united nations
educational, scientific
and cultural
organization

international atomic
energy agency

the
abdus salam
international centre for theoretical physics

ICTP 40th Anniversary

SCHOOL ON SYNCHROTRON RADIATION AND APPLICATIONS
In memory of J.C. Fuggle & L. Fonda

19 April - 21 May 2004

Miramare - Trieste, Italy

1561/16

Basic Concepts of X-ray Photoelectron Spectroscopy

C.S. Fadley

strada costiera, 11 - 34014 trieste italy - tel. +39 040 2240111 fax +39 040 224163 - sci_info@ictp.trieste.it - www.ictp.trieste.it

From Electron Spectroscopy, Theory,
Techniques, and Applications,
C.R. Brundle and A.D. Baker, Eds.
(Pergamon Press, 1978)
Volume II, Chapter 1.

1

Basic Concepts of X-ray Photoelectron Spectroscopy

C. S. FADLEY*

Department of Chemistry, University of Hawaii, Honolulu, Hawaii 96822

* Alfred P. Sloan Foundation Research Fellow.

I. INTRODUCTION

X-ray photoelectron spectroscopy has by now become a widely-used technique for studying the properties of atoms, molecules, solids, and surfaces. The extent of development between the first experiments of this type by Robinson and Rawlinson in 1914[1] and the present state of the art is indeed great, with most of this growth occurring within the last 10–20 years under the stimulation of pioneering studies begun in the early 1950s,[2, 3] particularly those carried out at Uppsala University.[3] From the first observations that core photoelectron peak intensities could be used for quantitative analysis by Steinhardt and co-workers[2] and that core electron binding energies exhibited chemically-induced shifts by Siegbahn and co-workers,[3] the number of distinct physical and chemical effects noted has expanded considerably. Thus, together with numerous developments in interpretive theory, this expansion has provided a rich panoply of information that can be derived by analysing different aspects of an x-ray photoelectron spectrum. To be sure, a greater understanding of the theoretical models underlying these phenomena has not always led to results as directly interpretable in simple chemical or physical terms as was initially imagined, but the overall scope of information derivable is nonetheless large enough to be useful in a broad range of disciplines.

The number of publications involving x-ray photoelectron spectroscopy (which is commonly referred to by one of the two acronyms *XPS* or *ESCA* ≡ electron spectroscopy for chemical analysis) is thus by now quite large, and includes several prior reviews[3, 4 10] and conference proceedings,[11, 12] as well as other chapters in this series on specific problems or areas of application.[13, 14] Thus, no comprehensive review of the literature will be attempted here, but rather only a concise discussion of various basic experimental and theoretical concepts, together with selected examples exhibiting different effects. In certain more newly developed areas, or for subjects in which confusion seems to exist in the literature, a somewhat more detailed treatment will be made. The instrumentation and experimental data discussed will be primarily restricted to that involving exciting radiation produced in a standard type of x-ray tube, thus providing an operational definition of XPS. Thus, photon energies of $\gtrsim 100$ eV will be considered, with principal emphasis on the most common 1·2–1·5 keV range. The more recently initiated photoemission studies utilizing synchrotron radiation[15] will thus not be included. The theoretical models discussed may, on the other hand, often apply directly to photoelectron emission experiments performed at lower photon energies as, for example, in conventional ultraviolet photoelectron spectroscopy (UPS) for which $h\nu$ is typically in the 5–40 eV range or in synchrotron studies. Alternatively, the models utilized in XPS may represent some particular

limit that cannot be used at lower energies. Thus, at several points, comparisons between low-energy- and high-energy-photoemission experiments will be made.

The fundamental experiment in photoelectron spectroscopy involves exposing the specimen to be studied to a flux of nearly monoenergetic radiation with mean energy $h\nu$, and then observing the resultant emission of photoelectrons, whose kinetic energies will be described most simply by the photoelectric equation:

$$h\nu = E_b^V(k) + E_{kin} \tag{1}$$

in which $E_b^V(k)$ is the binding energy or ionization potential of the kth level as referred to the vacuum level and E_{kin} is the photoelectron kinetic energy. (A more exact definition of binding energy, including a discussion of reference levels, is presented in Section II.B.3.) In general, both Auger electrons and secondary electrons (usually resulting from inelastic scattering processes) will also be emitted from the specimen, but it is generally possible to distinguish these electrons from true photoelectrons by methods to be discussed later in this section. There are three fundamental properties characterizing each emitted photoelectron: its kinetic energy, its direction of emission with respect to the specimen and the exciting radiation, and, for certain rather specialized experimental situations, the orientation of its spin. These three properties thus give rise to three basic types of measurements that are possible on the emitted electron flux.

(1) *The number distribution of photoelectrons with kinetic energy.* This measurement produces an electron spectrum or energy distribution curve (EDC) and, of course, requires some sort of electron energy analyser or spectrometer, of which several types are currently being utilized. In the dispersive spectrometers most commonly used in XPS, electron spectra are usually measured at fixed angles of electron emission (or over a small range of emission angles) relative to both the photon source and the specimen.

(2) *The distribution of photoelectron intensity with angle of emission.* Such angular-resolved measurements can be made relative to the photon propagation direction or to axes fixed with respect to the specimen. Generally, these measurements require kinetic energy distribution determinations at each of several angles of emission.

(3) *The spin polarization or spin distribution of the photoelectron intensity.* These measurements require a specimen that has somehow been magnetically polarized, usually by an external field, so that more photoelectrons may be emitted with one of the two possible spin orientations than with the other. Then the relative numbers of spin-up and spin-down photoelectrons are measured.[16] Such spin polarization measurements have so far only been

made with ultraviolet radiation for excitation, and they will not be discussed further here.

The additional time and experimental complexity required for angular distribution or spin polarization measurements have resulted in the fact that most XPS studies up to the present time have involved only kinetic energy distributions with a fixed geometry of the photon source, specimen, and spectrometer. However, measurements of both types (2) and (3) seem fruitful from several points of view, and angular-resolved XPS studies in particular have grown in importance in recent years.[17]

As an illustration of certain typical features observed in fixed-angle XPS spectra, Fig. 1 shows data obtained from an aluminum specimen exposed to monochromatized x-rays of 1487 eV energy. In Fig. 1(a), a broad-scan spectrum of 1000 eV width is displayed, and various prominent photoelectron peaks are labelled according to their level of origin from O1*s* to valence. The oxygen KLL Auger structure is also partially visible at the low-kinetic-energy end of the spectrum. The oxygen peaks arise from oxygen atoms present in a surface oxide layer; the C1*s* peak is due to an outermost surface layer of contaminants containing carbon. As is usually the case, the photoelectron peaks are considerably narrower and simpler in structure than the Auger peaks. Each electron peak exhibits to one degree or another an approximately constant background on its low-kinetic-energy side that is due to inelastic scattering; that is, electrons arising via the primary photoemission or Auger process that produces the sharp "no-loss" peak have been inelastically scattered in escaping from the specimen so as to appear in an "inelastic tail" or energy-loss spectrum.[18] Depending upon the types of excitation possible within the specimen, the inelastic tails may exhibit pronounced structure also, as is evident in the multiple peaks formed below the Al2*s* and Al2*p* no-loss features (which are due to the excitation of collective valence electron oscillations or plasmons[19] in aluminium metal), as well as the single broad peak in the O1*s* inelastic tail (which is due to one-electron excitations from the occupied to the unoccupied valence levels of aluminum oxide). The inelastic tail below C1*s* is considerably weaker due to the relatively thin layer of carbon-containing species present (approximately two atomic layers); thus, for this sample, C1*s* photoelectrons could escape with a relatively low probability of being inelastically scattered.

In Fig. 1(b), an expansion of the low-kinetic-energy region of the same aluminum spectrum is shown, and several other features are more clearly discernible. The plasmon loss structure is well resolved, and peaks associated with the excitation of up to four plasmons are seen. A magnified view of the rather low-intensity valence photoelectron region also shows complex spectral structure associated primarily with the overlapping metal- and oxide-valence levels. In general, XPS valence photoelectron intensities are approximately

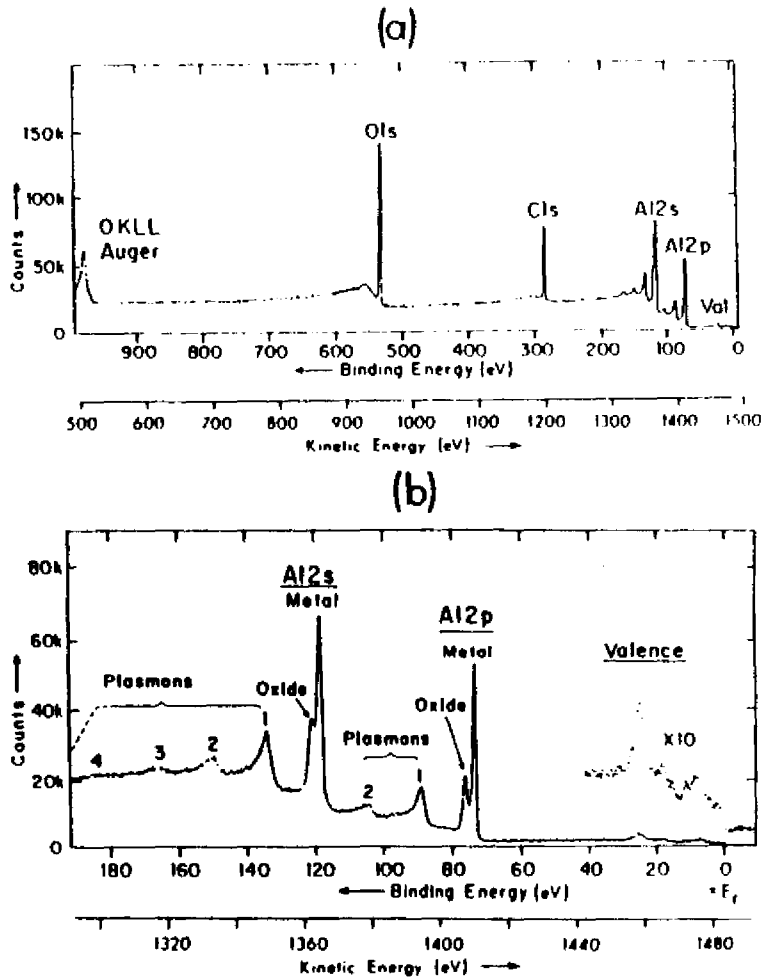

Fig. 1. Typical XPS spectra obtained from an oxidized aluminium specimen with a carbonaceous contaminant overlayer. Monochromatized AlKα radiation was used for excitation. (a) Overall spectrum with all major no-loss features labelled. (b) Expanded-scale spectrum of the Al2*s*, Al2*p*, and valence regions. Chemically-shifted oxide- and metal-core peaks are indicated, as well as inelastic loss peaks due to bulk plasmon creation.

an order of magnitude lower than those of the most intense core levels in a given specimen, but they are nonetheless high enough to be accurately measured and studied by using longer data acquisition times to improve statistics. An additional and chemically very significant feature in Fig. 1(b) is the splitting of the Al2*s* and Al2*p* photoelectron peaks into two components,

one associated with oxide and one associated with metal. This splitting or chemical shift is caused by the change in the aluminum chemical environment between oxide and metal.

In analysing XPS spectra, it is important to be able to distinguish as well as possible intensity resulting from Auger processes and inelastic scattering events. An Auger peak can be identified by: (1) comparing the observed peak energy with other experimental or theoretical Auger energies expected to be associated with the atom or atoms present, and (2) changing the photon energy by some amount $\Delta(h\nu)$ and then noting whether the peak shifts in kinetic energy by $\Delta(h\nu)$ according to Eq. (1) (and thus is a photoelectron peak) or remains fixed in kinetic energy (and thus has an Auger origin). Inelastic loss structure is often not as easily discernible in complex photoelectron spectra as for the examples shown in Fig. 1, but can be identified by: (1) looking for nearly identical features at kinetic energies below different no-loss peaks, as all high-energy electrons will be capable of the same excitations in inelastic scattering (although perhaps with probabilities that show a weak dependency on kinetic energy), and (2) comparing observed structure with independently-determined energy-loss spectra for the specimen material.[18]

A further very important point in connection with XPS studies of solid specimens is that the probability of inelastic scattering during escape from the sample is high enough that the mean depth of emission of no-loss electrons may be as small as a few atomic layers, and is never much larger than approximately 10 atomic layers.[20, 21] Thus, any analysis based on these no-loss peaks is inherently providing information about a very thin layer near the specimen surface, and this is, for example, the reason why O1*s* and C1*s* peaks due to thin surface overlayers are readily apparent in Fig. 1. This surface sensitivity of XPS (or any form of electron spectroscopy) can be exploited for studying various aspects of surface physics and chemistry,[22] but, on the other hand, must also be viewed as a potential source of error in trying to derive the true bulk properties of a given specimen.

In the following sections, various aspects of x-ray photoelectron spectroscopy are treated in more detail. In Section II, the instrumentation and experimental procedures required are reviewed. In Section III, the theoretical description of the photoemission process is discussed in detail so as to provide an accurate background for the consideration of various specific effects or areas of application; the use of XPS for the study of valence levels in molecules and solids is also considered. Section IV discusses chemical shifts of core-electron binding energies and various models used for interpreting them. Several effects primarily related to complexities in the final state of photoemission (namely relaxation phenomena, multiplet splittings, various many-electron interactions, and vibrational broadenings) are considered in Section V. In Section VI, various aspects of angular distribution measurements on

solids are considered. Finally, Section VII summarizes the present state of the technique and points out certain likely areas for future development.

II. EXPERIMENTAL CONSIDERATIONS

The basic components necessary for performing an XPS experiment consist of a radiation source for excitation, the specimen to be studied, an electron energy analyser, and some form of detection and control system. Each of these four distinct aspects of the experimental system is considered below. There are by now several commercial sources for complete XPS spectrometer systems[23-30] which represent various design approaches to each of these components.

A. Radiation Sources

The standard x-ray tube consists of a heated-filament cathode from which electrons are accelerated toward a suitable solid anode (usually water-cooled) over a potential of the order of 5-20 kV. Holes formed in the inner levels of the anode atoms by electron bombardment are then radiatively filled by transitions from higher-lying levels, with the resultant emission of x-rays. A thin, x-ray-transmitting window separates the excitation region from the specimen in most tubes. In general, more than one relatively sharp x-ray line will be emitted by any anode material, and the energy widths associated with various lines can also vary considerably from line to line or from element to element.[31] An additional source of radiation from such a tube is a continuous background of bremsstrahlung.[31] The choice of an anode material and operating conditions is thus made so as to achieve the closest possible approximation to a single, intense, monochromatic x-ray line. Various design geometries for such x-ray tubes are discussed in the literature,[3, 4, 31-36] with one obvious choice being whether to hold the anode or cathode at ground potential.

The anode materials most commonly utilized in XPS studies are Mg and Al, and, to a much lesser degree, Na and Si. Each of the members of this sequential series of second-row atoms gives rise to an x-ray spectrum that is dominated by a very intense, unresolved, $K\alpha_1$ $K\alpha_2$ doublet resulting from transitions of the type $2p_{\frac{3}{2}} \rightarrow 1s$ and $2p_{\frac{1}{2}} \rightarrow 1s$, respectively. The first demonstrations that such low-Z anodes could be utilized in XPS studies were by Henke.[32] These were followed approximately five years later by higher resolution applications by Siegbahn and co-workers.[3] The mean energies of the x-rays produced in such sources are: $NaK\alpha_{1,2}$ 1041·0 eV,[35] $MgK\alpha_{1,2}$ — 1253·6 eV,[37] $AlK\alpha_{1,2}$ 1486·6 eV[38] and $SiK\alpha_{1,2}$ 1739·5 eV.[39] At these x-ray energies, aluminium or beryllium windows of 10-30 μm thickness are sufficiently transmitting for use in separating the tube and specimen region. Additional x-ray lines are also produced in such tubes, as indicated in Fig. 2

for a magnesium anode[37] (note the logarithmic scale). These consist of satellites arising from $2p \rightarrow 1s$ transitions in atoms that are doubly-ionized (KL in Fig. 2), triply-ionized (KL^2), etc., and are denoted variously as Kα′, $K\alpha_3$, $K\alpha_4$, ..., $K\alpha_{14}$. $K\alpha_3$ and $K\alpha_4$ are by far the most intense, and, in Mg and Al, they occur at about 10 eV above the $K\alpha_{1,2}$ peak and with intensities of approximately 8% and 4% of $K\alpha_{1,2}$, respectively. Photoelectron spectra obtained with non-monochromatized sources of this type thus always exhibit a characteristic double peak at kinetic energies ~10 eV above the strong

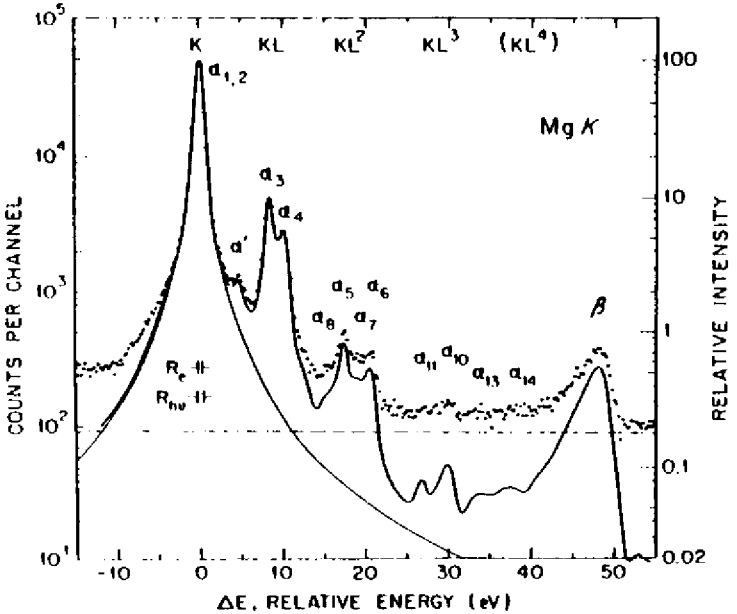

Fig. 2. The K x-ray emission spectrum of Mg metal as emitted by a non-monochromatized x-ray source. The peaks indicated $\alpha_{1,2}$, ..., β correspond to various transitions into the K = 1s subshell. The dashed line is an average background and the solid line is the net spectrum. Note the logarithmic intensity scale. The notation K corresponds to a single initial 1s hole, KL to initial holes in both 1s and 2s or 2p, KL^2 to a single initial hole in 1s and two initial holes in 2s, 2p, etc. (From Krause and Ferreira, ref. 37.)

$K\alpha_{1,2}$ peaks. The Kα′, $K\alpha_5$, ..., $K\alpha_{14}$ satellites are $\lesssim 1\%$ of $K\alpha_{1,2}$ in magnitude, and so, for most applications, can be neglected. An additional band of Kβ x-rays arises at energies approximately 45–50 eV above $K\alpha_{1,2}$ and is the result of valence $\rightarrow 1s$ transitions; the Kβ intensity is approximately 1% of $K\alpha_{1,2}$ for Mg and Al.[37] Thus, to a first approximation, the x-ray spectrum consists only of the very intense $K\alpha_{1,2}$ x-ray and most work has been based solely on an analysis of $K\alpha_{1,2}$-produced photoelectron peaks. However, in any study involving weak photoelectron peaks, or peaks generated by $K\alpha_{1,2}$ which overlap with satellite-generated peaks due to other

electronic levels, the non-monochromatic character of the x-ray source must be taken into account. For such non-monochromatized x-ray sources, the primary limiter of instrumental resolution is thus the natural linewidth of the $K\alpha_{1,2}$ line. As judged by the full width at half maximum intensity (FWHM), this resolution limit is approximately 0·4 eV for $NaK\alpha_{1,2}$,[35] 0·7 eV for $MgK\alpha_{1,2}$,[35] 0·8 eV for $AlK\alpha_{1,2}$,[38] and 1·0–1·2 eV for $SiK\alpha_{1,2}$.[39] This width decreases with decreasing atomic number for two reasons: the $2p_{\frac{1}{2}}$–$2p_{\frac{3}{2}}$ spin-orbit splitting decreases and the 1s hole lifetime increases. Materials of lower atomic number are thus favoured for width, but Mg and Al are generally utilized because of their lower chemical reactivity and vapor pressure in comparison to Na, and thus their easier fabrication and use as anodes. Although neon is expected to yield a $K\alpha_{1,2}$ line at 848·6 eV of only ~0·2–0·3 eV width, no attempts at constructing such a source for use in XPS have as yet been successful. The use of $K\alpha_{1,2}$ lines from elements below neon in atomic number is generally not possible because the valence 2p levels involved are broadened by bonding effects, introducing a corresponding broadening in the x-ray line. However, the $K\alpha_{1,2}$ x-rays of F in highly ionic compounds have been used recently in XPS.[40]

The monochromatization of such $K\alpha_{1,2}$ x-rays by Bragg reflection from a suitable single crystal has also been utilized to achieve narrower excitation sources, as well as to eliminate satellite lines and bremsstrahlung radiation.[3, 23, 25, 41, 42] Although the intensity loss in such reflections is considerable, photoelectron peaks as narrow as 0·4 eV have been observed with monochromatized AlKα excitation;[25, 41, 42] this width is to be compared to the $\gtrsim$0·9 eV typically found without monochromatization. To compensate for the loss in intensity due to monochromatization, various procedures have been utilized, including the use of very high-intensity x-ray tubes involving rotating anodes,[41] monochromator systems with more than one crystal,[25, 41] multichannel detection systems,[25, 41] and dispersion-compensating x-ray- and electron-optics.[3, 25] In dispersion compensation, all photon energies within the $K\alpha_{1,2}$ linewidth are spatially dispersed by Bragg reflection and utilized for photoelectron excitation, but their line-broadening influence is nullified by the action of the dispersive electron energy analyzer; the commercial Hewlett Packard system based upon this mode of operation yields optimum photoelectron peak widths with $AlK\alpha_{1,2}$ of ~0·5 eV FWHM.[25]

An additional type of ultra-soft x-ray transition that has been utilized successfully in XPS studies is the Mζ transition ($4p_{\frac{1}{2}} \rightarrow 3d_{\frac{3}{2}}$) in the sequential elements Y to Mo. The use of such x-rays in XPS was first suggested by Krause,[34] who pointed out that they yield sufficiently intense and monochromatic sources in the very interesting energy range of $100 \lesssim h\nu \lesssim 200$ eV, even though various satellite x-rays are present. The most narrow and thus

most used lines of this type are those for Y ($h\nu = 132{\cdot}3$ eV, FWHM $= 0{\cdot}5$ eV) and Zr ($h\nu = 151{\cdot}4$ eV, FWHM $= 0{\cdot}8$ eV), and they have been successfully applied to studies of both valence levels and outer core levels.[34-36] The ultrasoft character of these x-rays and their resultant decreased ability to penetrate through matter, as well as the significant sensitivity of their linewidths to surface chemical alterations of the anode surface, lead to several special features of tube design. Thin polymeric windows must be used. Relatively high excitation voltages as compared to $h\nu$ of $\sim$4–6 kV are also beneficial to maximize the intensity originating in the metallic anode interior (as distinct from its oxidized exterior).[35] And, in the highest resolution designs, a continuous deposition of fresh anode material is provided during operation.[34, 36]

A final rather new development in x-ray sources by Hovland[43] that deserves mention here leads to what has been termed *scanning* XPS. A thin layer of specimen material is directly deposited on one side of a thin Al foil ($\sim$6 μm thick). A high-resolution scanning electron beam is directed at the other side of this foil, so that, at any given time, AlKα x-rays are produced over only a very small spot with dimensions comparable to the beam diameter. These x-rays readily pass through the thin foil and specimen, exciting photoelectrons from a corresponding spot near the specimen surface. Lateral spatial resolutions of as low as 20 μm have so far been achieved, and a number of potential applications for such scanning XPS measurements exist.[43] The only significant limitation is that it must be possible to prepare sufficiently thin specimens ($\sim$1000–10,000 Å) that x-ray attenuation in penetrating to the surface is not appreciable.

The x-ray sources discussed up to this point thus permit high-resolution measurements to be carried out in the two approximate photon-energy ranges 100–200 eV and 1000–2000 eV, with a relatively little explored region from $\sim$200–1000 eV separating them. Another source of radiation in the photon energy region from 100 to 2000 eV of principal interest here is the so-called synchrotron radiation that is emitted in copious quantities by centripetally-accelerated electrons moving with highly relativistic velocities.[15, 44] This continuous spectrum of radiation is sufficiently intense to permit selection of a narrow range on the order of tenths of eV or lower with a suitable monochromator (usually a grating) while still maintaining fluxes adequate for photoemission studies. A number of excellent photoemission studies have by now been performed using such radiation,[15] although these have so far been restricted to photon energies between approximately 10 and 350 eV, principally because of the difficulty of achieving adequate monochromatization without severe intensity loss for soft x-rays of $\gtrsim$350 eV. Such radiation has the advantages of being both continuously variable in energy, as well as linearly polarized to a high degree;[44] thus, the exploration of phenomena dependent upon photon energy and/or polarization are much more easily studied than with more standard ultraviolet or soft x-ray sources. By contrast the soft x-ray tubes discussed previously emit radiation that is randomly polarized to a very good approximation.

B. Specimen Preparation

1. Introduction. X-ray photoelectron spectra have been obtained from specimens present as gases, solids, or liquids. The preparation and handling of any specimen requires considering two important factors: (1) In order to avoid excessive inelastic scattering during photoelectron traversal through the energy analyzer, pressures between the specimen and the detector must be maintained at $\lesssim 10^{-4}$ torr. This limit is easily estimated by considering a typical path length during analysis of 100 cm, and requiring that the total number of atoms/molecules encountered along this path be no greater than the analogous number encountered along the mean no-loss distance of emission from a typical solid specimen of $\sim$20 Å. (2) As the emission of photoelectrons, Auger electrons, and secondary electrons from any specimen constitutes a net loss of negative charge, it is also necessary to minimize or in some other way correct for the possible occurrence of a significant positive potential build-up in the emitting region. One way in which this is accomplished to some degree in any system is by the flux of similar electrons emitted *toward* the specimen by various portions of the specimen chamber and holder which are also in general exposed to exciting x-rays and/or electrons, although this can in fact lead to the opposite problem: a negative potential build-up.[45] The charging potential V_c produced by any net imbalance between charge input and output may vary throughout the specimen volume and in effect cause a range of energy level shifts from the values corresponding to the limiting situation in which no charging occurs. Thus, if $\mathbf{r}$ is the spatial coordinate of the emission point within the specimen, and $E_b^V(k)^0$ and E_{kin}^0 are the binding energy and kinetic energy expected for emission from level k in the absence of charging, the photoelectric equation [Eq. (1)] can be rewritten as

$$\begin{aligned} h\nu &= E_b^V(k, \mathbf{r}) + E_{kin}(\mathbf{r}) \\ &= E_b^V(k)^0 + E_{kin}(\mathbf{r}) + V_c(\mathbf{r}) \end{aligned} \tag{2}$$

Thus, if $V_c(\mathbf{r})$ is significant with respect to the typical instrumental resolution of $\sim$0·1 eV (which it indeed can be in certain cases[4, 45]), the measured binding energies $E_b^V(k, \mathbf{r})$ will in general be different from $E_b^V(k)^0$, and peak broadening also may occur. To minimize or correct for such effects, studies of peak position versus x-ray flux can be made,[45, 46] and a variable external source of electrons can be provided.[25] For gaseous specimens, the pressure can also be varied.[4] For solids, it is also customary to connect the specimen electrically to the specimen chamber as well as possible. Also, the presence

of a certain reference atom (for example, gold or carbon) on the surface of the specimen can be used to correct for charging,[47] although this procedure is often not completely unambiguous. A method recently developed by Grunthaner[18] involves floating a solid specimen at a variable negative potential and noting that potential at which an external source of monoenergetic electrons just begins to reach the surface; although not widely used as yet, this method seems to provide a very direct way of measuring surface potential distributions and thus correcting for them.

2. *Gaseous Specimens.* The basic requirement for gas-phase studies is a chamber to contain the gas with an x-ray-transparent window separating it from the x-ray source and a small opening or slit to permit photoelectron exit into the energy analyzer.[4, 33, 47, 49, 51] Typical gas pressures required in the chamber are from 10^{-2} to 1 torr, and therefore some form of differential pumping is generally necessary between the exit slit and the analyzer in order to minimize gas-phase inelastic scattering effects,[4] as discussed previously. Typical specimen volumes are of the order of 1 cm^3. The first gas-phase XPS studies were performed by Krause and Carlson,[49] followed shortly thereafter by the more extended investigations of Siegbahn *et al.*[4] The gas in the chamber can be provided by a room-temperature gas-phase source, or can be the result of heating liquid-[4] or solid-[33] phase reservoirs. With such devices, metals and other vaporizable solids can be studied by photoelectron spectroscopy in the gas phase.[33, 50] In certain studies, rather significant changes in peak positions and relative intensities due to the combined effects of charging and kinetic energy-dependent inelastic scattering have been noted,[4] but, in general, these are relatively small, especially at lower pressures.

For gas-phase spectra, the vacuum level is the naturally-occurring reference level, so that Eqs (1) and (2) are directly related to measurable quantities.

3. *Solid Specimens.* There are various methods of preparing solid specimens suitable for study by XPS. Typical specimen areas are ~ 1 cm^2 or smaller, and, because inelastic scattering effects limit the no-loss emission to a mean depth of only 10-80 Å below the surface (as discussed in more detail in Section III.E), this corresponds to an active specimen volume of only approximately 10^{-6} cm^3. Thus, total masses of only 1-10 μg are involved, and amounts of material on the order of 10^{-9} g can be detected under certain circumstances. Any change of the chemical composition in the first few atomic layers near the surface can thus also have a significant influence on results.

Machineable solids can simply be cut, cleaved, and/or polished into shapes suitable for mounting in the specimen position. For materials that can be prepared as fine powders at room temperature, specimens can also be prepared by pressing the powder into a uniform pellet (perhaps supported by an imbedded conducting-wire mesh) or by dusting the powder onto an adhesive backing such as that provided by double-sided tape (although this procedure has the rather undesirable characteristics of limiting temperature excursions and providing a steady source of surface-contaminating carbonaceous volatiles). In order to minimize atmospheric contamination or alteration of specimens, final preparation in an inert-atmosphere glove box or bag, perhaps attached to the specimen chamber, can be useful. Elements and certain compounds can also be heated *in situ* and vapor-deposited on a supporting substrate to form specimens. Alternatively, dissolved materials can be deposited from solution on a substrate, either by evaporating off the solvent or by selectively electroplating out various components.[52] Materials that normally exist as liquids or gases can also be condensed onto suitably cooled substrates for study in the solid state.[4] A broad range of specimen temperatures has by now been investigated, ranging from near that of liquid helium (4 K)[53] to several thousand degrees Kelvin.[54]

The extreme surface sensitivity of XPS also leads in many applications to the requirement that the specimen region be held at pressures of $\lesssim 10^{-9}$ torr in order to permit adequate control of surface composition. For example, for O_2 at 10^{-9} torr and 25 °C, the gas-phase collision rate with a surface will be such that, if each molecule striking the surface remains there (corresponding to a sticking coefficient of 1.0), a full atomic layer will be deposited in approximately 50 min.[55] This minimum monolayer coverage time varies inversely with pressure, so that pressures of the order of 10^{-10} torr are necessary to insure the maintenance of a highly reactive surface in a clean state over the period of time of several hours usually required for a series of XPS measurements. In preparing such surfaces, *in situ* cleaning by vapor deposition, cleaving, scraping, or inert-gas ion bombardment is thus often used.[55]

For the case of solid specimens, an electrical connection is made to the spectrometer in an attempt to minimize charging effects and maintain a well-defined and fixed potential during photoemission. For the simplest possible case of a metallic specimen in a metallic spectrometer, the energy levels and kinetic energies which result are as shown in Fig. 3. Thermodynamic equilibrium between specimen and spectrometer requires that their electron chemical potentials or Fermi levels be equal as shown. In a metal at absolute zero, the Fermi level E_F has the interpretation of being the highest occupied level, as indicated in the figure; this interpretation of E_F is also very nearly true for metals at normal experimental temperatures. For semiconductors and insulators, however, it is not so simple to locate the Fermi level, which lies somewhere between the filled valence bands and the empty conduction bands. The work function ϕ_s for a solid is defined to be the energy separation between the vacuum level and the Fermi level. When connected as shown in Fig. 3, the respective vacuum levels for specimen and spectrometer need not be equal, however, so that in passing from the surface of the specimen into the spectrometer, an electron will feel an accelerating or retarding potential

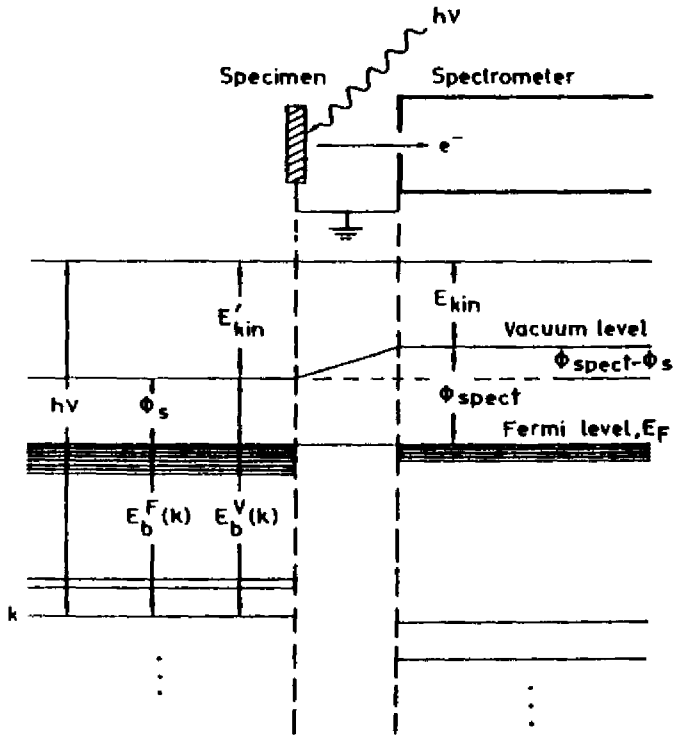

Fig. 3. Energy level diagram for a metallic specimen in electrical equilibrium with an electron spectrometer. The closely spaced levels near the Fermi level E_F represent the filled portions of the valence bands in specimen and spectrometer. The deeper levels are core levels. An analogous diagram also applies to semi-conducting or insulating specimens, with the only difference being that E_F lies somewhere between the filled valence bands and the empty conduction bands above.

equal to $\phi_s - \phi_{spect}$, where ϕ_s is the specimen work function and ϕ_{spect} is the spectrometer work function. Thus, an initial kinetic energy E_{kin}' at the surface of the specimen becomes E_{kin} inside the spectrometer, and

$$E_{kin} = E_{kin}' + \phi_s - \phi_{spect} \tag{3}$$

From Fig. 3 it is thus clear that binding energies in a metallic solid can be measured quite easily relative to the identical Fermi levels of specimen and spectrometer. The pertinent equation is

$$h\nu = E_b^F(k) + E_{kin} + \phi_{spect} \tag{4}$$

where the superscript F indicates a Fermi level reference. Provided that it is also possible to determine the specimen work function ϕ_s from some other

measurement, vacuum-referenced binding energies can then be obtained from

$$E_b^V(k) = E_b^F(k) + \phi_s \tag{5}$$

In fact, photoelectron spectra can be used to derive vacuum-referenced binding energies by measuring the position of the zero-kinetic-energy cut-off of the usually very intense secondary electron peak. Such a cut-off is shown in Fig. 4 in XPS data obtained for metallic Au by Baer.[56] This procedure for determining work functions has been used extensively in UPS studies,[57] but only in a more limited way in XPS[58, 58] due to the greater range of

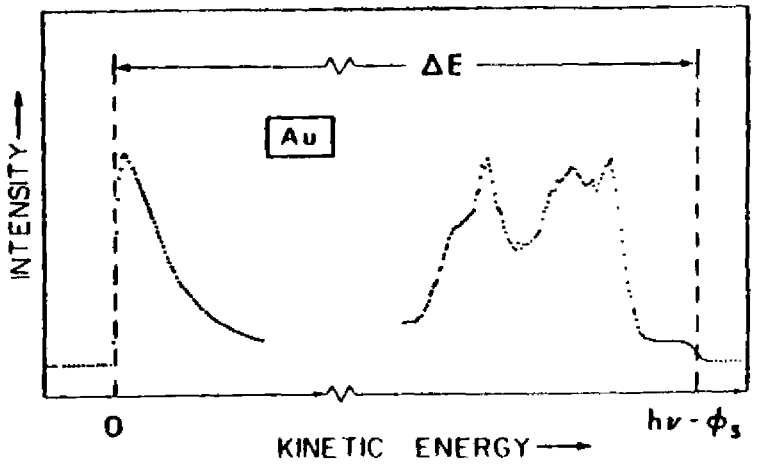

Fig. 4. Full XPS spectral scan for a polycrystalline Au specimen, showing both the cut-off of the secondary electron peak at zero kinetic energy and the high-energy cut-off for emission from levels at the metal Fermi level. The measurable distance ΔE thus equals $h\nu - \phi_s$, provided that suitable specimen biasing has been utilized. For this case, $h\nu$ was 1253·6 eV and ϕ_s was 5·1 eV. (From Baer, ref. 56.)

energies involved. In the simplest situation, both specimen and spectrometer are metallic and the energy diagram of Fig. 3 applies. All electrons emitted from the specimen are thus accelerated or decelerated by the same work function difference or contact potential $\phi_s - \phi_{spect}$ before analysis. With no voltage bias between specimen and spectrometer, the zero-energy cut-off corresponds to electrons propagating in final states exactly at the *spectrometer* vacuum level. For the implicit decelerating sign of $\phi_s - \phi_{spect}$ shown in Fig. 3, electrons propagating in final states at the *specimen* vacuum level are thus not observed. However, if the specimen is biased negatively with respect to the spectrometer by an amount greater than $\phi_s - \phi_{spect}$, then the low-energy cut-off does represent electrons at the specimen vacuum level or what can be defined as the true zero of kinetic energy. For the opposite accelerating sign of

$\phi_s - \phi_{spect}$, the true zero is observable and negative biasing is necessary only to insure that the cut-off is easily distinguishable against other sources of low-energy electrons.[56, 58] The low-energy cut-off thus establishes the zero of kinetic energy, and a distance $h\nu$ above this on the measured spectral scale corresponds to the point at which excitation from states at the specimen vacuum level would occur. On the same scale, the high-kinetic-energy cut-off observable for metal specimens (also shown in Fig. 4) is caused by excitation from occupied states at the Fermi level, and the difference between these two positions is thus the specimen work function. That is, if the measured difference in kinetic energy between the two cut-offs is denoted by ΔE, then

$$\phi_s = h\nu - \Delta E \tag{6}$$

In more complex situations where semiconducting or insulating specimens are involved, initial states at E_F are not occupied so as to yield the same type of high-energy cut-off, although the low-energy cut-off can still be determined. The location of E_F in spectra can in this case be determined by using a reference metal specimen under the same biasing conditions, and assuming that electronic equilibrium is fully established between specimen, reference, and spectrometer. Possible charging effects make the latter assumption uncertain in many cases, however.

Whether it is determined from photoemission measurements or not, in general some additional information concerning ϕ_s is necessary to determine $E_b^V(k)$ for a solid specimen. Inasmuch as ϕ_s is also very sensitive to changes in surface composition, it is thus often Eq. (4) that is used in analyzing data for metals and other solid specimens. From this discussion, it is clear that Fermi-referenced binding energies are operationally very convenient for solid specimens, although they may not always be the most directly comparable to the results of theoretical calculations, in which the vacuum level often emerges as the natural reference.

4. *Liquid Specimens.* The requirement that pressures in the analyzer region be maintained at reasonably low levels of $\lesssim 10^{-4}$ torr means that measurements on common liquids with relatively high vapor pressures can be performed only with difficulty. However, Siegbahn and co-workers[41, 59] have developed techniques for carrying out such studies; these involve a continuously-replenished liquid source in the form of either a free jet or a thin film carried on a translating wire, together with a high-speed differential pumping system between specimen chamber and analyzer. With such an apparatus, it has been possible to study relatively non-volatile liquids such as formamide ($HOCNH_2$), as well as solutions of the ionic solid KI dissolved in formamide. Certain liquid metals and other very low vapor pressure materials can, on the other hand, be studied with relatively little special equipment.[60]

C. *Electron Energy Analysis*

1. *Brief Overview.* The various specific types of energy analyzers utilized in electron spectroscopy are discussed in detail in the literature,[10, 61, 62] as well as in a special chapter in this series.[63] Thus, only certain salient features relevant to x-ray photoelectron studies will be reviewed here. In general, there are several criteria that an analyzer should satisfy: (1) A resolution capability of $\Delta E_{kin}/E_{kin} \approx 0.01\%$. This corresponds to 0.1 eV for 1000 eV electrons. Most XPS spectrometers presently operate in the 0.01–0.10% range. (2) The highest possible efficiency (sensitivity, intensity). That is, the highest possible fraction of electrons leaving the sample should be energy-analyzed and detected at the same time. (3) Unrestricted physical access to the sample and detector regions. This permits a wide variety of excitation sources, specimen geometries, and detector systems to be used.

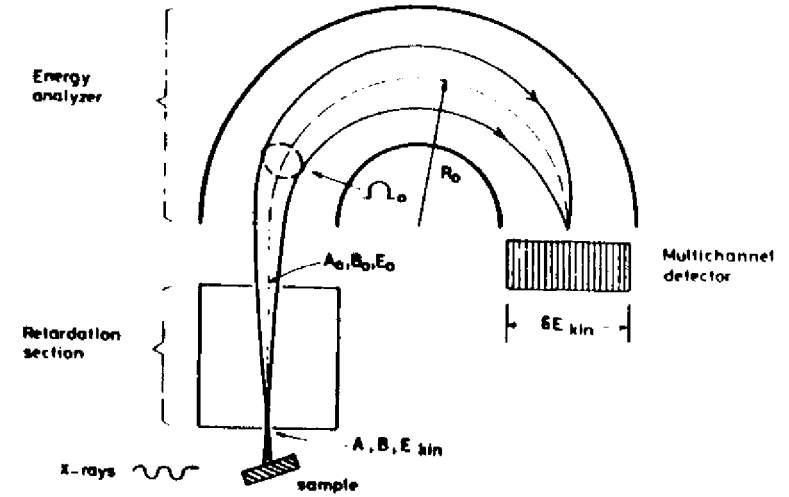

Fig. 5. Schematic illustration of an XPS spectrometer system indicating the primary components of radiation source, sample, electron energy analyser, and detector. For the specific example shown here, the energy analysis is accomplished by a pre-retardation section followed by a hemispherical electrostatic analyzer. A multichannel detector is also shown for generality.

(4) Ultra-high-vacuum capability for work on solid samples if surface composition is to be precisely controlled. (5) Ease of construction. One design philosophy often used for increasing the ease of construction is to insert a retardation section before the analyzer as shown schematically in Fig. 5, so that the energy of a given electron can be reduced from its initial value of E_{kin} to the final value at which it is analyzed of E_0. For a given *absolute* resolution of ΔE_{kin}, the *relative* resolution required from the analyzer is thus

reduced from $\Delta E_{kin}/E_{kin}$ to $\Delta E_{kin}/E_0$, thereby permitting looser tolerances on many mechanical and electrical components. The net effects of such retardations on intensity may or may not be deleterious, however, and are discussed in more detail in the next section. (6) Relative insensitivity to external environment, particularly as regards the shielding of extraneous magnetic fields. The vast majority of spectrometers currently in use are based on interaction with electrostatic fields and for these, μ-metal shielding is generally used to exclude extraneous magnetic fields. Only for the relatively few magnetic spectrometers in use are Helmholtz-coil systems required for magnetic field cancellation.[3, 4] Quantitative estimates of the degrees to which extraneous magnetic fields must be excluded for a given resolution have been calculated previously.[64] (7) If angular distribution studies are intended, well-defined, and perhaps also variable, angles of electron exit and x-ray incidence. This requirement generally acts counter to that for high efficiency, as it implies detecting only electrons emitted in a relatively small element of solid angle, thus reducing the total number that can be analyzed and detected.

With these constraints, there are several possible analyzer configurations,[61, 62] but the three that have been most used in XPS are all of the spatially dispersive type, and consist of the hemispherical electrostatic (schematically shown in cross-section in Fig. 5),[3, 61, 65] the cylindrical mirror electrostatic (CMA),[61, 66-68] and the double-focussing magnetic with a $1/\sqrt{r}$ field form.[3, 64, 69] In all of these analyzers, electrons are dispersed on the basis of kinetic energy along a radial or axial coordinate. For reasons of both ease of construction and magnetic shielding, the two electrostatic analyzers are much more common than the double-focussing magnetic, although a number of important early studies were performed on such instruments,[3, 33] and a fully-optimized spectrometer based upon the $1/\sqrt{r}$ field form is presently under construction.[64, 70] In addition to these dispersive analyzers, limited use has also been made in XPS of non-dispersive analyzers based upon the retarding grid principle.[71-73] Such analyzers are usually of relatively limited resolution ($\sim 1\%$), however, so that their use has been restricted to the obtaining of chemical composition information similar to that derived from Auger spectra. Such low-resolution Auger and XPS spectra can, in fact, be generated by using the spherical grids of a low-energy electron diffraction (LEED) system as a retarding grid analyzer. A further type of commercial analyzer developed specifically for XPS studies by the DuPont Corporation[24] is a hybrid with both dispersive and non-dispersive characteristics. Its first stage consists of an electrostatic deflection section that selects a band of energies in a dispersive mode; two subsequent retarding grid sections act as low-pass and high-pass filters with the net result that only a narrow band of energies is detected after the high-pass filter. A final type of XPS spectrometer with certain unique features is that formerly produced by the Hewlett Packard Company,[25] which makes use of dispersion-compensating x-ray- and electron-optics.[3, 74] In this system, an x-ray monochromator is matched to a retarding-lens/hemispherical-electrostatic-analyzer unit in such a way as to maximize intensity and minimize linewidths without the use of any slits in the x-ray optics; the detailed performance of this spectrometer has been analyzed recently.[74]

2. *Spectrometer Efficiency and Retardation.* The resolution and efficiency of any spectrometer are of critical importance. These properties are highly dependent upon one another, since for operation at lower resolution (higher $\Delta E_{kin}/E_{kin}$), a higher fraction of electrons can usually be energy-analyzed and detected. For operation at a given resolution, the overall efficiency E of a dispersive analyzer can be written as proportional to the following product[64]

$$E \propto BA\Omega \cdot \delta E_{kin} \tag{7a}$$

in which B is the brightness or intensity of the electron source for the energy analyzer in electrons per unit area *and* per unit solid angle, A is the area of the source, Ω is the solid angle over which electrons from the source are accepted into the energy analyzer and detected, and δE_{kin} is the range of electron energies or spectral width which can be analyzed at one time (as, for example, by a multi-channel detector). B, A, and Ω in general depend on E_{kin} for a given spectrometer. δE_{kin} will thus be proportional to N, the number of distinct energy channels simultaneously detected. If B and A vary over the area of the source, then a more correct statement of this efficiency involves an integration over the surface as

$$E \propto (\int B\Omega \cdot \mathrm{d}A) \cdot \delta E_{kin} \tag{7b}$$

The effective electron source as seen by the analyzer is often defined by an aperture in front of the photoemitting sample, and, depending upon the system, B, A, and Ω may refer to this aperture or to the true specimen surface. If a multichannel detector is utilized, δE_{kin} may in principle be as large as 10% of E_{kin},[25, 64] whereas the resolution ΔE_{kin} will be $\gtrsim 0{\cdot}01\%$ of E_{kin}. In this case, the detector would correspond to $\lesssim 1000$ channels. The notation used in this discussion is indicated in the schematic drawing of Fig. 5, where subscript zeros have been used on all quantities after a hypothetical retarding section. Such a retarding section may or may not be present, according to the specific system under consideration.

Helmer and Weichert[75] first pointed out that, for the general class of dispersive analyzers used in XPS, it is possible to retard before analysis, and, for a given absolute resolution ΔE_{kin}, to *gain* in overall efficiency in a system with single-channel detection (for which $\delta E_{kin} \approx \Delta E_{kin}$ and $N = 1$), and this result has proven useful in several specific spectrometer designs.[23, 25, 27, 28, 30]

Their analysis (which has also been extended to apply to systems with multichannel detection by Hagström and Fadley[6]) compares the operation of a given dispersive analyzer with and without retardation for a fixed resolution ΔE_{kin}, and with a primary electron source of fixed brightness B (cf. Fig. 5). It also requires that the source area A_0 and solid angle Ω_0 utilized at the analyzer entrance (and thus perhaps after the retardation section) be adjusted to the maximum values consistent with a resolution of ΔE_{kin} in either mode of operation *and* that the primary source (for example, a first entrance aperture) be capable of supplying electrons over sufficient area and solid angle to fill or illuminate both A_0 and Ω_0 with electrons. There are then two factors to be considered: (1) *The loss of brightness with retardation.* This loss of brightness has been derived for a few geometries involving a source and a *non-absorbing* retardation (or acceleration) section. If θ is defined to be the angle between the electron emission direction and a planar source surface, these geometries include a source emitting with a sin θ intensity distribution into an arbitrary point-to-point imaging lens system,[76] and a source with either a sin θ[77] or an isotropic[75] intensity distribution emitting into a uniform retarding field perpendicular to its surface. These derivations, which often (but not always) make use of the Abbe sine law[75, 76] or its paraxial-ray approximation the Langrange–Helmholtz relation,[3, 76] result in a simple brightness variation of the form:

$$B_0 = B\left(\frac{E_0}{E_{kin}}\right) \tag{8}$$

in which B_0 and E_0 are the brightness and kinetic energy after retardation. The cases for which this relationship has been shown to hold thus represent limits that are relatively easily achieved experimentally. Without retardation, the efficiency of a spectrometer conforming to this brightness law and possessing only a single channel of detection will be

$$E \propto BA\Omega \tag{9}$$

whereas with retardation it will be

$$E' \propto B_0 A_0 \Omega_0 \tag{10}$$

or, from Eq. (8),

$$E' \propto B\left(\frac{E_0}{E_{kin}}\right) A_0 \Omega_0 \tag{11}$$

(2) *The gain in efficiency associated with the increase of A_0 and Ω_0 relative to A and Ω permitted by the decrease in relative resolution from $(\Delta E_{kin}/E_{kin})$ to $(\Delta E_{kin}/E_0)$.* As a specific example, consider the hemispherical electrostatic analyzer, which is shown in Fig. 5. Its resolution is controlled by the radial source width s, the axial (out-of-plane) source height h, the radial detector width d, the radial angle of emission α_r, the axial (out-of-plane) angle of emission α_z, and the optic circle radius R_0, according to [3, 61]

$$\frac{\Delta E_{kin}}{E_{kin}} = \frac{s}{4R_0} + 0{\cdot}125\left(\frac{h}{R_0}\right)^2 + \frac{d}{4R_0} + 0{\cdot}61\alpha_r^2 + \text{smaller terms in } \alpha_r,\ \alpha_z^3, \text{ etc.} \tag{12}$$

The system is thus first-order focussing in h and α_r, and second-order focussing in α_z. Also, $sh = A$ (or A_0 with retardation) and $\alpha_z\alpha_r \propto \Omega$ (or Ω_0 with retardation). Optimizing the selection of each of the four parameters s, h, d and α_r by the reasonable procedure of requiring an approximately equal contribution from each term to $\Delta E_{kin}/E_{kin}$[69] thus means that

$$s \propto \frac{\Delta E_{kin}}{E_{kin}}, \quad h \propto \left(\frac{\Delta E_{kin}}{E_{kin}}\right)^{\frac{1}{2}}, \quad \alpha_r \propto \left(\frac{\Delta E_{kin}}{E_{kin}}\right)^{\frac{1}{2}} \tag{13}$$

and α_z can conservatively be assumed to be held constant. Thus, without retardation,

$$A \propto \left(\frac{\Delta E_{kin}}{E_{kin}}\right)^{1}, \quad \Omega \propto \left(\frac{\Delta E_{kin}}{E_{kin}}\right)^{\frac{1}{2}} \tag{14}$$

whereas with retardation

$$A_0 \propto \left(\frac{\Delta E_{kin}}{E_0}\right)^{1}, \quad \Omega_0 \propto \left(\frac{\Delta E_{kin}}{E_0}\right)^{\frac{1}{2}} \tag{15}$$

The ratio of efficiencies with and without retardation is then after cancellations

$$\frac{E'}{E} = \frac{E_{kin}}{E_0} \tag{16}$$

Thus, a tenfold retardation yields a tenfold loss in B, but a one hundredfold increase in the useable $A\Omega$ product, so that a net tenfold gain in efficiency results. Similar considerations apply to the other dispersive analyzers used in XPS,[75] provided that an appropriate retardation section is utilized. The application of such an analysis to a spectrometer in which a maximum degree of multichannel detection is incorporated is, by contrast, found to yield an approximately constant overall efficiency with retardation.[6]

D. Detection and Control

With very few exceptions, the detectors presently used in x-ray photoelectron spectroscopy are based on continuous-dynode electron mutipliers of the "channeltron" type.[62, 78, 79] These consist of fine-bore lead-doped glass tubes treated by hydrogen reduction at high temperature to leave the surface coated with a semiconducting material possessing a high secondary-electron emissive power.[62] Tube inner diameters vary from 1 mm down

to 10 μm. A high voltage of a few kV is applied between the ends of such a tube, and multiplications of 10^6–10^8 are achieved by repeated wall collisions as electrons travel down the inside of the tube. These multipliers are available in various configurations, often involving tube curvature to minimize ion-induced after-pulsing. Stacks of parallel tubes in the so-called "channel-plate" geometry are also available for use in multichannel detection schemes. Parallel-plate multipliers based upon the same principle have also been attempted.[80]

The efficiency gains concomitant with multichannel detection have led to the use of such a system in one commercial spectrometer,[25] in which the multiplied electron pulses from a channel plate are accelerated into a phosphorescent screen, behind which (and external to vacuum) is situated a vidicon camera for translating the optical signal into countable electronic pulses. Other forms of multichannel detection system based upon channel-plate/resistive strip combinations have also been used[81] to a limited degree, and solid-state image sensors of a different type appear to offer good possibilities for future applications of this nature.[82]

As the appropriate voltages or currents in the analyzer are swept so as to generate electron counts at different kinetic energies, there are various ways of storing and outputting the data. Most simply, a ratemeter can be directly coupled to a plotter or printer during a single continuous sweep. Generally, however, it is desirable to make repeated scans over a given spectral region to average out instrument drifts and certain types of noise; this results in the closest possible approximation to a spectrum with statistically-limited noise. Such repeated scanning requires some form of multiscalar memory, which is often expanded to involve on-line computer control.[33] The use of a more or less dedicated computer has additional advantages in that it can be used to control various functions of the spectrometer in a more automated way, as well as to carry out different types of data analysis such as background subtraction and curve fitting, and commercial systems usually offer this option.

E. Data Analysis

The aim of spectral analyses in XPS is to determine the locations, intensities, and, in certain cases, also the shapes of the various peaks observed, many of which are not clearly resolved from one another. Several complexities must be allowed for in doing this: (1) All peaks will exhibit inelastic tails toward low kinetic energy and these tails may in turn exhibit structure (see, for example, Fig. 1). As a rough approximation that is useful for many solid materials, a major portion of the inelastic tail can be assumed to have a linear or constant form, with extra features perhaps superimposed on it. Valence spectra from solids have been corrected for inelastic scattering by using a close-lying core level to derive the form of the inelastic tail,[33, 82] as well as by the more

approximate procedure of assuming an asymptotically-constant tail at low kinetic energy whose value at any energy is proportional to the integrated no-loss peak intensity at higher kinetic energies.[83] (2) All peaks ride on a background of secondary electrons from higher-kinetic-energy peaks. This background also can often be approximated as linear or constant. (3) The basic peak shapes observed in XPS are a convolution of several variable factors: the exciting x-ray lineshape, contributions from weaker x-rays such as satellites in non-monochromatized sources, the analyzer lineshape, possible non-uniform specimen charging, a Lorentzian hole-state lifetime contribution, Doppler broadening in gases,[4] and various final-state effects involving many-electron excitations[84] and vibrational excitations[41, 85] (as discussed further in Section V). Thus, no universal peak shape of, for example, Gaussian, Lorentzian, or Voigt-function form can be used, and most analyses have involved a somewhat trial-and-error fit for each specific problem. One rather general least-squares program for carrying out such fits permits choosing several basic peak shapes of Gaussian or Lorentzian form, to which are smoothly added an asymptotically-constant inelastic tail of variable height.[33] The effects of satellite x-rays can also automatically be included in the basic peak shape chosen, and a variable linear background is also present. Examples of spectral analyses for atomic 4d core levels using this program are shown in Fig. 6.[86] Lorentzian shapes have been used for Xe and Yb, and Gaussians for Eu, and the overall fits to these spectra are very good.

Beyond spectral analyses involving fits of certain functional forms to the data, Wertheim[87, 88] and Grunthaner[89] have also developed techniques for *deconvoluting* XPS spectra so as to mathematically remove instrumental linewidth contributions. The form of the instrumental linewidth has, in turn, been derived from the shape of the high-energy cut-off at the Fermi energy for a metallic specimen (cf. Fig. 4). This is possible because, to a good approximation, the density of occupied states ends in a vertical step function at E_F. The term "deconvolution" is also often incorrectly used to describe the results of peak-fitting procedures.

III. THE PHOTOEMISSION PROCESS

In this section, various aspects of the basic photoemission process are discussed in detail, with the primary aim of providing a unified theoretical framework for the subsequent discussion of various experimental observations. In discussing photoelectric cross-sections for atoms, molecules, and solids, applications to the interpretation of experimental results are also presented here.

A. Wave Functions, Total Energies, and Binding Energies

In any photoelectron emission experiment, the basic excitation process

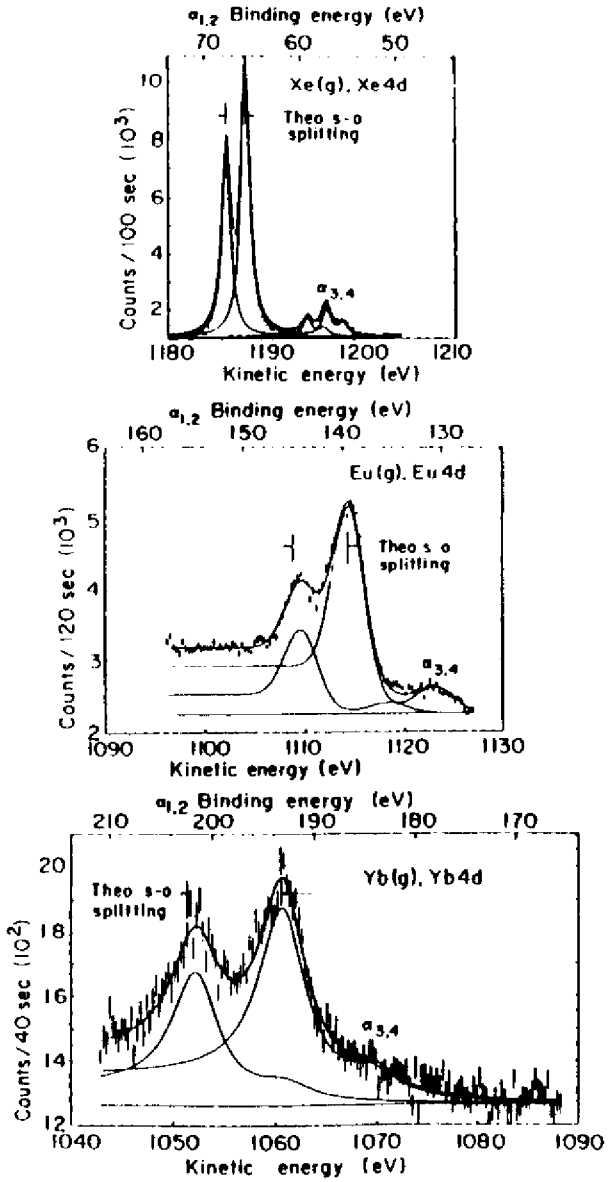

Fig. 6. 4*d* core photoelectron spectra from gaseous Xe, Eu, and Yb produced by excitation with non-monochromatized MgKα x-rays (cf. Fig. 2). The spectra have been resolved into components by least-squares fits of peak shapes including the $\alpha_{3,4}$ satellites and an asymptotically-constant inelastic tail. Lorentzian shapes were used for Xe and Yb, Gaussian for Eu. (From Fadley, ref. 33 (where the curve fitting program is described) and Fadley and Shirley, ref. 86.)

involves absorption of a photon of energy $h\nu$ according to

$$\overset{\text{Initial state}}{\Psi_{tot}^{I}(N),\ E_{tot}^{I}(N)} \xrightarrow{h\nu} \overset{\text{Final state}}{\Psi_{tot}^{J}(N, K),\ E_{tot}^{J}(N, K)} \tag{17}$$

Here $\Psi_{tot}^{I}(N)$ is the initial-state N-electron wave function corresponding to a total energy $E_{tot}^{I}(N)$, and $\Psi_{tot}^{J}(N, K)$ is the Kth final-state N-electron wave function (including the photoelectron) corresponding to a total energy of $E_{tot}^{J}(N, K)$. The relevant energy conservation equation is

$$E_{tot}^{I}(N) + h\nu = E_{tot}^{J}(N, K) \tag{18}$$

In the simplest situation, the index K thus labels the one-electron orbital k from which emission occurs (as discussed below), but in general it should describe all modes of excitation possible within the final state, including electronic, vibrational, and translational. In all forms of higher-energy photoelectron spectroscopy, it is customary to assume that the photoelectron is sufficiently weakly coupled to the $(N-1)$-electron ion left behind so as to permit separating the final state of the excitation process to yield

$$\overset{\text{Initial state}}{\Psi_{tot}^{I}(N),\ E_{tot}^{I}(N)} \xrightarrow{h\nu} \overset{\text{Final state ion}}{\Psi_{tot}^{J}(N-1, K),\ E_{tot}^{J}(N-1, K)} + \overset{\text{Photoelectron}}{\phi^{J}(1)\chi^{J}(1),\ E_{kin}} \tag{19}$$

in which $\Psi_{tot}^{J}(N-1, K)$ and $E_{tot}^{J}(N-1, K)$ refer to the Kth $(N-1)$-electron ionic state that can be formed, E_{kin} is the kinetic energy of the Kth photoelectron peak, $\phi^{J}(1)$ is the spatial part of a one-electron orbital describing the photoelectron and $\chi^{J}(1)$ is the spin part of the photoelectron orbital ($\chi = \alpha$ or β). The form of $\phi^{J}(1)$ thus depends on kinetic energy. (For simplicity here, any change in kinetic energy due to work function differences between specimen and analyzer is neglected.) $\Psi_{tot}^{J}(N-1, K)$ and $\phi^{J}(1)$ can, if desired, be combined in a suitable sum of products to yield the correct overall antisymmetry with respect to electronic coordinates necessary in the final state. This can be written with an antisymmetrizing operator $\hat{A}$ as:[90, 91]

$$\Psi_{tot}^{J}(N, K) = \hat{A}(\phi^{J}(1)\chi^{J}(1),\ \Psi_{tot}^{J}(N-1, K)) \tag{20}$$

The energy conservation equation which then results is that most useful in analyzing XPS spectra:

$$E_{tot}^{I}(N) + h\nu = E_{tot}^{J}(N-1, K) + E_{kin} \tag{21}$$

The binding energy corresponding to leaving the ion in a state describable by $\Psi_{tot}^{J}(N-1, K)$ is thus given by

$$E_b^{V}(K) = E_{tot}^{J}(N-1, K) - E_{tot}^{I}(N) \tag{22}$$

in which the vacuum-level reference is implicit.

One inherent source of linewidth in any binding energy measurement is thus energy broadening due to lifetime effects in either the initial or final state. If the relevant lifetime is denoted by τ, uncertainty principle arguments thus lead to a broadening that is Lorentzian in shape, with a FWHM in eV given by $\sim \hbar/\tau = 6.58 \times 10^{-16}/\tau(\text{s})$. The initial state lifetime is usually very long, and so contributes negligible broadening. However, final-state lifetimes are estimated to be as short as 10^{-18} s in certain cases, so that such effects can play a major role in limiting XPS resolution, particularly for inner subshell excitation.

In general, for a system containing N electrons with spatial coordinates $\mathbf{r}_1, \mathbf{r}_2, \ldots, \mathbf{r}_N$ and spin coordinates $\sigma_1, \sigma_2, \ldots, \sigma_N$ and P nuclei with spatial coordinates $\mathbf{R}_1, \mathbf{R}_2, \ldots, \mathbf{R}_P$, any of the total wave functions considered will depend upon all of these coordinates

$$\Psi_{\text{tot}}(N) = \Psi_{\text{tot}}(\mathbf{r}_1, \sigma_1, \mathbf{r}_2, \sigma_2, \ldots, \mathbf{r}_N, \sigma_N; \mathbf{R}_1, \mathbf{R}_2, \ldots, \mathbf{R}_P) \tag{23}$$

Nuclear spin coordinates can be neglected on the resolution scale of electron spectroscopy. In the non-relativistic limit that usually serves as the starting point for calculations on such systems, the relevant Hamiltonian in electrostatic units is

$$\hat{H}_{\text{tot}} = \underbrace{-\frac{\hbar^2}{2m}\sum_{i=1}^{N}\nabla_i^2}_{\substack{\text{Electron}\\ \text{kinetic}}} \underbrace{-\sum_{i=1}^{N}\sum_{I=1}^{P}\frac{Z_I e^2}{r_{iI}}}_{\substack{\text{Electron-}\\ \text{nuclear}\\ \text{attraction}}} + \underbrace{\sum_{i=1}^{N}\sum_{j>i}^{N}\frac{e^2}{r_{ij}}}_{\substack{\text{Electron-}\\ \text{electron}\\ \text{repulsion}}} + \underbrace{\sum_{I=1}^{P}\sum_{m>I}^{P}\frac{Z_I Z_m e^2}{r_{Im}}}_{\substack{\text{Nuclear-}\\ \text{nuclear}\\ \text{repulsion}}} - \underbrace{\frac{\hbar^2}{2}\sum_{I=1}^{P}\frac{\nabla_I^2}{M_I}}_{\substack{\text{Nuclear}\\ \text{kinetic}}} \tag{24}$$

Here, m is the electronic mass, Z_I is the charge of the Ith nucleus, $r_{iI} = |\mathbf{r}_i - \mathbf{R}_I|$, $r_{ij} = |\mathbf{r}_i - \mathbf{r}_j|$, $r_{Im} = |\mathbf{R}_I - \mathbf{R}_m|$ and M_I is the mass of the Ith nucleus. To this must be added relativistic effects, usually via a perturbation approach;[92-94] the additional term in the Hamiltonian most often considered is spin-orbit splitting, which for atomic orbitals has the form:[93, 95, 96]

$$\hat{H}_{\text{so}} = \sum_{i=1}^{N}\xi(r_i)\hat{l}_i \cdot \hat{s}_i \tag{25}$$

in which $\xi(r_i)$ is an appropriate function of the radial coordinate r_i,[95] $\hat{l}_i$ is the one-electron operator for orbital angular momentum, and $\hat{s}_i$ is the one-electron operator for spin angular momentum. The total wave function then must satisfy a time-independent Schroedinger equation of the form

$$\hat{H}_{\text{tot}}\Psi_{\text{tot}}(N) = E_{\text{tot}}(N)\Psi_{\text{tot}}(N)$$

For such an overall Hamiltonian, the Born-Oppenheimer approximation[95] permits separating the total wave function into a product of an electronic part Ψ and a nuclear part Ψ_{nuc} as

$$\Psi_{\text{tot}}(\mathbf{r}_1, \ldots, \mathbf{R}_P) = \Psi(\mathbf{r}_1, \sigma_1, \mathbf{r}_2, \sigma_2, \ldots, \mathbf{r}_N, \sigma_N)\Psi_{\text{nuc}}(\mathbf{R}_1, \mathbf{R}_2, \ldots, \mathbf{R}_P) \tag{26}$$

In this approximation, the electronic wave function $\Psi(N)$ depends only parametrically on $\mathbf{R}_1, \mathbf{R}_2, \ldots, \mathbf{R}_P$ via the nuclear-nuclear Coulombic repulsion potential, and is the solution to a Schroedinger equation in which the Hamiltonian is that of Eq. (24) with the nuclear kinetic energy term subtracted off:

$$\left(\hat{H}_{\text{tot}} + \frac{\hbar^2}{2}\sum_{I=1}^{P}\frac{\nabla_I^2}{M_I}\right)\Psi(N) = \hat{H}(N)\Psi(N) = E(N)\Psi(N) \tag{27}$$

($\hat{H}_{\text{tot}}$ here can include spin-orbit effects via Eq. (25) if desired). The total energy of the system can then be written as the sum of the electronic energy E and the nuclear energy E_{nuc}, as

$$E_{\text{tot}} = E + E_{\text{nuc}} \tag{28}$$

with E_{nuc} arising from various forms of internal nuclear motion such as vibrations, rotations, and translations (center-of-mass motions). If the various modes of nuclear motion are furthermore independent, the energy becomes

$$E_{\text{tot}} = E + E_{\text{vib}} + E_{\text{rot}} + E_{\text{trans}} + \ldots \tag{29}$$

The overall quantum numbers K describing any initial or final state thus must include a complete specification of all of these modes of motion.

For example, in the limit of a diatomic molecule with a very nearly harmonic oscillator form for the curve of electronic energy, E, versus internuclear separation,

$$E_{\text{vib}} = \hbar\nu_{\text{vib}}(v + \tfrac{1}{2}) \tag{30}$$

in which ν_{vib} is the classical vibration frequency and $v = 0, 1, 2, \ldots$, is the vibrational quantum number. Such vibrational excitations in the final state ion give rise to the pronounced vibrational bands well known in UPS studies of gas-phase molecules,[97] and have also recently been noted in XPS studies of both gases[41] and solids [85] (see Section V.E). Rotational excitations are sufficiently low in energy as to be so far unresolvable in XPS studies of molecules.

Translational motion of the center of mass of an atom or molecule can influence energies in two ways: (1) The conservation of linear momentum in the excitation process requires that

$$\mathbf{p}_{h\nu} + 0 = \mathbf{p}^f + \mathbf{p}_r \tag{31}$$

where $\mathbf{p}_{h\nu}$ is the photon momentum and has a magnitude of $h\nu/c$, the momentum associated with E^I is taken for simplicity to be zero, $\mathbf{p}^f$ is the photoelectron momentum, and $\mathbf{p}_r$ is the recoil momentum of the atom or molecule, treated as a center-of-mass translation. If v is the magnitude of the photoelectron velocity, for $E_{kin} = 500$ eV, $v/c = 0{\cdot}044$ and for $E_{kin} = 1500$ eV, $v/c = 0{\cdot}076$. Thus, the photoelectrons typically encountered in XPS can be considered to a good approximation to be non-relativistic. In this approximation, it is a simple matter to show that $|\mathbf{p}_{h\nu}| \approx v/2c\,|\mathbf{p}^f|$ for the example of photoelectrons originating from valence electronic levels (for which $E_{kin} \approx h\nu$). Therefore, in general $|\mathbf{p}_{h\nu}| \ll |\mathbf{p}^f|$ and $\mathbf{p}^f \approx \mathbf{p}_r$, indicating that the ion recoils in a direction opposite to that of photoelectron emission. By conserving both energy and momentum, it can be shown that for a given $h\nu$ and E_{kin}, the recoil energy $E_r = p_r^2/2M$ increases with decreasing atomic or molecular mass M.[3] For excitation of valence shell photoelectrons with Al Kα radiation ($h\nu = 1487$ eV), Siegbahn *et al.*[3] have calculated the following recoil energies for different atoms: H—0·9 eV, Li—0·1 eV, Na—0·04 eV, K—0·02 eV, and Rb—0·01 eV. It is thus clear that only for the lightest atoms H, He, and Li does the recoil energy have a significant magnitude in comparison with the present 0·4–1·0 eV instrumental linewidths in XPS spectra. For almost all cases, E_r can thus be neglected. (2) A more generally applicable limit on resolution in gas-phase studies is set by the Doppler broadening associated with the thermal translational motion of the emitting molcules. For center-of-mass motion of a molecule of total molecular weight M with a velocity V, the electron kinetic energy appropriate for use in Eq. (1) is

$$E_{kin}'' = \tfrac{1}{2}m|\mathbf{v} - \mathbf{V}|^2 \tag{32}$$

Thus, the measured kinetic energy $E_{kin} = \frac{1}{2}mv^2$ will differ from that of Eq. (32) by varying amounts, according to the thermal distribution of velocities. If the mean measured kinetic energy in a peak is denoted by $\overline{E_{kin}}$, then it can be shown using simple kinetic theory that the Doppler width ΔE_d (in eV) is given by [98]

$$\Delta E_d = 0{\cdot}723 \times 10^{-3}\left(\frac{T \cdot \overline{E_{kin}}}{M}\right)^{\frac{1}{2}} \tag{33}$$

in which E_{kin} is in eV, T is the absolute temperature in °K and M is the molecular weight. At room temperature and a typical XPS energy of 1000 eV, ΔE_d is thus $\lesssim 0{\cdot}10$ eV for molecules with $M \geq 10$. In general, such Doppler broadening is thus not a significant factor in comparison to typical XPS resolutions of $\sim 0{\cdot}4$–$1{\cdot}0$ eV, although they can be important in limiting gas-phase UPS resolution.

In many instances, it is adequate to neglect nuclear motion entirely, and use Eqs (17) and (19) with the quantities $\Psi^I(N)$, $E^I(N)$, $\Psi^f(N)$, $E^f(N)$, $\Psi^f(N-1, K)$, and $E^f(N-1, K)$ relating to only electronic motion. Note that this means

accurate calculations must in principle be made on both initial state and final state. The overall designations for such N-electron or $(N-1)$-electron states are obtained from the various irreducible representations of the symmetry group corresponding to the mean nuclear positions.[95] For example, in atoms for which spin–orbit coupling is small, Russell–Saunders or L, S coupling can be utilized, yielding states specified by L, S, and perhaps also M_L and M_S, where L is the quantum number for total orbital angular momentum L, S is the quantum number for total spin angular momentum S, and M_L and M_S relate to the z components of orbital and spin angular momentum. In the limit of zero spin–orbit splitting, energies depend only on L and S, yielding different L, S terms or multiplets with degeneracies of $(2L+1)(2S+1)$. Analogous overall quantum numbers apply for molecules,[95] but they are seldom used in describing total electronic wave functions in solids. Multiplet splittings such as those discussed in Section V.C are the result of energy differences between such many-electron states.

B. The Hartree–Fock Method and Koopmans' Theorem

In attempting to determine reasonably accurate approximations to N-electron wave functions, a common starting point is the non-relativistic Hartree–Fock (HF) self-consistent-field (SCF) method.[95, 99] As the Hartree–Fock method has been widely used in calculations on atoms, molecules, and solids at different levels of exactness and also serves as a reference method for several more accurate and less accurate methods of computing electronic energy levels, it is outlined here in simplest form. The wave function Ψ^I for an N-electron system is approximated as a single Slater determinant Φ of N orthonormal one-electron spin-orbitals. Each one-electron orbital is composed of a product of a spatial part $\phi_i(\mathbf{r})$ ($i = 1, 2, \ldots, N$) and a spin part $\chi_i(\sigma)$ which is equal to either α ($m_s = +\frac{1}{2}$), or β ($m_s = -\frac{1}{2}$), for which the orthonormality relations are

$$\int \phi_i^*(\mathbf{r})\phi_j(\mathbf{r})\,d\tau \equiv \langle \phi_i | \phi_j \rangle = \delta_{ij}$$

$$\int \chi_i^*(\sigma)\chi_j(\sigma)\,d\sigma \equiv \langle \chi_i | \chi_j \rangle = \delta_{m_{s,i},\, m_{s,j}} = \begin{cases} 1 & \text{for } \alpha\alpha \text{ or } \beta\beta \\ 0 & \text{for } \alpha\beta \text{ or } \beta\alpha \end{cases} \tag{34}$$

Ψ^I can then be written as a normalized determinant of the form:

$$\Psi^I \approx \Phi = \frac{1}{\sqrt{N!}}\begin{vmatrix} \phi_1(1)\chi_1(1) & \phi_2(1)\chi_2(1) & \cdots & \phi_{N-1}(1)\chi_{N-1}(1) & \phi_N(1)\chi_N(1) \\ \phi_1(2)\chi_1(2) & \phi_2(2)\chi_2(2) & \cdots & \phi_{N-1}(2)\chi_{N-1}(2) & \phi_N(2)\chi_N(2) \\ \cdot & \cdot & \cdot & \cdot & \cdot \\ \cdot & \cdot & \cdot & \cdot & \cdot \\ \cdot & \cdot & \cdot & \cdot & \cdot \\ \phi_1(N)\chi_1(N) & \phi_2(N)\chi_2(N) & \cdots & \phi_{N-1}(N)\chi_{N-1}(N) & \phi_N(N)\chi_N(N) \end{vmatrix} \tag{35a}$$

or in terms of the antisymmetrizer $\hat{A}$ as

$$\Phi = \hat{A}(\phi_1\chi_1, \phi_2\chi_2, \ldots, \phi_N\chi_N) \tag{35b}$$

where the integers 1, ..., N label the space and spin coordinates $\mathbf{r}_j$ and σ_j for each orbital.

The spatial one-electron orbitals are furthermore assumed to have symmetries belonging to the set of irreducible representations of the symmetry group of the equilibrium nuclear geometry, and are in this sense often referred to as "delocalized". Thus, for example, in atoms, the orbitals have the form[95]

$$\phi_{nlm_l}(r, \theta, \phi) = R_{nl}(r)\, Y_{lm_l}(\theta, \phi) \tag{36}$$

in which $R_{nl}(r)$ is the radial part and the angular part is given by the spherical harmonic $Y_{lm_l}(\theta, \phi)$. In molecules, various symmetry types arise, as, for example, $1\sigma\ 3\sigma_g\ 2a_1, \ldots$,[95] and the orbitals are often approximated as linear combinations of atomic orbitals (LCAO's). In solids, the translational periodicity of the crystal requires that all such delocalized orbitals be of the Bloch-function type:[95, 96, 99]

$$\phi_{\mathbf{k}}(\mathbf{r}) = u_{\mathbf{k}}(\mathbf{r}) \exp(i\mathbf{k}\cdot\mathbf{r}) \tag{37}$$

in which $\mathbf{k}$ is the electron wave vector with a quasi-continuous distribution of values and $u_{\mathbf{k}}(\mathbf{r})$ is a function characteristic of each $\phi_{\mathbf{k}}$ that has the same translational periodicity as the lattice. A free electron moving under the influence of no forces corresponds to a constant $u_{\mathbf{k}}(\mathbf{r})$, and yields a plane-wave (PW) one-electron orbital of the form

$$\phi_{\mathbf{k}}(\mathbf{r}) = C \exp(i\mathbf{k}\cdot\mathbf{r}) \tag{38}$$

in which C is a normalization constant and the momentum $\mathbf{p}$ and energy E are given by

$$\mathbf{p} = \hbar\mathbf{k} \tag{39}$$

$$E = E_{\mathbf{k}\ln} = p^2/2m = \hbar k^2/2m \tag{40}$$

In the often-used spin-restricted Hartree–Fock method, each spatial orbital ϕ_i is also taken to be multiplied by either α and β in the Slater determinant (that is, to have a maximum occupation number of two). Thus only $N/2$ unique ϕ_i's are involved in describing a system with an even number of electrons in doubly-occupied orbitals.

If the Hamiltonian of Eq. (27) is used together with the variational principle to determine the optimum Φ for which the total energy $E = \langle\Phi|\hat{H}|\Phi\rangle$ is a minimum, the Hartree–Fock equations are obtained. These N equations can be used to determine a self-consistent set of orbitals ϕ_i, as well as to calculate the total energy E of the state described by Φ. In atomic units (1 a.u. = 1 Hartree = 27·21 eV, 1 Bohr = a_0 = 0·529 Å), the Hartree–Fock equations in

diagonal form are

$$\underbrace{\left[-\tfrac{1}{2}\nabla_i^2 - \sum_{l=1}^{P}\frac{Z_l}{r_{il}}\right]}_{\substack{\text{Kinetic} \\ \text{Electron–nuclear} \\ \text{attraction}}}\phi_i(1) + \underbrace{\left[\sum_{j=1}^{N}\int\phi_j^*(2)\frac{1}{r_{12}}\phi_j(2)\,d\tau_2\right]}_{\substack{\text{Electron–electron} \\ \text{Coulombic} \\ \text{repulsion}}}\phi_i(1)$$

$$-\delta_{m_{s_i},\,m_{s_j}}\sum_{j=1}^{N}\underbrace{\left[\int\phi_j^*(2)\frac{1}{r_{12}}\phi_i(2)\,d\tau_2\right]}_{\substack{\text{Electron–electron} \\ \text{exchange}}}\phi_j(1) = \epsilon_i\phi_i(1), \quad i = 1, 2, \ldots, N \tag{41}$$

where the ϵ_i's are termed energy eigenvalues, one-electron energies, or orbital energies. The origins of the individual terms are labelled. The exchange interaction is only possible between spin-orbitals with parallel spins (that is, $\alpha\alpha$ or $\beta\beta$), and the Kronecker delta $\delta_{m_{s_i},\,m_{s_j}}$ allows for this. It is convenient to re-express Eq. (41) more simply in terms of the Fock operator $\hat{F}(1)$ as:

$$\hat{F}(1)\phi_i(1) \equiv \left\{-\tfrac{1}{2}\nabla_1^2 - \sum_{l=1}^{P}\frac{Z_l}{r_{1l}} + \sum_{j=1}^{N}[\hat{J}_j - \delta_{m_{s_i},\,m_{s_j}}\hat{K}_j]\right\}\phi_i(1) = \epsilon_i\phi_i(1) \tag{42}$$

by defining the Coulomb and exchange operators $\hat{J}_j$ and $\hat{K}_j$ such that

$$\hat{J}_j\phi_i(1) \equiv \int\phi_j^*(2)\frac{1}{r_{12}}\phi_j(2)\phi_i(1)\,d\tau_2 \tag{43}$$

$$\hat{K}_j\phi_i(1) \equiv \int\phi_j^*(2)\frac{1}{r_{12}}\phi_i(2)\phi_j(1)\,d\tau_2 \tag{44}$$

Thus, the matrix elements of these operators are the two-electron Coulomb integrals J_{ij} and exchange integrals K_{ij}:

$$J_{ij} \equiv \langle\phi_i(1)|\hat{J}_j|\phi_i(1)\rangle = \iint\phi_i^*(1)\phi_j^*(2)\frac{1}{r_{12}}\phi_i(1)\phi_j(2)\,d\tau_1\,d\tau_2 \tag{45}$$

$$K_{ij} \equiv \langle\phi_i(1)|\hat{J}_j|\phi_i(1)\rangle = \iint\phi_i^*(1)\phi_j^*(2)\frac{1}{r_{12}}\phi_i(2)\phi_j(1)\,d\tau_1\,d\tau_2 \tag{46}$$

From these definitions, it is clear that $J_{ij} = J_{ji}$, $K_{ij} = K_{ji}$, and $J_{ii} = K_{ii}$. Once the Hartree–Fock equations have been solved to the desired self-consistency, the orbitals energies ϵ_i can be obtained from

$$\epsilon_i = \epsilon_i^0 + \sum_{j=1}^{N}(J_{ij} - \delta_{m_{s_i},\,m_{s_j}}K_{ij}) \tag{47}$$

where ϵ_i^0 is the expectation value of the one-electron operator for kinetic energy and electron-nuclear attraction

$$\epsilon_i^0 = \langle\phi_i(1)|-\tfrac{1}{2}\nabla_1^2 - \sum_{l=1}^{P}\frac{Z_l}{r_{1l}}|\phi_i(1)\rangle \tag{48}$$

By comparison, the total energy of the state approximated by Φ is given by

$$E = \langle \Phi | \hat{H} | \Phi \rangle = \sum_{i=1}^{N} \epsilon_i^0 + \sum_{i=1}^{N} \sum_{j>i}^{N} (J_{ij} - \delta_{m_i, m_j} K_{ij}) + \sum_{l=1}^{P} \sum_{m>l}^{P} \frac{Z_l Z_m}{r_{lm}} \quad (49)$$

Note that the first two summations over electronic indices are not simply the sum of all of the one-electron energies for the N electrons in the system, as the sum of the Coulomb and exchange terms in the total energy is made with $i<j$ to avoid counting these terms twice. This means that measured binding energies (which will be shown shortly to be very close to the ϵ_i's in value) cannot be directly used to determine total energies and hence such quantities as reaction energies.

Mann[100] has compiled very useful tables of accurate Hartree–Fock calculations for all atoms in the periodic table. These include one-electron energies, Slater F^k and G^k integrals for calculating J_{ij} and K_{ij}, radial expectation values, and wave-function tabulations. Herman and Skillman[93] and Carlson *et al.*[101] have also calculated energies, radial expectation values, and local one-electron potentials for all atoms, using a Hartree–Fock Slater approximation with relativistic corrections.

In utilizing the Hartree–Fock method for computing binding energies, the most accurate procedure is to compute the difference between $E^f(N-1, K)$ and $E^i(N)$ corresponding to the Hartree–Fock wave functions $\Psi^f(N-1, K)$ and $\Psi^i(N)$, respectively. In the one-electron-orbital picture provided by this method, the final-state wave function can be characterized as having a hole in the kth subshell, and, for a closed-shell system with all ϕ_i's doubly occupied, the overall index K can be replaced simply by k. As the photoemission process by which this hole is formed occurs on a time scale very short compared to that of nuclear motion ($\sim 10^{-16}$ s compared to $\sim 10^{-13}$ s), the nuclear positions in $\Psi^f(N-1, K)$ can be assumed to be identical to those in $\Psi^i(N)$, and the nuclear–nuclear repulsion sum in Eq. (49) will thus cancel in an energy difference. However, the ion left behind by the exiting photoelectron may not possess a nuclear geometry consistent with the ionic ground-state vibrational motion, an effect which leads to the possibility of exciting various final vibrational states. If the excitation is also fast in comparison to the motions of the $(N-1)$ passive electrons in $\Psi^f(N-1, K)$ (a less rigorously justifiable limit termed the "sudden approximation"), it is also possible to show that various final electronic states can be reached. (See Sections III.D.1, V.D.2, and V.E for more detailed discussions.) For now, only the electronic ground state of the ion corresponding to the minimum binding energy will be considered. In this usually dominant final state, it is expected that the passive electrons will not have the same spatial distribution as those in $\Psi^i(N)$ due to relaxation or rearrangement around the k hole. Although the overall change in the spatial form of the passive orbitals due to relaxation around an inner hole is not large (for example, the mean radius of an atomic orbital changes by only ~ 1–10%),[102] the resulting change in energy can have an appreciable effect on calculated binding energies. Such relaxation effects can have significant consequences in interpreting binding energy data such as, for example, chemical shifts, and they are discussed in more detail in Sections IV and V.B. Hole-state calculations in which initial and final states are treated with equal accuracy in the Hartree–Fock sense have been performed by various authors for atoms,[103–105] small molecules,[106–109] and inorganic clusters.[110] If binding energies determined in this way are corrected for relativistic effects where necessary, very good agreement with experimental core electron binding energies has been obtained. For example, an agreement of approximately $0{\cdot}2\%$ is found between theoretical and experimental $1s$ binding energies of Ne ($E_b^V(1s) = 870$ eV) and Ar ($E_b^V(1s) = 3205$ eV).[103]

Relativistic effects generally increase core electron binding energies, as well as leading to spin–orbit splittings, and their magnitudes depend on the ratio of the characteristic orbital velocity to the velocity of light.[93, 94] The atomic Hartree–Fock Slater calculations of Herman and Skillman[93] and Carlson and Pullen[94] provide a direct tabulation of such corrections for all atoms as determined by perturbation theory. For example, the correction for $C1s$ is only about 0·2 eV out of 290 eV ($\sim 0{\cdot}08\%$), whereas for the deeper core level $Ar1s$, it is about 22 eV out of 3180 eV ($\sim 0{\cdot}69\%$).

An additional type of correction which should in principle be made to any type of Hartree–Fock calculation is that dealing with electron–electron correlation. In connection with hole-state Hartree–Fock binding energy calculations, the intuitive expectation for such corrections might be that because the initial-state SCF calculation does not include favorable correlation between a given core electron and the other $(N-1)$ electrons, the calculated E^i value would be too large and thus that the binding energy $E_b^V(K) = E^f(N-1, K) - E^i(N)$ would be too small. However, in comparing relativistically-corrected hole-state calculations on several small atoms and ions with experimental binding energies, the remaining error due to correlation has been found to change sign from level to level within the same system.[103, 111] Such deviations from simple expectations appear to have their origins primarily in the different types of correlation possible for final hole states in different core or valence levels. For example, $E_b^V(1s)$ for Ne shows a correlation correction δE_{corr} in the expected direction (that is, so as to increase E_b) of approximately 0·6 eV out of 870·2 eV ($\sim +0{\cdot}07\%$)[112] whereas δE_{corr} for $E_b^V(2s)$ acts in the opposite direction by approximately 0·9 eV out of 48·3 eV ($\sim -1{\cdot}8\%$).[111] For core levels in closed-shell systems such as Ne, such corrections can be computed approximately from a sum of electron pair correlation energies $\epsilon(i, j)$ calculated for the ground state of the system.[111] For example, in computing the $1s$ binding energy in Ne, the

correction has the form of a sum over pair correlation energies between the 1s electron and all other electrons in the atom. Such correlation energies are dependent upon both overlap and spin orientation, as the exchange interaction partially accounts for correlation of electrons with parallel spin. For Ne1s, this sum is thus:

$$\delta E_{\text{corr}} = \epsilon(1s\alpha, 1s\beta) + \epsilon(1s\alpha, 2s\alpha) + \epsilon(1s\alpha, 2s\beta) + 3\epsilon(1s\alpha, 2p\alpha) + 3\epsilon(1s\alpha, 2p\beta) \quad (50)$$

with values of $\epsilon(1s\alpha, 1s\beta) = +1{\cdot}09$ eV, $\epsilon(1s\alpha, 2s\alpha) = +0{\cdot}01$ eV, $\epsilon(1s\alpha, 2s\beta) = +0{\cdot}06$ eV, $\epsilon(1s\alpha, 2p\alpha) = +0{\cdot}11$ eV, $\epsilon(1s\alpha, 2p\beta) = +0{\cdot}15$ eV. Note the smaller magnitudes of $\epsilon(i, j)$ for electrons with parallel spins. Also, it is clear that most of the correlation correction arises from the strongly overlapping 1s electrons. Equation (50) is only a first approximation, however, and more exact calculations involving explicit estimates of all types of correlation in both Ne and Ne^+ with a 1s hole give better agreement with the experimental 1s binding energy.[112] The experimental value is $E_b^V(1s) = 870{\cdot}2$ eV, in comparison to $\delta E_{\text{corr}} = 1{\cdot}9$ eV, $E_b^V(1s) = 870{\cdot}8$ eV based on Eq. (50)[111] and $\delta E_{\text{corr}} = 0{\cdot}6$ eV, $E_b^V(1s) = 870{\cdot}0$ eV based on the more accurate calculation.[112] δE_{corr} is decreased in the latter calculation primarily because of correlation terms that are present in Ne^+ but not in Ne. The sum of pair correlation energies $\epsilon(i, j)$ in Ne^+ is larger than that in Ne by about 30%, and other terms not describable as pair interactions are present in Ne^+ but not Ne.

Aside from verifying that Hartree–Fock hole-state energy difference calculations can yield very accurate values for core electron binding energies in atoms and molecules, such investigations have also led to another important consideration concerning the final hole state formed by photoelectron emission. This concerns the correct extent of delocalization of the hole, which is implicitly assumed to have a symmetry dictated by the entire nuclear geometry (or to exhibit a maximum degree of delocalization) in the diagonal Hartree–Fock method discussed here. Hole-state calculations by Bagus and Schaefer[107] have shown that *core-orbital* holes will tend to be localized on one atomic center, as opposed to being distributed over all centers as might be expected in certain cases from a linear-combination-of-atomic-orbitals (LCAO) Hartree–Fock calculation including all electrons. In the simple example of O_2, a hole in the $1\sigma_g$ or $1\sigma_u$ molecular orbitals (which can be considered to a very good approximation to be made up of a sum or difference of 1s atomic orbitals on the two oxygen atoms, respectively) is predicted by such a calculation to result in a net charge of $+\frac{1}{2}e$ on each oxygen atom in the molecule. However, Snyder[108] has pointed out that such a state does not minimize the total energy associated with the final state Hamiltonian. Thus, the lowest energy state is found[107] to localize the 1s core hole entirely on

either oxygen atom. These pairs of equivalent final states (which no longer possess one-electron orbitals with the full symmetry of the molecule) yield the correct values of $E_f(N-1, K)$ for computing binding energies. For O_2, the localized hole states yield a value of $E_b^V(1s) = 542$ eV, in comparison with an experimental value of 543 eV, and a delocalized hole-state value of 554 eV. Thus, localizing the hole represents a large correction of 12 eV ($\sim 2{\cdot}2\%$). More recently, Cederbaum and Domcke[113] have shown from a more rigorous point of view why the use of such localized core-hole states is valid.

Although localization of final-state core holes is thus to be expected in general, the question of localization becomes more complex in dealing with valence electrons in molecules or solids. Molecular orbitals with lone-pair character or which exhibit a predominance of atomic-orbital make-up from a single atom in an LCAO description are inherently localized, even though they are describable in terms of the overall symmetry species of the molecule, and such orbitals would be expected to exhibit hole localization to a great degree. Other molecular valence hole states may or may not show localization that deviates significantly from a description with full-symmetry molecular orbitals. Similarly, the spatially-compact 4f valence levels in solid rare-earth elements and compounds are found to yield highly-localized hole states, as is evidenced by the atomic-like multiplet splittings observed[114] (see Section V.C). The valence d electrons in solid transition metals and their compounds or the valence electrons in free-electron-like metals may not always be so simply described, however. Nonetheless, Ley *et al.*[115] have concluded that, even for the highly delocalized valence states of free-electron metals such as Li, Na, Mg, and Al, the energy associated with final-state relaxation around a valence hole can be calculated equally well in terms of either a localized- or delocalized-hole-state description; in this case, however, the delocalized hole state is still best considered to be an itinerant localized hole propagating through the solid.

Although a localized-orbital description of the *initial* state can always be obtained from a Hartree–Fock determinant by means of a suitable unitary transformation of the various orbitals ϕ_i without changing the overall N-electron determinantal wave function or total energy,[116] the transformation is not unique. Payne[117] has also recently presented a new method for performing molecular Hartree–Fock calculations in which relatively unique localized-orbital character is built in by constraining each LCAO molecular orbital to be composed only of atomic orbitals centered on a small set of nearest-neighbor atoms. Although either of these two procedures for obtaining localized initial-state orbitals can provide chemically intuitive and transferable bonding orbitals between two or three bonding centers,[116, 117] it is not clear that they would necessarily lead to a more correct description of the final state with one electron removed. More theoretical and experimental work is thus necessary to characterize fully the best one-electron-orbital

description of the final states of many systems, *if* indeed such a one-electron picture is always adequate or necessary.

In order to avoid the difficulties associated with hole-state calculations in determining binding energies, a very often used approximation is to assume that Koopmans' Theorem well describes the relationship between initial and final state total energies. The basis of this theorem is the assumption that the initial one-electron orbitals ϕ_i making up the determinant $\Phi^I(N)$ are precisely equal to the final orbitals ϕ_i' making up $\Phi^J(N-1, k)$ with a single k-subshell hole. The final state total energy $E^J(N-1, k)$ can then be calculated from the formula for $E^I(N)$ [cf. Eq. (49)] simply by eliminating those terms dealing with the electron occupying the kth orbital initially. This procedure leaves as the Koopmans' Theorem value for $E^J(N-1, k)$ (neglecting nuclear repulsion):

$$\begin{aligned} E^J(N-1,k)^{\mathrm{KT}} = & \sum_{i\neq k}^{N} \epsilon_i^0 + \sum_{i\neq k}^{N} \sum_{j>i, j\neq k}^{N} (J_{ij} - \delta_{m_{s_i}, m_{s_j}} K_{ij}) \\ & - \sum_{i\neq k}^{N} \epsilon_i^0 + \sum_{i=1}^{N} \sum_{j>i}^{N} (J_{ij} - \delta_{m_{s_i}, m_{s_j}} K_{ij}) \\ & - \sum_{i=1}^{N} (J_{ik} - \delta_{m_{s_i}, m_{s_k}} K_{ik}) \end{aligned} \tag{51}$$

The Koopmans' Theorem binding energy of the kth electron is then by the difference method [cf. Eq. (22)],

$$\begin{aligned} E_b^{\mathrm{V}}(k)^{\mathrm{KT}} &= E^J(N-1,k)^{\mathrm{KT}} - E^I(N) \\ &= -\epsilon_k^0 - \sum_{i=1}^{N} (J_{ik} - \delta_{m_{s_i}, m_{s_k}} K_{ik}) \end{aligned}$$

or, making use of Eq. (47) for the orbital energy ϵ_k,

$$E_b^{\mathrm{V}}(k)^{\mathrm{KT}} = -\epsilon_k \tag{52}$$

Thus, the binding energy of the kth electron is in this approximation equal to the negative of the orbital energy ϵ_k. For bound-state orbitals ϵ_k is negative, so that the binding energy has the appropriate positive sign. This result is Koopmans' Theorem, as is indicated by the superscript KT. In reality, the relaxation of the $(N-1)$ passive orbitals about the k hole in the ionic ground state will tend to lower $E^J(N-1, k)^{\mathrm{KT}}$, and thus, as long as relativistic and correlation corrections are not too large, binding energies estimated with Koopmans' Theorem should be greater than the true values. If the error due to such electronic relaxation is denoted by $\delta E_{\mathrm{relax}} > 0$, then a binding energy can be written as (neglecting relativistic and correlation effects):

$$\begin{aligned} E_b^{\mathrm{V}}(k) &= E_b^{\mathrm{V}}(k)^{\mathrm{KT}} - \delta E_{\mathrm{relax}} \\ &= -\epsilon_k - \delta E_{\mathrm{relax}} \end{aligned} \tag{53}$$

It should be noted, however, that Koopmans' Theorem as it is derived here applies only to closed-shell systems (that is, systems that are adequately represented by a single Slater determinant with doubly-occupied one-electron orbitals), *or* to solids which contain many electrons in highly delocalized valence orbitals with quasi-continuous energy eigenvalues. For any other case, there will in general be several possible couplings of spin- and orbital-angular momenta in the open shell or shells, and each distinct coupling will give rise to a different initial or final state energy. These states in atoms might, for example, be described in terms of L, S coupling, and would in general be represented by a linear combination of Slater determinants.[118] Although each of these determinants would have the same gross electronic configuration (for example, $3d^5$), various possible combinations of $m_s = +\frac{1}{2}$ and m_l would be possible within the open shells. Provided that final-state relaxation is neglected, Slater[118] has pointed out that a binding energy $E_b^{\mathrm{V}}(k)^{\mathrm{KT}}$ computed as the difference between the *average* total energy for all states within the final configuration and the *average* total energy for all states within the initial configuration is equal to the one-electron energy ϵ_k computed from an initial-state Hartree–Fock calculation utilizing Coulomb and exchange potentials averaged over all states possible within the initial configuration. This we can write as

$$\bar{E}_b^{\mathrm{V}}(k)^{\mathrm{KT}} = \bar{E}^J(k)^{\mathrm{KT}} - \bar{E}^I = -\epsilon_k \tag{54}$$

and it represents a generalization of Koopmans' Theorem to open-shell systems. The various final states discussed here are the cause of the multiplet splittings to be considered in Section V.C.

Although the orbital energies ϵ_k in Koopmans' Theorem as stated here refer to fully delocalized orbitals, Payne[117] has recently pointed out that near-Hartree–Fock calculations in which different atomic-orbital basis sets are chosen for different molecular orbitals to yield effectively localized final results *also* yield a set of one-electron energies that can be interpreted via Koopmans' Theorem. As these one-electron energies are not the same as those for fully delocalized orbitals, it is thus of interest to determine whether any such localization effects are clearly discernible in experimental valence binding energies.

The most direct way of calculating $\delta E_{\mathrm{relax}}$ is of course to carry out SCF Hartree–Fock calculations on both the initial and final states and to compare $E_b^{\mathrm{V}}(k)$ as calculated by a total energy difference method with $E_b^{\mathrm{V}}(k)^{\mathrm{KT}} = -\epsilon_k$. Such calculations have been performed by various authors on both atoms and molecules.[3, 104-109] As representative examples of the magnitudes of these effects, for the neon atom, $E_b^{\mathrm{V}}(1s) = 868{\cdot}6$ eV and $E_b^{\mathrm{V}}(1s)^{\mathrm{KT}} = 891{\cdot}7$ eV, giving $\delta E_{\mathrm{relax}} \approx 23$ eV ($\sim 2{\cdot}6\%$), and $E_b^{\mathrm{V}}(2s) = 49{\cdot}3$ eV and $E_b^{\mathrm{V}}(2s)^{\mathrm{KT}} = 52{\cdot}5$ eV, giving $\delta E_{\mathrm{relax}} \approx 3$ eV ($\sim 6{\cdot}0\%$). Effects of similar magnitude are

found in the 1s levels of molecules containing first-row atoms.[106, 109] Also, in certain cases, the presence of a localized hole may cause considerable valence electron polarization relative to the initial state.[106, 107, 110] Thus δE_{relax} lies in the range of 1-10% of the binding energy involved, with greater *relative* values for more weakly bound electrons. Several procedures have also been advanced for estimating δE_{relax}[105, 119-121] and these are discussed in more detail in Section V.B. It has also been pointed out by Manne and Åberg[90] that a Koopmans' Theorem binding energy represents an average binding energy as measured over all states K associated with emission from the kth orbital, including those describable as both "one-electron" and "multi-electron" in character. This analysis is discussed in more detail in Section III.D.1. Implicit in the use of Koopmans' Theorem is the idea of a predominantly one-electron transition in which the $(N-1)$ passive electrons are little altered.

To summarize, the use of Hartree-Fock theory and Koopmans' Theorem permits writing any binding energy approximately as

$$E_b^{\,V}(k) = -\epsilon_k - \delta E_{relax} + \delta E_{relat} + \delta E_{corr} \tag{55}$$

in which δE_{relax}, δE_{relat}, and δE_{corr} are corrections for relaxation, relativisitic effects, and correlation effects, respectively.

C. More Accurate Wave Functions via Configuration Interaction

In explaining certain many-electron phenomena observed in XPS spectra it is absolutely essential to go beyond the single-configuration Hartree-Fock approximation, and the most common procedure for doing this is by the configuration interaction (CI) method.[122] In this method, an arbitrary N-electron wave function $\Psi(N)$ is represented as a linear combination of Slater determinants $\Phi_j(N)$ corresponding to different N-electron configurations:

$$\Psi(N) = \sum_{j=1} C_j \Phi_j(N) \tag{56}$$

The coefficients C_j, and perhaps also the set of one-electron orbitals ϕ_i used to make up the Φ_j's, are optimized by seeking a minimum in total energy to yield a more accurate approximation for $\Psi(N)$. In the limit of an infinite number of configurations, the exact wave function is obtained by such a procedure. In practice, the dominant C_j's are usually those multiplying determinants with the same configurations as those describing the Hartree-Fock wave function for the system.

For example, for Ne, a highly accurate CI calculation by Barr involving 1071 distinct configurations of spatial orbitals[123] yields the following absolute values for the coefficients multiplying the various members of a few more important configurations: $\Phi_1 = 1s^2 2s^2 2p^6$ = Hartree-Fock configuration 0·984; $\Phi_2 = 1s^2 2s^1 2p^6 3s^1$ − 0·005; $\Phi_3 = 1s^2 2s^2 2p^5 3p$ − 0·009; $\Phi_4 = 1s^2 2s^2 2p^4 4p^2$ − 0·007-0·030; and $\Phi_5 = 1s^2 2s^2 2p^4 3p 4p$ − 0·007 0·022. Approximately 70 distinct configurations have coefficients larger than 0·010 in magnitude, but only that for Φ_1 is larger than 0·030.

Manson[91] has discussed the influence of configuration interaction on the calculation of photoelectron peak intensities (see the more detailed discussion in the next section), and in particular has noted that it may be important to allow for CI effects in both initial and final states. Specific effects of configuration interaction in XPS spectra are also discussed in Sections V.C and V.D, as well as in the chapter by Martin and Shirley[14] in this series.

D. Transition Probabilities and Photoelectric Cross-sections

1. *General Considerations and the Sudden Approximation.* In order to predict the intensities with which various photoelectron peaks will occur, it is necessary to calculate their associated transition probabilities or photoelectric cross-sections. The photoelectric cross-section σ is defined as the transition probability per unit time for exciting a single atom, single molecule, or solid specimen from a state $\Psi^I(N)$ to a state $\Psi^f(N)$ with a unit incident photon flux of 1 cm^{-2} s^{-1}. If the direction of electron emission relative to the directions of photon propagation and polarization is specified in $\Psi^f(N)$, as well as perhaps its direction of emission with respect to axes fixed in the specimen, such a cross-section is termed differential, and is denoted by $d\sigma/d\Omega$. The differential solid angle $d\Omega$ is that into which electron emission occurs, and it is indicated in Fig. 7. From $d\sigma/d\Omega$ for a given system, the total cross-section for electron excitation into any direction is given by

$$\sigma = \int \frac{d\sigma}{d\Omega}\, d\Omega \tag{57}$$

Such differential or total cross-sections can be calculated by means of time-dependent perturbation theory, utilizing several basic assumptions that are discussed in detail elsewhere[124-131] and reviewed briefly below.

In a semi-classical treatment of the effect of electromagnetic radiation on an N-electron system, the perturbation $\hat{H}'$ due to the radiation can be approximated in a weak-field limit as:[131]

$$\hat{H}' = -\frac{e}{2mc}(\hat{p}\cdot\mathbf{A} + \mathbf{A}\cdot\hat{p}) \tag{58}$$

in which $\hat{p} = -i\hbar\nabla$ and $\mathbf{A} = \mathbf{A}(\mathbf{r}, t)$ is the vector potential corresponding to the field. For an electromagnetic wave traveling in a uniform medium, it is possible to choose $\mathbf{A}$ such that $\nabla\cdot\mathbf{A} = 0$ and thus $\hat{p}\cdot\mathbf{A} = 0$, so that in all applications to XPS it is appropriate to consider only the $\mathbf{A}\cdot\hat{p}$ term in Eq.

(58). (In UPS studies of solids, it has, however, been pointed out that the change in properties near a surface can result in a "surface photoeffect" due to the $\hat{p}\cdot\mathbf{A}$ term.[132]) The electromagnetic wave is further assumed to be a traveling plane wave of the form:

$$\mathbf{A}(\mathbf{r},t)=\mathbf{e}A_0\exp\left[i(\mathbf{k}_{h\nu}\cdot\mathbf{r}-2\pi\nu t)\right] \tag{59}$$

where $\mathbf{e}$ is a unit vector in the direction of polarization ($\mathbf{e}$ is parallel to the electric field E), A_0 is an amplitude factor, $\mathbf{k}_{h\nu}$ is the wave vector of propagation, $|k_{h\nu}|=2\pi/\lambda$, and λ is the wavelength of the radiation. Within this approximation the transition probability per unit time for a transition from $\Psi^i(N)$ to $\Psi^f(N)$ can be shown to be proportional to the following squared matrix-element[124, 131]

$$\begin{aligned}|M_{fi}|^2&=\left|\langle\Psi^f(N)|\sum_{t=1}^{N}\mathbf{A}(\mathbf{r}_t)\cdot\hat{p}_t|\Psi^i(N)\rangle\right|^2\\&=\hbar^2A_0^2\left|\langle\Psi^f(N)|\sum_{t=1}^{N}\exp(i\mathbf{k}_{h\nu}\cdot\mathbf{r}_t)\mathbf{e}\cdot\nabla_t|\Psi^i(N)\rangle\right|^2\end{aligned} \tag{60}$$

in which the time dependence of A has been integrated out and the integration remaining in the matrix element is over the space and spin coordinates of all N electrons. The intensity or photon flux of the incident radiation is proportional to A_0^2. If the final state $\Psi^f(N)$ corresponds to electron emission with a wave vector $\mathbf{k}^f$ (or momentum $\mathbf{p}^f=\hbar\mathbf{k}^f$) oriented within a solid angle $d\Omega$ (cf. Fig. 7), the differential cross-section can then be shown to be:[124]

$$\frac{d\sigma}{d\Omega}=C\left(\frac{1}{h\nu}\right)\left|\langle\Psi^f(N)|\sum_{t=1}^{N}\exp(i\mathbf{k}_{h\nu}\cdot\mathbf{r}_t)\mathbf{e}\cdot\nabla_t|\Psi^i(N)\rangle\right|^2 \tag{61}$$

in which C is a combination of fundamental constants, and A_0^2 is eliminated in the normalization to unit photon flux. In dealing with atoms and molecules, it is often necessary to sum further over various experimentally-indistinguishable symmetry-degenerate final states, *and* to average over various symmetry-degenerate initial states to determine a correct cross-section. If the degeneracy of the initial state is g_i and if each such initial state is equally populated, this yields

$$\frac{d\sigma}{d\Omega}=\frac{C}{g_i}\left(\frac{1}{h\nu}\right)\sum_{i,f}\left|\langle\Psi^f(N)|\sum_{t=1}^{N}\exp(i\mathbf{k}_{h\nu}\cdot\mathbf{r}_t)\mathbf{e}\cdot\nabla_t|\Psi^i(N)\rangle\right|^2 \tag{62}$$

Also, if unpolarized radiation is utilized for excitation, a summation or integration over the various possible orientations of $\mathbf{e}$ is necessary in deriving $d\sigma/d\Omega$, yielding finally a summation $\sum_{i,f,\mathbf{e}}$ in Eq. (62). Furthermore, for a randomly oriented set of atoms or molecules as appropriate to studies of gaseous- or polycrystalline-specimens, $d\sigma/d\Omega$ must also be averaged over all

possible orientations of the target system with respect to each possible relative geometry of the radiation and the emitted electron.

A final point of general concern is the influence of nuclear motion, specifically vibration, on such cross-sections. If the Born-Oppenheimer approximation [Eq. (26)] is valid and the influence of the perturbing radiation on

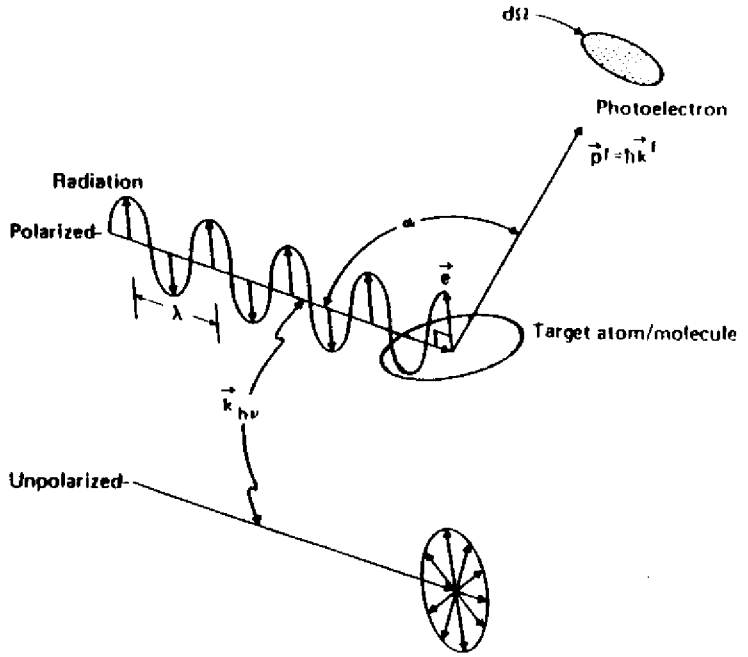

Fig. 7. General geometry for defining the differential cross-section $d\sigma/d\Omega$, showing both polarized and unpolarized incident radiation. The polarization vector $\mathbf{e}$ is parallel to the electric field F of the radiation. In order for the dipole approximation to be valid, the radiation wave length λ should be much larger than typical target dimensions (that is, the opposite of what is shown here).

the nuclear coordinates is neglected, the differential cross-section [Eq. (62)] becomes:

$$\frac{d\sigma}{d\Omega}=\frac{C}{g_i}\left(\frac{1}{h\nu}\right)\sum_{i,f}\left|\langle\Psi^f(N)|\sum_{t=1}^{N}\exp(i\mathbf{k}_{h\nu}\cdot\mathbf{r}_t)\mathbf{e}\cdot\nabla_t|\Psi^i(N)\rangle\right|^2 \left|\langle\Psi_{vib}^f(P)|\Psi_{vib}^i(P)\rangle\right|^2 \tag{63}$$

in which the squared overlap between the initial and final vibrational wave functions is simply a Franck-Condon factor. Vibrational effects in XPS spectra are discussed in Section V.E. Only the electronic aspects of matrix elements and cross-sections are considered further here.

In proceeding further, it is assumed that the photon wavelength λ is much larger than the typical dimensions of the system, which will generally be of the order of a few Å. This is a reasonably good, although borderline, approximation for MgKα or AlKα x-rays with $\lambda \approx 10$ Å. This assumption permits treating $\exp(i\mathbf{k}_{h\nu}\cdot\mathbf{r}_i)$ as unity in the integration, yielding for Eq. (62):

$$\frac{d\sigma}{d\Omega} = \frac{C}{g_i}\left(\frac{1}{h\nu}\right)\sum_{i,f}\left|\mathbf{e}\cdot\langle\Psi^f(N)|\sum_{i=1}^{N}\nabla_i|\Psi^i(N)\rangle\right|^2 \tag{64}$$

and is termed "neglect of retardation" or "the dipole approximation". A further convenience that thus arises is being able to write the matrix element in Eq. (64) in any of the three forms:[124]

$$\begin{aligned}\langle\Psi^f(N)|\sum_{i=1}^{N}\nabla_i|\Psi^i(N)\rangle &= \frac{i}{\hbar}\langle\Psi^f(N)|\sum_{i=1}^{N}\hat{p}_i|\Psi^i(N)\rangle \\ &= \frac{m(h\nu)}{\hbar^2}\langle\Psi^f(N)|\sum_{i=1}^{N}\mathbf{r}_i|\Psi^i(N)\rangle \\ &= \frac{1}{h\nu}\langle\Psi^f(N)|\sum_{i=1}^{N}\nabla_i V|\Psi^i(N)\rangle\end{aligned} \tag{65}$$

The equality of these three forms can be proven by means of commutation relations for the exact wave functions corresponding to any Hamiltonian of the form of Eq. (24); the first form is denoted "momentum" or "dipole-velocity", the second "dipole-length", and the third "dipole-acceleration". In the last form, $V = V(\mathbf{r}_1, \mathbf{r}_2, \ldots, \mathbf{r}_N)$ is the potential represented by the electron-electron repulsion and electron-nuclear attraction terms in the Hamiltonian.

There are several levels of accuracy that can be used for the evaluation of matrix elements such as those in Eq. (64). The most often used approximation begins by assuming a strongly "one-electron" character for the photoemission process, and represents the initial state as an antisymmetrized product of the "active" kth orbital $\phi_k(1)$ from which emission is assumed to occur and an $(N-1)$-electron remainder $\Psi_R(N-1)$ representing the "passive" electrons:

$$\Psi^i(N) = \hat{A}(\phi_k(1)\chi_k(1), \Psi_R(N-1)) \tag{66}$$

In the weak-coupling limit, the final state is further given very accurately by

$$\Psi^f(N) = \hat{A}(\phi^f(1)\chi^f(1), \Psi^f(N-1)) \tag{67}$$

where for brevity the index K (or most simply k) on the ionic wave function $\Psi^f(N-1)$ has been suppressed, and f specifies the kinetic energy and any additional quantum numbers necessary for the continuum orbital $\phi^f(1)$. If it is further assumed that the primary $k \rightarrow f$ excitation event is rapid or "sudden" with respect to the relaxation times of the passive-electron probability distribution, the evaluation of N-electron matrix elements for a general one-electron transition operator $\hat{t}$ depending only on spatial coordinates (such as any of those in Eq. 65)) yields:[90, 131]

$$\langle\Psi^f(N)|\sum_{i=1}^{N}\hat{t}_i|\Psi^i(N)\rangle = \langle\phi^f(1)|\hat{t}|\phi_k(1)\rangle\langle\Psi^f(N-1)|\Psi_R(N-1)\rangle \tag{68}$$

The use of this expression is often termed the "sudden approximation", and it has proven to be very successful for predicting the intensities of various types of many-electron fine structure observed in XPS spectra (see, for example, Sections V.C, and V.D). Transition probabilities and cross-sections are thus in this limit proportional to

$$|\langle\phi^f(1)|\hat{t}|\phi_k(1)\rangle|^2|\langle\Psi^f(N-1)|\Psi_R(N-1)\rangle|^2 \tag{69}$$

and involve a one-electron matrix element and an $(N-1)$-electron overlap integral between the ionic wave function and the passive-electron remainder $\Psi_R(N-1)$. It should be noted that $\Psi_R(N-1)$ is thus not a valid ionic wave function, but rather a non-unique "best" representation of the initial-state passive electrons. In order for the overlap integral to be non-zero, symmetry requirements further dictate that both $\Psi^f(N-1)$ and $\Psi_R(N-1)$ must correspond to the same overall irreducible representation; this is the origin of the so-called "monopole selection rule", which is discussed in more detail in Section V.D.2.

It is necessary also to consider criteria for determining whether the sudden approximation can be used or not.[133, 134] If the excitation from a given subshell k gives rise to a set of final state energies $E^f(N-1, K)$; $K = 1, 2, \ldots$, then the simplest criterion for the validity of the sudden approximation is that[133]

$$[E^f(N-1, K) - E^f(N-1, K')]\tau'/\hbar \ll 1 \tag{70}$$

where τ' is the time required for the $k \rightarrow f$ photoelectron to leave the system, and K and K' can range over any pair of final energies with significant intensity in the set. As an indication of the orders of magnitude occurring in this inequality, for a typical x-ray photoelectron of $E_{kin} = 1000$ eV, $v/c \approx 0.06$ or $v \approx 2 \times 10^9$ cm/s. For a typical atomic diameter of 2 Å, the escape time can thus be roughly estimated as $\tau' \approx (2 \times 10^{-8})/2 \times 10^9) \approx 10^{-17}$ s. Thus, $\tau'/\hbar \approx 1/65$ eV^{-1}, and for final state separations much larger than 10 eV, the sudden approximation would appear to be violated. However, calculations by Åberg[133] and by Carlson, Krause, and co-workers[135] using the sudden approximation have given reasonable agreement with experiment for several systems for which this inequality was not fully satisfied. On the other hand, Gadzuk and Sunjic[134] have considered in more detail the question of transit

times and relaxation times in XPS, and have concluded that even the typical excitation energies in XPS of ~1·5 keV may not be sufficient to reach fully the sudden limit. This question thus requires further study.

An alternative, and in certain respects more general, description of the initial and final states in the transition matrix element is to use single-determinant Hartree Fock wave functions. If these are calculated accurately for both states, thus including relaxation effects, the relevant wave functions are

$$\Psi^I(N) = \hat{A}(\phi_1\chi_1, \phi_2\chi_2, \ldots, \phi_k\chi_k, \ldots, \phi_N\chi_N) \tag{71}$$

$$\Psi^J(N) = \hat{A}(\phi_1'\chi_1, \phi_2'\chi_2, \ldots, \phi^J\chi^J, \ldots, \phi_N'\chi_N) \tag{72}$$

and the transition matrix element becomes[136, 137]

$$\langle\Psi^J(N)|\sum_{i=1}^{N} \hat{t}_i|\Psi^I(N)\rangle = \sum_m \sum_n \langle\phi_m'(1)|\hat{t}|\phi_n(1)\rangle D^{IJ}(m|n) \tag{73}$$

where the double sum on m and n is over *all* occupied orbitals and $D^{IJ}(m|n)$ is an $(N-1)\times(N-1)$ passive-electron overlap determinant. $D^{IJ}(m|n)$ is thus equal to the signed minor formed by removing the mth row and nth column from the $N\times N$ determinant D^{IJ} whose elements are overlaps between initial- and final-state one-electron orbitals. That is, the pq element is $(D^{IJ})_{pq} = \langle\phi_p'\chi_p|\phi_q\chi_q\rangle$. Many of the N^2 matrix elements contributing to Eq. (73) are zero or near-zero for three reasons: (1) one-electron matrix-element selection rules associated with $\langle\phi_m'(1)|\hat{t}|\phi_n(1)\rangle$; (2) monopole selection rules arising from the one-electron overlaps $\langle\phi_p'\chi_p|\phi_q\chi_q\rangle$, since ϕ_p' and ϕ_q must have the same spatial symmetry and the spin functions χ_p and χ_q must be equal for the overlap to be non-zero; and (3) the near orthonormality of the passive-orbital sets $\phi_1, \ldots, \phi_{k-1}, \phi_{k+1}, \ldots, \phi_N$ and $\phi_1', \ldots, \phi_{k-1}', \phi_{k+1}', \ldots, \phi_N'$, so that $\langle\phi_p'|\phi_p\rangle \approx 1{\cdot}0$ and $\langle\phi_p'|\phi_q\rangle \approx 0$ for $p \neq q$. Additional matrix elements corresponding to transitions other than $k \to f$ that cannot be ruled out on these bases have furthermore been shown by Åberg[133] to be negligible for a high-excitation-energy limit, which leaves finally a first-order result analogous to the sudden-approximation expression

$$\langle\Psi^J(N)|\sum_{i=1}^{N} \hat{t}_i|\Psi^I(N)\rangle = \langle\phi^J(1)|\hat{t}|\phi_k(1)\rangle D^{IJ}(f|k) \tag{74}$$

Various methods for calculating such overlap determinants for atoms have been investigated by Mehta *et al.*,[102] and it has been concluded that the use of a diagonal-element product is accurate to within ~1-2%:

$$\langle\Psi^J(N)|\sum_{i=1}^{N} \hat{t}_i|\Psi^I(N)\rangle = \langle\phi^J(1)|\hat{t}|\phi_k(1)\rangle \sum_{j=1, j\neq k}^{N} \langle\phi_j'|\phi_j\rangle \tag{75}$$

Proceeding one step further to an unrelaxed, "frozen orbital", or "Koopmans' Theorem" final state in which $\phi_j' = \phi_j$ for $j \neq k$ finally leads to the simplest approximation for such matrix elements:

$$\langle\Psi^J(N)|\sum_{i=1}^{N} \hat{t}_i|\Psi^I(N)\rangle = \langle\phi^J(1)|\hat{t}|\phi_k(1)\rangle \tag{76}$$

The majority of matrix element and cross-section calculations to date have used this last form.

At the level of sudden approximation calculations utilizing Eq. (68) or (74), two experimentally useful spectral sum rules have been pointed out. The first states that the weighted-average binding energy over all final ionic states $\Psi^J(N-1, K)$ associated with a given primary $k \to f$ excitation is simply equal to the Koopmans' Theorem binding energy of $-\epsilon_k$. That is, if I_K is the intensity of a transition to $\Psi^J(N-1, K)$ corresponding to a binding energy $E_b(K)$, then

$$-\epsilon_k = \sum_K I_K E_b(K) \Big/ \sum_K I_K = \sum_K |\langle\Psi^J(N-1, K)|\Psi^I_R(N-1)\rangle|^2 E_b(K) \tag{77}$$

This was first pointed out in connection with XPS by Manne and Åberg,[90] and has also been derived in a somewhat different context by Lundquist.[138] The significance of this sum rule is illustrated in Fig. 8, and it requires that,

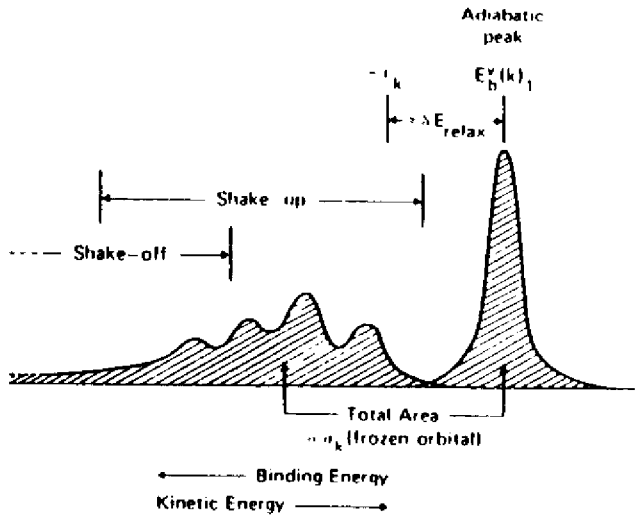

Fig. 8. Schematic illustration of a photoelectron spectrum involving shake-up and shake-off satellites. The weighted average of all binding energies yields the Koopmans' Theorem binding energy $-\epsilon_k$ [sum rule (77)], and the sum of all intensities is proportional to a frozen-orbital cross section σ_k [sum rule (78)]. The adiabatic peak corresponds to formation of the ground state of the ion [$E_b(k)_1 \equiv E_b(K=1)$].

in order for relaxation to occur in forming the lowest-binding-energy "primary" or "adiabatic" final state corresponding to the ionic ground state, excited ionic states corresponding to binding energies higher than $-\epsilon_k$ must also arise. The peaks due to these states have been variously called "shake-up", "shake-off", "many-electron transitions", "configuration-interaction satellites", or "correlation peaks", and more specific illustrations are given in Section V.D. The high-intensity lowest-binding-energy peak has often been associated with a "one-electron transition", although this name is unduly restrictive in view of the inherently many-electron nature of the photoemission process. Thus, the intimate relationship between relaxation and correlation is demonstrated, although it still is possible to determine uniquely a relaxation energy with initial- and final-state Hartree–Fock wave functions that are often assumed to be uncorrelated in the sense that E_{corr} is measured relative to them. The second sudden-approximation sum rule deals with intensities, and it states that the sum of all intensities associated with the states $\Psi^f(N-1, K)$ is given by

$$I_{tot} = \sum_K I_K = C \sum_k |\langle \phi^f(1)|\hat{l}|\phi_k(1)\rangle|^2 |\langle \Psi^f(N-1, K)|\Psi_R(N-1)\rangle|^2 = C|\langle \phi^f(1)|\hat{l}|\phi_k(1)\rangle|^2 \quad (78)$$

where C is a constant for a given photon energy. One experimental consequence of this sum rule is that matrix elements and cross-sections calculated with unrelaxed final-state orbitals and thus using Eq. (76) apply only to absolute intensities summed over all states $\Psi^f(N-1, K)$, as was first pointed out by Fadley.[137] Thus, absolute photoelectron intensities for the usually-dominant ionic-ground-state peaks may be below those predicted by unrelaxed or frozen-orbital cross-sections, as has been noted experimentally by Wuilleumier and Krause;[139] by contrast, x-ray absorption coefficients, which inherently sum over all final states for a given $k \to f$ excitation, are well predicted by unrelaxed cross-sections.[137]

At a higher level of accuracy than any of the approximations discussed up to this point, configuration-interaction wave functions can also be used in the calculation of matrix elements and cross-sections.[91, 127] In particular, Manson[91] has discussed in a general way the effects that this can have, pointing out several mechanisms by which calculated intensities can be significantly modified by the inclusion of CI in the initial-state wave function and the final-state wave function. For computational convenience, it is customary (although not essential) to use the same set of orthonormal one-electron orbitals $\phi_1, \phi_2, \ldots, \phi_M$ $(M > N)$ in making up the configurations of both initial and final states. This apparent lack of allowance for relaxation in the final state can be more than compensated by using a large number of configurations with mixing coefficients C_j^I and C_j^f that are optimized for both states:

$$\Psi^I(N) = \sum_j C_j^I \Phi_j^I(N) \quad (79)$$

$$\Psi^f(N) = \sum_m C_m^f \Phi_m^f(N) \quad (80)$$

The exact expressions for matrix elements determined with such wave functions are rather complex, particularly if more than one continuum orbital is included, corresponding to an allowance for continuum CI (also referred to as interchannel coupling or close coupling).[91] Although such continuum effects may be important in certain special cases (see Section V.D.5), several many-electron phenomena noted in XPS spectra can be well explained in terms of only initial-state CI and final-state-ion CI. In visualizing these effects, it is thus useful to take a sudden approximation point of view, in which a single primary $k \to f$ transition is considered and the individual configurations $\Phi_j^I(N)$ and $\Phi_m^f(N)$ are thus written as antisymmetrized products with forms analogous to Eqs (66) and (67):

$$\Phi_j^I(N) = \hat{A}(\phi_k(1)\chi_k(1), \Phi_j^I(N-1)) \quad (81)$$

$$\Phi_m^f(N) = \hat{A}(\phi^f(1)\chi^f(1), \Phi_m^f(N-1)) \quad (82)$$

In these equations, the $(N-1)$-electron factors can if desired be indexed identically, so that, for the fixed one-electron basis set, $\Phi_j^I(N-1) = \Phi_m^f(N-1)$ if $j = m$ and thus also $\langle \Phi_j^I(N-1)|\Phi_m^f(N-1)\rangle = \delta_{jm}$. Matrix elements in this limit are then given by repeated application of Eq. (68) as

$$\langle \Psi^f(N)|\sum_{i=1}^{N} \hat{l}_i|\Psi^I(N)\rangle = \langle \phi^f(1)|\hat{l}|\phi_k(1)\rangle [\sum_j (C_j^f)^* C_j^I] \quad (83)$$

Thus, the mixing of various configurations into either the initial or final states can affect the observed intensity of a given final state appreciably, as it is only if a certain configuration has a non-zero coefficient in both states that it will contribute a non-zero $(C_j^f)^* C_j^I$ product. For the useful limiting case in which a single configuration $j = 1$ dominates the initial state, then $C_j^I \approx 1.0$, $C_j^I \approx 0$ for $j \neq 1$, and the square of the matrix element (83) for transitions to a given final state is simply

$$\left|\langle \Psi^f(N)|\sum_{i=1}^{N} \hat{l}_i|\Psi^I(N)\rangle\right|^2 \propto |C_1^f|^2 \quad (84)$$

(If relaxation is permitted in the final-state one-electron orbitals, then overlap integrals of the form $\langle \Phi_m^f(N-1)|\Phi_j^I(N-1)\rangle = S_{jm}$ must be computed,[14] and Eqs (83) and (84) become more complex. However, in general $S_{jm} \approx \delta_{jm}$.) Such CI effects are important in understanding the simplest forms of multiplet

splittings (Section V.C), many-electron effects in multiplet splittings (Section V.C), and the intensities of various many-electron satellites (Section V.D).

The inherent requirement of relaxed final-state orbitals in sudden approximation calculations using single-determinant Hartree–Fock wave functions has led to a certain amount of confusion when comparing this model with the results of CI calculations. Manson,[91] for example, has pointed out that the use of relaxed final-state orbitals in such single-determinant calculations yields matrix elements of no higher accuracy than those resulting from the inclusion of only a limited form of initial-state configuration interaction. Thus, there are several types of effects that can only be adequately discussed in terms of a more complete CI treatment.

In the next three sections, matrix element and cross-section calculations for atoms, molecules, and solids are discussed at the often-used level of unrelaxed final-state orbitals that results in Eq. (76).

2. *Atoms.* For a closed-shell atom in the limit of no final-state passive-electron relaxation and a non-relativistic Hamiltonian, each emission event is characterized by a well-defined transition from spin-orbital $\phi_k\chi_k = \phi_{nlm_l}\chi_{m_s}$ to spin-orbital $\phi^f\chi^f = \phi_{E^f l^f m_l^f}\chi_{m_s^f}$, where E^f is the photoelectron kinetic energy $h\nu - E_b^V(nl)$. The usual dipole selection rules then require that

$$\Delta l = l^f - l = \pm 1 \tag{85}$$

$$\Delta m_l = m_l^f - m_l = 0, \pm 1 \tag{86}$$

$$\Delta m_s = m_s^f - m_s = 0$$

Photoemission is thus divided into two "channels" for $l^f = l+1$ and $l^f = l-1$, with the $l+1$ channel usually being much more important at XPS energies.

The most commonly encountered experimental situation is a collection of atoms whose orientations are random with respect to one another that is exposed to a flux of unpolarized radiation with an angle α between the propagation directions of the radiation and photoelectron (cf. Fig. 7). For this situation, the total photoelectric cross-section for all events involving emission from a given nl subshell can be calculated by summing transition probabilities for all possible one-electron events according to Eq. (63). A general derivation[124, 126, 127, 140] then shows that the total subshell cross section σ_{nl} is, in the dipole-length form,[141] given by

$$\sigma_{nl}(E^f) = \frac{4\pi\alpha_0 a_0^2}{3}(h\nu)[lR_{l-1}^2(E^f) + (l+1)R_{l+1}^2(E^f)] \tag{87}$$

in which α_0 is the fine structure constant, a_0 is the Bohr radius, and the $R_{l\pm1}(E^f)$ are radial matrix elements common to all one-electron dipole matrix elements between ϕ_{nlm_l} and $\phi_{E^f l^f m_l^f}$. (ϕ_{nlm_l} and $\phi_{E^f l^f m_l^f}$ both have the general form of Eq. (36).) These radial integrals are given by

$$R_{l\pm1}(E^f) = \int_0^\infty R_{nl}(r) r R_{E^f,\,l\pm1}(r) r^2\,dr = \int_0^\infty P_{nl}(r) r P_{E^f,\,l\pm1}(r)\,dr \tag{88}$$

where $P_{nl}(r)/r \equiv R_{nl}(r)$ is the radial part of the ϕ_{nlm_l} orbital and $P_{E^f,\,l\pm1}(r)/r \equiv R_{E^f,\,l\pm1}(r)$ is the radial part of the continuum photoelectron orbital $\phi_{E^f l^f m_l^f}$. The differential photoelectric cross-section for a given subshell is furthermore given by the expression[124, 127, 140]

$$\frac{d\sigma_{nl}}{d\Omega}(E^f) = \frac{\sigma_{nl}}{4\pi}[1 - \tfrac{1}{2}\beta_{nl}(E^f)P_2(\cos\alpha)]$$

$$= \frac{\sigma_{nl}}{4\pi}[1 + \tfrac{1}{2}\beta_{nl}(E^f)(\tfrac{3}{2}\sin^2\alpha - 1)] \tag{89}$$

where $\beta_{nl}(E^f)$ is termed the asymmetry parameter, α is the angle between photon propagation direction and electron emission direction, and $P_2(\cos\alpha) = \frac{1}{2}(3\cos^2\alpha - 1)$. $\beta_{nl}(E^f)$ can in turn be calculated from the radial integral $R_{l\pm1}(E^f)$ and certain continuum-orbital phase shifts $\delta_{l\pm1}(E^f)$ that represents the shift in the sinusoidally oscillating character of $R_{E^f,\,l\pm1}(r)$ at large radii relative to the continuum wave functions for a hydrogen atom at energy E^f. The equation for $\beta_{nl}(E^f)$ is

$$\beta_{nl}(E^f) = \frac{\{l(l-1)R_{l-1}^2(E^f) + (l+1)(l+2)R_{l+1}^2(E^f) - 6l(l+1)R_{l+1}(E^f)R_{l-1}(E^f)\cos[\delta_{l+1}(E^f) - \delta_{l-1}(E^f)]\}}{(2l+1)[lR_{l-1}^2(E^f) + (l+1)R_{l+1}^2(E^f)]} \tag{90}$$

and the term in $\cos[\delta_{l+1} - \delta_{l-1}]$ represents an interference between outgoing $l+1$ and $l-1$ waves. Such phase shifts are illustrated for C 2p emission into s and d waves at different $h\nu$ in Figs 9(d) and 9(e).

The allowed range for β_{nl} is $-1 \leq \beta \leq +2$. A positive value of β indicates that photoelectrons are preferentially emitted at angles perpendicular to the photon direction ($\alpha = 90°$), whereas a negative value indicates preferential emission either parallel or anti-parallel to this direction ($\alpha = 0°$ or 180°). A value of $\beta = 0$ yields an isotropic distribution. For s-electron emission, $l = 0$, and only transitions to $l^f = 1$ waves are possible. β is always $+2$ for this case, yielding a differential photoelectric cross-section of the form:

$$\frac{d\sigma_{ns}(E^f)}{d\Omega} = \frac{\sigma_{ns}(E^f)}{4\pi} \cdot \sin^2\alpha \tag{91}$$

with maximum intensity at $\alpha = 90°$ and zero intensity at $\alpha = 0°$ and 180°. For the other limiting case of $\beta = -1$,

$$\frac{d\sigma_{nl}(E^f)}{d\Omega} = \frac{\sigma_{nl}(E^f)}{4\pi} \cdot \cos^2\alpha \tag{92}$$

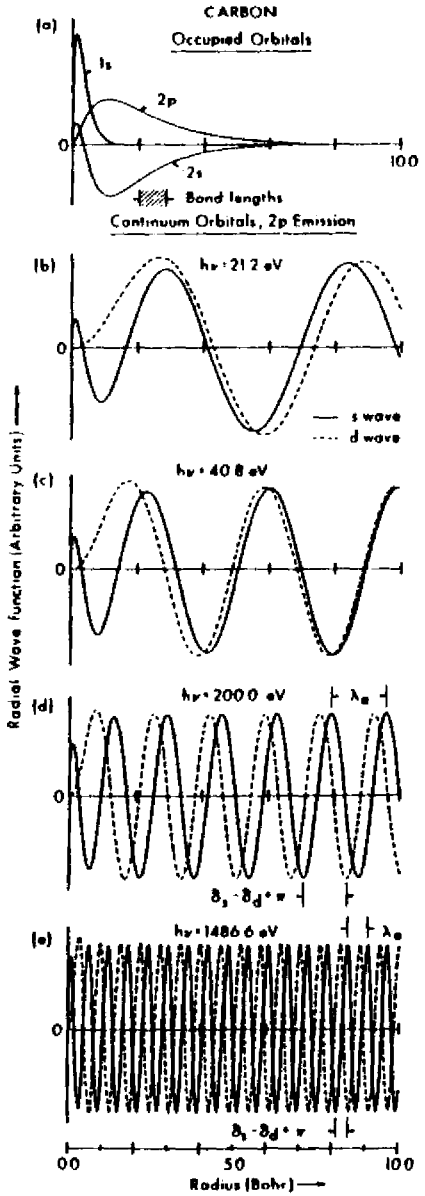

Fig. 9. Radial functions $P(r) = r \cdot R(r)$ for (a) the occupied orbitals of atomic carbon and (b) (c) the continuum photoelectron orbitals resulting from C 2*p* excitation at different photon energies as indicated. Continuum wave functions for both allowed emission channels are shown ($l + 1 = d$ wave, $l - 1 = s$ wave). Note the non-sinusoidal character near the nucleus, and the decrease in the electron deBroglie wavelength λ_e with increasing kinetic energy. The definition of the phase shift $\delta_s - \delta_d + \pi$ is also indicated for $h\nu = 200.0$ eV and 1486.6 eV. In (a), the range of typical bond lengths between carbon and low-to-medium *Z* atoms is also shown for comparison. (S. M. Goldberg and C. S. Fadley, unpublished results.)

the photoelectron intensity is zero at $\theta = 90°$, and has its maximum value at $\theta = 0°$ and 180°. No matter what the value of β is, the form of Eq. (89) dictates that the distribution should be cylindrically symmetric about the photon propagation direction.

Equation (89) is also equivalent to

$$\frac{d\sigma_{nl}(E)}{d\Omega} = A + B \sin^2\alpha \tag{93}$$

where A and B are constants given by $A = (\sigma_{nl}/4\pi)(1 - \beta_{nl}/2)$ and $B = (\sigma_{nl}/4\pi) \cdot 3\beta_{nl}/4$. From an empirical determination of A and B, β can thus be calculated from $\beta_{nl} = 4B/(3A + 2B)$. A comparison between the function predicted by Eq. (93) and experimental results made by Krause[142] is shown in Fig. 10. The parameters A and B have in this case been empirically adjusted to give the best fit to data obtained for photoemission from Kr 3*s*, Kr 3*p*, and Kr 3*d* levels with MgKα x-rays. The data are reasonably well described by Eq. (93), although a slight systematic deviation is apparent; this has been associated with effects due to the breakdown of the dipole approximation

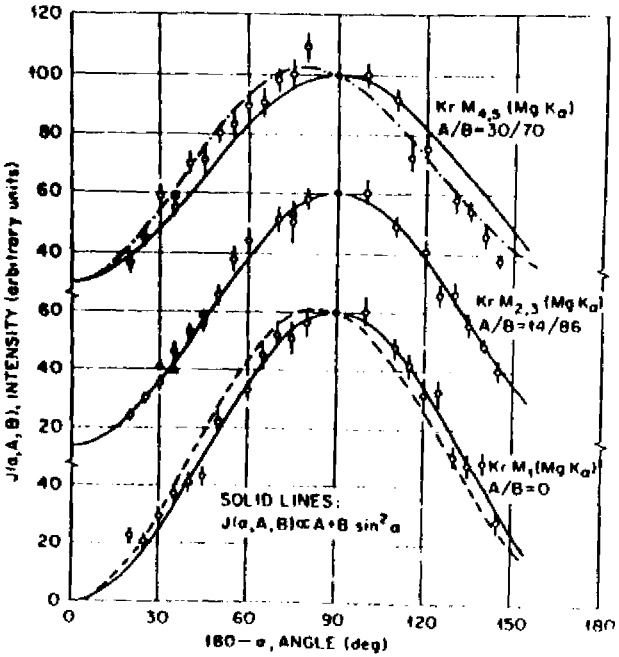

Fig. 10. Experimental angular distributions of 3*s* (= M_1), 3*p* (= $M_{2,3}$), and 3*d* (= $M_{4,5}$) photoelectrons excited from gaseous Kr with MgKα x-rays. The curves represent least-squares fits to the data points of a relationship of the form of Eq. (93), in which A and B were treated as empirical constants. (From Krause, ref. 142.)

(neglect of retardation).[142] Note that the 3s data are consistent with Eq. (91) as expected. Also, a decrease in β with increasing orbital angular momentum is observed, although β is clearly positive for all three cases presented in Fig. 10. Wuilleumier and Krause[139] have also presented a similar analysis for Ne2p emission that extends up to XPS excitation energies.

Total atomic subshell cross-sections for photon energies relevant to XPS have been calculated in various studies.[126, 143-151] These calculations have made use of both the non-relativistic theory outlined above, as well as relativistic methods based upon the Dirac equation.[144, 145, 151] In the non-relativistic calculations, the method introduced by Cooper and Manson[126, 146, 147] has been most utilized: cross-sections are calculated from matrix elements between initial-state orbitals determined in a Hartree-Fock Slater approximation (as those generated by Herman and Skillman for all atoms)[93] and final-state orbitals determined from a one-electron radial Schroedinger equation with a central potential $V(r)$ representing the interaction with the nucleus and $(N-1)$ electrons in the ion (again of the form determined by Herman and Skillman). More recently, Scofield[151] has used a relativistic analogue of this procedure to calculate MgKα and AlKα total subshell cross sections σ_{nlj}, $j=l\pm\frac{1}{2}$ for all elements in the periodic table; spin orbit effects split each subshell into two j components with occupancy $2j+1$. The use of such a cross-section tabulation in analyzing XPS spectral intensities is discussed below in Section III.F.3.

In general, it is found that for $h\nu$ well above threshold, as is the case in XPS measurements, transitions to $l'=l+1$ are much more probable than those to $l'=l-1$.[126, 147] Thus, the term $(l+1)R_{l+1}^2(E')$ dominates the term $lR_{l-1}^2(E')$ in Eq. (87). Also, $\sigma_{nl}(E')$ is generally a decreasing function of E' for $h\nu$ well above threshold. However, large oscillations and minima in the cross-section may occur as $h\nu$ is increased above threshold.[126, 146, 147] Such oscillations can be explained in terms of the changing overlap character of an oscillatory $P_{nl}(r)$ and an oscillatory $P_{E,l\pm1}(r)$ with changing E'.[126] As E' is increased, the effective wavelength of the radial oscillations in $P_{E,l\pm1}$ decreases and the oscillations penetrate more deeply into the region of non-zero $P_{nl}(r)$ "within" the atom. This effect is illustrated quantitatively in Fig. 9 for continuum orbitals corresponding to emission from a C2p subshell at $h\nu=21{\cdot}2$, 40·8, 200, and 1486·6 eV, as calculated by Goldberg and Fadley using the Manson/Cooper program. For a given $h\nu$, the matrix element $R_{l\pm1}(E')$ thus may consist of contributions due to the constructive overlap of one or more lobes in $P_{nl}(r)$ and $P_{E,l\pm1}$. If, as E' is varied, the relative signs of the overlapping lobes change, $R_{l\pm1}(E')$ may change sign, and therefore at some kinetic energy intermediate between the sign change, a zero or minimum in $E_{l\pm1}(E')$ and $\sigma_{nl}(E')$ can result. A corollary of this argument is that atomic orbitals $P_{nl}(r)$ which exhibit no oscillations with r should show cross-sections which decrease smoothly with increasing E' and exhibit no zeroes or minima.[126] Examples of such orbitals would be 1s, 2p, 3d, and 4f.

Comparisons of total cross-section calculations with experiment are often made through the total atomic absorption coefficient for x-rays, which at lower x-ray energies of $\lesssim 10$ eV consists essentially of a sum over the several subshell cross-sections. Such comparisons yield reasonably good agreement between experiment and theory (~ 5-10%) except near threshold where $h\nu \approx E_b^V(nl)$.[137, 143, 145, 150, 152] Cooper and Manson[147] have also calculated relative subshell cross-sections in XPS which compare favorably with the experimental values of Krause[142] shown in Fig. 10.

Asymmetry parameter calculations have also been performed for various atoms at the Manson/Cooper level, and the values obtained for $\beta_{nl}(E')$ are also in reasonable agreement with experiment ($\sim \pm 5\%$).[147] Manson[153] and Kennedy and Manson[149] have also pointed out that for certain subshells, theory predicts that $\beta_{nl}(E')$ may exhibit large oscillations with E'. Finally, Reilman *et al.*[154] have calculated β values spanning all elements in the periodic table for the two common XPS x-rays MgKα and AlKα; interpolations in this table can be made to any atomic subshell. Thus, the use of Scofield's σ_{nlj} values[151] together with the β_{nl} tables of Reilman *et al.*[154] permits determining a reasonably accurate differential cross-section for any situation encountered in typical XPS experiments (even though it does represent a mixture of relativistic and non-relativistic calculations). The data of Fig. 10 make it clear that in order for comparisons of peak intensities in photoelectron spectra to be meaningful, the angular geometry of the experiment must be known and allowed for via $d\sigma/d\Omega$. Neglecting the effect of the asymmetry parameter is equivalent to assuming

$$\frac{d\sigma}{d\Omega} = \frac{\sigma}{4\pi} \tag{94}$$

a relationship that is only rigorously true for a "magic-angle" experimental geometry with $P_2(\cos\alpha)=0$ or $\alpha=54{\cdot}74°$.

A further important point in connection with atomic cross-sections is that, for systems initially possessing an open shell, the calculations outlined above will represent a sum of cross-sections leading to the various allowed final multiplet states (generally describable as L, S terms).[125] Provided that these multiplets are degenerate, no observable effects are suppressed by such a summation. However, in many cases of both core-level and valence-level emission, these multiplets are resolvable from one another, so that some procedure within a one-electron-transition model is needed for predicting the partitioning of the cross-section into the various multiplets. For emission from a closed inner subshell, the weight of each multiplet is just its total

multiplicity,[155] so that

$$\text{Intensity} \propto (2S^f + 1)(2L^f + 1) \tag{95}$$

For emission from a partially-filled valence subshell, more complex expressions involving fractional parentage coefficients arise; these have been discussed in detail by Cox and co-workers,[155, 156] and by Bagus, Freeouf, and Eastman.[157] These references include extensive numerical tables. It has also recently been pointed out by Dill *et al.*[158] that for emission from a given nl subshell β_{nl} may vary from mutliplet to multiplet, but such effects are small enough to be neglected in first approximation.

Finally, it should be noted that, although all of the foregoing has assumed randomly oriented atoms (as would be characteristic of gas-phase or polycrystalline specimens), the situation of an array of atoms with definite orientation can be important for the case of chemical bonding at a well-defined single-crystal surface. Gadzuk[159] has considered the theoretical expressions resulting for oriented transition-metal atoms on surfaces, and finds potentially significant effects on the angular dependence of photoelectron emission from such atoms.

3. *Molecules and Molecular-orbital Studies.* In general, less is known both experimentally and theoretically about molecular cross-sections, primarily due to the greater difficulty of accurately calculating either the initial-state orbitals or especially the final-state orbitals involved.

For core-level emission to typical XPS energies of a few hundred eV or more, the use of atomic subshell cross-sections is probably a very good approximation at the level of a one-electron model of photoemission, because the initial-state orbital is very little altered by chemical bonding and the final-state hole is highly localized and atomic-like, thus leading to a continuum orbital with very nearly atomic properties. (At very low energies of excitation, it is interesting to note however, that even core levels are predicted to show cross-section resonances due to molecular geometry.[160]) Based upon theoretical calculations by Nefedov *et al.*,[161] changes in the magnitudes of core-level cross-sections with ionization state are further expected to be very small (~0-1% per unit charge), although in some cases such effects could be significant.

In valence-level emission, the determination of cross-sections becomes more complex. The initial-state orbital ϕ_k is usually written as a linear combination of atomic orbitals (LCAO):

$$\phi_k = \sum_{A\lambda} C_{A\lambda k}\phi_{A\lambda} \tag{96}$$

in which k represents a symmetry label appropriate for the molecule (e.g. $2\sigma_g$ or $1\pi_u$ in O_2), $\phi_{A\lambda}$ is an atomic orbital (AO) for which A designates the atom and λ the symmetry (e.g. A = oxygen and $\lambda = 1s$ in O_2), and the $C_{A\lambda k}$'s

are expansion coefficients. Such an LCAO description can be made at any of various levels of accuracy, as is common in quantum-chemical calculations. The final-state orbital ϕ^f presents more of a problem, however, as it must be computed so as to take account of the full molecular geometry, even though at high excitation energies and large distances from the center of mass it will look very much like an atomic continuum orbital of the same kinetic energy. Various approximations have been used for such final states in cross-section calculations relevant to XPS: (1) A simple plane-wave (PW) of the form $\exp(i\mathbf{k}\cdot\mathbf{r})$ has been used in several studies,[162, 163] although it seems doubtful that highly quantitative results can be achieved in this approximation because the plane-wave is in no way sensitive to the true potential near the atomic centers and neither is it properly orthogonal to the initial-state orbital. By analogy with the atomic case, one would expect correct final states to show behavior near the nucleus much like that shown in Fig. 9. (2) Plane-waves orthgonalized to the occupied core- and valence-orbitals (OPW's) have also been utilized, for example, by Rabalais, Ellison, and co-workers,[162] but doubts concerning their quantitative accuracy at high energies have also been raised by Ritchie.[164] Also, the use of either PW or OPW approximations in the atomic case has been shown by Williams and Shirley[165] to be grossly inadequate. (3) Ritchie[164] has used an expansion in terms of partial waves of different l character, noting that the non-spherical symmetry of the molecular geometry may mix these, introducing complexities not found in the atomic case. (4) More recently, Dill,[160] Dehmer,[160] and Davenport[166] have discussed the use of the multiple-scattering $X\alpha$[167] method in molecular cross-section calculations and, at this point, it shows considerable promise of being able to provide very useful and reasonably accurate numerical results. The calculation of molecular cross-sections has been reviewed recently by Dehmer,[168] as well as by Huang and Rabalais[130] elsewhere in this series.

An additional factor that must be considered in molcular cross-section and lineshape analyses is that various final vibrational states may be reached in a given photoemission event, even in the simple case for which only a single vibrational mode is initially populated. These vibrational excitations are responsible for the bands observed in gas-phase UPS spectra,[97] for example, and similar effects have been noted in core-level XPS emission (see Section V.E). If the Born-Oppenheimer approximation is used, then the electronic cross-section (differential or total) can be partitioned among the various vibrational states simply by multiplying by appropriate Franck Condon factors, as indicated previously in Eq. (63).

Whatever initial- and final-state approximations are utilized, it is nonetheless a general consequence of the conservation of parity and angular momentum that the overall form of the differential photoelectric cross-section of a randomly oriented collection of Born-Oppenheimer molecules exposed

to unpolarized radiation will have the same form as that for the atomic case,[140, 168] namely, Eqs (89) or (93). The calculation of σ_k and β_k proceeds by a different method from that in atoms, of course. The UPS angular distributions of a number of small molecules have been measured by Carlson *et al.*[169, 170] and they are found to follow the predicted form $A + B\sin^2\alpha$, with all members of each valence vibrational band showing very nearly the same distinct β value (with a few exceptions perhaps indicative of a partial breakdown of the Born–Oppenheimer approximation).

As in atoms, molecular cross-sections for open-shell systems also may represent emission into several non-degenerate multiplet states. Cox and Orchard[155] have derived the relative probabilities of reaching different final electronic states for emission from both filled and unfilled subshells. (A specialization of their results to filled-subshell emission from atoms yields Eq. (95).)

As a final general point concerning molecular cross-sections, it should be noted that, although all of the foregoing results assumed random orientation, the situation of surface chemical bonding on an atomically-ordered substrate may yield a set of molecules with a definite orientation. Dill[171] has presented a general theoretical formalism for evaluating such oriented-molecule differential cross-sections, and Davenport[160] has performed numerical calculations for oriented carbon monoxide based upon the $X\alpha$ method. Primary emphasis in all such theoretical studies to date has been on ultraviolet excitation, however.

In analyzing XPS emission from molecular valence levels, much use has also been made of an approximation first suggested by Gelius.[172] Although originally derived by assuming a plane-wave final state $\exp(i\mathbf{k}\cdot\mathbf{r})$, a slightly different procedure will be used here that both leads to the same result and also automatically includes certain correction terms that are often omitted. The initial-state molecular orbital (MO) ϕ_k is assumed to be of LCAO form [Eq. (96)] with the implicit restriction (not always stated) that the atomic orbitals $\phi_{A\lambda}$ be reasonable representations of *true* atomic orbitals, not just single-radial-lobe basis functions, for example, of Slater or Gaussian type. Consider a hypothetical final-state orbital ϕ^f corresponding to $E^f = h\nu - E_b^V(k)$ that has somehow been determined with arbitrary accuracy. The matrix element for photoemission from the molecular orbital will then be given by

$$\langle\phi^f|r|\phi_k\rangle = \langle\phi^f|r|\sum_{A\lambda} C_{A\lambda k}\phi_{A\lambda}\rangle$$

$$= \sum_{A\lambda} C_{A\lambda k}\langle\phi^f|r|\phi_{A\lambda}\rangle \qquad (97)$$

The photoelectric cross-section will be proportional to the square of this matrix element. If the atomic orbitals and LCAO coefficients are assumed to have been constructed as real, this square will be given by

$$|\langle\phi^f|r|\phi_k\rangle|^2 = \sum_{A'\lambda'}\sum_{A\lambda} C_{A'\lambda' k}C_{A\lambda k}\langle\phi^f|r|\phi_{A'\lambda'}\rangle\langle\phi^f|r|\phi_{A\lambda}\rangle$$

$$= \sum_{A\lambda} |C_{A\lambda k}|^2|\langle\phi^f|r|\phi_{A\lambda}\rangle|^2$$

$$+2\sum_{A'\lambda'}\sum_{\substack{A\lambda \\ (A\lambda > A'\lambda')}} C_{A'\lambda' k}C_{A\lambda k}\langle\phi^f|r|\phi_{A'\lambda'}\rangle\langle\phi^f|r|\phi_{A\lambda}\rangle \qquad (98)$$

The MO cross-section thus depends on matrix elements between a true molecular final state ϕ^f, and good approximations to atomic orbitals $\phi_{A\lambda}$. The strongly attractive potential near each atomic center will furthermore tend to make ϕ^f in the near-nuclear region look very much like the final-state orbital for photoemission from an isolated atom at the same kinetic energy. At XPS energies, the atomic continuum orbitals for all valence AO's should furthermore be very similar in oscillatory behavior, as the kinetic energies are all very close for a given $h\nu$. It can further be argued that it is the region near the nucleus in which most of the non-zero contributions to the matrix elements $\langle\phi^f|r|\phi_{A\lambda}\rangle$ arise, because as the distance from each nucleus is increased, ϕ^f rapidly becomes an oscillatory function with periods of only $\sim$0·35 Å (the de Broglie wavelength λ_e of the photoelectron). This is illustrated for C2*p* emission from atomic carbon in Fig. 9. Thus, it is only near the nucleus that the initial-state AO's have sufficiently dense spatial variations to yield a largely non-cancelling contribution to the matrix element; in the diffuse, slowly-varying tails of the valence AO's between the atoms, the oscillations in ϕ^f will yield an approximate cancellation in the matrix element integration. (This same argument is made by Gelius[172] using the more approximate plane-wave final state.) The squares of each of the matrix elements in Eq. (98) are therefore expected to be approximately proportional to the corresponding atomic cross-section:

$$|\langle\phi^f|r|\phi_{A\lambda}\rangle|^2 \propto d\sigma_{A\lambda}^{(AO)}/d\Omega$$

or

$$\langle\phi^f|r|\phi_{A\lambda}\rangle \propto \pm(d\sigma_{A\lambda}^{(AO)}/d\Omega)^{\frac{1}{2}} \qquad (99)$$

and the final result for the molecular cross-section can be rewritten as

$$d\sigma_k^{(MO)}/d\Omega \propto \sum_{A\lambda} |C_{A\lambda k}|^2(d\sigma_{A\lambda}^{(AO)}/d\Omega)$$

$$+2\sum_{A'\lambda'}\sum_{\substack{A\lambda \\ (A\lambda > A'\lambda')}} (\pm)C_{A'\lambda' k}C_{A\lambda k}(d\sigma_{A'\lambda'}^{(AO)}/d\Omega)^{\frac{1}{2}}(d\sigma_{A\lambda}^{(AO)}/d\Omega)^{\frac{1}{2}} \qquad (100)$$

The cross-terms in Eq. (100) are generally neglected, yielding the most commonly-used form of this model:

$$d\sigma_k^{(MO)}/d\Omega \propto \sum_{A\lambda} |C_{A\lambda k}|^2(d\sigma_{A\lambda}^{(AO)}/d\Omega) \qquad (101)$$

$|C_{A\lambda k}|^2$ is the net population of atomic orbital $A\lambda$ in molecular orbital k. In applications of Eq. (101), the net population is often replaced by the gross population $P_{A\lambda k}$ defined as

$$P_{A\lambda k} = |C_{A\lambda k}|^2 + \sum_{\substack{A'\lambda' \\ (A' \neq A)}} C_{A\lambda k} C_{A'\lambda' k} \langle \phi_{A\lambda} | \phi_{A'\lambda'} \rangle \qquad (102)$$

although Eq. (100) makes it clear that this is only a very crude way of allowing for overlap affects. Discussions of additional theoretical complexities have also appeared in several studies.[172-176]

The model summarized in Eqs (101) and (102) has been used with reasonable success in analyzing valence spectra of both molecules[172, 173] and solids in which quasi-molecular units (for example, polyatomic ions) exist.[174-176] In general, empirical relative atomic cross-sections are determined for atoms or simple molecules, and then used, together with an LCAO calculation for the system under study, to generate a theoretical spectrum. One such example for CF_4 is shown in Fig. 11, and it is clear that it correctly predicts relative intensities to a very high accuracy.

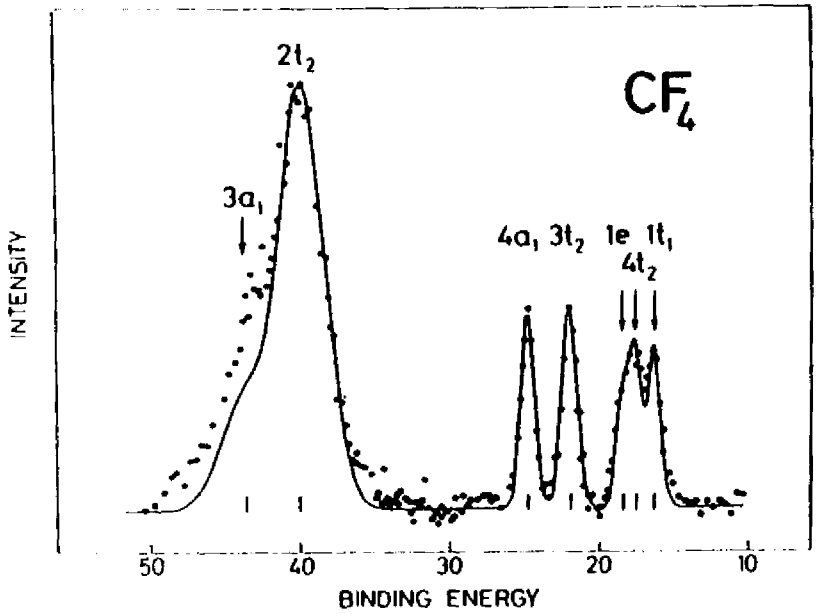

Fig. 11. Experimental XPS spectrum for the valence levels of gaseous CF_4 (points) in comparison with a theoretical curve based upon Eqs (101) and (102). Relative atomic subshell cross-sections were determined experimentally. MgKα radiation was used for excitation. (From Gelius, ref. 172.)

4. *Solids and Valence-band Studies.* X-ray photoemission from solids has been very successfully analyzed in terms of a three-step model first utilized in ultraviolet photoemission studies by Berglund and Spicer.[177] The steps involved are: (1) a one-electron excitation occurring somewhere below the solid surface from an initial-state orbital ϕ_k at energy E to a final-state orbital ϕ^f with an energy E^f greater by $h\nu$, (2) electron transport via ϕ^f to the surface, during which elastic and inelastic scattering events may occur, and (3) passage of the electron through the surface, at which a small potential barrier may cause refraction or back-reflection to occur. The electron states involved are generally assumed to be characteristic of the bulk material. The one-electron energies E and E^f may be measured with respect to the Fermi energy, the vacuum level, or some other reference; in any case E^f can be easily connected with the measured kinetic energy E_{kin}. An additional zeroth step involving penetration of the exciting radiation to the depth where excitation occurs might also be added to this model, but this has no significant consequence for XPS except at grazing incidence angles for which significant refraction and reflection begin to occur.[17, 178, 179] As x-ray photoelectron escape depths are only of the order of 10–30 Å, the assumption of an initial excitation involving pure bulk electronic states might be questioned, and one-step theoretical models in which the surface is explicitly included in the photoemission process have been presented.[180, 181] However, the bulk photoemission model correctly predicts most of the features noted in both UPS and XPS measurements on semiconductors and transition metals,[57, 182] and also permits separating out the various important physical aspects of photoemission. The presence of distinct surface effects on the photoemission process cannot be discounted, however,[132] with one much-discussed example being a surface-state peak observed in UPS spectra and other measurements on tungsten.[183] Primary emphasis here will be placed upon the excitation step in the three-step model, as it contains those elements of the problem that are most clearly related to the ground-state electronic structure of the system.

For emission from non-overlapping, highly-localized, core orbitals, the use of an atomic cross-section (differential or total) is a reasonable approximation for predicting the excitation strength. For emission from valence levels involved in only slightly overlapping quasi-molecular units, the methods discussed in the last section can be used. For emission from highly-overlapping band-like valence levels, a distinctly different procedure is necessary, as outlined below.

In a crystalline solid, both initial and final orbitals will be Bloch functions with wave vectors $\mathbf{k}$ and $\mathbf{k}^f$, respectively, so that $\phi_k(\mathbf{r}) = \phi_{\mathbf{k}}(\mathbf{r}) = u_{\mathbf{k}}(\mathbf{r}) \exp(i\mathbf{k}\cdot\mathbf{r})$ and $\phi^f(\mathbf{r}) \equiv \phi_{\mathbf{k}}{}^f(\mathbf{r}) = u_{\mathbf{k}}{}^f(\mathbf{r}) \exp(i\mathbf{k}^f\cdot\mathbf{r})$, consistent with Eq. (37). Such an excitation is shown in Fig. 12 on a plot of one-electron potential energy versus distance from the surface. In traversing the surface barrier, the electron

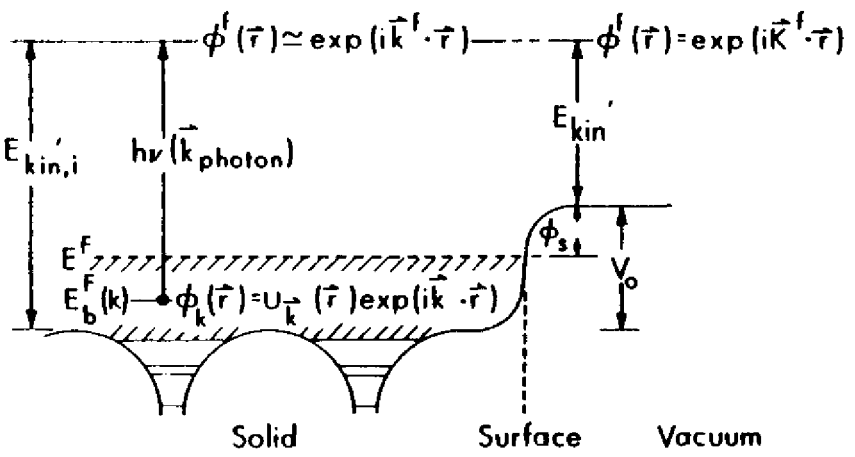

$$(1)\quad E'_{kin,i} = h\nu - E^F_b(k) + V_o - \phi_s \simeq \frac{\hbar^2(k^f)^2}{2m}$$

$$(2)\quad E'_{kin} = E'_{kin,i} + V_o = \frac{\hbar^2(K^f)^2}{2m}$$

$$(3)\quad \vec{k} + \vec{k}_{photon} + \vec{g} = \vec{k}^f$$

Fig. 12. One-electron model of photoemission in a metallic solid, shown as an energy-level diagram superimposed on the one-electron potential energy curve near the surface. The initial and final states inside the solid are assumed to have Bloch-wave character. Applicable conservation relations on energy and wave vector are also shown.

kinetic energy is reduced from its value inside the surface of E_{kin}', $_i$ by an amount equal to the barrier height or inner potential V_0. V_0 is generally measured with respect to the least negative portion of the potential energy inside the crystal which occurs midway between the strongly attractive atomic centers. Detection of an electron propagating in a definite direction outside of the surface implies a free-electron orbital $\phi_{\mathbf{K}^f}(\mathbf{r}) = C\exp(i\mathbf{K}^f \cdot \mathbf{r})$ with momentum $\mathbf{P}^f = \hbar\mathbf{K}^f$, but it should be noted that $\mathbf{K}^f$ need not be precisely equal to $\mathbf{k}^f$. One obvious source of a difference between $\mathbf{K}^f$ and $\mathbf{k}^f$ is refraction effects at the surface barrier, which are only expected to conserve the component of wave vector parallel to the surface ($\mathbf{k}_s{}^f = \mathbf{K}_s{}^f$), but such effects are rather small in XPS except for grazing-angles of electron emission with respect to the surface.[17] A convenient convention for describing the electron wave vectors involved in such a transition is to choose the initial $\mathbf{k}$ to lie inside the first or reduced Brillouin zone and the final $\mathbf{k}^f$ to be expressed in an extended-zone scheme. Thus, initial states at several different energies may

possess the same reduced $\mathbf{k}$ value, but each final state is associated with a unique $\mathbf{k}^f$ value.

The basic one-electron matrix element associated with the cross-section for excitation is most generally written as $\langle\phi_{\mathbf{k}^f}|\mathbf{A}\cdot\nabla|\phi_{\mathbf{k}}\rangle$. This represents the one-electron analogue of Eq. (60). It is then a simple matter to show[183] that the translational symmetry properties of Bloch functions [Eq. (37)] imply that this matrix element can only be non-zero when $\mathbf{k}$ and $\mathbf{k}^f$ are related by a reciprocal lattice vector $\mathbf{g}$:

$$\mathbf{k}^f = \mathbf{k} + \mathbf{g} \tag{103}$$

Transitions satisfying this selection rule are termed "direct", and have been found to be very important in the analysis of UPS spectra and other optical absorption experiments from a variety of materials.[52, 182] At the higher energies of excitation involved in XPS, it has been pointed out by Baird *et al.*[185] that the wave vector $\mathbf{k}_{h\nu}$ associated with the exciting x-ray in XPS has a magnitude sufficiently large that it must be included in this wave-vector conservation equation:

$$\mathbf{k}^f = \mathbf{k} + \mathbf{g} + \mathbf{k}_{h\nu} \tag{104}$$

For example, with $h\nu = 1486{\cdot}6$ eV, $|\mathbf{k}^f| \approx 2\pi/\lambda_e \approx 19{\cdot}7$ Å^{-1} for valence emission, $|\mathbf{k}_{h\nu}| = 2\pi/\lambda \approx 0{\cdot}7$ Å^{-1}, and typical magnitudes of the reduced wave vector are $|\mathbf{k}| \lesssim 2{\cdot}0$ Å^{-1}. Transitions violating such selection rules are termed "non-direct", and can be induced in various ways, for example, by interaction with lattice vibrations (phonons), by the introduction of atomic disorder, or by considering emission from very localized valence levels (for example, rare-earth 4*f*) for which the localized initial and final hole states suppress the effects of translational symmetry. Shevchik[186] has recently made the important observation that phonon effects may lead to an almost total obscuring of direct-transition effects in the XPS spectra of most materials at room temperature. Phonons with a range of wave vectors $\mathbf{k}_{phonon}$ are created or annihilated during the excitation process in a manner completely analogous to thermal diffuse scattering in x-ray diffraction,[187] with the net effect that only a certain fraction of the transitions are simply describable in terms of Eq. (104) (for which $\mathbf{k}_{phonon} \ll \mathbf{k}$). This fraction is most simply estimated from the Debye–Waller factor, as discussed in more detail in Section VI.D.2. Further study of such phonon effects is needed to assess quantitatively their importance, but they do appear to provide a likely mechanism whereby all occupied $\mathbf{k}$ values can contribute to XPS spectra, even if electrons are collected along only a finite solid-angle cone with respect to the axes of a single-crystal in an angle-resolved experiment (see further discussion in Section VI.D.2).

If it is assumed for the moment (as in most prior XPS studies) that direct transitions *are* important, the total rate of excitation of electrons to a given

energy E^f will be given by a summation over all allowed $\mathbf{k} \rightarrow \mathbf{k}^f$ transitions in which energy and wave vector conservation are satisfied. Also, for experiments at non-zero temperature each transition must be weighted by the probability of occupation of the initial state, as given by the Fermi function:

$$F(E) = \frac{1}{\exp\left[(E - E_F)/kT\right] + 1} \tag{105}$$

This function allows for the thermal excitation of electrons lying within $\sim kT$ of the Fermi level. Finally, each transition can be weighted by an average probability $\bar{T}$ for escape without inelastic scattering or back reflection at the surface, which will depend on both E^f and $\mathbf{k}^f$ and can be denoted $\bar{T}(E^f, \mathbf{k}^f)$. The average indicated is over various depths of excitation below the surface. The final result will be proportional to the no-loss photoelectron spectrum finally observed, and is thus given by

$$\begin{aligned} N(E_{kin}) &= N(E^f + \Delta) = N(E + h\nu + \Delta) \\ &\propto \sum_{\substack{\text{Occupied} \\ \text{bands}}} \int \left| \langle \phi_{\mathbf{k}}{}^f(E') \left| \mathbf{A} \cdot \nabla \right| \phi_{\mathbf{k}}(E) \rangle \right|^2 \\ &\quad \times F(E) \bar{T}(E^f, \mathbf{k}^f) \delta(E^f - E - h\nu) \delta(\mathbf{k}^f - \mathbf{k} - \mathbf{g} - \mathbf{k}_{h\nu}) \, d^3k \end{aligned} \tag{106}$$

where Δ is a trivial energy-scale shift that allows for the binding-energy reference chosen, as well as any work function difference between specimen and spectrometer.

In evaluating the matrix elements in this equation to permit comparisons with XPS spectra, Kono *et al.*[176] have assumed an orthogonalized plane wave for the final state $\phi_{\mathbf{k}}{}^f$ and a tight-binding (or LCAO) initial state $\phi_{\mathbf{k}}$. Similar analyses have also been carried out more recently by Aleshin and Kucherenko,[188] and in Section VI.D.2, the application of a simpler form of this model to the analysis of angle-resolved XPS valence spectra from single crystals is discussed.

Several basic simplifications of Equation (106) have often been made so as to obtain a rather direct relationship between observed XPS spectra and the initial density of electronic states $\rho(E)$.[82] Most of these simplifications cannot be made in considering UPS spectra, by contrast. The average no-loss escape function $\bar{T}(E^f, \mathbf{k}^f)$ will be essentially constant for all of the high-energy electrons in the XPS valence spectral region, and so can be eliminated. In UPS however, $\bar{T}(E^f, \mathbf{k}^f)$ can vary considerably over the spectrum. The Fermi function produces only relatively small effects within $\sim \pm kT$ of the Fermi energy, so that in either UPS or XPS carried out at or below room temperature, it is adequate to set it equal to a unit step function. A further simplification that can be justified in several ways for XPS but not UPS is

that the summation and integration in Eq. (106) ultimately yield *for a polycrystalline specimen* a result of the approximate form

$$N(E_{kin}) \propto \bar{\sigma}_E(h\nu)\rho(E) \tag{107}$$

in which $\bar{\sigma}_E(h\nu)$ is a mean photoelectric cross section for the initial states at energy E and $\rho(E)$ is the density of occupied initial states at energy E. The steps in this justification involve first noting the highly free-electron character of the very high energy final states in XPS (that is $\phi_{\mathbf{k}}{}^f \approx \exp(i\mathbf{k}^f \cdot \mathbf{r})$). Because the free-electron density of states is proportional to $(E^f)^{\frac{1}{2}}$, this results in an essentially constant total density of final states into which valence emission can occur.[82] Furthermore, the relatively short electron mean free paths in XPS have been argued by Feibelman and Eastman[181] to introduce an uncertainly-principle smearing in the surface-normal component of $\mathbf{k}^f$ that is larger than the mean $\Delta\mathbf{k}$ spacing between final-state bands at a given energy, and so permits all initial states in a polycrystalline specimen to be equally involved in direct transitions as far as $\mathbf{k}$-conservation is concerned. Phonon effects also may lead to a uniform sampling of all initial states, as suggested by Shevchik.[186] Finally, Baird, Wagner, and Fadley have carried out model direct-transition calculations for single crystals of Au[185] and Al[189] in which all matrix elements were assumed to be equal and the only $\mathbf{k}^f$ smearing included was associated with a finite spectrometer acceptance aperture; summing spectra predicted for all mean emission directions with respect to the crystal axes gave results essentially identical to the density of occupied states, suggesting again that all initial states are equally sampled. Thus, there are several reasons to expect XPS spectra from polycrystalline materials to have a form given approximately by Eq. (107).

XPS has been utilized to study the valence electronic structures of many solids.[82, 190–193] Examples of comparisons between experiment and theory for the three principal classes of solids (metal, semiconductor, and insulator) are shown in Figs 13,[191] 14,[192] and 15.[193] Here, total densities of initial states $\rho(E)$ are compared directly with experiment, in some cases after a suitable broadening has been applied to theory to simulate natural and instrumental linewidth contributions. These comparisons show that all of the main features noted in the experimental spectra are also seen in the theoretical densities of states, although peak intensities are not always well predicted, probably due to non-constant cross-section effects. For example, in Fig. 15, the dotted curve indicates an empirical estimate by Ley *et al.*[193] of the relative cross-section variation that would be necessary to yield agreement between experiment and Eq. (107) for diamond. The form of this curve is furthermore consistent with the increasing C2*s* character expected toward higher binding energies in the diamond valence bands, as the C2*s* atomic cross-section is expected to be considerably larger than that for C2*p*.[151] Similar conclusions have also been

reached for diamond in a recent more quantitative calculation of the matrix elements involved.[188] Cross-section variations over the valence bands thus clearly can play an important role in the analysis of such XPS data, but it is very encouraging that observed peak positions in general agree very well with those in the density of states. Thus, XPS has proven to be a very direct method for studying the density of states.

In summary, for studies of densities of states in solids, both UPS and XPS exhibit certain unique characteristics and advantages. Somewhat better resolution is possible in a UPS measurement, primarily due to the narrower

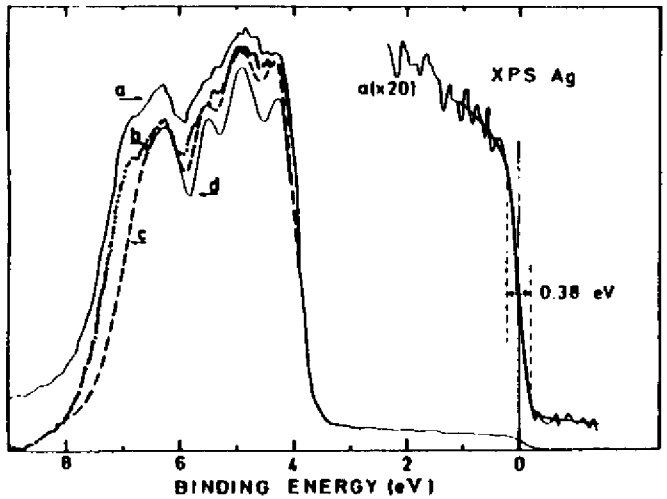

Fig. 13. XPS valence spectrum for polycrystalline silver excited by monochromatized AlKα radiation in comparison with a theoretical density of states. Curve *a* is the raw XPS data, curve *b* is the data after a smooth inelastic background correction has been subtracted, and curves *c* and *d* represent two different lineshape broadenings of the total theoretical density of states according to Eq. (158). These broadenings thus include effects due to both lifetime and shake-up type excitations in the metal. Note the steep cut-off in the data near $E_F - 0$, which can be used to determine the instrumental resolution function. (From Barrie and Christensen, ref. 191.)

radiation sources presently available. Also, UPS spectra contain in principle information on both the initial and final density of states functions, together with certain k-dependent aspects of these functions. The interpretation of an XPS spectrum in terms of the initial density of states appears to be more direct, however. Also, the effects of inelastic scattering are more easily corrected for in an XPS spectrum (cf. Section II.E). Finally, the two techniques are very complementary in the sense that they are controlled by cross-sections which may have different relative values for different bands, thereby providing further information on the types of states involved.

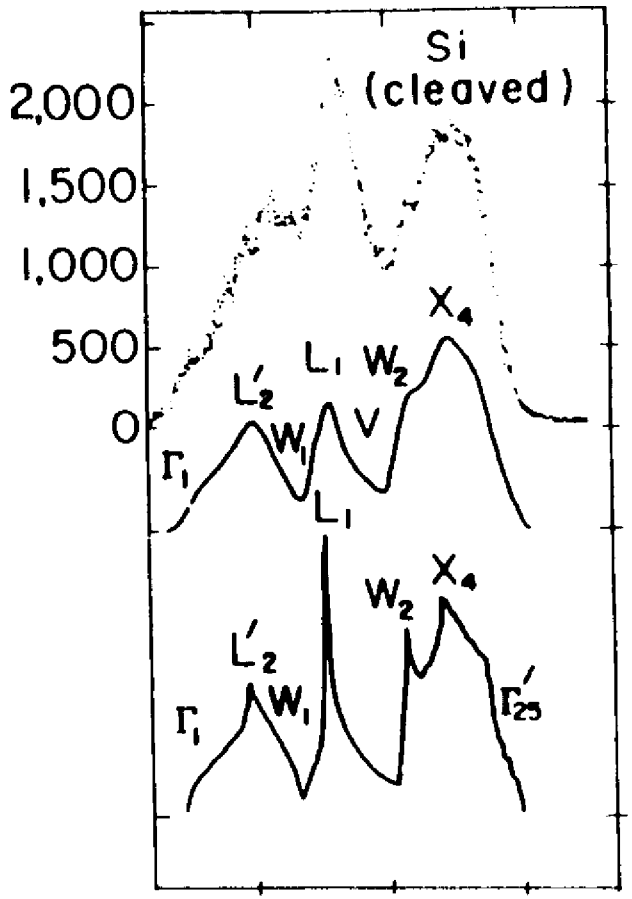

Fig. 14. XPS valence spectrum for a silicon single crystal cleaved in vacuum (points), together with a calculated total density of states (bottom curve), and a density of states broadened by the instrumental resolution function. Excitation was with monochromatized AlKα. The spectrum has been corrected for inelastic scattering. The energy locations of state density primarily due to various high-symmetry points in the reduced Brillouin zone are also indicated. (From Ley *et al.*, ref. 192.)

E. Inelastic Scattering in Solids

Inelastic scattering acts to diminish the no-loss photoelectron current for any type of specimen (gas, liquid, or solid). The processes involved can be one-electron excitations, vibrational excitations, or, in certain solids, plasmon excitations. As it is in measurements on solids that inelastic scattering plays the most significant role in limiting no-loss emission to a mean depth of only a few atomic layers, only such effects will be considered in detail here.

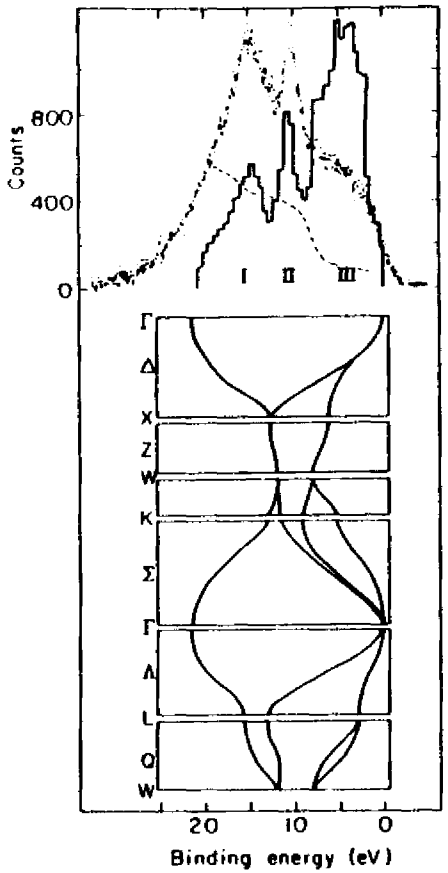

Fig. 15. Valence spectrum for diamond (points) in comparison with a calculated density of states (solid histogram). The dotted curve is an empirical estimate of the mean cross-section variation with energy that would be required to reconcile the spectrum and the density of states according to Eq. (107). Also shown in the lower portion of the figure is the detailed theoretical band structure along various high-symmetry directions in the reduced zone. The incident radiation was monochromatized AlKα. The spectrum has been corrected for inelastic scattering. (From Cavell *et al.*, ref. 193.)

Inelastic scattering in solids is generally discussed in terms of a characteristic length for decay of the no-loss intensity. Specifically, if a monoenergetic flux N_0 at energy E_{kin} is generated at a given point, the no-loss flux N remaining after traveling a distance l is assumed to be given by an exponential decay law

$$N = N_0 \exp\{-l/\Lambda_e(E_{kin})\} \tag{108}$$

where Λ_e is termed the electron attenuation length, mean free path, or penetration depth. Implicit in this definition is the idea that inelastic scattering

occurs *after* photoelectron excitation by means of what are often referred to as "extrinsic" loss processes. "Intrinsic" losses can however occur *during* excitation[194] and are discussed further in Section VI.B.

Such attenuation lengths are usually determined by measuring Auger or photoelectron peak intensities from uniform overlayers with varying thicknesses comparable in magnitude to Λ_e. Powell[20] and Lindau and Spicer[21] have recently presented very thorough reviews of attenuation length measurements in the 40–2000 eV range of most interest in XPS, and an on-going compilation of Λ_e values is also available through the National Physical Laboratory, U.K.[195] Powell's summary of experimental values obtained in various studies is shown in Fig. 16. (Note the log–log scales.) All data points

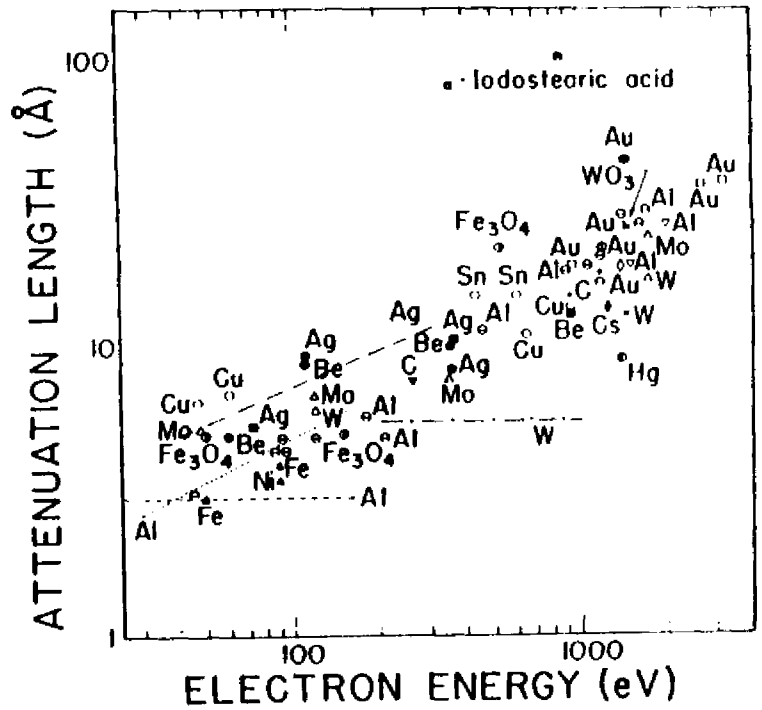

Fig. 16. Summary of experimental values for the electron inelastic attenuation length Λ_e for various solids. (From Powell, ref. 20.)

lie roughly on a common curve, which has been termed the "universal curve" of attenuation lengths (although it should be noted that it is universal to within only a factor of two to five). Extending a plot such as Fig. 16 to lower energies[21] reveals a minimum in Λ_e at ~30–100 eV and an increase at lower energies corresponding to typical UPS experiments. Thus, surface sensitivity

is a maximum in the 30–100 eV kinetic-energy range. For the log–log plot of Fig. 16, the higher energy data are fairly well described by a single straight line that ultimately yields an empirical energy dependence of the form

$$\Lambda_e(E_{kin}) \propto (E_{kin})^{0.52} \tag{109}$$

This relationship is useful in rough estimates of Λ_e variation from peak to peak in a given specimen, although between different materials it is certainly not very reliable.

Powell[20] and Penn[196] have also recently discussed various theoretical models that can be used to predict attenuation lengths at XPS kinetic energies in terms of microscopic system electronic properties. Penn divides the attenuation length up into two parts involving core- and valence-level excitations according to a reciprocal addition procedure expected if the two types of losses are independent of one another:

$$\frac{1}{\Lambda_{e,\,total}} = \frac{1}{\Lambda_{e,\,core}} + \frac{1}{\Lambda_{e,\,valence}} \tag{110}$$

$\Lambda_{e,\,core}$ is determined from an equation of the form given by Powell:[20]

$$\Lambda_{e,\,core} = 2{\cdot}55 \times 10^{-3}\, M E_{kin} \Big/ \rho \sum_i \frac{N_i}{E_i} \ln\left[\frac{4E_{kin}}{\Delta E_i}\right] \tag{111}$$

in which M is the atomic or molecular weight of the solid, E_{kin} is in electron volts, ρ is the density in g/cm^3, N_i is the number of electrons in the ith subshell at energy E_i, and ΔE_i is the mean energy loss involving these electrons (always greater than $E_i = E_b^F(i)$). $\Lambda_{e,\,valence}$ is determined by assuming that plasmon excitations are the dominant loss processes,[196] a situation that can also be shown to yield an overall relationship very similar to Eq. (111),[20] and the final results permit estimating XPS Λ_e values for all elements and compounds, albeit by means of a rather simplified model. In connection with such estimates, it is expected that *ratios* of Λ_e values for a given element or compound will be much more accurately determined than absolute values; this is a very useful result, as it is such ratios that are involved in quantitative analyses of homogeneous systems by XPS, as discussed further in the next section.

As a final comment concerning electron attenuation lengths, it has also been pointed out by Feibelman[197, 198] that Λ_e may vary in magnitude from the bulk of a specimen to its surface because of changes in the dominant mode of extrinsic inelastic scattering (for example, from bulk- to surface-plasmon excitation). Thus, Λ_e need not be an isotropic constant of the material, although it does not much deviate from this for a free electron metal.[197]

F. Photoelectron Peak Intensities

1. *Introduction.* The quantitative interpretation of x-ray photoelectron peak intensities requires developing a model for predicting their magnitudes from various properties of the excitation source, specimen, electron analyzer, and detection system. Detailed discussions of such models have been presented previously by Krause and Wuilleumier[199] for emission from gases and by Fadley[17] for emission from polycrystalline solids. A brief outline of the essential assumptions involved will be presented here, followed by a summary of several important special cases for emission from solids in the next section.

In general, the photoelectron peak intensity N_k produced by subshell k can be calculated within a three-step-like model by integrating the differential intensities dN_k originating in the various volume elements of the specimen. Each of these differential intensities can be written as the following product, in which x, y, z denotes position within the specimen:

$$\begin{aligned} dN_k = &\left[\begin{array}{c}\text{X-ray flux}\\ \text{at } x, y, z\end{array}\right] \times \left[\begin{array}{c}\text{Number of atoms (molecules)}\\ \text{in } dx\, dy\, dz\end{array}\right] \\ &\times \left[\begin{array}{c}\text{Differential cross-}\\ \text{section for } k \text{ subshell}\end{array}\right] \times \left[\begin{array}{c}\text{Acceptance solid angle of}\\ \text{electron analyzer at } x, y, z\end{array}\right] \\ &\times \left[\begin{array}{c}\text{Probability for no-loss}\\ \text{escape from specimen}\\ \text{with negligible}\\ \text{direction change}\end{array}\right] \times \left[\begin{array}{c}\text{Instrumental}\\ \text{detection}\\ \text{efficiency}\end{array}\right] \end{aligned} \tag{112}$$

In most spectrometer systems, a non-monochromatized x-ray source with a broad flux emission pattern is utilized, and for this case it is reasonable to set the x-ray flux equal to some constant value I_0 over the entire specimen volume that is active in producing detectable photoelectrons. This assumption is valid because the exciting radiation is attenuated much more slowly with distance of travel into the specimen than are the electrons as they escape from the specimen. Thus, the region active in producing no-loss electrons is exposed to an essentially constant flux. Exceptions to this situation are monochromatized x-ray sources for which a focused beam is produced,[74] as well as grazing-incidence experiments on solid specimens in which x-ray refraction at the surface much increases the x-ray attenuation with distance below the surface.[17, 178, 179] Neither of these special cases will be considered further here, but refraction effects are discussed in Section VI.C.

The acceptance solid angle Ω of the electron analyzer will vary over the specimen volume, becoming zero for those points from which emission is totally prohibited by the electron optics. Ω, as well as the effective specimen

area A over which $\Omega \neq 0$, also may vary with electron kinetic energy, as discussed previously in Sections II.C.1 and II.C.2.

The probability for no-loss escape from the specimen, which can in the present context be written as $T(E_{kin}, \mathbf{k}l, x, y, z)$, is most simply given by an expression such as Eq. (108) involving the electron attenuation length, provided that elastic scattering events that change direction but not energy are neglected. $\mathbf{k}l$ thus specifies the direction of electron motion along the path length l from the excitation point x, y, z. In gases, such an escape probability must also take into account variations in density (and thus also Λ_e) along the electron trajectories.

The instrumental detection efficiency D_0 is defined to be the probability that a no-loss electron escaping from the specimen in a direction encompassed by the acceptance solid angle will yield a single final count (or equivalent current). This efficiency thus allows for all non-idealities in the analysis and detection system, and it can also depend on E_{kin}.

If the atomic or molecular density in cm^{-3} is denoted $\rho(x, y, z)$, the differential intensity element thus becomes

$$dN_k = I_0 \cdot \rho(x, y, z)\, dx\, dy\, dz \cdot \frac{d\sigma_k}{d\Omega} \cdot \Omega(E_{kin}, x, y, z) \cdot T(E_{kin}, \mathbf{k}l, x, y, z) \cdot D_0(E_{kin}) \qquad (113)$$

or for a uniform-density, but bounded, specimen:

$$dN_k = I_0 \cdot \rho\, dx\, dy\, dz \cdot \frac{d\sigma_k}{d\Omega} \cdot \Omega(E_{kin}, x, y, z) \exp[-l/\Lambda_e(E_{kin})] \cdot D_0(E_{kin}) \qquad (114)$$

where l is the path length to escape from the specimen surface into vacuum.

2. *Peak Intensities from Solids.* With a few simplifying assumptions, Eq. (114) is readily integrated to obtain useful expressions for total peak intensity N_k for the idealized spectrometer shown in Fig. 17.[17, 178] The specimen surface is assumed to be atomically flat. The specimen is taken to be polycrystalline to avoid single-crystal anisotropies in emission[200] (see discussion in Section VI.D.1). An exponential inelastic attenuation law as in Eq. (108) is assumed, and elastic electron scattering effects are neglected. For a given kinetic energy, the electron spectrometer is further assumed to act as though a mean solid angle Ω_0 is applicable over all specimen volume included in the projection of an effective aperture A_0 along the mean electron emission direction (dotted lines in Fig. 17). Both Ω_0 and A_0 may be functions of the kinetic energy E_{kin}. The mean emission direction is assumed to be at an angle θ with respect to the surface. The exciting radiation is incident at an angle ϕ_x with respect to the surface, and, due to refraction, the internal

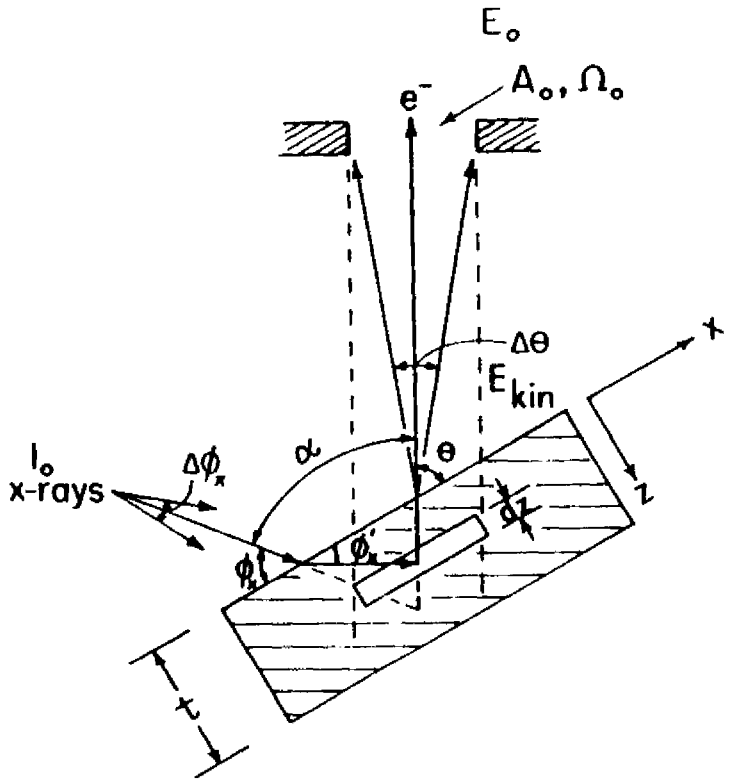

Fig. 17. Idealized spectrometer geometry for calculating photoelectron peak intensities from solid specimens.

angle ϕ_x' may be less than ϕ_x. Such refraction (and reflection) effects only occur for $\phi_x \lesssim 1°$,[178, 179] and will not be included here, although they are briefly discussed in Section VI.C. The angle α between the mean incidence- and exit-directions is held fixed at between approximately 45° and 105° in most current XPS spectrometers.

Within the approximations quoted above (which are very nearly achieved in a number of practical spectrometer systems), it is possible to derive intensity expressions for several important cases:[17, 178, 201]

(a) Semi-infinite specimen, atomically clean surface, peak k with $E_{kin} = E_k$:

$$N_k(0) = I_0 \Omega_0(E_k) A_0(E_k) D_0(E_k) \rho (d\sigma_k/d\Omega) \Lambda_e(E_k) \qquad (115)$$

This case corresponds to an optimal measurement on a homogeneous specimen for which no surface contaminant layer is present. The expression given permits predicting the absolute peak intensities resulting for a given

specimen, or, of much more interest in practice, the relative intensities of the various peaks. If absolute intensities are to be derived, then the incident flux I_0 must be determined, as well as the kinetic energy dependences of effective solid angle Ω_0, effective specimen area A_0, and detection efficiency D_0. In relative intensity measurements in which the quantity of interest is $N_k/N_{k'}$ for two peaks k and k', I_0 will cancel, although $\Omega_0 A_0 D_0$ need not due to its kinetic energy dependence. The density ρ of the atoms or molecules on which subshell k or k' is located may be known beforehand, or may also be the desired end result in quantitative analyses using XPS. The differential cross-section $d\sigma_k/d\Omega$ can be calculated by the various methods discussed in Sections III.D.2–III.D.4. For core levels, the tabulations of σ_{nl} by Scofield,[151] combined with the β_{nl} values given by Reilman *et al.*,[154] provide a suitable means for estimating $d\sigma_k/d\Omega$ with good accuracy within the framework of a one-electron-transition model. Possible effects of multi-electron processes on the use of such cross-sections are discussed in Sections III.D.1 and V.D. Within a given specimen, $\Lambda_e(E_k)$ can be estimated from Penn's treatment,[191] or, more simply, its dependence on kinetic energy can be assumed to follow the empirical square-root dependence of Eq. (109). Note that there is no θ dependence in N_k within this simple model, a prediction that has been verified experimentally by Henke;[178] this behavior is expected to hold as long as θ is not made so small that the edges of the specimen lie within the aperture A_0.[17, 222]

(b) Specimen of thickness t, atomically clean surface, peak k with $E_{kin} \equiv E_k$:

$$N_k(\theta) = I_0 \Omega_0(E_k) A_0(E_k) D_0(E_k) \rho (d\sigma_k/d\Omega) \Lambda_e(E_k) \times [1 - \exp(-t/\Lambda_e(E_k) \sin\theta)] \quad (116)$$

Here, the intensity of a peak originating in a specimen of finite thickness is predicted to increase with decreasing θ (again with the proviso that θ not be so small that the specimen edges lie within A_0).

(c) Semi-infinite substrate with uniform overlayer of thickness t—Peak k from substrate with $E_{kin} \equiv E_k$:

$$N_k(\theta) = I_0 \Omega_0(E_k) A_0(E_k) D_0(E_k) \rho (d\sigma_k/d\Omega) \Lambda_e(E_k) \times \exp(-t/\Lambda_e'(E_k) \sin\theta) \quad (117)$$

Peak l from overlayer with $E_{kin} \equiv E_l$:

$$N_l(\theta) = I_0 \Omega_0(E_l) A_0(E_l) D_0(E_l) \rho' (d\sigma_l/d\Omega) \Lambda_e'(E_l) \times [1 - \exp(-t/\Lambda_e'(E_l) \sin\theta)] \quad (118)$$

where

$\Lambda_e(E_k)$ = an attenuation length in the substrate

$\Lambda_e'(E_k)$ = an attenuation length in the overlayer

ρ = an atomic density in the substrate

ρ' = an atomic density in the overlayer.

Overlayer/substrate ratio:

$$\frac{N_l(\theta)}{N_k(\theta)} = \frac{\Omega_0(E_l) A_0(E_l) D_0(E_l) \rho' (d\sigma_l/d\Omega) \Lambda_e'(E_l)}{\Omega_0(E_k) A_0(E_k) D_0(E_k) \rho (d\sigma_k/d\Omega) \Lambda_e(E_k)} \times [1 - \exp(-t/\Lambda_e'(E_l) \sin\theta)] \exp(t/\Lambda_e'(E_k) \sin\theta \quad (119)$$

This case represents a much more common experimental situation in which the primary specimen acts as substrate and possesses an intentional or unintentional contaminant overlayer (for example, oxide on a metal or a layer deposited from the spectrometer residual gases). Substrate peaks are attenuated by inelastic scattering in the overlayer, an effect that is much enhanced at low θ. The overlayer/substrate ratio is thus predicted to increase strongly as θ decreases, an effect that suggests a general method for increasing surface sensitivity by using grazing angles of electron escape; such angular-dependent studies are discussed in more detail in Section VI.B.

(d) Semi-infinite substrate with a non-attenuating overlayer at fractional monolayer coverage—Peak k from substrate: Eq. (115).

Peak l from overlayer:

$$N_l(\theta) = I_0 \Omega_0(E_l) A_0(E_l) D_0(E_l) s' (d\sigma_l/d\Omega) (\sin\theta)^{-1} \quad (120a)$$

Overlayer/substrate ratio:

$$\frac{N_l(\theta)}{N_k(\theta)} = \frac{\Omega_0(E_l) A_0(E_l) D_0(E_l) s' (d\sigma_l/d\Omega)}{\Omega_0(E_k) A_0(E_k) D_0(E_k) s (d\sigma_k/d\Omega) (\Lambda_e(E_k) \sin\theta)/d} = \left[\frac{s'}{s}\right] \cdot \frac{D_0(E_l) \Omega_0(E_l) A_0(E_l) (d\sigma_l/d\Omega) d}{D_0(E_k) \Omega_0(E_k) A_0(E_k) (d\sigma_k/d\Omega) \Lambda_e \sin\theta} \quad (120b)$$

with

s' = the mean surface density of atoms in which peak l originates in cm^{-2}

s = the mean surface density of substrate atoms in cm^{-2}

s'/s = the fractional monolayer coverage of the atomic species in which peak l originates

d = the mean separation between layers of density s in the substrate (calculable from s/ρ).

These expressions are useful in surface-chemical studies at very low exposures to adsorbate molecules ($s'/s \lesssim 1$), as they permit an estimation of the fractional monolayer coverage from observed peak intensities. The assumption of no inelastic attenuation in the overlayer is an extreme one, but is justified because the macroscopic Λ_e' of case (c) is both difficult to estimate and dubious in its application to such thin, non-macroscopic layers, and also because it represents a correct limiting form for zero coverage.

The basic model presented here assumes an atomically-flat surface. As this will obtain only very rarely in actual experiments, assessments of the potential effects of surface roughness on XPS peak intensities have been made by Fadley *et al.*[17, 202] It is found that roughness can appreciably affect both absolute and relative intensities, especially for systems with inhomogeneity as measured vertical to the surface,[17, 203] with much depending upon the dimensional scale of the roughness relative to the attenuation lengths for x-rays and electrons involved. Roughness effects on angular-resolved measurements are discussed further in Section VI.B, and in considerably greater detail in other sources.[17, 202, 203]

As a final comment concerning the equations presented here, it should be noted that, for complete generality, an angle-dependent instrument response function $R(E_k, \theta)$ must be included as a further factor in all of Eqs (115)–(120). The definition and determination of this response function are discussed elsewhere.[17, 202] It is unity for the idealized geometry treated here (as long as θ is not too small). It has also been calculated and measured for one particular spectrometer system.[74] A further important property of this function is that it will generally be only weakly dependent on kinetic energy, and so will cancel to a very good approximation in peak intensity ratios obtained at a given angle θ. Thus, relative intensity measurements can be made in most cases without the necessity of evaluating the instrument response with θ.

3. *Applications to Quantitative Analysis.* The first detailed experimental tests of the simplest model for intensities originating in a uniform specimen represented by Eq. (115) above were carried out by Nefedov *et al.*[161] and Carter *et al.*[204] The study by Carter *et al.* made use of Eq. (94) to avoid the need of evaluating symmetry parameters, Eq. (109) for the energy dependence of attenuation lengths, and an empirically-determined instrument factor $\Omega_0(E_k)A_0(E_k)D_0(E_k)$. The Scofield calculations[151] provided the cross-sections required. Theoretical relative intensities were calculated for subshells in a number of elements and comparisons were made with several sets of experimental data, including tabulations of measured relative intensities (or elemental sensitivities) by Wagner[205] and Jorgensen and Berthou.[206] In general, agreement to within $\pm 10\%$ was found. Powell and Larson[207] have more recently considered the use of the same model from a somewhat more exact viewpoint, including a discussion of potential errors associated with determining experimental peak areas that are directly relatable to all of the processes involved in the differential photoelectric cross-section. Specifically, from 20% to 50% of the one-electron differential photoelectric cross-section is expected to appear as low-energy satellite intensity due to many-electron effects (cf. discussions in Sections III.F.1 and V.D.2). All of the factors in Eq. (115) were considered in detail, with the most accurate approximations being made whenever possible; for three pure compounds with carefully

cleaned surfaces, the agreement between experimental and theoretical relative intensities was $\sim \pm 5\%$. Thus, there are good reasons to be optimistic that XPS can be used for quantitative analyses of well-prepared homogeneous specimens with this accuracy. For systems exhibiting inhomogeneity near the surface (for example, a substrate/overlayer geometry), additional problems are encountered because at least two regions are involved, but, especially when coupled with angular-dependent measurements,[17] accuracies of $\sim \pm 10\%$ again seem achievable (see also discussion in Section VI.B). Thus, XPS does have considerable analytical potential, particularly as a near-surface probe that is at least complementary to, and probably somewhat more quantitative and less destructive than, electron-excited Auger electron spectroscopy (AES). Powell[208] has recently comparatively reviewed the use of XPS and AES in surface analysis.

IV. CORE ELECTRON BINDING ENERGY SHIFTS

A considerable fraction of XPS studies to date has been involved primarily with the precise measurement of core electron binding energies, and in particular with the measurement of chemical shifts in these binding energies. Such chemical shifts in fact provided much of the recent impetus for the development of XPS.[3] The technique is rather uniquely qualified for such studies, as the usual x-rays utilized ($MgK\alpha = 1254$ eV and $AlK\alpha = 1487$ eV) can penetrate to levels well below the vacuum level. The more common ultraviolet radiation sources presently limit UPS to valence levels and weakly bound core levels within ~ 40 eV of the vacuum level, on the other hand. Synchrotron radiation is also now beginning to be used to excite outer core levels with $E_b^V \lesssim 300$ eV.[15, 209]

The core levels of any atom can by definition be considered to represent filled subshells, and are found in XPS spectra to be relatively sharp in energy, with typical experimental widths of approximately 1–10 eV. The width observed for a core photoelectron peak depends upon several factors of both inherent and instrumental type. The most important inherent sources of width are:

(1) the lifetime of the k-subshell core hole created by photoemission,
(2) various possible values for the final state energy $E(N-1, K)$, as represented for example by multiplet splittings, multi-electron effects, or vibrational broadening (see Section V), and
(3) unresolvable chemically-shifted peaks.

For the present discussion, the final-state complexities of item (2) will be neglected so as to yield a description analogous to that for a simple, closed-shell system. The most important instrumental sources and their typical

magnitudes are:

(1) the exciting x-ray linewidth (approximately 1·0 eV for AlKα without monochromatization and approximately 0·4 eV with),
(2) the finite resolving power of the electron spectrometer (for example, 0·3 eV for 0·03% resolution at $E_{kin} = 1000$ eV), and
(3) non-uniform charging of the specimen (variable magnitude, as discussed in connection with Eq. (2)).

The minimum core linewidths observed to date have been a few tenths of an eV.[41, 210] Thus, provided that the various inherent sources of linewidth and non-uniform charging are not too large, it is possible in principle to measure chemical shifts of the order of 0·1 eV between two or more photoelectron peaks resulting from emission from the same subshell.

If the same atom A is considered as existing either in two chemically inequivalent sites in the same compound labelled 1 and 2 *or* in two different compounds which can be similarly labelled 1 and 2, then the chemical shift ΔE_b of the k electron binding energy can be written simply as the difference of two binding energies. For gaseous specimens with vacuum-referenced binding energies, this means that

$$\Delta E_b^V(A, k, 1\text{-}2) = (E_b^V(k))_1 - (E_b^V(k))_2 = (E_{kin})_2 - (E_{kin})_1 \quad \text{(gases)} \tag{121}$$

where A, k, 1 2 represent the minimum number of parameters required to specify a chemical shift, that is, the atom and level, and the two chemical sites or compounds involved. Here, we have neglected charging effects. For solids with Fermi-referenced binding energies, the corresponding equation is

$$\Delta E_b^F(A, k, 1\ 2) = (E_b^F(k))_1 - (E_b^F(k))_2 = (E_{kin})_2 - (E_{kin})_1 + (\phi_{spect})_2 - (\phi_{spect})_1 + (V_c)_2 - (V_c)_1 \tag{122}$$

where possible effects due to spectrometer work function changes or differences in charging potential have been included. Provided that both of the latter effects are negligible, Eq. (122) simplifies to a form identical to that of Eq. (121),

$$\Delta E_b^F(A, k, 1\text{-}2) = (E_b^F(k))_1 - (E_b^F(k))_2 = (E_{kin})_2 - (E_{kin})_1 \quad \text{(solids)} \tag{123}$$

As has been noted previously, many theoretical calculations of chemical shifts have an implicit vacuum reference level. This is quite satisfactory for gas-phase work, but not necessarily for work on solids. For the latter case, the relationship between vacuum-referenced and Fermi-referenced chemical shifts is, from Eq. (5):

$$\Delta E_b^V(A, k, 1\text{-}2) = \Delta E_b^F(A, k, 1\text{-}2) + (\phi_s)_1 - (\phi_s)_2 \tag{124}$$

Thus, in directly comparing vacuum-referenced theoretical calculations and Fermi-referenced experimental values, it is required to neglect the work function difference between the two solids, $(\phi_s)_1 - (\phi_s)_2$. In most work to date, no serious effects of work function differences have been observed, although there is generally more scatter on a plot of measured chemical shifts against calculated chemical shifts for solids than on a corresponding plot for gases.[3, 4, 7, 211] This additional scatter could be connected with reference level effects or specimen charging or both. Both of these effects deserve further study.

The theoretical interpretation of core-level chemical shifts has been attempted at various levels of sophistication, with each level providing a certain degree of agreement with experiment and interpretive utility. Several reviews of these procedures have been presented previously,[3, 4, 7, 8, 109] and therefore only a brief outline of the most important models, their uses, and their limitations will be given here. These procedures will be considered in approximate order of descending accuracy. From the outset, it is clear that the major goal of such analyses is to derive chemically-significant information concerning the initial state electronic structure of the system. Various final-state complexities (see Section V) can tend at times to obscure the initial-state chemical information, but it has nonetheless proven possible to derive it relatively straightforwardly for a number of systems.

The most accurate calculation of any binding energy shift must in general involve determining two binding energies, or a total of two initial-state calculations and two final hole-state calculations. The possible errors in shifts are thus approximately twice as large as for a single binding energy when calculations are performed at a given level. Various procedures for calculating binding energies have already been discussed in Sections III.A and III.B. Relative to a Koopmans' Theorem approach, corrections due to relaxation, relativistic, and correlation effects must be considered, as summarized in Eq. (55). A chemical shift in such binding energies between two chemically-inequivalent sites or compounds labelled 1 and 2 is thus

$$\Delta E_b^V(A, k, 1\text{-}2) = (E_b^V(k))_1 - (E_b^V(k))_2 = -(\epsilon_k)_1 + (\epsilon_k)_2 - (\delta E_{relax})_1 + (\delta E_{relax})_2 + (\delta E_{relat})_1 - (\delta E_{relat})_2 + (\delta E_{corr})_1 - (\delta E_{corr})_2$$

or

$$\Delta E_b^V(A, k, 1\text{-}2) = -\Delta\epsilon_k - \Delta(\delta E_{relax}) + \Delta(\delta E_{relat}) + \Delta(\delta E_{corr}) \tag{125}$$

In view of the physical origins of the relativistic and correlation corrections for a given core level, they will tend to have values of approximately the same magnitude from one site or compound to another. The same should also be true, but probably to a lesser degree, for relaxation corrections. Thus,

in many cases, it would be expected that $\Delta(\delta E_{relax})$, $\Delta(\delta E_{relat})$, and $\Delta(\delta E_{corr})$ would be considerably smaller in magnitude than the individual corrections to either $(E_b^V(k))_1$ or $(E_b^V(k))_2$, and therefore that the Koopmans' Theorem value $-\Delta\epsilon_k$ would represent a quite good approximation to the chemical shift $\Delta E_b^V(A, k, 1\text{-}2)$.[105] (This need not always be true, however, and we discuss both below and in Section V.B a few special examples in which $\Delta(\delta E_{relax})$ is very large.) For similar reasons, the quality of the wave function utilized in obtaining ϵ_k is often not as critical as might be imagined. That is, approximate wave functions with the same degree of self-consistency for both systems 1 and 2 may yield a reasonably accurate value of $\Delta\epsilon_k$ (which is, after all, a small perturbation primarily due to changes in valence electron charge distribution). Thus, the use of Koopmans' Theorem in conjunction with various approximate calculation procedures such as minimal-basis-set- or double-zeta-basis-set Hartree–Fock calculations has met with success in analyzing much chemical shift data. It appears that molecular wave functions of double-zeta quality can be utilized to predict chemical shifts from $-\Delta\epsilon_k$ which agree with experiment to within $\sim \pm 1$ eV for a carefully-chosen set of molecules not too much different in size, in spite of the fact that the orbital energies for such levels as C1*s* and N1*s* tend to be as much as 10–20 eV higher than the experimental binding energies due to relaxation. In Fig. 18, experimental C1*s* binding energies for different gaseous molecules are compared to 1*s* orbital energies from various theoretical calculations of roughly double-zeta accuracy. Although the two scales are shifted relative to one another by about 15 eV, the points lie very close to a straight line of unit slope. Thus, for sets of molecules chosen to minimize $\Delta(\delta E_{relax})$, $\Delta(\delta E_{relat})$, and $\Delta(\delta E_{corr})$, chemical shifts should be calculable from these orbital energies with an accuracy roughly equal to the scatter of points about the straight line or ± 1 eV.[7, 8, 109]

Although the use of Koopmans' Theorem in estimating binding energy shifts from reasonably accurate molecular-orbital calculations can thus be expected to yield fairly reliable values for well-chosen compounds, it is especially important to be able to include the effects of relaxation in such calculations. Such effects are treated in more detail in Section V.B, but at this point it is appropriate to mention a calculation procedure that lies intermediate between those of Koopmans' Theorem and doing accurate SCF calculations on both initial and final states. This method was developed by Goscinski *et al.*[212, 213] and is termed the transition-state or transition-operator method. In this method, relaxation effects are allowed for to second order in perturbation theory by solving a set of Hartree–Fock equations in which the Fock operator on the left-hand side of Eq. (42) is adjusted so as to involve an effective 1/2 occupation number as far as electron–electron interactions involving the kth spin-orbital from which emission is to occur. For

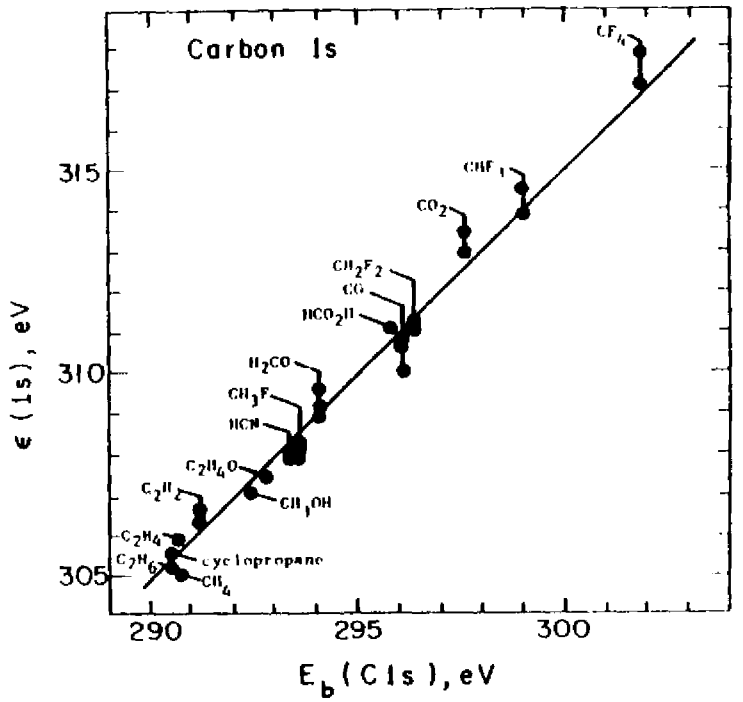

Fig. 18. Plot of carbon 1*s* binding energies calculated via Koopmans' Theorem against experimental binding energies for several carbon-containing gaseous molecules. For some molecules, more than one calculated value is presented. The slope of the straight line is unity. The two scales are shifted with respect to one another by 15 eV, largely due to relaxation effects. All of the theoretical calculations were of roughly double-zeta accuracy or better. (From Shirley, ref. 7.)

the fictitious "transition state" thus calculated for each initially-occupied spin-orbital, negatives of the one-electron energy eigenvalues yield estimates for binding energies that should include relaxation effects to second order. Comparisons of core- and valence-electron binding energy calculations for He, Li, Be, Ne, and Ar [212, 213] do indeed show that this method yields results in very good agreement with the more laborious procedure of calculating and subtracting accurate total energies for both the initial and final states.

The next approximation moving away from the Koopmans' Theorem method for calculating chemical shifts is the potential model that was used in the earliest quantitative discussions of chemical shifts by Siegbahn *et al.*[3] and Fadley *et al.*[105] In this model, the interaction of a given core electron with all other electrons and nuclei in a molecule or solid is divided into an intra-atomic term and an extra-atomic term. Furthermore, the assumption is made that each atom in the array has associated with it a net charge consistent with

overall electroneutrality. These net changes thus account in some way for the displacement of electronic charge which occurs in the formation of chemical bonds. In very covalent systems, this model is of questionable utility, but several variations of it have been applied to a wide variety of systems with considerable success.[3, 4, 105, 214-219] More recently, it has been termed a ground-state-potential model (GPM)[215] to emphasize its usual neglect of final-state effects (especially relaxation). Consider an atom A with a charge q_A situated in an array of atoms to which it is somehow bonded. The binding energy of the kth electron in this atom can then be expressed as a sum of two terms, one intra-atomic free-ion term and one extra-atomic potential:

$$\underset{\text{Compound}}{E_b^V(k)} = \underset{\substack{\text{Free ion of}\\ \text{charge } q_A}}{E_b^V(k, q_A)} + \underset{\substack{\text{Potential due}\\ \text{to all other atoms}}}{V} \tag{126}$$

The first term is a binding energy for the kth electron in a free-ion of charge q_A and the second term is the total potential due to all other atoms in the array. The first term might be evaluated by means of a free-ion Hartree-Fock calculation, for example (although much simpler procedures for dealing with it will also be discussed). The simplest way to calculate the second term is to assume that the other atoms behave as classical point charges in creating the potential V. Thus,

$$V = e^2 \sum_{i \neq A} \frac{q_i}{r_{iA}} \tag{127}$$

where the summation is over all atoms except that of interest in the array. If the array is a crystal, then V represents a convergent infinite sum that is closely related to the Madelung energy of the solid.[105] Thus, both terms in Eq. (126) may be relatively easy to obtain for a number of systems. Calculating a chemical shift using Eq. (126) gives

$$\Delta E_b^V(A, k, 1\text{-}2) = E_b^V(k, q_{A,1}) - E_b^V(k, q_{A,2}) + V_1 - V_2 \tag{128}$$

where $q_{A,1}$ and $q_{A,2}$ are the net charges on atom A in the sites 1 and 2, respectively. It is instructive to consider the predictions of this model for several simple systems, as it is found to explain qualitatively and semi-quantitatively several basic features of chemical shifts.

The difference of free-ion terms in Eq. (128) represents a change in binding energy concomitant with a change in the valence electron orbital occupation of the atom such that the net charge is altered from $q_{A,2}$ to $q_{A,1}$. In the first analyses based upon the potential model, Fadley *et al.*[105] calculated such changes for removal of successive valence electrons from various ionic states of I, Br, Cl, F, and Eu, using a minimum-basis-set Hartree-Fock calculation

and Koopmans' Theorem. These results are presented in Figs 19–23, where the shifts are plotted against the location of the maximum magnitude of the radial function for each orbital. Several systematic features of these results can be noted. For iodine, all core levels shift by very nearly the same amount. This is basically true also for Br and Cl, although as the atomic size decreases there is less constancy in the core shifts, with outer orbitals showing slightly

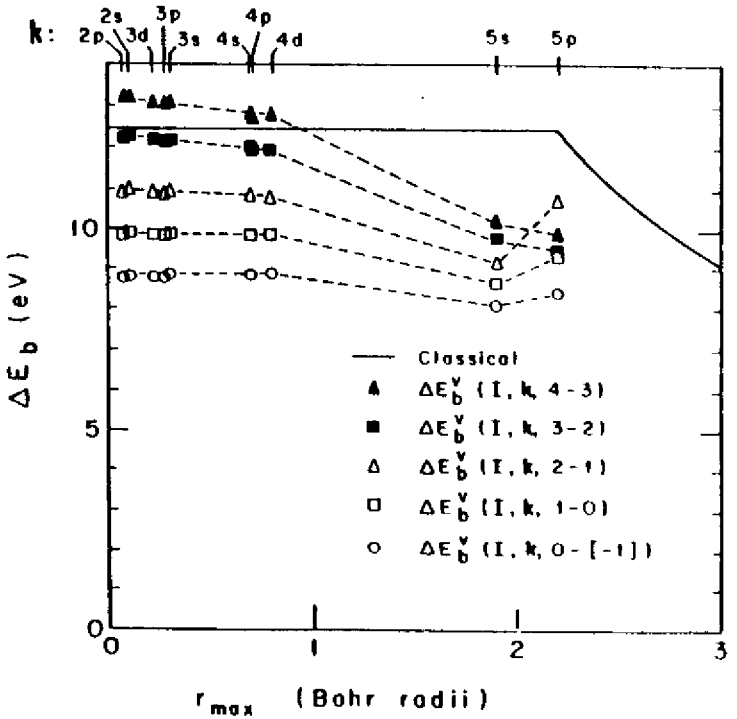

Fig. 19. Koopmans' Theorem free-ion binding energy shifts caused by the removal of a valence $5p$ electron from various configurations of iodine, plotted against the location of the radial maxima for the various orbitals. The configurations are: $+4 = 5s^25p$, $+3 = 5s^25p^2$, $+2 = 5s^25p^3$, $+1 = 5s^25p^4$, $0 = 5s^25p^5$, and $-1 = 5s^25p^6$. The solid curve shows the classical shift resulting from the removal of an electron from a thin spherical shell of charge with the radius of the $5p$ maximum. (From Fadley *et al.*, ref. 105.)

lower shifts. In all of the halogens, the p valence electrons are largely external to the core, as is evidenced by the location of the core- and valence-orbital radial maxima. For Eu, which by contrast has valence $4f$ electrons overlapping considerably with the core electrons, the core shifts are not at all constant, and furthermore can be about twice as large per unit change in valence shell occupancy as for the halogens. All of these results are qualitatively consistent with a very simple classical model of the interaction between core

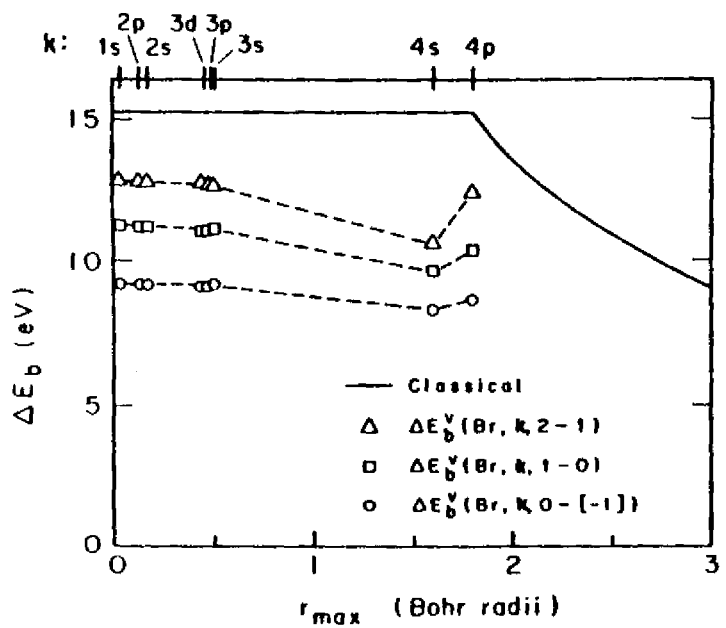

Fig. 20. Calculated free-ion binding energy shifts caused by the removal of a valence $4p$ electron from bromine, plotted as in Fig. 19. The configurations are: $+2 = 4s^2 4p^3$, $+1 = 4s^2 4p^4$, $0 = 4s^2 4p^5$, and $-1 = 4s^2 4p^6$. (From Fadley *et al.*, ref. 105.)

and valence electrons. The valence electron charge distribution can be approximated by a spherical charged shell of radius r_v, where r_v can reasonably be taken to be the average radius of the valence orbitals or the location of their radial function maximum. The classical potential inside this spherical shell will be constant and equal to q/r_v, where q is the total charge in the valence shell. If the charge on this shell is changed by δq, the potentials, and thus binding energies, of *all* the core electrons located well inside the shell will shift by an amount $\delta E_b{}^V = \delta q/r_v$. Such classical calculations are shown as the solid lines in Figs 19–23 and are found to give results that correctly predict the trends in relative shifts from subshell to subshell, as well as being in semi-quantitative agreement with the absolute magnitudes of the more accurate Hartree–Fock calculations. In general then, all core electrons which overlap relatively little with the valence shell are predicted to shift by approximately the same amount, and this prediction is verified experimentally.[105] The magnitude of the shift per unit change in charge should also increase as the valence shell radius r_v decreases, as is illustrated for the case of Eu. A more accurate estimate of $\delta E_b{}^V/\delta q$ for any atom is given by the change in Hartree Fock ϵ_k upon removal of one valence electron. From Eq. (47),

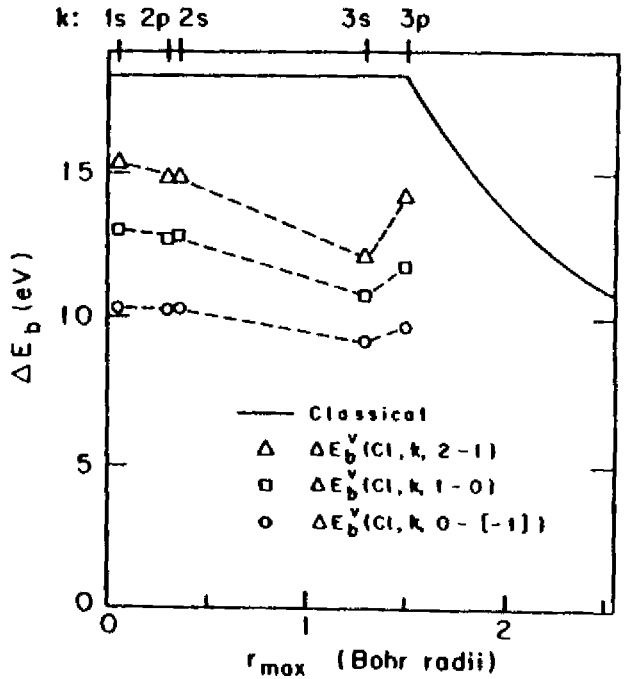

Fig. 21. Calculated free-ion binding energy shifts caused by the removal of a valence $3p$ electron from chlorine, plotted as in Fig. 19. The configurations are: $+2 = 3s^2 3p^3$, $+1 = 3s^2 3p^4$, $0 = 3s^2 3p^5$, and $-1 = 3s^2 3p^6$. (From Fadley *et al.*, ref. 105.)

this will be given by $J_{k\ \mathrm{valence}} - K_{k\ \mathrm{valence}}$ (spins parallel) or $J_{k\ \mathrm{valence}}$ (spins anti-parallel). As the core-valence exchange integral $K_{k\ \mathrm{valence}}$ will be of significant magnitude only if there is appreciable overlap between the core and valence orbitals, we can neglect $K_{k\ \mathrm{valence}}$ in comparison to $J_{k\ \mathrm{valence}}$. (For example, in carbon, $J_{1s,\,2s} = 22{\cdot}1$ eV, $K_{1s,\,2s} = 1{\cdot}4$ eV, $J_{1s,\,2p} = 20{\cdot}8$ eV, and $K_{1s,\,2p} = 0{\cdot}6$ eV.) Thus, $\delta E_b{}^V/\delta_q$ should be approximately equal to $J_{k\ \mathrm{valence}}$, the core-valence Coulomb integral. The magnitude of such Coulomb integrals are, in fact, found to be in good agreement with the shifts calculated in Figs 19–21 for I, Br, and Cl. As a final point, the free ion term $\delta E_b{}^V/\delta_q$ is of the order of 10–20 eV/electron charge for essentially all elements.

If the potential term V in Eq. (126) is now considered, it is found that its value also will be of the order of 10–20 eV for a transfer of unit electron charge from one atom to its nearest neighbors,[3, 105] as, for example, in a highly ionic alkali halide crystal. Furthermore, for a given molecule or solid the free-ion term $(\delta E_b{}^V/\delta_q)\cdot\delta_q$ will be opposite in sign to V, as V must account for the fact that charge is not displaced to infinity, but only to adjacent atoms during chemical bond formation. Thus, both the free-ion and potential terms

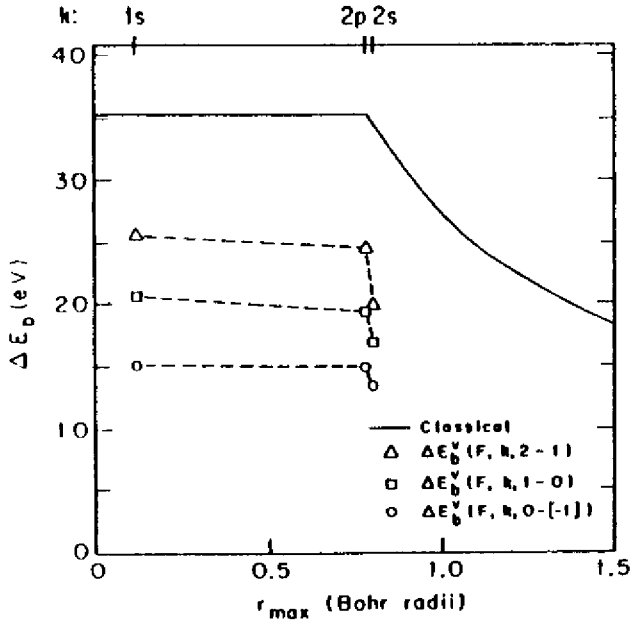

Fig. 22. Calculated free-ion binding energy shifts caused by the removal of a valence $2p$ electron from fluorine, plotted as in Fig. 19. The configurations are: $+2=2s^22p^3$, $+1=2s^22p^4$, $0=2s^22p^5$, and $-1=2s^22p^6$. (From Fadley *et al.*, ref. 105.)

in Eq. (126) must be calculated with similar accuracy if the resultant binding energy (or chemical shift) value is to have corresponding accuracy. This represents one of the possible drawbacks of such potential models.

Several other models based essentially on Eq. (126) have been utilized in analyzing core electron chemical shifts,[7, 8] and the detailed theoretical justifications for them have been discussed by Manne,[216] Basch,[217] and Schwartz.[218] For example, Siegbahn *et al.*[4] and Gelius *et al.*[211] have been able to describe the core binding energy shifts for a variety of compounds of C, N, O, F, and S with the following equation:

$$\Delta E_b^V(A, k, 1\text{-}2) = C_A q_A + V + I \tag{129}$$

where 2 represents a fixed reference compound. The various atomic charges q_i in each molecule were estimated using CNDO molecular-orbital theory, and these charges were then substituted into Eq. (127) to compute V. Then the constants C_A and I were determined empirically by a least-squares fit to the experimental data. Such fits give a reasonably consistent description of the data, as is shown in Fig. 24 for various compounds of carbon, and, in particular, the parameters C_A are found to be rather close to the 1s-valence

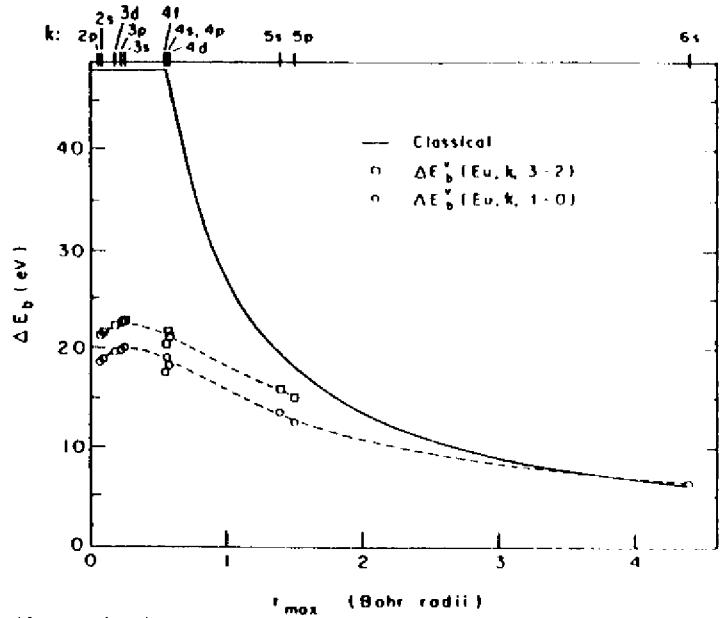

Fig. 23. Calculated free-ion binding energy shifts caused by the removal of a valence $4f$ electron from europium, plotted as in Fig. 19. The configurations are: $+3=4f^6$, $+2=4f^7$, $+1=4f^66s^2$, and $0=4f^76s^2$. Note the non-constancy of the core-level shifts by comparison to Figs 19-22. (From Fadley *et al.*, ref. 105.)

Coulomb integral $J_{1s\text{ valence}}$ computed for atom A. Thus, Eq. (129) as utilized in this semi-empirical way is consistent with a somewhat more exact theoretical model. Note, however, that all molecules are not adequately described by this model and that, for example, the points for CO and CS_2 lie far from the straight line predicted by Eq. (129). As might be expected, if an orbital energy difference based on near Hartree-Fock wave functions is used for the calculated shift of CO, much better agreement with experiment is obtained, as is shown in Fig. 18.

In another variant of the potential model proposed by Davis *et al.*,[219] a series of chemical shift measurements on core levels in all the atoms of several related molecules are used to derive a self-consistent set of atomic charges. For each atom in each molecule, the measured chemical shift is written in terms of undetermined atomic charges as

$$E_b^V(A, k, 1\text{-}2) = C_A' q_A + e^2 \sum_{i \neq A} \frac{q_i}{r_{Ai}} \tag{130}$$

where C_A' is set equal to $J_{1s\text{-valence}}$ for atom A. The resultant set of equations is solved self-consistently for the q_A values on each atom. Such calculations

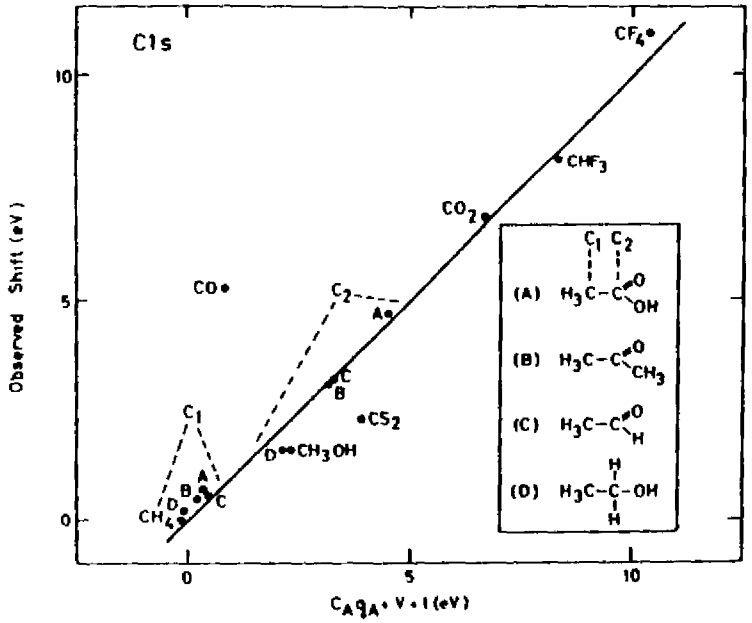

Fig. 24. A comparison of the experimental carbon 1s chemical shift values for several molecules with shifts calculated using the potential model of Eq. (129). The shifts were measured relative to CH_4. The parameters of the straight line were $C_A = 21{\cdot}9$ eV/unit charge and $I = 0{\cdot}80$ eV. (From Siegbahn *et al.*, ref. 4.)

on a series of fluorinated benzenes[219] give charges which agree rather well with charges obtained from calculations based upon the CNDO/2 method, as is apparent in Fig. 25.

Another procedure for analyzing chemical shift data that can be at least indirectly related to the various potential models is based on summing empirically determined shifts associated with each of the groups bonded to the atom of interest, and has been developed primarily by Gelius, Hedman, and co-workers.[211, 220] Each group shift is assumed to be constant and independent of the other groups present and is determined from a series of chemical shift measurements on reference compounds representing suitable combinations of the groups. The chemical shift associated with atom A in a given compound is thus written as

$$\Delta E_b(A, k, 1\text{-}2) = \sum_{\text{groups}} \Delta E_b(\text{group}) \qquad (131)$$

where 2 constitutes some reference compound against which all of the group shifts are determined. The applicability of this procedure has been demonstrated on a large number of carbon- and phosphorous-containing compounds,[211, 220] and a summary of results obtained for phosphorus compounds

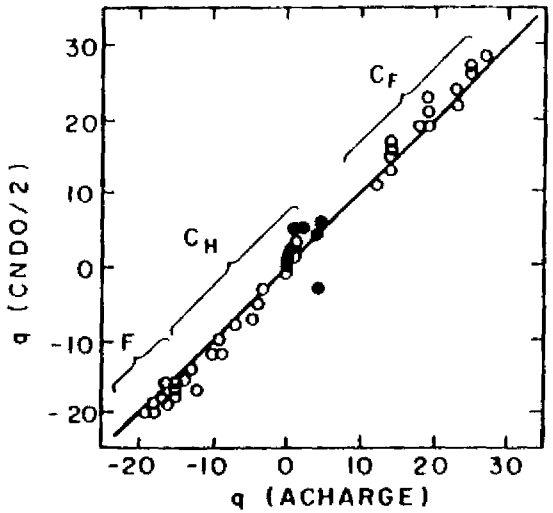

Fig. 25. Atomic charges for the various fluorinated benzenes as calculated by the CNDO/2 method and as derived experimentally ("ACHARGE") from chemical shift measurements on carbon and fluorine and Eq. (130). Charges are in units of 1/100 of an electronic charge. The filled circles represent average hydrogen charges. (From Davis *et al.*, ref. 219.)

is shown in Fig. 26. The relationship of this procedure to a potential model is possible if it is assumed that each group induces a valence electron charge change of δq(group) on the central atom and also possesses essentially the same intragroup atomic charge distribution regardless of the other groups present. Then both the free-ion and potential terms in Eq. (126) become simply additive for different groups, as is required in Eq. (131). In addition, however, the group shift can be considered to include empirically an approximately constant intragroup relaxation correction, thus going somewhat beyond a ground-state potential model in one sense.

Some of the first analyses of shift data were performed simply by plotting ΔE_b against atomic charges which were estimated by various procedures, among them CNDO or extended-Hückel calculations, or most crudely by electronegativity arguments. The implicit neglect of the potential terms of Eqs (126) and (128) in such a correlation of ΔE_b against q_A can, however, lead to a rather wide scatter of the points about a straight line or curve drawn through them. Hendrickson *et al.*,[221] for example, found two rather distinct clusters of data points described by two different curves in comparing nitrogen 1s shifts with charges calculated via CNDO. However, there *is* in general a systematic increase in E_b with increasing q_A for most compounds, particularly if the compounds are chosen to be rather similar in bonding type. One such series of compounds for which a simple electronegativity correlation has proven adequate is the halomethanes. Thomas[222] expressed the C1s

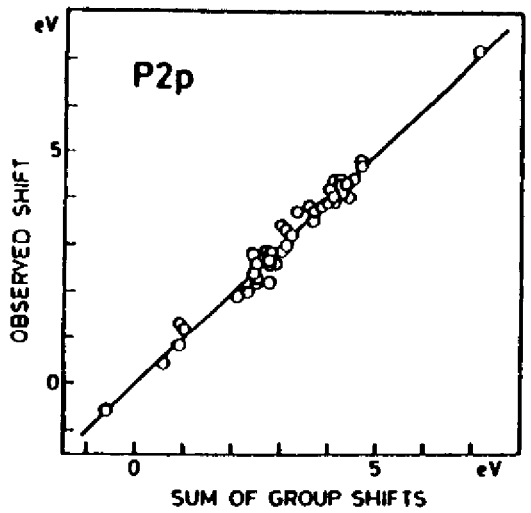

Fig. 26. A comparison of measured phosphorous 2*p* chemical shifts with shifts calculated using the group shift model of Eq. (131). The compounds were studied as solids. (From Hedman *et al.*, ref. 220.)

shifts between CH_4 and a given halomethane as a linear combination of the electronegativity differences between the various ligands present and hydrogen:

$$\Delta E_b^{V}(\text{C1}s,\ \text{halomethane-CH}_4) = C\sum_i (X_i - X_H) \qquad (132)$$

where C is an empirical constant, X_i is the ligand electronegativity, and X_H is the electronegativity of hydrogen. Such a correlation is shown in Fig. 27. The explanation for the success of this correlation would seem to be as a further simplification of the group shift approach, in which each monatomic ligand induces a charge transfer δq_i proportional to $X_i - X_H$, and the potential term involved is also simply proportional to δq_i for a nearly constant carbon–ligand bond length. Thus, the potential model of Eq. (128) can be reduced to the form of Eq. (132). Such correlations should be used very cautiously, however, as exceptions are relatively easy to encounter: for example, in the series of molecules generated by adding successive methyl groups to ammonia (NH_3, $NH_2(CH_3)$, $NH(CH_3)_2$, and $N(CH_3)_3$), the N1*s* binding energy is observed to *decrease* with the addition of CH_3 groups,[223] in complete disagreement with the greater positive charge expected on the central nitrogen because $X_C > X_H$. The major cause of this discrepancy is believed to be the greater relaxation energy associated with the $-CH_3$ group around the N1*s* hole,[223] a type of effect discussed in more detail in Section V.B.

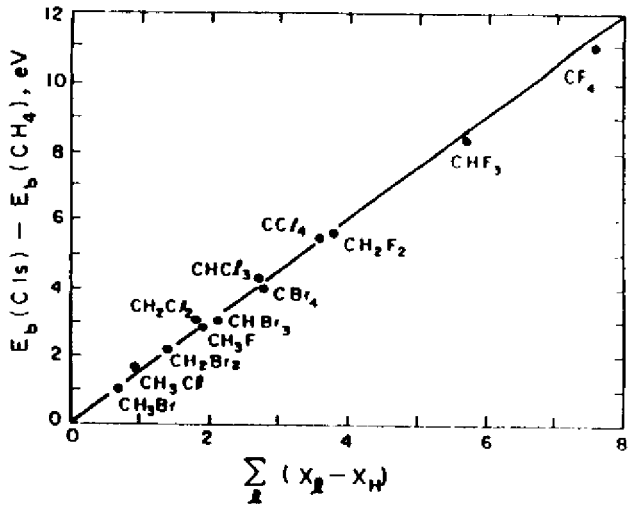

Fig. 27. Carbon 1*s* chemical shifts for halogenated methanes measured relative to CH_4 and plotted against shifts calculated on the basis of a sum of ligand-hydrogen electronegativity differences, as in Eq. (132). (From Thomas, ref. 222.)

Among the other methods utilized to analyze chemical shift data, mention should also be made of a procedure introduced by Jolly and Hendrickson[224, 225] for relating chemical shifts to thermochemical data. In this method, it is noted that to a good approximation the atomic core of an atom with nuclear charge Z and a single core-level hole acts on any surrounding electrons in an equivalent way to the filled core of an atom with nuclear charge $Z+1$. If the core electron overlap with the outer electrons is small, then the nuclear shielding should be nearly complete and this assumption is reasonable. As a more quantitative indicator of how good this approximation is for a medium-Z atom, Table I summarizes the results of highly-accurate numerical Hartree-Fock calculations by Mehta, Fadley, and Bagus[102] for atomic Kr with various core-level holes and its equivalent-core analogue Rb^{+1}. With neutral Kr as a reference, the fractional decreases in average subshell radii $1 - \langle r_{nl}\rangle/\langle r_{nl}\rangle_0$ are tabulated for different core-hole locations in Kr^{+1} and for the equivalent-core species Rb^{+1}. For the equivalent-core approach to be fully valid, these fractional changes should be nearly identical between true Kr hole states and Rb^{+1}, thus indicating the same degree of inward relaxation around both a core hole and a nuclear charge that is incremented from Z to $Z+1$. For the various true hole states in subshells that can be designated $n_{hole}l_{hole}$, the fractional decreases in $\langle r_{nl}\rangle$ range from ~ 0 for subshells with $n \lesssim n_{hole}$ up to 11% for the outermost 4*p* orbital. The equivalent-core Rb^{+1} orbitals by contrast show significant relaxation in all

TABLE 1

Average radii for the various subshells of neutral Kr $\langle r_{nl}\rangle_0$, together with the fractional changes in average radii between neutral Kr and all possible core-hole states. The changes between neutral Kr and the equivalent-core ion Rb^+ are also given. The units for $\langle r_{nl}\rangle_0$ are bohrs. The Kr^+ values are divided into those for $n \ll n_{hole}$ and $n > n_{hole}$ (from Mehta *et al.*, ref. 102)

Atom	L, S term	$1-\frac{\langle r_{1s}\rangle}{\langle r_{1s}\rangle_0}$	$\langle r_{2s}\rangle_0 =$	$1-\frac{\langle r_{2s}\rangle}{\langle r_{2s}\rangle_0}$	$\langle r_{2p}\rangle_0 =$	$1-\frac{\langle r_{2p}\rangle}{\langle r_{2p}\rangle_0}$	$\langle r_{3s}\rangle_0 =$	$1-\frac{\langle r_{3s}\rangle}{\langle r_{3s}\rangle_0}$	$\langle r_{3p}\rangle_0 =$	$1-\frac{\langle r_{3p}\rangle}{\langle r_{3p}\rangle_0}$	$\langle r_{3d}\rangle_0 =$	$1-\frac{\langle r_{3d}\rangle}{\langle r_{3d}\rangle_0}$	$\langle r_{4s}\rangle_0 =$	$1-\frac{\langle r_{4s}\rangle}{\langle r_{4s}\rangle_0}$	$\langle r_{4p}\rangle_0 =$	$1-\frac{\langle r_{4p}\rangle}{\langle r_{4p}\rangle_0}$
			0·0424		0·1873		0·1619		0·5378		0·5426		0·5509		1·6294		1·9516
$Kr^+(-1s)$	^2S	0·0049		0·0185		0·0267		0·0273		0·0381		0·0558		0·0722		0·1142
$Kr^+(-2s)$	^2S	0·0000		0·0010		0·0087		0·0194		0·0268		0·0534		0·0662		0·1078
$Kr^+(-2p)$	^2P	0·0008		0·0074		0·0026		0·0209		0·0304		0·0542		0·0683		0·1083
$Kr^+(-3s)$	^2S	0·0000		−0·0009		0·0004		0·0016		0·0105		0·0251		0·0606		0·1007
$Kr^+(-3p)$	^2P	0·0001		0·0006		−0·0006		0·0077		0·0028		0·0248		0·0617		0·1019
$Kr^+(-3d)$	^2D	0·0000		0·0003		0·0003		0·0089		0·0119		0·0272		0·0618		0·1003
Rb^+		0·0275		0·0294		0·0306		0·0366		0·0403		0·0537		0·0799		0·1150

subshells, with a range between 3% for 1*s* and 11% for 4*p*. Relaxation for subshells with $n \ll n_{hole}$ is thus much overestimated by the use of an equivalent core, whereas for $n > n_{hole}$, the overestimates range from only ~0·1% in absolute fractional radius change. Thus, the equivalent-core model is a reasonable and useful first approximation, although it is certainly expected to overestimate relaxation effects due to core-hole formation.

In applying the equivalent-core model to chemical-shift analyses, it is assumed[224, 225] that an exchange of cores can be made in the final-state ion without appreciably altering the valence electron charge distribution *or* equilibrium nuclear geometry. (The results in Table I for the 4*s* and 4*p* subshells suggest that this is a good approximation.) Thus, in considering core-level emission from a species containing nitrogen, an O^{+8} $1s^2$ core can be exchanged for the N^{+6} $1s = N^{+6*}$ core, where the asterisk denotes the presence of the 1*s* core hole. Such core exchanges can be utilized to write binding energy shifts in terms of thermodynamic heats of reaction, and hence to predict either shifts from thermodynamic data or thermodynamic data from shifts. As one example of the application of this procedure, let us consider 1*s* photoelectron emission from gaseous NH_3 and N_2 as chemical reactions in which the electron is assumed to be formed exactly at the vacuum level and therefore with no kinetic energy:

$$NH_3 \rightarrow NH_3^{+*} + e^-: \quad \Delta E_1 = E_b^V(N1s, NH_3)$$
$$N_2 \rightarrow N_2^{+*} + e^-: \quad \Delta E_2 = E_b^V(N1s, N_2)$$

These reactions are endothermic with internal energy changes ΔE_1 and ΔE_2 given by the 1*s* binding energies in NH_3 and N_2. Subtracting the second reaction from the first gives

$$NH_3 + N_2^{+*} \rightarrow NH_3^{+*} + N_2: \quad \Delta E = \Delta E_1 - \Delta E_2$$
$$= E_b^V(N1s, NH_3) - E_b^V(N1s, N_2)$$
$$= \Delta E_b^V(N1s, NH_3 - N_2)$$

with an internal energy change precisely equal to the N1*s* chemical shift between NH_3 and N_2. However, this reaction involves the unusual and very short-lived species N_2^{+*} and NH_3^{+*}. Now, it is assumed that the N^{6+*} core can be replaced by the O^{6+} core in either N_2^{+*} or NH_3^{+*} with only a small gain or loss of energy that can be termed the core-exchange energy ΔE_{ce}. As long as the core-exchange energy is very nearly the same in both N_2^{+*} and NH_3^{+*}, then the overall energy change associated with the reaction is not affected by core exchange. That is, we have a final reaction of

$$NH_3 + NO^+ \rightarrow OH_3^+ + N_2: \quad \Delta E - \Delta E_b^V(N1s, NH_3 - N_2) + \Delta E_{ce} - \Delta E_{ce}$$
$$= \Delta E_b^V(N1s, NH_3 - N_2)$$

Therefore, the chemical shift is equal to a thermodynamic heat of reaction involving well-known species. This procedure has been applied to an analysis of 1*s* shifts in compounds of N, C, O, B, and Xe, and very good agreement is obtained between experimental ΔE_b values and thermochemical estimates of these shifts. Such a comparison for nitrogen 1*s* is shown in Fig. 28. This analysis is closely related to the isodesmic processes discussed by Clark,[9] and is also reviewed in more detail by Jolly[13] in this series.

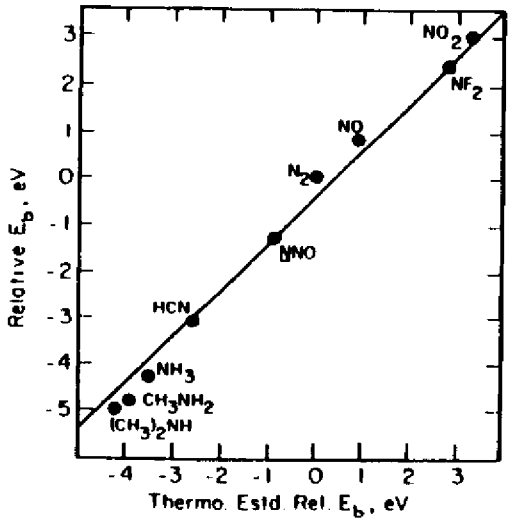

Fig. 28. Plot of experimental N1*s* binding energy shifts relative to N_2 for several molecules versus values calculated using equivalent-core exchange and thermodynamic data. The slope of the line is unity. (From Jolly, ref. 225.)

Finally, a few other methods in which core electron binding energy shifts can be used should be mentioned:

(1) Attempts have been made to derive bonding information from relative binding energy shifts of different levels in the same atom. From Figs 19–23, it is clear that the outer core and valence levels of a given atom need not shift by the same amount as inner core levels, especially if relatively penetrating valence levels are present as in Eu. Such *relative* shifts of different levels can for certain cases be simply related to the basic Coulomb and exchange integrals involved, and then utilized to determine properties of the valence electron charge distribution. In particular, the relative shifts of the inner core $3d_{\frac{3}{2}}$ and valence $5p_{\frac{3}{2}}$ levels have been measured for iodine in various alkyl iodides and III, and these shifts have been found by Hashmall *et al.*[226] to be consistent with a simple bonding model of the compounds involved. More

recently, Aono *et al.*[227] have carried out a similar relative shift study of rare-earth compounds that quantitatively confirms the non-constancy of the intra-atomic free-ion shifts as predicted, for example, for Eu in Fig. 23.

(2) In another type of analysis, core-level chemical shifts for several homologous series of the form RXH with X = O, N, P, and R = various substituent groups have also been found to be approximately equal to relative proton affinities.[228] Martin *et al.*[228] have explained this correlation by noting that the removal of a core electron from atom X to form a positive hole involves very nearly the same set of R-group relaxation energies (and to a less important degree also potential energies) as the addition of a proton. Thus, changes in X-atom core binding energy with R are expected to be approximately equal to changes in proton affinity with R, even though the absolute magnitudes of the two quantities are very different; this has been found to be true for a rather large number of small molecules.[228]

(3) It has also been proposed by Wagner[229] that the difference in kinetic energy between a core photoelectron peak and an Auger electron peak originating totally via core-level transitions in the same atom can be used as a sensitive indicator of chemical state that is free of any uncertainty as to binding energy reference or variable specimen surface charging. This difference, which has been termed the "Auger parameter",[229] changes with alterations in chemical environment because Auger energies are influenced much more strongly than photoelectron energies by final-state relaxation.[230, 231] In fact, Auger energy chemical shifts are roughly 3–4 times as large as corresponding core binding energy shifts.[229] Although a precise theoretical calculation of such extra-atomic relaxation effects may be difficult (see, for example, Section V.B), the Auger parameter appears to have considerable potential as a fingerprint for different chemical states.

(4) Finally, attempts have been made to correlate core binding energy shifts with the results of nuclear spectroscopic measurements such as NMR[232, 233] and Mössbauer spectroscopy,[234] as reviewed elsewhere by Carlson.[10] NMR diamagnetic shielding factors have been compared with core shifts, but the difficulty of separating out diamagnetic and paramagnetic contributions to shielding have prevented extensive application of this type of analysis. Also, binding energy shifts for a closely related set of tin compounds correlate reasonably well with Mössbauer chemical shift values,[234] but no detailed theoretical justification for this correlation has been presented.

It is clear that the theoretical interpretation of core electron binding energies or chemical shifts in these energies can be attempted in several ways at varying levels of sophistication. When binding energies are calculated by the most rigorous total-energy-difference method, including perhaps corrections for relativistic effects and electron electron correlation, values in very good agreement with experiment have been obtained for several atoms and

small molecules. This agreement verifies that all of the basic physical effects involved have been recognized and can be accounted for quantitatively. If binding energies are calculated from orbital energies via Koopmans' Theorem, errors primarily due to neglect of final state relaxation are incurred. Such errors can be from 1% to 10% of the total binding energy and can be estimated in several ways. In calculating chemical shifts of binding energies between two different sites or compounds by means of Koopmans' Theorem, however, a fortuitous cancellation of a large fraction of the relativistic, correlation, and relaxation corrections occurs. Thus, orbital energies can be used with reasonable success in predicting shifts, although anomalously large final-state relaxation around a localized hole represents an ever-present source of error in such analyses (see also Section V.B). The interaction of a core electron with its environment can be simplified even further, giving rise to several so-called potential models with varying degrees of quantum-mechanical and/or empirical input. All of these models can be useful in interpreting shifts, although it may be necessary to restrict attention to a systematic set of compounds for the most approximate of them. The direct connection of chemical shifts with thermochemical heats of reaction via the equivalent-core approximation is also possible. Finally, it is worthwhile to note that one of the primary reasons that chemical shifts can be analyzed by such a wide variety of methods is that their origin is so simply and directly connected to the molecular charge distribution. In turn, it is very often this charge distribution that is of primary interest in a given chemical or physical investigation.

V. FINAL-STATE EFFECTS

A. Introduction

In this section, several effects arising because of complexities in the final state of the photoemission process will be considered. Considerable use will be made of the theoretical developments of Sections III.A–D, from which it is already clear that unambiguously distinguishing various final-state effects in the electronic wave function may not always be possible, primarily due to many-electron effects that might, for example, be described by a configuration-interaction approach. Thus, the first four topics to be dealt with here (relaxation phenomena, multiplet splittings, shake-up and shake-off effects, and other many-electron effects) are all very much interrelated, as will become evident from subsequent discussion. However, for both historical and heuristic reasons, it is reasonable to consider them separately, using several examples for which distinctions can be made relatively easily. (Such final-state electronic effects have also been reviewed by Martin and Shirley[13] in more detail in this series.) The last subject to be treated here involves the influence of exciting various final vibrational states, for which theoretical background has already been presented in Sections III.A and III.D.

B. Relaxation Effects

The importance of relaxation corrections in accurately predicting binding energies has been emphasized in several prior discussions in this chapter. As a further example of how large such effects can be, it has been suggested by Ley *et al.*[235] that relaxation is the primary reason why free-atom vacuum-referenced core binding energies are higher by ~5–15 eV than corresponding vacuum-referenced binding energies in the pure elemental solid. Also, inert gas atoms implanted in noble metal lattices have been shown by Citrin and Hamann[236] to exhibit core binding energies 2–4 eV lower than in the free-atom state, again primarily due to relaxation. In a systematic study of the C1*s* binding energy in a set of linear alkanes C_nH_{2n+2} ($n = 1, 2, \ldots, 13$), Pireaux *et al.*[237] noted a monotonically increasing C1*s* chemical shift $\Delta E_b(C1s, CH_4\text{–}C_nH_{2n+2})$ with n, and a small overall shift of 0·6 eV between CH_4 and $C_{13}H_{28}$ with sign such that $C_{13}H_{28}$ has the lowest binding energy. Transition-operator calculations for these alkane molecules indicate that the relaxation energy increases by almost 2·0 eV in going from the smallest CH_4 to $C_{13}H_{28}$; thus, relaxation is a major contributing factor in producing these small chemical shifts, although it must act in conjunction with certain other effects with opposite sign to reduce the overall shift to 0·6 eV. Relaxation shifts of ~1–3 eV are also noted in *UPS* spectra of the valence levels of molecules chemisorbed on surfaces,[238] with the binding energies of molecular orbitals not directly involved in bonding to the surface being lower than in the free molecule, presumably due to extra relaxation in the substrate. In general for these systems, then, it is found that the more near-neighbor atoms there are surrounding a given final-state hole, the more relaxation can occur and the lower is the observed binding energy.

The relaxation energy δE_{relax} can be unambiguously defined as the difference between a Koopmans' Theorem binding energy $-\epsilon_k$ and a binding energy calculated by means of a difference of self-consistent Hartree–Fock total energies for both the initial and final states. Various methods have been utilized for estimating this energy in atoms, molecules, and solids,[119–121, 235, 239–242] but principal emphasis here will be on a relatively straightforward, yet easily visualized, procedure first used extensively by Shirley and co-workers.[121, 235, 239]

In this procedure,[121, 235, 239] the relaxation energy for a given core-level emission process is divided into two parts: an intra-atomic term (the only term present in the free-atom case) and an extra-atomic term that is important in molecules or solids. The extra-atomic term thus includes all relaxation

involving electrons primarily situated *in the initial state* on other atomic centers. Thus,

$$\delta E_{\text{relax}} = \delta E_{\text{relax}}^{\text{intra}} + \delta E_{\text{relax}}^{\text{extra}} \tag{133}$$

(This division of the relaxation correction was, in fact, made in the first discussion of the potential model for analyzing chemical shifts.[105]) The calculation of these two terms makes use of a general result derived by Hedin and Johansson,[120] which states that, for emission from an initial orbital ϕ_k in an atom of atomic number Z, the relaxation energy is given to a good approximation by

$$\delta E_{\text{relax}} = \tfrac{1}{2}\langle \phi_k | \hat{V}(N-1, Z) - \hat{V}(N, Z) | \phi_k \rangle \tag{134}$$

in which $\hat{V}(N-1, Z)$ is the total electronic Hartree–Fock potential operator acting on the kth orbital in the $(N-1)$-electron final state and $\hat{V}(N, Z)$ is the analogous total Hartree Fock potential operator for the N-electron initial state. (For a neutral atom, of course $N=Z$.) The expectation value in Eq. (134) thus involves sums over Coulomb and exchange integrals between ϕ_k and $(N-1)$ other spin-orbitals $\phi_j \neq \phi_k$. Two sets of orbitals ϕ_j are also needed, an initial-state set $\{\phi_j\}$ in $\hat{V}(N, Z)$ and a relaxed set $\{\phi_j'\}$ in $\hat{V}(N-1, Z)$. The determination of the relaxed orbitals is now further simplified by using the equivalent-core approximation, such that the integrals involving $\hat{V}(N-1, Z)$ are replaced by integrals for $\hat{V}(N+1, Z+1)$, the neutral atom with next higher atomic number; correspondingly, ϕ_k is taken to be an orbital in atom $Z+1$ in evaluating these integrals. This procedure is reasonable because the orbitals at larger mean radii than ϕ_k produce most of the relaxation and such orbitals in neutral atom $Z+1$ are very little different from those in atom Z with a hole in the k subshell (cf. Table I). Furthermore, even though inner-orbital relaxation occurs (including relaxation of ϕ_k), this inner-orbital relaxation is smaller (again see Table I), and thus the Coulomb and exchange integrals between inner and outer orbitals change little in atom $Z+1$ relative to the true hole state in atom Z.[121] Thus, the overall relaxation energy becomes finally

$$\delta E_{\text{relax}} = \tfrac{1}{2}(\langle \phi_k | \hat{V} | \phi_k \rangle_{Z+1} - \langle \phi_k | \hat{V} | \phi_k \rangle_Z) \tag{135}$$

with all relevant Coulomb and exchange integrals available from existing tabulated data for atoms.[100] Applying this calculation procedure to core emission from noble-gas atoms, Shirley[121] obtained very good estimates for relaxation energies as compared to direct total-energy-difference calculations.

The same procedure has also been applied to metals by Ley *et al.*,[235] for which the separation of Eq. (135) into intra-atomic and extra-atomic terms yields formally

$$\delta E_{\text{relax}} = \tfrac{1}{2}(\langle \phi_k | \hat{V} | \phi_k \rangle_{Z+1} - \langle \phi_k | \hat{V} | \phi_k \rangle_Z)^{\text{intra}} + \tfrac{1}{2}(\langle \phi_k | \hat{V} | \phi_k \rangle_{Z+1} - \langle \phi_k | \hat{V} | \phi_k \rangle_Z)^{\text{extra}} \tag{136}$$

The intra-atomic term in Eq. (136) is calculable as described previously. If a free atom A is placed into a pure solid lattice of the same species and it is further assumed that placement in the lattice has a small influence on the initial-state Hartree Fock energy eigenvalues ϵ_k (corresponding to an extra-atomic potential effect of approximately zero), then the difference between free-atom and solid binding energies is given simply by the extra-atomic relaxation term for the solid:

$$E_b^V(A, k, \text{atom}) - E_b^V(A, k, \text{solid}) = \tfrac{1}{2}(\langle \phi_k | \hat{V} | \phi_k \rangle_{Z+1} - \langle \phi_k | \hat{V} | \phi_k \rangle_Z)^{\text{extra}} \tag{137}$$

These extra-atomic terms have been derived[235] for a metal by assuming that the conduction electrons polarize to such an extent that a screening charge of approximately unit magnitude occupies an atomic-like orbital centered on the atom containing the core hole. As a reasonable choice for this orbital, that possessing the dominant character of the lowest unoccupied valence band in the solid is used, again together with an equivalent-cores approximation. Although this procedure overestimates screening because the orbital chosen is too localized, it does give approximately correct magnitudes for atom-solid shifts such as those in Eq. (137), as is illustrated in Fig. 29 for the $3d$ transition-metal series. Note the break in values at $Z=29$ (Cu) when the screening orbital changes from $3d$ to the more diffuse $4s$ because of filling of

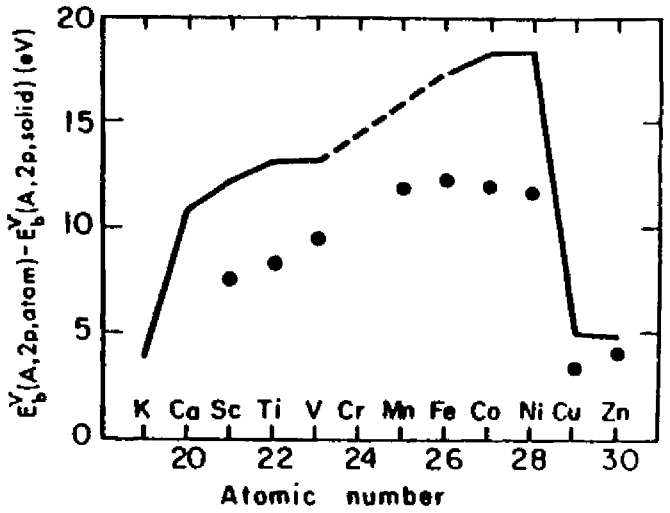

Fig. 29. Differences between vacuum-referenced free-atom $2p$ core binding energies and analogous binding energies in the corresponding elemental metal. The points represent experimental values and the line calculations based upon Eq. (137), which assumes that extra-atomic relaxation is the main cause of such differences. The break at $Z=29$ is caused by the filling of the $3d$ valence bands. (From Ley *et al.*, ref. 215 and 235).

the 3*d* bands. Alternate calculation procedures of a somewhat more rigorous nature have also been proposed to explain such atom-solid shifts[230, 240-242], including especially discussions of possible initial-state shifts in the solid. However, the scheme presented here clearly yields a semi-quantitative approximation for one of the most important factors, extra-atomic relaxation, as well as being very easy to apply to various systems.

As noted previously (Section III.B), it has also been pointed out by Ley *et al.*[115] that a localized-hole description can be used to estimate relaxation energies associated with *valence-level* excitations in free-electron metals. Such relaxation energies are calculated by assuming that in the final state a full single-electron screening charge occupies an initially unoccupied atomic-like valence orbital. Then, because there is minimal inner-orbital relaxation, the difference operator $\hat{V}(N-1, Z) - \hat{V}(N, Z)$ in Eq. (134) reduces to the single terms $\hat{J}_{\text{valence}} + \hat{K}_{\text{valence}}$, and the final relaxation energy is given by $\frac{1}{2}\langle\phi_{\text{valence}}|\hat{J}_{\text{valence}} + \hat{K}_{\text{valence}}|\phi_{\text{valence}}\rangle \approx \frac{1}{2}\langle\phi_{\text{valence}}|\hat{J}_{\text{valence}}|\phi_{\text{valence}}\rangle = \frac{1}{2}J_{\text{valence, valence}}$.

As a final comment concerning relaxation, the discussion surrounding Eq. (77) and Fig. 8 should be recalled. That is, the occurrence of relaxation requires by virtue of the Mauné–Åberg–Lundqvist sum rule given in Eq. (77) that additional photoelectron intensity arises at kinetic energies below that of the relaxed or adiabatic peak position. Thus, relaxation is very closely associated with various kinds of low-energy satellite structure of types to be discussed in Section V.D.

C. *Multiplet Splittings*

Multiplet splittings arise from the various possible non-degenerate total electronic states that can occur in the final hole states of open-shell systems, whether they be atoms, molecules, or solids with highly localized unfilled valence levels. The way in which multiple final states can be produced has already been briefly introduced in Section III.A, and for most systems it is adequate to consider a total spatial symmetry designation (e.g. $L=0, 1, 2, \ldots$ in atoms), a total spin designation (e.g. $S=0, 1, 2, \ldots$ in atoms or molecules), and perhaps also the perturbation of these via the relativistic spin–orbit interaction. The simplest interpretation of atomic multiplet splittings is thus in terms of various L, S terms. Such effects can occur in any system in which the outer subshell or subshells are only partially occupied. The partial occupation provides certain extra degrees of freedom in forming total final states relative to the closed-shell case via coupling with the unfilled shell left behind by photoelectron emission. Multiplet effects can occur for both core and valence emission, as long as the valence subshell(s) are not totally occupied initially. Multiplet splittings also possess the important feature of being describable *in first order* in terms of a single set of ground-state Hartree–Fock one-electron orbitals. Thus, electron–electron correlation effects beyond the ground-state Hartree–Fock approximation are not essential for predicting that multiplet effects will exist, although, as will be shown, the inclusion of correlation effects is absolutely essential for quantitatively describing these phenomena in certain instances.

Multiplet effects involving core-level holes are very commonly encountered in interpretations of the fine structure arising in x-ray emission spectra[243-245] and Auger electron spectra.[3, 246-248] However, it is more recently that such effects were first recognized and studied in detail in connection with core x-ray photoelectron spectra of paramagnetic free molecules[4, 249] and transition-metal compounds.[86, 250] Subsequently, numerous studies have been carried out, including applications to systems containing both transition-metal atoms[86, 157, 250-257] and rare-earth atoms,[156, 258-261] and a few comprehensive reviews have appeared.[262-265] Primary emphasis here will be on the elucidation of a few examples to illustrate the types of effects noted and their modes of interpretation.

As an introductory example of one type of multiplet splitting found in XPS studies,[86, 250] consider first the ground-state Hartree–Fock description of photoemission from the 3*s* level of a Mn^{2+} free ion, as shown on the left-hand side of Fig. 30. The ground state of this ion can be described in L, S (Russell–Saunders) coupling as $3d^5\,{}^6S$ (that is, $S=\frac{5}{2}$, $L=0$). In this state, the five 3*d* spins are coupled parallel. Upon ejecting a 3*s* electron, two final states may result: $3s3d^5\,{}^5S$ ($S=2$, $L=0$) or $3s3d^5\,{}^7S$ ($S=3$, $L=0$). The basic difference between these two is that in the ${}^5S$ state, the spin of the remaining 3*s* electron is coupled anti-parallel to those of the five 3*d* electrons, whereas in the ${}^7S$ state the 3*s* and 3*d* spins are coupled parallel. Because the exchange interaction acts only between electrons with parallel spins, the ${}^7S$ energy will be lowered relative to the ${}^5S$ energy because of the favorable effects of 3*s*–3*d* exchange. The magnitude of this energy separation will be proportional to the 3*s*–3*d* exchange integral $K_{3s,\,3d}$, and will be given by[118]

$$\begin{aligned}\Delta[E_b(3s)] &= E'(3s3d^5\,{}^5S) - E'(3s3d^5\,{}^7S) = \Delta E'(3s3d^5)\\ &= 6K_{3s,\,3d}\\ &= \frac{6e^2}{5}\int_0^\infty\int_0^\infty \frac{r_<^2}{r_>^3} P_{3s}(r_1)P_{3d}(r_2)P_{3s}(r_2)P_{3d}(r_1)\,dr_1\,dr_2 \qquad (138)\end{aligned}$$

where e is the electronic charge, $r_<$ and $r_>$ are chosen to be the smaller and larger of r_1 and r_2 in performing the integrations, and $P_{3s}(r)/r$ and $P_{3d}(r)/r$ are the radial wave functions for 3*s* and 3*d* electrons. The factor 1/5 results from angular integrations involved in computing $K_{3s,\,3d}$. A Hartree–Fock calculation of the energy splitting in Eq. (138) for Mn^{3+} gives a value of $\Delta E'(3s3d^5) \approx 13$ eV.[86, 250] As this predicted splitting is considerably larger

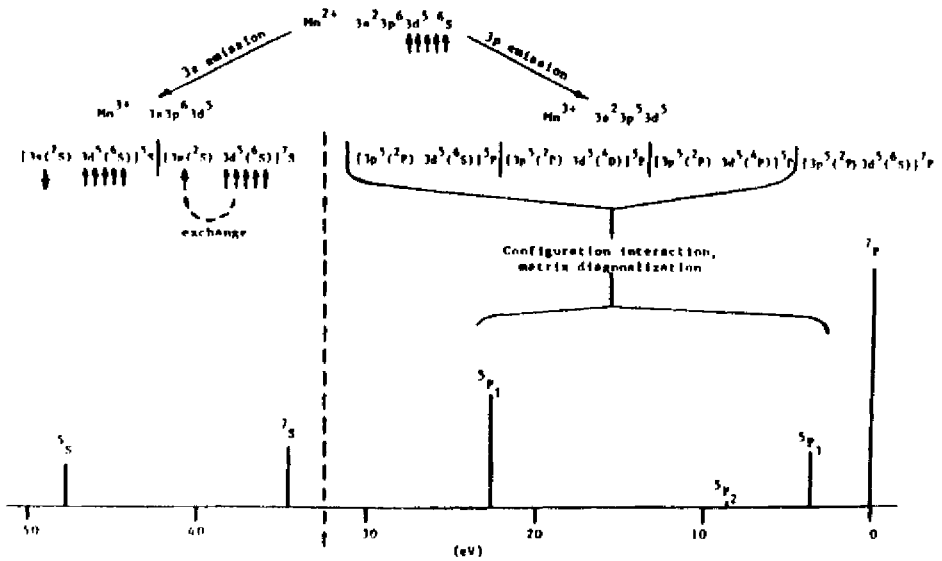

Fig. 30. The various final state L, S multiplets arising from 3s and 3p photoemission from a Mn^{2+} ion. Within the S and P manifolds, separations and relative intensities have been computed using simple atomic multiplet theory as discussed in the text. The separation and relative intensity of the ^7S and ^7P peaks were fixed at the values observed for 3s(1) and 3p(1) in the MnF_2 spectrum of Fig. 31 to facilitate comparison with experiment. (From Fadley, ref. 262.)

than typical XPS linewidths, it is not surprising that rather large 3s binding energy splittings have in fact been observed in solid compounds containing Mn^{2+}, and such splittings are clearly evident in the 3s regions of the first data of this type obtained by Fadley *et al.*,[86, 250] as shown in Fig. 31. Roughly the left half of each of these spectra represents 3s emission, and the splittings observed in MnF_2 and MnO are approximately one-half of those predicted from Eq. (138). The primary reason for this large discrepancy in magnitude appears to be correlation effects due to the highly overlapping character of the 3s and 3d orbitals, as discussed in more detail below.

In considering further such core binding energy splittings in non-relativistic atoms, it is worthwhile to present a more general discussion of the photoemission process, including the relevant selection rules.[8, 262, 263] If the photoelectron is ejected from a filled nl subshell containing q electrons, and an unfilled $n'l'$ valence subshell containing p electrons is present, the overall photoemission process can be written as

$$\underset{\text{(filled)}}{(nl)^q(n'l')^p} \xrightarrow{h\nu} \underset{(L',S')}{(nl)^{q-1}(n'l')^p} + \text{photoelectron} \qquad (139)$$

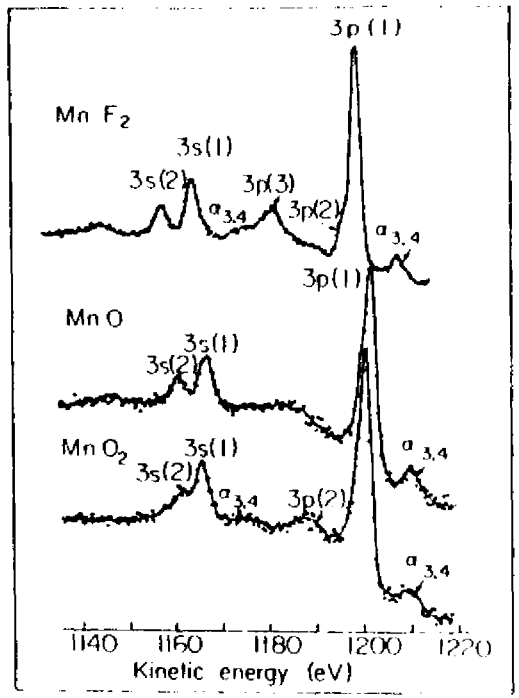

Fig. 31. XPS spectra from three solid compounds containing Mn, in the kinetic energy region corresponding to emission of Mn3s and 3p electrons. The initial-state ions present are $Mn^{+2}3d^5$ (MnF_2, MnO) and $Mn^{+4}3d^3$ (MnO_2). Peaks due to multiplet splittings are labelled 3s(1), 3s(2), etc. $K\alpha_{3,4}$ x-ray satellite structures are also indicated. (From Fadley and Shirley, ref. 86.)

Here, L and S denote the total orbital and spin angular momenta of the initial N-electron state and L' and S' represent the same quantities for the final ionic state with $(N-1)$ electrons. As $(nl)^n$ is a filled subshell, its total orbital and spin angular momenta must both be zero and therefore L and S correspond to the orbital and spin momenta of the valence subshell $(n'l')^p$. In the final state, L' and S' represent momenta resulting from the coupling of $(nl)^{q-1}$ (or, equivalently, a single core-electron hole) with $(n'l')^p$. The transition probability per unit time for photoelectron excitation is proportional to the square of a dipole matrix element between the initial and final state wave functions (see Section III.D.1 for a detailed discussion). In a nearly one-electron model of photoemission, this matrix element can be simplified to the sudden approximation forms given in Eqs (68) and (74). The selection rule on one-electron angular momentum is $\Delta l = l' - l = \pm 1$, as stated previously. Conservation of total spin and total orbital angular

momenta requires that

$$\Delta S = S' - S = \pm \tfrac{1}{2} \tag{140}$$

and

$$\Delta L = L' - L = 0, \pm 1, \pm 2, \ldots, \pm l \text{ or } L' = L + l, L + l - 1, \ldots, |L - l| \tag{141}$$

Also, the overlap factors in Eqs (68) and (74) yield an additional *monopole* selection rule on the passive electrons, as introduced in Section III.D.1. This rule implies that the coupling of the unfilled valence subshell $(n'l')^p$ in the final state must be the same as that in the initial state: that is to total spin and orbital angular momenta of L and S. Finally, any coupling scheme for $(nl)^{q-1}$ or $(n'l')^p$ must of course be consistent with the Pauli exclusion principle. Since $(nl)^{q-1}$ is assumed to represent a single hole in an otherwise filled subshell, it must therefore couple to a total spin of $\frac{1}{2}$ and a total orbital angular momentum of l. Within this model, it has been shown by Cox and Orchard[155] that the total intensity of a given final state specified by L', S' will be proportional to its total degeneracy, as well as to the one-electron matrix element squared. Thus, in Russell-Saunders coupling

$$I_{\text{tot}}(L', S') \propto (2S' + 1)(2L' + 1) \tag{142}$$

For the special case of atomic s-electron binding energy splittings, the relevant selection rules are thus:

$$\Delta S = S' - S = \pm \tfrac{1}{2} \tag{143}$$

$$\Delta L = L' - L = 0 \tag{144}$$

and the total intensity of a given peak is predicted to be proportional to the spin degeneracy of the final state:

$$I_{\text{tot}}(L', S') \propto 2S' + 1 \tag{145}$$

Thus, only two final states are possible corresponding to $S' = S \pm \frac{1}{2}$, and the relative intensities of these will be given by the ratio of their multiplicities, or

$$\frac{I_{\text{tot}}(L, S + \frac{1}{2})}{I_{\text{tot}}(L, S - \frac{1}{2})} = \frac{2S + 2}{2S} \tag{146}$$

The energy separation of these two states can further be calculated from simple atomic multiplet theory and is given by a result often referred to as the Van Vleck Theorem:[118]

$$\Delta[E_b(ns)] = E'(L, S - \tfrac{1}{2}) - E'(L, S + \tfrac{1}{2}) \tag{147}$$

$$\Delta[E_b(ns)] = (2S + 1)K_{ns,n'l'} \quad \text{for } S \neq 0 \tag{148}$$

$$\Delta[E_b(ns)] = 0 \quad \text{for } S = 0 \tag{149}$$

Here $K_{ns,n'l'}$ is the $ns - n'l'$ exchange integral and can be calculated from

$$K_{ns,n'l'} = \frac{e^2}{2l' + 1} \int_0^\infty \int_0^\infty \frac{r_<^{l'}}{r_>^{l'+1}} P_{ns}(r_1) P_{n'l'}(r_2) P_{ns}(r_2) P_{n'l'}(r_1)\, dr_1\, dr_2 \tag{150}$$

where the same notation as that in Eq. (138) has been used. Equations (146)–(150) indicate that such s-electron binding energy splittings should yield a doublet with a more intense component at lower binding energy (corresponding to an exchange-favored final state of $S' = S + \frac{1}{2}$) and a component separation that is directly associated with both the initial state spin and the spatial distributions of the core and valence electrons as reflected in the exchange integral. Thus, the potential for extracting certain types of useful and unique information from such splittings exists.

That Eq. (148) provides a good description of the systematics of such s-level multiplet splittings has been nicely demonstrated in studies of the 4s and 5s splittings in rare-earth metals and compounds with varying outer 4f subshell occupation numbers and spins S,[258, 259] as summarized in Fig. 32.

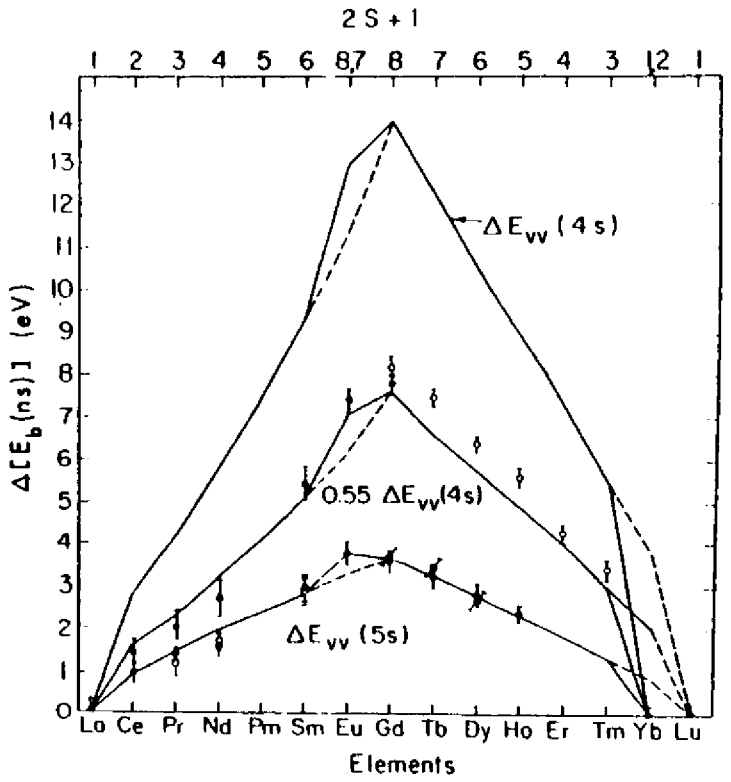

Fig. 32. Experimental (points) and theoretical (lines) 4s and 5s binding energy splittings in various rare-earth ions. The ΔE_{VV} values are calculated using Van Vleck's Theorem [Eq. (148)]. Experiment and theory are in excellent agreement for 5s, but the theoretical splittings must be reduced by a factor of 0·55 to agree with the 4s data because of correlation effects. (From McFeely *et al.*, ref. 259.)

The solid lines connect calculated values based upon Eq. (148) and are in excellent agreement with experiment for the 5*s* splittings, whereas for the 4*s* splittings, this simple theory must be reduced by a factor of ~0·55 to agree with experiment. These results also suggest that the 4*s* discrepancy may be due to the same type of correlation correction involved in Mn3*s*, as the 4*s*-4*f* spatial overlap is high, increasing correlation, whereas the 5*s*-4*f* overlap is much lower, decreasing it.

Configuration interaction calculations on Mn^{3+} by Bagus *et al.*[252] first provided a more quantitative understanding of such correlation corrections to intrashell *s*-level splittings such as 3*s*-3*d* and 4*s*-4*f*. They pointed out that, in a CI description of the true Mn^{3+} final states corresponding to 3*s* emission, several configurations would be of special importance in addition to the usual one-electron-transition final configuration as shown in the left half of Fig. 30. (In writing such configurations below, numbers in parentheses will denote the *L*, *S* coupling of the subshell to the left.) The ^7S final state is found to be composed almost completely of $3s^1(^2S)3p^6(^1S)3d^5(^6S)$, the one-electron configuration, and so is not much perturbed by CI. Another way of saying this is that there is already strong exchange correlation in ^7S, so that the addition of CI is not so significant. The ^5S final state is by contrast expected to have significant contributions from not only the one-electron configuration $\Phi_1(^5S) = 3s^1(^2S)3p^6(^1S)3d^5(^6S)$, but also from configurations in which it formally appears that one 3*p* electron has been transferred down to a 3*s* orbital while another 3*p* electron has been transferred up to a 3*d* orbital: $\Phi_2(^5S) = 3s^2(^1S)3p^4(^3P)3d^6(^3P_1)$, $\Phi_3(^5S) = 3s^2(^1S)3p^4(^3P)3d^6(^3P_2)$ and $\Phi_4(^5S) = 3s^2(^1S)3p^4(^1D)3d^6(^5D)$. (The notations $3d^6(^3P_1)$ and $3d^6(^3P_2)$ stand for two independent ways in which $3d^6$ can couple to ^3P.) Thus, there will be at least a fourfold manifold of ^5S states, and the lowest-energy member is expected to be lowered significantly (that is, to move toward ^7S). In fact, the ^5S state nearest ^7S is found to be only 4·71 eV away, in much better agreement with the experimental splitting for MnF_2 of 6·5 eV than the estimate of ~13 eV obtained from Eq. (138). Such intrashell *s*-level multiplet splittings can thus only be predicted accurately when correlation is allowed for, whereas intershell *s*-level splittings are, by contrast, well predicted by Eq. (148). A further significant effect predicted by these CI calculations for the Mn^{3+} ^5S states is the existence of additional experimental fine structure. Specifically, there are four ^5S states at E_1, E_2, E_3, and E_4, that can be written to a good approximation as

$$\begin{aligned}
\Psi_1(^5S) &= C_{11}\Phi_1(^5S) + C_{12}\Phi_2(^5S) + C_{13}\Phi_3(^5S) + C_{14}\Phi_5(^5S)\\
\Psi_2(^5S) &= C_{21}\Phi_1(^5S) + C_{22}\Phi_2(^5S) + C_{23}\Phi_3(^5S) + C_{24}\Phi_1(^5S)\\
\Psi_3(^5S) &= C_{31}\Phi_1(^5S) + C_{32}\Phi_2(^5S) + C_{33}\Phi_3(^5S) + C_{34}\Phi_4(^5S)\\
\Psi_4(^5S) &= C_{41}\Phi_1(^5S) + C_{42}\Phi_2(^5S) + C_{43}\Phi_3(^5S) + C_{44}\Phi_4(^5S)
\end{aligned} \qquad (151)$$

As the initial state is rather well described by a single configuration $3s^2(^1S)3p^6(^1S)3d^5(^6S)$ possessing the *d*-electron coupling of Φ_1, the sudden approximation result of Eq. (84) can immediately be used to show that the four ^5S intensities will be given by

$$I_1 \propto |C_{11}|^2, \quad I_2 \propto |C_{21}|^2, \quad I_3 \propto |C_{31}|^2, \quad I_4 \propto |C_{41}|^2 \qquad (152)$$

with the total intensity $I_1 + I_2 + I_3 + I_4$ still being proportional to the spin degeneracy of 5. Evaluating the energies and relative intensities in this way yields a prediction of a total of only *three* observable ^5S peaks (one is too weak to be seen easily) and one observable ^7S peak in the Mn^{2+} spectrum. Weak structures in good agreement with these predictions have, in fact, been observed by Kowalczyk *et al.*,[253] and their experimental results are shown in Fig. 33. These CI calculations also explain a peak intensity discrepancy noted relative to simple multiplet theory: namely that the intensity ratio $^5S(1)/^7S$ in Fig. 31 or Fig. 33 is significantly below the 5/7 predicted by

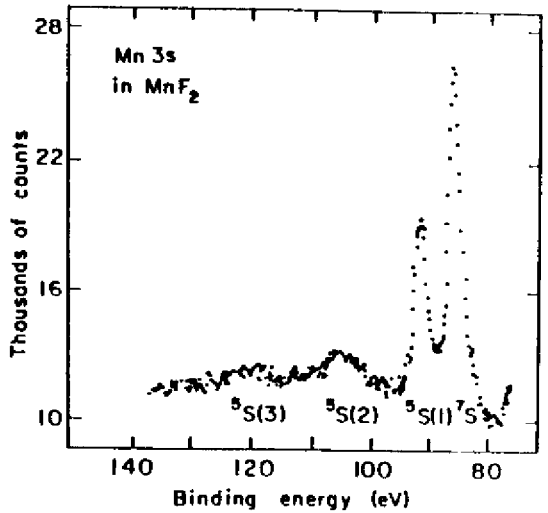

Fig. 33. Higher resolution Mn3*s* spectrum from MnF_2 obtained with monochromatized AlKα radiation (cf. Fig. 31). The peaks $^5S(2)$ and $^5S(3)$ arise from final-state configuration interaction (correlation effects) according to Eq. (151). (From Kowalczyk *et al.*, ref. 253.)

Eq. (146). It is thus clear, that, although a first-order description of multiplet effects is possible within a non-correlated Hartree-Fock approach, a detailed description of the numbers, positions, and relative intensities of peaks may require including correlation effects, especially where intrashell interactions dominate.

The first observations of *s*-electron core binding energy splittings analogous to those described by Eqs (146) (150) were in gaseous, paramagnetic

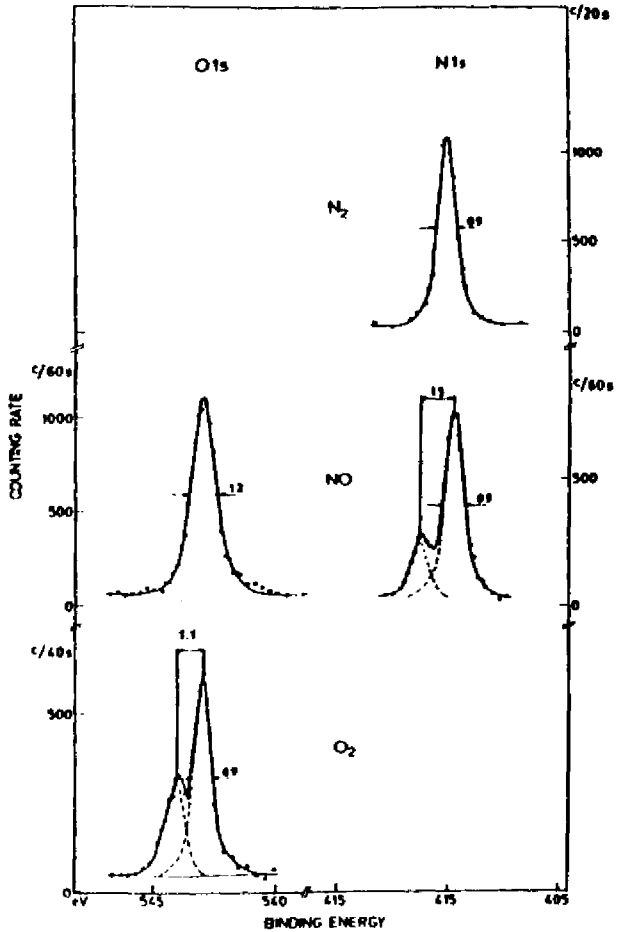

Fig. 34. XPS spectra from the 1s core electrons of the gaseous molecules N_2, NO, and O_2. The 1s peaks from the paramagnetic molecules NO and O_2 are split due to final-state multiplets. Diamagnetic N_2 shows no splitting. (From Siegbahn *et al.*, ref. 4.)

molecules.[4, 249] Hedman *et al.*[249] found splittings as large as 1·5 eV in the 1s photoelectron spectra of the molecules NO and O_2. These results are shown in Fig. 34 along with an unsplit 1s spectrum from the diamagnetic molecule N_2. In each case, it can be shown that the observed energy splitting should be proportional to an exchange integral between the unfilled valence molecular orbital and the 1s orbital of N or O,[4] in analogy with Eq. (148). Theoretical estimates of these splittings from molecular orbital calculations give values in good agreement with experiment,[4, 107] as expected for such

intershell interactions in which correlation effects are much decreased. The observed intensity ratios of the peaks are furthermore very close to the ratios of the final-state degeneracies, also in agreement with simple theory.

The analysis of binding energy splittings in emission from non-*s* core levels is not as straightforward as for *s*-level emission, primarily due to the fact that the core-electron hole represented by $(nl)^{q-1}$ (which now has associated with it a spin of $\frac{1}{2}$ and a non-zero orbital angular momentum of l) can couple in various ways with the valence subshell $(n'l')^p$ (which can have various spins S'' and orbital angular momenta L'', including the initial values S and L) to form a final state with a given total spin S' and total orbital angular momentum L'. Thus, the number of allowed final states increases and their energy separations will in general be determined by both Coulomb and exchange integrals through different coupling schemes. Additional complexities arising for non-*s* levels are caused by spin–orbit coupling and crystal-field splittings.

The simplest procedure for calculating such non-*s* energy separations is again to use non-relativistic atomic multiplet theory.[86, 250, 262, 263] As an illustrative example, consider 3*p* electron emission from Mn^{2+}, as indicated in the right-hand portion of Fig. 30. For this case, $(nl)^{q-1} = 3p^5$, $(n'l')^p = 3d^5$ and the initial state, as before, is $^6S\,(S=\frac{5}{2}, L=0)$. The previously stated selection rules imply that the allowed final states correspond to $^7P(S=3$ $L=1)$ and $^5P\,(S=2, L=1)$. Although a $^5S\,(S=2, L=0)$ final state would be, consistent with selection rule (141), it requires changing the coupling of $3d^5$ from its initial ^6S and so is not allowed. There is only one way for $3p^5$ to couple with $3d^5$ to form a ^7P state, that being with $3p^5$ (always coupled to total spin $= s = \frac{1}{2}$ and total orbital angular momentum $= l = 1$) coupled with $3d^5$ in its initial state coupling of $^6S\,(S=\frac{5}{2}, L=0)$. However, there are three ways to form the allowed ^5P final state by coupling

$$3p^5(s=\tfrac{1}{2}, l=1) \quad \text{with} \quad 3d^5\ {}^6S(S''=\tfrac{5}{2}, L''=0)$$
$$3p^5(s=\tfrac{1}{2}, l=1) \quad \text{with} \quad 3d^5\ {}^4D(S''=\tfrac{3}{2}, L''=2)$$

and

$$3p^5(s=\tfrac{1}{2}, l=1) \quad \text{with} \quad 3d^5\ {}^4P(S''=\tfrac{3}{2}, L''=1)$$

Thus, four distinct final states are possible for 3*p* emission from Mn^{2+}, one ^7P and three ^5P. As there are off-diagonal matrix elements of the Hamiltonian between the various ^5P coupling schemes,[118] they do not individually represent eigenfunctions. The eigenfunctions describing the ^5P final states will thus be linear combinations of the three schemes:

$$\begin{aligned}
\Psi_1(^5P) &= C_{11}\Phi(^6S) + C_{12}\Phi(^4D) + C_{13}\Phi(^4P) \\
\Psi_2(^5P) &= C_{21}\Phi(^6S) + C_{22}\Phi(^4D) + C_{23}\Phi(^4P) \\
\Psi_3(^5P) &= C_{31}\Phi(^6S) + C_{32}\Phi(^4D) + C_{33}\Phi(^4P)
\end{aligned} \tag{153}$$

where each ^5P configuration has been labelled by the $3d^5$ coupling involved and the C_{ij}'s are the usual expansion coefficients. The energy eigenvalues corresponding to these eigenfunctions will give the separations between the ^5P states. Such eigenfunctions and eigenvalues can most easily be determined by diagonalizing the 3×3 Hamiltonian matrix for the ^5P states, where each matrix element is expressed as some linear combination of $J_{3d,3d}$, $K_{3d,3d}$, $J_{3p,3d}$, and $K_{3p,3d}$.[33, 118] If Coulomb and exchange integrals from a Hartree–Fock calculation on Mn^{2+} are used, such matrix diagonalization calculations yield the relative separations indicated on the right-hand side of Fig. 30[86, 250] Once again, the sudden approximation result of Eq. (84) indicates that, because the initial state is rather purely $3d^5(^6S)$, only those components of the ^5P states represented by $C_{i1}\Phi(^6S)$ are accessible. Thus, the individual intensities of Ψ_1, Ψ_2, and Ψ_3 can be computed from $|C_{11}|^2$, $|C_{21}|^2$, and $|C_{31}|^2$, respectively. In determining the total intensity ratios for the ^5P and ^7P states, Eq. (142) can be used to give:

$$I_{tot}(^5P) : I_{tot}(^7P) = [I_1(^5P) + I_2(^5P) + I_3(^5P)] : I_{tot}(^7P) = 5 : 7$$

The relative peak heights in Fig. 30 have been calculated in this way, and the experimental 3s(1)–3p(1) separation and relative intensity for MnF_2 were used to empirically fix the scales between the 3s and 3p regions. The separations and relative intensities of the peaks observed are found to be at least semi-quantitatively predicted by this simple, atomic L, S coupling model,[86, 250] and these results have been confirmed in more detail by later experimental[255] and theoretical[256] studies. The remaining discrepancies between theory and experiment for this 3p case could be caused by a combination of effects due to correlation, spin–orbit coupling, and crystal-field splitting, although calculations by Gupta and Sen[250] indicate that the latter two are probably not so significant. Ekstig *et al.*[245] have carried out matrix diagonalization calculations like those described here but for more complex sets of final 3p-hole states in 3d transition metal atoms in an attempt to interpret soft x-ray emission spectra from solids. The theoretical aspects of calculating such non-s splittings have also recently been reviewed by Freeman *et al.*[263]

Deeper non-s core levels in 3d atoms should also exhibit similar splittings, although the magnitudes will be reduced because of the decreased interaction strengths between the core and 3d orbitals. For example, Fadley and Shirley[86] first noted that the Mn2p levels in MnF_2 are broadened by ~ 1.5 eV relative to those in low-spin (filled subshell) compounds, and suggested multiplet splittings as the origin of this broadening. Subsequent measurements at higher resolution by Kowalczyk *et al.*,[255] coupled with theoretical calculations by Gupta and Sen,[257] have confirmed this suggestion, and also verified the existence of peak asymmetries and anomalous $2p_{\frac{1}{2}}$–$2p_{\frac{3}{2}}$ separations. For this 2p case, both multiplet effects and spin–orbit coupling are of similar magnitude, and were included in calculations that successfully predicted the observed spectra.[257]

Analogous non-s core-level splittings have also been studied in systems with partially-filled f subshells,[86, 260, 266] and the anomalous shape and decreased spin–orbit splitting in the Eu4d spectrum of Fig. 6 is, in fact, attributable to such effects.[86]

Although only multiplet effects on core-level binding energies have been considered up to this point, such phenomena can play a considerable role in determining the fine structure observed in valence spectra (as has been apparent for some time in UPS studies of free molecules[97]). In particular, XPS valence spectra obtained from solids containing highly localized d levels or f levels are expected to be influenced by such multiplet effects,[82, 156, 157, 261, 266, 267] with the relative intensities of various allowed final states being determined by fractional parentage coefficients, as described in Section III.D.2 and elsewhere.[156, 157, 262] Heden *et al.*[267] first observed such effects in valence spectra of 4f metals. As an example of the occurrence and use of such splittings in studies of rare-earth compounds, the XPS results of Campagna *et al.*[261] and Chazalviel *et al.*[266] show strong multiplet splittings in the valence spectra of Sm-chalcogenides and a mixture of two markedly different multiplet structures in certain Sm compounds that are thought to exhibit valence fluctuations between Sm^{+2} $4f^7$ and Sm^{+3} $4f^6$. Some of these results for SmB_6[266] are presented in Fig. 35, in which the L, S multiplets expected for both Sm^{+2} and Sm^{+3} are labelled. Theoretical intensities have been calculated using fractional parentage coefficients,[156] and the agreement between the theoretically simulated spectrum and experiment is excellent. Baer[268] has also presented very high-resolution XPS spectra for various 4f metals that further confirm the existence of these atomic-like multiplet effects. In analogous multiplet effects in valence d orbitals, the inclusion of crystal-field effects is also expected to be important, as has been emphasized in a recent discussion by Bagus *et al.*[157]

In comparison to chemical shifts of core-electron binding energies, multiplet splittings of core- or valence-energies thus represent higher-order effects yielding a different type of information. In their simplest interpretation, chemical shift measurements detect a change in the spatially-averaged potential experienced by an electron, whereas analyses of multiplet effects have the capability of determining the valence electron configuration or the detailed strengths of various higher-order electronic interactions. The two types of measurements are thus complementary. Numerous applications of multiplet splittings measurements are thus possible in the study of the transition series metals, the rare earths, the transuranium elements, and open-shell systems in general.

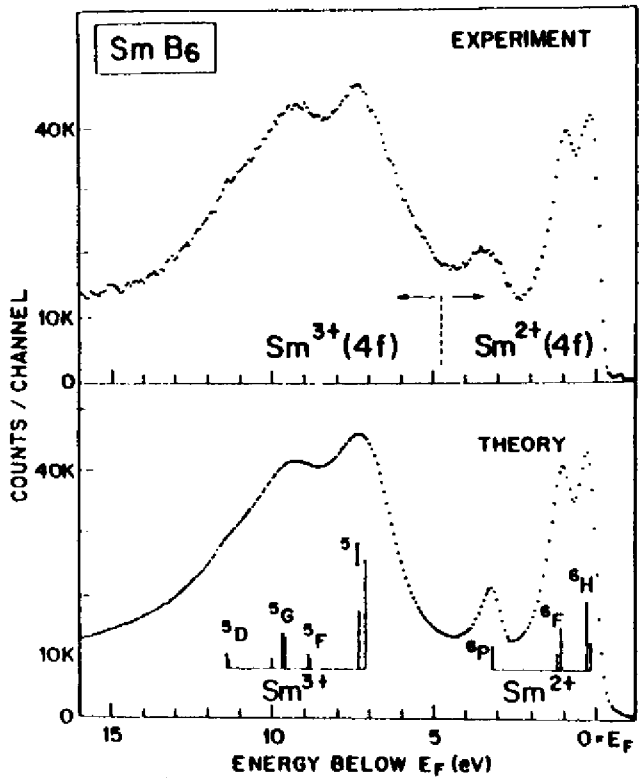

Fig. 35. Experimental and theoretical 4*f* valence spectra from SmB_6, a "mixed-valence" metallic compound believed to contain both Sm^{+2} $4f^6$ and Sm^{+3} $4f^5$. The intensities of the various final-state multiplets for $Sm^{+2} \rightarrow Sm^{+3}$ and $Sm^{+3} \rightarrow Sm^{+4}$ were computed using fractional parentage coefficients and are indicated as vertical bars. These calculations were broadened by an empirically-derived function of the form of Eq. (158) to generate the final theoretical curve. Monochromatized AlKα was used for excitation. (From Chazalviel *et al.*, ref. 266.)

D. Multi-electron Excitations

1. *Introduction.* In this section, several types of final-state effects (and, to a lesser degree, initial-state effects) that involve what appear to be "multi-electron" excitations during the photoemission process are considered. The term multi-electron is judged against a purely one-electron description in which no final-state relaxation occurs. From the outset, it is clear that relaxation *does* occur, so that all transitions are indeed *N*-electron. Also, in a configuration interaction picture, the various mixtures of initial- and final-state configurations involved could easily make it impossible to distinguish clearly a one-electron component of photoemission. Nonetheless, all effects discussed here do somehow represent final states that deviate in a well-defined way from the single initial-state Hartree–Fock determinant that best approximates the one-electron photoemission event. The discussion begins with relatively simple forms of multi-electron excitation (shake-up and shake-off), but then comes to involve more complex phenomena that are important in XPS studies of certain atoms, molecules, and solids.

2. *Shake-up, Shake-off, and Related Correlation Effects.* Multi-electron processes in connection with x-ray photoemission were first studied in detail by Carlson, Krause, and co-workers.[135] In these studies, gaseous neon and argon were exposed to x-rays with energies in a range from 270 eV to 1·5 keV. Measurements were then made of both the charge distributions of the resulting ions and the kinetic energy distributions of the ejected photoelectrons. From these measurements, it was concluded that two-electron and even three-electron transitions occur in photo-absorption, with total probabilities which may be as high as 20% for each absorbed photon. By far the most likely multi-electron process is a two-electron transition, which is approximately ten times more probable than a three-electron transition. Two types of two-electron transitions can further be distinguished, depending upon whether the second electron is excited to a higher bound state ("shake-up"[4]) or to an unbound continuum state ("shake-off"[135]). These are indicated in the transition below (cf. the corresponding one-electron transition in relation Eq. (139)):

Shake-up:

$$\underset{(L,S)}{(nl)^q(n'l')^p} \xrightarrow{h\nu} \underset{(L',S')}{(nl)^{q-1}(n'l')^{p-1}(n''l'')^1} + \text{photoelectron} \qquad (154)$$

Shake-off:

$$(nl)^q(n'l')^p \xrightarrow{h\nu} (nl)^{q-1}(n'l')^{p-1}(E_{\text{kin}}{}''l'')^1 + \text{photoelectron} \qquad (155)$$

Here $(n'l')^p$ represents some outer subshell from which the second electron is excited; it can be filled or partially filled. Either shake-up or shake-off requires energy that will lower the kinetic energy of the primary photoelectron. Thus, such multi-electron processes lead to satellite structure on the low-kinetic energy side of the one-electron photoelectron peak, as shown schematically in Fig. 8.

Higher resolution XPS spectra have been obtained more recently for neon and helium by Carlson *et al.*[269] and for neon by Sieghahn *et al.*[41, 270] A high-resolution Nels spectrum obtained by Gelius *et al.*[270] is shown in Fig. 36. The two-electron transitions that are believed to be responsible for the observed spectral features labelled 2 to 14 occurring at relative energies from 33 to 97 eV below the one-electron peak are listed in Table II. The total two-electron shake-up intensity in this spectrum is thus estimated to be approximately 12% of that of the one-electron peak. Both shake-up and shake-off together account for ~30% of all emission events.

TABLE II

Summary of data concerning multi-electron transitions accompanying the formation of a 1s hole in atomic neon by AlKα or MgKα x-rays (compare Fig. 36)

(a) *Shake-up transitions*

Line no.	Type of process	Final state	Experimental[a] excitation energy (eV)	Calculated[a, b] excitation energy (eV)	Experimental relative intensity (%)	Calculated[c] relative intensity (%)	Calculated[d] relative intensity (%)
0	One-electron transition	$1s2s^22p^6$ ^2S	(870·37)	(870·37)	100·00	100	100
1	Energy loss	$1s^22s^22p^53s$ ^2P	16·89 (6)	16·93			
2	Dipole shake-up	$1s2s^22p^53s$ ^2P lower	33·35 (9)		0·06 (1)		
3	Monopole shake-up	$1s2s^22p^53p$ ^2S lower	37·35 (2)	37·39	3·15 (8)	2·3	2·47
4	Monopole shake-up	$1s2s^22p^53p$ ^2S upper	40·76 (3)	41·26	3·13 (10)	2·9	2·60
5	Monopole shake-up	$1s2s^22p^54p$ ^2S lower	42·34 (4)	42·30	2·02 (10)		1·48
6	Monopole shake-up	$1s2s^22p^55p$ ^2S lower	44·08 (5)	44·18	0·42 (6)		0·43
7	Monopole shake-up	$1s2s^22p^56p$ ^2S lower	45·10 (7)		0·50 (15)		0·09
8	Monopole shake-up	$1s2s^22p^54p$ ^2S upper	46·44 (5)	46·42	0·96 (11)		0·70
9	Monopole shake-up	$1s2s^22p^55p$ ^2S upper	48·47 (7)	48·40	0·17 (5)		0·11
10	Monopole shake-up	$1s2s2p^63s$ ^2S lower	59·8 (1)	59·75	0·57 (5)		
11	Monopole shake-up	$1s2s2p^63s$ ^2S upper	65·9 (1)	65·93	0·49 (6)		
12	Two electron shake-up	$1s2s^22p^43p^2$ ^2S	93·14 (7)		0·08 (2)		
13	Two electron shake-up		95·9 (1)		0·10 (4)		
14	Two electron shake-up		97·23 (5)		0·24 (4)		
	Onset of shake-off	$1s2s^22p^5$ ^3P	47·4 (5)	46·96	11·89% = Partial sum of shake-up		
	Onset of shake-off	$1s2s^22p^5$ ^1P	51·7 (5)	51·27			

[a] From Gelius, ref. 270.

[b] All calculated excitation energies have been increased by 1·8 eV to allow for errors due to relativistic and correlation effects, particularly in the $1s2s^22p^6$ one-electron-transition final state.

[c] Calculated using one-electron wave functions only from Eq. (156) by Carlson *et al.*, ref. 269.

[d] Calculated using initial-state configuration interaction and Eq. (83) by Martin and Shirley, ref. 14.

TABLE II (*cont.*)

(b) *Shake-off transitions*

	Experimental[e] relative intensity (%)	Calculated[e] relative intensity (%)
Total intensity for shake-off of one electron from Ne 2s and 2p subshells ($Ne \rightarrow Ne^{2+}$)	16·5	16·1
Total intensity for shake-off of two electrons from Ne 2s and 2p subshells ($Ne \rightarrow Ne^{3+}$)	0·8	

[e] From Carlson, Krause, and co-workers, ref. 135. Intensity calculated using an extension of Eq. (156).

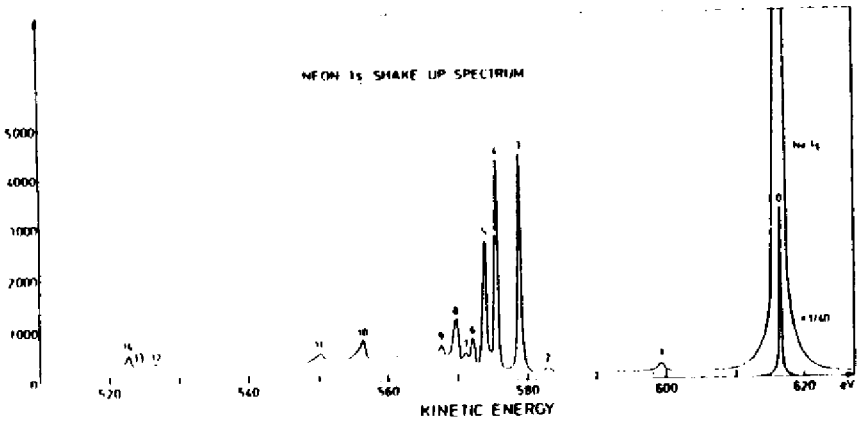

Fig. 36. High-resolution shake-up spectrum associated with excitation from Nels in gaseous neon. Table II lists the origins of the various satellite peaks labelled 1–14. The Nels FWHM was reduced to 0·4 eV in these measurements by using a monochromatized AlKα source. (From Gelius, ref. 270.)

Note that the initial and final states given in Table II are assumed to be composed of a single electronic configuration. This assumption, together with the sudden approximation as outlined in Section III.D.1, permits predicting such shake-up and shake-off peak intensities in a very straightforward way.[135] Namely, Eq. (75) is used for the relevant matrix element and it is noted that, in the passive-electron manifold, the only major change occurring for a two-electron transition is $\phi_{n'l'} \to \phi_{n''l''}$, with all other passive orbitals remaining in very nearly the same form. Thus, $\langle \phi_j' | \phi_j \rangle \approx 1{\cdot}0$ unless the overlap involved is $\langle \phi_{n''l''} | \phi_{n'l'} \rangle$, and the probability of a given transition is in simplest approximation[269]

$$P_{n'l' \to n''l''} \propto N_{n'l'} \left| \langle R_{n''l''} | R_{n'l'} \rangle \right|^2 \tag{156}$$

where $N_{n'l'}$ is the occupation number of the $n'l'$ subshell, and allows for a summation on $m_{l'}$-$m_{s'}$ (which must equal $m_{l''}$-$m_{s''}$). Here the radial function $R_{n''l''}$ must be calculated in the final-state ionic potential, and $R_{n'l'}$ is a radial function for the initial state. By virtue of symmetry, the overlap in Eq. (156) will only be non-zero if $l'' = l'$, a result that is often termed a one-electron monopole selection rule. Thus, for example, only $2s \to ns$ and $2p \to np$ monopole transitions yield large intensities as quoted in Table II (although a single, weak $2p \to 3s$ dipole transition is also thought to be present). The total symmetries for the $(N-1)$ passive electrons are also predicted to follow a monopole rule of the form predicted by Eq. (69)

$$\Delta J = \Delta L = \Delta S = \Delta M_J = \Delta M_L = \Delta M_S = \Delta\pi = 0 \tag{157}$$

where J is the quantum number for $\mathbf{L}+\mathbf{S}$, and π is the overall state parity.

Equation (156) has been used with reasonable success in predicting shake-up and shake-off intensities in core-level emission from rare gases,[4, 135, 269, 270 271] as well as from alkali-halides[271] for which the component ions possess rare-gas configurations. Some previous results for Nels emission are summarized in Table II, where calculated two-electron peak separations and relative intensities are compared with experiment. The various final-state configurations are noted and for this case the $\Psi_R(N-1)$ of Eq. (69) corresponds to an *unrelaxed* Ne^+ $1s2s^22p^6$ with an overall L, S coupling of ^2S. There is reasonable agreement between theoretical and experimental separations, but the theoretical values are uniformly high by about 1·8 eV out of 40 eV, and have been back-corrected by this amount before entry in the table.[270] The necessity for this correction has been explained as a $2p$-$2p$ correlation and relativistic error in the Hartree-Fock calculation for the one-electron $2p^6$ final state that is of much lower magnitude in the various $2p^5np$ two-electron final states because of the reduced $2p$ np overlap. Theoretical and experimental relative intensities are also in fair agreement. It should also be noted in connection with these data that the various L, S multiplets formed as final states must be considered. For example, the peaks indicated as "lower" and "upper" in Table II are due to a multiplet splitting of the same type noted on the right-hand side of Fig. 30 for the ^5P states of Mn^{3+}. In the case of Ne^+, ^2S states can be formed in two ways from the same total configuration $1s2s^22p^5np$: one in which the $1s$ electron is coupled with $2s^22p^5np(^1S)$ and one in which it is coupled with $2s^22p^5np(^3S)$.[4, 135] A similar effect occurs in $1s2s2p^6ns$ final states. Thus, there may be considerable interaction between multi-electron processes and multiplet splittings, and a complete specification of the final state must include possible multiplet effects.

The assumption of single-configuration final states used in the previous analysis clearly is open to question, especially since the best description of all states would presumbly be via a complete configuration-interaction treatment. Martin and Shirley[14] have performed CI calculations for Ne and the isoelectronic molecule HF that do indeed indicate that configuration-interaction effects can be significant. Their analysis proceeds via an equation analogous to Eq. (83), from which it is clear that both final-state CI and initial-state CI can complicate the calculation of intensities by opening up new options for non-zero $(C_j')^* C_j'$ products. In particular, the mixing of both the $1s^22s^22p^6$ and $1s^22s^22p^53p$ configurations into the initial state *and* the final states corresponding to the observed peaks 0, 3, and 4 is found to significantly alter the calculated intensities so as to yield better agreement with experiment, as shown in Table II.

It should also be noted that the total shake-up intensities associated with *valence-level* emission are generally observed to be higher than predicted by

the simple theory outlined above, a result that is consistent with much stronger intrashell correlation effects.[135, 269] For example, Chang and Poe[272] have recently performed theoretical calculations for Ne2p excitation at $h\nu \lesssim 200$ eV using more accurate many-body perturbation theory. Their results are in good agreement with available experimental data.

Similar core-level shake-up phenomena are also well known in molecules[4, 269, 270] and the same type of sudden approximation analysis as represented by Eqs (69) to (74) has been used with some success to predict intensities.[273, 274] In connection with valence-level emission a recent CI analysis of low-energy satellite structure in CO by Bagus and Viinikka[275] indicates that higher-order correlation effects are also highly significant, in agreement with the similar conclusions reached previously for atomic valence-level shake-up.

3. *Multi-electron Excitations in Metals.* Processes analogous to shake-up and shake-off are also expected to occur during core-level emission from solid metals, where the form of the density-of-states curve above the Fermi energy provides a continuous range of allowed one-electron excitation energies, rather than the discrete set available in atoms or molecules. Thus, rather than a sharp set of satellite lines below a roughly symmetric one-electron-transition peak (cf. Fig. 36), what is expected is an asymmetric tailing of the main peak. The detailed line shapes associated with such processes in XPS core-level emission were first discussed by Doniach and Sunjic[276] and are predicted to have the form:

$$I(E)=\frac{\cos\left[\pi\alpha/2+(1-\alpha)\tan^{-1}(E/\gamma)\right]}{(E^2+\gamma^2)^{(1-\alpha)/2}} \tag{158}$$

where

E = kinetic energy measured from the threshold of the unbroadened one-electron-transition peak

γ = the lifetime of the core hole

α = an asymmetry parameter

$$=2\sum_l (2l+1)(\delta_l/\pi)^2 \tag{159}$$

δ_l = the phase shift of the lth partial wave for electrons at the Fermi energy scattering from the core hole.

2γ is thus the natural FWHM of the core-level. If $\alpha = 0$ (as it is for insulators), then $I(E)$ merely reduces to a Lorentzian lifetime broadening. The phase shift δ_l thus has a meaning very close to those discussed in connection with atomic differential cross-sections in Section III.D.2 (cf. Fig. 9).

Citrin[277] first pointed out that XPS metal spectral shapes exhibited an asymmetry suggestive of Eq. (158). The first quantitative tests of the applicability of this line shape for describing such spectra were performed by Hüfner, Wertheim and co-workers.[84] They fitted Eq. (158) to core spectra for various simple metals and transition metals, empirically choosing the best values of γ and α. The spectra were corrected for instrumental resolution effects, but not for inelastic scattering. Examples of such a comparison between theory and experiment for Au and Pt[84] are shown in the right-hand panels of Fig. 37. It is significant here that Au with a low density of states near the Fermi level shows a much lower degree of asymmetry than Pt with a high density of states near the Fermi level. Hüfner, Wertheim *et al.*[84] concluded that this line shape does well describe the peaks observed in these metals, and that the values of γ and α obtained were physically reasonable. Similar conclusions have been reached in several other studies,[115, 191] and it thus seems likely that such shake-up-like effects do exert a significant influence on line shapes in metals.

A further closely-related effect that has been predicted to occur in metals is the creation of plasmon excitations during the formation of a core hole.[194, 278] Such "intrinsic" plasmons are distinguished from the "extrinsic" plasmons created during photoelectron escape from the material, although they occur at the same energy and are thus rather difficult to resolve from the experimental inelastic tail. Debate still continues as to how important intrinsic plasmons are in XPS spectra,[279] and some angular-resolved XPS results bearing on this question are discussed in Section VI.B.

4. *Core-peak Satellites in Transition-metal and Rare-earth Compounds.* Very strong low-kinetic-energy satellite lines were first observed in a study of Cu2p core levels in compounds such as CuS and Cu_2O by Novakov[280]. Similar results obtained more recently by Frost *et al.*[281] are shown in Fig. 38, and it is clear that the satellite peaks have intensities comparable to those of what might be referred to as the one-electron-transition peaks at lowest apparent binding energy. The appearances of these satellites also depend strongly on chemical state, being most intense in cupric compounds containing Cu^{+2} $3d^9$ ions, and almost unobservable in cupric compounds containing Cu^{+1} $3d^{10}$ ions. Similar strong satellites also occur in the core spectra of other open-shell transition-metal and rare-earth compounds.[114, 282-286] They are thus much higher in relative intensity than the 10–30% expected from typical atomic-like shake-up processes, and a great deal of discussion has gone on concerning their origins. Summaries of experimental data, as well as analyses of various proposed models, appear in several prior publications.[114, 280-286]

The most plausible explanation that has emerged for such effects is a significant involvement in the final state of a ligand-to-metal charge transfer

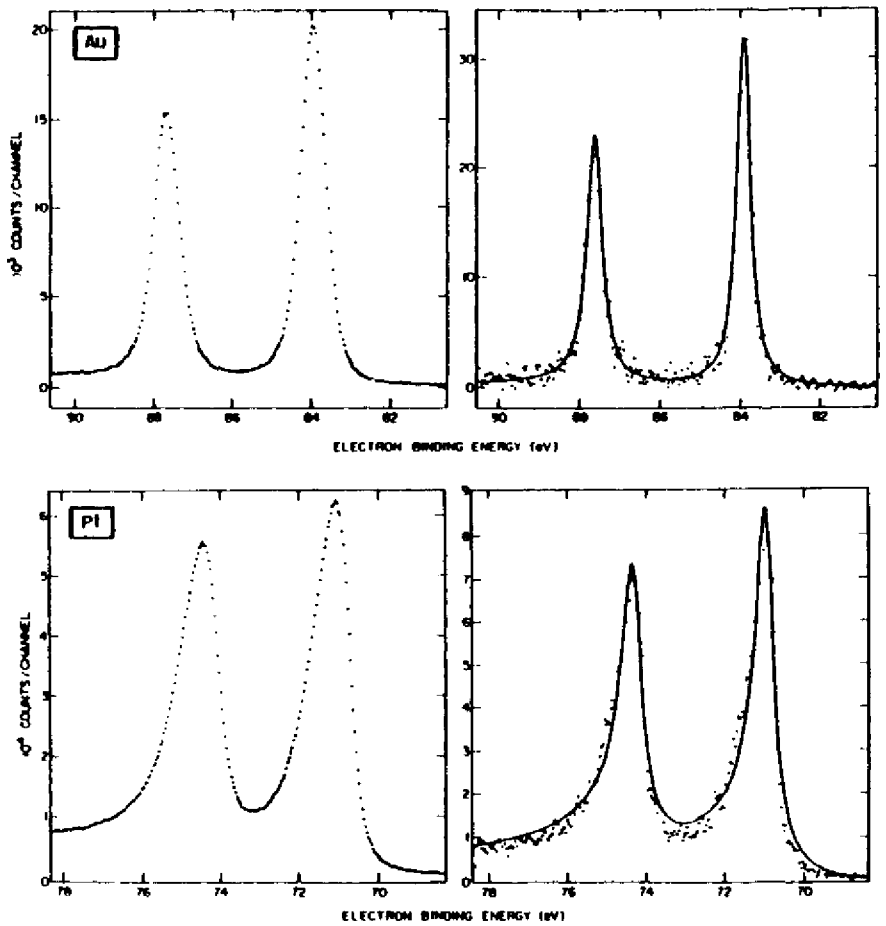

Fig. 37. 4*f* core spectra from polycrystalline Au and Pt (points) in comparison to a best fit of the asymmetric line shape predicted by Eq. (158) (curves). In the right panels, the data have been corrected by deconvolution of the instrumental line shape, but no correction for inelastic scattering effects has been made. The instrumental line shape was derived from the form of the cut-off near E_F (cf. Fig. 13). (From Hüfner and Wertheim, ref. 84.)

that results in a 3*d* or 4*f* configuration with one more *d* or *f* electron than in the initial state.[114, 282, 283, 285, 286] This idea was first suggested and qualitatively discussed by Wertheim *et al.*[114] for satellites in 4*f* compounds and by Kim[283] for 3*d* satellites. The importance of such $3d^n \rightarrow 3d^{n+1}$ and $4f^n \rightarrow 4f^{n+1}$ configurations is not surprising, since they represent an attempt to screen very effectively the core hole formed during final-state relaxation. In fact, there is a high degree of similarity between such final-state configurations

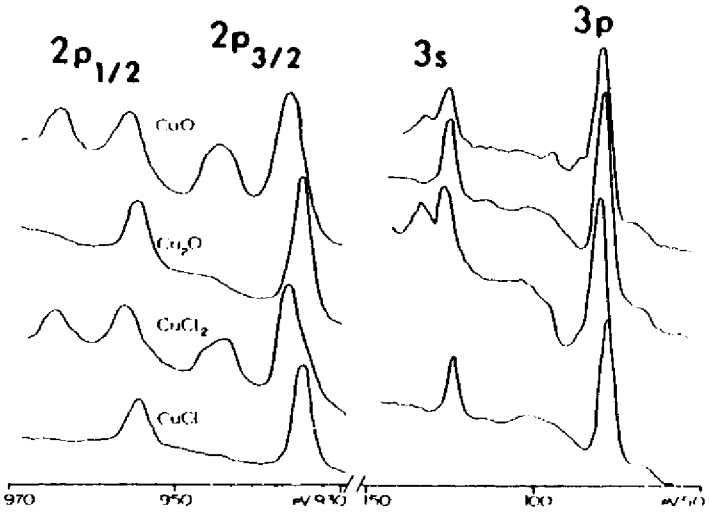

Fig. 38. 2*p*½, ½ and 3*s*, 3*p* core-level spectra from the copper compounds CuO, Cu_2O, $CuCl_2$, and CuCl. The low-energy satellites are very strong in Cu^{+2} $3d^9$ compounds (CuO, $CuCl_2$), and very weak in Cu^{+1} $3d^{10}$ compounds (Cu_2O, CuCl). (From Frost *et al.*, ref. 281.)

and those used by Ley *et al.*[235] to describe conduction-electron screening in metals (cf. Fig. 29 and discussion in Section V.B). The absence of satellites for closed-shell *d* or *f* systems is immediately explained in this picture, as such relaxation mechanisms are not possible. The most quantitative discussions of this model as applied to 3*d*-compound satellites have been presented by Larsson[285] and Asada and Sugano.[286] A two-configuration manifold is used to describe the final-state core-hole wave functions, with one configuration Φ_1 being the simplest final-state determinant with no change in valence-subshell occupations and the other Φ_2 being a determinant in which a single-electron ligand-to-metal transfer has occurred. Specifically, in an octahedrally-coordinated system, the transfer is ascribed to a monopole-allowed excitation of the type:[283, 285, 286] $e_g(\text{bonding}) \equiv e_g^b \rightarrow e_g(\text{anti-bonding}) \equiv e_g^a$. Both orbitals are expressed as linear combinations of metal *d* and ligand valence, with e_g^a being primarily metal 3*d*. The crystal-field-split octahedral symmetry designations are used, and the sudden approximation one-electron monopole selection rule must here be applied to these symmetries. If only the active orbitals are considered, the two final-state configurations can thus be written as:[286]

$$\Phi_1 = (\text{core hole})\,(e_g^b)^n(e_g^a)^m$$

$$\Phi_2 = (\text{core hole})\,(e_g^b)^{n-1}(e_g^a)^{m+1} \qquad (160)$$

Mixing these configurations produces two final states with differing degrees of charge transfer:

$$\Psi_1{}^f = C_{11}\Phi_1 + C_{12}\Phi_2 \quad \text{at} \quad E_1{}^f$$
$$\Psi_2{}^f = C_{21}\Phi_1 + C_{22}\Phi_2 \quad \text{at} \quad E_2{}^f \tag{161}$$

The "main" line occurs at lower E^f and thus higher kinetic energy and lower binding energy. If $\Psi_1{}^f$ is chosen to represent this main line, it is found to correspond to a net transfer of $\gtrsim 0.5$ electrons to the metal site.[110, 285] Thus, hole screening is predicted to be very appreciable as far as this state is concerned, and the mixing represented by Eq. (161) is highly significant. If the degree of one-electron-orbital relaxation is small, then Φ_1 is approximately equal to the $(N-1)$-electron remainder $\Psi_R(N-1)$ in Eq. (69), and the sudden approximation yields peak intensities via Eq. (84) of

$$I_1 \propto |C_{11}|^2, \quad I_2 \propto |C_{21}|^2 \tag{162}$$

Additional splittings due to crystal-field effects, multiplet effects, and spin–orbit interactions cause further fine structure in the predicted energies, and one-electron orbital relaxation has furthermore been included by means of the equivalent-core approximation.[286] With a limited degree of empirical parameter choice, numerical results based upon this model are in good agreement with experimental satellite data for $3d$ compounds as to intensities, widths, positions, and systematic trends with ligand character and d-orbital occupations.[285, 286] Finally, it is important to note that Viinikka and Bagus[110] have carried out more accurate self-consistent Hartree–Fock calculations with configuration interaction on fully-relaxed core-hole states in the cluster $[NiO_6]^{10}$. These results also show that a significant ligand-to-metal charge transfer of ~ 0.5 electrons is present in the state representing the main line. It is also concluded that the two primary final states contain significant admixtures of both configurations ($C_{11} \approx 0.9$, $C_{12} \approx 0.3$, $C_{21} \approx 0.3$, $C_{22} \approx 0.9$).

The occurrence of such two-configuration charge-transfer satellites has also been suggested in connection with the adsorption of CO on transition-metal surfaces.[287] In this case, satellites observed in the O1*s* spectrum are attributed to the strong involvement of a metal-to-molecule charge transfer (that is, the reverse of the direction discussed previously).

Thus, such satellites and the charge-transfer they represent can be extremely important considerations in the analysis of spectra in many systems. The term "shake-up" has been applied to these effects,[283, 285, 286] but such nomenclature can be a bit misleading in the sense that the final states are not pure configurations that are as simply related to the initial state as for the neon case of Table II. The most correct view would seem to be simply that a strong configuration interaction occurs in the final state due to relaxation about the inner hole.

It is finally worth noting that the presence or absence of such satellites has potential for use in a "fingerprint" mode for determining the oxidation state and/or valence configuration of $3d$ or $4f$ atoms in different chemical environments.

5. *Other Multi-electron Effects.* As a final example of multi-electron effects, we consider the observation first made by Gelius[270] that, for a series of elements with $Z \approx 50$–60, the $4p$ binding energy broadens into a many-electron resonance with complex structure, as shown in later data obtained by Kowalczyk *et al.*[215] in Fig. 39. This rather unique occurrence has been observed in both gases[270] and solids,[215] and has been explained by Wendin *et al.*[288, 289] as being caused by the particular one-electron energy-level spacings involved. Specifically, the single-configuration final-state after $4p$ emission is $\ldots 4p^5 4d^{10} 5s^2 \ldots$, with the remaining outer occupancies depending upon Z. However, the $4d$ binding energy is approximately $\frac{1}{2}$ that of $4p$ in this region of the periodic table, so that one $4d$ electron can be moved into the lower-energy $4p$ orbital and another $4d$ electron can be placed in a low-energy unoccupied bound orbital or continuum orbital to yield a set of configurations like $\ldots 4p^6 4d^8 5s^2 \ldots (n'l')^1$ or $\ldots 4p^6 4d^8 5s^2 \ldots (E_{kin} l')^1$ respectively that are nearly degenerate with the one-electron final-state configuration. Strong mixing thus occurs among these configurations, with a resultant smearing of the final states into a broad resonance with fine structure. The mixing in of continuum configurations can also be considered to result from a Coster–Kronig Auger de-excitation of the $4p$ hole via $4d \rightarrow 4p$, $4d \rightarrow$ continuum. The form of the interactions further dictates that orbitals with $l' = 2$ are dominant.[288, 289] (Note the similarity between the configurational degeneracy discussed here and that noted by Bagus *et al.*[252] in their analysis of $3s$ emission from Mn^{2+}, cf. Section V.C). It is thus rather fortunate that such resonances are rare phenomena throughout the periodic table, as one-electron energy levels would otherwise be a much less useful concept.

E. Vibrational Effects

The effects of exciting various final vibrational states on XPS spectra were first clearly observed in gas-phase data obtained with monochromatized radiation by Gelius and co-workers.[270] A C1*s* spectrum obtained from gaseous CH_4 is shown in Fig. 40, and it exhibits a three-component structure that can be explained as arising from the excitation of three different vibrational states of the symmetric C–H stretch type.[270] The relative intensities and positions of these peaks are furthermore found to be in good agreement with a theoretical model based upon the Born–Oppenheimer approximation as expressed in Eq. (63), provided that it is noted that the C1*s* hole alters

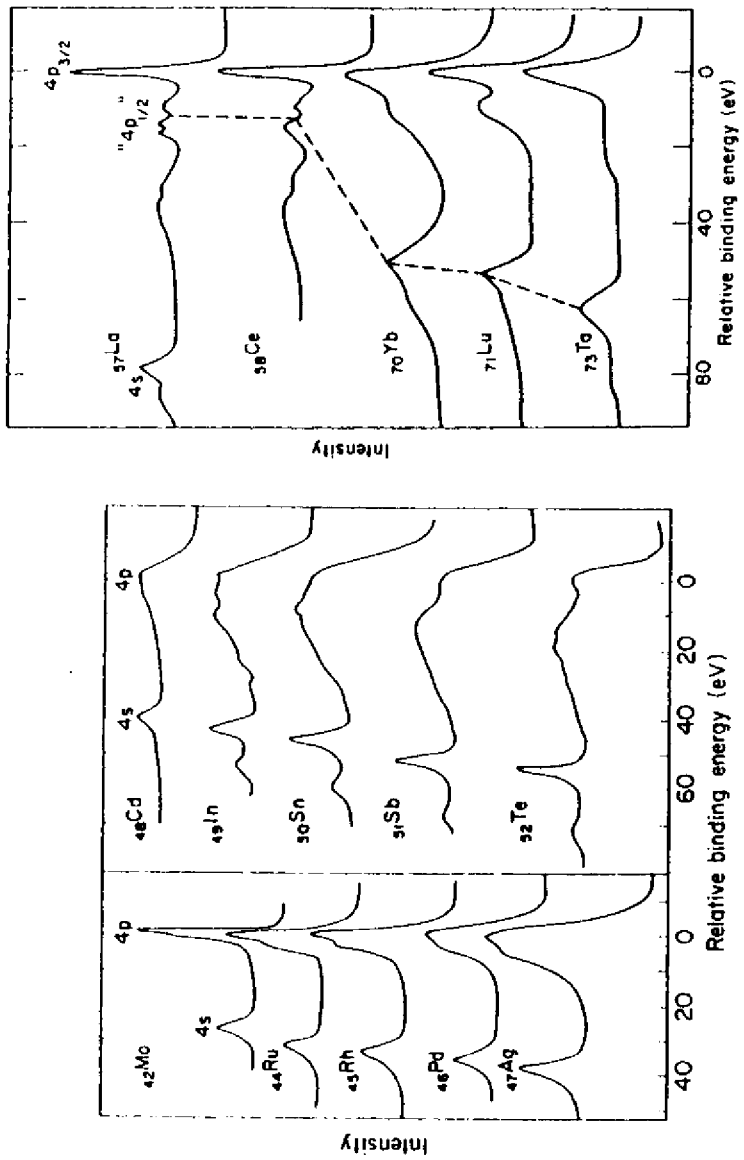

Fig. 39. 4s, 4p core-level spectra for a series of metals from Mo ($Z = 42$) to Ta ($Z = 73$). Note the broad 4p resonance that exists from $Z \gtrsim 49$ to $Z \gtrsim 60$. (From Shirley *et al.*, ref. 215.)

vibrational energies and wave functions appreciably in the final state. Similar vibrational effects appear to be present in other small molecules, and it is thus clear that XPS peak widths and positions can be significantly affected by final-state vibrational excitations.

Vibrational effects have also been noted in XPS studies of solids by Citrin *et al.*[85] In this work, core peaks in alkali halides were found to exhibit temperature-dependent line widths consistent with the excitation of lattice

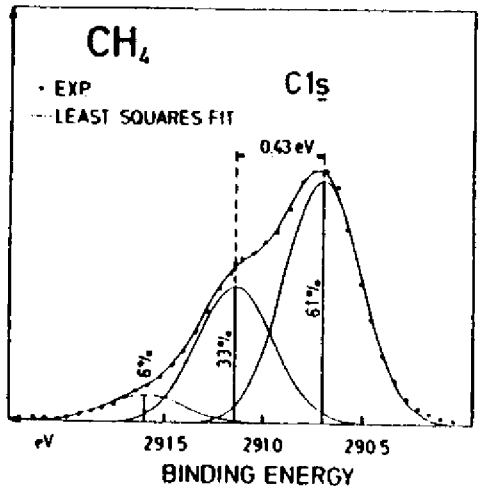

Fig. 40. A C1*s* spectrum from gaseous CH_4 obtained with very high instrumental resolution (FWHM ≈ 0·3 eV). The lowest-binding-energy primary peak shown here is found to exhibit three components due to vibrational excitations in the final state. (From Gelius, ref. 270.)

vibrations (phonons) during photoemission as shown in Fig. 41. A solid-state analysis based upon the Born–Oppenheimer approximation and Franck–Condon factors yields the proper variation with temperature, provided that the effects of specimen charging due to low conductivities at low temperatures are corrected for, as shown in the figure. Such effects are thus expected to be important in all polar solids for which electronic relaxation around the core hole cannot be complete enough to leave final vibrational states of very nearly the same form as the initial vibrational states. In metals, on the other hand, conduction electron screening is expected to be complete enough to leave the initial- and final-vibrational manifolds nearly identical. Thus, in metals the distribution of phonon excitation probabilities or Franck–Condon envelope is sharply peaked around the initial states (as can be seen by considering Eq. (63) for a single set of orthonormal functions); therefore, very little extra broadening is expected.

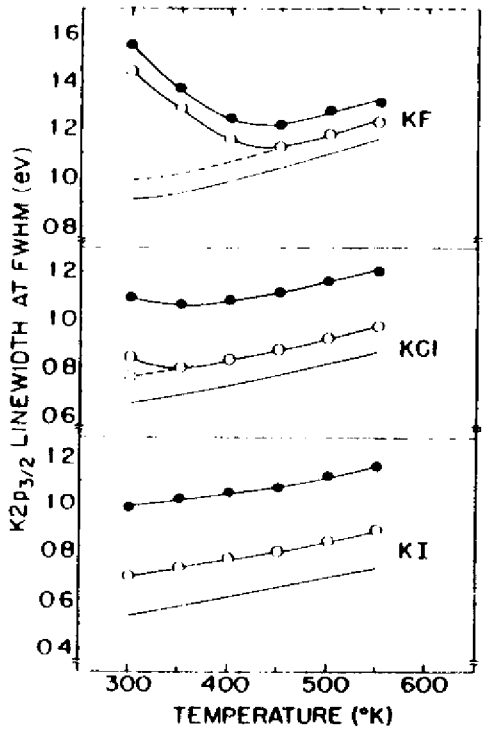

Fig. 41. Variation of the K2$p_{\frac{3}{2}}$ FWHM with temperature in solid KF, KCl, and KI. The curves ● ● are the unaltered experimental data. The curves –○—○– have been corrected for lifetime and instrumental width contributions. The dotted curves represent further corrections for specimen charging that occurred in KF and KI at low temperatures. The solid curves are theoretical calculations based upon final-state vibrational broadening. (From Citrin *et al.*, ref. 85.)

VI. ANGULAR-RESOLVED MEASUREMENTS ON SOLIDS

A. Introduction

Angular-resolved XPS studies of solids have very recently been reviewed by the author,[17] so only a brief outline of the most significant aspects and certain very new results will be presented here. The most generally occurring types of effects are those involving surface sensitivity enhancement for grazing angles of electron exit *or* x-ray incidence with respect to the surface and two types of anisotropies observed in the angular distributions of photoelectron intensities from single-crystal specimens.

The schematic geometry shown in Fig. 42 both reiterates the definitions of various angles as discussed previously here (cf. Figs 7 and 17) and also indicates that the electron emission direction can be made to have any

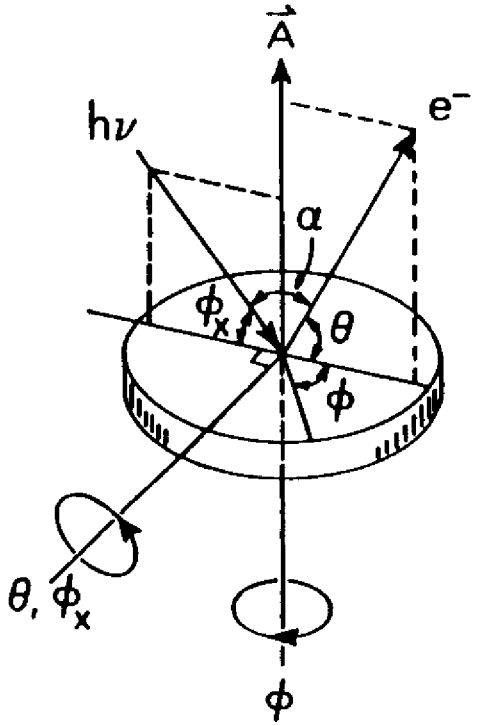

Fig. 42. General geometry for an angular-resolved XPS experiment. Rotations on the two perpendicular axes shown vary θ, ϕ_x and ϕ over their full allowed ranges. The angle α also may be varied, but is most commonly held constant.

orientation with respect to a set of axes fixed in the specimen if externally-accuated rotation is possible on the two perpendicular axes shown. Rotation on the axis perpendicular to the plane containing the photon and electron propagation directions varies the angles θ and ϕ_x describing electron exit and x-ray incidence, respectively. Rotation about the second axis parallel to the specimen surface normal varies the azimuthal angle ϕ as measured with respect to a specimen-fixed reference. Low ϕ or low ϕ_x thus corresponds to a grazing condition. The angle α is held fixed in most current XPS systems. Two-axis specimen goniometers for this purpose have been specially built for use in XPS studies, and various instrumental aspects of carrying out such measurements have been reviewed elsewhere.[17, 74, 202, 280]

B. Surface Sensitivity Enhancement at Grazing Electron Exit Angles

The achievement of greater relative surface sensitivity at conditions of grazing electron exit angles has already been discussed in connection with the

θ-dependent relationships describing peak intensities in Section III.F.2. The application of this procedure in XPS was first demonstrated by Fadley and Bergström,[291] and first quantitatively applied by Fraser *et al.*[201] As a simple illustration of the fundamental mechanism, Fig. 43 illustrates the way in which the mean depth of no-loss emission varies for a homogeneous, semi-infinite substrate. If Λ_e is assumed to be a direction-independent property of the material, this mean depth is given at any angle by $\Lambda_e \sin\theta$, so it is clear that a decrease of θ from say 90° to 5° will decrease the mean depth by about a factor of 6. This is a highly significant change that has by now been used in numerous studies to enable selectively altering the surface sensitivity of the XPS measurement.[17]

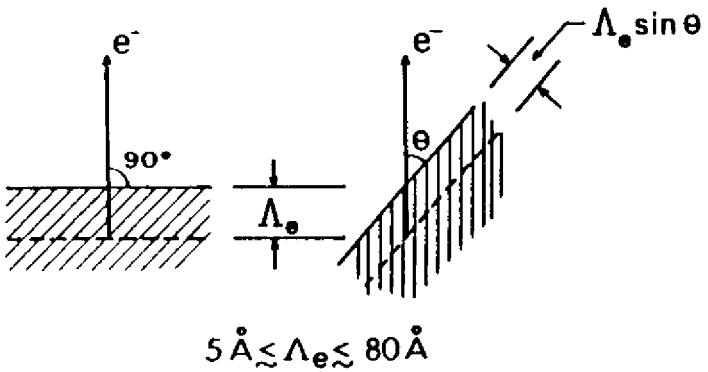

Fig. 43. Illustration of the basic mechanism producing surface sensitivity enhancement for low electron exit angles θ. The average depth for no-loss emission as measured perpendicular to the surface is given by $\Lambda_e \sin\theta$.

The only significant moderating factor that may in certain circumstances render such low-θ measurements somewhat less dramatic in capability is the presence of surface roughness. Surface roughness in general causes the local microscopic true angles of emission θ^t to differ from the experimental value θ as measured relative to the macroscopic planar average of the specimen surface. In general, for low θ values, roughness is expected to cause θ^t to be greater than θ, so that surface sensitivity enhancement is expected to be diminished.[17, 202, 290, 294] Roughness further has the effect of shading certain portions of the surface from x-ray incidence and/or electron exit. Such effects have been studied both experimentally and theoretically for a few systems,[17, 202, 203, 290, 294] and, although it is clear that large-scale roughness can significantly alter the type of surface enhancement achieved,[203] it has also been found for one system that, even with pressed powder pellets of the type often used as specimens in XPS, a usefully large surface enhancement can be achieved at low θ.[293] Thus, although roughness effects always need

to be considered in any quantitative analysis of such XPS data and the preparation of highly planar specimens is essential for some work,[294] there are good reasons to expect very general utility of the low-θ surface enhancement procedure. We now consider a few examples of the application of this method.

In Fig. 44, broad-scan spectra are shown at various angles for a highly-polished silicon specimen with an oxide overlayer 1–2 atomic layers in

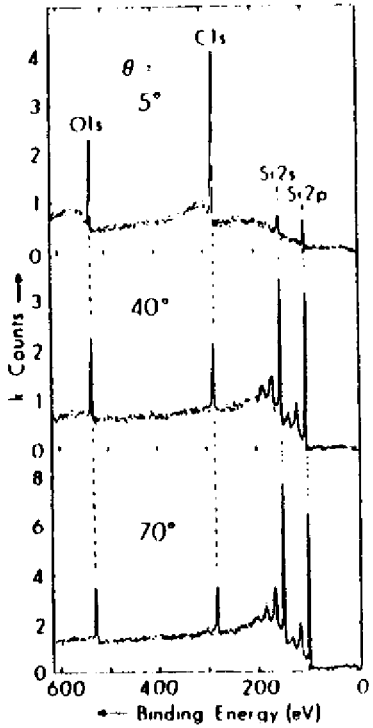

Fig. 44. Broad-scan core spectra at low and high exit angles for a Si specimen with a thin oxide overlayer (~4 Å) and an outermost carbon contaminant overlayer approximately 1–2 monolayers in thickness. The C1*s* and O1*s* signals are markedly enhanced in relative intensity at low θ due to the general effect presented in Fig. 43. (From Fadley, ref. 17.)

thickness, and an outermost overlayer of carbon-containing residual gas impurities of approximately the same thickness. (These thicknesses were estimated using Eqs such as (117) and (118).) Pronounced peaks due to the O1*s*, C1*s*, Si2*s*, and Si2*p* core levels are observed. At the higher emission angles of 40° and 70°, plasmon loss structure is also found to be associated with the Si peaks (cf. also Fig. 1 for Al). As θ is lowered to a grazing exit condition, marked changes occur in the relative intensities of all peaks, in

fact causing a complete inversion in ordering. At high θ where maximum bulk sensitivity is expected (Λ_e in Si is ~ 37 Å and Λ_e' in SiO_2 is ~ 27 Å[294]), the intensity order is Si2*s*, 2*p* ≫ O1*s* > C1*s*, where at low θ with maximum surface sensitivity, it is C1*s* > O1*s* ≫ Si2*s*, 2*p*. Such a three-angle scan thus clearly establishes the mean vertical displacement of all dominant species with respect to the surface, yielding very directly a qualitative concentration profile. If the Si2*p* region for this specimen is examined more closely, it is further found to exhibit a chemical shift between oxide and element, as shown in Fig. 45. However, the thin oxide layer present yields only a very weak relative intensity in the Si2*p* (oxide) peak at the relatively high angle of $\theta = 49°$.

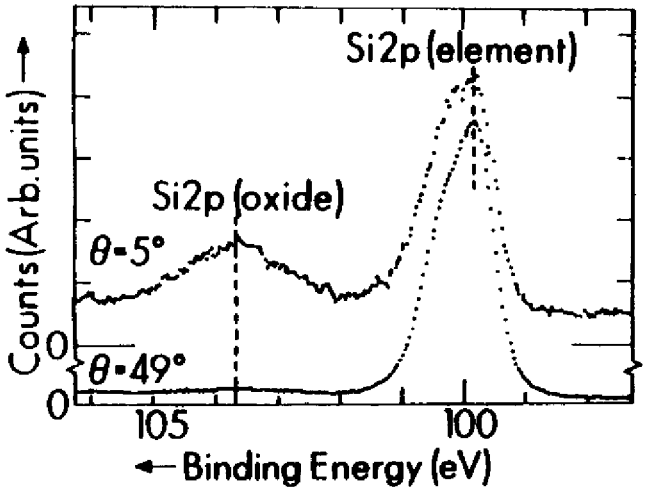

Fig. 45. Si2*p* core spectra at $\theta = 5°$ and 49° for the specimen of Fig. 44. The chemically-shifted Si2*p* (oxide) peak is enhanced in relative intensity by approximately a factor of 20 between 49° and 5°. (From Fadley, ref. 17.)

The spectrum obtained at $\theta = 5°$ by contrast exhibits marked enhancement by a factor of ~ 20 in the oxide relative intensity. More quantitative studies of such relative intensity changes with angle have also been made by Hill *et al.*,[294] and, although certain discrepancies are found to occur at low θ values with respect to the simple intensity expressions given in Section III.F.2, case (*c*), it nonetheless appears possible to extract highly quantitative data concerning specimen geometry and electron attenuation lengths.

An additional effect that is of interest in connection with the enhanced surface sensitivity achievable at low θ is a change in the relative intensities of various inelastic loss processes. For example, for an atomically clean surface of aluminium (which exhibits well-defined surface- and bulk-plasmon excitations at different energies), it has been found by Baird *et al.*[295] that

the surface plasmon losses are markedly enhanced in relative importance at low θ. Some data from this study are shown in Fig. 46. The reason for this enhancement is that the surface- and bulk-plasmons are spatially orthogonal.[107] Because decreasing the angle of exit also decreases the mean depth of emission, the relative probability of exciting a surface plasmon is thus also increased at low exit angles. Comparisons of such data with theoretical calculations for a free electron metal[194] furthermore yield good agreement with experimental relative intensities and further suggest that the creation of plasmons occurs by means of both extrinsic (after excitation) and intrinsic

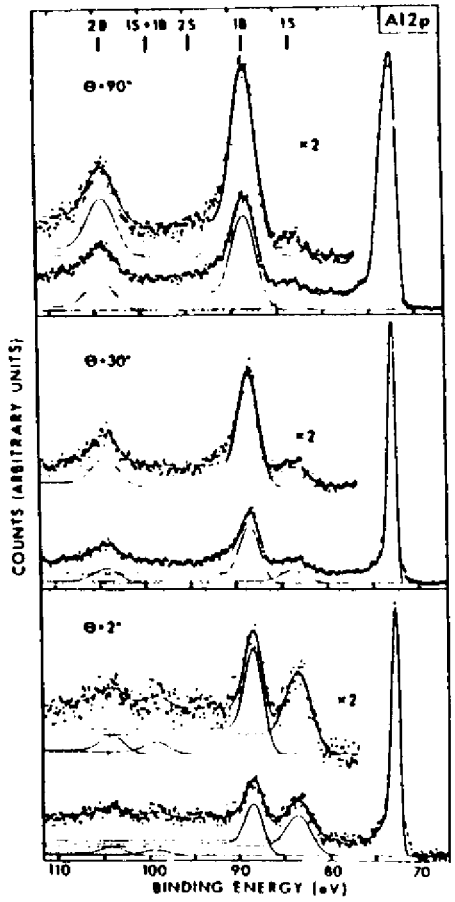

Fig. 46. Al2*p* plasmon loss spectra from a clean surface of polycrystalline aluminium at $\theta = 90°$, 30°, and 2°. The positions of various combinations of surface and bulk losses are denoted 1S, 1B, etc. Note the marked enhancement of the relative intensity of the surface plasmon loss (1S) for grazing exit angles. (From Baird *et al.*, ref. 295.)

(during excitation) processes.[295] An additional interesting feature of such angular-dependent loss measurements is that they can be used to determine the locations of adsorbed molecules relative to a surface. Specifically, the O1*s* loss spectrum for an ~0·2 monolayer coverage of oxygen on aluminium exhibits only surface plasmon peaks at grazing electron exit, indicating that the oxygen has not penetrated significantly below the surface plane.[295, 296] Thus, the angular dependence of such absorbate loss structures should provide useful complementary information concerning adsorption geometries and near-surface electronic structure.

The ground-state valence electronic structure of a solid is also predicted theoretically to change near its surface,[297] and it is of interest to determine whether angle-resolved XPS studies can detect this. One effect that should occur in transition metals is a narrowing of the FWHM of the *d*-bands near the surface due to reduced coordination number.[297] Such effects have been studied quantitatively by Mehta and Fadley[298] for the case of clean polycrystalline copper surfaces, and the experimental and theoretical *d*-band

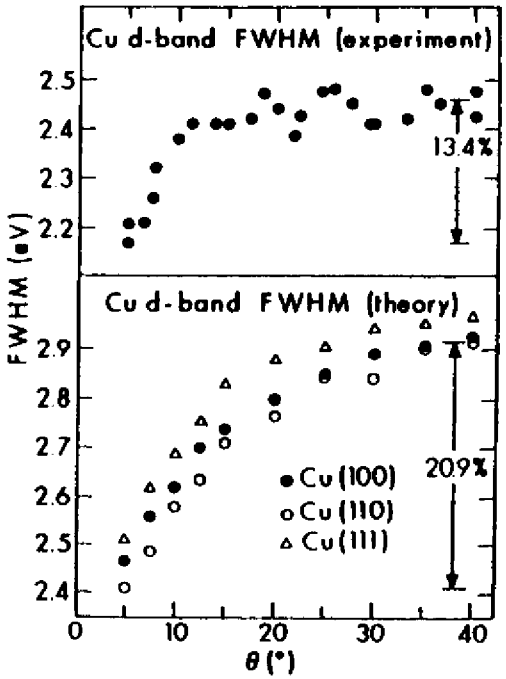

Fig. 47. Experimental and theoretical angular dependence of the FWHM of the Cu3*d* valence-band peak. The width decreases at low θ due to *d*-band narrowing near the surface that is in turn caused by reduced coordination number. (From Mehta and Fadley, ref. 298.)

FWHM values determined are summarized in Fig. 47. The small, but unambiguous decreases in FWHM observed at low θ are consistent with the theoretical calculations, with theory showing somewhat larger relative changes that could easily be explained by several effects.[298] Thus, such low-θ measurements can also be used to probe alterations in the near-surface valence electronic structure.

C. Surface Sensitivity Enhancement at Grazing X-ray Incidence Angles

A second mechanism producing enhanced surface sensitivity involves measurements carried out at very low x-ray incidence angles ϕ_x. For $\phi_x \lesssim 1°$, it was first noted by Henke[178] that the mean x-ray penetration depth in a typical XPS experiment (which is 10^3–10^5 Å for $\phi_x \gg 1°$) decreases markedly to values of the same order as the electron attenuation length Λ_e. This further suggests that surface-atom signals will be enhanced in relative intensity at low ϕ_x, as was first demonstrated by Mehta and Fadley.[179] The reason for this decrease in x-ray penetration depth is the onset of significant refraction such that $\phi_x' \ll \phi_x$ (cf. Fig. 17) and reflection at the solid surface. The interactions of typical XPS x-rays with a homogeneous medium are furthermore well described by a macroscopic classical treatment,[178] and detailed expressions for predicting penetration depths and expected surface sensitivity

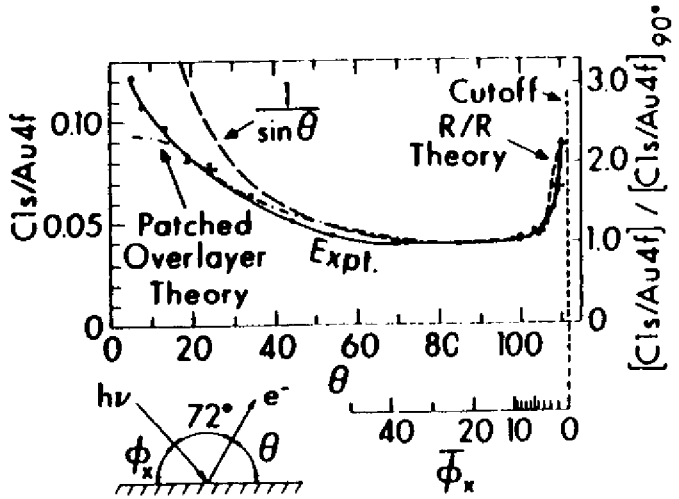

Fig. 48. Angular dependence of the C1*s*/Au4*f* intensity ratio for a gold specimen with a thin carbon-containing overlayer. Enhancement of the near-surface carbon signal is found for both grazing electron exit (low θ) and grazing x-ray incidence (low ϕ_x). The low-ϕ_x enhancement is well predicted by classical calculations allowing for x-ray refraction and reflection (R/R) at the surface, as shown by the dashed curve. (From Mehta and Fadley, ref. 179.)

enhancements in terms of the material optical constants and other parameters have been presented elsewhere.[17, 178, 179]

As an example of the surface sensitivity enhancement occuring at low ϕ_x, Fig. 48 shows data obtained from a gold specimen with ~2 atomic layers of carbon-containing material as an overlayer. The C1*s*/Au4*f* intensity ratio thus serves as a measure of relative surface sensitivity, and it is observed to increase at both low θ (for reasons discussed in the last section) and low ϕ_x. The increase at low ϕ_x is comparable to that at low θ (approximately a factor of 2–3), and there is good agreement between experiment and theoretical calculations including refraction and reflection effects. Note the very sharp onset of the low-ϕ_x enhancement over a region of only a few degrees near $\phi_x \sim 0$. Similar effects have also been noted in the Si2*p*(oxide)/Si2*p*(element) ratio for silicon with varying oxide overlayer thicknesses.[299] Also, the optical properties of several solids at XPS energies of ~1·5 keV have been used to predict that such phenomena should be of very general occurrence.[17]

It should be noted in connection with low-ϕ_x studies, however, that surface roughness effects can be very important in any attempt at quantitatively analyzing such data.[299] This is due to the very small incidence angles involved, so that if the true microscopic incidence angle ϕ_x^t deviates by even ~0·1° from the macroscopically measurable ϕ_x, a significant change occurs in the degree of refraction and reflection. Thus, surface preparation and accurate angle measurement are both very critical. A further practical problem is that surface shading by any roughness present will generally act to much diminish absolute photoelectron intensities at low ϕ_x. Thus, low ϕ_x surface enhancements may serve as a useful complement to those at low θ, but the measurement and interpretation of low-incidence-angle data may not be as straightforward.

D. Single-crystal Effects

Two rather distinct types of single-crystal effects have been noted in prior XPS studies. The physical origins and possible interpretations of these will be briefly discussed.

1. *Electron Channeling and Kikuchi Bands.* In measurements of core peak intensities or energy-integrated valence-spectral intensities from single-crystal specimens as a function of the emission angles θ and ϕ in Fig. 42, pronounced fine structure is noted. The first effects of this type were observed by Sieghahn *et al.*[300] in NaCl and by Fadley and Bergström[291] in Au. Baird *et al.*[200] have obtained the most detailed set of such data to date for Au4*f* emission from a Au crystal with (001) orientation and this is summarized in the stereographic projection intensity contour plot of Fig. 49(a). Considerable fine structure is evident in this plot, with many features possessing angular FWHM values of only ~5–10° and peak height : background ratios as high as ~2 : 1. It is thus clear that no peak intensity analysis involving a single crystal can neglect such effects.

The origin of this fine structure is primarily electron diffraction from the various sets of planes in the crystal. These effects are furthermore very closely related to the Kikuchi bands seen in low-energy electron diffraction (LEED) experiments carried out with $E_{kin} \gtrsim 300$ eV,[301] as well as to channeling phenomena seen in the emission of high-energy electrons (~10^4–10^6 eV) from radioactive nuclei imbedded in single crystals.[302] Based upon prior experimental and theoretical studies in these two areas,[301, 302] the qualitative expectation is for each set of planes denoted by Miller indices (*hkl*) to have associated with it a band of enhanced intensity for photoelectron emission that is parallel with the planes to within plus or minus the first-order Bragg angle θ_{hkl}, as defined from

$$\lambda_e = 2d_{hkl} \sin \theta_{hkl} \tag{163}$$

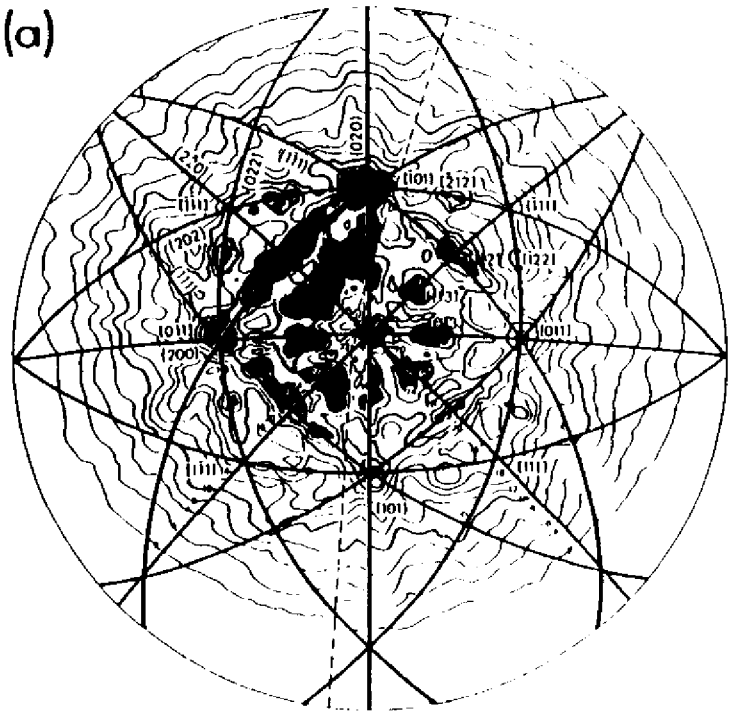

Fig. 49. (a) Experimental photoelectron intensity contours for Au4*f* emission from a Au(001) single-crystal surface. The contours are plotted in stereographic projection with various low-index directions indicated as [*hkl*]. The normal to the surface therefore lies in the centre of the figure. The arcs represent low-index planes available for electron diffraction or channelling.

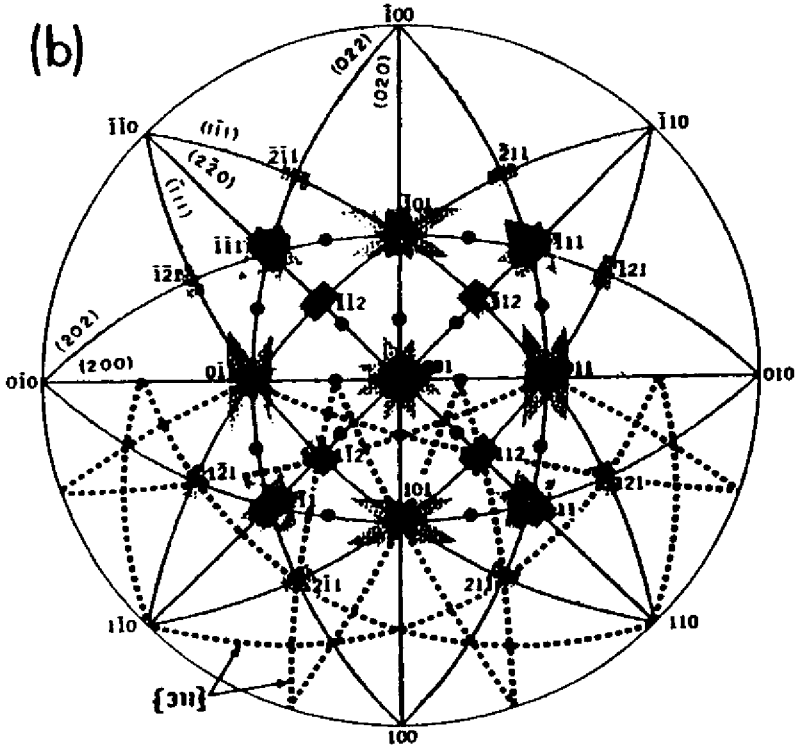

Fig. 49. (b) Qualitative theoretical simulation of the intensity pattern of (a) based on shaded rectangular Kikuchi bands of the form given by the dashed line in Fig. 50. The dotted lines in the lower half of the figure represent the centres of weaker, broader bands from lower-index planes that would also appear at mirror-symmetry-related points in the upper half. (From Baird *et al.*, ref. 200.)

with

$$\lambda_e\,(\text{in Å}) = \text{electron deBroglie wavelength} = [150/E_{\text{kin}}\,(\text{in eV})]^{\frac{1}{2}} \qquad (164)$$

$$d_{hkl} = \text{the interplanar spacing}$$

Such Kikuchi bands are furthermore expected to be approximately uniform in intensity over the $\pm\theta_{hkl}$ range, and to drop off rather sharply at the limits of this range, as shown schematically in Fig. 50. For typical higher-energy XPS photoelectrons and lower-index metal crystal planes, θ_{hkl} is found to lie in the range 3–15°. The overall photoelectron intensity distribution above a single-crystal surface is thus expected to be approximately given by a superposition of such bands for the various low-index planes within the crystal.

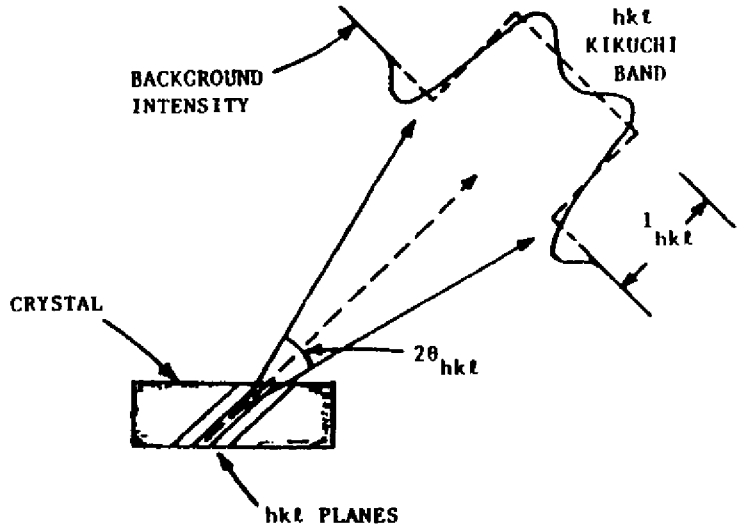

Fig. 50. The approximate form expected for a Kikuchi band from the (*hkl*) set of planes in a single crystal.

As a qualitative test of this interpretation, Fig. 49(b) presents a stereographic projection on which shaded bands corresponding in width and placement to those expected for the lowest index planes in Au have been inserted. Dotted lines in the lower half of the figure also indicate the centers of broader and weaker bands expected from higher-index planes. Comparison of Figs 49(a) and 49(b) indicates that there is good correspondence between experiment and theory as to the locations of high-intensity regions and fine structure. Recently, more quantitative calculations for copper have been carried out by Baird *et al.*[303] in which each band is given a height proportional to the Fourier coefficient V_{hkl} in the crystal potential; these calculations yield very good agreement with similar intensity contours for copper. Thus, the basic systematics of such effects is well established and relatively easily predicted, and such measurements can provide rather direct information concerning the near-surface atomic order and crystal orientation. Furthermore, in the very near future, more highly accurate theoretical calculations of such effects utilizing methods developed for LEED analyses should become available.[304]

A final important point in connection with such core-level angular distribution measurements is that it may be possible to utilize them for determining the bonding geometries of atoms or molecules adsorbed on single-crystal surfaces. That is, *if* core-level emission from an adsorbed atom does exhibit angular anisotropy, it must be primarily associated with final-state scattering effects that should, in turn, be strongly related to the nearest-neighbor

atomic geometry. Very recent measurements in our laboratory do in fact indicate that such anisotropies exist.

2. *Valence Spectra.* It was first noted by Baird *et al.*[185, 305] that XPS valence spectra from a single crystal exhibit considerable changes in fine structure as the electron emission direction is varied with respect to the crystal axes. As an example of these effects, Fig. 51 presents Au valence

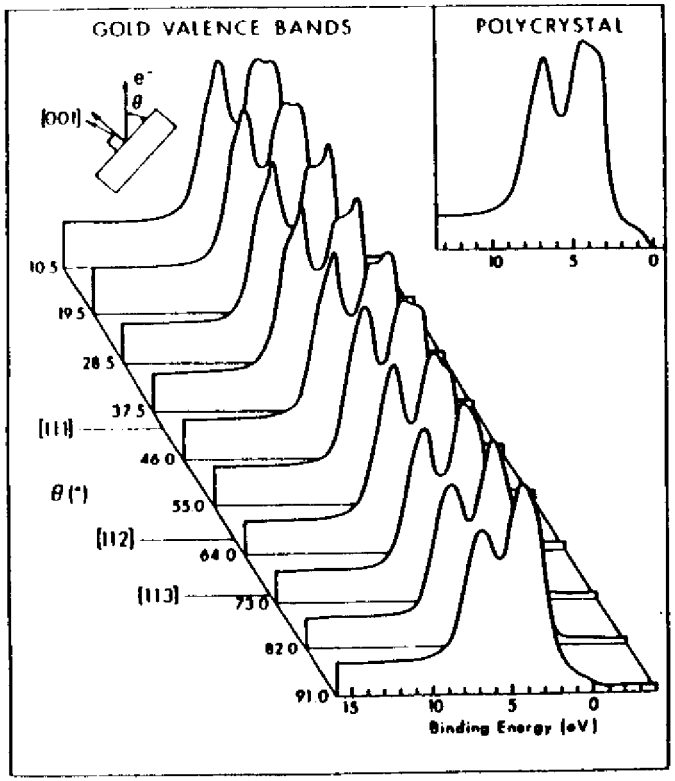

Fig. 51. Au valence spectra from a (001) single-crystal surface obtained at various θ values in a single polar scan passing through the [111], [112], and [113] directions. A polycrystalline spectrum is shown for reference. (From Baird *et al.*, ref. 200.)

spectra obtained with electron emission along various directions in a single θ scan. Although the basic two-peak structure in the dominant *d*-band peak is present for all directions, there are pronounced changes in the relative intensities and shapes of the two components. In particular, Au spectra obtained with emission along the [001], [101], and [111] directions exhibit probably the most pronounced differences relative to one another, as shown in Fig. 52. Similar changes in single-crystal XPS valence spectra with direction

have by now also been noted in Ag,[306] Cu,[307, 308] Pt,[309] and the layer compounds MoS_2, $GaSe_2$, and SnSe.[310]

The occurrence of such anisotropic effects thus means minimally that considerable care must be exercised in interpreting any XPS valence spectrum from a single crystal in terms of quantities such as the total density of states. That is, the total density of states $\rho(E)$ is by definition a non-directional quantity, as is the mean cross-section $\bar{\sigma}_E(h\nu)$, so that clearly such single-crystal effects add an element beyond the model summarized in Eq. (107). For example the Si spectrum shown in Fig. 14 may well exhibit an extra strength in the peak labelled "L_1" due to such effects.[305] As noted in Section III.D.4, the connection of XPS spectra to the density of states in a direct way implies a type of uniform averaging over initial states that need not be possible in a directionally-sensitive single-crystal experiment.

As it is reasonable to expect that the anisotropies noted in XPS valence emission from single crystals are associated somehow with the basic

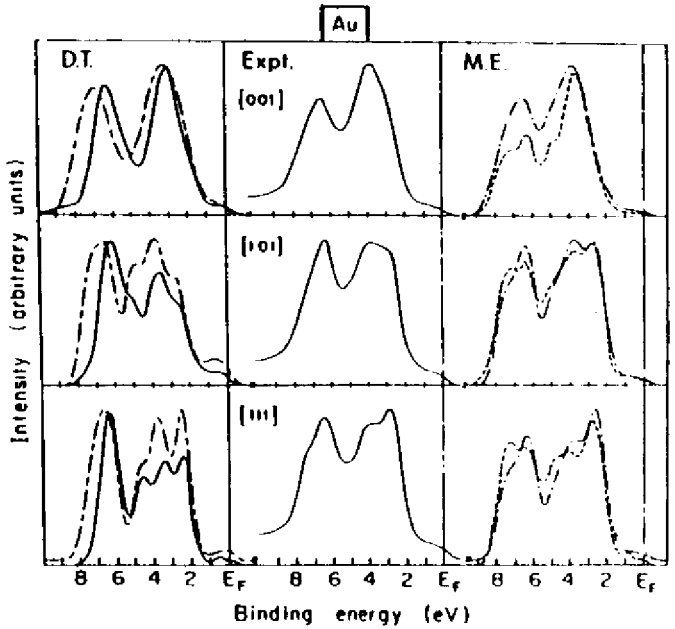

Fig. 52. Experimental and theoretical angular-resolved XPS Au valence spectra for electron emission along the [001], [101], and [111] directions. The data were obtained with monochromatized AlKα radiation. "D.T." represents calculations based upon the direct-transition model. "M.E." represents plane-wave matrix-element calculations. The band structures utilized in the theoretical calculations were: ——, Christensen's RAPW[315] and – – –, - - - - -, two slightly different choices for the spin orbit parameter in Smith's tight-binding interpolation scheme.[316] (From refs 185, 311, and 317.)

symmetries of the initial states involved, it is of considerable interest to develop theoretical models for the interpretation of such effects. Two different approaches to this problem have been proposed.[185, 306-312] Both of these models begin with the basic direct-transition expression given in Eq. (106), but the different assumptions made in each yields final predictions of a much different form. These two models are:

(1) *The Direct Transition Model.* In this model, the wave-vector conservation embodied in Eq. (104) is primarily emphasized. This viewpoint has been used previously to analyze angular-dependent UPS data from single crystals,[182, 313] and suitable modifications to permit its direct application to higher-energy photoemission experiments were first discussed by Baird *et al.*[185] Rigorous wave-vector conservation is used to connect each observed final-state wave vector $\mathbf{k}^f$ with a unique initial-state wave vector $\mathbf{k}$ within the reduced Brillouin zone by means of a suitable (and unique) reciprocal lattice vector $\mathbf{g}$. The *magnitude* of $\mathbf{k}^f$ is determined from the internal kinetic energy $E_{\mathrm{kin},i}$ (cf. Fig. 12) by assuming that the free-electron dispersion relation $E_{\mathrm{kin},i} = \hbar^2(k^f)^2/2m$ is valid at high excitation energies. At XPS energies, k^f furthermore varies very little over the valence spectrum: for example, in gold with lattice constant $a = 4{\cdot}08$ Å, it is found that $12{\cdot}84(2\pi/a) \leqslant k^f \leqslant 12{\cdot}88(2\pi a)$, where $2\pi/a$ is approximately the reduced zone radius. The *direction* of $\mathbf{k}^f$ (or, equivalently, the direction of the photoelectron momentum) with respect to the crystal axes is determined from the known crystal orientation relative to the spectrometer acceptance solid angle. (Small direction corrections due to electron refraction in crossing the surface barrier V_0 are necessary only for very low angles of electron exit.[17, 307]) The finite solid angle of acceptance of the electron energy analyzer distributes the

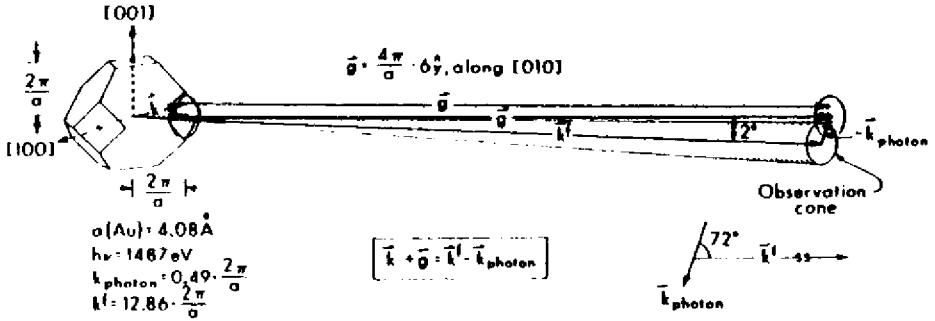

Fig. 53. Scale drawing in k-space of the direct transitions that would be involved in XPS emission along the [010] direction in a Au single crystal. The initial states from which emission could occur are represented by those k values in the shaded disc near the face of the reduced Brillouin zone at left. The additional involvement of variable-magnitude phonon wave vectors due to vibrational effects appears, however, to lead to rather full zone averaging in angular-resolved XPS spectra from Au at room temperatures, as discussed in the text.

observed $\mathbf{k}^f$ values over a disc-like region in k-space, as shown in the scale drawing for gold in Fig. 53, where the acceptance solid angle is taken for illustration to be conical with a 2·0° half angle. Each $\mathbf{k}^f$ value can then be corrected by the non-negligible $\mathbf{k}_{h\nu}$ associated with the photon to yield a set of vectors $\mathbf{k}^f - \mathbf{k}_{h\nu} = \mathbf{k} + \mathbf{g}$ (shown as the right-hand shaded disc in the figure) that permits uniquely determining the set of $\mathbf{k}$ values in the reduced zone from which allowed transitions can occur (shown as the left-hand shaded disc lying coincidentally very near a reduced-zone face). Due to the finite size of the disc (cf. its size to that of the reduced zone in Fig. 53), more than one $\mathbf{g}$ may be involved, depending on the exact placement of the disc in k-space or, equivalently, the observation direction in real space. It is further assumed in this model that the matrix elements for all $\mathbf{k} \rightarrow \mathbf{k}^f$ transitions are approximately equal, so that an angular-resolved spectrum is finally predicted to be proportional to the density of electronic states over the allowed $\mathbf{k}$ region (*not* the total density of states).

This model has been unambiguously demonstrated by Wagner *et al.*[314] to predict correctly all of the major spectral changes occurring with emission direction and photon energy for copper in the intermediate photon energy range $40 \lesssim h\nu \lesssim 200$ eV. XPS calculations based upon this model for Au with emission along [001], [101], and [111] are shown in Fig. 52, where they are indicated by "D.T." and compared with experimental spectra. Two different initial-state band structures have been utilized in the calculations,[315, 316] yielding two different sets of curves. The most accurate band structure was used for the solid curves, and comes from a relativistic augmented plane wave (RAPW) calculation by Christensen.[315] Both sets of direct-transition curves qualitatively predict the correct changes in both the relative intensities of the two main components and the shapes of each component, although the calculations do predict more change with direction than is noted experimentally. Similar agreement has been found for 9 other directions in Au,[317] as well as 6 directions in Cu,[307] leading to previous conclusions[185, 307] that the direct-transition model represents a good description of such effects in XPS. However, very recent data obtained by Hussain *et al.*[318] for Au with both MgKα and AlKα radiation are at variance with this model: specifically, for emission along [001], [111], and [112], theory predicts large changes in the spectra of a given direction when photon energy is changed (because the disc changes position in the reduced zone due to the change in the length of $\mathbf{k}^f$), whereas negligible differences are observed experimentally. In addition,[318] for excitation with AlKα, the free-electron metal Al is found not to exhibit *any* spectral changes with emission direction, again in disagreement with direct-transition predictions. It thus appears that some form of wave-vector smearing or reduced-zone averaging is occurring, probably due to the creation or annihilation of phonons, as suggested first by Shevchik[186] and discussed

previously in Section III.D.4. The fraction of direct transitions for which phonon smearing is absent is most simply estimated from the Debye–Waller factor:[187]

$$\text{Debye–Waller factor} = \exp\left(-\tfrac{1}{3}\langle u^2\rangle \mathbf{g}^2\right) \tag{165}$$

where

$\langle u^2\rangle$ = the mean squared vibrational displacement of atoms in the lattice

$\mathbf{g}^2 = |\mathbf{g}|^2$, with $\mathbf{g}$ the reciprocal lattice vector involved in a given direct transition

$\langle u^2\rangle$ is thus a function of material and temperature. In XPS, $\mathbf{g}^2$ is of the same order as $(k^f)^2$ (cf. Fig. 53) and therefore is much larger than the corresponding quantity in UPS. Thus, the Debye–Waller factor can be very small in XPS, as, for example, 0.04 in Au at 25 °C. Such small values suggest that rather complete zone averaging may occur in room-temperature angular-resolved XPS measurements on many systems, as previously noted. (In fact, Williams *et al.*[319] have recently noted the disappearance of direct-transition effects in UPS spectra of Cu obtained at high temperature that very nicely confirm phonon involvement.) The direct transition model as outlined here thus may not be applicable to room-temperature XPS measurements on many materials, even though it clearly is a valid description at lower excitation energies,[313, 314] and perhaps also at lower temperatures in XPS.

(2) *The Plane-wave Matrix-element Model.* This model was first discussed in connection with angular-dependent XPS spectra by McFeely *et al.*[306] Although k-conserving direct transitions are used as a starting point, it is further assumed that final-state complexities somehow smear out the determination of $\mathbf{k}$ and $\mathbf{k}^f$ to such a degree that essentially all $\mathbf{k}$ values in the reduced zone can contribute to emission in any direction. Mixing of different plane-wave components into the final electronic states by various scattering processes was first suggested as the source of such zone averaging,[306] but such effects do not seem to be strong for copper with $h\nu \leq 200$ eV.[314] More likely, the creation or annihilation of phonons in the photoelectron excitation event is responsible.

In the limit of complete zone averaging, anisotropies in XPS valence spectra are then assumed by McFeely *et al.*[306] to be due to directional matrix elements as summed over all occupied initial states. These matrix elements are in turn calculated by assuming a plane-wave final state of the form:

$$\phi_{\mathbf{k}}{}^f(\mathbf{r}) = \exp\left(i\mathbf{k}^f\cdot\mathbf{r}\right) \tag{166}$$

and a tight-binding or LCAO initial state of the form:[96, 99]

$$\phi_{\mathbf{k}}(\mathbf{r}) = \sum_{\mathbf{R}_l} \exp\left(i\mathbf{k}\cdot\mathbf{R}_l\right)\left\{\sum_{\mu} C_{\mu\mathbf{k}}\, X_\mu(\mathbf{r}-\mathbf{R}_l)\right\} \tag{167}$$

in which

$\mathbf{R}_l$ = the position of an atomic center in the lattice

$X_\mu(\mathbf{r}-\mathbf{R}_l)$ = an atomic orbital centered at $\mathbf{R}_l$

$X_\mu(\mathbf{r}) = R_\mu(r)\,Y_\mu(\theta,\phi)$ [cf. Eq. (36)]

$C_{\mu\mathbf{k}}$ = an expansion coefficient

Computing matrix elements $\langle\phi_{\mathbf{k}}{}^f|\mathbf{A}\cdot\nabla|\phi_{\mathbf{k}}\rangle$ can then be shown[159, 306, 312] to yield a linear combination of the Fourier transforms of the various atomic orbitals making up the initial-state orbital. Such Fourier transforms furthermore exhibit the same angular dependence in $\mathbf{k}^f$ space that the atomic function has in real space, and they can thus be written as

$$X_\mu(\mathbf{k}^f) = f_\mu(k^f)\,Y_\mu(\theta_{\mathbf{k}^f},\phi_{\mathbf{k}^f}) \tag{168}$$

with $\theta_{\mathbf{k}^f}$, $\phi_{\mathbf{k}^f}$ indicating the direction of $\mathbf{k}^f$, and $f_\mu(k^f)$ being a radial integral dependent on $|\mathbf{k}^f| = k^f$ only. For radiation with a polarization direction $\mathbf{e}$, it then directly results that

$$\left|\langle\phi_{\mathbf{k}}{}^f|\mathbf{A}\cdot\nabla|\phi_{\mathbf{k}}\rangle\right|^2 \propto (\mathbf{e}\cdot\mathbf{k}^f)^2\left|\sum_{\mu} C_{\mu\mathbf{k}}\, X_\mu(\mathbf{k}^f-\mathbf{k}_{hv})\right|^2 \tag{169}$$

In general, $\mathbf{e}\cdot\mathbf{k}^f$ has been held constant in prior experiments, and for a closely related set of orbitals such as d functions, it can further be assumed that the factor $f_\mu(k^f)$ is constant. Finally, each initial state is thus predicted to contribute photoelectron intensity with a weight of $\left|\sum_{\mu} C_{\mu\mathbf{k}}\, Y_\mu(\theta_{\mathbf{k}^f\,\mathbf{k}_{hv}},\phi_{\mathbf{k}^f\,\mathbf{k}_{hv}})\right|^2$ and a summation can be carried out over all such occupied states. Thus, for example, the contribution of a $d_{x^2-y^2}$ atomic orbital to such a matrix element is predicted to be a maximum along the same directions as the orbital maxima, namely the $\pm x$ and $\pm y$ directions. Orbital symmetry is thus predicted to be very directly reflected in the angular-dependent emission probability. Calculations based upon this model are presented in Fig. 52 for Au, where they are indicated by "M.E." Two different types of tight-binding parameterizations have been utilized, and it is clear that the results are sensitive to this choice. Nonetheless, there is generally good agreement between experiment and theory for the three directions shown, as well as others in Au[306, 311] which have been investigated, and a similar set in Cu.[311] The same type of plane-wave model has also been found by Ley *et al.*[310] to predict correctly changes in single-crystal valence spectra of the compounds MoS_2, $GaSe_2$, and $SnSe_2$. Thus, it at present appears that the plane-wave matrix element approach is the more correct of the two discussed here for describing room temperature XPS experiments on most materials, although significant questions do still remain as to the validity of using a free-electron plane-wave final state for

computing XPS matrix elements.[165, 186, 318] More accurate theoretical calculations of such effects are thus clearly of interest.

To the degree that such measurements do directly reflect orbital symmetries, such angular-resolved XPS studies should prove to be very useful probes of valence electronic structure.

VII. CONCLUDING REMARKS

The aim of this chapter has been to discuss in some detail the basic ideas involved in both performing and interpreting XPS measurements. It is clear that a relatively large number of distinct physical and chemical effects can be related to the observed spectra. This diversity can be both an advantage and a disadvantage in using the technique, depending upon the specific problem at hand and the phenomena encountered. On the positive side, however, is the fact that at least some degree of quantitative understanding has been achieved in connection with all of the effects noted to date. The theoretical interpretation of XPS spectra also involves a liberal mixture of concepts from atomic, molecular, and solid-state physics, thus making the technique truly interdisciplinary in character. A major goal of the discussion here has been to present these diverse ideas within a single, unified framework.

As an important example of the interdependency of different phenomena, final-state effects of various types can tend in certain situations to obscure the initial-state information that is of most interest in many applications. But, on the other hand, final-state effects can also be used to determine additional characteristics of the system. The essential reason for this initial-state/final-state dichotomy is that the photoemission event is inherently very disruptive to the system, leaving it with a hole in a certain subshell and thus a significantly altered set of electron-electron interactions. The interpretive material presented in Sections III–V therefore begins with a rather general discussion of the photoemission process that emphasizes the importance of both initial and final states (as well as inelastic scattering effects). However, the first areas of application considered are intentionally those which for many systems can exhibit the strongest initial-state component: valence-level studies in molecules and solids (Sections III.D.3 and III.D.4), quantitative analysis (Section III.F.3), and core-level binding energy shifts (Section IV). Nonetheless, care must always be exercised in analysing data in order to avoid having the different final-state effects discussed in Section V introduce a significant error in any conclusions concerning initial-state properties.

The potential range of information derivable from XPS spectra is indeed very broad, and a schematic summary of the interrelationships between various observable quantities or effects and basic system properties is presented in Table III. In this table, the possible interactions between different observables are also indicated.

TABLE III

Schematic illustration of the interrelationships between various observable XPS spectral features or their associated effects and the basic system properties potentially derivable from an analysis of such observations

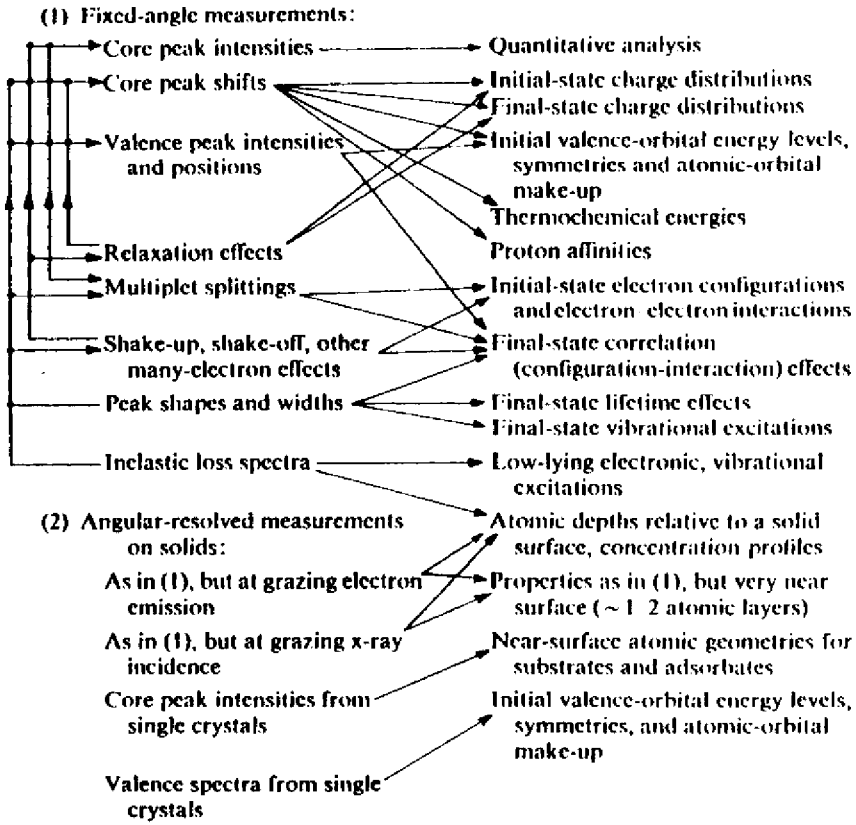

XPS has been and will no doubt continue to be fruitfully utilized for the study of free atoms, free molecules, and the *bulk* properties of solids and liquids. However, the inherent *surface* sensitivity of the technique when applied to solids and liquids leads to what is certainly one of the most significant areas of application, namely in studying the physics and chemistry of surfaces and interfaces. In this context, the relatively newly developed angular-resolved studies of solids have also clearly been demonstrated to enhance significantly the amount of information derivable, as is also indicated

in Table III. Two separate procedures exist for selectively increasing surface sensitivity by angle variations. For single-crystal specimens, information concerning both detailed atomic geometries and valence-orbital symmetries can also be derived from angular-distribution measurements.

No exhaustive elucidation of specific areas of application for XPS has been attempted here, but it is sufficient to note that by now the technique has been used in problems related to physical chemistry, inorganic chemistry, organic chemistry, biochemistry, solid-state physics, surface chemistry, surface physics, industrial chemistry, and environmental science. Future developments will no doubt involved all of these areas, but with special emphasis on problems related to surface science. A further significant component of future work will no doubt be the more extended use of XPS in combination with other spectroscopic methods such as, for example, the other surface-sensitive techniques of UPS, photoelectron spectroscopy utilizing synchrotron radiation sources, low-energy electron diffraction (LEED), Auger electron spectroscopy (AES), and secondary ion mass spectrometry (SIMS).

Thus, x-ray photoelectron spectroscopy is by now a relatively mature and well-established experimental tool. However, various major problems still remain to be solved concerning both the measurement and the analysis of XPS spectra. These include the ever-present and conflicting needs for higher resolution and higher intensity, which are at present being sought by means of more efficient x-ray monochromators combined with multichannel detection systems. More novel radiation sources and analyzer/detector systems might also provide a further solution to this problem. From the point of view of theory, more quantitative treatments of various final-state effects and electron–electron correlation effects are needed. More accurate calculations of both wave functions and photoelectric cross-sections for molecules and solids would also be very helpful, especially as related to angular-resolved studies of atoms and molecules interacting with solid surfaces.

Acknowledgements

I would like to thank the following agencies for financial support for those studies involving my research group at the University of Hawaii that are discussed here: The National Science Foundation, The Alfred P. Sloan Foundation, and The Petroleum Research Fund. I am also grateful to Dr S. Kono for helpful comments concerning this manuscript, and to Mr S. M. Goldberg for assistance with theoretical calculations relevant to it. Finally, I would like to thank Ms C. Carnate for invaluable assistance in preparing this manuscript.

REFERENCES

1. H. Robinson and W. F. Rawlinson, *Phil. Mag.* **28**, 277 (1914).
2. R. G. Steinhardt and E. J. Serfass, *Anal. Chem.* **25**, 697 (1953); and R. G. Steinhardt, F. A. D. Granados, and G. L. Post, *Anal. Chem.* **27**, 1046 (1955).
3. K. Siegbahn, C. Nordling, A. Fahlman, R. Nordberg, K. Hamrin, J. Hedman, G. Johansson, T. Bergmark, S.-E. Karlsson, I. Lindgren, and B. Lindberg, "ESCA: Atomic, Molecular, and Solid State Structure Studied by Means of Electron Spectroscopy", Nova Acta Regiae Soc. Sci. Upsaliensis, Ser. IV, Vol. 20 (Almqvist and Wiksells, Stockholm, 1967), also available as National Technical Information Service Report No. AD 844315, 1968, Dept of Commerce, Springfield, Va, U.S.A. See also earlier references therein, particularly S. Hagström, C. Nordling, and K. Siegbahn, *Z. Physik*, **178**, 439 (1964), in which the first association of core-binding energy shifts with chemical state was made.
4. K. Siegbahn, C. Nordling, G. Johansson, J. Hedman, P.-F. Hedén, K. Hamrin, U. Gelius, T. Bergmark, L. O. Werme, R. Manne, and Y. Baer, "ESCA Applied to Free Molecules" (North-Holland, Amsterdam, 1969).
5. The extensive XPS literature has been reviewed, for example, in D. M. Hercules, *Anal. Chem.* **44**, 106R (1972); W. E. Schwartz, *Anal. Chem.* **45**, 789A (1973); D. M. Hercules and J. C. Carver, *Anal. Chem.* **46**, 133R (1974), and D. M. Hercules, *Anal. Chem.* **48**, 294R (1976); A. D. Baker, M. Brisk and D. Liotta, *Anal. Chem.* **50**, 328, 1978R. Also, from 1972 on, numerous publications have appeared in the *Journal of Electron Spectroscopy and Related Phenomena*.
6. S. B. M. Hagström, and C. S. Fadley in "X-ray spectroscopy", L. V. Azaroff, ed. (McGraw-Hill, New York, 1974).
7. D. A. Shirley, *Adv. Chem. Phys.* **23**, 85 (1973).
8. C. S. Fadley in "Electron Emission Spectroscopy", W. Dekeyser *et al.*, eds (Reidel, Dordrecht, Netherlands, 1973).
9. D. T. Clark in "Electron Emission Spectroscopy", W. Dekeyser *et al.*, eds (Reidel, Dordrecht, Netherlands, 1973).
10. T. A. Carlson, "Photoelectron and Auger Spectroscopy" (Plenum Press, New York, 1975).
11. D. A. Shirley, ed., "Electron Spectroscopy" (North-Holland, Amsterdam, 1972). The proceedings of an international conference held at Asilomar, California, in September 1971.
12. R. Caudano and J. Verbist, eds, "Electron Spectroscopy: Progress in Research and Applications" (Elsevier, Amsterdam, 1974). The proceedings of an international conference held in Namur, Belgium, in April 1974. Also available as Volume 5 in the *Journal of Electron Spectroscopy* (1974).
13. W. L. Jolly in "Electron Spectroscopy: Theory, Techniques, and Applications", C. R. Brundle and A. D. Baker, eds (Academic Press, London and New York, 1977), Chapter 3, Vol. 1.
14. R. L. Martin and D. A. Shirley in "Electron Spectroscopy: Theory, Techniques, and Applications", C. R. Brundle and A. D. Baker, eds (Academic Press, London and New York, 1977), Chapter 2, Vol 1; and *Phys. Rev.* A13, 1475 (1976).
15. Detailed discussions of the application of synchrotron radiation to photoelectron spectroscopy have, for example, been given in papers by D. E. Eastman, by F. C. Brown, R. Z. Bachrach, S. B. M. Hagstrom, N. Lien,

and C. H. Pruitt, and by others in "Vacuum Ultraviolet Physics", E. E. Koch *et al.*, eds (Pergamon Press, New York, 1974); as well as in W. E. Spicer, K. Y. Yu, I. Lindau, P. Pianetta, and D. M. Collins in "Surface and Defect Properties of Solids", J. M. Thomas and M. W. Roberts, eds (Chem. Soc., London, 1976), Vol. V.

16. The general area of spin-polarized electron emission experiments has recently been reviewed in: M. Campagna, D. T. Pierce, F. Meier, L. Sattler, and H. C. Siegmann, in *Advances in Electronics and Electron Physics*, **41**, 113 (1976).
17. C. S. Fadley, *Prog. Sol. St. Chem.* **11**, 265 (1976).
18. For discussions of energy loss measurements at approximately XPS energies, see, for example, O. Klemperer and J. P. G. Shepherd, *Adv. Phys.* **12**, 355 (1963); H. Raether, *Springer Tracts in Modern Physics*, **38**, 84 (1965); J. Daniels, C. v. Festenburg, H. Raether, and K. Zeppenfeld, *Springer Tracts in Modern Physics*, **54**, 77 (1970), and G. R. Wight and C. E. Brion, *J. Electr. Spectr.* **3**, 191 (1974).
19. C. Kittel, "Introduction to Solid State Physics", 4th edn (Wiley, New York, 1971), Chapters 7 and 8.
20. C. J. Powell, *Surf. Sci.* **44**, 29 (1974).
21. I. Lindau and W. E. Spicer, *J. Electron Spectrosc.* **3**, 409 (1974).
22. C. R. Brundle, *J. Vac. Sci. Tech.* **11**, 212 (1974).
23. Kratos, 403 S. Raymond Avenue, Pasadena, California, U.S.A. is now marketing systems formerly manufactured by AEI Scientific Apparatus Ltd.
24. E. I. DuPont de Nemours and Co., Instrument Products Division, Wilmington, Delaware, U.S.A.
25. Hewlett Packard Co., Scientific Instruments Division, 1601 California Street, Palo Alto, California, U.S.A. Although no longer marketed, the special properties of this spectrometer are discussed in K. Siegbahn, D. Hammond, H. Fellner-Felldegg, and E. F. Barnett, *Science*, **176**, 245 (1972), as well as by R. J. Baird and C. S. Fadley in reference 74.
26. GCA/McPherson Instrument Corp., 530 Main Street, Acton, Massachusetts, U.S.A.
27. Leybold-Heraus GmbH, Gaedestrasse, 5000 Köln 51, West Germany. The electron optics of this system are described in detail in H. G. Nöller, H. D. Polaschegg, and H. Schillalies, *J. Electron Spectrosc.* **5**, 705 (1974).
28. Physical Electronics Industries, Inc., 6509 Flying Cloud Drive, Eden Prairie, Minnesota, U.S.A.
29. Vacuum Generators Inc., Charlwood Road, East Grinstead, Sussex, England.
30. Varian Associates, Analytical Instrument Devices, Palo Alto, California, U.S.A. This system is no longer marketed.
31. A. H. Compton and S. K. Allison, "X-rays in Theory and Experiment" (Macmillan and Co., London, 1935).
32. B. L. Henke in "Advances in X-ray analysis", Vol. 5 (Plenum Press, New York, 1962), p. 285; and in "X-ray Optics and Microanalysis" (Academic Press, New York and London, 1963), p. 157.
33. C. S. Fadley, Ph.D. Thesis, University of California at Berkeley, 1970 (Lawrence Berkeley Laboratory *Report UCRL-19535*).
34. M. O. Krause, *Chem. Phys. Lett.* **10**, 65 (1971).
35. M. S. Banna and D. A. Shirley, *J. Electr. Spectr.* **8**, 23, 255 (1976).
36. R. Nilsson, R. Nyholm, A. Berndtsson, J. Hedman, and C. Nordling, *J. Electr. Spectr.* **9**, 337 (1976).

37. M. O. Krause and J. G. Ferreira, *J. Phys.* **B8**, 2007 (1975).
38. E. Källne and T. Åberg, *X-ray Spect.* **4**, 26 (1975).
39. J. E. Castle, L. B. Hazell, and R. D. Whitehead, *J. Electron Spectrosc.* **9**, 246 (1976).
40. A. Berndtsson, R. Nyholm, R. Nilsson, J. Hedman, and C. Nordling, *J. Electron Spectrosc.* **13**, 131 (1978).
41. K. Siegbahn, *J. Electr. Spectr.* **5**, 3 (1974) and Uppsala University, *Institute of Physics Report, No. UUIP 909* (1975).
42. Y. Baer, G. Busch, and P. Cohn, *Rev. Sci. Inst.* **46**, 466 (1975).
43. C. T. Hovland, *Appl. Phys. Lett.* **30**, 274 (1977).
44. R. P. Godwin, "Synchrotron Radiation as a Light Source" in *Springer Tracts in Modern Physics*, **51** (1970).
45. J. F. McGilp and I. G. Main, *J. Electron Spectrosc.* **6**, 397 (1975).
46. C. S. Fadley, G. L. Geoffroy, S. B. M. Hagström, and J. M. Hollander, *Nucl. Inst. Methods*, **68**, 177 (1969).
47. G. Johansson, J. Hedman, A. Berndtsson, M. Klasson, and R. Nilsson, *J. Electron Spectrosc.* **2**, 295 (1973), and references therein.
48. F. J. Grunthaner, N.A.S.A. Technical Brief NPO-13772, Item 57, Spring 1977.
49. M. O. Krause, *Phys. Rev.* **A140**, 1845 (1965); T. A. Carlson and M. O. Krause, *Phys. Rev.* **A137**, 1655 (1965); **A140**, 1057 (1965); **A151**, 41 (1966).
50. J. Berkowitz in "Electron Spectroscopy", D. A. Shirley, ed. (North-Holland, Amsterdam, 1972), p. 391; and in "Electron Spectroscopy: Theory, Techniques, and Applications", C. R. Brundle and A. D. Baker, eds (Academic Press, London, 1977), Chap. 7, Vol 1.
51. See, for example, early gas-phase molecular studies in T. D. Thomas, *J. Chem. Phys.* **52**, 1373 (1970); *J. Am. Chem. Soc.* **92**, 4184 (1970); and D. W. Davis, D. A. Shirley, and T. D. Thomas in "Electron Spectroscopy", D. A. Shirley, ed. (North-Holland, Amsterdam, 1972), p. 707.
52. J. S. Brinen, *J. Electron Spectrosc.* **5**, 377 (1974); *Accts Chem. Res.* **9**, 86 (1976).
53. H. P. Hughes and R. A. Pollak, *Phil. Mag.* **34**, 1025 (1976).
54. T. E. Madey, J. T. Yates, and N. E. Erickson, *Chem. Phys. Lett.* **19**, 487 (1973); *Surf. Sci.* **43**, 526 (1974).
55. P. A. Redhead, J. P. Hobson, and E. V. Kornelsen, "The Physical Basis of Ultrahigh Vacuum" (Chapman and Hall, London, 1968); D. H. Holkeboer, D. W. Jones, F. Pagano, D. J. Santeler, "Vacuum Engineering" (Boston Technical, Boston, 1967).
56. Y. Baer, *Sol. St. Comm.* **19**, 669 (1976).
57. D. E. Eastman in "Electron Spectroscopy", D. A. Shirley, ed. (North-Holland, Amsterdam, 1972), p. 487.
58. S. Evans, *Chem. Phys. Lett.* **23**, 134 (1973).
59. H. Siegbahn and K. Siegbahn, *J. Electron Spectrosc.* **2**, 319 (1972); **5**, 1059 (1974).
60. UPS measurements on liquid Au are, for example, discussed in reference 57.
61. K. D. Sevier, "Low Energy Electron Spectrometry" (Wiley Interscience, New York, 1972).
62. H. Fellner-Felldegg, U. Gelius, B. Wannberg, A. G. Nilsson, E. Basilier, and K. Siegbahn, *J. Electron Spectrosc.* **5**, 643 (1974); B. Wannberg, U. Gelius, and K. Siegbahn, Uppsala University, *Institute of Physics Report No. UUIP-818* (1973).
63. C. E. Kuyatt, review of electron energy analyzers to appear in this series.

64. C. S. Fadley, C. E. Miner, and J. M. Hollander, *Appl. Phys. Letters*, **15**, 223 (1969); C. S. Fadley, R. N. Healey, J. M. Hollander, and C. E. Miner, *J. Appl. Phys.* **43**, 1085 (1972).
65. E. M. Purcell, *Phys. Rev.* **54**, 818 (1938).
66. H. Z. Sar-el, *Rev. Sci. Inst.* **38**, 1210 (1969).
67. S. Aksela, M. Karras, M. Pessa, and E. Suoninen, *Rev. Sci. Inst.* **41**, 351 (1970); S. Aksela, *Rev. Sci. Inst.* **42**, 810 (1971).
68. R. W. Shaw and T. D. Thomas in "Electron Spectroscopy", D. A. Shirley, ed. (North-Holland, Amsterdam, 1972), p. 105; K. Maeda, *op. cit.* p. 177.
69. K. Siegbahn in "Alpha-, Beta-, and Gamma-ray Spectroscopy", K. Siegbahn, ed. (North-Holland, 1965), Vol. 1, Chap. III.
70. K. Mills and D. A. Shirley, private communication.
71. L. B. Leder and J. A. Simpson, *Rev. Sci. Inst.* **29**, 571 (1958); J. A. Simpson, *Rev. Sci. Inst.* **32**, 1283 (1961).
72. C. N. Berglund and W. E. Spicer, *Rev. Sci. Inst.* **35**, 1665 (1964).
73. D. A. Huchital and J. D. Rigden in "Electron Spectroscopy", D. A. Shirley, ed. (North-Holland, Amsterdam, 1972), p. 79.
74. R. J. Baird and C. S. Fadley, *J. Electron Spectrosc.* **11**, 39 (1977).
75. J. C. Helmer, *Am. J. Phys.* **34**, 222 (1966); J. C. Helmer and N. H. Weichert, *Appl. Phys. Lett.* **13**, 266 (1968).
76. O. Klemperer, "Electron Optics", 3rd edn (Cambridge University Press, Cambridge, 1971), Chaps 1 and 2.
77. B. L. Henke, J. A. Smith, and D. T. Attwood, *J. Appl. Phys.* **48**, 1852 (1977).
78. Channeltron electron multipliers were originally marketed under a registered trademark of the Bendix Corporation. They are now available from various manufacturers.
79. The early development of such electron multipliers is reviewed in W. C. Wiley and C. F. Hendee, *I.R.E. Trans. Nucl. Sci.* NS-9, 103 (1962), D. S. Evans, *Rev. Sci. Inst.* **36**, 375 (1965).
80. Ö. Nilsson, L. Hasselgren, K. Siegbahn, S. Berg, L. P. Andersson, and P. A. Tore, *Nucl. Inst. and Meth.* **84**, 301 (1970).
81. C. D. Moak, S. Datz, F. Garcia-Santibanez, and T. A. Carlson, *J. Electron Spectrosc.* **6**, 151 (1975); M. Lampton and F. Paresec, *Rev. Sci. Inst.* **45**, 1098 (1974).
82. C. S. Fadley and D. A. Shirley, *J. Res. Nat. Bur. Stds*, **74A**, 543 (1970).
83. Various self-consistent inelastic loss subtraction procedures such as this have been utilized for XPS valence spectra, as discussed, for example, in references 82, 192, and 298.
84. S. Hüfner and G. K. Wertheim, *Phys. Rev.* **B11**, 678 (1975); *Phys. Rev.* **B11**, 5197 (1975); *Phys. Rev. Lett.* **35**, 53 (1975).
85. P. H. Citrin, P. Eisenberger, and D. R. Hamann, *Phys. Rev. Lett.* **33**, 965 (1974).
86. C. S. Fadley and D. A. Shirley, *Phys. Rev.* **A2**, 1109 (1970).
87. G. K. Wertheim, *J. Electr. Spectr.* **6**, 239 (1975). (As based on mathematical methods developed in ref. 88.)
88. P. H. van Zittert, *Z. Phys.* **69**, 298 (1931).
89. F. J. Grunthaner, Ph.D. Thesis, California Institute of Technology (1974).
90. R. Manne and T. Åberg, *Chem. Phys. Lett.* **7**, 282 (1970).
91. S. T. Manson, *J. Electron Spectrosc.* **9**, 21 (1976).
93. F. Herman and S. Skillman, "Atomic Structure Calculations" (Prentice-Hall, Inglewood Cliffs, New Jersey, 1963).
94. T. A. Carlson and B. P. Pullen, Oak Ridge National Laboratory, *Report No. ORNL-4323* (1969).

95. M. Tinkham, "Group Theory and Quantum Mechanics" McGraw-Hill, New York, 1964).
96. J. M. Ziman, "Principles of the Theory of Solids", 2nd edn (Cambridge University Press, Cambridge, 1972).
97. D. W. Turner, C. Baker, A. D. Baker, and C. R. Brundle, "Molecular Photoelectron Spectroscopy" (Wiley, London, 1970).
98. K. Siegbahn in "Electron Spectroscopy", D. A. Shirley, ed. (North-Holland, Amsterdam, 1972), p. 15.
99. J. Callaway, "Quantum Theory of the Solid State" (Academic Press, New York and London, 1974), Chap. 4.
100. J. B. Mann, Los Alamos Scientific Laboratory, *Reports LA-3690* (1967) and *LA-3691* (1968).
101. T. A. Carlson, C. C. Lu, T. C. Tucker, C. W. Nestor, and F. B. Malik, Oak Ridge National Laboratory, *Report ORNL-4614* (1970).
102. M. Mehta, C. S. Fadley, and P. S. Bagus, *Chem. Phys. Lett.* **37**, 454 (1975).
103. P. S. Bagus, *Phys. Rev.* **139**, A619 (1965).
104. A. Rosen and I. Lindgren, *Phys. Rev.* **176**, 114 (1968).
105. C. S. Fadley, S. B. M. Hagström, J. M. Hollander, M. P. Klein, and D. A. Shirley, *Science*, **157**, 1571 (1967); C. S. Fadley, S. B. M. Hagström, M. P. Klein, and D. A. Shirley, *J. Chem. Phys.* **48**, 3779 (1968).
106. M. E. Schwartz, *Chem. Phys. Lett.* **5**, 50 (1970).
107. P. S. Bagus and H. F. Schaefer, *J. Chem. Phys.* **55**, 1474 (1971); **56**, 224 (1972).
108. L. C. Snyder, *J. Chem. Phys.* **55**, 95 (1971).
109. H. Basch, *J. Electron Spectrosc.* **5**, 463 (1974).
110. E.-K. Viinikka and P. S. Bagus, extended abstract for the International Conference on the Physics of X-ray Spectra, 30 August-2 September, 1976, National Bureau of Standards, Gaithersberg, Md.
111. G. Verhaegen, J. J. Berger, J. P. Desclaux, and C. M. Moser, *Chem. Phys. Lett.* **9**, 479 (1971).
112. C. M. Moser, R. K. Nesbet, and G. Verhaegen, *Chem. Phys. Lett.* **12**, 330 (1971).
113. L. S. Cederbaum and W. Domcke, *J. Chem. Phys.* **66**, 5084 (1977).
114. G. K. Wertheim, R. L. Cohen, A. Rosencwaig, and H. J. Guggenheim in "Electron Spectroscopy", D. A. Shirley, ed. (North-Holland, Amsterdam, 1972), p. 813.
115. L. Ley, F. R. McFeely, J. G. Jenkin, and D. A. Shirley, *Phys. Rev.* **11**, 600 (1975).
116. See, for example, J. E. Lennard-Jones and J. A. Pople, *Proc. Roy. Soc.* **A202**, 166 (1950); C. Edmiston and K. Ruedenberg, *Rev. Mod. Phys.* **35**, 457 (1963).
117. P. W. Payne, *J. Am. Chem. Soc.* **99**, 3787 (1977).
118. J. C. Slater, "Quantum Theory of Atomic Structure" (McGraw-Hill, New York, 1960), Vol. II.
119. D. Liberman, *Bull. Am. Phys. Soc.* **9**, 731 (1964).
120. L. Hedin and A. Johansson, *J. Phys.* **B2**, 1336 (1969).
121. D. A. Shirley, *Chem. Phys. Lett.* **16**, 220 (1972).
122. H. F. Schaefer, "The Electronic Structure of Atoms and Molecules" (Addison-Wesley, Reading, Mass., 1972).
123. T. L. Barr, private communication.
124. H. A. Bethe and E. E. Salpeter, Quantum Mechanics of One- and Two-electron Atoms in "Handbuch der Physik" (Springer-Verlag, Berlin, 1955), Vol. 35, p. 88.
125. D. R. Bates, *Mon. Not. Roy. Astr. Soc.* **106**, 432 (1946).

126. J. W. Cooper, *Phys. Rev.* **128**, 681 (1962).
127. U. Fano and J. W. Cooper, *Rev. Mod. Phys.* **40**, 441 (1968).
128. J. W. Cooper, review in "Atomic Inner-shell Processes" (Academic Press, 1975).
129. S. T. Manson, review on atomic cross-section calculations to appear in this series, and S. T. Manson, *Advances in Electronics and Electron Physics*, **41**, 73 (1976).
130. J. J. Huang and J. W. Rabelais, review on molecular cross-sections to appear in this series.
131. See, for example, L. I. Schiff, "Quantum Mechanics" (McGraw-Hill, New York, 1968), Sections 35, 44, and 45, 3rd edn.
132. B. Feuerbacher and R. F. Willis, *J. Phys.* **C9**, 169 (1976).
133. T. Åberg, *Phys. Rev.* **156**, 35 (1967) and in "Inner-shell Ionization Phenomena and Future Applications", R. W. Fink *et al.*, eds (U.S.A.E.C., Conference-72-0404, 1973), p. 1409.
134. J. W. Gadzuk and M. Sunjic, *Phys. Rev.* **B12**, 524 (1975). See also the prior treatment of time scales in photoionization by H. W. Meldner and J. D. Perez, *Phys. Rev.* **A4**, 1388 (1971).
135. T. A. Carlson, *Phys. Rev.* **156**, 142 (1967); M. O. Krause and T. A. Carlson, *Phys. Rev.* **158**, 18 (1967); M. O. Krause, T. A. Carlson, and R. D. Dismukes, *Phys. Rev.* **170**, 37 (1968); M. O. Krause, *Phys. Rev.* **177**, 151 (1968).
136. P. O. Löwdin, *Phys. Rev.* **97**, 1474 (1955).
137. C. S. Fadley, *Chem. Phys. Lett.* **25**, 225 (1974); *J. Electr. Spectr.* **5**, 895 (1974).
138. B. I. Lundqvist, *Phys. Kondens. Materie*, **9**, 236 (1969).
139. F. Wuilleumier and M. O. Krause, *Phys. Rev.* **A10**, 242 (1974).
140. J. Cooper and R. N. Zare, *J. Chem. Phys.* **48**, 942 (1968); and in "Lectures in Theoretical Physics", S. Geltman, K. Mahanthappa, and W. Brittlin, eds (Gordon and Breach, New York, 1969), Vol. XIC.
141. In atomic cross-section calculations based upon typical approximation schemes, the three forms of the dipole operator need not give the same result. Recently, the degree of agreement between calculations using all three forms has been discussed for wave functions including correlation effects in M. S. Pindzola and H. P. Kelly, *Phys. Rev.* **A12**, 1419 (1975).
142. M. O. Krause, *Phys. Rev.* **177**, 151 (1969).
143. A. J. Bearden, *J. Appl. Phys.* **37**, 1681 (1966).
144. G. Rakavy and A. Ron, *Phys. Rev.* **159**, 50 (1967).
145. H. Bryskand C. D. Zerby, *Phys. Rev.* **171**, 292 (1968).
146. S. T. Manson and J. W. Cooper, *Phys. Rev.* **165**, 126 (1968).
147. J. W. Cooper and S. T. Manson, *Phys. Rev.* **177**, 157 (1969).
148. E. J. McGuire, *Phys. Rev.* **175**, 20 (1968).
149. D. J. Kennedy and S. T. Manson, *Phys. Rev.* **A5**, 227 (1972).
150. E. Storm and H. I. Israel, *Nuclear Data Tables* **A7**, 565 (1970).
151. J. H. Scofield, *J. Electr. Spectr.* **8**, 129 (1976).
152. B. L. Henke and E. S. Ebisu, in "Advances in X-ray Analysis" (Plenum Press, New York, 1974), Vol. 17.
153. S. T. Manson, *Phys. Rev. Lett.* **26**, 219 (1971).
154. R. F. Reilman, Alfred Msezane, and S. T. Manson, *J. Electr. Spectr.* **8**, 389 (1976).
155. P. A. Cox and F. A. Orchard, *Chem. Phys. Lett.* **7**, 273 (1970).
156. P. A. Cox, Y. Baer, and C. K. Jorgensen, *Chem. Phys. Lett.* **22**, 433 (1973); P. A. Cox, *Struct. Bonding*, **23**, 59 (1974).

157. P. S. Bagus, J. L. Freeouf, and D. E. Eastman, *Phys. Rev.* **B15**, 3661 (1977).
158. D. Dill, A. F. Starace, and S. T. Manson, *Phys. Rev.* **A11**, 1596 (1975).
159. J. W. Gadzuk, *Sol. St. Comm.* **15**, 1011 (1974); *Phys. Rev.* **B10**, 5030 (1974); *Phys. Rev.* **B12**, 5608 (1975).
160. D. Dill and J. L. Dehmer, *J. Chem. Phys.* **61**, 692 (1974); J. L. Dehmer and D. Dill, *Phys. Rev. Lett.* **35**, 213 (1975).
161. V. I. Nefedov, N. P. Sergushin, I. M. Band, and M. B. Trzhaskowskaya, *J. Electr. Spectr.* **2**, 383 (1973).
162. F. O. Ellison, *J. Chem. Phys.* **61**, 507 (1974); J. W. Rabelais, T. P. Debies, J. L. Berkosky, J. T. Huang, and F. O. Ellison, *J. Chem. Phys.* **61**, 516, 529 (1974).
163. M. J. S. Dewar, A. Komornicki, and W. Thiel, *Chem. Phys. Lett.* **31**, 286 (1975).
164. B. Ritchie, *J. Chem. Phys.* **60**, 898 (1974); **61**, 3279, 3291 (1974); **64**, 3050 (1976).
165. R. S. Williams and D. A. Shirley, *J. Chem. Phys.* **66**, 2378 (1977)
166. J. W. Davenport, *Phys. Rev. Lett.* **36**, 945 (1976).
167. K. H. Johnson in "Advances in Quantum Chemistry", P. O. Löwdin, ed. (Academic Press, New York and London, 1973), Vol. 7, p. 143.
168. J. L. Dehmer, *J. de Physique*, Coll. C4, 42 (1978).
169. T. A. Carlson and G. E. McGuire, *J. Electr. Spectr.* **1**, 209 (1972/73).
170. T. A. Carlson, G. E. McGuire, A. E. Jonas, K. L. Cheng, C. P. Anderson, C. C. Lu, and B. P. Pullen in "Electron Spectroscopy", D. A. Shirley, ed. (North Holland, Amsterdam, 1972), p. 207.
171. D. Dill, *J. Chem. Phys.* **65**, 1130 (1976).
172. U. Gelius in "Electron Spectroscopy", D. A. Shirley, ed. (North-Holland, Amsterdam, 1972), p. 311.
173. U. Gelius, C. J. Allen, G. Johansson, H. Siegbahn, D. A. Allison, and K. Siegbahn, *Phys. Scripta*, **3**, 237 (1971); C. J. Allen, U. Gelius, D. A. Allison, G. Johansson, H. Siegbahn, and K. Siegbahn, *J. Electr. Spectr.* **1**, 131 (1972).
174. R. Prins, *Chem. Phys. Lett.* **19**, 355 (1973).
175. A. Calabrese and R. G. Hayes, *Chem. Phys. Lett.* **27**, 376 (1974); *J. Am. Chem. Soc.* **95**, 2819 (1973); **96**, 505 (1974).
176. S. Kono, T. Ishii, T. Sagawa, and T. Kobayasi, *Phys. Rev. Lett.* **28**, 1385 (1972); *Phys. Rev.* **B8**, 795 (1973).
177. C. N. Berglund and W. E. Spicer, *Phys. Rev.* **A136**, 1030, 1044 (1964).
178. B. L. Henke, *Phys. Rev.* **A6**, 94 (1972).
179. M. Mehta and C. S. Fadley, *Phys. Lett.* **A55**, 59 (1975).
180. G. D. Mahan, *Phys. Rev.* **B2**, 4374 (1970); W. L. Schaich and N. W. Ashcroft, *Phys. Rev.* **B3**, 2452 (1970).
181. P. J. Feibelman and D. E. Eastman, *Phys. Rev.* **B10**, 4932 (1974).
182. N. V. Smith and M. M. Traum, *Phys. Rev. Lett.* **31**, 1247 (1973); M. M. Traum, N. V. Smith, and F. J. DiSalvo, *Phys. Rev. Lett.* **32**, 1241 (1974); N. V. Smith and M. M. Traum, *Phys. Rev.* **B11**, 2087 (1975), and references therein.
183. B. Feuerbacher and F. Fitton, *Phys. Rev. Lett.* **30**, 923 (1973); R. R. Tuttle and T. A. Callcott, *Phys. Rev. Lett.* **34**, 86 (1975); R. F. Willis, *Phys. Rev. Lett.* **34**, 670 (1975).
184. C. Kittel, "Quantum Theory of Solids" (Wiley, New York, 1963), Chap. 1.
185. R. J. Baird, L. F. Wagner, and C. S. Fadley, *Phys. Rev. Lett.* **37**, 111 (1976).
186. N. J. Shevchik, *Phys. Rev.* **16**, 3428 (1977); *J. Phys.* **C10**, L555 (1977).

187. R. W. James, "The Optical Principles of the Diffraction of X-rays" (Cornell University Press, Ithaca, 1967), Chap. V.
188. V. G. Aleshin and Y. N. Kucherenko, *J. Electr. Spectr.* **8**, 411 (1976).
189. L. F. Wagner and C. S. Fadley, unpublished results.
190. See, for example, R. A. Pollak, Ph.D. Thesis, University of California at Berkeley, 1972 (Lawrence Berkeley Laboratory Report LBL-1299); S. P. Kowalczyk, Ph.D. Thesis, University of California at Berkeley, 1976 (Report LBL 4319).
191. A. Barrie and N. E. Christensen, *Phys. Rev.* **B14**, 2442 (1976).
192. L. Ley, S. Kowalczyk, R. A. Pollak, and D. A. Shirley, *Phys. Rev. Lett.* **29**, 1088 (1972).
193. R. G. Cavell, S. P. Kowalczyk, L. Ley, R. A. Pollak, B. Mills, D. A. Shirley, and W. Perry, *Phys. Rev.* **B7**, 5313 (1973); F. R. McFeely, S. P. Kowalczyk, L. Ley, R. G. Cavell, R. A. Pollak, and D. A. Shirley, *Phys. Rev.* **B9**, 5268 (1974).
194. M. Sunjic, D. Sokcevic, and A. Lucas, *J. Electr. Spectr.* **5**, 963 (1974); M. Sunjic and D. Sokcevic, *Sol. St. Comm.* **15**, 165 (1974); **15**, 1703 (1974); **18**, 373 (1976).
195. This compilation of electron inelastic attenuation lengths is intended to contain all published determinations, and information concerning it is available through M. P. Seah, National Physical Laboratory, Electron Mean Free Path Versus Energy Compilation, Teddington, Middlesex, U.K.
196. D. R. Penn, *J. Electr. Spectr.* **9**, 29 (1976).
197. P. J. Feibelman, *Phys. Rev.* **B7**, 2305 (1973).
198. P. J. Feibelman, *Surf. Sci.* **36**, 558 (1973).
199. M. O. Krause and F. Wuilleumier, *Phys. Lett.* **A35**, 341 (1971), and in "Proceedings of the International Conference on Inner Shell Ionization Phenomena", Atlanta, Georgia, 1972, p. 2331.
200. R. J. Baird, C. S. Fadley, and L. F. Wagner, *Phys. Rev.* **B15**, 666 (1977).
201. W. A. Fraser, J. V. Florio, W. N. Delgass, and W. D. Robertson, *Surf. Sci.* **36**, 661 (1973).
202. C. S. Fadley, R. J. Baird, W. Siekhaus, T. Novakov, and S. Å. Bergström, *J. Electr. Spectr.* **4**, 93 (1974).
203. R. J. Baird, C. S. Fadley, S. Kawamoto, and M. Mehta, *Chem. Phys. Lett.* **34**, 49 (1975).
204. W. J. Carter, G. K. Schweitzer, and T. A. Carlson, *J. Electr. Spectr.* **5**, 827 (1974).
205. C. D. Wagner, *Anal. Chem.* **44**, 1050 (1972).
206. C. K. Jorgensen and H. Berthou, *Disc. Far. Soc.* **54**, 269 (1973); H. Berthou and C. K. Jorgensen, *Anal. Chem.* **47**, 482 (1975).
207. C. J. Powell and P. E. Larson, *Appl. Surf. Sci.* **1** (1977), in press.
208. C. J. Powell, in A.S.T.M. Special Technical Publication of the 1977 Symposium on Quantitative Surface Analysis, in press.
209. S. A. Flodström, R. Z. Bachrach, R. S. Bauer, and S. B. M. Hagström, *Phys. Rev. Lett.* **37**, 1282 (1976).
210. K. Siegbahn, Uppsala University, *Institute of Physics Report No. UUIP-940* (1976).
211. U. Gelius, P.-F. Heden, J. Hedman, B. J. Lindberg, R. Manne, R. Nordberg, C. Nordling, and K. Siegbahn, *Physica Scripta*, **2**, 70 (1970).
212. O. Goscinski, B. Pickup, and G. Purvis, *Chem. Phys. Lett.* **22**, 117 (1973).

213. G. Howat and O. Goscinski, *Chem. Phys. Lett.* **30**, 87 (1975).
214. P. H. Citrin, R. W. Shaw, A. Packer, and T. D. Thomas in "Electron Spectroscopy", D. A. Shirley, ed. (North Holland, Amsterdam, 1972), p. 691.
215. D. A. Shirley, R. L. Martin, F. R. McFeely, S. P. Kowalczyk, and L. Ley, *Far. Soc. Disc.* No. 60, 7 (1975).
216. R. Manne, *J. Chem. Phys.* **46**, 4645 (1967).
217. H. Basch, *Chem. Phys. Lett.* **5**, 337? (1970).
218. M. F. Schwartz, *Chem. Phys. Lett.* **5**, 50 (1970); **6**, 631 (1970).
219. D. W. Davis, D. A. Shirley, and T. D. Thomas, *J. Chem. Phys.* **56**, 671 (1972).
220. J. Hedman, M. Klasson, B. J. Lindberg, and C. Nordling in "Electron Spectroscopy", D. A. Shirley, ed. (North-Holland, Amsterdam, 1972), p. 681.
221. D. N. Hendrickson, J. M. Hollander, and W. L. Jolly, *J. Inorg. Chem.* **8**, 2642 (1969).
222. T. D. Thomas, *J. Am. Chem. Soc.* **92**, 4184 (1970).
223. P. Finn, R. K. Pearson, J. M. Hollander, and W. L. Jolly, *J. Inorg. Chem.* **10**, 378 (1971).
224. W. L. Jolly and D. N. Hendrickson, *J. Am. Chem. Soc.* **92**, 1863 (1970).
225. W. L. Jolly in "Electron Spectroscopy", D. A. Shirley, ed. (North-Holland, Amsterdam, 1972), p. 629.
226. J. A. Hashmall, B. E. Mills, D. A. Shirley, and A. Streitwieser, *J. Am. Chem. Soc.* **94**, 445 (1972).
227. M. Aono, M. Okusawa, T. Sagawa, Y. Takehana, and T. Nagatani, "Proceedings of the 7th International Conference on X-ray Optics and Microanalysis" (Moscow); M. Aono, S. Kawai, S. Kono, M. Okusawa, T. Sagawa, and Y. Takehana, *Sol. St. Comm.* **16**, 13 (1975).
228. R. L. Martin and D. A. Shirley, *J. Am. Chem. Soc.* **96**, 5299 (1974); B. E. Mills, R. L. Martin, and D. A. Shirley, *J. Am. Chem. Soc.* **98**, 2380 (1976).
229. C. D. Wagner, *Far. Soc. Disc.* No. 60, 291 (1975).
230. C. D. Wagner and P. Biloen, *Surf. Sci.* **35**, 82 (1973).
231. D. A. Shirley, *Phys. Rev.* **A7**, 1520 (1973).
232. G. D. Matecescu and J. L. Riemenschneider in "Electron Spectroscopy", D. A. Shirley, ed. (North Holland, Amsterdam, 1972), p. 661; B. J. Lindberg, *J. Electr. Spectr.* **5**, 149 (1974).
233. H. Basch, *Chem. Phys. Lett.* **5**, 337? (1970).
234. M. Barber, P. Swift, D. Cunnginham, and M. J. Frazer, *Chem. Commun.* **1970**, 1338 (1970).
235. L. Ley, S. P. Kowalczyk, F. R. McFeely, R. A. Pollak, and D. A. Shirley, *Phys. Rev.* **B8**, 2392 (1973).
236. P. H. Citrin and D. R. Hamann, *Phys. Rev.* **B10**, 4948 (1974).
237. J. J. Pireaux, S. Svensson, E. Basilier, P. A. Malmqvist, U. Gelius, R. Caudano, and K. Siegbahn, *Phys. Rev.* **A14**, 2133 (1976).
238. J. E. Demuth and D. E. Eastman, *Phys. Rev. Lett.* **32**, 1123 (1974).
239. D. W. Davis and D. A. Shirley, *Chem. Phys. Lett.* **15**, 185 (1972).
240. R. E. Watson, M. L. Perlman, and J. F. Herbst, *Phys. Rev.* **13**, 2358 (1976).
241. R. Hoogewijs, L. Fiermans, and J. Vennik, *Chem. Phys. Lett.* **37**, 87 (1976).
242. J. W. Gadzuk, *Phys. Rev.* **B14**, 2267 (1976).
243. D. Coster and M. J. Druyvesteyn, *Z. Physik*, **40**, 765 (1927).
244. V. I. Nefedov, *J. Struct. Chem.* **5**, 603, 605 (1964); **7**, 672 (1966).
245. B. Ekstig, E. Källne, E. Noreland, and R. Manne, *Physica Scripta*, **2**, 38 (1970).
246. W. N. Asaad and E. H. S. Burhop, *Proc. Phys. Soc.* **71**, 369 (1958).

247. F. H. S. Burhop, "The Auger Effect and Other Radiationless Transitions" (Cambridge University Press, London, 1952).
248. D. Stalherm, B. Cleff, H. Hillig, and W. Mehlhorn, *Naturforsch.* **24a**, 1728 (1969).
249. J. Hedman, P.-F. Heden, C. Nordling, and K. Siegbahn, *Phys. Lett.* **A29**, 178 (1969).
250. C. S. Fadley, D. A. Shirley, A. J. Freeman, P. S. Bagus, and J. V. Mallow, *Phys. Rev. Lett.* **23**, 1397 (1969).
251. J. C. Carver, T. A. Carlson, L. C. Cain, and G. K. Schweitzer, in "Electron Spectroscopy", D. A. Shirley, ed. (North-Holland, Amsterdam, 1972), p. 803.
252. P. S. Bagus, A. J. Freeman, and F. Sasaki, *Phys. Rev. Lett.* **30**, 850 (1973). These CI calculations actually use seven configurations for ^1S rather than the four discussed here, but the dominant contributors are found to be only those four.
253. S. P. Kowalczyk, L. Ley, R. A. Pollak, F. R. McFeely, and D. A. Shirley, *Phys. Rev.* **B7**, 4009 (1973).
254. S. P. Kowalczyk, F. R. McFeely, L. Ley, and D. A. Shirley in "Proceedings of the 20th Annual Conference on Magnetism and Magnetic Materials", 1974.
255. S. P. Kowalczyk, L. Ley, F. R. McFeely, and D. A. Shirley, *Phys. Rev.* **B11**, 1721 (1975).
256. R. P. Gupta and S. K. Sen, *Phys. Rev.* **B10**, 71 (1974).
257. R. P. Gupta and S. K. Sen, *Phys. Rev.* **B12**, 15 (1975).
258. R. L. Cohen, G. K. Wertheim, A. Rosencwaig, and H. J. Guggenheim, *Phys. Rev.* **B5**, 1037 (1972).
259. F. R. McFeely, S. P. Kowalczyk, L. Ley, and D. A. Shirley, *Phys. Lett.* **A49**, 301 (1974).
260. S. P. Kowalczyk, N. Edelstein, F. R. McFeely, L. Ley, and D. A. Shirley, *Chem. Phys. Lett.* **29**, 491 (1974).
261. M. Campagna, E. Bucher, G. K. Wertheim, and L. D. Longinotti, *Phys. Rev. Lett.* **33**, 165 (1974).
262. C. S. Fadley in "Electron Spectroscopy", D. A. Shirley, ed. (North-Holland, Amsterdam, 1972), p. 781.
263. A. J. Freeman, P. S. Bagus, and J. V. Mallow, *Int. J. Magnetism*, **4**, 35 (1973).
264. S. Sugano in "Proceedings of the NATO Advanced Study Institute on Spectroscopy of Excited States" (Plenum Press, New York, 1976).
265. T. A. Carlson, *Far. Soc. Disc.* No. 60, 30 (1975).
266. J. N. Chazalviel, M. Campagna, G. K. Wertheim, and P. H. Schmidt, *Phys. Rev.* **B10**, 4586 (1976).
267. P.-O. Heden, B. Löfgren, and S. B. M. Hagström, *Phys. Rev. Lett.* **26**, 432 (1971).
268. Y. Baer, *J. Electr. Spectr.* **5**, 611 (1974).
269. T. A. Carlson, M. O. Krause, and W. E. Moddeman, *J. de Physique*, **C2**, 102 (1971).
270. U. Gelius, *J. Electr. Spectr.* **5**, 985 (1974).
271. D. P. Spears, H. J. Fischbeck, and T. A. Carlson, *Phys. Rev.* **A9**, 1603 (1974).
272. T. N. Chang and R. T. Poe, *Phys. Rev.* **A12**, 1432 (1975).
273. H. Basch, *Chem. Phys.* **10**, 157 (1975); T. X. Carroll and T. D. Thomas, *J. Electr. Spectr.* **10**, 215 (1977).
274. D. T. Clark in *Far. Soc. Disc.* No. 60, 183 (1975).
275. P. S. Bagus and E.-K. Viinikka, *Phys. Rev.* **A15**, 1486 (1977).
276. S. Doniach and M. Sunjic, *J. Phys.* **C3**, 285 (1970).
277. P. H. Citrin, *Phys. Rev.* **B12**, 5545 (1973).
278. D. C. Langreth, *Phys. Rev. Lett.* **26**, 1229 (1971); J. J. Chang and D. C. Langreth, *Phys. Rev.* **B5**, 3512 (1972); **B8**, 4638 (1973); G. D. Mahan, *Phys. Stat. Solid.* **55**, 703 (1973).
279. W. J. Pardee, G. D. Mahan, D. E. Eastman, R. A. Pollak, L. Ley, F. R. McFeely, S. P. Kowalczyk, and D. A. Shirley, *Phys. Rev.* **B11**, 3614 (1975); J. C. Fuggle, D. J. Fabian, and L. M. Watson, *J. Electr. Spectr.* **9**, 99 (1976).
280. T. Novakov, *Phys. Rev.* **B3**, 2693 (1971).
281. D. C. Frost, A. Ishitani, and C. A. McDowell, *Molec. Phys.* **24**, 861 (1972).
282. T. A. Carlson, J. C. Carver, L. J. Saethre, and F. Garcia Santibanez, *J. Electr. Spectr.* **5**, 247 (1974); T. A. Carlson, J. C. Carver, and G. A. Vernon, *J. Chem. Phys.* **62**, 932 (1975).
283. K. S. Kim and R. E. Davis, *J. Electr. Spectr.* **1**, 251 (1972/73); K. S. Kim, *Phys. Rev.* **B11**, 2177 (1975).
284. L. Yin, I. Adler, T. Tsang, L. I. Matienzo, and S. O. Grim, *Chem. Phys. Lett.* **24**, 81 (1974).
285. S. Larsson, *Chem. Phys. Lett.* **32**, 401 (1975); **40**, 362 (1976).
286. S. Asada and S. Sugano, *J. Phys. Soc. Jap.* **41**, 1291 (1976).
287. E. W. Plummer and W. R. Salaneck in "Proceedings of the 5th International Conference on Vacuum Ultraviolet Radiation Physics", Montpellier, France (1977).
288. S. Lundqvist and G. Wendin, *J. Electr. Spectr.* **5**, 513 (1974).
289. G. Wendin and M. Ohno, *Physica Scripta*, **14**, 148 (1976); G. Wendin, M. Ohno, and S. Lundqvist, *Sol. St. Comm.* **19**, 165 (1976).
290. C. S. Fadley, *J. Electr. Spectr.* **5**, 725 (1974).
291. C. S. Fadley and S. Å. L. Bergström, *Phys. Lett.* **A35**, 375 (1971); in "Electron Spectroscopy", D. A. Shirley, ed. (North-Holland, Amsterdam, 1972), p. 233.
292. C. S. Fadley, *Far. Soc. Disc.* No. 60, 18 (1975).
293. R. J. Baird, C. S. Fadley, S. Kawamoto, M. Mehta, R. Alvarez, and J. A. Silva, *Anal. Chem.* **48**, 843 (1976).
294. J. M. Hill, D. G. Royce, C. S. Fadley, L. F. Wagner, and F. J. Grunthaner, *Chem. Phys. Lett.* **44**, 225 (1976).
295. R. J. Baird, C. S. Fadley, S. M. Goldberg, P. J. Feibelman, and M. Sunjic, *Surf. Sci.* **72**, 495 (1978).
296. A. M. Bradshaw, W. Domcke, and L. S. Cederbaum, *Phys. Rev.* **B16**, 1480 (1977).
297. R. Haydock and M. J. Kelly, *Surf. Sci.* **38**, 139 (1973); M. C. Dejonqueres and F. Cyrot-Lackmann, *Surf. Sci.* **53**, 429 (1975); K. S. Sohn, D. G. Dempsey, L. Kleinmann, and E. Caruthers, *Phys. Rev.* **B13**, 1515 (1976); **B14**, 3185, 3193 (1976).
298. M. Mehta and C. S. Fadley, *Phys. Rev. Lett.* **39**, 1569 (1977).
299. M. Mehta and C. S. Fadley, *Chem. Phys. Lett.* **46**, 225 (1977).
300. K. Siegbahn, U. Gelius, H. Siegbahn, and E. Olsen, *Phys. Lett.* **A32**, 221 (1970).
301. R. Baudoing, R. M. Stern, and H. Taub, *Surf. Sci.* **11**, 255 (1968); E. G. McRae, *Surf. Sci.* **44**, 321 (1974), and earlier references therein.
302. R. E. DeWames and W. F. Hall, *Acta Cryst.* **A24**, 206 (1968), and earlier experimental references therein.
303. R. J. Baird, C. S. Fadley, S. M. Goldberg, and S. Kono, to be published.

304. J. B. Pendry and R. Lindsay, private communication.
305. R. J. Baird, C. S. Fadley, and L. F. Wagner, *Far. Soc. Disc.* No. 60, 143 (1975).
306. F. R. McFeely, J. Stöhr, G. Apai, P. S. Wehner, and D. A. Shirley, *Phys. Rev.* **B14**, 3273 (1976).
307. L. F. Wagner, Z. Hussain, and C. S. Fadley, *Sol. St. Comm.* **21**, 453 (1977).
308. G. Apai, J. Stöhr, R. S. Williams, P. S. Wehner, S. P. Kowalczyk, and D. A. Shirley, *Phys. Rev.* **B15**, 584 (1977).
309. Z. Hussain, L. F. Wagner, and C. S. Fadley, to be published.
310. L. Ley, R. H. Williams, and P. Kemeny, *Bull. Am. Phys. Soc.* **24**, 942 (1976); R. H. Williams, P. C. Kemeny, and L. Ley, *Sol. St. Comm.* **19**, 495 (1976).
311. P. S. Wehner, J. Stöhr, G. Apai, F. R. McFeely, and D. A. Shirley, *Phys. Rev. Lett.* **38**, 169 (1977).
312. K.-F. Berggren and F. Martino, *Sol. St. Comm.* **20**, 1057 (1976).
313. P.-O. Nilsson and L. Ilver, *Sol. St. Comm.* **17**, 667 (1975); L. Ilver and P.-O. Nilsson, *Sol. St. Comm.* **18**, 677 (1976).
314. L. F. Wagner, Z. Hussain, and C. S. Fadley, *Sol. St. Comm.* **21**, 257 (1977).
315. N. E. Christensen and B. O. Seraphin, *Phys. Rev.* **B4**, 3321 (1972).
316. N. V. Smith, *Phys. Rev.* **B3**, 1862 (1971). Two different choices of spin orbit parameter were used in this tight-binding scheme for the calculations of Fig. 52.
317. R. J. Baird, L. F. Wagner, and C. S. Fadley, unpublished results.
318. Z. Hussain, N. F. T. Hall, L. F. Wagner, S. P. Kowalczyk, C. S. Fadley K. A. Thompson, and R. L. Dod, *Sol. St. Commun.* **25**, 907 (1978).
319. R. S. Williams, P. S. Wehner, J. Stöhr, and D. A. Shirley, *Phys. Rev. Lett.* **39**, 302 (1977).

Volume 16 Number 3 1984

Progress in Surface Science

An International Review Journal

ISBN 0 08 030892 9
ISSN 0079-6816
PSSFBP 16(3) 275-388 (1984)

PERGAMON PRESS New York / Oxford / Toronto
Paris / Frankfurt / Sydney

Progress in Surface Science, Vol. 16, pp. 275-388, 1984.
Printed in the USA.

0079-6816/84 $0.00 + .50

ANGLE-RESOLVED X-RAY PHOTOELECTRON SPECTROSCOPY

CHARLES S. FADLEY

Department of Chemistry, University of Hawaii at Manoa, Honolulu, Hawaii 96822

Abstract

In this review, various aspects of angle-resolved x-ray photoelectron spectroscopy (ARXPS) as applied to solid state- and surface chemical- studies are discussed. Special requirements for instrumentation are first considered. The use of grazing-emission angles to enhance surface sensitivity and study surface concentration profiles of various types is then discussed. Various effects that may limit the accuracy of such measurements such as surface roughness, electron refraction, and elastic scattering are considered. Several examples of surface-specific electronic structure changes as studied by grazing-emission ARXPS (e.g., valence-band narrowing and core-level shifts) are also reviewed. The use of grazing-incidence geometries for surface enhancement is also briefly considered. Single-crystal studies providing additional types of information via ARXPS are next discussed. For core-level emission from single-crystal substrates or adsorbed overlayers, x-ray photoelectron diffraction (XPD) is found to produce considerable fine structure in polar- or azimuthal- scans of intensity. Such XPD effects can be very directly related to the atomic geometry near a surface, for example, through simple intramolecular or intermolecular scattering processes. A straightforward single scattering or kinematical theory also appears to describe such effects rather well, thus far permitting several structures to be solved by analyses of azimuthal intensity scans. Likely future developments and possible limitations of such XPD structure studies are also discussed. Finally, valence-band ARXPS is considered, and it is shown that pronounced direct-transition effects can be observed provided that the specimen Debye-Waller factor is not too small. A simple free-electron final-state model is found to predict these direct-transition effects very well, and future studies at low temperatures and with higher angular resolution seem promising.

Contents

Abbreviations

ARUPS	Angle-Resolved Ultraviolet Photoelectron Spectroscopy
ARXPS	Angle-Resolved X-ray Photoelectron Spectroscopy
ARXUPS	Angle-Resolved XUV Photoelectron Spectroscopy
DT	Direct Transition
EXAFS	Extended X-ray Absorption Fine Structure
ESDIAD	Electron Stimulated Desorption Ion Angular Distribution
FWHM	Full Width at Half Maximum Intensity
LEED	Low Energy Electron Diffraction
ME	Matrix Element
MS	Multiple Scattering
NDT	Non-Direct Transition
NPD	Normal Photoelectron Diffraction
PhD	Photoelectron Diffraction
RHEED	Reflection High Energy Electron Diffraction
SEXAFS	Surface Extended X-ray Absorption Fine Structure
SIMS	Secondary Ion Mass Spectrometry
SSC	Single Scattering Cluster
UHV	Ultra-High Vacuum
UPS	Ultraviolet Photoelectron Spectroscopy
XPD	X-ray Photoelectron Diffraction
XPS	X-ray Photoelectron Spectroscopy

1. Introduction

Angle-resolved photoelectron spectroscopy in fact has a rather long history, as recently reviewed by Jenkin et al.[1]. However, the current interest in angle-resolved x-ray photoelectron spectroscopy (ARXPS) as applied to solids and surfaces is only approximately ten years old, having begun with observations of diffraction-induced channeling effects in single-crystal specimens by Siegbahn et al.[2] and by Fadley and Bergström[3] and of enhanced surface sensitivity for grazing angles of emission by Fadley and Bergström[3]. A number of other effects of interest in surface science have been noted since these first studies, and several quantitative models have been developed for describing them. This type of measurement has been treated in prior general reviews in 1974[4], 1976[5], and 1978[6], and the present discussion will thus principally stress those developments that have occurred in the past few years, particularly with regard to using ARXPS for quantitative surface analysis, surface atomic geometry investigations, and valence-band studies.

The XPS energy regime will here be defined in what might be termed the classical way so as to involve excitation at photon energies $\gtrsim$ 1.0 keV as derivable from standard x-ray tubes (e.g., using MgKα or AlKα radiation). The many very interesting studies performed to date at lower energies in angle-resolved uv- or xuv- photoelectron spectroscopy (ARUPS or ARXUPS) will thus not be considered in detail. However, at various points, comparisons of the characteristics of a given type of measurement (e.g., core-level photoelectron diffraction) as carried out in the low- and high- energy domains will be made. Further details concerning such lower-energy work as based upon both standard radiation sources and synchrotron radiation are contained in other reviews.[7-9]

It is useful to begin by considering a general experimental geometry for angle-resolved x-ray photoemission from a solid surface, as shown in Fig. 1. X-rays are incident at an angle $\theta_{h\nu}$ with respect to the surface. Photoelectrons are emitted into the acceptance solid angle of the analyzer Ω_o. The initial direction of a given trajectory into this solid angle is given by its polar angle θ (here measured with respect to the surface) and its azimuthal angle ϕ (measured with respect to some arbitrary direction in the plane of the surface). The angle between the direction of radiation propagation $\hat{k}_{h\nu}$ and the direction of electron emission $\hat{k}$ is defined to be α. In most current XPS systems, α is a constant fixed by the mechanical design, although much UPS work has been carried out with movable analyzers and thus variable α. In addition, the geometry shown here is somewhat special in that the directions of radiation propagation and electron emission

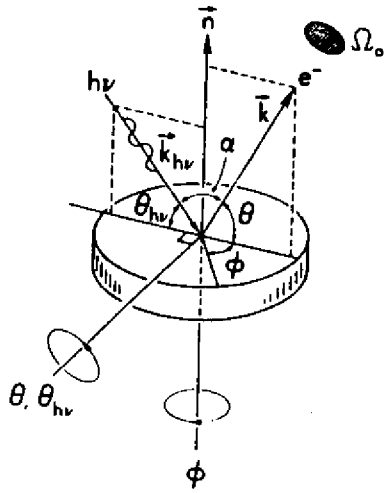

Fig. 1. General geometry for an angle-resolved photoemission experiment. Specimen rotations on the two perpendicular axes shown vary θ, ϕ, and $\theta_{h\nu}$ over their full allowed ranges. $\vec{n}$ is the surface normal. Movement of the electron analyzer relative to the radiation source also can be used to vary α and choose any θ, ϕ, $\theta_{h\nu}$, $\phi_{h\nu}$ combination, but in XPS this has been done very little to date.

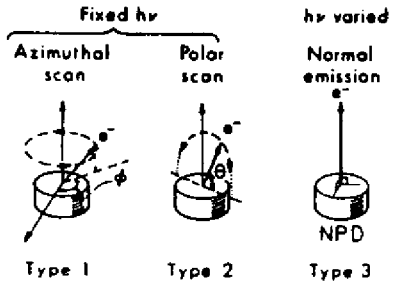

Fig. 2. Schematic illustration of three often-used types of angle-resolved photoemission experiments: (1) an azimuthal scan at constant polar angle, (2) a polar scan at constant azimuthal angle, and (3) a scan of hν at fixed normal emission (also referred to as normal photoelectron diffraction or NPD).

define a plane that also contains the surface normal. In this situation, rotation on the two perpendicular axes shown permits varying the angles θ, ϕ, and $\theta_{h\nu}$ over all possible values (consistent, of course with the geometric requirement that $\theta_{h\nu} + \alpha + \theta = \pi$). The θ, $\theta_{h\nu}$ axis is here taken to be perpendicular to the plane containing $\hat{k}_{h\nu}$, $\hat{k}$ and the surface normal, and the ϕ axis is parallel to the surface normal.

More general experimental geometries in which the analyzer can rotate on one or two axes with respect to the specimen and radiation source are also possible. In this case $\hat{k}_{h\nu}$ and $\hat{k}$ need not be co-planar with the surface normal and the four angles θ, ϕ, $\theta_{h\nu}$ and $\phi_{h\nu}$ are in general necessary to fully define the experiment. Such geometries have been used considerably in angle-resolved measurements at lower energies[7-9], but very little to date in the XPS regime. A final addition that is possible is the utilization of polarized radiation, as is just become practically possible in XPS studies with synchrotron radiation[10]; in this case, the angles θ_ε and ϕ_ε specifying the orientation of the polarization vector $\vec{\varepsilon}$ must also be known. However the standard XPS sources with which virtually all studies at $h\nu \gtrsim 1$ keV have to date been performed yield largely unpolarized radiation, so that we will only later comment briefly on polarization effects as an interesting subject for future investigation.

For a given photon energy $h\nu$, the two basic types of measurements possible in such experiments are thus an azimuthal scan at fixed polar angle (Type 1 of Fig. 2) and a polar scan at fixed azimuthal angle (Type 2 of Fig. 2). A third and more recently developed type of experiment[11] requiring the continuously tunable character of synchrotron radiation is also shown in Fig. 2; here, the emission direction is held parallel to the surface normal and $h\nu$ is swept. In core-level studies, this type of measurement has been termed normal photoelectron diffraction or NPD.

The remainder of this discussion will consider specific problems and areas of application. In Section 2, instrumentation requirements are briefly considered. In Section 3, the general ideas relating to surface sensitivity enhancement at grazing emission are introduced, and various examples of the uses of this effect such as concentration profile measurements, overlayer studies, and investigations of surface-specific electronic structure changes are discussed. The less-utilized effect of surface-sensitivity enhancement at grazing x-ray incidence is briefly considered in Section 4. Section 5 discusses various types of effects involved in core-level emission from single crystals, particularly as related to deriving surface atomic geometry information. In Section 6, valence-level emission from single crystals is considered, largely from the point of view of its relationship to bulk valence band structure.

2. Instrumentation

Beyond the normal instrumentation requirements for an XPS experiment, which are reviewed elsewhere[6], those for adding the capability to do angle-resolved measurements are relatively straightforward.

The solid angle Ω_o over which electrons are accepted into the analyzer (cf. Fig. 1) needs to be well defined and reasonably small. Depending upon the application intended, a range of angles corresponding to $\Delta\theta$ x $\Delta\phi$ from a minimum of $\sim$1° x $\sim$1° to a maximum of $\sim$10° x $\sim$10° could be suitable. For the two most commonly utilized analyzer configurations, the hemispherical electrostatic and cylindrical mirror electrostatic, some degree of baffling thus is in general required to adequately define the solid angle, and this will, of necessity, reduce the overall intensity of the instrument. In certain hemispherical analyzers with pre-retarding lens systems, the solid angle may already be relatively well defined, as discussed in detail for one system by Baird and Fadley[12], but in general this is not at all the case, with much larger angular deflections of $\sim\pm$20°-30° being allowed in a direction perpendicular to the central reference trajectory of the analyzer. This loss of intensity associated with reducing Ω_o also suggests the use of some form of multichannel detection as a compensating factor. A further problem that may be encountered with any analyzer is that Ω_o may vary over the effective emitting area of the specimen and also may depend upon electron kinetic energy or other analyzer parameters, as, for example, the degree of retardation.[5] Such changes in solid angle and also in emitting area can in addition lead to a purely instrumental change in intensity with angle, usually dependent on θ only. Such instrument response functions are discussed in Section 3.C and in prior reviews[4-6,12]. In addition, some instruments will exhibit a change in energy resolution with θ that must be allowed for in precise analyses of spectra[12]. Plummer[13] has also recently considered general criteria for designing analyzers for angle-resolved studies over a range of energies.

In addition to defining Ω_o, it is necessary to be able to rotate the specimen so as to change the angles θ, ϕ, and perhaps also $\theta_{h\nu}$. A single polar axis of rotation varying θ and $\theta_{h\nu}$ is very easy to add in an overall geometry such as that of Fig. 1. A second azimuthal axis for varying ϕ requires additional mechanical complexity, but commercial manipulators providing at least partial azimuthal rotation are available, and custom designs with greater flexibility exist in several laboratories for both ARXPS[5] and ARUPS[14,15] measurements.

As one example of a reasonably flexible system for performing ARXPS at ultra-high vacuum conditions, Figs. 3 and 4 show different aspects of one unit currently in use in our laboratory. (An earlier high-vacuum device with a simpler

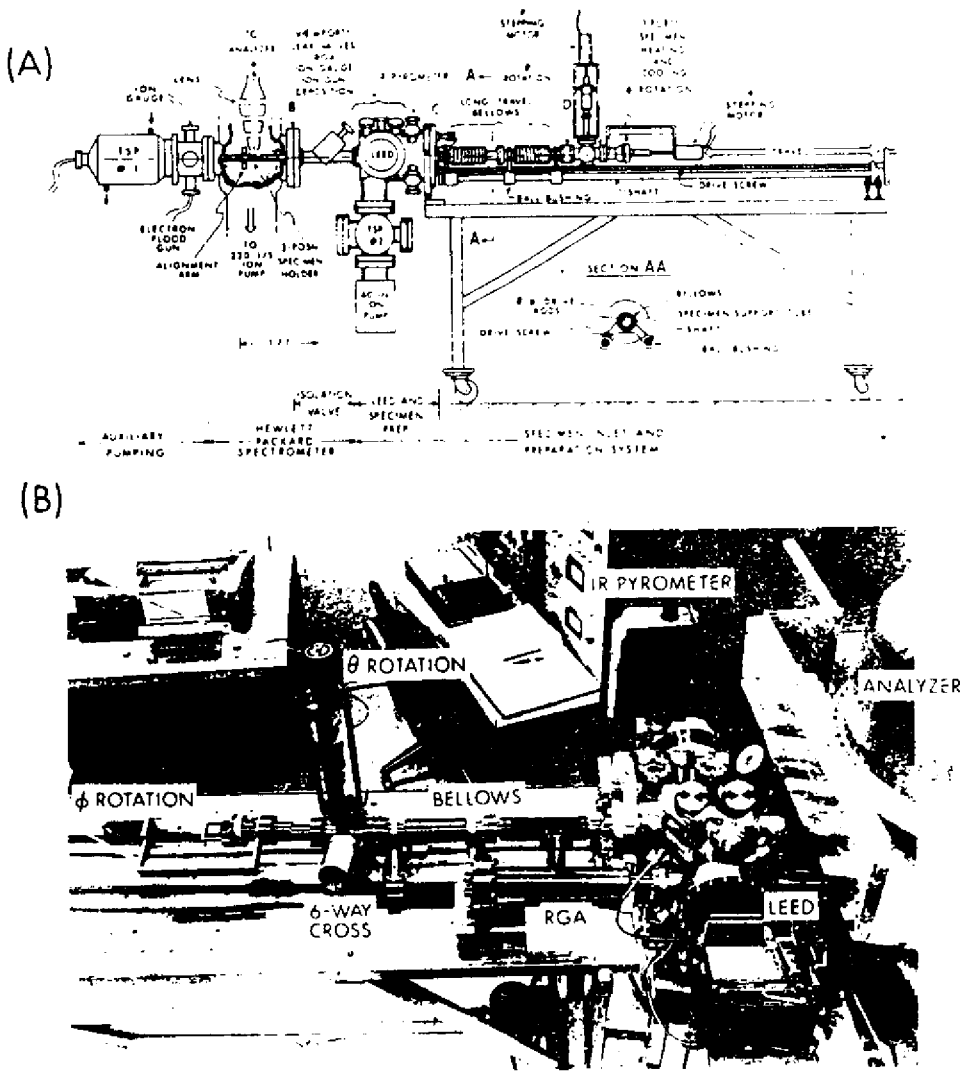

Fig. 3. (a) Schematic drawing of the specimen inlet side of a Hewlett Packard XPS spectrometer that has been specially modified for angle-resolved studies. Various components are labelled. (b) Overall photo of the system in (a) as viewed from the opposite side.

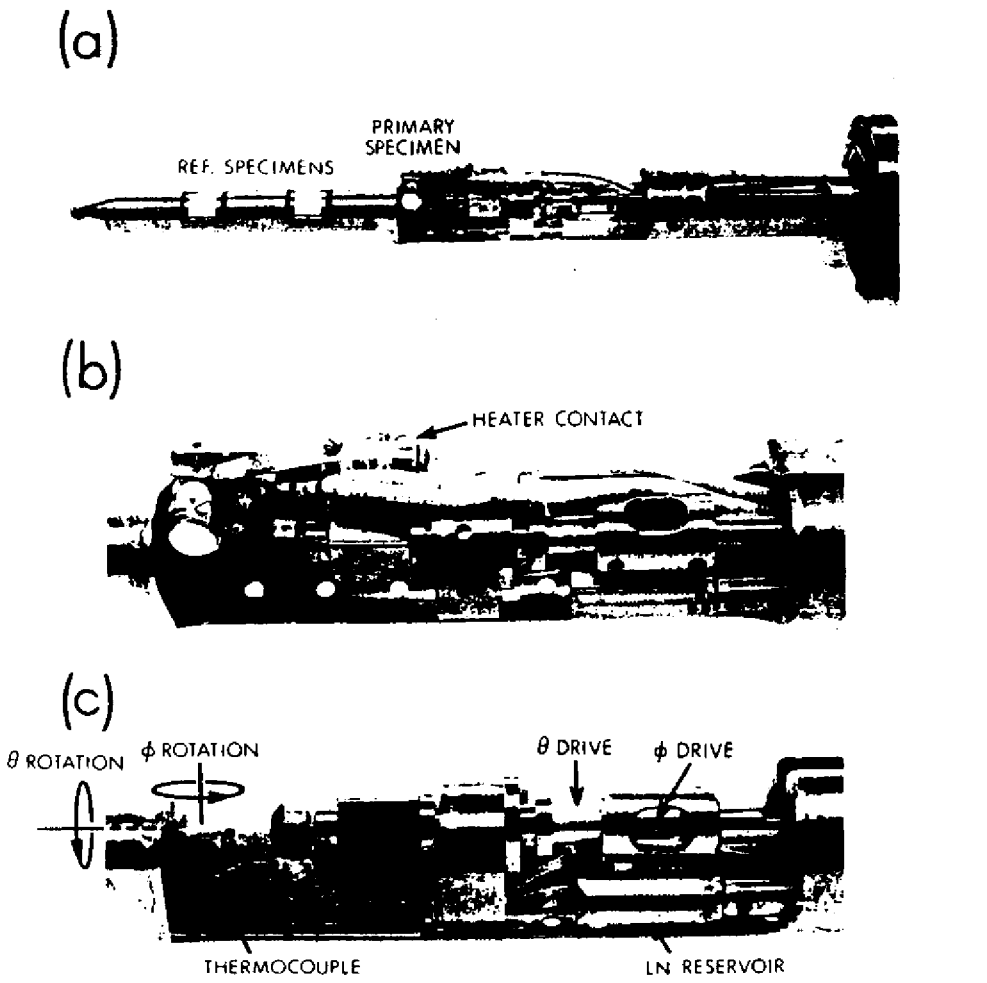

Fig. 4. Three different views of a two-axis goniometer used for variable-temperature ARXPS studies at angular accuracies of ≤±0.5°: (a) overview including reference sample positions, and (b),(c) two close ups with different polar orientation. The smaller-diameter section at left in (a) mates with an alignment arm in the analyzer (cf. Fig. 3(a)).

rack-and-pinion drive is described in ref. 5.) The basic XPS analyzer and chamber to which the specimen preparation chamber, specimen goniometer, and translating-bellows inlet system is mounted is a Hewlett-Packard Model 5950A. Fig. 3(a) is a line drawing of the overall system and Fig. 3(b) a photographic view from the isolation valve on the XPS chamber to the preparation chamber and inlet system. The interior specimen support tube translates on external ball bushings, and is controlled by a drive screw. Various standard components such as a LEED unit, residual gas analyzer, ion gun, leak valves, and infrared pyrometer permit cleaning, preparing, and characterizing specimens before admitting them to the XPS chamber through the isolation valve. Two rotary feedthrus driven by computer-controlled stepping motors permit precision scanning on the two axes shown in Fig. 1. These feedthrus are mounted on a six-way cross together with other feedthrus for electrical heating, thermocouple temperature measurement, and liquid nitrogen cooling. Full ultra-high vacuum operation is also achieved with this system, with base pressures in the XPS chamber of $\sim 4\text{-}6\times10^{-11}$ torr and in the preparation chamber of $\sim 8\text{-}10\times10^{-11}$ torr.

Fig. 4 shows three photographic views of the specimen end of this goniometer. The θ drive comes in on the vertical port of the six-way cross, turns a right angle with a set of bevel gears, and is then transmitted directly to the rotating specimen support arm via a 1/4" o.d. drive tube. This drive tube is supported on precision ball bearings over its entire length of ~110 cm. The φ drive enters via the rear port of the six-way cross and is transmitted via a straight internal drive shaft of 1/8" diameter to sets of bevel gears and then spur gears so as effect φ motion. The φ drive shaft is internal to and concentric with the θ drive tube. Precision stainless steel ball bearings are used at all rotation points. Although there is an overall lash in this system between the coupled θ and φ motions of $\lesssim 1°$ due to the various mechanical linkages involved, the consistent use of identical directions of rotation in making settings permits overall precisions and accuracies of $\lesssim 0.5°$ in both θ and φ. Particularly for the grazing-emission azimuthal scans to be discussed in Section 5, such accuracies appear to be absolutely required for obtaining reproducible data. The specimen can be heated up to ~1000°C with an internal resistive button heater (Varian No. 981-2058) to which current passes via a contact ring and a spring-loaded floating contact. Alternatively, an electron bombardment heater for temperatures up to ~2500°C can also be mounted in the same position. Thus, full azimuthal rotational freedom is maintained, an extremely useful feature in providing a self-consistency check on data from single crystals, where the crystal rotational symmetry should be mirrored in the azimuthal data. Thermocouple and liquid-nitrogen connections can also be made to points near the specimen as needed.

3. Surface Sensitivity Enhancement at Grazing Electron Emission Angles

A. Introduction

The basic mechanism of surface sensitivity enhancement at grazing emission angles is illustrated in Fig. 5 for the case of an idealized homogeneous, semi-infinite, flat-surface specimen in which any effects due to atomic positional order are assumed to be fully averaged over. The mean free path for inelastic scattering Λ_e is further taken to be a constant independent of emission angle. In this case, the mean depth of no-loss photoelectron emission as measured perpendicular to the surface is exactly equal to Λ_e for normal emission or $\theta = 90°$, but it decreases as $\Lambda_e \sin\theta$ for non-normal emission. For typical XPS mean free paths of 15-20 Å[16-18], this simple model thus predicts that between normal emission and grazing emission at $\theta = 10°$, the mean depth should decrease from roughly 8-10 atomic layers down to only ~2-3 atomic layers, respectively. Polar scans of photoelectron intensity are thus expected to exhibit varying degrees of surface sensitivity, as has been demonstrated in numerous prior investigations[4-6].

A qualitative illustration of how significant this low-θ effect can be is presented in Fig. 6, where broad-scan spectra are shown at three angles for a highly-polished Si specimen with an oxide overlayer approximately 1-2 atomic layers in thickness and an outermost overlayer of carbon-containing materials from the residual gas of approximately the same thickness[19]. The pronounced peaks due to the O1s, C1s, Si2s, and Si2p core levels are found to change dramatically in relative intensity as θ is changed from 70° (near normal) to 5° (grazing). With maximum bulk sensitivity at 70°, the Si peaks are most intense, then O1s, then C1s, but at 5°, this order is completely reversed. These results thus directly provide a qualitative depth profile of the specimen, with C lying outside O (present primarily as a Si oxide) and O lying outside the elemental Si of the substrate.

Closer examination of such oxidized Si spectra also shows Si core-level chemical shifts between oxide and element, with different angular behavior for the two, as illustrated in the results of Hill et al.[19] for a 14 Å oxide layer in Fig. 7. Here, the Si2p(oxide) peak is enhanced relative to Si2p(element) at low θ, as expected; the quantitative analysis of this type of overlayer data will be discussed further in Section 3.D.

A final and even more subtle example of the qualitative use of variable-θ data is provided by Si in some very recent results due to Grunthaner et al.[20] shown in Fig. 8. Here, the Si2p data from a chemically-cleaned surface exhibit a very small change in peak shape in going from $\theta = 38.5°$ to the more surface sensitive $\theta = 18.5°$. These results are also shown after a resolution enhancement procedure

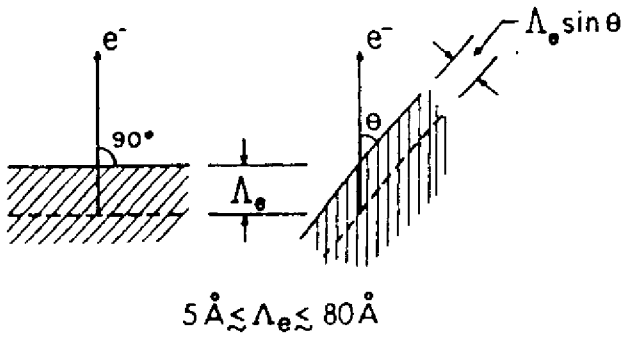

Fig. 5. Illustration of the basic mechanism producing surface sensitivity enhancement for low electron exit angles θ. The average depth for no-loss emission as measured perpendicular to the surface is $\Lambda_e \sin\theta$.

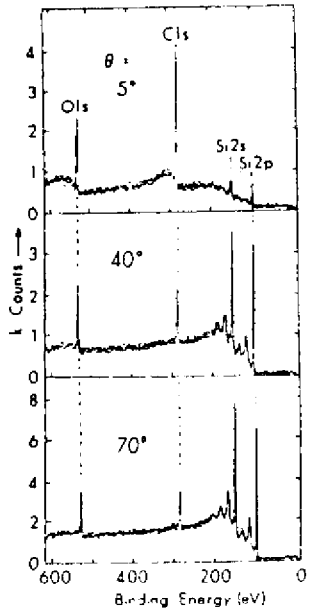

Fig. 6. Broad-scan core-level spectra at three electron exit angles between low and high values for a Si specimen with a thin oxide overlayer (~4Å) and an outermost carbon contaminant layer approximately 1 monolayer in thickness. Note the marked enhancement of the surface-associated O1s and C1s signals for low θ.

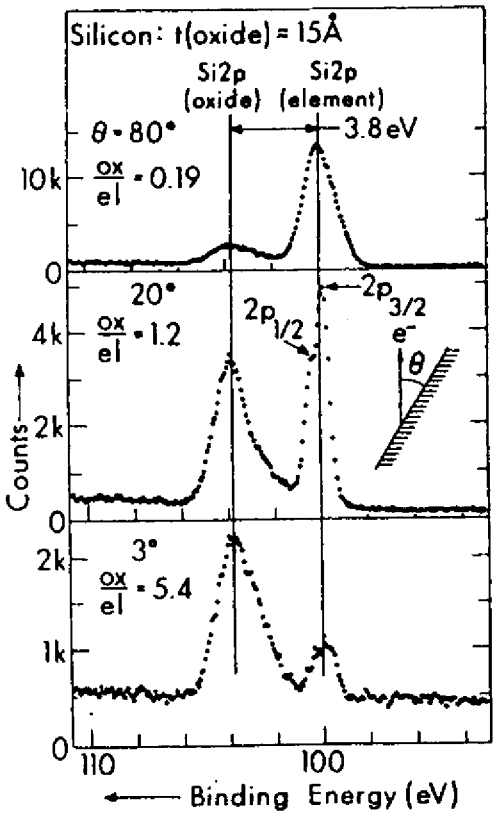

Fig. 7. Si2p spectra at three electron exit angles for a Si specimen with a 15-Å thick oxide overlayer. Note the complete reversal of the relative intensities of oxide and element between high and low θ. (From Hill et al., ref. (19).)

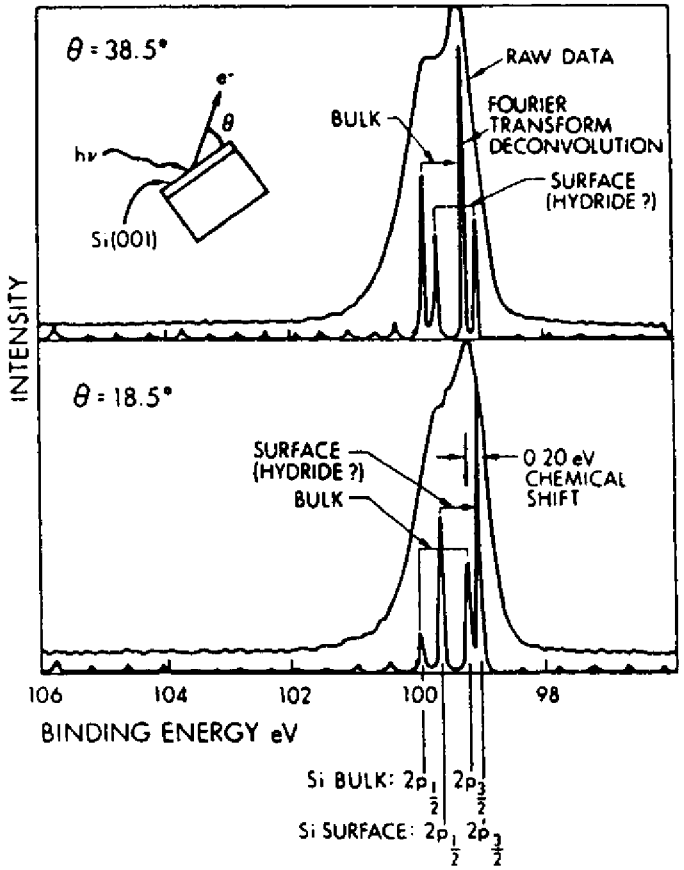

Fig. 8. Si2p spectra at two exit angles from a chemically-cleaned Si surface thought to have a surface hydride present. The raw data and curves obtained via a Fourier-transform (FT) deconvolution procedure are shown. Note the enhancement of the hydride FT peak at θ = 18.5°. (From Vasquez et al., ref. (20).)

using Fourier transform deconvolution to yield two doublets chemically shifted by only 0.30 eV from one another. The lower-binding-energy doublet is enhanced in relative intensity at low θ, suggesting a surface species. The fact that the 2:1 intensity ratio of the expected $2p_{3/2}$:$2p_{1/2}$ spin-orbit doublet is found in the area ratios of the peaks in each Fourier transform doublet for both angles lends further support to the results of the deconvolution procedure, and provides a further internal consistency check for it. The surface species is thought by the authors to be a chemically-produced hydride[20].

B. Simple quantitative models

In more quantitatively discussing such variations of peak intensities with polar angle, it is useful to consider the idealized spectrometer geometry shown in Fig. 9, as has been done in several prior studies[4-6,21,22]. Here, a uniform flux of x-rays I_0 is taken to be incident at $\theta_{h\nu}$ on the atomically flat surface of a specimen of arbitrary thickness t. The radiation may in general be refracted into $\theta_{h\nu}' \neq \theta_{h\nu}$ inside the specimen, after which it penetrates to a depth z below the surface and excites a photoelectron from some level k. X-ray refraction will be negligible for $\theta_{h\nu} \gtrsim$ 1-2°, so that it will not be considered further until the specific discussion of Section 4. Photoelectron excitation is described by the differential photoelectric cross section $d\sigma_k/d\Omega$. The k-level- derived photoelectrons travel to the surface, during which they can be inelastically attenuated according to $\exp\{-z/\lambda_e \sin\theta'\}$, where θ' is the internal propagation angle and $z/\sin\theta'$ is the path length to the surface. Elastic scattering in travelling to and escaping from the surface is for the moment neglected, although we will consider its possible effects later. In escaping from the surface, the photoelectrons may be refracted from θ' to the external propagation angle θ due to the surface barrier or inner potential V_0; refraction will also be neglected for the moment, although an estimate of the low-θ limit of validity of this approximation is presented later in this section. Next, the analyzer is assumed to be adequately described in terms of an effective solid angle of Ω_0 acting over an effective source area of A_0 (as measured perpendicular to the mean electron trajectory), so that all electrons emitted from within the dotted projection of A_0 (the active specimen volume) into Ω_0 are energy analyzed. Possible retardation from an initial energy of $E_{kin} \equiv E_k$ to a final energy of E_0 during analysis is also indicated in Fig. 9. Finally, a detection efficiency D_0 can be included which allows for either less than full counting of the electrons entering Ω_0 (in which case $D_0 < 1$) or the presence of a multichannel detection system (for which $D_0 >> 1$). In general, the mean free path, the effective solid angle, the effective

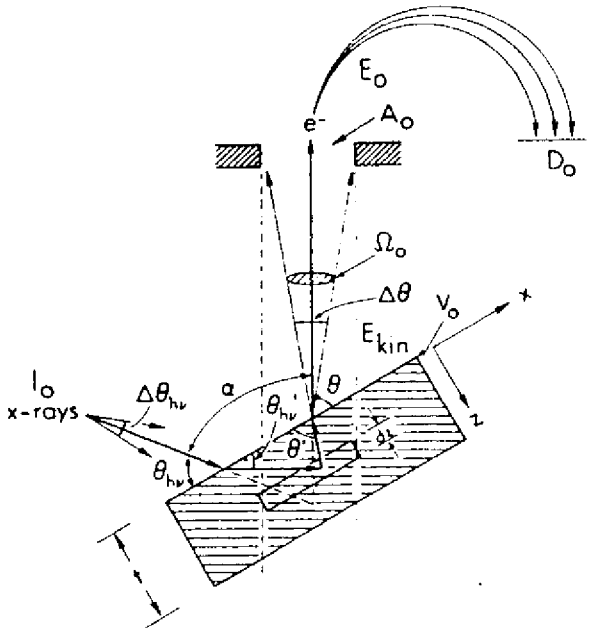

Fig. 9. Idealized spectrometer geometry for calculating angular-dependent photoelectron peak intensities, with various important parameters and variables indicated.

area, and the detection efficiency will depend on electron kinetic energy, so these will be written as $\Lambda_e(E_k)$, $\Omega_0(E_k)$, $A_0(E_k)$, and $D_0(E_k)$.

Within the assumptions of this simple, but for many experimental systems rather realistic, model, expressions for θ-dependent peak intensities can be directly derived for several useful specimen morphologies[4-6,21,22]. These are depicted in Fig. 10, where $N(\theta)$ denotes a θ-dependent photoelectron intensity, ρ denotes the atomic/molecular number density of the species on which the emitting level is located, a subscript k indicates a substrate level and a subscript ℓ denotes a level originating in an overlayer atom or molecule. Each of these cases will now be discussed, but we will return later in this section to consider several ways in which the model from which the equations have been derived may be somewhat oversimplified.

The different specimen morphologies are:

(i) Semi-infinite specimen, atomically clean surface, peak k with $E_{kin} \equiv E_k$. No θ dependence is predicted and the intensity is given by:

$$N_k^{\infty} \equiv I_0\Omega_0(E_k)A_0(E_k)D_0(E_k)\rho_k(d\sigma_k/d\Omega)\Lambda_e(E_k) \ . \qquad (1)$$

This case corresponds to an optimal measurement on a homogeneous specimen for which no surface chemical alteration or contaminant layer is present. The expression given permits predicting the absolute peak intensities resulting for a given specimen, or, of much more interest in practice, the relative intensities of the various peaks. If absolute intensities are to be derived, then the incident flux I_0 must be determined, as well as the kinetic energy dependences of the effective solid angle Ω_0, the effective specimen area A_0, and the detection efficiency D_0. In relative intensity measurements in which the quantity of interest is $N_k/N_{k'}$, for two peaks k and k', the I_0 factors will cancel, although the $\Omega_0 A_0 D_0$ factors need not due to their kinetic energy dependence. The densities ρ_k or $\rho_{k'}$ of the atoms or molecules on which subshell k or k' is located may be known beforehand, or may in many cases be the desired end result in quantitative chemical analyses using XPS. For core levels, the differential cross section $d\sigma_k/d\Omega$ can be calculated for either unpolarized or polarized radiation from a knowledge of the total subshell cross section σ_k and the asymmetry parameter β_k via[6,23-25]

$$\frac{d\sigma_k}{d\Omega} = \frac{\sigma_k}{4\pi}[1 + \beta_k(\tfrac{3}{2}\sin^2\alpha - 1)]. \qquad (2)$$

Within a one-electron central-potential model, tabulations of theoretical relativistic $\sigma_{n\ell j}$'s by Scofield[23] and non-relativistic $\beta_{n\ell}$'s by Reilman et al.[24] can be used to determine $d\sigma_{n\ell j}/d\Omega$, or the non-relativistic results of Goldberg et al.[25] for $\sigma_{n\ell}$ and $\beta_{n\ell}$ for a number of atoms can be used. All of these tabulations include the two most common XPS energies (MgKα at 1254.6 eV and AlKα at 1486.6

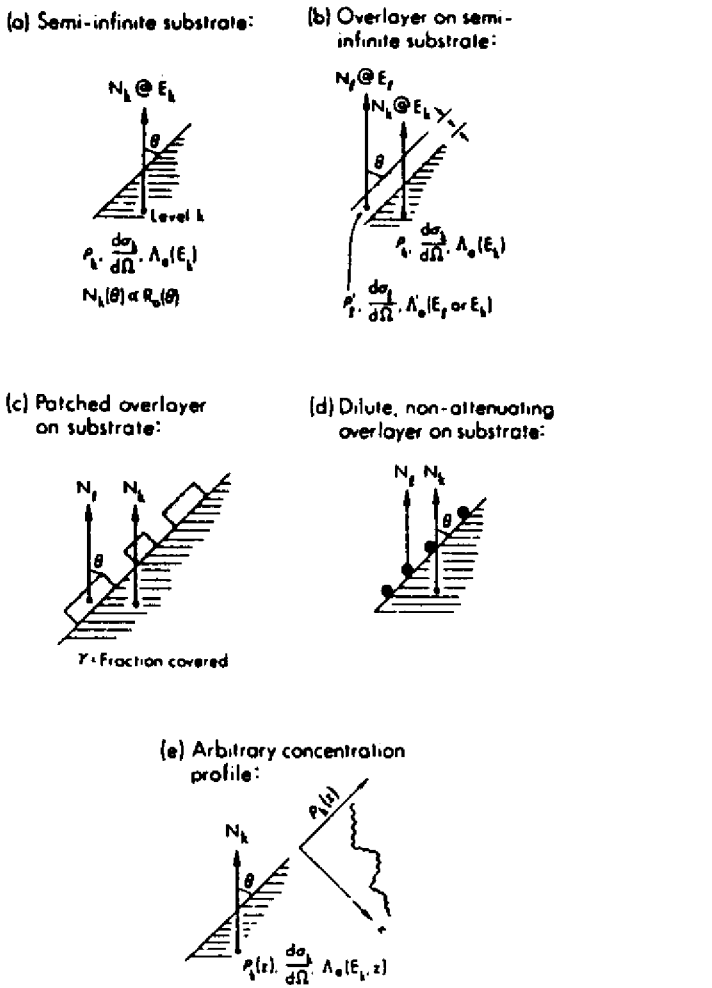

Fig. 10. Several specimen morphologies for which variable-θ peak intensities can be used in order to derive concentration profiles and other analytical information: (a) a uniform semi-infinite substrate, (b) a semi-infinite substrate with a uniform surface overlayer, (c) a semi-infinite substrate with a patched surface overlayer, (d) a semi-infinite substrate with a dilute, non-attenuating overlayer (e.g., a fractional monolayer coverage of an adsorbate), and (e) a semi-infinite substrate with arbitrary concentration profiles inward from the surface.

eV), as well as several lower energies[23,25]. Possible effects of multi-electron processes on the use of such cross sections are discussed elsewhere[6]. For valence levels involved in bonding, the determination of $d\sigma_k/d\Omega$ is more complex[6]. The last quantity involved is $\Lambda_e(E_k)$ which can either be taken from tabulations of previously measured values[18-18], or, within a given specimen, be estimated from Penn's theoretical treatment[26]. More simply, its dependence on kinetic energy for $E_k \gtrsim$ a few hundred eV can be assumed to follow an empirical square-root dependence as[6,18]: $\Lambda_e(E_k) \propto (E_k)^{1/2}$; this relationship thus permits determining Λ_e's at any energy for a given specimen provided that a single value is known.

Note that there is no θ dependence in N_k within this simple model, a prediction that was first made and verified experimentally by Henke[21]. Its origin lies in the fact that the effective emitting depth is $\Lambda_e\sin\theta$ (cf. Fig. 5), while the effective specimen surface area is $A_o/\sin\theta$ (cf. Fig. 9); the effective specimen volume at any θ is thus the product of the two, in which the $\sin\theta$ factors cancel. This behavior is expected to hold as long as θ is not made so small that the edges of the specimen lie within the aperture A_o[4,5]. For such low θ values an additional $\sin\theta$ factor appears in Eq. (1). This is one illustration of the origins of instrument-specific response functions modulating intensities[4,5,12]. This effect generally leads to the unfortunate characteristic that intensities at grazing emission are markedly reduced compared to those at higher θ.

Prior tests of Eq. (1) in the quantitative analysis of homogeneous samples at relatively high emission angles have generally yielded results in agreement with experimental peak ratios to within $\sim\pm$10%, as discussed elsewhere[6,27-29].

(ii) Specimen of thickness t, atomically clean surface, peak k with $E_{kin} \equiv E_k$. The intensity in this case is given by

$$N_k(\theta) = I_o\Omega_o(E_k)A_o(E_k)D_o(E_k)\rho_k(d\sigma_k/d\Omega)\Lambda_e(E_k)[(1-\exp(-t/\Lambda_e(E_k)\sin\theta)] = N_k^{\infty}[1-\exp(-t/\Lambda_e(E_k)\sin\theta)]. \quad (3)$$

Here, the intensity of a peak originating in a specimen of finite thickness is predicted to <u>increase</u> with decreasing θ (again with the proviso that θ not be so small that the specimen edges lie within A_o).

(iii) <u>Semi-infinite substrate with uniform overlayer of thickness t</u>. As first discussed by Fraser et al.[22], the two types of intensities here are:

Peak k from substrate with $E_{kin} \equiv E_k$:

$$N_k(\theta) = I_o\Omega_o(E_k)A_o(E_k)D_o(E_k)\rho_k(d\sigma_k/d\Omega)\Lambda_e(E_k)\exp(-t/\Lambda_e'(E_k)\sin\theta) = N_k^{\infty}\exp(-t/\Lambda_e'(E_k)\sin\theta), \quad (4)$$

Peak ℓ from overlayer with $E_{kin} \equiv E_\ell$:

$$N_\ell(\theta) = I_o\Omega_o(E_\ell)A_o(E_\ell)D_o(E_\ell)\rho_\ell'(d\sigma_\ell/d\Omega)\Lambda_e'(E_\ell)[1-\exp(-t/\Lambda_e'(E_\ell)\sin\theta] = N_\ell^{\infty}[1-\exp(-t/\Lambda_e'(E_\ell)\sin\theta)] \quad (5)$$

where

Λ_e = an attenuation length in the substrate

Λ_e' = an attenuation length in the overlayer

ρ = an atomic density in the substrate

ρ' = an atomic density in the overlayer .

Or, it is often more convenient to deal with peak ratios in which I_o and any purely instrumental variations with θ cancel:

<u>Overlayer/substrate ratio</u>:

$$R(\theta) \equiv \frac{N_\ell(\theta)}{N_k(\theta)} = \frac{\Omega_o(E_\ell)A_o(E_\ell)D_o(E_\ell)\rho_\ell'(d\sigma_\ell/d\Omega)\Lambda_e'(E_\ell)}{\Omega_o(E_k)A_o(E_k)D_o(E_k)\rho_k(d\sigma_k/d\Omega)\Lambda_e(E_k)} \times [1-\exp(-t/\Lambda_e'(E_\ell)\sin\theta)]\exp(t/\Lambda_e'(E_k)\sin\theta) = \frac{N_\ell^{\infty}}{N_k^{\infty}} \times [1-\exp(-t/\Lambda_e'(E_\ell)\sin\theta)]\exp(t/\Lambda_e'(E_k)\sin\theta). \quad (6)$$

This case represents a much more common experimental situation in which the primary specimen acts as substrate and possesses an intentional or unintentional contaminant overlayer (for example, an oxide on a semiconductor as in Figs. 6 and 7 or a layer deposited from the spectrometer residual gases). Substrate peaks are attenuated by inelastic scattering in the overlayer, an effect that is much enhanced at low θ. The overlayer/substrate ratio is thus predicted to increase strongly as θ decreases, and this model provides a quantitative description of the effects discussed qualitatively in the previous section. It is also useful to consider several trivial modifications of Eqs. (4)-(6) that have been found useful in analyzing data. Rearranging Eq. (4) and taking the logarithm yields[30]

$$\ln\left[\frac{N_k(\theta)}{N_k^{\infty}}\right] = -\frac{t}{\Lambda_e'(E_k)\sin\theta}, \quad (7)$$

and proceeding similarly for Eq. (5) gives

$$\ln\left[1-\frac{N_\ell(\theta)}{N_\ell^{\infty}}\right] = \frac{t}{\Lambda_e'(E_\ell)\sin\theta}. \quad (8)$$

In Eq. (6), if the two kinetic energies E_k and E_ℓ are very nearly equal (as, for example, in chemically-shifted peaks such as those of Fig. 7), then $\Lambda_e'(E_k) = \Lambda_e'(E_\ell)$ (although in general $\Lambda_e'(E_\ell) \neq \Lambda_e(E_k)$ because they apply to different materials) and the $\Omega_oA_oD_o$ products will cancel in the ratio. Defining

$K \equiv \frac{N_\ell^\infty}{N_k^\infty}$ then yields after similar manipulation[19]

$$\ell n\left[\frac{R(\theta)}{K}+1\right] = \frac{t}{\Lambda_e'(E_k)\sin\theta} . \quad (9)$$

Eqs. (7)-(9) thus represent linearized methods for plotting data versus $1/\sin\theta$ that will be considered further in Section (3.D), where the quantitative use of this model is discussed. The slopes of such plots are thus given by plus or minus the effective overlayer thickness $\tau \equiv t/\Lambda_e'$.

(iv) Semi-infinite substrate with a uniform, but patched, overlayer of thickness t[5,31,32]. If the fraction of surface area covered by the overlayer is γ, that uncovered is thus $(1-\gamma)$, and the resultant intensities are given by:

Peak k from substrate:

$$N_k(\theta) = (1-\gamma)(\text{Eq. (1)}) + \gamma(\text{Eq. (4)})$$
$$= N_k^\infty[(1-\gamma) + \gamma\exp(-t/\Lambda_e'(E_k)\sin\theta)] \quad (10)$$

Peak ℓ from overlayer:

$$N_\ell(\theta) = \gamma(\text{Eq. (5)})$$
$$= \gamma N_\ell^\infty [1-\exp(-t/\Lambda_e'(E_\ell)\sin\theta)] \quad (11)$$

Overlayer/substrate ratio:

$$\frac{N_\ell(\theta)}{N_k(\theta)} = \frac{N_\ell^\infty}{N_k^\infty}\,\gamma\,[1-\exp(-t/\Lambda_e'(E_\ell)\sin\theta)] \times [(1-\gamma) + \gamma\exp(-t/\Lambda_e'(E_k)\sin\theta)]^{-1} . \quad (12)$$

The overlayer/substrate ratio thus has a θ dependence different from Eq. (6), and, in particular, the enhancement of the overlayer relative intensity at low θ is predicted to be less pronounced in the presence of patching or clustering. This model might be expected to apply for overlayer growth in which the overlayer material (for example, a metal) is more compatible with itself than the substrate, or could also be qualitatively useful as an extreme representation of the effects of non-uniform overlayer growth (for example, in certain types of oxide formation). This model has been compared previously with experimental results[31,32], although it is not clear that patching effects can be clearly distinguished from those due to other phenomena such as surface roughness (to be discussed below).

(v) Semi-infinite substrate with a very thin, non-attenuating overlayer. One important example of such a specimen type is an adsorbate present on a substrate at fractional monolayer coverage. The relevant intensities are[5,6]:

Peak k from substrate:

$$N_k(\theta) = N_k^\infty \text{ as Eq. (1)} \quad (13)$$

Peak ℓ from overlayer:

$$N_\ell(\theta) = I_0\Omega_0(E_\ell)A_0(E_\ell)D_0(E_\ell)s'(d\sigma_\ell/d\Omega)(\sin\theta)^{-1} \quad (14)$$

Overlayer/substrate ratio:

$$\frac{N_\ell(\theta)}{N_k(\theta)} = \frac{\Omega_0(E_\ell)A_0(E_\ell)D_0(E_\ell)s'(d\sigma_\ell/d\Omega)d}{\Omega_0(E_k)A_0(E_k)D_0(E_k)s(d\sigma_k/d\Omega)\Lambda_e(E_k)\sin\theta} = \left[\frac{s'}{s}\right] \times \frac{D_0(E_\ell)\Omega_0(E_\ell)A_0(E_\ell)(d\sigma_\ell/d\Omega)d}{D_0(E_k)\Omega_0(E_k)A_0(E_k)(d\sigma_k/d\Omega)\Lambda_e(E_k)\sin\theta} \quad (15)$$

with

s' = the mean surface density of overlayer atoms in which peak ℓ originates (in cm^{-2})

s = the mean surface density of substrate atoms (in cm^{-2})

s'/s = the fractional monolayer coverage of the atomic species in which peak ℓ originates

d = the mean separation between layers of density s in the substrate (calculable from s/ρ).

These expressions are useful in surface-chemical studies at very low exposures to adsorbate molecules ($s'/s \lesssim 1$), as they permit an estimation of the fractional monolayer coverage from observed peak intensities. The assumption of no inelastic attenuation in the overlayer is an extreme one, but is justified because the macroscopic Λ_e' of case (iii) is both difficult to estimate and dubious in its application to such thin, non-macroscopic layers, and also because it represents a correct limiting form for zero coverage. A recent attempt to quantitatively assess the utility of this analysis[33] is discussed below in Section 3.E.

(vi) An arbitrary concentration profile $\rho_k(z)$ of a given species in a semi-infinite substrate[34].

Peak k from a species of interest:

As a first approximation to such a situation, if the mean free path $\Lambda_e(E_k)$ can be assumed to be constant with depth z and thus independent of the composition change associated with $\rho_k(z)$, a simple summation over atomic layers with spacing d at depths of $z_n = nd$ ($n = 1,2, .. \infty$) can be made to yield:

$$N_k(\theta) = I_0\Omega_0(E_k)A_0(E_k)D_0(E_k)\Lambda_e(E_k)(d\sigma_k/d\Omega) \times \sum_{n=1}^{\infty} \rho_k(z_n)\exp(-z_n/\Lambda_e(E_k)\sin\theta) . \quad (16)$$

If Λ_e depends on z also as $\Lambda_e(E_k,z)$, the resulting expression is, however, considerably more complex[34]:

$$N_k(\theta) = I_o\Omega_o(E_k)A_o(E_k)D_o(E_k)(d\sigma_k/d\Omega) \times \sum_{n=1}^{\infty} [\rho_k(z_n)\{1-\exp(-d/\Lambda_e(E_k,z_n)\sin\theta)\} \prod_{m=1}^{n-1} \exp(-d/\Lambda_e(E_k,z_n)\sin\theta)] \quad (n\geq 2) \quad (17)$$

Taking ratios of two such intensities N_k and N_k' as derived from species with different concentration profiles has been suggested as a method for deriving profiles by Hollinger et al.[34], although a complex, multiparameter fit to the θ-dependent data results, and it appears that physically reasonable constraints must be placed on the forms of $\rho_k(z)$ to yield unique solutions. Vasquez and Grunthaner[35] have also considered a very similar model for oxide growth in fixed-angle XPS measurements. This method is discussed in more detail in Section 3.F.

C. Additional complicating effects

With reference to the idealized spectrometer geometry of Fig. 9 and a few further assumptions made in arriving at the results of the last section, there are several additional effects that need to be considered in order to fully understand the behavior of experimental data.

(i) The instrument response function. Beyond the extreme low-θ deviation of intensities from the constancy predicted by Eq. (1) that we have mentioned before, additional purely instrumental effects can be introduced by a non-uniform x-ray flux (as, for example, will be produced by most x-ray monochromators[12]) and a solid angle that varies over the active portion of the specimen. All of these factors can be combined into an effective instrument response function, as discussed in detail in prior reviews[4-6]. Denoting this by $R_o(E_k,\theta)$, it is conveniently defined in terms of an integral over differential surface elements of the product of spatially varying x-ray flux I, solid angle Ω, and detection efficiency D. The specimen surface can be considered to lie in the x,y plane, thus yielding[5]

$$R_o(E_k,\theta) \equiv \sin\theta \int_A I(\theta,x,y)\Omega(E_k,\theta,x,y)D(E_k,\theta,x,y)dxdy . \quad (18)$$

The detection efficiency will depend principally on E_k and so can probably be removed from the integral. With this definition, any of Eqs. (1) and (3)-(17) can be modified so as to apply to an arbitrary spectrometer simply by replacing the

combined factor $I_o(E_k)\Omega_o(E_k)A_o(E_k)D_o(E_k)$ by $R_o(E_k,\theta)$. Inspection of Eq. (1) with and without R_o inserted shows that the form of such a response function can be empirically determined simply by measuring the θ dependence (and perhaps also the E_k dependence) of the k photoelectron intensity originating from a homogeneous semi-infinite specimen with a clean surface (cf. Fig. 10(a)).

Examples of non-ideal response functions are shown in Fig. 11. Here, curves calculated with a slightly simplified version of Eq. (18) are compared with experimental points obtained with a Hewlett Packard spectrometer[12]. These results are for a system with monochromatized radiation in which I is very strongly peaked in the middle of the specimen surface, but for which the Ω_o, A_o approximation of Fig. 9 is essentially valid. Also shown in Fig. 11 is the measured response function for a Vacuum Generators ESCALAB spectrometer; note that it comes much closer to the constancy with θ predicted by Eq. (1), as its non-monochromatized source yields a much more nearly uniform x-ray flux.

It is finally reasonable to suppose that for some spectrometers, $R_o(E_k,\theta)$ will have the same functional form in θ regardless of E_k[5,12], and in this case, that any intensity ratio $N_k(\theta)/N_{k'}(\theta)$ from a given specimen will yield θ variations independent of instrument effects. (Clark and co-workers[36] have noted, however, that this simplification may not hold for all analyzer systems.) Thus, such peak ratios should in general be more amenable to straightforward analysis, although they still may carry information on the E_k dependence of R_o. For example, an energy dependence of Ω_o as shown in Fig. 12[37] must be considered in analyzing peak ratios at any θ for the Hewlett Packard instrument of Figs. 3 and 11.

(ii) Surface roughness effects. The qualitative effects of surface roughness are illustrated in Fig. 13(a), and they are twofold: (1) For a given macroscopic or experimental angle of emission θ as measured with respect to the planar average of the roughness, the microscopic or true emission angle θ^t at an arbitrary surface point may be significantly different. Thus, the true degree of surface enhancement at low θ may differ appreciably from that expected on the basis of the macroscopic θ alone. (2) Certain regions on the surface may be shaded for emission at a given θ by adjacent raised areas, as indicated by the cross-hatched regions in Fig. 13(a). Such shading will tend to be fully effective if the roughness contours are large with respect to typical Λ_e values of 10-40 Å, or only partial if the contours are on the scale of Λ_e. In any case, regions of the surface will be selected by shading as being more active in emission, and over these regions, it is an integration of the true-angle emission behavior that will correctly predict the observed intensities.

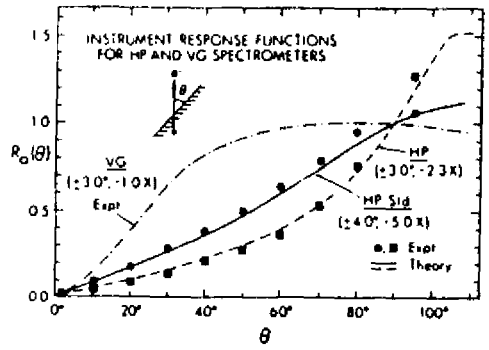

Fig. 11. Instrument response functions $R_0(\theta)$ for two different spectrometer systems, a Hewlett Packard 5950A with monochromatized AlKα x-ray source and α = 72° and a VG ESCALAB5 with a standard AlKα source and α = 48°. All curves have arbitrarily been set to 1.0 at θ = 90° (electron emission normal to the surface). For the HP system, two different entry lens magnifications have been used: standard of 5.0X and a second option of 2.3X. Cls intensities were used for the HP results; $Cu2p_{3/2}$ for the VG. Note the different shapes of the curves, with the monochromatized system showing greater deviations from the simple predictions of Eq. (1) of a constant response function. (From ref. (12) plus R.C. White and C.S. Fadley, unpublished results.)

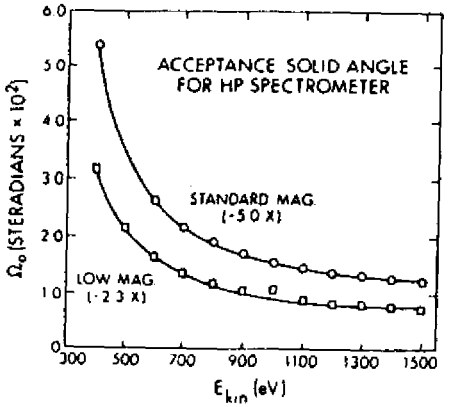

Fig. 12. Kinetic energy dependence of the solid angle of acceptance into a Hewlett Packard 5950A spectrometer, as determined from detailed electron trajectory calculations for two different entry lens magnifications. (From Baird, ref. (37).

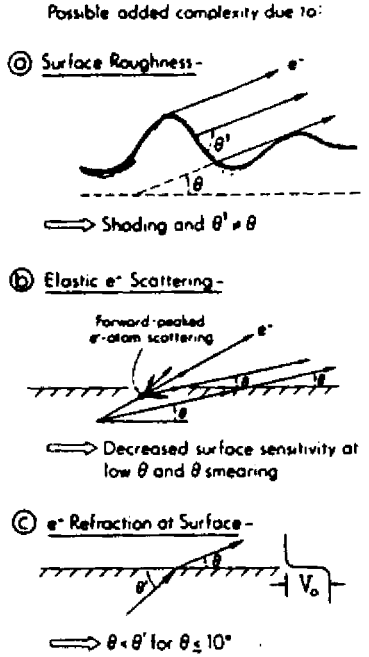

Fig. 13. Illustration of three effects providing additional complexities in the analysis of angle-resolved peak intensities: (a) surface roughness, (b) elastic electron scattering, and (c) electron refraction in crossing the surface barrier V_0.

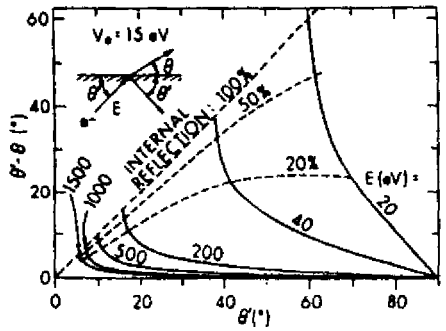

Fig. 14. Calculation of electron refraction effects for different electron kinetic energies and a typical V_0 value of 15eV. The degree of refraction is indicated by the difference θ' (internal) − θ (external). Contours of equal probability of internal reflection are also shown. (From ref. (5).)

In prior investigations[4,5,38,39], roughness effects have been considered for several idealized topographies from both a theoretical and experimental point of view. For example, the triangular-periodic surfaces of aluminum diffraction gratings with thin oxide overlayers exhibit dramatic angular variations in the Al2p(oxide)/Al2p(metal) ratio that are fully consistent with theoretical calculations incorporating the two effects mentioned above[33]. The precise form of the effects seen depends strongly on the exact nature of the profile, which is usually not known for an arbitrary specimen unless it has been very carefully prepared. However, it is possible to conclude that the presence of roughness will in general reduce the degree of surface sensitivity enhancement possible at low θ, although in the limit of very low θ, roughness with rounded contours should again give reasonable enhancement (i.e., an average $\theta_t \gtrsim \theta \gtrsim 0°$)[5].

Thus, roughness must be kept in mind as a possible source of deviations from the simple models of the last section for all specimens. However, even for rather randomly roughened surfaces, such effects do not seem to preclude the use of high-θ and low-θ comparisons to do qualitative depth profiling[39], as discussed in Section 3.A. Also, a procedure as simple as unidirectional course polishing of an aluminum surface and subsequent θ scanning in a plane parallel to the polishing grooves and normal to the surface is, for example, found to significantly enhance the amount of surface sensitivity enhancement at low θ[39].

(iii) Elastic electron scattering. Elastic electron scattering during photoelectron travel to and escape from the surface has been neglected in this simple model, but it could lead to several effects. Each interaction of the photoelectron wave with an atomic center will produce scattered intensity deviating from the initial propagation direction. Thus, the simple straight-line paths assumed in the model are not a fully accurate representation. Fortunately, at typical XPS energies of $\sim 10^3$ eV, the scattered intensity due to each atom will be strongly forward peaked; that is, most of the intensity will lie very close to the initial direction and will in fact be within $\sim \pm 10°$-$15°$ of it. (Such effects will be discussed in much more detail in Section 5, as they have been found to produce pronounced photoelectron diffraction effects in single-crystal studies.) But even in that case, there may be sufficient displacement of intensity to alter the final emission distribution significantly, especially at low θ. The possible effects of elastic scattering on grazing-emission surface enhancement have been discussed qualitatively for some time[5,19], but only rather recently have Nefedov et al.[40] attempted to quantitatively determine their nature and importance.

One important effect of elastic scattering will be to reduce surface sensitivity enhancement at low θ according to the mechanism of Fig. 13(b). For some very low

emission angle θ, the direct or unscattered wave travels along a long path of inelastic attenuation in reaching the surface. It is possible, however, that a wave initially propagating at some higher angle (and thus with a shorter path length to the surface) can be scattered just before escaping so as to yield significant intensity in the θ direction with respect to that of the direct wave. Thus, higher-θ relative intensities for different peaks can be scattered into lower-θ regions, reducing surface sensitivity enhancement. This discussion implicitly neglects any diffraction or interference effects between waves by assuming that the positions of the atomic scatterers are random and averaged over in different emission events. (For single-crystal specimens, such averaging does not occur and diffraction effects can be very strong.)

A second type of effect discussed by Nefedov et al.[40] is the effective lengthening of the average path length of a photoelectron caused by a random walk of elastic scattering events. Thus, they postulate that measured inelastic mean free paths λ_e are too large due to a lack of allowance for such elastic effects.

An example of possible elastic scattering effects is presented in Section 3.D in discussing ARXPS data for the SiO_2/Si system.

(iv) Electron refraction at the surface. As the photoelectron escapes from the surface, it must surmount a potential barrier or inner potential V_o that can be from 5-25 eV in magnitude for typical clean surfaces[41,42]. In doing so, the component of momentum perpendicular to the surface will be reduced, along with the kinetic energy, and a net refraction as shown in Fig. 13(c) will be produced. A fraction of the intensity can also be reflected back into the solid. As the internal angle θ' will thus always be greater than the external angle θ, refraction will act to decrease the degree of surface sensitivity enhancement relative to that expected at θ.

Such refraction and reflection effects can be easily calculated provided that V_o is known[5], and a family of curves for different kinetic energies E and a typical V_o of 15 eV is shown in Fig. 14. The equations utilized in calculating θ and the fractional internal reflection R_e for a given θ' are:

$$\theta = \tan^{-1}[(\sin^2\theta' - V_o/E)^{1/2}/\cos\theta'] \tag{19}$$

and

$$R_e = \left[\frac{1-(1-V_o/E\sin^2\theta')^{1/2}}{1+(1-V_o/E\sin^2\theta')^{1/2}}\right]^2 . \tag{20}$$

The difference θ'-θ between the internal and external angles is used as a gauge of the degree of refraction, and contours of equal percentage of internal reflection are also shown. From these results, it is clear that such refraction and

reflection effects can be very serious problems in measurements in the UPS regime of 20-40 eV. In the XPS region of ~500-1500 eV by contrast, refraction and reflection should not be significant for $\theta \gtrsim 10\text{-}15°$, where $\theta'-\theta \lesssim 3°$ and the internal reflection is $\lesssim 10\%$. Nonetheless, such effects should be taken into account whenever possible in any fully quantitative analysis of ARXPS data for $\theta \lesssim 20\text{-}30°$.

Having considered both the simple quantitative models applicable to ARXPS intensities and several effects which could cause deviations from them, we now turn to illustrative examples involving several specimen morphologies and several types of phenomena that it has been possible to study.

D. Applications to uniform overlayers

As one example of ARXPS as applied to the study of uniform overlayers, we consider work by Clark and co-workers[36] on polymer films deposited in situ on metal substrates. In this study, poly(p-xylylene) films of different thicknesses were deposited on a smooth Au substrate. Thicknesses t were measured with a quartz crystal deposition monitor. The Cls intensity from the film and $Au4f_{7/2}$ intensity from the substrate were measured at several θ values for each film, including values obtained in the limit of infinite thickness. Plots of

$$\ln\left[1-\frac{N_{Cls}(\theta)}{N_{Cls}^{\infty}}\right] \text{ and } \ln\left[\frac{N_{Au4f_{7/2}}(\theta)}{N_{Au4f_{7/2}}^{\infty}}\right] \text{ vs } t/\sin\theta$$

were then made, according to the linearized relations of Eqs. (7) and (8). Such data are shown in Fig. 15 and it is clear that the points for various thicknesses and θ values are very well described by a straight line. There is also very good agreement in the overlayer λ_e' values obtained via least-squares fits for data at different θ's, as given for both the Cls and $Au4f_{7/2}$ kinetic energies on the figure. Varying θ thus provides a very useful additional dimension in such data. We note, however, that high θ values were utilized, being from 90° (normal emission) down to 40°, and thus that various additional effects expected to be stronger at low θ such as roughness, elastic scattering, and refraction have probably been minimized.

As a second case, we consider SiO_2 overlayers thermally grown on highly polished single-crystal Si substrates; some example data have already been shown in Fig. 7. In the first ARXPS study of this type by Hill et al.[19], four oxide thicknesses as determined by ellipsometry were studied and the θ dependence of the Si2p(oxide)/Si2p(element) ratio measured. As the kinetic energies of the two peaks are essentially identical, Eq. (9) provides a useful method for analyzing

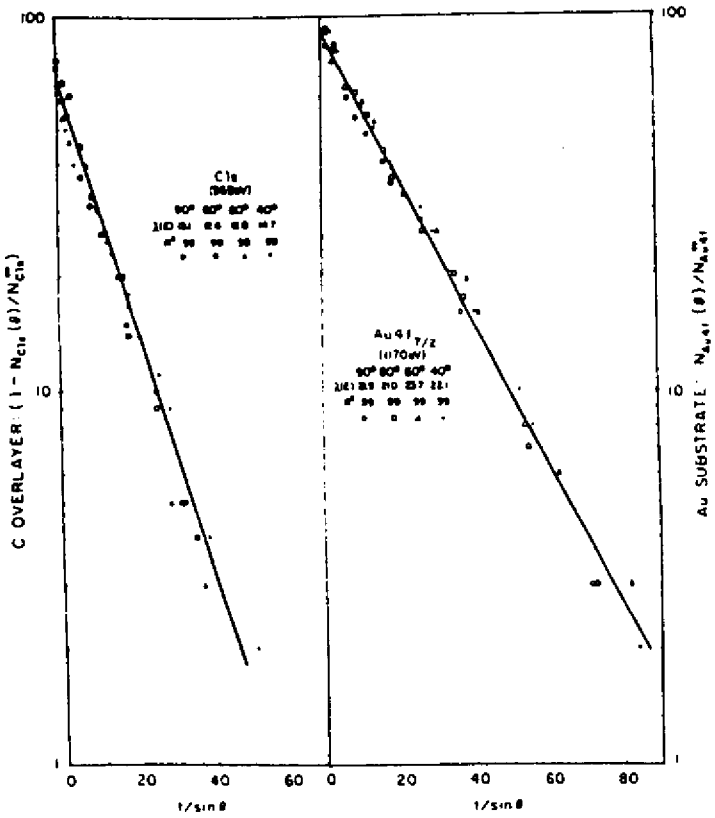

Fig. 15. Angle-resolved core-level intensities from a specimen consisting of a uniform overlayer of poly(p-xylylene) on a polycrystalline Au substrate. Overlayer Cls and substrate $Au4f_{7/2}$ intensities were measured at four θ values and for different overlayer thicknesses, and then plotted according to Eqs. (7) and (8). Line slopes were then used to derive $\lambda_e(E)$ values in the overlayer (here indicated as $\lambda(E)$). (After Clark and Thomas, ref. (36).

the data, and a plot of $\ln[\frac{R(\theta)}{K} + 1]$ versus t/sinθ is shown in Fig. 16 over a broad θ range from 90° to as low at 5°. The data were found to be linear over the θ range of 90° to 30°-40°, but showed similar deviations from linearity for lower θ values in a direction so as to reduce the relative intensity of the oxide peak. These deviations could be due to a combinations of factors: roughness, elastic scattering, electron refraction, incomplete averaging over single crystal effects, and the presence of a non-abrupt transition region between SiO_2 and Si[19]. More recently, Nefedov et al.[40] have reanalyzed this data with the incorporation of only elastic scattering effects, and they find good agreement as to the qualitative form of the deviations from linearity expected at low θ. Pijolet and Hollinger[34] have also very recently analyzed similar Si2p(oxide)/Si2p(element) data using a simplified version of Eq. (17) which allows for an interface layer of intermediate composition between SiO_2 and Si; This analysis suggests that the transition region is rather abrupt and does not exceed ∿ 3 Å for an oxide film of ∿28 Å thickness. However, even this small a transition region also could account for some of the low-θ deviations, as was noted previously in the analysis by Hill et al.[19]. But in any case, the use of $\tau = t/\Lambda_e'$ values derived over the linear regions for the three thickest SiO_2 overlayers permitted deriving a Λ_e'(oxide) of 37±4 Å and, via the experimentally determined constant K (cf. Eqs. (1) and (9)), also a Λ_e(element) of 27±6 Å[19]. These values have subsequently been found to be accurate by other investigators[35,43,44]. Thus, provided that such data are tested via Eq. (9) and the appropriate high-θ range used, this type of analysis seems capable of providing accurate Λ_e' or Λ_e values (or, once Λ_e' is known, accurate t values).

E. Analysis of adsorbate overlayers at fractional monolayer coverage

In chemisorption studies, one is often dealing with fractional monolayer coverages of some adsorbate, and it is thus of interest to ask how accurate ARXPS is for both determining the coverage and also perhaps detecting whether an adsorbate has penetrated into the surface. Single-crystal effects are also often present in such studies, so that some allowance for them needs to be made also.

The example chosen here is from a recent study by Connelly et al.[33] of the very well characterized system c(2x2)S on Ni(001), for which an ordered half-monolayer of S atoms is present, occupying every other fourfold hole site on the Ni surface. Previous structural studies[45] indicate further that the S atoms are 1.3 Å above the first plane of Ni atoms, as will be discussed further in Section 5.E.

Polar scans of S2p(E_{kin} = 1317 eV), Ni2$p_{3/2}$(627 eV), and Ni3p(1413 eV) core-level intensities were made for two different azimuthal orientations

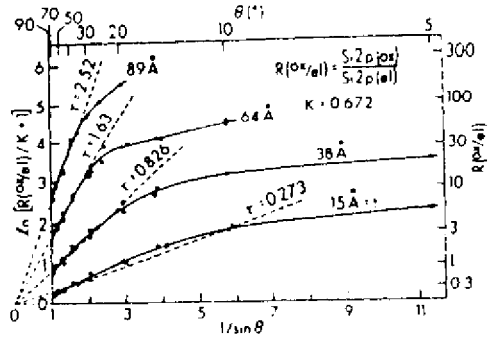

Fig. 16. Angle-resolved core-level intensity ratios from Si specimens with four different oxide overlayer thicknesses from 15Å to 89Å. The Si2p oxide/element ratio (cf. Fig. 7) has been plotted according to Eq. (9) so as to derive Λ_e(oxide) = t/τ. (From Hill et al., ref. (19).)

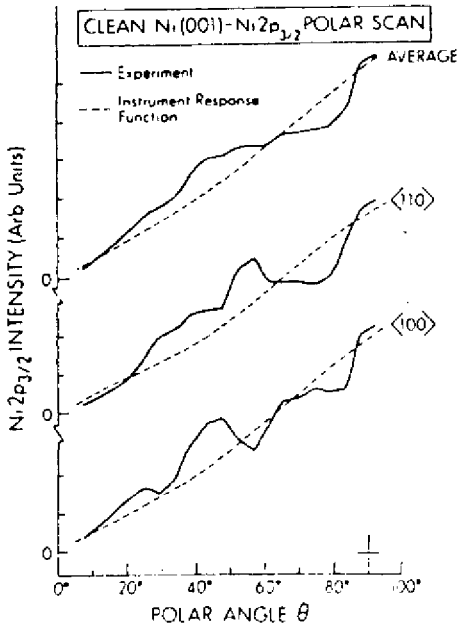

Fig. 17. Polar-scans of Ni2$p_{3/2}$ intensities above a (001) Ni surface. Shown are two scans along the symmetry-inequivalent azimuths ⟨100⟩ and ⟨110⟩, together with an average of these two scans. Before averaging strong diffraction features are evident. Also shown is the instrument response function (cf. Fig. 11). (From ref. (33).)

corresponding to [100] and [111] directions. (For $Ni2p_{3/2}$, it was important to include the intensity of the satellite at ~6 eV.) As expected, the Ni levels showed marked single-crystal channeling effects in their polar scans, but these were very nearly averaged out in a sum of the two scans at different azimuths. This is illustrated in Fig. 17, where the summed data for each Ni level also fit rather well the form expected for the Hewlett-Packard instrument response function (cf. Fig. 11).

The adsorbate/substrate ratios S2p/Ni3p and $S2p/Ni2p_{3/2}$ were calculated from Eq. (15), with all parameters being evaluated as accurately as possible for the specimen and experimental geometry utilized. This included utilizing the known coverage of s'/s = 0.5, theoretical photoelectric cross sections[25], and energy dependences of both Λ_e in the substrate as given by $(E_k)^{1/2}$ and Ω_0 as given by Fig. 12. The calculated curves are directly compared with experiment in Fig. 18, and there is very good agreement as to both the $1/\sin\theta$ form and the absolute magnitude of the ratio, even though the θ range covered is extremely broad (90°-7°). The two sets of data never disagree with theory by more than ~±10%. Theory is however above experiment at low θ for the $2p_{3/2}$ ratio, whereas it is below in the same region for the 3p ratio. This could be due to the much shorter mean free path for the lower energy $Ni2p_{3/2}$ peak, a fact which could lead to some low-θ inelastic attenuation in the overlayer that is not included in the model of Eq. (15). Nonetheless, these effects are not large, and, particularly if higher energy peaks are utilized, it appears that such azimuthally-summed measurements should permit rather accurate coverage measurements to be made, even in the presence of strong single crystal effects. In addition, differences in the forms of such ratio curves as a function of exposure or annealing could be useful in detecting adsorbate penetration into the substrate, as the degree of increase in an adsorbate/substrate ratio at low θ should decrease in the presence of any penetration. For too high adsorbate coverages, however, there could be concern as to the validity of the non-attenuating assumption for the overlayer[5].

F. Studies of more complex concentration profiles

In the category of more complex concentration profiles, we begin by considering a single-crystal specimen of LaB_6 with alternating layers of La atoms and B_6 octahedra perpendicular to the (001) surface (cf. Fig. 19(a)). When such a surface is polished, cleaned in situ by ion bombardment, and annealed to form a well-ordered system, the question arises as to whether La or B_6 layers will lie on the surface. Aono et al.[46] have studied this with ARXPS, measuring polar scans of both La and B core levels, as shown in Fig. 19(b) at two different azimuths. Although there are pronounced single-crystal channeling effects in the intensities

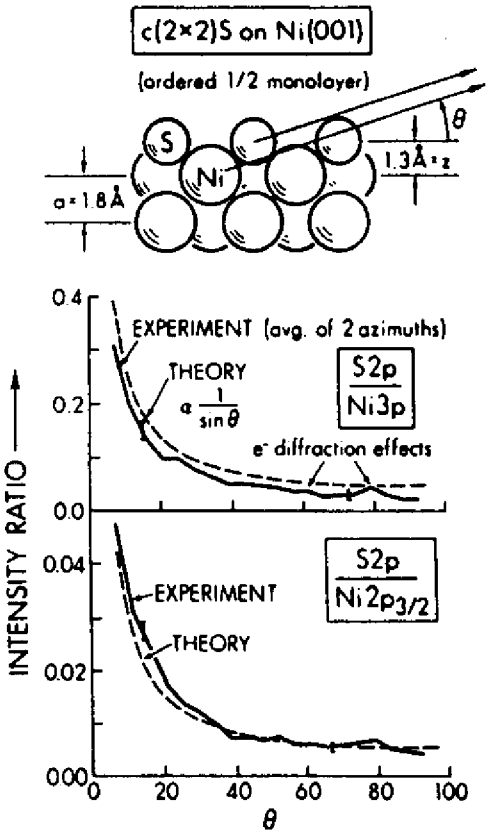

Fig. 18. Comparison of experiment and theory for the polar-angle dependence of an adsorbate/substrate intensity ratio for the very well defined overlayer of c(2x2)S on Ni(001). The $Ni2p_{3/2}$ and Ni3p intensities are averages of two azimuths (cf. Fig. 17). The theoretical curves are calculated according to Eq. (15) with no adjustable parameters. (From ref. (33).)

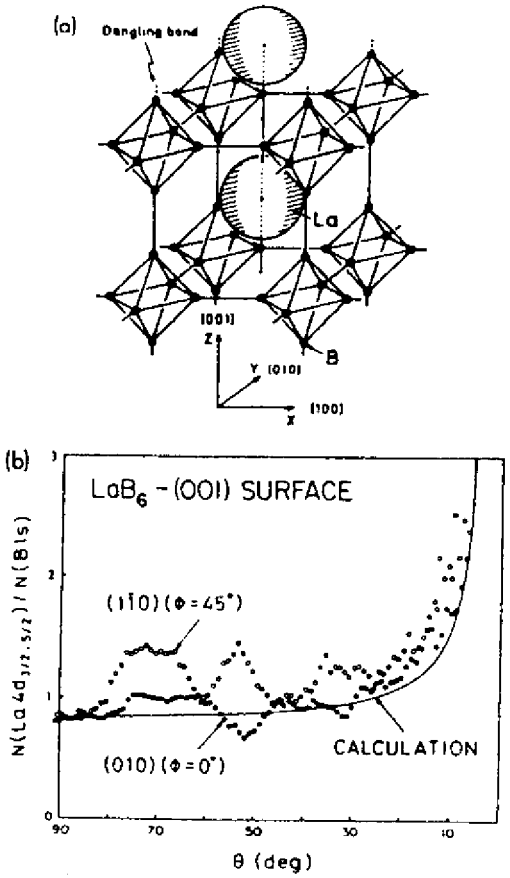

Fig. 19. The crystal structure of LaB_6 is shown in (a), together with the measured and calculated θ dependence of the La4d/B1s intensity ratio in (b). Two different azimuths are shown for the experimental results. (After Aono et al., ref. (46).)

of both peaks, it is nonetheless clear that the La relative intensity is enhanced at low θ. This system represents a straightforward application of Eq. (16) in which Λ_e does not vary with z, but it can be set up in two ways depending upon whether La atoms or B_6 moieties make up layer 1 (the surface layer). Aono and co-workers have carried out calculations of the $La4d_{3/2,5/2}/B1s$ ratio in both ways and it is clear that the agreement with experiment is much better for a La surface layer. This observation via ARXPS has thus assisted in explaining the unusually low work function of LaB_6, and should be generally useful for ordered structures with layering of this type.

Binary metal alloys provide another example for which concentration profiles can be much more complex, with one component often segregating preferentially at the surface[47]. The concentration of this species may then monotonically decay into the bulk until it reaches the average bulk value, or it may in certain cases exhibit single-layer oscillations as it approaches the bulk value. Ion bombardment may, on the other hand, cause preferential depletion of one species at such a surface. As a qualitative illustration of such effects, Nefedov et al.[48] have studied permalloy with a composition of about $Fe_{0.2}Ni_{0.8}$. They compared the polar dependence of the Fe3p/Ni3p intensity ratio for an air-exposed film and for the same film after ion bombardment. Their results are shown in Fig. 20, where it is clear that Fe is surface segregated for the air-exposed film, but that very little segregation of either species is present after ion bombardment. Thus, it is possible to conclude that the ion bombardment has selectively removed Fe, perhaps leading to a slight enrichment of Ni at the surface.

Beyond such qualitatively useful conclusions concerning alloys, the question also arises as to whether the detailed $\rho_k(z)$ profile can be determined by analyzing such ARXPS data. Pijolet and Hollinger[34] have recently discussed this general problem from the point of view of using peak ratios $N_k(\theta)/N_{k'}(\theta)$ based upon Eq. (17). A simplex method is used to choose the best $\rho_k(z)$ and $\rho_{k'}(z)$ by minimizing the difference between the experimental and theoretical ratios. However, the ρ curves so derived are found to be extremely sensitive to the exact data points fit and the convergence criteria used, so that effectively, multiple solutions can result if quite arbitrary profiles are utilized. However, by incorporating physically realistic constraints on ρ_k and $\rho_{k'}$ as they are derived, much better results can be obtained. These constraints include limiting maximum and minimum values, and usually requiring a monotonically increasing or decreasing function of z. (The latter of course eliminates the possibility of seeing the oscillations in ρ(z) that are expected for certain systems.) An example of their results for a Cu/Ni alloy ion bombarded and annealed in UHV are shown in Fig. 21, together with the % Ni profile yielding the solid curve that

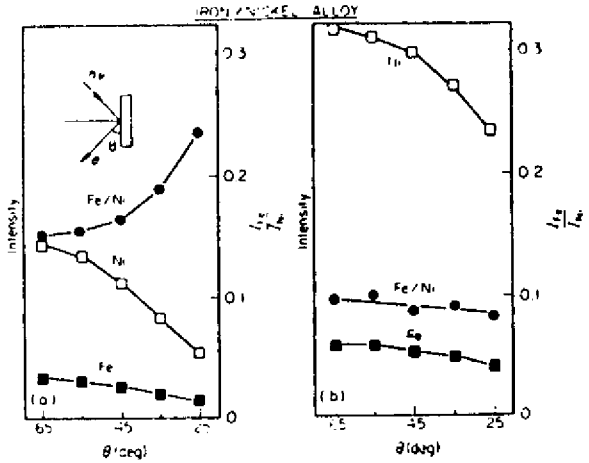

Fig. 20. The θ dependence of Fe3p and Ni3p core intensities for an Fe/Ni alloy before and after ion bombardment of the surface. Note particularly the marked change in the variation of the Fe/Ni ratio with bombardment. (After Nefedov et al., ref. (48).)

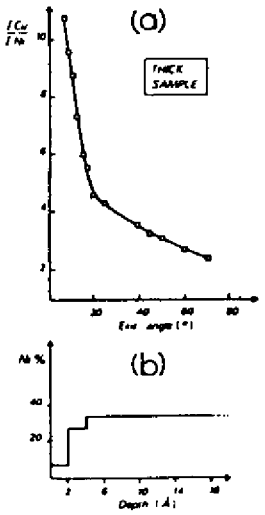

Fig. 21. Experimental $Cu2p_{3/2}$ / $Ni2p_{3/2}$ relative intensities from a Cu/Ni alloy are shown as a function of θ in (a). In (b), the Ni concentration profile as derived from these measurements using an analysis based on a simplified revision of Eq. (17) is presented. (From Pijolat and Hollinger, ref. (34).)

very well describes the $Cu2p_{3/2}/Ni2p_{3/2}$ ratio data. The profile also agrees qualitatively with that expected from theory. However, the layer-by-layer variation of ρ provides essentially a multiparameter fit, so that good agreement between theory and experiment does not assure meaningful theoretical numbers. Also, the inclusion of low-θ data down to ~6° could bring in errors due to roughness, refraction, or elastic scattering; it would be interesting to repeat the analysis for say θ ≳ 15-20° to check self-consistency. Nonetheless, this general idea for trying to derive arbitrary monotonic profiles is promising and well worth further investigation.

As a final and even more complex type of concentration distribution, mention should be made of systems that may exhibit concentration gradients both laterally along the surface as well as inward from the surface. Thus in general the density will be given by ρ(x,y,z). One important class of specimens exhibiting such character is supported heterogenous catalysts, in which active metal atoms may reside within pores in the support, or may coalesce under sintering to form very small metal particles along the surface of the support. This complex concentration distribution, together with the generally very rough character of the support surface, will make any sort of angle-resolved measurement rather difficult to interpret unambiguously, for reasons we have discussed previously. However, fixed-angle intensity measurements, together with specialized models incorporating some of the ideas in the patched overlayer of Eqs. (10) and (11), have been used to derive useful information concerning atomic migration and particle sizes on heterogenous catalysts, as discussed recently by Delgass and co-workers[49] and by Meisel et al.[50].

G. Studies of surface-specific electronic structure changes

(1) Surface core-level shifts. ARXPS has also been used to verify that core-level binding energies of atoms in the outermost layer of a material can be shifted relative to the bulk. This effect was first unambiguously observed by Citrin et al.[51], who used very high resolution (~ 0.25 eV) XPS to study the θ dependence of core levels in Au, Ag, and Cu. Some of their results are summarized in Fig. 22. For Ag and Cu there is little change with θ, but for Au, a shoulder grows in on the low-binding-energy side of the $4f_{7/2}$ peak for low θ. This is reminiscent of the discussion of the Si data in Fig. 8, and suggests a less-tightly-bound species near the surface. The Au data they have analyzed using a two-component model (i.e., a one-monolayer Au(surface) layer and Au(bulk)) with θ-dependent intensities given by Eqs. (4) and (5). This model is found to provide a self-consistent analysis of the data with a surface-to-bulk shift of 0.40 eV and a surface component localized entirely in the first atomic layer. Such

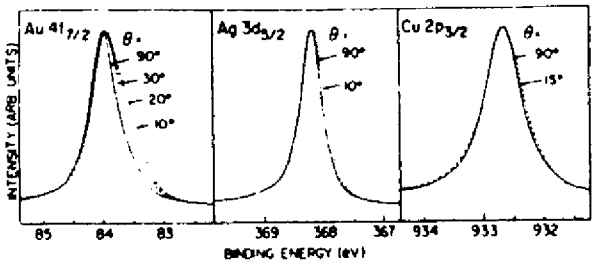

Fig. 22. The θ dependence of core line shapes from the noble metals Au, Ag, and Cu. For near-grazing emission, a shoulder is observed at lower binding energy for Au; This is interpreted as being due to a surface chemical shift of the $Au4f_{7/2}$ binding energy. (From Citrin and Wertheim, ref. (51).)

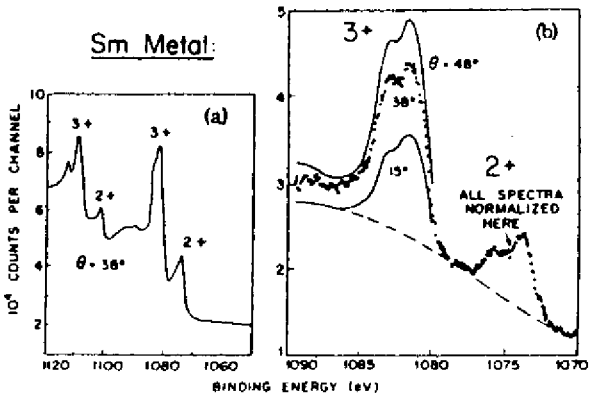

Fig. 23. The θ dependence of 3d core spectra from samarium metal. In (a), the overall 3d spectrum is shown, with both 3/2 and 5/2 regions exhibiting double peaks due to the presence of 3+ and 2+ configurations. In (b), the $3d_{5/2}$ region is shown at three different emission angles, with the 3+ peak being less important for grazing emission angles. (From Wertheim and Crecelius, ref. (53).)

surface-layer chemical shifts have subsequently been confirmed for other metals in higher-resolution synchrotron radiation studies[52]. The Si data of Fig. 8 also represents a similar observation of a surface-specific core shift, in this case thought to be due to hydride formation[20].

Thus, although both of these examples have strained the resolution of the technique to its limits, the ability to vary angle has provided an absolutely essential feature in arriving at the final conclusions.

(ii) Surface valence-state alterations. A further surface-specific effect that has been detected in ARXPS is a change in the average valency of certain rare earth species near the surface. Wertheim and Crecelius[53] first noted this effect for metallic Sm. This material is trivalent in the bulk, and exhibits corresponding multiplet splittings in both core and valence levels that can be used as fingerprints of this 3+ state. However, 2+ multiplets are also seen in the XPS spectra and they are found to increase in relative intensity as θ is decreased, as illustrated for the 3d core levels in Fig. 23. These data were successfully analyzed in terms of Eqs. (4) and (5), but with the added assumption that all Sm^{2+} was located in the first layer, although not all first-layer ions were Sm^{2+}.

(iii) Surface density-of-states changes. Inasmuch as the surface atoms of any material experience a different and usually lower coordination number in comparison to their bulk companions, it might be expected that the distribution of valence states in energy would also be different from the bulk. Such a difference, as measured by the density of states, has been predicted in numerous theoretical studies to occur on the surfaces of transition metals, where the general expectation is for a reduced d-band width as measured most accurately by the first moment of the d-band density of states[54].

One of the most convincing observations of such effects to date is based on ARXPS. Mehta and Fadley[55] studied clean polycrystalline surfaces of Cu and Ni, and for grazing emission found unambiguous narrowing of the second moment of the d band peaks by ∿ 19% and 21%, respectively. Experimental data for Cu are shown in Fig. 24. Calculations were performed to simulate these effects by taking theoretical densities of states as computed for each layer[56] $\rho(E)_j$, j = 1,2,3,... and summing them with allowance for inelastic scattering to yield a weighted density of states that should be seen in first order in the XPS measurement as:

$$\overline{\rho(E)} = \sum_{j=1}^{\infty} \rho(E)_j \exp(-z_j/\Lambda_e \sin\theta'). \qquad (21)$$

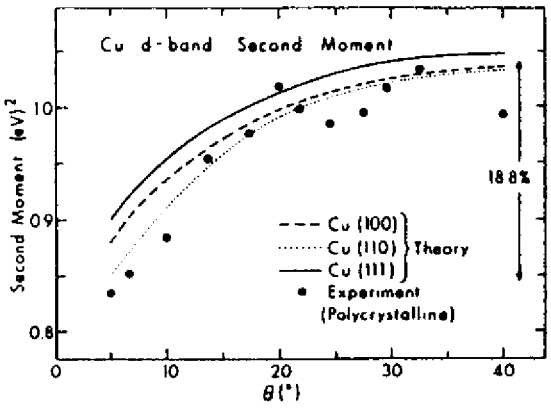

Fig. 24. Comparison of experimental and theoretical Cu 3d-band widths as a function of θ. The width is here measured using the second moment of the 3d intensity, although very similar results are obtained in using the FWHM. Theory is shown for the three lowest-index surfaces. (From Mehta and Fadley, ref. (55).)

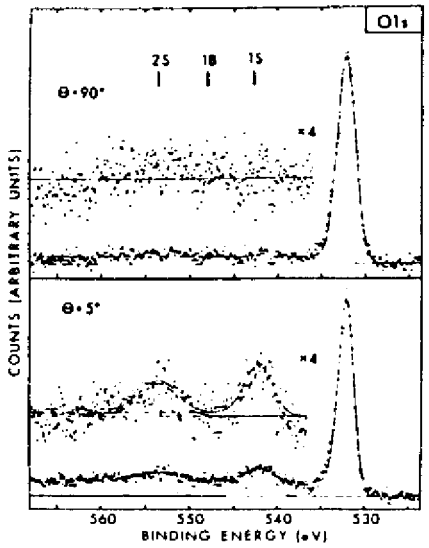

Fig. 25. Polar dependence of plasmon inelastic losses for O1s from oxygen adsorbed on a polycrystalline aluminum surface. The expected positions of bulk- and surface- plasmon loss peaks are also shown. (From Baird et al., ref. (57).)

Here, z_j is the depth of the jth layer and electron refraction has been allowed for in using θ' instead of θ. The curves calculated in this way for three low-index faces of Cu agree very well with the experimental curve, as shown in Fig. 24. The forms of the curves also agree for Ni, although theory predicts a larger effect than that observed. However, in view of the simple initial-state-only model used and the likely greater influence of many-electron effects in nickel d-band emission, the overall conclusion can certainly be made that these ARXPS results display surface d-band narrowing effects for both metals. The fact that decent agreement is obtained even at angles as low as θ=5° also suggests that surface roughness may not be a major problem for very carefully prepared surfaces (In this case, the metals were deposited in situ on ultra-smooth glass substrates.)

Citrin et al.[51] have subsequently used similar measurements on Au to isolate the surface and bulk components of the density of states, thus illustrating surface narrowing and other featural changes. The model used in analyzing this data is analogous to that described in Section 3.G(i) for surface core-level shifts. Their assumption that only the density of states of the first surface layer differs from that of the bulk deviates somewhat from theory, however[54,56], which suggests that the first 2-3 layers may differ. In any case, their results appear to be at least qualitatively correct.

Overall then, such ARXPS measurements have provided another type of information concerning the surface electronic structure of metals, and their application to other classes of materials should also be of interest.

(iv) Surface plasmon losses. A final effect that is of interest in connection with the enhanced surface sensitivity achievable at low θ is a change in the relative intensities of various inelastic loss processes. For example, for an atomically clean surface of aluminum (which exhibits well-defined surface- and bulk-plasmon excitations at different energies), it has been found by Baird et al.[57] that the surface plasmon losses are markedly enhanced in relative importance at low θ. The reason for this enhancement is that the surface- and bulk-plasmons are spatially orthogonal. Thus, because decreasing the angle of exit also decreases the mean depth of emission, the relative probability of exciting a surface plasmon is also increased at low exit angles. Comparisons of such data with theoretical calculations for a free electron metal furthermore yield good agreement with experimental relative intensities and further indicate that the creation of plasmons occurs by means of both extrinsic processes occuring after photoelectron excitation and intrinsic processes occuring during excitation[57]. A further feature of such angular-dependent loss measurements that is of interest in

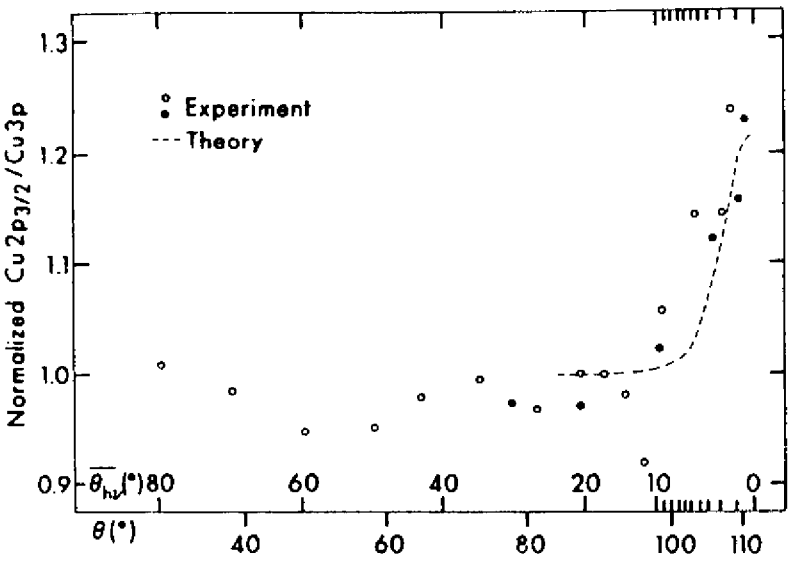

Fig. 26. Experimental and theoretical $Cu2p_{3/2}/Cu3p$ ratios for a smooth polycrystalline Cu specimen as a function of x-ray incidence angle $\theta_{h\nu}$. The $Cu2p_{3/2}$ intensity is enhanced in relative importance as $\theta_{h\nu}$ goes to zero due to its lower Λ_e value and the reduced x-ray penetration depth. (M. Mehta and C. S. Fadley, unpublished results.)

a surface-chemical sense is that they may be useful in determining the locations of adsorbed molecules relative to a surface as noted by Baird et al.[57] and Bradshaw et al.[58]. Specifically, the O1s loss spectrum for an ~0.2 monolayer coverage of oxygen on aluminum exhibits only surface plasmon peaks at grazing electron exit, as shown in Fig. 25, thus suggesting that the oxygen has not penetrated significantly below the surface plane. Thus, the angular dependence of such adsorbate loss structures should provide useful complementary information concerning adsorption geometries and near-surface electronic structure.

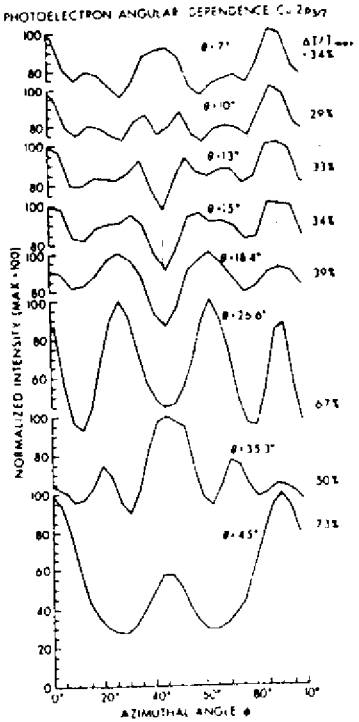

Fig. 27. Experimental azimuthal dependence of $Cu2p_{3/2}$ intensity above a Cu(001) surface for 8 different polar angles of emission. The data have been fourfold-averaged into one quadrant from a full 360° scan, but no mirror symmetrization about $\phi = 45°$ has been performed. Overall anisotropies $\Delta I/I_{max}$ are indicated as percentages. For certain θ values shown here, however (e.g., $\theta = 45°$), it has subsequently been determined that a non-linearity in the videcon multichannel detector used resulted in ~ 1.5X overestimates of the degree of an anisotropy. Compare the more accurate $\Delta I/I_{max}$ values at $\theta = 45°$ of Fig. 31. (From Kono et al., ref. (63).)

4. Surface Sensitivity Enhancement at Grazing X-ray Incidence Angles

A second mechanism producing enhanced surface sensitivity involves measurements carried out at very low x-ray incidence angles $\theta_{h\nu}$. For $\theta_{h\nu} \lesssim 1°$, it was first noted by Henke[21] that the mean x-ray penetration depth in a typical XPS experiment (which is a very large 10^3-10^5 Å for $\theta_{h\nu} >> 1°$) decreases markedly to values of the same order as the electron attenuation length λ_e. This further suggests that surface-atom signals will be enhanced in relative intensity at low $\theta_{h\nu}$, as was first demonstrated by Mehta and Fadley[59]. The reason for this decrease in x-ray penetration depth is the onset of significant refraction such that $\theta_{h\nu}' << \theta_{h\nu}$ (cf. Fig. 9) at the solid surface. The interactions of typical XPS x-rays with a homogeneous medium are furthermore well described by a macroscopic classical treatment,[21] and detailed expressions for predicting penetration depths and expected surface sensitivity enhancements in terms of the material optical constants and other parameters have been presented elsewhere.[5,21,59]

As a recent example indicating the surface sensitivity enhancement possible at low $\theta_{h\nu}$, Fig. 26 shows data obtained from a clean polycrystalline Cu surface for which the $Cu2p_{3/2}/Cu3p$ ratio was measured as a function of the mean x-ray incidence angle $\overline{\theta}_{h\nu}$[60]. Because the kinetic energy of the $Cu2p_{3/2}$ peak (549 eV) is much lower than that of the Cu3p peak (1406 eV), its mean free path will be significantly lower. Thus, the mean depth of $2p_{3/2}$ emission will be less than that of 3p emission under normal circumstances of x-ray incidence, and any significant reduction in the x-ray penetration depth at low $\theta_{h\nu}$ will act preferentially to turn off more of the 3p signal. Therefore, the ~25% increase in the $Cu2p_{3/2}/Cu3p$ ratio noted for $\overline{\theta}_{h\nu} \approx 0°$ is a clear indication of surface sensitivity enhancement. There is also good agreement between experiment and theoretical calculations including both refraction and reflection effects, as also shown in Fig. 26. Note the very sharp onset of the low-$\theta_{h\nu}$ enhancement over a region of only a few degrees near $\theta_{h\nu} = 0°$. More pronounced effects have also been noted in the Cls/Au4f ratio for Au with a carbonaceous overlayer[59], and in the Si2p(oxide)/Si2p(element) ratio for silicon with varying oxide overlayer thicknesses.[61] Also, the known optical properties of several solids at XPS energies of ~1.5 keV have been used to predict that such phenomena should be of very general occurrence.[5]

It should be noted in connection with such grazing-incidence studies, however, that surface roughness effects can be extremely important in any attempt at quantitatively analyzing such data.[61] This is due to the very small incidence angles involved, so that if the true microsopic incidence angle $\theta_{h\nu}^t$ deviates by even ~0.1° from the macroscopically measureable $\theta_{h\nu}$, a significant change occurs

in the degree of refraction and reflection. Thus, surface preparation and accurate angle measurement are both very critical. Further practical problems are that the x-ray source ought to have a very well defined direction of incidence ($\Delta\theta_{h\nu} \lesssim 1°$ in Fig. 9) and that surface shading by any roughness present will generally act to much diminish absolute photoelectron intensities at low $\theta_{h\nu}$. Thus, grazing-x-ray-incidence surface enhancements may serve as a useful complement to those at grazing electron emission, but the measurement and interpretation of the former data may not be as straightforward.

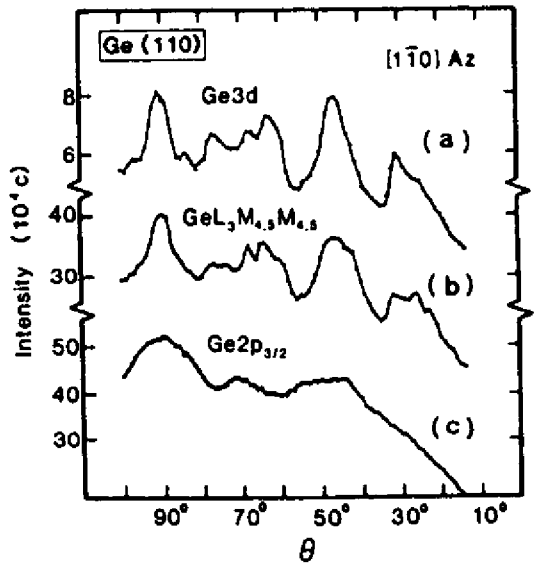

Fig. 28. Experimental polar dependence of Ge XPS and Auger intensities above a Ge(110) surface for θ scans in a [1$\bar{1}$0] azimuth. Ge3d and $Ge2p_{3/2}$ XPS intensities are shown together with the Ge $L_3M_{4,5}M_{4,5}$ Auger intensity. No allowance has been made for the instrument response function. (From Owari et al., ref. (64).)

5. Core-Level Emission from Single Crystals: X-ray Photoelectron Diffraction(XPD)

A. Introduction

In this section, we begin the consideration of effects observed in angle-resolved x-ray photoemission studies of highly-ordered single-crystal specimens. Here, emission from highly-localized, atomic-like core levels will be discussed; in Section 6 following, the more complex case of emission from delocalized valence levels will be considered. In both situations, a consideration of diffraction phenomena associated with the wave character of the emitted photoelectrons will prove essential for understanding the observed angular distributions. It is thus useful to immediately introduce the appropriate non-relativistic relationship between photoelectron wavelength λ_e and kinetic energy E_{kin}:

$$\lambda_e = h/[2mE_{kin}]^{1/2}, \tag{22}$$

where h = Planck's constant and m = the electron mass. In convenient units, this reduces to approximately

$$\lambda_e(\text{in } \mathring{A}) = [150/E_{kin}(\text{in eV})]^{1/2}. \tag{23}$$

Thus the relevant wavelengths over the typical XPS range of energies of ~500-1500 will be from 0.55 Å at 500 eV to 0.32 Å at 1500 eV. The magnitude of the associated electron wave vector $\vec{k}$ is in turn given by $k = 2\pi/\lambda_e$, and $\hat{k} = \vec{k}/k$.

In order to qualitatively introduce the different types of effects seen in such x-ray photoelectron diffraction (XPD) experiments, some typical experimental data are shown in Figs. 27-30[62-64]. These are illustrative of the various types of data which can be obtained, in that Figs. 27 and 28 both represent emission from core-levels in the single-crystal substrate (Cu with (001) orientation and Ge with (110) orientation, respectively), whereas Figs. 29 and 30 represent emission from species adsorbed on such a substrate (c(2x2)CO on Ni(001) and c(2x2)O on Cu(001), respectively. Also, two of the figures (27 and 30) represent azimuthal scans (cf. Fig. 2) whereas the other two (28 and 29) show polar scans.

From these figures, one can directly draw several useful qualitative conclusions: There are pronounced anisotropies in all of these photoelectron angular distributions. If the degree of anisotropy is measured as $(I_{max}-I_{min})/I_{max} = \Delta I/I_{max}$, we see that the values vary from as large as 73% for $Cu2p_{3/2}$ substrate emission in Fig. 27 to as small as 6% for O1s adsorbate emission at large θ values in Fig. 30. There are also some rather narrow features in these angular distributions, with widths as small as ~ 4-5°, and this indicates the possible importance of having adequate angular resolution (as discussed further below). Not surprisingly, the patterns seen exhibit certain symmetries of the underlying substrate: for example, the azimuthal data of Figs. 27 and 30 for a Cu(001)

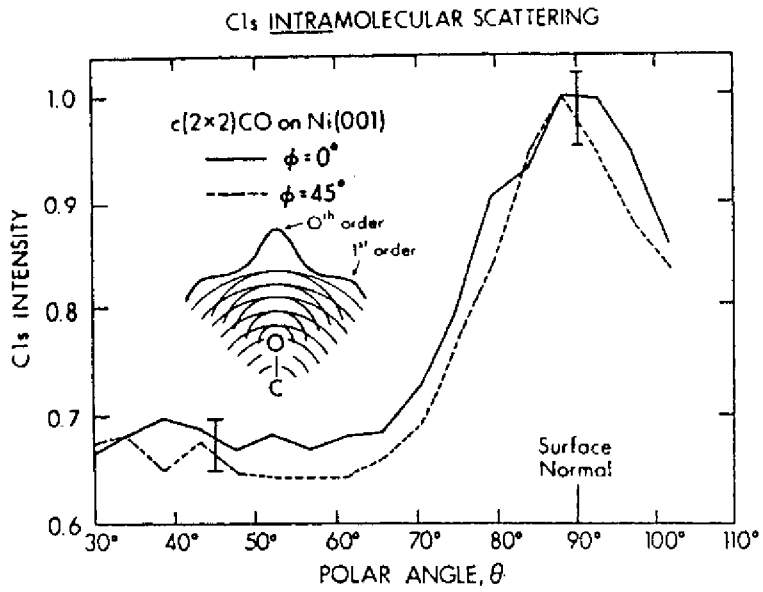

Fig. 29. Experimental polar dependence of the C1s intensity for a c(2x2) overlayer of CO on a Ni(001) surface. The data have been obtained in two symmetry-inequivalent azimuths. Also shown is a schematic illustration of the intramolecular scattering and diffraction producing such effects. (From Petersson et al., ref. (62) and Orders and Fadley, ref. (81).)

surface with C_{4v} symmetry exhibit near mirror symmetry about a [110] azimuth for ϕ = 45°, a point we will amplify on below. The strongest substrate diffraction features are also most often seen along high-symmetry azimuths as well, and this suggests the possible use of such features for determining crystal orientations. Finally, if the substrate angular distributions of Fig. 28 are considered, it is clear that the lower-energy photoelectron peaks exhibit broader features than those at higher energy: specifically, the $Ge2p_{3/2}$ angular distribution at 270 eV has less fine structure than that of Ge3d at 1457 eV. This last observation is a straightforward consequence of the change in de Broglie wavelength with energy, with shorter wavelengths at higher energies being capable of producing sharper diffraction features due to interference effects.

The previous point concerning the desirability of high angular resolution is further illustrated in Fig. 31, where experimental $Cu2p_{3/2}$ azimuthal data from Cu(001) at a polar emission angle of 45° is shown for two different analyzer angular acceptances: cones with half angles of 4.5° and 1.5°. The angle steps used in accumulating the data were $\Delta\phi$ = 1.0° for both cases. It is clear that the ±1.5° aperture yields data with considerably more fine structure, including some features of only a few degrees in width. Although most of these features can also be seen in the ±4.5° data, they are much easier to resolve in the ±1.5 curves. Thus the optimum use of XPD in deriving structural information will in many cases require instrumental angular resolutions of approximately 1-2°.

The azimuthal data of Figs. 27 and 30 further illustrate some important points concerning data analysis. The raw data of Fig. 30 for O1s emission from c(2x2)O on Cu(001), which is shown as dashed curves, has been obtained by scanning over a full 360° in azimuth. Thus, in view of the C_{4v} symmetry of the surface, there is redundancy in the data that can be used to average out noise and to check for the reliability of various features. One useful method is to fourfold average such data by adding the points at ϕ, ϕ+90°, ϕ+180°, and ϕ+270°, thus partially accounting for the known symmetry associated with the surface; in general, this averaging reduces the anisotropy $\Delta I/I_{max}$. Subtracting off the minimum intensity and replotting then yields the "flower" patterns shown as solid curves. These can in turn be compared with the raw data to be sure that all features present in the fourfold-averaged data are consistent with similar features in each quadrant of the raw data. Any misalignment of the azimuthal rotation axis with respect to the [001] surface normal also becomes very evident in such comparisons. Finally, since the symmetry operations of mirror reflection across ϕ=0°, 45°, etc. have not been included in the fourfold averaging, the presence or absence of such mirror symmetry can be used to judge feature accuracy and overall statistical reliability. For example, in Fig. 27, such fourfold-averaged data for $Cu2p_{3/2}$

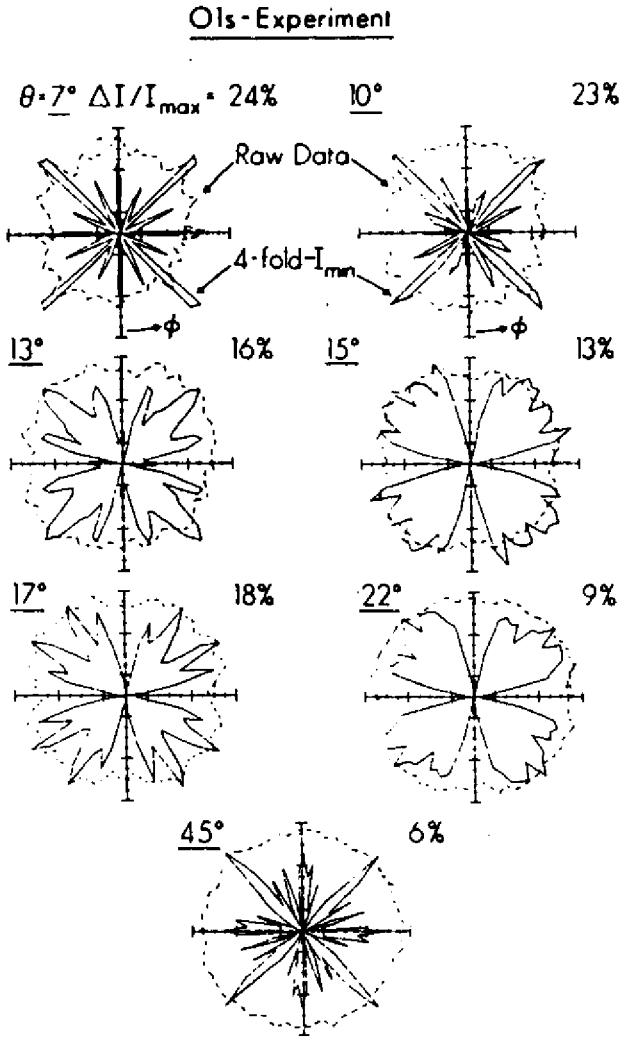

Fig. 30. Experimental azimuthal dependence of the O1s intensity for a c(2x2) overlayer of oxygen on a Cu(001) surface. Seven different polar angles of emission are shown. Both the raw data of a full 360° scan and fourfold-averaged data from which the minimum intensity has been subtracted are shown. The overall anisotropies $\Delta I/I_{max}$ are also indicated for each set of fourfold-averaged data. (From Kono et al., ref. (63).)

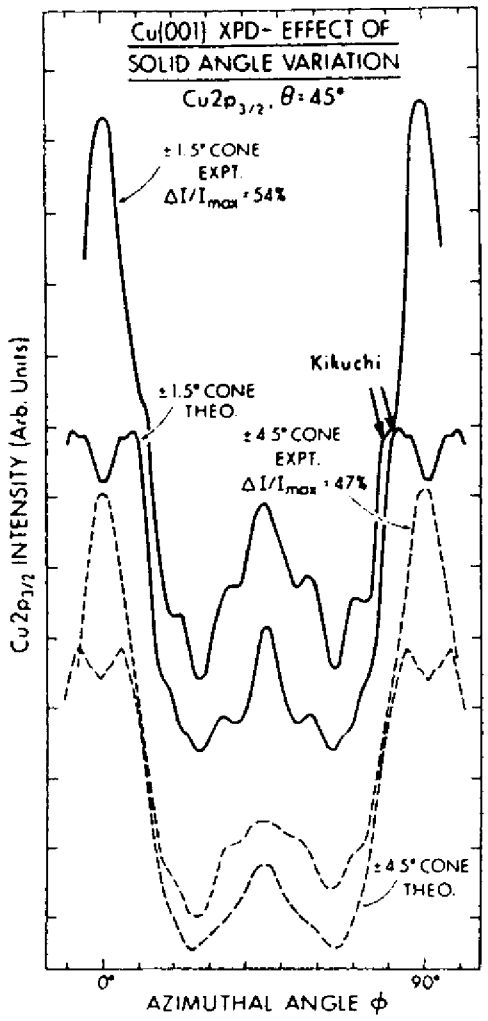

Fig. 31. Effect of analyzer solid angle variation on the experimental and theoretical azimuthal dependences of the $Cu2p_{3/2}$ intensity observed at 45° above a Cu(001) surface. Curves are shown for both a ±1.5° cone of acceptance solid angle and a ±4.5° cone of acceptance. The theoretical curves are based on the single-scattering cluster model. (R. C. White, B. Sinkovic, P. J. Orders, and C. S. Fadley, unpublished results.)

emission from Cu(001) is plotted in Cartesian form and is found to be very close to mirror symmetric about φ = 45°. Other forms of azimuthal data averaging would be appropriate for surfaces with different symmetry (as a three-fold (111) surface or the stepped surfaces to be discussed in Sec. 5.E.), but in general it seems to be very useful to obtain the fullest angle scans possible to enable carrying out such analyses. Similarly, doing symmetry-equivalent polar scans (e.g., at φ = 0°, 90°, 180°, 270° for a fourfold surface) and averaging these to check orientational accuracy and reduce spurious intensity variations is also very useful.

It is also worthwhile to note here that the typical mean free paths for inelastic scattering in XPS of ~10-30 Å imply that all of the features seen in Figures 27-30 must be associated with atomic order very near the surface. In fact, we have found in general that the type of surface pre-treatment utilized (for example, as to times and temperatures for ion bombardment and annealing) can have a dramatic effect on the degree of anisotropy found, even when simultaneous observation with low energy electron diffraction (LEED) shows very little visual difference in the sharpness of a pattern for different pre-treatment procedures. Thus, such XPS measurements seem to be very sensitive and quantitative indicators of the degree of near-surface order.

Before proceeding to a more quantitative discussion of these effects, we consider a few examples of how such x-ray photoelectron diffraction patterns can be used in more or less a fingerprint fashion to derive very useful information. First, the fact that substrate photoelectron emission along low-index directions in the crystal is generally associated with pronounced peaks in the XPD pattern can be used to carry out very precise crystal orientations in situ. (This peaking along low-index directions can be qualitatively explained in terms of Kikuchi bands associated with different sets of low-index planes[65], as discussed in more detail in Section 5.B.) For example, in our laboratory, the polar- and azimuthal-orientations of (001)-metal crystals are routinely determined to within ±0.5° by using a combination of polar scans through the [001] surface normal and azimuthal scans through a series of <110> directions at 45° with respect to the normal. For single crystals containing more than one type of atom, a second type of information concerns the nature of the crystal site in which a given substrate atom is sitting: for example, is it in well-defined lattice sites, has it been interstitially incorporated, or has it been randomly incorporated with respect to the other atoms of the lattice? This use of XPD was first made for a Au/Ag alloy by Fadley and Bergstrom[3]. Some more recent XPD data obtained by Thomas and co-workers[66] from a single crystal of the mineral muscovite are shown in Figure 32. Here, polar scans of different peak intensity ratios are shown. These have been analyzed by noting that photoelectrons arising from two atoms occupying

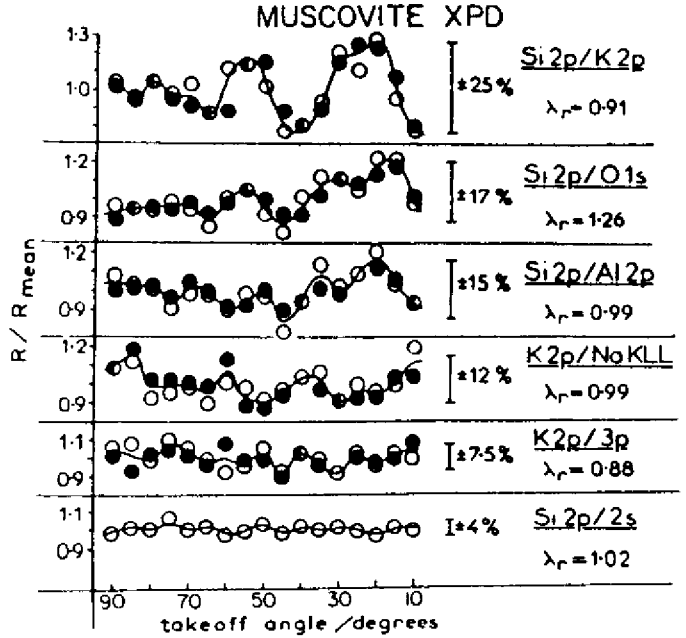

Fig. 32. Experimental polar dependence of normalized core intensity ratios for different peaks resulting from a single crystal of the mineral muscovite ($K(Al_2)(Si_3Al)O_{10}(OH)_2$). The full range of excursion is indicated as a percentage, and λ_r denotes the ratio of de Broglie wavelengths of the two peaks involved in a given ratio. (From Adams, Evans, and Thomas, ref. (66).)

exactly the same type(s) of lattice site(s) in the crystal should show exactly the same XPD pattern, as long as their de Broglie wavelengths are not different by more than ~30%; thus, their normalized ratio should be very near unity regardless of polar angle. This is trivially the case for the K2p/K3p and Si2p/Si2s ratios arising in a single atom. By contrast, photoelectrons arising from atoms with very different sites should exhibit the greatest excursions from unity, as for the ~±25% deviations in the Si2p/K2p ratio; this is consistent with the known structure of this mineral. The reduced value of the Si2p/Al2p excursions of ±15% (as compared, for example to Si2p/K2p) is furthermore suggestive of some Al in stoichiometric excess of that needed to occupy normal octahedral sites going into tetrahedral sites that are predominantly Si. As a second example of site-type determination, Fig. 33 shows polar-scan data obtained by Nihei et al.[67] for a Au overlayer of ~85 Å thickness grown onto a (110) surface of GaSb. With annealing at 400°C only, the Au4f XPD pattern is relatively featureless, suggesting an amorphous overlayer, whereas both the Ga3d and Sb4d patterns exhibit considerable fine structure. After annealing at 540°C, however, the Au4f pattern becomes very nearly identical to the Ga3d pattern; as these two peaks are furthermore very close in kinetic energy, it is thus suggested that Au has preferentially displaced Ga in the GaSb lattice. This kind of atom-specific order and site information would be difficult to obtain in any other way.

As a final introductory comment, we note that Liebsch[68] first pointed out from a theoretical point of view how adsorbate core-level photoelectron diffraction might be used to determine surface structural information. This work involved multiple-scattering theory for low energies as appropriate to an ARUPS experiment.

B. The single-scattering cluster (SSC) model

In discussing more quantitatively such XPD effects, it is necessary to introduce a more detailed model of the scattering and interference phenomena that are expected to occur for photoelectrons in the ~500-1500 eV energy regime. Such a model can be formulated at varying levels of complexity from a straightforward single-scattering or kinematical approach[62,63,69] to more complex dynamical treatments incorporating some degree of multiple scattering[68,70,71]. Fortunately, we have found that a very simple single-scattering model as applied over a finite cluster of atoms appears to very well describe most of the features in XPD[62,63,69], and it is thus this approach that will be discussed below.

The essential elements of this single-scattering cluster (SSC) model are shown schematically in Fig. 34. The basic assumptions are essentially identical to those used in describing extended x-ray absorption fine structure (EXAFS)[72,73] and a similar model has also been applied (although rather unsuccessfully) to angle-

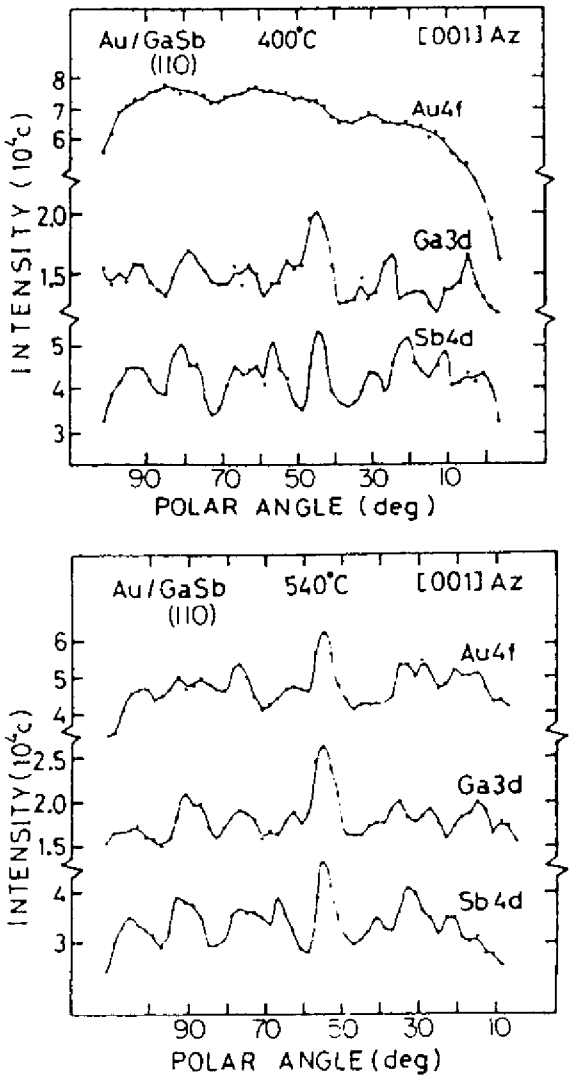

Fig. 33. Experimental polar dependence of the Au4f, Ga3d, and Sb4d peaks resulting from a Au overlayer of approximately 85Å thickness on a GaSb(110) surface. Scanning was in a [001] azimuth, and results for two different annealing temperatures of 400° and 540° are shown. Note the strong similarity of the Au4f and Ga3d curves after the higher temperature anneal. (From Koshizaki et al., ref. (67).)

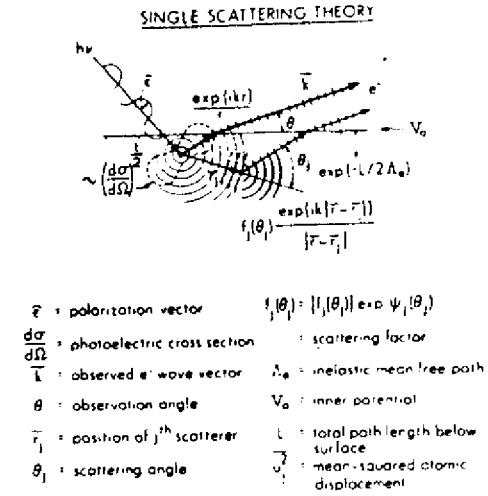

Fig. 34. Schematic illustration of the assumptions used in the single scattering cluster (SSC) model, with various important quantities defined.

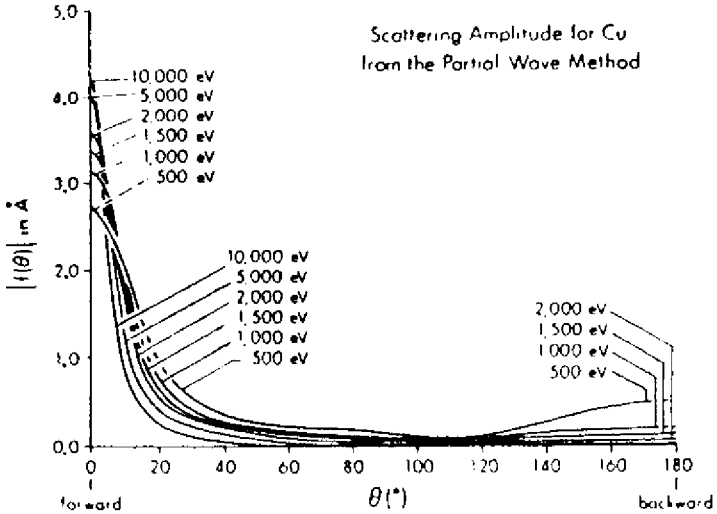

Fig. 35. The magnitude of the atomic scattering factor $|f(\theta)|$ for Cu as a function of scattering angle θ for various electron kinetic energies from 500 to 10,000 eV. Note the enhanced forward peaking as energy increases, and the concomitant decrease in the importance of any backscattering. (From Thompson, ref. (80).)

resolved Auger emission at very low energies of $\lesssim$100 eV[74]. The SSC model as appropriate to XPD is discussed in more detail elsewhere[62,63], so that only the essential assumptions and mathematical results will be outlined here.

Radiation with polarization $\hat{\epsilon}$ is incident on some atom in the cluster, from which it ejects a core-level photoelectron. (In Fig. 34, the emitting atom is shown near the surface, but it could as well be any atom in the substrate.) The problem is then to describe the single scattering of this wave from all other atoms j in the cluster, keeping track of the phase shifts introduced by both the scattering and path length differences and finally to sum the wave <u>amplitudes</u> so produced to yield the total photoelectron amplitude. Squaring this amplitude then yields the intensity expected in a given emission direction, as denoted by the wave vector $\vec{k}$. That is, if $\phi_0(\vec{r},\vec{k})$ is the photoelectron wave at $\vec{r}$ as emitted directly into direction $\vec{k}$ and $\phi(\vec{r},\vec{r}_j\rightarrow\vec{k})$ is the wave resulting from initial ϕ_0 emission toward a scatterer j at $\vec{r}_j$ and then subsequent scattering so as to emerge from the surface in the direction of $\vec{k}$, the overall wave amplitude will be given by

$$\psi(\vec{r},\vec{k}) = \phi_0(\vec{r},\vec{k}) + \sum_j \phi_j(\vec{r},\vec{r}_j\rightarrow\vec{k}) \qquad (24)$$

and the photoelectron intensity by

$$I(\vec{k}) \propto |\psi(\vec{r},\vec{k})|^2 \quad . \qquad (25)$$

Because the detector is situated at essentially $\vec{r} = \infty$ along $\vec{k}$, all of the waves in (24) can finally be taken to have the limiting spherical forms $\phi_0 \propto \exp(ikr)/r$ or $\phi_j \propto \exp(ik|\vec{r}-\vec{r}_j|)/|\vec{r}-\vec{r}_j|$, although the actual amplitudes of each type in a given direction will be modulated by the photoexcitation matrix element and, for the ϕ_j's, also the scattering cross section. It is further assumed that the portion of ϕ_0 which passes to the scatterer j to produce ϕ_j also decays in amplitude according to a spherical wave assumption, or as $1/r_j$. If the scattering angle is θ_j, the overall path length difference between ϕ_0 and ϕ_j is then $r_j(1-\cos\theta_j)$.

The directional modulation of the initial photoelectron wave ϕ_0 would most accurately be treated by considering both the $\ell+1$ and $\ell-1$ components produced in a dipole excitation from an $n\ell$ subshell, and determining the matrix element involved[70-72]. Fujikawa, for example, has recently discussed this approach[71]. For the special case of ns emission, however, this reduces simply to an $\hat{\epsilon}\cdot\hat{k}$ dependence[25], and it is this form that has been used in most prior XPD analyses[63,69]. Since the differential photoelectric cross section $d\sigma_{n\ell}(\hat{\epsilon},\hat{k})/d\Omega$ is proportional to intensity rather than amplitude, another approximation would be to use a ϕ_0 modulation of $[d\sigma_{n\ell}(\hat{\epsilon},\hat{k})/d\Omega]^{1/2}$ [64]. Although this is not strictly correct and does not account for possible sign changes in the matrix element with direction due to the photoelectron parity[75], it is probably an adequate approximation for XPD in which the electron scattering process will be seen to select out $\vec{r}_j$ choices very nearly parallel to $\vec{k}$; that is, for the range of $\vec{r}_j$ directions near the $\vec{k}$ direction that produce significant scattering, the matrix element varies little, so that a very precise description of it is not required. In fact, predicted XPD patterns have not been found to be very sensitive to the exact way in which the matrix-element modulation is included, particularly as regards averaging over $\hat{\epsilon}$ in an unpolarized source[62,63]. We shall thus use the simple $\hat{\epsilon}\cdot\hat{k}$ form in what follows.

The electron-atom scattering that produces ϕ_j is assumed to be adequately described by a complex scattering factor

$$f_j(\theta_j) = |f_j(\theta_j)|\exp[i\psi_j(\theta_j)], \qquad (26)$$

where $\psi_j(\theta_j)$ is the phase shift associated with the scattering. The scattered wave ϕ_j is thus proportional to $f_j(\theta_j)\exp ik|\vec{r}-\vec{r}_j|/|\vec{r}-\vec{r}_j|$, with an overall phase shift relative to ϕ_0 of $kr_j(1-\cos\theta_j) + \psi_j(\theta_j)$ that is due to both path length difference and scattering. The use of this form for ϕ_j implicitly assumes that the portion of ϕ_0 incident on the <u>jth</u> scatterer has sufficiently low curvature compared to the scattering potential dimensions to be treated as a plane wave. This is the so-called "small-atom" approximation[76], and it should be fully adequate in XPD for all but perhaps the nearest-neighbor atoms to the emitter. Even for such nearest-neighbor atoms, the only effect of inclusion of ϕ_0 curvature will probably be to somewhat reduce the amplitudes of certain forward-scattering peaks in $I(\vec{k})$ in comparison to those predicted with the use of Eq. (26)[77], so that its neglect should not be serious. A further important point here is that, as energy is increased, the region of the potential well that is effective in the scattering is reduced in diameter, so that the small-atom approximation should because of this be more valid than prior criteria[76] might indicate.

The scattering factor $f_j(\theta_j)$ is most accurately determined by applying the partial-wave method to a suitable spherically symmetric-scattering potential for each atomic type in the cluster. The number of partial-wave phase shifts needed goes up with energy, and for a typical scattering potential of effective radius 1.5 Å, would be $\gtrsim$ 8 for E_{kin} = 500 eV and $\gtrsim$ 24 for 1500 eV. Tabulations of free-atom scattering factors at energies spanning the XPS regime exist[79]. Alternatively, scattering potentials more appropriate to a cluster of atoms with overlapping charge densities and potentials can be constructed via the muffin-tin model employed, for example, in LEED[41,42]. The free-atom f_j's generally are larger in magnitude than their muffin-tin counterparts due to their neglect of charge and potential overlap[62,63]. Both types of f_j's have been employed in XPD calculations, and they do not yield significantly different $I(\vec{k})$ curves, although

the use of free atom f_j's might be expected to predict slightly higher peak intensities due to their larger amplitudes. In the limit of very high energy, the use of the first Born approximation[78] for determining scattering factors might also be expected to be adequate. However, recent studies by Goldberg, Thompson et al. have shown that the Born approximation is not sufficiently accurate for XPD calculations at $\lesssim$5 keV[63,80].

Some typical scattering factor amplitudes and phase shifts for Cu are shown in Figs. 35 and 36. These curves and other available data[79] show that, over the typical energies in XPS of ~500-1500 eV, the amplitude $|f_j(\theta_j)|$ is very strongly peaked in the forward direction or near $\theta_j = 0°$, with a FWHM of only ~10-30°. This forward peaking is even more pronounced at higher energies, as illustrated in Fig. 35. The only other appreciable scattering strength occurs near $\theta_j = 180°$, but this is down by roughly an order of magnitude in comparison to the forward scattering peak. At higher energies, the back scattering peak is reduced even further, essentially disappearing at 10,000 eV. Considering the phase shifts in Figure 36 and other available data[79] also permits concluding that for XPD, ψ_j is rather small ($\lesssim$30-50°) for the θ_j region in which $|f_j|$ is large. Thus, for electron elastic scattering in XPD from atoms of low- to moderate- atomic number, the scattered waves ϕ_j are expected to be significant only for θ_j rather near zero, and in this case the scattering phase shift will also be rather small. (The optical theorem prevents ψ_j from being exactly zero unless the total scattering cross section is also zero[78].) For substrate-atom emission from well below the surface, the condition of near-forward scattering from neighbors above is geometrically possible for emission into a large number of directions $\vec{k}$ above the surface. However, for adsorbates or near-surface substrate atoms, observation at special emission directions may be necessary to see significant XPD. This is why, for example, most of the polar angles θ in Fig. 30 are near-grazing with respect to the surface. It also explains why the anisotropy in Fig. 30 falls off as the polar angle is increased away from the surface, becoming almost undetectable at θ = 45°.

The effects of inelastic scattering on wave amplitudes during propagation below the surface must also be included. Intensity falls off as $\exp(-L/\Lambda_e)$, where L is an arbitrary path length, so that amplitude is expected to fall off as the square root of this or $\exp(-L/2\Lambda_e) \equiv \exp(-\gamma L)$. Thus, $\gamma = 1/2\Lambda_e$, although γ values up to ~2-3 times this have been suggested in prior EXAFS[72] and Auger[74] analyses. Each wave ϕ_0 or ϕ_j can thus be multiplied by such a factor involving an L value which includes the total path length below some surface cutoff point. This surface cutoff is usually chosen to be the substrate surface as defined by hard-sphere atoms[62,63], although the exact choice is not found to influence the XPD patterns

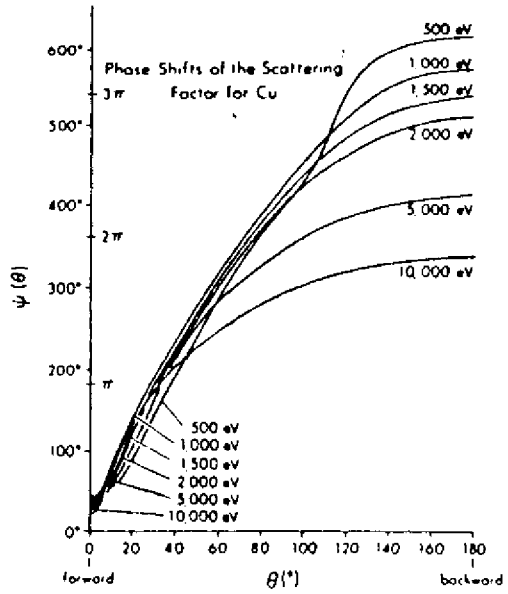

Fig. 36. The phase shift $\psi(\theta)$ for Cu as a function of scattering angle θ for various electron kinetic energies from 500 to 10,000 eV. (From Thompson, ref. (80).)

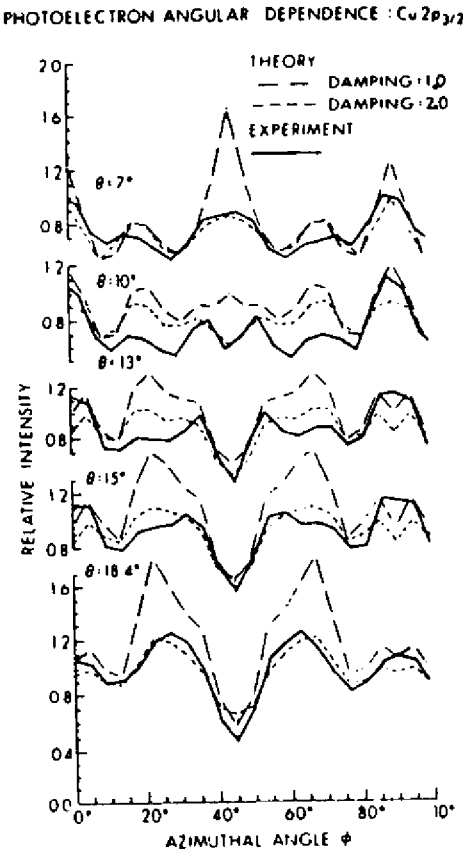

Fig. 37. Comparison of experiment and single-scattering cluster (SSC) theory for the azimuthal dependence of $Cu2p_{3/2}$ emission from Cu(001) at various polar angles between 7° and 18.4°. The notation damping = 1.0 refers to the use of $|f_j(\theta)_j|$ values with no empirical reduction factor, whereas damping = 2.0 refers to the use of values reduced by ½ to optimize agreement with experiment. Note that the only significant changes produced by the use of such damping are for two fine structure features near $\phi = 45°$ and for $\theta = 7°$ and 10°. (From Kono et al., ref. (63).)

significantly. Λ_e values can be taken from prior experimental or theoretical tabulations, but it is found that this choice also is not critical: for example, Λ_e for Cu has been varied by ~±25% without changing the substrate XPD patterns significantly[62,63].

Vibrational attenuation of interference effects is furthermore potentially important, and can be included in a standard way by multiplying each ϕ_j by its associated temperature-dependent Debye-Waller factor:

$$W_j(T) = \exp[-\Delta k^2 \overline{U_j^2}(T)] = \exp[-2k^2(1-\cos\theta_j)\overline{U_j^2}(T)] \quad (27)$$

where Δk is the magnitude of the change in wave vector produced by the scattering, and $\overline{U_j^2}(T)$ is the temperature-dependent one-dimensional mean-squared vibrational displacement of atom j with respect to the emitter. At this level of approximation, $\overline{U_j^2}$ is assumed to be isotropic in space and any correlations in the movements of near-neighbor atoms are neglected. $\overline{U_j^2}$ values can be obtained from, for example, LEED analyses[62,63]. However, the fact that the electron scattering is significant only when θ_j is rather close to zero acts through the $(1-\cos\theta_j)$ factor in the argument of Eq. (27) to yield W_j's very close to unity for all important scattered waves. Thus, the $\overline{U_j^2}$ values chosen for Cu can in fact be increased by a factor of four without appreciably altering the $I(\vec{k})$ curves[63]. So, vibrational effects are to first order not very important in forward-scattering dominated XPD, although they are, for example, very important in LEED, EXAFS, and normal photoelectron diffraction where back scattering is the dominant diffraction mode (and thus $\theta_j \gtrsim 180°$). An alternate method for allowing for vibrational effects is to assume some probability distribution of atomic positions due to vibration (as, for example, a harmonic oscillator envelope) and then to sum separate weighted diffraction intensities for all possible combinations of atomic positions. This is cumbersome, but it has been used to quantitatively look at the effects of specific types of molecular vibrations at surfaces[77,81].

The expression for intensity $I(\vec{k})$ can now be written down directly as:

$$I(\vec{k}) \propto \int \left| \hat{\varepsilon}\cdot\hat{k} e^{-\gamma L} + \sum_j \frac{\hat{\varepsilon}\cdot\hat{r}_j}{r_j} |f_j(\theta_j)| W_j e^{-\gamma L_j} \{\exp i[k r_j(1-\cos\theta_j) + \psi_j(\theta_j)]\} \right|^2 d\hat{\varepsilon}$$

$$+ \sum_j \int (\hat{\varepsilon}\cdot\hat{r}_j)^2 \frac{|f_j(\theta_j)|^2}{r_j^2} (1-W_j^2) e^{-2\gamma L_j} d\hat{\varepsilon}. \quad (28)$$

Here, $\hat{\varepsilon}\cdot\hat{k}$ and $\hat{\varepsilon}\cdot\hat{r}_j$ represent photoemission matrix-element modulations along the unit vectors $\hat{k}$ and $\hat{r}_j$, respectively, and $\exp(-\gamma L)$ and $\exp(-\gamma L_j)$ are appropriate inelastic attentuation factors. Thus, $(\hat{\varepsilon}\cdot\hat{k})\exp(-\gamma L)$ is the amplitude of the direct wave $\phi_o(\vec{r},\vec{k})$ and $(\hat{\varepsilon}\cdot\hat{r}_j)|f_j(\theta_j)|W_j \exp(-\gamma L_j)/r_j$ is the effective amplitude

of $\phi_j(\vec{r}, \vec{r}_j-\vec{k})$ after allowance for both inelastic scattering and vibrational attenuation of interference. The complex exponential allows for the total final phase difference between ϕ_o and each ϕ_j. The integrals on $\hat{\varepsilon}$ simply sum over different polarizations perpendicular to the radiation progagation direction, as appropriate to the usual case of a largely unpolarized x-ray source in XPS. The second $\sum_j$ corrects the first absolute value squared for the incorrect inclusion of Debye-Waller attenuations in terms involving a product of a scattered wave with itself. That is, in expanding the absolute value squared, only products involving unlike waves as $\phi_o\phi_j^*$ or $\phi_j\phi_\ell^*$ $(j \neq \ell)$ should include Debye-Waller products of W_j or W_jW_ℓ, respectively. The $(1-W_j^2)$ factor in the second summation is thus necessary to yield overall correct products of the form $\phi_j\phi_j^*$ without any W_j^2 factor. The second sum is termed the thermal diffuse scattering term and it is usually quite small with respect to the overall XPD modulations, because, as we have already noted, W_j is very close to unity for all strong scatterers. Eq. (28) is thus the basic starting point of the single scattering cluster model. It is also worth noting here that such a cluster sum makes no explicit use of the 2- or 3- dimensional translational periodicities that may be present, even though the atomic coordinates $\vec{r}_j$ used as inputs may incorporate such periodicities. Thus, neither surface- nor bulk- reciprocal lattice vectors are explicitly involved, and it makes no sense at this level of description to speak of diffraction "beams" associated with certain $\vec{g}$'s as in LEED.

Averaging over a totally unpolarized source leads to a more complex expression for $I(\vec{k})$ in terms of various geometric angles, but it can be shown that the strong forward peaking in $f_j(\theta_j)$ permits using the following relatively simple expression[62,63]:

$$I(\vec{k}) \propto |I_o + \sum_j I_j W_j \exp\{i[k r_j(1-\cos\theta_j) + \psi_j(\theta_j)]\}|^2 + \sum_j I_j^2(1-W_j^2), \quad (29)$$

where θ_k or θ_{r_j} are the angles between the direction of radiation propagation and $\vec{k}$ or $\vec{r}_j$, respectively, and I_o and I_j are defined as

$$I_o = \sin\theta_k \exp(-\gamma L)$$

$$I_j = \sin\theta_{r_j} |f_j(\theta_j)| \exp(-\gamma L_j)/r_j .$$

That is, in averaging over $\hat{\varepsilon}$, $\hat{\varepsilon}\cdot\hat{k}$ has been replaced by $\sin\theta_k$ and $\hat{\varepsilon}\cdot\hat{r}_j$ by $\sin\theta_{r_j}$. It is this result that has been used in most XPD calculations to date.

The last parameter of importance in actually using Eqs. (28) or (29) is the range of j or the choice of a suitable cluster of atoms. This is done empirically so as to include all significant scatterers by verifying that the predicted XPD patterns do not change in any significant way with the addition of further atoms at the periphery of the cluster. The inherent weakness of all scattering events

for which θ_j is appreciably different from zero tends to limit cluster sizes in most cases. They thus can range from 2 atoms for near-normal emission from a vertically oriented diatomic molecule on a surface[77] to as many as several hundred atoms for substrate emission in which both the emission and scattering must be summed over several layers into the bulk[62,63]. However, even for the largest clusters so far considered, the inherent simplicity of Eqs. (28) and (29) still yields calculations which do not consume excessive amounts of computer time, especially by comparison with those necessary for LEED or UPS simulations.

A further physical effect of importance in making comparisons to experiment is the possibility of electron refraction at the surface, as discussed previously in Section 3.C. Fig. 14 indicates that, even at the relatively high energies of XPS, for emission near grazing, angle changes $\theta'-\theta$ of a few degrees can be produced by refraction. Thus, especially for adsorbate studies such as that shown in Fig. 30, a proper allowance for refraction is necessary, at least for θ values $\lesssim 10°$. This is done by using a suitable inner potential V_0 derived from experiment and/or theory and Eq. (19) to predict θ for a given internal propagation direction θ'. In the presence of an adsorbate, the exact form of the surface potential barrier thus becomes important, as it may not then be possible to assume an abrupt rise to the vacuum level at the substrate surface. Also, the presence of adsorbate atoms may alter V_0 through changes in the work function, and these atoms also may occupy positions above the surface in which only a fraction of V_0 is appropriate. Although a prior study of O on Cu(001) indicates that the predicted XPD results are not particularly sensitive to the choice of V_0[62,63], it is important to realize that not properly allowing for it may shift theoretical XPD patterns by as much as a few degrees with respect to the actual θ values at which they will be observed.

A final step in any realistic calculation based upon this model is to integrate the direction of emission $\hat{k}$ over the solid angle Ω_0 accepted into the electron analyzer[62,63]. For most of the calculations reported here, this has been over a cone of ±3.0-3.5° half angle, although for certain cases a smaller cone of ±1.5° has been used.

There are several reasons, however, why the XPD effects predicted by such SSC calculations are from the outset expected to be larger in amplitude than those observed experimentally. (This is a common type of discrepancy in other diffraction calculations as well, as, for example, in LEED.) These have been discussed previously in connection wtih XPD[63], and are: (1) The actual surface may have irregularities on an atomic scale that are not included in the usually idealized model cluster. Also, adsorbates may exhibit more than one type of bonding site, especially if unobserved steps or dislocations are present on the surface to some degree. These effects will in general tend to average out XPD effects in experimental data relative to a highly ideal calculation. (2) The lack of a fully-converged cluster of atoms in the calculations would also tend to produce greater anisotropy, as atoms near the periphery of a larger cluster add so as to produce a nearly isotropic background. (3) The inclusion of spherical-wave character for nearest-neighbor scattering will qualitatively tend to reduce the scattering strength, at least in the forward direction. This effect has been quantitatively estimated in XPD calculations for C1s emission from molecular CO, where it appears to reduce the forward scattering diffraction peak by about 1/2 as measured with respect to the background intensity[77]*. (4) Vibrational effects, especially at a surface or for an adsorbate, may not be adequately described by simple Debye-Waller factors, and lead to enhanced supression of XPD features. (5) Multiple-scattering effects also may be present to some degree, and these would generally be expected to smear out some features. (6) The presence of a non-isotropic inelastic scattering mechanism (for example, associated with excitations of rather localized valence electrons) also could reduce the relative intensities of diffraction features. Such phenomena have been noted as a source of reduced diffraction effects in EXAFS back scattering, for example, although it appears that for forward scattering the optical theorem[78] will require an increase in $|f_j|$ due to inelastic processes[82]. Such effects need to be further investigated for forward scattering at the $\sim 10^3$ eV energies appropriate to XPS. The last four of these effects thus need to be explored in further theoretical treatments of XPD, but we shall show that the much simpler SSC model not incorporating them still seems to describe the observed experimental phenomena rather well.

As a final comment concerning the SSC model, we note that it can be directly reduced to an expression very close to that used in EXAFS analyses[72] if it is assumed that all scattered waves ϕ_j are small in magnitude in comparison to ϕ_0. Then, if we begin at Eq. (28) (for simplicity neglecting any averaging over $\hat{\epsilon}$), we see that all terms such as $\phi_j\phi_\ell^*$ and $\phi_j\phi_j^*$ can be neglected in expanding the absolute value squared. The thermal diffuse scattering term thus can also be neglected. After some simple algebra, it can then be shown that

$$I(\hat{k}) \propto (\hat{\epsilon}\cdot\hat{k})^2 e^{-2\gamma L} + 2(\hat{\epsilon}\cdot\hat{k})e^{-\gamma L}\sum_j \frac{\hat{\epsilon}\cdot\hat{r}_j}{r_j}|f_j(\theta_j)|W_j e^{-\gamma L_j} \times \cos(kr_j(1-\cos\theta_j) + \psi_j(\theta_j)). \quad (30)$$

This simplified form has in fact been used recently by Orders and Fadley in successfully describing several aspects of normal photoelectron diffraction data[83].

*This factor of approximately 0.4-0.5 for nearest-neighbor scattering has also been verified in recent much more detailed XPD spherical-wave calculations by Sagurton, Bullock, and Fadley(to be published).

In subsequent sections, we will consider several applications of this SSC model to the interpretation of XPD data, including especially several substrate- and adsorbate- systems of known geometry to test the degree of its validity.

C. Substrate emission

The first quantitative comparisons of theoretical and experimental XPD curves were for azimuthal scans above a Cu(001) surface[62,63]. Some of this data for $Cu2p_{3/2}$ emission is shown in Fig. 37 (cf. Fig. 27), and a more recent comparison using higher and lower angular resolutions has been presented in Fig. 31. Consider first the theoretical curves labelled "damping = 1.0" in Fig. 37, which represent non-adjusted SSC calculations according to Eq. (29), as do the theoretical curves of Fig. 31. It is clear from these figures that simple SSC calculations are capable of predicting the positions and approximate relative intensities of most of the features observed, even down to the very narrow peaks noted for $15° \lesssim \phi \lesssim 75°$ in Fig. 31. There are, to be sure, some minor discrepancies as to features, as for example, in Figure 37 where the local minimum in experiment is not present in theory for $\phi = 45°$ and $\theta = 10°$ and the maxima in experiment for $\phi = 90°$ and $\theta = 13°$, 15°, 18.4°, and 45° are local minima in theory. Also, the degree of anisotropy is overestimated by theory by a factor of $\sim$1.5-2.0, but this is not surprising in view of our prior discussion of the model.

The overall agreement between theory and experiment for Cu is improved somewhat by the empirical reduction of each scattering amplitude $|f_j|$ by a factor of 1/2[63]: such curves are denoted by "damping = 2.0" in Figure 37. Such an empirical reduction in $|f_j|$ might be justified in allowing for some or all of the last four factors discussed in the preceding section as being responsible for overestimates of anisotropy by theory,* but its magnitude has been rather arbitrarily chosen to optimize agreement, so that such adjustments will not generally be utilized in what follows and, if so, will be specifically indicated.

As more recent examples of such comparisons, we note that the closely-related crystal Ni(001) exhibits XPD azimuthal patterns very close to those of Cu(001), and somewhat better agreement with non-adjusted SSC calculations[84].

Also, Kono[85] has recently compared SSC calculations and experiment for polar scans above a LaB_6 crystal. Fig. 38 shows such a comparison for La4d emission, and it is clear that all main features are correctly predicted as to position and approximate relative intensity. (The experimental data here have not been corrected for a smooth-curve modulation due to the instrument response function.) Takahashi et al.[86] have also recently compared azimuthal XPD data for Ag3d

*Such empirical adjustments in $|f_j|$ by approximately 0.4-0.5x have also been found to improve agreement with experiment in more recent work (ref. 100 and Trehan and Fadley, to appear in Phys. Rev. B), and their principal origin in spherical-wave effects(ref. 77) has also been confirmed by Sagurton, Bullock, and Fadley(to be published).

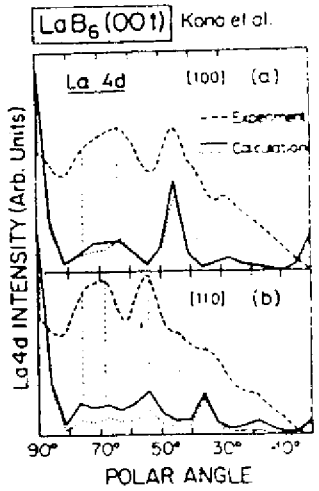

Fig. 38. Comparison of experiment and SSC theory for the polar dependence of La4d emission from LaB_6(001) along the [100] and [110] azimuths. The solid-curve theory includes both La and B atoms as scatterers; the dotted-curve theory includes only the much heavier La atoms as scatterers. No allowance for the instrument response function has been made in plotting the experimental data. (After Kono, ref. (85).)

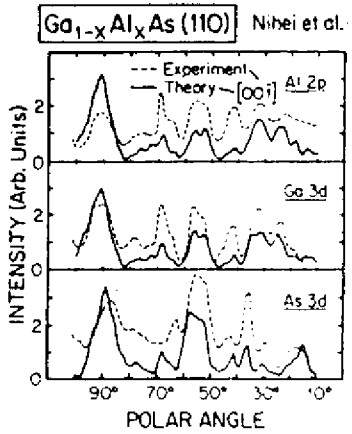

Fig. 39. Comparison of experiment and SSC theory for the polar dependence of Al2p, Ga3d, and As3d emission from $Ga_{1-x}Al_xAs$(110). (After Owari et al., ref. (87).)

emission from a Ag (110) crystal wtih SSC theory and found very good agreement for all major features.

As a final example, we show in Figure 39 a very recent comparison of SSC calculations and experimental results obtained by Nihei et al.[87] for polar scans of three core peaks in a crystal of $Ga_{1-x}Al_xAs$ ($x \lesssim 0.5$) with (110) orientation. The SSC model utilized was somewhat simplified from that discussed here. Again, almost all of the features are correctly predicted in position and relative intensity, with the sole exception being a shift of ~6° of two features for As3d in the range $50° \lesssim \theta \lesssim 70°$.

Overall, the test cases studied to date thus permit tentatively concluding that SSC calculations provide a very good description of the XPD effects associated with substrate core-level emission. The degree of agreement found is even somewhat surprising in view of the fact that emission along or near lines of atoms in the crystal might be expected to enhance the importance of multiple scattering effects. (Perhaps this is the reason for the slight featural disagreements seen in Fig. 31 near $\phi = 0°$ and 90°, as this corresponds to emission along <110> directions.) Comparing SSC calculations with experimental measurements thus should much increase the certainty of site-type determinations, such as those represented by Figs. 32 and 33. Anticipating the next sections on adsorbate emission, we also note that emission along lines of atoms is generally not possible, so that SSC results might be expected to better describe experiment in at least this respect.

In concluding on substrate emission, we also note an alternate description of such effects in terms of Kikuchi bands[2,6,65,88]. This emphasizes photoelectron diffraction from different sets of planes in the crystal as denoted by Miller indices (hkℓ), and each set is expected to have associated with it a band of enhanced intensity for photoelectron emission within plus or minus the Bragg angle $\theta_{hk\ell}$ of being parallel to these planes. If the interplanar spacing is $d_{hk\ell}$, then the Bragg angle is determined from

$$\lambda_e = 2d_{hk\ell} \sin \theta_{hk\ell} . \qquad (31)$$

One thus qualitatively expects peaks of intensity for emission along low-index directions in which several sets of planes intersect, as discussed previously. Maxima at $\sim\pm\theta_{hk\ell}$ away from the planes are also expected and such features are seen in both experiment and SSC theory in Fig. 31 for $\phi \lesssim 10°$, 80°. This model has been compared to experimental data both qualitatively[65] and quantitatively (using a simple superposition of independent (hkℓ) Kikuchi bands)[88,89], and found to provide a semi-quantitative zeroth-order description of substrate XPD. A more detailed comparison of the Kikuchi-band and SSC models appears elsewhere[88].

D. Emission from molecular adsorbates

Although the first adsorbate XPD was actually observed for an atomic adsorbate (O on Cu(001)[62,63]), it is heuristically useful to begin by considering two simple effects arising in small-molecule adsorption. These have both been studied for the system c(2x2)CO on Ni(001)[77,81].

(1) Intramolecular Scattering. Fig. 29 shows polar-scan experimental data for C1s emission from c(2x2)CO on Ni(001) for two different high-symmetry azimuthal orientations[62,80]. The C1s intensity has been normalized by dividing by the featureless O1s intensity to allow for the instrument response function, and a clear peak along the surface normal is found. A qualitative explanation of this in terms of intramolecular scattering is indicated in the inset of this figure. C1s photoelectrons are preferentially forward-scattered by the O atom in the same molecule so as to produce a constructive interference and therefore a peak in intensity directly along the C-O bond direction. This forward-scattering peak can also be termed a 0th order diffraction peak, as the scattering phase shift is very small (it is shown for simplicity to be zero in the schematic drawing). At larger angles away from the bond direction, 1st order diffraction effects might also be expected, but they cannot be resolved for certain in this data.

A more quantitative description of this data requires using the SSC model, as has been done in two prior studies[77,81]. Because the electron emission directions of interest are rather near the surface normal, the substrate Ni atoms or other CO molecules around a given emitter will be associated with scattering angles of $\gtrsim 90°$. Thus, it has been shown that they have a negligible influence on such intramolecular XPD and a two-atom cluster (a C emitter and an O scatterer) is sufficient. The other important parameters of the calculation are the tilt angle θ_t of the bond axis away from the surface normal and an rms vibrational amplitude θ_{rms} for a wagging or frustrated rotational motion of the CO. θ_{rms} is incorporated via a ground-state harmonic oscillator probability distribution, and is expected to be near 10° for CO on Ni(001) at ambient temperature.

Fig. 40 compares experiment and theory for $\theta_{rms} = 10°$ and various choices of θ_t. (Again, theory predicts $\lesssim 2$ times larger XPD effects than are observed and at least half of this overestimate has been shown to be neglect of curved-wave effects due to the short C-O distance[77].) An intensity maximum along the surface normal such as that observed experimentally is found in the SSC curves for all tilt angles $\lesssim 14°$. Considering further the FWHM of this 0th order peak is found to limit the tilt to $\theta_t \lesssim 10°$. This conclusion is also possible in the presence of greater degrees of vibrational motion[81].

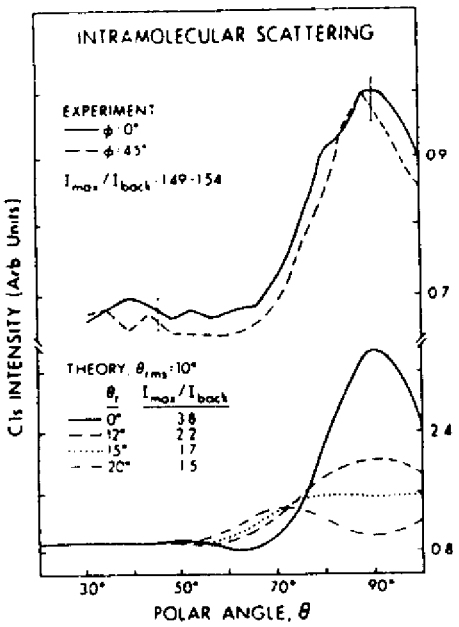

Fig. 40. Comparison of experiment and SSC theory for the polar dependence of Cls emission from c(2x2)CO on Ni(001). The calculations have been performed with a fixed root-mean-squared vibrational displacement of 10° and several tilt angles θ_t of the CO molecule relative to the Ni surface. The amplitudes of these intramolecular scattering phenomena are indicated here by the maximum-to-background ratio I_{max}/I_{back}. (From Orders and Fadley, ref. (81).)

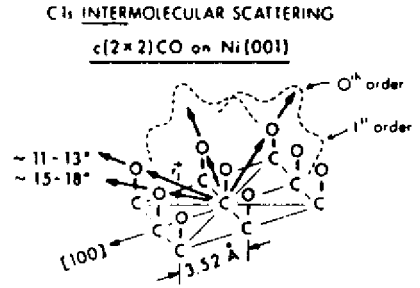

Fig. 41. Schematic illustration of the mechanism by which intermolecular scattering produces azimuthal anisotropy in Cls emission from c(2x2)CO on Ni(001). (From Orders and Fadley, ref. (81).)

Thus, this analysis permits rather straightforwardly determining the orientation of CO on this surface to within ~10°. It also suggests the general utility of such effects in studying the orientations of small molecules on surfaces, as the 0th order peak intensity in general follows the bond direction. All that is required is for an atom of reasonable scattering power (that is, of atomic number $\gtrsim$4-8) to lie between the emitting atom and the detector. Such intramolecular scattering effects thus provide a type of information very similar to that available from electron stimulated desorption ion angular distributions (ESDIAD)[90] and polarization-dependent core-level absorption edge structure measurements[91]. However, the theoretical picture in XPD seems both simpler and more clearly understood than either of these other two methods, and a synchrotron radiation source is not needed to carry out the XPD measurements, although it is for absorption edge studies.

(ii) Intermolecular scattering. A further type of XPD effect possible for an ordered overlayer of adsorbed molecules is illustrated for the case of c(2x2)CO on Ni(001) in Fig. 41. Cls emission is again considered, but in this case, for near-grazing emission directions for which scattering by O atoms in near-neighbor molecules along the surface is possible. Each O atom thus may generate both 0th order and 1st order XPD structure. For the expected C-O bond length, these effects are expected to occur for emission angles of ~10°-20° with respect to the surface. At lower angles, intermolecular scattering by C atoms in adjacent molecules also may be significant. The qualitative expectation is thus that azimuthal scans of Cls intensity should exhibit 0th order peaks at ϕ = 0°, 45°, 90°, ... (as measured from the [100] direction), with extra structure at intermediate angles possible due to 1st order effects.

Such intermolecular effects have been experimentally observed[81], as illustrated in Fig. 42 for scans at various polar angles. These data have been fourfold-averaged over a full 360° scan to reduce noise. As noted previously, the degree of mirror symmetry about ϕ = 45° can be used to judge the statistical accuracy of a given feature. Although low intensities make the statistical scatter of these measurements rather high, intermolecular scattering effects are clearly seen at the two lowest angles of θ = 7° and 11°, including 1st order peaks at ϕ positions of ~22° and ~68°. The overall anisotropies are ~15% for these low θ values, with rapidly decreasing values as θ is increased to a maximum of 18°. Also shown in Fig. 42 are SSC theoretical curves incorporating the effects of both types of adjacent CO molecules (that is, those at ϕ = 0° and 45°). Independent wagging vibrations of these molecules have also been included, with a θ_{rms} value of 10°.[81] Although theory again overestimates the degree of anisotropy, this time by ~4

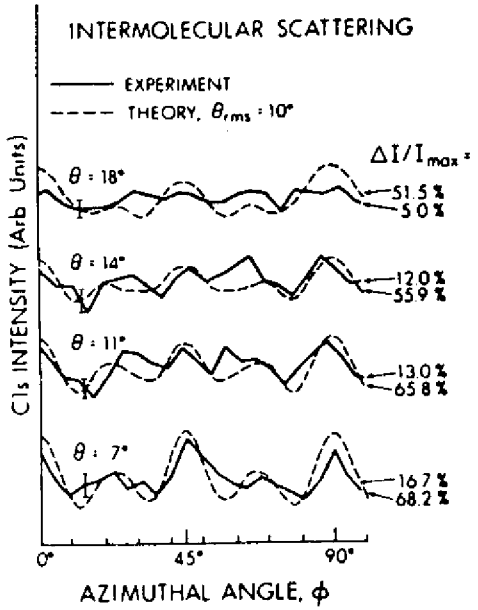

Fig. 42. Comparison of experiment and SSC theory for the azimuthal dependence of C1s emission from c(2x2)CO on Ni(001). The diffraction effects seen are due to intermolecular scattering (cf. Fig. 41). (From Orders and Fadley, ref. (81).)

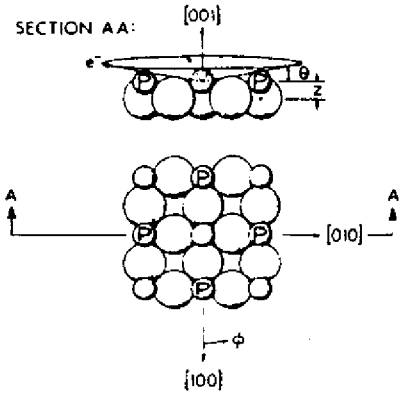

Fig. 43. General atomic geometry for c(2x2) and p(2x2) adsorbate overlayers on a [001] surface of an fcc metal, assuming that adsorption is in fourfold-hollow sites. In c(2x2), all sites are occupied; in p(2x2) only those denoted by "P".

times, the peak positions and approximate relative intensities agree very well with experiment, especially at the two lowest θ values. A more detailed discussion of these effects, including theoretical curves for varying degrees of vibrational motion, appears elsewhere.[81]

Thus, such intermolecular scattering effects should provide rather direct information on the short-range order in an adsorbate overlayer. This is by contrast with measurements such as LEED, for which long-range order over distances of $\sim 10^2$ Å is necessary for sharp patterns to be observed. Particularly with further developments in instrumentation to increase intensity, as well as angular precision and accuracy, such XPD effects thus should provide very useful surface structural information.

E. Emission from atomic adsorbates

We begin here by discussing several recent test cases designed to explore the angular sensitivity of x-ray photoelectron emission from core levels of atomic adsorbates, as well as to determine the degree to which the single scattering cluster model can be used to quantitatively describe such effects. Several practical applications to structural determinations are then discussed, together with estimates of structural sensitivity for different types of adsorption, and suggestions for improving the structural sensitivity. The use of polarized and energy-tunable synchrotron radiation for such XPD studies is also considered.

(i) Well-defined test cases. Fig. 30 makes it clear that XPD effects can be observed in emission from a core level of an atomic adsorbate, and furthermore that the resulting azimuthal patterns are very sensitive to the polar angle of emission. The discussions of the preceding two sections on substrate- and molecular adsorbate- emission also strongly suggest that a single scattering cluster model should be adequate for describing these effects. However, it is nonetheless necessary to test this idea by comparing experiment and SSC calculations for some well-defined adsorbate geometries. This has been done recently by Orders et al.[69] for c(2x2)S and c(2x2)Se on Ni(001). These overlayers have been studied previously by LEED and NPD and both consist of atomic adsorption in fourfold hollow sites, with S at a vertical distance of z = 1.30-1.35 Å above the first Ni layer[45] and Se at a distance of z = 1.55-1.60 Å; every other fourfold site is occupied, as illustrated in Fig. 43.

A series of azimuthal scans for S2p emission from c(2x2)S on Ni(001) at different polar angles θ between 7° and 17° are shown in Fig. 44 in comparison to SSC theoretical curves for z = 1.30 Å. Note that some of the θ steps here are only 1° in magnitude. Considering first only the dashed experimental curves, we

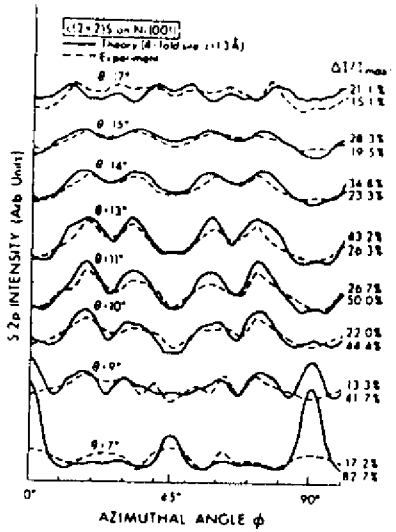

Fig. 44. Comparison of experiment and SSC theory for the azimuthal dependence of S2p emission from c(2x2)S on Ni(001) at eight closely-spaced polar angles. The theoretical calculations were performed for the generally accepted geometry of 4-fold S bonding at a vertical distance of z = 1.30Å (cf. Fig. 43). (From Connelly, ref. (33).)

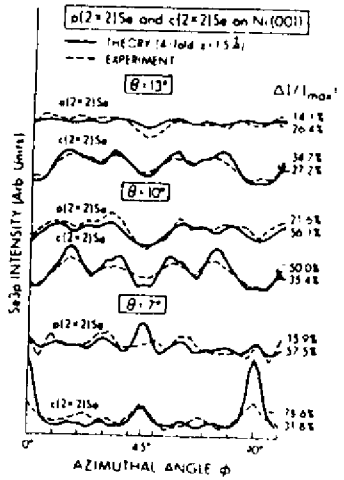

Fig. 45. Comparison of experiment and SSC theory for the azimuthal dependence of Se3p emission from p(2x2)Se and c(2x2)Se on Ni(001) at three different polar angles. The calculations were performed for the accepted geometry of 4-fold Se at z = 1.5Å. (From R. E. Connelly and R. C. White, unpublished results.)

see that the patterns change very much with θ, particularly in the range of ∿7°-11°. The expected mirror symmetry about φ = 45° is also seen in all of the experimental data, and provides strong confirmation of all of the features present in these curves. A comparison now of experiment with the SSC calculations shows that, with very few exceptions, all of the peak positions and relative intensities, and by implication thus also the changes in structure with θ, are correctly predicted by this simple model. As usual, theory predicts more anisotropy than experiment, here by ∿1.4-4.9 times, depending on the θ value. However, the only significant discrepancies as to features between experiment and theory are associated with the symmetry-identical peaks at φ = 0° and 90° for θ = 7° and 9° (and very slightly also for 10°); these peaks are predicted to be ∿2-3 times too high in theory for θ = 7°, and for this reason also persist as significant features at θ = 9° even though they are not observed experimentally. A consideration of the SSC calculations shows that, for low θ values $\lesssim$7°, the peaks at φ = 0°, 90° are produced by forward scattering or 0th order diffraction from nearest-neighbor S atoms to the emitter which are located along <100>-type directions (cf. Fig. 43). Similarly, the peak for very low θ values at φ = 45° is associated with forward scattering by next-nearest neighbor S atoms along <110>-type directions. One likely reason for overestimating the strength of nearest-neighbor scattering is that these SSC calculations assumed no refraction in scattering events from the adsorbate, thereby emphasizing smaller-angle adsorbate events too much in the final angular averaging. Also, for such close distances between emitter and scatterer, the use of the small-atom approximation may not be fully valid, and curved-wave corrections would thus be expected to effectively reduce the forward-scattering strength. It is also possible that surface non-idealities and microscopic roughness could become more important for very low takeoff angles (as discussed in another context in Sec. 3.C), and that both non-isotropic inelastic scattering and multiple scattering effects could be more important for this type of nearest-neighbor forward scattering. In any case, the overall agreement is very encouraging.

A similar comparison of experiment and SSC calculations has also been made for c(2x2)Se or Ni(001)[69], and it yields essentially identical conclusions. Some of this data is shown in Fig. 45, where the only significant discrepancies are again in the relative intensities of the φ = 0°, 90° peaks at θ = 7°, as well as in slight position shifts of ∿3-4° in the doublets for 10° $\lesssim$ φ $\lesssim$ 35° and 55° $\lesssim$ φ $\lesssim$ 80°. Overall, then, these two test cases thus provide further strong support for the quantitative utility of SSC in describing XPD from adsorbates. (Further experimental and theoretical studies aimed at explaining the few discrepancies noted are nonetheless desirable.)

(ii) Structural sensitivity and structural determinations. In addition to the test cases discussed in the prior section, adsorbate XPD measurements combined with SSC calculations have been used to study the atomic geometries of several more complex systems: c(2x2)O on Cu(001)[62,63], p(2x2)O and c(2x2)O on Ni(001)[92], and O on the stepped Cu surfaces (211) and (410)[80]. We begin by discussing the apparent structural sensitivities seen in some of these studies from both experimental and theoretical points of view.

As a first example of sensitivity to the type of overlayer structure present, Fig. 45 compares experimental and theoretical azimuthal scans from the well-defined overlayers c(2x2)Se on Ni(001) and p(2x2)Se on Ni(001). Considering experiment first, we see that there are major differences between c(2x2) and p(2x2) for all three polar angles shown. Thus, XPD is clearly very sensitive to this change in overlayer structure, albeit a rather large one. Again with only a few exceptions as to relative intensity, the theoretical curves very well predict the experimental curves for both overlayers; in fact, the only points of significant disagreement are for c(2x2)Se at $\theta = 7°$, and have been discussed in the last section. This comparison thus also lends further support to the applicability of the SSC model for describing XPD data.

In proceeding further to consider structural sensitivity, the adsorbate vertical position emerges as a critical parameter of interest. As a first illustration of how this can affect adsorbate XPD, we consider in Figs. 46 and 47 comparisons of experiment and theory at different z values for O1s emission from the expected fourfold hollow sites of c(2x2)O on Cu(001)[62,63]. (Although most of the theoretical curves shown are for $\beta \equiv$ damping = 2.0 and thus have had the $|f_j|$ values reduced by 1/2, their forms do not change significantly for $\beta = 1.0$, and thus none of the discussion below is altered with the use of unadjusted $|f_j|$'s.) Comparing experiment and theory here for z values above and below the atomic centers of the Ni surface plane at $z = 0.0$ Å shows that at $\theta = 10°$ the region of best agreement is for ~ -0.1 Å to +0.1 Å. For $\theta = 13°$, it would seem that 0.0 Å to -0.1 Å is the region of maximum agreement. Similar comparisons at a total of five θ values ultimately permitted Kono et al.[62,63] to propose that c(2x2)O is bonded in 4-fold hollow sites at a position that is co-planar with the surface Cu atoms to within $\sim \pm 0.1$ Å (that is, at $z = 0.0 \pm 0.1$ Å). Including the Cu atom immediately below the hollow, this yields a five-fold coordination for O with a Cu-O bond distance of 1.81 Å that is not very different from the 1.85 Å in the compound Cu_2O. Although no prior definitive determination of this structure has been made, very recent NPD measurements on this system are also at least partly consistent with a nearly in-plane adsorption[93], and previous LEED[94] and SIMS

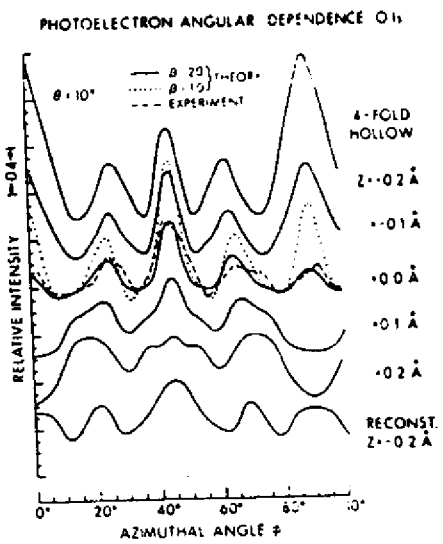

Fig. 46. Comparison of experiment and SSC theory for the azimuthal dependence of O1s emission from c(2x2)O on Cu(001) at $\theta = 10°$ and for different adsorption geometries. $\beta = 2.0$ has the same significance as damping = 2.0 in Fig. 37; $\beta = 1.0$ corresponds to damping = 1.0 or no adjustment of the $|f_j(\theta_j)|$ values. Experiment and theory are compared for five z positions of 4-fold bonding and for the empirically optimum value for a previously proposed reconstructed geometry. (From Kono et al., ref. (63).)

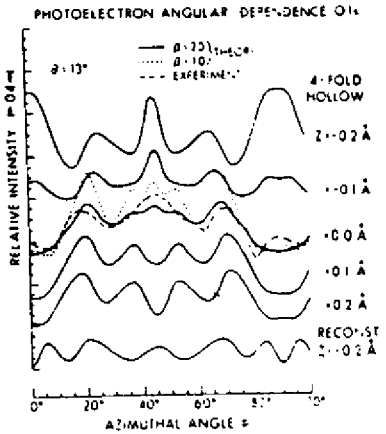

Fig. 47. As Fig. 46, but for $\theta = 13°$.

angular distribution[95] studies have also found this geometry to give one of the best fits to experiment.

A further indication of structural sensitivity is shown by the bottom curves in Figs. 46 and 47, which were calculated for another trial adsorption geometry: a reconstructed Cu surface in which O replaces every other Cu atom in the first layer. The z distance of -0.2 Å was chosen to optimally fit experiment at all θ values, but this fit is clearly very poor at θ = 13°, even though it is reasonable at θ = 10°. The reconstructed geometry thus could be ruled out. This illustrates both the necessity of using a rather full XPD data set at multiple polar angles and also the potential sensitivity of XPD to the bonding site type.

A similar XPD study of various O exposures on Ni(001) spanning the p(2x2) to c(2x2) transition in LEED[92,99] also permitted concluding that lower exposures involve fourfold O atoms at $z \lesssim 0.8 \pm 0.2$ Å, whereas at higher exposures, a considerable fraction of the fourfold O is nearly co-planar with Ni at $z = 0.1 \pm 0.2$ Å. This conclusion has subsequently been confirmed in high-resolution electron energy loss measurements on the same system[96], although it is at variance with recent NPD[97] and SEXAFS[98] measurements, which suggest above-plane adsorptions for both p(2x2) and c(2x2). Possible explanations for this apparent discrepancy are a variable degree of above-plane and co-planar mixing with different specimen preparation treatments, as well as an enhanced sensitivity of XPD to O in the co-planar sites where smaller-angle substrate scattering is possible[92].

However, the situation concerning vertical sensitivity is not quite as simple for all cases as that illustrated in Figs. 46 and 47. Fig. 48 shows a similar comparison of experiment and theory at different z values for c(2x2)S on Ni(001). Although significant changes in features occur with z for z values up to ~1.0 Å, beyond this point, the pattern is rather stable, with only very subtle changes in fine structure. Thus it would be difficult to conclude much more than $z \gtrsim 1.0$ Å by comparing experiment and theory for this case, and similar conclusions obtain for the other polar angles of emission in Fig. 44[99]. The same sorts of trends are seen also for c(2x2)Se on Ni(001)[99], and lead to the conclusion that vertical position sensitivity is lost if the adsorbate is too far above the surface plane.

The explanation of this lies straightforwardly in the forward-peaked nature of electron-atom scattering in XPS, and is illustrated schematically in Fig. 49. For low θ values and an adsorbate lying closer to the substrate surface, small-angle scattering is possible from both other adsorbate and substrate atoms. Since only substrate scattering can provide information on the adsorbate-substrate distances, a high z sensitivity of the order of ±0.1 Å results. On the other hand, when the adsorbate is too far above the surface ($\gtrsim$1.3 Å for O on Ni, $\gtrsim$1.0 Å for S on Ni, $\gtrsim$ 0.8 Å for Se on Ni, and $\gtrsim$0.7 Å for Te on Ni[99]), the scattering angles from the

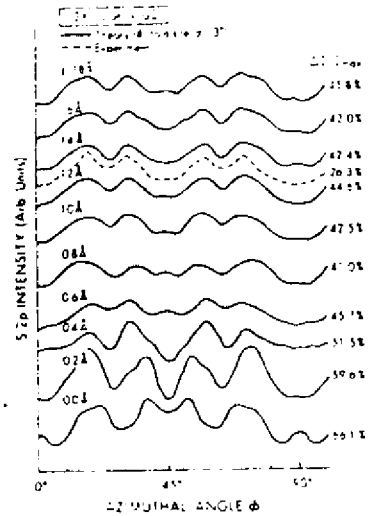

Fig. 48. As Fig. 47, but for c(2x2)S in 4-fold coordination on Ni(001) and a broader range of z values; θ = 1.0 for all curves. (From Connelly, ref. (33).)

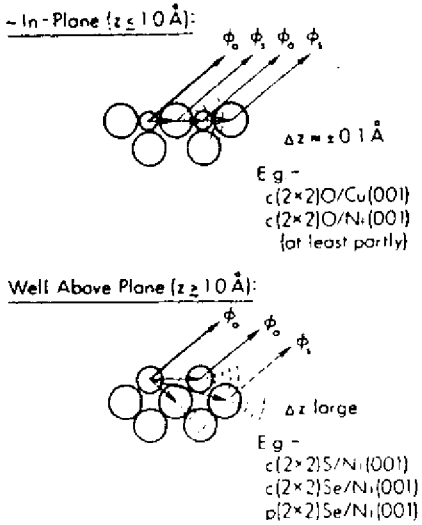

Fig. 49. Schematic explanation of the differing sensitivity of azimuthal XPD depending upon the height of the adsorbate above the substrate, with specific examples of each type of bonding indicated.

near-neighbor substrate atoms of most significance are too large to yield appreciable scattered waves ϕ_j, and the z sensitivity is very low. In fact, the XPD is predominantly produced by scattering in the two-dimensional adsorbate overlayer, as is found to be the case, e.g., for both S and Se on Ni(001). The inherent scattering strengths of the atoms involved also are important parameters here, and one can see a systematic trend through the chalcogenides in the values given above. Thus, a very low atomic number adsorbate on a very high atomic number substrate would tend to show more site type and z sensitivity at higher z values, and vice versa.

Thus, although there are to be sure a great many surface chemical problems for which adsorbed or reacting species will occupy sites at $z \lesssim 1.0$ Å with respect to the substrate surface and thus be amenable to high-precision study by XPD, the amount of information derivable for other problems involving greater z distances will be more limited. The question thus arises as to whether the method of carrying out such measurements can be changed in some way so as to improve z sensitivity, and two possible solutions seem promising. The simplest is to increase the angular resolution of the analyzer, so that more fine structure can be resolved in the XPD patterns. A theoretical simulation of this for c(2x2)S on Ni(001) is shown in Fig. 50, where curves for a cone of 3.0° half angle are compared to those for a cone of 1.5° half angle at various z values. Although the ±3.0° curves are essentially constant in form for $z > 1.2$ Å, those for ±1.5° continue to show changes in fine structure up to the rather high value of 1.8 Å. Thus, especially if a family of such azimuthal scans at high angular resolution and for various θ values were analyzed simultaneously, it should be possible to increase the sensitivity to both site type and z for higher z values. (On the negative side, however, would be the unavoidable intensity loss in increasing the angular resolution.)

A second possibility for improving z sensitivity is to use polarized synchrotron radiation and preferentially direct the primary photoelectron emission toward the substrate, as shown in Fig. 51. In so-called s polarization with the $\vec{\epsilon}$ vector lying in the plane of the surface, the maximum emission from a level exhibiting a typical XPS differential cross section will be toward the other adsorbate atoms, thus minimizing substrate scattering and lowering the z sensitivity. By contrast, in a p polarization geometry chosen to maximize the emission toward the substrate and minimize that toward the other adsorbate atoms and in the direct wave ϕ_0, the influence of the substrate should be markedly enhanced in the observed XPD. (Although to be sure a potential disadvantage of such a geometry is that the overall photoelectron intensity may also be markedly reduced.) As an illustration of the possible magnitudes of such polarization effects, Fig. 52 shows a

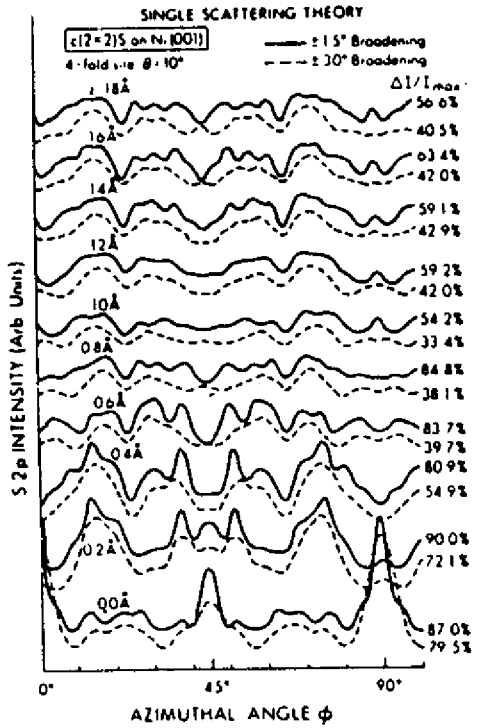

Fig. 50. The effect of reducing analyzer acceptance from ±3.0° to ±1.5° on azimuthal XPD. Theoretical SSC curves for the azimuthal dependence of S2p intensity from c(2x2)S on Ni(001) at $\theta = 10°$ are shown for the two angular acceptances and a range of 4-fold-coordinate z values from 0.0Å to 1.8Å. (From Connelly, ref. (33).)

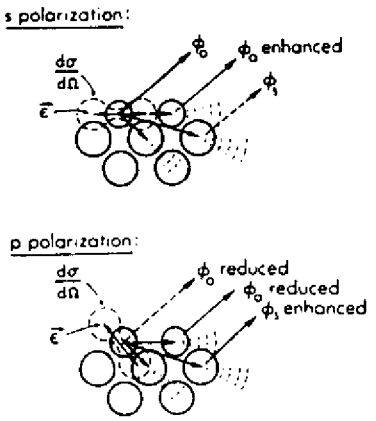

Fig. 51. Schematic explanation of how azimuthal XPD experiments in a p-polarized geometry would be expected to increase the sensitivity to adsorbate-substrate vertical displacement.

comparison of calculated XPD curves for c(2x2)S on Ni(001) with s- and p-polarization, and for various z values. The forms of these curves at $\theta = 10°$ (as well as at other angles not shown) are very much changed by the change in polarization, and the anisotropies for the p-polarized cases are larger by as much as a factor of 2. Recent experiments by our group at the Stanford Synchrotron Radiation Laboratory have confirmed this polarization sensitivity in XPD.[100] Also, although the curves for s polarization cease changing appreciably with z for $z \gtrsim 1.4$ Å in p polarization, changes in fine structure continue to occur all the way up to $z = 2.0$ Å. Thus, with increased angular resolution and/or the use of polarization variation, it appears that the high-z limitations on z sensitivity in XPD could be substantially improved.

As a further example of structural determinations using XPD, we briefly consider a recent study by Thompson and Fadley[80] of O adsorbed on the stepped Cu surfaces (211) and (410). Such surfaces are of considerable interest as controlled models of what may be the active sites on metal catalysts. As one illustration from this work, the (211) surface is found via LEED examination to reconstruct under oxygen exposure to the geometry shown in Fig. 53. It consists of a regular series of 5-atom terraces of (111) orientation and 2-atom step faces of (100) orientation. The most likely high-symmetry adsorption sites for atomic oxygen are also shown as A-C, and these can be further designated as A = 4-fold top, B = 4-fold bottom, and C = 3-fold. However, there is no prior evidence to suggest which of these sites will be occupied first, or whether a mixture of occupied sites may arise. Prior chemisorption studies on the separate low-index (111) and (100) faces do suggest however that (100) atoms should be much more reactive than (111) atoms, and it is also expected that atoms on or near step faces may exhibit higher reactivity as well.

It is thus of considerable interest to see whether oxygen adsorbed on this stepped surface exhibits any XPD features that are clearly influenced by the presence of the steps. A 5 Langmuir exposure to O_2 was found via an analysis of XPS core-peak intensities to yield a coverage equivalent to ~1 atom per high-symmetry site along the step face (or about 11% of a monolayer); this exposure also occurs at a distinct break in the curve of coverage vs. exposure for which the surface can be considered nearly saturated with O. Full 360° azimuthal scans of the O1s intensity for this system showed pronounced XPD effects, as illustrated in Fig. 54 for $\theta = 10°$. $\phi = 0°$ here corresponds to emission in an azimuth perpendicular to and away from the step faces. The reproducibility of features between the two halves of the scan (which should be mirror symmetric due to the presence of the steps) is also very good, especially for the most pronounced peaks between $\phi \gtrsim 60°$ and $\phi \gtrsim 140°$. Similar reproducibility was found for data obtained

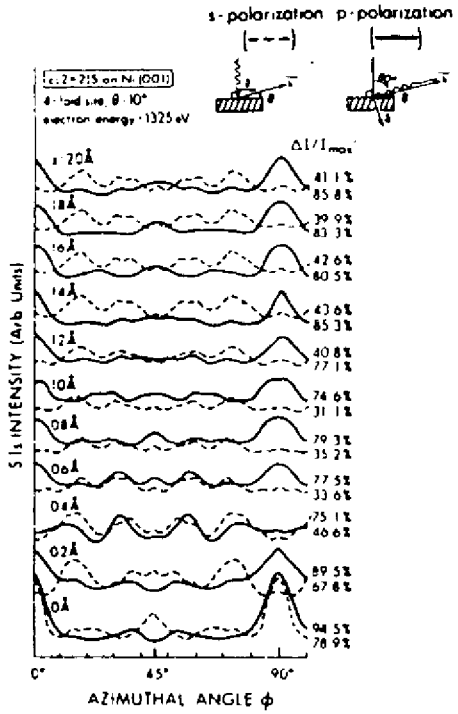

Fig. 52. The effect of changing from s- to p- polarization on azimuthal XPD. Theoretical curves for the azimuthal dependence of S2p intensity from c(2x2)S on Ni(001) at $\theta = 10°$ are shown for the two polarizations and a range of 4-fold-coordinate z values from 0.0Å to 2.0Å. (P. J. Orders and C. S. Fadley, unpublished results, plus new experimental and theoretical results in ref. 100.)

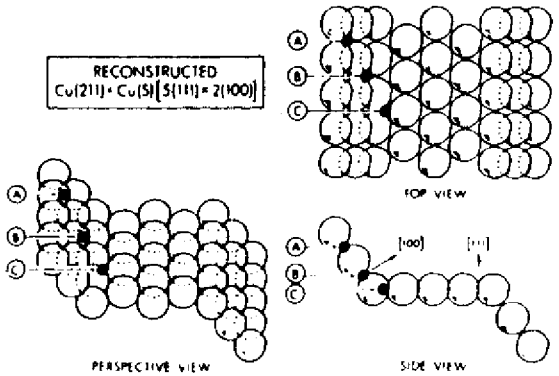

Fig. 53. Three views of a stepped Cu(211) surface as it is found to reconstruct under oxygen exposure. Included are the three possible high-symmetry coordination sites expected for oxygen bonding on or near the step faces: A = 4-fold top, B = 4-fold bottom, and C = 3-fold. (From Thompson, ref. (80).)

from (211) and (410) surfaces at different exposures.[80] In general, a mirror average of these two halves will give the best representation of the true XPD peaks, and that also is shown in Fig. 54. A full set of such mirror-averaged experimental data for six θ values between 7° and 23° is shown as dashed curves in Fig. 55, and it is clear that the diffraction features are very sensitive to polar angle as well. The anisotropies are as high as 31% for (211) and 40% for (410). The most reliable data range is for $10° \lesssim \theta \lesssim 20°$, as below this the count rates are much lower due to the instrument response function and possible residual roughness effects, and above it, the anisotropies are too low due to the large scattering angles required.

In order to next ask what the experimental data in Fig. 55 can tell us concerning the adsorption geometry, a series of SSC calculations was performed for various physically reasonable vertical positions z of oxygen in the different sites A, B and C of Fig. 53. Comparison of these theoretical curves with experiment showed that the B = 4-fold bottom site clearly gave the best fit to experiment, with A = 4-fold top being reasonably good as well, and C = 3-fold being very poor. Choosing the optimum z value for each site type proceeded via comparisons like Fig. 56 for the 4-fold bottom site at θ = 17°: it is clear here that a z distance of 0.4-0.6 Å above the centers of the Cu atoms in the step face gives the best fit to experiment. Overall use of all six θ values yields 0.6±0.2 Å as the best estimate, and the final theoretical curves for this value are summarized in Fig. 55. Although not all features are correctly predicted, especially as to relative intensity, the overall agreement in the structure-rich region for $\phi > 90°$ is very good, especially for the region $10° \lesssim \theta \lesssim 20°$ expected to be most reliable. The search and optimization procedure used thus strongly suggests a predominant 4-fold bottom adsorption site for this O exposure on Cu(211). A minority admixture of 4-fold top adsorption also is possible.

Having tentatively solved this structure it is also of interest to see whether any of the XPD features are capable of simple physical interpretation. In fact, the strong peaks seen near $\phi = 135°$ for $7° \leq \theta \leq 20°$ are all found to be due to forward scattering or 0th order diffraction from the two nearest-neighbor Cu atoms just above a B-site oxygen on the (100) step face (cf. Fig. 53). (The symmetry of the surface also dictates that similar peaks would arise in A-site emission as well, but they are found to be slightly shifted in position relative to experiment.) Also, the general dip in intensity seen at $\phi \gtrsim 100°$-120° is found to be due to enhanced inelastic scattering for emission through the step face at angles nearly parallel to it. The excellent agreement between experiment and theory for these simply explicable features thus further reinforces the 4-fold site assignment.

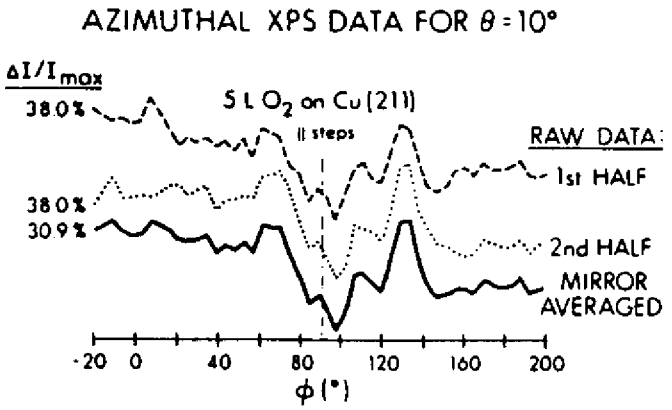

Fig. 54. Azimuthal XPD data for O1s emission from a 5L exposure of O_2 on a stepped Cu(211) surface. The mirror symmetry of the surface across a plane perpendicular to the steps is reflected in the excellent agreement between the two halves of the full 360° scan. The average of these two halves has been used for subsequent structural analysis. (Thompson, ref. (80).)

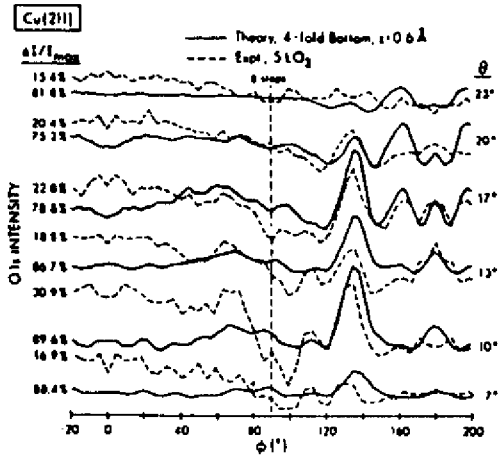

Fig. 55. Comparison of experiment and SSC theory for the data of Fig. 54, with experiment being shown here as dashed curves. The theoretical curves are for oxygen in all sites of type B in Fig. 53 and at a distance of 0.6Å above the first layer of Cu atoms on the step face; this geometry is found to optimize agreement with experiment.

It has thus been possible using this type of XPD analysis to tentatively suggest adsorption geometries for several exposures of O on Cu(211) and (410)[80]. More importantly, this work indicates that XPD may be able to provide unique structural information for this complex, yet chemically very important, class of surfaces about which rather little is known. Determination of adsorbate bonding geometries from LEED for such surfaces is a very difficult matter, for example, due to the much larger unit cells and relatively weaker substrate effects involved[101].

As a final and very recent example of the use of XPD in a surface-structural study, Kono and co-workers[102] investigated the $(\sqrt{3}\times\sqrt{3})$R30° Ag overlayer on Si(111). They see strong XPD features in azimuthal scans of Ag3d intensity, and have made use of kinematical theory to propose a new structure for this overlayer. (See below.)

F. XPD Measurements Using Synchrotron Radiation

We have already noted in the last section that the use of polarized synchrotron radiation may permit enhancing the sensitivity of XPD to adsorbate site type and vertical position, and preliminary experiments of this type have recently been performed[100]. A further interesting question is whether it would be advantageous to be able to tune the radiation energy so as to have photoelectron energies either below or above those fixed by the usual XPS sources of $h\nu$ = 1.2-1.5 keV.

Going to lower kinetic energies of say 200-500 eV would have the advantage of yielding scattering factors less strongly forward peaked, and therefore possibly more substrate sensitivity in azimuthal scans. Also, a useful degree of anisotropy might persist up to higher θ values, thus avoiding the need for extremely small-angle grazing emission with its attendant low intensity and possible surface roughness problems. Possible problems at lower energies, however, are the need for a more complicated theoretical model involving multiple scattering (MS) effects. Very complex MS calculations are, for example, clearly necessary in the very low energy (~30-100 eV) adsorbate core-level photoelectron diffraction studies pioneered by Smith, Woodruff, Norman and co-workers[103]. A partial answer to these questions has been obtained in recent measurements by Orders et al.[100] They obtained Sls azimuthal scans from the well-defined c(2x2)S overlayer on Ni(001), tuning the x-ray radiation so as to sweep the photoelectron energy from 230 eV to 900 eV. Some of this experimental data for θ = 10° is shown as solid curves in Fig. 57, and it is clear that the XPD effects are very sensitive to photoelectron kinetic energy. This directly suggests the alternate possibility of fixing θ at some convenient value and making φ scans for various hν values to build up a data set for structural determinations. Also shown in Fig. 57 are SSC curves for the known adsorbate geometry and the agreement between theory and experiment for all three energies is extremely good: all peaks are

Since the writing of this review, two additional aspects of XPD have been explored: (1) The use of near-neighbor forward scattering such as that in Figs. 40 and 41 in the analysis of epitaxial overlayer growth (W. F. Egelhoff, Phys. Rev., B30, 1052 (1984) - expt.; E. L. Bullock and C. S. Fadley, Phys. Rev., B31, 1212 (1985) - theory; and (2) The use of multiplet-split core levels to permit spin-polarized photoelectron diffraction studies of magnetic materials (B. Sinkovic and C. S. Fadley, Phys. Rev., B31, 4665 (1985) - theory; B. Sinkovic, B. Hermsmeier, and C. S. Fadley - expt., to be published, Phys. Rev. Lett. 55, 1227 (1985)).

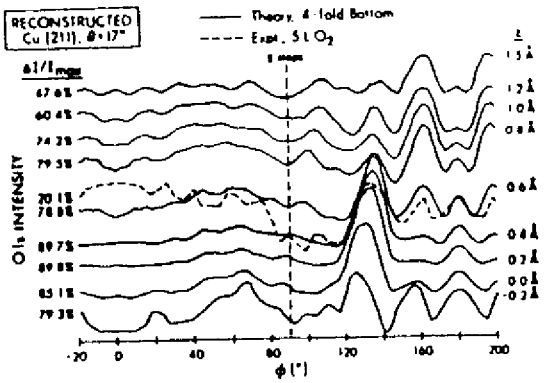

Fig. 56. Illustration of the sensitivity of the theoretical curves of Fig. 55 to the choice of z for the 4-fold bottom site. Calculations for different z values are compared to experiment for a θ = 17° emission angle.

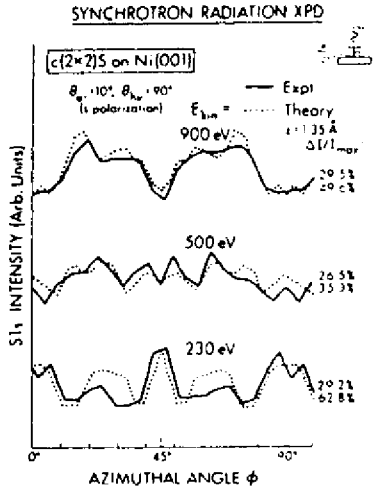

Fig. 57. Comparison of SSC theory to the results of the first azimuthal XPD experiments using synchrotron radiation for excitation. The system is again c(2x2)S on Ni(001), and photon energies have been chosen to yield electron kinetic energies of 900 eV, 500 eV, and 230 eV. The electron emission angle is θ = 10° and the radiation is s-polarized (Ē is parallel to the surface). (From Orders et al., ref. (100).)

correctly predicted as to position, and generally also as to relative intensity, although a few deviations as to the latter are seen, especially at the lowest energy of 230 eV. Thus, the SSC model definitely seems useful down to a few hundred eV in energy, making this region a potentially very fruitful one for future XPD studies. A more detailed account of this study is in preparation[100].

On the opposite end of the energy scale, would higher photoelectron energies of say 10,000 eV be of any advantage? Scattering factors would be more sharply forward peaked (cf. Fig. 35) and a single-scattering approach probably more likely to be highly accurate. However, on the negative side, the total scattering cross sections would be lower and effects thus smaller, and angles even closer to grazing would be needed to see significant substrate scattering. Also, the smaller deBroglie wavelengths would lead to very fine features in the XPD patterns perhaps difficult to resolve.

A recent theoretical study by Thompson and Fadley[80] used SSC calculations to compare typical XPD effects at 1000 eV with those at 10,000 eV. The cases chosen for study were polar-scan intramolecular scattering in a vertically-oriented CO molecule with differing degrees of wagging vibration, and grazing emission azimuthal scans from c(2x2)O on Cu(001) at two z positions: in-plane at z = 0.0 Å and above plane at z = 1.0 Å. Some of these results are summarized in Figs. 58 and 59. In Fig. 58, the sharper intramolecular peak in a polar scan for 10,000 eV and no vibration (θ_{rms} = 0°) could permit more precisely determining the molecular orientation relative to a surface, but adding in a reasonable amount of vibration (θ_{rms} = 10°) quickly leads to comparable FWHM's for both energies, and an even lower anisotropy $\Delta I/I_{max}$ for 10,000 eV. The negative effect of the lowered <u>total</u> scattering cross section at 10,000 eV is also seen in the larger relative importance of the unscattered waves. In Fig. 59, the overall anisotropy $\Delta I/I_{max}$ in an O1s azimuthal scan is shown as a function of the polar angle at which the scan is made. The two energies and two adsorbate vertical positions are shown separately. These curves make it clear that for either in-plane or above-plane adsorption, the degree of anisotropy falls off much more rapidly with θ for 10,000 eV electrons, and that angles $\lesssim$5-10° would be necessary to see significant effects. For θ $\gtrsim$ 10°, almost no anisotropy is seen at 10,000 eV. This is a direct result of the additional peaking in the scattering factors at higher energy. The effects of increasing energy on the detailed form of the azimuthal XPD patterns is also considered elsewhere in detail[80]. Overall, however, it can be concluded that increasing kinetic energy markedly from the present XPD regime of 10^3 eV does not seem to provide any significant advantages for XPD work, even though going to lower energies does seem promising in several respects.

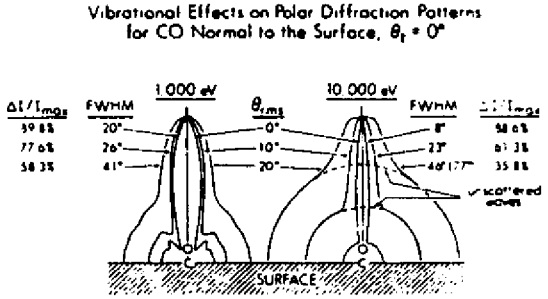

Fig. 58. Vibrational effects on C1s polar dependence in emission from CO oriented normal to a surface (θ_t = 0°) for two electron kinetic energies: 1,000 eV and 10,000 eV. Only the root-mean-squared angular displacement due to vibration is varied from 0° to 20°. (From Thompson, ref. (80).)

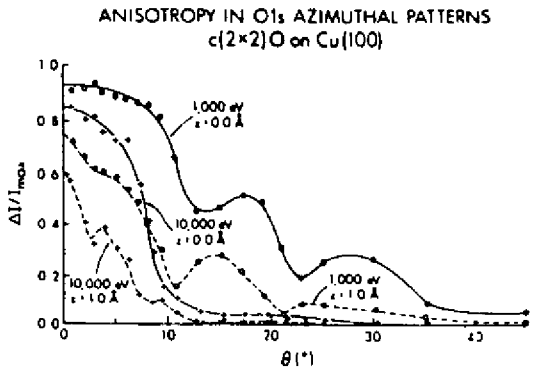

Fig. 59. Dependence of overall XPD anisotropy $\Delta I/I_{max}$ on emission angle θ, adsorbate z position, and electron kinetic energy for c(2x2)O on Cu(001). In general, increasing θ, moving the adsorbate from in-plane (z = 0.0Å) to above-plane (z = 1.0Å), or increasing energy from 1,000 eV to 10,000 eV tends to decrease the anisotropy. (From Thompson, ref. (80).)

G. Diffraction in core-level Auger emission

Inasmuch as Auger emission inevitably accompanies x-ray photoelectron excitation, and also can be produced very easily by other forms of bombardment, for example by electrons, it is of interest to ask whether similar kinds of Auger diffraction effects may arise in emission from a single crystal. For simplicity, we will concentrate on Auger energies in the 500-1500 eV XPS range and on transitions of the core-core-core type that are minimally influenced by chemical effects or valence-level complexities. (In fact, prior studies of the angular distributions of very low energy ($\lesssim$150 eV) core-valence-valence Auger electrons have proven to be rather difficult to interpret, even with the use of multiple-scattering theory[73,105].)

Fig. 28 due to Owari et al.[64] already contains some polar-scan substrate Auger data of this type for the Ge $L_3M_{4,5}M_{4,5}$ transition, which in this case has a kinetic energy of 1147 eV not very different from the Ge3d photoelectron peak at 1457 eV (the deBroglie wavelengths would have a ratio of 1.13, rather close to unity). Comparison of the observed XPD curves (a) and (b) for these two transitions reveals that they are very close in structure. Fig. 60 shows similar azimuthal-scan data due to Orders et al.[69] for adsorbate core-core-core Auger emission from c(2x2)Se on Ni(001). The Auger transition here is the same as that studied for Ge ($L_3M_{4,5}M_{4,5}$) and it has an energy of 1311 eV extremely close to the Se3p photoelectron peak at 1322 eV; the de Broglie wavelengths here are thus essentially identical. The five curves shown for different polar angles of emission are essentially identical for the Auger and photoelectron peaks. It thus seems clear that in the $\sim 10^3$ eV energy regime and for core-core-core transitions, the predominant source of such Auger anisotropies is final-state scattering and diffraction of exactly the same nature as that discussed in detail here for XPD. By implication, one would also thus expect a single-scattering theory to provide a reasonably good description of such Auger phenomena.

Because of the much different natures of the basic emission processes for photoelectrons and Auger electrons, it might at first sight seem difficult to understand why their overall diffraction effects should be essentially identical for emission at the same kinetic energy. This, however, is easily explained qualitatively in terms of the forward-peaked nature of the electron-atom scattering at these energies. That is, even though the basic Auger emission intensity will be essentially isotropic for a core-core-core transition, in contrast to the polarization-associated directionality of the photoelectron emission (cf. Fig. 34), in either case, it is only for initial emission rather close to the final observation direction $\hat{k}$ that the scattering can be significant enough to produce measureable diffraction effects. Thus, for most current XPS

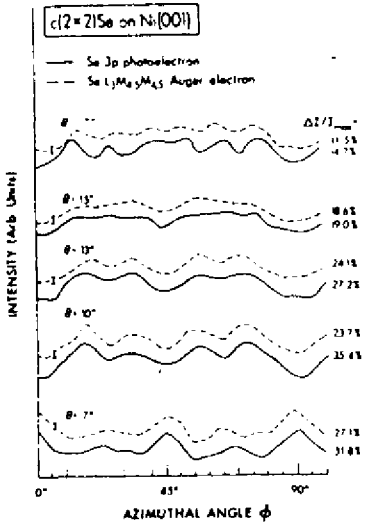

Fig. 60. Comparison of experimentally-observed diffraction effects in azimuthal scans of Se3p photoelectron- and Se$L_3M_{4,5}M_{4,5}$ Auger- emission from c(2x2)Se on Ni(001).

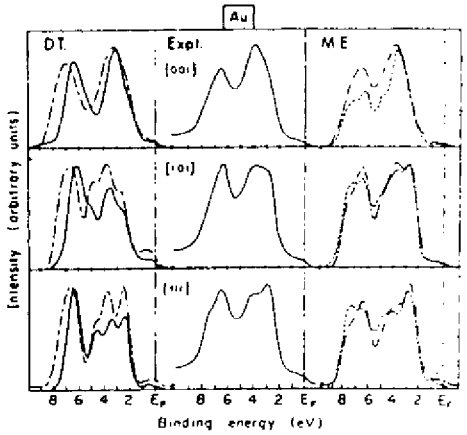

Fig. 61. Some early experimental and theoretical angle-resolved XPS valence spectra for single-crystal Au with electron emission along the [001], [101], and [111] directions. "D.T." represents calculations based upon the direct-transition model, and "M.E." calculations using the plane-wave matrix-element model. The two sets of theoretical curves in each case represent slightly different choices of the band structure used as a starting point (cf. refs. 6, 110, and 111).

experimental geometries, the variation of the primary emission intensity over the solid angle that is effective in producing the diffraction effects will be rather small; overall then, the XPD patterns should look very much like their isotropically-excited Auger counterparts, as is observed experimentally. However, for very special polarization geometries in XPS such as the p case shown in Fig. 51, one would expect the anisotropic character of the primary emission to be more important, and this should lead to inherent differences between photoelectron- and Auger- diffraction effects.

In any case, it is of considerable interest that Auger electrons exhibit effects completely analogous to those of XPD, and this suggests that future cross comparisons of the two types of data could be very useful in structure studies. The same sort of SSC model should also be valuable for interpreting Auger data, perhaps modified so as to assume isotropic initial emission simply by removing the $\hat{e}\cdot\hat{k}$ and $\hat{e}\cdot\hat{r}_j$ factors in Eq. (28).

H. Concluding remarks and comparison to other techniques

Overall then, XPD appears to have considerable potential as a surface structural tool, especially with expected improvements in angular resolution and intensity, as well as with the use of polarized, energy-tunable, synchrotron radiation for excitation. The fact that a very simple single scattering theory appears to describe these effects very well is also an advantage. Intra- and intermolecular scattering effects can provide very direct and simply interpretable information on adsorbate structures, and similarly simple through-bond scattering has also been observed for adsorption on stepped surfaces. Azimuthal-scan data can also be analyzed by comparison to single-scattering theory so as to derive geometries with accuracies that can be as high as ± 0.1 Å, although for adsorbates situated well above the substrate surface ($\gtrsim 1.0$ Å), further improvements will be needed to achieve high positional accuracy. Analogous Auger diffraction effects at comparable energies of $\sim$500-1500 eV may also be useful for structural studies.

A brief comparison to some other currently used surface structural techniques is also worthwhile here. LEED[41,42] is certainly the most used method to date, but the accumulation of accurate I-V data is a difficult task (certainly of the same order as an XPD experiment) and the final analysis must then proceed via very complex multiple-scattering calculations. Also, rather long-range order over a region of $\gtrsim$100 Å in diameter is needed to do LEED, whereas XPD should require only very short range order, or, for certain effects, no long-range order at all beyond that in the substrate. Reflection high-energy electron diffraction (RHEED) with energies of $\sim 10^4$ eV and grazing incidence angles of $\sim 5°$[104] is also a close relative of both LEED (in general experimental geometry) and XPD (in using rather high

energies). However, to date only preliminary attempts have been made at deriving quantitative structural information from RHEED[104], even though it is very generally useful in a qualitative sense.

Angle-resolved UPS of valence levels has been shown to provide very useful structural information as well[7-9], but this must often rely on a rather complex theoretical analysis of the valence states involved. This analysis may also have to include the detailed matrix elements involved in the photoemission process, although in certain cases, symmetry-based selection rules can be used to semi-quantitatively derive structural information. Angle-resolved UPS of core levels (often referred to as "PhD" for photoelectron diffraction) attempts to do the same thing as XPD, but at much lower energies where a more complex multiple-scattering theory must be used[104]; here again long-range order is not necessary. In general, synchrotron radiation is necessary to fully exploit either form of ARUPS.

Two other diffraction-based techniques requiring synchrotron radiation are normal photoelectron diffraction (NPD)[11,106] (and the closely-related off-normal photoelectron diffraction[107]), as well as surface EXAFS or SEXAFS[98,108]. Neither of these require long-range adsorbate order. Both involve scans of photon energy, but NPD is experimentally more difficult in requiring that a certain core photoelectron peak intensity be monitored accurately throughout this scan; thus the monochromator flux and electron analyzer acceptance must be measured carefully at each $h\nu$, and Auger peaks also may cause interferences at certain $h\nu$ values. By contrast, detection can be much simplified in SEXAFS. NPD seems to require multiple-scattering calculations for comparison to experiment in order to derive adsorbate structures. Prior suggestions of the possibility of Fourier transforming NPD data to more easily derive distance information[11,106] do not seem to be fully quantitatively justifiable or useful[83]. By contrast, Fourier transformations of SEXAFS data are routinely used, with accuracies of $\sim\pm 0.05$ Å appearing to be possible. Thus, although each of these electron-based techniques has certain unique aspects as far as information context, it is also clear that each has certain limitations and/or practical problems of execution.

The use of intramolecular scattering in XPD has already been compared to deriving analogous bond-orientation information from electron stimulated desorption (ESDIAD)[90] and core-level absorption edge structure measurements[91] in Section 5.c.

Finally, other surface structural techniques involving, for example, different types of ion scattering and x-ray scattering have been reviewed recently by Eisenberger and Feldman[109]. It is again clear that each of these techniques has its advantages and disadvantages.

Overall, XPD thus appears to provide various types of structural information that should well complement these other methods and be of general utility in surface science.

6. VALENCE-LEVEL EMISSION FROM SINGLE CRYSTALS

A. Introduction

As the last major subject, we turn to angle-resolved XPS spectra from the valence levels of single-crystals. It was first noted by Baird et al.[110] that such angle-resolved valence spectra for Au exhibited significant changes with emission direction, and some of these earliest experimental results are shown in Fig. 61. For electron emission along the three low-index directions [001], [101], and [111], the relative intensities of the two main 5d-band components vary considerably, and there are also noticeable changes in the fine structure within these components. Such angular sensitivity has subsequently been observed in a number of systems encompassing both transition metals and semiconductors, including Ag[111], Cu[112], Pt[113], Si[114], MoS_2,[115] GaSe[115], and W[116]. It is thus clear that there may be no simple connection of a given single-crystal valence band spectrum with something as straightforward as the non-directional total density of electronic states, even though angle-integrated or polycrystalline XPS studies have previously been shown to be capable of deriving density-of-states information[6]. However, the angular dependence of such spectra may provide much more detailed kinds of information concerning the electronic states, and it is toward this end that two rather simple limiting theoretical models have been developed for interpreting such effects. Although much more general treatments of the photoemission process have been presented by several authors[117-119], these have not been applied to XPS in a quantitative way, and in fact, the higher energy of excitation (vis a vis UPS) makes certain simplifications readily possible. These two simplified models are introduced briefly below, and their likely limitations and domains of applicability are discussed. Comparisons of theory with illustrative experimental spectra are then given.

B. Simple theoretical models

(i) Introduction. A detailed treatment of angle-resolved XPS valence emission would require accurate wave functions for both the initial state and the final state, which involves a photoelectron at $\sim 10^3$ eV. Matrix elements between these two would then have to be evaluated. Although very accurate and complete methods for doing this have been discussed[117-119], it is convenient and adequate in discussing ARXPS to use as a starting point the simple one-electron, three-step model of photoemission. This model predicts the kinetic energy distribution just outside the surface to be given by:

$$N(E_{kin}) = N(E^f - V_o) = N(E^i + h\nu - V_o)$$
$$\propto \sum_{\substack{\text{Occ.}\\ \text{Bands}}} \int |\langle \phi_{\vec{k}^f}(E^f = E^i + h\nu)|\vec{A}\cdot\vec{\nabla}|\phi_{\vec{k}^i}(E^i)\rangle|^2 F(E^i) T(E^f, \vec{k}^f)$$
$$\times\, \delta(\vec{k}^f - \vec{k}^i - \vec{g} - \vec{k}_{h\nu})\, d^3k^i \ ,$$

where E^f is the final energy of the excitation as measured inside the crystal, E^i is the initial energy from which excitation occurs, $\phi_{\vec{k}^f}$ is a final-state one-electron function corresponding to wave vector $\vec{k}^f$ and energy E^f, $\phi_{\vec{k}^i}$ is the initial-state one-electron function, $\vec{A}\cdot\vec{\nabla}$ is the relevant operator for the radiation, F(E) is the Fermi function ($\lesssim 1.0$ for $E<E_{Fermi}$ and $\lesssim 0$ for $E>E_{Fermi}$) and T is an escape function that could allow for inelastic scattering effects and internal reflection at the potential barrier V_o. Energy conservation is implied in setting $E^f = E^i + h\nu$. In XPS, the energies and mean free paths are high enough to assume that emission involves pure bulk states and to set T = 1.0 for all but grazing angles of emission (cf. Figs. 5 and 14). The sum is over all occupied bands and the integral over all initial wave vectors $\vec{k}^i$ inside the reduced Brillouin zone. The initial-state band-structure can thus be denoted $E^i(\vec{k}^i)$. The relevant one electron functions are assumed to be Bloch functions due to the full translational periodicity assumed for the crystal, so that the evaluation of the $\vec{A}\cdot\vec{\nabla}$ matrix directly results in a wave-vector conservation relation implied by the delta function:

$$\vec{k}^f = \vec{k}^i + \vec{g} + \vec{k}_{h\nu} \ . \qquad (33)$$

Here $\vec{k}^f$ is the final-state wave vector expressed in an extended zone scheme, $\vec{k}^i$ is the initial-state wave vector expressed in a reduced-zone scheme, $\vec{g}$ is a unique bulk reciprocal lattice vector connecting the two, and $\vec{k}_{h\nu}$ is the wave vector associated with the radiation. In general, $|\vec{k}_{h\nu}| = 2\pi/(\text{radiation wavelength})$. $\vec{k}_{h\nu}$ can be neglected with respect to reduced-zone dimensions in experiments at uv energies, but it cannot be in typical XPS measurements, as will be illustrated below for a specific example. Transitions satisfying Eq. (33) are termed direct transitions or wave-vector conserving transitions. Eqs. (32) and (33) thus implicitly assume long-range order, neglect surface effects except as a potential barrier which may produce refraction at lower takeoff angles, and do not include any consideration of vibrational effects (which can be considered to be the introduction of a type of positional disorder).

At very high energies of excitation such as those in XPS, a further approximation that seems reasonable is to assume a free-electron final state inside the crystal with momentum

$$\vec{p}^{\,f} = \hbar\vec{k}^{\,f} \tag{34}$$

and energy

$$E^f = E^i + h\nu = \frac{\hbar^2(k^f)^2}{2m} \tag{35}$$

The observed photoelectron just outside the surface would then have a momentum

$$\vec{p}^{\,f} = \hbar\vec{K}^{\,f} \tag{36}$$

and energy

$$E_{kin} = E^f - V_o = \frac{\hbar^2(K^f)^2}{2m} \quad , \tag{37}$$

with $\vec{K}^f$ being most simply related to $\vec{k}^f$ by refraction at the surface barrier V_o, as discussed previously in Sec. 3.C. An angle-resolved measurement of E_{kin} and the direction of emission thus determines $\vec{K}^f$, and, if V_o is known, $\vec{K}^f$ can then be used to derive $\vec{k}^f$ inside the crystal.

A further point first made by Shevchik[120] is that vibrational effects can effectively weaken the wave-vector conservation requirement in XPS and introduce a degree of averaging over the entire Brillouin zone such that all $\vec{k}^i$ points can be excited for all emission directions $\vec{k}^f \rightarrow \vec{K}^f$. Such phonon-induced non-direct transitions thus can be described in terms of Eq. (32) simply by removing the delta function so that the integral on $\vec{k}^i$ now can have non-zero contributions for all possible $\vec{k}^i$ values. Let us call this zone-averaged non-direct transition component of emission $N_{NDT}(E_{kin})$ and the direct-transition component as given by Eq. (32) without modification $N_{DT}(E_{kin})$. Since a direct transition can be viewed as a diffraction process, the observed strength of N_{DT} is furthermore reduced by vibrational effects according to a bulk temperature-dependent Debye-Waller factor W(T) as given by Eq. (27): the relevant $\Delta\vec{k}$ is here the reciprocal lattice vector $\vec{g}$. Then finally the total spectrum can be written as:

$$N_{tot}(E_{kin},T) = W(T)N_{DT}(E_{kin}) + [1-W(T)]N_{NDT}(E_{kin}) \quad , \tag{38}$$

from which it is clear that the Debye-Waller factor represents the fraction of transitions that are direct. Shevchik pointed out that the $\vec{g}$ vectors involved in XPS are sufficiently large that Debye-Waller factors of ~0.05-0.10 are not uncommon at room temperature, and thus that direct transitions might be very difficult to observe. Experiments with temperature variation also clearly may involve changes in the relative importances of the two component N_{DT} and N_{NDT}.

With this general background, we now discuss the two limiting models.

(ii) The direct-transition model. This model emphasizes the component N_{DT} of Eq. (38) (as calculated from Eq. (32)), and was first proposed by Baird, Wagner, and Fadley for interpreting angle-resolved XPS spectra[110]. Rigorous wave-vector conservation according to Eq. (33) is required for a transition to be allowed. The matrix elements $\langle\phi_{\vec{k}}^f|\vec{A}\cdot\vec{\nabla}|\phi_{\vec{k}}^i\rangle$ in Eq. (32) are also assumed to be constant for all allowed transitions, so that each transition is equally weighted in summing and integrating over the band structure $E_i(\vec{k}_i)$. The free-electron dispersion relation of Eq. (35) is also assumed, so that with Eq. (37) and perhaps an allowance for refraction at the surface, the observed energy and wave vector can finally be calculated. As noted previously in XPS, such refraction corrections will only be important for very low take-off angles $\lesssim 10°$, but in applying this same model at lower energies of ~40-160 eV they have been shown to become more important[121,122].

To illustrate the nature of $\vec{k}$ conservation for a typical XPS transition, Fig. 62 shows a scale drawing in $\vec{k}$ space of a possible direct transition in W involving photoelectron emission nearly along the [010] direction. The Brillouin zone radius is approximately $2\pi/a$, where a is the W lattice constant. MgKα radiation is assumed for excitation, leading to k^f values via Eq. (35) that range from $9.18(2\pi/a)$ for emission from the bottom of the 5d bands to $9.20(2\pi/a)$ for emission from the Fermi energy. Thus, the magnitude of $\vec{k}^f$ in XPS is very nearly constant over the full spectrum as judged against the Brillouin zone dimension within which $\vec{k}^i$ is eventually to be located, although this is not true in UPS. The finite solid angle cone of observation of the electron analyzer further distributes the observed $\vec{k}^f$ values over a disc-like region in $\vec{k}$-space: in Fig. 62, this is taken for illustration to be a cone of 1.5° half angle. $\vec{k}_{h\nu}$ will in this case be $0.32(2\pi/a)$ and thus clearly non-negligible with respect to Brillouin zone dimensions. Thus, its effect on wave vector conservation must be included. The effect of $\vec{k}_{h\nu}$ can be allowed for by shifting all points on the $\vec{k}^f$ disc of the observation cone by $-\vec{k}_{h\nu}$ as shown in Fig. 62. For an assumed angle of 48° between x-ray incidence and electron exit (a characteristic of the spectrometer geometry), this yields the right-hand shaded disc. This disc can then be projected back via one or more $\vec{g}$ vectors to yield $\vec{k}^i$ points within the zone from which emission can occur. The emission geometry here has been arbitrarily chosen so that the $\vec{k}^i$ set is centered along the x axis or [010] direction, and is shown as the left-hand shaded disc. Thus, the large value of $\vec{k}^f$ in XPS produces some degree of averaging in $\vec{k}^i$ via the finite disc sizes involved; in UPS by contrast very little averaging is produced by this effect. Also, this finite size in XPS may make it necessary to use different $\vec{g}$ vectors for different regions of the disc. Thus, this model finally predicts that an angle-resolved N_{DT} spectrum will be proportional to the

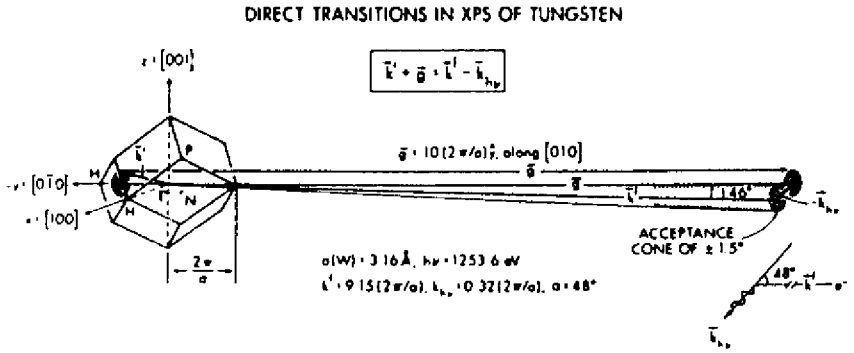

Fig. 62. Scale drawing in $\vec{k}$-space of the direct transitions that would be allowed for electron emission very nearly along the [010] direction from a W single crystal. An angle α of 48° between photon incidence and electron exit is assumed, together with an analyzer acceptance of ±1.5°. MgKα is used for excitation. The emission angle has been chosen so that $\vec{k}^f - \vec{k}_{h\nu} = \vec{k}^i + \vec{g}$ lies exactly along the [010] direction. The angular shift between $\vec{k}^f$ and $\vec{k}^f - \vec{k}_{h\nu}$ is 1.46°, as indicated. Those $\vec{k}^i$ values from which emission could occur will lie on the shaded disc inside of the Brillouin zone at left; the center of this disc lies −5/8 of the way from Γ to H along the [0$\bar{1}$0] direction.

density of electronic states as computed over the allowed $\vec{k}^i$ region or disc, a quantity much different from the total density of states.

This direct-transition model was first shown to successfully describe normal emission angle-resolved UPS spectra from Cu at the lower energies of $40 \lesssim h\nu \lesssim 200$ eV by Wagner et al.[123], and it has subsequently also been used to map band structures of metals[121-125] and semiconductors[126] in both normal-[124,125] and off-normal[121,122,126] emission (where refraction may become important). Its utility in describing XPS spectra we discuss in the next section, but it is important to note that a Debye-Waller factor of too small magnitude would make direct-transition effects very difficult to see. In fact, for the example of Au in Fig. 61 at room temperature, W = 0.04, so that direct transition effects would certainly be very weak at that temperature; cooling Au to 4°K would by contrast yield approximately 65% direct transitions in Eq. (38).

(iii) The plane-wave matrix-element model. The second approach was first discussed in connection with XPS by McFeely et al.[111] Although Eq. (32) is again used as a starting point, it is here assumed that $\vec{k}$ conservation is somehow not an important selection rule, or equivalently that all $\vec{k}^i$ values in the zone can contribute to emission in a given $\vec{k}^f$ direction. The most likely source of this full $\vec{k}^i$ averaging is vibrational effects, as pointed out by Shevchik[120], but it was also originally suggested that final-state complexities due to electron scattering might cause such averaging as well[111]. In this limit of complete zone averaging, only the matrix elements of Eq. (32) remain as weighting factors of all of the occupied initial states to produce variations in spectra with direction. These matrix elements are further assumed to be calculable by using plane-wave or free-electron final states of the form $\phi_{\vec{k}^f}(\vec{r}) = \exp(i\vec{k}^f\cdot\vec{r})$, and tight-binding or LCAO initial states. The matrix elements then can be shown to have the form of linear combinations of Fourier transforms of atomic orbitals. There is also a further simplification in that the angular shape of the orbital in real space (for example, p_x or $d_{x^2-y^2}$) is preserved in the Fourier transform in $\vec{k}^f$ space (for example, a p_x orbital shows preferred emission along ±x, and a $d_{x^2-y^2}$ orbital along ±x,±y). Thus, information concerning the atomic-orbital makeup of a given set of levels is in principle derivable by analyzing the directionality of emission.

This plane-wave matrix-element model would not be expected to be useful at low energies where direct transitions are generally more important, and moreover the final states are expected to be much more complex than plane waves. In fact, the use of such matrix elements in Eq. (32) in an attempt to improve upon

direct-transition model calculations for Cu at ∿40-200 eV was found to markedly decrease agreement with experiment[123].

C. Comparisons of experiment and theory

Fig. 61 shows results of some of the earliest XPS studies of this type and compares XPS spectra for Au with emission along [001], [101], and [111] with theoretical curves generated by both the direct-transition (DT) and plane-wave matrix-element (ME) models[6,110,111]. Although the DT model predicts more change than is seen experimentally, both models qualitatively agree with the spectral variations seen experimentally. However, as already pointed out, the Debye-Waller factor for this case is only 0.04, so that the DT model is not appropriate for this particular case and its agreement with experiment must be viewed as fortuitous. However, Sayers and McFeely[127] and Goldberg et al.[25] have subsequently made more accurate matrix-element calculations relevant to zone-averaged tight-binding matrix-elements and they conclude that much of the ME agreement in Fig. 61 is fortuitious as well. Ley et al.[115] have however, been able to use this model in describing changes in angle-resolved XPS spectra from MoS_2, $GaSe_2$, and $SnSe_2$. Thus, it remains to fully resolve the degree to which the plane-wave matrix-element model can be used in XPS for systems where full zone averaging is expected.

A final important question is thus whether direct transitions can be observed at all in XPS, but this has been unambiguously resolved in the affirmative with recent studies by Hussain and co-workers[10,116]. The tungsten system chosen for study has an especially high Debye-Waller factor at room temperature: W = 0.55 at 300K. Thus ∿55% of the transitions at this temperature ought to be direct, and angle scans might be expected to produce spectral variations predictable by the direct-transition model. Also, raising the temperature would be expected according to Eq. (38) to reduce the effect of direct transitions, leading to more importance of zone-averaged matrix elements via N_{NDT}; thus, any significant change in spectra with temperature would be suggestive of direct transitions.

Fig. 63 shows a room-temperature azimuthal scan of W valence spectra at a polar angle of $\theta = 63.4°$ with respect to the (001)-oriented crystal surface; the azimuthal steps were 5°. The solid-curve experimental spectra show marked changes with angle, particularly as to the relative intensities of the components labelled 1-3. Component 1 at ∿4.8 eV below E_F in particular is very strong at $\phi = 0°$ and 45°, and very weak at $\phi \gtrsim 15°$. The dashed curves in the figure are based on the direct-transition model and make use of Eq. (38) with N_{NDT} taken to be the total density of states for W as a reasonable first approximation to this quantity that

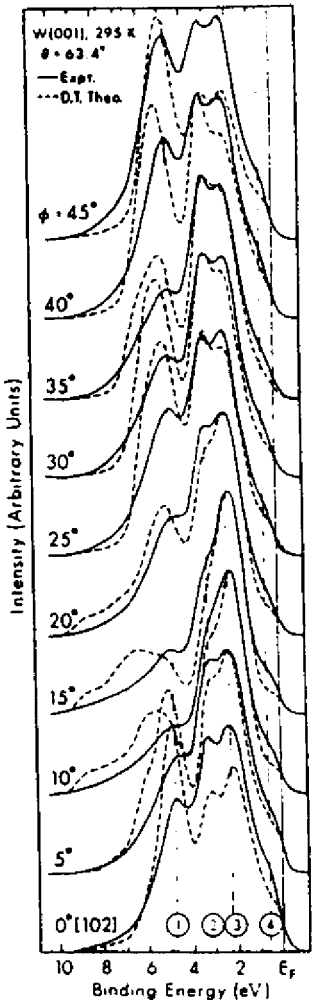

Fig. 63. Tungsten XPS valence-band spectra at T = 295°K for a 5°-step azimuthal scan from $\phi = 0°$ to 45° and a polar angle of 63.4°. Experimental curves (solid lines) are compared to theoretical curves (dashed lines) as calculated using Eq. (38), with $I_{NDT}(E)$ assumed to be proportional to the total density of states. (From Hussain et al., ref. (116).)

is in any case not expected to change rapidly with direction. Even though this theory thus totally neglects matrix element effects in both N_{DT} and N_{NDT}, it correctly predicts all of the trends in relative intensity change found experimentally, including for example, the marked drop in importance of the 4.8 eV peak at $\phi \gtrsim 15°$. As a more quantitative indicator of the peak intensity changes with ϕ, Fig. 64 shows the ratio of the 4.8 eV peak to that at 2.3 eV for the azimuthal scan of Fig. 63 and another at θ=33°. Here again all of the experimental features are predicted by the direct-transition model, even if somewhat more dramatically than is actually observed. Some of the small discrepancies remaining are no doubt due to the neglect of matrix elements in the model. Similar agreement is found also for peak intensity ratios from polar scans of spectra[116].

A further important observation made in this work[116] is that the photon wave vector clearly influences the wave vector conservation in the manner expected. Fig. 65 overlays a pair of 2°-step symmetry-related polar scans around the [102] and [201] directions, and these would be superimposable with the [102] spectrum over that at [201] if $\vec{k}_{h\nu}$ were not significant. Including the effect of $\vec{k}_{h\nu}$ (as shown in the figure insets) produces a 4.0° shift in matching the two scans. This shift, together with a 0.6° refraction correction, yields an overall value of 4.6° in very good agreement with the 6.0° empirical shift needed to make the spectra optimally agree with one another. Without such a shift, the agreement is very poor, for example, the [102] and [201] spectra are very different.

The pronounced temperature dependence of W valence spectra also supports the presence of direct transitions in W near room temperature[116], as is shown in Fig. 66. Here, spectra obtained at two azimuths that are 6° apart for θ = 33° are shown as a function of temperature. At 295 K with a Debye-Waller factor of 0.55, the two spectra are very different, particularly as regards the 4.8 eV component, but they become essentially identical at 1000K where the Debye-Waller factor is down to 0.14. The marked difference at 295K suggests direct transitions, as zone-averaged matrix elements by themselves would not be expected to alter intensities that rapidly with ϕ. Conversely, the near identity of the spectra at 1000K is thus attributed to the slow variation of the now dominant zone-averaged matrix elements with direction.

Such temperature-dependent data can also be used to decompose spectra into their N_{DT} and N_{NDT} components[116], as Eq. (38) indicates that measurements of N_{tot} at any two temperatures, together with calculated W values at those temperatures, can be used to solve for N_{DT} and N_{NDT}. This is found to yield self-consistent decompositions into components for various spectra and various pairs of temperatures, as shown in Fig. 67. The direct-transition components so isolated

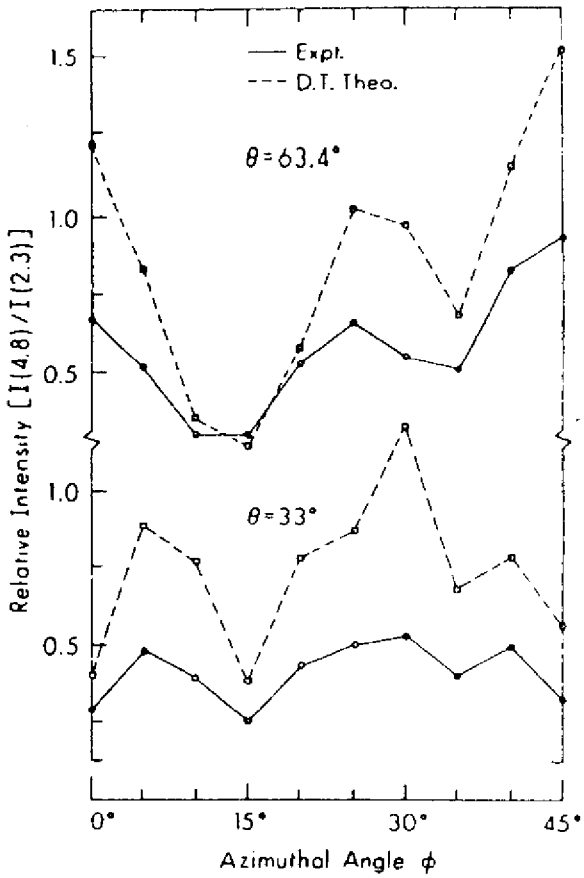

Fig. 64. Azimuthal dependence at T = 295°K of the relative intensity of the W valence-band peak at − 4.8 eV (cf. Fig. 63). The intensity of this peak is measured with respect to that at − 2.3 eV, and results are shown for polar angles of both 63.4° and 33°. Both experimental and direct-transition theoretical curves are shown. (From Hussain et al., ref. (116).)

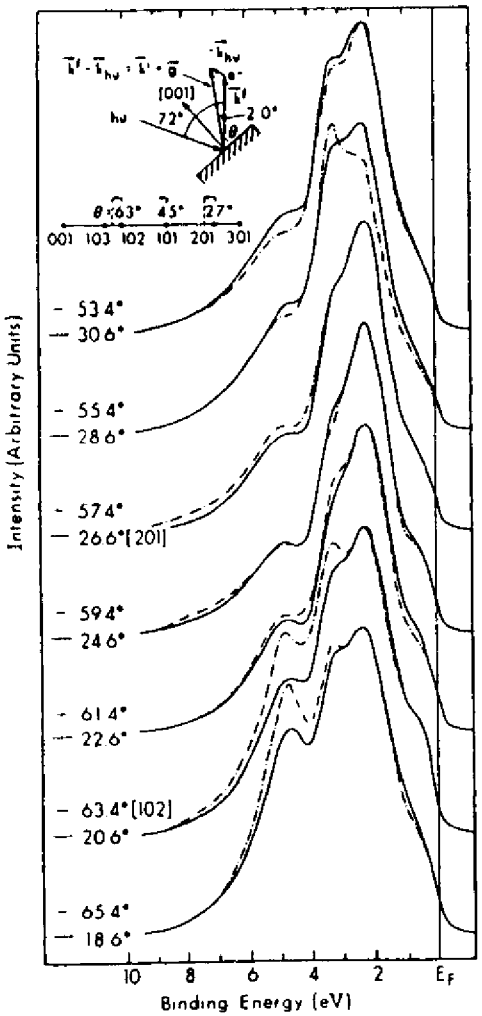

Fig. 65. Effect of photon wave vector $\vec{k}_{h\nu}$ on wave vector conservation in W valence-band emission at T = 295°K. A shift of 6.0° is needed in order to match spectra obtained at $\phi = 0°$ and various θ values near the symmetry-equivalent [201] and [102] directions; most of this shift is due to $\vec{k}_{h\nu}$, as explained in the insets. (From Hussain et al., ref. (116).)

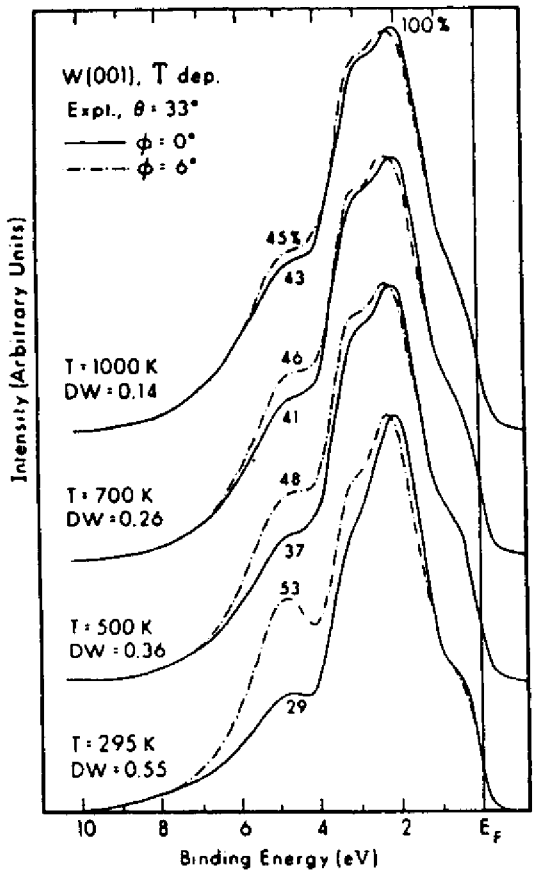

Fig. 66. Temperature dependence of W valence-band spectra for $\theta = 33°$ and emission along two azimuths separated by 6°. The temperatures and their associated Debye-Waller factors are also given, along with the relative intensity of the peak at − 4.8 eV (as measured in % of that at − 2.3 eV). (From Hussain et al., ref. (116).)

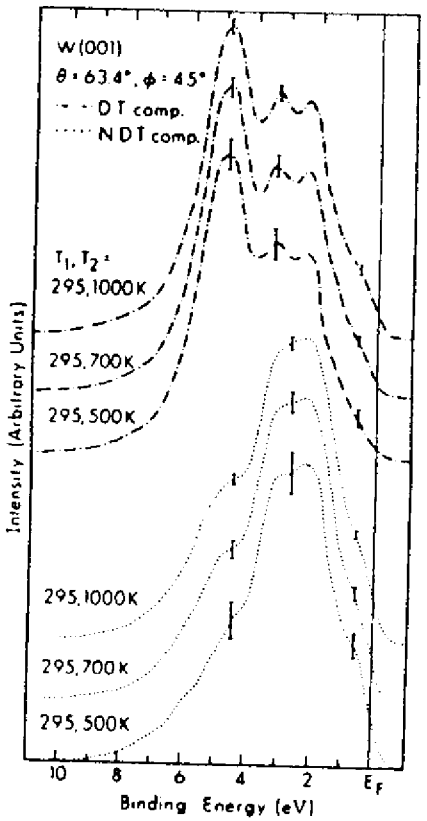

Fig. 67. Use of temperature-dependent W valence spectra to decompose measured intensities into their direct-transition and non-direct transition components with the use of Eq. (38). Different pairs of temperatures yield essentially the same results. (From Hussain et al., ref. (116).)

furthermore agree very well with pure direct-transition calculations of N_{DT} only. This method thus could be very useful in future band-mapping studies using XPS.

As a further example, Hussain et al.[10] have carried out the first swept-hν angle-resolved XPS study of valence spectra, again on tungsten to emphasize direct transition involvement. These measurements were done in normal emission from W (011) with monochromatized synchrotron radiation in the range 1100-1250 eV. Some of the results are shown in Fig. 68 together with direct transition calculations of the same type as those in Fig. 63. The agreement with experiment is thus excellent, especially with regard to the relative intensity change of the peak at ~4.8 eV, thereby providing more support for the applicability of the simple direct-transition model.

As a final point concerning the direct-transition model, one can ask why it works as well as it does and why, for example, complexities in the final state wave function do not cause significant deviations from it[111,128]. Such final-state complexities can be considered most simply as the mixing in of other plane-wave components $\exp(i(\vec{k}^f+\vec{g}')\cdot\vec{r})$ to an initial $\exp(i\vec{k}^f\cdot\vec{r})$ excitation via diffraction events associated with the reciprocal lattice vectors $\vec{g}'$. Here, $\vec{g}'$ is not the same as the $\vec{g}$ involved in the primary $\vec{k}$ conservation, but may be another bulk $\vec{g}$ vector or a vector associated with the reciprocal lattice of the surface. That such $\vec{g}'$ mixing events may be very weak in XPS is reasonable in view of the forward-peaked nature of the electron-atom scattering factors (cf. discussion of Sec. 5.B) that must be involved in producing such diffracted waves. An additional effect of possible importance is a smearing in $\vec{k}^f$ due to the inelastic scattering that effectively limits the wave function to a region of order Λ_e in size along its propagation direction[119]. Thus, the uncertainty principle dictates $\Delta k^f \Lambda_e \sim 1/2$ or $\Delta k \gtrsim 1/2\Lambda_e$ as a reasonable estimate of such smearing. That is, a $\vec{k}^f$ disc such as that in Fig. 62 will come to have an added thickness Δk^f along $\vec{k}^f$. However, for the specific example of W with a mean free path in XPS of ~13 Å, $\Delta k^f \gtrsim 0.02(2\pi/a)$, which is not very large compared to the Brillouin zone size as represented by $(2\pi/a)$. Direct calculations also verify that this much smearing along the propagation direction does not significantly alter the predicted XPS spectra,[116] even though such Δk^f effects appear to be important for understanding UPS spectra in the 40-200 eV region[122]. Thus neither of these two final-state complexities appears to be highly significant in describing XPS valence spectra.

D. Concluding remarks

In conclusion, although it may at first sight appear to be difficult to see direct-transition effects in the XPS spectra of many systems due to Debye-Waller

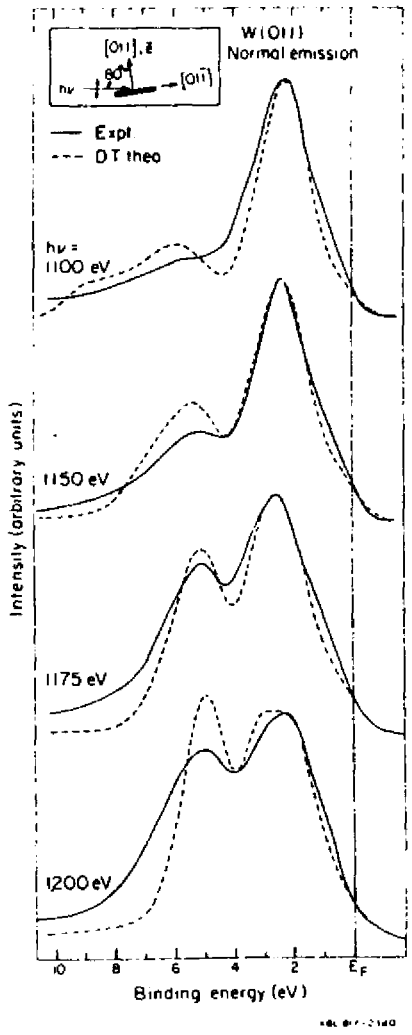

Fig. 68. Comparison of direct-transition theory to the first XPS valence-band experiments making use of tunable synchrotron radiation. Emission was normal to a W(011) surface; the geometry is shown as an inset. (From Hussain et al., ref. (10).)

attenuation, the inherent simplicity of the theoretical model which describes such effects at high energies of emission makes such measurements very appealing for band-structure studies. In fact, with the possible use of cryogenic cooling to increase W (see table of representative values for different elements in ref. 116) and multi-temperature measurements to permit isolating the direct-transition component, it should be possible to expand the range of systems that could be studied in this way. Using synchrotron radiation at lower energies of $\sim$ 200-400 eV would also reduce $|\vec{g}|$ and thus increase W while at the same time probably retaining the desired theoretical simplicity. Also, decreasing the angular acceptance of the analyzer would be very beneficial in reducing the size of the disc over which $\vec{k}^i$ is averaged, thereby providing more precise band mapping information.

To provide some indication as to how much increased angular resolution might affect such spectra, Fig. 69 shows recent direct-transition theoretical curves by Hussain and Fadley[129] for several very close-lying emission directions above a W (001) surface at two different angular apertures: ±1.5° and ±3.0° (at about which all prior XPS experiments have been carried out). It is clear that the ±1.5° curves are much more sensitive than the ±3.0° curves to small changes in emission direction. The ±3.0° curves are expected to show a greater degree of zone averaging, and this is borne out by the fact that at least some non-zero direct-transition intensity is predicted over the entire valence band region from 0-7 eV for all of the angles shown. By contrast, the ±1.5° curves exhibit greater differences, sharper features, and regions of zero predicted intensity (e.g., at ~3 eV for θ = 56° and 57°). Furthermore, an analysis of these calculations shows that the ±1.5 curves for certain angles directly reflect that the $\vec{k}^i$ disc is centered very near a high-symmetry Brillouin zone point. For example, for θ = 53°, the disc center is near N and the 3-peaked structure reflects the 3 bands there[130], whereas for θ = 56°, 57°, the disc is near H where only a single low-lying band lies below the Fermi level[130]. The positions of the major peaks noted at these angles also correlate very well with band positions. Thus, for the first time, it is possible to predict that high-angular-resolution XPS can provide detailed point-by-point mapping of band structures. Recent experiments on W in our laboratory at a ±1.5° resolution[131] also confirm this enhanced sensitivity to angle, and the results are also consistent with direct-transition theory.

Finally, it would certainly be of interest from a theoretical point of view to further explore the calculation of the relevant $\vec{A}\cdot\vec{\nabla}$ matrix elements involved in such studies, as a fully accurate treatment of either direct transitions or zone-averaged non-direct transitions requires accounting for them and it is at present unclear as to whether a simple model can be reliably used to include them.

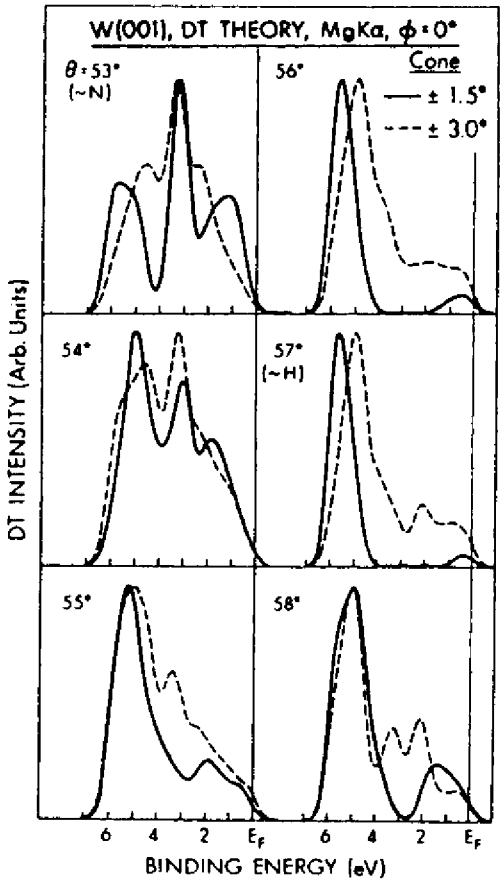

Fig. 69. The effect of increased angular resolution on the direct-transition component of W valence-band emission. Pure direct-transition theoretical curves are compared for a ±3.0° analyzer acceptance (dashed curves) and for a ±1.5° acceptance (solid curves). ϕ is fixed at 0° and θ is scanned in 1°-steps from 53° to 58°. For θ = 53° and 57°, the discs of allowed $\vec{k}_i$ points are very close to the N and H points in the Brillouin zone, respectively, as indicated (cf. Fig. 62).

As a final comparison to the closely-related use of angle-resolved UPS to study valence levels[7-9], it is clear that this technique has contributed very much to our understanding of both bulk- and surface- electronic structure. In general, it can be carried out at higher resolutions than ARXPS (~0.2-0.3 eV in UPS compared to ~0.5-1.0 eV in XPS), and both phonon effects and $\vec{k}$ smearing due to the finite analyzer acceptance core are much less as problems due to the much smaller energies involved. However, a detailed analysis of ARUPS data may require knowledge of both the initial- and final- state band structures, as well as a proper inclusion of both matrix elements and multiple-scattering effects. In ARXPS, by contrast, a very simple theory seems to describe the data very well, at least as far as the direct transition component is concerned. Thus, it seems that ARXPS will serve as a very useful complement to ARUPS, especially in bulk band structure studies.

Acknowledgements

In connection with those aspects of this review involving work at the University of Hawaii, the author is very much indebted to his several colleagues for their considerable contributions to the development of angle-resolved x-ray photoelectron spectroscopy. This group includes R. J. Baird, S. M. Goldberg, Z. Hussain, P. F. Heden, S. Kono, P. J. Orders, L.-G. Petersson, K. A. Thompson, and L. F. Wagner. Many helpful comments from B. L. Henke are also appreciated. The support of the National Science Foundation, the Petroleum Research Fund, and N.A.T.O. is also gratefully acknowledged. The hospitality of the Department of Physics, Montana State University during a portion of the writing of this manuscript is also very much appreciated. The author is also grateful to E. A. Stern for some very helpful comments concerning EXAFS theory and its relationship to XPD.

References

1. J. Jenkin, J. Elect. Spect., 23, 187 (1981).
2. K. Siegbahn, U. Gelius, H. Siegbahn, and E. Olsen, Phys. Lett., 32A, 221 (1970).
3. C. S. Fadley and S. A. L. Bergstrom, Phys. Lett., 35A, 375 (1971); and in Electron Spectroscopy, D. A. Shirley, ed., North Holland, Amsterdam (1972), p. 233.
4. C. S. Fadley, R. J. Baird, W. Siekhaus, T. Novakov, and S. A. L. Bergstrom, review in J. Elect. Spect., 4, 93 (1974).
5. C. S. Fadley, review in Prog. in Sol. St. Chem., G. A. Samorjai and J. O. McCaldin, eds., Pergamon Press, New York (1976), Vol. 11, p. 265.
6. C. S. Fadley, review in Electron Spectroscopy: Theory, Techniques, and Applications, C. R. Brundle and A.D. Baker, eds., Academic Press, London (1978), Vol. 2, Ch. 1.
7. B. Feuerbacher, B. Fitton, and R. F. Willis, eds., Photoemission and the Electronic Properties of Surfaces, Wiley, New York (1978).
8. M. Cardona and L. Ley, eds., Photoemission in Solids, Springer-Verlag, Berlin (1978), Vols. 1 and 2.
9. E. W. Plummer and W. Eberhardt, review in Adv. in Chem. Phys., L. Prigogine and S. A. Rice, eds., John Wiley, New York (1982), Vol. XLIX, p. 533.
10. Z. Hussain, E. Umbach, J. J. Barton, J. G. Tobin, and D. A. Shirley, Phys. Rev., B 25, 672 (1982).
11. S. D. Kevan, D. H. Rosenblatt, D. Denley, B.-C. Lu, and D. A. Shirley, Phys. Rev., B 20, 4133 (1979); Z. Hussain, D. A. Shirley, C. H. Li, and S. Y. Tong, Proc. Nat. Acad. Sci. (U.S.A.), 78, 5293 (1981).
12. R. J. Baird and C. S. Fadley, J. Elect. Spect., 11, 39 (1977).
13. E. W. Plummer, Nucl. Inst. and Meth., 177, 179 (1980).
14. N. V. Smith, in Photoemission in Solids, M. Cardona and L. Ley, eds., Springer-Verlag, Berlin (1978), Ch. 6.; N. V. Smith, P. K. Larsen, and M. M. Traum, Rev. Sci. Inst., 48, 454 (1977).
15. R. Z. Bachrach, S. B. M. Hagstrom, and F. C. Brown, in Vacuum Ultraviolet Radiation Physics, E. E. Koch, R. Haensel, and C. Kunz, eds., Pergamon, London (1974), p. 795; G. V. Hansson, B. Goldberg, and R. Z. Bachrach, Rev. Sci. Inst., 52, 517 (1981).
16. C. J. Powell, Surf. Sci., 44, 29 (1974).
17. I. Lindau and W. E. Spicer, J. Elect. Spect., 3, 409 (1974).
18. M. P. Seah and D. P. Dench, Surf. Int. Anal., 1, 2 (1979).
19. J. M. Hill, D. G. Royce, C. S. Fadley, L. F. Wagner, and F. J. Grunthaner, Chem. Phys. Lett., 44, 225 (1976).
20. R. P. Vasquez, J. D. Klein, J. J. Barton, and F. J. Grunthaner, J. Elect. Spect., 23, 63 (1981).
21. B. L. Henke, Phys. Rev., A 6, 94 (1972).
22. W. A. Fraser, J. V. Florio, W. N. Delgass, and W. D. Robertson, Surf. Sci., 36, 661 (1973).
23. J. H. Scofield, J. Elect. Spect., 8, 129 (1976).
24. R. F. Rielman, Alfred Msezone, and S. T. Manson, J. Elect. Spect., 8, 389 (1976).
25. S. M. Goldberg, C. S. Fadley, and S. Kono, J. Elect. Spect., 21, 285 (1981); Solid State Commun., 28, 459 (1978).
26. D. R. Penn, J. Elect. Spect., 9, 29 (1976) and J. Vac. Sci. Tech., 13, 221 (1976).
27. V. I. Nefedov, N. P. Sergushin, I. M. Band, and M. B. Trzhaskowskaya, J. Elect. Spect., 2, 383 (1973).
28. W. J. Carter, G. K. Schweitzer, and T. A. Carlson, J. Elect. Spect., 5, 827 (1974); T. A. Carlson, Surf. and Int. Anal., 4, 125 (1982).

29. C. J. Powell and P. E. Larson, Appl. Surf. Sci., 1, 186 (1977).
30. D. T. Clark and H. R. Thomas, J. Polym. Sci. (Polym. Chem, Ed.), 15, 1093 (1977).
31. C. S. Fadley, J. Elect. Spect., 5, 725 (1974).
32. J. Brunner and H. Zogg, J. Elect. Spect., 5, 911 (1977).
*33. R. E. Connelly, M.S. Thesis, Univ. of Hawaii (1982); and R. E. Connelly and C. S. Fadley, to be published.
34. G. Hollinger and M. Pijolat, Surf. Sci., 105, 114 (1981); and M. Pijolat, doctoral thesis, Univ. Claude Bernard, Lyon, France (1980).
35. R. P. Vasquez and F. J. Grunthaner, Surf. Sci., 99, 681 (1980), and references therein.
36. D. T. Clark and H. R. Thomas, J. Polym. Sci. (Polym. Chem., Ed.), 15, 2843 (1977).
37. R. J. Baird, Ph.D. thesis, Univ. of Hawaii (1977).
38. R. J. Baird, C.S.Fadley, S. Kawamoto, and M. Mehta, Chem. Phys. Lett., 34, 49 (1975).
39. R. J. Baird, C. S. Fadley, S. Kawamoto, M. Mehta, R. Alvarez, and J. A. Silva, Anal. Chem., 48, 843 (1976).
40. O. A. Baschenko and V. I. Nefedov, J. Elect. Spect., 17, 405 (1979); 21, 153 (1980); and 26, 109 (1982).
41. J. B. Pendry, Low Energy Electron Diffraction, Academic Press, London (1974).
42. M. A. Van Hove and S. Y. Tong, Surface Crystallography by LEED, Springer-Verlag, New York (1979).
43. M. F. Ebel and W. Liebe, J. Elect. Spect., 16, 463 (1979).
44. J. C. Ashley and V. E. Anderson, J. Elect. Spect., 24, 127 (1981) and IEEE Trans. on Nucl. Sci., NS-28, 4132 (1981).
45. J. E. Demuth, D. W. Jepsen, and P. M. Marcus, Phys. Rev. Lett., 32, 1182 (1974); D. H. Rosenblatt et al., Phys. Rev., B 23, 3828 (1981); S. Brennan, J. Stöhr, and R. Jaeger, Phys. Rev., B 24, 4871 (1981).
46. M. Aono, C. Oshima, T. Tanaka, E. Bannai, and S. Kawai, J. Appl. Phys., 49, 2761 (1978).
47. A. Jablonski, Adv. in Coll. and Int. Sci., 8, 213 (1977).
48. V. I. Nefedov, P. P. Pozdeyev, V. F. Dorfman, and B. N. Pypkin, Surf. and Int. Anal., 2, 26 (1980).
49. W. N. Delgass, G. L. Haller, and J. H. Lunsford, Spectroscopy in Heterogeneous Catalysis, Academic Press, New York (1979), Ch. 8; P. J. Angevine, J. C. Vartuli, and W. N. Delgass, Proc. 6th Int. Cong. Catal., London, 1976, 2, 611 (1977).
50. J. Finster, P. Lorenz, and A. Meisel, Surf. and Int. Anal., 1, 179 (1979).
51. P. H. Citrin and G. K. Wertheim, Phys. Rev. Lett., 41, 1425 (1978).
52. T. M. Duc, C. Guillot, Y. Lassailly, J. Lecante, Y. Jugnet, and J. C. Vedrine, Phys. Rev. Lett., 43, 789 (1979); J. F. van der Veen, F. J. Himpsel, and D. E. Eastman, Phys. Rev. Lett., 44, 189 (1980).
53. G. K. Wertheim and G. Crecelius, Phys. Rev. Lett., 40, 813 (1978).
54. R. Haydock and M. J. Kelly, Surf. Sci., 38, 139 (1973); M. C. Dejonqueres and M. Cyrot-Lackmann, Surf. Sci., 53, 429 (1975); K. S. Sohn, D. G. Dempsey, L. Kleinmann, and E. Caruthers, Phys. Rev., B 13, 1515 (1976); B 14, 3185, 3193 (1976).
55. M. Mehta and C. S. Fadley, Phys. Rev. Lett., 39, 1569 (1977); Phys. Rev., B 20, 2280 (1979).
56. D. G. Dempsey and L. Kleinman, private communication.
57. R. J. Baird, C. S. Fadley, S. M. Goldberg, P. J. Feibelman, and M. Sunjic, Surf. Sci., 72, 495 (1978).
58. A. B. Bradshaw, W. Domcke, and L. S. Cederbaum, Phys. Rev., B 16, 1480 (1977).

---

* Now appearing as:

33. R. E. Connelly, C. S. Fadley, and P. J. Orders, J. Vac. Sci. Tech., A2, 1333 (1984).

59. M. Mehta and C. S. Fadley, Phys. Lett., A55, 59 (1975).
60. M. Mehta and C. S. Fadley, unpublished results.
61. M. Mehta and C. S. Fadley, Chem. Phys. Lett., 46, 225 (1977).
62. S. Kono, S. M. Goldberg, N. F. T. Hall, and C. S. Fadley, Phys. Rev. Lett., 41, 1831 (1978); L.-G. Petersson, S. Kono, N. F. T. Hall, C. S. Fadley, and J. B. Pendry, Phys. Rev. Lett., 42,1545 (1979).
63. S. Kono, S. M. Goldberg, N. F. T. Hall, and C. S. Fadley, Phys. Rev., B 22, 6085 (1980).
64. M. Owari, M. Kudo, Y. Nihei, and H. Kamada, J. Elect. Spect., 21, 131 (1981).
65. R. J. Baird, C. S. Fadley, and L. F. Wagner, Phys. Rev., B 15, 666 (1977).
66. J. M. Adams, S. Evans, J. M. Thomas, J. Am. Chem. Soc., 100, 3260 (1978); S. Evans, E. Raftery, and J. M. Thomas, Surf. Sci., 89, 64 (1979).
67. N. Koshizaki, M. Kudo, M. Owari, Y. Nihei, and H. Kamada, Jap. J. Appl. Phys., 19, L349 (1980).
68. A. Liebsch, Phys. Rev. Lett., 32, 1203 (1974); Phys. Rev., B 13, 544 (1976).
69. P. J. Orders, R. E. Connelly, N. F. T. Hall, and C. S. Fadley, Phys. Rev., B 24, 6163 (1981).
70. R. N. Lindsay, C. G. Kinnibergh, and J. B. Pendry, J. Elect. Spect., 15, 157 (1979).
71. T. Fujikawa, J. Phys. Soc. Jap., 50, 1321 (1981); 51, 251 (1982); and J. Elect. Spect., 26, 79 (1982).
72. P. A. Lee, Phys. Rev., B 13, 5261 (1976).
73. P. A. Lee and G. Beni, Phys. Rev., B 15, 2862 (1977).
74. L. McDonnell, D. P. Woodruff, and B. W. Holland, Surf. Sci., 51, 249 (1975).
75. Z. Hussain and D. A. Shirley, NPD results for sulfur s- and p- emission to be published. (Cf. also ref. 107.)
76. P. A. Lee and J. B. Pendry, Phys. Rev., B 11, 2795 (1975).
77. L.-G. Petersson, S. Kono, N. F. T. Hall, C. S. Fadley, and J. B. Pendry, Phys. Rev. Lett., 42, 1545 (1979).
78. L. I. Schiff, Quantum Mechanics, McGraw-Hill, New York (1968), pp. 136-137 and 324-325.
79. M. Fink and A. C. Yates, At. Data, 1, 385 (1970); M. Fink and J. Ingram, At. Data, 4, 129 (1972).
*80. K. A. Thompson, Ph.D. Thesis, Univ. of Hawaii (1981); K. A. Thompson and C. S. Fadley, to be published.
81. P. J. Orders, S. Kono, C. S. Fadley, R. Trehan, and J. T. Lloyd, Surf. Sci., 119, 371 (1982).
82. B. K. Teo and P. A. Lee, J. Am. Chem. Soc., 101, 2815 (1979).
*83. P. J. Orders and C. S. Fadley, Phys. Rev., B, to appear.
84. P. J. Orders, J. T. Lloyd, and C. S. Fadley, unpublished results for substrate Ni azimuthal XPD.
85. S. Kono, Hyomen Kagaku (Surface Science), 2, 153 (1981).
86. S. Takahashi, S. Kono, H. Sakurai, and T. Sagawa, J. Phys. Soc. Jap., 51, 3296 (1982).
*87. M. Owari, M. Kudo, Y. Nihei, and H. Kamada; and Y. Nihei, M. Owari, M. Kudo, and H. Kamada, papers presented at the 9th Int. Conf. on Atomic Spectroscopy/XXII Colloquium Spectroscopicum Internationale, Sept. 1981, Tokyo, Japan.
88. S. M. Goldberg, R. J.Baird, S. Kono, N. F. T. Hall, and C. S. Fadley, J. Elect. Spect., 21, 1 (1980).
89. M. Kudo, M. Owari, Y. Nihei, Y. Gohshi, H. Kamada, Jap. J. Appl. Phys., 17, Supp. 17-2, 275 (1978).

---

* Now appearing as:

80. K. A. Thompson and C. S. Fadley, J. Elect. Spect., 33, 29 (1984), and Surf. Sci., 146, 231 (1984).

83. P. J. Orders and C. S. Fadley, Phys. Rev., B27, 781 (1983); E. L. Bullock, C. S. Fadley, and P. J. Orders, Phys. Rev., B28, 4867 (1983); M. Sagurton, E. L. Bullock, and C. S. Fadley, Phys. Rev., B30, 7332 (1984).

87. M. Owari et al., J. Elect. Spect., 34, 215 (1984).

90. T. E. Madey, Surf. Sci., 79, 575 (1979) plus earlier references therein.
91. J. Stohr, K. Baberschke, R. Jaeger, R. Treichler, and S. Brennan, Phys. Rev. Lett., 47, 381 (1981).
92. L.-G. Petersson, S. Kono, N. F. T. Hall, S. Goldberg, J. T. Lloyd, and C. S. Fadley, Mat. Sci. and Eng., 42, 111 (1980).
93. D. H. Rosenblatt, J. G. Tobin, M. G. Mason, R. F. Davis, S. D. Kevan, D. A. Shirley, C. H. Li, and S. Y. Tong, Phys. Rev., B 23, 3828 (1981); D. A. Shirley, private communication.
94. J. H. Onuferko and D. P. Woodruff, Surf. Sci., 95, 555 (1980) and references therein.
95. B. J. Garrison, N. Winograd, and D. E. Harrison, Phys. Rev., B 18, 6000 (1978); S. P. Holland, B. J. Garrison, and N. Winograd, Phys. Rev. Lett., 43, 220 (1979).
96. T. S. Rahman, J. E. Black, and D. L. Mills, Phys. Rev. Lett., 46, 1469 (1981) and references therein.
97. D. H. Rosenblatt, J. G. Tobin, M. G. Mason, R. F. Davis, S. D. Kevan, and D. A. Shirley, private communication.
98. J. Stohr, R. Jaeger, and T. Kendelewicz, Phys. Rev. Lett., 49, 142 (1982) and references therein.
99. N. F. T. Hall, Ph.D. Thesis, Univ. of Hawaii (1982); N. F. T. Hall and C. S. Fadley, to be published.
*100. P. J. Orders, C. S. Fadley, R. Trehan, B. Sinkovic, Z. Hussain, and J. Lecante, to be published.
101. D. W. Jepsen, Phys. Rev., B 22, 5701 (1980) and references therein.
102. S. Kono, H. Sakurai, K. Higashiyama, and T.Sagawa, Surf. Sci., to appear.
103. D. P. Woodruff, D. Norman, B. W. Holland, N. V. Smith, H. H. Farrell, and M. M. Traum, Phys. Rev. Lett., 41, 1130 (1978); N. V. Smith, H. H. Farrell, M. M. Traum, D. P. Woodruff, D. Norman, M. S. Woolfson, and B. W. Holland, Phys. Rev., B 21, 3119 (1980); H. H. Farrell, M. M. Traum, N. V. Smith, W. A. Royer, D. P. Woodruff, and P. D. Johnson, Surf. Sci., 102, 527 (1981); W. M. Kang et al., Phys. Rev. Lett., 47, 931 (1981).
104. T. Matsudaira, N. Nishijima, and M. Onchi, Surf. Sci., 61, 651 (1976); D. Aberdam, R. Baudoing, E. Blanc, and C. Gaubert, Surf. Sci., 71, 279 (1978).
105. J. L. Beeby, Surf. Sci., 80, 55 (1979); S. Holloway, Surf. Sci., 80, 62 (1979); P. A. Maksym and J. L. Beeby, Surf. Sci., 110, 423 (1981).
106. S. D. Kevan, R. F. Davis, D. H. Rosenblatt, J. G. Tobin, M. G. Mason, D. A. Shirley, C. H. Li, and S. Y. Tong, Phys. Rev. Lett., 46, 1629 (1981) and references therein; S. Y. Tong and J. C. Tang, Phys. Rev., B 25, 6526 (1982).
*107. D. H. Rosenblatt, S. D. Kevan, J. G. Tobin, R. F. Davis, M. G. Mason, D. A. Shirley, J. C. Tang, and S. Y. Tong, Phys. Rev.,B 26, 3181 (1982).
108. P. H. Citrin, P. Eisenberger, and R. C. Hewitt, Phys. Rev. Lett., 41, 309 (1978); 45, 1948 (1980); S. Brennan, J. Stohr, and R. Jaeger, Phys. Rev., B 24, 4871 (1981); and references therein.
109. P. Eisenberger and L. C. Feldman, Science, 214, 300 (1981).
110. C. S. Fadley, Far. Soc. Disc., 60, 18 (1975); R. J. Baird, C. S. Fadley, and L. F. Wagner, Phys. Rev. Lett., 37, 111 (1976).
111. F. R. McFeely, J. Stohr, G. Apai, P. S. Wehner, and D. A. Shirley, Phys. Rev., B 14, 3273 (1976).
112. L. F.Wagner, Z. Hussain, C. S. Fadley, and R. J. Baird, Solid State Commun., 21, 453 (1977); G. Apai, J. Stohr, R. S. Williams, S. P. Kowalczyk, and D. A. Shirley, Phys. Rev., B 15, 584 (1977).

---

* Now appearing as:

100. B. Sinkovic et al., Phys. Rev., B30, 1833 (1984); P. J. Orders et al., Phys. Rev. B30, 1838 (1984).

107. An additional reference for swept-energy studies is: J. J. Barton et. al., Phys. Rev. Lett., 51, 272 (1983).

113. Z. Hussain, L. F. Wagner, and C. S. Fadley, unpublished ARXPS results for the valence bands of Pt.
114. N. Erikson, Phys. Scr., 16, 462 (1977).
115. R. H. Williams, P. C. Kemeny, and L. Ley, Solid State Commun., 19, 495 (1976).
116. Z. Hussain, S. Kono, R. E. Connelly, and C. S. Fadley, Phys. Rev. Lett., 44, 895 (1980); Z. Hussain, C. S. Fadley, S. Kono, and L. F. Wagner, Phys. Rev., B 22, 3750 (1980).
117. G. D. Mahan, Phys. Rev., B 2, 4334 (1970), and review in Electron and Ion Spectroscopy of Solids, L. Fiermans, J. Vennik, and W. Dekeyser, eds., Plenum Press, New York (1978).
118. C. Caroli, D. Lederer-Rozenblatt, B. Roulet, and D. Saint-James, Phys. Rev., B 8, 4552 (1973).
119. P. J. Feibelman and D. E. Eastman, Phys. Rev., B 10, 4932 (1974).
120. N. J. Shevchik, J. Phys., C 10, L555 (1977); Phys. Rev., B 16, 3428 (1977).
121. L.-G. Petersson, Z. Hussain, S. Kono, and C. S. Fadley, Solid State Commun., 34, 549 (1980).
122. Z. Hussain, S. Kono, L.-G. Petersson, C. S. Fadley, and L. F. Wagner, Phys. Rev., B 23, 724 (1981).
123. L. F. Wagner, Z. Hussain, and C. S. Fadley, Solid State Commun., 21, 257 (1977).
124. J. Stohr, P. S. Wehner, R. S. Williams, G. Apai, and D. A. Shirley, Phys. Rev., B 17, 587 (1978).
125. P. Thiry, D. Chandesri, J. Lecante, C. Guillot, R. Pinchaux, and Y. Petroff, Phys. Rev. Lett., 43, 82 (1979).
126. T. C. Chiang, J. A. Knapp, M. Aono, and D. E. Eastman, Phys. Rev., B 21, 3513 (1980).
127. M. J. Sayers and F. R. McFeely, Phys. Rev., B 17, 3867 (1978).
128. G. Paasch, Phys. Status Solidi, B 87, 191 (1978).
129. Z. Hussain and C. S. Fadley, unpublished results of ARXPS direct-transition calculations for W with high angular resolution.
130. N. E. Christensen and B. Feuerbacher, Phys. Rev., B 10, 2349 (1974).
131. R. C. White, Z. Hussain, D. W. Shinn, and C. S. Fadley, unpublished experimental ARXPS valence data for W with ± 1.5° resolution.

The Study of Surface Structures by Photoelectron Diffraction and Auger Electron Diffraction

Charles S. Fadley

ABBREVIATIONS AND ACRONYMS

AED	Auger electron diffraction
APD	azimuthal photoelectron diffraction
ARPEFS	angle-resolved photoemission fine structure (acronym for scanned-energy photoelectron diffraction)
CMA	cylindrical mirror analyzer
DL	double-layer model
EELS	electron energy loss spectroscopy
ESDIAD	electron stimulated desorption ion angular distributions
EXAFS	extended X-ray absorption fine structure
FT	Fourier transform
FWHM	full width at half maximum intensity
GIXS	grazing incidence X-ray scattering
HT	high temperature limit (in SPPD experiment)
LEED	low energy electron diffraction
LT	lower temperature of measurement (in SPPD experiment)
ML	monolayer
MEIS	medium-energy ion scattering
MQNE	magnetic quantum number expansion
MS	multiple scattering
MSC	multiple scattering cluster
MTL	missing-top-layer model
NEXAFS	near edge X-ray absorption fine structure = XANES

Charles S. Fadley • Department of Chemistry, University of Hawaii, Honolulu, Hawaii 96822. *Present address:* Department of Physics, University of California–Davis, Davis, California 95616, *and* Materials Science Division, Lawrence Berkeley Laboratory, Berkeley, California 94720.

Synchrotron Radiation Research: Advances in Surface and Interface Science, Volume 1: Techniques, edited by Robert Z. Bachrach, Plenum Press, New York, 1992.

NPD	scanned-energy photoelectron diffraction with normal emission
ODAC	one-dimensional alkali-chain model
OPD	scanned-energy photoelectron diffraction with off-normal emission
PD, PhD	photoelectron diffraction
PLD	path-length difference
PPD	polar photoelectron diffraction
PW	plane-wave scattering
RBS	Rutherford back scattering
SEXAFS	surface extended X-ray absorption fine structure
SMSI	strong metal support interaction
SPAED	spin polarized Auger electron diffraction
SPPD	spin polarized photoelectron diffraction
SRMO	short-range magnetic order
SS	single scattering
SSC	single scattering cluster
STM	scanning tunneling microscopy
SW	spherical-wave scattering
XANES	X-ray absorption near-edge structure = NEXAFS
XPD	X-ray photoelectron diffraction, typically at energies of 500–1400 eV
XPS	X-ray photoelectron spectroscopy

1. INTRODUCTION

A knowledge of the atomic identities, positions, and bonding mechanisms within the first 3–5 layers of a surface is essential to any quantitative microscopic understanding of surface phenomena. This implies knowing bond directions, bond distances, site symmetries, coordination numbers, and the degree of both short-range and long-range order present in this selvedge region. A number of surface-structure probes have thus been developed in recent years in an attempt to provide this information.[1] Each of these methods has certain unique advantages and disadvantages, and they are often complementary to one another.

We will here concentrate on the basic experimental and theoretical aspects of photoelectron diffraction (PD or PhD) and its close relative, Auger electron diffraction (AED). Although the first observations of strong diffraction effects in X-ray photoelectron emission from single-crystal substrates by Siegbahn *et al.*[2] and by Fadley and Bergstrom[3] took place almost 20 years ago, and the use of such effects at lower energies to determine surface structures was proposed by Liebsch[4] 15 years ago, it was not until about 10 years ago that quantitative experimental surface-structure studies were initiated by Kono *et al.*,[5] Woodruff *et al.*,[6] and Kevan *et al.*[7] By now both photoelectron diffraction and Auger electron diffraction are becoming more widely used to study surface atomic geometries.[8–13] We will thus consider here both the present status and future prospects of these methods, and then return at the conclusion of this chapter to make a critical comparison of them with several other surface-structure probes such as LEED, grazing incidence X-ray scattering (GIXS), and scanning tunneling microscopy (STM).

The basic experiment in PD or AED involves exciting a core photoelectron or a relatively simple core-like Auger transition from an atom in a single-crystal environment and then observing modulations in the resulting peak intensities that are due to final-state scattering from atoms neighboring the emitter. For a general Auger peak of the type XYZ, it is thus important that the upper levels Y and Z involved are not so strongly influenced by chemical bonding as to induce an anisotropy in emission that is more associated with initial-state electronic structure. The directly emitted photoelectron- or Auger electron–wave exhibits interference with various scattered waves, and this interference pattern is analyzed to derive structural information. Peak intensities can be monitored as a function either of the emission direction or, in the case of photoelectron diffraction, of the exciting photon energy. In AED, excitation can also derive from anything producing core holes: an electron beam, VUV/soft-X-ray radiation, or even an ion beam.

The three basic types of measurement possible are as shown in Fig. 1: an azimuthal or ϕ scan, a polar or θ scan, and, for photoelectron diffraction, a scan of energy in a normal or off-normal geometry. Several abbreviations and acronyms have arisen in connection with such measurements. With soft X-ray excitation at about 1.2–1.5 keV at the typical X-ray photoelectron spectroscopy (XPS) limit, scanned-angle measurements have been termed X-ray photoelectron diffraction (XPD).[5,9] Scanned-energy photoelectron measurements spanning the VUV-to-soft-X-ray regime have also been called normal photoelectron diffraction (NPD),[7,8,14] off-normal photoelectron diffraction (OPD),[15] or angle-resolved photoemission fine structure (ARPEFS)[8] to emphasize their similarity to the more familiar surface extended X-ray absorption fine structure (SEXAFS).[16] Both standard X-ray sources and synchrotron radiation can be used for excitation, with photon energies being as low as 60 eV[6,17,18] and as high as a few keV.[7,8,19] Synchrotron radiation adds the capability of varying the photon energy continuously and of studying the dependence of the diffraction on polarization.

The degree of modulation of intensity observed in PD or AED experiments can be very large, with overall values of anisotropy as high as $(I_{max}-I_{min})/I_{max} = \Delta I/I_{max} = 0.5$–$0.7$. Thus, it is not uncommon to observe 30–50% changes in the peak intensity as a function of direction or energy, and such effects are relatively easy to measure. This is by contrast with the related surface-structure technique

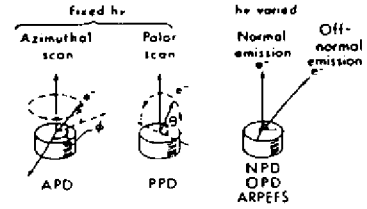

FIGURE 1. The three basic types of photoelectron or Auger electron diffraction measurement: an azimuthal (ϕ) scan at constant polar angle, sometimes referred to as azimuthal photoelectron diffraction or APD; a polar (θ) scan at constant azimuthal angle, referred to as polar photoelectron diffraction or PPD; and a scan of $h\nu$ in fixed geometry that can be done only in photoelectron diffraction and for emission either normal or off-normal to the surface (denoted NPD or OPD, respectively). The scanned-energy type has also been referred to as angle-resolved photoemission fine structure or ARPEFS. Note that θ is measured with respect to the surface.

of SEXAFS,[16] in which typical modulations are about one tenth as large. This difference arises from the fact that SEXAFS effectively measures an angle-integrated photo electron diffraction pattern as a function of energy, and it is not surprising that this integration averages over various phases and leads to considerably lower relative effects.

We shall consider both scanned-angle photoelectron and Auger results and scanned-energy photoelectron results here. To date, scanned-angle studies are much more numerous; this is due to their greater simplicity, since scanned-energy work has several requirements in addition: the sweeping of photon energy with a synchrotron radiation source, the correct normalization of photon fluxes and electron-analyzer transmissions as a function of energy, and the possibility of allowing for interference between Auger peaks and photoelectron peaks in certain kinetic-energy ranges. Finally, it requires more-complex theoretical calculations in that scattering phase shifts and other nonstructural parameters have to be generated for all of the energies in a scan.[8,19–22] However, an advantage in scanned-energy work is that Fourier transform (FT) methods can be used to estimate the path-length differences for various strong scatterers.[8,20–22]

A key element in either photoelectron or Auger electron diffraction is the energy dependence of the relevant elastic-scattering factors. Figure 2 illustrates this for the case of atomic Ni with curves of the plane-wave scattering amplitude $|f_{Ni}|$ as a function of both the scattering angle θ_{Ni} and the electron energy. For low energies of 50–200 eV, it is clear that there is a high amplitude for scattering into all angles. For the intermediate range of about 200–500 eV, it is a reasonable approximation to think of only forward scattering ($\theta_{Ni} = 0°$) and backscattering ($\theta_{Ni} = 180°$) as being important. However, at energies above 500 eV, we see that the scattering amplitude is significant only in the forward direction, in which it is strongly peaked. The degree of forward peaking increases as the energy is increased. The utility of such forward scattering at higher energies in surface-structural studies was noted in very early XPD investigations,[5,23] and it has more recently been termed a "searchlight effect"[13] or "forward focusing"[24] in connection with XPD analyses of epitaxial overlayers. This effect turns out to be one of the most useful and simply interpretable aspects of higher-energy photoelectron or Auger electron diffraction, and we will make reference to it in several of the examples considered in following sections. These qualitative observations concerning the energy dependence of the scattering factor will later also assist in explaining which multiple scattering effects may be the most significant. A special aspect of such scattering factors is that they may exhibit zeroes for certain angles and energies; this has been termed a generalized Ramsauer–Townsend effect, and its influence on the analysis of ARPEFS data is considered elsewhere.[21,25]

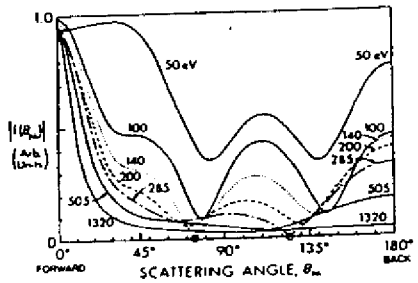

FIGURE 2. Nickel plane-wave scattering factor amplitudes $|f_{Ni}|$ as a function of both the scattering angle θ_{Ni} and the photoelectron kinetic energy. Note the zeroes occurring for both 140 eV and 285 eV, which have been termed a generalized Ramsauer–Townsend effect. (From Ref. 21.)

A final important aspect of either photoelectron or Auger electron diffraction is that both are *atom-specific* probes of *short-range order*. Thus, each type of atom in a sample can in principle be studied, and each will have a unique diffraction signature associated with the neighbors around it. Previous work shows that the principal features of diffraction curves are due to the geometry of the first 3–5 spheres of scatterers around a given emitter, although data may exhibit useful fine structure that is associated with scatterers as far as 20 Å away.[20,26] This short-range sensitivity is thus shared with SEXAFS. We will later point out the potential uses of PD and AED in studying the degree of order present in the near neighbors of the emitter.

The remainder of this chapter begins by briefly reviewing the experimental requirements of these methods and considering both the simplest single-scattering model and other more accurate models that have been used to analyze both PD and AED data. The bulk of the text discusses several illustrative cases to which these techniques have been applied. This is not intended to be an exhaustive listing of all such studies to date, but the examples have been chosen to demonstrate certain basic phenomena, to illustrate the range of structural information that can be obtained, and to provide some idea of the different classes of systems that can be fruitfully studied. In certain cases, the limitations of the analysis or the need for future improvements are pointed out. Finally, some particularly interesting new directions for the future are discussed, and comparisons to other currently used structural probes are also made.

The studies discussed represent a mixture of work utilizing both standard X-ray or electron excitation sources and synchrotron radiation, with the number of investigations using standard sources certainly being greater to date. Thus, the methods discussed here are not limited to synchrotron radiation, by contrast with several others discussed in this volume.[27,28] However, both PD and AED will benefit greatly by the use of the higher-intensity facilities in the vacuum ultraviolet/soft X-ray range that are now becoming more available, and we return to this point toward the end of the chapter.

2. EXPERIMENTAL CONSIDERATIONS

The basic experimental requirements for carrying out photoelectron or Auger electron diffraction measurements are relatively simple. A minimal experiment can consist of the excitation source, a specimen holder with only one axis of angular motion (usually the polar angle as defined in Fig. 1), and an electron energy analyzer with an angular resolution of at least approximately ±5°. Thus, most of the commercially available hemispherical analyzers are suitable, and even a cylindrical mirror analyzer (CMA) with some sort of baffle at its entry slit can be used. Peak intensities can be measured very simply as the difference in

height between some point at the maximum and a point in the high-energy background. Measurements at this level are thus quite easy to take, and interesting surface-structural information has been obtained from them.[11]

Going beyond this minimal experiment to be able to tap all of the information available in the diffraction pattern involves several possible elaborations:

- The specimen holder should have both polar and azimuthal axes of rotation (cf. Fig. 1) so that the electron emission direction can be oriented arbitrarily with respect to the surface. The optimal scanning capabilities in this case are to be able to vary θ from grazing excitation incidence to grazing electron exit and to vary ϕ over a full 360° or more. The latter is very useful for establishing the symmetry of the surface and for verifying the reproducibility of features from one symmetry-equivalent azimuthal direction to another. Scanning ϕ over its full range is the most difficult to achieve in practice if there are electrical or mechanical connections to the sample for heating, cooling, or measuring temperature, but designs of this type have been in use for some time.[9] The reproducibility and accuracy of both of these motions should be at least ±0.5°, with even smaller values on the order of ±0.1° being required for very high angular resolution work.
- Automated scanning of spectra, determining of peak intensities by more accurate area-integration and/or peak-fitting procedures, and stepping of angles under computer control are also essential for efficiently obtaining the most reliable data. Systems for doing this are discussed elsewhere.[9,29]
- It also may be desirable to rotate both the specimen and the analyzer (or excitation source) on two axes so as to be able to orient the excitation source at various positions with respect to the electron emission direction. In photoelectron diffraction, this permits making use of the radiation polarization to preferentially excite the direct wave toward different scatterers while at the same time observing the electron intensity along a special direction.[8,19] This is particularly important in studies utilizing synchrotron radiation. In Auger electron diffraction, it can also be useful for assessing the degree to which the penetration of the exciting flux along different incidence directions influences the outgoing diffraction pattern, even though results to date indicate that such effects are minor.[30] (Similar anisotropic penetration might also be expected with X-rays due to Bragg reflections,[2,3] but such effects have so far not been found to be significant in photoelectron diffraction patterns.)
- Improving the angular resolution of the analyzer to the order of ±1.0° has also been found to yield data at higher energies with considerably more fine structure.[10,26] Achieving this may involve specially designed entrance optics,[31,32] or more simply the use of movable tube-array baffles at the entry to a more standard analyzer.[33] High-resolution results of this kind will be discussed in more detail in sections 4.2.1, 4.2.2, and 5.1.
- Improving the energy resolution of the system to on the order of 0.1 eV is also desirable, because it permits resolving small chemical shifts or surface shifts of core levels and studying the diffraction patterns of these species separately.[18]
- Scanning angle or energy obviously involves an added cost in time for any study, and so it is desirable to have the highest overall count rates. This can be achieved by using a more-intense excitation source (as, for example, from insertion-device-generated synchrotron radiation) and/or the most efficient and highest-speed electron analyzer and detection system. Making the latter as effective as possible is important, since there are always potentially deleterious effects of radiation damage as the excitation intensity is increased. Analyzer improvements include the use of multichannel energy-detection systems involving several single-channel electron multipliers or a microchannel plate[32,34] and the use of special spectrometer geometries in which spectra at several angles can be recorded at the same time.[35–37] However, a potential disadvantage of systems recording several angles at once is that the angular resolution may be limited, particularly if it is desired to scan kinetic energies to several hundred eV. A final method for increasing data acquisition rates with a pulsed synchrotron radiation source is to use a time-of-flight analysis system;[38] a logistical problem with such systems however, is that they may require running the storage ring in a less frequently used "timing" mode with fewer electron bunches. Leckey[39] has recently reviewed many of the more novel proposals for analyzers with high energy resolution, high angular resolution, and/or high data acquisition rates.
- Finally, if scanned-energy photoelectron diffraction is to be performed, it is essential to use a reasonably stable synchrotron radiation source and to have an analyzer system whose transmission properties as a function of energy are well understood. This is because photon energies must be scanned in small steps over a total period on the order of hours in present experiments, and the influences of both the decay of photon flux with time and the change of the analyzer's sensitivity with kinetic energy must be corrected out of the final intensity data so as to yield something that is truly proportional to the energy-dependent photoelectric cross section in a given emission direction. Methods for making these corrections are discussed elsewhere.[8,20]

3. THEORETICAL MODELING

3.1. Single-Scattering Theory

3.1.1. Overview of Model

Since the first theoretical paper on low-energy photoelectron diffraction by Liebsch,[4] several detailed discussions of the modeling of photoelectron and Auger electron diffraction have appeared in the literature.[9,15,21,24,25,40–45] Thus, we will begin here by presenting only the essential ingredients of the simplest approach, the single-scattering cluster (SSC) model, and then comment toward the end of this section on several improvements that can be made to it, as well as on some effects expected due to multiple scattering (MS) events.

The basic elements of this single-scattering cluster model are shown schematically in Fig. 3(a). The fundamental assumptions are essentially identical to those used in describing extended X-ray absorption fine structure (EXAFS),[41] and a similar model has also been applied some time ago to angle-resolved Auger emission at very low energies of ≤100 eV.[40] We consider photoelectron emission first and then discuss the modifications required to describe Auger emission.

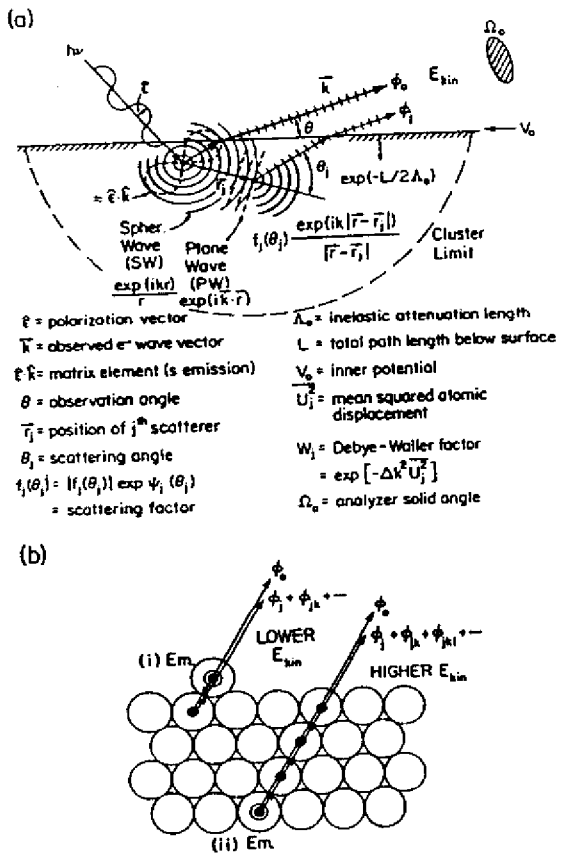

FIGURE 3. (a) Illustration of the assumptions used in the single-scattering cluster (SSC) model, with various important quantities indicated. (b) Two types of multiple-scattering corrections to the SSC model that may be significant for certain energies and geometries: (i) at lower energies of <200 eV, backscattering from a nearest-neighbor atom behind the emitter and then forward scattering by the emitter (from Ref. 25); (ii) multiple forward scattering along lines of closely spaced atoms that leads to a reduction of the expected intensity enhancement, particularly at higher energies of >500 eV (from Refs. 24 and 73).

Radiation with polarization $\hat{\varepsilon}$ is incident on some atom in a cluster, from which it ejects a core-level photoelectron. (In Fig. 3a, the emitting atom is shown near the surface, but it could as well be any atom in the substrate.) If the initial core-electron wave function is denoted by $\psi_c(\mathbf{r})$ and the final photoelectron wave function corresponding to emission with wave vector $\mathbf{k}$ by $\psi(\mathbf{r}, \mathbf{k})$, then the

observed intensity will be given in the dipole approximation by

$$I(\mathbf{k}) \propto |\langle \psi(\mathbf{r}, \mathbf{k}) | \hat{\varepsilon} \cdot \mathbf{r} | \psi_c(\mathbf{r}) \rangle|^2. \quad (1)$$

The final-state wave function in single scattering is further described as being the superposition of a direct wave $\phi_0(\mathbf{r}, \mathbf{k})$ and all singly scattered waves $\phi_j(\mathbf{r}, \mathbf{r}_j \rightarrow \mathbf{k})$ that result from initial ϕ_0 emission toward a scatterer j at $\mathbf{r}_j$ and then subsequent scattering so as to emerge from the surface in the direction of $\mathbf{k}$. Thus, the overall wave function can be written as[21,41]

$$\psi(\mathbf{r}, \mathbf{k}) = \phi_0(\mathbf{r}, \mathbf{k}) + \sum_j \phi_j(\mathbf{r}, \mathbf{r}_j \rightarrow \mathbf{k}). \quad (2)$$

Because the detector is situated at essentially infinity along $\mathbf{k}$, all of the waves in Eq. (2) can finally be taken to have the limiting spherical forms $\phi_0 \propto \exp(ikr)/r$ or $\phi_j \propto \exp(ik|\mathbf{r} - \mathbf{r}_j|)/|\mathbf{r} - \mathbf{r}_j|$, although the effective amplitudes and phases of each type in a given direction will be modulated by the photoexcitation matrix element and, for each ϕ_j, also $\exp(ikr_j)/r_j$ and the scattering factor. Flux conservation also dictates that the portion of ϕ_0 which passes to the scatterer j to produce ϕ_j decays in amplitude as a spherical wave, or as $1/r_j$. This decay is a principal reason why PD and AED are short-range probes, although the effects of inelastic scattering contribute additionally to this. If the scattering angle is θ_j, the overall path length difference (PLD) between ϕ_0 and any ϕ_j is $r_j(1 - \cos\theta_j)$, and it is these PLDs that provide most of the bond-length information in photoelectron or Auger electron diffraction.

3.1.2. Matrix Elements and Final-State Interference

When this model has been applied to photoelectron emission, the dipole matrix element has usually been treated as involving a p-wave final state (that is, the case that is appropriate for emission from an s subshell). This yields a matrix-element modulation of the form $\hat{\varepsilon} \cdot \hat{\mathbf{k}}$ for an arbitrary direction of emission $\hat{\mathbf{k}}$.[21,41] For emission from other subshells with l not equal to zero, more complex expressions including both of the interfering $l + 1$ and $l - 1$ channels are involved,[43,45–47] and we return below to consider how important these effects can be. However, at higher energies, the assumption of a p-wave final state has been found to be reasonably adequate in several prior studies of non-s emission.[9,10,48–50]

Since the differential photoelectric cross section $d\sigma_{nl}(\hat{\varepsilon}, \mathbf{k})/d\Omega$ is proportional to intensity rather than amplitude, another possible approximation might be to use a ϕ_0 modulation of $[d\sigma_{nl}(\hat{\varepsilon}, \mathbf{k})/d\Omega]^{1/2}$.[51] Although this is not strictly correct and it also does not account for possible sign changes in the matrix element with direction due to the photoelectron parity,[15,52] it may be a reasonably adequate approximation for higher-energy XPD in which the forward-dominated electron-scattering process selects out $\mathbf{r}_j$ choices very nearly parallel to $\mathbf{k}$. That is, for the range of $\mathbf{r}_j$ directions near the $\mathbf{k}$ direction that produce significant scattering, the matrix element varies little, so that a very precise description of it is not required. In fact, predicted XPD patterns have not been found to be very sensitive to the

exact way in which the matrix-element modulation is included. At lower energies, such simplifications are not generally possible, however, and Treglia[53] has, for example, recently shown that not using the correct final-state angular momenta can have a strong effect on predicted azimuthal diffraction patterns at energies of about 30 eV.

Such final-state momentum and interference effects have been studied in more detail recently by Friedman and Fadley,[47] who have made use of a newly developed Green's function matrix approach due to Rehr and Albers.[54] Representative results as a function of electron kinetic energy are presented in Fig. 4. Here, a Cu emitter is 3.5 Å away from a single Cu scatterer, and three different electron kinetic energies of 100, 300, and 1000 eV are considered. Scattering is in all cases full spherical wave. The intensity fluctuations as a function of scattering angle are normalized to the unscattered intensity I_0 as $\chi = [I - I_0]/I_0$. In order to illustrate in these calculations only the effects of changing the final-state angular momenta that are involved, emission from a Cu 2*p* orbital was taken as a reference. For this *p*-emission case, the correct final-state interference involves *s*

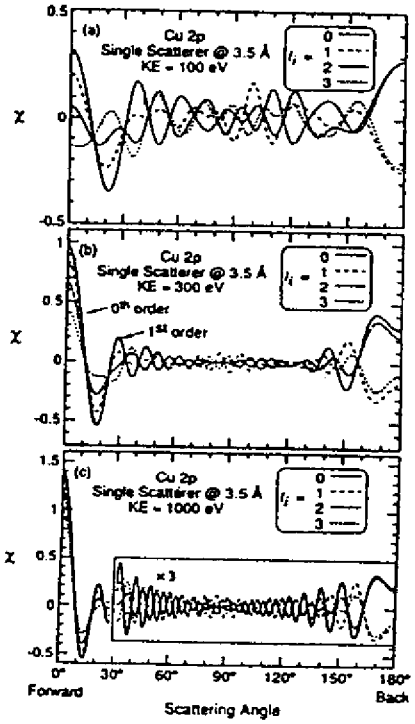

FIGURE 4. Theoretical calculations of electron scattering from a single Cu atom at a distance of 3.5 Å from the emitter and for energies of (a) 100 eV, (b) 300 eV, and (c) 1000 eV. Intensity is shown as the normalized function $\chi = (I - I_0)/I_0$. Full spherical-wave (SW) scattering is used, and different final-state assumptions are compared: l_f = 0 (*s* to a single *p* channel), l_f = 1 (*p* to interfering *s* + *d* channels), l_f = 2 (*d* to *p* + *f*), and l_f = 3 (*f* to *d* + *g*). The radiation is taken to be unpolarized, with the plane of polarization lying in the plane of r_{Cu} and k. Note the sign reversals due to photoelectron parity in the backscattering direction. (From Ref. 47.)

and *d* waves, and includes the radial matrix elements R_s and R_d and the phase shifts δ_s and δ_d. These have been calculated using an atomic cross-section program due to Manson.[55] The ratio R_d/R_s changes relatively little, from 4.62 to 3.91, as we go from 100 eV to 1000 eV. The curves shown for $l_f = 0$ are the simple limit, discussed previously, of an *s* initial state and single *p* final state with no interference. The results for $l_i = 1$ are the correct description of Cu 2*p* emission. For the other two cases of $l_i = 2$ and $l_i = 3$ shown, emission into final waves at $l_f = 1$ and 3 and $l_f = 2$ and 4, respectively, is allowed, and the same radial matrix elements R_s and R_d and phase shifts δ_s and δ_d were used for the $l_f = l_i + 1$ and $l_f = l_i - 1$ channels in both cases. These sets of four curves thus permit systematically observing only the effect of the different final-state character and interference associated with the dipole matrix element.

Several general conclusions can be drawn from the curves of Fig. 4:

- Increasing the angular momenta in the final state from 1 to 0 + 2 to 1 + 3 to 2 + 4 is found to decrease systematically the amplitude of forward scattering, thus constituting a reason for which calculations using the *p* final state may overpredict the degree of anisotropy for emission from subshells with $l_i \geq 1$.
- In the backscattering direction, the parity of the photoelectron waves is evident, since the odd waves from $l_i = 0$ and 2 exhibit the same sign of χ, and the opposite sign is seen for the even waves from $l_i = 1$ and 3. The previously discussed approximation of using the square root of the differential cross section neglects these sign differences. It implicitly assumes photoelectron waves of even character unless an *ad hoc* sign change is introduced as appropriate for emission angles greater than 90° with respect to the polarization vector.[15]
- The smallest differences between different final-state angular momenta are for the highest energy, where, in the dominant forward direction, the main effect is a reduction of amplitudes in the forward scattering direction, but little change occurs in the shapes of the '0th-order' peak at a scattering angle of 0° and, for $l_i < 3$, also in the 1st-order peak at about 22°. However, as energy is decreased to 100 eV, the differences between the curves become increasingly more significant, and they begin also to involve phase changes in the regions of both of these peaks nearest forward scattering.
- At the highest energy typical of the XPS limit, one thus expects the general shape of the 0th order or forward scattering peak to be the same regardless of final-state angular momenta, and to see a general suppression of the relative importance of the higher-order features.

Overall, these results indicate that the use of the correct final-state angular momenta with interference will probably be important for energies below about 500 eV. For higher energies of 1000 eV or move, forward scattering should be reasonably well treated by the simple *p* final state (as has been verified in prior XPD studies), although both overall anisotropies and the relative intensities of higher-order features may be overestimated. Similar conclusions concerning the suppression of higher-order diffraction features have been reached by both Parry[46] and Sagurton[56] using more approximate calculations based upon plane-wave scattering and/or plane-wave final states.

Keeping in mind the discussion of the last paragraphs, we shall for simplicity and heuristic reasons in what follows still use the p final state and its factor $\hat{\epsilon} \cdot \hat{\mathbf{k}}$ in describing photoelectron emission.

3.1.3. Electron–Atom Scattering

The electron–atom scattering that produces ϕ_j is most simply described by a complex plane-wave (PW) scattering factor

$$f_j(\theta_j) = |f_j(\theta_j)| \exp[i\psi_j(\theta_j)]. \tag{3}$$

where $\psi_j(\theta_j)$ is the phase shift associated with the scattering. The scattering factor is in turn calculated from partial-wave phase shifts δ_l according to the usual expression:

$$f(\theta) = (2ik)^{-1} \sum_{l=0}^{\infty} (2l + 1)[\exp(2i\delta_l) - 1]P_l(\cos\theta), \tag{3'}$$

where the P_l are Legendre polynomials. For large r, the scattered wave ϕ_j is thus proportional to $f_j(\theta_j) \exp(ik|\mathbf{r} - \mathbf{r}_j|)/|\mathbf{r} - \mathbf{r}_j|$, with an overall phase shift relative to ϕ_0 of $kr_j(1 - \cos\theta_j) + \psi_j(\theta_j)$ that is due to both path-length difference and scattering. The use of this form for ϕ_j implicitly assumes that the portion of ϕ_0 incident on the jth scatter has sufficiently low curvature compared to the scattering potential dimensions to be treated as a plane wave. This is the so-called small-atom approximation,[57] and its limitations in comparison to the more accurate spherical-wave (SW) scattering[21,25,58,59] of Fig. 4 are discussed below.

The PW scattering factor $f_j(\theta_j)$ is thus determined by applying the partial-wave method to a suitable spherically symmetric scattering potential for each atomic type in the cluster. The number of partial-wave phase shifts needed for convergence goes up with energy, and for a typical scattering potential of effective radius 1.5 Å would be $\gtrsim 8$ for $E_{kin} = 500$ eV and $\gtrsim 24$ for 1500 eV. Tabulations of free-atom scattering factors at energies going up to the XPS regime also exist.[60] Alternatively, scattering potentials more appropriate to a cluster of atoms with overlapping charge densities and potentials can be constructed via the muffin-tin model employed, for example, in LEED theory.[61] The free-atom f_j is generally larger in magnitude in the forward direction than its muffin-tin counterparts due to the neglect of charge and potential overlap.[42] Both types of f_j have been employed in higher-energy PD and AED calculations, and they usually do not yield markedly different $I(\mathbf{k})$ curves, although the use of the free-atom f_j is expected to predict slightly higher peak intensities due to its larger amplitudes in the forward direction. The PW scattering factor amplitudes in Fig. 2 were calculated using the more accurate muffin-tin procedure. Whatever procedure is used to calculate these scattering factors, there are two useful generalizations concerning their behavior as atomic number is varied:

- The forward scattering amplitude $|f_j|$ at higher energy is found to be primarily sensitive to the radius of the atom (or muffin tin) involved. It is for this reason that free-atom forward scattering amplitudes are always larger than those for a muffin tin in which the potential is effectively truncated at the tin radius. This behavior can be rationalized by a classsical argument in which it is noted that forward scattering trajectories graze the outer reaches of the scattering potential and so are only deflected slightly; these trajectories are thus primarily sensitive to the outer regions of the potential.
- The backscattering amplitude at higher energy is by contrast found to increase monotonically with atomic number. This also is expected from a classical argument in which backscattering involves strongly deflected trajectories that pass close to the nucleus.

3.1.4. Inelastic Scattering

The effects of *inelastic* scattering on wave amplitudes during propagation below the surface must also be included. If intensity falls off as $\exp(-L/\Lambda_e)$, where L is an arbitrary path length below the surface and Λ_e is the inelastic attenuation length, then *amplitude* is expected phenomenologically to fall off as the square root of this or $\exp(-L/2\Lambda_e) \equiv \exp(-\gamma L)$. Each wave ϕ_0 or ϕ_j is multiplied by such an exponential factor involving an L value which includes the total path length below some surface cutoff point (cf. Fig. 3*a*). This surface cutoff is often chosen to be the substrate surface as defined by hard-sphere atoms,[42] although this choice should not influence the diffraction patterns unless some atoms are positioned above the cutoff. Thus, the attenuation coefficient $\gamma = 1/2\Lambda_e$, although γ values up to 1.3–2 times this have been suggested in prior EXAFS,[41,62] AED,[12] and PD[42,48,63] analyses. That is, the effective inelastic attenuation length Λ_e in these diffraction experiments is suggested to be about 0.50–0.75 times literature values based upon intensity-attenuation measurements or theoretical calculations.[64] In fact, some inelastic attenuation lengths derived from EXAFS measurements do not appear to take account of the difference between amplitude and intensity mentioned above.[62]

These reduced values of Λ_e are not surprising in view of several factors: Uncertainties of at least ±20% are common in measurements of attenuation lengths,[64,65] and some recent measurements in fact yield values that are significantly lower than others in the literature.[65] The effects of elastic scattering and diffraction on intensities can introduce additional uncertainties of this order,[66,67] and it is, for example, now well recognized that the actual mean free path between inelastic scattering events is about 1.4 times the attenuation length discussed above. Finally, the effective attenuation length in a diffraction measurement should be shorter than in a simple intensity-attenuation experiment, because quasielastic scattering events of small energy (e.g., from phonons) that leave the electron kinetic energy within the peak being measured[68] can still introduce direction changes and phase shifts that effectively remove such electrons from the coherent intensity for diffraction. In addition, multiple elastic-scattering events similarly cause a reduction of the effective coherent intensity in a single-scattering theory. Thus, one overall expects effective attenuation lengths related as Λ_e(intensity) > Λ_e(multiple-scattering diffraction) > Λ_e(single-scattering diffraction).

Fortunately, electron diffraction features for most cases are not strongly affected by varying Λ_e over its plausible range, and so its choice is in general not crucial to final structural conclusions. Nonetheless, it is desirable to verify this insensitivity by varying Λ_e in model calculations.[42,48,63]

3.1.5. Vibrational Effects

Vibrational attenuation of interference effects is furthermore potentially important and can be included in the simplest way by multiplying each ϕ_j by its associated temperature-dependent Debye–Waller factor:

$$W_j(T) = \exp[-\Delta k_j^2 \overline{U_j^2}(T)] = \exp[-2k^2(1 - \cos\theta_j)\overline{U_j^2}(T)], \quad (4)$$

where Δk_j is the magnitude of the change in wave vector produced by the scattering, and $\overline{U_j^2}(T)$ is the temperature-dependent one-dimensional mean-squared vibrational displacement of atom j. At this level of approximation, $\overline{U_j^2}$ is assumed to be isotropic in space, and any correlations in the movements of near-neighbor atoms are neglected. (The importance of *correlated* vibrational motion in certain types of lower-energy diffraction experiments is considered below.) Suitable bulk and surface $\overline{U_j^2}$ values or Debye temperatures can be obtained from the literature. At high energy, the electron scattering is significant only when θ_j is rather close to zero, and this acts through the $(1 - \cos\theta_j)$ factor in the argument of Eq. (4) to yield W_j very close to unity for all important scattered waves. So vibrational effects are to first order not very significant in forward-scattering-dominated XPD or AED, although they can be very important in LEED, EXAFS, and lower-energy PD and AED, where backscattering is the dominant diffraction mode and thus $1 - \cos\theta_j$ is a maximum.

An alternate method for allowing for vibrational effects is to assume some probability distribution of atomic positions due to vibration (as, for example, a harmonic-oscillator envelope) and then to numerically sum separate weighted diffraction intensities for all possible combinations of atomic positions. This is cumbersome, but it has been used to quantitatively look at the effects of specific types of wagging molecular vibrations at surface.[23,69]

3.1.6. Single-Scattering Cluster Model

With these assumptions, the simplest SSC–PW expression for photoelectron intensity $I(\mathbf{k})$ can now be written down from Eqs. (1–3) as

$$I(\mathbf{k}) \propto \int \left| \hat{\boldsymbol{\varepsilon}} \cdot \hat{\mathbf{k}} e^{-\gamma L} + \sum_j \frac{\hat{\boldsymbol{\varepsilon}} \cdot \hat{\mathbf{r}}_j}{r_j} |f_j(\theta_j)| W_j e^{-\gamma L_j} \{\exp i[kr_j(1 - \cos\theta_j) + \psi_j(\theta_j)]\} \right|^2 d\hat{\boldsymbol{\varepsilon}}$$
$$+ \sum_j \int (\hat{\boldsymbol{\varepsilon}} \cdot \hat{\mathbf{r}}_j)^2 \frac{|f_j(\theta_j)|^2}{r_j^2} (1 - W_j^2) e^{-2\gamma L_j} d\hat{\boldsymbol{\varepsilon}}. \quad (5)$$

Here, $\hat{\boldsymbol{\varepsilon}} \cdot \hat{\mathbf{k}}$ and $\hat{\boldsymbol{\varepsilon}} \cdot \hat{\mathbf{r}}_j$ represent p-wave photoemission matrix-element modulations along the unit vectors $\hat{\mathbf{k}}$ and $\hat{\mathbf{r}}_j$, respectively, and $\exp(-\gamma L)$ and $\exp(-\gamma L_j)$ are

appropriate inelastic attenuation factors. Thus, $(\hat{\boldsymbol{\varepsilon}} \cdot \hat{\mathbf{k}}) \exp(-\gamma L)$ is the amplitude of the direct wave $\phi_0(\mathbf{r}, \mathbf{k})$ and $(\hat{\boldsymbol{\varepsilon}} \cdot \hat{\mathbf{r}}_j) |f_j(\theta_j)| W_j \exp(-\gamma L_j)/r_j$ is the effective amplitude of $\phi_j(\mathbf{r}, \mathbf{r}_j \rightarrow \mathbf{k})$ after allowance for both inelastic scattering and vibrational attenuation of interference. The complex exponential allows for the total final phase difference between ϕ_0 and each ϕ_j.

The integrals on $\hat{\boldsymbol{\varepsilon}}$ simply sum over the different polarizations perpendicular to the radiation progagation direction, as appropriate to the particular case at hand. Closed-form expressions for a totally unpolarized source that are applicable to high-energy work are given elsewhere;[42] however, the simplest way to carry out this integration for a general case is just to sum the intensities for two perpendicular polarizations of convenient orientation.

The second $\sum_j$ corrects the first absolute value squared for the incorrect inclusion of Debye–Waller attenuations in terms involving a product of a scattered wave with itself. That is, in expanding the absolute value squared, only products involving unlike waves like $\phi_0 \phi_j^*$ or $\phi_j \phi_l (j \neq l)$ should include Debye–Waller products of W_j or $W_j W_l$, respectively. The $(1 - W_j^2)$ factor in the second summation is thus necessary to yield overall correct products of the form $\phi_j \phi_j^*$ without any W_j^2 factor. The second sum has been called thermal diffuse scattering,[40] and it is often quite small with respect to the overall modulations. Equation (5) is thus the basic starting point of the single-scattering cluster model.

In modifying this model to describe Auger emission, the usual assumption is that the much freer mixing of angular momenta in the final state overall leads to an outgoing wave with s character.[12,40,70–73] Although selection rules do limit the allowed final angular momentum states in Auger emission,[72] for certain cases, the $l = 0$ channel is dominant. Also, if filled subshells are involved in both the initial and final levels of the transition, the implicit sums over all initial and final m_l values would be expected to produce an overall distribution of emitted primary intensity that could be approximated as an s wave. Although it is possible for higher-l components to be present in the final state that could affect the scattering,[72,73] these are often found at higher energies to be minor effects.[12,70,71] For Auger emission into such an assumed s final state, we thus simply remove all factors involving $\hat{\boldsymbol{\varepsilon}} \cdot \hat{\mathbf{k}}$ and $\hat{\boldsymbol{\varepsilon}} \cdot \hat{\mathbf{r}}_j$ in Eq. (5). Non-s character in Auger final states deserves further study however.

It is also worth noting here that the cluster sum on j in Eq. (5) makes no explicit use of the 2- or 3-dimensional translational periodicities that may be present, even though the atomic coordinates $\mathbf{r}_j$ used as inputs may incorporate such periodicities. Thus, neither surface- nor bulk-reciprocal lattice vectors $\mathbf{g}$ are explicitly involved, and it is not appropriate at this level of description to speak of diffraction "beams" associated with certain $\mathbf{g}$ vectors as in LEED. However, in section 5.1 we will consider the relationship of this model to an alternative Kikuchi-band picture that does involve $\mathbf{g}$ vectors and the idea of Bragg reflections from sets of planes.

The last parameter of importance in actually using Eq. (5) is the range of j or the choice of a suitable cluster of atoms. This is done empirically so as to include all significant scatterers by verifying that the predicted diffraction patterns do not change in any significant way with the addition of further atoms at the periphery of the cluster. Clusters can range from a few atoms for near-normal high-energy emission from a vertically oriented diatomic molecule on a surface[23] to as many as

several hundred atoms for substrate emission in which both the emission and the scattering must be summed over several layers into the bulk.[42] In the latter case, each structurally unique type of atom emits incoherently with respect to the other, so that intensities from each must be added layer by layer. However, even for the largest clusters so far considered, the inherent simplicity of Eq. (5) still yields calculations which do not consume excessive amounts of computer time, especially by comparison with those necessary for such procedures as multiple-scattering LEED simulations.

A further physical effect of importance in making comparisons to experiment is the possibility of electron refraction at the surface in crossing the surface barrier or inner potential of height V_0. Even at the relatively high energies of XPS, for emission angles near grazing, refraction effects of a few degrees can be produced (cf. Fig. 14 in Ref. 9). Thus, for lower takeoff angles relative to the surface and/or lower kinetic energies, a proper allowance for refraction is necessary. This is accomplished most simply by using a suitable inner potential V_0 derived from experiment and/or theory to predict the internal angle of emission θ' for a given external propagation direction θ.[9] The resulting expression for an electron energy of $E'_{kin} = E_{kin} + V_0$ inside the surface is

$$\theta' = \cos^{-1}\left\{\left[\frac{E_{kin}}{E_{kin} + V_0}\right]^{1/2} \cos\theta\right\}, \tag{6}$$

where, as before, θ and θ' are measured with respect to the surface. In the presence of an adsorbate, the exact form of the surface potential barrier thus becomes important, as it may not then be possible to assume an abrupt rise to the vacuum level at the substrate surface. Also, the presence of adsorbate atoms may alter V_0 through changes in the work function, and these atoms also may occupy positions above the surface in which only a fraction of V_0 is appropriate. In some photoelectron diffraction studies, V_0 has also been treated as an adjustable parameter.[20,25,63] Although prior studies indicate that structural conclusions are not particularly sensitive to the choice of V_0,[25,42] it is important to realize that not allowing for it properly may shift theoretical diffraction patterns by as much as a few degrees with respect to the actual θ values at which they will be observed. The precise method of allowing for inner potential and related image–force effects has also been considered in more detail theoretically.[25]

We stress also at this point that any uncertainties in final structures associated with the choices of nonstructural parameters such as the scattering phase shifts, the attenuation length for inelastic scattering, vibrational attenuation, and the inner potential are equally well shared with the techniques of LEED, EXAFS, and SEXAFS, although in EXAFS/SEXAFS, empirical phase shifts from known structures can sometimes be used.

A final step in any realistic calculation based upon this model is to integrate the direction of emission $\mathbf{k}$ over the solid angle Ω_0 accepted into the electron analyzer. For most of the calculations reported here, this has been over a cone of ±3.0–3.5° half angle, although for certain high-resolution cases a smaller cone of ±1.0–1.5° has been used.

3.1.7. Improvements to the Model

We now consider some possible improvements to this simple SSC–PW model:

- A first possible correction is to choose a *more correct form for the primary wave as it leaves the emitter*. The SSC–PW result of Eq. (5) assumes a simple outgoing plane wave from the emitter which then scatters to produce an outgoing spherical wave from each scatterer. In fact, the correct primary wave should be of the type used in free-atom photoelectric cross sections and should consist of an ingoing spherical wave plus the outgoing plane wave.[21,41,45,74] Such a primary wave experiences the emitter potential and represents the correct solution to the Schrödinger equation inside of a muffin-tin-like region centered on the emitter. If this form of the primary wave is used, the equivalent of Eq. (5) with neglect of effects due to vibrations is:[21,41]

$$I(\mathbf{k}) \propto \int \left| \hat{\boldsymbol{\epsilon}} \cdot \hat{\mathbf{k}} e^{-r_L} + \sum_j \frac{\hat{\boldsymbol{\epsilon}} \cdot \hat{\mathbf{r}}_j}{r_j} |f_j(\theta_j)| e^{-r_{L_j}} \{\exp i[kr_j(1 - \cos\theta_j) + \psi_j(\theta_j)]\} \right.$$
$$\left. + \sum_j \frac{\hat{\boldsymbol{\epsilon}} \cdot \hat{\mathbf{r}}_j}{r_j^2} f_j(\pi) f_{sm}(\pi - \theta_j) e^{-r(L+2r_j)} \{\exp i[2kr_j]\} \right|^2 d\hat{\boldsymbol{\epsilon}}. \tag{7}$$

This result, although still single scattering in assumption, now contains, through the scattering of the incoming wave, a second sum of terms that are the classic double scattering events of the type emitter → scatterer → emitter → detector discussed in EXAFS theory.[41] Because these added terms are in effect double scattering and also exhibit stronger attenuation due to both $1/r_j^2$ and e_j^{-2r}, this sum is expected for many cases to be a small correction to Eq. (5). This should be especially true for higher energies where backscattering is negligible. In fact, the inclusion of this sum can be shown to lead to the central-atom (emitter) phase shift that is always present in EXAFS theory, and we comment further on this later in this section.

- A next important correction is the use of *spherical-wave (SW) scattering* instead of the asymptotic and much simpler plane-wave (PW) scattering. The nature of such SW corrections in reducing forward scattering amplitudes in XPD was first pointed out some time ago,[23] but more recent studies have presented detailed comparisons of PW and SW results for different systems.[58,59] For example, Fig. 5 compares PW and SW scattering at energies from 50 eV to 950 eV,[58] with the results being displayed in a format identical to that of Fig. 4. Emission from an s level ($l_i = 0, l_f = 1$) to a single Ni scatterer 2.49 Å away is considered. For larger scattering angles (≳40°) and higher energies (≳200 eV), the PW and SW results are essentially identical. However, for lower energies and in the forward scattering direction, there are significant differences. In particular, for energies ≳100 eV, the forward scattering peak is significantly reduced in amplitude by a factor that can be as low as 0.5. As expected, the differences between PW and SW curves also decrease as the scatterer is moved away from the emitter,[58] because in the limit of a scatterer at infinity, the incident wave is

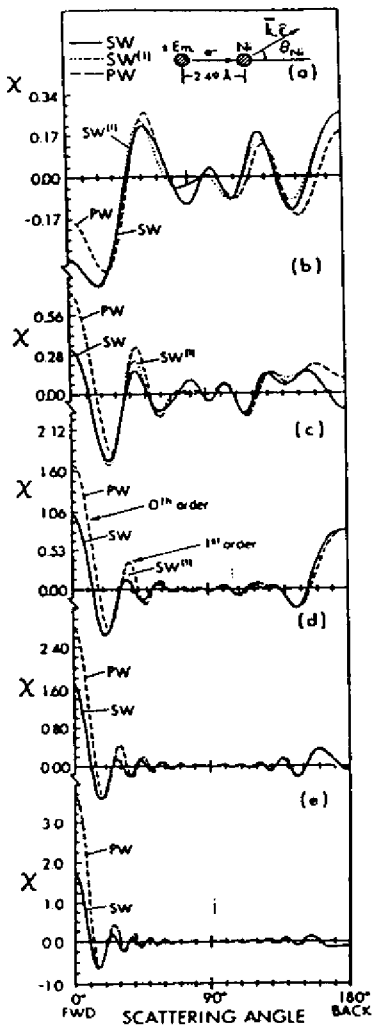

FIGURE 5. As in Fig. 4, but comparing plane-wave (PW) and spherical-wave (SW) scattering from a single Ni scatterer at a distance of 2.5 Å from the emitter with energies of (a) 50 eV, (b) 100 eV, (c) 200 eV, (d) 500 eV, and (e) 950 eV. Here, PW results are compared to SW results for the case of $l = 0$ (s emission to a single p channel). Polarization is parallel to the emission direction. The curves labelled $SW^{(1)}$ represent a first-order approximation to the full SW scattering. (From Refs. 21 and 58.)

planar. One general conclusion from these results is thus that, at higher energies, the primary effect of including curvature in ϕ_0 is to reduce the amplitudes of the forward-scattering peaks in $I(\mathbf{k})$ for near-neighbor atoms as compared to those predicted from Eq. (3).

Fortunately, such SW corrections can now be very simply and accurately

incorporated into the SSC framework via effective SW scattering factors developed by Barton and Shirley using a Taylor-series magnetic quantum number expansion (MQNE)[25] and by Rehr *et al.* using separable Green's function approaches.[45,54] For example, Rehr *et al.*[45] derive an equation identical to Eq. (7) in form, but in which the plane-wave scattering factors $f_j(\theta)$ are replaced by three effective spherical-wave scattering factors $f^{(1)}_{j,\text{eff}}(\theta, r_j)$, $f^{(2)}_{j,\text{eff}}(\pi, r_j)$, and $f^{(3)}_{\text{em,eff}}(\pi - \theta, r_j)$ that are used to describe the three types of scattering events present. These effective scattering factors depend on r_j, as they must converge to the PW result as r_j goes to infinity. They are also very simply calculable, involving expressions closely related to that in Eq. (3').

However, particularly at higher energies, the much simpler PW approximation is still found to yield results very similar in form to those with SW scattering, and it has been found possible to draw useful structural conclusions with it. Sometimes, PW scattering at high energy has been used together with an empirical reduction factor of forward scattering amplitudes by a factor of 0.4–0.5[42] that can be largely justified as being due to SW effects (cf. Fig. 5).

• An additional important correction for some cases is the use of *correlated vibrational motion* in which atoms that are near neighbors of the emitter have lower vibrational amplitudes relative to the emitter, and thus Debye–Waller factors for diffraction that are nearer unity. This correction is more important in special geometries and at lower energies for which large-angle or, particularly, backscattering events become more important, as first pointed out in connection with the interpretation of scanned-energy data by Sagurton *et al.*[21] and also discussed by Barton and Shirley.[25] This more correct form for vibrational attenuation involves a factor W_j^{corr} of the form:[21]

$$W_j^{\text{corr}}(T) = \exp\left[\frac{-\Delta k_j^2 \sigma_j^2(T)}{2}\right] = \exp\left[-k^2(1 - \cos\theta_j)\sigma_j^2(T)\right], \tag{8}$$

where $\sigma_j^2(T) = \langle(\Delta\hat{\mathbf{k}}_j \cdot \mathbf{u}_j)^2\rangle$ is a thermal average of the projection of the atomic displacement $\mathbf{u}_j$ as measured with respect to the emitter onto the direction of the change in wave vector produced by the scattering $\Delta\hat{\mathbf{k}}_j$. Thus, each scatterer in a photoelectron diffraction experiment is sensitive to a different type of vibrational displacement, varying from no effects for forward scattering, to small effects for small-angle scattering associated with components of $\mathbf{u}_j$ perpendicular to the emitter–scatterer axis, to maximum effects for backscattering associated with components of $\mathbf{u}_j$ along this axis. By contrast, in SEXAFS, it is only the along-axis components that contribute. Correlation effects are also expected to be largest for atoms that are backscatterers, because along-axis vibrations will be reduced more than those perpendicular to this axis. Ultimately, this might make it possible to measure anisotropies in vibration in a more precise way with temperature-dependent photoelectron diffraction, for example, by looking at the variation of different peaks in Fourier transforms of scanned-energy data. A first attempt at this has recently been made by Wang *et al.*[75] Also, even forward scattering features at high energy contain vibrational information because of peak broadening by motion perpendicular to a bond,[23,69] and this has permitted

Wesner *et al.*[76] to determine the vibrational amplitude anisotropy for an adsorbed molecule, as discussed further in section 4.1.3.

• A final aspect of the model which might be improved but which has only been discussed in a limited way to date is *more accurate allowance for both surface refraction and attenuation due to inelastic scattering*. Refraction has been treated differently from the phenomenological approach indicated here both by Lee[41] and by Tong and Poon,[77] who have considered the proper matching of the attenuated photoelectron wave inside the surface to the free electron wave outside the surface. However, the latter have found that, if refraction is allowed for in the way described here in calculating the path length for inelastic scattering in approaching the surface, the net result is very little different from the correct treatment of the wave matching. Another more complex problem is choosing the proper value for the inelastic attenuation length: As we have noted above, these lengths in electron-diffraction problems appear empirically to be only about 0.5–0.75 times the typical literature values based upon intensity attenuation. It would be desirable to understand these attenuation lengths more quantitatively, including both elastic and inelastic effects, for example, within the framework of more accurate methods of measuring peak intensities developed by Tougaard.[78] Finally, it might be useful to consider the possibility of *nonuniform or anisotropic inelastic scattering*. Such effects have been considered in both LEED[79a] and EXAFS,[79b] where the use of complex scattering phase shifts is proposed; but the influence of such effects on predicted diffraction patterns in PD or AED has not been assessed. More recently, Treglia *et al.*[80a] have used SSC–SW calculations to describe very low energy photoelectron diffraction at about 30 eV from different surfaces of *W*. They see evidence for a significantly different inelastic attenuation length in emission from W (001) and W (110). This could well be possible, but at this low energy, it would also be useful to carry out full MS calculations to eliminate such effects as another cause of effective anisotropic attenuation. In another recent paper, Frank *et al.*[80b] have discussed Auger electron diffraction data from Pt(111) with various adsorbates and for energies varying from about 65 eV to 420 eV. They have analyzed these results in terms of a classical model of anisotropic inelastic attenuation which totally neglects all wave inteferences and diffraction phenomena. Unfortunately, there is no basis in prior experiment or theory for this extreme model, even though it seems to fortuitously fit some of the features in the experimental data. Thus, this classical analysis by Frank *et al.* provides neither a useful method for analyzing AED data, nor any new information concerning the possibility of anisotropic inelastic attenuation. Such attenuation is in any case expected to produce only small corrections to the strong anisotropies associated with diffraction effects.

3.1.8. Relationship to EXAFS/SEXAFS Theory

As a further aspect of the SSC model, we note that it can be directly reduced to an expression very close to that used in EXAFS/SEXAFS analyses if it is assumed that all scattered waves ϕ_j are small in magnitude in comparison to ϕ_0.[15] Then, if we begin at Eq. (5) (for simplicity neglecting any averaging over $\hat{\boldsymbol{\varepsilon}}$), we see that all terms such as $\phi_j\phi_j^*$ and $\phi_j\phi_j^*$ can be neglected in expanding the absolute value squared. The thermal diffuse scattering term can also be neglected. After some simple algebra, it can then be shown that

$$I(\mathbf{k}) \propto (\hat{\boldsymbol{\varepsilon}}\cdot\hat{\mathbf{k}})^2 e^{-2\gamma L} + 2(\hat{\boldsymbol{\varepsilon}}\cdot\hat{\mathbf{k}})e^{-\gamma L}\sum_j \frac{\hat{\boldsymbol{\varepsilon}}\cdot\hat{\mathbf{r}}_j}{r_j}|f_j(\theta_j)|\,W_j e^{-\gamma L_j} \times \cos[kr_j(1-\cos\theta_j)+\psi_j(\theta_j)]. \quad (9)$$

and that this can be converted to a normalized function $\chi(\mathbf{k})$ if we take the unscattered intensity to be $I_0 = (\hat{\boldsymbol{\varepsilon}}\cdot\hat{\mathbf{k}})^2 e^{-2\gamma L}$ and finally write

$$\chi(\mathbf{k}) \equiv \frac{I(\mathbf{k})-I_0}{I_0} \propto \frac{2}{(\hat{\boldsymbol{\varepsilon}}\cdot\hat{\mathbf{k}})e^{-\gamma L}}\sum_j \frac{\hat{\boldsymbol{\varepsilon}}\cdot\hat{\mathbf{r}}_j}{r_j}|f_j(\theta_j)|\,W_j e^{-\gamma L_j} \times \cos[kr_j(1-\cos\theta_j)+\psi_j(\theta_j)]. \quad (10)$$

This last equation thus has a form very close to the standard kinematical expression for EXAFS/SEXAFS, with the only differences being that double scattering events of the type emitter → scatterer → emitter → detector in Eq. (7) are included in the integration over direction in EXAFS to better describe the primary wave,[41] with these producing the central-atom phase shift; and the integration over direction changes the cosine function here finally to a sine function for EXAFS/SEXAFS. Equations (9) and (10) were first used in connection with the interpretation of ARPEFS data by Orders and Fadley,[15] and they have later been refined in this context by Sagurton *et al.*[21] Their form also suggests the possibility of using Fourier transform methods in scanned-energy PD to derive information concerning the set of path-length differences associated with a given structure, as discussed first by Hussain *et al.*[14] and now in active use by Shirley and co-workers[20,25] as a preliminary step of ARPEFS analysis.

As a final comment concerning this level of the diffraction theory, we consider the conservation of photoelectron flux. In the small-atom (or large r_j) limit, where PW scattering is adequate, the usual optical theorem assures that flux will be conserved if it is integrated over 4π.[81] Thus, even if high-energy scattering produces forward-scattering peaks, there will be, somewhere else, sufficient phase space with reduced intensity to exactly cancel them. However, in using the SSC–PW model for cases in which some scatterer distances require SW corrections, it is doubtful that flux will be conserved properly.[40] Nonetheless, with SW scattering correctly included, Rehr *et al.*[45] have shown that their SW equivalent of Eq. (7) does conserve flux and lead to a generalized optical theorem on each l channel involved.

In subsequent sections, we will consider several applications of this SSC model to the interpretation of experimental data, including especially several substrate and adsorbate systems of known geometry to test the degree of its validity.

3.2 *Effects beyond Single Scattering*

Finally, the possible importance of multiple scattering (MS), particularly along rows of atoms in a multilayer substrate, has been discussed qualitatively for some time,[9,42] and more recent papers have presented quantitative estimates of such effects and suggested improved methods for including MS corrections if they

are needed.[24,25,54,82-84] In general, the MS analogue of Eq. (2) can be written as

$$\psi(\mathbf{r},\mathbf{k}) = \phi_0(\mathbf{r},\mathbf{k}) + \sum_j \phi_j(\mathbf{r},\mathbf{r}_j \rightarrow \mathbf{k}) + \sum_j \sum_k \phi_{jk}(\mathbf{r},\mathbf{r}_j \rightarrow \mathbf{r}_k \rightarrow \mathbf{k}) + \sum_j \sum_k \sum_l \phi_{jkl}(\mathbf{r},\mathbf{r}_j \rightarrow \mathbf{r}_k \rightarrow \mathbf{r}_l \rightarrow \mathbf{k}) + \sum_j \sum_k \sum_l \sum_m \phi_{jklm}(\mathbf{r},\mathbf{r}_j \rightarrow \mathbf{r}_k \rightarrow \mathbf{r}_l \rightarrow \mathbf{r}_m \rightarrow \mathbf{k}) + \text{higher orders}, \quad (11)$$

where events up to fourth order are shown here and, in the multiple scattering sums, the combinations of j, k, l, and m are limited only in that they do not involve consecutive scattering by the same scatterer. Such MS calculations have been done in two basic ways: first by Tong and co-workers using LEED-type methods that require full translational symmetry along the surface,[24] and more

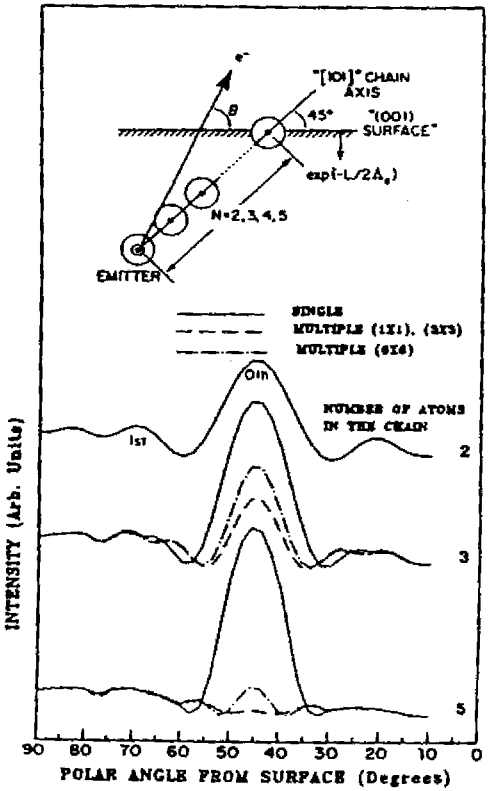

FIGURE 6. Calculated Auger electron diffraction patterns at 917 eV from linear chains of Cu atoms in single and multiple scattering. The geometry of the calculation with the emitter at the base of the chain is shown at the top. The primary outgoing Auger wave is treated as having s character. The multiple scattering results are shown at three levels of the matrix used to describe the scattering: (1 × 1), (3 × 3), and the most accurate, (6 × 6). The (1 × 1) and (3 × 3) cases are found to be superimposable for this case. (From Ref. 84, with similar results also appearing in Refs. 73 and 83(b).)

recently by Barton and co-workers using a cluster approach with SW scattering and the Taylor series MQNE method to simplify the calculations.[25,82,83] The cluster method is really more appropriate to the physics of such a short-range order probe, and we will term it MSC–SW. More recently, Rehr and Albers[54] have proposed a Green's-function matrix method for such MSC–SW calculations that shows promise as an alternate approach in extensive applications by Kaduwela *et al.*[84]

One effect of MS first discussed by Poon and Tong[24] is a defocusing of intensity occurring in multiple forward scattering at higher energies along a dense row of atoms, such that an SSC–PW or SSC–SW calculation along such a row may overestimate the intensity by a factor of two or more. This is illustrated schematically in Fig. 3b(ii). For an embedded species at some distance from the surface but again emitting along such a row, it has more recently been shown that these defocusing effects may be even more dramatic.[73,82,83]

Such defocusing effects have been very nicely illustrated in recent MSC–SW calculations by Barton, Xu, and van Hove[73,82,83] and by Kaduwela *et al.*[84] for emission from chains of Cu atoms of variable length. Some recent results of this type are shown in Figs. 6 and 7. In both figures, chains of 2, 3, or 5 atoms with the emitter at their base are tilted at 45° with respect to the surface of a medium of uniform density that simply serves to attenuate the emitted waves inelastically (see inset in Fig. 6). This geometry thus simulates the intensity distribution expected for emission from the 2nd, 3rd, and 5th layers along a low-index [110]

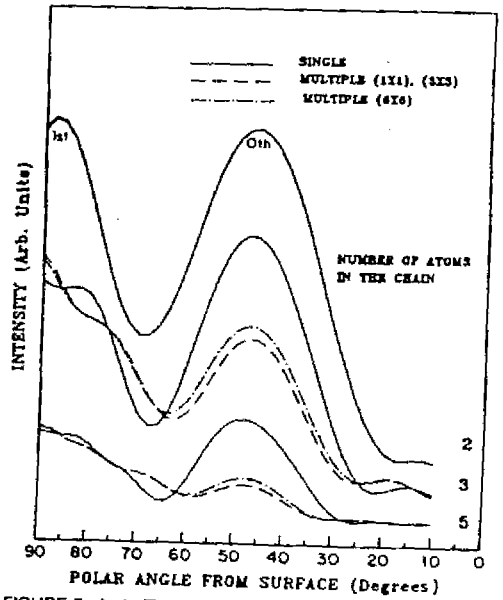

FIGURE 7. As in Fig. 6 (bottom), but for an energy of 100 eV.

row of Cu with (001) orientation, but without any diffraction effects due to scatterers adjacent to the row. Emission into a simple *s*-wave final state approximating Auger emission is treated. Both single-scattering and fully converged (6 × 6) multiple-scattering calculations are shown for each case.

In Fig. 6, for an emission energy of 917 eV, it is clear that the single- and multiple-scattering curves are identical for the two-atom case (as appropriate to a diatomic adsorbate, for example), but they diverge more and more as additional scatterers are added between the emitter and the detector. For the five-atom chain, the forward scattering peak is suppressed to only about 10–15% of its value for single scattering. There is also a systematic narrowing of the width of this peak as more defocussing due to multiple scattering comes into play. For scattering angles more than about ±15° from the chain axis, the differences between single and multiple scattering are much more subtle, as is to be expected since strong multiple forward scattering is no longer possible directly in the emission direction. At the much lower energy of 100 eV in Fig. 7, one expects less strongly peaked forward scattering, as shown by the wider peaks along a polar angle of 45°. Here again, the single-scattering and multiple-scattering results are identical for a two-atom chain, but one sees a suppression and narrowing of the forward scattering peak with increasing chain length that is qualitatively similar to, but less severe than, that observed at the higher energy.

Overall, these and other recently published results by Xu and van Hove[73] indicate that, for emitters in the first one or two layers of a surface and/or for which the emission direction does not involve near parallelism with a dense row of scatterers, a single scattering model should be quite accurate. For atoms further below the surface and/or for emission directions along such high-density rows, certain forward scattering features are expected to be suppressed by multiple scattering, but single-scattering calculations should nonetheless predict their positions with good accuracy.

An additional important multiple scattering effect pointed out by Barton *et al.*[25] is due to strong nearest-neighbor backscattering at lower energies. This they find in certain scanned-energy cases to significantly increase intensity due to events of the type emitter → neighbor → emitter → detector, as illustrated in Fig. 3b(i).

A further important point in connection with such multiple-scattering calculations is that events up to at least the fifth order have to be included to assure reasonable convergence.[25,84] In fact, it is found that including only second-order events can often lead to curves which are in much poorer agreement with experiment than the corresponding first-order calculation![84] This is similar to the experience in EXAFS theory, in which including only lower-order multiple-scattering corrections can yield worse results than those of single scattering.[57,85] A more reasonable procedure is to include events up to, say, the fifth order if the total path length $r_j + r_{jk} + r_{kl} + \cdots$ is less than some cutoff value of 10–20 Å,[20,25,57,85] although an inproved cutoff criterion has been suggested by Kaduwela *et al.*[84]

As noted previously, there is by now a considerable body of data which indicates that useful structural information can be derived at the SSC–SW or even SSC–PW level, and we will show illustrations of this in subsequent sections. Nonetheless, MS effects such as those described above can cause discrepancies

between experiment and theory for certain classes of system, and full MS treatments of both photoelectron and Auger electron diffraction are beginning to be more often used. Several advances in the simplification of these methods, as well as rapid improvements in computer technology, should lead to a greater reliance on MS approaches in future work. In the examples which follow, a variety of theoretical models have been used, and the specific approach followed will be indicated with each set of results to permit the reader to draw his or her own conclusions.

4. ILLUSTRATIVE STUDIES OF DIFFERENT TYPES

4.1. Small-Molecule Adsorption and Orientation

We here consider primarily the case of small-molecule adsorption as studied by higher-energy XPD. The cases treated are thus of considerable interest in studies of surface chemistry and catalysis, and they provide the first simple illustrations of the utility of the forward-scattering peaks discussed in the preceding section. Auger peaks at similar energies of about 1000 eV could also in principle be used for such studies, but all of the cases to date involve photoelectron diffraction.

4.1.1. CO/Ni (001)

We begin with the first system of this type studied by Petersson *et al.*[23] and Orders *et al.*:[69] $c(2 \times 2)$ CO on Ni (001). Figure 8 compares experimental C 1*s*

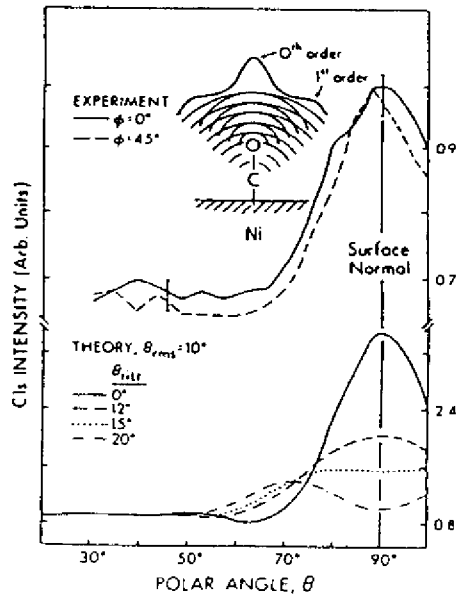

FIGURE 8. Comparison of polar-scan C 1*s* XPD data from $c(2 \times 2)$ CO on Ni (001) at a kinetic energy of 1202 eV with SSC-PW theory. The inset indicates the type of intramolecular forward scattering and interference involved. Note definitions of zeroth-order and first-order effects, as shown also in Figs. 4 and 5. (From Ref. 69.)

polar scans in two high-symmetry azimuths (normalized by dividing by the O 1*s* intensity to eliminate the θ-dependent instrument-response function) to SSC–PW calculations for varying degrees of CO tilt relative to the surface normal.[69] The theoretical model also includes a wagging or "frustrated-rotation" molecular vibration with an rms displacement of 10 Å. The experimental curves are essentially identical along both azimuths and show a strong peak along the surface normal that represents about a 35% anisotropy. Comparing experiment and theory furthermore permits concluding very conservatively that CO is within 10° of normal for this overlayer and that it has no preferential azimuthal orientation.

The inset in this figure also indicates that, in addition to the forward scattering or zeroth-order diffraction peak, one expects higher-order features such as the first-order peak indicated. (These also appear in the single-scatterer calculations of Figs. 4 and 5, where higher orders also are shown.) The first-order peak corresponds to a 2π phase difference between the direct wave and the scattered wave, or a path length difference of approximately one deBroglie wavelength. We will further consider such higher-order features in the next case and subsequent examples.

4.1.2. CO/Fe (001)

A more recent and more complex case of CO adsorption is that on Fe (001). In Figs. 9a and 9b, we show both polar and azimuthal C 1*s* data obtained by Saiki *et al.*[86] from CO adsorbed at room temperature on Fe (001) so as to form predominantly the so-called α_3 state. This rather unusual species has been the subject of prior studies by several techniques, including EELS, ESDIAD, and NEXAFS.[87] Its structure is of considerable interest because it is thought to be bound in a highly tilted geometry with a significantly weakened C–O bond and thus to be a possible intermediate state for the dissociation of the molecule. However, the best that the tilt angle could be determined from NEXAFS data was 45 ± 10°, and no information was obtained on the most likely azimuthal orientation(s) of the molecules. It is thus of interest to see what more can be learned about such a species from XPD.

The strong peak in the normalized C 1*s* polar-scan results for the [100] azimuth shown in Fig. 9a immediately permits a direct estimate of the tilt angle with respect to the surface normal as $\theta_{tilt} = 55 \pm 2°$ (that is, with the molecule oriented 35° from the surface). Also, the fact that this forward scattering peak is not seen in polar scans along the [1$\bar{1}$0] azimuth indicates that the preferred tilt is along ⟨100⟩ directions, or into the open sides of the fourfold-hollow sites that are the sterically most reasonable choices for the bonding location. Complementary evidence confirming this structure comes from the azimuthal data at a polar angle with respect to the surface of $\theta = 35°$ in Fig. 9b. These results again show the preferred tilt in the ⟨100⟩ azimuths via strong peaks along $\phi = 0°$ and 90°. It is thus concluded that the CO molecules are tilted along the four ⟨100⟩ axes, perhaps in separate but equally populated domains, as illustrated schematically for one fourfold-hollow site in Fig. 9c.

As a self-consistency check of these data, it is also of interest that the overall effects seen in both parts a and b of Fig. 9 are of very nearly the same magnitude.

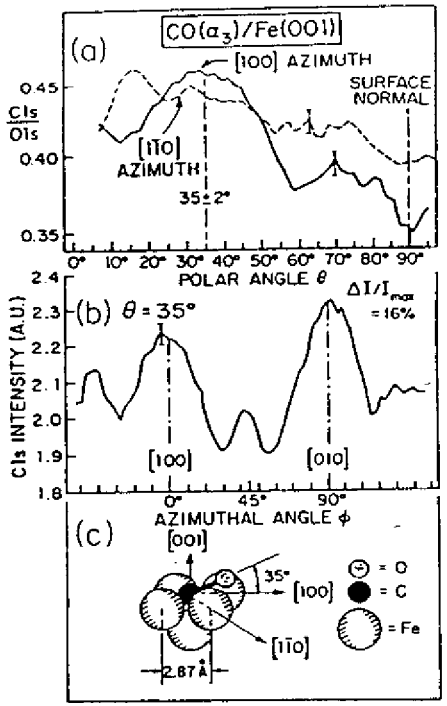

FIGURE 9. (a) Experimental polar scans of the C 1*s*/O 1*s* intensity ratio for the α_3 state of CO on Fe (100). The C 1*s* kinetic energy is 1202 eV. Curves are shown for two azimuths: [100] (solid curve) and [1, 1, 0] (dashed curve). (b) Experimental azimuthal scan of C 1*s* intensity for the α_3 state of CO at a polar angle of 35° chosen to coincide with the peak in the [100] data of part (a). (c) The bonding geometry as deduced from these data. (From Ref. 86.)

That is, if the overall anisotropy as mentioned previously is measured as a percentage by $\Delta I/I_{max}$, we find about a 14% effect in Fig. 9a and a 16% effect in Fig. 9b. Thus, it is possible to reliably measure rather small diffraction effects with XPD, particularly in the azimuthal data, which do not need to be corrected for any systematic instrumental changes in intensity. By contrast, polar scans will always be influenced by a θ-dependent instrument-response function[9] and must somehow be corrected for this. Since the O 1*s* intensity is not expected to be very much affected by final-state scattering and diffraction, using the C 1*s*/O 1*s* ratio in Fig. 9a acts to normalize out any such instrumental effects.

Another useful observation from Figs. 9a and b is that the main peaks exhibit very similar full widths at half-maximum intensity (FWHM) of 30–35°. Thus, the resolutions for determining both the polar and the azimuthal senses of the tilt are about the same.

The results in Fig. 9b also exhibit much smaller but quite reproducible peaks along the ⟨110⟩ azimuths (that is, at $\phi = 45°$) that could be due to scattering from Fe atoms in the ⟨110⟩ corners of the hollow. A more detailed theoretical analysis of these azimuthal results using the SSC–SW model in fact shows that these peaks are due to constructive addition of first-order scattering from oxygen

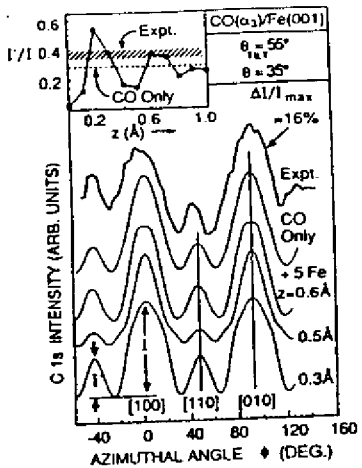

FIGURE 10. Experimental results of Fig. 9(b) are compared with theoretical SSC-SW calculations of C 1s azimuthal scans for CO on Fe (001) tilted at 35° with respect to the surface along the ⟨100⟩ directions and assumed to be in four equally populated domains. In the top theoretical curve, no Fe scatterers are included. In the lower theoretical curves, five Fe scatterers are added, as in Fig. 9(c). The C atom is centered in the fourfold hollow, and the distance z with respect to the Fe surface plane is varied. The inset shows the ratio of the two main peak intensities I'/I as a function of z. (From Ref. 86.)

(see inset in Fig. 8) and second- or third-order scattering from the corner Fe atoms, depending upon the distance z of the tilted CO from the Fe surface. Some results of these calculations of the azimuthal scan of Fig. 9b are compared to experiment in Fig. 10. The top theoretical curve is from a calculation in which only CO molecules are present; these are assumed to be present in four equally populated domains tilted at $\theta = 35°$. This very simple calculation correctly predicts the positions and approximate widths of the strong forward scattering peaks along ⟨100⟩ azimuths, as well as the additional weaker first-order features seen along ⟨110⟩ at $\theta = 45°$. However, if the five Fe nearest neighbors are also included as scatterers (as shown in Fig. 9c) and the C atom is further assumed to be centered in the fourfold hollow but with variable vertical distance z relative to the first Fe layer, we arrive at what should be a more realistic set of curves. These are striking in that the small peaks along ⟨110⟩ are predicted to oscillate in intensity, as shown in the figure inset. Comparing experiment and theory for the ratio I'/I as indicated yields z values of both about 0.22 ± 0.10 Å and 0.63 ± 0.10 Å that agree best; these z values also correspond to very reasonable C–Fe distances of 1.6–2.0 Å. Multiple-scattering calculations for this system by Kaduwela *et al.*[84] also quantitatively confirm the single-scattering results shown here; this is as expected in view of the high energy and high takeoff angles relative to the surface.

Figure 11 shows a further aspect of this analysis in which the experimental polar scans of Fig. 9a are compared to SSC–SW theory for the two azimuths involved and for several z distances. Polar scans are also seen to be sensitive to both azimuth and vertical distance, with in particular the results for the [110] azimuth favoring a z value nearer 0.3 Å. This study thus indicates the significant advantage of having both polar and azimuthal XPD data for such systems.

The theoretical anisotropies $\Delta I/I_{max}$ in Figs. 8, 10, and 11 are found to be about 2–3 times larger than those of experiment. This kind of discrepancy has

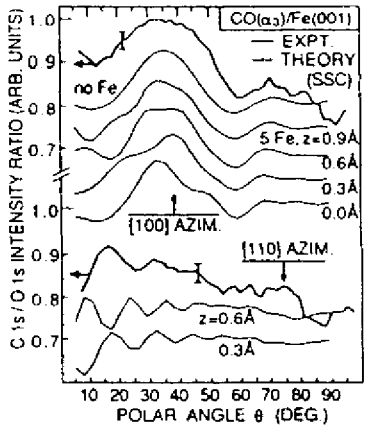

FIGURE 11. Comparison of experimental C 1s polar scans for α_3 CO on Fe (001) to SSC-SW theory for two azimuths and different vertical distances z. (From Ref. 86.)

been found in most previous XPD studies of adsorbates[9,10,23,69] and can be explained by the combined effects of the following:

- Molecular vibration. This has not been included in the calculations for CO/Fe (001) shown here, but is considered in prior work for CO/Ni (001).[23,69]
- The presence of more than one type of emitter on the surface. For the present case, this could be due either to the method of formation of the α_3 state or to adsorption at defects. There could also be additional C-containing impurities beyond those associated with CO and its dissociation products on the surface. All of these act to diminish diffraction features relative to background and thus to reduce the experimental anisotropy. Such effects will tend to be present in any adsorbate system to some degree.

4.1.3. CO/Ni (110)

A final example of a molecular adsorbate system is that of CO on Ni (110), as studied with polar-scan measurements by Wesner, Coenen, and Bonzel.[76,88] For this case, Fig. 12 shows a comparison of normalized C 1s polar scans from CO adsorbed to saturation on Ni (110) at two different temperatures of 300 K and 120 K. The polar scans are markedly different, with the high-temperature results being very similar to those of CO on Ni (001) (cf. Fig. 8), and thus suggestive of a simple vertical adsorption of the CO, and the low-temperature results being widely split into a doublet along the [001] azimuth, but retaining a weaker peak along the normal for the [1$\bar{1}$0] azimuth. The low-tempeature, higher-coverage results have been explained by a structure in which the CO molecules are tilted by ±21° along the [001] azimuth, as shown in Fig. 12d.[89] This structure is nicely confirmed in Fig. 12c, where SSC–PW calculations with an rms vibrational amplitude of 8° are found to yield excellent agreement with experiment.

Wesner *et al.*[88] have also considered the effect of adsorbing CO on a Ni (110)

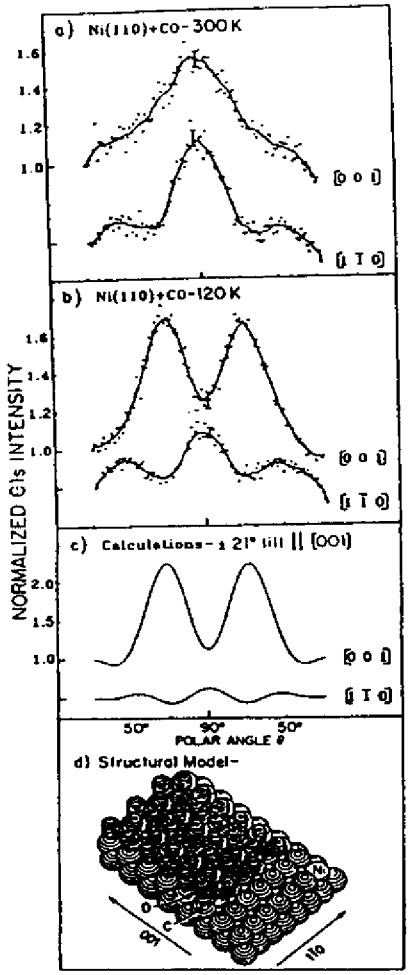

FIGURE 12. (a) Experimental polar scans in two azimuths of the C 1s intensity from CO adsorbed on Ni (110) at 300 K. The kinetic energy is 970 eV. (b) As in (a), but for adsorption at 120 K. (c) SSC-PW calculations modeling the data in (b), with an assumed tilt of ±21° along [001] and an rms vibrational amplitude of 8°. (d) The geometric model assumed for the calculations of (c). [(a)–(c) from Ref. 68. (d) from Ref. 89.]

surface pretreated with K, which is known to act as a promoter in many catalytic reactions. This system is found to have both vertical and more highly tilted CO species present. Finally, the same group has made use of the temperature dependence of the widths of peaks such as those in Fig. 12 for CO on Ni (011) to study the anisotropy of wagging vibrational amplitudes in different azimuths.[76]

4.1.4. Other Systems and Other Techniques

These simple examples thus show that XPD (or in principle also higher-energy AED) is a very powerful tool for studying the orientations and bonding of small molecules on surfaces, and that it is well suited to even very highly tilted species that may exhibit enhanced reactivity and thus be important in such phenomena as catalysis. Each of the cases discussed here is also significant in that other surface structural probes have been applied to the same problem without being capable of a clean resolution of the structure. Similar XPD measurements and theoretical analyses have also recently been applied to several other systems: CO and CH_3O on Cu (110) by Prince *et al.*[90] and CO on Pt (111) treated with K as a promoter by Wesner *et al.*[91]

Similar forward-scattering effects have also been seen by Thompson and Fadley[92] in emission from an atomic adsorbate on stepped surfaces: oxygen on Cu (410) and Cu (211). For this case, scattering by near-neighbor atoms up the step face from the emitter is found to be particularly strong. Stepped surfaces in fact represent a particularly attractive kind of system for study by this technique, since any atomic or molecular adsorbate that bonds preferentially at the base of the step has atoms on the step face as nearest-neighbor forward scatterers in the upstep direction.

The use of intramolecular forward scattering also appears to have several advantages for determining molecular or fragment orientations on surfaces in comparison to other techniques such as high-resolution electron energy loss spectroscopy (EELS),[93] electron stimulated desorption-ion angular distributions (ESDIAD),[94] and NEXAFS[95] or SEXAFS.[16] In EELS, the presence of a titled species can be detected by which vibrational modes are excited, but estimating the magnitude of the tilt is difficult.[87a,93] In ESDIAD, the ion angular distributions for bond tilts away from normal can be significantly distorted by image forces and ion-neutralization effects,[87b,94] and tilts further away from normal than 25–30° therefore cannot in practice be measured accurately, if at all. In NEXAFS[95] and SEXAFS,[16] the experimental intensities of different features vary only relatively slowly with polarization, as $\sin^2\alpha$ or $\cos^2\alpha$, if α is the angle between the radiation polarization and the appropriate molecular symmetry axis. In forward-scattering XPD or AED, by contrast, it is the much narrower peak in the scattering amplitude $|f|$ near 0° (cf. Fig. 2 and Fig. 8) that controls the precision of orientation determinations, leading to FMWHs of 25–35° for all molecules studied to date. Comparing these values to the effective widths of $\sin^2\alpha$ or $\cos^2\alpha$ thus leads to the conclusion that forward scattering in XPD or AED should be about 3–4 times more precise in determining bond directions. An additional problem in NEXAFS is that a correct assignment of the peak(s) to be studied is necessary.

We close this section by noting that scanned-energy photoelectron diffraction or ARPEFS also has been applied recently to the study of small-molecule fragments such as formate (HCOO) and methoxy (CH_3O) adsorbed on Cu (100). The lower energies involved in this work imply that information on bond distances to backscattering neighbors below the adsorbate are also derivable. Such studies are described in more detail in the chapter by Haase and Bradshaw in Volume 2 of this set.

...c. 1. Oxygen/Ni (001)

Saiki and co-workers[26] have carried out an XPD/LEED investigation of the interaction of oxygen with Ni (001) over the broad exposure range from $c(2 \times 2)$ O at 30 Langmuirs (L) to saturated oxide at 1200 L. Scanned-angle measurements were performed with Al $K\alpha$ radiation at 1486.6 eV for excitation. Although this system has been extensively studied in the past by various structural and spectroscopic probes,[96-98] several questions remain as to the exact structures formed. The combined use of XPD and LEED proves capable of answering several of these, as well as pointing out some new features of XPD that should be generally useful in surface-structure studies.

For example, in Fig. 13a, we show azimuthal scans of O 1*s* intensity at a relatively high polar angle θ of 46° with respect to the surface for four oxygen exposures from the onset of sharp $c(2 \times 2)$ LEED spots (30 L) to full oxide saturation (1200 L). The experimental curves are compared to SSC–SW calculations for a $c(2 \times 2)$ overlayer in simple fourfold sites with a vertical oxygen distance of $z = 0.85$ Å above the first Ni layer (the by now generally accepted structure), for two monolayers (ML) of NiO (001) with ideal long-range order, and for two monolayers of NiO (111) with long-range order. The dominant peaks at $\phi = 0°$ and 90° for the highest two exposures of 150 L and 1200 L are correctly predicted by theory and are due to simple forward scattering of photoelectrons emitted from oxygen atoms below the surface by oxygen atoms situated in the upper layers of the oxide, as indicated by the arrows in Fig. 13b. These peaks furthermore persist as the strongest features down to 30 L, indicating very clearly the existence of buried oxygen emitters, probably in small nuclei of NiO (001), over the full region of observation of the $c(2 \times 2)$ overlayer. The presence of such oxide nuclei in varying degrees on Ni (001) surfaces prepared in different laboratories is thus a likely cause of some of the previous controversy surrounding the vertical positions of both $c(2 \times 2)$ and $p(2 \times 2)$ oxygen on this surface,[96,97] but XPD provides a sensitive probe of the presence of any sort of buried species via such forward-scattering effects.

Comparing the 1200-L experimental curve and the theoretical curve for 2 ML of ideal Ni (001) in Fig. 13a for the region near $\phi = 45°$ shows qualitative agreement as to the existence of a region of enhanced intensity for $30° < \phi < 60°$, but disagreement as to exact fine structure, with theory showing a doublet where experiment shows a single broad peak. However, annealing this saturated oxide to approximately 250 °C for ≈10 minutes to increase its degree of long-range order parallel to the surface (as well as perhaps its thickness)[97] is found to yield a significantly altered XPD curve, with a doublet centered at $\phi = 45°$ that is in very good agreement with theory for NiO (001), as shown in the higher-resolution results of Fig. 14. It is also striking that the annealed oxide overlayer shows much more fine structure and generally narrower features, even though the dominant peaks in both the unannealed and annealed data are still those for simple forward scattering along ⟨101⟩ directions (i.e., at $\phi = 0°$ and 90°). The theoretical curves for 2 ML or 3 ML of ideal NiO (001) in Fig. 14 are

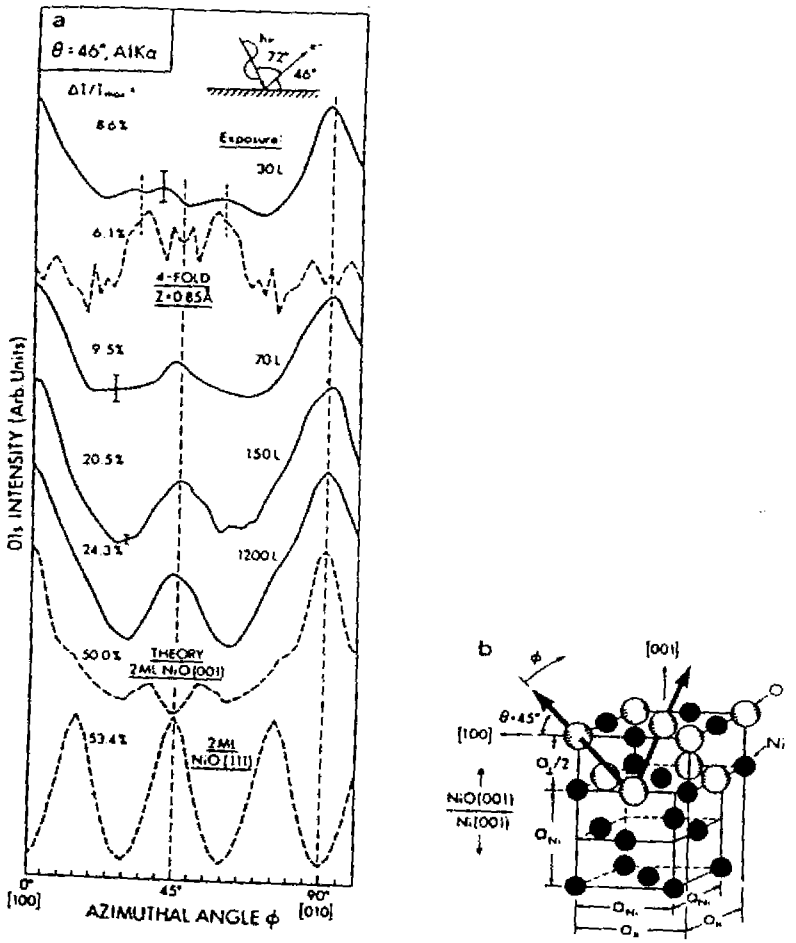

FIGURE 13. (a) O 1*s* azimuthal XPD data from oxygen on Ni (001) at four exposures from the $c(2 \times 2)$ regime (30 L) to saturated oxide (1200 L). The kinetic energy is 945 eV. The polar angle of 46° involves scanning very close to the ⟨110⟩ directions at $\theta = 45°$ and $\phi = 0°$ and 90°. Also shown are SSC-SW calculations for fourfold $c(2 \times 2)$ oxygen at $z = 0.85$ Å and fully ordered 2 ML overlayers of NiO with both (001) and (111) orientations. (b) An approximate representation of the structure of the dominant Ni (001) formed at high exposures, indicating the oxide lattice expansion and strain involved. Also shown as arrows are the directions of the strong forward-scattering peaks observed at $\phi = 0°$, 90° in (a). (From Ref. 26.)

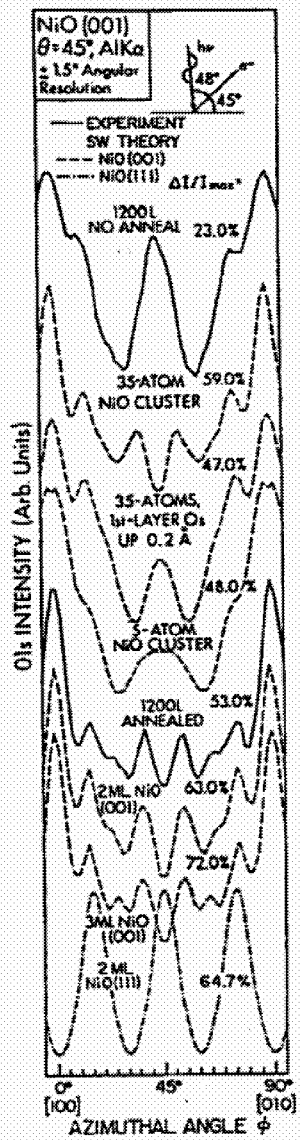

FIGURE 14. O 1s azimuthal XPD data from the saturated oxide formed at 1200 L exposure on Ni (001) obtained at a high angular resolution of ±1.5° with an emission angle of 45° with respect to the surface. Experimental curves are shown for both the ambient-temperature oxide and the same overlayer after a brief low-temperature anneal. SSC-SW calculations are also shown for several cases: smaller five-atom and 35-atom clusters to simulate loss of long-range order and strain and large fully converged clusters to simulate ideal NiO growing in either the (001) orientation (with 2 ML or 3 ML thickness) or the (111) orientation (with 2 ML thickness). (From Ref. 26.)

also in remarkably good agreement with the annealed data, verifying that annealing has produced a very highly ordered overlayer, and suggesting that the unannealed oxide exhibits diffraction effects due to strain and disorder.

The data shown in Fig. 14 are different from all results presented up to this point in being obtained at a very high angular resolution of ±1.5° or less; precise angular resolution has in this case been obtained by using interchangeable tube arrays of the proper length-to-diameter ratio, as discussed in detail by White *et al.*[33] Note the additional fine structure in the unannealed 1200-L curve of Fig. 14 as compared to that of Fig. 13a.

The bottom theoretical curves in Figs. 13a and 14 are for 2 ML of NiO (111), an orientation of oxide growth which is also thought from LEED to coexist with NiO (001) on this surface.[97] The total lack of agreement of the NiO (111) curve with experiment makes it clear that this is only a minority species affecting no more than 5% of the NiO present.

In order to better understand the unannealed oxide data in Figs. 13a and 14, we also show in Fig. 14 theoretical curves for smaller 35-atom and 5-atom clusters of NiO (001). The previous calculations discussed involved much larger clusters with about 100 atoms per layer to insure full convergence. The 35-atom cluster includes atoms in about the first $1\frac{1}{2}$ unit cells around a given oxygen emitter; the 5-atom cluster is minimal and represents only nearest-neighbor and next-nearest-neighbor scatterers. The results for the full 2-ML cluster and the 35-atom cluster are found to be very close except for somewhat more fine structure in the full-cluster curve. This is consistent with prior XPD studies which have concluded that near-neighbor scatterers dominate in producing the observed patterns. However, much better agreement with the unannealed oxide results is seen if either the first-layer oxygen atoms (but not the nickel atoms) in the 35-atom cluster are relaxed upward by 0.2 Å or the effective cluster size is reduced to five atoms. Both of these models are consistent with a highly strained unannealed oxide overlayer of (001) orientation in which the long-range order is severely disturbed. The LEED spots for NiO (001) in fact indicate a lattice expanded by very nearly $\frac{1}{2}$ relative to the underlying Ni (001) surface, as indicated schematically in Fig. 13b. Although these results do not permit choosing between these two possibilities for stress relief in such a disordered system, they are significant in that both the experimental and theoretical XPD curves are quite sensitive to these more subtle deviations from an ideal NiO (001) overlayer with long-range order. This suggests a broad range of applications of XPD or higher-energy AED to studies of epitaxy and overlayer growth.

It is also significant in the comparisons of experimental data for annealed oxide with theory for 2–3 ML of NiO (001) in Fig. 14 that the agreement extends even to the overall degree of anisotropy, as judged again by $\Delta I/I_{max}$. The theoretical anisotropies are only about 1.2–1.3 times those of experiment. As noted previously, theory is in general expected to overestimate these anisotropies, in some previous cases by as much as factors of 2–3. One important reason for this kind of discrepancy is the lack of allowance in the calculations for atoms bound at various defect or impurity sites along or below the surface, as these are expected to produce a rather diffuse background of intensity, thus lowering the overall anisotropy. However, for the present case, the very good

agreement suggests that the annealed oxide overlayer consists of oxygen atoms that are almost completely bound in a highly ordered NiO (001) structure.

At lower exposures, XPD has also been used to determine the $c(2 \times 2)$ *oxygen structure on Ni* (001).[26] The high θ values of Figs. 13 and 14 minimize the effects of any forward-scattering events in emission from oxygen in the $c(2 \times 2)$ overlayer (cf. Fig. 2), so that the 30-L curves here are dominated by the

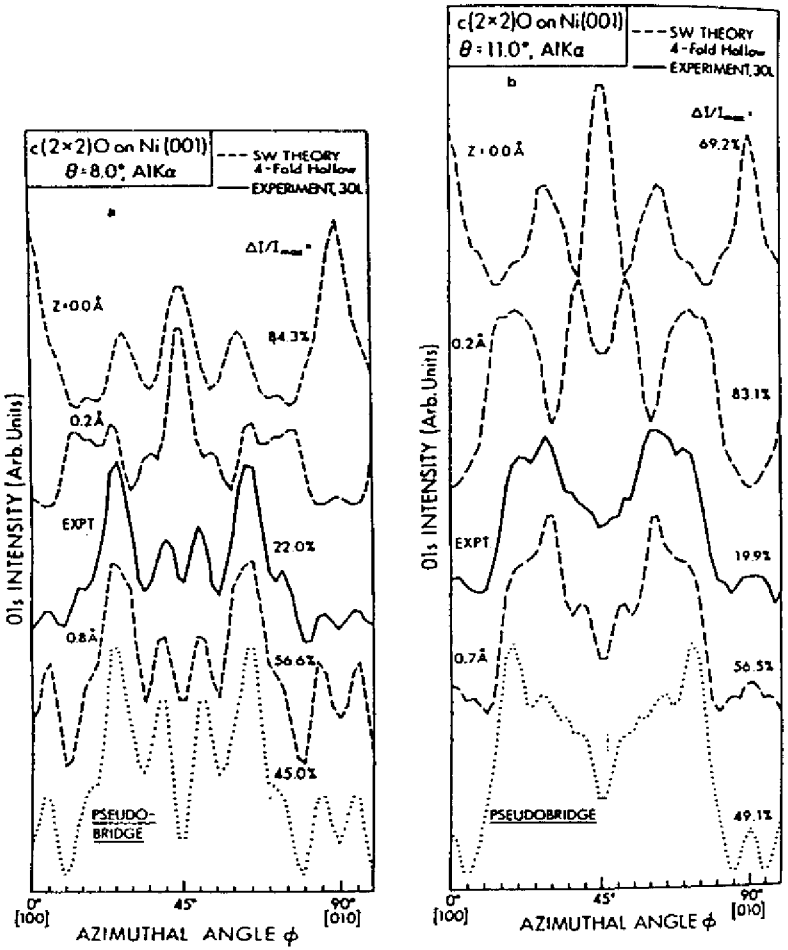

FIGURE 15. (a) Grazing-emission O 1s azimuthal data from $c(2 \times 2)$ O on Ni (001) at $\theta = 8°$. The experimental data are compared to SSC-SW curves for four possible fourfold-hollow $c(2 \times 2)$ structures, including the pseudobridge geometry of Ref. 98. (b) As in (a), but for $\theta = 11°$. (From Ref. 26.)

presence of a certain fraction of buried oxygen, probably in oxide nuclei. However, at very low takeoff angles with respect to the surface of approximately 8°–15°, forward elastic scattering from adsorbed oxygen becomes much stronger, and the signal from buried oxygen is also suppressed by enhanced inelastic scattering.[9] Thus, the diffraction patterns at such low θ values are expected to be more strongly associated with overlayer effects.

Figure 15 shows such experimental and theoretical results for two representative θ values, 8° and 11,° of the four angles studied (data were also obtained for 14° and 17°). Experiment is here compared with SSC–SW theoretical curves for four possible $c(2 \times 2)$ structures: in-plane fourfold bonding ($z = 0.0$ Å); slightly-above-plane fourfold bonding ($z = 0.2$ Å); the vertical distance in fourfold bonding yielding the empirical best fit to experiment at that θ value as judged both visually and by R factors;[26d] and the so-called pseudobridge geometry suggested by Demuth *et al.* on the basis of a LEED analysis.[98] For this last geometry, $z = 0.8$ Å and the oxygen atoms are offset horizontally by 0.3 Å in the fourfold hollow toward any of the four symmetry-equivalent ⟨110⟩ directions.

In Fig. 15a for $\theta = 8°$, it is very clear that $c(2 \times 2)$ oxygen does not occupy a position in the 0.0-to-0.2-Å range, although certain prior studies have suggested this as the most likely bonding position.[96,97] Simple fourfold bonding at $z = 0.80$ Å, by contrast, yields excellent agreement with experiment, with all observed features being present in the theoretical curve. The only points of disagreement are the relative intensity of the weak doublets centered at $\phi = 0°$ and 90°, which is too strong in theory; and the degree of anisotropy $\Delta I/I_{max}$, which is predicted to be too high by approximately a factor of 2.6. The latter discrepancy could be due to a significant fraction of oxygen atoms occupying defect or buried sites, e.g., in the oxide nuclei mentioned previously. Also, for such a low takeoff angle that begins to be within the forward scattering cone at this kinetic energy (≈954 eV), there may be some defocusing and reduction of peak heights due to multiple scattering effects; in fact, $\phi = 0°$ and 90° are the directions of nearest-neighbor oxygen scatterers in the $c(2 \times 2)$ structure, as shown in Fig. 16a. The pseudobridge geometry does not fit experiment as well, since the relative intensity of the doublet centered at $\phi = 45°$ is too high.

In Fig. 15b, for $\theta = 11°$, the two geometries close to being in plane again do not agree at all with experiment, which is very well described by simple fourfold bonding at an optimum z of 0.70 Å. The pseudobridge geometry in this case also differs considerably from experiment as to the shape of the two main peaks. When these results are combined with those at the other two θ values studied,[26] it can overall be concluded that $c(2 \times 2)$ oxygen does not bond in either simple fourfold positions at $0.0 < z < 0.3$ Å or in the pseudobridge geometry, but does occupy simple fourfold positions at $z = 0.80 \pm 0.10$ Å. This choice of structure is also confirmed by an R-factor comparison of experiment and various theoretical curves. The z distance found here also agrees very well with several more recent structural studies of this system.[96,97]

A final point in connection with the results of Fig. 15 is that, in order for theory to adequately reflect all of the fine structure seen in experiment, the cluster used in the calculations must include all O and Ni atoms within the first few layers of the surface (adsorbate plus two layers of Ni) and out to a relatively

large radius of about 20 Å from the emitter. The rate of convergence with cluster size is illustrated in Fig. 16. Due to the rotational symmetry of the surface, calculations need be performed only over the 45° wedge indicated in Fig. 16a, but it is important to include sufficient atoms at the edge of this wedge. It is clear from the diffraction curves in Fig. 16b that going out to only 10 Å in radius does not yield the correct diffraction fine structure. This indicates sensitivity in forward scattering at grazing emission to well beyond the first 3–5 spheres of neighbors. The effective *diameter* of the cluster is thus about 40 Å.

Thus, these results for a prototypical surface oxidation over a broad exposure range, from ordered overlayers at partial monolayer coverage to saturated oxide, indicate several very useful types of structural information that can be derived from XPD (or by implication also by high-energy AED) in conjunction with SSC calculations.

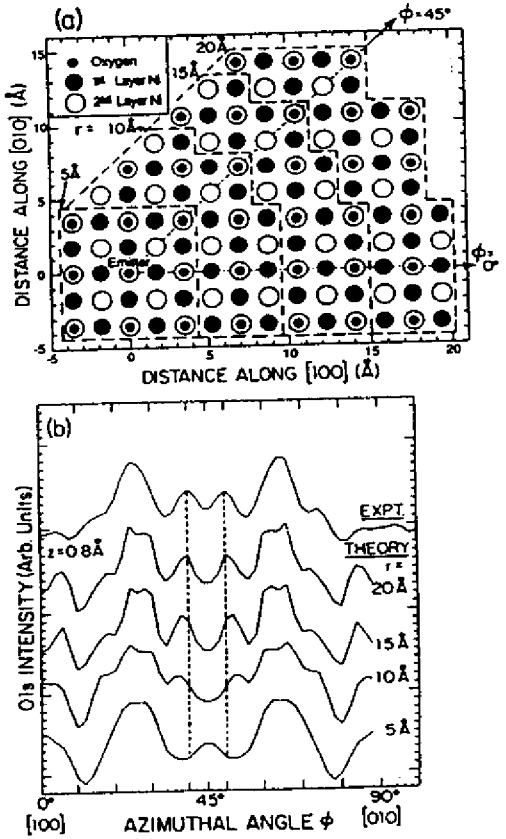

FIGURE 16. (a) Choices of cluster. Different-sized clusters used in testing the convergence of the SSC-SW curves for $\theta = 8°$ in Fig. 15(a), labelled with the approximate radii outward from the emitter that they represent. (b) Convergence with cluster size. Calculated curves for the clusters of (a) with $z = 0.8$ Å are compared to experiment. Note that a radius of at least 20 Å is required to yield optimum agreement. (From Ref. 26.)

4.2.2. Sulfur/Ni (001)

The sulfur/Ni (001) system has been much used as a test case for surface-structure techniques because it represents a rather unique example of a system for which there is a general consensus on a structure: the $c(2 \times 2)$ sulfur overlayer is bound with atomic S in fourfold sites at a distance z of 1.3–1.4 Å above the first Ni plane.[99] Several photoelectron diffraction studies have been made of this system,[14,15,19,21,25,99] including both scanned-angle and scanned-energy measurements, and we will consider a few of these.

Higher-energy scanned-angle XPD measurements have been made for this system by Connelly *et al.* (Fig. 44 in Ref. 9), and experimental azimuthal scans of S 2*p* emission at grazing takeoff angles are found to be in good agreement with SSC–PW calculations for the known structure. However, for a structure with this high a distance above the Ni surface, the effects of forward scattering become weaker, since the scattering angle from any near-neighbor Ni atom becomes larger. For example, for the Ni nearest neighbors in the fourfold hollow, a very low emission angle of 5° with respect to the surface still corresponds to a minimum scattering angle of approximately 43° that is well outside of the forward scattering cone at high energy (cf. Fig. 2). Thus, the strongest contribution to azimuthal anisotropy is scattering from the other (coplanar) S adsorbate atoms, for which the scattering angle is simply the emission angle with respect to the surface. The sensitivity of such XPD measurements to the vertical S–Ni distance is thus expected to be lower than for more nearly in-plane or below-plane adsorption, and it has been questioned as to whether such measurements will be sensitive enough to determine structures for any adsorbate sitting well above the surface.[9] Several possibilities appear to exist for improving the positional sensitivity for such cases: working at higher angular resolutions and taking advantage of additional diffraction fine structure, using lower energies for which large-angle and backscattering are stronger, and/or using special polarization geometries to enhance certain substrate scatterers. Some of these possibilities thus involve synchrotron radiation, and we consider now their application to the S/Ni case in both the scanned-angle and scanned-energy modes.

We first look at the influence of higher angular resolution. S 2*p* azimuthal XPD data at a polar angle of 13° obtained by Saiki *et al.*[100] with a high angular resolution of about ±1.0° are shown in Fig. 17. The data were obtained in scans over 100° in ϕ and then mirror-averaged across [110] to improve statistical accuracy, but all of the features shown were reproduced in the full scan. These results exhibit considerably more fine structure than similar data obtained with a ±3.0° resolution, and the anisotropy is found to go up from 31% to a very high 40% with increased resolution. Also, when these data are compared with the SSC–SW curves shown in this figure for different z positions of S above the fourfold hollow, they exhibit a high sensitivity to position. A more quantitative analysis of these high-resolution results by Saiki *et al.*[100] using R factors for comparing experiment and theory[26d] in fact yields a z value of 1.39 Å for this structure that is in excellent agreement with prior work. This analysis furthermore permits estimating the first nickel–nickel interplanar distance (d_{12}), which is found to be expanded to about 1.86 Å from the bulk value of 1.76 Å. Thus, there

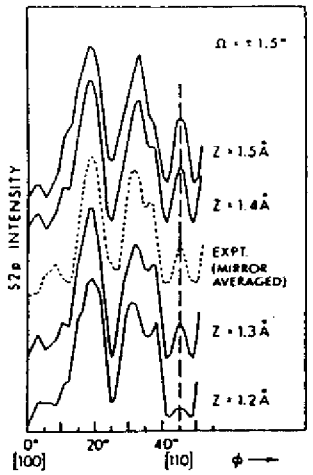

FIGURE 17. Azimuthal XPD data for S 2p emission from $c(2 \times 2)$ S on Ni (001) at a kinetic energy of 1085 eV obtained with a high angular resolution of approximately ±1.5°. The polar angle is 13° with respect to the surface. The anisotropy $\Delta I/I_{max}$ is a high 40% for these results, compared to only 31% for the same measurement with a ±3.0° angular resolution; the fine structure is also considerably enhanced with higher resolution. SSC-SW calculations are shown for various distances z of the S above the Ni surface. (From Ref. 100.)

is considerable potential in using high-energy measurements with high angular resolution, even for adsorption at large z distances above approximately 1.0Å.

Going to lower energies with synchrotron radiation in such azimuthal measurements also has potential for such studies. We show in Fig. 18 results for S 1s emission from the $c(2 \times 2)$S overlayer on Ni (001) obtained by Orders *et al.*[19b] Here, the experimental geometry was chosen so that the polarization vector

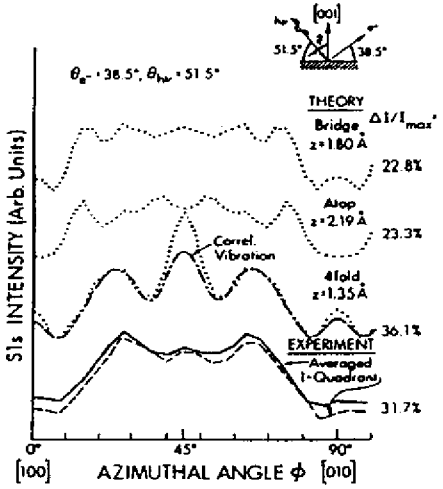

FIGURE 18. Synchrotron radiation excited S 1s intensity from $c(2 \times 2)$ S on Ni (001) at a kinetic energy of 282 eV. The geometry chosen emphasized nearest-neighbor backscattering because the polarization vector was oriented directly toward the relevant Ni nearest neighbor, as shown in the inset at upper right. SSC-PW calculations for three possible adsorption sites of bridge, atop, and fourfold are shown as dotted curves. The dashed-dotted fourfold curve involves a more correct inclusion of correlated vibrational effects. (From Refs. 19(b) and 101.)

was directed rather precisely toward nearest-neighbor Ni atoms for certain azimuthal positions in a ϕ scan. Backscattering from this type of Ni atom should also be rather strong at the photoelectron energy of 282 eV chosen (cf. Fig. 2). This energy is nonetheless high enough that a single-scattering model should still be reasonably quantitative. The experimental data is here compared with SSC–PW calculations for three different bonding sites (bridge, atop, and fourfold) with reasonable S–Ni bond distances, and the correct fourfold site is clearly in better agreement with experiment. The agreement is also significantly improved if a more accurate allowance for correlated vibrations is included in the SSC calculations, as shown by the dashed–dotted curve.[101]

However, a note of caution is in order concerning the use of different polarization orientations, since experimental and theoretical work on S/Ni by Sinkovic *et al.*[19a] indicates that a geometry in which the polarization is nearly perpendicular to the electron emission direction (instead of parallel, as in Fig. 18) increases the importance of multiple-scattering events and causes more significant deviations from a simple theoretical model. This is thought to occur through a weakening of that portion of the photoelectron wave emitted directly in the detection direction in comparison to the various scattered waves that can interfere with it. The intensity distribution is thus produced by the interference of direct and scattered waves that are all of the same magnitude, a situation rather like that in LEED where all contributions to intensity are those due to relatively weak backscattering; thus, MS effects might be expected to be more important. In most photoelectron and Auger experiments, the direct-wave amplitudes are stronger than those of the scattered waves, and it can be argued that this is a fundamental reason for the higher degree of applicability of a single-scattering approach.

Finally, we consider scanned-energy or ARPEFS measurements on S/Ni (001) of the type pioneered by Shirley and co-workers.[8,25] In this type of experiment, an adsorbate core intensity is measured as a function of $h\nu$ in a fixed θ, ϕ geometry, and the resulting EXAFS-like oscillations are analyzed in order to derive the adsorbate position. The data are usually analyzed as a normalized $\chi(E)$ or $\chi(k)$ function. Figure 19 shows typical experimental data of this type in a normal-emission geometry, for S 1s emission from $c(2 \times 2)$ S/Ni (001).[8] Allowance has been made here for the interference between the S Auger peak at 155–160 eV and the S 1s photoelectron peak. These results are compared to both MSC–SW calculations by Barton and Shirley[25] in Fig. 19a and SSC–SW calculations by Sagurton *et al.*[21] in Fig. 19b. The agreement is very good for both sets of theoretical curves, provided that the first nickel–nickel interlayer distance (d_{12}) is relaxed outward from the bulk value of 1.76 Å to 1.84 Å (cf. the two theory curves in Fig. 19b). This interlayer relaxation, as first pointed out by Barton and Shirley, thus illustrates the high sensitivity of photoelectron diffraction to subtle structural changes on the order of 0.10 Å or less.

It is also clear from this figure and other work on the S/Ni system[21,22] that both the single-scattering and multiple-scattering approaches describe the experimental results well and that they also lead to very similar structural conclusions, with only the perpendicular distance for S being different by 0.05 Å between the two analyses. Thus, although the MSC–SW approach is certainly in principle more accurate and does lead to $\chi(k)$ amplitudes in better agreement

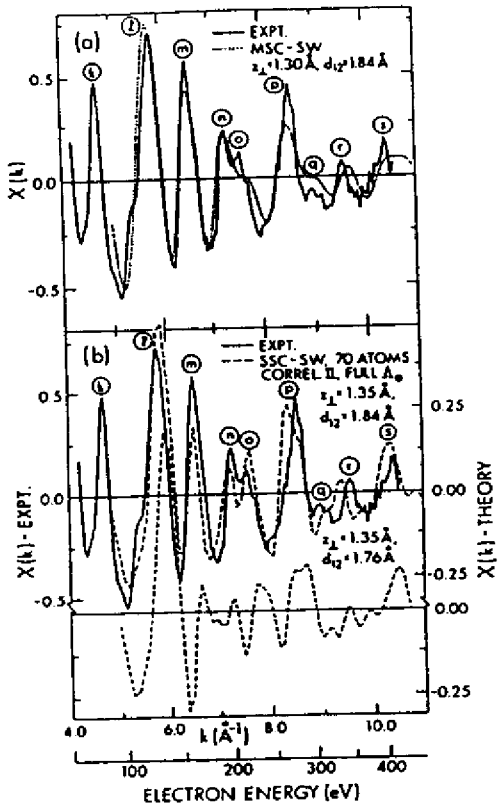

FIGURE 19. Comparison of scanned-energy S 1s data for $c(2 \times 2)$ S on Ni (001), θ_{in} = 70°, θ_{e-} = 0° (From Ref. 8) with: (a) a multiple-scattering cluster spherical-wave (MSC-SW) calculation due to Barton and Shirley (From Ref. 25), and (b) single-scattering cluster spherical wave (SSC-SW) calculations due to Sagurton *et al.* (From Ref. 21). Both the sulfur vertical distance z and the first Ni–Ni interplanar distance d_{12} are specified. (Fig. from Ref. 21.)

with experiment, the SSC–SW method appears capable of a usefully quantitative description of the observed oscillations and fine structure.

Another aspect of this analysis noted by Barton and Shirley[25] is that nearest-neighbor backscattering followed by emitter forward scattering (cf. Fig. 3b–i) can be an important factor in producing the full amplitude of the ARPEFS oscillations at low energies. This may be the reason why the single-scattering curves in Fig. 19b have lower amplitudes, although a different allowance for vibrational effects also could play a role.[21]

An additional useful aspect of such ARPEFS data is in being able to Fourier transform $\chi(k)$ curves to yield peaks which are for some (but not necessarily all) of the strongest scatterers rather directly related to interatomic distances via the path-length difference and the scattering angle [cf. Eq. (10)]. The degree to which Fourier transforms can be used in this way is discussed in detail elsewhere.[21,25] However, ARPEFS Fourier transforms (FTs) need not be as simply associated with certain spheres of neighbors as are those of EXAFS and SEXAFS; the reason for this

is the potentially large number of scattering events and various possible scattering angles that can be associated with a given region in the transform.[21] Nonetheless, such FTs have been used to rule out certain structures as part of a more detailed structure determination; we consider such an example in the next section.

4.2.3. Sulfur/Cr (001)

We now turn to a recent study of $c(2 \times 2)$ S/Cr (001) by Terminello *et al.*[20] that serves to represent a state-of-the-art analysis of scanned-energy or ARPEFS data. In this work, S 1*s* intensities were scanned as a function of energy up to about 475 eV above threshold; two different emission directions were studied; [001] and [011], with polarizations oriented in general along the emission direction (35° off normal toward [011] for [001] emission and along [011] for [011] emission). Special care was taken to avoid spurious energy-dependent effects in the measuring of intensities, with normalization being needed for both the incident photon flux and the transmission function of the electron-energy analyzer. As for S/Ni (001), the interference between the S Auger peak at 155–160 eV and the S 1*s* photoelectron peak was allowed for by carefully subtracting out the former. Fourier transforms of the data were made, with the inner potential being treated as an adjustable parameter and the $\chi(k)$ data being multiplied by a Gaussian window function to reduce ringing effects in the final FTs. The strongest peaks in these transforms were then taken to be semiquantitatively indicative of certain near-neighbor path-length differences; this analysis thus implicitly assumes that the single-scattering Eq. (10) represents a good first-order description of the diffraction and that there are no significant interferences between the effects of different near-neighbor scatterers. The approximate geometric information from the FT peak positions was found to point to the fourfold-hollow site as the adsorption position.

The final quantitative determination of the site type and the structure was made by directly comparing the experimental $\chi(k)$ curves (Fourier filtered to remove effects due to path-length differences beyond about 20 Å) with multiple-scattering cluster calculations using spherical-wave scattering. As one example of these results, Fig. 20*a* compares experimental curves along the two directions with curves calculated for S adsorbed on three types of sites. It is very clear here that the fit is best for the fourfold site (cf. similar comparison for the scanned-angle S/Ni results in Fig. 18).

Pursuing the fourfold site further by means of an R-factor comparison of experiment and MSC–SW theory, the authors derive a geometry that includes a determination of S–Cr distances down to the fifth layer of the substrate. Some of the results of this R-factor analysis are shown in Fig. 21. It is interesting here that the two sets of data for emission along [001] and [011] azimuths and with polarization nearly parallel to each emission direction are complementary in their sensitivities to different structural parameters. The [001] results are much more sensitive to the Cr_2-atop position because strong single and multiple backscattering can be involved (cf. Fig. 3b–i). By contrast, the [011] data is much more sensitive to the Cr_2-open position for the same reason. The polarization orientations enhance these effects by preferentially directing the initial photoelectron wave toward these scatterers (cf. Fig. 3a). The final results of this

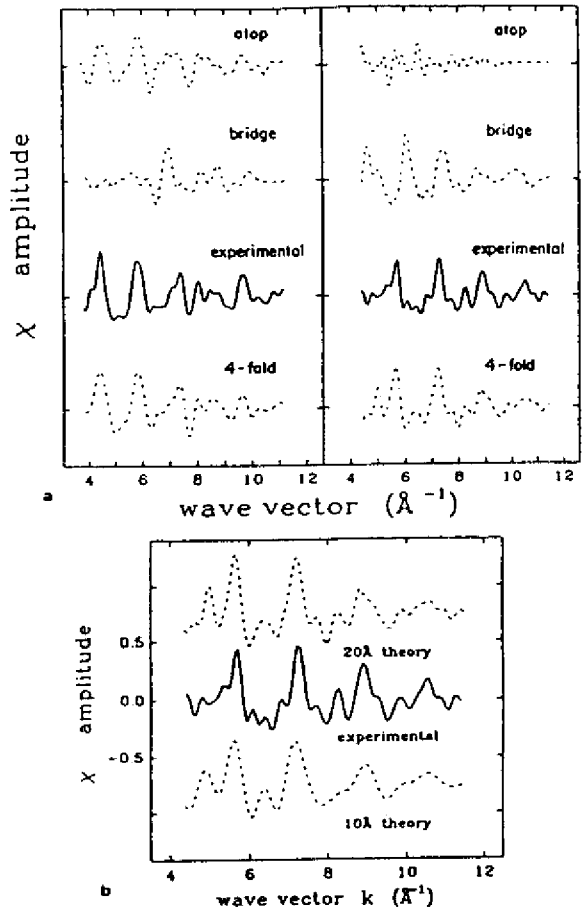

FIGURE 20. (a) Comparison of scanned-energy S 1s experimental data for emission from $c(2 \times 2)$ S on Cr (001) along the [001] direction (left panel) and [110] direction (right panel) with MSC-SW calculations for different adsorption sites of atop, bridge, and fourfold. (b) As in (a), but comparing the data obtained in the [011] azimuth to MSC-SW theory for the final optimized fourfold-hollow structure with different path-length cutoffs of 20 Å and 10 Å. (From Ref. 20.)

R-factor analysis show an 8% reduction of the mean separation of the first and second Cr layers (compare the 3% expansion in similar S/Ni results in Fig. 19) and further suggest a slight corrugation of the second layer and a slight expansion of the separation of the second and third layers, although the latter are not fully conclusive within the error limits of 0.02–0.03 Å estimated by the authors.

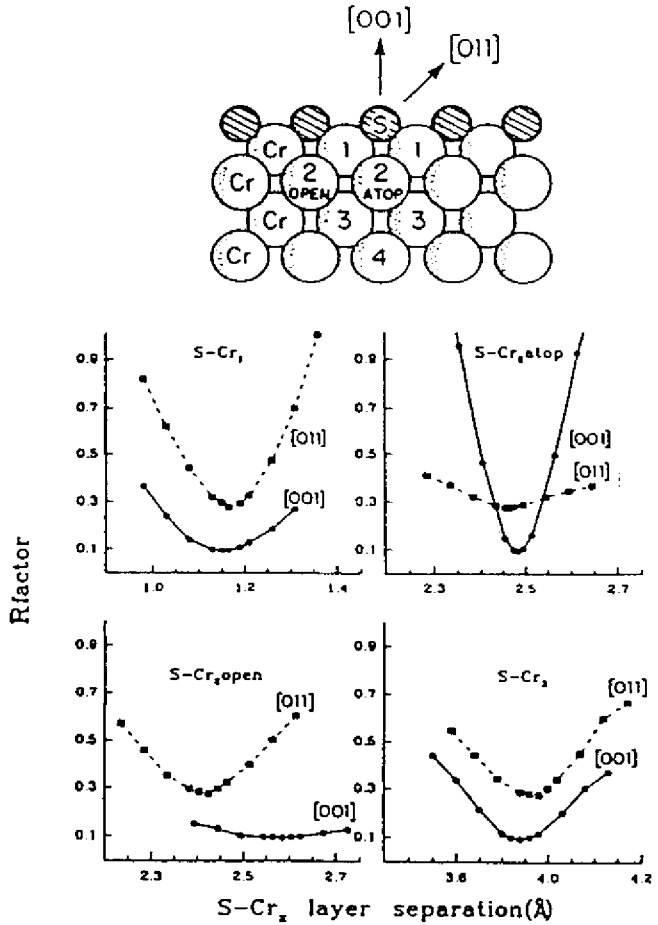

FIGURE 21. *R*-factor analysis of the scanned-energy results of Fig. 20, showing the geometry involved and the variation of the *R* factor with various S–Cr layer separations. (From Ref. 20.)

A further important point made in this work is that the $\chi(k)$ curves exhibit fine structure associated with path-length differences out to about 20 Å. Such fine structure in ARPEFS data and the need to use rather large clusters of up 50–100 atoms to adequately model S/Ni data have also been discussed previously (see Fig. 19 and Ref. 21). The work by Terminello *et al.* shows this explicitly by comparing experimental $\chi(k)$ curves for S/Cr with MSC–SW curves that have

been cut off at both 10 Å and 20 Å total scattering lengths; these results are presented in Fig. 20b, where it is clear that the fine structure in experiment is better modeled by the 20-Å curve, especially for wave vectors above about 7 $Å^{-1}$. This sensitivity permitted a final determination of Cr layer spacings down to that between the fourth and fifth layers, although the accuracy decreases from an estimated ±0.02–0.03 Å for the first three spacings to ±0.07 Å for the fourth spacing measured. It is, finally, worth noting that the approximately 20 Å limit noted here is in the same range as that found in the higher-energy scanned-angle O/Ni results presented in Fig. 16. Thus, both methods seem to have similar sensitivity to more-distant neighbors.

This work demonstrates the full power of the scanned-energy approach, provided that the initial intensities are measured carefully and that the final results are analyzed by means of a quantitative comparison of experimental $\chi(k)$ curves with calculations for a range of choices of geometrical parameters. A very similar analysis has been carried out for the system $c(2 \times 2)$ S/Fe (001) by Zhang *et al.*[102] Although much more time-consuming multiple-scattering calculations were used for all of the geometries tried in these cases, it should be possible in general to do a much more rapid search for promising geometries in single scattering, with only fine tuning of the parameters then being required in multiple scattering.

4.3. Epitaxial Oxide, Metal, and Semiconductor Overlayers

4.3.1. NiO/Ni (001)

Although the case of NiO grown on Ni (001) considered in the previous section does not represent perfect epitaxy, the degree of agreement between experiment at 1200 L and theory in Figs. 13a and 14 clearly shows that the predominant form of NiO present is of (001) orientation. Certain structural conclusions concerning the form of this oxide and its degree of long-range order before and after annealing have also been made (section 4.2.1 and Refs. 26b,c). An analysis of the LEED spot patterns (including a splitting of the NiO (001) spots and corresponding XPD data in fact suggests a two-dimensional superlattice growth of NiO (001) with a lattice constant expanded by exactly ¼ with respect to the underlying Ni substrate (cf. Fig. 13b). Although LEED patterns for the unannealed oxide also exhibit a 12-spot ring throught to be due to NiO (111),[97] the XPD results of Figs. 13a and 14 indicate that it is at most a minority species of the total NiO present, since NiO (111) would produce 12-fold symmetric XPD patterns (bottom theory curves in Figs. 13a and 14) that are not seen experimentally. This example thus indicates a very useful sensitivity of high-energy XPD to the orientation of an epitaxial overlayer and its degree of short-range order under various conditions of annealing and deposition.

4.3.2. Cu/Ni (001) and Fe/Cu (001)

We now consider two very different limits of metal-on-metal epitaxial growth taken from some of the first experimental studies in this field, those by Egelhoff and co-workers and Chambers and co-workers: pseudomorphic epitaxial growth of Cu on Ni[11,103] and island formation by Fe on Cu (001).[104]

Figure 22 illustrates high-energy AED for the first case of Cu on Ni (001). The different near-neighbor forward scattering events allowed as each new Cu layer is added are illustrated by the arrows in Fig. 22a. In Fig. 22b, experimental data from Egelhoff[11] are compared to theoretical SSC–PW curves from Bullock and Fadley.[71] In Fig. 22c, some of the same experimental data are compared to very recent multiple-scattering calculations by Xu and van Hove.[73]

In Fig. 22b, the relatively abrupt appearance at certain overlayer thicknesses of forward-scattering features such as those at $\theta = 45°$ and 90° (normal emission) can be used as a direct measure of the number of overlayers in the range of about 0–3 ML. Comparison with Fig. 22a also shows that the appearance of each of these two peaks corresponds to the onset of forward scattering by the two nearest neighbors encountered in this polar scan from [100] to [001]. The simple origin of these two peaks has also been directly verified by comparing SSC calculations with and without these important scatterers present.[71]

Thus, simple forward scattering peaks from nearest and next-nearest neighbors are very useful in studies of epitaxy, as we have also discussed for the oxide case in the last section. However, the interpretation of weaker features such as those at $\phi \approx 20°$ and 70° in Fig. 22b need not be so simple. Calculations with various atoms removed from the cluster show that these have more complex origins which require at least a full SSC calculation for their explanation.[71] For example, the peak near 70° is a superposition of simple forward scattering by atoms along [103] and [102] and, more importantly, first-order effects (cf. the inset of Fig. 8) from the atoms along [001] and [101]. Thus, for atoms that are further away than the first three or four spheres of neighbors, a mixed origin in forward scattering and higher-order interference effects is generally to be expected. This conclusion has also been confirmed in a recent analysis by Osterwalder *et al.*[48] of an extensive set of high-resolution Ni $2p_{3/2}$ data from bulk Ni (001) that we discuss further in section 5.1.

Figure 22a also makes it clear that, in pseudomorphic growth with the lateral lattice constants locked to those of Ni, the vertical spacing of the Cu layers will determine the θ position of the peak near 45°. A ±1° change in this peak position from 45° would correspond to a ±0.12-Å change in the vertical lattice parameter or a ±0.06-Å change in the interplanar spacing. This sensitivity has in fact recently been used by Chambers *et al.*[12a,b] to measure the degree of outward vertical relaxation in thin Cu overlayers on Ni (001). It should thus be possible to measure interlayer spacings with accuracies of better than 0.1 Å in this way[24,71,73] although doing some sort of theoretical modeling at least at the SSC–PW or SSC–SW level (as Chambers *et al.* have done[12]) is advisable to verify peak origins, shapes, and predicted shifts with relaxation. Using higher angular resolution also should be beneficial for such studies by making it possible to determine forward-scattering peak positions more precisely.

The main point of discrepancy between experiment and SSC–PW theory in Fig. 22b is that the peak for forward scattering along the nearest-neighbor [101] direction has a relative intensity too high for thicker overlayers by about a factor of about 2. As expected from the prior discussion of Fig. 5, using spherical-wave

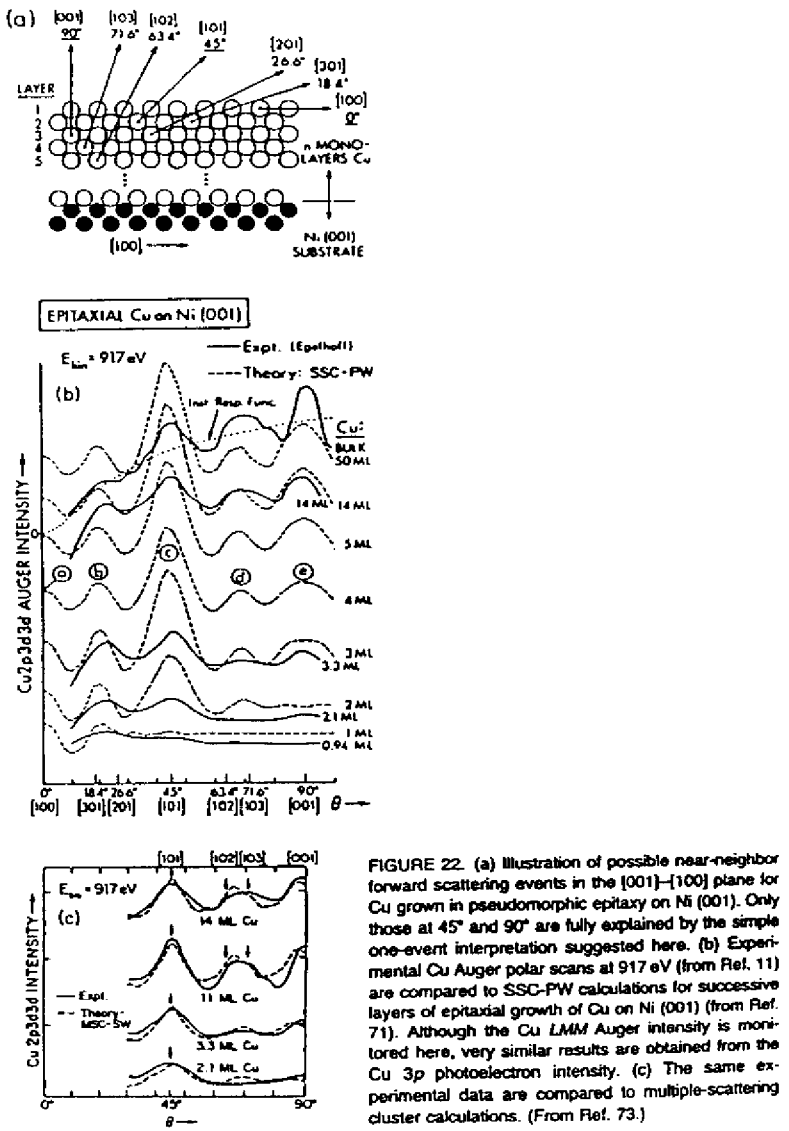

FIGURE 22. (a) Illustration of possible near-neighbor forward scattering events in the [001]–[100] plane for Cu grown in pseudomorphic epitaxy on Ni (001). Only those at 45° and 90° are fully explained by the simple one-event interpretation suggested here. (b) Experimental Cu Auger polar scans at 917 eV (from Ref. 11) are compared to SSC-PW calculations for successive layers of epitaxial growth of Cu on Ni (001) (from Ref. 71). Although the Cu *LMM* Auger intensity is monitored here, very similar results are obtained from the Cu 3*p* photoelectron intensity. (c) The same experimental data are compared to multiple-scattering cluster calculations. (From Ref. 73.)

scattering in the SSC model is found to significantly improve agreement for this relative intensity by reducing it to about $\frac{3}{4}$ of the magnitudes seen in Fig. 22b for thicknesses >3.0 ML[50b]; it is nonetheless still too high by 1.3–1.5 times in comparison with experiment. The remaining discrepancy is due to multiple scattering effects, and the calculations of Fig. 22c include the additional defocusing of intensity along the [101] direction. Much more quantitative agreement with experiment is obtained here. However, even though certain forward-scattering peaks may have their relative intensities decreased by multiple scattering, it should nonetheless still be possible to use the peaks along [001] and [101] in the simple way described in the preceding paragraphs to monitor overlayer thicknesses and determine interlayer relaxations.[71,73]

A more recent paper by Egelhoff[103] has also looked experimentally at a single pseudomorphic Cu (001) layer on Ni (001) buried under various numbers of Ni (001) overlayers. In this work, the attenuation and broadening of certain features with increasing layer thickness is interpreted as evidence of stronger multiple-scattering effects in emission from greater depths. Although the defocusing effects seen in the MS results of Fig. 6 make this a plausible conclusion, Herman *et al.*[105] have made SSC–SW predictions for the cases studied, and these are found to show very similar attenuation to the experimental data. As one example of this comparison of experiment and SSC–SW theory, Fig. 23 shows results for the 917 Auger peak; the experimental data have been corrected for the θ-dependent instrument response by dividing by the curve for a single Cu

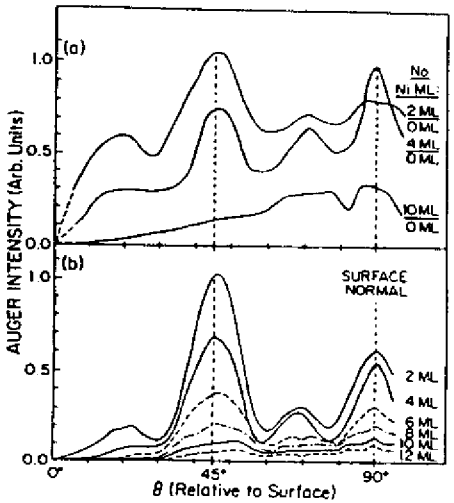

FIGURE 23. (a) Experimental data for Auger emission from a single pseudomorphic Cu (001) layer on top of Ni (001) buried underneath different numbers of layers of epitaxial Ni, also in (001) orientation. (From Ref. 103) (b) Theoretical calculations within the SSC-SW approximation of the results in (a), including curves for other overlayer thicknesses. (From Ref. 105.)

monolayer with no overlying Ni (shown as "0 ML"). Although the relative intensity of the peak at 45° compared to that at 90° is again predicted in theory to be too high, the trends in experiment as the Ni overlayer is increased in thickness are surprisingly well reproduced by the SSC calculations. In particular, the change in the absolute intensity of the peak at 45° with thickness is well reproduced by the calculations, and its final broadening out and diminution of importance in comparison to the peak at 90° is also correctly predicted. Discrepancies noted are that the broad, flat feature seen in experiment at about 70° is not fully developed in the single scattering theory and that an initial narrowing of the peak along 45° that may be due to multiple-scattering effects (cf. the discussion of Fig. 6 and Fig. 22c) is not seen. Experimental errors of as much as ±10–20% in measuring the number of monolayers (cf. calculated curves at other thicknesses), as well as the possible presence of defects in the growing Ni layer,[12a,b] could also affect the agreement between experiment and theory. More recent multiple-scattering calculations for this buried-monolayer system by Xu and van Hove[73] and by Kaduwela *et al.*[84] yield a more quantitative description of the decrease in intensity of the peak at $\theta = 45°$, although the experimental overlayer thicknesses have to be decreased by from 0.6 to 1.5 ML in the calculations to yield optimum agreement. However, on going to thicker overlayers on the order of ten layers, there is still a stronger peak in MS theory than in experiment near $\theta = 70°$.

Thus, although such a deeply imbedded emitter layer clearly represents an extreme case of the type shown in Fig. 3b–ii, for which multiple-scattering effects ought to be maximized, the case for these data definitely exhibiting such effects is not as strong as might be expected, and the SSC approach still yields at least a semiquantitative description of the data.

A final note of caution in connection with this study[103] concerns the idea that classical trajectories can be used to predict when and how multiple scattering will be important in AED or XPD. Although classical arguments can be didactically useful once the correct answer is known, taking them further seems to be very risky, particularly when the quite simple and wave-mechanical SSC model is already available for comparisons to experiment and to more-accurate calculations including higher-order multiple scattering.

We now turn to the second system: Fe/Cu (001) as studied by Chambers, Wagener, and Weaver[104a] and by Steigerwald and Egelhoff.[104b] Figure 24 shows a similar set of AED data from the latter study for the case of Fe deposited on Cu (001) at ambient temperature and compares it to results like those in Fig. 22b. It is striking here that coverages of one monolayer or less (even down to 0.1 ML) already exhibit the strong forward-scattering peak at 45° characteristic of *fcc* Fe in islands or clusters at least two layers thick, as well as the beginning of the peak along the surface normal associated with three-layer structures. In fact, the 1-ML Fe curve looks very similar to that for 3.3 ML of pseudomorphic Cu in Fig. 22b. These results[104b] and a more detailed set of polar and azimuthal data discussed by Chambers *et al.*[104a] thus show that at least the first one or two layers of Fe grown under these conditions have a strong tendency to agglomerate on Cu (001), a conclusion that has important implications for the magnetic properties of such overlayers.[104] This work nicely demonstrates the general usefulness of such

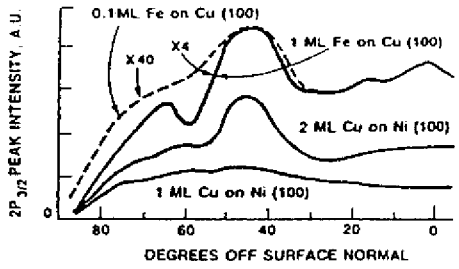

FIGURE 24. Experimental polar scan data for Fe $2p_{3/2}$ emission at 780 eV from Fe deposited at ambient temperature on Cu (001). Data for both 0.1 ML and 1 ML total coverages are compared to similar results for Auger emission from Cu deposited up to 1 ML and 2 ML on Ni (001); cf. Fig. 22(b). Note the presence of strong forward scattering peaks at 45° in both Fe curves and the beginning of a peak along normal for the 1-ML Fe data. [From Ref. 104(b), with more detailed polar and azimuthal data appearing in Ref. 104(a).]

scanned-angle measurements for detecting the presence of island or cluster formation, as discussed further in section 4.5.

4.3.3. Fe/GaAs (001)

We now consider another example from the work of Chambers *et al.*[12a,b] in which Auger electron diffraction has been applied to the growth of epitaxial layers of Fe on GaAs (001). This system has been studied extensively because of its interesting magnetic anisotropies in the surface plane, as first discussed by Krebs, Jonker, and Prinz.[106] It is complicated by the fact that outward diffusion of As is thought to occur, even though at the same time the Fe atoms appear in LEED to be growing in (001) epitaxy. A polar scan in the [100] azimuth of the $L_3M_{4,5}M_{4,5}$ Fe Auger peak at approximately 710 eV kinetic energy provides further information on how this might be occurring, as illustrated in Fig. 25. Here, the experimental AED curve of Chambers *et al.* for a 10-ML Fe overlayer on GaAs is compared to an analogous experimental Fe $2p_{3/2}$ XPD curve for a clean *bcc* Fe (001) surface due to Herman *et al.*[107]; the XPD peak furthermore has a kinetic energy of about 780 eV, very close to that of the Auger peak, so that the two diffraction patterns would be expected to be very similar for a given crystal structure. In fact, the two experimental curves are very different, with the *bcc* Fe (001) showing a much lower intensity for the peak along [101] and different fine structure at polar angles of about 15–30° and 60–75°.

Also shown in Fig. 25 are SSC–PW theoretical curves for three overlayer crystal structures: *bcc* Fe with $a = 2.82$ Å [the bulk-lattice constant which also gives a very good match to the GaAs (001)], primitive cubic (*pc*) Fe with $a = 2.82$ Å, and *fcc* Fe with $a = 2.82$ Å. It is clear that the *fcc* calculation gives the best agreement with the Fe/GaAs experimental data as to both the relative intensity of the [101] peak and the fine structure. The calculations for the other two structures seriously underestimate the intensity of the peak along the [101] direction. The *bcc* calculation also agrees best with the XPD curve from clean Fe (001), particularly as to the relative intensities of the weaker features from $\theta = 15°$ to 75°, even if all of the fine structure is not correctly predicted. All

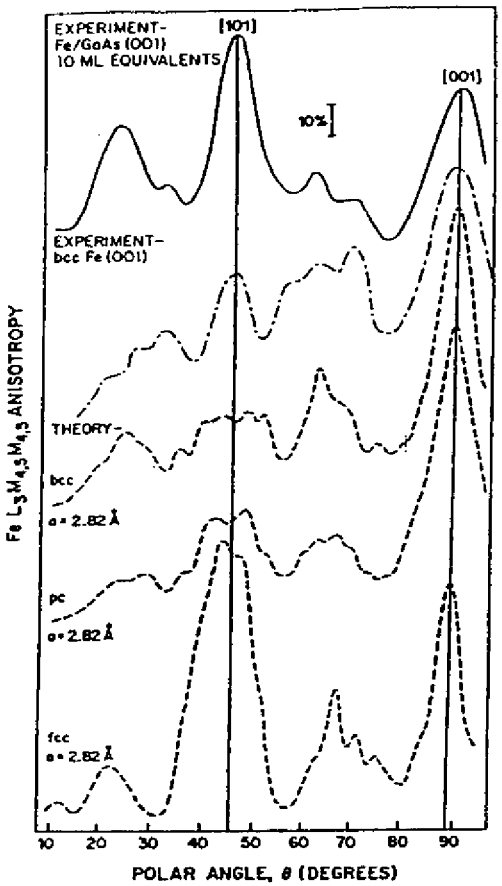

FIGURE 25. Experimental polar scan of the Fe *LMM* Auger intensity at 703 eV from 10 ML of Fe deposited on GaAs (001) (solid curve) is compared to theoretical calculations for various Fe lattices (dashed curves). (From Ref. 12(b).) The scans are in the [100] azimuth ($\phi = 0°$), with the directions [101] and [001] indicated. The calculations are at the SSC-PW level, and they are shown for Fe in three crystal structures: *bcc*, *pc* (primitive cubic), and *fcc* (which is proposed to be *bcc* Fe with As atoms outwardly diffused into the *fcc* interstitial sites). Also shown for comparison is an experimental polar scan for bulk Fe (001) in the same azimuth (dot-dash curve) from a separate study. (From *ref.* 107.)

calculations predict a strong peak along the normal or [001] direction; this is due to forward scattering from atoms with a closest spacing of $1.000a$ for all three structures. Along the [101] direction, by contrast, the *fcc* structure has nearest-neighbor scatterers at a distance of $a/\sqrt{2} = 0.707a$ (cf. Fig. 22a) whereas, in the *bcc* and *pc* structures, the nearest scatterers are twice that distance away at $\sqrt{2}a = 1.414a$. This explains the stronger forward-scattering peak along [101] in the *fcc* theory.

The combined experimental and theoretical results in Fig. 25 thus suggest that the local structure in Fe/GaAs has scatterers that are at the *fcc* positions. These results have been explained by the interesting proposal[12a,b] that the outward-diffusing As atoms occupy the face-centered positions in a *bcc* Fe lattice so as to yield an overall AED pattern that is essentially *fcc* in nature. Although Fe and As are slightly separated in atomic number (26 and 33, respectively) so that the all-Fe calculations of Fig. 25 are not in that case strictly correct, the forward-scattering strength that is dominant at these energies is not a strong function of atomic number (but rather of atomic size, as noted in section 3.1.3), and thus these theoretical simulations should be reasonably accurate for the hypothesized structure as well.

This work thus illustrates another aspect of higher-energy AED and XPD that should be generally useful in studying the detailed structures of complex epitaxial overlayers that may have impurities present, such as atoms diffusing outward from the substrate or inward from the surface. An obvious complementary and useful type of data that could be derived for such a system would be to look at the AED or the XPD of the impurity. For the example of Fe/GaAs, if the hypothesized structure is correct, As also should show an *fcc* type of diffraction pattern, although perhaps weaker or with less fine structure if it is preferentially segregated to the surface of the Fe overlayer. Another recent example of this type is a combined AED/XPD study of dopant P and Sb atoms in Ge epitaxial layers on GaAs (001) by Chambers and Irwin;[12c] here P was found to occupy lattice sites, whereas Sb was segregated to the surface.

4.3.4. $Hg_{1-x}Cd_xTe$ (111)

As a final example of an epitaxial system, we consider a recent scanned-angle XPD study by Granozzi, Herman *et al.*[108] of $Hg_{1-x}Cd_xTe$ (111) grown by liquid-phase epitaxy. This sample underwent transport at atmospheric pressure before being studied and was minimally ion-bombarded so as to remove a thin oxide layer from the surface. It was not subjected to bakeout or annealing after ion bombardment, to avoid depleting Hg from the surface region. At the time of measurement, the value of x was approximately 0.4. In spite of the less-than-ideal surface expected to remain after such a treatment, XPD modulations of $\Delta I/I_{max} \approx 15$–$25\%$ were seen in all of the major photoelectron peaks observable (Hg $4f_{7/2}$ at a kinetic energy of 1383 eV, Cd $d_{5/2}$ at 1078 eV, and Te $3d_{5/2}$ at 910 eV). Qualitatively comparing Hg, Cd, and Te diffractions curves immediately indicated that the Hg and Cd atoms were occupying similar lattice sites, as expected.

As another more subtle structural problem resolvable from this data, the question of the nature of the termination of the surface also was addressed. That is, was the surface terminated preferentially with double layers having cationic Cd (or Hg) on top and anionic Te on the bottom (termed Model *A*) or with the reverse (termed Model *B*)? Comparing the azimuthal XPD patterns for Cd and Te obtained at several polar angles with SSC–SW calculations for both Models *A* and *B* permits determining the dominant type of termination, even for a surface that probably has a reasonable amount of damage on it. Some of this data is shown in Fig. 26, where Cd emission at $\theta = 19°$ and 35° (both chosen to pass through near-neighbor scattering directions) is considered. It is clear that, for both angles of emission, the agreement between experiment and theory as to both visual fit and *R* factor[26d] is much better for a Model *A* termination; peak relative intensities, positions, and fine structure are much better predicted. Similar conclusions can be drawn from analogous Te azimuthal scans.

As one further aspect of this study, we consider the forward scattering origin of the various major peaks observed in Fig. 26 with the aid of Fig. 27, which indicates the several near-neighbor forward-scattering events possible in a surface terminated as in Model *A*. For the data at $\theta = 19°$, the effects of the event labelled as $\theta = 19°$, $\phi = 0°$ are clear in both experiment and theory. For the data at $\theta = 35°$, the principal peaks are due to events of the types labelled $\theta = 35°$, $\phi = 60°$ and $\theta = 30°$, $\phi = 30°$, 90°.

The analogous Te curves at these polar angles are very different from those of Cd in both experiment and theory, with peak shifts and relative intensity

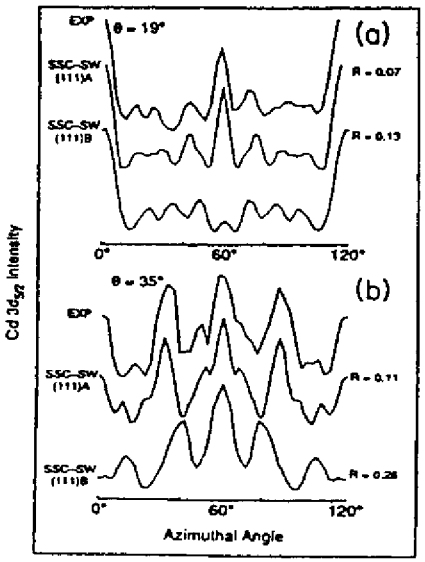

FIGURE 26. Al $K\alpha$-excited azimuthal scans of Cd $3d_{5/2}$ intensities from $Hg_{1-x}Cd_xTe$ (111) ($x = 0.4$) at polar angles of (a) 19° and (b) 35° passing through or very close to forward-scattering low-index directions shown in Fig. 27 as $\theta = 19°$, $\phi = 0°$, $\theta = 35°$, $\phi = 60°$, and $\theta = 30°$, $\phi = 30°$, 90°. Also shown are SSC–SW curves for the two possible surface terminations (Model A = Cd or Hg on top, Model B = Te on top), together with *R* factors comparing experiment and theory. (From Ref. 108.)

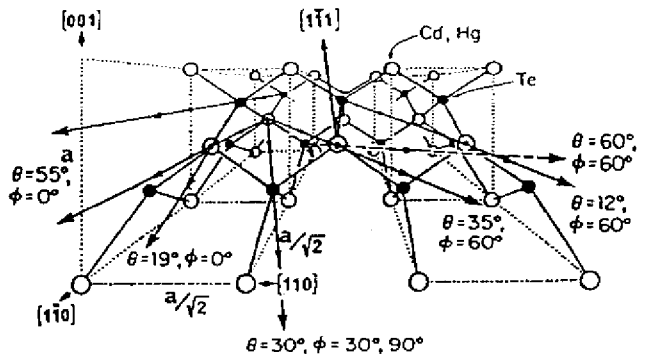

FIGURE 27. Perspective view of the unreconstructed (111) surface of $Hg_{1-x}Cd_xTe$ (111) in the Model *A* surface termination of Fig. 26, with the θ, ϕ coordinates of various near-neighbor/low-index directions along which forward scattering might be expected to be strong. These directions would be the same for the unreconstructed (111) surfaces of any material with the zincblende or diamond structure, as will be used later in discussing Fig. 36.

changes. In particular, the peaks at $\theta = 35°$, $\phi = 30,°$ and 90° for Cd disappear in Te and are replaced by two weaker features at $\theta = 35°$, $\phi = 38°$ and 80°. This is easily explained, since Fig. 27 shows that, in an *A*-type termination, the peaks that disappear are only strong forward-scattering events in the first double layer for Cd emission; thus, they are not expected to be seen for Te.

Inspection of other azimuthal data of this type shows that most of the strong features can be assigned an origin in the various simple near-neighbor forward-scattering effects illustrated in Fig. 27, although it is again important to realize that higher-order interference effects can significantly influence the intensities due to forward scattering by atoms further from the emitter (cf. the discussion of Fig. 22 and, below, Figs. 37 and 38).

This study thus illustrates the further use of higher-energy XPD for epitaxial systems, for which bonding sites of substitutional atoms and the type of surface termination of a compound semiconductor can be determined.

4.3.5. Diffraction Effects in Quantitative Analysis and Photoelectron-detected EXAFS

We conclude this discussion of epitaxial systems with two notes of caution concerning the strong diffraction effects that are expected in either photoelectron or Auger emission from well-ordered lattices.

Diffraction Effects Must Be Carefully Allowed for in Any Attempt to Do Quantitative Analyses of Surface Composition. Methods of correcting for such effects have been considered by both Connelly *et al.*, for simple adsorption on a metal,[109] and more recently for semiconductor surfaces by Alnot *et al.*[110] Not adequately allowing for such effects can lead to errors of as high as ±50% in

measured stoichiometries! Some of the methods for such corrections are averaging over diffraction curves obtained in more than one polar or azimuthal scan, taking advantage of the crystal-structure symmetry to find scans in which different constituents will have nearly identical diffraction patterns (e.g., this is possible in the zincblende structure[110]), or using theoretical calculations to try to determine directions in which diffraction effects can be neglected.

By contrast, a potentially useful aspect of diffraction effects for surface analysis is in monitoring intensities along different directions as a function of coverage during epitaxial growth, as suggested by Idzerda *et al.*[67] Model calculations of such curves in the SSC–PW model suggest that it should be possible to resolve the completion of the first few layers of growth.

The Use of Photoelectron Intensities to Monitor EXAFS-like Oscillations Requires Sufficient Angular Averaging. The idea of using photoelectron intensities to measure EXAFS oscillations for near-surface species has recently been proposed by Rothberg *et al.*[111] and applied to semiconductor systems by Choudhary *et al.*[112] It is clear from the strong oscillations of up to 70% seen in scanned-energy photoelectron diffraction and their dramatic dependence on emission direction (cf. Fig. 20) that an adequate averaging over direction must be undertaken to yield something related to the 4π-averaged EXAFS signal. Although this is automatic for disordered or polycrystalline systems,[111] it is problematic in single-crystal studies. Lee[41] has in fact questioned on theoretical grounds whether even the maximum 2π averaging possible in photoemission for such cases is sufficient to yield the EXAFS limit. Nonetheless, preliminary experimental results of this type[112] using the modest type of averaging inherent in the conical solid angle of a cylindrical mirror analyzer (CMA) appear to yield EXAFS-like data. However, it is the author's opinion that a single-geometry CMA measurement does not represent sufficient angular averaging to reliably yield the EXAFS limit and that the close similarity of these result to EXAFS data may have a fortuitous component. Perhaps measuring intensities for several different orientations of the specimen with respect to the analyzer would improve the reliability of this approach, but it is not clear that this has been done to date. The solid-angle averaging of a particular analyzer could also be checked by carrying out SSC calculations over the directions involved and summing these intensities, as was done recently by Idzerda *et al.* in another context.[67]

Overall, both XPD and AED thus have considerable potential for the study of the morphology of the first 1–5 layers of an epitaxial system. The strongest peaks are expected to be directly connected with simple forward scattering from the first few spheres of neighbors around a given emitter. Weaker features may involve a superposition of several types of scattering events. Thus, a quantitative analysis of the full intensity profile will require calculations at least at the SSC level. Predicting peak relative intensities correctly if emission along a dense row of atoms is involved may also require the inclusion of multiple scattering. However, much useful information about the surface structure, layer thickness, morphology, impurity-site type, and surface termination should be derivable from a consideration of the possible strong forward-scattering peaks due to the nearest

neighbors (cf. Figs. 22 and 27) combined with theoretical modeling at the single scattering level.

4.4. Metal–Semiconductor Interface Formation

We now consider two recent examples of the application of higher-energy XPD to the study of metal–semiconductor interface formation. This kind of XPD study was pioneered by Kono and co-workers, and more detailed discussions appear elsewhere, including work on other metal–semiconductor combinations.[49,113,114] The examples chosen here both involve the initial stage of metal reaction with Si surfaces and represent structures over which controversy still exists. The examples differ in the final structure proposed. The first case, K/Si (001), is a metal overlayer relatively far above the Si surface. The second case, Ag/Si (111), is a metal layer nearly coplanar with the first Si layer. This strongly affects the degree and manner in which forward scattering by Si or metal atoms influences the observed diffraction patterns.

4.4.1. K/Si (001)

In this study by Abukawa and Kono,[114] azimuthal K 2*p* XPD data have been obtained for the structure formed by depositing K to saturation onto the Si (001) (2 × 1) reconstructed surface. The substrate surface is thought from a number of previous studies to consist of rows of dimers, as shown by the small open circles in Fig. 28. The most-often-discussed model for the potassium structure on this surface is the so-called one-dimensional-alkali-chain (ODAC) model illustrated in Fig. 28a; it corresponds to a $\frac{1}{2}$ ML coverage, and leaves open grooves adjacent to each high-lying row. However, there is still considerable controversy surrounding the structure of K adsorbed on Si (001), and this geometry has not been directly determined.[115] There is also disagreement as to what constitutes the saturation coverage of K on the surface.[114,115b]

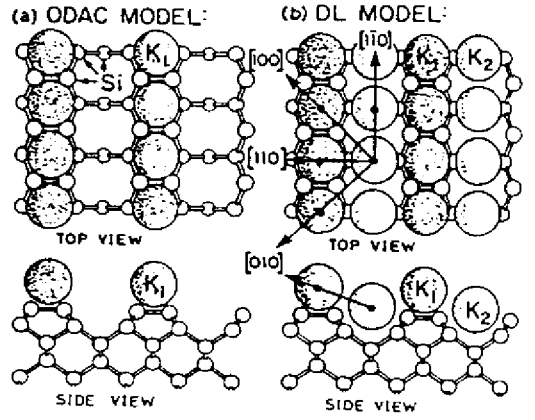

FIGURE 28. Schematic illustration of two structural models for the Si (001) (2 × 1) surface saturated with K: (a) one-dimensional-alkali-chain (ODAC) model, (b) double-layer (DL) model proposed from an analysis of azimuthal XPD data (see Fig 29). Silicon dimers appear along the [1, −1, 0] rows in both models. Each model can exist in two domains rotated by 90° with respect to one another. Some strong forward-scattering directions in the DL model are shown by arrows. (From Ref. 114.)

Even before considering the actual XPD data, we note that, if only atoms of type K_1 in the ODAC structure are present, the diffraction patterns would be dominated by forward scattering from other K_1 atoms, and this would furthermore be strong only for very low θ and along the $\langle 1,-1,0\rangle$ rows for which the interatomic distances are shortest. The Si atoms should play only a minor role, perhaps producing fine structure in the azimuthal curves for very low takeoff angles.

A set of azimuthal experimental data for this system with emission angles relative to the surface of 14°–22° is shown as the points in Fig. 29. The strongest peak is seen along $\langle 100\rangle$ for a relatively high value of $\theta = 14°$, an observation which already seems at odds with the ODAC model. Considering also the experimental anisotropy $\Delta I/I_{max}$ (scale along left of figure), we see that it can be as high as about 30%, a value which is significantly above those expected in general for such higher-θ scattering from neighbor atoms that are either all in-plane or all below-plane relative to the emitter (cf. Fig. 15 for $c(2\times 2)$ O/Ni (001) as a typical example).

These results suggest trying in addition to the ODAC model another structure in which there are scatterers well above some K emitters. One such model is the obvious one of putting rows of atoms of type K_2 in all of the grooves to yield a 1-ML coverage, as illustrated in Fig. 28b. For this double-layer (DL) model, strong forward scattering can occur for higher takeoff angles, as indicated by the arrows along both $\langle 110\rangle$ and $\langle 100\rangle$ directions. For very low takeoff angles approaching zero, either model is expected to show strong forward scattering for emission along the K rows parallel to $\langle 1,-1,0\rangle$. The presence of two equivalent domains of either structure rotated by 90° with respect to one another also implies

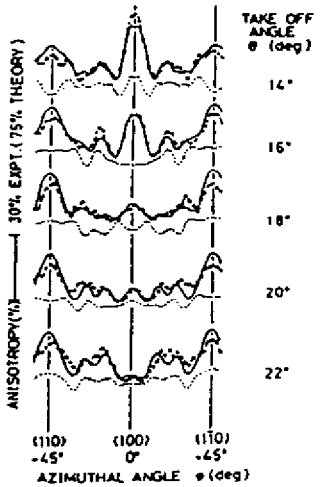

FIGURE 29. Azimuthal data for Al $K\alpha$-excited K 2p emission from the Si(001) (2 × 1) surface saturated with K at polar angles from 14° to 22° above the surface. Experiment is compared with SSC-PW calculations for the two models shown in Fig. 28: ODAC = dashed curves and DL model best fitting data = solid curves. Very similar curves were also obtained with SSC-SW calculations. (From Ref. 114.)

summing two diffraction patterns in the analysis and overall C_{4v} symmetry in both the observed and calculated patterns.

Comparing these experimental data to SSC–PW (or very similar SSC–SW) calculations for the two models[114] is now found to yield clearly superior agreement for the DL model (solid curves in Fig. 29). The strong peak at $\phi = 0°$ which grows in for θ approaching 14° can be explained as being due to emission from K_2 atoms and scattering by their second-nearest K_1 neighbors along $\langle 100\rangle$. The peaks along $\langle 110\rangle$ and $\langle 1,-1,0\rangle$ are due to K_2 emission again, but now involve scattering from nearest-neighbor K_1 atoms (and a sum over domains 90° apart). Additional azimuthal data for θ as low as 4°[114] show strong peaks for $\phi = \pm 45°$ that can be ascribed to the expected forward scattering along $\langle 1,-1,0\rangle$ directions within either K_1 or K_2 rows. Not surprisingly, these latter peaks are also present for very low θ in the theoretical curves for both models, and they are the most significant features in calculations for the ODAC model. Comparing experiment and theory for these lower-θ data also is found to support the DL model. By testing various vertical placements of the two K row types, the authors were able to determine a 1.1 Å vertical separation between the two K rows, and less accurately to determine that the bottom K row was not lower than about 0.5 Å above the first Si layer. For such a 1.1-Å separation, the K_1–K_2 distance is 3.99 Å and slightly larger than the K–K distance of 3.84 Å along either the K_1 or K_2 rows. It is also interesting that, for this structure, the $K_2 \rightarrow K_1$ forward scattering peaks should occur at $\theta \approx 16°$ along [110] and $\theta = 11°$ along [100]; this explains the strong peaks seen in the data over this range of polar angles. The registry of the DL along $\langle 1,-1,0\rangle$ with respect to the underlying Si surface was not determined, but the six-coordinate site shown in Fig. 28b for atoms of type K_1 is that predicted by theory to be the lowest energy.[115a,d]

In a more recent theoretical study of this system by Ramirez,[115d] it is found that adsorption in groove sites (including type K_2 in Fig. 28b) is significantly lower in energy than the six-coordinate site shown for K_1 atoms. Thus, adsorption in the grooves is supported by theory as well. However, the 1-ML structure proposed in this study is different from Fig. 28b in that the atoms of type K_2 are shifted along the $\langle 1,-1,0\rangle$ direction so as to be directly opposite the Si dimers. The K_2 atoms in this model are also predicted to be approximately in-plane with respect to the Si dimers. However, it is doubtful that this structure would yield the strong forward scattering peak seen in XPD along $\phi = 0°$ for relatively high theta values of 12–16°. Thus, even though these calculations[115d] indicate that a double layer with such shifted K_2 atoms is lower in energy than the structure shown in Fig. 28b, the latter structure still represents a better choice based upon the XPD data.

Overall, these XPD results thus provide important new insights into the bonding of K on Si (001) and illustrate several aspects of the use of this technique for metal–semiconductor studies.

4.4.2. Ag/Si (111)

The Ag/Si (111) system has been studied by almost every modern surface-science technique and is known to exhibit, among other things, a well-ordered

($\sqrt{3} \times \sqrt{3}$) Ag structure and the formation of *fcc* Ag clusters or islands with (111) orientation for exposures that go above the 0.7–1.0 ML needed just to form the ($\sqrt{3} \times \sqrt{3}$) structure.[49,50,116,117] In the following section, we consider the use of XPD in studying such clusters; here, we concentrate on a recent XPD study by Bullock *et al.* of the ($\sqrt{3} \times \sqrt{3}$) structure.[50a,b]

In this study, polar and azimuthal Ag $3d_{5/2}$ XPD data were obtained for a well-ordered and very stable ($\sqrt{3} \times \sqrt{3}$)Ag structure, and these experimental results are summarized in Figs. 30a and 31. The smooth and structureless nature of the polar scans in Fig. 30a indicates an absence of strong forward scattering effects, except perhaps at very low takeoff angles of $\theta \approx 4$–$8°$ where a four-peak structure is seen in Fig. 31. A simple geometric calculation then permits the conclusion that the Ag cannot be more than approximately 0.5 Å below the surface Si layer. This is also consistent with the lower anisotropy values of no more than 21% that are found for the azimuthal scans of Fig. 31. It can thus be concluded that there are no strong forward scatterers above the Ag. The azimuthal data are also fully consistent with an earlier XPD study of this system by Kono *et al.*,[49] but they are more detailed in involving full 360° ϕ scans and more θ values.

It is beyond the scope of this review to discuss the many models that have been and are being proposed for this structure, but all known structures have been tested against this azimuthal data by Bullock *et al.*, using *R* factors[26d] as the final quantitative measure of goodness of fit. The calculations were carried out at the SSC–SW level, and in final optimizations also with the full final-state interference of 3*d* emission into *p* and *f* channels. (This latter correction was not found to alter the structural conclusions, a result which is expected to be true in general for higher-energy XPD, but certainly not for work at less than a few hundred eV, as discussed in section 3.1.2).

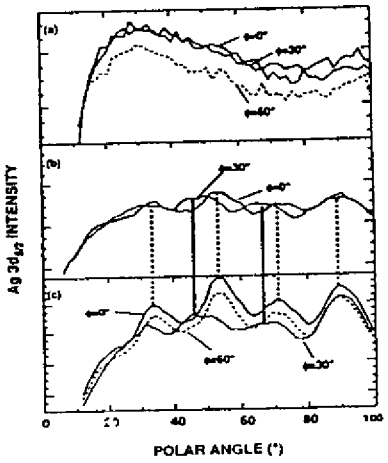

FIGURE 30. Polar XPD scans of Ag $3d_{5/2}$ intensity at 1120 eV from: (a) the ($\sqrt{3} \times \sqrt{3}$) Ag structure on Si (111) formed after annealing an ~1.3-ML Ag overlayer to 550°C; (b) a Ag overlayer of approximately 2 ML average thickness at 450°C; and (c) a thick Ag overlayer of approximately 6 ML thickness at ambient temperature. (From Ref. 50.)

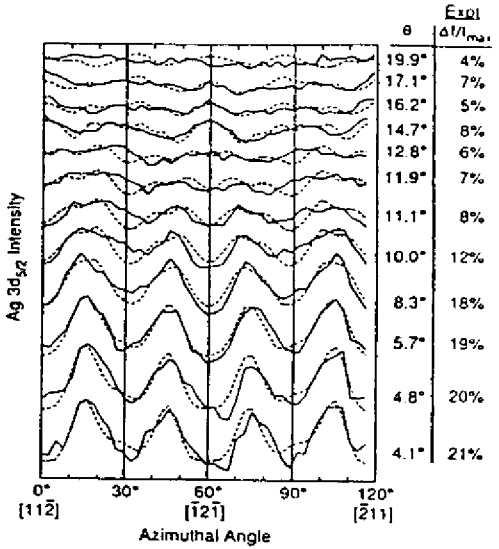

FIGURE 31. Azimuthal XPD scans of Ag $3d_{5/2}$ intensity from ($\sqrt{3} \times \sqrt{3}$) Ag/Si (111) at polar angles from 4° to 20° (solid lines) are compared to SSC-SW calculations for the optimized two-domain model of Fig. 32 (broken lines), for which $s_1 = s_2 = 0.86$ Å; $z_1 = -0.10$ Å, $z_2 = -0.30$ Å, and a 50:50 mixture of the two domains. Full final-state interference in the *d*- to $-p + f$ emission process has been included. This comparison yields an *R* factor of 0.14 (cf. values in Figs. 21 and 26). (From Ref. 50.)

The final model proposed on the basis of this work is for two nearly equivalent domains of Ag in a honeycomb array on a Si surface that has had the top layer of the first Si double layer removed. This two-domain missing-top-layer (MTL) model is illustrated in top view in Fig. 32. The optimized structural parameters are a contraction of the Si trimers toward one another in both domains of $s_1 = s_2 = 0.86$ Å, vertical distances of the Ag relative to the Si layer of $z_1 = -0.1$ Å for Domain 1 and $z_2 = -0.3$ Å for Domain 2 (that is, the Ag is very nearly coplanar with the Si in both domains, but just slightly below it), and a mixture of the two domain types that is between 50:50 and 40:60, with Domain 2 perhaps being slightly more predominant. The fits between experiment and theory for this fully optimized structure are shown in Fig. 31. All other models that have been tried yield significantly worse agreement as judged both visually and by *R* factors. This two-domain model is also closely related to one derived in a prior XPD study by Kono *et al.*: a single-domain MTL Ag honeycomb structure of type 1 with $s = 0.66$ Å and a vertical distance of -0.15 Å. The presence of Domain 2 is suggested to explain the four-peak structure at low θ values in Fig. 31, as illustrated by the nearest-neighbor forward-scattering peaks for the two domains shown at the bottom of Fig. 32. For

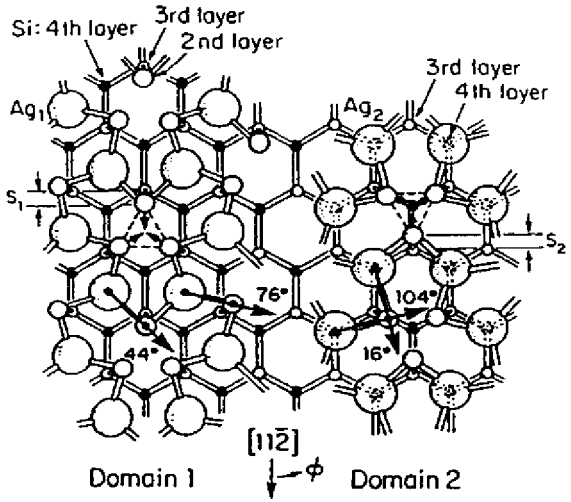

FIGURE 32. The two-domain missing-top-layer (MTL) honeycomb model proposed for ($\sqrt{3} \times \sqrt{3}$) Ag/Si (111). The parameters characterizing it are: vertical positions $z_1 = -0.1$ Å and $z_2 = -0.3$ Å, Si trimer contractions of $s_1 = s_2 = 0.86$ Å, and a 50:50 mixture of Domains 1 and 2. The lower half of the figure shows the two sets of nearest-neighbor Si forward-scattering peaks that produce the four-peak structure seen at low θ values in Fig. 31. (From Ref. 50.)

the lowest θ values near 4°, an additional correction of possible importance is the reduction of nearest-neighbor Si forward-scattering strengths due to multiple scattering effects along the nearly linear rows of atoms that can be labelled Ag emitter → Si first-neighbor scatterer → Si second-neighbor scatterer (cf. Figs. 32, 3b, and 6); very recent MS calculations by Herman *et al.*[50c] show that this reduces the absolute peak intensities for $\theta = 4°$ and $\phi = 16°$, 44°, 76°, and 104° by about 30%, thus improving the agreement of theoretical and experimental anisotropies.

A further interesting point in connection with this structure is that a recent LEED study of the clean Si (111) surface by Fan *et al.*[117] concludes that a little-studied ($\sqrt{3} \times \sqrt{3}$) Si reconstruction has very nearly the same geometry as Domain 1 in Fig. 32 if Ag adatoms are replaced by Si adatoms. Although these authors do not consider the possibility of a second domain of type 2 for ($\sqrt{3} \times \sqrt{3}$) Si, it might be expected to have approximately the same energy (due to weak fourth-layer interactions) and thus also to exist on the clean surface. This work thus lends support to the two-domain model for ($\sqrt{3} \times \sqrt{3}$) Ag, since one can imagine its growth simply by replacing the Si adatoms with Ag atoms.

This structure is still very controversial, and these results thus cannot be called conclusive, but they further illustrate the way XPD can be used for such metal–semiconductor studies. This study is also state-of-the-art for XPD in that it

involves a large azimuthal data set, SSC–SW calculations with correct final-state interference, and the use of R factors[26d] to judge goodness of fit. As one qualitative figure of merit in connection with this study, the minimum R factors of 0.14 found are about $\frac{1}{2}$ of those found in recent LEED studies of the same system.[117,118]

4.5. *Supported Clusters*

In this section, we briefly consider two examples of how higher-energy XPD has been used to study the formation of three-dimensional clusters on surfaces. (A third example has already been considered in the data for Fe deposited on Cu (001) shown in Fig. 24, where agglomeration effects are visible even for very low coverages.)

4.5.1. Ag/Si (111)

We have noted in the last section that Ag readily forms islands and three-dimensional clusters on the Si (111) surface if the coverage exceeds the 0.7–1.0 ML needed for the ($\sqrt{3} \times \sqrt{3}$) Ag structure. If these clusters are more than one atomic layer in thickness, then strong forward-scattering effects are expected for emitters in the lower layer(s) of the cluster. Such effects are illustrated in Fig. 30b,c, where polar scans of Ag $3d_{5/2}$ intensity have been measured first in Fig. 30c for a thick Ag reference layer of approximately 6 ML thickness, and then after heating to 450 °C so as to desorb all but an average coverage of about 2 ML. In Fig. 30c, a LEED pattern characteristic of the epitaxial Ag (111) that is known to grow on Si (111) is seen, and strong diffraction peaks due to buried-atom emission from this thick overlayer are found. In Fig. 30b, the Ag (111) LEED pattern is weakly present and there are still clear remnants of the photoelectron-diffraction features seen in the thick overlayer. Thus, such XPD patterns are very sensitive to the presence of three-dimensional islands.

The previous discussion of Figs. 22 and 23 also suggests that it might be possible to estimate the average thickness of such clusters up to about 5 ML, where the XPD features begin to converge to the bulk pattern. An additional type of information that could be very useful for some systems is the orientation of the cluster crystal axes with respect to the surface normal. In fact, even if clusters grow in a textured way (that is, without preferred azimuthal orientation), polar scans of the type shown here should permit determining whether there is any preferred vertical axis. Bullock and Fadley[50b,119] have also recently pointed out that, even for two-dimensional islands, it should be possible to use low-θ azimuthal scans to determine the island orientation and, for smaller islands, the average number of atoms present.

4.5.2. Pt/TiO_2

As a second example of cluster studies using XPD, Tamura *et al.*[120] have considered the interaction of Pt with three low-index faces of TiO_2, a system of interest in catalysis and for which the so-called strong metal-support interaction

(SMSI) can occur. In this study, Pt was deposited at room temperature to a mean thickness of about 10 ML onto the (110), (100), and (001) surfaces of TiO_2, and azimuthal XPD measurements were made at different polar angles for the Ti 2*p* and O 1*s* photoelectron peaks before deposition and for the Pt 4*f* peaks after deposition. Similar Pt 4*f* measurements were made after annealing the samples up to 800 K.

Some of these results are shown in Fig. 33a for the (110) surface at $\theta = 40°$ and Fig. 33b for (100) at $\theta = 45°$. Considering first Fig. 33a, we see that curves (i) and (ii) show weak diffraction features for both Ti 2*p* (clean) and Pt 4*f* (just after the deposition). The nonconstant background under these curves, particularly for (ii), is thought to be due to a nonuniform deposition over the region of the sample seen by the electron analyzer; thus, with changes in ϕ, a slightly different area and average Pt thickness might be seen. After the high-temperature anneal, the Pt 4*f* features in (iii) are strongly enhanced, with a concomitant increase in the anisotropy $\Delta I/I_{max}$ from 16% to 29%. This is consistent with the growth of thicker or larger clusters upon annealing, although (ii) indicates that some sort of ordering must be present even without annealing. Finally, (iv) shows a theoretical calculation based upon PW-cluster calculations with the effects of double scattering included. (The possible risk of including only double-scattering events has been mentioned already in section 3.2). The Pt clusters assumed had (111) orientation and contained 13 atoms in three planes; two symmetry-equivalent orientations with respect to the substrate 180° apart were considered. The resulting curve in (iv) is found to agree rather well with the annealed Pt 4*f* experimental results, suggesting that the clusters are growing with preferred (111) orientation.

A similar set of data for the (100) surface are shown in Fig. 33b. Here, (i) and (ii) exhibit strong diffraction from the O 1*s* and Ti 2*p* peaks of the substrate. Curve (iii) shows the strong diffraction of Pt 4*f* after the anneal. (A more uniform deposition of Pt has here made the background levels very flat.) Finally, curve (iv) is calculated for the same type of two-domain, three-layer Pt cluster [but with different assumed registry with the (100) surface], and it again shows good agreement with experiment, suggesting (111) orientation for the clusters on this surface as well.

For the third (001) surface studied, it is interesting that the Pt 4*f* oscillations were weak both before and after annealing, indicating a different kind of overlayer growth and/or a lower degree of cluster formation.

Together the three studies related to clusters that have been considered up to this point illustrate the utility of both polar and azimuthal XPD or AED data for studying the amount of cluster formation present and the average orientation and morphology of the aggregates formed. Two possible limitations of this kind of study are that XPD and AED average over all of the clusters present and so cannot easily be used to estimate the cluster-size distribution. In certain cases, it might even be difficult to detect the difference between, for example, a full 4-ML epitaxial overlayer and a collection of independent clusters with an average thickness of 4 ML, even if the crystallographic orientation could be easily determined. Although with careful measurements of both substrate and deposited-atom intensities before and after deposition and/or heat treatment, the

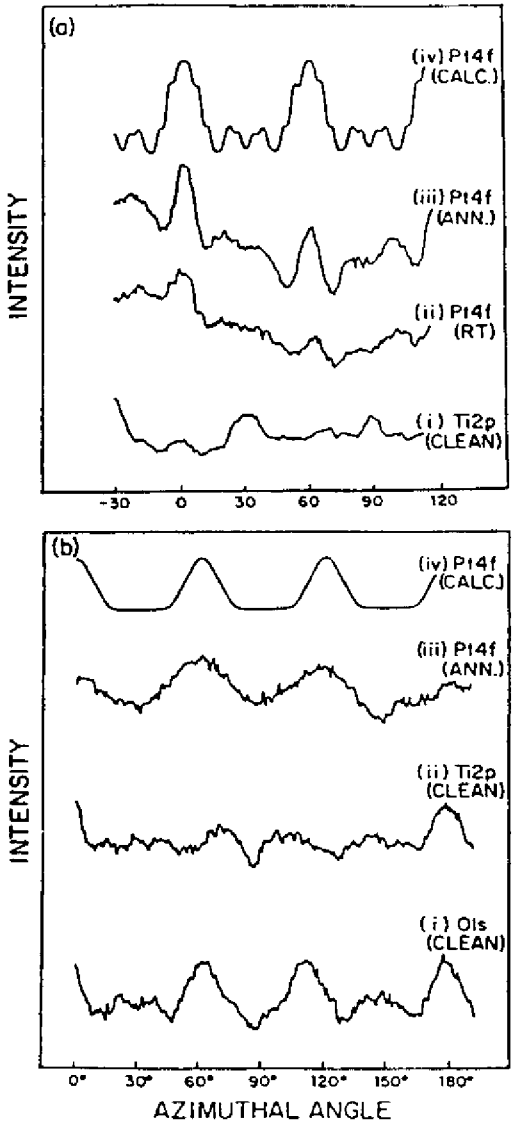

FIGURE 33. (a) Azimuthal XPD data for Pt 4*f* and Ti 2*p* emission from Pt on TiO_2 (110) at $\theta = 40°$ are compared to PW cluster calculations including double scattering for Pt emission from a (111)-oriented metal cluster of about 15 Å diameter. Al $K\alpha$ radiation was used for excitation. (b) As in (a) but for Pt 4*f*, Ti 2*p*, and O 1*s* emission from Pt on TiO_2 (100) at $\theta = 45°$. (From Ref. 120.)

implicit effects of "patching" in cluster growth should be evident in deposited-atom–substrate relative intensities. Simple formulas for analyzing such patched-overlayer relative intensities appear elsewhere.[9] It is also clear that combining XPD or higher-energy AED with scanning tunneling microscopy (STM) would yield a particularly powerful set of data for cluster and epitaxial growth studies. This is because STM can be used to measure directly both the cluster size distribution and the step and defect densities that are averaged over in XPD/AED. But it may be difficult or impossible with STM to see into a cluster or overlayer so as to determine its crystallographic orientation or thickness. This is because STM cannot probe below the surface density of states and also is not atom-specific.

4.6. Core Level Surface Shifts and Chemical Shifts

A further type of problem that has been studied by low-energy photoelectron diffraction using synchrotron radiation for excitation is metal core level surface shifts.[18,53,80,121,122] In particular, Sebilleau, Treglia *et al.*[18,53,80] have tuned the photoelectron energy to low values to achieve high surface sensitivity and have looked with high energy resolution at photoelectron diffraction from such surface-shifted core levels.

Some of their results for tungsten $4f$ emission from W (100) are illustrated in Fig. 34, where both the surface and bulk peaks are shown, together with their individual azimuthal diffraction patterns and corresponding SSC–PW theoretical curves. The two types of peaks clearly exhibit very different diffraction patterns, and both of these are rather well predicted by the SSC model, even at this quite low photoelectron energy of approximately 30 eV. It is remarkable that a single-scattering approach is so quantitative at such a low energy, and this may to some degree be fortuitous. However, later work by Treglia *et al.*[18c,53,80] has reached similar conclusions, with the only qualification being that it is necessary at such energies to use the correct final-state angular momenta, as expected from the discussion of Fig. 4 in section 3.1.2. For the low energy of this case, the $4f$-to-εd channel is assumed to be dominant.

This work thus illustrates the added ability of photoelectron diffraction to carry out independent structure determinations of physically or chemically different species of the same atom through core level shifts. These shifts are not limited to the clean-surface type considered above, but may also involve the well-known chemical shifts commonly seen when different chemical bonding or oxidation states are present. Such state-specific structure studies should be a very powerful probe of surface reactions, overlayer growth, and interface formation. They will, however, require very high energy resolutions of 0.3 eV or better to be fully effective in resolving small shifts.

As an obvious example for future work, it should also be possible to do state-specific diffraction studies on semiconductor surfaces, since both clean surfaces[123a,b] and chemically reacted surfaces[123c] exhibit shifted core levels characteristic of the different bonding sites and/or oxidation states.

One technologically important example of a semiconductor system for which more structural information concerning different chemical species would be useful

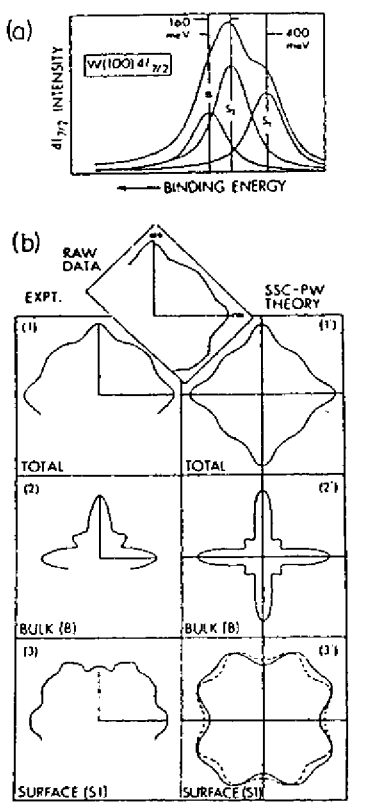

FIGURE 34. (a) A W $4f_{7/2}$ spectrum from W (001) at a kinetic energy of ≈30 eV, showing two surface-shifted core levels (S_1 and S_2) as well as a bulk peak (B). (b) The azimuthal dependences of these intensities at a polar angle of 60° above the surface: (1) represents the total $4f_{7/2}$ intensity, (2) the bulk intensity (B), and (3) the surface intensity (S_1). SSC-PW calculations of these intensities are shown in (1'), (2'), and (3'), respectively. The inset represents raw data for the total intensity. (From Ref. 18(a).)

is the formation of the interface between SiO_2 and Si. Figure 35 shows high-resolution Si $2p_{3/2}$ core spectra obtained by Himpsel *et al.*[123c] from Si (100) and Si (111) surfaces that were thermally oxidized in UHV conditions (2.5 Torr O_2, 750° C, 20 sec) so as to produce a very thin 5-Å oxide film. The overall resolution here was 0.3 eV, and it is striking that all of the oxidation states of Si are clearly seen, from the elemental substrate to the 4+ dioxide. The different nature of the oxidizing surface for Si (111) is further found to lead to a suppression of the Si^{2+} state. These intermediate oxidation states are thought to be associated with the interface, and, from quantitative estimates of the different depth distributions of these states, it is concluded that an extended rather than abrupt interface is involved. Models of such an extended interface have been proposed by Himpsel *et al.*, but these cannot be tested in detail without additional data. It seems clear that separately measuring the scanned-angle photoelectron diffraction patterns of the different oxidation states would provide some very useful information in this

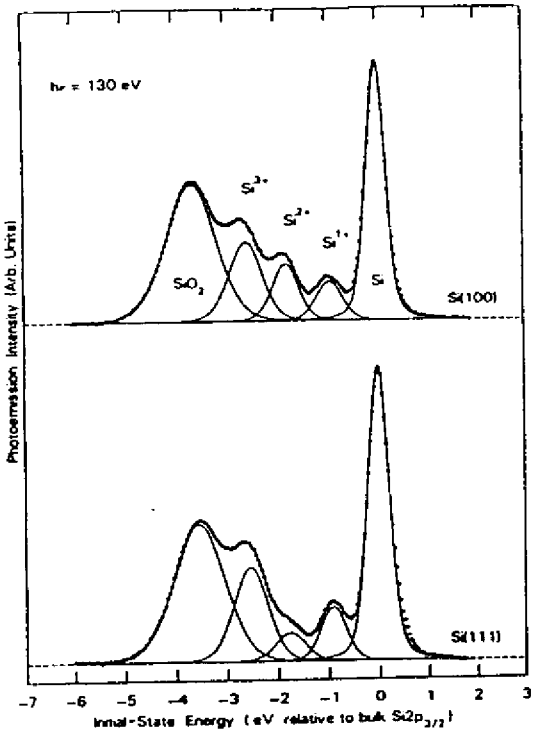

FIGURE 35. The Si $2p_{3/2}$ components of Si $2p$ spectra from thin oxide films of approximately 5 Å thickness thermally grown on Si (100) and Si (111) surfaces. Note the reduced intensity of Si^{2+} for Si (111), assumed to be due to structural differences in the interface. [From Ref. 123(c).]

direction, since each state is hypothesized to occupy one or at most a few distinct site types relative to the substrate lattice.

Although these are difficult experiments at present, the detailed state-by-state information derivable should help in unraveling the microscopic structures of many surface and interface systems. Being able to tune photon energy so as to vary surface sensitivity or to move on or off of resonant photoemission conditions would also be an advantage, as noted in prior studies.[123] Going to higher photon energy not only permits looking deeper into the material and assessing the relative depth distributions of the different species, but should also lead to more simply interpretable forward-scattering peaks for emission from interface-associated atoms. A disadvantage of higher energies is that the substrate signal tends to dominate the spectrum, but with high enough resolution and suitable reference spectra for subtracting the substrate signal, such high-energy measurements should be possible. Synchrotron radiation will thus be necessary to fully exploit this potential for studying interface growth by state-specific photoelectron diffraction.

4.7. Surface Phase Transitions

We conclude this discussion of applications of photoelectron diffraction and Auger electron diffraction by considering briefly their possible use in studying various types of surface phase transitions such as surface premelting, roughening, or disordering at a temperature below the bulk melting temperature,[124] as well as surface reconstructions that are temperature-dependent.[123a,b] The short-range order and directional sensitivity of both PD and AED suggest that they should be useful probes of such surface phase transitions, which may involve changes in near-neighbor atom positions and/or the introduction of considerably more disorder in these positions. The number of such studies is still very small, but the most recent are quite promising.

An unsuccessful attempt at observing surface premelting for Cu (001) in grazing-emission XPD was made some time ago by Trehan and Fadley.[63a] For this surface, roughening and possibly faceting was observed before any evidence was seen in the XPD anisotropies of the extra disorder associated with surface melting. However, much more recently, evidence for surface phase transitions involving surface disordering and perhaps premelting has been seen in XPD from two separate systems: Pb (110) by Breuer, Knauff, and Bonzel[125] and Ge (111) by Friedman, Tran, and Fadley.[126]

For the case of Ge (111), prior LEED studies and theoretical modeling by McRae and co-workers[127] indicate that there is a reversible surface order–disorder transition at a temperature of 1060 K that is 0.88 times the bulk melting temperature. Is this transition visible in XPD? In Fig. 36, we show such XPD data in which the Ge $3d$ azimuthal anisotropy was monitored as a function of temperature. The polar angle of 19° chosen here causes the emission direction to sweep through nearest-neighbor forward-scattering directions in the unreconstructed surface, as shown in Fig. 27. This relatively low θ value also leads to higher surface sensitivity.

Figure 36a shows four azimuthal scans taken at temperatures from ambient to about 50 K above the transition. (Note the expected similarity of the azimuthal scan at ambient temperature to that for $Hg_{1-x}Cd_xTe$ (111) in Fig. 26a.) As the temperature is increased, the azimuthal curves gradually lose much of their fine structure, and upon passing above the transition point, only two main peaks remain in the azimuths $[1, 1, -2]$ ($\phi = 0°$) and $[-1, 2, -1]$ ($\phi = 60°$). In Fig. 36b, the intensity of the $[1, 1, -2]$ peak corresponding to nearest-neighbor scattering is plotted against temperature, and it is clear that an abrupt drop occurs over the interval 850–1050 K. This drop furthermore cannot be explained by simple Debye–Waller modeling.

McRae *et al.*[127a] have measured the intensities of several LEED beams for the same system as a function of temperature, and their data is similar to Fig. 36b in that the intensities drop sharply toward 1060 K and level off thereafter. Some of the LEED intensities drop more rapidly than the curve of Fig. 36b near 1060 K;

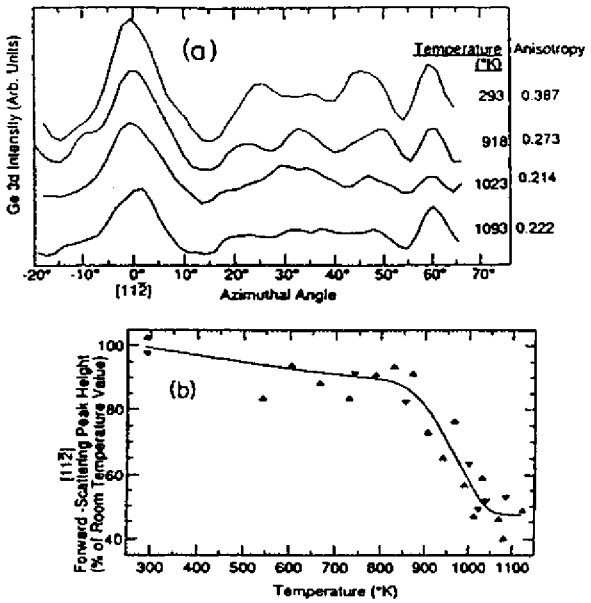

FIGURE 36. Temperature-dependent azimuthal XPD data for Ge 3*d* emission at 1458 eV from Ge(111) at low takeoff angle of $\theta = 19°$. This θ value corresponds to scanning through nearest-neighbor scattering directions for $\phi = 0°$, as shown in Fig. 27. (a) Four azimuthal scans at temperatures from ambient to above the order-disorder transition. (b) The detailed temperature dependence of the height of the peak along $\phi = 0°$. 1060 K is where a prior LEED study (Ref. 127(a)) has seen evidence for a surface-disordering transition. Upright triangles represent increasing temperature; inverted triangles, decreasing temperature. (From Ref. 126.)

some have a form very similar to this curve. Thus, it can be concluded that the same transition is observed in both sets of data, even though the LEED measurement is expected to be sensitive to longer-range order on a scale of approximately 100 Å, whereas XPD should probe distances on the order of 10–20 Å.

Although these XPD results have not as yet been analyzed in detail so as to derive additional structural information, it is clear that obtaining both polar and azimuthal data at temperatures below and above the transition temperature and comparing the diffraction structures seen with calculations for different types of disorder models should yield a better understanding of this and other surface phase transitions.

Similar abrupt changes in polar-scan diffraction anisotropies have also been seen by Breuer *et al.*[125] for the surface disordering of Pb(110), which has been observed previously with Rutherford backscattering and low-energy electron diffraction.[128]

As one interesting future direction for such work, the study of surface phase transitions should also benefit greatly from doing separate diffraction measurements on the various core peaks observed. For example, the Ge(111) surface exhibits one bulk peak and two surface peaks[123a,b] that could all be studied separately. However, the small shifts of only about 0.3–0.7 eV involved here would require very-high-resolution data and the use of curve-deconvolution procedures.

5. FUTURE DIRECTIONS

5.1. Measurements with High Angular Resolution and Bragg-like Reflections

As noted previously, most prior PD and AED measurements have been carried out with resolutions of at best a few degrees in half angle. In many systems, the acceptance solid angle is also not a simple cone, but may have different dimensions along two perpendicular axes.[29] For future work, the question thus arises as to what additional information might be gained by going to much better conic resolutions of, for example, ±1.0°.

As discussed in section 2, various methods exist for limiting angular spreads upon entry into the analyzer, but one which has the advantages of being very certain in its limits and operationally very convenient is the insertion of externally selectable angle-defining tube or channel arrays between sample and analyzer entry. The use of such channel arrays has been discussed by White *et al.*,[33] and they have been used to precisely limit angles to ±1.5° or better (that is, $<\frac{1}{4}$ of typical prior solid angles).

We have already discussed two examples of this kind of data: for NiO grown on Ni(001) in Fig. 14 and for $c(2 \times 2)$ S on Ni(001) in Fig. 17. For these cases, we have pointed out the greater sensitivity to the degree of short-range order and the adsorbate position, respectively.

As a final example of the dramatic effects seen in going to high angular resolution, we compare in Figs. 37a and b low- and high-resolution XPD data obtained by Osterwalder, Stewart *et al.*[48] for Ni $2p_{3/2}$ emission from a clean Ni(001) surface at $\theta = 47°$. A great deal more fine structure is seen in the data with ±1.5° resolution, and the form of the fine structure for $\phi = 25°$–$65°$ is in fact completely changed due to a lower degree of angular averaging over such structures. Very narrow features of only a few degrees at FWHM are also seen in the results at high resolution.

Figure 37c summarizes a more complete set of such high-resolution azimuthal data for Ni $2p_{3/2}$ that represents the most detailed investigation of XPD fine structure to date. Here, the polar angle of emission was varied in 1° steps from $\theta = 40°$ to 50°, passing through the high-symmetry value of $\theta = 45°$ which contains the ⟨110⟩ directions of nearest-neighbor scattering in its ϕ scan. Full 360° scans were used to generate each curve, and fourfold averages of this data into one quadrant shown elsewhere[10,48] agree excellently with the single-quadrant results presented here. This three-dimensional plot makes it clear that high-energy electron diffraction features can change extremely rapidly with either θ or

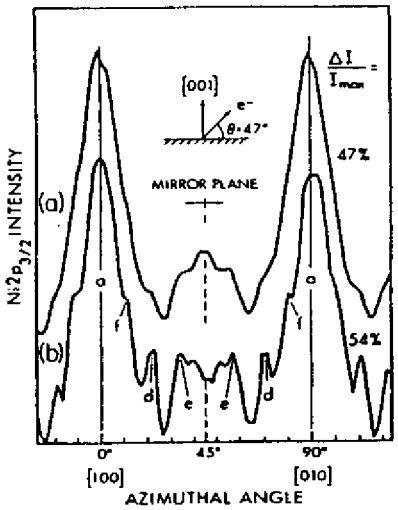

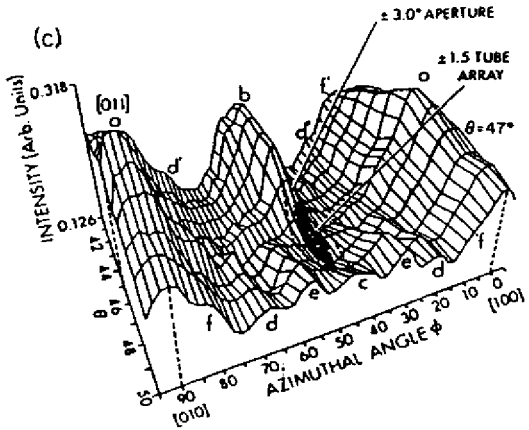

FIGURE 37. Effect of increasing angular resolution on Ni $2p_{3/2}$ azimuthal XPD data from a clean Ni (001) surface at 632 eV. (a) and (b) show single scans at $\theta = 47°$ with resolutions defined by a single aperture of nominal ±3.0° acceptance and a tube array yielding ±1.5° or less, respectively. (c) a three-dimensional summary of a series of single-quadrant high-resolution Ni $2p_{3/2}$ scans with a ϕ step of only 1°. The regions averaged over with the two different angle-defining devices in (a) and (b) are shown as shaded. (From Ref. 48.)

ϕ. These results also qualitatively explain how the approximately ±3.0° averaging in Fig. 37a yields features for $\phi = 25°$–$65°$ that are so different from those for the high-angular-resolution curve in Fig. 37b. That is, Fig. 37a represents an average over all of the curves in Fig. 37c from $\theta = 44°$ to $\theta = 50°$, as bounded by the lighter-shaded elliptical area, and the steeply rising ridge toward $\theta = 44°$ thus accounts for the peak seen at $\phi = 45°$ with lower resolution. The results in Fig. 37b, by contrast, represent an average over only the darker-shaded area in Fig. 37c, and so retain a minimum at $\phi = 45°$.

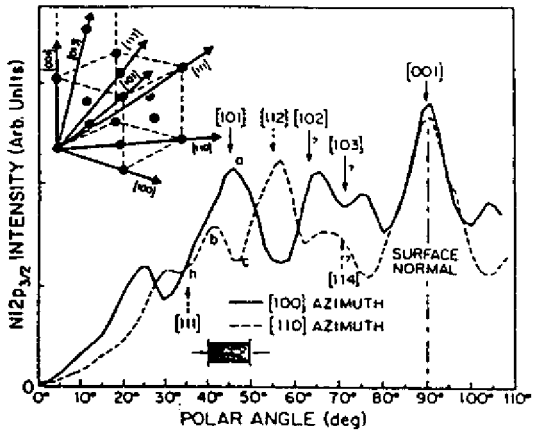

FIGURE 38. High-resolution Al Kα polar scans of Ni $2p_{3/2}$ intensity above Ni (001) in two different azimuths, with certain low-index directions and special points noted [cf. lower-case letter labeling in Fig. 37(c)]. The region covered by Fig. 37(c) is shaded. The inset shows the near-neighbor/low-index directions within an *fcc* unit cell. (From Ref. 48.)

Figure 38 shows two high-resolution polar scans from the same study of Ni (001). The unit cell of the metal and various near-neighbor scatterers along low-index directions is also indicated to permit judging how well various strong features correlate with them (cf. also Fig. 22a). These polar scans also show considerable extra fine structure, for example, as compared to the same sort of [100] polar scan for higher-energy Auger emission from bulk Cu (001) shown in Fig. 22b. These high-resolution data are found to exhibit peaks for emission along some, but not all, of the near-neighbor directions shown. Peaks are found at positions corresponding closely to the nearest neighbors (and fourth-nearest neighbors) along [101], the second neighbors along [001], and the third neighbors along [112]. However, minima and/or significant peak shifts are seen for the fifth neighbors along [103] and the sixth neighbors along [111]. Neighbors even further away along [102] and [114] are also found to show significant shifts compared with the observed peaks. In particular, the [111] direction corresponds to a local minimum (indicated as point *h*), with enhanced intensity on either side of the minimum; a ϕ scan through [111] at $\theta = 35°$ shows the same sort of profile. As noted previously in the discussion of Fig. 22, this is due to the influence of higher orders of interference[71] and perhaps multiple scattering effects.[73] Thus, we conclude that the first 3–4 spheres of neighbors in any lattice will probably produce strong and simply interpretable forward scattering peaks. Beyond these spheres, more-complex origins will require modelling at least at the SSC–PW level for interpretation.

Three-dimensional data of the type shown in Fig. 37c have also been obtained at lower angular resolution by Baird, Fadley and Wagner for XPD from

Au (001)[129] and by Li and Tonner for high-energy AED from Cu (001).[29] These two data sets span a high fraction of the 2π solid angle above these two surfaces, and they exhibit very similar intensity contours, as expected since they both represent high-energy emission from the same *fcc* crystal structure. The more recent data of Li and Tonner serves as a more accurate reference for the overall features of such *fcc* XPD/AED patterns at lower angular resolution. These studies also agree with the preceding paragraph and the discussion of section 4.3.2 in seeing simple correlations of peaks with near-neighbor forward-scattering directions out only to the fourth shell, with directions such as [111], [114], [102], and [103] showing more complex behavior.

The Ni data discussed here and the other high-resolution results discussed previously thus make it clear that, at least in higher-energy XPD and AED, using resolutions that are much worse than ±1.0° will blur out some features and lead to a loss of structural information. Such sharp features are generally the result of superpositions of several scattering events, since the relevant scattering factor by itself exhibits nothing narrower than the forward scattering peak of some 20–25° FWHM. These features also tend to involve scatterers further away from the emitter and thus to be associated with the degree of short-range order around the emitter. (This is nicely illustrated by the NiO/Ni (001) results of Fig. 14.) Thus, there is little doubt that XPD or AED with high resolution will contain more fine details of the structure under study.

At lower energies, by contrast, one expects generally wider features due to the broader, more diffuse scattering factors involved (cf. Fig. 2) and the larger de Broglie wavelengths that spread out different orders of interference (cf. the curves in Figs. 4 and 5). However, even for such energies, it is possible for superpositions of multiple events to produce rather narrow features, and high resolution might also be a benefit in this case.

The most obvious disadvantage of working at high angular resolution is the longer data-acquisition times, which may be 10–30 times those of typical low-resolution operation.[33] A second disadvantage is that it is likely that the effects of multiple scattering will tend to be averaged out somewhat in lower-resolution data because of cancellations of phases in the many events involved.[21] Conversely, in high-resolution data, such MS effects may be more important, even though the information content is inherently greater.

A further aspect of the relationship of such high-resolution data to more complex interference effects and more distant neighbors is the influence of Bragg-like diffraction effects from planes in multilayer substrate emission. In the presence of the strong inelastic damping characteristic of both PD and AED, such Bragg-like events lead to what has been termed a Kikuchi-band model of these phenomena.[2,3,63b,129,130] Although a fully quantitative Kikuchi-band theory of higher-energy PD or AED based upon the superposition of many Bragg-like scattered waves is lacking, simple model calculations have been carried out by Baird *et al.*,[129] by Goldberg *et al.*,[130] and more recently also by Trehan *et al.*,[63b] and they are found to semiquantitatively reproduce the results of XPD measurements on both Au (001) and Cu (001). In particular, the superposition of several Kikuchi bands along low-index directions yields the forward-scattering peaks seen in both experiment and SSC calculations.

More interestingly, there are features in experimental data at high angular resolution that appear to be associated with specific Bragg events from low-index planes (such as features *d* and *f* in Fig. 37b here and as discussed in connection with Fig. 31 of Ref. 9). This suggestion has been given more quantitative support in a recent high-resolution study of Ni (001) by Osterwalder *et al.*[48a] Furthermore, calculations with the SSC model exhibit these same Bragg-like features if the cluster size is permitted to be large enough and/or the inelastic damping is sufficiently reduced,[48a,63b] thus verifying that a cluster-based theory can be used for problems varying from short-range order to long-range order.

This formal equivalence of the SSC model and the Kikuchi-band picture for describing bulk-like multilayer emission was first pointed out some time ago,[9,42,130] but additional clarification seems appropriate in view of misleading statements concerning the role of the Kikuchi model in the interpretation of XPD and AED that have nonetheless appeared in the more recent literature.[11] From an experimental point of view, the essentially identical intensity profiles for LMM Auger electron diffraction and backscattered LEED "Kikuchi patterns" from Ni (001) at 850 eV observed by Hilferink *et al.*[70a] provide a particularly clear verification of this equivalence. From a theoretical point of view, the relationship of the two approaches, if both are carried to comparable quantitative accuracy, is analogous to the equivalence of the so-called short-range-order and long-range-order theories of EXAFS, as discussed elsewhere.[63b,131] It is clear, however, that the SSC and MSC approaches are of greater generality in that they can be applied to both surface- and bulk- emission and to problems of differing degrees of order. The Kikuchi-band picture is, by contrast, formulated on a basis of inelastically attenuated Bloch states that reflect long-range translational order. Thus, the cluster-based theories are inherently more rapidly convergent and are more appropriate ways to look at near-surface diffraction from adsorbates and thin overlayers, as noted previously.[42,130] But it is absolutely incorrect to say that the ability of the cluster approach to explain forward-scattering features makes the Kikuchi-band model invalid for describing substrate emission.[11]

In summary, the use of high angular resolutions on the order of ±1.0° should permit even more precise structural conclusions to be derivable from both photoelectron diffraction and Auger electron diffraction, especially at energies of >500 eV. Such data should contain information on neighbors further away from the emitter, including features related to Bragg-like scattering events. It is also clear that the use of resolutions of ±3.0° or worse may conceal a great deal of fine structure inherent in the experimental curves.

5.2. *Spin-Polarized Photoelectron and Auger Electron Diffraction*

Beyond increasing both the energy resolution and the angular resolution in PD and AED as means of deriving more detailed structural information, we can also ask what is to be gained if the last property of the electron, its spin, is also somehow resolved in the experiment. This prospect has so far been considered quantitatively and observed experimentally only in the case of photoelectron diffraction, but we return at the end of this section to comment on how it might also be possible in Auger electron diffraction.

In the first attempts at what has been termed spin-polarized photoelectron diffraction (SPPD), the fundamental idea has been to use core-level multiplet splittings to produce internally referenced spin-polarized sources of photoelectrons that can subsequently scatter from arrays of ordered magnetic moments in magnetic materials. Figure 39a illustrates how such a splitting can give rise to spin-polarized photoelectrons for 3*s* emission from high-spin Mn^{2+}. The splitting is intra-atomic in origin and arises from the simple *LS* terms of ^5S and ^7S in the final ionic state of Mn^{+3} with a 3*s* hole.[132] The net effect is to cause the peaks in the doublet to be very highly spin-polarized, with ^5S predicted to be 100% spin-up and ^7S to be 71% spin-down relative to the net 3*d* spin of the emitting atom.[133,134] The relatively large exchange interaction between the highly overlapping 3*s* and 3*d* electrons is responsible for the easily resolvable splitting of 6.7 eV between the ^5S and ^7S final states of the photoemission process.

The basic experiment in SPPD thus involves looking for spin-dependent scattering effects that make two such peaks behave slightly differently in the presence of a magnetically ordered set of scatterers. Such effects were first discussed theoretically by Sinkovic and Fadley,[134a] and they have several special properties:[135,136]

- There is no need for any kind of external spin detector beyond an electron spectrometer capable of resolving the two peaks in energy.

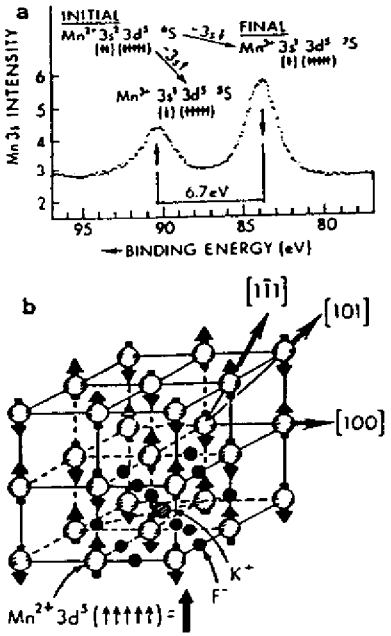

FIGURE 39. (a) The Al $K\alpha$-excited Mn 3*s* spectrum of $KMnF_3$, with the initial and final states leading to the multiplet splitting indicated, together with the predominant photoelectron spin expected in each peak. (b) The crystal structure of $KMnF_3$, with the antiferromagnetic ordering of the Mn^{2+} spins also indicated. [From Ref. 134(a).]

- The fact that the photoelectron spins are referenced to that of the emitting atom or ion means that SPPD should be capable of sensing magnetically ordered scatterers even when the specimen has no net magnetization. Thus, studies of both ferromagnetic and antiferromagnetic materials should be possible, and meaningful measurements should also be feasible above the relevant macroscopic transition temperatures (Curie or Neel temperatures, respectively). For the latter case, the photoelectrons in each peak would be unpolarized with respect to any external axis of measurement but still polarized relative to the emitting atom.
- The photoelectron emission process is also very fast, with a time scale of only about 10^{-16} to 10^{-17} seconds; thus, such measurements should provide an instantaneous picture of the spin configuration around each emitter, with no averaging due to spin–flip processes, which are much slower at roughly 10^{-12} seconds.
- Finally, the previously discussed strong sensitivity of any form of photoelectron diffraction to the first few spheres of neighboring atoms means that SPPD should be a probe of short-range magnetic order (SRMO) in the first 10–20 Å around a given emitter. Thus, provided that a sufficiently well-characterized and resolved multiplet exists for a given material, this technique has considerable potential as a rather unique probe of SRMO for a broad variety of materials and temperatures.

Before discussing the first observations of such spin-dependent scattering and diffraction effects, it is appropriate to ask to what degree final-state effects such as core-hole screening may alter or obscure these multiplets. We note first that the cases of principal interest in SPPD are outer core holes, which are more diffuse spatially than inner core holes and for which the interaction with the surrounding valence electrons is thus not as strongly polarizing as for inner core holes (which can often be very well described in the equivalent-core approximation). Nonetheless, it has been suggested by Veal and Paulikas[137] that both screened and unscreened multiplets corresponding to $3d^{n+1}$ and $3d^n$ configurations, respectively, are present in the 3*s* spectra of even highly ionic compounds such as MnF_2.

As such effects would make the carrying out of SPPD measurements more difficult (although still certainly not impossible) due to the potential overlap of peaks of different spin polarization, Hermsmeier *et al.*[138] have explored this problem in a study of Mn 3*s* and 3*p* multiplets for which the experimental spectra from several reasonably ionic solid compounds have been directly compared to the analogous spectra from gaseous Mn, a simple free-atom system in which no extra-atomic screening can occur. In Fig. 40, we show their compilation of 3*s* spectra for the diluted magnetic semiconductor $Cd_{0.3}Mn_{0.7}Te$ (a), single-crystal MnO with (001) orientation (b), polycrystalline MnF_2 as obtained some time ago by Kowalczyk *et al.*[139] (c), gaseous atomic Mn (d), and a free-ion theoretical calculation of these multiplets by Bagus *et al.* including configuration interaction, but totally neglecting extra-atomic screening (e).[140] From a consideration of the experimental data only, it is striking that for both 3*s* multiplets and 3*p* multiplets (not shown here, but discussed in Ref. 138) the solid-state spectra are very similar to the gas-phase spectra, with the only differences being some extra broadening in the solid state and some small changes in peak positions that are not at all surprising. Thus, even without resorting to theory, it seems clear that these

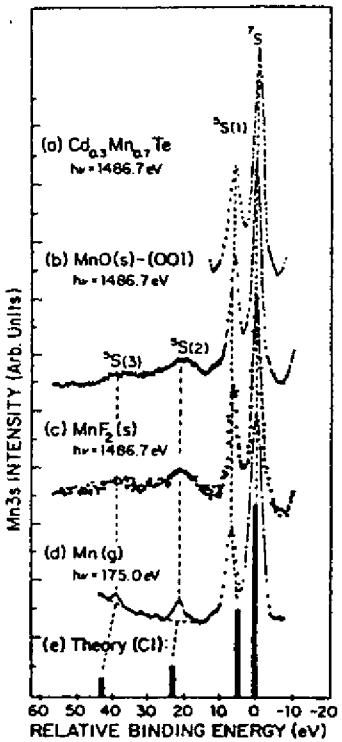

FIGURE 40. Experimental Mn 3*s* spectra for (a) the diluted magnetic semiconductor $Cd_{0.3}Mn_{0.7}Te$, (b) MnO (001), (c) polycrystalline MnF_2 (Ref. 139), and (d) gaseous atomic Mn are compared to (e) theoretical calculations for emission from a free Mn^{2+} ion including final-state configuration interaction (Ref. 140). (From Ref. 138.)

spectra are very free-atom–free-ion like, and that a simple multiplet interpretation such as that in Fig. 39a should rather accurately describe the spin polarizations of the photoelectrons involved.

If we consider now the best available free-ion theoretical prediction for the 3*s* spectra, this conclusion becomes even more convincing. In Fig. 40e, the results of a calculation by Bagus, Freeman, and Sasaki[140] for Mn^{3+} with a 3*s* hole and limited configuration interaction (CI) are shown. There is excellent agreement with experiment not only for the two dominant members of the multiplet that would be most useful in SPPD, but also for the two much weaker satellites that directly result from including CI. Similar conclusions are reached in a comparison of experiment and theory for analogous 3*p* spectra.[138] We thus conclude that extra-atomic screening does not cause a major perturbation of these multiplet splittings and thus also that outer core holes such as 3*s* and 3*p* should exhibit relatively free-atom–free-ion like multiplets for a variety of high-spin systems. Such multiplets in turn should be useful as spin-resolved sources in SPPD.

Direct experimental evidence of spin polarization in core spectra also exists. A recent measurement with an external spin detector of the spin polarization over the 3*p* peak from ferromagnetic Fe by Kisker and Carbone[141] yields significant spin-up polarization at lower kinetic energy and spin-down polarization at higher kinetic energy that are in the same sense as those expected for a simple 3*p* multiplet.[138] These results thus suggest that SPPD should be possible with ferromagnetic metals as well, particularly on the simpler and more widely split 3*s* peaks.

Returning now to a consideration of the SPPD experiments carried out to date, we have shown in Fig. 39b the crystal structure of the first material for which such effects were observed: a (110)-oriented sample of the simple antiferromagnet $KMnF_3$. It is clear from this that the relative spins of the emitter and the first scatterer encountered can be different for different directions of emission, as for example, between [100] and [101]. Spin-dependent scattering effects were first observed for this system by Sinkovic, Hermsmeier, and Fadley[142] as small changes of up to about 15% in the ratios of the $^5S(1)$ (spin-up) and ^7S (spin-down) peaks in the dominant doublet shown in Fig. 39a. For this study, a lower energy of excitation of 192.6 eV (Mo Mζ radiation) was used in order to yield lower-energy photoelectrons at approximately 100 eV, which are expected to exhibit significant spin-dependent effects in scattering.[134a] This requirement of low kinetic energies thus makes SPPD inherently well suited to synchrotron radiation with its tunable energy.

The $^5S(1):^7S = I(\uparrow)/I(\downarrow)$ intensity ratio was found to be sensitive to both direction of emission (as qualitatively expected from Fig. 39a) and temperature. Its variation with temperature is furthermore found to exhibit a surprisingly sharp transition at a point considerably above the Neel temperature (T_N), as shown in Fig. 41a. Here, we plot a normalized intensity ratio or "spin asymmetry" S_{expt} that is measured relative to the value of $I(\uparrow)/I(\downarrow)$ at a limiting high-temperature (HT) paramagnetic limit. This asymmetry is defined in the inset of Fig. 41a; it goes to zero at high temperature.

The abrupt high-temperature change observed in S_{expt} has been suggested to be due to the final destruction of the short-range magnetic order that is expected to dominate in producing such spin-polarized photoelectron diffraction effects. Note also that the short-range-order transition temperature T_{SR} at which this occurs is approximately $2.7T_N$.

In an important confirmation and extension of this earlier work, very similar SPPD effects have also more recently been observed by Hermsmeier *et al.* for (100)-oriented MnO,[143] and two of their curves for the temperature dependence of the spin asymmetry are shown in Fig. 41b. As for $KMnF_3$, there is a relatively sharp change in the $^5S(1):^7S$ ratio at a temperature that is again well above the long-range-order transition temperature at $T_{SR} = 4.5T_N$. For both $KMnF_3$ and MnO, it is also interesting that the form of the short-range order transition is very sensitive to emission direction, being steepest for the nearest-neighbor scattering direction in Fig. 41a and changing sign with only a 15° shift of emission direction in Fig. 41b. This sensitivity to direction is qualitatively consistent with single-scattering calculations of the spin-dependent exchange-scattering processes that may be involved.[134,143,144]

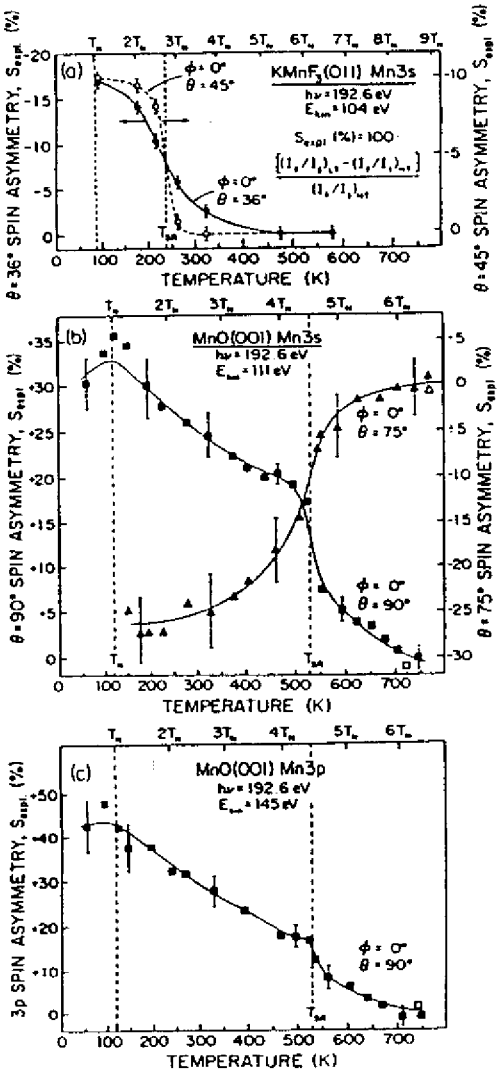

FIGURE 41. Spin-polarized photoelectron diffraction data indicating the presence of a high-temperature transition in antiferromagnetic short-range order. (a) Experimental spin asymmetries for the Mn 3*s* doublet from $KMnF_3$ with (110) orientation, as a function of temperature. Mo $M\zeta$ radiation at 192.6 eV was used for excitation to photoelectron energies of approximately 100 eV. The spin asymmetry is defined in the inset, where $I(\uparrow)/I(\downarrow)$ is the ratio of spin-up (^8S) to spin-down (^7S) intensities, HT refers to the highest temperature of measurement. Data are shown for two emission directions, one of which is along the [100] nearest-neighbor direction and the other 9° away from this. (From Ref. 142.) (b) As in (a), but for Mn 3*s* emission from MnO with (001) orientation. Note the different signs of the spin asymmetries for this case. (From Ref. 143.) (c) As in (b), but for Mn 3*p* emission from MnO with (001) orientation and treating the spin-up (^8P) and spin-down (^7P) peaks. (From Ref. 143.)

Although we have discussed only 3*s* emission thus far, the more complex 3*p* multiplets also should be spin polarized.[138,143] And in fact, a very similar transition has also been seen for MnO in the more widely split $^5P(1):^7P = I(\uparrow)/I(\downarrow)$ doublet at the same temperature T_{SR},[143] as shown in Fig. 41c. The fact that the same sort of transition is seen for these two peaks in spite of the fact that they are different from $^5S(1):^7S$ in both energy separation and mean kinetic energy provides strong support for the conclusion that this is a new type of magnetic transition.

It is also interesting that the T_{SR} values are, for both cases, approximately equal to the Curie–Weiss temperatures of the two materials, a connection which may be associated with the fact that this constant is proportional in mean-field theory to the sum of the short-range magnetic interactions.[145]

A final observation concerning this data is that the results for MnO in Figs. 41b and c show a possible indication of sensitivity to the long-range-order transition at T_N, as both curves possess a weak peak at T_N which is just outside of the estimated-error bar of the ratio measurement. If this is true, it is perhaps not surprising in view of the longer-range sensitivity of PD to neighbors that may be 20 Å from the emitter, as discussed in connection with both Figs. 16 and 20b.

A number of questions are thus raised by these results concerning the nature of short-range order above the long-range-order transition temperature and the way in which such effects can be incorporated in a spin-polarized variant of photoelectron diffraction theory. Although a quantitative theory of all aspects of the short-range-order transition and its inclusion in a spin-dependent modeling of the diffraction process does not yet exist, results in qualitative or semiquantitative agreement with experiment have been obtained in a few previous studies.[134,136,143,144]

The observation that Auger spectra from ferromagnetic materials exhibit strong spin polarization from one part of the manifold of features to another by Landolt and co-workers[146] also suggests that spin-polarized Auger electron diffraction (SPAED) should be possible. The more complex nature of Auger spectra in general will make the *a priori* prediction of the type of spin polarization more difficult, but for ferromagnets with net magnetization, an external spin detector could be used to first calibrate the spectrum for polarization.[146] Then, measurements of spin-up–spin-down ratios as functions of direction and/or temperature could be taken in the same way as for the spin-split core multiplets in SPPD. Even in antiferromagnetic systems with equal numbers of up and down 3*d* moments so that external calibration is impossible, any transition involving the polarized 3*d* valence electrons might be expected to show a net polarization that would again be internally referenced to the emitter.

A final aspect of such spin-polarized studies is to make use of left or right circularly polarized radiation, in conjunction with spin–orbit interaction in the energy levels involved, to preferentially excite one or the other spin polarization, as discussed recently by both Schuetz and co-workers[147] and Schoenhense and co-workers.[148] The use of such radiation already has produced very interesting spin-polarized NEXAFS and EXAFS structure from ferromagnets and ferrimagnets[147] and circular dichroism angular distributions (CDAD) from nonmagnetic surfaces and adsorbates.[148] In CDAD for light elements with negligible spin–orbit effects,

no net spin polarization of the photoelectron flux is involved, but such measurements provide the interesting possibility of measuring the contributions of individual m_l components to photoemission and photoelectron diffraction.[148] The CDAD studies require lifting the degeneracy of the m_l sublevels, and so have been carried out on valence levels; however, with very high energy resolution, it might be possible to do similar measurements on outer core levels with, for example, small crystal-field and/or spin–orbit splittings present.

With the availability of higher-intensity sources of circularly polarized radiation from next-generation insertion devices, it should be possible to greatly expand both of these kinds of study so as to look in more detail at both the angle and the energy dependence of the photoelectron intensities. For example, spin-polarized EXAFS requires measuring very accurately the differences in absorption for right and left polarizations, because the overall effects may be as small as a few times 10^{-4} in K-shell absorption.[147] However, studying L_2- and L_3 absorption for heavier elements with $Z \geq 60$ leads to considerably larger effects that can be on the order of 10^{-3}–10^{-2}. Extending this to do SPPD would thus imply measuring similarly accurate ratios or differences of photoelectron intensities. In this case, the magnitudes of the photoelectron spin polarizations are only on the order of 1% for K-shell emission, but for heavier elements, they can be up to 40–50% in L_2 emission and 20–25% in L_3 emission.[147] The latter two cases are thus about $\frac{1}{3}$–$\frac{1}{2}$ as highly polarized sources as a high-spin multiplet such as that in Fig. 39a. One advantage of such an approach would be to expand such studies to cases for which a suitable high-spin multiplet is not available. A disadvantage is that an external axis of polarization is involved, so that only ferro- or ferrimagnetic specimens could be studied. However, in CDAD experiments, this last restriction is not present.[148]

SPPD is thus a very new area of photoelectron diffraction, but it has considerable potential for providing information on the short-range spin order and spin–spin correlation functions around a given type of emitter site in the near-surface region of magnetic materials. Other antiferromagnetic and also ferromagnetic materials are currently being studied in order to better establish the systematics of the short-range-order transition and the range of utility of this method. Spin-polarized Auger electron diffraction and other measurements making use of circularly polarized radiation for excitation also should be possible.

5.3. Synchrotron Radiation–Based Experiments

Looking ahead to the much more intense and/or much brighter synchrotron radiation sources in the VUV/soft X-ray region that are currently either coming into operation or being conceived as next-generation devices based upon undulators or wigglers, one can see much-expanded possibilities for all of the types of photoelectron diffraction measurements discussed up to this point.

Measurements with both high-energy resolution (to distinguish different surface layers or chemical states as shown in Figs. 34 and 35, respectively) and high angular resolution (to enhance fine structure and thus structural sensitivity) should be possible. For some types of experiments (e.g., with maximum surface sensitivity and/or with spin-polarized diffraction in mind), lower photoelectron

energies of approximately 50–100 eV may be necessary, but for much structural work, energies of 1000 eV or even higher will be beneficial in yielding strongly peaked forward scattering and more nearly single-scattering phenomena. Being able to go to much higher photoelectron energies of up to 5000–10,000 eV may also be of interest in yielding even narrower forward-scattering peaks (as considered from a theoretical viewpoint by Thompson and Fadley[149]), more true bulk sensitivity via the longer electron attenuation lengths, and simpler theoretical interpretation. Being able to tune energy is also essential for the scanned-energy or ARPEFS experiments; it should be possible to carry these out much more rapidly and over a broader energy range above threshold. The polarization vector can also be oriented in either scanned-angle or scanned-energy measurements so as to enhance the contributions of various important scatterers (cf. Figs. 3a and 18). And we have already considered in the last section the possibility of using circularly polarized radiation. Finally, photoelectron *microscopy* with resolutions on the order of 500 Å or less is currently being developed,[150] and the additional dimension of using simultaneous photoelectron diffraction to probe the local atomic structure in such a small spot is quite exciting.

Auger electron diffraction may not benefit as much from synchrotron radiation, because excitation can be achieved with either photons or electrons and because the spectral form is not dependent on the excitation utilized if the initial hole is formed well above threshold. However, even for this case, synchrotron radiation could provide a more intense and less destructive excitation source than, for example, an electron beam or a standard X-ray tube. Also, it would be interesting to look at the diffraction process as the excitation energy is swept through threshold, so as to yield a purer one-hole initial state.

5.4. Combined Methods and Novel Data-Analysis Procedures: Photoelectron Holography?

It is clear from the foregoing examples that both scanned-angle and scanned-energy photoelectron diffraction measurements can provide useful information concerning surface structures, but that scanned-angle measurements are simpler in general to perform. Going to higher energies leads to easily interpretable forward-scattering features for many systems, but at the same time provides little information on the atoms that are below or behind the emitting atom as viewed from the detection direction. Thus, there are clear advantages to using lower energies as well, even if these lead to a potentially greater influence of multiple scattering. In the scanned-energy ARPEFS work discussed in sections 4.2.2 and 4.2.3, a major reason why interlayer spacings down into the bulk were derivable is that these lower energies exhibit the strongest backscattering effects and provide the largest oscillations in the $\chi(k)$ curves (cf. Fig. 20).

It is thus easy to suggest that the ideal photoelectron diffraction experiment based upon present methodology would consist of carrying out both high-energy measurements at kinetic energies greater than approximately 500 eV and low-energy measurements at approximately 50–100 eV. Being able to scan $h\nu$ would also be desirable, but not essential. A typical structure could then be analyzed by first making scanned-angle measurements at high energy and using the real-space

aspects of any forward-scattering effects to narrow down the range of possible structures (cf., for example the discussion of Figs. 29 and 30). Combining scanned-angle measurements at high and low energies then should permit determining structures in detail, including atomic positions both below and above the emitter in the sense mentioned above. Or scanned-energy measurements could be performed as a second step as well, leading to the utility of Fourier transform methods for narrowing down the number of structures. Using an electron spectrometer that can simultaneously analyze and detect electrons over a range of emission directions[35-38] would also clearly speed up such studies, with the only likely drawback being that angular resolution is often lower in such systems, particularly when working at higher energies. In all of these methods, the final precise structural determination would require comparison of experimental diffraction curves or χ functions with calculated curves for a number of geometries, with the most quantitative method of comparison being via some sort of R factor.[20,26d] This is thus exactly the same methodology employed in LEED, except that in photoelectron diffraction, a single scattering approach should already provide useful information for many cases and there is additional readily available structural information concerning the type of local bonding site that can assist in ruling out structures.

As a final new direction in the analysis of scanned-angle data, we consider the recent interesting proposal by Barton,[151] based on an earlier suggestion by Szoeke,[152] that it should be possible to directly determine atomic positions via photoelectron holography. According to this idea, the photoelectron leaving the emitter is treated in first approximation as a spherical outgoing wave that, by virtue of the scattering and diffraction from its neighbors, produces an intensity modulation outside of the surface that can be considered a hologram. This hologram is then simply the intensity distribution of a given peak over a two-dimensional range in θ, ϕ (or, equivalently, some two-dimensional range in k_x, k_y). This intensity distribution can then be described by a formula of exactly the same type as Eq. (10), but with some important generalizations. These generalizations are that the scattering amplitude $|f_j|$ and phase shift ψ_j, together with the factors for the excitation matrix element and attenuation due to spherical wave, inelastic, and vibrational effects, must be replaced by an overall wave amplitude $|F_j|$ and phase ψ_j for each scatterer that sums over all single- and multiple-scattering events which terminate in atom j as the last scatterer before the detector. It can then be shown[151] that inverting this two-dimensional hologram mathematically to produce a real image is equivalent to a double Fourier integral in k_x and k_y, in which the desired z plane of the image is a variable paremeter within the integral. Thus, two dimensional x–y cross sections at different z positions are in principle possible with this method.

Barton has carried out a theoretical simulation of this new method using MSC–SW intensity distributions in θ, ϕ for the $c(2 \times 2)$ S/Ni (001) system at a kinetic energy of 548 eV and with a width of angular detection in both the k_x and k_y directions of $\pm 40°$. The inversion of this hologram is found to have maxima that can be directly related to different near-neighbor Ni atoms, with an estimated resolution in x and y of 0.5 Å and in z of a much higher 2.3 Å. The x and y resolutions are ultimately limited by the Rayleigh criterion for a lens

(hologram) of a given opening angle. For the maximum reasonable detection-angle ranges in a spectrometer of $\pm 40°$ to $\pm 60°$, this in turn yields resolution limits Δx and Δy that are very close to the de Broglie wavelength of the electron (i.e., 0.52 Å at 548 eV). This is a likely reason why a rather high kinetic energy in the typical XPS range was used for this simulation.

As noted by Barton, some limitations and/or problems that need to be addressed in the further development of this technique are the relatively low position-resolution obtainable, particularly in z; the presence of twin images at $\pm z$ for each atom (a universal effect in holography), which could cause serious overlap problems for bonding geometries involving atoms that are below-plane; the fact that multiple scattering effects on the F_j may cause deviations of the image positions from the actual sites, thus requiring an iterative correction via theoretical calculations of these generalized scattering amplitudes for an assumed geometry; the fact that several images at different energies, or even an additional Fourier transform of energy-dependent data at each θ, ϕ, may be necessary to effect this correction; and the added experimental difficulty in requiring some sort of high-speed multichannel electron analyzer that can obtain such large data sets in a reasonable amount of time.[35]

Another limitation not mentioned in connection with this theoretical simulation is that the high energy used implies relatively weak backscattering effects of only 15% or so compared to forward scattering (cf. Fig. 2); thus, the actual degree of modulation in intensity observed may be quite small, making the measurements rather difficult. Going to higher energies to improve resolution via shorter de Broglie wavelengths will make this problem worse due to even weaker backscattering. Thus, for an adsorbate or surface atom that has not significantly penetrated a surface, there will always be a tradeoff between resolution and ease of measurement in photoelectron holography. Of course, if the emitter is found below the surface, then strong forward scattering of the type discussed previously here can take place, and the resulting hologram should then show larger intensity modulations; however, forward scattering effects by themselves contain bond direction information, but not bond length information, so that the weaker modulations due to higher-order features would still need to be accurately measured in order for the inversion of the hologram to yield the full structure.

As a potentially more convenient experimental alternative for holography, a suitable Auger peak involving three filled levels might be useful as a source of a more nearly spherical wave as assumed in the image reconstruction, although the poorly understood mixing in of other l components could complicate a precise theoretical analysis of the effective amplitudes $|F_j|$ and phases ψ_j. Also, using Auger peaks that are too broad in energy would reduce the degree of monochromaticity (i.e., coherence) required in the source.[21b]

No matter how these problems are dealt with, even low-resolution three-dimensional images from such holography could be useful in ruling out certain bonding geometries in a semiquantitative way, much as Fourier transforms in ARPEFS can be useful through the approximate path-length differences they provide. It will be interesting to see what the first inversion of an experimental photoelectron hologram brings. (Please see the added note on holographic methods at the end of this chapter.)

6. COMPARISONS TO OTHER TECHNIQUES AND CONCLUDING REMARKS

We begin this concluding section by comparing photoelectron and Auger electron diffraction to several other current probes of surface structure in order to assess their relative strengths and weaknesses. As a first overall comment, it is clear from any perusal of the current literature (e.g., Ref. 1) that no one surface-structure probe directly and unambiguously provides all of the desired information on atomic identities, relative numbers, chemical states, positions, bond distances and bond directions in the first 3–5 layers of the surface. The very small number of surface structures for which there is a general consensus in spite of several decades of careful study of some of them testifies to the need for using complementary information from several methods.

To provide some idea of this complementarity of approaches, we show in Table 1 several techniques assessed according to a number of characteristics: photoelectron diffraction (PD) in both scanned-angle and scanned-energy forms, Auger electron diffraction (AED), surface extended X-ray absorption fine structure (SEXAFS),[16] near-edge X-ray absorption fine structure NEXAFS,[95,133,154] low-energy electron diffraction (LEED),[61] surface-sensitive grazing incidence X-ray scattering (GIXS),[27] scanning tunneling microscopy (STM),[155] and Rutherford backscattering (RBS) or medium-energy ion scattering (MEIS).[156] This is not intended to be a complete list of modern structure probes, but it roughly represents the group most used at present.

These techniques are rated, first, according to whether they directly provide information on atomic identity (a positive feature of all techniques except for LEED, GIXS, and STM) and chemical state (possible only with PD, AED, and NEXAFS). Atom identification is possible in GIXS only if use is made of anomalous dispersion near a certain absorption edge. State-specific information is not derivable in typical SEXAFS measurements because of the overlap of different oscillatory absorption structures above a given edge.

Also, we assess whether other subsidiary types of structural and bonding information can be obtained in a straightforward manner. Of course, once a structure has been determined and optimized to fit the data of any one of these methods, it has implicit in it bond directions, bond distances, site symmetries, and coordination numbers, but the table entries have been chosen to reflect the directness with which these can be extracted from the raw data with a minimum of data analysis. The types of information considered are valence electronic levels or excitations (directly accessible only in NEXAFS and STM), bond directions (particularly easy to determine in high-energy PD/AED with forward scattering—as discussed in comparison to other techniques in section 4.1.4—and RBS/MEIS with shadowing and blocking), bond distances (very direct in SEXAFS Fourier transforms), local bonding-site symmetries (easiest to determine with PD, AED, SEXAFS, and RBS/MEIS), and coordination numbers (derivable directly from high-energy PD and AED and less directly from the amplitudes of SEXAFS oscillations). STM can also directly image surface atoms and thus provide coordination numbers, but it is limited to looking at only the outermost surface density of states, and so does not probe the bonding below this level in a direct

way. Distinguishing between structures that are related to atomic positions and protrusions in the density of states can also be a problem in STM. It has been suggested that NEXAFS resonance energies can be used to measure bond distances,[153] but this approach may be limited to well-calibrated series of homologous molecules, and has been called into question.[154]

The estimated accuracies of finally determining atomic positions with the current state of these techniques is also indicated. Numbers smaller or larger than these will be found for some cases in the literature, but it is the author's opinion that the numbers in the table are a better representation of the true absolute accuracies if all of the various uncertainties in both experimental parameters and the modelling or treatment of the data are taken into account. Surface X-ray diffraction is the most accurate, but its principal sensitivity is to horizontal positions, with vertical positions being derivable only via the more difficult method of measuring rod profiles normal to the surface. PD in any of its forms and AED should be inherently as accurate as SEXAFS, if not more so, particularly if the latter has been analyzed only with transform and back-transform methods without any final theoretical modeling. PD should also ultimately be as accurate as LEED,[73] particularly for a given amount of input to the theoretical analysis.

The degree to which these techniques probe short-range order in the first 10–20 Å around a given site versus longer-range order over 100 Å or more is also considered. Except for LEED and X-ray diffraction, all of the techniques are primarily sensitive to short-range order, although we have also pointed out that PD and AED actually have sensitivity extending over a region of diameter as large as 40 Å. Although inherently larger-scale probes, LEED and X-ray diffraction can with spot profile analysis be used to study the breakdown of long-range order in such phenomena as surface phase transitions.

Next, several characteristics relating to the ease of obtaining data and analyzing it theoretically are indicated: the overall percentage change in intensity as one measure of the ease of determining the signal (which is particularly large for PD, AED, and LEED); the possibility of using a simple, usually kinematical, theory to analyze the results; and the feasibility of using Fourier transform methods to more directly derive structural parameters. The overall figures for percentage effect should be assessed carefully, however, since the inelastic background under some photoelectron and Auger spectra can be high, thus making even a 50% modulation of the peak intensity difficult to measure. By contrast, for some applications of SEXAFS, background effects can be much reduced by using X-ray fluorescence detection,[157] although surface specificity is then lost. Problematic background effects can also arise in SEXAFS scans such as Auger-photoelectron interferences if either type of peak is being used to monitor the absorption and sharp spikes or glitches of intensity due to Bragg reflection of X-rays from very well-ordered crystals such as semiconductors. Auger-photoelectron interferences can also make the use of scanned-energy photoelectron diffraction more difficult if there are any Auger peaks from the sample that lie in the kinetic-energy range from about 100 eV to 400 eV. Standard Auger tabulations show that this could yield difficult background subtraction problems for the atomic number ranges 4–7, 14–22, and 37 upward. As examples of this, sulfur at 16 involves such an interference, as noted previously in sections 4.2.2 and 4.2.3,

TABLE 1. Comparison of Several Surface-Structure Techniques by Different Criteria ("yes" and "no" responses based on deriving a given type of information with minimal data analysis)

	Scanned-angle PD	Scanned-energy PD	AED	SEXAFS	NEXAFS	LEED	GIXS	STM	RBS/MEIS
Atom specific?	Yes	Yes	Yes	Yes	Yes	No	No[a]	No	Yes
Chemical-state specific?	Yes[b]	Yes[b]	Yes[b]?	No	Yes	No	No	No	No
Bond directions?	Yes[c]	Yes	Yes[c]	Yes[c]	Yes[c]	No	No	Yes[d]	Yes[d]
Bond distances?	Yes	Yes[f]	Yes	Yes[f]	No[g]	No	No	Yes[d]	Yes[d]
Adsorption site symmetries?	Yes[h]	Yes?	Yes[h]	Yes?	No	No	No	Yes[d]	Yes
Coordination numbers?	Yes[c]	Yes	Yes[c]	Yes	No	No	No	Yes[d]	Yes
Position accuracies?	~0.02–0.05 Å	~0.02–0.05 Å	≤0.05 Å	~0.02–0.05 Å	?[i]	~0.01–0.05 Å	~0.001 Å (Horizontal) ?[j] (Vertical)	~0.3 Å (Horizontal) ~0.05 Å (Vertical)	~0.01 Å
Valence-electron states?	No	No	No	No	Yes	No	No	Yes	No
Short-range order (~10–20 Å)?	Yes	Yes	Yes	Yes	Yes	No	No	Yes[d]	Yes
Long-range order (>100 Å)?	No	No	No	No	No	Yes	Yes	Yes[d]	No
Overall % effects?	20–70%	20–70%	20–70%	~5%	Variable	70–90% in I–V	Weaker surface peaks	Large	~10%[e]
Kinematical theory?	Yes[f]	Yes[f]	Yes[f]	Yes[f]	No	No	Yes	No	Yes
Fourier transform analysis?	No[k]	Yes[f]	No	Yes[f]	No	No	Yes	Yes[l]	No
Requires synchrotron radiation?	No	Yes	No	Yes	Yes	No	Yes	No	No

[a] GIXS only atom-specific if anomalous dispersion used
[b] If core shifts/fine structure can be resolved in PD/AED, but more difficult in Auger spectra
[c] Forward scattering in high-energy PD and AED yields ~3 times better resolution for bond directions than in polarization-dependent NEXAFS and SEXAFS. Also directly gives coordination numbers for neighbors between emitter and detector.
[d] STM senses only *surface* density of state contours, so that structural parameters are for outermost atoms only.
[e] Via shadowing and blocking in RBS/MEIS.
[f] Fourier transforms to yield path-length differences in scanned energy PD may be complicated by overlap of close-lying differences; SEXAFS Fourier transforms are simpler in this respect.
[g] Only via correlation of bond length with NEXAFS resonance energies that may be limited in application (see Refs. 153 and 154).
[h] May be very direct from azimuthal PD or AED data.
[i] Vertical position information in GIXS less accurate and available only by measuring vertical rod profiles.
[j] Some multiple scattering effects may have to be considered in all of PD, AED, and SEXAFS (see Refs. 57 and 85), and dynamical effects also may have to be included in the analysis of GIXS data for some scattering geometries (see Ref. 27).
[k] Only if holographic imaging is possible.
[l] Fourier transforms of STM images are useful for detecting lateral symmetries present.

and the Ag/Si system considered in section 4.4.2 was found in a recent scanned-energy experiment[50(c)] to exhibit extensive interferences over the full 90–350 eV range due to the various peaks in both the Si *KLL* and the Ag *MNN* spectra.

As a last and important criterion for the present volume, we indicate whether a given technique requires synchrotron radiation, as about half of them do.

The ideal structural probe would have "yes" for all of the nonquantitative characteristics in this table except the last one, which for reasons of broadest utility would be "no." It is clear that each method has positive features, but none constitutes this ideal probe. Thus, complementary information from several methods is in general desirable for fully resolving any structure. PD and AED are positive on sufficient points to be attractive additions to this list. AED is easier to excite (e.g., with photons or electrons), but the more complex nature of Auger spectra will prevent doing state-specific diffraction measurements for many cases, and an accurate theory, especially for lower energies, will be more difficult. Not being able to use radiation polarization to selectively excite towards a given scatterer is also a disadvantage of AED. As one disadvantage of scanned-angle PD and AED, we note the present lack of being able to use Fourier transform methods to determine structure directly (although photoelectron holography is a proposal to do this); thus it may be necessary to carry out a number of calculations for various structures, a procedure analogous to that used in LEED. However, some aspects of the data (e.g., forward scattering peaks at high energy) provide structural information very directly, and a good deal of any analysis should be possible within the framework of a simple single scattering picture. And in any case, the final test of any structural model derived in PD, AED, or SEXAFS should be to compare experiment to a diffraction calculation on a cluster of atoms of sufficient size to adequately include all significant scatterers.

Thus, although photoelectron diffraction and its close relative Auger electron diffraction are relatively new additions to the array of tools for studying surface structures, they have already proven to be useful for a broad variety of systems. Even at the present stage of development of both techniques with, for example, standard X-ray tubes or electron guns as excitation sources, and theory at the single-scattering-cluster–spherical-wave level, structurally useful and unique information can be derived for a range of problems including adsorption, molecular orientation, oxidation, epitaxial growth, metal–semiconductor interface formation, cluster growth, surface phase transitions, and short-range magnetic order. The use of higher angular resolutions promises to provide more precise structural information, particularly concerning longer-range order. The wider availability of synchrotron radiation, especially from the next generation of high-brightness insertion devices, will enormously increase the speed of both scanned-angle and scanned-energy measurements, thus permitting more studies of surface dynamics. The accurate-intensity ratio measurements at low kinetic energy required in spin-polarized photoelectron diffraction will also become easier. Some degree of lateral-resolution photoelectron microscopy-plus-diffraction should also become possible. And with focused electron beams, Auger electron microscopy-plus-diffraction is also feasible. Also, high-brightness radiation sources should permit increased energy resolutions of the order of 0.3 eV even at the higher photon

energies of 1.0–2.0 keV that are optimum for taking advantage of forward scattering and a single-scattering approach. Separate diffraction patterns will be obtainable for the various peaks in a given spectral region that are produced by chemical shifts, multiplet splittings, or more complex final-state effects. Using both linearly and circularly polarized radiation will also permit the selection of specific scatterers and spin-polarized final states, respectively. State-specific structural parameters should thus be derivable in a way that is not possible with other methods.

NOTE ON HOLOGRAPHIC METHODS

Since the original writing of this review, the use of holographically motivated Fourier-transform inversion methods for deriving surface structural information from both photoelectron- and Auger electron-diffraction data (cf. discussion in section 5.4) has advanced considerably. Some of these developments are discussed below.

The first experimental data have successfully been inverted to yield direct images of atomic positions near Cu surfaces by Tonner *et al.*[158] More recently, the same types of images have been observed for the semiconductors Si and Ge by Herman *et al.*[159] and for the simple adsorbate system $c(2 \times 2)$ S/Ni (001) by Saiki *et al.*[100] In general, these images are accurate to within about ±0.2–0.3 Å in planes parallel to the surface and more or less perpendicular to strong forward scattering directions, but only to within about ±0.5–1.0 Å in planes perpendicular to the surface or containing forward scattering directions.

Methods have been proposed for eliminating the observed distortions in atomic images due to both the anisotropic nature of the electron–atom scattering and the phase shift associated with the scattering by Saldin *et al.*,[160] Tong *et al.*,[161] and Thevuthasan *et al.*[162] Preliminary tests of these methods are encouraging, but more applications to experimental data are needed to assess them fully. Further image distortions due to anisotropies in the electron emission process have been discussed,[160,161] and corrections for these also appear to be useful. Additional spurious features that may arise in images due to the strength of the electron–atom scattering and resultant self-interference effects have been pointed out by Thevuthasan *et al.*[162] By contrast, the multiple scattering defocusing illustrated in Figs. 3b–ii and 6 has been shown to reduce the image distortions for the special case of buried emitters that are separated by several atoms from the detector.[162]

Finally, Barton[163] has shown in theoretical simulations that the simultaneous analysis of photoelectron holographic data obtained at several different photon energies, involving in effect an additional Fourier sum on energy, should act to reduce the influence of both twin images and multiple scattering on atomic images.

Thus, the holographic analysis of both photoelectron and Auger electron data is in an intense period of evaluation, with several indications already that it may ultimately provide reasonably good starting-point structures which can then be refined by the more classic trial-and-error methods discussed previously in this review, but in much reduced time.

ACKNOWLEDGMENTS

Some of the work reported here has been supported by the Office of Naval Research under Contract N00014-87-K-0512, the National Science Foundation under Grant CHE83-20200, and the New Energy Development Organization (NEDO) of Japan. Some of the studies discussed here have also benefitted by grants of Cray XMP/48 time at the San Diego Supercomputer Center. The author is also very grateful to his various former and present co-workers at the University of Hawaii for their significant contributions to the development of these techniques. J. J. Rehr has also provided various ideas concerning efficient methods of treating both spherical-wave effects and multiple scattering. Special thanks also go to D. J. Friedman for critically reading this chapter, and to S. A. Chambers and G. Schoenhense for providing helpful comments concerning it. The fine work of M. Prins on many of the figures is also gratefully acknowledged. I also thank J. Hanatani for assistance with preparing this manuscript.

REFERENCES

1. Excellent summaries of the current status of most of these techniques can be found in the proceedings of three International Conferences on the Structure of Surfaces: (a) *The Structure of Surfaces* (M. A. Van Hove and S. Y. Tong, eds.), Springer Verlag, Berlin (1985); (b) *The Structure of Surfaces II* (J. F. van der Veen and M. A. van Hove, eds.), Springer-Verlag, Berlin (1988); (c) *The Structure of Surfaces III* (S. Y. Tong, M. A. Van Hove, K. Takayanagi, and X. D. Xie, eds.), Springer-Verlag, Berlin (1991).
2. K. Siegbahn, U. Gelius, H. Siegbahn, and E. Olsen, *Phys. Lett.* **32A**, 221 (1970).
3. C. S. Fadley and S. A. L. Bergstrom, *Phys. Lett.* **35A**, 375 (1971).
4. A. Liebsch, *Phys. Rev. Lett.* **32**, 1203 (1974); *Phys. Rev.* **B13**, 544 (1976).
5. S. Kono, C. S. Fadley, N. F. T. Hall, and Z. Hussain, *Phys. Rev. Lett.* **41**, 117 (1978); S. Kono, S. M. Goldberg, N. F. T. Hall, and C. S. Fadley, *Phys. Rev. Lett.* **41**, 1831 (1978).
6. D. P. Woodruff, D. Norman, B. W. Holland, N. V. Smith, H. H. Farrell, and M. M. Traum, *Phys. Rev. Lett.* **41**, 1130 (1978).
7. S. D. Kevan, D. H. Rosenblatt, D. Denley, B.-C. Lu, and D. A. Shirley, *Phys. Rev. Lett.* **41**, 1565 (1978).
8. J. J. Barton, C. C. Bahr, Z. Hussain, S. W. Robey, J. G. Tobin, L. E. Klebanoff, and D. A. Shirley, *Phys. Rev. Lett.* **51**, 272 (1983); J. J. Barton, C. C. Bahr, Z. Hussain, S. W. Robey, L. E. Klebanoff, and D. A. Shirley, *J. Vac. Sci. Technol.* **A2**, 847 (1984); J. J. Barton, S. W. Robey, C. C. Bahr, and D. A. Shirley in *The Structure of Surfaces* (M. A. van Hove and S. Y. Tong, eds.), Springer Verlag, Berlin (1985) p. 191.
9. C. S. Fadley, *Prog. in Surf. Sci.* **16**, 275 (1984).
10. C. S. Fadley, Phys. Scr. **T17**, 39 (1987) and earlier references therein.
11. (a) W. F. Egelhoff, *Phys. Rev.* **B30**, 1052 (1984); (b) R. A. Armstrong and W. F. Egelhoff, *Surf. Sci.* **154**, L225 (1985); (c) W. F. Egelhoff, *Phys. Rev. Lett.* **59**, 559 (1987).
12. (a) S. A. Chambers, H. W. Chen, I. M. Vitomirov, S. B. Anderson, and J. H. Weaver, *Phys. Rev.* **B33**, 8810 (1986); (b) S. A. Chambers, I. M. Vitomirov, S. B. Anderson, H. W. Chen, T. J. Wagener, and J. H. Weaver, *Superlattices and Microstructures* **3**, 563 (1987); (c) S. A. Chambers and T. J. Irwin, *Phys. Rev.* **B38**, 7858 (1988); and earlier references therein.
13. C. S. Fadley, in *Core-Level Spectroscopy in Condensed Systems* (J. Kanamori and A. Kotani, eds.), Springer Verlag, Berlin (1988), p. 236.
14. Z. Hussain, D. A. Shirley, C. H. Li, and S. Y. Tong, *Proc. Natl. Acad. Sci. USA.* **78**, 5293 (1981). The use of Fourier transforms was here first thought to yield interlayer distances but later shown to provide path-length difference information, as discussed in Refs. 15 and 21.

15. P. J. Orders and C. S. Fadley, *Phys. Rev.* **B27**, 781 (1983).
16. (a) P. Citrin, in *Springer Series on Surface Science*, Vol. II, Springer Verlag, Berlin (1985), p. 49; (b) D. Norman, *J. Phys.* **C19**, 3273 (1986); (c) J. Stohr, in *X-Ray Absorption: Principles, Applications, Techniques of EXAFS, SEXAFS, and XANES* (R. Prins and D. Konigsberger, eds.), Wiley, New York (1987).
17. N. V. Smith, H. H. Farrell, M. M. Traum, D. P. Woodruff, D. Norman, M. S. Woolfson, and B. W. Holland, *Phys. Rev.* **B21**, 3119 (1980); H. H. Farrell, M. M. Traum, N. V. Smith, W. A. Royer, D. P. Woodruff, and P. D. Johnson, *Surf. Sci.* **102**, 527 (1981).
18. (a) D. Sebilleau, M. C. Desjonqueres, D. Chauveau, C. Guillot, J. Lecante, G. Treglia, and D. Spanjaard, *Surf. Sci. Lett.* **185**, L527 (1987); (b) M. C. Desjonqueres, D. Sebilleau, G. Treglia, D. Spanjaard, C. Guillot, D. Chauveau, and J. Lecante, *Scanning Electron Microsc.* **1** 1557 (1987); (c) D. Sebilleau, G. Treglia, M. C. Desjonqueres, D. Spanjaard, C. Guillot, D. Chauveau, and J. Lecante, *J. Phys. (Paris)* **49**, 227 (1988).
19. (a) B. Sinkovic, P. J. Orders, C. S. Fadley, R. Trehan, Z. Hussain, and J. Lecante, *Phys. Rev.* **B30**, 1833 (1984); (b) P. J. Orders, B. Sinkovic, C. S. Fadley, Z. Hussain, and J. Lecante, *Phys. Rev.* **B30**, 1838 (1984).
20. L. J. Terminello, X. S. Zhang, Z. Q. Huang, S. Kim, A. E. Schach von Wittenau, K. T. Leung, and D. A. Shirley, *Phys. Rev.* **B38**, 3879 (1988).
21. (a) M. Sagurton, E. L. Bullock, and C. S. Fadley, *Phys. Rev.* **B30**, 7332 (1984); and (b) *Surf. Sci.* **182**, 287 (1987).
22. D. P. Woodruff, *Surf. Sci.* **166**, 377 (1986).
23. L. G. Petersson, S. Kono, N. F. T. Hall, C. S. Fadley, and J. B. Pendry, *Phys. Rev. Lett.* **42**, 1545 (1979).
24. H. C. Poon and S. Y. Tong, *Phys. Rev.* **B30**, 6211 (1984); S. Y. Tong, H. C. Poon, and D. R. Snider, *Phys. Rev.* **B32**, 2096 (1985).
25. J. J. Barton and D. A. Shirley, (a) *Phys. Rev.* **B32**, 1892 (1985) and (b) *Phys. Rev.* **B32**, 1906 (1985); (c) J. J. Barton, Ph.D. Thesis, U. Cal., Berkeley (1985); J. J. Barton, S. W. Robey, and D. A. Shirley, *Phys. Rev.* **B34**, 778 (1986).
26. (a) R. S. Saiki, A. P. Kaduwela, J. Osterwalder, M. Sagurton, C. S. Fadley, and C. R. Brundle, *J. Vac. Sci. Technol* **A5**, 932 (1987); (b) R. S. Saiki, A. P. Kaduwela, J. Osterwalder, C. S. Fadley, and C. R. Brundle, *Phys. Rev.* **B40**, 1586 (1989); (c) R. S. Saiki, A. P. Kaduwela, J. Osterwalder, C. S. Fadley, and C. R. Brundle, to be published; (d) The *R* factors used in this study are generally the *R*1 defined in M. A. van Hove, S. Y. Tong, and M. H. Elconin, *Surf. Sci.* **64**, 85 (1977), although final checks have also been made with the other possibilities *R*2–*R*5 discussed there.
27. Chapter 8 in this volume by P. H. Fuoss, K. S. Liang, and P. Eisenberger.
28. Chapter 3 of Vol. 2 of this set by J. Haase and A. M. Bradshaw.
29. H. Li and B. P. Tonner, *Phys. Rev.* **B37**, 3959 (1988).
30. S. A. Chambers, H. W. Chen, S. B. Anderson, and J. H. Weaver, *Phys. Rev.* **B34**, 3055 (1986).
31. S. D. Kevan, *Rev. Sci. Instrum.* **54**, 1441 (1983).
32. S. D. Kevan, Ph.D. thesis, U. Cal., Berkeley (1980).
33. R. C. White, C. S. Fadley, and R. Trehan, *J. Electron Spectros. Relat. Phenom.* **41**, 95 (1986).
34. J. Osterwalder, M. Sagurton, P. J. Orders, C. S. Fadley, B. D. Hermsmeier, and D. J. Friedman, *J. Electron. Spectros. Relat. Phenom.* **48**, 55 (1989).
35. D. E. Eastman, J. J. Donelon, N. C. Hien, and F. J. Himpsel, *Nucl. Instrum Methods* **172**, 327 (1980).
36. R. C. G. Leckey and J. D. Riley, *Appl. Surf. Sci.* **22/23**, 196 (1985).
37. H. A. Engelhardt, W. Back, and D. Menzel, *Rev. Sci. Instrum.* **52**, 835 (1981); H. A. Engelhardt, A. Zartner, and D. Menzel, *Rev. Sci. Instrum.* **52**, 1161 (1981).
38. M. G. White, R. A. Rosenberg, G. Gabor, E. D. Poliakoff, G. Thornton, S. H. Southworth, and D. A. Shirley, *Rev. Sci. Instrum.* **50**, 1268 (1979); Z. Hussain and D. A. Shirley, private communication.
39. R. C. G. Leckey, *J. Electron Spectros. Relat. Phenom.* **43**, 183 (1987).
40. L. McDonnell, D. P. Woodruff, and B. W. Holland, *Surf. Sci.* **51**, 249 (1975).
41. P. A. Lee, *Phys. Rev.* **B13**, 5261 (1976).
42. S. Kono, S. M. Goldberg, N. F. T. Hall, and C. S. Fadley, *Phys. Rev. Lett.* **41**, 1831 (1978); *Phys. Rev.* **B22**, 6085 (1980).

43. T. Fujikawa, *J. Phys. Soc. Jpn.* **50**, 1321 (1981); **51**, 251 (1982); **54**, 2747 (1985); *J. Electron. Spectros. Relat. Phenom.* **26**, 79 (1982).
44. H. Daimon, H. Ito, S. Shin, and Y. Murata, *J. Phys. Soc. Jpn.* **54**, 3488 (1984).
45. J. J. Rehr, R. Albers, C. Natoli, and E. A. Stern, *Phys. Rev.* **B34**, 4350 (1986); J. J. Rehr, J. Mustre de Leon, C. R. Natoli, and C. S. Fadley, *J. Phys. (Paris)* **C8**, Suppl. 12, 213 (1986); J. J. Rehr, J. Mustre de Leon, C. R. Natoli, C. S. Fadley, and J. Osterwalder, *Phys. Rev.* **B39**, 5632 (1989).
46. D. E. Parry, *J. Electron. Spectros. Relat. Phenom.* **49**, 23 (1989).
47. D. J. Friedman and C. S. Fadley, *J. Electron Spectrosc.* **51**, 689 (1990).
48. (a) J. Osterwalder, E. A. Stewart, D. Cyr, C. S. Fadley, J. Mustre de Leon, and J. J. Rehr, *Phys. Rev.* **B35**, 9859 (1987); (b) J. Osterwalder, A. Stuck, D. J. Friedman, A. P. Kaduwela, C. S. Fadley, J. Mustre de Leon, and J. J. Rehr, *Phys. Scr.* **41**, 990 (1990); (c) J. Osterwalder, E. A. Stewart, D. J. Friedman, A. P. Kaduwela, C. S. Fadley, J. Mustre de Leon, and J. J. Rehr, unpublished results.
49. S. Kono, K. Higashiyama, and T. Sagawa, *Surf. Sci.* **165**, 21 (1986) and references to prior structure studies therein.
50. (a) E. L. Bullock, G. S. Herman, M. Yamada, D. J. Friedman, and C. S. Fadley, *Phys. Rev.* B, **41**, 1703 (1990); (b) E. L. Bullock, Ph.D. thesis, U. Hawaii (1988); (c) A. P. Kaduwela, D. J. Friedman, M. Yamada, E. L. Bullock, C. S. Fadley, Th. Lindner, D. Ricker, A. W. Robinson, and A. M. Bradshaw in *Structure of Surfaces III* (S. Y. Tong, M. A. Van Hove, K. Takayanagi, and X. D. Xie, eds.), Springer-Verlag, Berlin (1991), p. 600; and to be published.
51. M. Owari, M. Kudo, Y. Nihei, and H. Kamada, *J. Electron. Spectros. Relat. Phenom.* **21**, 131 (1981).
52. D. H. Rosenblatt, S. D. Kevan, J. G. Tobin, R. F. Davis, M. G. Mason, D. A. Shirley, J. C. Tang, and S. Y. Tong, *Phys. Rev.* **B26**, 3181 (1982).
53. G. Treglia, in *Core-Level Spectroscopy in Condensed Systems* (J. Kanamori and A. Kotani, eds.), Springer Verlag, Berlin (1988), p. 281.
54. J. J. Rehr and E. A. Albers, *Phys. Rev.* **B41**, 8139 (1990).
55. S. T. Manson, *Adv. Electron. Electron. Phys.* **41**, 73 (1976).
56. M. Sagurton, private communication.
57. P. A. Lee and J. B. Pendry, *Phys. Rev.* **B11**, 2795 (1975).
58. M. Sagurton, E. L. Bullock, R. Saiki, A. P. Kaduwela, C. R. Brundle, C. S. Fadley, and J. J. Rehr, *Phys. Rev.* **B33**, 2207 (1986).
59. H. C. Poon, D. Snider, and S. Y. Tong, *Phys. Rev.* **B33**, 2198 (1986).
60. M. Fink and A. C. Yates, *At. Data Nucl. Data Tables* **1**, 385 (1970); M. Fink and J. Ingram, *At. Data Nucl. Data Tables* **4**, 129 (1972); D. Gregory and M. Fink, *At. Data Nucl. Data Tables* **14**, 39 (1974).
61. J. B. Pendry, *Low Energy Electron Diffraction*, Academic Press, London (1974); M. A. van Hove and S. Y. Tong, *Surface Crystallography by LEED*, Springer-Verlag, New York (1979).
62. E. A. Stern, B. A. Bunker, and S. M. Heald, *Phys. Rev.* **B21**, 5521 (1980).
63. (a) R. Trehan and C. S. Fadley, *Phys. Rev.* **B34**, 6784 (1986); (b) R. Trehan, J. Osterwalder, and C. S. Fadley, *J. Electron. Spectros. Relat. Phenom.* **42**, 187 (1987).
64. M. P. Seah and W. A. Dench, *SIA, Surf. Interface Anal.* **1**, 2 (1979); C. J. Powell, *Scanning Electron Micros.* **4**, 1649 (1984); S. Tanuma, C. J. Powell, and D. R. Penn, *SIA Surf. Interface Anal.* **11**, 577 (1988).
65. P. M. Cadman and G. M. Gossedge, *J. Electron. Spectros. Relat. Phenom.* **18**, 161 (1980); C. M. Schneider, J. J. de Miguel, P. Bressler, J. Garbe, S. Ferrer, R. Miranda, and J. Kirscher, *J. Phys. (Paris) C*, Suppl. 12, **49**, 1657 (1988).
66. O. A. Baschenko and V. I. Nefedov, *J. Electron. Spectros. Relat. Phenom.* **21**, 153 (1980) and **27**, 109 (1982) and earlier references therein.
67. Y. U. Idzerda, D. M. Lind, and G. A. Prinz, *J. Vac. Sci. Technol.* **A7**, 1341 (1989).
68. N. E. Erickson and C. J. Powell, *Phys. Rev.* **B40**, 7284 (1989).
69. P. J. Orders, S. Kono, C. S. Fadley, R. Trehan, and J. T. Lloyd, *Surf. Sci.* **119**, 371 (1981).
70. (a) H. Helferink, E. Lang, and K. Heinz, *Surf. Sci.* **93**, 398 (1980); (b) P. J. Orders, R. E. Connelly, N. F. T. Hall, and C. S. Fadley, *Phys. Rev.* **B24**, 6161 (1981).
71. E. L. Bullock and C. S. Fadley, *Phys. Rev.* **B31**, 1212 (1985).

72. R. G. Weissman and K. Muller, *Surf. Sci. Rep.* **1**, 251 (1981).
73. M. L. Xu and M. A. van Hove, *Surf. Sci.* **207**, 215 (1989).
74. G. Breit and H. Bethe, *Phys. Rev.* **94**, 888 (1954).
75. L.-Q. Wang, A. E. Schach von Wittenau, Z. G. Ji, L. S. Wang, Z. Q. Huang, and D. A. Shirley, *Phys. Rev.* **B44**, 1292 (1991); and unpublished results.
76. D. A. Wesner, F. P. Coenen, and H. P. Bonzel, *Surf. Sci.* **199**, L419 (1988).
77. S. Y. Tong and H. C. Poon, *Phys. Rev.* **B37**, 2884 (1988).
78. S. Tougaard, *SIA, Surf. Interface Anal.* **11**, 453 (1988) and earlier references therein.
79. (a) J. B. Pendry and B. S. Ing, *J. Phys.* **C8**, 1087 (1975); (b) B. K. Teo and P. Lee, *J. Am. Chem. Soc.* **1979**, 101 (1979).
80. (a) G. Treglia, M. C. Desjonqueres, D. Spanjaard, D. Sebilleau, C. Guillot, D. Chauveau, and J. Lecante, *J. Phys. (Paris)* **1**, 1879 (1989); (b) D. G. Frank, N. Batina, T. Golden, F. Lu, and A. T. Hubbard, *Science* **247**, 182 (1990) and references therein.
81. L. I. Schiff, *Quantum Mechanics*, 3rd ed., McGraw-Hill, New York (1968), p. 136.
82. J. J. Barton, M.-L. Xu, and M. A. van Hove, *Phys. Rev.* **B37**, 10475 (1988).
83. (a) M.-L. Xu, J. J. Barton, and M. A. van Hove, *J. Vac. Sci. Technol* **A6**, 2093 (1988) and (b) *Phys. Rev.* **B39**, 8275 (1989).
84. A. P. Kaduwela, G. S. Herman, D. J. Friedman, C. S. Fadley, and J. J. Rehr, *Phys. Scr.* **41**, 948 (1990); A. P. Kaduwela, G. S. Herman, D. J. Friedman, and C. S. Fadley, *J. Electron Spectrosc. Relat. Phenom.* **57**, 223 (1991).
85. (a) R. C. Albers and J. J. Rehr, to be published; (b) K. Baberschke, in *The Structure of Surfaces II* (J. F. van der Veen and M. A. van Hove, eds.), Springer-Verlag, Berlin (1988), p. 174; (c) P. Rennert and N. V. Hung, *Phys. Status Solid* **148**, 49 (1988).
86. R. S. Saiki, G. S. Herman, M. Yamada, J. Osterwalder, and C. S. Fadley, *Phys. Rev. Lett.* **63**, 283 (1989).
87. (a) D. W. Moon, S. L. Bernasek, D. J. Dwyer, and J. L. Gland, *J. Am. Chem. Soc.* **107**, 4363 (1985); (b) C. Benndorf, B. Kruger, and F. Thieme, *Surf. Sci.* **163**, L675 (1985); (c) D. W. Moon, S. Cameron, F. Zaera, W. Eberhardt, R. Carr, S. L. Bernasek, J. L. Gland, and D. J. Dwyer, *Surf. Sci.* **180**, L123 (1987).
88. (a) D. A. Wesner, F. P. Coenen, and H. P. Bonzel, *Phys. Rev. Lett.* **60**, 1045 (1988); (b) *Phys. Rev.* **B39**, 10770 (1989).
89. H. Kuhlenbeck, M. Neumann, and H.-J. Freund, *Surf. Sci.* **173**, 194 (1986).
90. K. C. Prince, E. Holub-Krappe, K. Horn, and D. P. Woodruff, *Phys. Rev.* **B32**, 4249 (1985); E. Holub-Krabbe, K. C. Prince, K. Horn, and D. P. Woodruff, *Surf. Sci.* **173**, 176 (1986).
91. D. R. Wesner, F. P. Coenen, and H. P. Bonzel, *Phys. Rev.* **B33**, 8837 (1986).
92. K. A. Thompson and C. S. Fadley, *Surf. Sci.* **146**, 281 (1984).
93. H. Ibach and D. L. Mills, *Electron Energy Loss Spectroscopy*, Academic Press, New York (1982).
94. T. E. Madey, David E. Ramaker, and R. Stockbauer, *Ann. Rev. Phys. Chem.* **35**, 215 (1984).
95. J. Stohr and R. Jaeger, *Phys. Rev.* **B26**, 4111 (1982); A. L. Johnson, E. I. Muetterties, J. Stohr, and F. Sette, *J. Phys. Chem.* **89**, 4071 (1985); J. Stohr and D. A. Outka, *Phys. Rev.* **B36**, 7891 (1987).
96. See discussion and references in I. P. Batra and J. A. Barker, *Phys. Rev.* **B29**, 5286 (1984) and R. L. Strong and J. L. Erskine, *Phys. Rev.* **B31**, 6305 (1985).
97. An excellent review of the O/Ni (001) system is by C. R. Brundle and J. Q. Broughton in *The Chemical Physics of Solid Surfaces and Heterogeneous Catalysis* (D. A. King and D. P. Woodruff, eds.), Elsevier, Amsterdam (1991), Vol. 3a.
98. J. E. Demuth, N. J. DiNardo, and C. S. Cargill, *Phys. Rev. Lett.* **50**, 1373 (1983).
99. J. J. Barton, C. C. Bahr, Z. Hussain, S. W. Robey, J. G. Tobin, L. E. Klebanoff, and D. A. Shirley, *Phys. Rev. Lett.* **51**, 272 (1983) and earlier references therein.
100. R. S. Saiki, A. P. Kaduwela, Y. J. Kim, D. J. Friedman, J. Osterwalder, S. Thevuthasan, E. Tober, R. Ynzunza and C. S. Fadley, to be published.
101. M. Sagurton, B. Sinkovic, and C. S. Fadley, unpublished results.
102. X. S. Zhang, L. J. Terminello, S. Kim, Z. Q. Huang, A. E. Schach von Wittenau, and D. A. Shirley, *J. Chem. Phys.* **89**, 6583 (1988).
103. W. F. Egelhoff, *Phys. Rev. Lett.* **59**, 559 (1987).

104. (a) S. A. Chambers, T. J. Wagener, and J. H. Weaver, *Phys. Rev.* **B36**, 8992 (1987); (b) D. A. Steigerwald and W. F. Egelhoff, *Phys. Rev. Lett.* **60**, 2558 (1988).
105. G. Herman, J. Osterwalder, and C. S. Fadley, unpublished results.
106. J. J. Krebs, B. T. Jonker, and G. A. Prinz, *J. Appl. Phys.* **61**, 2596 (1987).
107. G. S. Herman, T. Lindner, R. S. Saiki, and C. S. Fadley, unpublished results.
108. G. Granozzi, A. Rizzi, G. S. Herman, D. J. Friedman, C. S. Fadley, J. Osterwalder, and S. Bernardi, *Phys. Scr.*, **41**, 913 (1990); G. S. Herman, D. J. Friedman, C. S. Fadley, G. Granozzi, G. A. Rizzi, J. Osterwalder, and S. Bernardi, *J. Vac. Sci. Technol.* **B9**, 1870 (1991).
109. R. E. Connelly, C. S. Fadley, and P. J. Orders, *J. Vac. Sci. Technol.* **A2**, 1333 (1984).
110. P. Alnot, J. Olivier, F. Wyczisk, and C. S. Fadley, *J. Electron. Spectros. Relat. Phenom.* **43**, 263 (1987); P. Alnot, J. Olivier, and C. S. Fadley, *J. Electron. Spectros. Relat. Phenom.* **49**, 159 (1989).
111. G. M. Rothberg, K. M. Choudhary, M. L. denBoer, G. P. Williams, M. H. Hecht, and I. Lindau, *Phys. Rev. Lett.* **53**, 1183 (1984).
112. K. M. Choudhary, P. S. Mangat, A. E. Miller, D. Kilday, A. Filipponi, and G. Margaritondo, *Phys. Rev.* **B38**, 1566 (1988).
113. S. Kono in *Core-Level Spectroscopy in Condensed Systems* (J. Kanamori and A. Kotani, eds.), Springer-Verlag, Berlin (1988), p. 253.
114. T. Abukawa and S. Kono, *Phys. Rev.* **B37**, 9097 (1988).
115. (a) S. Ciraci and I. P. Batra, *Phys. Rev. Lett.* **56**, 877 (1986); (b) E. M. Oellig and R. Miranda, *Surf. Sci.* **177**, L947 (1986); (c) T. Kendelewicz, P. Soukassian, R. S. List, J. C. Woicik, P. Pianetta, I. Lindau, and W. E. Spicer, *Phys. Rev.* **B37**, 7115 (1988); (d) R. Ramirez, *Phys. Rev.* **B40**, 3962 (1989).
116. E. J. van Loenen, J. E. Demuth, R. M. Tromp, and R. J. Hamers, *Phys. Rev. Lett.* **58**, 373 (1987); R. J. Wilson and S. Chiang, *Phys. Rev. Lett.* **59**, 2329 (1987) and *J. Vac. Sci. Technol* **A6**, 800 (1988); T. L. Porter, C. S. Chang, and I. S. T. Tsong, *Phys. Rev. Lett.* **60**, 1739 (1988); and earlier references therein.
117. W. C. Fan, A. Ignatiev, H. Huang, and S. Y. Tong, *Phys. Rev. Lett.* **62**, 1516 (1989).
118. S. Y. Tong, H. Huang, C. M. Wei, W. E. Packard, F. K. Men, G. Glander, and M. B. Webb, *J. Vac. Sci. Technol* **A6**, 615 (1988).
119. E. L. Bullock and C. S. Fadley, unpublished results.
120. K. Tamura, U. Bardi, M. Owari, and Y. Nihei, in *The Structure of Surfaces II* (J. F. van der Veen and M. A. van Hove, eds.), Springer-Verlag, Berlin (1988), p. 404.
121. D. Spanjaard, C. Guillot, M. C. Desjonqueres, G. Treglia, and J. Lecante, *Surf. Sci. Rep.* **5**, 1 (1985).
122. Y. Jugnet, N. S. Prakash, L. Porte, T. M. Duc, T. T. A. Nyugen, R. Cinti, H. C. Poon, and G. Grenet, *Phys. Rev.* **B37**, 8066 (1988).
123. (a) T. Miller, T. C. Hsieh, and T.-C. Chiang, *Phys. Rev.* **B33**, 6983 (1986); (b) J. Aarts, A.-J. Hoeven, and P. K. Larsen, *Phys. Rev.* **B38**, 3925 (1988); (c) F. J. Himpsel, F. R. McFeely, A. Taleb-Ibrahimim, J. A. Yarmoff, and G. Hollinger, *Phys. Rev.* **B38**, 6084 (1988).
124. E. Tosatti, in *The Structure of Surfaces II* (J. F. van der Veen and M. A. van Hove, eds.), Springer-Verlag, Berlin (1988), p. 535.
125. U. Breuer, O. Knauff, and H. P. Bonzel, *J. Vac. Sci. Tech.*, **A8**, 2489 (1990).
126. T. Tran, D. J. Friedman, Y. J. Kim, G. A. Rizzi, and C. S. Fadley, *Structure of Surfaces III* (S. Y. Tong, M. A. Van Hove, K. Takayanagi, and X. D. Xie, eds.) Springer-Verlag (1991), p. 522; T. Tran, S. Thevuthasan, Y. J. Kim, G. S. Herman, D. J. Friedman and C. S. Fadley, to be published.
127. (a) E. G. McRae and R. A. Malic, *Phys. Rev. Lett.* **58**, 1437 (1987) and *Phys. Rev.* **B38**, 13183 (1988); (b) E. G. McRae, J. M. Landwehr, J. E. McRae, G. H. Gilmer, and M. H. Grabow, *Phys. Rev.* **B38**, 13178 (1988).
128. J. W. M. Frenken, J. P. Toennies, Ch. Woell, B. Pluis, A. W. Denier van der Gon, and J. F. van der Veen, in *The Structure of Surfaces II* (J. F. van der Veen and M. A. van Hove, eds.), Springer-Verlag, Berlin (1988), p. 547.
129. R. J. Baird, C. S. Fadley, and L. F. Wagner, *Phys. Rev.* B15, 666 (1977).
130. S. M. Goldberg, R. J. Baird, S. Kono, N. F. T. Hall, and C. S. Fadley, *J. Electron. Spectros. Relat. Phenom.* **21**, 1 (1980).

131. W. Schaich, *Phys. Rev.* **B8**, 4078 (1973); E. A. Stern, *Phys. Rev.* **B10**, 3027 (1974).
132. See, for example, discussion of multiplets by C. S. Fadley in *Electron Spectroscopy: Theory, Techniques, and Applications* (C. R. Brundle and A. D. Baker, eds.), Vol. 2, Academic Press, London (1978), Ch. 1.
133. G. M. Rothberg, *J. Magn. Magn. Mater.* **15–18**, 323 (1980).
134. (a) B. Sinkovic and C. S. Fadley, *Phys. Rev.* **B31**, 4665 (1985); (b) B. Sinkovic, Ph.D. thesis, U. Hawaii (1988); (c) B. Sinkovic, D. J. Friedman, and C. S. Fadley, *J. Magn. Magn. Mater.* **92**, 301 (1991).
135. B. Hermsmeier, B. Sinkovic, J. Osterwalder, and C. S. Fadley, *J. Vac. Sci. Technol* **A5**, 1082 (1987).
136. C. S. Fadley in (*Magnetic Properties of Low-Dimensional Systems II. New Developments* (L. R. Falicov, F. Mejia-Lira, and J.-L. Moran-Lopez, eds.), Springer-Verlag, Berlin (1990), p. 36; See especially calculations by J. M. Sanchez and J.-L. Moran-Lopez for a frustrated antiferromagnetic system discussed therein.
137. B. W. Veal and A. P. Paulikas, *Phys. Rev. Lett.* **51**, 1995 (1983).
138. B. Hermsmeier, C. S. Fadley, B. Sinkovic, M. O. Krause, J. Jiminez-Mier, P. Gerard, and S. T. Manson, *Phys. Rev. Lett.* **61**, 2592 (1988).
139. S. P. Kowalczyk, L. Ley, R. A. Pollak, F. R. McFeely, and D. A. Shirley, *Phys. Rev.* **B7**, 4009 (1973).
140. P. S. Bagus, A. J. Freeman, and F. Sasaki, *Phys. Rev. Lett.* **30**, 850 (1973).
141. E. Kisker and C. Carbone, *Solid State Commun.* **65**, 1107 (1988).
142. B. Sinkovic, B. Hermsmeier, and C. S. Fadley, *Phys. Rev. Lett.* **55**, 1227 (1985).
143. B. Hermsmeier, J. Osterwalder, D. J. Friedman, and C. S. Fadley, *Phys. Rev. Lett.* **62**, 478 (1989); B. D. Hermsmeier, Ph.D. thesis, U. Hawaii (1989); B. Hermsmeier, J. Osterwalder, D. J. Friedman, B. Sinkovic, T. Tran, and C. S. Fadley, *Phys. Rev.* **B42**, 11895 (1990).
144. D. J. Friedman, B. Sinkovic, C. S. Fadley, *Phys. Scr.* **41**, 909 (1990).
145. J. E. Smart, *Effective Field Theories of Magnetism*, Saunders, New York (1966), Ch. 4.
146. M. Landolt and D. Mauri, *Phys. Rev. Lett.* **49**, 1783 (1982); D. Mauri, R. Allenspach, and M. Landolt, *Phys. Rev. Lett.* **52**, 152 (1984); M. Taborelli, R. Allenspach, and M. Landolt, *Phys. Rev.* **B34**, 6112 (1996); R. Allenspach, D. Mauri, M. Taborelli, and M. Landolt, *Phys. Rev.* **B35**, 4801 (1987).
147. G. Schuetz, W. Wagner, W. Wilhelm, P. Keinle, R. Zeller, R. Frahm, and G. Materlik, *Phys. Rev. Lett.* **58**, 737 (1987); G. Schuetz, R. Frahm, P. Mautner, R. Wienke, W. Wagner, W. Wilhelm, and P. Kienle, *Phys. Rev. Lett.* **62**, 2620 (1989); G. Schuetz, *Phys. Scr.* **T29**, 172 (1989); G. Schuetz and R. Wienke, *Hyperfine Interactions* **50**, 457 (1989).
148. G. Schoenhense, *Appl. Phys.* **A41**, 39 (1986); C. Westphal, J. Bansmann, M. Getzlaff, and G. Schoenhense, *Phys. Rev. Lett.* **63**, 151 (1989); G. Schoenhense, *Phys. Scr.*, **T31**, 255 (1990).
149. K. A. Thompson and C. S. Fadley, *J. Electron, Spectros. Relat. Phenom.* **33**, 29 (1984).
150. P. L. King, A. Borg, P. Pianetta, I. Lindau, G. Knapp, and M. Keenlyside, *Phys. Scr.* **41**, 413 (1990); B. P. Tonner, *Phys. Scr.* **T31**, (1990); W. Ng, A. K. Ray-Chaudhuri, R. K. Cole, S. Crossley, D. Crossley, C. Gong, M. Green, J. Guo, R. W. C. Hansen, F. Cerrina, G. Margaritondo, J. H. Underwood, J. Kortright, and R. C. C. Perera, *Phys. Scr.* **41**, (1990); H. Ade, J. Kirz, S. L. Hulbert, E. D. Johnson, E. Anderson, and D. Kern, *Appl. Phys. Lett.* **56**, 1841 (1990).
151. J. J. Barton, *Phys. Rev. Lett.* **61**, 1356 (1988) and private communication.
152. A. Szoeke, in *Short Wavelength Coherent Radiation: Generation and Applications* (D. T. Attwood and J. Bokor, eds.), AIP Conf. Proc. No. 147, American Institute of Physics, New York (1986).
153. J. Stohr, J. L. Gland, W. Eberhardt, D. A. Outka, R. J. Madix, F. Sette, R. J. Koestner, and U. Doebler, *Phys. Rev. Lett.* **51**, 2414 (1983); J. Stohr, F. Sette, and A. L. Johnson, *Phys. Rev. Lett.* **53**, 1684 (1984); A. P. Hitchcock and J. Stohr, *J. Chem. Phys.* **87**, 3253 (1986).
154. M. N. Piancastelli, D. W. Lindle, T. A. Ferrett, and D. A. Shirley, *J. Chem. Phys.* **86**, 2765 (1987) and **87**, 3255 (1987).
155. P. K. Hansma and J. Tersoff, *J. Appl. Phys.* 61, R1 (1987); J. Tersoff, in *The Structure of Surfaces II* (J. F. van der Veen and M. A. van Hove, eds.) Springer-Verlag, Berlin (1988), p. 4; and references therein.

156. T. Gustafsson, M. Copel, and P. Fenter, in *The Structure of Surfaces II* (J. F. van der Veen and M. A. van Hove, eds.) Springer-Verlag, Berlin (1988), p. 110; and references therein.
157. F. Sette, S. J. Pearton, J. M. Poate, J. E. Rowe, and J. Stohr, *Phys. Rev. Lett.* 56, 2637 (1986).
158. G. R. Harp, D. K. Saldin, and B. P. Tonner, *Phys. Rev. Lett.* 65, 1012 (1990), and *Phys. Rev.* **B42**, 9199 (1990).
159. G. S. Herman, S. Thevuthasan, T. T. Tran, Y. J. Kim, and C. S. Fadley, *Phys. Rev. Lett.* 3 Feb., 1991.
160. D. K. Saldin, G. R. Harp, B. L. Chen, and B. P. Tonner, *Phys. Rev.* **B44**, 2480 (1991) and earlier references therein.
161. S. Y. Tong, C. M. Wei, T. C. Zhao, H. Huang, and H. Li, *Phys. Rev. Lett.* **66**, 60 (1991); S. Y. Tong, H. Li, and H. Huang, *Phys. Rev. Lett.* **67**, 3102 (1991).
162. S. Thevuthasan, G. S. Herman, A. P. Kaduwela, R. S. Saiki, Y. J. Kim, W. Niemczura, M. Burger, and C. S. Fadley, *Phys. Rev. Lett.* **67**, 469 (1991).
163. J. J. Barton, *Phys. Rev. Lett.* **67**, 3406 (1991).

ELSEVIER

Journal of Electron Spectroscopy and Related Phenomena 75 (1995) 273–297

JOURNAL OF ELECTRON SPECTROSCOPY and Related Phenomena

Photoelectron diffraction: new dimensions in space, time, and spin

C.S. Fadley[a,b,*], M.A. Van Hove[b], Z. Hussain[c], A.P. Kaduwela[a,b]

[a] *Department of Physics, University of California–Davis, Davis, CA 95616, USA*
[b] *Materials Science Division, Lawrence Berkeley National Laboratory, Berkeley, CA 94720, USA*
[c] *Advanced Light Source, Lawrence Berkeley National Laboratory, Berkeley, CA 94720, USA*

Received 13 October 1995; accepted 1 November 1995

Abstract

The current status of photoelectron diffraction studies of surface structures is briefly reviewed, and several recent developments and proposals for future areas of application are then discussed. The application of full-solid-angle diffraction data, together with simultaneous characterization by low energy electron diffraction and scanning tunneling microscopy, to epitaxial growth is first considered. New instrumentation for carrying out such studies with third-generation synchrotron radiation is then presented and several types of results obtained with it are discussed. These results include photoelectron diffraction from surface and interface atoms, the possibility of time-resolved measurements, and circular dichroism in photoelectron angular distributions. The addition of spin to the photoelectron diffraction measurement is also considered, and can be achieved either through core-level multiplet splittings or by circular-polarized excitation of spin–orbit-split levels. This last development makes it possible to study short-range magnetic order, perhaps even in a holographic fashion.

Keywords: Holography; Photoelectron diffraction; Photoelectron spectroscopy; Surface structure; Synchrotron radiation

1. Introduction

In photoelectron diffraction (PD), a photon excites an electron from a core level, and the outgoing photoelectron wave is scattered from the atoms neighboring the emitter, producing an interference pattern. Strong modulations in intensity of as much as ±40% are observed as a function of either the direction of electron emission or the energy of excitation, leading to what have been termed scanned-angle or scanned-energy measurements, respectively. The first set of papers on PD began appearing 25 years ago [1], and the Shirley group was a pioneer in scanned-energy PD, publishing the initial paper in 1978 [1f]. The aim of these measurements is to deduce information about the atomic structure around the emitter, or perhaps also the type of magnetic order surrounding it. There are by now a number of groups in the world engaged in such experiments, using both laboratory X-ray sources and synchrotron radiation (SR), and a variety of systems have been studied to date with this technique, including systems exhibiting surface core-level shifts, adsorbed atoms and molecules, epitaxial overlayers, and atoms at buried interfaces. Several reviews of this field have appeared in recent years [2–7], and it will thus not be our aim to survey it in detail. Rather, we will

* Corresponding author.

SSDI 0368-2048(95)02545-6

begin by briefly describing those basic characteristics that make PD an attractive structural probe, consider some of its limitations and difficulties, and then go on to concentrate on several more recent developments involving both laboratory and next-generation SR sources that promise to make it an even more widely used tool for surface, interface, and nanostructure studies in the future.

We begin with the positive aspects of PD, several of which will be illustrated with more specific examples in the following sections.

(i) Atom specificity. PD is an atom-specific probe by virtue of the fact that a certain core level is probed. Thus, the structure around each type of atom in the sample can be probed separately.

(ii) Chemical-state or site specificity. With sufficient resolution, core binding energy shifts with chemical state (e.g. the different oxidation states of a given atom) or binding site (e.g. between the bulk and surface of a metal or semiconductor) can be used to study the atomic structure around each type of atom separately [8].

(iii) Spin-specificity. Although not nearly as much explored, the diffraction patterns of photoelectrons of different spins can also be studied separately, yielding the promise of determining the local magnetic order around both magnetic atoms and non-magnetic atoms surrounded by magnetic atoms. Such spin sensitivity can be achieved by using the multiplet splitting inherent in the core spectra of various transition metals or rare-earth elements, by exciting spin-orbit-split core levels with circularly polarized radiation, or by some combination of these two effects. This leads to what has been termed spin polarized photoelectron diffraction (SPPD) [9].

(iv) Polarization dependence. Beyond using circular polarization to produce spin polarization, varying polarization from linear to left or right circular to unpolarized further permits selectively directing the outgoing photoelectron probe wave into different regions of the atomic structure surrounding the emitter, so that complementary structural information can be obtained for different relative orientations of light and sample [2,4].

(v) Energy dependence. PD makes use of energy dependence in three basic ways. At higher energies of more than 500 eV, the electron–atom scattering factor is highly peaked in the forward direction, producing pronounced peaks in diffraction patterns along, for example, bond directions in adsorbed molecules and low-index directions in epitaxial layers [2,3,5]. For lower energies below 300 eV, the scattering factor is more uniform over all directions, and usually has a strong peak in the backward direction; thus, the locations of atoms behind the emitter as viewed from the detector can be studied [4,6], although their bond directions cannot be as directly determined as in forward scattering. Being able to vary energy between these two limits using synchrotron radiation thus permits the full structural environment of a given emitter to be studied. Going to lower energies in the 50–100 eV range further leads to increased sensitivity to the surface (via the reduced inelastic attenuation length) and to magnetic scattering effects, (via the enhanced exchange interaction); such energies are thus those of relevance in SPPD measurements [9]. Finally, the energy dependence of the photoelectron de Broglie wavelength is also what leads to the modulations measured in scanned-energy photoelectron diffraction.

(vi) Simple first-order theoretical interpretation. In a number of studies to date, it has proven possible to derive useful surface structural information by comparing experimental data with the results of rather straightforward single-scattering (SS or kinematical) theoretical calculations [2,3a]. However, it is also by now clear that a fully quantitative treatment of all of the features in both low-energy and high-energy diffraction patterns will require more sophisticated calculations at a fully converged multiple scattering (MS) level [10] that have many similarities to those used in low energy electron diffraction (LEED) analyses. We shall illustrate below both types of theoretical analysis.

(vii) Direct derivation of structural parameters. A final advantage is that there are several ways in which it is possible to directly derive structural parameters from PD data. We have already noted that forward scattering peaks directly give bond or low-index directions [2,3,5]. Beyond this, a Fourier transform of scanned-energy PD data yields path-length differences for different scatterers that can often be used to rule out some adsorbate geometries in a search for the true structure [2,4,6b,11].

Finally, taking a larger data set that involves varying both energy and angle over some volume in the momentum space of the photoelectron can be used with several recently suggested transform algorithms to holographically derive atomic positions in three dimensions [12–19], a topic to which we shall return in connection with spin-resolved studies.

By contrast, some difficulties with PD are as follows.

(i) More complex equipment. Relative to a standard laboratory photoelectron spectroscopy system, a more precise, computer-driven sample manipulator is required. For the most versatile and powerful experiments with variable energy and/or variable polarization, access to a synchrotron radiation beamline is also necessary.

(ii) Long measuring times. Measuring hundreds or perhaps even a few thousand separate core spectra to produce a single angle or energy scan or a more complex scan over both angle and energy that can be used in a holographic sense [12–19] can be very time consuming, and take between hours and days with most present systems. However, next-generation synchrotron radiation beamlines, coupled to appropriately high-throughput spectrometers and detectors, promise to reduce these times to the minutes-to-hours range. This should also permit a broader range of dynamical studies on surfaces.

(iii) Macroscopic domain averaging. At present, PD data are taken from the full area illuminated by the radiation, which is typically of the order of 1 mm^2 to 10 mm^2. Thus, many domains are averaged over, and structural conclusions can be confused by the resulting overlap of diffraction patterns from different site types. Various kinds of photoelectron microscopy are currently being tested at different synchrotron radiation sources around the world, as discussed in the article in this issue by Tonner et al. [20]. These developments may ultimately permit PD to be carried out on areas as small as a few hundred angstroms in radius, thus focussing on a single domain or nanostructure on the surface. This last prospect is to be sure a tour de force experiment for third-generation (or even fourth-generation) synchrotron radiation sources, but realizing it would be exciting indeed, because a further space dimension could then be accessed.

(iv) Complex multiple-scattering theoretical interpretation. We have already noted above that data can often be analyzed to a useful point within a single-scattering framework, but future studies will no doubt make more use of the more quantitative multiple-scattering model. However, a number of groups by now have multiple scattering programs operating [10], and these will no doubt become faster, more accurate, and more user friendly; as they have in LEED analysis.

We will now turn to a few recent examples of PD data and its theoretical interpretation, and to the development of next-generation instrumentation for such measurements. These examples are chosen primarily from the work of our groups, but we hope that they are illustrative of both some current forefronts of PD studies and some of the more exciting future directions in this field.

2. Full-solid-angle diffraction data

Although the first full-solid-angle PD pattern was measured some time ago [21a], it is only in recent years that these time-consuming experiments have been performed on a more routine basis, beginning particularly in the Osterwalder group [7,21b–e]. We here illustrate the utility of this kind of data for a recent study of the growth of iron oxides on Pt(111) [22]. In this work, another noteworthy element was added in that X-ray photoelectron diffraction (XPD) measurements in a laboratory-based system were combined with in situ characterization by both LEED and scanning tunneling microscopy (STM), such that the complementary nature of these surface structure probes could be exploited.

Some of the data from this study for a 1 monolayer (ML) overlayer of FeO on Pt(111) are shown in Fig. 1, where a LEED pattern, STM image, and full-solid-angle XPD patterns for all three atoms present (Pt, Fe, and O) are compared for the same surface preparation. The LEED pattern shows the basic Pt(111) spots, but with a rosette of superstructure spots around each one indicative of some longer range order. This longer range

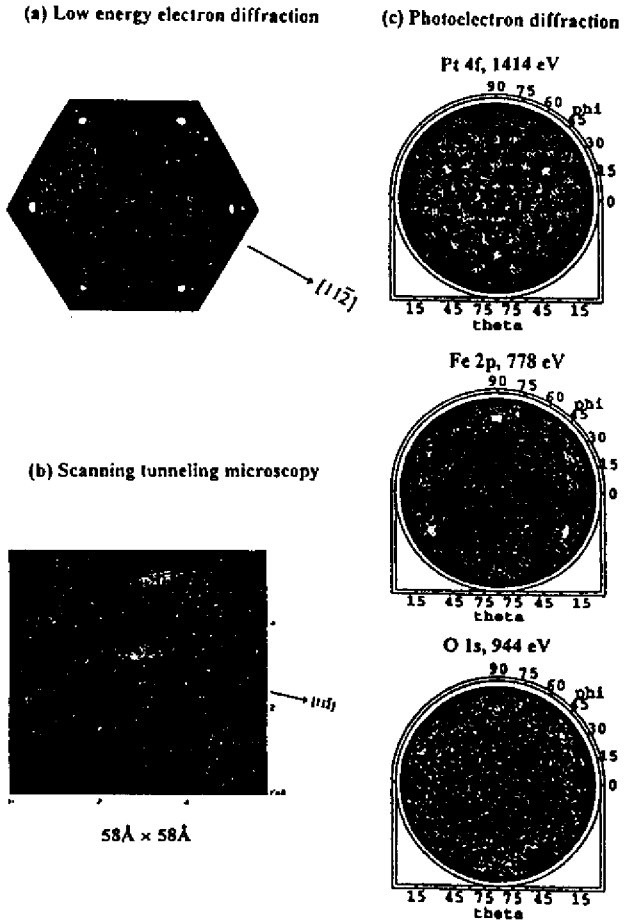

Fig. 1. LEED, STM, and XPD data for 1 ML of FeO on Pt(111). The full-solid-angle XPD patterns for Pt4f, Fe2p, and O1s emission are shown. (From Ref. [22].)

order is directly imaged by STM, with a hexagonal unit cell of approximately 26 Å × 26 Å superimposed on the atomic-resolution hexagonal oxide unit cell of 3.1 Å × 3.1 Å. Such combined LEED and STM data led Galloway et al. [23] to propose a particular superstructure or lateral Moiré pattern consisting of a hexagonal-symmetry bilayer of FeO(111) composed of a layer of Fe atoms on top of, or below, a layer of O atoms. However, this model left several questions about this overlayer unanswered. Among these questions were: Which atomic layer is outermost, Fe or O? What is the interplanar distance between Fe and O? Is there a preferred relative orientation of the FeO bilayer in its growth with respect to the underlying Pt?

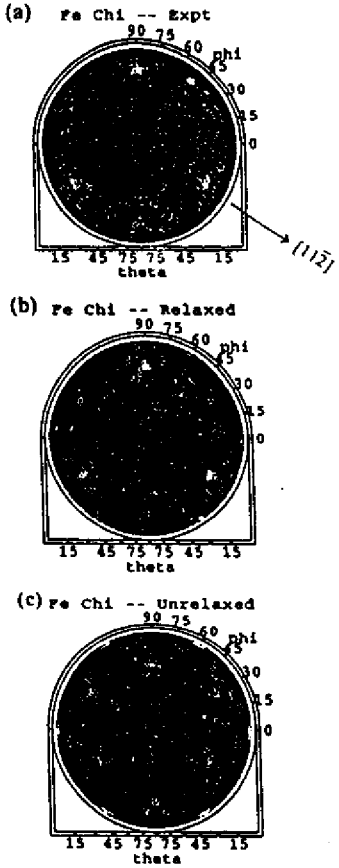

Fig. 2. The full-solid-angle Fe2p XPD pattern for 1 ML of FeO on Pt(111): (a) experimental data; (b) single scattering theory with an Fe–O interplanar distance of 0.65 Å; (c) single-scattering theory with an Fe–O interplanar distance of 1.25 Å as in bulk FeO. (From Ref. [22].)

The XPD results in Fig. 1 serve to answer all three of these questions. The Pt4f diffraction pattern is dominated by scattering in the substrate crystal, and so does not contain any easily-derivable information concerning the structure of the overlayer. It does, however, provide a direct internal reference in the data for the orientation of the overlayer. The Fe2p diffraction pattern contains three strong peaks with some fine structure around them, immediately suggesting that there are forward scattering atoms between Fe and the detector. Thus, O appears to be the outermost layer. Finally, the O1s pattern is devoid of any significant diffraction features, further confirming that it is the outermost layer. The second question regarding interlayer spacing is also easily answered by measuring the polar angle at which the Fe–O forward scattering peaks occur, and combining this with the lateral unit cell dimensions of the FeO overlayer from LEED and/or STM. Simple trigonometry then yields an interplanar distance of only 0.65 Å that is much contracted from the 1.25 Å between (111) planes in bulk FeO. This distance can be further checked by carrying out single-scattering diffraction calculations for this overlayer, with single-scattering being a very good approximation for this situation in which there are no chains of forward scattering atoms [2]. Theoretical calculations for both 0.65 Å and 1.25 Å interplanar spacings are compared to experiment in Fig. 2. The agreement between experiment and the calculation for 0.65 Å is excellent, including even the weak diffraction features around the forward scattering peaks. For a 1.25 Å spacing, agreement is poor, both for the polar angle position of the forward scattering peaks and the weaker features. Finally, the fact that there are only three forward scattering peaks in the Fe diffraction pattern immediately implies that only one orientation of the hexagonal O overlayer with respect to the underlying Pt surface exists, even though two O overlayer orientations rotated by 180° with respect to one another are equally likely as far as the Fe layer is concerned. Thus, there is an O–Pt interaction through the Fe layer that is strong enough to select only one orientation of

the O overlayer, a subtle aspect of the growth process that would be difficult to determine with any other method.

This is thus an illustrative example of both how useful full-solid-angle diffraction patterns can be (see also Refs. [7] and [21] for other examples) and how important it is to have additional complementary structural probes in the same experimental chamber, with LEED and STM being two particularly useful ones.

3. A next-generation photoelectron spectrometer/diffractometer

In Fig. 3, we show a schematic view of a photoelectron spectrometer that has been configured for high-resolution, high-intensity spectroscopy and diffraction measurements, and initially installed on bending magnet beamline 9.3.2 at the Advanced Light Source in Berkeley. Fig. 4 shows a photograph of the system, with major components labelled. The electron energy analyzer is a tuneable-resolution large-diameter hemispherical electrostatic system (Scienta ES200) that has been incorporated into a chamber which can rotate over 60° in the plane of the electron storage ring. This rotation is made possible by a large-diameter bellows linking the chamber to the beamline, as shown in these figures. Such in-plane analyzer rotation, although common for much smaller analyzers mounted inside the vacuum system, has not been attempted before in such an ex situ mounting, and it permits selectively varying of the fundamental excitation cross section, keeping the photon-sample geometry fixed while measuring intensities over a large fraction of the 2π solid angle above the surface, and scanning the analyzer with the sample polar-angle motion to keep the photoelectron escape process constant. The analyzer is presently equipped with a single multichannel detector capable of an integrated count rate of about 100 kHz, but will in the near future be modified to include a much higher speed multichannel detector operating up to the gigahertz range, together with an alternative spin detector of the so-called microMott type that will be interchangeable in situ. The spherical grating monochromator and analyzer together should be capable of operating at energy resolutions of $1:10^4$. The analyzer is also equipped with a demountable collimator at its entry to limit the solid angle of acceptance to ±1.5° for high angular resolution studies. The beamline optics also permit radiation to be taken both above and below the plane of the electron orbit, thus obtaining a high degree of left or right circular polarization, and linear polarization with in-plane operation. This beamline and end station has been constructed as a collaborative project with the Shirley group. We now briefly consider some first results obtained with this instrumentation.

3.1. Full-solid-angle photoelectron diffraction from surface and bulk atoms of a clean surface

In Fig. 5(a), we show the geometry for an experiment in which the surface and bulk W4f peaks from a clean W(110) surface have been measured with this system. It is well known that the clean (110) surface exhibits a surface component shifted to lower binding energy by 320 meV [8a,24a], and this is cleanly resolved in the spectrum of Fig. 5(b). The 120 meV full width at half maximum (FWHM) for the bulk peak is slightly narrower than anything measured before [24a], and is essentially limited by the various sources of natural linewidth for this level. PD has been measured before for this case [8a,24b,c], but has only involved a few scans in azimuthal angle or in energy. The high rate of data acquisition possible with this new system (a spectrum like that in Fig. 5(b) can be obtained in 20 s or less) has now permitted measuring essentially the full solid angle of data for both the bulk and surface peaks, as shown in Figs. 5(c) and 5(d), respectively [25]. The photoelectron energies here are in the very surface sensitive 39–40 eV range. Thus, it is obvious that it will be possible in the future to obtain much more complete photoelectron diffraction information than in prior studies.

One immediate benefit of such data sets is the possibility of making more rigorous tests of the multiple scattering theory that is now being used by several groups to analyze PD data. In particular, we have carried out multiple-scattering and single-scattering calculations to simulate the surface-atom

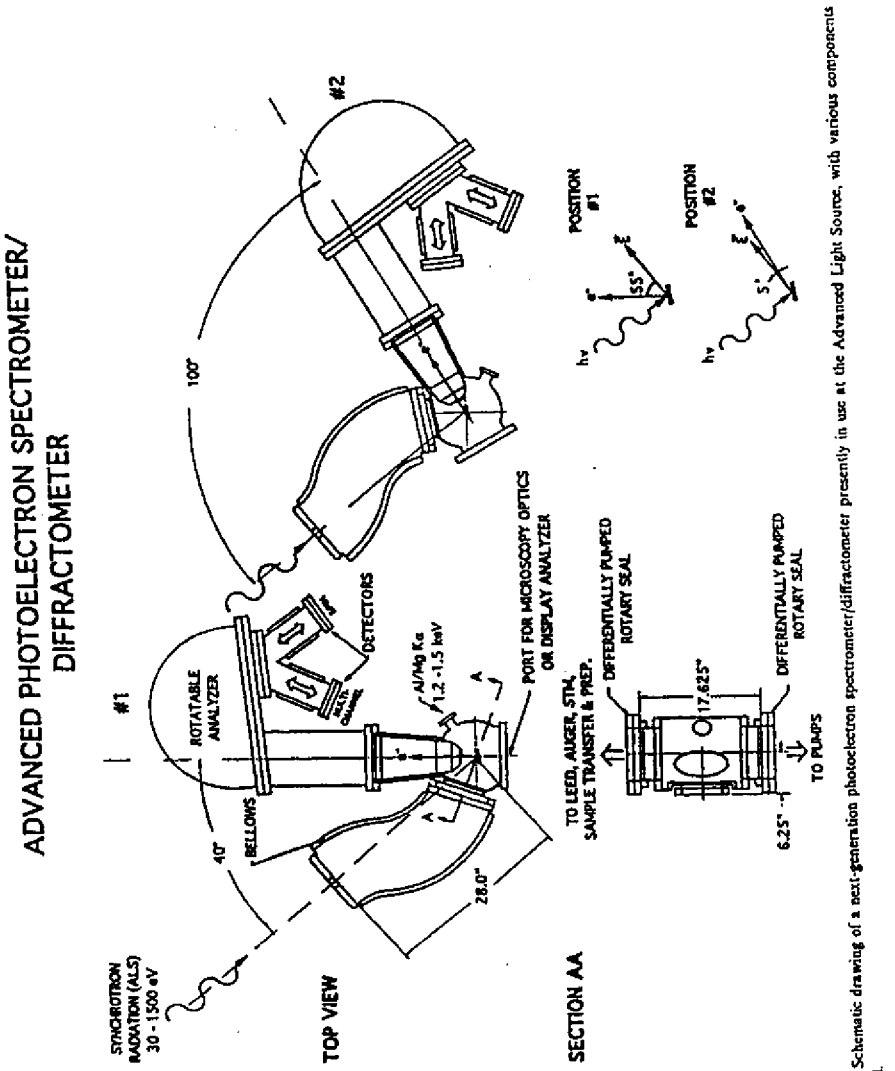

Fig. 3. Schematic drawing of a next-generation photoelectron spectrometer/diffractometer presently in use at the Advanced Light Source, with various components labelled.

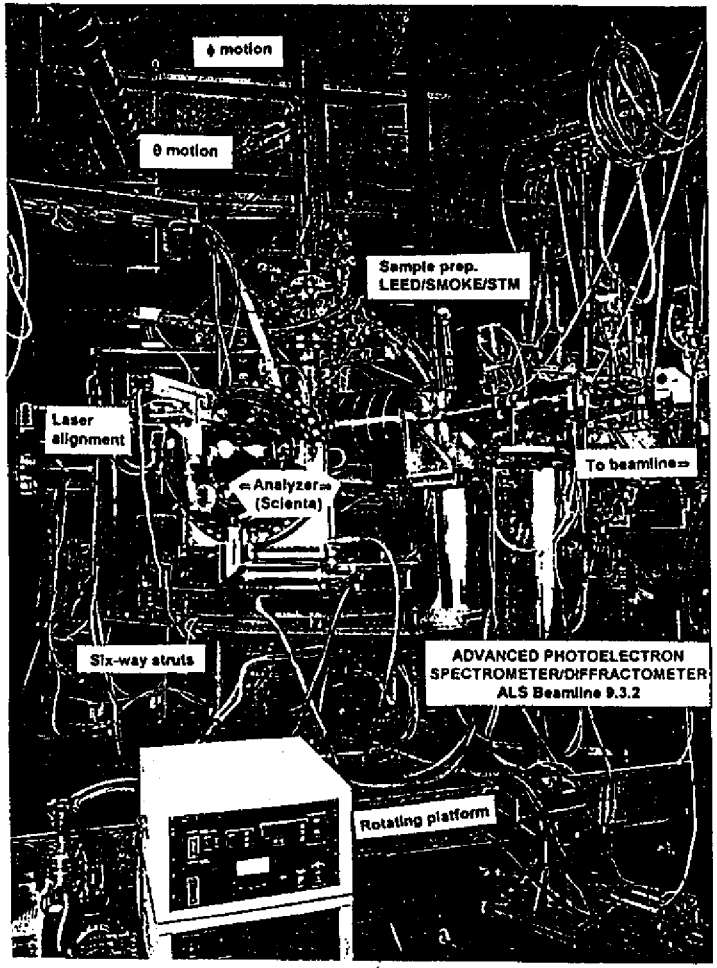

Fig. 4. Photograph of the photoelectron spectrometer/diffractometer of Fig. 3.

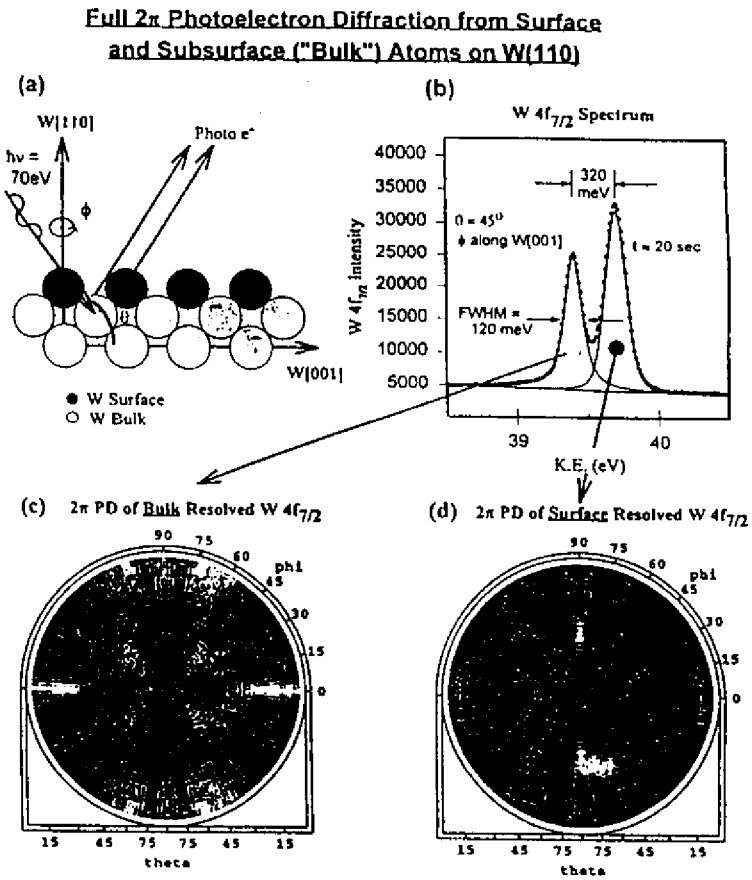

Fig. 5. Full-solid-angle photoelectron diffraction from clean W(110): (a) the experimental geometry; (b) a high-resolution W4f$_{7/2}$ spectrum, resolved into surface and bulk components; (c) the full diffraction pattern for the bulk component; (d) the full diffraction pattern for the surface component. (From Ref. [25].)

diffraction pattern in Fig. 5(d), using a program developed by Kaduwela et al. [10e] and based on the convenient Rehr–Albers approximation for treating multiple scattering [10d]. The experimental data for surface emission are shown again in Fig. 6(a), where they are compared to both multiple scattering and single-scattering results. The "non-structural" parameters for the calculations of inner potential V_0 and inelastic attenuation length Λ_e were determined from the PD data by optimizing the fit of the MS calculations to experiment and analyzing azimuthally-averaged surface-to-bulk ratios as a function of photoelectron takeoff angle relative to the surface; the values of

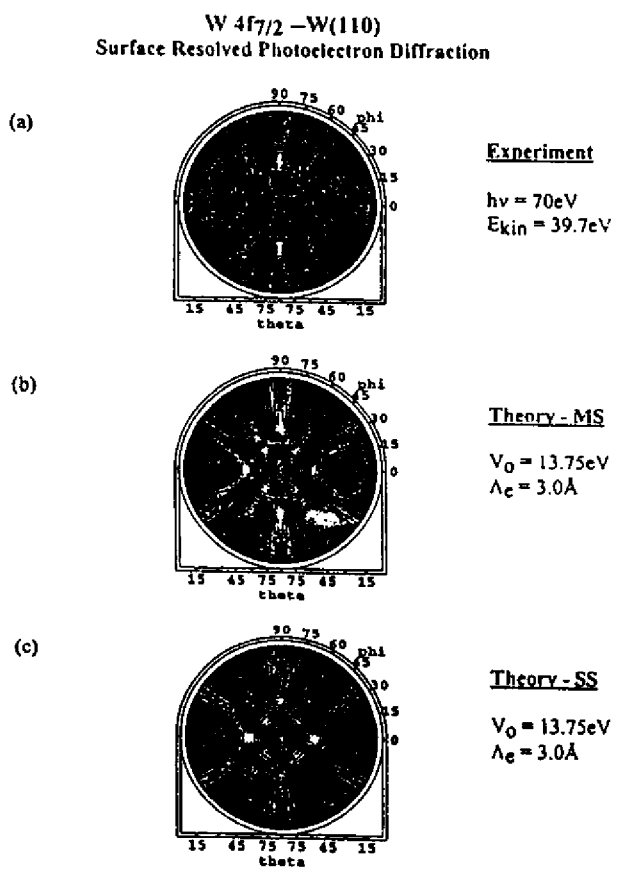

Fig. 6. Full-solid-angle diffraction from the surface atoms of W(110): (a) experimental data; (b) multiple scattering theory; (c) single scattering theory. (From Ref. [25].)

13.75 eV and 3.0–4.0 Å so derived are in excellent agreement with independent determinations from band structure and other theoretical calculations. Moreover, the MS calculations are in excellent agreement with experiment for all the major diffraction features, thus showing that existing PD theory is capable of an accurate description of such data even at such low kinetic energies. The SS calculations based on the same input parameters show similar diffraction features, but clearly do not describe the data as well as the MS results; thus MS effects will definitely need to be included for a quantitative description of such low-energy data.

3.2. Photoelectron diffraction from interface atoms

The detailed structure of interfaces, e.g. between an epitaxial overlayer and the substrate on which it is grown, is clearly one of the most important current surface-structure problems. It is also a difficult problem to solve, because most surface structure probes either cannot uniquely resolve interface atoms from their neighbors or cannot probe very deeply below the surface. PD with high energy resolution has been shown to be capable of studying interface atoms that are at least a few atomic layers below the surface [8d], and future experimental capabilities promise to expand this application dramatically.

As one illustration of what is possible, we show in Fig. 7 results obtained with the system in Figs. 1 and 2 for the case of 1.2 ML of Gd deposited on W(110) [26]. It has been shown by Tober et al. [27] in a combined STM and LEED study that this first monolayer forms a lateral superstructure or Moiré pattern with (7 × 14) periodicity in which a hexagonal Gd(0001) layer is formed on the surface with relatively little lattice constant change compared to bulk Gd. However, this layer is only weakly bound to the underlying W, and many types of Gd–W bonding sites are involved over the (7 × 14) unit cell. Fig. 7(b) shows that it is nonetheless possible to clearly resolve the interface W atoms via the 4f spectrum, and that these interface atoms exhibit a binding energy that is even lower than that for the clean W surface. A likely reason for this lowering of binding energy is the additional core-hole screening possible in the Gd monolayer, which has only a very weak bonding interaction with the substrate. It has also been possible to measure the separate PD patterns for the bulk and interface W peaks in this system, and they are compared in Fig. 7(c), (d) with the corresponding patterns for the clean surface. Because there are many scattering geometries between either an interface W atom or a bulk W atom and the overlying Gd atoms, it is not surprising that the interface diffraction curve is very much like the surface diffraction curve, and that the two bulk curves are also very similar. Overall the Gd scattering here acts to simply produce a nearly uniform background of intensity underneath the dominant pattern associated with W-atom scattering. However, for other kinds of metal–metal epitaxy such as pseudomorphic growth in registry with the substrate, the overlayer would be expected to produce more dramatic changes in the diffraction. Future applications of high-resolution interface PD to metal–metal, metal–semiconductor, and oxide semiconductor overlayer growth are thus very promising.

3.3. Time-dependent measurements

As one illustration of how rapidly it should be possible to take PD data in the future, we show in Fig. 8(a), (b) two lower-resolution spectra from W(110) that were the beginning and end points of a rapid accumulation of over 180 spectra taken in a 70 min time interval. Each spectrum was obtained in only about 4 s. The initially nearly clean surface was exposed to about 6×10^{-10} Torr of O_2 above a 2×10^{-10} Torr base pressure over this time, and the surface peak thus slowly decreased in intensity and shifted toward the bulk peak in energy (an effect that has been seen before [24a]), while a weak oxide peak grew in at about 0.35 eV higher binding energy than the bulk peak. The curves in Fig. 8(c) illustrate the time dependence of the surface and oxide intensities and the surface peak position (which becomes more uncertain as its intensity dies away). These data thus clearly indicate the potential for kinetics studies in which intensities are measured at several key energies or directions as a function of time, thus yielding time-resolved PD. With further optimization of the beamline and end station on which these data were obtained, and/or carrying out the same type of measurement on a more intense third-generation undulator beamline, we estimate that it should be possible to improve these data acquisition speeds by at least one order of magnitude, if not two.

4. Circular dichroism in photoelectron angular distributions

Circular dichroism in photoelectron angular distribution (often termed CDAD) was first

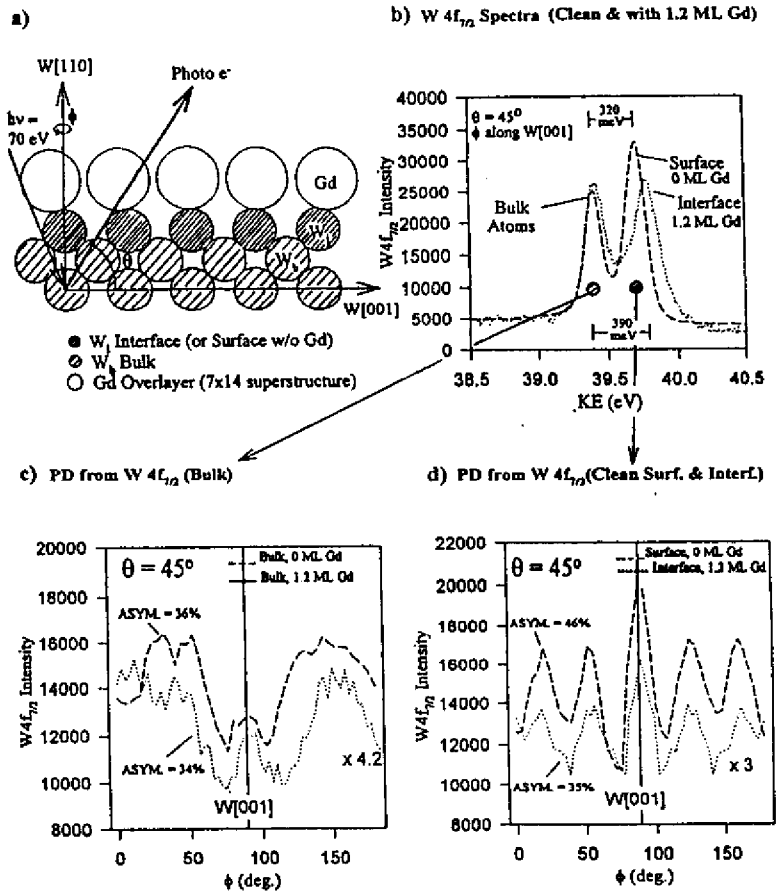

Fig. 7. Photoelectron diffraction from interface W atoms below one monolayer of Gd on W(110): (a) the experimental geometry; (b) comparison of W4f$_{7/2}$ spectra for clean W(110) and 1.2 ML of Gd on W(110) at a takeoff angle of 45° with respect to the surface; (c), (d) azimuthal photoelectron diffraction data at a takeoff angle of 45° for both the clean W(110) and 1 ML Gd/W(110). In (c), the bulk diffraction is compared for the two cases, and in (d) the surface-atom and interface-atom diffraction is compared for the two cases. (From Ref. [26].)

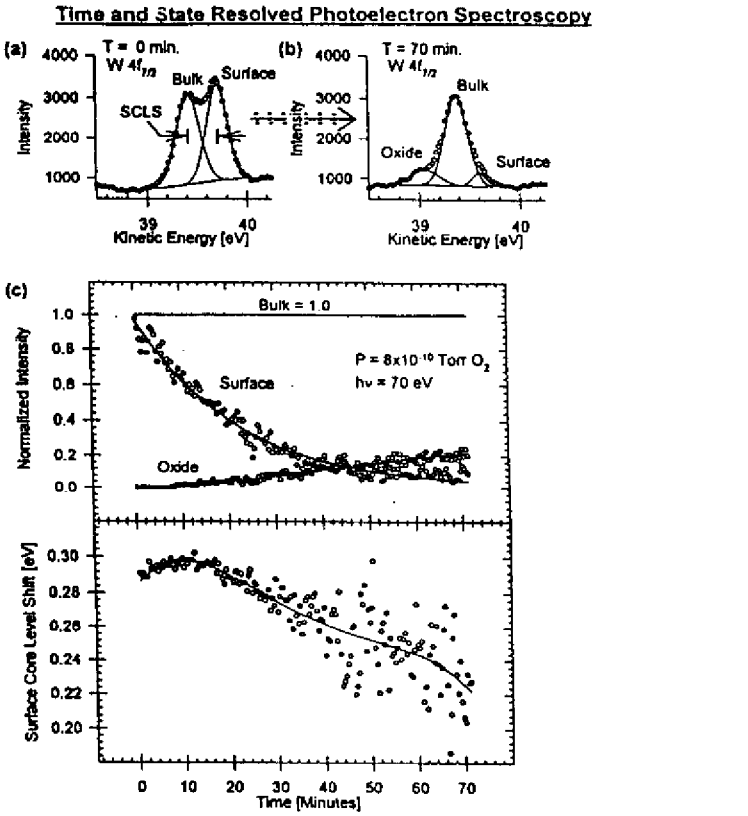

Fig. 8. Time and state resolved photoelectron spectra for a clean W(110) surface exposed to oxygen: (a) clean surface W4f$_{7/2}$ spectrum at start of scans ($T = 0$); (b) surface after 70 min, with depleted surface peak and "oxide" peak associated with adsorbed oxygen, (c) time dependence of surface and "oxide" intensities, together with surface core level shift. (From Ref. [25].)

observed for emission from a core level for the case of an adsorbed molecule on a surface (C1s emission from CO/Pd(111)) by Schönhense and co-workers [28]. This dichroism, or difference between the intensities with left and right circularly polarized light (I^{RCP} and I^{LCP}, respectively), is most conveniently measured via a normalized asymmetry that is defined as

$$A_{CDAD} = \frac{[I^{RCP}(\hat{k}) - I^{LCP}(\hat{k})]}{[I^{RCP}(\hat{k}) + I^{LCP}(\hat{k})]} \quad (1)$$

where $\hat{k}$ is the direction of electron emission. Changes in this asymmetry with direction by as much as ±75% were observed for CO/Pd. These measurements thus made it clear that even a non-chiral molecule can exhibit circular dichroism when

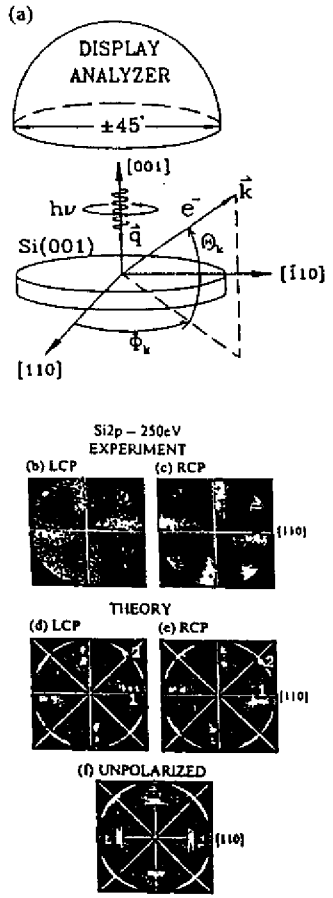

Fig. 9. Circular dichroism in the angular distributions of photoelectrons from Si(001): (a) the experimental geometry, with radiation incident normal to the surface and a display analyzer being used to simultaneously detect electrons over a ±45° cone; (b), (c) experimental Si2p intensity distributions at a kinetic energy of 250 eV and with left-circularly polarized (LCP) and right-circularly polarized (RCP) excitation, respectively; (d), (e) as (b), (c), but multiple scattering photoelectron diffraction theory; (f) analogous multiple scattering theory for excitation with unpolarized radiation. (From Refs. [30] and [31].)

it is fixed to a surface, provided that a certain geometrical condition is satisfied between the molecular axis $\hat{n}$, the light incidence direction $\hat{q}$, and $\hat{k}$: in particular A_{CDAD} can be non-zero whenever these three vectors are not co-planar. Such data were first interpreted using quantum-chemical theoretical methods for the isolated adsorbate molecule [29a]. However, the chirality must be associated with the final-state photoelectron wave function, because the initial core state is spherically symmetrical. This suggests using a PD point of view to interpret such results, as has been done more recently [29b]. In this picture, all information on the chirality is carried in the geometry of the light incidence, the locations of all scatterers around the emitter, and the direction of electron emission. This approach thus permits easy inclusion of contributions to the dichroism from atoms in the substrate. PD calculations were in fact also found to correctly predict the effects seen for CO/Pd(111) [29b].

More generally, it has now been realized that the emission from *any* core level in a single crystal specimen can exhibit non-zero CDAD effects, provided that the plane containing $\hat{q}$ and $\hat{k}$ does not also coincide with a plane of mirror symmetry perpendicular to the surface [30,31]. In particular, intensity distribution measurements for Si2s and Si2p emission from a Si(001) surface in a geometry with the light incident along the normal (see geometry in Fig. 9(a)) have shown that there are not only very strong CDAD effects of as high as about ±20%, but that the observed diffraction patterns exhibit what can in a first approximation be described as peak "rotations" across mirror planes. Some of these experimental data are shown in Fig. 9(b), (c), where all the main diffraction peaks clearly appear to move counterclockwise with LCP excitation, and clockwise with RCP excitation. Also shown in Fig. 9(d), (e) are corresponding diffraction patterns calculated from MS PD theory, and the agreement with the observed effects is excellent for both peaks of types "1" and "2" that can be seen in both experiment and theory. For reference, the theoretical pattern with unpolarized excitation (for which I^{UNP} can rigorously be shown to equal simply $I^{RCP} + I^{LCP}$ [31]) is shown in Fig. 9(f). Exciting with circularly polarized

radiation thus yields one or the other of the two components present in the unpolarized diffraction pattern, with unpolarized radiation producing broader features that are the sum of the two.

Considerable physical insight into the origin of the peak rotations seen in Fig. 9 can also be gained via an approximate model first introduced by Daimon et al. [30]. This notes that, for emission from a given $n_i l_i m_i$ state, the dipole selection rules for circularly-polarized radiation $\Delta m^{RCP} = m_f - m_i = -1$, and $\Delta m^{LCP} = m_f - m_i = +1$, coupled with the angular and radial integrations involved in calculating the photoelectric cross section, lead to a dominance in the final-state photoelectron wave of the spherical harmonics $l_f = l_i + 1$, $m_f = m_{f,min/max} = \mp(l_i + 1)$, respectively. These spherical harmonics then have an azimuthal dependence of $\exp(im_f\phi)$ which yields spiral, rather than cylindrical, constant-phase surfaces. Because photoelectron current will propagate perpendicular to such constant-phase planes, these two dominant components, which have spirals of opposite sense, will "rotate" any diffraction feature (for example, a forward scattering peak) in opposite directions. For circularly-polarized radiation incident perpendicular to a surface, a simple formula even results for these azimuthal rotations $\Delta\phi_{m_f}$

$$\Delta\phi_{m_f} = \frac{m_f}{R_\parallel k_\parallel} \qquad (2)$$

where $R_\parallel$ is the component of the nearest-neighbor distance along some forward scattering direction along the surface, and $k_\parallel$ is the component of the photoelectron wave vector along the surface. This simple formula is in fact very successful in predicting the peak rotations seen in Fig. 9(b), (c), as indicated by the black crosses. It is not however, expected to be fully quantitative for emission directions too far from the surface plane, nor for cases where there is significant mixing of different l_f, m_f components in the final state.

More recent data obtained with the system of Figs. 1 and 2 confirm the generality of such peak rotations, but also more quantitatively show the additional peak distortions that can occur in changing from LCP to RCP [32]. The case studied was a (1 × 1) oxide overlayer on W(110), prepared in a manner described previously [33]. The experimental geometry was very similar to that of the Si(001) experiment, as shown in Fig. 10(a). The W4f spectra for this surface shown in Fig. 10(b) are clearly split into oxide and bulk components, with a separation between them of about 0.70 eV. In Fig. 10(c), we show single azimuthal scans of the bulk and oxide peaks for a takeoff angle θ with respect to the surface of 26.5°, with excitation by linearly-polarized light (LP), and LCP and RCP light. The correct mirror symmetry across the [001] azimuth at 90° is seen in both bulk and oxide for LP excitation, but peak rotations and considerable distortions, are seen with LCP and RCP excitation. The overall diffraction patterns furthermore obey the symmetry expected from the normal-incidence experimental geometry, because the mirror image of the LCP intensities for both oxide and bulk are essentially identical to the RCP intensities. These symmetries and rotations are even more clearly seen in the oxide/bulk ratios of Fig. 10(d), in which various sources of absolute experimental intensity drift with time (and thus angle) are eliminated: in particular, a ±6° rotation is seen here between LCP and RCP. MS PD calculations furthermore well predict both the overall rotations of features and the peak distortions seen here [32].

Thus, such circular dichroism in photoelectron angular distributions is expected to be a very general phenomenon for any non-magnetic (or by implication also magnetic) system, and it can also be quantitatively described by PD theory. One reason for being interested in this effect is that circular dichroism in magnetic systems (magnetic circular dichroism or MCD) is usually a much more subtle difference in intensities that may be only a few percent in magnitude [34]. MCD effects in photoelectron angular distributions are due to a combination of the spin–orbit and multiplet splittings inherent in core spectra [34a] and possible spin-dependent exchange scattering from magnetic atoms during photoelectron escape from the surface. By contrast, the CDAD effects discussed in this section are due to the strong coulomb-plus-exchange scattering from every atom in the speci-

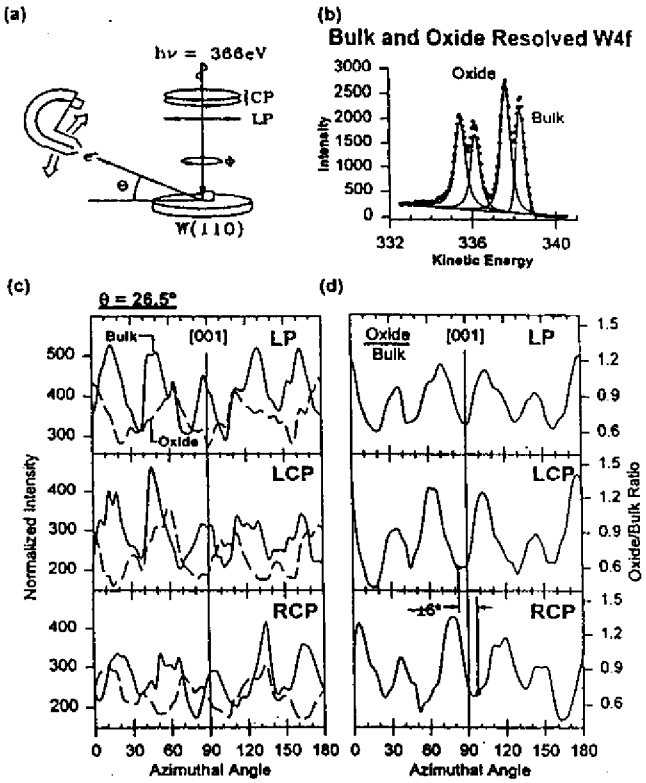

Fig. 10. Circular dichroism in the angular distributions of photoelectrons from (1 × 1) O/W(110) with a (1 × 12) oxide superstructure: (a) the experimental geometry, with radiation incident normal to the surface and the rotating analyzer of Figs. 3 and 4 being used to measure at various takeoff angles θ; (b) a W4f spectrum with oxide and bulk peaks resolved; (c) azimuthal scans at a takeoff angle of 26.5° for both bulk and oxide W4f components for linearly-polarized (LP) light, LCP light, and RCP light; (d) the oxide/bulk ratio over the same azimuthal scan, again for LP, LCP, and RCP excitation. (From Ref. [32].)

men. Thus, properly allowing for the latter will be essential to accurately measuring the former [29].

We also note that the interplay between strong non-magnetic scattering and diffraction effects and weaker magnetic dichroism effects will no doubt also exist in the more recently discovered magnetic linear dichroism (MLD) [35a, b] and magnetic unpolarized dichrosim (MUD) [35c–e], both of which effects manifest themselves in core-photoelectron angular distributions.

We now address the more subtle spin-dependent scattering effects in more detail.

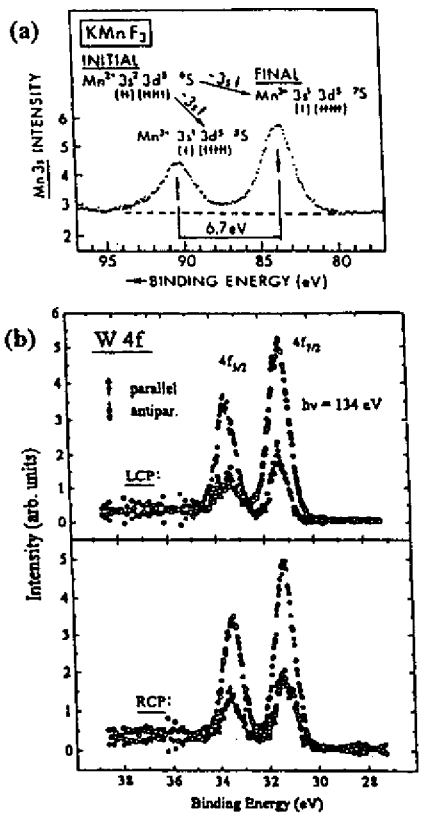

Fig. 11. Spin-polarized core photoelectron spectra: (a) a Mn3s spectrum from $KMnF_3$, with the electronic states and spin polarizations relative to the emitting Mn^{2+} ion indicated (from Ref. [9c]; (b) a W4f spectrum from W(110), excited by LCP light (top panel) and by RCP light (bottom panel). In (b), the spin-resolved intensities as measured parallel or antiparallel to the light incidence direction q are indicated. (From Ref. [39].)

5. Spin-polarized photoelectron diffraction and holography

5.1. Multiplet splittings and spin-polarized photoelectron diffraction

We have already noted that being able to separately measure intensity distributions for spin-up and spin-down photoelectrons should in principle make it possible to determine the short-range magnetic order around a given type of emitter via what can be called spin-polarized photoelectron diffraction (SPPD). The use of multiplet splittings for this purpose is by now well-established for both simple antiferromagnets [9] and ferromagnetic metals [36], and we show in Fig. 11(a) an exchange-split 3s spectrum from antiferromagnetic $KMnF_3$ (100) that is one of the few cases studied to date by SPPD. The predominant spin polarizations of the two components are indicated in this figure, together with the overall electron configurations and L–S multiplets associated with each peak: the ^5S peak at lower kinetic energy is expected to be 100% up-spin and the ^7S peak 71% down-spin; spin polarizations are here measured with respect to the emitting Mn^{2+} ion. In Fig. 12, some experimental [9c, d] and theoretical [37] results related to SPPD from the similar antiferromagnetic system MnO(001) are presented. Plotted in Fig. 12(a) is the temperature dependence of the spin asymmetry S, a normalized spin-up/spin-down intensity ratio that is defined to go to zero at the high-temperature (HT) "paramagnetic" limit of the experimental data via $S(T) = 100[R_T - R_{HT}]$ (in %) [9b–e]. Here $R = I_\uparrow/I_\downarrow$, and the subscripts indicate the temperature at which the ratio was measured. For a low average kinetic energy of 111 eV, this asymmetry shows dramatic changes at about 4.5 times the bulk Néel temperature, with the sense of this change being opposite for two different directions of observation. For a high kinetic energy of 1405 eV for which exchange scattering effects are expected to be negligibly small, no such effect is observed. These experimental results are in qualitative agreement with PD calculations assuming that there is an abrupt loss of short-range antiferromagnetic order at this high temperature, even

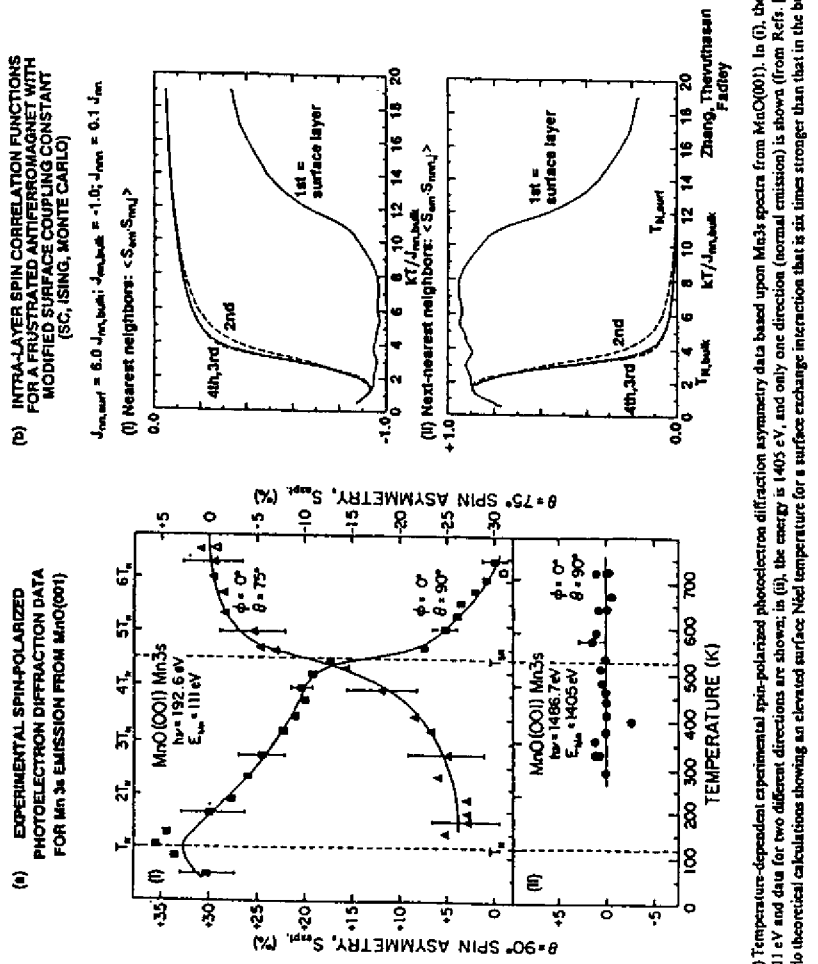

Fig. 12. (a) Temperature-dependent experimental spin-polarized photoelectron diffraction asymmetry data based upon Mn3s spectra from MnO(001). In (i), the electron energy is 111 eV and data for two different directions are shown; in (ii), the energy is 1405 eV, and only one direction (normal emission) is shown (from Refs. [9c,d]). (b) Monte Carlo theoretical calculations showing an elevated surface Néel temperature for a surface exchange interaction that is six times stronger than that in the bulk (from Ref. [37]).

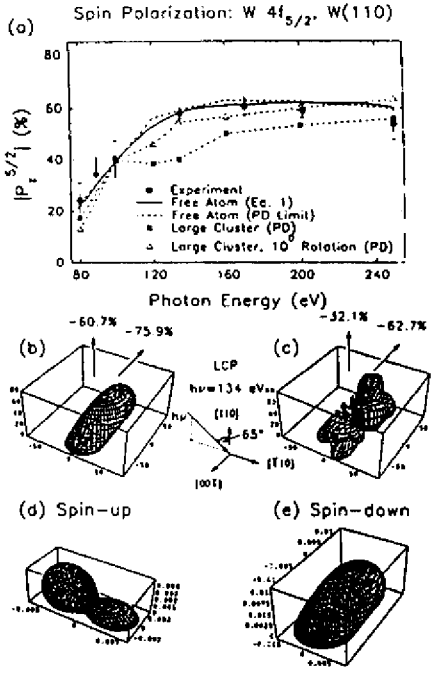

Fig. 13. Spin-polarization in W4f spectra excited by circularly-polarized light from W(110): (a) the absolute value of the $4f_{5/2}$ polarization as a function of photon energy, with experiment compared to both free-atom and MS cluster PD calculations; (b) the three-dimensional spin polarization for a free atom in the geometry shown in the inset and with an excitation energy of 134 eV; (c) as 9b), but for a MS cluster PD calculation in a five-atom cluster (an emitter below four surface scatterers); (d), (e) the separate spin-up and spin-down intensities excited in a free-atom. (From Ref. [39].)

though the bulk long-range order is lost at the much lower Néel temperature [9d]. One possible explanation for this effect is that there are local domains of short-range order that persist up to this higher temperature and then abruptly disappear. Another recently discussed possibility is that the surface Néel temperature could be significantly higher than that in the bulk [37]. Fig. 12(b) shows the results of Monte Carlo calculations for a simple-cubic Ising antiferromagnet of Mn^{2+} ions in which the surface exchange coupling between Mn^{2+} spins has been set to be 6.0 times that in the bulk. For this simple model, it is seen that the spin–spin correlation functions for both nearest neighbor Mn^{2+} ions and next neighbor Mn^{2+} ions show a relatively sharp transition in the surface layer (here indicated as the first layer) at a temperature that is a few times the transition temperature for the rest of the layers (i.e. the bulk in this model). Thus, it is also possible that these SPPD experiments have detected a highly elevated surface Néel temperature for this system. Although further experiments and theory will be necessary to fully clarify the nature of these observations, this work and other prior studies [9] indicates the potential of SPPD for studying short-range magnetic order. Exploiting this potential should be assisted enormously by the use of next-generation synchrotron radiation facilities.

5.2. Spin polarization from circular-polarized excitation

Spin-polarized photoelectrons can also be produced by exciting a spin–orbit-split core level, making use of the well known Fano effect from atomic physics [38]. We illustrate this with some very recent data obtained by Starke et al. for the non-magnetic system W(110) [39]. Fig. 11(b) shows spin-resolved W4f spectra in which the spin polarizations are here measured externally along the direction of light incidence, and the light has been changed from RCP to LCP. The experimental geometry is indicated in the inset of Fig. 13(b). There is a clear and strong spin polarization in both the 5/2 and 7/2 components, with the expected change of sign as the polarization of the light is changed. In Fig. 13(a), we show the absolute value of the spin polarization of the $W4f_{5/2}$ peak excited with circularly-polarized radiation, as a function of photon energy. Over the range from about 130 eV to 250 eV, the experimental polarization is very large and about 50–60%. The 7/2 peak is found to have the opposite sign of polarization to the 5/2 peak for RCP or LCP excitation, and a magnitude only 3/4 as large (the inverse ratio of subshell occupation numbers), as expected from

simple atomic considerations [39]. These polarizations are thus comparable to the 70–100% expected for simple 3s multiplets of the type discussed previously, and immediately suggest using such spectra as internal sources of spin-polarized photoelectrons for SPPD studies. Such SPPD studies based on circularly-polarized excitation have in fact been attempted for the first time recently [40]. Theoretical curves for the energy dependence of the 5/2 spin polarization are also shown in Fig. 13(a). Simple free-atom calculations based on the work of Cherepkov [41] agree very well with experiment, but with some deviations at lower and higher energies. PD calculations with only one emitter and no scatterers present (i.e. the free-atom limit of the algorithm) agree with the analytical free-atom results, an important self-consistency check. MS PD calculations from a large W(110) cluster in the nominal geometry of the experiment show the same general trend of polarization variation with energy as experiment, but have a significant dip at about 125 eV that is not seen in experiment. However, a small azimuthal rotation of the cluster by 10° that is within the experimental uncertainty of alignment suppresses this dip, and also yields excellent agreement with experiment. The change in the PD polarizations with cluster orientation, however, suggests that photoelectron scattering, even in a non-magnetic lattice, can significantly alter the degree of spin polarization in a core spectrum. To explore this effect further, we show in Fig. 13(b), (c) the full three-dimensional contours of the absolute value of the W4$f_{5/2}$ spin polarization, as plotted relative to the origin of the coordinate system. In Fig. 13(b) is shown the contour for a free atom, tilted toward the upper right due to the light incidence direction, as shown in the inset geometry. This is a smooth curve, with basically a donut shape and overall negative polarization. Fig. 13(c) shows the same kind of contour for a W emitter beneath four W scatterers: a five-atom cluster in the W(110) geometry. It is here obvious that scattering and diffraction effects cause a strong modulation of the spin polarization with direction, with one manifestation of this being the dip seen at 125 eV in Fig. 13(a). The origin of these dramatic changes is that the separate spin-up and spin-down intensity distributions excited from the 5/2 level have very different shapes, as shown in the plots of Fig. 13(d), (e), and they thus sample differently the non-magnetic scatterers around the emitting atom. Such effects should be very general, very strong, and occur in both non-magnetic and magnetic surroundings.

5.3. Spin-polarized photoelectron holography

Finally, we turn to another intriguing prospect for the future of spin-resolved photoelectron diffraction studies: the possibility of directly imaging the spins around a given emitter via holographic inversion methods. So-called "direct methods" for deriving three-dimensional atomic structures have been discussed in two other papers in this volume by Schaff et al. [6b] and by Terminello et al. [16e], and we thus introduce them here only briefly, to be able to discuss adding a spin-dependent aspect. All direct methods involve carrying out some kind of mathematical operation that is closely akin to a Fourier transform on a large set of data involving perhaps 1500–4000 distinct intensity measurements. In general, the photoelectron intensity $I(k)$ for a certain wave vector k is converted to a normalized χ function in a standard way via

$$\chi(k) = \frac{I(k) - I_0(k)}{I_0(k)} \quad \text{or} \quad \frac{I(k) - I_0(k)}{I_0(k)^{1/2}} \qquad (3)$$

where $I_0(k)$ is the intensity in the absence of any scatterers. Measurements of $\chi(k)$ are made at several directions of emission (several $\hat{k}$), and also perhaps at several energies of excitation (several $|k|$). The most common way to holographically invert such a $\chi(k)$ data set is to carry out the following transform over the relevant volume in k-space [12d,14a,b]

$$U(r) = \left| \int_{|k|} \exp(-i|k||r|) \iint_{\hat{k}} \times \exp(ik \cdot r)\chi(k)|k|^2 \, d|k| \sin\theta_k \, d\theta_k \, d\phi_k \right| \qquad (4)$$

where θ_k and ϕ_k are the angles defining the direction $\hat{k}$. Several prior studies have obtained successful three-dimensional images of near-neighbor

atoms using this approach or close relatives of it [12–19], and it seems clear that, at least for back scattering atoms around a given emitter, very useful structural conclusions can be drawn. These images include some obtained with only one energy (e.g. Refs. [13,15a,b,d,16]) and others in which the transform of Eq. (4) is modified to allow for non-ideal scattering effects and/or to somehow focus on the region of image space that is most nearly ideal (e.g. Refs. [13,14,15,17b,18,19]).

We have already noted that two core photoelectron peaks can often be found at relatively close-lying energies that are strongly spin-polarized in an opposite sense. This might be due to a core multiplet splitting or a spin–orbit doublet excited with circular polarization, or some mixture of these two effects. Thus, it is in principle possible to separately measure $\chi_\uparrow$ and $\chi_\downarrow$ for the two different spin orientations, and this could lead via spin-dependent scattering effects to the holographic imaging of the local magnetic order around a given type of emitter [42]. There are two obvious spin-sensitive imaging algorithms based on Eq. (4) and $\chi_\uparrow$ and $\chi_\downarrow$ [42b]

$$\Delta(r) = U_\uparrow(r) - U_\downarrow(r) \qquad (5)$$

with obvious notation, and

$$\Delta'(r) = \left| \int_{|k|} \exp(-i|k||r|) \iint_{\hat{k}} \exp(ik \cdot r)[\chi_\uparrow(k) - \chi_\downarrow(k)]|k|^2 \, d|k| \sin\theta_k \, d\theta_k \, d\phi_k \right| \qquad (6)$$

which is simply the image $U(r)$ calculated only on the difference of the spin-up and spin-down χ values. Additional vector-based spin-sensitive holographic imaging functions have also been proposed [42a].

As a brief indication of the potential of this kind of photoelectron holography, we show in Fig. 14 holographic inversions of multiple scattering calculations for emission of spin-up and spin-down electrons from Mn^{2+} ions in a small planar cluster representing a portion of the MnO(001) surface [42c]. The cluster is shown in Fig. 14(a). Spin-up Mn^{2+} scatterers in this cluster have been distinguished from spin-down scatterers by having an additional exchange potential due to five unpaired 3d electrons that interacts only with spin-up photoelectrons. Spin-down scatterers have the same 3d exchange potential, but it interacts only with spin-down photoelectrons. Thus, the potential is slightly more attractive when the photoelectron spin is parallel to that of the scatterer. Spin-up and spin-down holograms were calculated in a fully-converged MS way for 10 energies between 127 eV and 278 eV, and holographic images then derived via Eqs. (4)–(6). The normal images U in the plane of the cluster for spin-up and spin-down electrons are shown in Fig. 14(b), (c) together with the corresponding spin-sensitive images $\Delta(r)$ nd $\Delta'(r)$ in Fig. 14(d), (e). The normal images show features for all of the atoms in the cluster, including the four non-magnetic O atoms. These spin-up and spin-down images are also very similar, as expected because the 3d exchange scattering is only 5–15% of the total effective scattering potential at these energies. By contrast, neither $\Delta(r)$ nor $\Delta'(r)$ contains any image intensity for the O atoms, verifying that either of these choices of imaging algorithm is predominantly sensitive to only the magnetic scatterers. The peaks and valleys in the spin-sensitive images are in general about 7–9% as strong in transform amplitude as the normal images, suggesting the experimental possibility of carrying out such imaging, albeit a non-trivial exercise. $\Delta(r)$ and $\Delta'(r)$ are also inherently different in that $\Delta(r)$ images both orientations of scatterers in the same way, due the absolute value in Eq. (6), while $\Delta'(r)$ changes sign when the scatterer is flipped, and thus also is sensitive to the orientation of a given scatterer. $\Delta'(r)$ also involves the phase of the scattering factor, and thus can show sign changes over the region of a magnetic scatterer; however, it is clear from this and other calculations that the sign changes are exactly reversed if the orientation of the scatterer spin is flipped from up to down.

Thus, spin-polarized photoelectron holography represents an intriguing and challenging experimental possibility for the future, but one well matched to the new synchrotron radiation sources that are now becoming available.

6. Concluding remarks

Photoelectron diffraction is thus in some respects

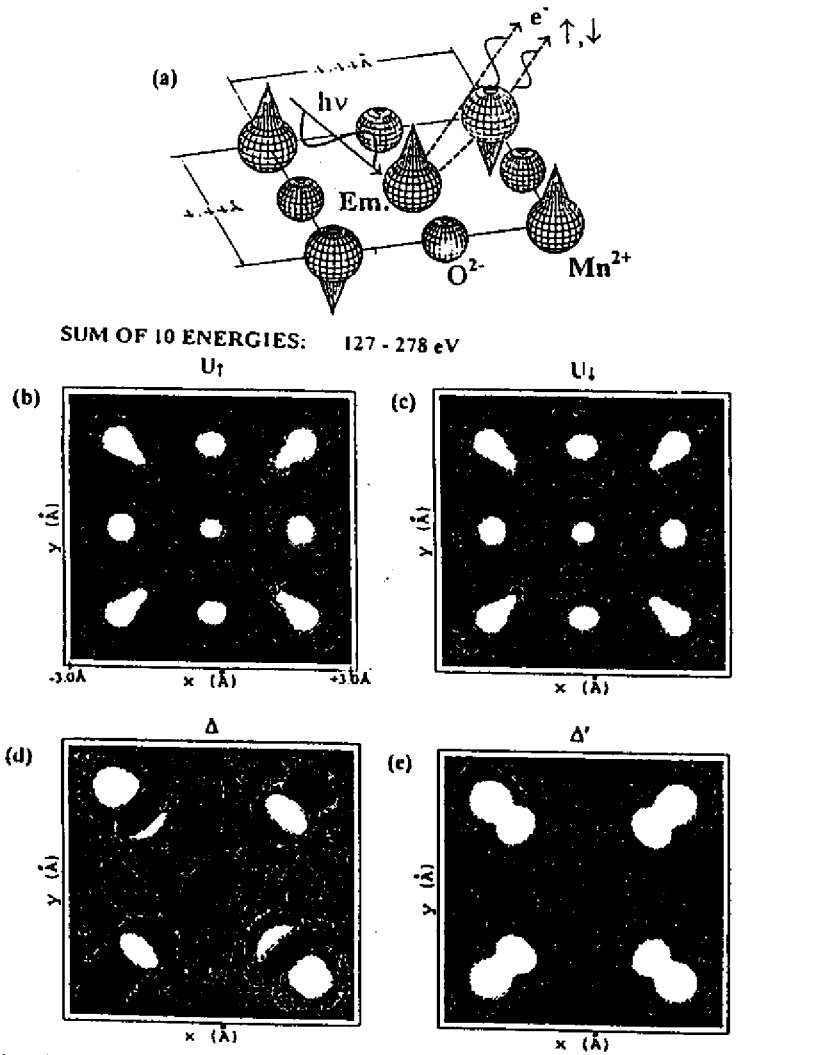

Fig. 14. A theoretical simulation of spin-polarized photoelectron holography: (a) a nine-atom cluster representing the (001) surface of MnO, with an emitter in its center; (b), (c) normal holographic images $U(r)$ generated by using Eq. (4) for ten energies between 127 and 278 eV; (d) the spin-sensitive holographic image $\Delta(r)$ generated by using Eq. (5); (e) the spin-sensitive holographic image $\Delta'(r)$ generated by using Eq. (6). (From Ref. [42b].)

a mature field, but at the same time one in which several exciting new possibilities for surface and magnetic structure studies are found. The simple extension to taking full-solid-angle data often permits much clearer conclusions regarding structures, especially when high energies with forward scattering are present, and complementary structure probes such as LEED and STM are used in situ with it. Next-generation instrumentation, particularly at third-generation synchrotron radiation sources, will much expand the use of state-resolved photoelectron diffraction, including the resolution of surface atoms and atoms at buried interfaces, time-dependent structural studies, and different types of dichroism in both non-magnetic and magnetic systems. The use of circularly-polarized radiation for excitation shows up new phenomena in diffraction peak rotations and distortions, and makes it possible to excite spin-polarized photoelectrons from any spin–orbit split level. Spin-polarized photoelectron diffraction and its more difficult cousin spin-polarized photoelectron holography also promise to provide information on local magnetic order in an element-specific, and also a site-specific, way.

Acknowledgments

We are grateful to R.X. Ynzunza and E.D. Tober for assistance with preparing some of the figures in this paper. We also thank our various co-workers who have contributed greatly to the equipment fabrication and the several specific studies presented here: R. Couch, C. Cummings, H. Daimon, K. Higashiyama, W.R.A. Huff, P.D. Johnson, S.A. Kellar, Y.J. Kim, T. Lauritzen, P. Len, G. Miner, E.J. Moler, J. Palomares, S. Ryce, S. Ruebush, W. Schattke, D.A. Shirley, K. Starke, S. Thevuthasan, E.D. Tober, Z. Wang, C. Westphal, R. Wright, H. Xiao, R.X. Ynzunza, and F. Zhang. This work has been supported by the Director, U.S. Department of Energy, Office of Basic Energy Sciences, Division of Materials Sciences under Contract DOE-AC03-76SF00098 and the U.S. Office of Naval Research under Contract No. N00014-94-0162.

References

[1] (a) K. Siegbahn, U. Gelius, H. Siegbahn and E. Olsen, Phys. Lett. A, 32 (1970) 221.
(b) C.S. Fadley and S.A.L. Bergstrom, Phys. Lett. A, 35 (1971) 375.
(c) A. Liebsch, Phys. Rev. Lett., 32 (1974) 1203; Phys. Rev. B, 13 (1976) 544.
(d) S. Kono, C.S. Fadley, N.F.T. Hall and Z. Hussain, Phys. Rev. Lett., 41 (1978) 117.
(e) D.P. Woodruff, D. Norman, B.W. Holland, N.V. Smith, H.H. Farrell and M.M. Traum, Phys. Rev. Lett., 41 (1978) 1130.
(f) S.D. Kevan, D.H. Rosenblatt, D. Denley, B.-C. Lu and D.A. Shirley, Phys. Rev. Lett., 41 (1978) 1565.
(g) S. Kono, S.M. Goldberg, N.F.T. Hall and C.S. Fadley, Phys. Rev. Lett., 41 (1978) 1831.
[2] (a) C.S. Fadley, Phys. Scr. T, 17 (1987) 39.
(b) C.S. Fadley, in R.Z. Bachrach (Ed.), Synchrotron Radiation Research: Advances in Surface Science, Plenum Press, New York, 1993.
(c) C.S. Fadley, Surf. Sci. Rep., 19 (1993) 231.
(d) C.S. Fadley, S. Thevuthasan, A.P. Kaduwela, C. Westphal, Y.J. Kim, R. Ynzunza, P. Len, E. Tober, F. Zhang, Z. Wang, S. Ruebush, A. Budge and M.A. Van Hove, J. Electron Spectrosc. Relat. Phenom., 68 (1994) 19.
(e) C.S. Fadley, in X. Xide, S.Y. Tong and M.A. Van Hove (Eds.), The Structure of Surfaces IV, World Scientific, Singapore, 1994b, pp. 1–28.
[3] (a) S.A. Chambers, Adv. Phys., 40 (1990) 357; Surf. Sci. Rep., 16 (1992) 261.
(b) W.F. Egelhoff, Jr., Crit. Rev. Solid State Mater. Sci., 16 (1990) 213.
[4] (a) L.J. Terminello, X.S. Zhang, Z.Q. Huang, S. Kim, A.E. Schach von Wittenau, K.T. Leung and D.A. Shirley, Phys. Rev. B, 38 (1988) 3879.
(b) L.-Q. Wang, Z. Hussain, Z.Q. Huang, A.E. Sachach von Wittenau, D.A. Shirley and D.W. Lindle, Phys. Rev. B, 44 (1991) 13771.
(c) D.A. Shirley, Y. Zhang, B.L. Petersen, Z. Hussain, W.A. Huff, J.J. Barton and L.J. Terminello, J. Electron Spectrosc. Relat. Phenom., 68 (1994) 49.
[5] H.P. Bonzel, Prog. Surf. Sci., 42 (1993) 219.
[6] (a) A.M. Bradshaw and D.P. Woodruff, in W. Eberhardt (Ed.), Applications of Synchrotron Radiation: High-Resolution Studies of Molecules and Molecular Adsorbates on Surfaces, Springer-Verlag, Berlin, 1993.
(b) O. Schaff, G. Hess, V. Fernandez, K.-M. Schindler, A. Theobald, Ph. Hofmann, A.M. Bradshaw, V. Fritzsche, R. Davis and D.P. Woodruff, J. Electron Spectrosc. Relat. Phenom., 75 (1995) 117.
[7] J. Osterwalder, P. Aebi, R. Fasel, D. Naumovic, P. Schwaller, T. Treutz, L. Schlapbach, T. Abukawa and S. Kono, Surf. Sci., 331–333 (1995) 1002.
[8] (a) D. Sebilleau, M.C. Desjonqueres, D. Chaveau, C. Guillot, J. Lecante, G. Treglia and D. Spanjaard, Surf. Sci. Lett., 185 (1987) L527.

(b) A. Nilsson, H. Tillborg and N. Mårtensson, Phys. Rev. Lett., 67 (1991) 1015.
(c). K.U. Weiss, R. Doppel, K.M. Schindler, P. Gardner, V. Fritsche, A.M. Bradshaw, A.L.D. Kilcoyne and D.P. Woodruff, Phys. Rev. Lett., 69 (1992) 3196.
(d) J.D. Denlinger, E. Rotenberg, U. Hessinger, M. Leskovar and M.A. Olmstead, Appl. Phys. Lett., 62 (1993) 2057; E. Rotenberg, J.D. Denlinger, U. Hessinger, M. Leskovar and M.A. Olmstead, J. Vac. Sci. Technol. B, 11 (1993) 1444.
[9] (a) B. Sinkovic and C.S. Fadley, Phys. Rev. B, 31 (1985) 4665.
(b) B. Sinkovic, B.D. Hermsmeier and C.S. Fadley, Phys. Rev. Lett., 55 (1985) 1227.
(c) B.D. Hermsmeier, J. Osterwalder, D.J. Friedman and C.S. Fadley, Phys. Rev. Lett., 62 (1989) 478.
(d) B.D. Hermsmeier, J. Osterwalder, D.J. Friedman, B. Sinkovic, T.T. Tran and C.S. Fadley, Phys. Rev. B, 42 (1990) 11895.
(e) B. Sinkovic, D.J. Friedman and C.S. Fadley, J. Magn. Magn. Mater., 92 (1991) 301.
[10] (a) C.H. Li and S.Y. Tong, Phys. Rev. Lett., 42 (1979) 901.
(b) J.J. Barton and D.A. Shirley, Phys. Rev. B, 32 (1985) 1892, 1906.
(c) A.P. Kaduwela, G.S. Herman, D.J. Friedman and C.S. Fadley, Phys. Scr., 41 (1990) 948.
(d) J.J. Rehr and R.C. Albers, Phys. Rev. B, 41 (1990) 8139.
(e) A.P. Kaduwela, D.J. Friedman and C.S. Fadley, J. Electron Spectrosc. Relat. Phenom., 57 (1991) 223.
[11] (a) P.J. Orders and C.S. Fadley, Phys. Rev. B, 27 (1983) 781.
(b) M. Sagurton, E.L. Bullock and C.S. Fadley, Phys. Rev. B, 30 (1984) 7332; Surf. Sci., 182 (1987) 287.
(c) V. Fritzsche and D.P. Woodruff, Phys. Rev. B, 46 (1992) 16128.
(d) P. Hofmann and K.M. Schindler, Phys. Rev. B, 47 (1993) 13942.
[12] (a) A. Szöke, in D.T. Attwood and J. Bokor (Eds.), Short Wavelength Coherent Radiation: Generation and Applications, AIP Conference Proceedings No. 147, AIP, New York, 1986.
(b) J.J. Barton, Phys. Rev. Lett., 61 (1988) 1356.
(c) J.J. Barton, J. Electron Spectrosc. Relat. Phenom., 51 (1990) 37.
(d) J.J. Barton, Phys. Rev. Lett., 67 (1991) 3106.
[13] (a) G.R. Harp, D.K. Saldin and B.P. Tonner, Phys. Rev. Lett., 65 (1990) 1012; Phys. Rev. B, 42 (1990) 9199.
(b) B.P. Tonner, Z.-L. Han, G.R. Harp and D.K. Saldin, Phys. Rev. B, 43 (1991) 14423.
(c) G.R. Harp, D.K. Saldin, X. Chen, Z.L. Han and B.P. Tonner, J. Electron Spectrosc. Relat. Phenom., 57 (1991) 331.
(d) D.K. Saldin, G.R. Harp, B.L. Chen and B.P. Tonner, Phys. Rev. B, 44 (1992) 2480.
(e) D.K. Saldin, G.R. Harp and B.P. Tonner, Phys. Rev. B, 45 (1992) 9629.
[14] (a) S.Y. Tong, C.M. Wei, T.C. Zhao, H. Huang and H. Li, Phys. Rev. Lett., 66 (1991) 60.
(b) S.Y. Tong, H. Li and H. Huang, Phys. Rev. Lett., 67 (1992) 3102.
(c) S.Y. Tong, H. Huang and C.M. Wei, Phys. Rev. B, 46 (1992) 2452.
(d) J.G. Tobin, G.D. Waddill, H. Li and S.Y. Tong, Phys. Rev. Lett., 70 (1993) 4150.
[15] (a) S. Thevuthasan, G.S. Herman, A.P. Kaduwela, R.S. Saiki, Y.J. Kim, W. Niemczura, M. Burger and C.S. Fadley, Phys. Rev. Lett., 67 (1991) 469.
(b) G.S. Herman, S. Thevuthasan, T.T. Tran, Y.J. Kim and C.S. Fadley, Phys. Rev. Lett., 68 (1992) 650.
(c) S. Thevuthasan, G.S. Herman, A.P. Kaduwela, T.T. Tran, Y.J. Kim, R.S. Saiki and C.S. Fadley, J. Vac. Sci. Technol. A, 10 (1992) 2261.
(d) S. Thevuthasan, R.X. Ynzunza, E.D. Tober, C.S. Fadley, A.P. Kaduwela and M.A. van Hove, Phys. Rev. Lett., 70 (1993) 595.
(e) P.M. Len, S. Thevuthasan, A.P. Kaduwela, M.A. van Hove and C.S. Fadley, Surf. Sci., in press.
(f) P.M. Len, F. Zhang, S. Thevuthasan, A.P. Kaduwela, M.A. van Hove and C.S. Fadley, J. Electron Spectrosc., Relat. Phenom., 76 (1995) 351.
[16] (a) L.J. Terminello, J.J. Barton and D.A. Lapiano-Smith, J. Vac. Sci. Technol. B, 10 (1992) 2088; Phys. Rev. Lett., 70 (1993) 599.
(b) B.L. Petersen, L.J. Terminello and D.A. Shirley, Mat. Res. Soc. Symp. Proc., 307 (1993) 285.
(c) B.L. Petersen, L.J. Terminello, J.J. Barton and D.A. Shirley, Chem. Phys. Lett., 220 (1994) 46.
(d) B.L. Petersen, Ph.D. Thesis, University of California-Berkeley, 1995.
(e) L.J. Terminello, B.L. Petersen and J.J. Barton, J. Electron Spectrosc. Relat. Phenom., 75 (1995) 299.
(f) Y. Zhou, X. Chen, J.C. Campuzano, G. Jennings, H. Ding and D.K. Saldin, Mat. Res. Soc. Symp. Proc., 307 (1993) 279.
[17] (a) H. Wu, G.J. Lapeyre, H. Huang and S.Y. Tong, Phys. Rev. Lett., 71 (1993) 251.
(b) H. Wu and G.J. Lapeyre, Phys. Rev. B, 51 (1995) 14549.
[18] S.Y. Tong, H. Li and H. Huang, Phys. Rev. B, 51 (1995) 1850.
[19] M.T. Sieger, J.M. Roesler, D.-S. Lin, T. Miller and T.-C. Chiang, Phys. Rev. Lett., 73 (1994) 311.
[20] B.P. Tonner, D. Dunham, T. Droubay, J. Kikuma, J. Denlinger and E. Rotenberg, J. Electron Spectrosc. Relat. Phenom., 75 (1995) 309.
[21] (a) R.J. Baird, C.S. Fadley and L.F. Wagner, Phys. Rev. B, 15 (1977) 666.
(b) J. Osterwalder, T. Greber, S. Hüfner and L. Schlapbach, Phys. Rev. B, 41 (1990) 12495.
(c) S. Hüfner, J. Osterwalder, T. Greber and L. Schlapbach, Phys. Rev. B, 42 (1990) 7350.
(d) G.S. Herman and C.S. Fadley, Phys. Rev. B, 43 (1991) 6792.
(e) T. Greber, J. Osterwalder, S. Hüfner and L. Schlapbach, Phys. Rev. B, 44 (1991) 8958.

[22] (a) Y.J. Kim, C. Westphal, R.X. Ynzunza, H. Xiao, Z. Wang, H.C. Galloway, M. Salmeron, M.A. Van Hove and C.S. Fadley, paper presented at the 1995 Natl. Symp. Am. Vac. Soc., to be published.
(b) Y.J. Kim, Ph.D. Thesis, University of Hawaii-Manoa, 1995.
[23] H.C. Galloway, J.J. Benitez and M. Salmeron, Surf. Sci., 198 (1993) 127; J. Vac. Sci. Technol. A, 12 (1994) 2302.
[24] (a) D.M. Riffe, G.K. Wertheim and P.H. Citrin, Phys. Rev. Lett., 63 (1989) 1976.
(b) D. Spanjaard, C. Guillot, M.-C. Desjonquères, G. Tréglia and J. Lecante, Surf. Sci. Rep., 5 (1985) 1.
(c) B. Kim, J. Chen, J.L. Erskine, W.N. Mei and C.M. Wei, Phys. Rev. B, 48 (1993) 4735.
[25] R.X. Ynzunza, E.D. Tober, J. Palomares, Z. Wang, Z. Hussain, A.P. Kaduwela and C.S. Fadley, to be published.
[26] E.D. Tober, R.X. Ynzunza, Z. Wang, J. Palomares, Z. Hussain, A.P. Kaduwela and C.S. Fadley, to be published.
[27] E.D. Tober, R.X. Ynzunza, C. Westphal and C.S. Fadley, Phys. Rev. B, May 1996.
[28] (a) G. Schönhense, Phys. Scr. T, 31 (1990) 255.
(b) J. Bansmann, Ch. Ostertag, G. Schönhense, F. Fegel, C. Westphal, M. Getzlaff, F. Schafers and H. Petersen, Phys. Rev. B, 46 (1992) 13496.
[29] (a) V. McKoy and J.A. Stephens, personal communication, 1994.
(b) C. Westphal, A.P. Kaduwela, M.A. Van Hove and C.S. Fadley, Phys. Rev. B, 50 (1994) 6203.
[30] (a) H. Daimon, T. Nakatani, S. Imada, S. Suga, Y. Kagoshima and T. Miyahara, Jpn. J. Appl. Phys., 32 (1993) L1480.
(b) H. Daimon, personal communication, 1994.
[31] A.P. Kaduwela, H. Xiao, S. Thevuthasan, M.A. Van Hove and C.S. Fadley, Phys. Rev. B, 52 (1995) 14927.
[32] H. Daimon, R. Ynzunza, J. Palomares, Z. Wang, Z. Hussain, A.P. Kaduwela and C.S. Fadley, to be published.
[33] K.E. Johnson, R.J. Wilson and S. Chiang, Phys. Rev. Lett., 71 (1993) 1055.
[34] (a) L. Baumgarten, C.M. Schneider, H. Petersen, F. Schafers and J. Kirschner, Phys. Rev. Lett., 65 (1990) 492.
(b) H. Ebert, L. Baumgarten, C.M. Schneider and J. Kirschner, Phys. Rev. B, 44 (1991) 4406.
(c) G.D. Waddill, J. Tobin and D.R. Pappas, Phys. Rev. B, 46 (1992) 552.
[35] (a) Ch. Roth, F.U. Hillebrecht, H.B. Rose and E. Kisker, Phys. Rev. Lett., 70 (1993) 3479.
(b) F. Sirotti and G. Rossi, Phys. Rev. B, 49 (1994) 15682.
(c) M. Getzlaff, Ch. Ostertag, G.H. Fecher, N.A. Cherepkov and G. Schönhense, Phys. Rev. Lett., 73 (1994) 3030.
(d) N.A. Cherepkov, Phys. Rev. B, 50 (1994) 13813.
(e) E. Kisker, paper presented at VUV 11, Tokyo, Japan, August 1995. To be published in J. Electron Spectrosc. Relat. Phenom.
[36] F.U. Hillebrecht, R. Jungblut and E. Kisker, Phys. Rev. Lett., 65 (1990) 2450.
(b) R. Jungblut, Ch. Roth, F.U. Hillebrecht and E. Kisker, J. Appl. Phys., 70 (1991) 5923.
(c) R. Jungblut, Ch. Roth, F.U. Hillebrecht and E. Kisker, Surf. Sci., 269/270 (1992) 615.
(d) T. Kachel, C. Carbone and W. Gudat, Phys. Rev. B, 47 (1993) 15391.
(e) D.G. van Campen, R.J. Pouliot and L.E. Klebanoff, Phys. Rev. B, 48 (1993) 17533.
(f) P.D. Johnson, Y. Liu, Z. Xu and D.J. Huang, J. Electron Spectrosc. Relat. Phenom., 75 (1995) 245.
[37] F. Zhang, S. Thevuthasan, R.T. Schalettar, R.R.P. Singh and C.S. Fadley, Phys. Rev. B, 51 (1995) 12468.
[38] (a) U. Fano, Phys. Rev., 178 (1969) 131.
(b) U. Heinzmann, J. Kessler and J. Lorenz, Phys. Rev. Lett., 25 (1970) 1325.
[39] K. Starke, A.P. Kaduwela, Y. Liu, P.D. Johnson, M.A. Van Hove, C.S. Fadley, V. Chakarian, E.E. Chaban, G. Meigs and C.T. Chen, to be published.
[40] J.G. Tobin, C.D. Waddill, D.P. Pappas, E. Tamura and P. Sterne, J. Vac. Sci. Technol. A, 14 (1995) 1574.
[41] N.A. Cherepkov, Phys. Lett. A, 40 (1972) 119; Adv. At. Mol. Phys., 19 (1983) 395.
[42] (a) E.M.E. Timmermans, G.T. Trammell and J.P. Hannon, Appl. Phys., 73 (1993) 6183; Phys. Rev. Lett., 72 (1994) 832.
(b) A.P. Kaduwela, Z. Wang, M.A. Van Hove and C.S. Fadley, Phys. Rev. B, 50 (1994) 9656; to be published.
(c) Z. Wang and A.P. Kaduwela, to be published.

Pergamon

Progress in Surface Science, Vol. 54, No. 3/4, pp. 341-386, 1997

0079-6816/97 $32.00

PII: S0079-6816(97)00013-0

DIFFRACTION AND HOLOGRAPHY WITH PHOTOELECTRONS AND FLUORESCENT X-RAYS

C. S. FADLEY[#*]

With:

Y. Chen[*], R.E. Couch[#], H. Daimon[‡], R. Denecke[#*], J.D. Denlinger[/], H. Galloway[*@], Z. Hussain[†], A.P. Kaduwela[#*], Y.J. Kim[*&], P.M. Len[#*], J. Liesegang[£], J. Menchero[@*], J. Morais[#], J. Palomares[#*], S.D. Ruebush[#*], E. Rotenberg[+], M. B. Salmeron[*], R. Scalettar[#], W. Schattke[§], R. Singh[#], S. Thevuthasan[#], E.D. Tober[#*], M.A. Van Hove[*], Z. Wang[#*], and R.X. Ynzunza[#*]

[#]Department of Physics, University of California-Davis, Davis, CA 95616

[*]Materials Sciences Division, Lawrence Berkeley National Laboratory, Berkeley, CA 94720

[†]Advanced Light Source, Lawrence Berkeley National Laboratory, Berkeley CA 94720

[@]Department of Physics, University of California-Berkeley, Berkeley, CA 94720

[&]Department of Chemistry, University of Hawaii, Honolulu, Hawaii 96822

[‡]Dept. of Materials Physics, Osaka University, Toyonaka, Osaka 560, Japan

[/]University of Wisconsin-Milwaukee, Milwaukee, WI 53201

[+]University of Oregon, Eugene, OR 97403

[§]Institut für Theoretische Physik, Universität Kiel, D-24118 Kiel, Germany

[£]Dept. of Physics, Latrobe University, Bundoora 3083, Victoria, Australia

Abstract

We consider studies of the atomic and magnetic structure near surfaces by photoelectron diffraction and by the holographic inversion of both photoelectron diffraction data and diffraction data involving the emission of fluorescent x-rays. The current status of photoelectron diffraction studies of surfaces, interfaces, and other nanostructures is first briefly reviewed, and then several recent developments and proposals for future areas of application are discussed. The application of full-solid-angle diffraction data, together with simultaneous characterization by low energy electron diffraction and scanning tunneling microscopy, to the epitaxial growth of oxides and metals is considered. Several new avenues that are being opened up by third-generation synchrotron radiation sources are also discussed. These include site-resolved photoelectron diffraction from surface and interface atoms, the possibility of time-resolved measurements of surface reactions with chemical-state resolution, and circular dichroism in photoelectron angular distributions from both non-magnetic and magnetic systems. The addition of spin to the photoelectron diffraction measurement is also considered as a method for studying short-range magnetic order, including the measurement of surface magnetic phase transitions. This spin sensitivity can be achieved through either core-level

multiplet splittings or circular-polarized excitation of spin-orbit-split levels. The direct imaging of short-range atomic structure by both photoelectron holography and two distinct types of x-ray holography involving fluorescent emission is also discussed. Both photoelectron and x-ray holography have demonstrated the ability to directly determine at least approximate atomic structures in three dimensions. Photoelectron holography with spin resolution may make it possible also to study short-range magnetic order in a holographic fashion. Although much more recent in its first experimental demonstrations, x-ray fluorescence holography should permit deriving more accurate atomic images for a variety of materials, including both surface and bulk regions.

Acronyms

ALS	Advanced Light Source
CDAD	Circular dichroism in photoelectron angular distributions
FWHM	Full width at half-maximum intensity
LCP	Left circularly-polarized radiation
LEED	Low energy electron diffraction
LP	Linearly-polarized radiation
MCD	Magnetic circular dichroism
MCDAD	Magnetic circular dichroism in photoelectron angular distributions
MEXH	Multi-energy x-ray holography
ML	Monolayer
MLD	Magnetic linear dichroism
MS	Multiple scattering
MSC	Multiple scattering cluster
MUD	Magnetic unpolarized dichroism
PD	Photoelectron diffraction
PH	Photoelectron holography
RCP	Right circularly-polarized radiation
SR	Synchrotron radiation
SPPD	Spin-polarized photoelectron diffraction
SS	Single scattering
SSC	Single scattering cluster
STM	Scanning tunneling microscopy
UP	Unpolarized radiation
XFH	X-ray fluorescence holography
XH	X-ray holography using fluorescence emission (2 types)
XPD	X-ray photoelectron diffraction
XPS	X-ray photoelectron spectroscopy
XRD	X-ray diffraction

1. Introduction

A. Photoelectron Diffraction and Holography

The basic process involved in photoelectron diffraction (PD) is illustrated in Fig. 1. A photon excites an electron from a core level that is necessarily well localized in space, and the outgoing approximately-spherical photoelectron wave is scattered from the atoms neighboring the emitter, producing an interference pattern. It is the interference of the unscattered component ϕ_0 with the scattered components ϕ_j, (where j = 1, 2, 3, ...and is summed over an atomic cluster of sufficiently large size to be convergent) that produces the final diffraction pattern. Some of the key physical parameters controlling this process are indicated in the figure. These parameters are: $\vec{\varepsilon}$ = the light polarization which influences the initial photoelectron excitation matrix element, $\vec{q}$ = the photon wave vector, $\vec{k}$ = the electron wave vector directly related to the momentum $\vec{p} = \hbar\vec{k}$ and the electron de Broglie wavelength $\lambda_e = 2\pi/|\vec{k}|$, $f_j(\theta_j)$ = the electron-atom scattering factor for a given scattering angle θ_j (describable in first order via plane-wave scattering but more accurately via spherical-wave scattering), Λ_e = the attenuation length controlling the exponential damping of the elastic photoelectron signal due to inelastic scattering, $\overline{U_j^2}$ = the mean-squared atomic vibrational amplitude involved in the damping of the diffraction pattern due to vibrational effects (as included most simply in a Debye-Waller factor), V_0 = the inner potential which produces refraction of the photoelectron in crossing this surface potential barrier, and Ω_0 = the effective analyzer acceptance solid over which the diffraction pattern is averaged in the actual experiment. All of these aspects will be included in the theoretical calculations presented here.

Beginning with the first experiments of this type [1], strong modulations in intensity of as much as ±50% have been observed as a function of either the direction of electron emission or the energy of excitation, leading to what have been termed *scanned-angle* or *scanned-energy* measurements, respectively. The aim of these measurements is to deduce information about the atomic structure around a given type of emitter, or perhaps also the type of magnetic order surrounding such an emitter. There are by now a number of groups in the world engaged in such experiments, using both laboratory x-ray sources and synchrotron radiation (SR), and a variety of systems have been studied to date with this technique, including adsorbed atoms and molecules, systems exhibiting surface and interface core-level shifts, epitaxial overlayers, surface structural and magnetic phase transitions, and atoms at buried interfaces. Several reviews of this field have appeared in recent years [2-7], and it will thus not be our aim to survey it in detail. Rather, we will begin by briefly describing those basic characteristics that make PD an attractive structural probe, consider some of its limitations and difficulties, and then go on to concentrate on several more recent developments involving both laboratory x-ray sources and next-generation SR sources that promise to make it an even more widely used tool for surface, interface, and nanostructure studies in the future.

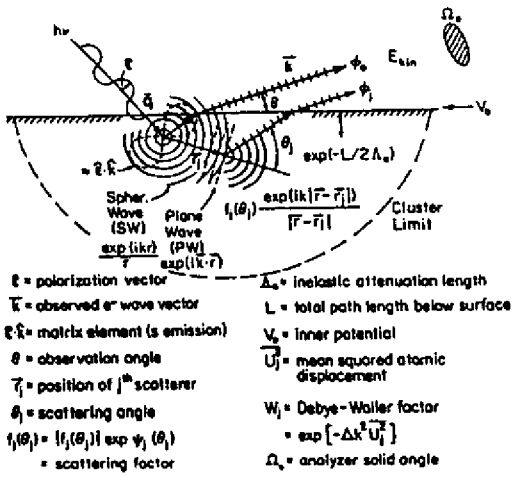

Fig. 1. Illustration of the basic photoelectron diffraction process, with various key physical quantities necessary for theoretically modeling such phenomena labelled and defined.

We begin with the positive aspects of PD, several of which will be illustrated with more specific examples in the following sections:

- *Atom specificity*: PD is an atom-specific probe by virtue of the fact that a certain core level is excited. Thus, the structure around each type of atom in the sample can be probed separately.
- *Chemical-state or site specificity*: With sufficient resolution, core binding energy shifts with chemical state (e.g., the different oxidation states of a given atom) or binding site (e.g, between the bulk and surface of a metal or semiconductor) can be used to study the atomic structure around each type of atom separately [8].
- *Spin-specificity:* Although not nearly as much explored, the diffraction patterns of photoelectrons of different spins can also be studied separately, yielding the promise of determining the local magnetic order around both magnetic atoms and non-magnetic atoms surrounded by magnetic atoms. Such spin sensitivity can be achieved by using the multiplet splitting inherent in the core spectra of various transition metals or rare-earth elements, by exciting spin-orbit-split core levels with circular-polarized radiation, or by some unavoidable combination of these two effects. This leads to what has been termed spin polarized photoelectron diffraction (SPPD). [9].

• *Variation of light polarization:* Beyond using circular polarization to produce spin polarization, varying polarization from linear (LP) to left or right circular (LCP or RCP, respectively) to unpolarized (UP) further permits selectively directing the outgoing photoelectron probe wave into different regions of the atomic structure surrounding the emitter, so that complementary structural information can be obtained for different relative orientations of light and sample [2,4].

• *Variation of excitation energy:* PD makes use of the ability to vary the excitation energy (and thus also the photoelectron kinetic energy) in several ways. At higher kinetic energies of ≥500 eV, the magnitude of the electron-atom scattering factor $|f_j(\theta_j)|$ is highly peaked in the forward direction, producing pronounced peaks in diffraction patterns along e.g. bond directions in adsorbed molecules and low-index directions in epitaxial layers [2,3,5]. For lower energies of ≤300 eV, the scattering factor for lower-Z atoms is more uniform over all directions, and often has a strong peak in the backward direction; thus, the locations of atoms behind the emitter as viewed from the detector can be fruitfully studied [2,4,6], although their bond directions cannot be as directly determined as in forward scattering. Being able to vary energy between these two limits using synchrotron radiation thus permits studying the full structural environment of a given emitter. Going to lower energies in the 50-100 eV range further leads to increased sensitivity to the surface, as this is where most materials possess a minimum in the inelastic attenuation length Λ_e for electrons.. Also, the 50-100 eV range is one in which magnetic scattering effects, particularly due to the exchange interaction are strongest; thus, such energies are those of relevance in SPPD measurements [9]. Being able to tune the photoelectron energy to maxima, minima, and/or resonances in the various photoelectric cross sections is a useful possibility in SR studies. And finally, the dependence of the photoelectron de Broglie wavelength on kinetic energy E_{kin}, which is given by $\lambda_e(\text{Å}) \approx \sqrt{150/E_{kin}(eV)}$, is of course also what leads to the modulations measured in scanned-energy photoelectron diffraction.

• *Simple first-order theoretical interpretation:* In a number of studies to date, it has proven possible to derive useful surface structural information by comparing experimental data to the results of rather straightforward single-scattering (SS or kinematical) theoretical calculations [2,3(a)]. However, it is also by now clear that a fully quantitative treatment of all of the features in both low-energy and high-energy diffraction patterns will require more sophisticated calculations at a fully-converged multiple scattering (MS) level [10]. These calculations have many similarities to those used in low energy electron diffraction (LEED) analyses . We will below illustrate both types of theoretical analysis.

• *Short-range order sensitivity:* The nature of the photoelectron emission process (into an outgoing spherical wave which decays as 1/r) and the inelastic scattering process (with very short attenuation lengths Λ_e in the ~5-20Å range) can be shown to make PD a probe of short-range atomic or magnetic structure, with primary sensitivity to the first 5 or so spheres of neighbors around a given emitting site, or within a sphere of maximum radius ~20 Å [2,4]. This can be of advantage in studying any sort of nanostructure which does not exhibit long-range order over a surface. LEED by comparison is generally used to probe longer-range order over perhaps 50-100 Å, although spot profile analysis is now being used to derive shorter-range information.

• *Direct derivation of structural parameters and photoelectron holography:* A final advantage is that there are at least three distinct ways in which it is possible to directly derive structural parameters from PD data with a minimum recourse to theoretical modeling. We have already noted that *forward scattering peaks* directly give bond or low-index directions [2,3,5]. Beyond this, *Fourier transforms of scanned-energy PD data* yield path-length differences for different scatterers that can often be used to rule out some adsorbate geometries in a search for the true structure [2,4,6(b),11]. Finally, *holographic transforms of larger data sets* that involve varying both energy and angle over some volume in the momentum space or $\vec{k}$-space of the photoelectron can be used to directly derive atomic positions in three dimensions [12-21]. This was first suggested by Szöke [12(a)]. The process is illustrated in Fig. 2(b), in which the unscattered component ϕ_0 is now identified with the holographic reference wave and the scattered components $\phi_1, \phi_2, \phi_3, \ldots$ with the object or subject waves. Various attempts have been made to derive atomic structures by photoelectron holography (PH), including several methodologies for generating atomic images [12-21]. Comparisons of these methods and general criteria for optimizing the taking of such holographic data so as to minimize measuring times also have been presented recently [15(e)-(g)].

By contrast, some difficulties and limitations of PD are:

• *More complex instrumentation:* Relative to a standard laboratory x-ray photoelectron spectroscopy (XPS) system, a more precise, computer-driven sample manipulator is required. However, adequate manipulators are now available from various commercial sources. For the most versatile and powerful experiments with variable energy and/or variable polarization, access to a synchrotron radiation beamline is also necessary, although much can still be done with a standard laboratory XPS system.

• *Longer measuring times:* Measuring hundreds or perhaps even a few thousand separate core spectra to produce a single angle or energy scan or a more complex scan over both angle and energy that can be used in a holographic sense [12-21] can be very time consuming, and may take between hours and days with most present systems. However, state-of-the-art laboratory XPS systems and next-generation synchrotron radiation beamlines, coupled with appropriately high-throughput spectrometers and detectors, promise to reduce these times to the minutes to hours range. Such instrumentation should also permit a broader range of dynamical studies on surfaces. We discuss below one such experimental system at the Advanced Light Source in Berkeley, and some time-resolved surface kinetics measurements that have been performed with it.

• *Macroscopic domain averaging:* As presently carried out, PD data is taken from the full area illuminated by the radiation, which is typically of the order of 1 mm^2 to 10 mm^2. Thus, many atomic domains are averaged over, and structural conclusions can be confused by the resulting overlap of diffraction patterns from different site types. Various kinds of photoelectron *microscopy* are currently being tested at different synchrotron radiation sources around the world, as reviewed recently elsewhere by Tonner et al. [22]. These developments may ultimately permit doing PD on

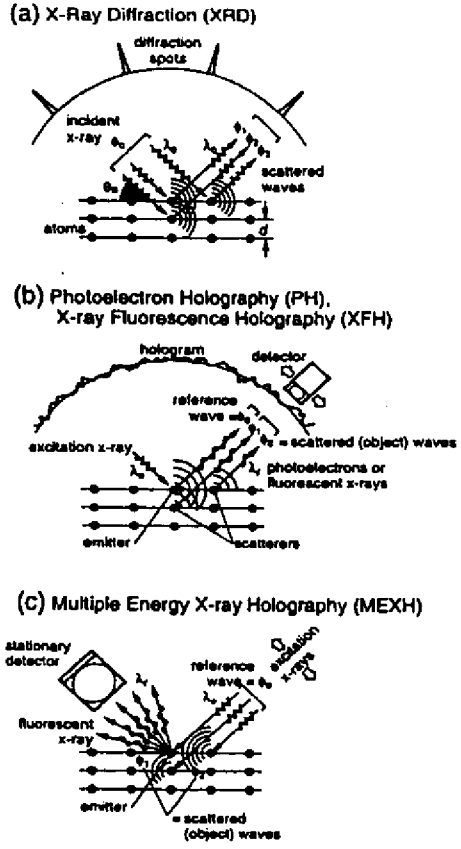

Fig. 2. Schematic illustration of some methods for determining atomic structure. (a) Conventional x-ray diffraction from a crystal, in which the incident wavefront ϕ_0 does not usually contribute to the diffracted intensity spots . (b) Localized-source holography in which a certain atom emits either a core photoelectron, yielding photoelectron holography (PH) or a core-derived fluorescent x-ray, yielding x-ray fluorescence holography (XFH). (c) A second type of x-ray holography in which the incident x-ray scatters from near-nrighbor atoms to create an interference at a certain emitter of fluorescent x-rays. This is the time-reversed version of XFH in (b).

areas as small as a few hundred Å in radius, thus focussing on a single domain or nanostructure on the surface. This last prospect is to be sure a *tour de force* experiment for third-generation (or even fourth-generation) synchrotron radiation sources, but realizing it would be exciting indeed, as two further spatial dimensions could then be accessed in the experiment.

• *More complex multiple-scattering theoretical interpretation:* We have already noted above that data can often be analyzed in a useful way within a single-scattering framework, but future studies will no doubt make more use of the more quantitative multiple-scattering model. However, a number of groups by now have multiple scattering programs operating [10], and these will no doubt become faster, more accurate, and more user friendly, as they have in the LEED community. We illustrate the need for this more accurate modeling in specific cases discussed below.

In what follows, we will present a few recent examples of PD data and its theoretical interpretation, and also consider the development of next-generation instrumentation for such measurements These examples are chosen primarily from the work of our group, but we believe that they are illustrative of both some current forefronts of PD studies and some of the more exciting future directions in this field.

B. X-Ray Fluorescence Holography

We will also consider a much more newly developed technique for directly determining short-range atomic structures, but one which is a very close relative of photoelectron holography (PH): x-ray holography (XH) [23,24]. In PH, the photoelectric effect creates an outgoing photoelectron wave from a given atomic center. As noted previously, the unscattered component of this wave is treated as a reference wave which interferes with the scattered components, with the latter being treated as the object or subject waves in a standard holographic exposure (cf. Fig. 2(b)). In the first method of doing XH, the deexcitation of a core hole in a given atom creates an outgoing fluorescent x-ray, with the unscattered and scattered components of this wave again serving as reference and subject in a holographic exposure. This also is shown in Fig. 2(b), and it has been termed x-ray flourescence holography (XFH). A second XH method called multi-energy x-ray holography (MEXH) and illustrated in Fig. 2(c) is in a sense the time-reversed version of XFH and will be introduced in more detail later.

Because x-rays scatter much more ideally from atoms than electrons (i.e., much more weakly and isotropically, and with negligible scattering phase shifts ψ_j), one expects either way of doing XH to yield more accurate holographic images than those from PH. However, the intensity modulations in an x-ray hologram are also expected to be much weaker (by a factor of $\sim 10^{-3}$-10^{-4}), so that such experiments will be inherently more difficult to perform. The much greater penetration depths of x-rays in matter also means that XH can be used to probe nanostructures quite far below a surface, with surface or interface specific studies being possible only if a certain atomic type is present only in the near-surface region to be studied. XH thus shares some of the advantages of PD/PH : atom specificity, variation of exciting light polarization, an even simpler kinematical theoretical interpretation, short-range order sensitivity, and direct derivation of three-dimensional atomic

structures. And it also shares some of the disadvantages: complex instrumentation, even longer measuring times, and macroscopic domain averaging. Nonetheless, the exciting promise of XH as a complement to the well-developed x-ray diffraction (XRD) methods for studies of atomic structure (cf. Fig. 2(a)) has led to a few pioneering measurements of this type [24] that we will briefly overview below.

2. Full-Solid-Angle XPD in Combination with LEED and STM

Although the first full-solid-angle photoelectron diffraction pattern was measured some time ago [25(a)], it is only in recent years that these time-consuming experiments have been performed on a more routine basis, beginning particularly in the Osterwalder group [7, 25(b),(c)]. We here illustrate the utility of this kind of data in two recent studies of epitaxial growth: iron oxide on Pt(111) [26] and Cu on Ru(0001) [27]. In the iron oxide work, another noteworthy element was added in that x-ray photoelectron diffraction (XPD) measurements in a laboratory-based system were combined with in situ characterization by both LEED and scanning tunneling microscopy (STM), such that the complementary nature of these surface structure probes could be exploited [26(b)].

Some data for a 1 monolayer (ML) overlayer of FeO on Pt(111) obtained by Kim et al. [26(b)] are shown in Fig. 3, where a LEED pattern, STM image, and full-solid-angle XPD patterns from all three atoms present (Pt, Fe, and O), as excited by Al Kα radiation at 1,487 eV, are compared for the same surface preparation. The LEED pattern in Fig. 3(a) shows the basic Pt(111) spots, but with a rosette of superstructure spots around each one indicative of some longer range order. This longer range order can in turn be directly imaged by STM [26(a)] as shown in Fig. 3(b), and it consists of a hexagonal unit cell of approximately 26 Å x26 Å superimposed on the atomic-resolution hexagonal oxide unit cell of 3.1 Å x 3.1 Å. Such combined LEED and STM data led Galloway et al. [26(a)] to first propose a particular superstructure or lateral Moiré pattern consisting of a hexagonal-symmetry bilayer of FeO(111) type and composed of a layer of Fe atoms on top of (or perhaps below) a layer of O atoms. But this model left several questions about this overlayer unanswered. Among these questions were: Which atomic layer is outermost, Fe or O? What is the interplanar distance between Fe and O? Is there a preferred relative orientation of the FeO bilayer in its growth with respect to the underlying Pt?

The XPD results in Fig. 3(c) serve to answer all three of these questions. The Pt 4f diffraction pattern is dominated by scattering in the substrate crystal, and so does not contain any easily-derivable information concerning the structure of the overlayer. It does however provide a direct internal reference in the data for the orientation of the overlayer, with the [11$\bar{2}$] direction lying in the Pt(111) surface indicated on the figure. The Fe 2p XPD pattern contains three strong peaks with some fine structure around them, immediately indicating that there are forward scattering atoms between Fe and the detector. Thus, O is immediately suggested to be in the outermost layer and responsible for this forward scattering. Finally, the O 1s pattern is devoid of any significant

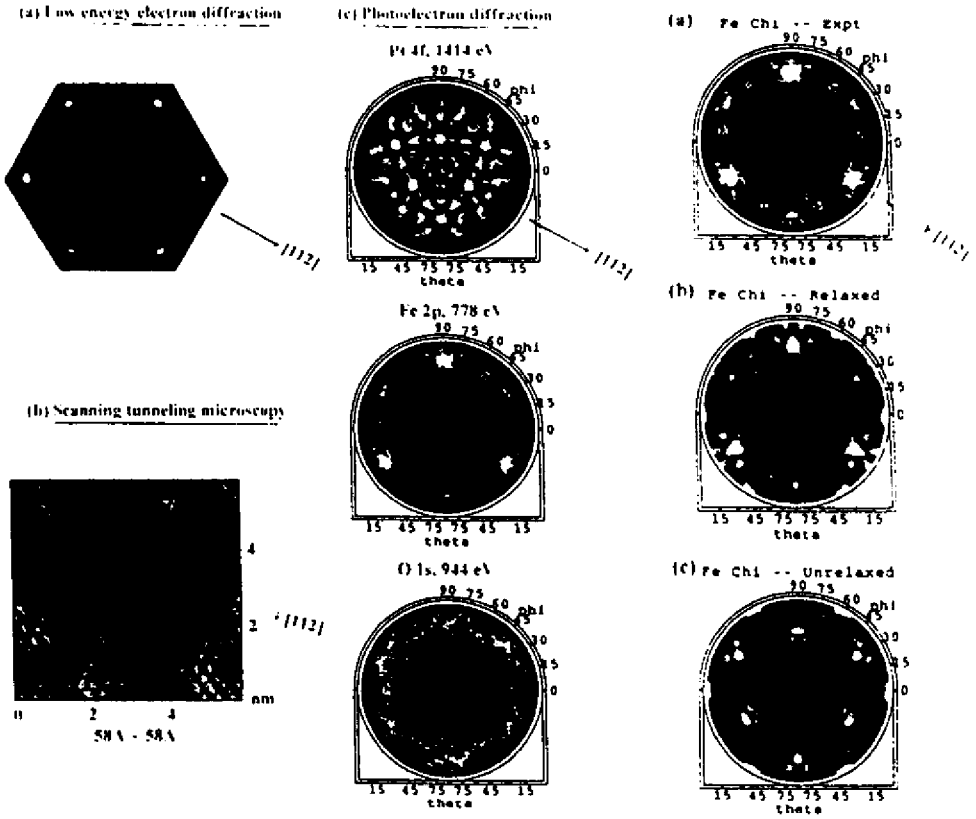

Fig. 3. (Upper left) (a) LEED, (b) STM, and (c) full-solid-angle XPD data for 1 monolayer (ML) of FeO on Pt(111). The XPD patterns for Pt 4f, Fe 2p, and O 1s emission are shown in stereographic projection. [From ref. 26(b).]

Fig. 4. (Upper right) Full-solid-angle Fe 2p XPD pattern for 1 ML of FeO on Pt(111): (a) experimental data, (b) single scattering theory with a best-fit Fe-O interplanar distance of 0.68 Å, (c) single-scattering theory with an Fe-O interplanar distance of 1.25 Å as in bulk FeO. [From ref. 26(b).]

diffraction features, further confirming that it is the outermost layer. The second question as to interlayer spacing is also easily answered by measuring the polar angle of 20° (measured with respect to the surface) at which the Fe-O forward scattering peaks occur, and combining this with the lateral unit-cell dimensions of the FeO overlayer as derived from LEED and/or STM. Simple trigonometry then yields an interplanar distance of only 0.65 Å that is much contracted from the 1.25 Å between (111) planes in bulk FeO. This distance can be further checked by carrying out single-scattering diffraction calculations for this overlayer, with single-scattering being an excellent approximation for this situation in which there are no chains of forward scattering atoms [2]. Comparing such calculations with experiment via R-factors developed specifically for the analysis of PD data [26(c)] [(as done also in quantitative LEED structural analyses) finally yields the most accurate interplanar distance of 0.68 Å that is very close to the simple estimate based on the forward scattering direction. Theoretical calculations for both 0.68 Å and 1.25 Å interplanar spacings are compared to experiment in Fig. 4. The agreement between experiment and the calculation for 0.68 Å is excellent, including even the weak diffraction features around the forward scattering peaks. For a 1.25 Å spacing, agreement is poor, both as to the polar angle position of the forward scattering peaks and the weaker features. Finally, the fact that there are only three forward scattering peaks in the Fe diffraction pattern immediately implies that only one orientation of the hexagonal O overlayer with respect to the underlying Pt surface exists, even though two O overlayer orientations rotated by 180° with respect to one another are equally likely as far as the Fe layer is concerned. Thus, there is an O-Pt interaction through the Fe layer that is strong enough to select only one orientation of the O overlayer; in fact, this interaction must involve second-layer Pt atoms. Thus, XPD can be used to determine a final subtle aspect of the growth process that would be difficult to arrive at with other methods.

Thus, this is an illustrative example of both how useful full-solid-angle diffraction patterns can be (see also refs. 7 and 25 for other examples, including a very recent application to C_{60} in ref. 25(c)) and how important it is to have additional complementary structural probes in the same experimental chamber, with LEED and STM being two particularly useful ones.

A second example of epitaxy recently studied using data from these combined techniques is Cu/Ru(0001), a system that at one level exhibits classic Stranski-Krastanov growth, but which on closer examination with STM by Günther et al. [27(a)] shows four stages of growth from a pseudomorphic first layer through various types of lateral contraction until finally reaching Cu(111)-like islands with essentially the bulk Cu structure. Subsequent theoretical analysis of these results by Hamilton and Foiles have successfully predicted these stages of growth as well [27(b)]. Ruebush, Couch et al. [27(c)] have now measured full-solid-angle XPD from both Cu and Ru for this system, and analyzed these results together with the STM results obtained by Günther et al. [27(a)]. Some of their experimental data for 1, 2, 3 and 4 ML Cu coverages are shown in Fig. 5 together with theoretical calculations based upon both multiple-scattering cluster (MSC) [10(e)] and single-scattering cluster (SSC) [10(c)] methods. In general, MSC theory better describes these data, for example, as to the sharpness of the two sets of sixfold rings seen for 1 ML, and the relative

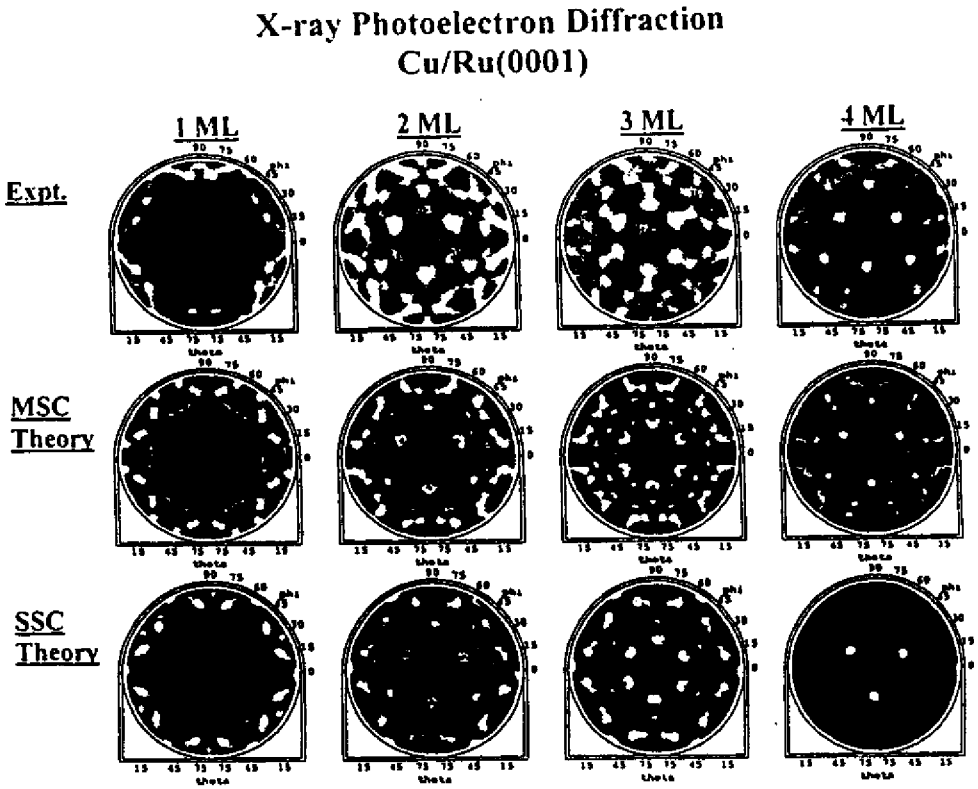

Fig. 5. X-ray photoelectron diffraction from the Cu $2p_{3/2}$ level of Cu on Ru(0001), for coverages of Cu from 1 to 4 ML. The kinetic energy is 556 eV. Also shown are the results of multiple scattering cluster (MSC) and single scattering cluster (SSC) calculations in which the interplanar spacings have first been varied to achieve best agreement with experiment. [From ref. 27(c).]

intensities of the most intense forward scattering peaks for 4 ML (which are too strong along these low-index directions in SSC). However, as noted before [2], SSC theory nonetheless predicts most of the major features away from such low-index directions. Comparing these XPD data with theory via PD-specific R-factors [26(c)] has furthermore permitted determining the average interlayer spacing of the Cu overlayers as a function of overlayer thickness, with the interesting result that significant contraction is found to persist even up to 5-8 ML coverages. A simple theoretical picture based on the Frenkel-Kontorova model [27(c)] on the other hand predicts a much quicker convergence to the bulk interlayer spacing than is seen in experiment. Accurately knowing such interlayer spacings is clearly important for an understanding of both the chemical reactivity and magnetic properties of such epitaxial metal overlayers, and full-solid-angle XPD can play a very useful role in such studies.

3. Photoelectron Diffraction Studies with Third Generation Synchrotron Radiation

There are at present several "third-generation" synchrotron radiation facilities either already operating or under construction, and these sources of very bright vacuum ultraviolet and soft x-ray radiation in roughly the 30-2000 eV range will permit a number of exciting new directions to be explored in both photoelectron diffraction and photoelectron holography. We illustrate some of these possibilities with data obtained at the Advanced Light Source (ALS) in Berkeley, using a new high-resolution spectrometer/diffractometer that has recently been built for use there.

A. Next-Generation Photoelectron Spectrometer/Diffractometer

In Fig. 6, we show a schematic view of a photoelectron spectrometer that has been configured for high-resolution, high-intensity photoelectron spectroscopy, diffraction, and holography measurements, and initially installed on bending magnet beamline 9.3.2 at the Advanced Light Source in Berkeley [2(f)]. Figure 7 shows a photograph of the system, with major components labelled. The electron energy analyzer is a tuneable-resolution large-diameter hemispherical electrostatic system (Scienta ES200) that has been incorporated into a chamber which can rotate over 60° in the plane of the electron storage ring. This rotation is made possible by a large-diameter bellows linking the chamber to the beamline, as shown in these figures. Such in-plane analyzer rotation, although common for much smaller analyzers mounted inside the vacuum system, has not been attempted before in such an *ex situ* mounting, and it permits probing the angular dependence of the fundamental photoelectron excitation cross section, keeping the photon-sample geometry fixed while measuring intensities over a large fraction of the 2π solid angle above the surface, and keeping the photoelectron-sample geometry fixed by scanning the analyzer synchronously with the sample polar-angle motion while measuring intensities as a function of light incidence direction. This analyzer is presently equipped with a single multichannel detector capable of an integrated count rate of about 500 kHz, but it will in the near future be modified so as to include a much higher speed multichannel detector operating up to the GHz range, as well as an alternative spin detector of the so-called microMott type that will be interchangeable *in situ*. The spherical grating monochromator in this beamline, together with the Scienta analyzer , are capable of operating at overall kinetic energy resolutions of $\Delta E/E_{kin} \approx 1:10^4$. The analyzer is also equipped with a demountable collimator at its entry to limit both the solid angle of acceptance to ~±1.5° for high angular resolution studies and the area of the sample surface seen by the analyzer. The 9.3.2 beamline optics also permit taking radiation both above and below the plane of the electron orbit, thus obtaining a high degree of left or right circular polarization, as well as linear polarization with in-plane operation. We discuss below the use of this capability in measuring circular dichroism effects in photoelectron angular distributions (CDAD). We now briefly consider some first results obtained with this instrumentation.

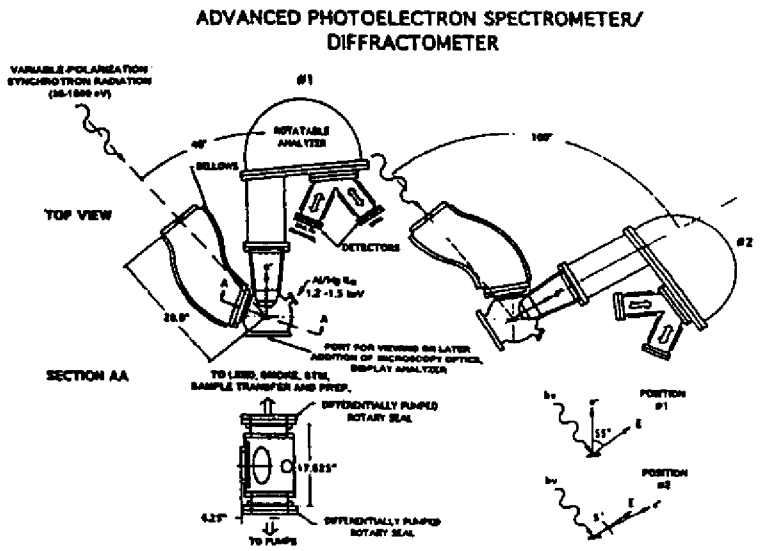

Fig. 6. Schematic drawing of the advanced photoelectron spectrometer/diffractometer (APSD) presently situated on beamline 9.3.2 of the Advanced Light Source. The rotation of the main chamber, including electron analyzer, and the range of photon-electron geometries possible are also indicated.

B. Full-Solid-Angle Photoelectron Diffraction from Clean-Surface and Bulk Atoms

In Fig. 8(a), we show the geometry for an experiment in which the surface and bulk W 4f peaks from a clean W(110) surface have been measured with this system. It is well-known that the clean (110) surface exhibits a surface component shifted to lower binding energy by 320 meV

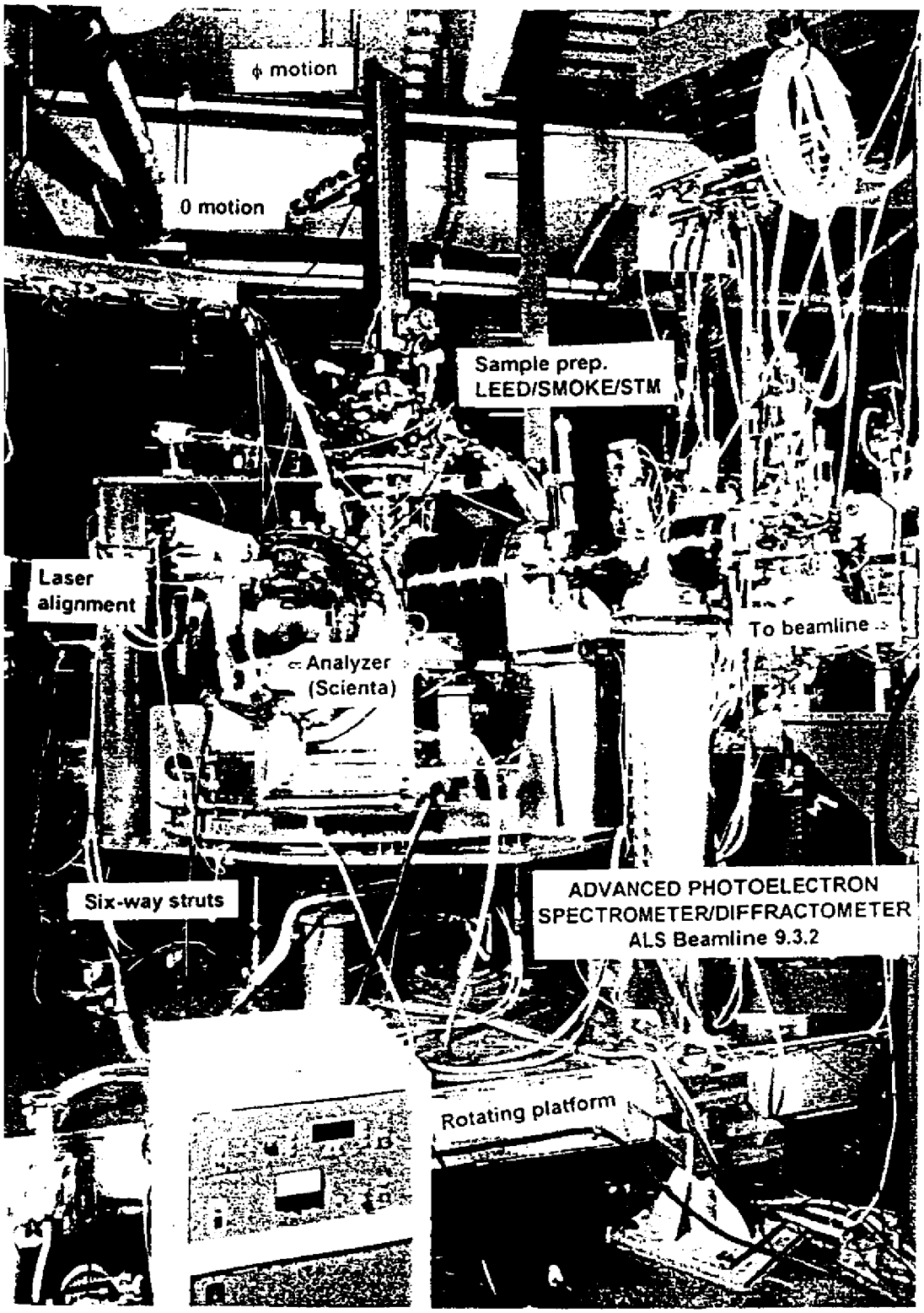

Fig. 7. Photograph of the APSD system in Fig. 6.

[8(a),28], and this is cleanly resolved in the spectrum of Fig. 8(b). The 120 meV full width at half maximum (FWHM) for the bulk peak is slightly narrower than anything measured before [28(a)], and is essentially limited by the various sources of natural linewidth for this level. PD has been measured before for this case [28(b)], but these studies involved only a few scans in azimuthal angle or in energy. The high rate of data acquisition possible with this new system (a spectrum like that in Fig. 8(b) can be obtained in 20 sec or less) has now permitted measuring essentially the full solid angle of data for both the bulk and surface peaks, as shown in Figs. 9(a) and 9(b), respectively [29]. The photoelectron energies here are also in the very surface sensitive 39-40 eV range. Thus, it will be possible in the future to obtain much more complete site-specific photoelectron diffraction information, and we discuss the application of this to holography below.

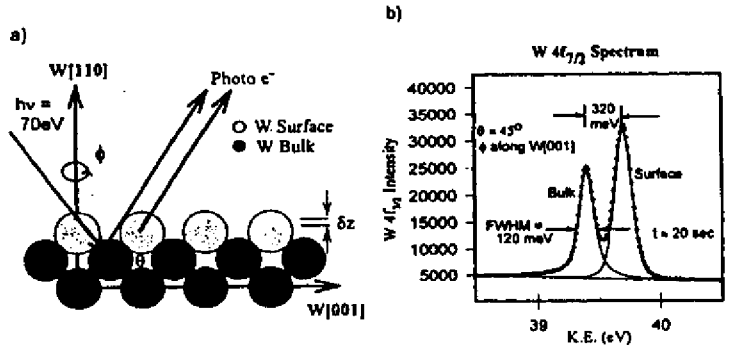

Fig. 8. (a) Experimental geometry used to study clean W(110), showing the two types of W atom sites resolved. (b) High-resolution W $4f_{7/2}$ spectrum from W(110), showing surface and bulk components. [From ref. 29.]

One immediate benefit of such data sets is the possibility of making more rigorous tests of the multiple scattering theory that is now being used by several groups to analyze PD data [10]. In particular, multiple-scattering and single-scattering calculations have been carried out to simulate these diffraction patterns [29], using programs developed by Kaduwela et al. [10(e)] and by Chen et al. [10(g)] and based on the convenient Rehr-Albers approximation for treating multiple scattering [10(d)]. These calculations have been carried out for a range of interlayer spacings z between the surface W layer and the second layer below, with PD-specific R-factors [26(c)] once more being used to determine the best estimate of the structure. Experiment and theory for the optimized

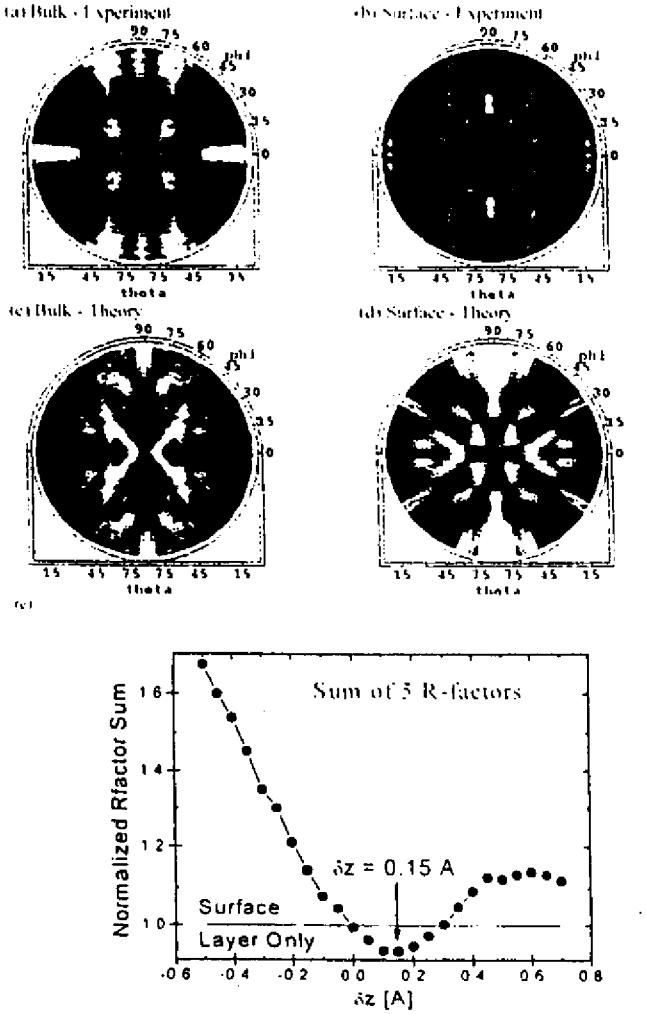

Fig. 9. Full-solid-angle W $4f_{7/2}$ photoelectron diffraction patterns (a) bulk-resolved experiment, (b) surface-resolved experiment, (c) bulk theory for the optimum interlayer distance, (d) surface theory for the optimum interlayer distance; and (e) R-factor comparison between experiment and multiple-scattering theory for the surface-atom W $4f_{7/2}$ photoelectron diffraction pattern of Fig. 9(b). The curve represents a normalized sum of five R-factors. The horizontal line corresponds to an R-factor for calculations in which no bulk scatterers were present [From ref. 29.]

distance are compared in Figs. 9(a)-(d), and the resultant R-factor curve from the more sensitive analysis of the surface-atom data is shown in Fig. 9(e). There is excellent agreement between experiment and theory for most of the features in the surface-atom diffraction pattern and very good agreement for the more complex bulk case, which involves emitters in various layers below the surface. The overall conclusion based on the surface diffraction pattern is that the surface W layer relaxes outward from the bulk position by 0.10-0.15±0.05 Å, corresponding to a very small change of 4.4-6.7% of the bulk interlayer spacing. These results furthermore agree in general with prior studies of this surface by PD and LEED [28(b) and refs. therein]. Corresponding SSC calculations based on the same input parameters show similar diffraction features, but are not found to describe the data as well as the MSC results shown in Fig. 9. Thus, MS effects will definitely need to be included for a quantitative description of such low-energy data.

C. Photoelectron Diffraction from Interface Atoms

The detailed structure of interfaces, e.g. between an epitaxial overlayer and the substrate on which it is grown, is clearly one of the most important current surface-structure problems. It is also a difficult problem to solve, because most surface structure probes either cannot uniquely resolve interface atoms from their neighbors or cannot probe very deeply below the surface. PD with high energy resolution has been shown capable of studying interface atoms that are at least a few atomic layers below the surface in studies by Olmstead and co-workers of insulator growth on a semiconductor [8(d)], and future experimental capabilities promise to expand this application dramatically.

As one illustration of what is now possible, we show in Fig. 10 photoelectron spectra obtained with the same experimental system at the ALS for the case of ~1 ML of Fe and ~1 ML of Gd deposited on W(110) [30]. The first monolayer of Fe is known to grow in a (1x1) structure on W(110), with presumably a single unique bonding site for every Fe atom [31]. On the other hand, it has been shown by Tober et al [32] in a combined STM and LEED study that the first monolayer of Gd forms a lateral superstructure or Moiré pattern with (7x14) periodicity in which a hexagonal Gd(0001) layer is formed on the surface with relatively little lattice constant change relative to bulk Gd. However, this layer appears to be only weakly bound to the underlying W, and many types of Gd/W bonding sites are involved over the (7x14) unit cell. Fig. 10 compares W $4f_{7/2}$ photoelectron spectra from the clean surface in (a) with those from Fe/W in (b) and Gd/W in (c). The W atoms at the Fe/W and Gd/W interfaces are clearly resolved from those in the bulk. For Fe/W, the second-layer W atoms are even displaced from the bulk due to their strong interaction with the Fe, as noted previously by Shinn et al. [31]. Thus, it has been possible to measure separate PD patterns for the bulk and interface W atoms in these systems, and for Fe/W also for the second-layer W atoms, and to use these data to directly probe the metal-metal interface structure [30]. Some of these results for Fe/W are shown in Fig. 11. Because there are many scattering geometries between either an interface W atom or a bulk W atom and the overlying Gd atoms, we find that the interface Gd/W diffraction patterns are very much like the clean-surface diffraction patterns, and that the two bulk

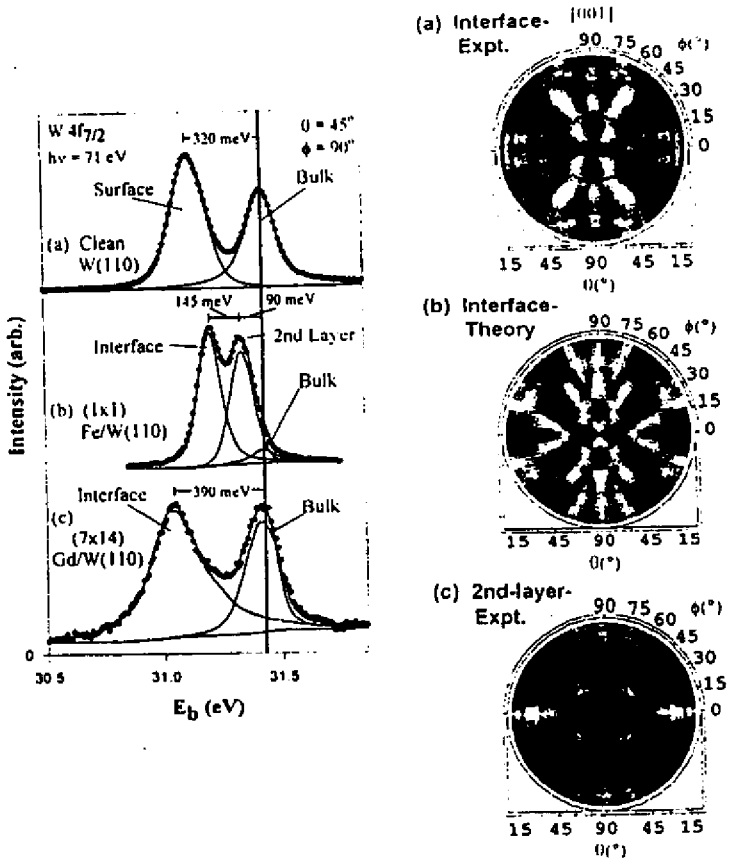

Fig. 10. (Upper left) W $4f_{7/2}$ photoelectron spectra taken with a photon energy of 71 eV from (a) the clean W(110) surface, (b) 1 ML of Fe in a (1x1) overlayer on W(110), and (c) 1 ML of Gd in a (7x14) Moiré superstructure on W(110). [From ref. 30.]

Fig. 11. (Upper right) Full-solid-angle W $4f_{7/2}$ photoelectron diffraction patterns for the (1x1) Fe/W(110) system taken from (a) experimental data for the -235 meV-shifted W interface peak, (b) theoretical multiple scattering calculations for the (1x1) Fe/W(110) interface with an optimized two-fold bridge adsorption site for Fe, and (c) experimental data for the -90 meV-shifted W 2nd-layer peak. The photoelectron kinetic energy outside the surface was E_{kin} = ~40 eV in all cases. The data shown span takeoff angles relative to the surface from 12° to 90°(normal emission), and the W(100) azimuth is toward the top of the page in each of these stereographic projections. [From ref. 30.]

patterns are also very similar [30] Thus, The Gd scattering here overall acts to simply produce a nearly uniform background of intensity underneath the dominant pattern associated with W-atom scattering. But for the Fe/Gd case, the interface-atom diffraction is much different from the clean surface diffraction (compare Fig. 11(a) with Fig. 9(b)) . Therefore, for this case, comparisons of experiment with theory for different Fe bonding geometries via R-factors [26(c)] has permitted determining the bonding site (a twofold bridge site which corresponds to continuing the W crystal) and the Fe-W interlayer distance (2.17 Å) for the first time. Future applications of high-resolution interface PD to metal-metal, metal-semiconductor, and oxide semiconductor overlayer growth are therefore very promising.

D. Time-Dependent Measurements

We now consider the possibility of time-resolved measurements of surface reaction kinetics and atomic structure. To illustrate this, Ynzunza et al. [29] studied an initially clean W(110) surface which was exposed to a constant O_2 pressure of 3×10^{-9} torr (riding on a base pressure in the system of 2×10^{-10} torr). The reaction of this surface with oxygen was monitored over 70 min. by taking many photoelectron spectra in rapid succession. We show in Figs. 12(a)-(c) three W $4f_{7/2}$ spectra that were taken at the beginning, middle, and end of this rapid accumulation of over 180 spectra. Each spectrum was obtained in 20 sec, and this provides some idea as to how rapidly it should be possible to accumulate PD data in parallel to such time-resolved spectra in the future. Four distinct states of W are seen in these spectra (as described below). The quantitative time evolution of these states is shown in Fig. 12(d), where intensities have been derived by fitting appropriate peak shapes to each spectrum of the series. The clean-surface peak decays to zero intensity over about the first 20 min. and concomitant with this, the bulk peak actually grows in intensity over about the first 10 min. Simultaneously, a peak due to W atoms in interaction with chemisorbed oxygen begins to grow in at about 0.35 eV higher binding energy than the bulk peak, reaching its maximum intensity (corresponding to about 0.5 ML coverage) after about 30 min. Finally, a peak due to W atoms more strongly bound to oxygen in an incipient-oxide like state begins to grow in just as the chemisorbed species reaches its maximum intensity. This state can grow finally to a 1.0 ML coverage before saturating, although this is not reached during the time of our measurements. These data thus clearly indicate a strong interrelationship of these states via the kinetic mechanisms that are operative for this oxidation reaction, and further analysis of these results in this context is now underway. However, these data already illustrate the considerable potential for future studies of nanostructure growth kinetics in which intensities are measured at several key energies or directions as a function of time, thus yielding also time-resolved PD. With further optimization of the bend-magnet beamline and end station on which these data were obtained, and/or making the same type of measurement on a more intense third-generation undulator beamline, we estimate that it should be possible to improve these data acquisition speeds by at least one order of magnitude, and probably two, so that individual spectra could ultimately be obtained in ~0.1-1.0 seconds.

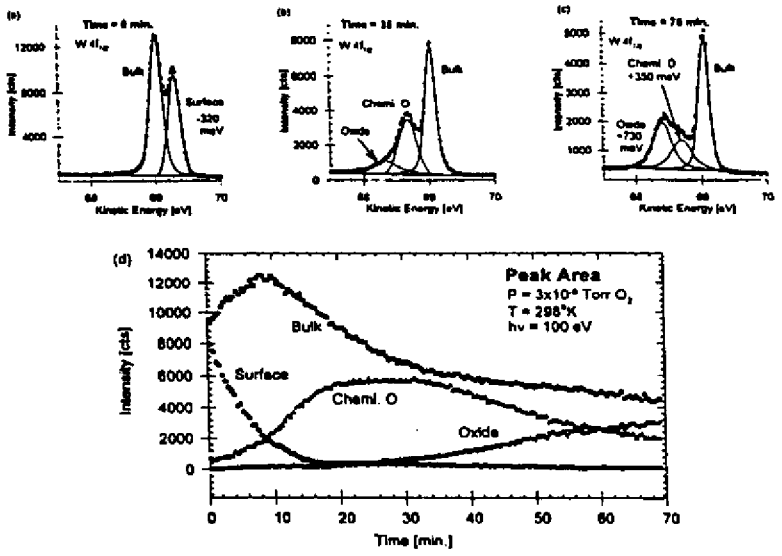

Fig. 12. Time- and state- resolved W $4f_{7/2}$ photoelectron spectra for a clean W(110) surface exposed to oxygen at 3×10^{-9} torr for 70 min.: (a) t = 0 min.--initial clean surface showing the surface core level shifted peak at -320 meV with respect to bulk; (b) t = 35 min--surface after 35 min., showing the two oxygen-induced peaks at -350 meV and -730 meV; (c) t = 70 min.--final spectrum of the series after 70 min, showing the increase of the oxide peak at the expense of the chemisorbed oxygen peak; (d) time dependence of the intensities of the four peaks observed in these spectra. [From ref. 29.]

E. Circular Dichroism in Photoelectron Diffraction

(i) Non-magnetic systems. Circular dichroism represents another aspect of photoelectron diffraction that can be explored with synchrotron radiation, and we here briefly discuss its essentials, with more detailed accounts appearing elsewhere [33-37]. Circular dichroism in photoelectron angular distributions (often termed CDAD) was first observed for emission from a core-level for the case of an adsorbed molecule on a surface (C 1s emission from CO/Pd(111)) by Schönhense and co-workers [33(b)]. Such dichroism is defined via the difference between the intensities with left and right circular-polarized light (I^{RCP} and I^{LCP}, respectively), and is most conveniently measured using

a normalized asymmetry : $A_{CDAD} = \left[I^{RCP}(\hat{k}) - I^{LCP}(\hat{k})\right] / \left[I^{RCP}(\hat{k}) + I^{LCP}(\hat{k})\right]$, where $\hat{k}$ is the direction of electron emission. Changes in this asymmetry with direction by as much as ±75% were observed for CO/Pd. These measurements thus made it clear that even a non-chiral molecule can exhibit circular dichroism when it is fixed to a surface, provided that a certain geometrical condition is satisfied between the molecular axis $\hat{n}$, the light incidence direction $\hat{q}$, and $\hat{k}$: in particular A_{CDAD} can be non-zero whenever these three vectors are not co-planar. Such data were first interpreted using quantum-chemical theoretical methods for the isolated adsorbate molecule [33(b),34(a)]. However, the chirality must be associated with the final-state photoelectron wave function, since the initial core state is spherically symmetric. This suggests using a photoelectron diffraction point of view to interpret such results, as has been done more recently [34(b)]. In this picture, all information on the chirality is carried in the geometry of the light incidence, the locations of all scatterers around the emitter, and the direction of electron emission. This approach thus permits easily including contributions to the dichroism from atoms in the substrate. PD calculations were in fact found to correctly predict the effects seen for CO/Pd(111) [34(b)].

More generally, it has now been realized that the emission from *any* core level in a single crystal specimen can exhibit non-zero CDAD effects, provided that the plane containing $\hat{q}$ and $\hat{k}$ does not also coincide with a plane of mirror symmetry perpendicular to the surface [35,36]. In particular, intensity distribution measurements for Si 2s and 2p emission from a Si(001) surface in a geometry with the light incident along the normal by Daimon et al. [35] have shown that there are not only very strong CDAD effects of as high as ~±20%, but that the observed diffraction patterns exhibit what can in first approximation be described as peak "rotations" across mirror planes perpendicular to the surface. Daimon et al. [35] have also discussed a simple physical model for understanding why individual features should appear to rotate one way in azimuth with one polarization and the other way with the other polarization. This model considers the transfer of the z-component of angular momentum from the radiation to the outgoing photoelectron wave, and its influence on forward scattering diffraction peaks. In addition, more quantitative multiple scattering PD calculations have been shown to well predict these alterations in diffraction patterns with a change in polarization [36].

More recent data obtained at the ALS by Daimon, Ynzunza et al. [37] confirm the generality of such peak rotations, but also more quantitatively show that additional peak distortions beyond a simple rotation can occur in changing from LCP to RCP. The case studied was a 1 ML coverage of oxygen on W(110) in the incipient oxide overlayer associated with the +730 meV peak in Fig. 12(c), and prepared in a manner described previously [38]. The experimental geometry was very similar to that of the Si(001) experiment [35], and is shown in Fig. 13(a). The W 4f spectra for this surface shown in Fig. 13(b) are clearly split into oxide and bulk components, with a separation between them of 0.73 eV. In the solid curves of Figs. 13(c),(d), we show single azimuthal scans of the oxide and bulk peaks for a takeoff angle θ with respect to the surface of 26.5°, and with excitation by linear-polarized (LP) light, as well as circular-polarized LCP and RCP light. With LP excitation, the

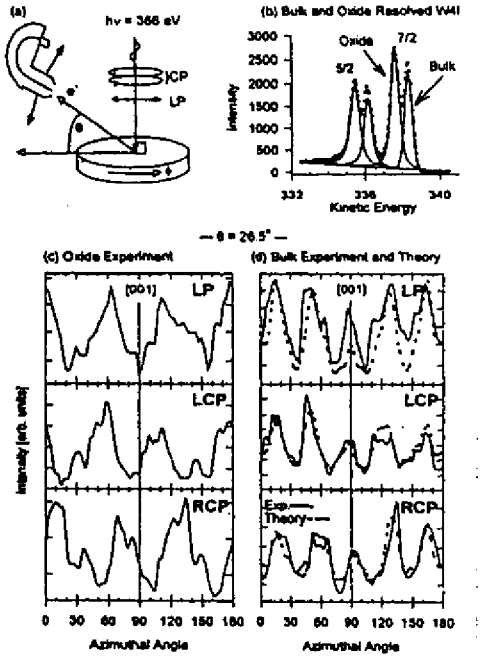

Fig. 13. Circular dichroism in the angular distributions of photoelectrons from (1x1)O/W(110) with a (1x12) incipient-oxide superstructure: (a) the experimental geometry, with radiation incident normal to the surface and the rotating analyzer of Figs. 6 and 7 being used to measure at various takeoff angles θ with respect to the surface; (b) a W 4f spectrum with oxide and bulk peaks resolved; (c),(d) azimuthal scans at a takeoff angle of 26.5° for both oxide and bulk W 4f components for linear-polarized (LP) light, left-circular-polarized (LCP) light, and right-circular-polarized (RCP) light (solid curves). In (d) is also a comparison of the experimental curve for bulk emission with theoretical photoelectron diffraction calculations (dashed curve). [From ref. 37.]

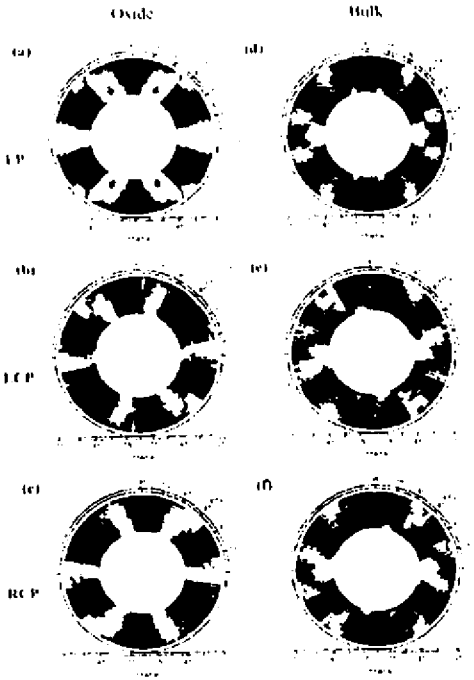

Fig. 14. Large-solid-angle photoelectron diffraction patterns for oxide [(a),(b),(c)] and bulk [(d),(e),(f)] W 4f emission from a (1x1)-(1x12) oxygen overlayer on W(110). Panels (a) and (d) are for LP excitation, (b) and (e) are for LCP excitation, and (c) and (f) are for RCP excitation. Note the apparent rotation of certain major features in the patterns between LCP and RCP, particularly for the oxide patterns [From ref. 37.]

correct mirror symmetry across the [001] azimuth at ϕ = 90°is seen to within statistical uncertainty in both oxide and bulk. But with LCP and RCP excitation, differences which can be interpreted as peak "rotations", as well as other relative intensity changes and distortions, are found. The rotations appear as a general leftward movement of peaks and valleys with LCP, and a general rightward movement with RCP. The overall diffraction patterns furthermore obey the symmetry expected from the normal-incidence experimental geometry, as the mirror image of the LCP intensities across [001] for both oxide and bulk are within statistics identical to the RCP intensities. These symmetries and rotations are even more clearly seen in the large-solid-angle data sets in Fig. 14. In particular, an approximately ±5-6° rotation of the most prominent peaks is very clear in the oxide data between LCP and RCP. MSC PD calculations furthermore well predict both the overall rotations of features and the peak distortions seen here [37], and the dashed curves in Fig. 13(d) present some preliminary theoretical results.

Thus, such circular dichroism in photoelectron angular distributions is expected to be a very general phenomenon for any non-magnetic system (or by implication, also any magnetic system), and such effects can also be quantitatively described by PD theory. One reason for being interested in this phenomenon is that circular dichroism in magnetic systems (*magnetic* circular dichroism or MCD) is usually a much more subtle difference in intensities that may be only a few % in magnitude [39]. MCD effects in photoelectron angular distributions are due to a combination of the spin-orbit and multiplet splittings inherent in core spectra [39(a)], as well as possible spin-dependent exchange scattering from magnetic atoms during photoelectron escape from the surface [9]. By contrast, the CDAD effects discussed in this section are due to the strong Coulomb-plus-exchange scattering from every atom in the specimen. Thus, properly allowing for the latter will be essential to accurately measuring the former [34(b),35,36]. The same kind of allowance will be necessary in the more recently discovered magnetic linear dichroism (MLD) [40(a)] and magnetic unpolarized dichroism (MUD) [40(b)] effects in core photoelectron angular distributions.

(ii) Magnetic systems. As a recent example of the kinds of magnetic circular dichroism effects seen in ferromagnetic systems, we show in Fig. 15(a) some Gd 4d spectra from Gd(0001) obtained by Morais, Denecke et al. [41]. Both of these spectra are split into various final-state multiplets, with the five-component fine structure clearly resolved for the higher energy peak. The Gd has been magnetized in a mirror plane of the crystal, along $\vec{M}$ as shown in the inset, and the two spectra correspond to having $\vec{M}$ parallel or anti-parallel to the plane containing $\hat{q}$, the surface normal $\hat{n}$, and $\hat{k}$ (i.e., the angle ϕ_M = 0° or 180°, respectively). There is a dramatic difference between these spectra, and it results in the MCD signal shown in Fig. 15(b), which is as large as ±30%. Figure 15(c) now shows a free-atom theoretical calculation of such effects by Van der Laan et al. [42], and the agreement with experiment is excellent, including a state-by-state prediction of the degree of MCD.

Figure 16 now shows the azimuthal angular dependence of this Gd MCD, with the sample being rotated about its normal so as to vary ϕ_M and the MCD always being measured as a difference

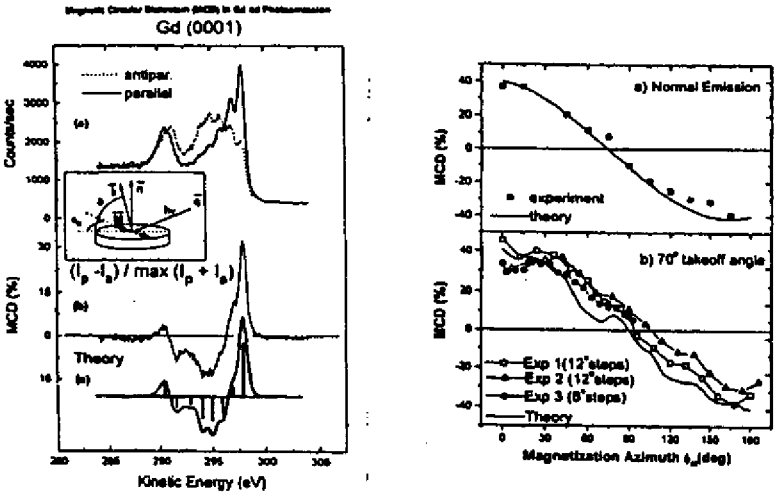

Fig. 15. (Upper left) (a) Gd 4d photoemission spectra taken at a photon energy of 450 eV using left circular polarized light. The solid-curve spectrum was taken with the sample magnetization $\vec{M}$ parallel to the azimuth of the light incidence direction (Φ_M=0°), and the dotted-curve spectrum an antiparallel arrangement (Φ_M = 180°). (b) The normalized difference of the spectra in (a) or MCD asymmetry. (c) A free-atom theoretical calculation of the MCD asymmetry, taken from ref. 42. The inset shows the experimental geometry. [From ref. 41.]

Fig. 16. (Upper right) Angle dependence of the overall MCD effect for Gd 4d core-level emission. (a) Normal emission, (b) Electron takeoff angle = 70° (20° from normal). In both cases the solid lines show theoretical curves calculated for the respective cases. In (a) the calculation is for a free atom, in (b) it is for emission from an atomic cluster three layers thick in order to account for photoelectron diffraction effects. [From ref. 41.]

of spectra for ϕ_M and ϕ_M + 180°. There is a strong ~±35% variation of this signal with ϕ_M, including an overall cosine-like behavior that is characteristic of the free atom and dominant in Fig. 16(a) for normal emission. But additional reproducible fine structure in the ~±5% range is also present in Fig. 16(b) for emission 20° off normal. Such magnetic circular dichroism effects in photoelectron angular distributions (MCDAD) thus will be useful in studying magnetic order and local structure in an element-specific way, but it is clear that a fully quantitative understanding and use of them will require considering final state photoelectron scattering and diffraction.

4. Spin Polarization in Photoelectron Diffraction

A. Multiplet Splittings and Spin-Polarized Photoelectron Diffraction

Being able to separately measure intensity distributions for spin-up and spin-down photoelectrons should in principle make it possible to determine the short-range magnetic order around a given type of emitter via what has been termed spin-polarized photoelectron diffraction (SPPD) by Sinkovic et al. [9(a),(b)]. This is because the scattering of spin-up and spin-down photoelectrons is slightly different in the presence of magnetic order, primarily due to the exchange interaction between the photoelectron and the unfilled d or f valence shells responsible for the magnetic order. The use of multiplet splittings for deriving such spin-resolved spectra is by now well-established for both simple antiferromagnets [9] and ferromagnetic metals [43], and we show in Fig. 17(a) a multiplet-split 3s spectrum from antiferromagnetic $KMnF_3$(100) that is one of the few cases studied to date by SPPD. The predominant spin polarizations of the two components are indicated in this figure, together with the overall electron configurations and L-S multiplets associated with each peak: the $3s^1...3d^5\ ^5S$ peak at lower kinetic energy is expected to be 100% up-spin and the $3s^1...3d^5\ ^7S$ peak to be 71% down-spin. *Spin polarizations are in the case of such multiplets measured with respect to the emitting atom or ion.* The spin-up/spin-down intensity ratio $I_\uparrow / I_\downarrow$ in such multiplets has been measured previously for both $KMnF_3$(110) and MnO(001) as a function of both temperature and direction [9(b)-(d)], and these results indicate some sort of high-temperature magnetic phase transition which occurs at 3-5 times the bulk transition temperature or Néel temperature of these materials. Some of these results due to Hermsmeier et al. [9(c),(d)] are shown in Fig. 18(a). Plotted in this figure is the temperature dependence of the spin asymmetry S(T), a normalized spin-up/spin-down intensity ratio that is defined so as to go to zero at the high-temperature (HT) "paramagnetic" limit of the experimental data via $S(T) = 100[R_T - R_{HT}]$ (in %)[9(b)-(e)]. Here, $R = I_\uparrow / I_\downarrow$, with the subscripts indicating the temperature at which the ratio was measured. For a low average kinetic energy of 111 eV, this asymmetry shows dramatic changes at about 540 K or 4.5 times the bulk Néel temperature, with the sense of this change being opposite for two different directions of observation. Thus, the effect shows a strong dependence on emission direction. For a high kinetic energy of 1405 eV for which exchange scattering effects are expected to be negligibly small, no such effects are observed. These experimental results are in qualitative agreement with PD calculations assuming that there is an

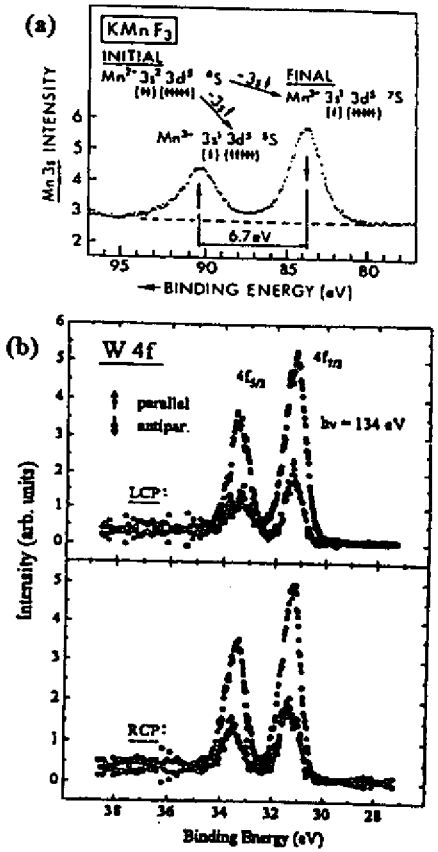

Fig. 17. Spin-polarized core photoelectron spectra: (a) a Mn 3s spectrum from $KMnF_3$, with the electronic states and spin polarizations relative to the emitting Mn^{2+} ion indicated [From ref. 9(e).]; (b) a spin-resolved W 4f spectrum from W(110), excited by LCP light (top panel) and by RCP light (bottom panel). [From ref. 46.] In (b), the spin-resolved intensities as measured parallel or antiparallel to the light incidence direction $\hat{q}$ are indicated.

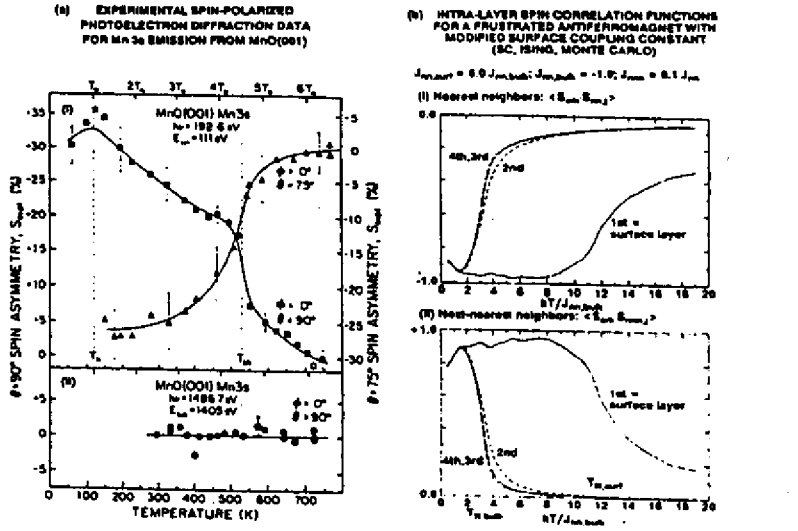

Fig. 18. (a) Temperature-dependent experimental spin-polarized photoelectron diffraction asymmetry data based upon Mn 3s spectra from MnO(001): In the top panel (i), the electron energy is 111 eV and data for two different directions are shown; in the lower panel (ii), the energy is 1405 eV, and only one direction (normal emission) is shown. [From refs. 9(c),(d).] (b) Monte Carlo theoretical calculations showing an elevated surface Néel temperature for a surface exchange interaction that is six times stronger than that in the bulk. [From ref. 44.]

abrupt loss of short-range antiferromagnetic order at this high temperature, even though the bulk long-range order is lost at the much lower Néel temperature [9(d)]. One possible explanation for this effect is that there are local domains of short-range order that persist up to this higher temperature and then abruptly disappear. Another possibility recently discussed by Zhang et al. [44] is that the surface Néel temperature could be significantly higher than that in the bulk. Figure 18(b) shows the results of Monte Carlo calculations for a simple-cubic Ising antiferromagnet of Mn^{2+} ions in which the surface exchange coupling between Mn^{2+} spins has been set to be 6.0 times that in the bulk. For this simple model, it is seen that the spin-spin correlation functions for both nearest neighbor Mn^{2+} ions and next nearest neighbor Mn^{2+} ions show a relatively sharp transition in the surface layer (here indicated as the first layer) at a temperature that is a few times the transition temperature for the rest of the layers (i.e., the bulk in this model). Thus, it is also possible that these SPPD experiments have detected a highly elevated surface Néel temperature for this system, although it remains to be seen whether the surface exchange coupling is really enough higher than that in the bulk to produce such an effect.

In a more recent study, Tober et al. [45] have used the analogous Gd 4s and 5s multiplets to carry out SPPD measurements on Gd(0001), an interesting system because it is thought to have a surface Curie temperature that is 20-60 K above that of the bulk [46]. For this case, the relevant multiplets are $ns^1...4f^7$ ^7S and ^9S in symmetry, and they again yield the predominantly spin-up and spin-down intensities, respectively. The temperature dependence of the spin asymmetry S for this case is shown in Fig. 19 for four different cases, three directions with 5s emission and one direction with 4s emission. There is strong angular dependence in the 5s results, with broad peaks spanning ~ 275-375 K for the first two cases in Figs. 19(a) and (b), and no visible effect of temperature beyond a monotonic decrease for the third case in (c). This angular dependence is found to be consistent with diffraction theory [45]. The presence of two distinct transitions is particularly dramatic in the Gd 4s results of Fig. 19(d). Overall, these results thus confirm that there are two different magnetic transitions about 60-80 K apart, with the bulk Curie temperature being at 293 K and the surface Curie temperature at about 360-380 K.

Although further experiments and theory will be necessary to fully clarify the nature of the magnetic transitions observed in SPPD experiments to date [9,45], these studies indicate the considerable potential of this technique for studying short-range magnetic order in both antiferromagnetic and ferromagnetic systems. Exploiting this potential should be assisted enormously by the use of next-generation synchrotron radiation facilities.

B. Spin Polarization from Circular-Polarized Excitation

Spin-polarized photoelectrons can also be produced by exciting a spin-orbit-split core level with circular-polarized radiation, making use of the well-known Fano effect from atomic physics [47]. We illustrate this with some very recent data obtained by Starke et al. [48] for the non-magnetic system W(110), in the experimental geometry shown in the inset between Figs. 20(b) and (c). Figure 17(b) shows spin-resolved W 4f spectra for the two different circular polarizations of the

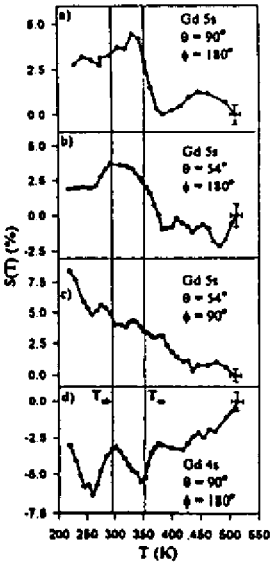

Fig. 19. Experimental spin asymmetry S(T) derived from Gd 5s and 4s multiplet intensity ratios $R = I_\uparrow / I_\downarrow$ as a function of temperature T for (a) Gd 5s emission along the normal ($\theta = 90°$, $\phi = 180°$ along the "c" axis), (b) Gd 5s emission ($\theta = 54°$, $\phi = 180°$ along the "-b" axis), (c) Gd 5s emission ($\theta = 54°$, $\phi = 90°$ along the "a" axis), and (d) Gd 4s emission ($\theta = 90°$, $\phi = 180°$ along the "c" axis). Note the strong angle and level dependence of these results, with broad peaks in (a) and (b) for 5s, no visible effect in (c) for 5s, and two distinct features in (d) for 4s.

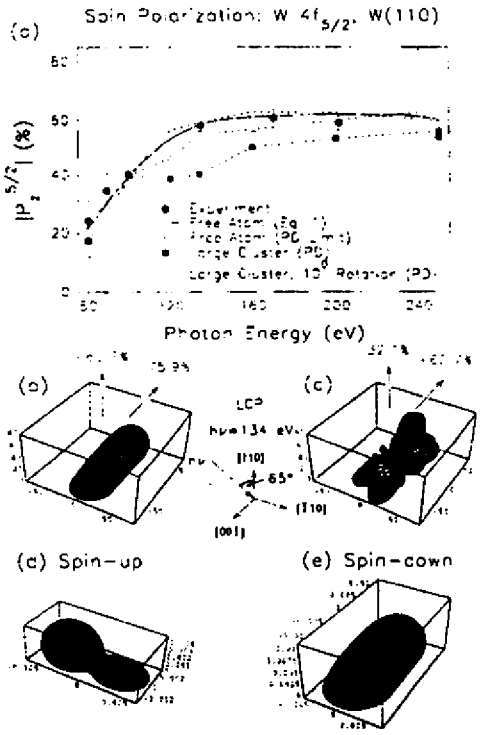

Fig. 20. Spin-polarization in W 4f spectra excited by circular-polarized light from W(110): (a) the absolute value of the $4f_{5/2}$ polarization as a function of photon energy, with experiment compared to both free-atom and MS cluster PD calculations; (b) the three-dimensional spin polarization for a free atom in the experimental geometry shown in the inset and with an excitation energy of 134 eV; (c) as (b), but for a MS cluster PD calculation in a 5-atom cluster (an emitter below 4 surface scatterers); (d),(e) the separate spin-up and spin-down intensities excited in a free-atom. [From ref. 48.]

incident radiation, with the photoelectron spin being measured either parallel or antiparallel to the resulting direction of the light helicity, which is in turn parallel or antiparallel to the light incidence direction. That is, for this case, the *spin polarizations are referenced externally to the direction of light incidence*. There is a clear and strong spin polarization in both the 5/2 and 7/2 components, with the expected change of sign as the polarization of the light is changed. These spin polarizations are also found to increase markedly with photon energy from 80 eV to about 130 eV, and to remain large at about 50-60% over the range from 130 eV to 240 eV, as shown in Fig. 20(a). These polarizations are thus comparable to the 70-100% expected for simple *ns* multiplets in high-spin atoms of the type discussed previously for Mn [9] and Gd [45], and immediately suggest using such spectra also as internal sources of spin-polarized photoelectrons for SPPD studies. Such SPPD studies based on circular-polarized excitation have in fact been attempted for the first time recently [49]. Theoretical calculations of such effects have also been carried out. For example, for the W $4f_{5/2}$ results in Fig. 20(a), the simple free-atom calculations [50] shown as the solid curve agree very well with the energy dependence seen in experiment. MSC PD calculations from a large W(110) cluster in the nominal geometry of the experiment show the same general trend of polarization variation with energy as experiment, but have a significant dip at about 125 eV that is not observed experimentally. However, a small azimuthal rotation of the cluster by 10° that is within the experimental uncertainty of alignment suppresses this dip, and yields very good agreement with experiment as well. This predicted change in the PD polarizations with cluster orientation however suggests that photoelectron scattering, *even in a non-magnetic lattice*, can significantly alter the degree of spin polarization in a core spectrum [48]. The origin of these changes is that the separate spin-up and spin-down intensity distributions excited from the 5/2 or 7/2 levels have very different shapes, and that they thus sample differently the non-magnetic scatterers around the emitting atom. These effects are illustrated in the theoretical calculations in Figs. 20(b)-(e): the three-dimensional distribution of polarization for the free-atom in (b) is significantly altered when emission from a 5-atom cluster is considered in (b). This alteration can furthermore be qualitatively understood from the dramatic differences in the separate spin-up and spin-down intensity distributions for the free-atom in (d) and (e). Such effects should be very general, very strong, and occur in both non-magnetic and magnetic surroundings.

Finally, we note that the separate measurement of spin-up and spin-down intensities over a range of directions and/or energies can in principle lead to spin-polarized photoelectron *holography* [51], a prospect that we discuss briefly below.

5. Photoelectron Holography

We now turn to the potential for directly determining short-range atomic structures by holographically inverting data sets that may span both photoelectron direction and energy. All of these so-called "direct" methods involve carrying out some kind of mathematical operation that is closely akin to a Fourier transform on a large set of data involving ≥1000 distinct intensity

measurements. In general, the photoelectron intensity $I(\vec{k})$ for a certain wave vector $\vec{k}$ is converted to a normalized χ function in a standard way via:

$$\chi(\vec{k}) = \frac{I(\vec{k}) - I_0(\vec{k})}{I_0(\vec{k})} \quad \text{or} \quad \frac{I(\vec{k}) - I_0(\vec{k})}{I_0(\vec{k})^{1/2}} , \tag{1}$$

where $I_0(\vec{k}) \propto |\phi_0|^2$ is the intensity in the absence of any scatterers. Measurements of $\chi(\vec{k})$ are made at several directions of emission (several $\hat{k}$), and also perhaps at several energies of excitation (several $|\vec{k}|$). The most common way to holographically invert such a $\chi(\vec{k})$ data set is to carry out the following transform over the relevant volume in k-space, as first suggested by Szöke for single-energy data [12(a)], and amplified upon by Barton et al. [12(d)], and by Tong et al. [14(a)] for multi-energy data:

$$U(\vec{r}) = \left| \int_{|\vec{k}|} \exp(-i|\vec{k}||\vec{r}|) \iint_{\hat{k}} \exp(i\vec{k}\cdot\vec{r}) \chi(\vec{k}) |\vec{k}|^2 \, d|\vec{k}| \sin\theta_k \, d\theta_k \, d\phi_k \right| . \tag{2}$$

Here θ_k and ϕ_k are the angles defining the direction $\hat{k}$. Several prior experimental and theoretical studies have obtained successful three-dimensional images of near-neighbor atoms using this approach or close relatives of it [12-21], and it seems clear that, at least for back scattering atoms around a given emitter, useful structural conclusions can be drawn. These images include some obtained with only one energy [e.g., 15(a),(b),(d); 17], and others in which the transform of Eq. (2) is modified to allow for non-ideal scattering effects and/or to somehow focus on the region of image space that is most nearly ideal [e.g., 13,14,15,18(b),(c),20].

We will illustrate this method as applied to a first-of-a-kind extended data set obtained by Denlinger, Rotenberg et al. on beamline 7.0 at the Advanced Light Source, and analyzed recently by Len et al. [52]. The clean W(110) surface discussed previously has been used as a test case, with the intensities of the bulk and surface peaks in spectra such as that in Fig. 8(b) being measured over essentially the full hemisphere above the surface and for kinetic energies between 41 eV (about like that in Figs. 8(b) and 9) and 302 eV. A total of about 20,000 unique intensities was thus measured. Figure 21 shows the separate data sets thus derived for both bulk and surface emission, in a cutaway volume representation. Fig. 22(a) now shows a holographic atomic image reconstructed via Eq. (2) (here referred to as Method A from among several considered elsewhere [15(g),52]) from the surface-atom intensity data, as first normalized to produce $\chi(\vec{k})$ via Eq. (1). This image is in the vertical $(\bar{1}\,1\bar{2})$ plane, the emitter position is indicated by a dashed square, and the ideal positions of the neighboring atoms are indicated by circles. We see that the back scattering atom just below the emitter (denoted $[\bar{1}\,\bar{1}\,0]$) is very well imaged, with a sharp peak that is centered very close to the true atomic position (within ~0.2 Å). The side scattering atoms surface atoms just next to the emitter (denoted $[\frac{1}{2}\frac{\bar{1}}{2}\frac{\bar{1}}{2}]$ and $[\frac{\bar{1}}{2}\frac{1}{2}\frac{1}{2}]$) are also clearly imaged, but with some smearing in the vertical

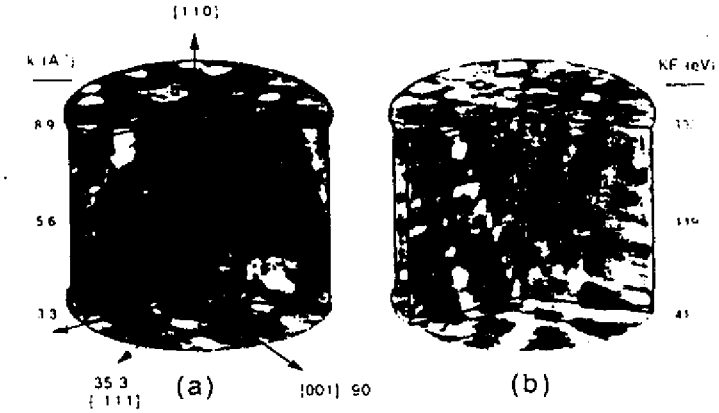

Fig. 21. Cutaway views of volume representations of the normalized intensities $\chi(k)$ for W $4f_{7/2}$ emission from clean W(110), with (a) from the bulk peak and (b) from the surface peak (as shown in Fig. 8(b)). The vertical scales are kinetic energy (KE) and wavevector, and each plane represents a stereographic projection of a nearly full-hemisphere data set taken over directions from the surface normal to within 10° of the surface. [From ref. 50.]

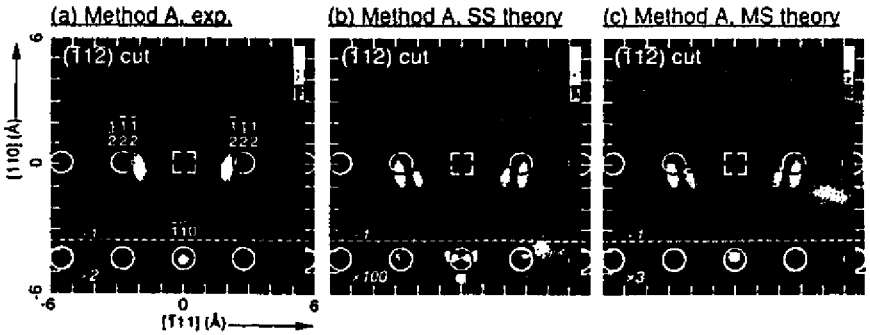

Fig. 22. W(110) holographic atomic images in the vertical $(\bar{1}\,1\bar{2})$ plane, as reconstructed using Eq. (2) from (a) the experimental surface-resolved W $4f_{7/2}$ data set of Fig. 21(b), (b) corresponding single scattering calculations, and (c) corresponding multiple scattering calculations. The surface-atom emitter is indicated by a dashed square, and the near-neighbor scatterers by circles. Image intensities for vertical coordinates ≤-3.5 Å have been rescaled, with the scale factors indicated on the figures. [From ref. 50.]

direction, and positions that are further from the true positions, being shifted inward toward the emitter by about 0.7 Å and downward from the surface plane by about 0.2 Å. Nonetheless, this experimental image could be used to provide a good first-order estimate of the local geometry around these W surface atoms if it were not already known (e.g. via the PD analysis in Fig. 9 and other prior studies discussed in ref. 28).

In Figs. 22(b) and (c) are now shown corresponding images derived from both single scattering and multiple scattering calculations. Single scattering is found not to agree as well with experiment, for example for the form and relative intensity of the image of the back scattering atom. The image of this atom is found to be split and much weaker in intensity than is found in experiment. Multiple scattering is found to much better predict the image of this back scattering atom in both form and intensity. Both theoretical images are found to show a doubling of the side scattering atomic images that is not as evident in experiment, but they agree in predicting inward and downward shifts in the center of gravity of these images, as seen in experiment. Thus, experiment and multiple scattering theory are in very good agreement, but with the experimental images being even cleaner representations of these nearest-neighbor atomic images than found in theory.

Similar results for a bulk emitter are not as encouraging, with the forward scattering atoms above a typical emitter showing elongated and shifted images that would make it difficult to use them for a precise structural prediction [52]. Various other imaging algorithms (denoted Methods A', B-D) have also been applied to these surface and bulk holographic data to assess the degree to which they improve the atomic images [52]. Overall, it is concluded that backscattering atoms below and side-scattering atoms beside a given emitter that is in turn at or near the surface can be imaged successfully, with forward scattering atoms above an emitter that is below the surface not being imaged as accurately. Large data sets of the type considered here should permit exploiting holographic imaging to a maximum degree in the future, although it should not be necessary for most cases to obtain more that 3,000-5,000 intensities to accurately image the near-neighbor region [15(e),(f)].

6. Spin-Polarized Photoelectron Holography

We turn now to another intriguing prospect for the future of spin-resolved photoelectron diffraction studies: the possibility of directly imaging the scatterer spins around a given emitter via holographic inversion methods. We have already noted that two core photoelectron peaks can often be found at relatively close-lying energies that are strongly spin-polarized in an opposite sense. This might be due to a core multiplet splitting or a spin-orbit doublet excited with circular polarization, or some mixture of these two effects. Thus, it is in principle possible to separately measure $\chi_\uparrow(\bar{k})$ and $\chi_\downarrow(\bar{k})$ for the two different spin orientations, and this could lead via spin-dependent scattering effects to the holographic imaging of the local magnetic order around a given type of emitter [51]. There are two obvious spin-sensitive imaging algorithms based on Eq. (2) and separate measurements of $\chi_\uparrow(\bar{k})$ and $\chi_\downarrow(\bar{k})$ [51(b),(c)]:

$$\Delta(\bar{r}) = U_\uparrow(\bar{r}) - U_\downarrow(\bar{r}) , \qquad (3)$$

with obvious notation, and

$$\Delta'(\bar{r}) = \left| \int_{|\bar{k}|} \exp(-i|\bar{k}||\bar{r}|) \iint_{\bar{k}} \exp(i\bar{k}\cdot\bar{r}) \left[\chi_\uparrow(\bar{k}) - \chi_\downarrow(\bar{k}) \right] |\bar{k}|^2 \, d|\bar{k}| \sin\theta_k d\theta_k d\phi_k \right| , \qquad (4)$$

which is simply an image like $U(\bar{r})$ but calculated only on the difference of the spin-up and spin-down χ's. Additional vector-based spin-sensitive holographic imaging functions have also been proposed by Timmermans et al. [51(a)].

As a brief indication of the potential of this kind of photoelectron holography, we show in Fig. 23 holographic inversions of multiple scattering calculations for emission of spin-up and spin-down electrons from Mn^{2+} ions in a small planar cluster representing a portion of the MnO(001) surface [51(c)]. The cluster is shown in Fig. 23(a). Spin-up Mn^{2+} scatterers in this cluster have been distinguished from spin-down scatterers by having an additional exchange potential due to five unpaired 3d electrons that interacts only with spin-up photoelectrons. Spin-down scatterers have the same 3d exchange potential, but it interacts only with spin-down photoelectrons. Thus, the potential is slightly more attractive when the photoelectron spin is parallel to that of the scatterer. Spin-up and spin-down holograms were calculated in a fully-converged MSC way for 10 energies between 127 eV and 278 eV, and holographic images then derived via Eqs. (1)-(4). The normal images $U_\uparrow$ and $U_\downarrow$ in the plane of the cluster for spin-up and spin-down electrons are shown in Figs. 23(b),(c), together with the corresponding spin-sensitive images $\Delta(\bar{r})$ and $\Delta'(\bar{r})$ in Figs. 23(d),(e). The normal images show features for all of the atoms in the cluster, including the four non-magnetic O atoms. These spin-up and spin-down images are also very similar, as expected since the 3d exchange scattering is only 5-15% of the total effective scattering potential at these energies. By contrast, neither $\Delta(\bar{r})$ nor $\Delta'(\bar{r})$ contains any image intensity for the O atoms, verifying that either of these choices of imaging algorithm are predominantly sensitive to only the magnetic scatterers. The peaks and valleys in the spin-sensitive images are in general about 7-9% as strong in transform amplitude as the normal images, suggesting the experimental possibility of carrying out such imaging, albeit a non-trivial exercise. $\Delta(\bar{r})$ and $\Delta'(\bar{r})$ are also inherently different in that $\Delta'(\bar{r})$ images both orientations of scatterers in the same way, due the absolute value in Eq. (4), while $\Delta(\bar{r})$ changes sign when the scatterer is flipped, and thus also is sensitive to the orientation of a given scatterer. $\Delta(\bar{r})$ also involves the phase of the scattering factor, and thus can show sign changes over the region of a magnetic scatterer; however, it is clear from this and other calculations that the sign changes are exactly reversed if the orientation of the scatterer spin is flipped from up to down.

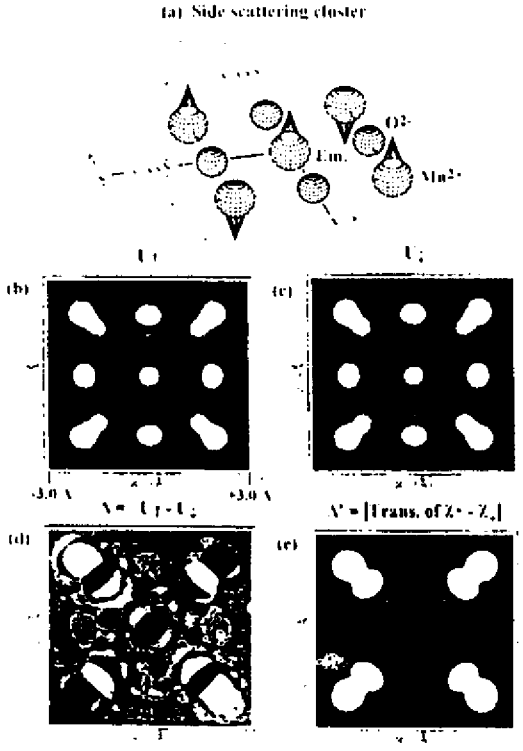

Fig. 23. A theoretical simulation of spin-polarized photoelectron holography: (a) a nine-atom cluster representing the (001) surface of MnO, with an emitter in its center, (b),(c) normal holographic images $U(\vec{r})$ $U(\vec{r})$ generated for the two different photoelectron spins by using Eq. (2) and holograms at 10 energies between 127 and 278 eV, (d) the spin-sensitive holographic image Δ generated by using Eq. (3), (e) the spin-sensitive holographic image $\Delta'(r)$ generated by using Eq (4) [From refs. 49(c),(d)]

Thus, spin-polarized photoelectron holography represents an intriguing and challenging experimental possibility for the future, but one well matched to the new synchrotron radiation sources that are now becoming available.

7. X-Ray Holography Using Fluorescence Emission

A. X-Ray Fluorescence Holography

We now consider an alternative type of holography involving the scattering of x-rays by the near neighbors to a given atom that is emitting fluorescent x-rays. This method has been discussed previously from a theoretical point of view [23], but the the much weaker diffraction modulations involved have prevented the first experimental explorations of it until very recently [24(a),(c),(d)]. The first method for doing such x-ray holography, which has been termed x-ray fluorescence holography (XFH), is illustrated in Fig. 2(b). As indicated, it is identical in philosophy to photoelectron holography, except that it is now a fluorescent x-ray which scatters instead of a photoelectron. This makes the scattering much weaker, by 10^{-3} or 10^{-4}, but much more ideal and optical in character. The former means that such measurements will be more difficult to measure, but the latter means that they should be more accurate, and thus worth assessing. Comparing Fig. 2(a) with Fig. 2(b) also points out the fundamental difference between a classic x-ray diffraction (XRD) measurement and XFH. In XRD, scattered waves ϕ_1, ϕ_2, ϕ_3,...from the various atomic planes in a sample *with long-range order* constructively interfere to yield various Bragg reflections, and the reference wave ϕ_0 is lost into the crystal. Thus, a direct holographic inversion of such data is not possible, although there are by now several well-established approaches for solving the resulting "phase problem" so as to determine unique atomic structures [53], and more recently, the use of x-ray standing waves has also been discussed for this purpose [54(a)]. In XFH by contrast, the reference wave is involved in producing the diffraction pattern, which is created by the scattering from the near neighbor atoms involved in the *short-range order* around a given emitter. Thus, a true hologram is generated, and inversion of it using Eqs. (1) and (2) becomes feasible. Scattering of fluorescent x-rays from the *long-range order* in the crystal also can occur, and this produces features known as *Kossel lines* which have also been suggested as an alternate way of doing x-ray holography [54(b)]. In fact, photoelectrons exhibit such features as well, which are called *Kikuchi bands* [55]. But we will focus here on the short-range-order effects in XFH that are completely analogous to the dominant effects in a normal photoelectron diffraction pattern.

The first XFH measurements were performed recently by Tegze and Faigel [24(a)]. They measured the hologram by monitoring the single-energy Sr Kα emission (E = 14.10 keV, k = 7.145 Å) from a single crystal of $SrTiO_3$. Approximately 2,400 intensities were measured over a cone of 60° half angle above the surface. The final hologram was found to have anisotropies in intensity of $\Delta I/I_0 \approx 0.3\%$. These small effects mean that much more demanding detector counting statistics are required in x-ray holography measurements than with comparable photoelectron holography measurements in which $\Delta I/I_0$ can be 50%. The reconstruction of this hologram via the algorithm of

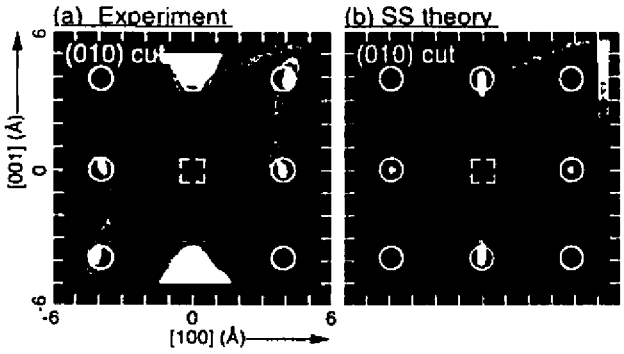

Fig. 24. Single-energy x-ray fluorescence holography (XFH) atomic images of $SrTiO_3$ in the vertical (010) plane, obtained from (a) experimental [24(a)] and (b) theoretical [24(b)] Sr Kα $\chi(k)$ data sets, via Eq. (2). The Sr emitter site is indicated by the dashed square, and nearest-neighbor and next-nearest-neighbor Sr scatterers are indicated by circles.

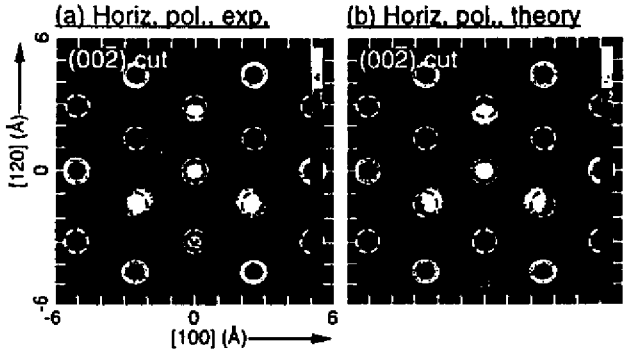

Fig. 25. Multiple energy x-ray holography (MEXH) atomic images of α-Fe_2O_3(001) in the horizontal (00$\bar{2}$) plane situated 6.89Å below each of the two types of Fe emitters, obtained from (a) experimental and (b) theoretical Fe Kα $\chi(k)$ data sets, via Eq. (2) [24(c)]. Fe scatterers in the bi-layer just above or below this plane are indicated by dashed circles, and Fe scatterers in relative positions common to both inequivalent Fe emitters are indicated by bold circles.

Eq. (2) (as now reduced to a single integral over direction) yields images of the Sr atoms only, as the much weaker scattering strength of the Ti and O atoms renders their images invisible compared to those of the Sr atoms. Fig. 24(a) shows the experimental image reconstructed in the vertical (010) plane [24(a)], and it is compared in Fig. 24(b) to an image reconstructed from a theoretical $\chi(\vec{k})$ for Sr Kα emission from a simple-cubic Sr cluster of 27 atoms (24(b)). Based on previously discussed criteria [13(d)], the expected atomic image resolutions at this hologram energy and angular range are $\delta x \approx 0.3$Å in the horizontal [100] direction, and $\delta z \approx 0.9$Å in the vertical [001] direction, and these numbers are in general agreement with the atomic images of Figs. 24(a),(b).

Reconstructing three-dimensional atomic images from a single-wavenumber hologram is known to yield twin images [12-15, 23]. That is, each $U(\vec{r})$ has associated with it a $U(-\vec{r})$ of equal magnitude. In any structure without inversion symmetry, these twins can overlap with real atomic images so as to confuse structural interpretation. In addition, the real and twin atomic images for a particular wavenumber and system can overlap completely out of phase, leading to an artificial suppression of atomic image intensities [23]. As in photoelectron holography [12(c),12(d),23(c)], it is thus advantageous to reconstruct direct atomic images from multiple-wavenumber $\chi(\vec{k})$ data sets so as to avoid such real-twin image overlaps. However, such XFH holograms cannot be measured at arbitrary wavenumbers, with the latter being limited by the intensity and number of fluorescence lines of the photoemitting species.

B. Multi-Energy Time-Reversed X-Ray Holography

To overcome this single-energy, or at most few-energy, limitation in XFH, another method for obtaining x-ray holographic information at conveniently chosen multiple energies has also very recently been proposed and demonstrated experimentally for the first time by Gog et al. [24(c)]. This method has been termed multiple energy x-ray holography (MEXH), and its basic principle is illustrated in Fig. 2(c). MEXH is essentially the time-reversed version of the conventional geometry of XFH (Fig. 2(b)), in that the wave motions are reversed, and the emitter and detector positions are interchanged. The exciting external x-ray beam now produces the reference and object waves, and the fluorescing atom acts only to detect the interference between the direct and scattered wavefronts. That is, the strength of the angle-integrated fluorescence signal is used to monitor the x-ray field strength at the emitting atom. The emitted x-rays are now collected by a distant detector with a large acceptance solid angle, in principle yielding much higher effective counting rates. The excitation x-ray source can also now be set to any energy above the fluorescence edge of the emitting species, thus permitting holograms at multiple wavenumbers and yielding in principle atomic images with no real-twin image overlaps [12(c),12(d),14(a),24(c)]. Specifically, multiple-wavenumber x-ray holograms have been measured to date for hematite (α-Fe_2O_3(001))[24(c)], and for Ge(001) [24(d)].

We illustrate the results of applying the inversion algorithm of Eq. (2) to both experimental MEXH data for (α-Fe_2O_3(001)) measured by Gog and co-workers on Beamline X-14A of the National Synchrotron Light Source at Brookhaven National Laboratory [24(c)] and to theoretical

simulations of this data. Fe Kα fluorescence was excited by horizontally polarized radiation at three energies in the range hν= 9.00keV to 10.30keV (k = 4.561Å^{-1} to 5.220Å^{-1}) that was incident on the sample surface over a polar range of $60° \le \theta \le 90°$ = surface normal. These data points were measured at three wavenumbers with intervals of δk = 0.329Å^{-1} (δE = 650eV), and at angular intervals of $(\delta\theta,\delta\phi)$ = (5°,5°), making a total of 435 unique measurements in a symmetry-reduced 1/3rd of the total solid-angle above the sample. The resulting modulation in $\chi(\vec{k})$ was ~0.5% and so similar to that found in the XFH results for $SrTiO_3$ [24(a)].

For comparison to the experimental results, a single-scattering model [23(c)] was used to calculate a theoretical $\chi(\vec{k})$ for an ideal α-Fe_2O_3(001) cluster containing 384 Fe atoms with two inequivalent Fe emitter sites, as appropriate to the hematite lattice. The O atoms were not included due to their much smaller scattering power. The orientation of the radiation polarization with respect to the crystal during the crystal rotation of the measurement was also taken into account.. In particular, because the incident radiation is linearly polarized, the x-ray scattering factor must be further multiplied by the Thomson scattering factor, which has the form $\sin^2\Theta_\varepsilon^{\hat{q}'}$, where $\Theta_\varepsilon^{\hat{q}'}$ is the angle between the polarization vector of the incident radiation $\vec{\varepsilon}$, and the direction $\hat{q}'$ of the scattered radiation. Thus, there will be nodes in the incoming scattered object waves along the polarization direction, and emitter atoms near this direction will not be as strongly influenced by x-ray scattering.

Figures 25(a) and (b) show the resulting MEXH atomic images for experiment and theory, respectively, in the [00$\bar{2}$] plane situated at z = -6.89Å below the emitter. There is excellent agreement between experiment and theory, and the positions of the atoms are very close to those in the known lattice (~0.2 Å inward displacement toward the emitter in experiment, and ~0.4 Å inward displacement in theory. The expected image resolutions in the horizontal ([100] and [1$\bar{2}$0]) directions are $\delta x = \delta y$ = 0.6Å [13(d)] The experimental and theoretical images are very similar in that three of the Fe atoms from the neighboring upper Fe bi-layer intrude into the [00$\bar{2}$] image plane. This intrusion is due to the limited wavenumber and angular range of the $\chi(\vec{k})$ data points in $\vec{k}$-space (as compared to the larger wavenumber and angular range for the electron $\chi(\vec{k})$'s in the previous section). This results in atomic images much less resolved in the vertical [001] direction and a resolution limit of δz ≈ 2.5 Å [13(d)]. Still, since these images are reconstructed from a multiple-wavenumber $\chi(\vec{k})$ data set, they should be freer of real-twin image overlaps [23(c)]. And they do indicate for the first time that such multi-energy data can be obtained and analyzed.

Thus, although x-ray holography using fluorescent x-rays is really just beginning to become a reality, it already shows considerable promise of becoming a complementary tool to x-ray diffraction and other surface and bulk structure probes. Its key advantages are that it is element-specific, that the theoretical interpretation is much simpler than for electrons, and that it can probe the short-range structure in systems for which long-range order may be lacking (as for example, in mosaic crystals). For certain kinds of surface, interface, and nanostructure work, both XFH and MEXH thus could be very useful, as discussed in more detail in recent comparative papers [24(e),24(f)]. Fully exploiting these new methods will also require the high brightness excitation sources of third-generation synchrotron radiation facilities

8. Concluding Remarks

Photoelectron diffraction is thus in some respects a mature technique, but at the same time it is one in which several exciting new possibilities for surface, interface, and nanostructure structure studies are found. The simple extension to taking full-solid-angle data often permits much clearer conclusions as to structures, especially when high energies with forward scattering are present, and complementary structure probes such as LEED and STM are used *in situ* with it. Next-generation instrumentation, particularly at third-generation synchrotron radiation sources, will much expand the use of chemical state- or site- resolved photoelectron diffraction, including the resolution of surface atoms and atoms at buried interfaces, time-dependent structural studies, and different types of dichroism in both non-magnetic and magnetic systems. The use of circular-polarized radiation for excitation shows up new phenomena in diffraction peak rotations and distortions, as well as making it possible to excite spin-polarized photoelectrons from any spin-orbit split level. Spin-polarized photoelectron diffraction and its more difficult cousin spin-polarized photoelectron holography also promise to provide information on local magnetic order in an element-specific, and also site-specific, way. Photoelectron holography also are beginning to provide direct three-dimensional images of short-range atomic structure, with useful accuracy for neighbors beside or below an emitter that is a surface of near-surface species. Finally, x-ray holography of either the x-ray fluorescence type or the multi-energy time-reversed type represents a new and closely related technique with considerable potential for imaging short-range atomic structure with higher accuracy.

Acknowledgments

We are very grateful to various co-workers and collaborators who have contributed greatly to the beamline installation and testing, equipment fabrication, and some of the specific studies presented here: T. Anderson, C. Cummings, P. Dyer, T. Gog, K. Higashiyama, B. Holbrook, W.R.A. Huff, P.D. Johnson, S.A. Kellar, J. Kortright, T. Lauritzen, G. Materlik, C.E. Miner, E.J. Moler, M. Rice, S. Ryce, D.A. Shirley, K. Starke, C. Westphal, R. Wright, H . Xiao, J.J. Zaninovich, and F. Zhang. This work has been supported by the Director, Office of Energy Research, Office of Basic Energy Sciences, Division of Division of Materials Sciences, of the U.S. Department of Energy, under Contract DOE-AC03-76SF00098 and the U.S. Office of Naval Research under Contract No. N00014-94-0162.

References

1. (a) K. Siegbahn, U. Gelius, H. Siegbahn and E. Olsen, Phys. Lett. 32A, 221 (1970); (b) C.S. Fadley and S.A.L. Bergstrom, Phys. Lett. 35A, 375 (1971); (c) A. Liebsch, Phys. Rev. Lett. 32, 1203 (1974); and Phys. Rev. B13, 544 (1976); (d) S. Kono, C.S. Fadley, N.F.T. Hall and Z. Hussain, Phys. Rev. Lett. 41, 117 (1978); (e) D.P. Woodruff, D. Norman, B.W. Holland, N.V. Smith, H.H. Farrell, and M.M. Traum, Phys. Rev. Lett. 41, 1130 (1978); (f) S.D. Kevan, D.H. Rosenblatt, D. Denley, B.-C. Lu, and D.A. Shirley, Phys. Rev. Lett. 41, 1565 (1978); (g) S. Kono, S.M. Goldberg, N.F.T. Hall, and C.S. Fadley, Phys. Rev. Lett. 41, 1831 (1978)
2. (a) C.S. Fadley, Phys. Scripta T17, 39 (1987); (b) C.S. Fadley in *Synchrotron Radiation Research: Advances in Surface Science*, R.Z. Bachrach (Ed.), (Plenum Press, New York, 1993); (c) C.S. Fadley, Surf. Sci. Repts. 19, 231 (1993); (d) C.S. Fadley et al., J. Electron Spectrosc. 68, 19 (1994); (e) C.S. Fadley, in *The Structure of Surfaces IV*, X. Xide, S.Y. Tong, and M.A. Van Hove (Eds.), (World Scientific, 1994); (f) C.S. Fadley, M.A. Van Hove, Z. Hussain, and A.P. Kaduwela, J. Electron Spectrosc. 75, 273 (1995).
3. (a) S.A. Chambers, Adv. in Phys. 40, 357 (1990); S.A. Chambers, Surf. Sci. Rep. 16, 261 (1992); (b) W.F. Egelhoff, Jr. in *Critical Reviews in Solid State and Materials Sciences*, 16, 213 (1990).
4. (a) L.J. Terminello, X.S. Zhang, Z.Q. Huang, S. Kim, A.E. Schach von Wittenau, K.T. Leung, and D.A. Shirley, Phys. Rev. B 38, 3879 (1988); (b) L.-Q. Wang, Z. Hussain, Z.Q. Huang, A.E. Schach von Wittenau, D.A. Shirley, and D.W. Lindle, Phys. Rev. B 44 , 13771 (1991); (c) D.A. Shirley et al., J. Electron Spectrosc. 68, 49 (1994).
5. H.P. Bonzel, Prog. in Surf. Sci. 42, 219 (1993) and references therein.
6. (a) A.M. Bradshaw and D.P. Woodruff, in *Applications of Synchrotron Radiation: High-Resolution Studies of Molecules and Molecular Adsorbates on Surfaces*, W. Eberhardt (Ed.), (Springer-Verlag, Berlin, 1993); (b) O. Schaff, G. Hess, V. Fernandez, K.-M. Schindler, A. Theobald, Ph. Hofmann, A.M. Bradshaw, V. Fritzsche, R. Davis, and D.P. Woodruff, J. Electron Spectrosc. 75, 117 (1995).
7. J. Osterwalder, P. Aebi, R. Fasel, D. Naumovic, P. Schwaller, T. Treutz, L. Schlapbach, T. Abukawa, and S. Kono, Surf. Sci. 331-333, 1002 (1995)
8. (a) D. Sebilleau, M.C. Desjonqueres, D. Chaveau, C. Guillot, J. Lecante, G. Treglia, and D. Spanjaard, Surf. Sci. Lett. 185, L527, (1987); (b) A. Nilsson, H. Tillborg, and N. Mårtensson, Phys. Rev. Lett. 67, 1015 (1991); (c) K.U. Weiss et al., Phys. Rev. Lett. 69, 3196 (1992); (d) J.D. Denlinger, E. Rotenberg, U. Hessinger, M. Leskovar, and M.A. Olmstead, Appl. Phys. Lett. 62, 2057 (1993), and E. Rotenberg, J.D. Denlinger, U. Hessinger, M. Leskovar, and M.A. Olmstead, J. Vac. Sci. Tech. B11, 1444 (1993).
9. (a) B. Sinkovic and C.S. Fadley, Phys. Rev. B31, 4665 (1985); (b) B. Sinkovic, B.D. Hermsmeier, and C.S. Fadley, Phys. Rev. Lett. 55, 1227 (1985); (c) B.D. Hermsmeier, J. Osterwalder, D.J. Friedman, and C.S. Fadley, Phys. Rev. Lett. 62, 478 (1989); (d) B.D. Hermsmeier, J. Osterwalder, D.J. Friedman, B. Sinkovic, T.T. Tran, and C.S. Fadley, Phys. Rev. B42, 11895 (1990); (e) B. Sinkovic, D.J. Friedman, and C.S. Fadley, J. Magn. Magn. Mater. 92, 301 (1991).
10. (a) C.H. Li and S.Y. Tong, Phys. Rev. Lett. 42, 901 (1979); (b) J.J. Barton and D.A. Shirley, Phys. Rev. B32, 1892 (1985); and Phys. Rev. B32, 1906 (1985); (c) A.P. Kaduwela, G.S. Herman, D.J. Friedman and C.S. Fadley, Phys. Scripta 41, 948 (1990), as based on a method described in (d); (d) J.J. Rehr and R.C. Albers, Phys. Rev. B41, 81139 (1990); (e) A.P. Kaduwela, D.J. Friedman, and C.S. Fadley, J. Electron Spectrosc. 57, 223 (1991); (f) D.K. Saldin, G.R. Harp, and X.Chen, Phys. Rev. B48, 8234 (1993); (g) Y. Chen, H. Wu, and D.A. Shirley, private communication.
11. (a) P.J. Orders and C.S. Fadley, Phys. Rev. B27, 781 (1983); (b) M. Sagurton, E.L. Bullock, and C.S. Fadley, Phys. Rev. B30, 7332 (1984) and (c) Surf. Sci. 182, 287 (1987); (d) V. Fritzsche and D.P. Woodruff, Phys. Rev. B46, 16128 (1992); and (e) P. Hofmann and K.M. Schindler, Phys. Rev. B47, 13942 (1993).
12. (a) A. Szöke, in *Short Wavelength Coherent Radiation: Generation and Applications*, D.T. Attwood and J. Bokor (Eds.), AIP Conference Proceedings No. 147 (AIP, New York, 1986); (b) J.J. Barton, Phys. Rev. Lett. 61, 1356 (1988); (c) J.J. Barton, J. Electron Spectrosc. 51, 37 (1990); (d) J.J.Barton,, and L.J. Terminello, paper presented at the Third International Conference on the Structure of Surfaces, Milwaukee, July 1990, and in *Structure of Surfaces III*, S. Y. Tong, M. A. Van Hove, X. Xide, and K. Takanayagi, eds., (Springer Verlag, Berlin, 1991) p. 107, and J.J. Barton, Phys. Rev. Lett. 67, 3106 (1991).
13. (a) G.R. Harp, D.K. Saldin, and B.P. Tonner, Phys. Rev. Lett. 65, 1012 (1990); (b) G.R. Harp, D.K. Saldin, and B.P. Tonner, Phys. Rev. B42, 9199 (1990); (c) B.P. Tonner, Z.-L. Han, G.R. Harp, and D.K. Saldin, Phys. Rev. B43, 14423 (1991); (d) G.R. Harp, D.K. Saldin, X. Chen, Z.L. Han, and B.P. Tonner, J. Electron Spectrosc. 57, 331 (1991); (e) D.K. Saldin, G.R. Harp, B.L. Chen and B.P. Tonner, Phys. Rev. B44, 2480 (1992); (f) D.K. Saldin, G.R. Harp, and B.P. Tonner, Phys. Rev. B45, 9629 (1992)
14. (a) S.Y. Tong, C.M. Wei, T.C. Zhao, H. Huang, and H. Li, Phys. Rev. Lett. 66, 60 (1991); (b) S.Y. Tong, H. Li, and H. Huang, Phys. Rev. Lett. 67, 3102 (1992); (c) S.Y. Tong, H. Huang, and C.M. Wei, Phys. Rev. B46, 2452 (1992); (d) J.G. Tobin, G.D. Waddill, H. Li, and S.Y. Tong, Phys. Rev. Lett. 70, 4150 (1993).
15. (a) S. Thevuthasan, G.S. Herman, A.P. Kaduwela, R.S. Saiki, Y.J. Kim, W. Niemczura, M. Burger and C.S. Fadley, Phys. Rev. Lett. 67, 469 (1991); (b) G.S. Herman, S. Thevuthasan, T.T. Tran, Y.J. Kim, and C.S. Fadley, Phys. Rev. Lett. 68, 650 (1992); (c) S. Thevuthasan, G.S. Herman, A.P. Kaduwela, T.T. Tran, Y.J. Kim, R.S. Saiki, and C.S. Fadley, J. Vac. Sci. Technol. A10, 2261 (1992); (d) S. Thevuthasan, R.X. Ynzunza, E.D. Tober, C.S. Fadley, A.P. Kaduwela, and M.A. van Hove, Phy. Rev. Lett. 70, 595 (1993); (e) P.M. Len, F.Zhang, S. Thevuthasan, A.P. Kaduwela, M.A. van Hove, and C.S. Fadley, J. Electron Spectrosc. 76, 351 (1995); (f) P.M Len, S. Thevuthasan, A.P. Kaduwela, M.A. van Hove, and C.S. Fadley, Surf. Sci. 365, 535 (1996); P.M. Len, S. Thevuthasan, A.P. Kaduwela, and C.S. Fadley, J. Electron Spectrosc., to appear.
16. (a) L.J. Terminello, J.J. Barton, and D.A. Lapiano-Smith, J. Vac. Sci. Technol. B10, 2088 (1992) and Phys. Rev. Lett. 70, 599 (1993); (b) B.L. Petersen, L.J. Terminello, and D.A. Shirley, Mat. Res. Soc. Symp. Proc. 307, 285 (1993); (c) B.L. Petersen, L.J. Terminello, J.J. Barton, and D.A. Shirley, Chem. Phys. Lett. 220, 46 (1994); (d) B.L. Petersen, Ph.D. Thesis, University of California-Berkeley, 1995; (e) L.J. Terminello, B.L. Petersen, and J.J. Barton, J. Electron Spectrosc. 75, 299 (1995).
17. Y. Zhou, X. Chen, J.C. Campuzano, G. Jennings, H. Ding, and D.K. Saldin, Mat. Res. Soc. Symp. Proc. 307, 279 (1993).
18. (a) H. Wu, G.J. Lapeyre, H. Huang, and S.Y. Tong, Phys. Rev. Lett. 71, 251 (1993); (b) H. Wu and G.J. Lapeyre, Phys. Rev. B51, 14549 (1995); (c) S.Y. Tong, H. Li, and H. Huang, Phys. Rev. B51, 1850 (1995)
19. M. Zharnikov, M. Weinelt, P. Zebisch, M. Stichler, H.-P. Steinrück, Surf. Sci. 334, 114-134 (1995), and references therein.
20. M.T. Sieger, J.M. Roesler, D.-S. Lin, T. Miller, and T.-C. Chiang, Phys. Rev Lett. 73, 311 (1994).
21. R. Denecke, R. Eckstein, L. Ley, A.E. Bocquet, J.D. Riley, and R.C.G. Leckey, Surface Science 331-333, 1085 (1995).
22. B.P. Tonner, D. Dunham, T. Droubay, J. Kikuma, J. Denlinger, and E. Rotenberg, J. Electron Spectrosc. 75, 309 (1995).

23. (a) M.Tegze and G. Faigel, Europhys. Lett. 16, 41 (1991); (b) C.S. Fadley. Mat. Res. Soc. Symp. Proc. 307, 261 (1993); (c) P.M. Len S. Thevuthasan, C.S. Fadley, A.P. Kaduwela, and M.A. Van Hove, Phys. Rev. B, Rap. Comm. 50, 11275 (1994).
24. (a) M. Tegze and G. Faigel, Nature 380, 49 (1996); (b) C.S. Fadley and P.M. Len, Nature 380, 27 (1996) and unpublished results; (c) T. Gog, P.M. Len, G. Materlik, G. Bahr, C. Sanchez-Hanke, and C.S. Fadley, Phys. Rev. Letters 76, 3132 (1996); (d) T. Gog, R.-H. Menk, F. Arfelli, P.M. Len, C.S. Fadley, and G. Materlik, Synchrotron Radiation News 9, 30 (1996); (e) P.M. Len, T. Gog, C.S. Fadley, and G. Materlik, Phys. Rev. B 55, February, 1997; (f) P.M. Len, C.S. Fadley, and G. Materlik, Proceedings of the X-96 Conference, Hamburg, September, 1996, AIP Proceedings, to appear., 1997.
25. (a) R.J. Baird, C.S. Fadley, and L.F. Wagner, Phys. Rev. B15, 666 (1977); (b) J. Osterwalder, T. Greber, S. Hüfner, and L. Schlapbach, Phys. Rev. B41, 12495 (1990); S. Hüfner, J. Osterwalder, T. Greber, and L. Schlapbach, Phys. Rev. B42, 7350 (1990); G.S. Herman and C.S. Fadley, Phys. Rev. B43, 6792 (1991); T. Greber, J. Osterwalder, S. Hüfner, and L. Schlapbach, Phys. Rev. B44, 8958 (1991); (c) R. Fasel, P. Aebi, R.G. Agostino, D. Naumovic, J. Osterwalder, A. Santaniello, and L. Schlapbach, Phys. Rev. Letters 76, 4733 (1996).
26. (a) H.C. Galloway, J.J. Benitez, and M. Salmeron, Surf. Sci. 198, 127 (1993) and J. Vac. Sci. Technol. A12, 2302 (1994); (b) ; Y.J. Kim, Ph. D. thesis, University of Hawaii-Manoa, 1995; Y.J. Kim, C. Westphal, R.X. Ynzunza, Z. Wang, H.C. Galloway, M. Salmeron, M.A. Van Hove, and C.S. Fadley, to be published; (c) R. Saiki, A. P. Kaduwela, J. Osterwalder, D.J. Friedman, C. S. Fadley, and C. R. Brundle, Surf. Sci. 282, 33 (1993).
27. (a) C. Günther, J. Vrijmoeth, R.Q. Hwang, and R.J. Behm, Phys. Rev. Lett. 74, 754 (1995); (b) J.C. Hamilton and S.M. Foiles, Phys. Rev. Lett. 75, 882 (1995); (c) S.D. Ruebush, R.E. Couch, S. Thevuthasan, Z. Wang, and C.S. Fadley, Surf. Sci. Lett., to appear.
28. (a) D.M. Riffe, G.K. Wertheim, and P.H. Citrin, Phys. Rev. Lett. 63, 1976 (1989); (b) D. Spanjaard, C. Guillot, M.-C. Desjonquères, G. Treglia, and J. Lecante, Surf. Sci. Repts. 5, 1 (1985); B. Kim, J. Chen, J.L. Erskine, W.N. Mei, and C.M. Wei, Phys. Rev. B48, 4735 (1993).
29. R.X. Ynzunza, F.J. Palomares, E.D. Tober, Z. Wang, H. Daimon, Y. Chen, Z. Hussain, J. Liesegang, M.A. VanHove, and C.S. Fadley, to be published.
30. E. D. Tober, R. X. Ynzunza, F. J. Palomares, Z. Wang, Z. Hussain, M. A. Van Hove, and C. S. Fadley, Phys. Rev. Lett, to appear.
31. N.D. Shinn, B. Kim, A.B. Andrews, J.L. Erskine, K.J. Kim, and T.-H. Kang, Mat. Res. Soc. Symp. Proc. 307, 167 (1993).
32. E.D. Tober, R.X. Ynzunza, C. Westphal, and C.S. Fadley, Phys. Rev. B53, 5444 (1996).
33. (a) G. Schönhense, Physica Scripta T31, 255 (1990); (b) J. Bansmann, Ch. Ostertag, G. Schönhense, F. Fegel, C. Westphal, M. Getzlaff, F. Schafers, and H. Petersen, Phys. Rev. B46, 13496 (1992); (c) G. Schönhense and J. Hormes, in *VUV and Soft X-Ray Photoionization*, U. Becker and D.A. Shirley (Eds.), (Plenum Press, New York, 1996).
34. (a) V. McKoy and J.A. Stephens, private communication; (b) C. Westphal, A.P. Kaduwela, M.A. Van Hove, and C.S. Fadley, Phys. Rev. B50, 6203 (1994).
35. H. Daimon, T. Nakatani, S. Imada, S. Suga, Y. Kagoshima, and T. Miyahara, Jpn. J. Appl. Phys. 32, L1480 (1993); and H. Daimon, private communication.
36. A.P. Kaduwela, H. Xiao, S. Thevuthasan, M.A. Van Hove, and C.S. Fadley, Phys. Rev. B 52, 14297 (1995).
37. H. Daimon, R.X. Ynzunza, F.J. Palomares, E.D. Tober, Z. Wang, Z. Hussain, M.A. Van Hove, and C.S. Fadley, to be published.
38. K.E. Johnson, R.J. Wilson, and S. Chiang, Phys. Rev. Lett. 71, 1055 (1993) and refs. therein.
39. (a) L. Baumgarten, C.M. Schneider, H. Petersen, F. Schafers, and J. Kirschner, Phys. Rev. Lett. 65, 492 (1990); (b) H. Ebert, L. Baumgarten, C.M. Schneider, and J. Kirschner, Phys. Rev. B44, 4406 (1991); (c) G.D. Waddill, J. Tobin, and D.R. Pappas, Phys. Rev. B46, 552 (1992).
40. (a) Ch. Roth, F.U. Hillebrecht, H.B. Rose, and E. Kisker, Phys. Rev. Lett. 70, 3479 (1993); F. Sirotti and G. Rossi, Phys. Rev. B49, 15682 (1994); (b) M. Getzlaff, Ch. Ostertag, G. H. Fecher, N.A. Cherepkov, and G. Schönhense, Phys. Rev. Lett. 73, 3030 (1994); N.A. Cherepkov, Phys. Rev. B50, 13813 (1994); A. Fanelsa, R. Schellenberg, F.U. Hillebrecht, E. Kisker, J.G. Menchero, A.P. Kaduwela, C.S. Fadley, and M.A. Van Hove, Phys. Rev. B54, 17962 (1996).
41. J. Morais, R. Denecke, R. X. Ynzunza, J.G. Menchero, J. Liesegang, J. Kortright, Z. Hussain, and C.S. Fadley, to be published.
42. G. van der Laan, E. Arenholz, E. Navas, A. Bauer, and G. Kaindl, Phys. Rev. B53, R5998 (1996).
43. F.U. Hillebrecht, R. Jungblut, and E. Kisker, Phys. Rev. Lett. 65, 2450 (1990); R. Jungblut, Ch. Roth, F.U. Hillebrecht, and E. Kisker, J. Appl. Phys. 70, 5923 (1991); R. Jungblut, Ch. Roth, F.U. Hillebrecht, and E. Kisker, Surf. Sci. 269/270, 615 (1992); T. Kachel, C. Carbone, and W. Gudat, Phys. Rev. B47, 15391 (1993); D.G. van Campen, R.J. Pouliot and L.E. Klebanoff, Phys. Rev. B48, 17533 (1993); P.D. Johnson, Y. Liu, Z. Xu, and D.J. Huang, J. Electron Spectrosc. 75, 245 (1995).
44. F. Zhang, S. Thevuthasan, R.T. Scalettar, R.R.P.Singh, and C.S. Fadley, Phys. Rev. B51, 12468 (1995).
45. E.D. Tober, F. J. Palomares, R.X. Ynzunza, Z. Wang, Z. Hussain, and C.S. Fadley, to be published.
46. D. Weller, S. F. Alvarado, W. Gudat, K. Scröder, and M. Campagna, Phys. Rev. Lett. 54, 1555 (1985); B. Kim, A. B. Andrews, J. L. Erskine, K. J. Kim, and B. N. Harmon, Phys. Rev. Lett. 68, 1931 (1992); H. Tang, D. Weller, T. G. Walker, J. C. Scott, C. Chapert et al., Phys. Rev. Lett. 71, 444 (1993); C. Rau and M. Robert, Phys. Rev. Lett. 58, 2714 (1987);C. Rau, J. Mag. and Mag. Mat. 31-34, 874 (1983);C. Rau and S. Eichner, Phys. Rev. B34, 6347 (1986) & in *Nuclear Methods in Materials Research*, K. Bethge, H. Burman, H. Jex, and F. Rauch (Eds.), (Viewig, Braunschweig, 1980), p. 354.
47. U. Fano, Phys. Rev. 178, 131 (1969); U. Heinzmann, J. Kessler, and J. Lorenz, Phys. Rev. Lett. 25, 1325 (1970).
48. K. Starke, A.P. Kaduwela, Y. Liu, P.D. Johnson, M.A. Van Hove, C.S. Fadley, V. Chakarian, E.E. Chaban, G. Meigs, and C.T. Chen, Phys. Rev. B53, R10544 (1996).
49. J.G. Tobin, C.D. Waddill, D.P. Pappas, E. Tamura, and P. Sterne, J. Vac. Sci. Tech. A13, 1574 (1995).
50. N.A. Cherepkov, Phys. Lett. A40, 119 (1972) and Adv. At. Mol. Phys. 19, 395 (1983).
51. (a) E.M.E. Timmermans, G.T. Trammell, and J.P. Hannon, Appl Phys. 73, 6183 (1993) and Phys. Rev. Lett. 72, 832 (1994); (b) C.S. Fadley, Mat. Res. Soc. Symp. Proc. 307, 261 (1993) and Surf. Sci. Rep. 19, 231 (1993); (c) A.P. Kaduwela, Z. Wang, M.A. Van Hove, and C.S. Fadley, Phys. Rev. B50, R9656 (1994); (c)Z.Wang, A.P. Kaduwela, S. Thevuthasan, M.A. Van Hove, and C.S. Fadley, to be published.
52. P.M. Len, E. Rotenberg, J.D. Denlinger, B.P. Tonner, S.D. Kevan, M.A. Van Hove, and C.S. Fadley,to be published.
53. W.N. Lipscomb, Acta Crystallographica 2, 193 (1949); J. Karla and H.A. Hauptmann, Acta Crystallographica 3, 18 (1950); K. Hümmer and H. Billy, Acta Crystallographica A38, 841 (1982); S. L. Chang, Phys. Rev. Letters 48, 163 (1982).
54. (a) M.J. Bedyzk and G. Materlik, Physical Review B32, 6456 (1985); (b) J.T. Hutton, G.T. Trammell, and J.P. Hannon, Phys. Rev. B31, 420 (1985), and Phy. Rev.B31, 743 (1985).

55. S. M. Goldberg, R. J. Baird, S. Kono, N. F. T. Hall, and C. S. Fadley, J. Electron Spectrosc. 21, 1 (1980); R. Trehan, C. S. Fadley and J. Osterwalder, J. Electron Spectrosc. 42, 187 (1987).

LBNL-39580

Invited paper appearing in
X-Ray and Inner-Shell Processes; 17th International Conference
R.L. Johnson, H. Schmidt-Boekering, and B.F. Sonntag, Eds.
AIP Conference Proceedings No. 389 (AIP, New York, 1997) pp. 295-319.

Atomic Holography with Electrons and X-rays

P. M. Len[1], C. S. Fadley[1,2], G. Materlik[3]

[1]*Department of Physics, University of California, Davis, CA 95616 USA*

[2]*Materials Sciences Division, Lawrence Berkeley National Laboratory, Berkeley, CA 94720 USA*

[3]*Hamburger Synchrotronstrahlungslabor (HASYLAB) am Deutsches Elektronen-Synchrotron (DESY), 22603 Hamburg, Germany*

Gabor first proposed holography in 1948 as a means to experimentally record the amplitude and phase of scattered wavefronts, relative to a direct unscattered wave, and to use such a "hologram" to directly image atomic structure. But imaging at atomic resolution has not yet been possible in the way he proposed. Much more recently, Szöke in 1986 noted that photoexcited atoms can emit photoelectron or fluorescent x-ray wavefronts that are scattered by neighboring atoms, thus yielding the direct and scattered wavefronts as detected in the far field that can then be interpreted as holographic in nature. By now, several algorithms for directly reconstructing three-dimensional atomic images from electron holograms have been proposed (*e.g.* by Barton) and successfully tested against experiment and theory. Very recently, Tegze and Faigel, and Gog *et al.* have recorded experimental x-ray fluorescence holograms, and these are found to yield atomic images that are more free of the kinds of aberrations caused by the non-ideal emission or scattering of electrons. The basic principles of these holographic atomic imaging methods are reviewed, including illustrative applications of the reconstruction algorithms to both theoretical and experimental electron and x-ray holograms. We also discuss the prospects and limitations of these newly emerging atomic structural probes.

INTRODUCTION

Historical Origin of Atomic Holography

Dennis Gabor first outlined in 1948 a direct experimental method of recording diffraction phases as well as intensities in an effort to surpass the then current resolution and lens aberration limits of electron microscopy and thus achieve atomic-scale image resolution (1). In Gabor's original scheme, an electron

wavefront (of wavenumber k_0 and wavelength λ_0) diverging from a point focus illuminates an object as well as a detector (or image plate) directly. The interference pattern at this detector involves the wavefronts scattered by the object, and explicitly records the phases of these wavefronts relative to the direct or reference wavefront (Fig. 1(a)). This interference "hologram" thus contains spatial information about the scattering object, which can be retrieved as an image in several ways. Gabor suggested that the developed image plate could simply be re-illuminated by a visible light reference wavefront (of wavenumber k *and wavelength* λ), as shown in Fig. 1(b). The wavefronts thus diffracted by the image plate would create a virtual image of the original object visible to the naked eye, and magnified by a factor of k_0/k. But the image reconstruction can also be performed numerically using a Fourier-transform-like integral, as first pointed out by Wolf (2). Holography is now of course widespread in science and technology, with lasers at usually optical wavelengths providing the reference waves. Note that, since the three-dimensional information of the r-space object field $u(\mathbf{r})$ (shown in Fig. 1 as an optical mask of the letter "F") is "encoded" holographically into a single-wavenumber two-dimensional k-space diffraction pattern $\chi(\hat{\mathbf{k}})$, both a real and twin image of the optical mask are retrieved. This is due to the loss of spatial information perpendicular to the plane of the image plate recording the diffraction pattern, and is by now overcome in optical holography by recording a volume of holographic intensities by means of a thick recording medium (3).

Until recently, Gabor's goal of imaging at atomic resolution had not been attained, due to the lack of a source of sufficiently coherent radiation at such short wavelengths. However, in 1986, Szöke observed that there is an atomic-scale analog of Gabor's holographic scheme: photoexcited atoms produce outgoing photoelectron or fluorescent-x-ray wavefronts, which then reach a far field detector either directly, or after scattering by neighboring atoms surrounding the emitter (5). With a sub-Ångström source size and wavelength, scattered wavefront amplitudes and phases from atoms surrounding the emitter can thus be referenced to the directly emitted wavefront, as shown for the case of fluorescence in Fig. 2(a). It was also pointed out a little later by Barton (4a,4b) and subsequently by Tong *et al.* (4c) that, by measuring diffraction patterns at different wavenumbers, three-dimensional spatial information could be completely encoded into a three-dimensional k-space volume of diffraction intensities $\chi(\mathbf{k})$, from which atomic images free of twin-image effects and other aberrations should be directly obtainable.

Two other approaches for obtaining structural information at the atomic scale should also be mentioned, as illustrated in Fig. 3. First, atomic order and electron density maps can be determined by so-called direct methods from the kinematical (single-scattering) diffraction technique, which exploits the translational symmetry (Bragg planes) of a crystal (6) (Fig. 3(a)). The second is the use of multiple, dynamical scattering from single crystals to solve the phase

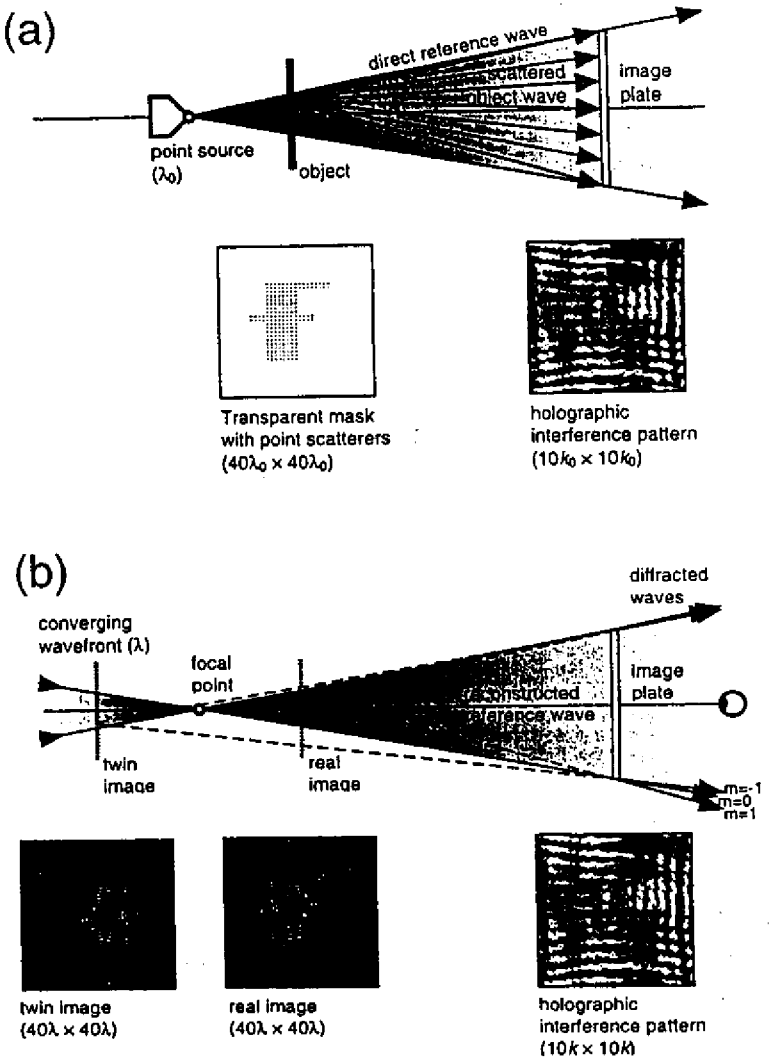

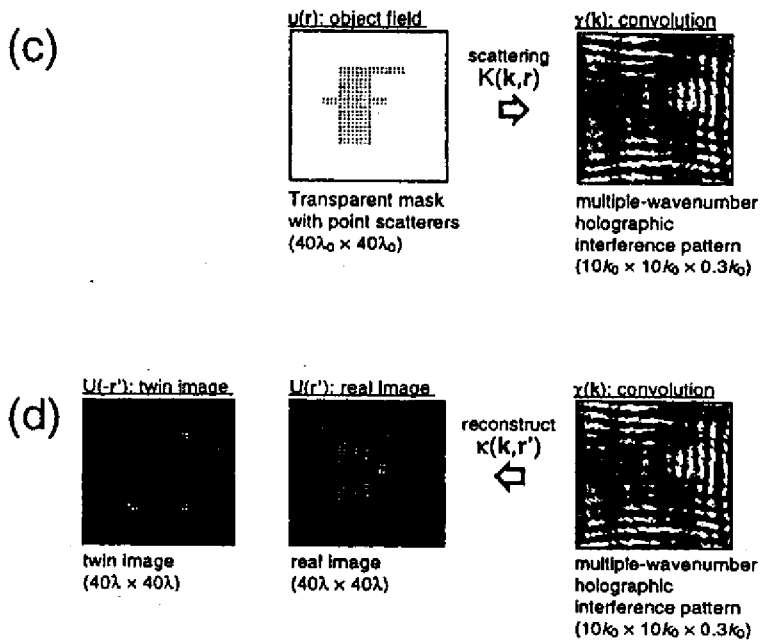

FIGURE 1. (a)-(b) An idealized numerical demonstration of the creation and inversion of single-wavenumber optical Gabor in-line holograms. (a) A point source of coherent radiation at the origin illuminates a transparent mask with point scatterers creating the letter "F" at r, as well as an image plate. This image plate is then exposed by a direct wavefront, as well as by the wavefronts scattered by the mask, which produces a holographic interference pattern. (b) The developed image plate is later re-illuminated by a reference wavefront. The wavefronts diffracted by the image plate produce a virtual (real) image of the mask at *r*, and a virtual conjugate twin image at the inverse position -r. (c)-(d) An analogous demonstration of the creation and inversion of optical multiple-wavenumber holograms. (c) A multiple-wavenumber normalized $\chi(k)$ hologram data set (of which one wavenumber is shown) is calculated from the object field $u(r)$ by means of an r-space convolution, using a kernel $K(k,r)$ that describes the emission and scattering physics involved (here, optical scattering in the far field regime). (d) The object field $u(r)$ is recovered as an image intensity $U(r')$ by a k-space deconvolution of $\chi(k)$, using a kernel $\kappa(k,r')$ that is sufficiently orthogonal to $K(k,r)$. Note that the conjugate twin image $U(r = -r')$ has been suppressed, due to the volume of k-space enclosed in the multiple-wavenumber $\chi(k)$ considered here.

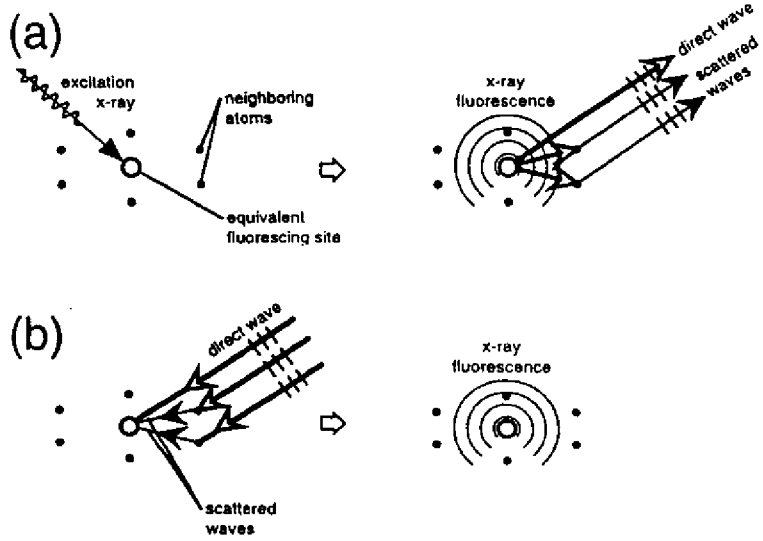

FIGURE 2. Atomic-scale analogs of Gabor holography. (a) The first scheme suggested by Szöke (5), in which an excitation x-ray first creates an inner-shell hole in one of many equivalent fluorescing atoms, and this atom then emits fluorescent x-ray (or electron) wavefronts that illuminate neighboring atoms, as well as a far field detector. This detector senses the interference between the direct wavefront and wavefronts scattered by the neighboring atoms. Moving the detector over a large solid-angle range builds up a holographic interference pattern. (b) The time-reversed case of (a) as suggested by Gog *et al.* (15), where a coherent far field excitation x-ray illuminates and photoexcites an emitter, and also illuminates and is scattered from atoms neighboring the emitter. The emitting atom senses the interference between the direct wavefront and wavefronts elastically scattered by the neighboring atoms. The net photoexcitation is then detected by a stationary, large solid-angle detector. Moving the far field source over a large solid-angle range builds up a holographic interference pattern. In both (a) and (b), atomic images can be reconstructed numerically.

problem of crystallography (7-9), either via Kossel lines (Fig. 3(b)) (10) or standing-wave methods (Fig. 3(c)) (11). The holographic approach is different from these two methods in that it uses the interference pattern which results from the direct unscattered wavefront emitted by a source atom, and the wavefronts which have been singly scattered from neighboring atoms. This does not require translational order (only rotational alignment) between the atomic neighborhoods to be imaged.

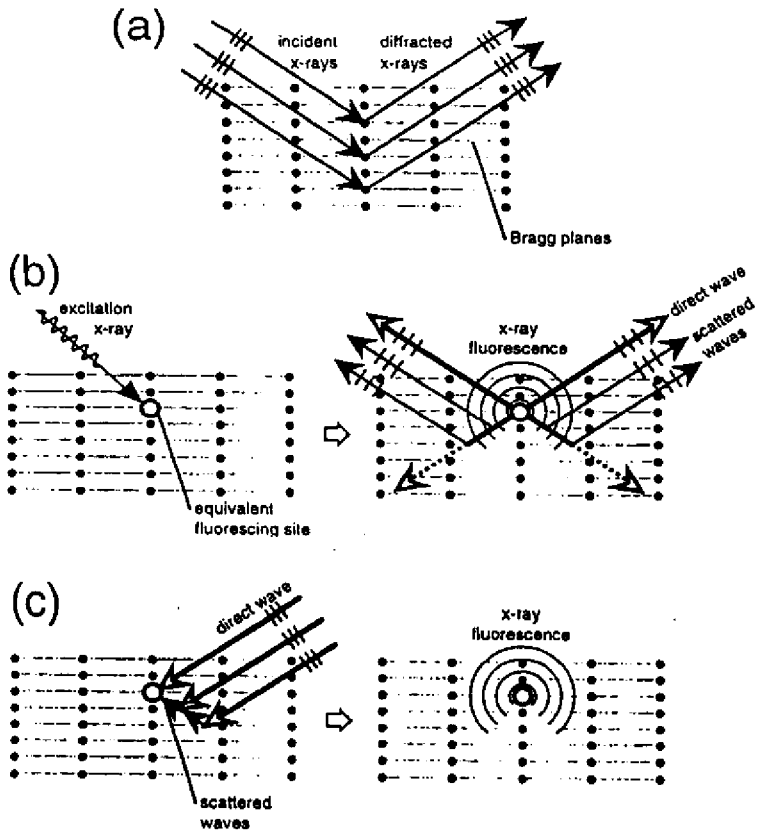

FIGURE 3. Diffraction probes of atomic structure related to atomic holography. (a) Conventional x-ray crystallography, where x-rays are diffracted by Bragg planes of atoms. Diffraction phases are determined by the simultaneous analysis of many Bragg intensities and other methods. (b) Kossel patterns (or Kikuchi bands, for the case of electrons). Fluorescent x-rays (or electrons) from a photoexcited emitter are diffracted by Bragg planes of atoms. Diffraction phases are thus here directly referenced to the unscattered portion of the fluorescence. (c) X-ray standing waves. This is the optical reciprocal of (b), where a coherent plane wave illuminates a fluorescing atom either directly, or after being scattered by Bragg planes of atoms. The interference between these wavefronts determines the amount of fluorescence by the emitter. Note that in all these above cases, the structure to be determined must have long-range atomic order, in contrast to the methods illustrated in Fig. 2.

Basic Principles of Atomic Holography

The process by which three-dimensional atomic image intensities are numerically reconstructed is to first measure the intensity $I(\mathbf{k})$ from a localized source over some range of directions $\hat{\mathbf{k}} = \mathbf{k}/k$ and perhaps also some range of wavenumbers k. Normalized holographic intensities $\chi(\mathbf{k})$ are then derived from either $[I(\mathbf{k})-I_0(\mathbf{k})]/\sqrt{I_0(\mathbf{k})}$ or $[I(\mathbf{k})-I_0(\mathbf{k})]/I_0(\mathbf{k})$, where $I(\mathbf{k})$ is the raw measured intensity, and $I_0(\mathbf{k})$ is the intensity that would be measured in the absence of atomic scattering; that is, $I_0(\mathbf{k})$ is the unperturbed intensity of the reference wave. The overall imaging process can be understood by first considering the hologram to be a convolution of the r-space object field $u(\mathbf{r})$:

$$\chi(\mathbf{k}) = \iiint_R d^3\mathbf{r}\cdot K(\mathbf{k},\mathbf{r})u(\mathbf{r}) + \iiint_R d^3\mathbf{r}\cdot K^*(\mathbf{k},\mathbf{r})u^*(\mathbf{r}), \tag{1}$$

where the convolution kernel $K(\mathbf{k},\mathbf{r})$ somehow describes the physics of the emission and atomic scattering of the photoexcited wavefronts, and R denotes the volume in real space over which the object exists. This produces a three-dimensional $\chi(\mathbf{k})$ volume in k-space, so as to completely encode three-dimensional spatial information of the object field $u(\mathbf{r})$. The reconstruction algorithm is then most simply a k-space deconvolution of $\chi(\mathbf{k})$ to obtain a real-space $U(\mathbf{r}')$ image intensity:

$$U(\mathbf{r}') = \iiint_K d^3\mathbf{k}\cdot\kappa^*(\mathbf{k},\mathbf{r}')\chi(\mathbf{k}), \tag{2}$$

where the reconstruction kernel $\kappa(\mathbf{k},\mathbf{r}')$ has been chosen to be orthogonal to the scattering kernel $K(\mathbf{k},\mathbf{r})$, as integrated over a sufficiently large k-space volume, that is, so that:

$$\begin{aligned} &\iiint_K d^3\mathbf{k}\cdot\kappa^*(\mathbf{k},\mathbf{r}')K(\mathbf{k},\mathbf{r}) \propto \delta(\mathbf{r}-\mathbf{r}'), \\ &\iiint_K d^3\mathbf{k}\cdot\kappa^*(\mathbf{k},\mathbf{r}')K^*(\mathbf{k},\mathbf{r}) \approx 0 \end{aligned} \tag{3}$$

If such a $\kappa(\mathbf{k},\mathbf{r}')$ can be found, then the object field $u(\mathbf{r})$ can thus be recovered as the image intensity $U(\mathbf{r}')$ from Eqs. (1)-(3):

$$\begin{aligned} U(\mathbf{r}') &= \iiint_R d^3\mathbf{r}\cdot\left[u(\mathbf{r})\iiint_K d^3\mathbf{k}\cdot\kappa^*(\mathbf{k},\mathbf{r}')K(\mathbf{k},\mathbf{r}) + u^*(\mathbf{r})\iiint_K d^3\mathbf{k}\cdot\kappa^*(\mathbf{k},\mathbf{r}')K^*(\mathbf{k},\mathbf{r})\right] \\ &= \iiint_R d^3\mathbf{r}'u(\mathbf{r})\delta(\mathbf{r}-\mathbf{r}') \\ &= u(\mathbf{r}'). \end{aligned} \tag{4}$$

So once the emission and scattering process that creates $\chi(\mathbf{k})$ can be sufficiently modeled by a $K(\mathbf{k},\mathbf{r})$ convolution kernel, then a deconvolution kernel $\kappa(\mathbf{k},\mathbf{r}')$ can in principle be formulated so as to directly reconstruct atomic images using Eq. (2).

Atomic Holography Reconstruction

The basic algorithms used in reconstructing atomic holographic images can be understood in the context of a single scattering (or kinematical) model of the scattering process. We consider e^{-ikr}/kr to represent the photoexcited electron or x-ray spherical wavefront that illuminates the (point-like) scattering atoms surrounding the emitter (with the emitted wave assumed to be isotropic for simplicity), $f(\Theta_r^k)$ to be the complex plane-wave atomic scattering factor ($\equiv |f(\Theta_r^k)|\exp[i\psi(\Theta_r^k)]$), where Θ_r^k is the scattering angle, and $\mathbf{k}\cdot\mathbf{r}$ is the phase of the scattered portion of this wavefront as it reaches the far field detector (Fig. 4). Thus the total geometrical path-length phase difference between the reference and scattered wavefronts is ($\mathbf{k}\cdot\mathbf{r} - kr$). The convolution kernel for this scattering process can then be expressed as:

$$K(\mathbf{k},\mathbf{r}) = \frac{f(\Theta_r^k)}{kr} e^{i(\mathbf{k}\cdot\mathbf{r}-kr)}. \tag{5}$$

This choice for $K(\mathbf{k},\mathbf{r})$ does not include any allowance for anisotropy in magnitude or phase of the outgoing reference wave, which for the simple example of *s*-level photoemission, takes the form of an additional factor of $\boldsymbol{\varepsilon}\cdot\mathbf{k}$, where $\boldsymbol{\varepsilon}$ is the polarization vector of the radiation (12). Thus, in photoemission, reference wave anisotropy is almost always present. However, for the case of Kα x-ray fluorescence to be considered below, the outgoing reference wave should be isotropic *and* randomly polarized, and thus be well described by Eq. (5).

Another advantage of x-rays lies in the nature of $f(\Theta_r^k)$. Figure 5 shows the magnitudes and phases of Ni atomic scattering factors for both x-rays and electrons with wavelength $\lambda = 0.79$Å (or wavenumber $k = 8.0$Å^{-1}). Note that the x-ray scattering factors (Fig. 5(a)) are much weaker (by ~1/2000) and more nearly constant in magnitude than those for electrons (Fig. 5(b)), and that the scattering phase shifts for x-rays are also much smaller (by ~1/100) and more nearly constant than those for electrons. Thus, for x-rays $|f(\Theta_r^k)| \approx$ constant $= f_0$, and $\psi(\Theta_r^k) \approx \psi_0 \approx 0$, such that the simplest possible optical scattering kernel results: $K_O(\mathbf{k},\mathbf{r}) \propto e^{i(\mathbf{k}\cdot\mathbf{r}-kr)}$. The reconstruction kernel that is most simply orthogonal to this optical scattering kernel is thus $\kappa_O(\mathbf{k},\mathbf{r}') \equiv e^{i(\mathbf{k}\cdot\mathbf{r}'-kr')}$, as first suggested by Barton and Terminello (4b). Thus for the scattering of fluorescent x-rays, the

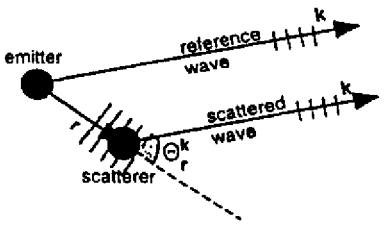

FIGURE 4. Scattering geometry between a photoemitter and a neighboring scattering atom. The photoemitter is placed at the origin, while the scatterer is located at the relative position r. The far field detector lies in the direction k. The portion of the direct wavefront that is scattered by the neighboring atom into the detector at r depends on the scattering angle Θ_r^k between r and k according to the complex phase factor $f(\Theta_r^k)$.

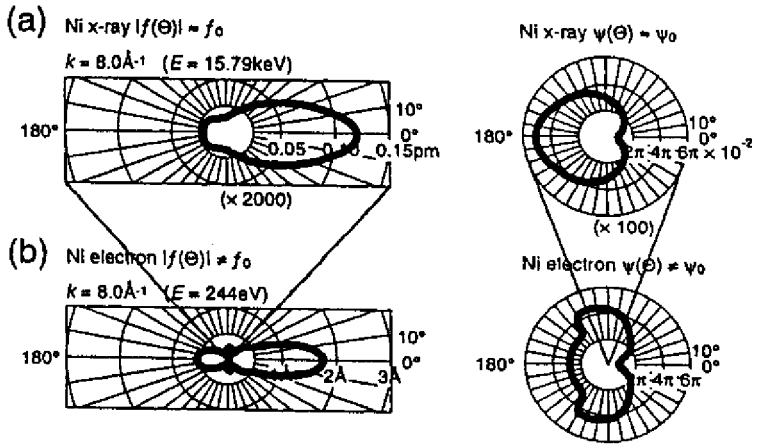

FIGURE 5. Ni scattering factor magnitudes ($|f(\Theta_r^k)|$) and phases ($\psi(\Theta_r^k)$), as a function of scattering angle Θ_r^k for (a) k = 8.0 Å^{-1} (E = 15.79keV) x-rays. (b) k = 8.0 Å^{-1} (E = 244eV) electrons. Θ_r^k = 0° is the forward scattering direction, Θ_r^k = 180° is the backscattering direction.

reconstruction algorithm of Eq. (2) becomes to a good approximation:

$$U(\mathbf{r}') = \iiint_K d^3\mathbf{k}\cdot e^{-i(\mathbf{k}\cdot\mathbf{r}'-kr')}\chi(\mathbf{k}). \tag{6}$$

This simple optical reconstruction algorithm has been used recently to obtain direct atomic images from experimental single-wavenumber (13,14) and multiple-

wavenumber (15,16) x-ray holographic data sets, as discussed further below.

For example, Fig. 1(c) schematically shows the optical holographic $\chi(k)$ intensities that were numerically calculated from the transparent "F" mask using Eqs. (1) and (5), over a range of different directions ($\hat{k}$) and wavenumbers (k). Figure 1(d) shows the numerically reconstructed real and twin images obtained from the volume $\chi(k)$ of Fig. 1(c). Due to the three-dimensional spatial information that was encoded in the k-space volume encompassed by $\chi(k)$, the reconstruction algorithm of Eq. (6) suppresses the spurious twin image, while increasing the fidelity of the desired real image (*cf.* Fig. 1(b)).

The optical reconstruction algorithm of Eq. (6) was in fact first used to reconstruct data from electron holographic data sets, *e.g.* from photoelectron diffraction (17-21). However, because of the generally anisotropic nature of the photoemitted source wave, and the strong, non-optical and often multiple nature of electron scattering, the single-scattering optical convolution kernel $K_o(\mathbf{k},\mathbf{r}') \propto e^{i(\mathbf{k}\cdot\mathbf{r}'-kr')}$ does not accurately describe the process by which electron holograms are produced, and consequently the optical reconstruction kernel $\kappa_o(\mathbf{k},\mathbf{r}') = e^{-i(\mathbf{k}\cdot\mathbf{r}'-kr')}$ will not in general satisfy the orthogonality condition (Eq. (3)) for electrons. Thus Eq. (6), when applied to electron holograms, often results in images which suffer from aberrations and position shifts (22-24). Nonetheless, useful atomic structure information has been derived from electron holography, with various modifications to the basic optical reconstruction kernel $\kappa_o(\mathbf{k},\mathbf{r}')$, and to the definition of the reconstruction integral (Eq. (2)) itself being proposed (25-29), and comparative reviews of different methods appearing elsewhere (30,31).

In summary, the atomic scattering of x-rays is much more nearly ideal than that of electrons, and this suggests that a simple optical reconstruction kernel as in Eq. (6) can be straightforwardly used to directly obtain atomic images from holographic x-ray intensities. However, more sophisticated reconstruction kernels and deconvolution integrals will probably be necessary to account for the non-ideal nature of the propagation and scattering of electrons, in order to successfully obtain the most accurate atomic images from holographic electron intensities, as discussed elsewhere (25-31).

ATOMIC ELECTRON HOLOGRAPHY

In this section, we discuss the results of applying the imaging algorithm of Eq. (6) to experimental and theoretical photoelectron diffraction results for W 4*f* emission from the surface atoms of clean W(110), with the experimental data being obtained by Denlinger, Rotenberg, and co-workers at Beamline 7.0 of the Advanced Light Source at the Lawrence Berkeley National Laboratory (31). The 4*f* photoelectron peak (which contains *d* and *g* components due to the dipole selection rule) can be resolved into bulk and surface core-level-shifted components, of which atomic images reconstructed from only surface photoemission will be considered here. Photoelectron spectra were measured for kinetic energies of $E = 41$eV to 197eV (wavenumbers $k = 3.3\text{Å}^{-1}$ to 7.2Å^{-1}), and collected over a polar takeoff angle range of $14° \le \theta \le 90°$ = normal emission. These data points were measured at wavenumber intervals corresponding to $\delta k = 0.1\text{Å}^{-1}$, and angular intervals of $(\delta\theta,\delta\phi) = (3°, 3°\cos\theta)$ corresponding roughly to equal solid angle elements, making a total of 12,280 unique measurements in a symmetry-reduced 1/4th of the total solid-angle above the sample. For each different wavenumber and direction, the W 4*f* peak was resolved into bulk and surface emission components by integrating the areas under the lower and higher flanks of the bulk and surface W 4*f* peaks, respectively, as shown in Fig. 6(a). Figures 6(b)-(c) show the bulk and surface $I(\mathbf{k})$ data sets in k-space, respectively, as viewed down along $[\bar{1}\,\bar{1}\,0]$. Data points in the lower right quadrant have been cut away to reveal the intensities $I(\mathbf{k})$ for the minimum $k = 3.3\text{Å}^{-1}$; the other quadrants show the intensities $I(\mathbf{k})$ for the maximum $k = 7.2\text{Å}^{-1}$. The dark bands at the perimeter indicate the locations in k-space on these iso-wavenumber surfaces where data was not collected. Due to the strong atomic scattering of electrons, the anisotropy of the raw $I(\mathbf{k})$ data, which we measure as $\Delta I / I_0 = (I_{max} - I_{min}) / I_0$, is found to be $\approx 30\%$, and is easily discernible with this gray scale.

In order to determine the normalized $\chi(\mathbf{k})$ from the raw $I(\mathbf{k})$ intensities of Figs. 6(b)-(c), $I_0(\mathbf{k})$ was determined by fitting a low order polynomial in wavenumber k and polar angle θ to $I(\mathbf{k})$:

$$I_0(\mathbf{k}) = a_{00} + \sum_{m=1}^{3}\sum_{n=1}^{3} a_{mn} k^m \cos[(2n-1)\theta], \qquad (11)$$

where the coefficients a_{mn} are determined by a least-squares fit to $I(\mathbf{k})$. This is in contrast to previous more approximate methods for determining $I_0(\mathbf{k})$ where simple linear, low-order polynomial, or spline fits were separately made for each set of different wavenumbers along a given direction: $I_k(\hat{\mathbf{k}})$, or each set of different directions at a given wavenumber: $I_{\hat{\mathbf{k}}}(k)$. Such separate normalizations within each scanned-wavenumber or scanned-angle set of data points in $I(\mathbf{k})$ arose from the historical development of electron holography, in which data tended to be collected with k-space resolution that was either fine-in-direction/coarse-in-wavenumber or coarse-in-direction/fine-in-wavenumber (30,31). There has in fact been a recent proposal to consider these k-space sampling choices as distinct atomic structure probes (17(e)), but these choices simply represent extremes of a continuous range of k-space sampling, of which the optimal choice has been shown to be in the intermediate range of roughly equally resolved direction and wavenumber data steps (30). Thus, this distinction (17(e)) is artificial, and not

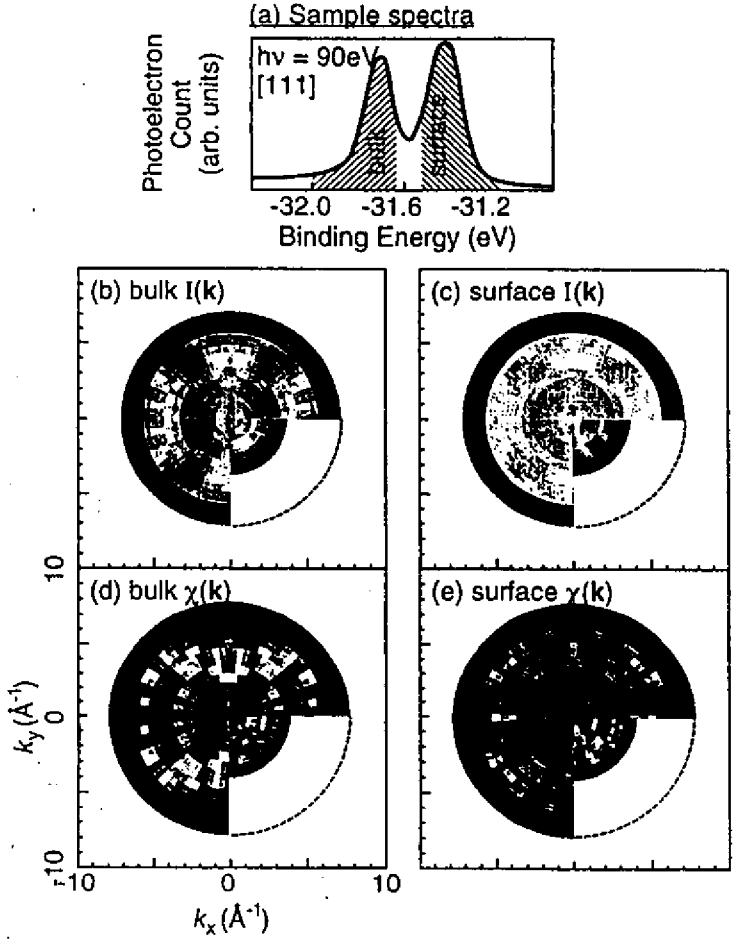

FIGURE 6. (a) Example W $4f_{7/2}$ photoelectron spectrum from clean W(110), with the bulk and surface emitter contributions used to generate the $I(k)$ intensity data points of (b)-(c) shaded in. (b)-(c) Schematic k-space representations of the raw $I(k)$ intensity data sets for bulk and surface W $4f_{7/2}$ emission, respectively. (d)-(e). Normalized bulk and surface emission $\chi(k)$ data sets, respectively, corrected for the unscattered intensity I_0 (as derived from Eq. (11)) and an inner potential of $V_0 = 14V$.

consistent with the optimal use of the holographic methodology. As a consequence, the normalization of $I(k)$ intensities should ideally be made via the determination of a general wavenumber and direction dependent $I_0(k)$ background, as done here, rather than determined separately for each wavenumber or direction in the $I(k)$ data set.

Figures 6(d)-(e) show the normalized bulk and surface $\chi(k)$ functions obtained from the raw $I(k)$ intensities of Figs. 7(b)-(c), using the wavenumber and angle fit $I_0(k)$ of Eq. (11), and after correcting for an inner potential of $V_0 = 14V$ (32) to yield electron wavenumbers and directions beneath the surface of the sample. These data points were then remapped to a $\delta k = 0.1Å^{-1}$, and $(\delta\theta,\delta\phi) = (5°,5°)$ grid over the range $k = 3.85Å^{-1}$ to $7.45Å^{-1}$ ($E = 56eV$ to $211eV$), and $40° \le \theta \le 90°$ range, for a final total of 6,697 unique intensities in the symmetry-reduced 1/4th of the solid angle above the sample.

For comparison, single-scattering and multiple-scattering models were used to calculate the surface emission $I(k)$ from a theoretical W(110) cluster (33). These theoretical photoemission intensities were then also normalized using Eq. (11).

Figure 7 shows the reconstructed images in the vertical $(\bar{1}\,1\,\bar{2})$ plane obtained from applying the optical reconstruction kernel of Eq. (6) to: (a) the experimental surface emission $\chi(k)$ of Fig. 6(e); (b) the theoretical single-scattering $\chi(k)$; and (c) the theoretical multiple-scattering $\chi(k)$. The expected atomic image resolution for this wavenumber and angular range of $\chi(k)$ in the horizontal $[\bar{1}\,1\,1]$ direction is given by $\delta x \approx \pi/\Delta k_x = \pi/(2k_{max}sin(\theta_{max}-\theta_{min})) \approx 0.3Å$, and in the vertical [110] direction is given by $\delta z \approx \pi/\Delta k_z = \pi/(k_{max}-k_{min}\cos(\theta_{max}-\theta_{min})) \approx 0.6Å$ (34), and these numbers are comparable to the actual atomic image resolutions in Fig. 7. As noted above, Eq. (6) makes no special effort to suppress aberrations due to the non-optical nature of the electron scattering process. In all of these images, the $\bar{1}\,\bar{1}\,0$ backscattering atom and the $\frac{1}{2}\frac{1}{2}\frac{1}{2}$ and $\frac{1}{2}\frac{1}{2}\frac{1}{2}$ side scattering atoms are well-resolved, with experiment and the more accurate multiple-scattering theory showing the sharpest features for the backscattering atoms. In the experimental image of Fig. 7(a), the $\frac{1}{2}\frac{1}{2}\frac{1}{2}$ and $\frac{1}{2}\frac{1}{2}\frac{1}{2}$ atoms are shifted in toward the emitter (by ≈ 0.7Å), and downward from the $z = 0Å$ surface (by ≈ 0.2Å), this is probably primarily due to anisotropies in the photoemitted source wave and the atomic scattering factor for such side-scattering directions. As expected, the backscattering $\bar{1}\,\bar{1}\,0$ atom is better resolved due to the more ideal nature of electron backscattering (*cf.* Fig. 5), with no significant position shift. The experimental backscattering image is also less intense (≈50%) than the side scattering atomic images; and image intensities above and below $z = -3.5Å$ have been scaled accordingly. This difference in relative image intensity is qualitatively expected due to the longer inelastic attenuation path of the wavefront that illuminates, and is subsequently scattered by, the backscattering atom, as compared to the wavefront paths that involve the side scattering atoms. Despite these

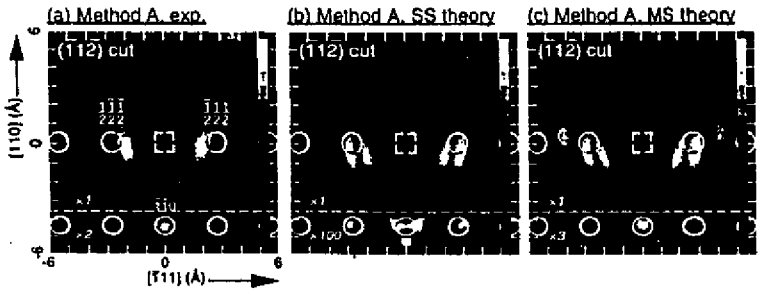

FIGURE 7. (a) W(110) atomic images obtained in the vertical $(\bar{1}1\bar{2})$ plane from experimental and theoretical W $4f_{7/2}$ surface emission $\chi(k)$ data sets, via (Eq. (6)). The surface emitter site is indicated by the dashed square, and the positions of the scatterers (assuming no surface relaxation) are indicated by circles. The nearest and next-nearest scattering positions have been labeled. Axes are marked off in 1Å units. Image intensities for $z \leq -3.5$Å have been rescaled, with the scale factors indicated on the figures. (a) Images reconstructed from the experimental $\chi(k)$ data set of Fig. 6(e). (b) Images reconstructed from a theoretical single scattering $\chi(k)$ data set. (c). Images reconstructed from a theoretical multiple scattering $\chi(k)$ data set.

position shifts and aberrations, this atomic image overall gives good *ab initio* estimates of the positions of the atoms surrounding the surface W(110) emitter, which could then be refined *e.g.*, using *R*-factor comparisons of experiment with model diffraction calculations for various structures.

The single and multiple scattering images of Figs. 7(b)-(c) are similar to experiment in that the $\frac{\bar{1}\bar{1}\bar{1}}{2\,2\,2}$ and $\frac{\bar{1}\,1\,1}{2\,2\,2}$ side scatterers exhibit side lobes which are shifted in towards the emitter, and downward from the surface. However, the side scattering atomic images of Figs. 7(b)-(c) differ from those of Fig. 7(a) in that the theoretical image peaks are split. This splitting may be due to a number of reasons, among them the differences between the theoretical and actual wavenumber-dependent photoexcitation cross-sections, photoemitted source wave angular distributions, and atomic scattering factors. Still, these single- and multiple-scattering models produce other image features that rather closely match the experimental image of Fig. 7(a), even including the faint aberrations seen at $(x,z) \approx (\pm 4\text{Å}, 0\text{Å})$. The most marked difference between the experimental image of Fig. 7(a) and the single-scattering image of Fig. 7(b) is the triply-split backscattering $\bar{1}\,\bar{1}\,0$ atom in the latter, which is also very much weaker in intensity ($\approx$ 1%) relative to the $\frac{\bar{1}\bar{1}\bar{1}}{2\,2\,2}$ and $\frac{\bar{1}\,1\,1}{2\,2\,2}$ image peaks. This is mainly due to the oversimplification of the single-scattering model, as seen by comparing Figs. 7(b) and (c). Note that in the multiple-scattering image of Fig. 7(c), the backscattering $\bar{1}\,\bar{1}\,0$ peak intensity relative to the side scattering $\frac{\bar{1}\bar{1}\bar{1}}{2\,2\,2}$ and $\frac{\bar{1}\,1\,1}{2\,2\,2}$ image peaks ($\approx$ 33%) is more nearly that of Fig. 7(a) ($\approx$ 50%). This dramatic difference between single and multiple scattering can arise because each of the atoms in the multiple-scattering model becomes a secondary emitter, which can then illuminate the atoms surrounding them, especially the atom located at the $\bar{1}\,\bar{1}\,0$ relative position. In this way more scattering events contribute to the backscattering signal in the resulting holographic $\chi(k)$ intensities, and as such the reconstructed $\bar{1}\,\bar{1}\,0$ atomic intensity is much stronger for the image reconstructed from the multiple-scattering model than that from the single-scattering model. Thus, the closer match between Fig. 7(c) and the experimental image of Fig. 7(a) graphically illustrates that multiple-scattering more accurately describes the nature of the creation of the experimental holographic photoelectron intensities $I(k)$.

Atomic electron holography has been extensively tested on both bulk and surface structures, with some notable successes to date being the determination of structures of adsorbate overlayers (17c,19a,20a,27b-c,) and reconstructed surface structures (17e,19b). This technique is most useful in that initial atomic position estimates can be determined, which can then be refined using a more standard comparison of experiment and theory. Further improvements of image quality in atomic electron holography will lie primarily in the refinement of reconstruction kernels and algorithms that more accurately account for the non-ideal atomic scattering and propagation of electron wavefronts, as well as the wavenumber dependences and anisotropies in the source wave. Other holographic experiments that await implementation in the near future are the monitoring of temperature and coverage dependent structural phase changes; and spin-polarized photoelectron holography (SPPH) (35), where spin-specific photoemission (or detection) could be exploited to yield images of local atomic spin order.

ATOMIC X-RAY HOLOGRAPHY

In this section we review two experimental techniques for acquiring holographic x-ray data, and show the results of imaging experimental and theoretical x-ray holographic data sets involving both single and multiple wavenumbers.

The first atomic x-ray holographic images were recently obtained using what can be termed *x-ray fluorescence holography (XFH)*, as shown in Fig. 2(a). In this work, Tegze and Faigel (13) measured the hologram by monitoring the single-wavenumber Sr Kα emission ($k = 7.145\text{Å}^{-1}$, $E = 14.10$keV) from a single crystal of $SrTiO_3$. 2,402 intensities were measured over a full cone of 60° half angle above the surface. The final hologram was found to have anisotropies in intensity

of $\Delta I / I_0 \approx 0.3\%$. These much smaller effects mean that more demanding detector counting statistics are required in x-ray holographic measurements than with comparable atomic electron holography measurements. The reconstruction of this hologram via the optical kernel algorithm of Eq. (6) yields images of the Sr atoms only, as the much weaker scattering strength of the Ti and O atoms renders their images invisible compared to those of the Sr atoms. Figure 8(a) shows the experimental image reconstructed in the (010) plane (36), and it is compared in Fig. 8(b) to an image reconstructed from a theoretical $\chi(k)$ for Sr Kα emission from a simple-cubic Sr cluster of 27 atoms (14). The expected atomic image resolutions at this hologram wavenumber and angular range are $\delta x \approx 0.3$Å in the horizontal [100] direction, and $\delta z \approx 0.9$Å in the vertical [001] direction (34), and are roughly comparable to the atomic images of Figs. 8(a)-(b).

Reconstructing three-dimensional atomic images from a single-wavenumber hologram yields twin images. In any structure with inversion symmetry, these twins can overlap with real atomic images so as to confuse structural interpretation (37,38). In addition, the real and twin atomic images for a particular wavenumber and system can overlap completely out of phase, leading to an artificial suppression of atomic image intensities (37,38). It is thus advantageous to reconstruct direct atomic images from multiple-wavenumber $\chi(k)$ data sets so as to avoid such real-twin image overlaps (4a,4b,38). However, such XFH holograms cannot be measured at arbitrary wavenumbers, with the latter being limited by the intensity and number of fluorescence lines of the photoemitting species (38,39).

Another method for obtaining x-ray holographic information at conveniently chosen multiple wavenumbers has also very recently been demonstrated for the first time by Gog *et al.* (15,16), and its basic principle is illustrated in Fig. 2(b). This method has been termed *multiple energy x-ray holography* (MEXH). MEXH is the time-reversed version of the conventional geometry of XFH (Fig. 2(a)), in that the wave motions are reversed, and the emitter and detector positions are interchanged (Fig. 2(b)) (15,16,39,40). The exciting external x-ray beam now produces the reference and object waves, and the fluorescent atom acts only to detect the interference between the direct and scattered wavefronts in the near field. The emitted x-rays are now collected by a distant detector with a large acceptance solid angle, in principle yielding much higher effective counting rates. The far field source wave can be set to any wavenumber (energy) above the fluorescence edge of the emitting species. thus permitting holograms at multiple wavenumbers and yielding in principle atomic images with no real-twin image overlaps (15,16,39). Specifically, multiple-wavenumber x-ray holograms have been measured to date for hematite ($\alpha - Fe_2O_3(001)$) (15,40), and for Ge(001) (16).

We show the results of applying the optical kernel algorithm of Eq. (6) to experimental and theoretical MEXH data for $\alpha - Fe_2O_3(001)$ as measured by Gog and co-workers on Beamline X-14A of the National Synchrotron Light

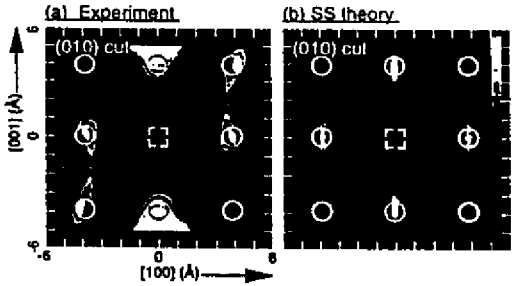

FIGURE 8. X-ray fluorescence holography atomic images of $SrTiO_3$ in the vertical (010) plane, obtained from (a) experimental (13) and (b) theoretical (14) Sr Kα $\chi(k)$ data sets, via Eq. (6). The Sr emitter site is indicated by the dashed square, and nearest-neighbor and next-nearest-neighbor Sr scatterers are indicated by circles. Axes are marked off in 1Å units.

Source at Brookhaven National Laboratory (15,40). Fe Kα fluorescence was excited by horizontally polarized radiation in the range $k = 4.561$Å^{-1} to 5.220Å^{-1} (E = 9.00keV to 10.30keV) that was incident on the $\alpha - Fe_2O_3(001)$ sample surface over a polar angle range of $60° \le \theta \le 90°$ = surface normal. These data points were measured at three wavenumbers with intervals of $\delta k = 0.329$Å^{-1} (δE = 650eV), and at angular intervals of $(\delta\theta, \delta\phi) = (5°, 5°)$, making a total of 435 unique measurements in a symmetry-reduced 1/3rd of the total solid-angle above the sample. Figure 9(a) illustrates the orientation of the sample with respect to the horizontal ($\hat{e}_1$) polarization vector, with the vertical ($\hat{e}_2$) polarization vector shown also to permit discussing other possible experimental geometries. Figure 9(b) shows the raw measured $I(k)$ data set in k-space, as viewed down along $[00\bar{1}]$, in the same format as Figs. 6(b)-(d). Data points in the fourth quadrant have been cut away to reveal the $k = 4.561$Å^{-1} $I(k)$ intensities, while the other quadrants show the $k = 5.220$Å^{-1} $I(k)$ intensities. Note that the much weaker atomic scattering of x-rays renders the anisotropy of the raw $I(k)$ data ($\Delta I / I_0 \approx 0.5\%$) barely discernible with this linear gray scale.

Due to the limited wavenumber range of this $I(k)$ data set, a separate $I_0(k)$ was determined for each of the three different wavenumber holograms via a low-pass filter (34), thereby including in $I_0(k)$ the reference wave, as well as corrections for the effects of x-ray absorption during both excitation and emission. Figure 9(c) shows the normalized $\chi(k)$ obtained by this method from the raw $I(k)$ intensities of Fig. 9(b).

For comparison to the experimental results, a single-scattering model (38,41)

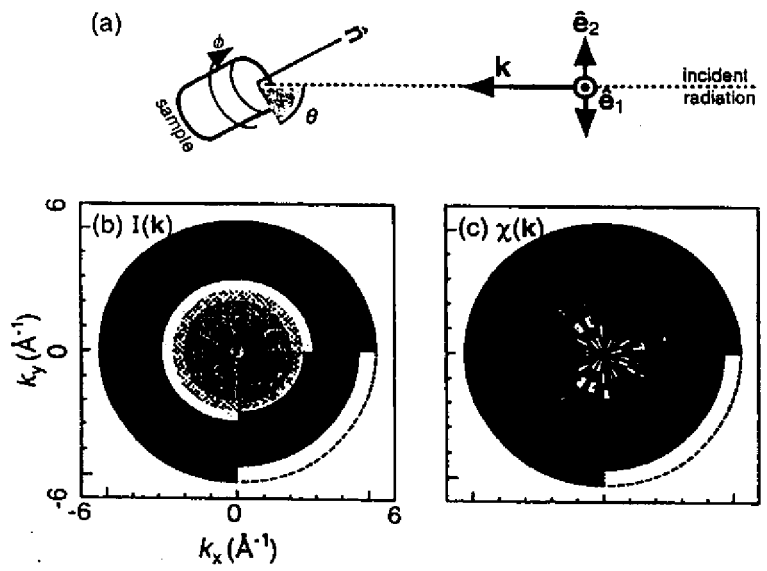

FIGURE 9. (a) Orientation of the sample (where $\hat{n}$ is the surface normal) with respect to the horizontal ($\hat{e}_1$) and vertical ($\hat{e}_2$) polarization vectors of the incident radiation k. (b) Schematic k-space representation of the raw measured $I(k)$ intensity data set for Fe Kα fluorescence from α-Fe_2O_3(001) excited by horizontally polarized radiation. (c) The normalized χ(k) data set. The format is the same as Figs. 6(b)-(d).

was used to calculate a theoretical χ(k) from an ideal $\alpha-Fe_2O_3(001)$ cluster containing 384 Fe atoms with two inequivalent Fe emitter sites as appropriate to the hematite lattice. The O atoms were not included due to their much smaller scattering power (15). The incident radiation in this model calculation is polarized horizontally with respect to the $\hat{\theta}$ and $\hat{\phi}$ rotation axes of the cluster (*cf.* Fig. 9(a)), as was the case in the measurement of the experimental $I(k)$ data set discussed above. Because the incident radiation is polarized, the x-ray scattering factor in Fig. 5(a) must be further multiplied by the Thomson scattering factor, which has the form $\sin^2\Theta_\varepsilon^{k'}$, where $\Theta_\varepsilon^{k'}$ is the angle between the polarization vector of the incident radiation ε, and the direction k' of the scattered radiation. Thus, there will be nodes in the incoming scattered object waves along the polarization direction, and emitter atoms near this direction will not be strongly influenced by x-ray scattering. For the present case, the use of horizontal polarization is therefore a

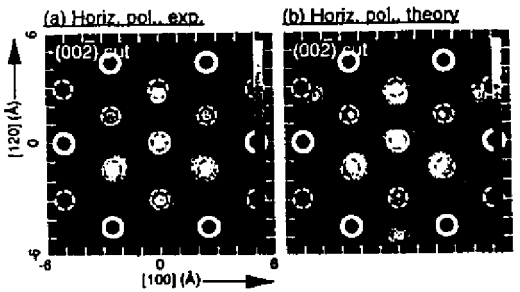

FIGURE 10. Multiple energy x-ray holography (MEXH) atomic images of α-Fe_2O_3(001) in the horizontal $(00\bar{2})$ plane situated 6.89Å below each of the two types of Fe emitters, obtained from (a) experimental and (b) theoretical Fe Kα χ(k) data sets, via Eq. (6). Fe scatterers in the bi-layer just above or below this plane are indicated by dashed circles, and Fe scatterers in relative positions common to both inequivalent Fe emitters are indicated by bold circles. Axes are marked off in 1Å units.

disadvantage in the imaging of horizontal planar structures such as those in $\alpha-Fe_2O_3(001)$, which is comprised of closely stacked horizontal Fe bi-layers with (001) orientation. The effect of such horizontally polarized incident radiation (via the Thomson cross section) is thus to strongly suppress atomic images in the basal (001) plane of the emitter, but to much less suppress images in horizontal planes farther above and below the emitter plane (40).

Figures 10(a) and (b) show the reconstructed atomic images in the $(00\bar{2})$ plane situated at z = -6.89Å below the emitter and obtained by applying Eq. (6) to the experimental and single-scattering theoretical χ(k) data sets, respectively. The expected image resolutions in the horizontal ([100] and $[1\bar{2}0]$) directions are $\delta x = \delta y \approx 0.6$Å (34). The experimental and theoretical images are very similar in that three of the Fe atoms from the neighboring upper bi-layer intrude into the $(00\bar{2})$ image plane. This intrusion is due to the limited wavenumber and angular range of the χ(k) data points in k-space (as compared to the larger wavenumber and angular range for the electron χ(k)'s in the previous section), which results in atomic images much less resolved in the vertical [001] direction: $\delta z \approx 2.5$Å (34). Still, since these images are reconstructed from a multiple-wavenumber χ(k) data set, they should be freer of real-twin image overlaps (4,15,16,38-40).

As a future prospect, using unpolarized incident radiation in MEXH, or perhaps rotating the entire sample-detector complex by 90° so as to measure holograms with both horizontal polarization and vertical polarization (with the polarization vector in the plane formed by the azimuthal rotation axis (the normal

of the sample surface) and the x-ray incidence direction, would allow atomic images to be reconstructed for atoms in all horizontal and vertical planes.

In fact, however, there also exist some classes of structures where it would be sufficient to utilize horizontally polarized incident radiation, and for which vertical structural information is more important than horizontal planar structure. These include some surface structure problems and buried epitaxial atomic layers. We specifically illustrate what might be learned for a buried atomic layer by considering theoretically a single Ge "δ-layer" buried in Si(001) (40). The Ge atoms in the δ-layer are assumed to lie in horizontal epitaxial sites with respect to the surrounding Si(001), such that structural information in the horizontal plane of a Ge emitter is relatively unimportant compared to the possibly strained vertical distances between the Ge δ-layer atoms and the Si neighbors above and below them (42). Thus using horizontally polarized incident radiation to record a MEXH Ge Kα $\chi(k)$ data set for this system may prove to be sufficient, and perhaps even advantageous.

As an example, Figs. 11(a)-(c) show the Thomson scattering factors for unpolarized, horizontally polarized, and vertically polarized incident radiation, respectively. Figs. 11(d)-(f) show the reconstructed atomic images in the vertical $(1\bar{1}0)$ plane obtained from applying Eq. (6) to a theoretical single-scattering $\chi(k)$ data set calculated for these polarization modes (unpolarized, horizontally polarized, and vertically polarized) for an ideal Ge δ-layer buried in a Si(001) cluster with no vertical strain. These MEXH $\chi(k)$ intensities were calculated at 7 wavenumbers (energies) for radiation of $k = 6.081\text{Å}^{-1}$ to 9.122Å^{-1} ($E = 12.00$keV to 18.00keV) that was incident over a polar takeoff angle range of $10° \le \theta \le 90°$, and with wavenumber (energy) steps of $\delta k = 0.507\text{Å}^{-1}$ ($\delta E = 1.00$keV) and angle steps of $(\delta\theta,\delta\phi) = (5°,5°)$, yielding a total of 1,897 unique data points in the symmetry-reduced 1/4th of the total solid-angle above the cluster. The higher wavenumber and larger wavenumber and angular ranges of these MEXH $\chi(k)$ data sets ensure better resolved atomic images ($\delta x = \delta y \approx 0.2\text{Å}$; $\delta z \approx 0.4\text{Å}$) than those of Fig. 10 (34). The Ge δ-layer atoms are well-defined in the image obtained with unpolarized radiation (Fig. 11(d)), and the Si atoms in the layer directly above the Ge δ-layer are fairly well resolved, but the Si atoms in the top center of the image along the [001] direction are poorly resolved, being farther away from the emitter. In contrast, in the image obtained with horizontally polarized radiation (Fig. 11(e)), the Si atoms above and below the Ge δ-layer, including those at top center and bottom center of the image along the [001] direction, are clearly imaged compared to those in the basal plane of the Ge δ-layer. Thus, it appears that the strained vertical interlayer distances could be determined in an MEXH experiment on this system using horizontally polarized incident radiation. Figure 11(f) shows the image obtained with vertically polarized incident radiation, where in contrast to Fig. 11(e), the Ge δ-layer atoms are strongly evident, compared to the suppressed images of the Si atoms above and below. Should both vertical *and* horizontal

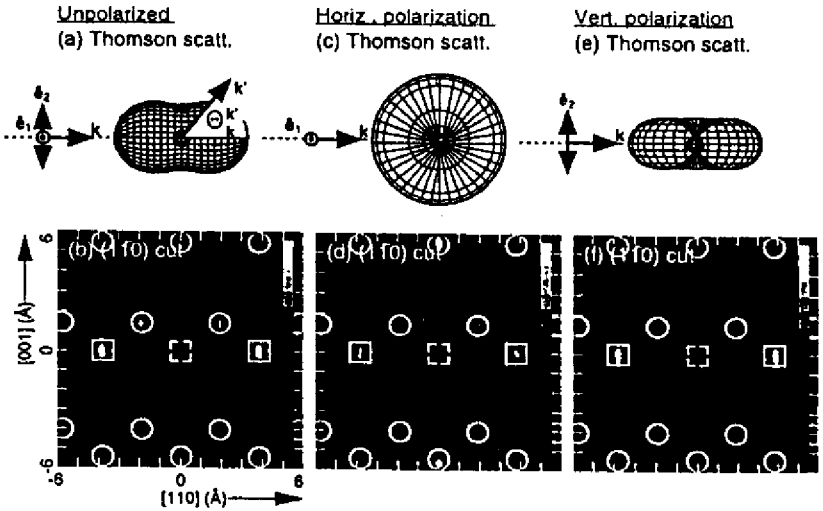

FIGURE 11. (a)-(c) Thomson scattering factors for unpolarized, horizontally polarized, and vertical polarized incident radiation, respectively. (d)-(f) Multiple energy x-ray holography images of a single Ge layer embedded in Si(001) (Si(001)/Ge-δ/Si(001)) in the vertical $(1\bar{1}0)$ plane obtained from theoretical Ge Kα $\chi(k)$ data sets via Eq. (6), for unpolarized, horizontally polarized, and vertically polarized incident radiation, respectively. The Ge emitter site is indicated by the dashed square, and the Ge δ-layer scatterers are indicated by solid squares. The Si atoms directly above and below the Ge δ-layer are indicated by circles. Axes are marked off in 1Å units.

structural information be desired for a given system with only linearly polarized incident radiation for excitation, then $\chi(k)$ intensities measured using horizontally and vertically polarized radiation separately could simply be added to determine the MEXH $\chi(k)$ intensities for most of the solid angle above the sample that one would measure using unpolarized incident radiation (40). The use of circularly polarized incident radiation should also be advantageous in this respect (40). In order to determine the vertical strain in this system (an effect of a few percent), increased spatial resolution of atomic images could be obtained by measuring holographic $\chi(k)$ intensities at higher wavenumbers (34).

Thus atomic x-ray holography holds much promise for the imaging of local atomic structure surrounding a specific emitter species of interest. The more ideal atomic scattering nature of x-rays produces reconstructed images that are relatively free of the aberrations, artifacts, and position shifts that are usually found in comparable electron atomic holographic images. XFH and MEXH also share

the advantage of being element specific; thus the local structure around each atomic type in a sample can be determined. In addition, neither XFH or MEXH requires a sample with long range crystalline order; it need only be minimally ordered to within the potential imaging volume surrounding the emitter site that can be resolved with the k-space resolution of a given $\chi(k)$ data set (30,38). In contrast to the bulk structures considered in the initial implementation of this technique, atomic x-ray holography would be advantageously used to image structures with only short-range order which cannot be determined using conventional x-ray diffraction probes, such as surface and buried atomic layers; strained atomic lattice positions surrounding dopant sites (Fig. 12(a)); as well as

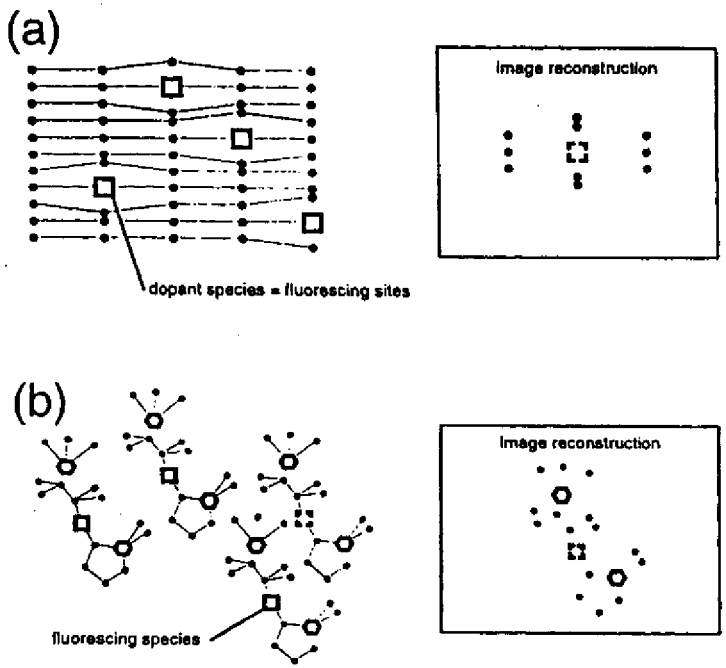

FIGURE 12. Schematic representation of two types of short-range-order atomic structures that could be fruitfully studied using atomic x-ray holography, together with their expected reconstructed images. (a) Strained lattice atoms surrounding dopant sites. (b) Rotationally aligned macromolecules with poor long-range translational symmetry.

the structure of macromolecules which do not exhibit perfect translational symmetry in crystal form (Fig. 12(b)). But one can also imagine using x-ray holography as a adjunct to conventional x-ray diffraction, with good estimates of local structures and phase relationships being derived to assist the diffraction analysis. Exploitation of linear and circularly polarized incident radiation in MEXH may also be utilized to emphasize horizontal and/or vertical structures of interest.

CONCLUDING REMARKS

In conclusion, holographic atomic imaging with localized single-atom sources of electrons or x-rays promises to become an important structural probe that will complement, or in some respects even surpass, conventional diffraction methods or other atomic structure probes. These holographic methods should be applicable to a wide variety of systems of practical and fundamental interest. X-ray holography of either the single-wavenumber fluorescence type or the multiple-wavenumber (inverse) type promises to yield more accurate images due to the more ideal scattering of x-rays, although the much weaker diffraction effects observed with x-rays also present challenges in measurement. However, with brighter sources of x-rays at next-generation synchrotron radiation facilities, and the development of faster detectors, these experimental problems should be surmountable. Thus, although much experimental and theoretical work lies ahead if we are to develop both the electron and x-ray techniques to their fullest potential, the final fulfillment of Gabor's dream for atomic-resolution holography seems well worth the effort.

ACKNOWLEDGEMENTS

Research at UC-Davis was supported in part by the Office of Naval Research (Contract Nos. N00014-90-5-1457 and N00014-94-1-0162), by the Director, Office of Energy Research, Office of Basic Energy Sciences, Materials Sciences Division of the U. S. Department of Energy (Contract No. DE-AC03-76SF00098), the National Energy Research Supercomputer Center, and by the International Centre for Diffraction Data. The authors would like to thank T. Gog, J. D. Denlinger, E. Rotenberg, F. Arfelli, R. A. Eisenhower, A. P. Kaduwela, R. H. Menk, D. Novikov, and S. Thevuthasan for their experimental and theoretical collaborative efforts, and M. A. Van Hove and R. L. Johnson for their useful comments during the preparation of this manuscript. Use of a preliminary version of a new multiple-scattering photoelectron diffraction program package was made possible by Y. Chen, H. Wu, and D. A. Shirley.

REFERENCES

1. Gabor, D. *Nature* (London) **161**, 777-778 (1948).
2. Wolf, E. *Optics Communications* **1**, 153-156 (1969), and *Optical Society of America* 60, 18-20 (1970).
3. Syms, R. R. A., *Practical Volume Holography*, Oxford: Clarendon Press, 1990, ch. 1, pp. 21-28.
4. (a) Barton, J. J., *Physical Review Letters* **61**, 1356-1359 (1988), and *Physical Review Letters* 67, 3106-3109 (1991). (b) Barton, J. J., and Terminello, L. J., paper presented at the Third International Conference on the Structure of Surfaces, Milwaukee, July 1990, and in *Structure of Surfaces III*, S. Y. Tong, M. A. Van Hove, X. Xide, and K. Takanayagi, eds., (Springer Verlag, Berlin, 1991) p. 107. (c) Tong, S. Y., Huang, H., and Wei, C. M., *Physical Review B* **46**, 2452-2459 (1992), and references therein.
5. Szöke, A., *Short Wavelength Coherent Radiation: Generation and Applications*, T. Attwood, J. Boker (eds.), AIP Conference Proceedings No. 147, (AIP, New York, 1986) pp. 361-367.
6. Karla, J., and Hauptmann, H. A., *Acta Crystallographica* **3**, 18 (1950).
7. Lipscomb, W. N., *Acta Crystallographica* **2**, 193 (1949).
8. Hümmer, K., Billy, H., *Acta Crystallographica A* **38**, 841 (1982).
9. Chang., S., L., *Physical Review Letters* **48**, 163 (1982).
10. Hutton, J. T., Trammell, G. T., and Hannon, J. P., *Physical Review B* **31**, 743 (1985), and *Physical Review B* **31**, 6420 (1985).
11. Bedyzk, M. J., and Materlik, G., *Physical Review B* **32**, 6456 (1985).
12. Saldin, D. K., Harp, G. R., Tonner, B. P., *Physical Review B* **45**, 9629 (1992).
13. Tegze, M., and Faigel, G., *Nature* **380**, 49-51 (1996).
14. Fadley, C. S., and Len, P. M., *Nature* **380**, 27-28 (1996), and unpublished results.
15. Gog, T., Len, P. M., Materlik, G., Bahr, D., Sanchez-Hanke, C., and Fadley, C. S., *Physical Review Letters* **76**, 3132-3135 (1996).
16. Gog., T., Menk, R.-H., Arfelli, F., Len, P. M., Fadley, C. S., and Materlik, G., *Synchrotron Radiation News* **9**, 30-35 (1996).
17. (a) Terminello, L. J., Petersen, B. L., and Barton, J. J., *Journal of Electron Spectroscopy and Related Phenomena* 75, 229-308 (1995), and references therein. (b) Wu, H., Lapeyre, G. J. Huang, H., and Tong, S. Y., *Physical Review Letters* **71**, 251-254 (1993) and references therein. (c) Zharnikov, M., Weinelt, M., Zebisch, P., Stichler, M., Steinrück, H.-P., *Surface Science* 334, 114-134 (1995), and references therein. (d) Denecke, R., Eckstein, R., Ley, L., Bocquet, A. E., Riley, J. D., Leckey, R. C. G., *Surface Science* **331-333**, 1085-1092 (1995). (e) Tobin, J. G., Waddill, G. D., Li, H., Tong, S. Y., *Surface Science* **334**, 263-275 (1995), and references therein.
18. (a) Li, H., Tong, S. Y., Naumovic, D., Stuck, A., and Osterwalder, J., *Physical Review B* 47, 10036-10039 (1993). (b) Saldin, D. K., Harp, G. R. and Chen, X., *Physical Review B* **48**, 8234-8245 (1993), and references therein.
19. (a) Han, Z.-L., Hardcastle, S., Harp, G. R., Li, H., Wang, ,X.-D. Zhang, J., and Tonner, B. P., *Surface Science* **258**, 313-327 (1991), and references therein. (b) Hong, I. H., Shyu, S. C., Chou, Y. C., and Wei, C. M., *Physical Review B* **52**, 16884-16891 (1995), and references therein.
20. (a) Mendez, M. A., Glück, C., Guerrero, J., Andres, P. L., Heinz, K., Saldin, D. K., and Pendry, J. B., *Physical Review B* 45, 9402-9405 (1992), and references therein. (b) Wei, C. M., Tong, S. Y., Wedler, H., Mendez, M. A., and Heinz, K., *Physical Review Letters* 72, 2434-2437 (1994), and references therein.
21. Tong, S. Y., Huang, H., and Guo, X. Q., *Physical Review Letters* 69, 3654-3657 (1992).
22. Saldin, D. K., Harp, G. R., Chen, B. L., and Tonner, B. P., *Physical Review B* **44**, 2480-2494 (1991).
23. (a) Thevuthasan, S., Herman, G. S., Kaduwela, A. P., Tran, T. T., Kim, Y. J., Saiki, R. S., and Fadley, C. S., *Journal of Vacuum Science and Technology A* 10, 2261-2270 (1992). (b) Herman, G. S., Thevuthasan, S., Tran, T. T., Kim, Y. J., and Fadley, C. S., *Physical Review Letters* **68**, 650-653 (1992). (c) Tran, T. T., Thevuthasan, S., Kim, Y. J., Friedman, D. J., Fadley, C. S., *Physical Review B* **45**, 12106-12109 (1992), and *Surface Science* **281**, 270-284 (1993). (d) Thevuthasan, S., Ynzunza, R. X., Tober, E. D., Fadley, C. S., Kaduwela, A. P., and Van Hove, M. A., *Physical Review Letters* 70, 595-598 (1993).
24. Hu, P. and King, D. A., *Physical Review B* **46**, 13615-13618 (1992).
25. Tonner, B. P., Han, Z.-L., Harp, G. R., and Saldin, D. K., *Physical Review B* **43**, 14423-14433 (1991).
26. Thevuthasan, S., Ynzunza, R. X., Tober, E. D., Fadley, C. S., Kaduwela, A. P., and Van Hove, M. A., *Physical Review Letters* 70, 595 (1993).
27. (a) Tong, S. Y., Li, H., and Huang, H., *Physical Review B* 51, 1850-1854 (1995). (b) Wu, H., and Lapeyre, G. J. *Physical Review B* 51, 14549-14553 (1995). (c) Roesler, J. M., Sieger, M. T., and Chiang, T.-C., *Surface Science* 329, L588-592 (1995), and references therein.
28. Rous, P. J. and Rubin, M. H., *Surface Science* 316, L1068-1074 (1994).
29. Hofmann, P., Schindler, K.-M., Fritzsche, V., Bao, S., Bradshaw, A. M., and Woodruff, D. P., *Journal of Vacuum Science and Technology A* 12, 2045-2050 (1994), *Surface Science* 337, 169-176 (1995), and references therein.
30. (a) Len, P. M., Thevuthasan, S., Kaduwela, A. P., Van Hove, M. A., and Fadley, C. S., *Surface Science* 365, 535-546 (1996). (b) Len, P. M., Zhang, F., Thevuthasan, S., Kaduwela, A. P., Van Hove, M. A., and Fadley, C. S., *Journal of Electron Spectroscopy and Related Phenomena* 76, 351-357 (1995). (c) Len, P. M., Zhang, F., Thevuthasan, S., Kaduwela, A. P., Fadley, C. S., and Van Hove, M. A., submitted to the *Journal of Electron Spectroscopy and Related Phenomena*.
31. Denlinger, J. D., Rotenberg, E., Len, P. M., Kevan, S. D., Tonner, B. P., and Fadley, C. S., in preparation.
32. Ynzunza, R. X., private communication.
33. SCAT photoelectron diffraction program package, Chen, Y., Wu, H., and Shirley, D. A., private communication.
34. Harp, G. R., Saldin, D. K., Chen, X., Han, Z.-L., and Tonner, B. P., *Journal of Electron Spectroscopy and Related Phenomena* 57, 331-355 (1991).
35. (a) Timmermans, E. M. E., Trammell, G. T., and Hannon, J. P., *Physical Review Letters* 72, 832-835 (1994). (b) Kaduwela, A. P., Wang, Z., Thevuthasan, S., Van Hove, M. A., and Fadley, C. S., *Physical Review B* 50, 9656-9659 (1994).
36. Faigel, G., private communication.
37. Tegze, M., Faigel, G., *Europhysics Letters* 16, 41-46 (1991).
38. Len, P. M., Thevuthasan, S., Fadley, C. S., Kaduwela, A. P., and Van Hove, M. A., *Physical Review B* 50, 11275-11278 (1994).
39. Len, P. M., Gog, T., Fadley, C. S., and Materlik, G., submitted to *Physical Review B*.
40. Len, P. M., Gog, T., Novikov, D., Eisenhower, R. A., Materlik, G., and Fadley, C. S., submitted to *Physical Review B*.
41. *International Tables for X-ray Crystallography*, edited by K. Lonsdale (Reidel, Dordrecht, 1968), Vol. III.
42. Falta, J., Gog, T., Materlik, G., Muller, B. H., and Horn-von Hoegen, M., *Physical Review B* 51 7598-7602 (1995), and references therein.

UNITED NATIONS EDUCATIONAL, SCIENTIFIC AND CULTURAL ORGANIZATION
INTERNATIONAL ATOMIC ENERGY AGENCY
INTERNATIONAL CENTRE FOR THEORETICAL PHYSICS
I.C.T.P., P.O. BOX 586, 34100 TRIESTE, ITALY, CABLE: CENTRATOM TRIESTE

H4.SMR/1013-7

SCHOOL ON THE USE OF SYNCHROTRON RADIATION
IN SCIENCE AND TECHNOLOGY:
"John Fuggle Memorial"

3 November - 5 December 1997

Miramare - Trieste, Italy

Theoretical Aspects of Electron Emission Holography [2)]

Luciano Fonda
ICTP - Trieste, Italy

Review Article

phys. stat. sol. (b) 188, 599 (1995)

Subject classification: 79.60; 61.14

Department of Theoretical Physics, University of Trieste, and International Center for Theoretical Physics, Trieste[1])

Theoretical Aspects of Electron Emission Holography[2])

By

L. FONDA

Contents

1. Introduction

Starting from a suggestion of Szöke [1] and Barton [2], a new surface structure determination approach, called either photoelectron or Auger electron holography depending on the process under consideration, to get three-dimensional images of the close vicinity of a given near-surface atom emitter, has recently been developed. The idea goes back to Gabor's discovery of holography [3]. He realized that, by recording on a photographic plate the interference pattern (hologram) of a known *reference* wave with an unknown *object* wave and then illuminating with an appropriate decoding wave the so obtained hologram, one can obtain the image of the object.

In the case of a photoelectron or of an Auger electron, the reference wave is assumed to be the direct wave emitted by the excited atom a. The object wave is then the superposition of the waves emitted coherently by the atoms surrounding a as a consequence of the process of single double ... multiple scattering experienced by the emitted electron. By taking the detector to be a spherical photographic film, the decoding wave referred to above is then chosen to be the spherical wave, converging on the film, obtained from the asymptotic reference wave via the operation of time reversal [1, 2]. This wave is transmitted through

[1]) POB 586, Strada Costiera 11, I-34100 Trieste, Italy.

[2]) Supported in part by the Istituto Nazionale Fisica Nucleare.

the film and in this process it collects the information contained in the hologram. The images of the atoms of the object are then obtained by means of computer reconstruction using a mathematical method similar to the one employed in optical holography.

In this way, one therefore realizes the inverse process of recovering the structure of the object from the knowledge of the hologram.

The advantage of this holographic method lies in the knowledge of the reference wave, a point which is not shared by structure determination approaches using an external beam of particles, such as e.g. X-ray and neutron diffractions, where the reference wave is lost and the experimentalist is therefore faced with the so-called "phase problem".

In Section 2, the theory of electron emission holography is expounded in full detail. In Sections 3 and 4, the weak points of the theory, such as the appearance of twin images, of "ghost atoms", and of some other artificial byproducts of the method, are discussed and ways to eliminate them are reviewed.

Applications of this holographic technique have appeared in the literature. For a complete list of references, the reader is referred to the review papers by Chambers [4] and Fadley [5].

2. Photoelectron and Auger Electron Holography

Let us first consider the way the hologram is obtained. We place a spherical photographic film around our object. The centre of the sphere is at the origin 0 of the reference frame placed at the centre of the atom emitter a. The radius of the sphere is R. Each point of the film is characterized by the polar angles defining the vector R.

The interference pattern is encoded on this photographic film. It is obtained by evaluating the component of the emitted electron vector probability current density in the direction perpendicular to the sphere surface (for simplicity, we neglect the refraction of the electron wave at the surface of the sample subject to measurement),

$$I(R) \equiv j(R) \cdot R/R \,. \tag{2.1}$$

If the detector is in the far field (R large with respect to the dimensions of the object), this probability is just proportional to the modulus square of the emitted electron wave function $\psi(R)$ evaluated at the position R,

$$I(R) \propto |\psi(R)|^2 \,. \tag{2.2}$$

On the sphere surface the wave function $\psi(R)$ can be expressed in terms of the scattering matrix

$$\psi(R)_{R\,\text{large}} \approx -\frac{m(2\pi)^{1/2}}{\hbar^2}\,\frac{e^{ikR}}{R}\,T_{f-i} \,. \tag{2.3}$$

T_{f-i} is the T-matrix for the process evaluated on the energy shell. In the standard single-particle approach, it is given by

$$T_{f-i} \equiv \langle \psi_f^{(-)}(k) \,|\, A_c \rangle \,, \tag{2.4}$$

where the PhotoElectron state vector $|A_c^{\text{PhE}}\rangle$ and the Auger $|A_{c12}^{\text{Auger}}\rangle$ are defined by (see [6], Sections 2 and 6)

$$|A_c^{\text{PhE}}\rangle = \langle 0|\, H_1 \,|I_i\rangle\, |\psi_c\rangle \,, \tag{2.5a}$$

$$\langle r_2 \,|\, A_{c12}^{\text{Auger}}\rangle = \int \mathrm{d}^3 r_1\, \psi_c^*(r_1)\, \frac{e^2}{|r_2 - r_1|}\, [\psi_{i1}(r_1)\, \psi_{i2}(r_2) - \psi_{i2}(r_1)\, \psi_{i1}(r_2)] \,. \tag{2.5b}$$

In the case of photoemission, the initial state vector is the product of the incoming free photon state vector $|1_i\rangle$ (the subscript i symbolizes the initial photon momentum and the polarization) times the vector $|\psi_c\rangle$ which represents the initial single-electron normalized bound state relative to the *core* level c. The final state is given by the product of the normalized photon vacuum $|0\rangle$ times the single-electron scattering state $|\psi_f^{(-)}(k)\rangle$, satisfying an incoming wave boundary condition, describing the emitted electron, with asymptotic momentum $\hbar k \equiv \hbar kR/R$, in interaction with the ionized atom emitter a and with its neighbours in the condensed material. For simplicity, in this paper we shall forget about the spin of the emitted electron. To the first order in the radiation field, the interaction Hamiltonian is given by: $H_I = -(e/mc)\, A \cdot p$, where m and p are the electron mass and momentum operator, respectively, and $A(r)$ is the quantized photon field in the Coulomb gauge $\nabla \cdot A(r) = 0$.

In the case of Auger emission, the process is one in which an electron of the ionized atom a makes a transition from the core level 1 (core level 2) to the empty core level c, while an electron from the core level 2 (core level 1) is ejected from the atom a. This emitted Auger electron, represented in (2.4) by the usual scattering state $|\psi_f^{(-)}(k)\rangle$, propagates then in the material and suffers multiple scatterings from the atoms surrounding the doubly ionized atom a until, after having finally assumed the momentum $\hbar k$, it reaches the detector.

The expression of the T-matrix in terms of all multiple scatterings is known from the literature. We write here (3.37) of [6] (L is a combined orbital angular momentum index $L \equiv l, m$),

$$T_{f\leftarrow i} = \sum_L \mathscr{T}_{L'} \mathscr{M}_{cL}\,, \tag{2.6a}$$

$$\mathscr{T}_L = \sum_{L'} (2\pi)^{-3/2} (-i)^{l'} Y_{L'}(k) \times \left\{ \delta_{LL'} + \sum_{\substack{p=a \\ q=a}} \sum_{L_p L_q} [\delta_{L'L_q} e^{ik\cdot R_{aq}} + t_l^a g_{L'L_q}(R_{aq})]\, \tau^{qp}_{L_q L_p} g_{L_p L}(R_{pa}) \right\}. \tag{2.6b}$$

Apart from the consideration of inelasticities and thermal vibrations, to be introduced with proper attenuation factors [5], (2.6) is, within the single-particle framework, the correct T-matrix.

The matrix $\tau^{qp}_{L_q L_p}$ is the representative in angular momentum space of the scattering path operator [7]. The integral equation defining this operator is given by (3.38) of [6],

$$\tau^{qp}_{L_q L_p} = t_p^p \delta_{qp} \delta_{L_q L_p} + \sum_{m\neq q} \sum_{L_m} t_q^q [g_{L_q L_m}(R_{qm})]\, \tau^{mp}_{L_m L_p}\,, \tag{2.7}$$

$R_{qp} = R_q - R_p$ is the bond vector pointing from atom p to atom q, $t_l^p = -e^{i\delta_l^p} \sin \delta_l^p$ is the l-th wave T-matrix for scattering of the electron from the atom p, the form factor $\mathscr{M}_{cL}$ is given by

$$\mathscr{M}_{cL} = \int d^3r \frac{\psi_{al}^{(+)}(k, r)}{kr} Y_L^*(r) \langle r | A_c \rangle\,, \tag{2.8}$$

where $\psi_{al}^{(+)}(k, r)$ is the physical radial scattering wave function, satisfying an outgoing wave boundary condition, belonging to the angular momentum l, for the emitted electron in the field of the potential U_a of the atom emitter a.

The g-propagator (structure factor) is given by

$$g_{L_p L_q}(R_{pq}) = -i \sum_L 4\pi i^{l+l_p-l_q} \langle Y_{L_p} Y_L \,|\, Y_{L_q} \rangle\, Y_L(R_{pq})\, h_l^{(+)}(kR_{pq})\,. \tag{2.9}$$

Using (2.3), (2.6), and (2.7), we can easily split the wave function, at the sphere surface, into *reference* and *object* terms,

$$\psi(R) = \psi_{ref}(R) + \psi_{obj}(R) \equiv -\frac{m(2\pi)^{1/2}}{\hbar^2} \frac{e^{ikR}}{R} \sum_L [\mathscr{T}_L^{ref} + \mathscr{T}_L^{obj}]\, \mathscr{M}_{cL}\,, \tag{2.10a}$$

$$\mathscr{T}_L^{ref} = (2\pi)^{-3/2} (-i)^l Y_L(k)\,, \tag{2.10b}$$

$$\mathscr{T}_L^{obj} = (2\pi)^{-3/2} \sum_{p,q} \sum_{L_p L_q} (-i)^{l_q} Y_{L_q}(k)\, e^{ik\cdot R_{aq}}\, \tau^{qp}_{L_q L_p} (1 - \delta_{pa})\, g_{L_p L}(R_{pa})\,. \tag{2.10c}$$

Note that the object wave contains also all waves which, after having undergone multiple scattering, have atom a as the last scatterer (term $q = a$ of (2.10c)). These particular multiple-scattering contributions are unknown and therefore, even though consisting of waves eventually outgoing from the atom emitter, cannot be included in the reference wave. They are at least of second order with respect to the latter wave.

To decode the information contained in the interference pattern appearing on the spherical film, we imagine to illuminate the film with a converging spherical wave

$$\psi_{decoding}(r) = \frac{e^{-ikr}}{r}; \qquad r > R \tag{2.11}$$

obtained, apart from a constant, from the asymptotic expression of the reference wave via the operation of time reversal. This converging wave is transmitted through the film. We suppose that the interference pattern $I(R)$ is imprinted on a positive photographic film which, by proper development, has the contrast value $\gamma = 2$ [8]. As a consequence, the transmittance is linearly related to the intensity $I(R)$ measured on the film and the *transmitted wave* ψ_T on the internal side of the surface of the sphere is therefore given by:

$$\psi_T(R) = (1 + CI(R)) \frac{e^{-ikR}}{R}\,. \tag{2.12}$$

The transmitted wave satisfies the Helmholtz wave equation

$$(\Delta + k^2)\, \psi_T(r) = -4\pi C_0 \delta^3(r); \qquad r \leqq R \tag{2.13}$$

subject to the (Dirichelet) boundary condition (2.12) on the surface of the sphere. $\psi_T(r)$ is singular in the origin $r = 0$ (position of the atom emitter a). This can be understood from the fact that, if there is no hologram ($I = 0$), ψ_T must coincide with the decoding wave (2.11) which satisfies (2.13) with $C_0 = 1$.

In order to find ψ_T in a given point P_0 (of coordinate vector r_0) inside the sphere, we consider the Green's function $K(r \,|\, r_0)$ satisfying the Helmholtz equation,

$$(\Delta + k^2)\, K(r \,|\, r_0) = -4\pi \delta^3(r - r_0) \tag{2.14}$$

with boundary condition to be specified in a moment.

We multiply (2.13) by $K(r \mid r_0)$ and (2.14) by $\psi_T(r)$ and subtract member by member one equation from the other. We integrate the so obtained expression on the whole volume of the sphere. Using then the Green's theorem, we get

$$\psi_T(r_0) - C_0 K(0 \mid r_0) = \frac{1}{4\pi} \int [K(r \mid r_0)\, \Delta\psi_T(r) - \psi_T(r)\, \Delta K(r \mid r_0)]\, dV$$

$$= \frac{1}{4\pi} \int \left[\psi_T(r) \frac{\partial K(r \mid r_0)}{\partial n} - K(r \mid r_0) \frac{\partial \psi_T(r)}{\partial n} \right]_{r=R} dS, \quad (2.15)$$

where ∂n is the normal to the surface directed into the interior of the sphere.

A natural choice for the Green's function would be [2, 9]: $K(r \mid r_0) = (\exp ik|r - r_0|)/|r - r_0|$. In that case, however, from (2.15) we see that knowledge of ψ_T and $\partial\psi_T/\partial n$ on the whole surface should be required to solve our problem. Apart from the fact that on the boundary we know only the values of ψ_T (from (2.12)), this might lead to the following mathematical contradiction: In practice the hologram can cover at most the 2π-hemisphere hanging over the sample subject to measurement; if symmetry arguments are not available in order to obtain mathematically the hologram on the "opaque" sides of the measuring apparatus, one usually assumes the vanishing of the surface integral (2.15) just on those opaque parts of the surface, which implies $\psi_T = \partial\psi_T/\partial n = 0$ there; but this implies, by a well-known theorem, that ψ_T vanishes identically in the whole space.

I shall require that the Green's function vanishes on the boundary surface.

$$K(R \mid r_0) = 0 \quad (2.16)$$

so that (2.15) can be rewritten as

$$\psi_T(r_0) = C_0 K(0 \mid r_0) + \frac{1}{4\pi} \int_S \psi_T(R) \left. \frac{\partial K(r \mid r_0)}{\partial n} \right|_{r=R} dS. \quad (2.17)$$

We see that only the knowledge of ψ_T on the boundary is now required.

The integral on the right-hand side of (2.17) may extend now only on the portion S of the surface on which the hologram is actually measured. On the "opaque" parts of the surface we can safely place $\psi_T = 0$ without meeting contradictions of any sort.

We must now solve the Dirichlet boundary value problem posed by (2.14) and (2.16). The solution in the whole space can be found only by means of computer calculations. In fact, for the Helmholtz equation (2.14) an analytic solution satisfying (2.16) cannot be written down. Fortunately, however, we need only to know $\partial K/\partial n$ on the surface of the sphere. In order to find it there explicitly, I shall make a variation of the well-known method of images. This method has been invented for the case of a flat boundary [10]. Let us see which changes are needed for our curved boundary.

Suppose I want to find the value of $\partial K/\partial n$ in a given point $P_s \subset S$. I draw, through the point P_s, the plane T tangent to the surface S. I perform then the space reflection with respect to T and find the image of P_0 (see Fig. 1). Call this new point P_0^*, whose position vector is r_0^*. Consider now the auxiliary Green's function:

$$\tilde{K}(r \mid r_0) = \frac{e^{ikr_1}}{r_1} - \frac{e^{ikr_2}}{r_2}, \quad (2.18)$$

where $r_1 = r - r_0$ and $r_2 = r - r_0^*$. In the interior of the sphere, $\tilde{K}$ satisfies the Helmholtz equation (2.14) and it vanishes on the plane T (where $r_1 = r_2$), in particular in the point P_s.

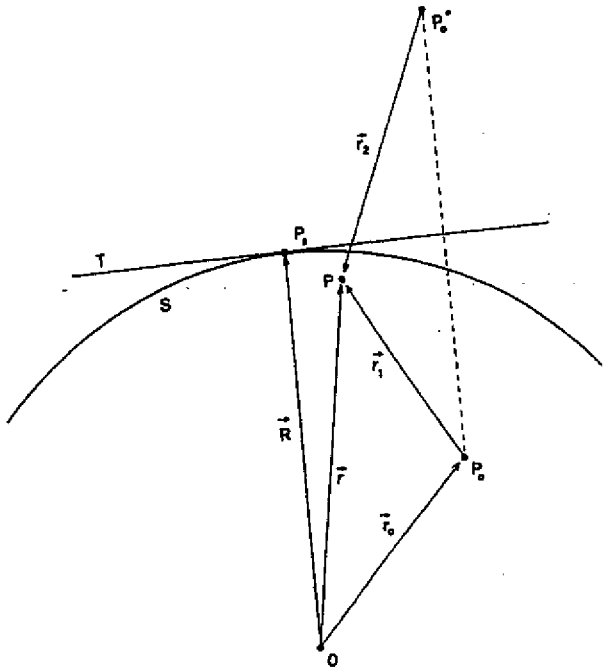

Fig. 1. Definition of points and vectors relative to the construction of the derivative of the Green's function with respect to the normal to the boundary surface

By construction, in any infinitesimal spherical neighbourhood of P_s, the Green's functions K and $\tilde{K}$ differ by infinitesimal quantities and the same holds for their derivatives. We obtain then

$$\left. \frac{\partial K(r \mid r_0)}{\partial n} \right|_{P=P_s} = \left. \frac{\partial \tilde{K}(r \mid r_0)}{\partial n} \right|_{P=P_s}$$

$$= \left[\left(ik - \frac{1}{r_1} \right) \frac{e^{ikr_1}}{r_1} \frac{\partial r_1}{\partial n} - \left(ik - \frac{1}{r_2} \right) \frac{e^{ikr_2}}{r_2} \frac{\partial r_2}{\partial n} \right]_{P=P_s}. \quad (2.19)$$

The evaluation of the derivatives $\partial r_1/\partial n$ and $\partial r_2/\partial n$ in the point P_s is straightforward under the consideration that r_0 is a typical vector spanning the object. Since holography is a short-range order probe ($r_0 < 1.5$ to 2.0 nm) we have that $r_0 \ll R$ and $r_0^* \approx 2R$. Indicating by R the position vector of P_s, we get

$$\left. \frac{\partial r_1}{\partial n} \right|_{P=P_s} \equiv - \frac{\partial |R - r_0|}{\partial R} = - \frac{R - (r_0 \cdot R/R)}{|R - r_0|} \underset{r_0 \ll R}{=} -1, \quad (2.20a)$$

$$\left. \frac{\partial r_2}{\partial n} \right|_{P=P_s} \equiv - \frac{\partial |R - r_0^*|}{\partial R} = - \frac{R - (r_0^* \cdot R/R)}{|R - r_0^*|} \underset{r_0^* \approx 2R}{=} +1. \quad (2.20b)$$

We therefore obtain

$$\left.\frac{\partial K(r \mid r_0)}{\partial n}\right|_{r=R_s} = -2\left(ik - \frac{1}{r_1}\right)\frac{e^{ikr_1}}{r_1}\bigg|_{r=R_s} \underset{kR\gg 1}{\simeq} -2ik\frac{e^{ik|R-r_0|}}{|R-r_0|}; \quad r_0 \ll R, \quad (2.21)$$

where we have dropped a term of the order $(kR)^{-1}$ since $kR \gg 1$ (kR is 10^8 to 10^9 in our case).

Using again the smallness of r_0, on the right-hand side of (2.21) for $|R - r_0|$ we can substitute R in the denominator and $R - (R \cdot r_0/R)$ in the exponent. We finally get

$$\frac{\partial K(R \mid r_0)}{\partial n} = -2ik\frac{e^{ikR}}{R}e^{-ik\cdot r_0}; \quad r_0 \ll R, \quad (2.22)$$

where $k \equiv kR/R$. Using (2.12) and (2.22), and writing $dS \equiv R^2\, d\Omega_k$, (2.17) finally reads

$$\psi_T(r_0) = A_0 + A_1 \int_S d\Omega_k\, I(k)\, e^{-ik\cdot r_0}, \quad (2.23)$$

where $A_0 = C_0 K(0 \mid r_0) - (ik/2\pi)\int_S d\Omega_k\, e^{-ik\cdot r_0}$, $A_1 = -ikC/2\pi$, and $I(k) \equiv I(R)$. A_0 constitutes an uninteresting background; as a function of r_0 it may peak only at the position $r_0 = 0$ of the atom emitter a. Therefore we shall drop it in what follows.

Since all quantities on the right-hand side of (2.23) are known, the wave function $\psi_T(r_0)$ is therefore determined. In the literature, (2.23) is referred to as the Helmholtz-Kirchhoff integral.

Now, also for ψ_T we define *reference* and *object* terms.

$$\psi_T = \psi_{T\,ref} + \psi_{T\,obj}. \quad (2.24)$$

Using (2.2), (2.10a), and (2.23) we get

$$\psi_{T\,ref}(r_0) = A\int_S d\Omega_k\, |\psi_{ref}(R)|^2\, e^{-ik\cdot r_0}, \quad (2.25a)$$

$$\psi_{T\,obj}(r_0) = A\int_S d\Omega_k [\psi^*_{obj}(R)\,\psi_{ref}(R) + \psi_{obj}(R)\,\psi^*_{ref}(R) + |\psi_{obj}(R)|^2]\, e^{-ik\cdot r_0}. \quad (2.25b)$$

The function appearing in the integral (2.25b):

$$\chi(k) \equiv |\psi(R)|^2 - |\psi_{ref}(R)|^2 = \psi^*_{obj}(R)\,\psi_{ref}(R) + \psi_{obj}(R)\,\psi^*_{ref}(R) + \psi^*_{obj}(R)\,\psi_{obj}(R) \quad (2.26)$$

is termed *anisotropy* in the literature. It must be obtained experimentally via subtraction of the reference wave flux. The reference flux is calculated theoretically. One must evaluate carefully the matrix elements $\mathcal{M}_{cL}$ given by (2.8). In the case of photoemission, the dipole excitation of an initial l-wave subshell leads to the interfering $l + 1$ and $l - 1$ final orbital angular momentum channels. The case of Auger emission is much more complex: in practical calculations it is often assumed that the initial state has an s-wave character [4, 5, 11].

Equation (2.25b) is the relevant integral to be evaluated in order to get the image of our object. It transforms the two-dimensional hologram into a three-dimensional image. The first two terms of the integral on the right-hand side of (2.25b) contain the usual hologram of optical holography, while the third term represents the self-interference or self-hologram.

From (2.10), the reference and object waves can be written as

$$\psi_{ref}(R) = \sum_L Y_L(k)\, A_L, \quad (2.27a)$$

$$\psi_{obj}(R) = \sum_q \sum_{L_q} Y_{L_q}(k)\, e^{ik\cdot R_{aq}}\, B^q_{L_q}. \quad (2.27b)$$

Using (2.25b) and (2.27), from a stationary-phase argument [2] we expect that $\psi_{T\,obj}(r_0)$ will yield peaks at

$$r_0 \simeq \pm R_{aq}, \quad (2.28a)$$

$$r_0 = R_q - R_p. \quad (2.28b)$$

This is certainly correct for s-waves (as in the optical case, where s-wave scattering dominates), or in the case of s-wave emission combined with moderately angle dependent scatterings from the neighbours. The latter condition is better realized at low energies since electron scattering presents a high angular anisotropy and relevant phase shifts as the energy increases. As a consequence, artifacts, such as shifts of the position of the atoms and image asymmetry or broadening, appear in the Helmholtz-Kirchhoff integral (2.25b). In Section 4 we shall discuss possible ways to cure these unpleasant features.

In (2.28a), the minus sign is related to the peaks present in the first term of the Helmholtz-Kirchhoff integral (2.25b) and it corresponds to the real images of the atoms of the object; the plus sign corresponds to their twin images. For $q = a$ one gets the image (twin = real) of the atom emitter. The presence of both real and twin images is a problem shared with optical holography.

The uncertainty principle of course limits the ultimate resolution with which the positions of the atoms can be determined by this method [20, 4, 5]: $\Delta r \gtrsim 1/(k_{max} - k_{min})$, where the projections of $\hbar(k_{max} - k_{min})$ on the coordinate axes are the uncertainties on the measured electron momenta.

If one centres the relevant part of the hologram along the z-axis and calls θ the half opening angle of the corresponding cone, the Heisenberg principle yields $\Delta x = \Delta y = \pi/(k \sin\theta) = \lambda_e/(2 \sin\theta)$ and $\Delta z = 2\pi/[k(1 - \cos\theta)] = \lambda_e/(1 - \cos\theta)$ showing that the resolution of the images of the atoms should improve for wider θ (with upper limit $\pi/2$) and using higher energy electrons.[3])

Equation (2.28b) corresponds to the third term of (2.25b) and yields peaks at the $\pm$ interdistances of all pairs of atoms, as an expression of the self-hologram; for $q = p$ one gets peaks at $r_0 = 0$, i.e. at the position of the atom emitter a, which after all is not too bad, but, more importantly, for $q \neq p$ peaks appear at positions where there are no atoms. These *ghost* images, which actually appear to be 10 to 20% in size of the real and twin

[3]) For $\theta = 60°$, at the electron energy of 100 eV one gets $\Delta x = \Delta y = 0.071$ nm, $\Delta z = 0.25$ nm. At 1000 eV: $\Delta x = \Delta y = 0.022$ nm, $\Delta z = 0.076$ nm.

images [12], would not be there if the holographic requirement $|\psi_{ref}| \gg |\psi_{obj}|$ were satisfied, as it happens in the simpler optical case. In the photoelectron or Auger electron holography this is not so since the electron–atom interaction is in general stronger, particularly for scattering in forward directions along a chain of atoms at high energies.

We shall see in Section 3 how one can eliminate the twin images and the noise due to the self-hologram in the case of photoelectrons.

We end this section by pointing out that the holographic method has the potential of getting information on near-surface atoms beyond nearest neighbours [4, 5], something which is not obtainable by the photoelectron or Auger electron diffraction approaches.

Methods of the type discussed in this section can also be applied to core level X-ray fluorescence [1, 13], to DLEED (diffuse low-energy electron diffraction) [14], and to Kikuchi patterns [15]. Spin-polarized photoelectron holography has been treated in [16, 17].

3. Elimination of Twin Images and Self-Hologram Effects in Photoelectron Holography

We shall treat in this section a method devised to cope with unphysical artifacts such as twin images and self-hologram effects in photoelectron holography.

The method suggested by Barton, Tong, and coworkers [18 to 23] introduces a Fourier transform operation in energy on $\psi_{Tobj}(r_0)$. In order to see this in detail, let us first apply the plane wave approximation (PWA) to our formulas. This approximation is able to render explicit the energy dependence of the propagators. It consists in fact in replacing, in the g-propagator, the Hankel function $h_l^{(+)}(kR)$ with its expression for large kR: $(-i)^{l+1}\, e^{ikR}/kR$.

For the g-propagator one then obtains

$$(g_{L_p L_q}(R_{pq}))_{PWA} = -\frac{4\pi}{k}\, i^{l_p - l_q} Y^*_{L_p}(R_{pq})\, \frac{e^{ikR_{qp}}}{R_{pq}}\, Y_{L_q}(R_{pq}). \tag{3.1}$$

We finally get the PWA expression of the object part of the wave function

$$\{\psi_{obj}(R)\}_{PWA} = -\frac{m}{2\pi\hbar^2}\, \frac{e^{ikR}}{R} \sum_L (-1)^l c_L \sum_{\substack{p \neq a \\ q}} e^{ikr_{aq}}\, F^{PWA}_{qp}(k_{rq}; k_{pa})\, \frac{e^{ikR_{pa}}}{R_{pa}}\, (-i)^l\, Y_L(R_{pa}), \tag{3.2}$$

where the multiple scattering amplitude $F^{PWA}_{qp}(k_{xq}; k_{pa})$ is defined by (see [6], Section 4).

$$F^{PWA}_{qp}(k_{xq}; k_{pa}) = -\frac{4\pi}{k} \sum_{L_p L_q} i^{l_p - l_q} Y_{L_q}(k_{xq})\, (\tau^p_{q L_p})_{PWA}\, Y^*_{L_p}(k_{pa}). \tag{3.3}$$

In terms of the scattering factor (scattering amplitude) f_p it satisfies the following multiple-scattering matrix equation:

$$F^{PWA}_{qp}(k_{xq}; k_{pa}) = \delta_{qp} f_p(k_{xp}; k_{pa}) + \sum_m f_q(k_{xq}; k_{qm})\, \frac{e^{ikR_{qm}}}{R_{qm}}\, (1 - \delta_{qm})\, F^{PWA}_{mp}(k_{qm}; k_{pa}) \tag{3.4}$$

with its perturbation expansion[4])

$$F^{PWA}_{qp}(k_{xq}; k_{pa}) = \delta_{qp} f_p(k_{xp}; k_{pa}) + f_q(k_{xq}; k_{qp})\, \frac{e^{ikR_{qp}}}{R_{qp}}(1 - \delta_{qp})\, f_p(k_{qp}; k_{pa}) + \sum_m f_q(k_{xq}; k_{qm}) \frac{e^{ikR_{qm}}}{R_{qm}} (1 - \delta_{qm})\, f_m(k_{qm}; k_{mp}) \frac{e^{ikR_{mp}}}{R_{mp}} (1 - \delta_{mp}) \times f_p(k_{mp}; k_{pa}) + \dots . \tag{3.5}$$

Let us now discuss the general structure, as far as the energy dependence of the propagators is concerned, of the terms appearing under the sign of integration of the Helmholtz-Kirchhoff integral (2.25b). For the first term, using (3.2) and (3.5), we can write

$$\begin{aligned} &\int_S d\Omega_k\, e^{-ik\cdot r_0} \{\psi^*_{obj}(R)\, \psi_{ref}(R)\}_{PWA} \\ &= \int_S d\Omega_k\, e^{-ik\cdot r_0} \left\{ \sum_q M^*_q\, e^{-ik\cdot R_{aq}} \frac{e^{-ikR_{aq}}}{R_{qa}} (1 - \delta_{qa}) \right. \\ &+ \sum_{q,p} M^*_{qp}\, e^{-ik\cdot R_{aq}} \frac{e^{-ikR_{qp}}}{R_{qp}} (1 - \delta_{qp}) \frac{e^{-ikR_{pa}}}{R_{pa}} (1 - \delta_{pa}) \\ &\left. + \sum_{q,p,m} M^*_{qpm}\, e^{-ik\cdot R_{aq}} \frac{e^{-ikR_{qp}}}{R_{qp}} (1 - \delta_{qp}) \frac{e^{-ikR_{pm}}}{R_{pm}} (1 - \delta_{pm}) \frac{e^{-ikR_{ma}}}{R_{ma}} (1 - \delta_{ma}) + \dots \right\}. \end{aligned} \tag{3.6}$$

As suggested in [18 to 23], we now take the following energy Fourier transform on the Helmholtz-Kirchhoff integral (2.25b):

$$\psi'_{Tobj}(r_0) = \int_0^{+\infty} \{\psi_{Tobj}(r_0)\}_{PWA}\, e^{ikr_0}\, w(k)\, dk, \tag{3.7}$$

$w(k)$ is a proper weight function which can limit the integration interval. It could be a sum of Dirac δ-functions.

After application of the Fourier transform (3.7) to (3.6), we discover that, apart from particular cases which we shall discuss in a while, we are able to get the suppression of all but the first term on the right-hand side (which represents the single-scattering contributions from the neighbours of the atom a (note that $q \neq a$)): For this term in fact, the peaks which appear at the real positions of the atoms $r_0 = R_{qa} \equiv R_q - R_a$ after integrating over angles, get reinforced after the energy Fourier transform (3.7) is performed, as can be understood from the stationary phase argument applied to the phase factor $\exp[ik(r_0 - R_{qa})]$. On the

[4]) $f_q(k_{xq}; k_{qp}) \equiv f_q(\theta_{xqp})$ is the scattering factor describing the electron as being shot from the atom p, scattering from the atom q, and emerging in the direction x (θ_{xqp} is the corresponding polar angle of scattering). For the differential cross section one has: $d\sigma/d\Omega = |f(\theta)|^2$. The scattering factor is connected with the partial wave T-matrix as follows: $f_q(\theta) = -(4\pi/k) \sum_L Y^*_L(k)\, t^q_l Y_L(k')$. (Note that formulae like (3.5) must be read from right to left in order to follow the correct time arrow of the process.)

contrary, the other, multiple-scattering, terms of (3.6) are in general suppressed, since the peak resulting from the energy integration does not coincide with that obtained from the angular integration.

As mentioned above, there are, however, particular cases where multiple scatterings contribute.

Consider for example the second term of (3.6). The angular integral peaks again at $r_0 = R_{qa} \equiv R_q - R_a$. When its Fourier transform (3.7) is taken, the energy phase factor $\exp[ik(r_0 - R_{qp} - R_{pa})]$ will give a contribution if the atom p is aligned with q and atom a so that $R_{qp} + R_{pa} = R_{qa}$ (i.e. p lies in between a and q), since in this way the peaks resulting from angular and energy integrations coincide. The contribution of this a pq chain will then add up to the q-term of the first term of (3.6). Similar considerations hold for the other terms of (3.6) which contribute if chains a $jk \ldots pq$ of aligned atoms are realized so that $R_{qp} + \ldots + R_{kj} + R_{ja} = R_{qa}$.

However, the contribution of these multiple scatterings is not harmful since it enhances the single-scattering term corresponding to the end atom of the chain.

Another possibility, which we have already mentioned in Section 2, is the case $q = a$ which yields a peak at the position $r_0 = 0$. It represents the image (true = twin) of the atom emitter, and it appears at least as a second-order effect.

Let us now consider the second term of the Helmholtz-Kirchhoff integral (2.25b),

$$\int_S d\Omega_k \, e^{-ik\cdot r_0} \{\psi_{obj}(R)\, \psi^*_{ref}(R)\}_{PWA}$$

$$= \int_S d\Omega_k \, e^{-ik\cdot r_0} \left\{ \sum_q M_q \, e^{ik\cdot R_{aq}} \frac{e^{ikR_{aq}}}{R_{qa}} (1 - \delta_{qa}) \right.$$

$$\left. + \sum_{q,p} M_{qp} \, e^{ik\cdot R_{aq}} \frac{e^{ikR_{qp}}}{R_{qp}} (1 - \delta_{qp}) \frac{e^{ikR_{pa}}}{R_{pa}} (1 - \delta_{pa}) + \ldots \right\}. \tag{3.8}$$

The angular integration yields the twin images of the atoms of the object, at the positions $r_0 = -R_{qa} \equiv R_a - R_q$, space reflected of the positions of the true images. However, the Fourier transform (3.7) of expression (3.8) suppresses all the terms since the energy phase factors $\exp(ik(r_0 + R_{qa}))$ $(q \neq a)$ or $\exp(ik(r_0 + R_{qp} + \ldots + R_{ja}))$ are always highly oscillating whichever the positions of the atoms. At most, a little contribution to the "background" bump at the position $r_0 = 0$ of the emitter is obtained.

The purpose of eliminating the twin images has therefore been achieved.

We come now to the discussion of the third (self-hologram) term of (2.25b). Its energy Fourier transform is

$$\int_0^{+\infty} dk \, w(k) \, e^{ikr_0} \int_S d\Omega_k \, e^{-ik\cdot r_0} \{|\psi_{obj}(R)|^2\}_{PWA}$$

$$= \int_0^{+\infty} dk \, w(k) \, e^{ikr_0} \int_S d\Omega_k \, e^{-ik\cdot r_0} \left\{ \sum_{p,q} H_{qp} \, e^{ik\cdot(R_{ap} - R_{aq})} \frac{e^{ik(R_{pa} - R_{qa})}}{R_{pa} R_{qa}} (1 - \delta_{pa})(1 - \delta_{qa}) \right.$$

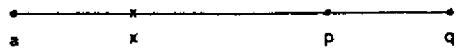

Fig. 2. After Fourier transform on the energy, in the self-hologram there still appear false atom (ghost) images along forward scattering chains of at least three atoms

$$+ \sum_{n,p,q} \left[H_{qpn} \, e^{ik\cdot(R_{ap} - R_{aq})} \frac{e^{ik(R_{pa} - R_{qn} - R_{na})}}{R_{pa} R_{qn} R_{na}} (1 - \delta_{pa})(1 - \delta_{qn})(1 - \delta_{na}) + \text{c.c.} \right]$$

$$+ \sum_{m,n,p,q} H_{qpnm} \, e^{ik\cdot(R_{ap} - R_{aq})} \frac{e^{ik(R_{pa} + R_{na} - R_{qm} - R_{ma})}}{R_{pn} R_{na} R_{qm} R_{ma}}$$

$$\left. \times (1 - \delta_{pn})(1 - \delta_{na})(1 - \delta_{qm})(1 - \delta_{ma}) + \ldots \right\}. \tag{3.9}$$

Let us first consider the first, single-scattering, term on the right-hand side of (3.9). From the stationary phase argument, the integration over angles would peak at $r_0 = R_{ap} - R_{aq}$, while the integration over energies would peak at $r_0 = R_{qa} - R_{pa} > 0$. Only if these two maxima coincide we get a sizeable contribution to the integral, and this means $|R_{ap} - R_{aq}| \approx R_{qa} - R_{pa} > 0$ which is satisfied only if the vectors R_{ap} and R_{aq} are parallel: the atoms p and q are aligned with atom a (and the atom p lies in between a and q). Therefore, as shown in Fig. 2, we obtain a ghost image at the point x defined by $r_x = R_{ap} - R_{aq} \equiv R_q - R_p$ on the chain apq. If $q = p$ we of course get a contribution to the background at $r_0 = 0$.

Much the same can be said about the other, multiple-scattering, terms of (3.9). They all give contributions for forward scattering along chains of atoms and an enhancement of the background at $r_0 = 0$.

We see therefore that, by making a Fourier transform on the energy of the Helmholtz-Kirchhoff integral (2.25b), one is able to suppress the twin images and most of the self-hologram. As far as the latter is concerned, the only contribution left is the appearance of ghost images (i.e. false atoms) along forward scattering chains of at least three atoms.

A very good point of this procedure is that, having practically cancelled the multiple-scattering contributions, one is left only with the consideration of single scatterings (first term on the right-hand side of (3.6)).

4. Treatment of Angular Anisotropies

The angular anisotropies, arising both from the directly emitted (reference) wave and from the scattered (object) waves, lead to aberrations which include shifts of the atom positions and image distortions. As far as the scattered waves are concerned, while at low energy the atomic scattering factor is rather isotropic, as the energy increases it becomes increasingly anisotropic being very large in the forward direction.

In the literature, ways have been conceived to cope with this problem [19, 21, 24 to 28]. In these approaches the beauty of the holographic approach is a bit lost, as we shall see.

As a result of the considerations of Section 3, for the case of photoemission the image wave field is given by

$$\psi'_{T\,obj}(r_0) \equiv A \int_0^{+\infty} dk\, w(k)\, e^{ikr_0} \int_S d\Omega_k\, \chi(k)\, e^{-ik\cdot r_0}$$

$$\approx A \int_0^{+\infty} dk\, w(k)\, e^{ikr_0} \int_S d\Omega_k\, \psi^*_{obj}(R)\, \psi_{ref}(R)\, e^{-ik\cdot r_0} \qquad (4.1)$$

and we can stick to single scatterings only.

The case of Auger emission will be treated here on the same basis, being understood that in the integral (4.1) one has $w(k) = \delta(k - k_f)$, where $\hbar k_f$ is the final momentum of the emitted Auger electron.

The single-scattering (SS) part of the wave function (2.10) reads

$$\psi^{SS}(R) = \psi_{ref}(R) + \psi^{SS}_{obj}(R)$$

$$= \bar{A}\frac{e^{ikR}}{R}\left\{\sum_L (-i)^l\, Y_L(k)\, \mathcal{M}_{cL} + \sum_{p\neq a} e^{ik\cdot R_{ap}} \sum_L O^L_p(k; R_{ap})\, \mathcal{M}_{cL}\right\}, \qquad (4.2)$$

where $\bar{A} = -m/(2\pi\hbar^2)$ and the object scattered-wave function O^L_p, and its plane wave approximation, is given by

$$O^L_p(k; R_{ap}) = \sum_{L_p} (-i)^{l_p}\, Y_{L_p}(k)\, t^l_p g_{L_pL}(R_{pa}) \underset{PWA}{\Rightarrow} f_p(\theta_{fpa})\frac{e^{ikR_{pa}}}{R_{pa}}(-i)^l\, Y_L(R_{pa}), \qquad (4.3)$$

where θ_{fpa} is the angle of scattering from the atom p defined by $\cos\theta_{fpa} = k \cdot R_{pa}/kR_{pa}$.

The presence of scattering phase shifts in (4.2) (see also (4.4) and (4.5) below) is responsible for the shift in the positions of the images of the atoms.

In the case of dipole photoemission from an s-subshell, (4.2) is very simply given in the PWA,

$$\{\psi^{SS}_{s\text{-subshell}}(R)\}^{dipole}_{PWA} = \hat{A}\mathcal{M}_{l=1}(k)\frac{e^{ikR}}{R}\left\{\frac{\varepsilon\cdot k}{k} + \sum_{p\neq a}\frac{\varepsilon\cdot R_{pa}}{R_{pa}}\frac{e^{i[kR_{pa}(1-\cos\theta_{fpa})+\varphi_p(\theta_{fpa})]}}{R_{pa}}|f_p(\theta_{fpa})|\right\}. \qquad (4.4)$$

where $\hat{A} = em(\hbar\omega)^{1/2}/(2(2\pi)^3\hbar^2 k)$ is slowly energy dependent, ε and $\hbar\omega$ are the polarization unit vector and the energy of the incoming photon, and $\mathcal{M}_{l=1}(k) = \int_0^\infty r\, dr\, \psi^{(+)}_{a,l=1}(k, r)\, R_{l=0}(r)$.

We have written explicitly the amplitude $|f_p|$ and the phase φ_p of the scattering factor f_p.

In the case of Auger emission of an electron with final $L \equiv l, m$ angular momentum, in the PWA (4.2) reads

$$\{\psi^{SS}_L(R)\}^{Auger}_{PWA}$$

$$= \hat{B}_L\frac{e^{ikR}}{R}\left\{Y_L(k) + \sum_{p\neq a}\frac{e^{i[kR_{pa}(1-\cos\theta_{fpa})+\varphi_p(\theta_{fpa})]}}{R_{pa}}|f_p(\theta_{fpa})|\, Y_L(R_{pa})\right\}, \qquad (4.5)$$

where $\hat{B}_L = \hat{A}(-i)^l\mathcal{M}^{Auger}_{cL}$.

From the structure of (4.2) we see that, if we divide the experimental photoemission anisotropy function $\chi(k)$ by the angular part of the reference wave,

$$\chi(k) \to \tilde{\chi}(k) = \frac{\chi(k)}{D_{ref}(k)}, \qquad (4.6a)$$

$$D_{ref}(k) = \sum_L (-i)^l\, Y_L(k)\, \mathcal{M}_{cL}, \qquad (4.6b)$$

we eliminate altogether the distortions caused by this angular asymmetry. Note that for a dipole photoemission from an s-core level, (4.6) is tantamount to dividing by $\varepsilon\cdot k/k$, while for Auger s-wave emission the denominator $D_{ref}(k)$ is of course a constant. The operation (4.6) can be considered as a redefinition of the boundary condition (2.12).

We need now to discuss how to cope with the anisotropies present in the object waves of the integrand of (4.1).

4.1 The SWEEP method

A first possible procedure is that proposed by Tong and collaborators [19, 21, 24]. To be consistent with our procedures, we shall rephrase it a bit.

We first evaluate (4.1) using the experimental $\chi(k)$ corrected as in (4.6) for the angular anisotropy of the reference wave. We then fix our attention on a particular bump p appearing at the distance R'_{ap} from the atom a and representing a neighbour of a. Pre-existing knowledge about the system in question, will avoid the risk that a self-hologram false atom of the type discussed at the end of Section 3 is taken for a good atom. We now perform the following operation on $\tilde{\chi}(k)$:

$$\tilde{\chi}(k) \to \chi_{SWEEP}(k) = \frac{\tilde{\chi}(k)}{D_{obj}(k; R'_{pa})}, \qquad (4.7a)$$

$$D_{obj}(k; R'_{pa}) = e^{-ikR'_{pa}} R'_{pa} \sum_L O^L_p(k; R'_{pa})\, \mathcal{M}_{cL} \underset{PWA}{\approx} f_p(\theta_{fpa}) \sum_L (-i)^l\, Y_L(R'_{pa})\, \mathcal{M}_{cL}, \qquad (4.7b)$$

and carry out the integration (4.1). In the original papers, Tong et al. actually integrate only over the forward, or backward, peak on a small angular window of half angle $\approx 30°$ centred along R'_{ap}. Their formalism is then known as the SWEEP method (for small-window energy extension process).

In (4.7), the outgoing scattered-wave function $O^L_p(k; R'_{ap})$, and the scattering factor $f_p(\theta_{fpa})$, are theoretical expressions evaluated for an atom p of a given chemical species. This second step should have yielded an improved position R''_{ap}. The procedure is repeated by dividing $\tilde{\chi}(k)$ as shown in (4.7), where now R'_{ap} is replaced by R''_{ap}. By iteration one should converge to a final value R_{ap} for the position vector of the atom p. One must repeat the same procedure also for the other bumps in order to complete the determination of the structure around the atom a.

4.2 The SWIFT method

A second procedure, proposed by Saldin and coworkers [25 to 28], is an original variation of the above approach. For coherence with the rest of our text, we discuss it within the framework of (4.1), i.e. by including also the energy Fourier transform.

After having corrected the experimental $\chi(k)$ as in (4.6) for the angular anisotropy of the reference wave, let us perform the following operation on $\tilde{\chi}(k)$ [25 to 28]:

$$\tilde{\chi}(k) \to \chi_{\text{SWIFT}}(k) = \frac{\tilde{\chi}(k)}{D_{\text{obj}}(k; r_0)}, \tag{4.8a}$$

$$D_{\text{obj}}(k; r_0) = e^{-ikr_0} r_0 \sum_L O_p^L(k; r_0)\, \mathcal{N}_{cL} \underset{\text{PWA}}{\approx} f(\theta_{r0a}) \sum_L (-i)^l Y_L(r_0)\, \mathcal{N}_{cL}, \tag{4.8b}$$

and then carry out the integration (4.1).

Here the angle θ_{r0_a} is defined by: $\cos\theta_{r0_a} = k \cdot r_0/kr_0$ and the outgoing scattering-wave function $O_p^L(k; r_0)$ (or the scattering factor $f(\theta_{r0_a})$) is now a generalized scattering amplitude evaluated at the position of the image point r_0 as if a hypotetical atom would be sitting there. Since the transformation involves the scattering amplitude, the authors have named it SWIFT, for scattered-wave-included Fourier transform.

According to the calculations performed in [25 to 28], with this method an improvement of the atom positions and image distortions is actually realized at the stationary-phase points $r_0 = R_{sp}$. As in the case of the SWEEP method, due care has to be applied to spot the existence of possible ghosts.

A good point of this procedure is that the entire interference pattern is inverted in only one step. No prior knowledge of the forward scattering directions locating the atoms is required. This method spoils, however, the simple structure of Fourier transform over the angles possessed by the Helmholtz-Kirchhoff algorithm (2.25b) (and also by (4.1)), as naturally obtained from the holographic approach.

Also operations (4.7) and (4.8), even within their artificiality, could be thought of as being redefinitions of the boundary condition (2.12).

5. Conclusions

In this article we have reviewed the theory of electron emission holography. Its formulation has been provided in Section 2 on a sound mathematical basis.

We have seen that, as in the optical case, one is faced with the presence of twin images. Besides, however, other artifacts appear in electron emission holography due to the fact that, at variance with the optical case, here the object wave is not small with respect to the reference wave and the scattering is in general not dominated by s-waves.

Sections 3 and 4 have been devoted to the discussion of these artifacts and to a review of the various correction procedures proposed in the literature for their elimination. In doing so, we have also seen that the proposal by Barton, Tong, and collaborators of performing an energy Fourier transform of the holography integral (2.23) is able to eliminate most of the multiple-scattering contributions to the hologram.

Apart from the complications mentioned above, the holographic method has the merit of being rather direct. One has to remember that in electron emission diffraction methods the structure information is obtained only after a lengthy trial-and-error procedure of comparing experimental spectra with those obtained by means of extensive multiple-scattering calculations. Holography requires, however, an increased amount of experimental data, and therefore of data acquisition times, with respect to the diffraction methods. But this is at hand now at the new high brightness synchrotron radiation sources.

We have seen in Section 2 that, with the use of the simple Helmholtz-Kirchoff holography integral (2.23), atoms can be located with an accuracy of a few hundredth nm at best. Taking

also into account the fact that, by performing an energy Fourier transform, one can improve this spatial resolution, we feel that, before the investigator involves himself with the more sophisticated trial-and-error method mentioned above, electron emission holography provides him with a quick tool to get within shooting range of a more accurate determination of the positions of atoms at or near a surface.

References

[1] A. Szöke, AIP Conf. Proc. 147, 361 (1986).
[2] J. J. Barton, Phys. Rev. Letters 61, 1356 (1988).
[3] D. Gabor, Proc. Roy. Soc. A 197, 454 (1949); Proc. Phys. Soc. B 64, 449 (1951).
[4] S. A. Chambers, Surface Sci. Rep. 16, 261 (1992).
[5] C. S. Fadley, Surface Sci. Rep., 19, 231 (1993).
[6] L. Fonda, phys. stat. sol. (b) 182, 9 (1994).
[7] B. L. Gyorffy and M. J. Stott, Solid State Commun. 9, 613 (1971).
[8] F. T. S. Yu, Optical Information Processing, J. Wiley & Sons, New York 1983.
[9] M. Born and E. Wolf, Principles of Optics, Pergamon Press, Oxford 1980 (p. 374).
[10] A. Sommerfeld, Optics, Academic Press, New York/London 1964 (p. 200).
[11] C. S. Fadley, in: Synchrotron Radiation Research: Advances in Surface and Interface Science, Vol. 1, Techniques. Ed. R. Z. Bachrach, Plenum Press, New York 1992 (p. 421).
[12] S. Thevuthasan, G. S. Herman A. P. Kaduwela, R. S. Saiki, Y. J. Kim, W. Niemczura, M. Burger, and C. S. Fadley, Phys. Rev. Letters 67, 469 (1991).
[13] P. M. Len, S. Thevuthasan, C. S. Fadley, A. P. Kaduwela, and M. A. Van Hove, to be published.
[14] D. K. Saldin and P. L. de Andres, Phys. Rev. Letters 64, 1270 (1990).
[15] G. R. Harp, D. K. Saldin, and B. P. Tonner, Phys. Rev. Letters 65, 1012 (1990).
[16] A. P. Kaduwela, Z. Wang, M. A. Van Hove, and C. S. Fadley, to be published.
[17] E. M. E. Timmermans, G. T. Trammel, and J. P. Hannon, J. appl. Phys. 73, 6183 (1993).
[18] J. J. Barton and L. J. Terminello, in: Structure of Surfaces III, Ed. S. Y. Tong, M. A. Van Hove, X. Xide, and K. Takayanagi, Springer-Verlag, Berlin 1991 (p. 107).
[19] S. Y. Tong, Hua Li, and H. Huang, Phys. Rev. Letters 67, 3102 (1991).
[20] J. J. Barton, Phys. Rev. Letters 67, 3106 (1991).
[21] S. Y. Tong, H. Huang, and Hua Li, Mater. Res. Soc. Symp. Proc. 208, 13 (1991).
[22] H. Huang, Hua Li, and S. Y. Tong, Phys. Rev. B 44, 3240 (1991).
[23] L. J. Terminello, J. J. Barton, and D. A. Lapiano-Smith, J. Vacuum Sci. Technol. B 10, 2088 (1992), Phys. Rev. Letters 70, 599 (1993).
[24] S. Y. Tong, C. M. Wei, T. C. Zhao, H. Huang, and Hua Li, Phys. Rev. Letters 66, 60 (1991).
[25] S. Hardcastle, Z.-L. Han, G. R. Harp, J. Zhang, B. L. Chen, D. K. Saldin, and B. P. Tonner, Surface Sci. 245, L190 (1991).
[26] B. P. Tonner, Z.-L. Han, G. R. Harp, and D. K. Saldin, Phys. Rev. B 43, 14423 (1991).
[27] D. K. Saldin, G. R. Harp, B. L. Chen, and B. P. Tonner, Phys. Rev. B 44, 2480 (1991).
[28] D. K. Saldin, G. R. Harp, and B. P. Tonner, Phys. Rev. B 45, 9629 (1992).

(Received November 10, 1994)

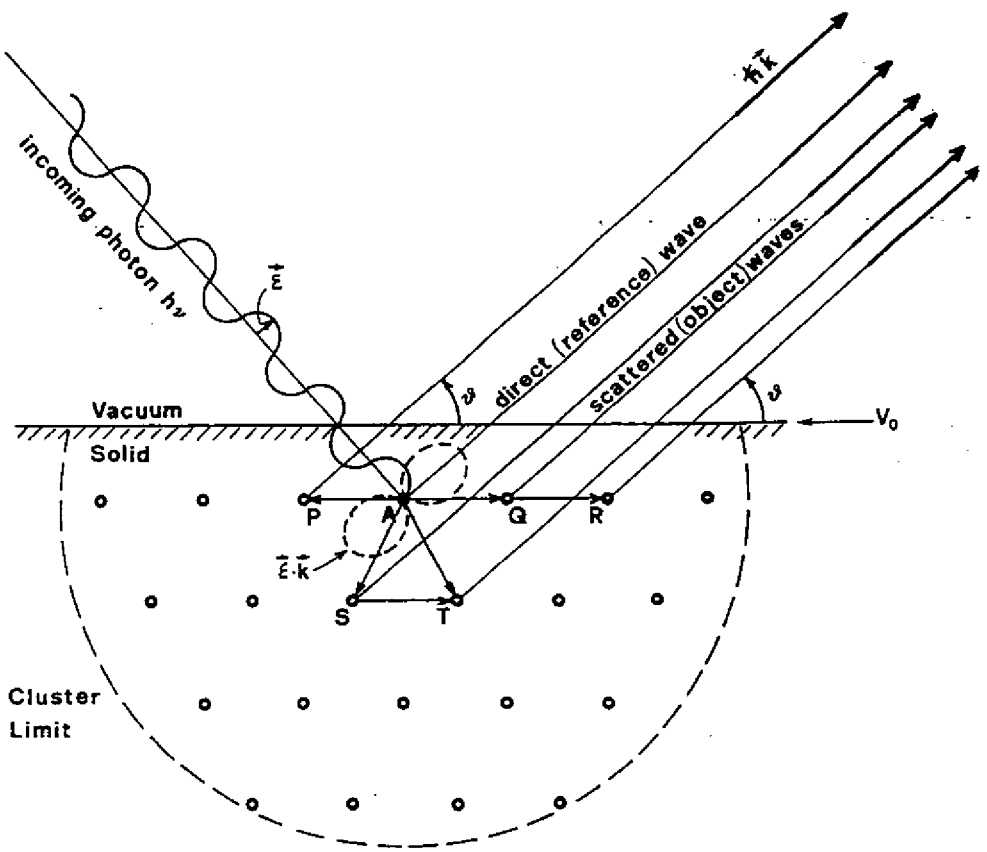
incoming photon hν
ħk
direct (reference) wave
scattered (object) waves
Vacuum
Solid
V_0
P
A
Q
R
S
T
$\vec{\varepsilon}\cdot\vec{k}$
Cluster
Limit

Fig. 1

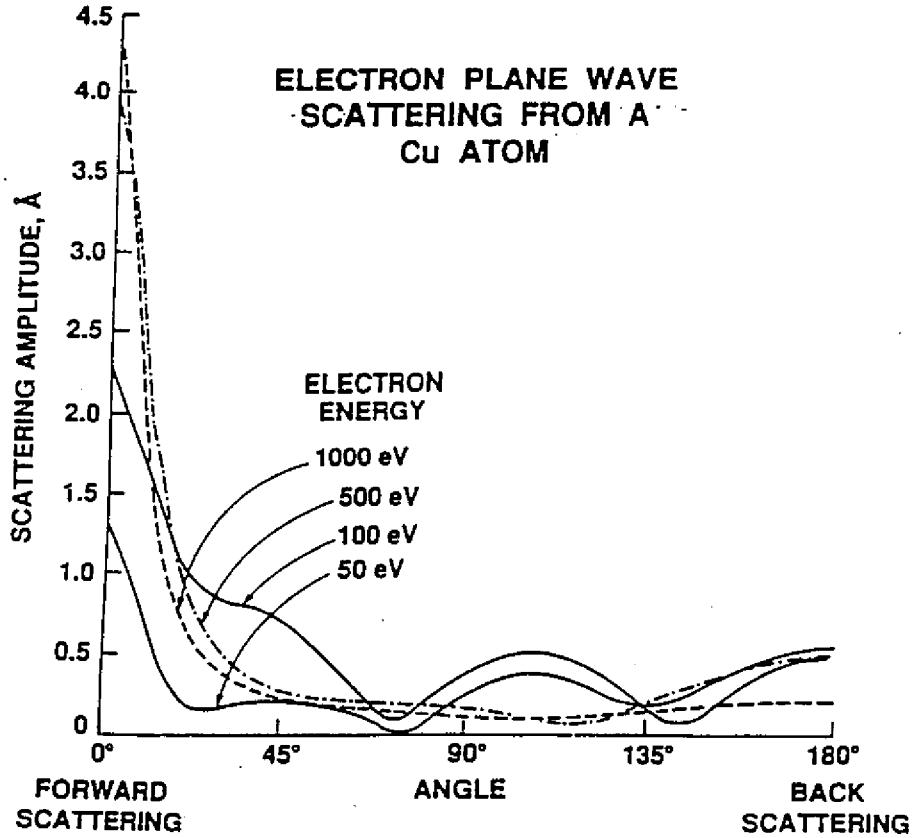
ELECTRON PLANE WAVE
SCATTERING FROM A
Cu ATOM
SCATTERING AMPLITUDE, Å
4.5
4.0
3.5
3.0
2.5
2.0
1.5
1.0
0.5
0
ELECTRON
ENERGY
1000 eV
500 eV
100 eV
50 eV
0°
45°
90°
135°
180°
FORWARD
SCATTERING
ANGLE
BACK
SCATTERING

Fig. 2

A.P. KADUWELA, D.K. SALDIN and B.P. TONNER

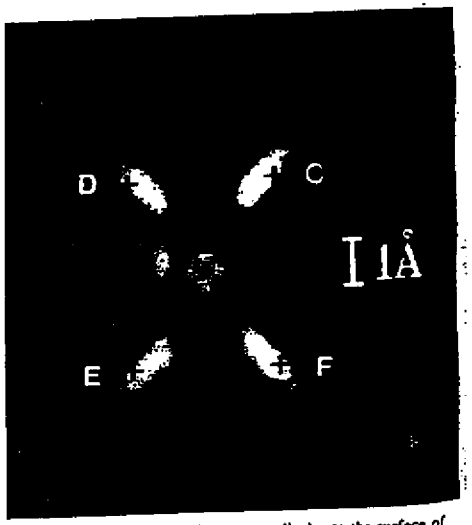

FIG. 4. A view in the plane perpendicular to the surface of the holographic reconstruction of the data from Fig. 1. The crosses mark positions of atoms in the ideal lattice. The elongated shape of the atom image is due to a reduction in resolution parallel to the electron emission direction.

Phys. Rev. Letters 65, 1012 (1990)

PETERSEN, TERMINELLO, BARTON and SHIRLEY

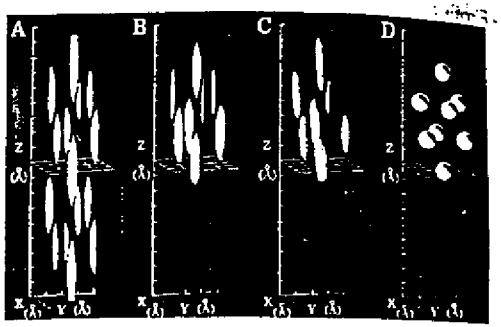

Fig. 10. Elimination of twin images as a result of the application of energy FT holography. Panel A shows a symmetry-averaged $\chi(k)$ at $k = 9.8$ Å^{-1} (366 eV). Twin images appear for $z < 0$. Panel B shows the result of phase-summing on eight values of k in the interval 8.8-10.2 Å^{-1}. Panel C shows the same pattern without symmetry averaging. Panel D represents a model showing the atoms in the positions as expected. (From Ref. 89.)

Chem. Phys. Lett. 213, 412(1993); 220, 46 (1994)

PHYSICAL REVIEW B, VOLUME 63, 115119

Multiatom resonant photoemission

A. W. Kay,[1,2] F. J. Garcia de Abajo,[2,3] S.-H. Yang,[2] E. Arenholz,[4] B. S. Mun,[1,2] N. Mannella,[1,2] Z. Hussain,[4] M. A. Van Hove,[1,2] and C. S. Fadley[1,2]

[1]*Department of Physics, University of California-Davis, Davis, California 95616*

[2]*Materials Sciences Division, Lawrence Berkeley National Laboratory, Berkeley, California 94720*

[3]*Centro Mixto CSIC-UPV/EHU, San Sebastian, Spain*

[4]*Advanced Light Source, Lawrence Berkeley National Laboratory, Berkeley, California 94720*

(Received 21 July 2000; revised manuscript received 17 November 2000; published 2 March 2001)

We present experimental and theoretical results related to multiatom resonant photoemission, in which the photoelectron intensity from a core level on one atom is influenced by a core-level absorption resonance on another. We point out that some prior experimental data has been strongly influenced by detector nonlinearity and that the effects seen in new corrected data are smaller and of different form. Corrected data are found to be well described by an extension of resonant photoemission theory to the interatomic case, provided that interactions beyond the usual second-order Kramers-Heisenberg treatment are included. This microscopic theory is also found to simplify under certain conditions so as to yield results equivalent to a classical x-ray optical approach, with the latter providing an alternative, although less detailed and general, physical picture of these effects. The potential utility of these effects as near-neighbor probes, as well as their implications for x-ray emission and x-ray scattering experiments, are also discussed.

DOI: 10.1103/PhysRevB.63.115119 PACS number(s): 79.60.−i, 68.35.−p, 78.20.Ci, 78.70.Dm

I. INTRODUCTION

In several recent papers by our group,[1–5] it has been suggested that photoemission associated with a certain core electronic level of a given atom "*A*" can be significantly enhanced in intensity by tuning the photon energy through core-level absorption edges of a near-neighbor atom "*B*." The apparent enhancements seen in experimental data for several metal oxides (e.g., MnO, Fe_2O_3, and $La_{0.7}Sr_{0.3}MnO_3$),[1,2] as well as in a series of Cr/Fe alloys and bilayers[3b] were very large, ranging up to 40–100% of the nonresonant intensity, and they were furthermore observed to follow closely the x-ray absorption coefficient of atom *B* in shape.[1–3] The effects observed have been termed multiatom resonant photoemission (MARPE) to distinguish them from the better-known intra-atomic single-atom resonant photoemission (SARPE). Similar effects have also been reported in other transition metal compounds[6] and in adsorbates[7] by other groups. Analogous and presumed related enhancements also appeared to be present in the secondary decay processes of Auger electron and fluorescent x-ray emission, again tracking very closely the x-ray absorption coefficient in form.[4] A theoretical model based on an extension of normal SARPE theory has also been presented to describe these results, and the first comparisons of calculations based on it yielded encouraging agreement with experiment.[5] The potential utility of such effects for studying near-neighbor atom identities and bonding have also been pointed out.[1–4] Independent of this work on *core-core* multiatom resonant photoemission, other groups have reported the enhancement of *valence* photoemission intensities primarily associated with emission from a certain atom *A* upon tuning the photon energy through the core-level absorption edges of a nearby atom *B*, with this work including measurements near solid-solid interfaces[8,9] and on a free molecule.[10] No attempts have as yet been made to theoretically model this latter type of valence-core MARPE effect.

In this paper, we first point out that the measurement of the core-core multiatom resonant photoemission effects mentioned above (or indeed any resonant-or nonresonant-photoemission effect) must be carried out with extreme care to avoid nonlinearities in the electron detector response, and illustrate these effects by carrying out corrections on a few representative data sets for O 1 s emission from MnO in resonance with the Mn 2*p* excitations. The corrected results are found to show significantly smaller MARPE effects on photoelectron intensities, with shapes now considerably different from the x-ray absorption coefficient. In addition, theoretical calculations based on the previously discussed microscopic model,[5] and on a simpler classical theory of x-ray optics[11] are presented and found to yield excellent agreement with the remaining experimental effects, thus clarifying the physics involved. We also comment on the implications of this work for other recent core-core and valence-core MARPE measurements,[6–10,12,13] as well as for x-ray emission[4,14] and x-ray scattering experiments.

II. EXPERIMENTAL PROCEDURE AND DATA ANALYSIS

All photoelectrons were analyzed in energy and detected with a Scienta ES200 electron spectrometer system,[15a] as situated either on a bend-magnet beamline[15b] (9.3.2) or an undulator beamline (4.0.2) at the Berkeley Advanced Light Source. The final multichannel detection system used is that provided as part of the standard equipment by the manufacturer: a microchannel plate multiplier followed by a phosphor screen at high voltage in a vacuum, and a charge-coupled device (CCD) video camera outside of the vacuum to finally convert light pulses into counts. We have operated this detector in the "greyscale" or "analog" mode in which an integrated CCD charge is used for counting, rather than in the alternate "black-and-white" or "digital mode," in

which individual pulses are counted. The detector has in addition been used as delivered and installed by the manufacturer; thus, the discriminator setting was left at its recommended value at setup. This spectrometer and detector system is furthermore the same as that used by some other groups attempting to measure multiatom resonant photoemission effects.[6,7] We have in the present study calibrated our detector system in both analog and black-and-white modes by using a standard x-ray tube with a continuously variable emission current at a fixed high voltage, verifying initially that the total electron current from the sample tracked linearly with the emission current: thus, the emission current is directly proportional to the x-ray flux incident on the sample. The general methodology for this calibration and the final correction of spectra is discussed elsewhere,[16,17] and in one case, discussed together with previous data for a similar electron detection system.[16]

III. RESULTS AND DISCUSSION

In Fig. 1(a) and its inset, we show the measured (dashed curve) vs ideal or "true" (straight line) response of this detector as used in analog mode over a countrate range spanning 0 to 500 Hz in a typical *x*-*y* pixel of the approximately 70 000 pixels in the CCD camera used in normal operation. We have verified that all spatial regions of the detector behave in essentially the same manner,[17] so the performance shown can be applied over the entire active region. The inset makes it clear that there is curvature in the response, with falloff and incipient saturation being seen as the countrate increases. Although one might then expect linearity for the lowest countrates, the blowup of the 0–20 Hz region (the maximum used in all of our measurements to avoid falloff and saturation) shown in the main figure makes it clear that there is still significant nonlinearity, including what is found to be a quadratic component as compared to an ideal detector with linear response that we define to be equal to that of the real detector in the limit of zero countrate (solid line of the unit slope in the figure and inset). For reference, the 20 Hz per pixel rate would correspond to a global countrate of 1.4 MHz (before a "multiple counting" divisor introduced by the manufacturer's software is applied) for the entire useable portion of the detector phosphor and if the phosphor were evenly illuminated.

Thus, although measured and true rates can be conveniently defined to yield the same unit slope as countrates go to zero, the measured rates deviate significantly from linearity, showing quadratic overcounting over the full range of our earlier measurements. Almost identical quadratic effects were also found in the black-and-white mode, although this mode was not used in our measurements.[17] An additional effect of such quadratic overcounting is the narrowing or broadening of the photoelectron peaks in energy as a high-intensity resonance is passed, depending on which portion of the nonlinear response a given photon energy scan occupies, and we have in prior work[1–4] also used the additional criterion of constant peak width over an energy scan to try to minimize nonlinearities. However, this criterion of constant peak width proves to be inadequate for avoiding spurious effects on peak intensity measurements. Using methods described in detail elsewhere,[16,17] the detector response curve in Fig. 1(a) can be turned into an efficiency, and the inverse of this efficiency then used to correct individual spectra in a point-by-point fashion. Although it is possible that adjusting the discriminator setting on the detector could reduce these nonlinearities, several other groups appear to have encountered the same type of nonlinearity with the standard manufacturer's settings.[6,7,18] It has also been suggested that a change in the CCD camera might improve this behavior,[19] and this is another direction for future investigation.

Both uncorrected (as measured) and corrected ("true") spectra are shown in Fig. 1(b) for O 1*s* emission from MnO, where the photon energies of 637.6 and 640.2 eV have been chosen to be just below the strong Mn $2p_{3/2}$ resonance and just on this resonance, respectively.[1] Because of the significantly increased background level associated with secondary decay processes and inelastically scattered electrons arising from the Mn $2p_{3/2}$ absorption, which in turn forces the detector countrate further up its nonlinear response curve, the correction procedure acts to a greater degree on resonance. Thus, the intensity on resonance is artificially enhanced. In fact, in order to decrease these nonlinear correction effects to negligibly low levels, we have found in data not shown here that the countrates had to be lowered by another order of magnitude from our prior typical operating points, or to about 2 Hz per pixel.[17]

In Fig. 1(c), we now show uncorrected and corrected O 1*s* intensities, measured as areas by fitting analytical peak shapes plus backgrounds to spectra such as those in Fig. 1(b), as a function of photon energy, with curves such as these being discussed previously in terms of multiatom resonant photoemission.[1–4] It is clear that the uncorrected MARPE scan follows very closely the previously published x-ray absorption curve for MnO in the Mn $2p_{3/2}$ region,[1–3] which we also show in Fig. 1(c) as derived from the inelastic electron background under the O 1*s* spectra,[1] with about a 32% enhancement of intensity of the O 1*s* intensity at the Mn $2p_{3/2}$ peak.[1–4] However, the corrected MARPE scan shows a much smaller effect of about 12% in overall excursion, and also of a much different form, being negative just below the resonance and then going positive. In data obtained at other x-ray incidence angles over the range of 5–30°,[17] we have also found that these corrected effects are strongly dependent on angle, being largest for more grazing x-ray incidence angles, such as the analogous results for 10° shown in Fig. 1(c), which exhibit about 37% overall excursion, and quickly decaying in magnitude as this angle is increased. We estimate our overall systematic error in the corrected spectra as ±2%, with some channel-to-channel statistical scatter around this.

As a final point on this correction, it appears that, with constant UHV conditions of operation, the correction function does not change significantly over a period of months, with older data obtained via the same detector setup showing reasonable correctability. However, the correction function should in any case be checked frequently to avoid any drifts with time.

It is thus clear that detector nonlinearity can have a dra-

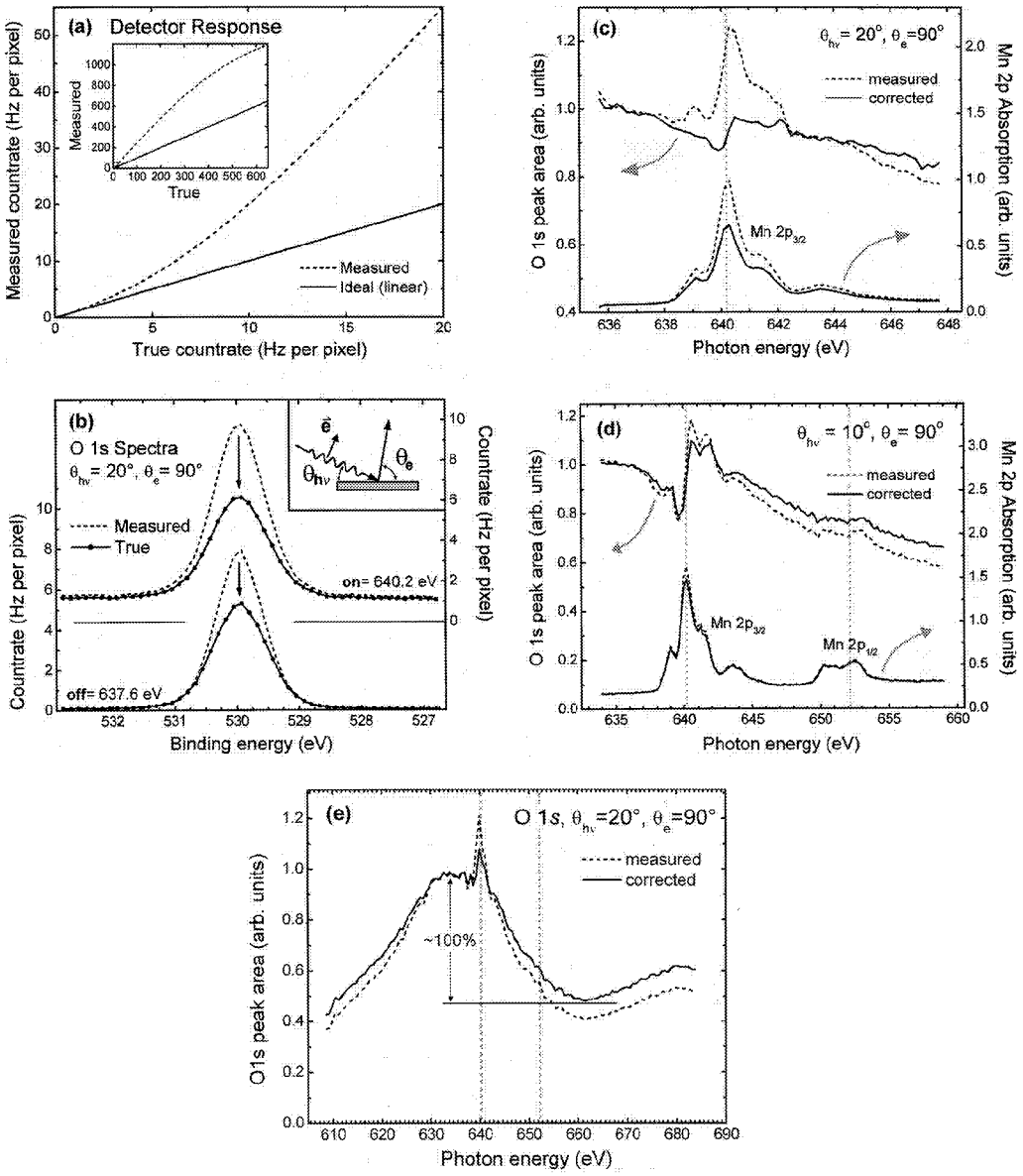

FIG. 1. (a) The measured response function of our multichannel detection system (dashed curves), as plotted against the linear reference of an ideal detector (solid lines). The ordinate is measured counts per energy pixel, and the abscissa is proportional to the "true countrate" expected, which is in turn proportional to the emission current of the x-ray tube and, thus, incident x-ray flux. The inset shows the same kind of plot over a much broader countrate range. The solid lines for the ideal detector are chosen to asymptotically agree with the slope of the measured curve at the lowest countrates, although the final corrected results in (b)–(d) do not depend on this choice of reference. (b) O 1s spectra from MnO(001) off resonance (photon energy $h\nu=637.6$ eV) and on resonance ($h\nu=640.2$ eV) are shown before (dashed curves) and after (solid curves) applying the correction for detector nonlinearity. The inset shows the experimental geometry, with x-ray incidence for this case at $\theta_{h\nu}=20°$ and electron exit along the surface normal at $\theta_e=90°$. The radiation is linear p-polarized, with the electric field vector **e** lying in the plane of the figure. (c) O 1s intensities derived from fitting analytical peak shapes to uncorrected (dashed curve) and corrected (solid curve) spectra such as those in (b) as a function of photon energy over the Mn $2p_{3/2}$ absorption range and still for $\theta_{h\nu}=20°$, $\theta_e=90°$. Also shown in the bottom of the panel is the Mn $2p_{3/2}$ absorption coefficient, as measured via the inelastic background underneath the O 1s peak. (d) As (c), but for $\theta_{h\nu}=10°$, $\theta_e=90°$ and extending over the full Mn $2p_{3/2,1/2}$ range. The countrates here were actually higher than in (c), but spanned a smaller portion of the detector dynamic range, and hence, the corrections are smaller in magnitude. (e) As (b), but with a broader energy range that clearly shows the oscillation associated with scanned-energy photoelectron diffraction.

matic effect on such measurements, with the solid curves in Figs. 1(b), 1(c), and 1(d) now representing much more accurately any effects beyond a simple one-electron picture of O 1s emission from MnO. Without such interatomic effects, one should observe a simple smooth curve of negative slope over this region in energy due to a combination of subshell cross section and electron inelastic attenuation length variation,[11,20] as perhaps modulated by energy-dependent

photoelectron diffraction (PD).[17,21] The effects of scanned-energy photoelectron diffraction are in fact clearly shown in Fig. 1(e), which represents a broader energy scan for the same experimental conditions as in Fig. 1(c). Here, the long-wavelength oscillation with a maximum at ~634 eV has been verified via theoretical calculations to be due to PD effects.[17]

We also note that, in addition to affecting photoemission results, prior measurements of secondary Auger and x-ray emission effects[4] also appear to have been strongly influenced by such detector nonlinearities, for the former, just as for the photoelectron case due to the identical instrumentation, and for the latter via an x-ray absorption coefficient necessary for a self-absorption correction that was measured via secondary electrons in the same electron spectrometer.

Beyond the particular case of MARPE considered here, we also point out that such detector nonlinearities need to be corrected for and/or minimized in any use of this detector system for quantitative peak intensity analysis, as any comparison of intensities obtained over a range of countrates, even in a single spectrum, can be significantly altered by these effects.

IV. THEORY AND DISCUSSION

A. Interatomic resonant photoemission model

We now consider several levels of theory in order to explain the remaining effects that link the O $1s$ intensity to the Mn $2p$ absorption process as seen in Figs. 1(c) and 1(d), first considering these effects via a prior microscopic many-body theoretical treatment of MARPE based on a resonant photoemission model,[5] and then showing that this approach can be successively simplified for the case at hand to yield results essentially identical to those from classical x-ray optical theory. Focusing still on the case of O $1s$ photoemission from MnO(001) and the system initially prepared in its many-body ground state $|g\rangle$, the contribution of the direct or unscattered wave function to the photoelectron intensity can be written

$$I(\mathbf{k}) \propto |\phi_k^0(\mathbf{r})|^2 \propto \left| \sum_{l\mu} Y_{l\mu}(\hat{\mathbf{k}}) i^l h_l^{(+)}(kr) M_{El\mu} \right|^2, \quad (1)$$

where $\mathbf{k}$ is the photoelectron wave vector, $\phi_k^0(\mathbf{r})$ is the wave function at the detector, $Y_{l\mu}$ is a spherical harmonic, $h_l^{(+)}(kr)$ is a spherical Hankel function, and

$$M_{El\mu} = \langle El\mu, \mathrm{O}1s | T | g \rangle \quad (2)$$

is the matrix element describing the transition to the final state with a photoelectron $|El\mu\rangle$ of energy $E = \hbar^2 k^2/2m$ and an O $1s$ hole. Final-state photoelectron diffraction effects can also be incorporated in this model by using $M_{El\mu}$ as input for self-consistent multiple-electron-scattering equations.[22]

The transition matrix T can be conveniently expanded in a power series with respect to the perturbation of the radiation field V. One then has[23]

$$T = V + VG_0V + VG_0VG_0V + \cdots, \quad (3)$$

where G_0 is the Green function of the unperturbed solid. If we keep only terms up to second order in V, the part of Eq. (3) that makes a nonzero contribution to Eq. (2) reduces to the well-known Kramers-Heisenberg formula for resonant photoemission[24]

$$T = V_{\mathrm{rad}}^0 + \sum_{j,m} V_{\mathrm{AI}}^j \frac{|m,j\rangle\langle m,j|}{\hbar\omega + E_g - E_m + i\Gamma_m/2} V_{\mathrm{rad}}^j, \quad (4)$$

where V_{rad}^0 is the interaction of the radiation with the emitter, V_{rad}^j is the interaction with the resonating atom j, V_{AI}^i is the autoionizing Coulomb interaction between the emitter and atom j, E_g is the ground state energy, and the sums are over both Mn atoms j and their intermediate many-body states $|m,j\rangle$ of energy E_m and width Γ_m. We have here neglected exchange-type interactions via two-electron autoionization processes like $\langle El\mu; g | V_{\mathrm{AI}}^j | m,j; \mathrm{O}1\,\mathrm{s}\rangle$ that would lead to a greater overall similarity with the coulomb-plus-exchange matrix elements describing an interatomic Auger process, but such processes should be negligible for non-nearest neighbors and small for nearest neighbors due to their strict dependence on nonzero orbital overlap. Such orbital overlap is not required for the Coulombic term we have included here,[1,5] which is associated with two-electron processes like $\langle El\mu; g | V_{\mathrm{AI}}^j | \mathrm{O}1\mathrm{s}; m,j\rangle$. A fully general theory of MARPE should include these exchange effects however. We also point out that the connection between MARPE and an interatomic Auger electron emission is primarily formal, since the same sorts of matrix elements are embedded in the expressions describing both. However, the overall processes are fundamentally different.

We now note two special points that have been considered previously:[5] Retardation effects must be considered in the interaction with the external radiation and in the autoionization interaction [see Eq. (4) in Ref. 5], and the interatomic autoionization interaction must be generalized to the fully relativistic Møller formula used previously in the high-energy Auger theory[25,26] [see Eq. (5) in Ref. 5]. At this level, the treatment should be capable of describing all many-electron interactions up to second order in the perturbation via Eq. (4), or up to arbitrary order via Eq. (3), including those for nearest neighbors with the greatest overlap and thus enhanced many-electron interactions with the emitting atom.

If we now sacrifice some accuracy in describing nearest-neighbor behavior, the autoionization interaction can be conveniently expanded in multipoles that should be valid for resonator distances from the emitter $R_j \gg r_1, r_2$, where r_1 and r_2 are electron-nuclear distances and are of the order of the relevant dimensions of the two core orbitals involved (here O $1s$ and Mn $2p$). With these assumptions, and the further neglect of multipoles higher than dipoles, the effective interaction can be reduced to the following, in which several quantities are written out more explicitly than in prior work[5]

$$V_{\mathrm{AI}}^{j} \approx e^2 r_1 r_2 \sum_{\mu_1 \mu_2} F_{\mu_1 \mu_2}^{R_j} Y_{1\mu_1}(\hat{\mathbf{r}}_1) Y_{1\mu_2}^{*}(\hat{\mathbf{r}}_2), \tag{5}$$

where

$$F_{\mu_1 \mu_2}^{R} = \frac{-4\pi k^3}{3}\left[\frac{\delta_{\mu_1 \mu_2}}{2\pi} h_0^{(+)}(kR) + h_2^{(+)}(kR) Y_{2\mu_2-\mu_1}(\hat{\mathbf{R}}) \times \langle Y_{1\mu_2} | Y_{2\mu_2-\mu_1} Y_{1\mu_1} \rangle\right] \tag{6}$$

and the bracket represents a Gaunt integral with standard normalization.[27] Equations (5) and (6) can also be derived in a more rigorous way using nonrelativistic quantum electrodynamics,[22,28,29] where Eq. (6) is found to be simply proportional to the Green function of the photon field in the transverse gauge,[28] and the remaining short-range longitudinal Coulomb coupling is neglected.[29]

Combining results, we now find, in slightly different notation form, but equivalent meaning to that in Ref. 5

$$M_{E1\mu} = A\langle E1|r|\mathrm{O}1s\rangle \delta_{1,1} \sum_{\lambda} \varepsilon_{\lambda}^{\mathrm{eff}} \langle Y_{1\mu}|Y_{1\lambda}|Y_{00}\rangle = A\langle E1|r|\mathrm{O}1s\rangle \delta_{1,1} \varepsilon_{\mu}^{\mathrm{eff}}/\sqrt{4\pi}, \tag{7}$$

where A is a light-intensity normalization constant,

$$\varepsilon_{\lambda}^{\mathrm{eff}} = \varepsilon_{\lambda} - \sum_{\lambda' \mu_2} F_{\lambda \mu_2} \alpha_{\mu_2 \lambda'} \varepsilon_{\lambda'} \tag{8}$$

is now the effective polarization vector that includes the effect of x-ray scattering at the Mn sites, and the magnitude of the resonance is controlled by a product of a structure-factor type of sum over Mn sites

$$F_{\lambda \mu_2} = \sum_{j} F_{\lambda \mu_2}^{R_j} e^{i\mathbf{k}_{h\nu}\cdot\mathbf{R}_j}, \tag{9}$$

and the Mn^{2+} polarizability tensor,

$$\alpha_{\mu_2 \lambda'} = -\frac{4\pi e^2}{3} \sum_{m} \frac{\langle g|rY_{1\mu_2}^{*}|m\rangle\langle m|rY_{1\lambda'}|g\rangle}{\hbar\omega + E_g - E_m + i\Gamma_m/2}. \tag{10}$$

The form for the polarizability given here makes it clear that it is directly related to the usual description of resonant photoemission in Eq. (4) and Ref. 24.

The polarizability has been calculated using a configuration interaction scheme for a central Mn^{2+} ion surrounded by six O^{2-} ions in an octahedral cluster,[5,24] with interaction parameters derived previously from fits to both SARPE and x-ray absorption data, and an average over orientations of Mn magnetic moments, since the experiments have been performed above the MnO Néel temperature. In addition, $\alpha_{\mu_2 \lambda'}$ can be well approximated by a quantity averaged over diagonal elements, as $\bar{\alpha}\delta_{\mu_2 \lambda'}$, where $\bar{\alpha} = (\alpha_{-1-1} + \alpha_{00} + \alpha_{11})/3$.[5] The above equations were used in Ref. 5 to calculate O $1s$ intensities. However, all resonant contributions to the O $1s$ intensities [i.e., the second term in Eq. (4)] were incorrectly multiplied by an extra factor of -4 in the computer calculations. Here, we present corrected theoretical results from this model, as well as results going beyond the earlier approximations used by considering higher-order interactions in Eq. (3), and also compare these two sets of results to a theoretical approach based on more standard x-ray optical theory.

In Fig. 2(a) we compare experimental and theoretical results for the O $1s$ intensity as a function of photon energy and for light incident at an angle of 10° with respect to the surface. The connected points represent the corrected experimental results from Fig. 1(d) and the thin solid curve the theoretical results based on Eq. (3) above. The experimental data show a steeper negative slope than the theory as energy is increased, that we have verified by measurements and calculations, to be due to a combination of decreasing photoelectric cross sections and strong modulations due to photoelectron diffraction [cf. Fig. 1(e)],[17] both well-understood effects.[20,21] If this difference in slope is allowed for, the agreement between experiment and theory is qualitatively good, although the amplitude of the intensity modulations is too small by a factor of 2–3 in theory. Now, going beyond this level of microscopic theory, we note that the remaining terms in the series expansion (3) describe processes in which an incoming photon is scattered by more than one Mn atom before it reaches the O emitter. In particular, they incorporate higher-order Mn-Mn interactions via the Møller formula.[5,25,26] This gives rise to extra terms in the effective polarizability of Eq. (7), which now becomes

$$\varepsilon_{\lambda}^{\mathrm{eff}} = \varepsilon_{\lambda} - \bar{\alpha} \sum_{\lambda', j} \mathbf{F}_{\lambda\lambda'}^{\mathbf{R}_j} e^{i\mathbf{k}_{h\nu}\cdot\mathbf{R}_j} \varepsilon_{\lambda'} + \bar{\alpha}^2 \sum_{\lambda' \lambda'', jj'} \mathbf{F}_{\lambda\lambda''}^{R_j} \mathbf{F}_{\lambda'\lambda''}^{R_j - R_{j'}} e^{i\mathbf{k}_{h\nu}\cdot R_{j'}} \varepsilon_{\lambda''} + \cdots, \tag{11}$$

where the first two terms are the same as in Eq. (8) after approximating the polarizability by the average scalar $\bar{\alpha}$. This series can be summed up to an infinite order for a slab formed by a finite set of atomic planes,[22] and a semi-infinite medium can be simulated by using a sufficiently large number of layers. The result obtained in that case for the O $1s$ intensity is shown in Fig. 2(a) as a solid curve. The new terms in Eq. (11) bring the theoretical result much closer to the experimental one, making it evident that it is essential to include what is in effect multiple scattering of the incoming radiation in order to accurately describe such strong soft x-ray resonances. To our knowledge, this point has not been made before in discussing such resonances.

B. Relationship to an x-ray optical (dielectric) model

We now consider the relationship of this microscopic many-body theory to another related theoretical method for dealing with such effects: an x-ray optical approach based on Maxwell's and Fresnel's equations, as described in detail elsewhere.[11,30] Equation (11) involves sums over Mn positions in the MnO crystal. However, the details of the atomic structure of the Mn sublattice should be irrelevant in the limit of long radiation wavelengths λ_x for which phase shifts along the scattered paths can be neglected. In this limit, Eq.

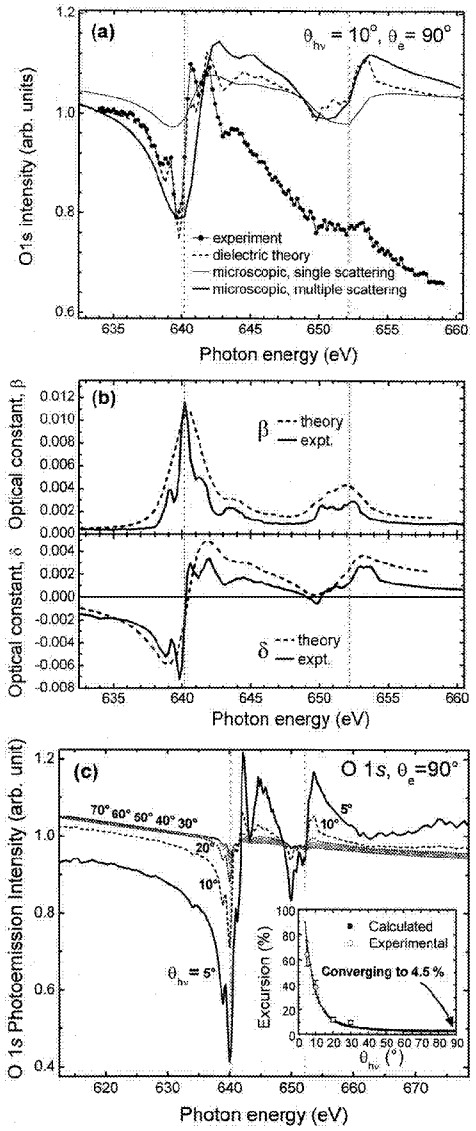

FIG. 2. (a) O 1*s* intensity from MnO(001) as a function of photon energy and for $\theta_{h\nu}=10°$, $\theta_e=90°$: experimental data (connected points) are compared to theoretical curves calculated using Eq. (8) (thin solid line, second-order microscopic many-body theory=single radiation scattering), Eq. (11) (thick solid line, infinite-order microscopic theory=multiple radiation scattering), and x-ray optical dielectric theory based on Eq. (15) and the experimental constants shown in (b) (dashed curve). (b) The x-ray optical constants δ and β of MnO over the Mn 2*p* absorption region, as derived from microscopic many-body theory (dashed curves) and from experiment with corrected data for the absorption coefficient μ and Kramers-Kronig analysis. (c) Calculations of the O 1*s* intensity as a function of photon energy based on the experimental optical constants in (b) and Eq. (15) from x-ray optical theory. Curves are shown for various x-ray incidence angles. The inset shows the normalized magnitude of the negative-to-positive excursion in percent as a function of x-ray incidence angle, as calculated using x-ray optical theory (solid points) and as measured in this study (large open circles).

(11) can be shown to reduce to the polarization vector derived from a macroscopic dielectric description based upon Maxwell's equations, in which the solid is represented by a local frequency-dependent dielectric function ε that is related to the atomic polarizability as $\varepsilon=1+4\pi n_{\mathrm{Mn}}\bar{\alpha}$, where n_{Mn} is the density of Mn atoms. This relationship between ε and $\bar{\alpha}$ can be derived from the Clausius-Mossotti relationship with the assumption that $\varepsilon\approx 1$, as is reasonable in the soft x-ray region. More specifically, for the case of the Mn2*p* resonance in MnO, the ratio of the wavelength to the Mn-Mn nearest-neighbor distance is ≈6.1. Therefore, one would expect reasonable results to come out of the macroscopic description. We have here also implicitly assumed that the O atoms contribute only a small amount to the total polarizability in the vicinity of the Mn 2*p* resonances.[5,22,30b,31]

Thus, an alternative, although more empirically oriented, approach for calculating such effects is to derive the energy-dependent x-ray optical constants $\delta(h\nu)$ and $\beta(h\nu)$ in the index of refraction $n_r=\sqrt{\varepsilon}=1-\delta+i\beta$ (Ref. 32) by measuring the absorption coefficient $\mu(h\nu)=4\pi\beta(h\nu)/\lambda_x$ over the edges in question (here, Mn2*p*), matching it in the nonresonant region to accurate theoretical and/or experimental data,[30b,31] and then using a Kramers-Kronig analysis to derive δ. These two parameters, as derived experimentally in this study, are shown as a function of photon energy in Fig. 2(b) (solid curves), where they are compared also to the same parameters as derived from the parameterized many-body model (dashed curves). The measured β has been fully corrected for the inelastic attenuation of the outgoing secondary electrons used to measure it via a set of measurements at varying takeoff angles;[17,33] taken together with the corrections for detector nonlinearity, we thus believe that this curve, and the associated δ values, are within ~1–2% of the true values. However, such absorption coefficient measurements need to be made with care, so that neither the measurement method (e.g., partial yield, total yield, fluorescence, collection angle) nor nonlinearity in the detector distorts the final curves. The agreement between experiment and theory here is very good, with more fine structure in experiment, as expected. Note also that the variation in the experimental O 1*s* intensity in Fig. 2(a) about a mean value follows very closely the behavior of δ, a point to which we return below. Proceeding now via the Fresnel equations to calculate the photoemission intensity as a function of photon energy, it can be shown that, for *p*-polarized radiation incident on a planar surface from vacuum with $n=1$, and for a conducting or nonconducting, but nonmagnetic, reflective medium, the ratio of the complex electric field magnitude just below the surface $[E(z=0+)]$ to the incident complex field magnitude just above the surface in vacuum $[E_{\mathrm{vac}}^{\mathrm{inc}}(z=0-)]$ is given by

$$t\equiv\frac{E(0+)}{E_{\mathrm{vac}}^{\mathrm{inc}}(0-)}=\frac{2\sin\theta_{h\nu}}{\sin\theta'_{h\nu}+n_r\sin\theta_{h\nu}}, \tag{12}$$

where z is the coordinate perpendicular to the surface and $\theta'_{h\nu}$ is the complex angle of propagation below the surface, again measured relative to the surface. $\theta'_{h\nu}$ is further related

to $\theta_{h\nu}$ via Snell's Law: $\cos\theta_{h\nu}=n_r\cos\theta'_{h\nu}$, with $\theta_{h\nu}$ real. The complex character of n_r also implies that E attenuates with z only according to $\exp[-\mathrm{Im}(k'z\sin\theta'_{h\nu})]$, where k' is the complex propagation wave vector inside the medium and equal to $2\pi n_r/\lambda_x$, and λ_x is the wavelength of the radiation. Normalizing the electric field inside the medium to the incident field just above the surface then gives for the electric field strength at depth z relevant for photoemission

$$|E(z)|^2=|t|^2\exp(-\mathrm{Im}\{4\pi n_r z\sin\theta'_{h\nu}/\lambda_x\}). \quad (13)$$

The photoemission intensity $I(h\nu)$ can now be obtained by introducing the energy-dependent differential photoelectron cross section $d\sigma/d\Omega$ appropriate to the experimental geometry (which may in general also include the effects of photoelectron diffraction), the energy-dependent inelastic attenuation length for electrons Λ_e, and integrating over z as

$$I(h\nu)\propto\frac{d\sigma}{d\Omega}\int_0^\infty|E(z)|^2\exp\left(-\frac{z}{\Lambda_e\sin\theta}\right)dz, \quad (14)$$

where we have not included factors of atomic density and solid angle acceptance of the analyzer that will be constant over an energy scan. Substituting Eq. (13) into Eq. (14) and integrating then yields finally

$$I(h\nu)\propto\frac{d\sigma}{d\Omega}(h\nu)\times\frac{|t(h\nu)|^2}{\dfrac{\mathrm{Im}\{4\pi n_r(h\nu)\sin\theta_{h\nu}'(h\nu)\}}{\lambda_x(h\nu)}+\dfrac{1}{\Lambda_e(h\nu)\sin\theta}}, \quad (15)$$

which is a completely general formula for photoemission intensity from a conducting or nonconduction, nonmagnetic, semi-infinite substrate, with all dependences on energy explicitly indicated. Making use of Eq. (15) and the experimental values for δ and β in Fig. 2(b), we arrive at the dashed curve in Fig. 2(a), which is in excellent agreement with experiment, including all aspects of the fine structure. A similar degree of agreement is also found for other incidence angles $\theta_{h\nu}$.

This x-ray optical approach furthermore exhibits only small differences in fine structure with respect to the microscopic description based upon Eq. (11). These differences are due to differences in δ and β between theory and measurement [cf. Fig. 2(b)] and perhaps also to the fact that only the Mn polarizability has been considered in the microscopic theory, thus neglecting the small contributions from nonresonant O scattering over this energy range.[30b,31] In addition, we find that, if the infinite-order microscopic Eq. (11) is used together with the experimental x-ray optical constants to derive the polarizability, the calculated curve is essentially indistinguishable from that of Eq. (15), thus verifying the accuracy of the microscopic approach and its exact reduction to the x-ray optical model, provided that multiple scattering effects are included and certain conditions mentioned above are met.

In Fig. 2(c), we finally show normalized curves of the multiatom effect on the O $1s$ intensity as a function of an x-ray incidence angle, as calculated using the x-ray optical approach of Eq. (15). These curves make it clear that the effects are strongly sensitive to an x-ray incidence angle, being much smaller for angles greater than about 30°, although very similar in shape for all angles. The calculated normalized +/− excursion of the effect as a function of an incidence angle is further shown in the inset of Fig. 2(c), where it is compared to experimental results at four incidence angles. There is excellent agreement between experiment and theory, and theory furthermore predicts an asymptotic value of about 4.5% for the excursion at normal incidence. These results thus further confirm the accuracy of the x-ray optical analysis as compared to experiment, and also imply that such effects should be observable on crossing strong core-level resonances for *all* angles of x-ray incidence, although with greater difficulty of observation as $\theta_{h\nu}$ goes above about 20–30°.

We also note that recent measurements have found similar MARPE effects in O $1s$ emission from CuO with Cu $2p_{3/2}$ resonance, and these show a overall excursion of ~20% that is similar to the magnitudes observed here for MnO.[13] Here, the effects have been termed "anti-resonances" to distinguish them from the all-positive effects reported in previous uncorrected data [cf. Fig. 1(c)], but the present paper makes it clear that they are manifestations of the same interatomic resonant phenomenon. Although it was not possible in this paper to see similar effects in O $1s$ emission from NiO,[13] we believe that this could be due to the relatively high x-ray incidence angle of 35° used in this paper, combined with the ~±2% statistical error in the data as compared to the few percent effect that might be expected at this incidence angle [cf. inset of Fig. 2(c)].

It is now useful to compare these theoretical results with those from prior work by Henke on calculating photoelectron intensities via x-ray optics.[30a] We first note that he was interested in scanning the incidence angle $\theta_{h\nu}$ only, in which case δ, β, λ_x, and Λ_e all remain constant, and he was thus able to make certain approximations that we cannot, due to the strong variation of both δ and β over a scan in photon energy. Nonetheless, if $|\delta|,\beta\ll 1$ over the energy scan, which Fig. 2(b) makes clear is an excellent assumption, our Eq. (15) can be simplified to

$$I(h\nu)\approx\frac{d\sigma}{d\Omega}(h\nu)\times\frac{|t(h\nu)|^2}{\dfrac{4\pi\beta(h\nu)\sin\theta_{h\nu}(h\nu)}{\lambda_x(h\nu)}+\dfrac{1}{\Lambda_e(h\nu)\sin\theta}}, \quad (16)$$

which permits more direct comparison with this prior work. In particular, our use of $|t|^2$ to represent the strength of the electric field squared below the surface is inherently more accurate and versatile in application than the factor $[1-R]\times[\sin\theta_{h\nu}/\sin\theta_{h\nu}']$ used by Henke in his prior analysis. An additional difference in the two approaches is that all quantities in the last expression are treated as real by Henke, whereas we have shown that a more accurate expression re-

lated to this earlier formalism is a factor $[I-R][\sin\theta_{h\nu}/(\mathrm{Re}\{n_r \sin\theta'_{h\nu}\})]$, with n_r and $\theta_{h\nu}'$ here treated as complex. In addition, the inverse x-ray attenuation length perpendicular to the surface in this prior work and appearing here as the first term in the denominator of Eq. (16) was further simplified by Henke, and finally is different from ours by a factor of $1/[\sin\theta_{h\nu}']^2$. In describing scanned-energy resonant data however, we find it essential to use the form in Eq. (15), or with some approximation, that in Eq. (16).

To gain further insight into the relationship of photoemission intensity of δ and β, we can further approximate Eq. (15) to the conditions of the measurements shown here, for which δ and β are both much less than unity [cf. Fig. 2(b)] and the reflectivity R is also small (with a maximum value for all cases considered here of 0.18 at $\theta_{h\nu}=5°$), and this finally yields, after suppressing the obvious dependences on photon energy

$$I(h\nu)\approx\frac{d\sigma}{d\Omega}\frac{1+\delta}{\dfrac{4\pi\beta\sin\theta_{h\nu}}{\lambda_x}+\dfrac{1}{\Lambda_e\sin\theta}}. \tag{17}$$

From this expression, it is clear that the variation of intensity with photon energy as normalized to the values on either side of a resonance should qualitatively follow δ, just as observed. The magnitude of this variation is also enhanced by the change in β, whose increase over the resonance generally acts to decrease intensity over the same region. The negative excursion of δ just before the resonance, together with the increase in β, thus produces the strong dips in intensity seen at about 639.5 eV in Figs. 2(a) and 2(d).

Although the numerical results from the microscopic model embodied in Eqs. (1)–(11) can be reduced to a continuum x-ray optical picture, provided we include higher-order effects representing multiple light scattering, it should nonetheless permit future calculations of such interatomic resonant photoemission effects from first principles, including in particular, an allowance for nearest-neighbor many-body interactions that are only effectively included in the optical approach. Of course, any microscopic model is in a sense simply calculating the x-ray optical response of the system, but for nearest-neighbor effects, in free molecules, and for small clusters of atoms on the nanometer scale, it is not clear that an x-ray optical approach is particularly useful, or even appropriate. Beyond this, the excellent numerical agreement between the microscopic and macroscopic continuum dielectric descriptions presented above is expected to break down when the wavelength of the radiation is of the order of, or smaller than, the relevant interatomic distances. Thus, if the resonating atoms do not form a compact enough lattice (as Mn does in MnO), the continuum dielectric treatment is not appropriate. Some possible examples of this are atoms situated inside the cages of fullerites or zeolites, and/or systems subjected to resonant excitation by shorter-wavelength radiation. The continuum dielectric model also is not appropriate for calculating such effects in nanometer-scale objects or systems with nanometer-scale heterogeneity or clustering in which the detailed atomic positions are to be allowed for, even if this model can be extended via methods such as the Mie theory so as to apply to special cases such as small metal clusters of regular shape.[34] Neither is the continuum model appropriate for free molecules, in which core-core interatomic resonance effects appear to have recently been observed in angular distributions.[12]

We also comment briefly on an intermediate theoretical approach that would involve assigning each atom a complex scattering factor based on some combination of measured and/or calculated optical constants, somehow partitioned among the different constituents so as to allow for element-specific resonance effects, with standard formulas for this appearing elsewhere.[30b] This method could in principle be applied to any arbitrary cluster of atoms, and with sufficient long-range order, would lead to Bragg scattering effects at shorter wavelengths. However, this approach could not incorporate any unique nearest-neighbor effects, nor in its standard formulation would it explicity allow for the multiple scattering effects on resonance that we find to be important.

Regardless of the theoretical model that is most appropriate to use, such interatomic resonance effects (even though generally smaller and of different form than discussed previously) still represent an experimental probe that should be able, for various situations, to provide information on the near-neighbor identities and bonding of atoms B that surround a given emitter A, as suggested in prior work.[1–4]

Finally, we note that both of the theoretical models discussed above can be extended to describe fluorescent x-ray emission. For the x-ray optical model, and for the case of a fluorescent energy that is far from any resonance and at a fluorescence exit angle θ^F that is large enough to minimize refraction and reflection at the surface, this would involve simply replacing $\Lambda_e\sin\theta$ with $\Lambda_x^F\sin\theta^F$ in Eqs. (15)–(17), with Λ_x^F equal to the fluorescent x-ray attenuation length along path length or $\lambda_x^F/[4\pi\beta^F]$ in obvious notation. With this replacement, Eqs. (15)–(17) thus represent different levels of approximation for handling what essentially reduces to the well-known self-absorption effects in x-ray fluorescence that have been discussed previously in connection with MARPE.[4,14] In fact, viewed in this light, MARPE in x-ray emission can be seen as having self-absorption as a key ingredient, but due to near-neighbor effects not the only ingredient. The microscopic model could also be similarly extended to predict fluorescence intensities, but we will not present these details here.

V. CONCLUSIONS

In summary, we have pointed out that a proper allowance for detector nonlinearity is essential for accurately measuring multiatom resonant photoemission effects, with the magnitude and form of the corrected results being significantly different from previous reports.[1–4,6,7a] A microscopic theoretical model proposed previously for describing these results[5] is found to well describe the observed effects, and confirms, via agreement with experiment, that they can be considered as interatomic resonance phenomenon. For the specific case of O $1s$ emission from MnO in the vicinity of the Mn$2p$ resonances treated here, this microscopic model, with the inclusion of higher-order interactions not considered previ-

ously, is also found to be reducible to a classical x-ray optical treatment using experimental optical constants. The x-ray optical model is furthermore found to well describe the observed intensity profiles as a function of both photon energy and x-ray incidence angle. It is thus of interest in future studies to explore the degree to which such effects (particularly with the expected enhancement of nearest-neighbor interactions, for more spatially dispersed resonating atoms so as to go beyond the simple x-ray optical picture, in nanometer-scale objects, and/or in free molecules) can provide an element-specific probe of near-neighbor properties and many-electron interactions. The experimental and theoretical approaches outlined here should provide a sound framework for such work, both for photoelectron and fluorescent x-ray emission. The microscopic theoretical model outlined here should also be capable of describing such core-core interatomic resonance effects in the intensities and angular distributions in photoemission from free molecules,[12] as well as with straightforward generalization the valence-core interatomic resonance effects mentioned previously.[8–10] Finally, we point out that the demonstrated importance of multiple scattering of soft x-ray radiation in the vicinity of strong core-level resonances should be of relevance in the analysis of resonant elastic and inelastic x-ray scattering, and other topics of high current interest.[35]

ACKNOWLEDGMENTS

We are grateful to M. G. Garnier, D. Nordlund, A. Nilsson, and R. Denecke for pointing out the potential importance of detector nonlinearity in our measurements, and to A. Kikas, M. P. Seah, J. B. Kortright, N. Brookes, M. Finazzi, G. Paolucci, and K. Prince for helpful comments. This work was supported by the U.S. Department of Energy, Office of Science, Office of Basic Energy Sciences, Materials Sciences Division, under Contract No. DE-AC03-76SF00098. Additional support was provided by the Basque Government and by the Fulbright Foundation (J. G. de A., Grant No. 22726216-98), as well as the Miller Institute, U. C. Berkeley (E. A.).

[1] A. Kay, E. Arenholz, B. S. Mun, F. J. Garcia de Abajo, C. S. Fadley, R. Denecke, Z. Hussain, and M. A. Van Hove, Science **281**, 679 (1998).

[2] A. W. Kay, E. Arenholz, B. S. Mun, F. J. Garcia de Abajo, C. S. Fadley, R. Denecke, Z. Hussain, and M. A. Van Hove, J. Electron Spectrosc. Relat. Phenom. **103**, 647 (1999).

[3] (a) C. S. Fadley, E. Arenholz, A. W. Kay, J. Garcia de Abajo, B. S. Mun, S.-H. Yang, Z. Hussain, and M. A. Van Hove, in *X-ray and Inner-Shell Processes*, edited by R. W. Dunford, D. S. Gemmell, E. P. Kanter, B. Krässig, S. H. Southwartor, and L. Young, AIP Conf. Proc. No. 506 (AIP, Melville, NY, 2000), pp. 251–272; (b) E. Arenholz and A. W. Kay (unpublished).

[4] E. Arenholz, A. W. Kay, C. S. Fadley, M. M. Grush, T. A. Callcott, D. L. Ederer, C. Heske, and Z. Hussain, Phys. Rev. B **61**, 7183 (2000).

[5] F. J. Garica de Abajo, C. S. Fadley, and M. A. Van Hove, Phys. Rev. Lett. **82**, 4126 (1999).

[6] A. Kikas, E. Nommiste, R. Ruus, A. Saar, and I. Martinson, Solid State Commun. **115**, 275 (2000).

[7] (a) M. G. Garnier, N. Witkowski, R. Denecke, D. Nordlund, A. Nilsson, M. Nagasono, N. Mårtensson, and A. Föhlisch, Maxlab Annual Report for 1999 and (private communication) correcting this data; (b) D. Nordlund, M. G. Garnier, N. Witowsky, R. Denecke, A. Nilsson, M. Nagasono, N. Mårtensson, and A. Föhlisch (unpublished).

[8] K. L. I. Kobayashi, N. Watanabe, H. Nakashima, M. Kubota, H. Daimon, and Y. Murata, Phys. Rev. Lett. **52**, 160 (1984).

[9] P. Pervan, M. Milun, and D. P. Woodruff, Phys. Rev. Lett. **81**, 4995 (1999).

[10] Y. F. Hu, G. M. Bancroft, and K. H. Tan, Inorg. Chem. **39**, 1255 (2000).

[11] S.-H. Yang, B. S. Mun, A. W. Kay, S.-K. Kim, J. B. Kortright, J. H. Underwood, Z. Hussain, C. S. Fadley, Surf. Sci. **461**, 557 (2000).

[12] H. Wang, O. Hemmers, P. Focke, M. M. Sant'Anna, D. Lukic, C. Heske, R. C. C. Perera, I. Sellin, and D. Lindle (unpublished).

[13] M. Finazzi, G. Ghiringhelli, O. Tjernberg, L. Duo, A. Tagliaferri, P. Ohressser, and N. B. Brookes (unpublished).

[14] A. Moewes, E. Z. Kurmaev, D. L. Ederer, and T. A. Callcott (unpublished).

[15] (a) N. Mårtensson, P. Baltzer, P. A. Bruhwiler, J. -O. Forsell, A. Nilsson, A. Stenborg, and B. Wannberg, J. Electron Spectrosc. Relat. Phenom. **70**, 117 (1994); (b) C. S. Fadley, Prog. Surf. Sci. **54**, 341 (1997).

[16] M. P. Seah, I. S. Gilmore, and S. J. Spencer, J. Electron Spectrosc. Relat. Phenom. **104**, 73 (1999), and earlier references therein.

[17] A. W. Kay, Ph.D. dissertation, University of California-Davis, 2000, Chap. 4 and 5.

[18] A. Gromko, C. Yi, A. Fedorov, and D. Dessau (private communication).

[19] T. Valla and P. D. Johnson (private communication).

[20] J. J. Yeh and I. Lindau, At. Data Nucl. Data Tables **32**, 1 (1985).

[21] C. S. Fadley, Prog. Surf. Sci. **54**, 341 (1997), and references therein.

[22] F. J. Garía de Abajo, M. A. Van Hove, and C. S. Fadley, Phys. Rev. B (to be published).

[23] A. Messiah, *Quantum Mechanics* (North-Holland, New York, 1969), Vol. II, p. 849.

[24] A. Tanaka and T. Jo, J. Phys. Soc. Jpn. **63**, 2788 (1994).

[25] N. F. Mott and I. N. Sneddon, *Wave Mechanics and its Applications* (London, Oxford University Press, 1948), pp. 338–339.

[26] J. P. Desclaux, in *Relativistic Effects in Atoms, Molecules, and Solids*, edited by G. L. Malli (Plenum Press, New York, 1981), pp. 115–143.

[27] The Gaunt normalization is chosen such that $\langle Y_{1\mu}|Y_{1\lambda}Y_{00}\rangle$ = the integral over solid angle Ω of $Y^*_{1\mu}(\Omega)Y_{1\lambda}(\Omega)Y_{00}(\Omega) = \delta(\mu,\lambda)/\sqrt{4\pi}$.

[28] Y. Nishino and G. Materlik, Phys. Rev. B **60**, 15 074 (1999).

[29] C. Cohen-Tannoudji, J. Dupont-Roc, and G. Grynberg, *Photon &*

Atoms. Introduction to Quantum Electrodynamics (Wiley, New York, 1989).

[30] (a) B. L. Henke, Phys. Rev. A **6**, 94 (1972); (b) B. L. Henke, E. M. Gullikson, J. C. Davis, At. Data Nucl. Data Tables **55**, 34 (1993).

[31] C. T. Chantler, J. Phys. Chem. Ref. Data **24**, 71 (1995).

[32] The sign convention for the imaginary part of the index of refraction used here is different from that used elsewhere of $n_r = 1 - \alpha - i\beta$ (Refs. 25, 27), but we choose it to be consistent with the use of retarded Green functions for G_0.

[33] G. van der Laan and B. T. Thole, J. Electron Spectrosc. Relat. Phenom. **46**, 123 (1988).

[34] S. V. Fomichev and D. F. Zaretsky, J. Phys. B **32**, 5083 (1999), and references therein.

[35] P. M. Platzman and E. D. Isaacs, Phys. Rev. B **57**, 11 107 (1998); P. Kuiper, J. H. Guo, C. Sathe, J. Nordgren, J. J. M. Pothuizen, F. M. F. deGroot, and G. A. Sawatzky, Phys. Rev. Lett. **80**, 5204 (1998).

Phys. Rev. B, to appear

Multiple scattering of electrons in solids and molecules: a novel cluster-model approach

F. J. García de Abajo,[1,2,*] M. A. Van Hove,[1,3] and C. S. Fadley[1,3]
[1] *Materials Sciences Division, Lawrence Berkeley National Laboratory, Berkeley, CA 94720, USA*
[2] *Centro Mixto CSIC-UPV/EHU, San Sebastián, Spain*
[3] *Department of Physics, University of California, Davis, CA 95616, USA*
(May 26, 2000)

A new method for the simulation of electron scattering and diffraction in solids and molecules within the cluster approach is presented with explicit applications to photoelectron diffraction, electron scattering in molecules, and LEED. No approximations are made beyond the muffin-tin model, and in particular, an exact representation of the free-electron Green function is used. All multiple scattering paths are accounted for up to an order of scattering that ensures convergence. The new method relies upon a convenient separation of the free-electron Green function in rotation matrices and translations along the z axis, which greatly reduces the computation time and storage demand. The evaluation of the multiple scattering expansion is implemented using the divergent-free recursion method, which permits performing an iterative refinement of the final-state wave function, as expressed in the basis set of spherical harmonics attached to each atom of the cluster. Examples are offered in which divergences encountered when using either direct multiple scattering or the more sophisticated simultaneous relaxation method are eliminated by using the recursion method. The computation time needed by the resulting computer program of electron diffraction in atomic clusters (EDAC) to determine the self-consistently-scattered wave function is proportional to $N^2(l_{max}+1)^4$, where N is the number of atoms in the cluster and l_{max} is the maximum angular momentum for which the scattering phase shifts take non-negligible values. Within this method it is possible to establish that in practical cases $N > 1000$ might be needed for convergence of the cluster size, although the angular averaging inherent in many experiments may reduce this. The recursion method has also been modified to reduce the effort in computing angular distributions of photoelectrons and low-energy diffracted electrons, which now take negligible time for each angle of emission once the wave function has been determined for a given electron energy. Angle and energy distributions of core-level photoemission, elastic scattering of electrons from a free molecule, and low-energy electron diffraction in large-unit-cell surfaces are calculated.

61.14.-x, 61.14.Dc, 61.14.Qp

I. INTRODUCTION

Multiple elastic scattering (MS) plays a central role in the description of electron transport inside solids and molecules in different experimental spectroscopies like photoelectron diffraction (PD),[1–3] low-energy electron diffraction (LEED),[4,5] Auger electron diffraction (AED),[6] x-ray-absorption fine structure (XAFS),[7] and related techniques.

Various approximations are customarily employed to efficiently calculate MS effects. For relatively high electron energies like the ones considered in this work (> 50 eV above the Fermi level), electron scattering is rather insensitive to the outermost region of the atomic potentials that make up the solid or molecule. Therefore, the atomic potentials can be well approximated by spherically-symmetric muffin-tin potentials.[4] In addition, inelastic scattering is usually treated in a phenomenological way via a complex optical potential, or equivalently, inelastic mean free paths.[4]

Two different categories of computational schemes can be distinguished, depending on the use made of the symmetry of the atomic structure in the case of solids: layer-by-layer methods and cluster methods. The former have been primarily developed in the context of LEED and take advantage of the fact that the atoms of an oriented crystal are disposed in layers parallel to the surface, resulting in remarkably efficient algorithms for the transport between layers.[4,8–10] The latter do not require any sort of long-range order and can be applied to other classes of problems.[11–17]

In particular, when translational crystal symmetry is broken due to either the presence of randomly distributed adsorbates and defects or a localised character of the electron source as in the case of PD and AED, cluster models provide a natural approach for simulating MS effects that is suggested by the fact that excited electrons cannot travel large distances in real solids without suffering inelastic losses, so that the region which actually contributes to the emission of elastically scattered electrons defines a finite cluster surrounding the adsorbate, defect, or emitter.[11–17] This approach is also suitable for dealing with similar scattering phenomena in adsorbed or free molecules.

A hybrid model consisting of treating MS within a cluster formed by concentric spherical shells was proposed by Pendry[18] and implemented by Saldin *et al.*[19–21] to simulate x-ray-absorption near-edge structure (XANES),[19] LEED,[20] AED, and PD.[21] This method can in fact be advantageous in LEED calculations when large surface unit cells are considered.[20]

The more straightforward cluster approach adopted in the present work has been extensively employed in the past within a single-scattering approximation, and it has been found to reproduce qualitatively, and in several respects quantitatively, many of the experimental features in both XAFS[7,22] and PD.[2,6,23] However, higher orders of MS are needed to improve accuracy and structural analyses.[24] For example, by interpreting the terms of the MS series as paths that the electron follows connecting atoms in the cluster in all possible ways,[25] characteristic MS effects like forward focussing and defocussing along rows of atoms have been discerned in PD experiments.[24]

A basis set suited to describe the electron wave function is provided by spherical harmonics and spherical Bessel functions attached to each atom of the cluster. This incorporates curved-wave effects in a natural way. Unfortunately, the propagation of these functions between cluster atoms is computationally very demanding.[26,27,4] Since no intensive use of crystal symmetry is made in cluster models, further approximations have been introduced in the past in order to make feasible the calculation of the MS series.[28–37,2,7,6,11,13–15,21,22]

In the high-energy limit, the propagation reduces to plane-wave factors (hence the name plane-wave approximation) and each term in the MS series becomes a product of scattering amplitudes.[7] Different expansions of the propagated wave function in the finite region centered around each cluster atom lead to the so-called small-atom approximations.[33,11] Among them, the point-scattering approximation goes beyond the plane-wave approximation by multiplying the scattering amplitude by appropriate curved-wave factors.[35]

As the experimental resolution increases, more accurate theoretical analyses become necessary. These are complicated by the fact that the number of multipole terms that are needed rises rapidly with increasing electron energies. The maximum of the significant angular momentum quantum numbers scales roughly as $l_{max} \sim kr_{mt}$, where k is the electron momentum and r_{mt} is the muffin-tin radius of the scatterers. Upon inspection of actual calculations, l_{max} is of the order of $5-20$ for electron energies in the range $50-700$ eV. Since the number of different multipole components (l,m) used to describe the electron wave function around each atom is $(l_{max}+1)^2$, the aforementioned propagation between each pair of atoms involves multiplication by propagation matrices, requiring $(l_{max}+1)^4$ complex products.

On the other hand, the number of atoms N needed in a cluster to reach convergence is also important in the evaluation of the computational demand of the problem. This number scales as the cube of the electron inelastic mean free path (imfp), λ_i. We estimate N as the number of sites of a simple cubic lattice of lattice constant 2.5 Å that are contained in a sphere of radius $1.5\lambda_i$. The dependence of the universal imfp curve on the electron energy must be also allowed for.[38–40] The relation between l_{max} and the electron momentum discussed above has been assumed for a typical muffin-tin radius $r_{mt} = 1.5$ Å. In this way, one obtains the relation between N and l_{max} shown in Fig. 1 by the solid curve.

In order to overcome the rapidly-growing computational demand with increasing l_{max}, Rehr and Albers[13] (R-A) provided a clever procedure based upon a separable representation of the free-electron Green function that allows one to generalize the scattering amplitudes, substituting them by matrices that describe each scattering event for a given type of atoms in such a way that the leading element of each matrix reproduces the point-scattering approximation. Their method, which produces reliable results when keeping only a few more relevant elements in those matrices,[13] is particularly suitable to calculate the contribution of different individual electron paths, and it has been implemented for PD calculations by Kaduwela *et al.*[17] and by Chen *et al.*[41]

Rather than including all possible electron paths, Zabinsky *et al.*[36] have also shown that only a small fraction of all paths contribute significantly to the MS series in XAFS. This has permitted them to reduce substantially the total computational effort by only including in the calculation selected paths whose contributions are non-negligible already within the plane-wave approximation. Their approach is very efficient in particular if the so-called second-order R-A separable representation is used, where each scattering event within a given electron path is typically represented by a 6×6 matrix.

More recently, Chen *et al.*[41] have used a similar approach in the case of PD, incorporating an iterative evaluation of the MS expansion within the framework of the R-A separable representation.[13] In this approach, the number of complex multiplications per iteration is $36N^3$.

In the present work, the MS expansion is evaluated using an exact representation of the Green function propagator. An iterative procedure is followed that requires $\approx (10/3)N^2(l_{max}+1)^3$ multiplications per iteration. Wu and Tong[42] have reported divergences in the exact MS expansion and claimed that these divergences can be prevented by using the simultaneous relaxation method,[43] consisting of both mixing the result of each iteration with that of the previous one and using the updated components of the wave function as they are calculated rather than waiting for a given iteration to be completed. That iteration procedure is compared in the present paper with the Haydock recursion method,[44–46] which is shown to be more robust and to prevent divergences not avoided by the former. In addition, the recursion method results in faster convergence as compared with either the direct MS expansion or the simultaneous relaxation method. These ideas have been implemented in a new fully-automated computer code for calculating electron diffraction in atomic clusters (EDAC). A similar approach has been recently employed in the description of photon scattering in nanostructures.[47] The computational performance of EDAC as compared with

Submitted to Phys. Rev. B

second-order R-A is shown in Fig. 1 (broken curve): the EDAC method is faster outside the shadowed area.

The MS theory is reviewed in Sec. II in a way suitable to be employed within the selected iterative scheme. Further computational details are given in Sec. III. In particular, several iteration methods are discussed and a modification of the recursion method is introduced to allow calculating scattered or emitted electron intensities for multiple directions simultaneously from a single MS calculation (Sec. III A). Moreover, the free electron propagators are decomposed into rotations and translations along the z axis, resulting in a significant reduction both in time and in storage demand (Sec. III B). Particular examples of application to PD, elastic electron scattering from molecules, and LEED from surface structures with large unit cells are presented in in Secs. IV, V, and VI, respectively. Finally, the main conclusions are summarized in Sec. VII.

Atomic units (a.u., i.e., $e = m = \hbar = 1$) will be used from now on, unless otherwise specified. The notation of Messiah[48] for spherical Bessel and Hankel functions, spherical harmonics, and rotation matrices will be adopted.

II. MULTIPLE SCATTERING THEORY

Let us begin by introducing the standard elements of multiple scattering theory in a Green's function approach. Consider an electron of energy E described by the wave function $\varphi^0(\mathbf{r})$ that satisfies the free-electron Schrödinger equation

$$(H_0 - E)\varphi^0 = 0, \tag{1}$$

where $H_0 = -\nabla^2/2$.

The presence of a solid or molecule introduces a strong perturbation that can be represented by the potential

$$V(\mathbf{r}) = \sum_\alpha V_\alpha(\mathbf{r}),$$

where the sum is extended over atomic positions $\mathbf{R}_\alpha$. Within the muffin-tin model adopted here, each atomic potential V_α vanishes outside a sphere of radius $r^\alpha_{\rm mt}$ (the muffin-tin radius) centered at $\mathbf{R}_\alpha$. These are non-overlapping spheres and $V(\mathbf{r})$ is set to a constant (the muffin-tin zero) in the interstitial region.

The wave function φ that satisfies the full Schrödinger equation $(H_0 + V - E)\varphi = 0$ can be written $\varphi = \varphi^0 + \phi$, where ϕ is the scattered part. Using matrix notation,[49] the latter can be expressed in terms of the atomic-cluster T matrix as

$$\phi = G_0 T \varphi^0, \tag{2}$$

where G_0 is the free-electron propagator that satisfies $(E - H_0)G_0 = 1$ and $k = \sqrt{2E}$ is the electron momentum. Defining the cluster Green function G via $(E - H_0 - V)G = 1$, the T matrix can be written $T = V + VGV$. An implicit dependence on E is understood in these expressions.

The key ingredient of MS theories is the reduction of the T matrix of the cluster to the T_α matrices of the individual muffin-tin potentials V_α. The latter are defined by the self-consistent relation

$$T_\alpha = V_\alpha + V_\alpha T_\alpha V_\alpha. \tag{3}$$

Following Beeby,[25] T can be written as a series expansion whose terms represent all possible electron scattering paths. More precisely,

$$T = \sum_\alpha \Lambda_\alpha,$$

where

$$\Lambda_\alpha = T_\alpha + \sum_{\beta\neq\alpha} T_\beta G_0 T_\alpha + \sum_{\gamma\neq\beta}\sum_{\beta\neq\alpha} T_\gamma G_0 T_\beta G_0 T_\alpha + \dots \tag{4}$$

accounts for MS paths in which the first scattering event occurs at atom α and two consecutive scattering events take place always at different atoms of the cluster. From Eq. (4), T can alternatively be defined as

$$T = \sum_\alpha (T_\alpha + \sum_{\beta\neq\alpha} \Lambda_\beta G_0 T_\alpha), \tag{5}$$
$$= T_{\alpha_0} + \sum_{\beta\neq\alpha_0} (\Lambda_\beta + \Lambda_\beta G_0 T_{\alpha_0}),$$

for any atom α_0.

Inserting Eq. (5) into Eq. (2), the scattered wave reduces to

$$\phi = \sum_\alpha (\phi^0_\alpha + \sum_{\beta\neq\alpha} G_0 \Lambda_\beta \phi^0_\alpha), \tag{6}$$

where

$$\phi^0_\alpha = G_0 T_\alpha \varphi^0 \tag{7}$$

represents the first-order contribution to MS. The second term on the right hand side of Eq. (6) can be understood as the propagation of the results of scattering at atom α to every other atom of the cluster β, followed by subsequent MS starting at the latter.

Some information on the structure of the scattered wave function can be gained by considering explicit expressions for G_0. Namely,

$$G_0(\mathbf{r} - \mathbf{r}') = \frac{-1}{2r}\frac{e^{ik|\mathbf{r}-\mathbf{r}'|}}{|\mathbf{r}-\mathbf{r}'|} \tag{8}$$
$$= -2k \sum_L h^{(+)}_L(k\mathbf{r}) j_{l-m}(k\mathbf{r}')(-1)^{l+m}, \qquad (r > r')$$

where $h^{(+)}_L(k\mathbf{r}) = i^l h^{(+)}_l(kr) Y_L(\Omega_r)$ represents an outgoing spherical wave, $j_L(k\mathbf{r}') = i^l j_l(kr') Y_L(\Omega_{r'})$ is a mixture of outgoing and incoming spherical waves that exhibits no net flux into or out of a closed surface containing the origin, $h^{(+)}_l$ is a spherical Hankel function,[48] j_l is a spherical Bessel function, and $L = (l, m)$ labels spherical harmonics Y_L. Since, by virtue of Eq. (3), T_α vanishes outside the muffin-tin sphere α, one finds, using Eqs. (7) and (8),

$$\phi^0_\alpha(\mathbf{r}) = \sum_L h^{(+)}_L[k(\mathbf{r} - \mathbf{R}_\alpha)]\, \phi^0_{\alpha,L} \tag{9}$$

for $|\mathbf{r} - \mathbf{R}_\alpha| > r^\alpha_{\rm mt}$.[50] Therefore, ϕ^0_α is a superposition of outgoing spherical waves centered on $\mathbf{R}_\alpha$. Following a similar argument, the self-consistently scattered wave can be written

$$\phi(\mathbf{r}) = \sum_\alpha \sum_L h^{(+)}_L[k(\mathbf{r} - \mathbf{R}_\alpha)]\, \phi_{\alpha,L} \tag{10}$$

for $\mathbf{r}$ outside the muffin-tin spheres. Eq. (10) states that the scattered wave finds its sources in the muffin-tin spheres, from where it emerges as a combination of outgoing spherical waves.

The propagation of ϕ^0_α from atom α to atom β, which is needed in the evaluation of Eq. (6), can be performed by using Eq. (9) and the translation formula of spherical harmonics[26,27,4]

$$h^{(+)}_{L'}[k(\mathbf{r} - \mathbf{R}_\beta)] = \sum_L j_L[k(\mathbf{r} - \mathbf{R}_\alpha)] G_{\alpha\beta,LL'}, \tag{11}$$

where

$$G_{\alpha\beta,LL'} = 4\pi \sum_{L''} h^{(+)}_{L''}[k(\mathbf{R}_\alpha - \mathbf{R}_\beta)] \times \int d\Omega\, Y_L(\Omega) Y_{L''}(\Omega) Y^*_{L'}(\Omega).$$

Eq. (11) is valid provided that $|\mathbf{r} - \mathbf{R}_\alpha| < |\mathbf{R}_\alpha - \mathbf{R}_\beta|$; this condition is satisfied when $\mathbf{r}$ is contained inside the muffin-tin sphere $\beta \neq \alpha$ and non-overlapping spheres are considered. It is also convenient to represent G_0 in the basis set of spherical harmonics attached to each atom of the cluster. Using Eqs. (8) and (11), one finds[26,27,4]

$$G_0(\mathbf{r} - \mathbf{r}') = -2k \sum_{LL'} j_L[k(\mathbf{r} - \mathbf{R}_\alpha)] j_{l'-m'}[k(\mathbf{r}' - \mathbf{R}_\beta)] \times (-1)^{l'+m'} G_{\alpha\beta,LL'}, \tag{12}$$

and this expression is valid in the present context for $\alpha \neq \beta$, and $\mathbf{r}$ and $\mathbf{r}'$ lying inside different non-overlapping muffin-tin spheres.

With the help of these expressions, all spatial integrals that are implicit in Eqs. (4) and (6) (see Ref. [49]) can be collected in the so-called scattering matrix elements,

$$t_{\alpha,LL'} = -2k \int d\mathbf{r} d\mathbf{r}'\, j_{l-m}[k(\mathbf{r} - \mathbf{R}_\alpha)](-1)^{l+m} \times T_\alpha(\mathbf{r}, \mathbf{r}')\, j_{L'}[k(\mathbf{r}' - \mathbf{R}_\alpha)]. \tag{13}$$

For spherically-symmetric potentials, $t_{\alpha,LL'}$ becomes diagonal and it is given in terms of the scattering phase shifts δ^α_l as[48]

$$t_{\alpha,LL'} = t_{\alpha,l}\delta_{LL'} = \sin\delta^\alpha_l e^{i\delta^\alpha_l}\delta_{LL'}. \tag{14}$$

Finally, using Eqs. (4) and (9)–(13), and identifying coefficients that multiply into the same functions $h^{(+)}_L[k(\mathbf{r} - \mathbf{R}_\alpha)]$, Eq. (6) reduces to

$$\bar{\phi}_\alpha = \bar{\phi}^0_\alpha + \sum_{\beta\neq\alpha} t_\alpha G_{\alpha\beta} \bar{\phi}^0_\beta + \sum_{\gamma\neq\beta}\sum_{\beta\neq\alpha} t_\alpha G_{\alpha\beta} t_\beta G_{\beta\gamma} \bar{\phi}^0_\gamma + \dots, \tag{15}$$

where $\bar{\phi}^0_\alpha$ and $\bar{\phi}_\alpha$ denote column vectors of components $\phi^0_{\alpha,L}$ and $\phi_{\alpha,L}$, respectively, $G_{\alpha\beta}$ represents the matrix of components $G_{\alpha\beta,LL'}$, the scattering matrix t_α has components given by Eq. (14), and matrix multiplication involves summation over indices L, L', etc.

III. COMPUTATIONAL PROCEDURE

The time employed in the direct evaluation of Eq. (15) grows exponentially with the number of terms on the right hand side. However, an iterative procedure makes it feasible to evaluate the MS series until convergence is achieved, as discussed below in Sec. III A,[41,42,47] where several iteration methods are examined in connection with the solution of that equation, including a new modification of the recursion method that allows us to calculate intensities simultaneously for many angles in the far electron field from a single MS calculation.

An exact representation of the free electron Green function is used in the present work, and this is made possible in part thanks to the saving in both computation time and storage demand achieved through the method introduced in Sec. III B: decomposition of the Green function into elementary rotations and translations while keeping track of the latter, so that they are not unnecessarily re-calculated during the full MS evaluation.

A. Iterative solution of the MS series

It is easy to see that the sum of the first $n+1$ terms on the right hand side of Eq. (15), $\bar{\phi}^n_\alpha$, obeys the following recurrence relation:

$$\bar{\phi}^n_\alpha = \bar{\phi}^0_\alpha + t_\alpha \sum_{\beta\neq\alpha} G_{\alpha\beta} \bar{\phi}^{n-1}_\beta, \quad (n > 0). \tag{16}$$

That is, the difference between $\bar{\phi}^n_\alpha$ and $\bar{\phi}^{n-1}_\alpha$ is just the $n^{\rm th}$ sum on the right hand side of Eq. (15). Each term in that sum contains n products by matrices t_α, that is,

it can be interpreted as the contribution of paths along which the electron undergoes n atomic-scattering events.

Taking the $n \to \infty$ limit in Eq. (16), one finds

$$\bar{\phi}_\alpha = \bar{\phi}^0_\alpha + t_\alpha \sum_{\beta \neq \alpha} G_{\alpha\beta} \bar{\phi}_\beta. \tag{17}$$

The direct inversion of Eq. (17), sometimes called giant-matrix inversion (GMI), is prohibitive in many cases, since it requires performing $\sim N^3(l_{\max}+1)^6$ complex products. However, this has been carried out by some authors for small values of N and $l_{\max}$[51,52] and is also commonly used within individual layers in a surface with small number of atoms per surface unit cell.[4,5]

Three different iterative techniques have been used and compared in the present work to evaluate Eq. (15): (a) direct Jacobi iteration, (b) simultaneous relaxation,[43] previously used in this context,[42] and (c) the Haydock recursion method.[44–46]

(a) *Direct Jacobi iteration.* This method is based upon the iterative evaluation of Eq. (16). Starting with $\bar{\phi}^0_\alpha$, each iteration of Eq. (16) leads to the next order of scattering, and this procedure has to be carried out until convergence is achieved. Substituting $\phi^n_{\alpha,L}$ for $\phi_{\alpha,L}$ in Eq. (10), one obtains the approximate wave function calculated up to order n of MS. Since the wave function coefficients $\phi_{\alpha,L}$ span a space of dimension $(l_{\max}+1)^2N$, Eq. (16) can also be regarded as the power series inversion formula $1/(1-X)|\phi\rangle = (1+X+X^2+\ldots)|\phi\rangle$, where X is a matrix that operates on that space, defined in terms of t_α and $G_{\alpha\beta}$, and $|\phi\rangle$ is the vector of coefficients $\phi_{\alpha,L}$. Unfortunately, when any of the eigenvalues of X has a magnitude larger than 1, this expansion series fails to converge. This problem has already been discussed in the context of LEED[4] and PD.[42] Faster convergent schemes can be found that do not require an extra computational effort, at the price of dismissing the intuitive physical picture of going to the next order of scattering with each iteration step. This is the case of the simultaneous relaxation method and the recursion method discussed next.

(b) *Simultaneous relaxation method* (SR). This consists of using the latest values of $\bar{\phi}^n_\alpha$ as soon as they are calculated. In addition, the result obtained from its iteration is mixed with the previous result to improve convergence. Then, the iteration formula becomes

$$\bar{\phi}'^n_\alpha = \bar{\phi}^0_\alpha + t_\alpha \sum_{\beta \neq \alpha} G_{\alpha\beta} \bar{\phi}'^n_\beta$$

and

$$\bar{\phi}^n_\alpha = \eta \bar{\phi}'^n_\alpha + (1-\eta)\bar{\phi}^{n-1}_\alpha,$$

where $\bar{\phi}'^n_\beta = \bar{\phi}'^n_\beta$ for $\beta < \alpha$ and $\bar{\phi}'^n_\beta = \bar{\phi}^{n-1}_\beta$ otherwise, and η is a mixing parameter typically adjusted in the range $0 < \eta < 2$ in order to accelerate convergence. For $0 < \eta < 1$ one has what is termed underrelaxation.[43]

(c) *Modified recursion method.* With the notation of point (a) above, Eq. (17) can be written $|\phi\rangle = (\lambda - X)^{-1}|\phi^0\rangle$ ($\lambda = 1$). The relevant magnitude in which we are interested is the electron current at the detector, which is proportional to $|\langle f|\phi\rangle|^2$ with a suitable definition of the final detected wave function in a given direction $\langle f|$ (e.g., see Sec. IV below). Haydock's recursion method[44–46] permits obtaining this matrix element by iterative refinement. Here, λ plays the same role as the energy in calculations of solid ground state properties.[45,46] Although we are only interested in the value $\lambda = 1$ in the present case, the recursion method is advantageous because it is fully convergent for any matrix X. Actually, it produces rigorously exact values when the iteration is carried out $(l_{\max}+1)^2N$ times, although convergence is achieved much earlier, typically in less than 20 iterations in the examples presented in the present work.

In many cases, one is interested in calculating angular distributions of emitted or scattered electrons (e.g., in Fig. 3). Unfortunately, the recursion method requires carrying out the MS iteration procedure for each direction of emission (i.e., for each $\langle f|$). Here, we have modified the recursion method so that it allows one to obtain intensities for various directions of emission with a single MS calculation, provided one stores the moments $\mu_n = \langle f|X^n|\phi^0\rangle$ for each $\langle f|$ and each iteration step n. Our modified method is based upon the double recurrence

$$|\alpha_{p+1}\rangle = [(X^\dagger - a^*_p)|\alpha_p\rangle - b^*_p|\alpha_{p-1}\rangle]/b^*_{p+1} \tag{18}$$

and

$$|\beta_{q+1}\rangle = [(X - a_q)|\beta_q\rangle - b_q|\beta_{q-1}\rangle]/b_{q+1}, \tag{19}$$

where the starting values are $|\alpha_{-1}\rangle = |\beta_{-1}\rangle = 0$, $|\alpha_0\rangle = |f\rangle/\sqrt{\mu^*_0}$, and $|\beta_0\rangle = |\phi_0\rangle/\sqrt{\mu_0}$, and a_n and b_n are complex numbers. Upon inspection, one can easily prove that

$$\langle \alpha_i|\beta_j\rangle = \delta_{ij} \tag{20}$$

if one chooses

$$a_n = \langle \alpha_n|X|\beta_n\rangle \tag{21}$$

and b_{p+1} such that $\langle \alpha_{p+1}|\beta_{p+1}\rangle = 1$. Haydock's recursion method is recovered in the special case where $X = X^\dagger$ and $|f\rangle = |\phi_0\rangle$.[44] These recurrences share in common with Haydock's method the property that the matrix of components $\langle \alpha_i|X|\beta_j\rangle$ is tridiagonal, as can be seen from Eqs. (18), (19), and (20), and this permits writing the desired matrix element as the continued fraction[44]

$$\langle f|(\lambda - X)^{-1}|\phi_0\rangle = \cfrac{\langle f|\phi 0\rangle}{\lambda - a_1 - \cfrac{b_1^2}{\lambda - a_2 - \cfrac{b_2^2}{\lambda - a_3 - \ldots}}}. \tag{22}$$

Different terminations of the iteration procedure have been proposed,[44] but in the present context, our results are quite insensitive to the particular choice.

Rather than directly evaluating these recurrences, an equivalent recurrence can instead be constructed using the quantities

$$I^n_{pq} = \langle \alpha_p|X^n|\beta_q\rangle.$$

Multiplying Eq. (19) by $\langle \alpha_p|$, one finds

$$I^n_{pq+1} = [I^{n+1}_{pq} - a_q I^n_{pq} - b_q I^n_{pq-1}]/b_{q+1}, \tag{23}$$

and similarly, from Eq. (18),

$$I^n_{p+1,q} = [I^{n+1}_{pq} - a_p I^n_{pq} - b_p I^n_{p-1,q}]/b_{p+1}. \tag{24}$$

Moreover, Eq. (21) can be recast

$$a_p = I^1_{p,p} \tag{25}$$

and the normalization factor b_{p+1} becomes

$$b_{p+1} = \sqrt{I^2_{pp} - a^2_p - b^2_p}. \tag{26}$$

Now, a_p and b_p, and therefore also Eq. (22), can be evaluated using Eqs (23), (24), (25), and (26) recursively with the starting values $I^n_{00} = \mu_n/\mu_0$ and $I^n_{p,-1} = I^n_{-1,q} = 0$. The relevance of this procedure is that it permits calculating the matrix element (22) directly from the moments μ_n, which are in turn obtained from a single MS calculation for as many $\langle f|$'s as desired.

Comparisons of rapidity of convergence using these iteration methods are offered in Figs. 2, 3, and 4 for PD, and in Fig. 7 for electron scattering. The results are discussed in more detail in Secs. IV and V.

An important point about the iteration methods just described is that the number of products of scattering matrices t_α per iteration is N in all of them, whereas the number of $G_{\alpha\beta}\bar{\phi}_\beta$ products is $N(N-1)$. Therefore, in realistic clusters, where $N > 100$ (see Fig. 1), no substantial relative increase in computational effort is introduced if one goes beyond the commonly used spherical muffin-tin approximation, that is, if non-diagonal scattering matrices like those needed to represent non-spherical potentials[53–55] (e.g., in photoelectron diffraction in oriented molecules[56]) or spin-orbit coupling[53] are considered.

Since most of the computational effort is invested in products by $G_{\alpha\beta}$ matrices (vector addition takes a negligible time), we have devoted Sec. III B to a description of how to minimize their computational cost.

B. Optimization of products of Green functions

Following previous authors,[26,13,14] the Green function $G_{\alpha\beta}$ that propagates a free electron along an inter-atomic bond vector $\mathbf{d}_{\alpha\beta} = \mathbf{R}_\alpha - \mathbf{R}_\beta$ will be expressed in terms of the propagator along the z axis by using rotation matrices $R^{(l)}_{mm'}(\alpha\beta\gamma)$, where $(\alpha\beta\gamma)$ are the corresponding Euler angles.[48] In a first step, the bond vector $\mathbf{d}_{\alpha\beta}$ is rotated onto the z axis by applying the matrix[13,48]

$$R_{\alpha\beta,LL'} = \delta_{ll'} R^{(l)}_{mm'}(0,\theta,\pi-\varphi), \tag{27}$$

where (θ,φ) are the polar angles of $\mathbf{d}_{\alpha\beta}$. Then, the electron is propagated along the bond vector, directed now along the z axis and for which the Green function reduces to

$$G^z_{\alpha\beta,LL'} = \delta_{mm'}\sqrt{4\pi}\sum_{l''}\sqrt{2l''+1}\,i^{l''}h^{(+)}_{l''}(kd_{\alpha\beta}) \times \int d\Omega\, Y_{lm}(\Omega)Y_{l''0}(\Omega)Y^*_{l'm}(\Omega). \tag{28}$$

Finally, the bond vector is rotated back to the original position, and one finds[13,41]

$$G_{\alpha\beta} = R^{-1}_{\alpha\beta}G^z_{\alpha\beta}R_{\alpha\beta}. \tag{29}$$

A recurrence relation has been reported that permits evaluating Eq. (28) efficiently.[15] The rotation matrices can be in turn decomposed into azimuthal and polar rotations as[48]

$$R^{(l)}_{mm'}(0,\theta,\pi-\varphi) = R^{(l)}_{mm'}(0,\theta,0)\,(-1)^{m'}e^{i\varphi m'}.$$

This decomposition of the Green function permits us to reduce both *(i)* the storage required to evaluate the MS series and *(ii)* the computational effort.

(i) A significant reduction in memory demand can be accomplished if the coefficients of each polar rotation $R^{(l)}_{mm'}(0,\theta,0)$, each azimuthal rotation $(-1)^{m'}e^{i\varphi m'}$, and each propagation along a bond distance $G^z_{\alpha\beta,LL'}$ are computed and stored once and for all the first time that they are encountered during the full calculation. Since actual clusters on which MS calculations are to be performed possess in general a certain degree of symmetry, the total number of different bond distances and bond polar angles is considerably reduced as compared with the total number of bond vectors. To illustrate this, let us take the example of a simple-cubic-lattice cube of side p in units of the lattice constant; this cluster contains p^3 atoms and $(2p-1)^3-1$ different bond vectors, a number that has to be compared with at most $3p^2$ bond distances, since the square of the distance between any pair of atoms has to be equal to an integral number, and the distance between opposite corners is $\sqrt{3}p$. A better estimate for this case results in $\approx 1.8p^2$ different bond distances.

(ii) For a given maximum value of the angular momentum number $l_{\max}$, the dimension of each vector $\bar{\phi}_\alpha$ is $(l_{\max}+1)^2$, so that every matrix-vector product $G_{\alpha\beta}\bar{\phi}_\beta$ involves $(l_{\max}+1)^4$ complex multiplications. However, all of the three matrices that appear on the right hand side of Eq. (29) are sparse, as can be seen from Eqs. (27) and (28). A detailed inspection leads to the conclusion that only $\approx (10/3)(l_{\max}+1)^3$ complex multiplications are needed to evaluate the product $G_{\alpha\beta}\bar{\phi}_\beta$ when $G_{\alpha\beta}$ is decomposed as shown in Eq. (29). This is a factor of

$\approx 3l_{max}/10$ smaller than the direct matrix-vector product.

Further reduction in computational and storage demand can be achieved if symmetry relations for the Green function and the rotation matrices[48] are used (e.g., $G^z_{\alpha\beta,lm,l'm} = G^z_{\alpha\beta,l'-m,l-m}$).

In the examples reported below, the time needed to calculate and store the matrices defined in Eqs. (27) and (28) is negligible compared with the time spent in the iterative evaluation of Eq. (16).

C. Electron attenuation, temperature effects, and surface barrier

The effect of electron inelastic scattering is easily accounted for in a phenomenological way by multiplying the propagator $G^z_{\alpha\beta}$ of Eq. (28) by an exponentially-decaying function of the bond distance, $\exp(-d_{\alpha\beta}/2\lambda_i)$, where λ_i is the inelastic electron mean free path[38–40] and the 1/2 factor reflects the fact that this function goes inside the wave function rather than the electron probability. Also, the propagation from each atom to the detector has to be accompanied by the corresponding exponential attenuation that takes care of the part of the path contained inside the cluster (or below the surface in the case of a solid sample, of which the cluster represents just a part). Inelastic scattering, together with MS, reduces the scattering range, making LEED and PD excellent surface analysis techniques. In the case of core-level photoemission, the photoelectrons ejected from a solid or molecule thus provide information only on the vicinity of the ionised atom, and features coming from the interaction with distant atoms are attenuated by a finite inelastic mean free path.

The effect of thermal vibrations has been incorporated as is generally done in LEED analyses[4] by means of temperature dependent phase shifts that take into account an average displacement of the cluster atoms in their thermal motion.

Refraction at the surface barrier or inner potential V_0 requires correlating the direction of emission as seen from inside a solid with the actual direction of detection outside of it. The relation between these two is easily obtained by invoking conservation of electron momentum parallel to the surface and taking into account the loss of electron kinetic energy in the motion normal to the surface. A transmission factor is also needed,[47] specially for nearly grazing emission (i.e., when the normal kinetic energy is only a few eV above the vacuum threshold). Diffraction of electron components reflected back from the surface has been neglected, although we note that this can play a very important role at very low normal kinetic energies.

We now apply this general methodology to three important classes of experiment: core-level photoelectron diffraction, elastic electron scattering from molecules, and low-energy electron diffraction at surfaces.

IV. CORE-LEVEL PHOTOELECTRON DIFFRACTION

In this section, our methods are applied to the case of photoelectron diffraction. Describing the interaction with the external radiation H_{rad} to first order, the perturbed part of the time-dependent wave function, $\phi(\mathbf{r})\exp(-i\mathrm{E}t)$, is given by

$$\phi(\mathbf{r}) = \int d\mathbf{r}'\, G(\mathbf{r},\mathbf{r}')H_{rad}(\mathbf{r}')\phi_i(\mathbf{r}'), \qquad (30)$$

where $\phi_i(\mathbf{r})$ is the initial-state core-electron wave function and $G(\mathbf{r},\mathbf{r}')$ is the cluster Green function discussed in Sec. II and evaluated at the final electron energy E. The photo-excitation of a core-level electron in a solid or molecule can be well described within the dipole approximation when the radiation wavelength is much larger than the dimensions of the initial core-electron state, in which case one can take $H_{rad} = C\hat{\epsilon}\cdot\mathbf{r}$, where $\hat{\epsilon}$ is the photon-polarization unit vector and C is a normalization constant.

In matrix notation, expressing G in terms of T as $G = G_0 + G_0TG_0$ and using Eq. (5), Eq. (30) becomes

$$\begin{aligned}\phi = {} & G_0H_{rad}\phi_i + G_0T_{\alpha_0}G_0H_{rad}\phi_i \\ & + \sum_{\beta\neq\alpha_0} G_0\Lambda_\beta G_0H_{rad}\phi_i \\ & + \sum_{\beta\neq\alpha_0} G_0\Lambda_\beta G_0T_{\alpha_0}G_0H_{rad}\phi_i,\end{aligned}$$

where α_0 is taken to be the emitter. Noticing that $G_{\alpha_0} = G_0 + G_0T_{\alpha_0}G_0$ is the Green function of atom α_0, one finds

$$\phi = G_{\alpha_0}H_{rad}\phi_i + \sum_{\beta\neq\alpha_0} G_0\Lambda_\beta G_{\alpha_0}H_{rad}\phi_i,$$

which can be compared to Eq. (6) to redefine

$$\phi^0_{\alpha}(\mathbf{r}) = \delta_{\alpha\alpha_0}C\int d\mathbf{r}'\, G_{\alpha_0}(\mathbf{r},\mathbf{r}')\,\hat{\epsilon}\cdot\mathbf{r}'\,\phi_i(\mathbf{r}'). \qquad (31)$$

We are interested in values of $\mathbf{r}$ outside the muffin-tin sphere of the emitter α_0, whereas the integral in Eq. (31) involves $\mathbf{r}'$ inside the muffin-tin sphere (i.e., the region where the core-electron wave function takes non-negligible values). Under these conditions, G_{α_0} can be written as[48]

$$\begin{aligned}& G_{\alpha_0}(\mathbf{r},\mathbf{r}') \\ & = -2k\sum_L h^{(+)}_L[k(\mathbf{r}-\mathbf{R}_{\alpha_0})]F^*_L(\mathbf{r}')\exp(i\delta^{\alpha_0}_l), \qquad (32)\end{aligned}$$

where $F_L(\mathbf{r}) = i^l F_l(r)Y_L(\Omega_r)$ is a solution of $(H_0 + V_{\alpha_0} - E)F_L = 0$ and F_l is chosen such that it is finite at the origin (the regular solution). Inserting Eq. (32) into Eq. (31) and comparing the result with Eq. (9), one obtains

$$\phi^0_{\alpha,L} = -2kC\delta_{\alpha\alpha_0}e^{i\delta^{\alpha_0}_l}\langle F_L|\epsilon\cdot\mathbf{r}|\phi_i\rangle,$$

which includes the dipole matrix elements $\langle F_L|\epsilon\cdot\mathbf{r}|\phi_i\rangle$ and phase shifts $\delta^{\alpha_0}_l$ that are well known in the theory of atomic photoelectric cross sections.[46] Finally, the MS coefficients $\phi_{\alpha,L}$ are obtained from $\phi^0_{\alpha,L}$ as explained in Sec. III and $\phi(\mathbf{r})$ is given by Eq. (10) outside the muffin-tin spheres.

When $\mathbf{r}$ lies at the electron detector (i.e., for r much larger than the interatomic distances of the cluster) we are in the far-field limit and can approximate $h_L[k(\mathbf{r}-\mathbf{R}_\alpha)] \approx \exp(ikr - ik_f\cdot\mathbf{R}_\alpha)Y_L(\Omega)/kr$, where $\mathbf{k}_f = k\mathbf{r}/r$ and Ω is the polar direction of $\mathbf{r}$ (i.e., the detector). Therefore, using Eq. (10), the measured electron intensity per unit of solid angle in the far field becomes

$$I(\Omega) = \left|\frac{C}{k}\sum_\alpha e^{-ik_f\cdot\mathbf{R}_\alpha - \zeta_\alpha/2\lambda_i}\sum_L Y_L(\Omega)\phi_{\alpha,L}\right|^2, \qquad (33)$$

where ζ_α is the distance from atom α to the surface along the direction of emission and λ_i is the inelastic electron mean free path. In general, comparison with experiments requires performing an incoherent sum over different degenerate initial states and possibly over various emitters α_0.

For PD from atoms on or below a solid surface, and for which the entire (focussed) photon beam is intercepted by the sample, the intensity can be given in electrons per steradian per incoming photon by choosing the normalisation constant as $|C|^2 = 4\pi k\sigma(\omega/c)^2/\cos\theta_i$, where ω is the photon energy, c is the speed of light, θ_i is the polar angle of incidence of the light with respect to the surface normal, and σ is the surface density of emitters equivalent to α_0 (i.e., those of a given layer parallel to the surface).

The present formalism is particularly efficient when calculating photoelectron angular distributions: once the coefficients $\phi_{\alpha_0,L}$ have been obtained for a given electron energy, the photoelectron intensity for each emission direction is readily calculated using Eq. (33). When using the modified recursion method outlined in Sec. III A, $\langle f|\phi\rangle$ corresponds to the expression inside the modulus in Eq. (33) and the moment n is given by $\mu_n = \langle f|\phi^n\rangle - \langle f|\phi^{n-1}\rangle$, where $\langle f|\phi^n\rangle$ is calculated from the coefficients $\phi^n_{\alpha L}$ obtained in the n^{th} iteration.

The relative performances of the various iteration methods discussed in Sec. III A for calculating PD from a simple sample consisting of two carbon atoms is analyzed in Fig. 2, where the inset illustrates the details of the geometry (the interatomic distance corresponds to nearest neighbors in graphite). This constitutes a severe test of multiple scattering, since the interatomic distance is relatively small. Within the resolution of the figure, the recursion method (solid circles) converges in just seven iterations to the result of the exact giant-matrix inversion (GMI). In single scattering (SS), that is, at iteration 1, the direct Jacobi iteration (open circles) is already much worse, and subsequent scattering orders lead to divergence. Neither are such divergences prevented by using the SR method (broken curves) over a wide range of the relaxation parameter η. The lower the value of η, the slower is the increase in intensity with iteration step, but the divergent behavior remains.

Divergences such as these are encountered in MS when the absolute value of any of the eigenvalues of the matrix X discussed in Sec. III A is larger than 1. In a basis set that makes this matrix diagonal, each eigenvalue x_i enters the direct Jacobi MS expansion of $1/(1-X)$ as $1/(1-x_i) = 1 + x_i + x_i^2 + \ldots$, and this expansion is only convergent when $|x_i| < 1$. This is a well-known problem in LEED,[4,5] where various schemes have been devised to prevent it, such as renormalized forward scattering[4,5,9] and reverse scattering perturbation.[5,19] The SR method provides a cure in many cases,[42] but it is not sufficiently general, as illustrated by Fig. 2. Instead, the recursion method has a well-established convergent behavior,[44] and therefore, it will be employed from now on unless otherwise specified.

Fig. 3(a) shows our choice of the cluster used to represent photoemission from a given atom (darker circle) within a solid surface. The cluster is formed by those atoms contained within a parabolic surface where the emitter coincides with its focus. The parameter d_{max} determines the size of the cluster (see figure). The parabolic surface comes from the condition that the maximum electron path length inside the solid, where the inelastic attenuation is effective, be at most d_{max} within SS for normal emission.

Convergence with the number of cluster atoms $N \propto d^3_{max}$ is analyzed in Fig. 3(b) for photoemission from a Cu2s level situated on the third layer of a Cu(111) surface and at a polar emission angle of $\theta = 35°$. The geometry under consideration is illustrated schematically in the lower left corner of the figure, and the atoms are again within the paraboloid of Fig. 3(a). Plotted here is the reliability factor defined as[52]

$$R_{ave} = \frac{\overline{|I^N - I^\infty|}}{\overline{I^\infty}}, \qquad (34)$$

where the average is taken over all azimuthal directions of emission (cf. inset), I^N is the intensity calculated for an N-atom cluster, and I^∞ is actually obtained for $N = 1856$. The solid curve and circles correspond to the result obtained from the recursion method, where convergence is achieved in less than 20 iterations. A smooth convergence can be seen in the $N \to \infty$ limit. For $N \approx 160$, which is suggested by Fig. 1 as a convergence criterion for the electron energy under consideration (100 eV), one has $R_{ave} = 0.16$. The inset shows azimuthal scans obtained for different cluster sizes, in order to facilitate the understanding of the actual meaning of R_{ave} in terms of curve comparisons. For $N = 944$ (dot-

ted curve in the inset), one has $R_{ave} = 0.03$ and convergence is already quite good as compared to the $N = 1856$ case, although some small discrepancies can still be distinguished in the height of the peaks around 30°, 60°, and 90°, so that over 1000 atoms are needed to obtain convergence within the resolution of the figure. We note however that most real experimental situations involve averaging over some finite solid angles, and this can lead to an effective reduction in the cluster size needed.

The open circles in Fig. 3(b) show the reliability factor obtained from the Jacobi method for various scattering orders (5, 9, 13, 17, 21, and 25), where the spread in the position of the circles makes evident a divergent behavior. The latter is more pronounced for larger clusters. In this sense, the Jacobi method has to be regarded as an asymptotic series unable to converge below a certain reliability factor in the present case.

Figs. 4(a) and 4(b) show the performance of the recursion method (solid circles, for which only odd iteration orders introduce variations by construction of the method) as compared with that of direct Jacobi iteration (open circles) as a function of iteration step for 4f photoemission from the third W layer in a W(110) surface covered with one monolayer of (1 × 1) O and with an emission angle of 46°.[59] Two different definitions of the reliability factor have been used, based upon either the relative average deviation given by Eq. (34) by substituting N by the iteration step n (R_{ave}, thick curves), or the maximum deviation over the azimuthal scan (thin curves)

$$R_{max} = \frac{\max\{|I^n - I^\infty|\}}{I^\infty}, \tag{35}$$

respectively, where the average is performed over azimuthal scans for a polar angle of emission $\theta = 46°$. Both iteration methods show similar convergence behavior for the relatively small cluster of Fig. 4(a), consisting of $N = 65$ atoms. However, for the larger cluster of Fig. 4(b) ($N = 189$), the Jacobi method fails to converge, whereas the recursion method shows a steady convergent trend.

As pointed out above, the computational cost of EDAC scales as $(l_{max} + 1)^3$ with l_{max}. Consequently, it is desirable to have a criterion to limit the value of l_{max} used in actual MS calculations while maintaining the required degree of accuracy. This criterion is provided by the reliability factor for the atomic scattering amplitude f,

$$R_f \simeq \frac{1}{3}\sqrt{\frac{\int d\Omega\,|f^{l_{max}} - f^{l_{max}=\infty}|^2}{\int d\Omega\,|f^{l_{max}=\infty}|^2}}, \tag{36}$$

where the integrals are extended over all scattering directions Ω. Fig. 4(c) shows the dependence of R_f on l_{max} for 250-eV electrons scattered on W atoms (open circles) as compared with the reliability factor for MS under the same conditions as in Fig. 4(a) for $N = 123$ atoms (solid circles). The latter has been obtained from Eq. (34) by varying l_{max} rather than N for azimuthal scans with polar angle of emission $\theta = 46°$. Both Eq. (34) and Eq. (36) are proportional to relative variations of the atomic scattering amplitude, so that one is comparing quantities of the same order of magnitude. Actually, they exhibit a similar behavior with l_{max}, as shown in Fig. 4(c), which indicates that Eq. (36), whose computation requires a negligible time as compared with MS calculations, offers a good estimate of the error that is made when finite values of l_{max} are used, thus providing a criterion to determine the appropriate value of l_{max} before performing actual MS calculations. Similar results are obtained for other values of θ. Interestingly, all angles of scattering enter in the definition of R_f, and this is consistent with the fact that MS in a solid involves a dense set of single scattering angles. Also shown in Fig. 4(c) is the l_{max} value obtained from the simple criterion mentioned earlier ($l_{max} = kr_{mt}$), which is 11.3.

As another PD example, Fig. 5 shows the angular distribution over the upper-hemisphere for W4f photoelectrons coming from the outer W layer of a W(110) surface covered with one monolayer of (1 × 1) O and illuminated with left-circularly polarized (LCP) light under normal incidence, as shown in the insets. The quantity actually plotted is $[I(\theta,\varphi) - I_0(\theta)]/I_0(\theta)$, where I_0 is the average of the intensity over azimuthal angles. In calculating the data displayed in Fig. 5(a), the MS procedure has been carried out only once for all directions of emission, as explained in Sec. III A, thus saving considerable time. Fig. 5(a) exhibits reduced symmetry with respect to that expected for W(110) owing to the fact that LCP light is used and also because the oxygen atoms are displaced with respect to a center of symmetry of the surface (see the schematic top view). Two different domains can also exist on this surface:[59] the one depicted in the insets and another one with the oxygen lying in a mirror-image symmetry-equivalent W valley. The average over the result obtained from both domains has been performed. The maximum intensity (bright regions) near the [001] azimuthal direction is rotated clockwise, as expected from the use of LCP light and f core levels.[60,61,59] This rotation reproduces very well the available experimental data shown in Fig. 5(b) and taken from Ref. [59].

As a last example of PD, we consider photoemission from atoms near surface steps, where the lack of symmetry makes it difficult to use layer-by-layer methods in simulations, while the cluster approach is perfectly suited for that purpose. Prior x-ray PD experiments on O adsorbed on stepped Cu surfaces have, for instance, indicated high sensitivity to structure via SS calculations.[62] Here, we show calculated azimuthal scans of photoelectrons coming from Xe atoms adsorbed near a step on a Pt(111) surface (Fig. 6). The insets on the right hand side of the figure show schematically the geometry under consideration. Two different possible structures have been studied: one row of Xe atoms located either on the lower terrace (upper part of the figure) or on the upper terrace (lower part), continuing the bulk Pt structure in both cases. Experimental evidence coming from low-energy ion scattering[63] indicates that the lower terrace is the preferred geometry. The results presented in Fig. 6 permit concluding that the features exhibited by PD scans would allow one to distinguish between the two possibilities, although no actual experimental data is available for this case. Moreover, at least 100 atoms are needed to obtain the dominant features when the Xe atoms are sitting on the upper terrace. However, strong forward scattering, dominated by nearest neighbors of the emitter, occurs when the Xe atoms are sitting on the lower terrace, and therefore, a 22-atom cluster produces good qualitative results. In both cases, convergence in the fine structure requires approximately 500 atoms.

V. ELASTIC ELECTRON SCATTERING FROM MOLECULES

The scattering of an external electron beam from a molecule represented by an atomic cluster is discussed in this section. The initial electron state of Eq. (1) will be described by a plane wave $\varphi^0(\mathbf{r}) = \exp(i\mathbf{k}_i\cdot\mathbf{r})$, which can be expanded in partial waves around each of the cluster atoms, and using Eqs. (7)-(9) and (13), one finds

$$\phi^0_{\alpha,L} = 4\pi i^l Y_{l-m}(\Omega_{\mathbf{k}})(-1)^m e^{i\mathbf{k}_i\cdot\mathbf{R}_\alpha - \zeta_\alpha/2\lambda_i}, \tag{37}$$

where ζ_α has the same meaning as in Eq. (33), with the *surface* now defined as the boundary of the molecular electronic charge distribution. These are the input wavefunction coefficients from which one can obtain those of the self-consistent wave function (10), $\phi_{\alpha,L}$, after MS is performed using the methods described in Sec. III. The latter permits, upon insertion into Eq. (33), computing the diffracted electron intensity. Choosing $C = 1$, Eq. (33) represents the scattering cross section.

This has been done for C_{60} molecules and 809-eV electrons in Fig. 7(a), where experimental results taken from Ref. [64] are compared with single scattering (SS, also reported in Ref. [64]) and MS calculations represented by broken and solid curves, respectively, as a function of scattering angle. MS results in better agreement for the relative height of the prominent diffraction peaks at around 5° and 8.5°, as compared with the SS analysis.

In order to emphasize the contribution of MS, lower electron energies (100 eV) and a back-scattering geometry have been considered in Fig. 7(b) for electron scattering by C_{60} molecules. The thick solid curve represents the fully-converged result obtained by using the recursion method (convergence has been obtained after 11 iterations within the scale of the figure). The thin solid curve shows the results obtained after only 5 iterations, which are in qualitative good agreement with the exact result. By contrast, direct Jacobi iteration is far from convergence even after 25 iterations (thick broken curve). The C_{60} molecule, like the C-C cluster of Sec. IV, is a severe test of multiple scattering because the carbon atoms are reasonably strong scatterers placed relatively close together.

VI. LOW-ENERGY ELECTRON DIFFRACTION

The cluster approach followed in this work finds application in the simulation of LEED intensities for large-unit-cell surfaces, where conventional layer-by-layer schemes become quite expensive computationally. It is also directly applicable to non-periodic surfaces, including disordered overlayers, disordered alloys, point defects, steps and kinks, adsorbed clusters, quasicrystals, etc.

In a periodic surface, the scattering of electrons in any surface unit cell differs from that of the first unit cell by a phase factor, $\exp[i(\mathbf{k}_i - \mathbf{k}_f)\mathbf{R}_a]$, where $\mathbf{k}_i$ ($\mathbf{k}_f$) is the incoming (outgoing) electron momentum vector, and $\mathbf{R}_a$ is a Bravais lattice vector. Therefore, LEED intensities can be calculated within the present cluster approach by taking ϕ^0_α as in Eq. (37) for the atoms of the first unit cell and zero elsewhere. One obtains

$$I_{LEED}(\Omega) = I(\Omega)|S(\mathbf{k}_i^{\parallel} - \mathbf{k}_f^{\parallel})|^2, \tag{38}$$

where

$$S = \sum_a e^{i(\mathbf{k}_i - \mathbf{k}_f)\mathbf{R}_a},$$

is the surface structure factor[4] and $I(\Omega)$ is an envelope function given by Eq. (33), where the coefficients $\phi_{\alpha,L}$ are obtained from a MS calculation within a cluster containing the first unit cell and atoms around it up to a distance far enough to guarantee convergence. The cluster size is thus determined by the electron inelastic mean free path and the size of the first unit cell, with the cluster extending beyond the unit cell by roughly the electron inelastic attenuation length.

For an infinitely extended incoming beam and a perfect infinite surface, the two-dimensional structure factor S vanishes except along those directions for which the components of $\mathbf{k}_i - \mathbf{k}_f$ parallel to the surface equal a reciprocal surface lattice vector G denoted by Miller indices (hk), giving rise to a factor $\delta(\mathbf{k}_i^{\parallel} - \mathbf{k}_f^{\parallel} - \mathbf{G})$; this corresponds to the so-called (hk) beam at the polar direction Ω_G. Integrating over directions of emission around Ω_G, the probability that the electron is reflected along such a direction is found to be

$$P_G = \left(\frac{2\pi}{Ak}\right)^2 \frac{I(\Omega_G)}{\cos\theta_i \cos\theta_f},$$

where θ_i (θ_f) is the polar angle of incidence (reflection) with respect to the surface normal, A is the surface unit-cell area, and k is the electron momentum. With the normalization of Eq. (37) and taking $C = 1$ in Eq. (33), P_G is actually the fraction of incoming electrons that are reflected in the G beam.

In practice, the electron beam has a finite coherence width of the order of 100 Å, depending on the angular and energy spread of the electron gun. This effect can be accounted for in a phenomenological way by considering that only a fraction of the unit cells contribute coherently with respect to an arbitrarily chosen central unit cell. Assuming a Gaussian profile for this effect with half width H and furthermore that there is no substantial variation of coherence across any given unit cell, one finds

$$S = \sum_{\alpha} e^{-R_\alpha^2/2H^2} e^{i(\mathbf{k}_i - \mathbf{k}_f)\mathbf{R}_\alpha}$$
$$= (2\pi)^3 \frac{H^2}{A} \sum_{\mathbf{G}} e^{-|\mathbf{k}_i^{\parallel} - \mathbf{k}_f^{\parallel} - \mathbf{G}|^2 H^2/2}, \qquad (39)$$

where the first (last) sum is extended over surface lattice sites $\mathbf{R}_\alpha$ (reciprocal surface lattice vectors G). Obviously, the sum in reciprocal space reduces to a single term at most in the $H \to \infty$ limit, and a few more terms allow achieving good convergence for typical values of $H \sim 100$ Å. Inserting Eq. (39) into Eq. (38), one finds a finite reflection probability for every direction Ω.

The present formalism has been applied to the Si(111)-(7 × 7) surface. The atomic positions have been taken from a previous LEED analysis,[65] in which intensive use was made of the symmetry of the surface. By contrast, the results presented here have been obtained directly without any symmetry considerations beyond the surface unit-cell geometry. Fig. 8 shows the final LEED pattern I_{LEED} (right figure) as well as the surface structure factor S^2 (upper left figure) and the envelope function I (lower left figure) for an incident beam of 50-eV electrons coming along the surface normal. The axis labels represent the components of the electron momentum parallel to the surface. The structure factor exhibits a dense spot pattern that reflects the symmetry of the large unit cell of the Si(111)-(7 × 7) surface. This is a purely geometrical quantity which does not contain any information about the actual positions of the atoms within the surface unit cell, but does reflect the quality of the electron beam via Eq. (39). That information is fully contained in the envelope function (lower left figure), which presents marked maxima near the positions expected for the LEED spots of the unreconstructed Si(111) surface (see the six prominent peaks in the figure). The envelope function modulates the intensity that is observed around each of the spots of the structure factor, leading to the complex LEED pattern shown in the right part of the figure.

The calculation of the envelope function $I(\Omega)$ has been performed using a cluster consisting of 1545 atoms, of which only 494 are contained within the surface unit cell. The cluster extends up to 15 Å below the surface and the electron inelastic mean free path has been taken as 5.5 Å.

This calculation has been compared with experimental observations in Fig. 9 both for 50-eV electrons and for 75-eV electrons (left and right side of the figure, respectively).[66] Note the large change in the measured distribution of the brightest spots when one goes from 50 eV to 75 eV (upper figures), which is well reproduced by the present calculation (lower figures) using an inner potential of 10 eV.

As another example of application of the present method to LEED with a large unit cell, the case of a W(110) surface covered with one monolayer of Gd is considered in Fig. 10. Various experimental LEED studies of this structure have been reported in the past.[67,68] Fig. 10(a) shows the model (A) proposed by Tober *et al.*,[68] wherein the Gd overlayer forms a rectangular coincidence lattice with (7 × 14) periodicity and with a mismatch of 0.6% area increase relative to bulk Gd(0001). The calculated LEED pattern represented in Fig. 10(b) for this model has been obtained from Eqs. (38) and (39) for an electron beam diameter of 100 Å and an energy of 102 eV. The surface has been described by five W layers below the Gd overlayer, so that 648 atoms are contained in the surface unit cell, and 2516 atoms have been used in the calculation to include the regions surrounding the surface unit cell.. Some of the spots are clearly highlighted by the envelope function, and in particular the six brighter spots coming from the Gd overlayer. Six satellites around each of them are clearly highlighted forming a quasi-six-fold satellite pattern (see the white lines drawn to guide the eye), in reasonable agreement with the experimental result shown in Fig. 10(c) (taken from Ref. [68]).

Since the spot pattern imposed by S for this model is a rectangular one, leading to the emergence of spurious satellites not observed in the experiment, a different model structure (model B) with a 1.8% overall area reduction relative to Gd(0001) has been tried, as represented in Figs. 8(c)-(d). Two different domains are possible in this case. The corresponding LEED pattern averaged over both domains is shown in Fig. 8(d). This results in a somewhat poorer agreement with experimental observations[68] [Fig. 10(e)] and demonstrates the power of such simulations to assist in structural studies.

In summary, the present method allows calculating LEED patterns for complex structures using large clusters of up to several thousand atoms, which are now beyond practical reach of currently available layer-by-layer methods of LEED simulation.

VII. CONCLUSIONS

A new method for the simulation of electron diffraction in atomic clusters (EDAC) has been introduced. The computation time has been shown to behave like $N^2(l_{\max}+1)^3$, where N is the number of atoms and $l_{\max}$ is the maximum angular momentum quantum number. Actual calculations using above 1000 atoms have been presented. This is made possible via a convenient separation of the exact free-electron Green functions into rotation matrices and propagators along the z axis.

The resulting EDAC code relies on the iterative solution of the multiple scattering (MS) secular equation, for which various iteration techniques have been compared. In particular, the recursion method has been shown to prevent divergences and to result in faster convergence as compared with the direct MS approach. A modified recursion method has been introduced in order to be able to quickly obtain angular distributions of scattered or emitted electrons from a single MS calculation (see Sec. III A.

The computational effort in EDAC is not very sensitive to the detailed form of the atomic scattering $t-$matrices (e.g., diagonal vs non-diagonal), and it therefore constitutes a good platform for including the effects of nonspherical atoms in MS. Further research in this direction is in progress.[56]

Examples of application of EDAC to PD have been given for Cu(111), O/W(110), and Xe adsorbed near steps of a Pt(111) surface. The present cluster approach is particularly suitable for these cases due to the lack of translational symmetry. Also, PD from a C-C dimer has been shown to lead to divergences in the MS expansion (even at a relatively large electron energy of 850 eV), which are easily prevented by using the recursion method.

Electron elastic scattering on C_{60} molecules has also been discussed, and MS has been shown to result in improved agreement with experiment as compared to single scattering.

Finally, a formalism for studying LEED within the cluster approach has been presented and applied to LEED from large-unit-cell surfaces. In particular, the relative intensity of the different LEED spots observed experimentally for the Si(111)-(7×7) are well reproduced by this theory. Also, two different models for the surface structure of one monolayer of Gd on W(110) have been considered, and the resulting LEED patterns have been discussed in the light of the available experimental results. The formalism can also be applied to a wide variety of non-periodic surface structures, including free molecules.

ACKNOWLEDGMENTS

The authors would like to thank R. X. Ynsunza, F. J. Palomares, and E. Tober for providing the experimental data of Figs. 5, 9, and 10, respectively. This work was supported in part by the University of the Basque Country and the Spanish Ministerio de Educación y Cultura (Fulbright grant FU-98-22726216), and by the Director, Office of Science, Basic Energy Sciences, Materials Sciences Division of the U.S. Department of Energy under Contract No. DE-AC03-76SF00098.

* E-mail: ccpgaabf@photon.lbl.gov

[1] C. S. Fadley and S. Å. L. Bergström, Phys. Lett. A 35, 375 (1971).
[2] A. Liebsch, Phys. Rev. Lett. 32, 1203 (1974).
[3] S. Kono, C. S. Fadley, N. F. T. Hall, and Z. Hussain, Phys. Rev. Lett. 41, 117 (1978); D. P. Woodruff, D. Norman, B. W. Holland, N. V. Smith, H. H. Farrell, and M. M. Traum, Phys. Rev. Lett. 41, 1130 (1978); S. D. Kevan, D. H. Rosenblatt, D. Denley, B.-C. Lu, and D. A. Shirley, Phys. Rev. Lett. 41, 1565 (1978); S. Kono, S. M. Goldberg, N. F. T. Hall, and C. S. Fadley, Phys. Rev. Lett. 41, 1831 (1978).
[4] J. B. Pendry, *Low Energy Electron Diffraction* (Academic Press, London, 1974).
[5] M. A. Van Hove, W. H. Weinberg, and C.-M. Chan, *Low Energy Electron Diffraction* (Springer-Verlag, Heidelberg, 1986).
[6] S. A. Chambers, Adv. Phys. 40, 357 (1991).
[7] P. A. Lee and J. B. Pendry, Phys. Rev. B 11, 2795 (1975).
[8] J. B. Pendry, Surf. Sci. 57, 679 (1976).
[9] C. H. Li, A. R. Lubinsky, and S. Y. Tong, Phys. Rev. B 17, 3128 (1978).
[10] C. H. Li and S. Y. Tong, Phys. Rev. Lett. 42, 901 (1979).
[11] J. J. Barton and D. A. Shirley, Phys. Rev. B 32, 1906 (1985).
[12] J. J. Barton, M.-L. Xu, and M. A. Van Hove, Phys. Rev. B 37, 10475 (1988).
[13] J. J. Rehr and R. C. Albers, Phys. Rev. B 41, 8139 (1990).
[14] V. Fritzsche, J. Phys.: Condens. Matter 2, 1413 (1990).
[15] V. Fritzsche, J. Phys.: Condens. Matter 2, 9735 (1990).
[16] D. J. Friedman and C. S. Fadley, J. Electron Spectrosc. 51, 689 (1990).
[17] A. P. Kaduwela, D. J. Friedman, and C. S. Fadley, J. Electron Spectrosc. 57, 223 (1991).
[18] J. B. Pendry, in *Determination of Surface Structure by LEED*, edited by P. M. Marcus and F. Jona (Plenum Press, New York, 1984), p. 3.
[19] D. D. Vvedensky, D. K. Saldin, and J. B. Pendry, Surf. Sci. 156, 845 (1985).
[20] D. K. Saldin and J. B. Pendry, Surf. Sci. 162, 941 (1985).
[21] D. K. Saldin, G. R. Harp, and X. Chen, Phys. Rev. B 48, 8234 (1993).
[22] J. E. Müller and W. L. Schaich, Phys. Rev. B 27, 6489 (1983).
[23] C. S. Fadley, in *Synchrotron Radiation Research: Advances in Surface and Interface Science*, edited by R. Z. Bachrach (Plenum Press, New York, 1992), p. 421.
[24] C. S. Fadley *et al.*, Prog. in Surf. Sci. 54, 341 (1997).
[25] J. L. Beeby, Proc. R. Soc. A 302, 113 (1967).
[26] M. Danos and L. C. Maximon, J. Math. Phys. 6, 766 (1965).
[27] R. Nozawa, Nucl. Instrum. Methods B 100, 1 (1966).
[28] W. L. Schaich, Phys. Rev. B 8, 4028 (1973).

[29] C. A. Ashley and S. Doniach, Phys. Rev. B 11, 1279 (1975).
[30] W. L. Schaich, Phys. Rev. B 29, 6513 (1984).
[31] S. J. Gurman, N. Binsted, and I. Ross, J. Phys.: Condens. Matter 17, 143 (1984).
[32] S. J. Gurman, N. Binsted, and I. Ross, J. Phys.: Condens. Matter 19, 1845 (1986).
[33] J. J. Barton and D. A. Shirley, Phys. Rev. A 32, 1019 (1985).
[34] M. Sagurton, E. L. Bullock, R. Saiki, A. Kaduwela, C. R. Brundle, C. S. Fadley, and J. J. Rehr, Phys. Rev. B 33, 2207 (1986).
[35] J. Mustre de Leon, J. J. Rehr, C. R. Natoli, C. S. Fadley, and J. Osterwalder, Phys. Rev. B 39, 5632 (1989).
[36] S. I. Zabinsky, J. J. Rehr, A. Ankudinov, R. C. Albers, and M. J. Eller, Phys. Rev. B 39, 5632 (1989).
[37] A. Ankudinov and J. J. Rehr, Phys. Rev. B 52, 10214 (1995).
[38] G. E. Laramore, C. B. Duke, and N. O. Lipari, Phys. Rev. B 10, 2246 (1974).
[39] C. J. Tung and R. H. Ritchie, Phys. Rev. B 16, 4302 (1977).
[40] C. J. Powell and A. Jablonski, Physical and Chemical Reference Data 28, 19 (1999).
[41] Y. Chen, F. J. García de Abajo, A. Chassé, R. X. Ynzunza, A. P. Kaduwela, M. A. Van Hove, and C. S. Fadley, Phys. Rev. B 58, 13121 (1998).
[42] H. Wu and S. Y. Tong, Phys. Rev. B 59, 1657 (1999).
[43] W. H. Press, S. A. Teukolsky, W. T. Vetterling, and B. P. Flannery, *Numerical Recipes* (Cambridge University Press, New York, 1992).
[44] R. Haydock, Solid State Physics 35, 215 (1980).
[45] V. Heine, Solid State Physics 35, 1 (1980).
[46] R. Haydock, Phys. Rev. B 61, 7953 (2000).
[47] F. J. García de Abajo, Phys. Rev. Lett. 82, 2776 (1999).
[48] A. Messiah, *Quantum Mechanics* (North-Holland, New York, 1966).
[49] Matrices will be represented in upper case (e.g., T) and vectors in lower case (e.g., φ^0). Spatial coordinates are providing matrix and vector indices, so that, products like $T\varphi^0$ involve spatial integrals: $\int d\mathbf{r}' T(\mathbf{r},\mathbf{r}')\varphi^0(\mathbf{r}')$. The unit matrix stands for $\delta(\mathbf{r}-\mathbf{r}')$, and the potential V, when understood as a matrix, represents $V(\mathbf{r})\delta(\mathbf{r}-\mathbf{r}')$.
[50] The explicit form of the coefficients $\phi^0_{\alpha,L}$ is not relevant, but the important point is that $\phi^0_\alpha(\mathbf{r})$ is a superposition of outgoing spherical waves $h^{(+)}_L[k(\mathbf{r}-\mathbf{R}_\alpha)]$ for $\mathbf{r}$ outside the muffin-tin sphere α.
[51] C. R. Natoli and M. Benfatto, J. Physique Colloque 47, C8 (1986).
[52] V. L. Shneerson, W. T. Tysoe, and D. K. Saldin, Phys. Rev. B 53, 10177 (1996).
[53] P. Strange, J. Staunton, and B. L. Gyorffy, J. Phys. C 17, 3355 (1984).
[54] H. Ebert, Phys. Rev. B 38, 9390 (1988).
[55] P. Strange, H. Ebert, J. Staunton, and B. L. Gyorffy, J. Phys.: Condens. Matter 1, 2959 (1989).
[56] R. Diez Muiño, S. Rolles, F. J. García de Abajo, M. A. Van Hove, and C. S. Fadley (in preparation).
[57] M. Rösler and F. J. García de Abajo, Phys. Rev. B 54, 17158 (1996).
[58] The choice of the reliability factor $R_{\rm ave}$ is appropriate here, since we are comparing different theoretical calculations in which no experimental uncertainties in the zero of energy and angle scales are introduced.
[59] R. X. Ynzunza *et al.*, J. Electron Spectrosc. 106, 7 (2000).
[60] T. Nakatani, S. Imaga, S. Suga, Y. Kagoshima, and T. Miyahara, Jpn. J. Appl. Phys. 32, L1480 (1993).
[61] M. A. Van Hove, A. P. Kaduwela, H. Xiao, W. Schattke, and C. S. Fadley, J. Electron Spectrosc. 80, 137 (1996).
[62] K. A. Thompson and C. S. Fadley, Surf. Sci. 146, 281 (1984).
[63] V. Pouthier, C. Ramseyer, C. Girardet, K. Kuhnke, V. Marsico, M. Blanc, R. Schuster, and K. Kern, Phys. Rev. B 56, 4211 (1997).
[64] L. G. Gerchikov, P. V. Efimov, V. M. Mikoushkin, and A. V. Solov'yov, Phys. Rev. Lett. 81, 2707 (1998).
[65] S. Y. Tong, H. Huang, C. M. Wei, W. E. Packard, F. K. Men, G. Glander, and M. B. Webb, J. of Vacuum Sci. and Technology A 6, 615 (1987).
[66] F. J. Palomares, unpublished.
[67] J. Kolaczkiewicz and E. Bauer, Surf. Sci. 175, 487 (1986).
[68] E. D. Tober, R. X. Ynzunza, C. Westphal, and C. S. Fadley, Phys. Rev. B 53, 5444 (1996).

FIG. 1. Minimum criteria for convergence on cluster size and angular momenta in multiple scattering calculations (solid curve) and relative speeds of the present EDAC method versus the second-order Rehr-Albers (R-A) separable representation (broken curve). Criteria are expressed in terms of the number of atoms N as a function of the maximum angular-momentum quantum number $l_{\rm max}$. The value of N for which convergence is achieved (solid curve) is estimated as the number of atoms contained within a sphere of radius equal to 1.5 times the universal inelastic mean free path, λ_l, assuming an average nearest-neighbor separation of 2.5 Å. λ_l depends upon the electron momentum k, which is in turn related to $l_{\rm max}$ via $l_{\rm max} = kr_{\rm mt}$ for a typical muffin-tin radius of $r_{\rm mt} = 1.5\text{Å}$. The number of complex multiplications needed per iteration is $(10/3)N^2(l_{\rm max}+1)^3$ in EDAC and $36N^3$ in R-A, and therefore, EDAC requires a shorter computation time as compared with R-A when $N > 0.1(l_{\rm max}+1)^3$ (white area above the broken curve) if all scattering paths are accounted for.

FIG. 2. C1s photoemission intensity in a cluster formed by two carbon atoms separated by 1.4 Å as a function of iteration step. The incoming light is linearly polarized with the polarization vector parallel to the interatomic axis. The emission occurs in the forward scattering direction (see inset). The electron energy is 850 eV. Results obtained from different iteration methods are compared: the recursion method of this work (solid circles), which converges rapidly to the exact result derived via giant-matrix inversion (GMI); the direct Jacobi iteration (open circles), for which the number of iteration steps equals the scattering order; and the simultaneous relaxation (SR) method[42,48] for various values of the relaxation parameter η (thin broken curves). The intensity has been normalized to that of the isolated C atom.

FIG. 3. (a): Schematic representation of the cluster used in photoelectron diffraction calculations. Only atoms whose sum of distances to the emitter (darkest atom) and to the surface is smaller than $d_{\rm max}$ are included in the calculation (gray atoms). This criterion leads to a parabolic surface with the focus coinciding with the emitter. (b): R–factor [Eq. (34)] variation with the number of atoms N for Cu2s photoemission from the third layer of a Cu(111) surface. Azimuthal scans have been considered with a polar angle of emission of 35°, a photoelectron energy of 100 eV, and p-polarized light under normal incidence conditions, as shown schematically in the lower left corner of the figure. The inset shows the intensity as a function of azimuthal angle for various cluster sizes, as indicated by labels, normalized to that of the direct emission without inelastic attenuation.

FIG. 4. (a): R–factor variation with scattering order for azimuthal scans of W4f photoemission from a W(110) surface covered with one monolayer of (1×1) O.[58] The emitter is taken to be in the third W layer, the photoelectron is emitted with an energy of 250 eV and polar angle of 46°, and the incident light is circularly polarized and coming perpendicular to the surface (see inset). The cluster consists of $N = 65$ atoms [$d_{\rm max} = 1$ nm; see Fig. 3(a)]. Results derived from the recursion method (solid curves and circles) are compared with those obtained using direct Jacobi iteration (broken curves and open circles). Thick and thin curves show R–factor values according to the definitions of Eqs. (34) and (35), respectively (i.e., the relative value of the average deviation and the maximum deviation, respectively). (b): Same as (a) for $N = 189$ atoms [$d_{\rm max} = 1.4$ nm; see Fig. 3(a)]. (c): R–factor variation with $l_{\rm max}$ under the same conditions as in (a) for $d_{\rm max} = 1.2$ nm (solid curve and solid circles). The variation of the R factor for the atomic scattering amplitude as defined by Eq. (36) is shown by the broken curve and open circles. Also shown is the expected $l_{\rm max}$ value based on the simple criterion of $l_{\rm max} = kr_{\rm mt}$.

FIG. 5. W4f photoemission intensity as a function of the polar direction of emission for a W(110) surface covered with one monolayer of (1×1) O and illuminated with left-circularly-polarized light.[59] Represented is $[I(\theta,\varphi) - I_0(\theta)]/I_0(\theta)$, where $I_0(\theta)$ is the average of the intensity over azimuthal angles. The photoelectron energy is 250 eV. The emission takes place from the top-most (oxide) W layer. Dark regions correspond to high intensity. (a): EDAC calculation for a cluster consisting of $N = 393$ atoms ($d_{\rm max} = 18\text{Å}$). The position of the oxygen is shown schematically in the inset. The average over the two symmetry-equivalent positions of the oxygen has been performed. The direction of normal emission corresponds to the center of the figure, and the polar angle θ is proportional to the distance to that point (the range actually plotted is $46° \le \theta \le 63.5°$). (b): Experimental results taken from Ref. [59].

FIG. 6. Azimuthal dependence of the photoemission intensity from s levels of a row of Xe atoms adsorbed near a step in a Pt(111) surface. Top part: the Xe atom is on the lower terrace at the step edge. Bottom part: the Xe atom is on the upper terrace. In all cases, the Xe atoms are located in Pt continuation sites. (See the schematic representations on the right hand side.) The photoelectron kinetic energy is 60 eV. The electron take-off angle is 30°. The light is unpolarized and incident perpendicular to the terraces.

FIG. 7. (a): Scattering probability of 809-eV electrons from C_{60} molecules as a function of scattering angle. Experimental results (circles) taken from Ref. [64] are compared with single-scattering (broken curve) and multiple-scattering (solid curve) calculations. An average over molecular orientations has been performed. (b): Scattering probability of 100-eV electrons from C_{60} molecules as a function of scattering angle calculated for various iteration steps (see labels) using the recursion method (solid curves) and direct Jacobi iteration (broken curves).

FIG. 8. Calculation of the LEED pattern of the Si(111)-(7 × 7) surface for 50-eV electrons coming along the surface normal. The surface structure factor S^2 (upper-left figure) has been obtained for the symmetry of the Si(111)-(7×7) surface and for a beam diameter of 100 Å. The envelope function I (lower-left figure, in logarithmic scale), which contains all the information about the atomic positions within a given surface unit cell as well as near-neighbor scattering, stands for the angular distribution of scattered electrons assuming that the first atomic scattering event occurs within the selected unit cell. The full LEED pattern (right figure, in linear scale) is obtained as the direct product of the structure factor and the envelope function [Eq. (38)]. The axis labels represent the components of the electron momentum parallel to the surface.

FIG. 9. Comparison of observed (upper figures, from Ref. [66]) and calculated (lower figures) LEED patterns for the Si(111)-(7 × 7) surface using two different electron energies: 50 eV (left) and 75 eV (right). The electron beam is coming perpendicular to the surface and it has a diameter of 100 Å. The axis labels represent the components of the electron momentum parallel to the surface. Some white lines have been drawn to guide the eye.

FIG. 10. (a)-(d): Calculated LEED patterns for a W(110) surface covered with one monolayer of Gd. The electron energy is 102 eV. The electron beam is coming along the surface normal and its diameter is 100 Å. (a): Schematic representation of model A for the structure with W (solid circles) and Gd (open circles) shown, leading to a large Moiré structure. (b): LEED intensity for model A. (c)-(d): Same as (a)-(b) for model B as shown in (c). The average over the geometry depicted in (c) and its mirror reflection with respect to the W[001] direction has been performed in (d). (f): Experimental result, taken from Ref. [68]. The axis labels represent the components of the electron momentum parallel to the surface. Some white lines have been drawn on the LEED images to guide the eye.

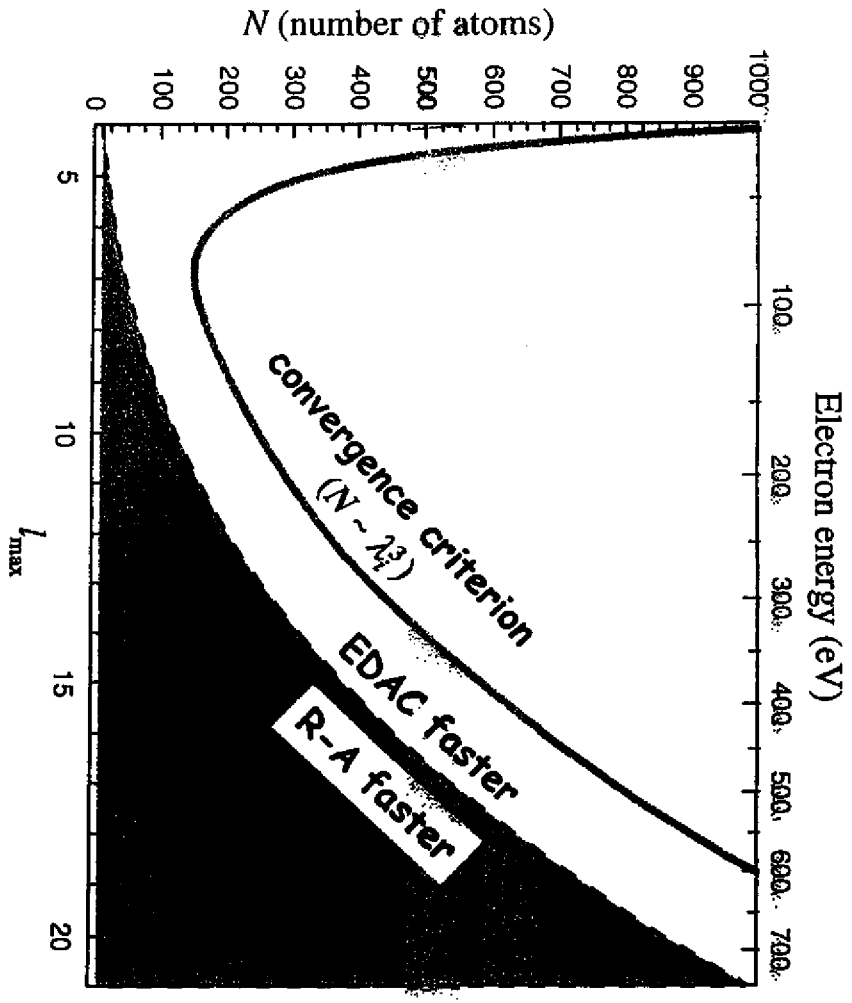

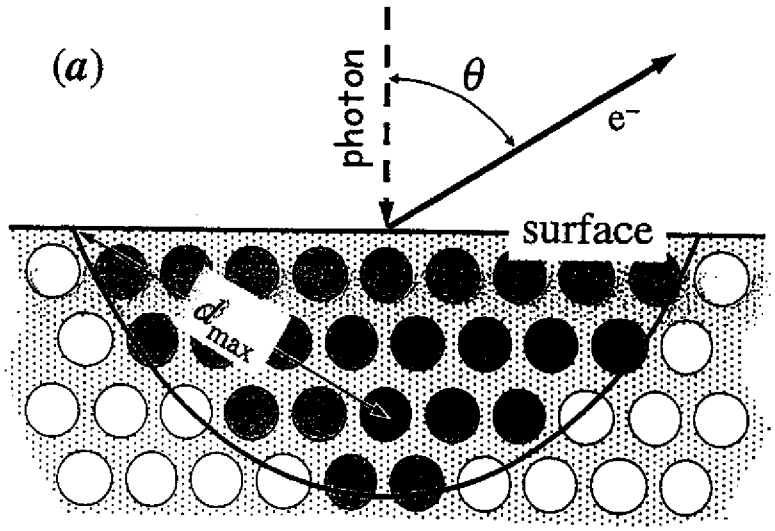
(a)
photon
θ
e⁻
surface
d max

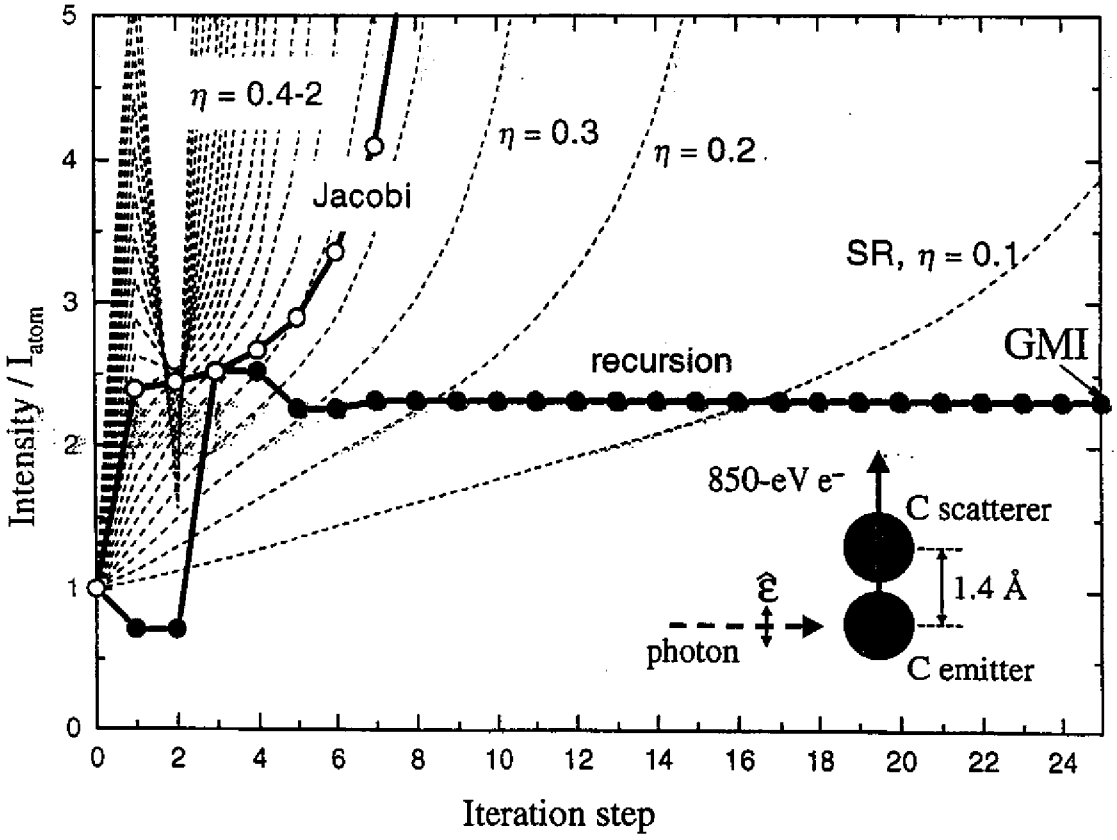
η = 0.4-2
η = 0.3
η = 0.2
Jacobi
SR, η = 0.1
recursion
GMI
850-eV e⁻
C scatterer
1.4 Å
ε̂
photon
C emitter
Intensity / I atom
Iteration step
0
1
2
3
4
5
0
2
4
6
8
10
12
14
16
18
20
22
24

4ab

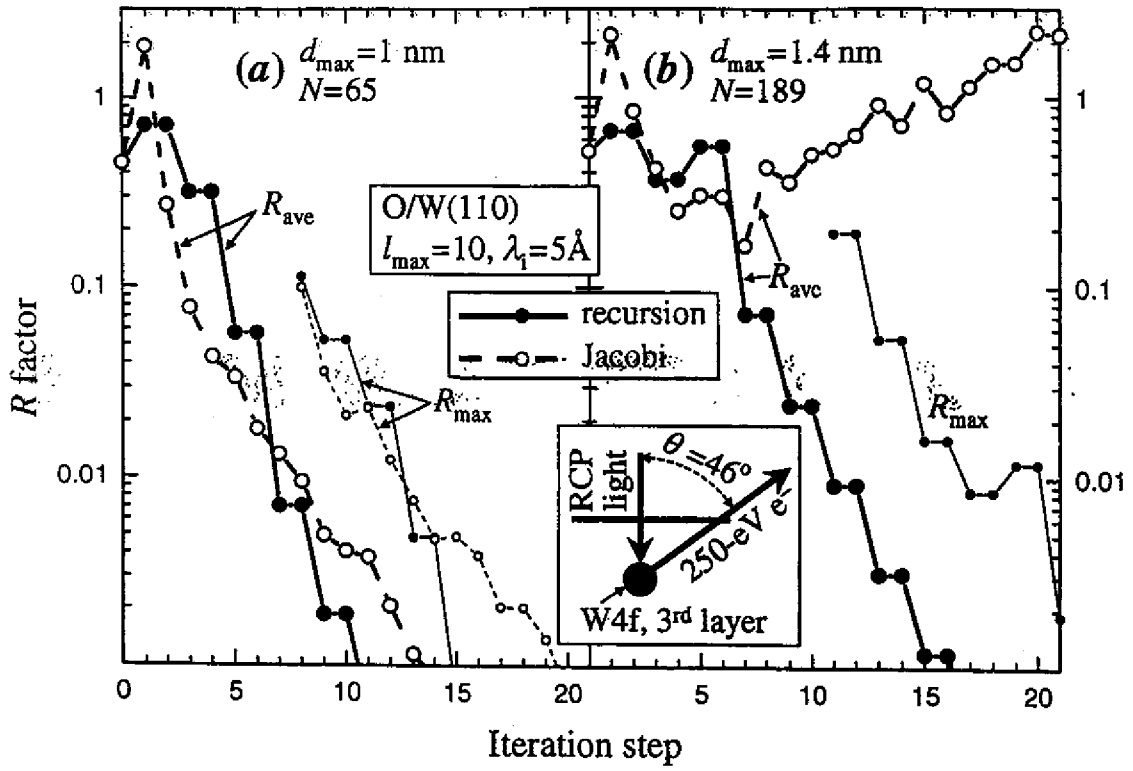
(a) d_{max}=1 nm
N=65
(b) d_{max}=1.4 nm
N=189
O/W(110)
l_{max}=10, λ_1=5Å
recursion
Jacobi
R_{ave}
R_{max}
RCP light
θ=46°
250-eV e⁻
W4f, 3rd layer
R factor
Iteration step

3b

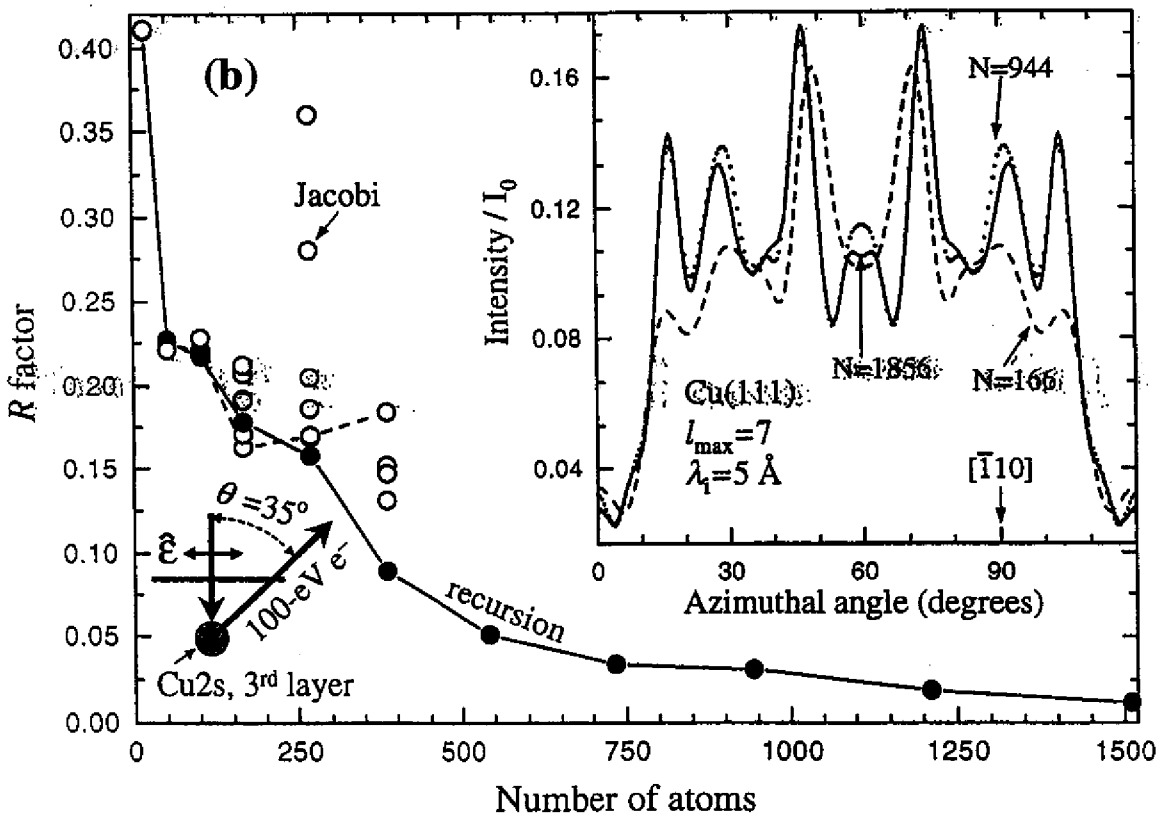
(b)
Jacobi
recursion
θ=35°
100-eV e⁻
Cu2s, 3rd layer
R factor
Number of atoms
Intensity / I_0
N=944
N=1856
N=166
Cu(111)
l_{max}=7
λ_1=5 Å
[$\bar{1}$10]
Azimuthal angle (degrees)

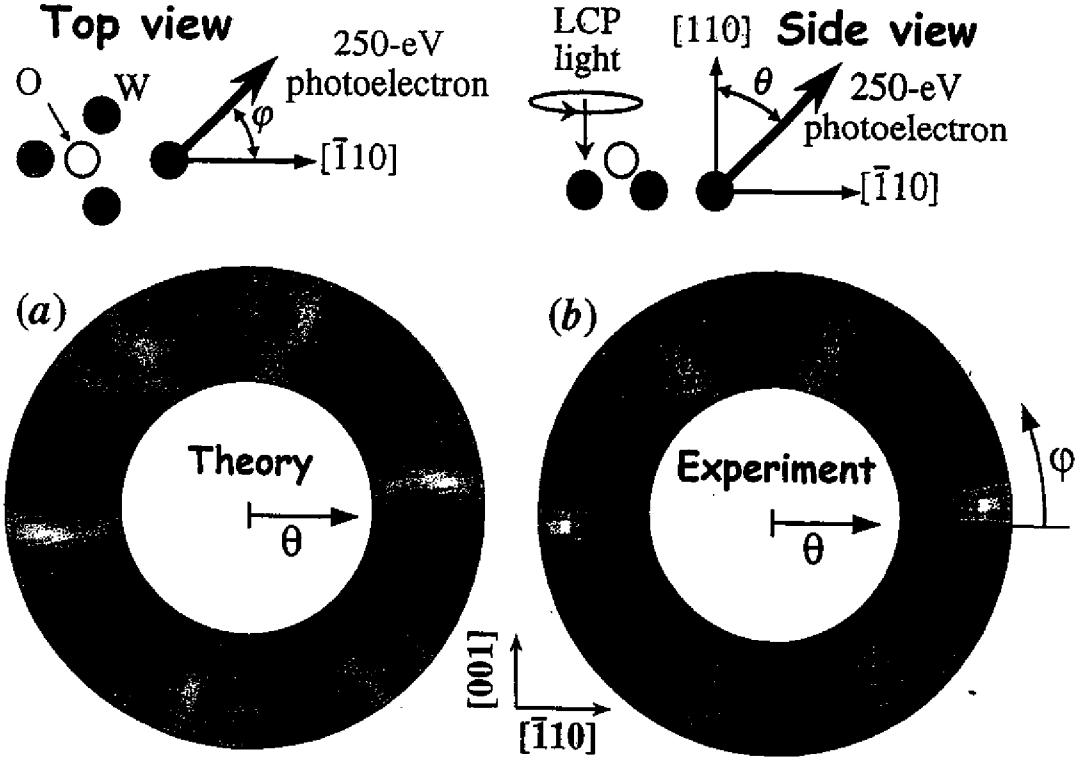
Top view
O
W
250-eV
photoelectron
φ
[1̄10]
LCP
light
[110]
Side view
θ
250-eV
photoelectron
[1̄10]
(a)
Theory
θ
(b)
Experiment
θ
φ
[001]
[1̄10]

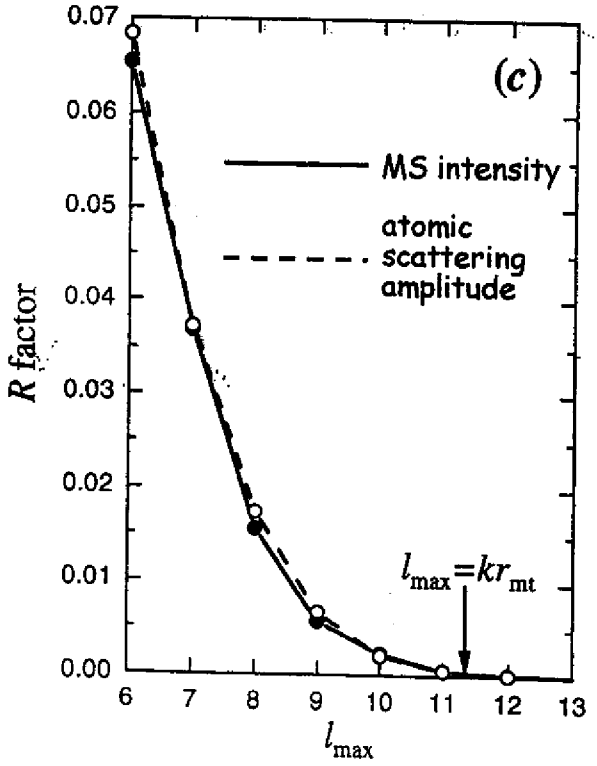
(c)
MS intensity
atomic
scattering
amplitude
R factor
$l_{max}=kr_{mt}$
l_{max}
0.07
0.06
0.05
0.04
0.03
0.02
0.01
0.00
6
7
8
9
10
11
12
13

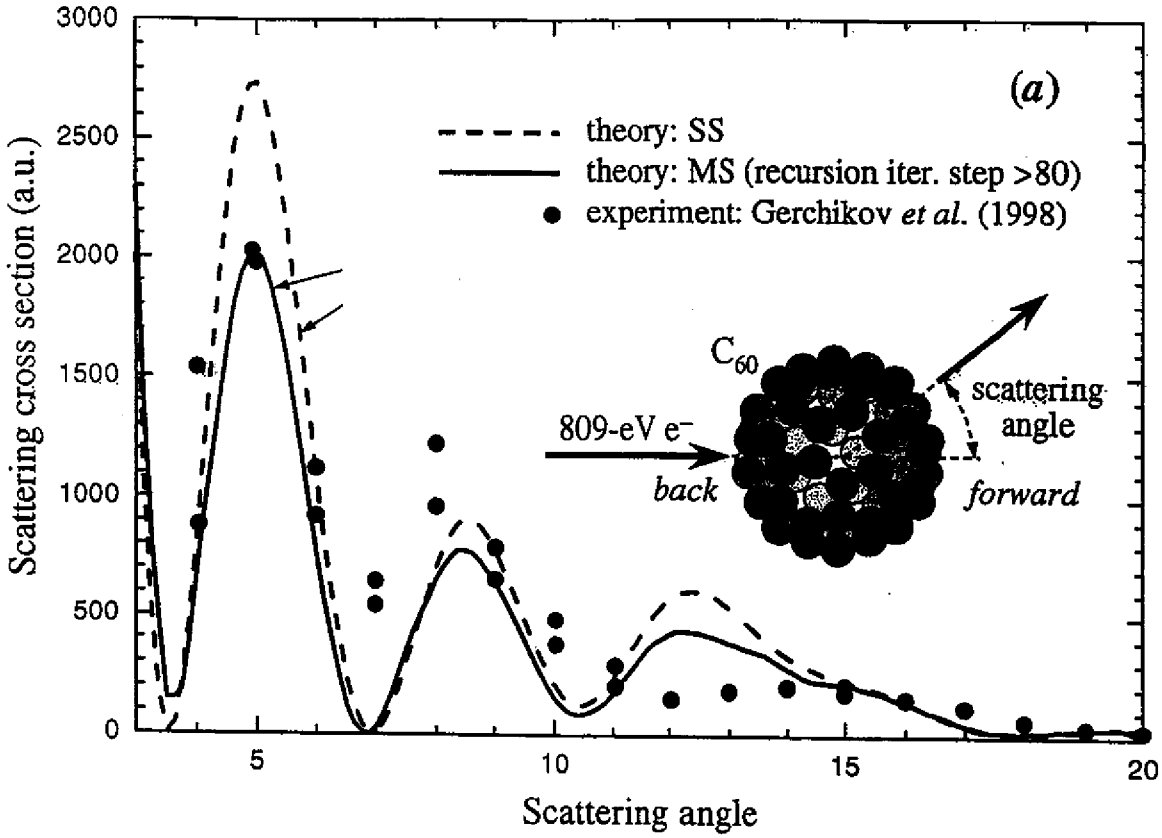
(a)
theory: SS
theory: MS (recursion iter. step >80)
experiment: Gerchikov et al. (1998)
C60
809-eV e⁻
back
forward
scattering angle
Scattering cross section (a.u.)
Scattering angle
3000
2500
2000
1500
1000
500
0
5
10
15
20

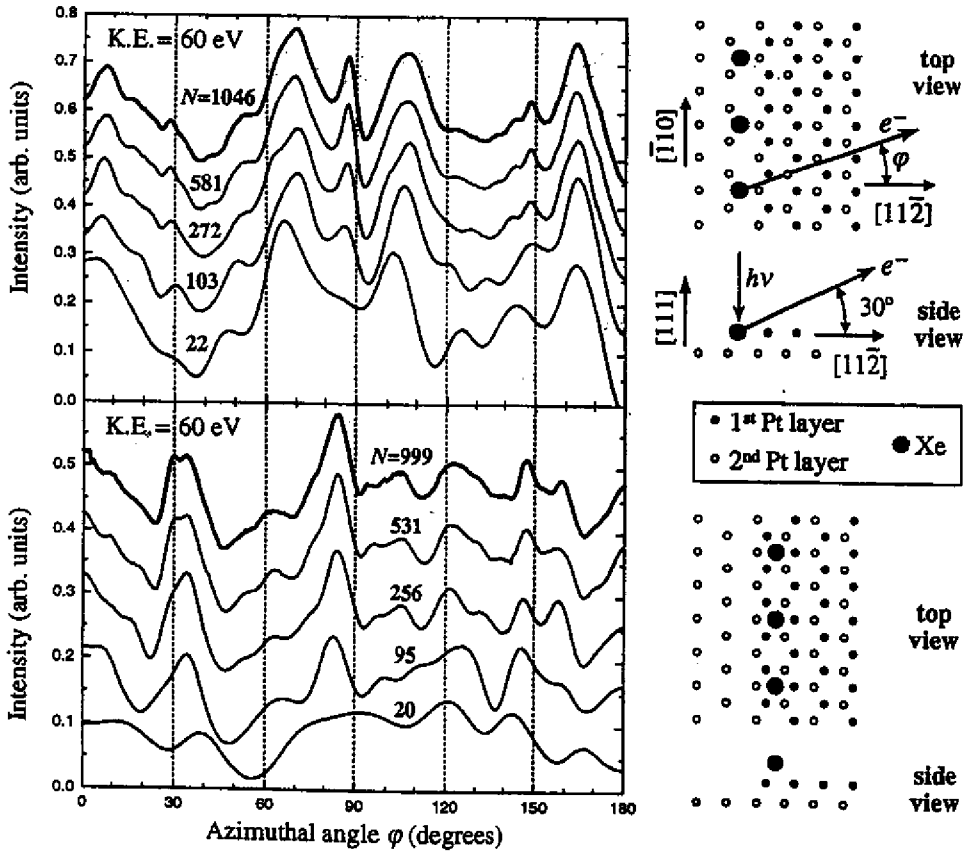
K.E.=60 eV
N=1046
581
272
103
22
K.E.=60 eV
N=999
531
256
95
20
Intensity (arb. units)
Azimuthal angle φ (degrees)
top view
side view
[1̄10]
[11̄2]
[111]
hν
e⁻
φ
30°
1st Pt layer
2nd Pt layer
Xe

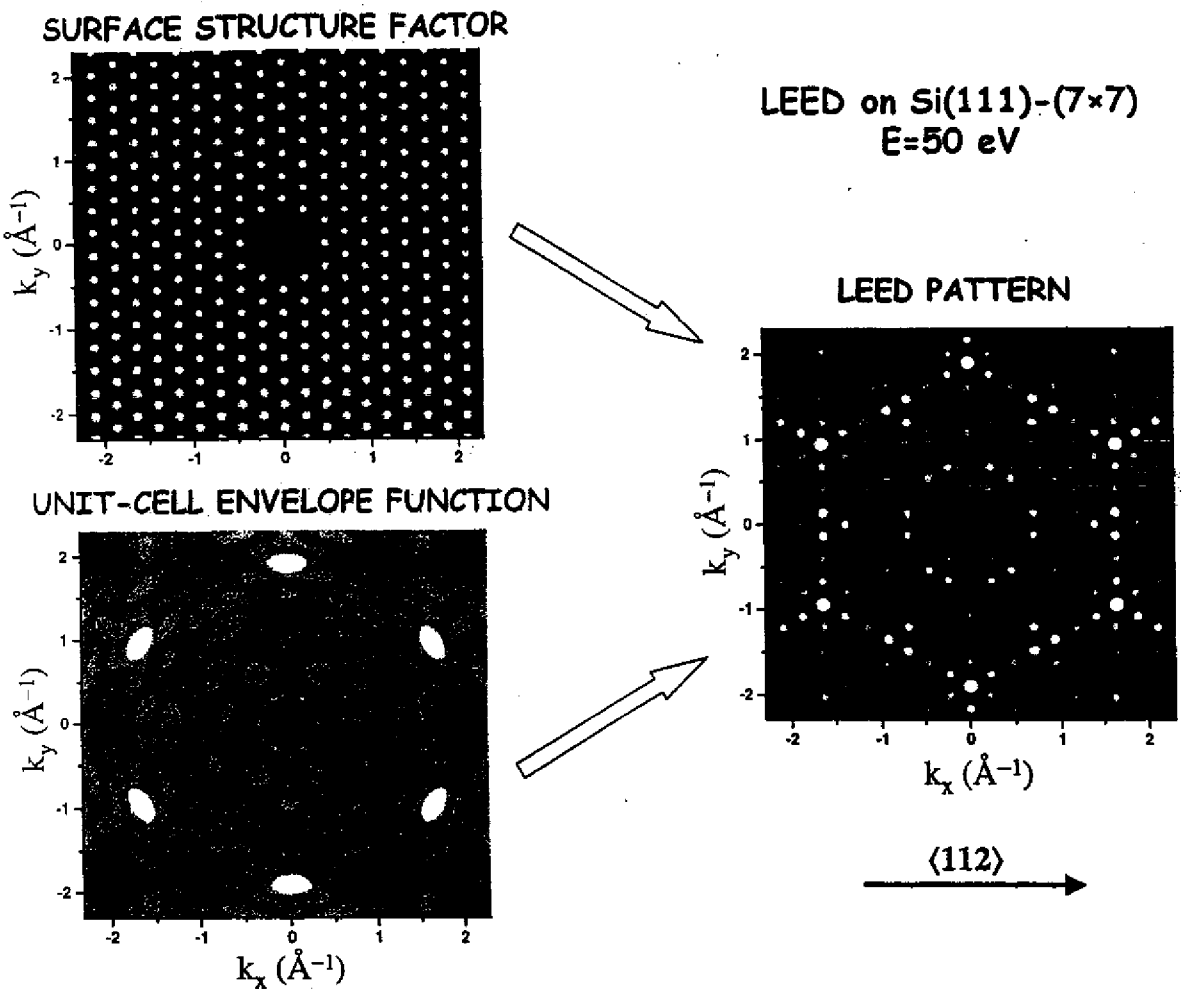
SURFACE STRUCTURE FACTOR
LEED on Si(111)-(7×7)
E=50 eV
LEED PATTERN
UNIT-CELL ENVELOPE FUNCTION
k_y (Å^{-1})
k_x (Å^{-1})
⟨112⟩

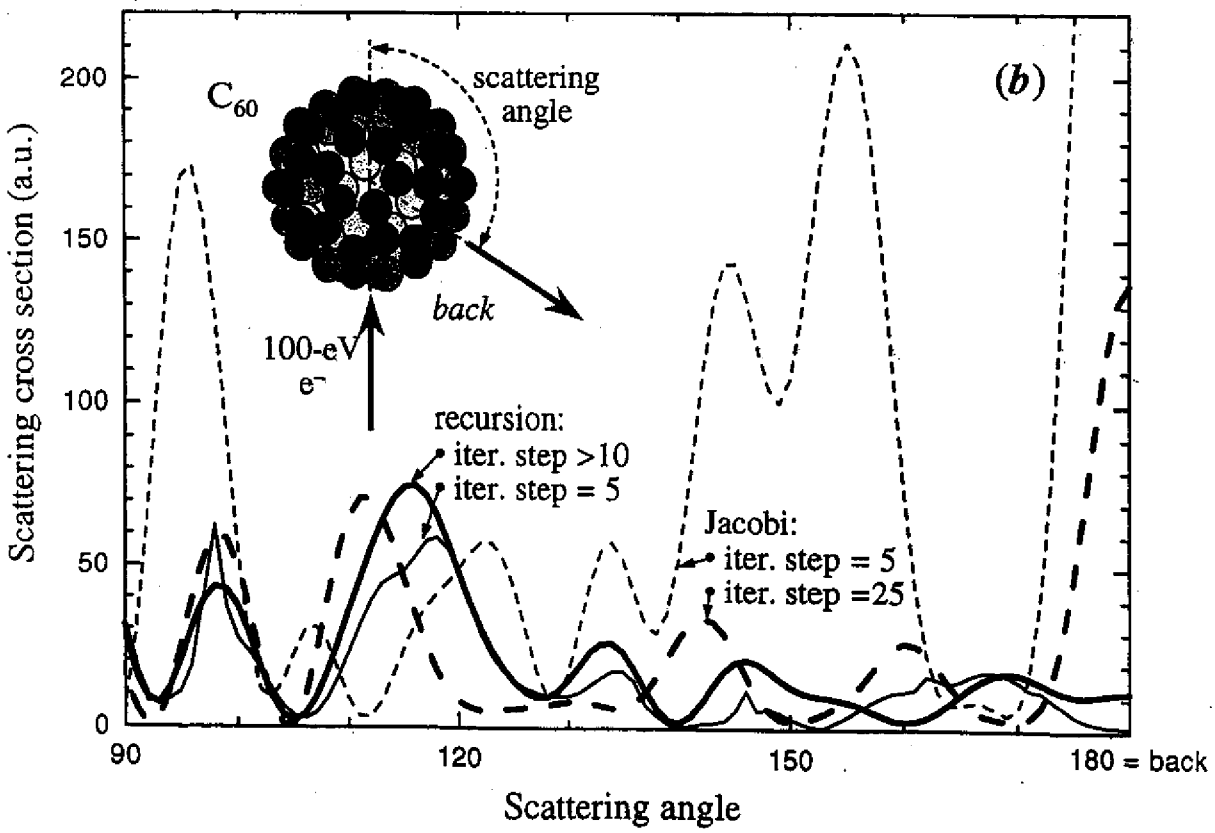
(b)
C_{60}
scattering angle
back
100-eV e⁻
recursion:
iter. step >10
iter. step = 5
Jacobi:
iter. step = 5
iter. step =25
Scattering cross section (a.u.)
Scattering angle
90
120
150
180 = back

(10)

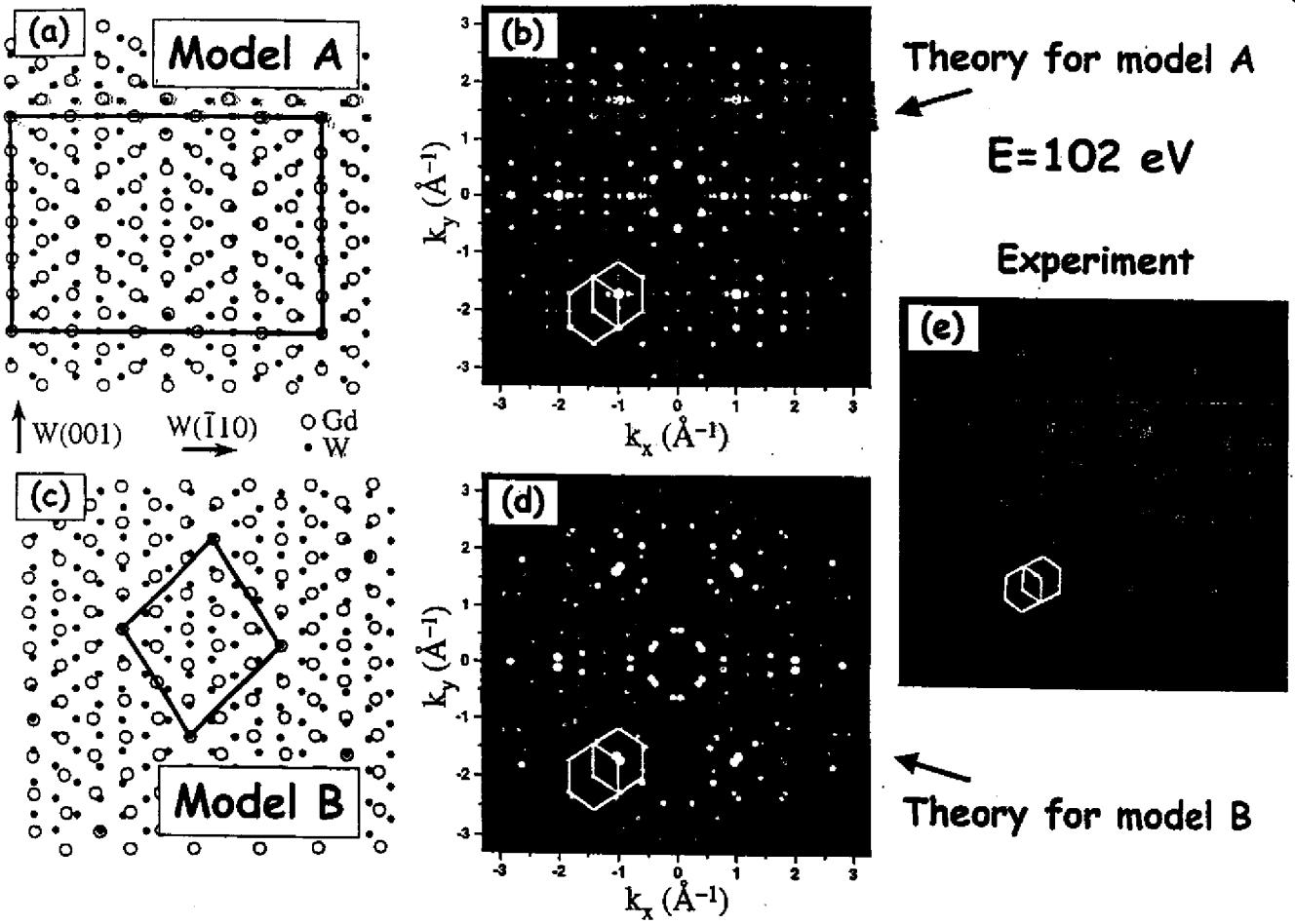
(a)
Model A
W(001)
W(1̄10)
Gd
W
(c)
Model B
(b)
(d)
k_y (Å^{-1})
k_x (Å^{-1})
Theory for model A
E=102 eV
Experiment
(e)
Theory for model B

(9)

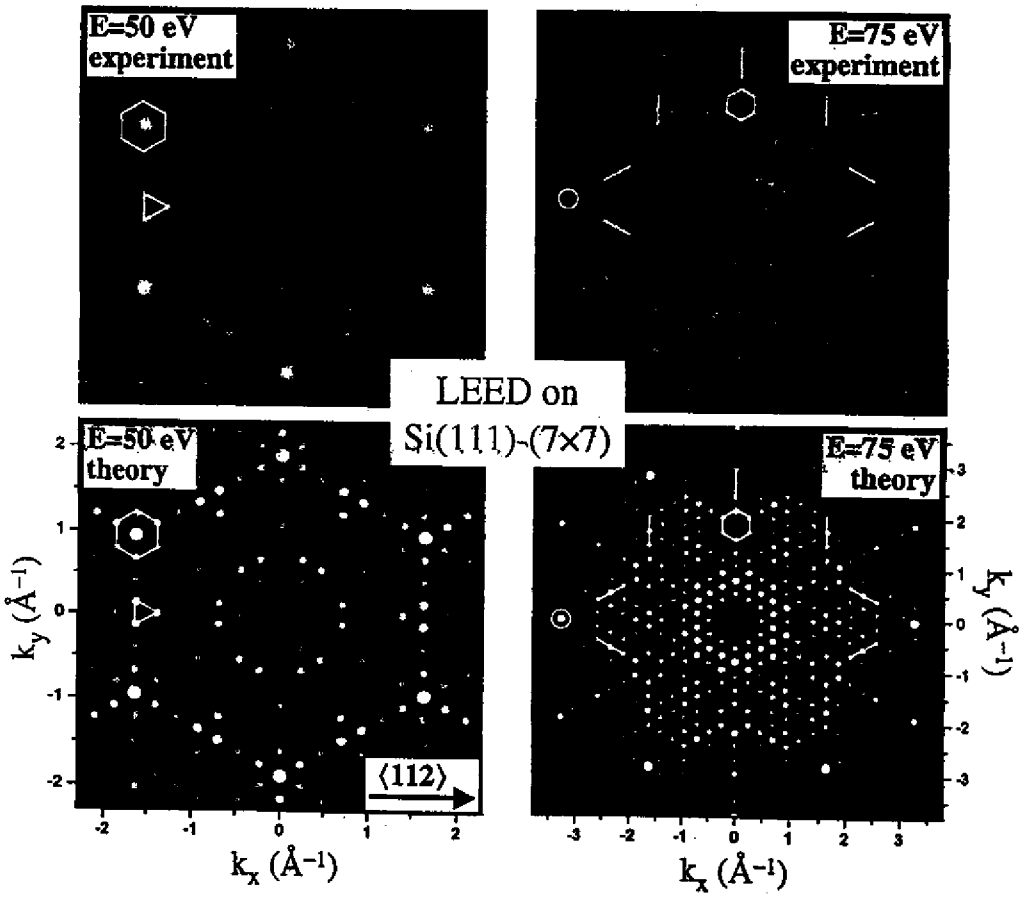
E=50 eV
experiment
E=75 eV
experiment
LEED on
Si(111)-(7×7)
E=50 eV
theory
E=75 eV
theory
⟨112⟩
k_y (Å^{-1})
k_x (Å^{-1})

Surface Review and Letters, Vol. 4, No. 2 (1997) 391–408

FERMI SURFACE MAPPING BY PHOTOEMISSION*

J. OSTERWALDER
Physik-Institut, Universität Zürich-Irchel,
Winterhurerstr. 190, CH-8057 Zürich, Switzerland

Received 13 March 1996

Angle-resolved ultraviolet photoelectron spectroscopy (ARUPS) data are usually measured spectrum by spectrum at various emission angles or photon energies in order to observe the dispersion of energy bands in solids and on their surfaces. In these lecture notes an alternative experimental procedure is described which yields a direct mapping of constant energy surfaces within the band structure, and specifically of the Fermi surface. This approach appears very promising, in particular when applied to magnetic systems and systems with narrow bands. Fermi surfaces of surface states are seen in direct relation to the underlying bulk Fermi surface.

1. Introduction

The shape and volume of the Fermi surface of a metal are intimately related to many of its physical properties.[1] It is therefore not surprising that some of the first precise measurements of the electronic structure of metals were carried out at their Fermi surfaces using the de-Haas–van-Alphen (dHvA) and related effects where the oscillatory behavior of some physical property, such as the magnetic susceptibility, is recorded as a function of the applied magnetic field. Extremal orbits on the Fermi surface within the plane perpendicular to the magnetic field direction are determined very accurately, and by combining the information on such orbits for many field orientations the whole Fermi surface can be reconstructed. Other Fermi surface probes have been developed since, using for example Compton scattering[2] or positron annihilation.[3] While these other techniques put much less stringent requirements on sample quality and temperature, they offer relatively limited resolution in k space. All these methods are volume-sensitive probes and provide no surface-related information.

In the meantime, angle-resolved ultraviolet photoelectron spectroscopy (ARUPS) has been developed into a powerful tool for studying occupied electronic bands also further away from the Fermi energy, providing both volume- and surface-sensitive information.[4] Early on, Fermi surface data from dHvA experiments were used for calibrating the absolute k locations of certain bands crossing the Fermi level. This calibration was found necessary as the photoelectron carries direct information on $k_\parallel$, the k component parallel to the surface, while its normal component $k_\perp$ is affected by the surface potential energy step, by details of the final state dispersion relation $E(k)$, and by the smearing associated with the short photoelectron escape depth.[4] On the other hand, it was soon realized that this technique provided access to the complete band structure, including the Fermi surface, of two-dimensional (2D) systems, including surface states, where $k_\parallel$ is the relevant quantum number. These latter experiments locate Fermi level crossings of energy bands in measured angle-resolved energy spectra in order to trace Fermi surface contours.[5]

*These lecture notes are based on experimental results obtained at the Université de Fribourg in collaboration with P. Aebi, R. Fasel and L. Schlapbach of the Institut de Physique, Université de Fribourg, and with T. J. Kreutz and P. Schwaller of the Physik-Institut, Universität Zürich.

Alternatively, a few groups have recently begun to map Fermi surfaces by measuring intensities of photoelectrons emitted from the Fermi edge as a function of emission angles relative to the crystal axes[6–12] and thus as a function of $k_\parallel$. In principle, the two experimental procedures for locating Fermi surface contours are equivalent: at those $k_\parallel$ positions where a band crosses the Fermi level, the photoemission intensity at the Fermi level rises sharply, contributing to the measured contour in the intensity map.

In this lecture this latter experimental technique will be introduced. The important test case of copper will be discussed, providing a simple and intuitive connection between the measured 2D contours and the well-known Fermi surface of 3D copper. Recent measurements on ferromagnetic nickel will be given and compared with Fermi surface data from dHvA experiments. Applications to 2D systems include high temperature superconductors, where the relevant conduction electrons are quasi-2D, and sp-derived surface states on Cu and Al surfaces.

2. Angle-Resolved Photoemission

The theory of angle-resolved photoemission has been excellently reviewed by Hüfner.[4] We limit our discussion here to a few simple concepts that are necessary in order to intuitively understand the Fermi surface mapping experiments. For conceptual simplicity we shall remain within the so-called three-step model, which describes the photoemission process as a sequence of (i) the photoexcitation of a band electron into an empty band, (ii) the propagation of this excited electron to the surface, and (iii) the transmission of this electron through the surface into the vacuum. We make the approximation of a free electron final state to describe the photoexcited electron within the solid, which often is a good starting point for the interpretation of ARUPS data.

In the photoexcitation process (i), energy and crystal momentum are conserved. For a given photon energy $h\nu$ and for an initial state with wave vector k_i and energy $E_i(k_i)$, we thus have

$$E_f(k_f) = E_i(k_i) + h\nu\,, \qquad (1)$$

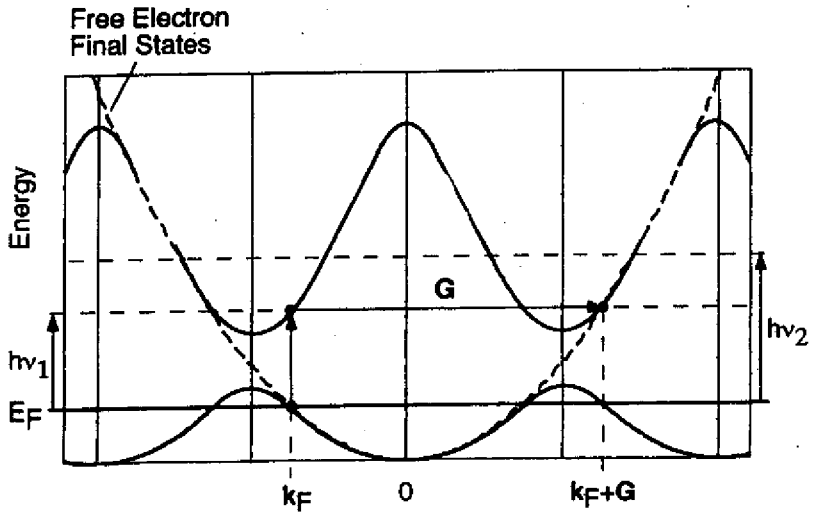

Fig. 1. Illustration of a direct transition (DT) from the Fermi surface of a solid. The band structure $E(k)$ (solid curves) is given in the repeated zone scheme while the free electron final state parabola (dashed curve) is drawn in the extended zone scheme. Along this particular direction of k there is a DT for the photon energy $h\nu_1$ and not for $h\nu_2$.

$$\mathbf{k}_f = \mathbf{k}_i + \mathbf{k}_{h\nu} + \mathbf{G}. \qquad (2)$$

For photon energies of the order of 20 eV the associated photon wave vector $\mathbf{k}_{h\nu}$ is not more than a percent of typical Brillouin zone dimensions and can thus be neglected in Eq. (2). The 3D reciprocal lattice vector G is needed in order to provide the momentum for the electron to escape from the crystal. These conservation laws imply that the dominant emission features appear as vertical or direct transitions (DT's) within the band structure of a solid, as is depicted in Fig. 1. If we now consider transitions from the Fermi surface only, we must find locations $\mathbf{k}_F$, where a band crosses the Fermi energy E_F, and which is separated vertically from some empty band by the photon energy used in the experiment. Figure 1 illustrates how such locations can be conveniently found by viewing the initial state band, and thus the Fermi surface, in the repeated zone scheme and the free electron final state parabola in the extended zone scheme. The figure also makes clear that these conservation laws put rather stringent conditions on k and that they can be fulfilled only along a few directions for a given photon energy. In order to provide an overview of where such transitions are to be expected in reciprocal space, Fig. 2 shows a planar section through k space parallel to the (1̄10) plane of the face-centered cubic lattice of copper and containing the origin Γ. Brillouin zones are indicated and the Fermi surface is given in the repeated zone scheme. The large circles give the possible free electron wave vectors for the final states associated with two different photon energies, specifically He I (21.2 eV) and He II (40.8 eV) radiation. According to Fig. 1 direct transitions occur at intersections of these spheres with the Fermi surface. Since the free electron final state sphere and the Fermi surface represent intersecting hypersurfaces in 3D reciprocal space, we expect these locations to be sets of continuous lines. Figure 3 illustrates such a set of lines as one should observe for Fermi surface emission from a Cu(001) surface using He I radiation. Within the (1̄10) plane shown in Fig. 2, there is no intersection as the final state falls into the well-known necks associated with the zone boundaries near equivalent L points. However, for emission planes other than that a Fermi level crossing should be observed, thus giving a rounded-square-like Fermi contour, and so providing a direct mapping of the Fermi surface.

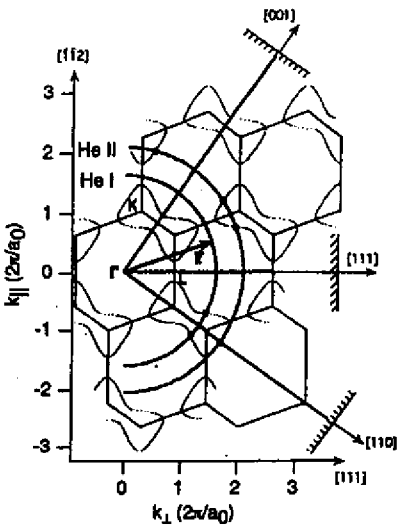

Fig. 2. High symmetry plane perpendicular to the {1̄10} direction in the reciprocal lattice of copper. The solid polygons correspond to a section through the bulk Brillouin zones. Fermi surface sections are given by dotted curves. Large circles indicate free electron final states for He I and He II radiation (21.2 eV and 40.8 eV, respectively). The orientation of three low index surfaces is indicated.

We neglect the scattering processes that the excited electrons undergo while propagating to the surface in step (ii). They affect essentially the transition intensities and widths and not their positions. On the other hand we have to consider the refraction effects due to the surface potential energy step (iii). For a given photon energy $h\nu$, the measured kinetic energy E^m_{kin} of the electrons emitted from the Fermi level is given by

$$E^m_{kin} = h\nu - \Phi, \qquad (3)$$

where Φ is the work function of the sample. Inside the solid the kinetic energy of the same electrons is higher by an amount given by the inner potential V_0, i.e. the average attractive potential due to the Coulomb interaction with the ion cores and the other

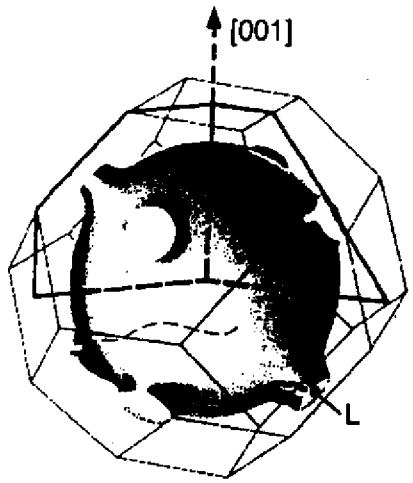

Fig. 3. 3D representation of the Fermi surface of copper, displaying the necks at equivalent L points. The solid and dashed curves near the bottom indicate the section measured at a photon energy of 21.2 eV.

valence electrons. We thus have

$$E_f(\mathbf{k}_f) = E^m_{kin} + V_0. \qquad (4)$$

Assuming free electron dispersion relations in both cases, i.e.

$$E_f(\mathbf{k}_f) = \frac{\hbar^2 \mathbf{k}_f{}^2}{2m}, \quad E^m_{kin} = \frac{\hbar^2 \mathbf{k}_m{}^2}{2m}, \qquad (5)$$

and considering the conservation of parallel momentum, one arrives at the equivalent of Snell's law of refraction (Fig. 4):

$$\sin\theta = \sin\theta_m \sqrt{\frac{h\nu - \Phi}{h\nu - \Phi + V_0}}. \qquad (6)$$

Here, θ_m is the polar angle relative to the surface normal under which the photoelectrons are detected while θ is the internal polar angle of the same electrons prior to leaving the surface. Values for V_0 and Φ can be found in the literature for many crystal surfaces. By taking E^m_{kin} according to Eq. (3) and by defining theelectron detection direction by the polar

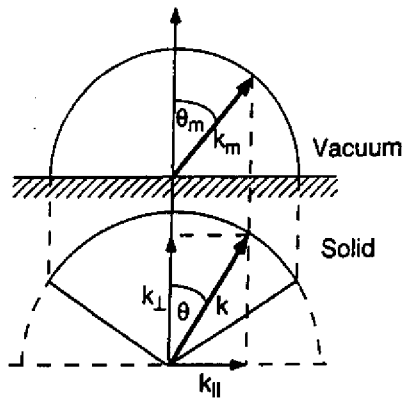

Fig. 4. Refraction at the surface potential step: photoelectrons have longer wave vectors inside the solid (larger circle) than outside. For periodic surfaces $\mathbf{k}_\parallel$ is strictly conserved.

angle θ_m (Fig. 4) and the azimuthal angle ϕ_m, one can thus determine, within this simplified model, absolute k positions inside the solid:

$$\mathbf{k} = \frac{1}{\hbar}\sqrt{2m(h\nu - \Phi + V_0)} \times(\sin\theta\cos\phi_m, \sin\theta\sin\phi_m, \cos\theta), \qquad (7)$$

where ϕ_m is usually measured relative to some high symmetry direction of the crystal.

These concepts can be readily transposed to the case of a 2D system. In this case the initial states are defined by $\mathbf{k}_\parallel$ while we consider the same 3D free electron final states. Since $\mathbf{k}_\parallel$ is conserved rigorously and since the final state can pick up any amount of $\mathbf{k}_\perp$ needed from the underlying crystal — there is no quantization of $\mathbf{k}_\perp$ for a 2D system — the same intuitive picture arises if the Fermi surface is viewed as a prismatic hypersurface in 3D k space with the 2D Fermi surface as its base in the $\mathbf{k}_\parallel$ plane (Fig. 5). Obviously, one can here map the entire Fermi surface out to the refraction-corrected free electron sphere using a single photon energy, while one obtains only slices in the 3D case. However, using tunable synchrotron radiation for excitation, such slices can be measured for various sphere radii and the full Fermi

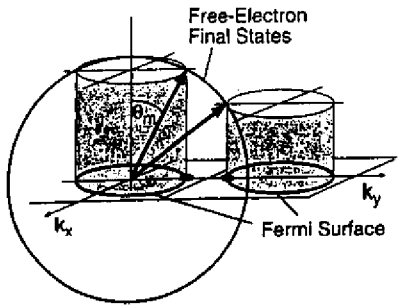

Fig. 5. Condition for the occurrence of a direct transition in k space for a 2D system: the Fermi surface is represented by a prismatic hypersurface in 3D k space. Free electron final states are indicated by the solid circle.

surface can in principle be constructed also for a 3D crystal.

3. Experimental Considerations

As outlined in the preceding section, mapping a Fermi surface consists in finding all those k vectors where direct transitions from the Fermi surface produce photoelectron intensities. In fact elastic and quasielastic electron–electron, electron–phonon and electron–defect scattering leads to non-k-conserving, so-called nondirect transitions[13] that produce intensities also away from the direct transitions, though usually much weaker. For a fixed photon energy the detected electron emission direction is swept over a large part of the hemisphere above the surface while the emission intensity at the Fermi level is monitored. Two different experimental approaches have been followed for this procedure. In the first Fermi surface mapping experiment presented by Santoni *et al.*,[9] a display type analyzer[14] was used for parallel detection of a large piece of solid angle. While this device permits a very efficient data collection with acquisition times of the order of a few minutes, it has certain limitations due to angular distortions, low signal-to-background ratios, detector inhomogeneities, and limited energy resolution by today's standards. The first three points make a set of careful calibration measurements necessary each time, which reduces somewhat the efficiency of this approach.

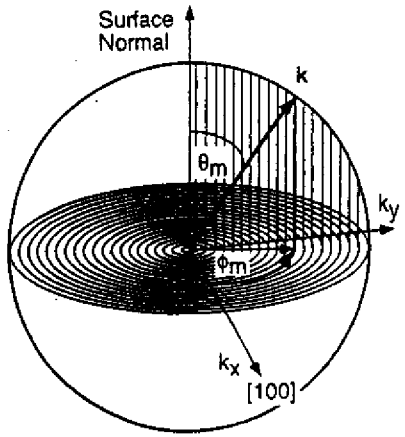

Fig. 6. Sequential angle-scanning mode for a mapping of $k_\parallel$ with a uniform sampling density by crystal rotation. Scanning starts at grazing emission angles and proceeds in an azimuthal fashion up to the surface normal, covering several thousand angular settings.

More accurate measurements have been carried out using a sequential data acquisition of one angle at a time. In this case a highly optimized angle- and energy-resolving electron detector can be used. The setup used in the University of Fribourg laboratory, from which all the data presented in these notes are taken, has a geometry in which this analyzer sits fixed in space while the sample is rotated so as to cover all emission directions relative to the crystal axes. The angle scanning is done by computer-controlled stepping motors that drive both a polar tilt axis and an azimuthal rotation of the sample about its normal. A sequence of azimuthal circles at decreasing polar angles (Fig. 6) has proven very successful, as each closing circle provides a consistency test for experimental stability and reproducibility.[15] A uniform sampling density in $k_\parallel$ is achieved by varying the polar step size with $1/\cos\theta_m$ and by increasing azimuthal steps with decreasing polar angle. Typically more than 4000 angles are sampled and mapped onto $k_\parallel$, with intensity values represented in a linear gray scale, with acquisition times being in the range of one to several hours. Even though

surface cleanliness is a concern with such measuring times, ultrahigh vacuum conditions in the low 10^{-11} mbar range have made it possible to study reactive systems such as Na layers on Al surfaces.[16] In this procedure the detection efficiency as well as the angular and energy resolution are completely uniform for the entire solid angle which is measured. Resolutions of $< 1°$ in angle and about 30 meV in energy are routinely achieved. The He discharge lamp can be maintained at stable conditions to within 5% for extended measuring times. Due to the low background intensities and the constant detection efficiency, even weak features on the Fermi surface can be observed.

One additional mode of operation could be to keep the sample fixed in space and to sweep a small angle-resolving analyzer across the emission hemisphere. In fact, this measuring mode for intensity mapping has been successfully applied to Auger electron diffraction,[17] and more recently also to Fermi surface mapping.[12] There is one principal difference between the fixed crystal (which is present also for the display type analyzer) and rotating crystal approaches: in the first case the light inincidence is at a fixed angle relative to the crystal lattice, while in the second case it is at a fixed angle relative to the electron emission direction. In the latter case we expect the excitation matrix element to be constant for equivalent initial and final states, and the produced Fermi surface maps should thus present the full symmetry of the surface under study. As a matter of fact, if the light incidence is outside the plane swept by the surface normal (Fig. 7), mirror symmetries will be broken due to light polarization effects, as we shall see below. In the first case, with the light polarization residing fixed inside the crystal, very strong asymmetries are seen in the resulting images.[11] These asymmetries can provide information on the orbital character of the states on the Fermi surface, but they can also obscure its shape in unfavorable cases. Quite generally it can be said that any feature containing well-defined contours, regardless of their intensities, provides information on the location and shape of the Fermi surface. Caution is indicated if the used excitation radiation is not "clean," i.e. if weak satellites produce additional weak contours that are associated with a different photon energy.

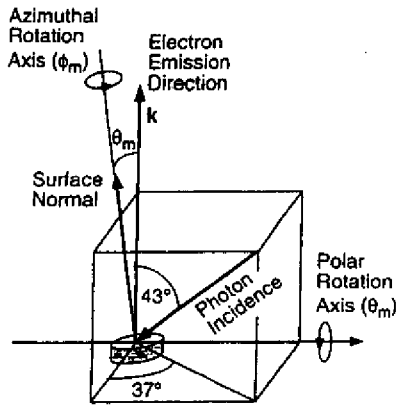

Fig. 7. Geometry of the experimental setup used for all data presented in this paper. Note that the photon incidence direction is outside the plane swept by the surface normal.

4. Three-Dimensional Systems

4.1. *Copper as a test case*

The Fermi surface of Cu is maybe the best studied of all solids and its dimensions and shape are well known from dHvA experiments[1,18] (see Fig. 3). Also, from the point of view of the photoemission experiment, Cu has the advantage of producing clean and nonreconstructed low index surfaces after standard preparation techniques, which remain stable for extended periods of time under ultrahigh vacuum conditions.

In Figs. 8(a)–8(c) we present Fermi surface maps from three differently oriented Cu surfaces, all taken at a photon energy of 21.2 eV.[8] As expected, we observe sets of well-defined, continuous lines for all three cases. Figure 9 illustrates, for one azimuthal trace of the measurement of Fig. 8(b) ($\theta_m = 66°$), how these lines of high emission intensities are actually formed by direct transitions moving through the Fermi level: the fast-dispersing sp band is occupied along the $[\bar{1}\bar{1}2]$ azimuth of the Cu(111) surface. Rotation away from this azimuth finds the

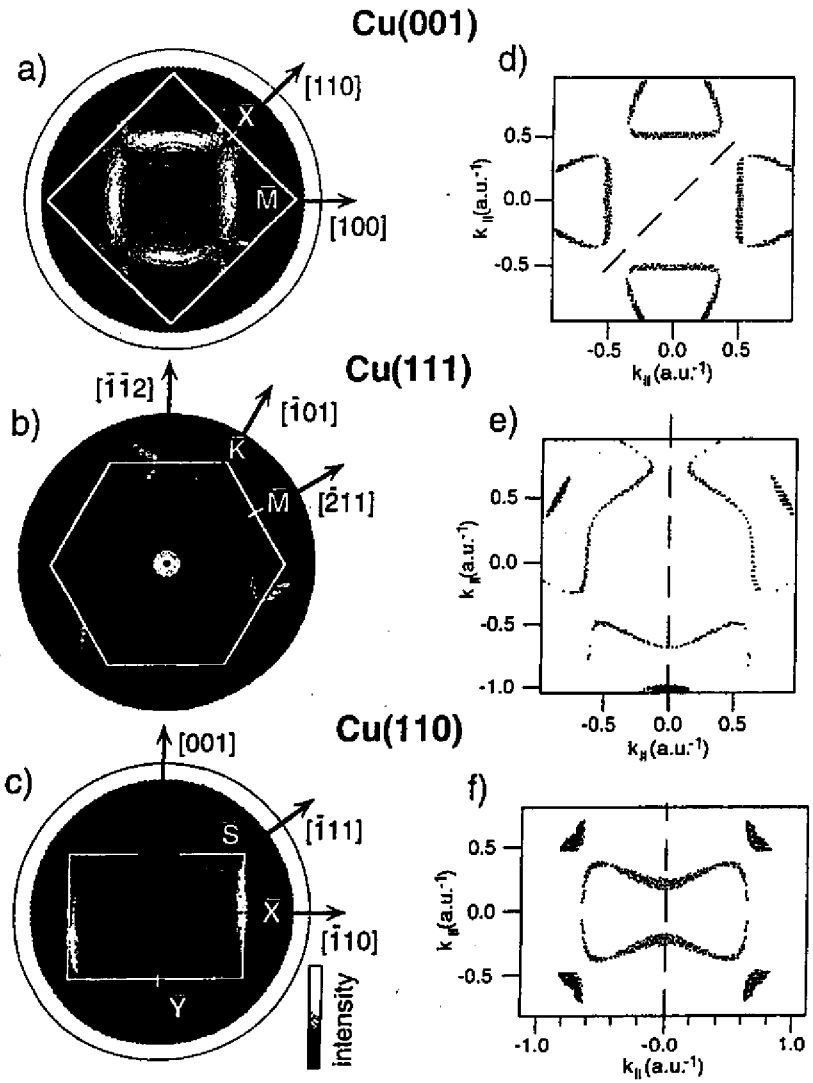

Fig. 8. Fermi surface maps from (a) Cu(001), (b) Cu(111) and (c) Cu(110). The different surface Brillouin zones (white lines) and high symmetry points and directions are indicated. Normal emission is at the center of each figure. (d)–(f) Calculated sections through the bulk Fermi surface using a free electron final state (see text). The dashed lines represent the plane shown in Fig. 2.

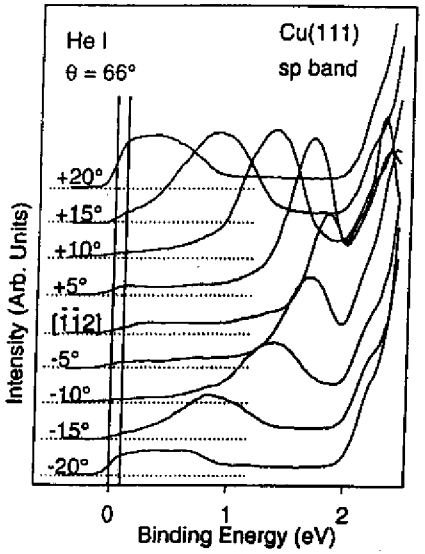

Fig. 9. He I excited energy spectra from Cu(111) at a polar angle of 66°. Azimuthal angles around the [$\bar{1}\bar{1}$2] direction are indicated. Vertical lines limit the energy window applied to the angle scans of Fig. 8.

transition moving towards E_F, where it crosses at some azimuthal angle. If the DT peak in the energy spectrum were infinitely sharp, this crossing would produce an equally sharp intensity rise at the crossing angles. As can be seen in Fig. 9, the energy peaks are by no means sharp delta functions but they are broadened, in this case by limited angle and energy resolution, or intrinsically by electron–phonon, electron–defect and electron–electron scattering.[19,20] Consequently, the Fermi level crossings will have some width as a function of the emission angle and thus in k space. It is clear that experimental energy and angular resolution are intimately interconnected by the band structure $E(\mathbf{k})$.

Now that we have seen the formation of Fermi contours, we have to establish the precision and reliability with which the real Fermi surface is represented by these contours when using free electron final states for data interpretation. For to this purpose we give in Figs. 8(d)–8(f) the results of a theoretical calculation for these contours. A Fermi surface of Cu was calculated using the layer Korringa–Kohn–Rostocker (LKKR) formalism, which is in good agreement with dHvA data. This Fermi surface was then intersected with the free electron final state sphere [the dashed lines indicate the ($\bar{1}$10) plane of Fig. 2], which had previously been corrected for refraction effects (Fig. 4) in order to give a one-to-one comparison with the measured contours. In doing so, a value of 13.5 eV was taken for V_0 [21] and 4.7 eV for Φ. The agreement found in Fig. 8 for the main contours puts in evidence that this is a viable technique to obtain reliable Fermi surface information and that the free electron final state approximation is a very good starting point for accurate 3D k space mapping. It further appears that $k_\perp$ is relatively well defined, otherwise the contours should be much more smeared out.

As mentioned earlier, photon polarization effects manifest themselves, for the given experimental configuration of Fig. 7, as asymmetries in contour intensities for k points that are otherwise related to each other by mirror symmetry operations. This phenomenon can be seen, for example in the data from the (111) surface [Fig. 8(b)], where the measurement touches the L-point necks at three places. Each time the intensity on the clockwise side of the neck is significantly weaker than it is on the counterclockwise side. Although the experiment has been carried out with unpolarized radiation, the oblique orientation of the photon incidence direction nevertheless means a tilt of the polarization plane with respect to the scattering plane, defined by the photoelectron emission direction and the surface normal. Clockwise rotation then moves the states near the neck further away from the polarization plane while the opposite sense moves them closer. Similar mirror-symmetry-breaking effects have been observed in core level photoelectron diffraction and Auger electron diffraction experiments.[22]

Besides the main contours seen both in experiment and in theory, the measured images show additional structure. Most prominently, there is a very bright small ring at the center of the surface Brillouin zone of the Cu(111) surface [Fig. 8(b)], which is absent in the calculations [Fig. 8(e)].

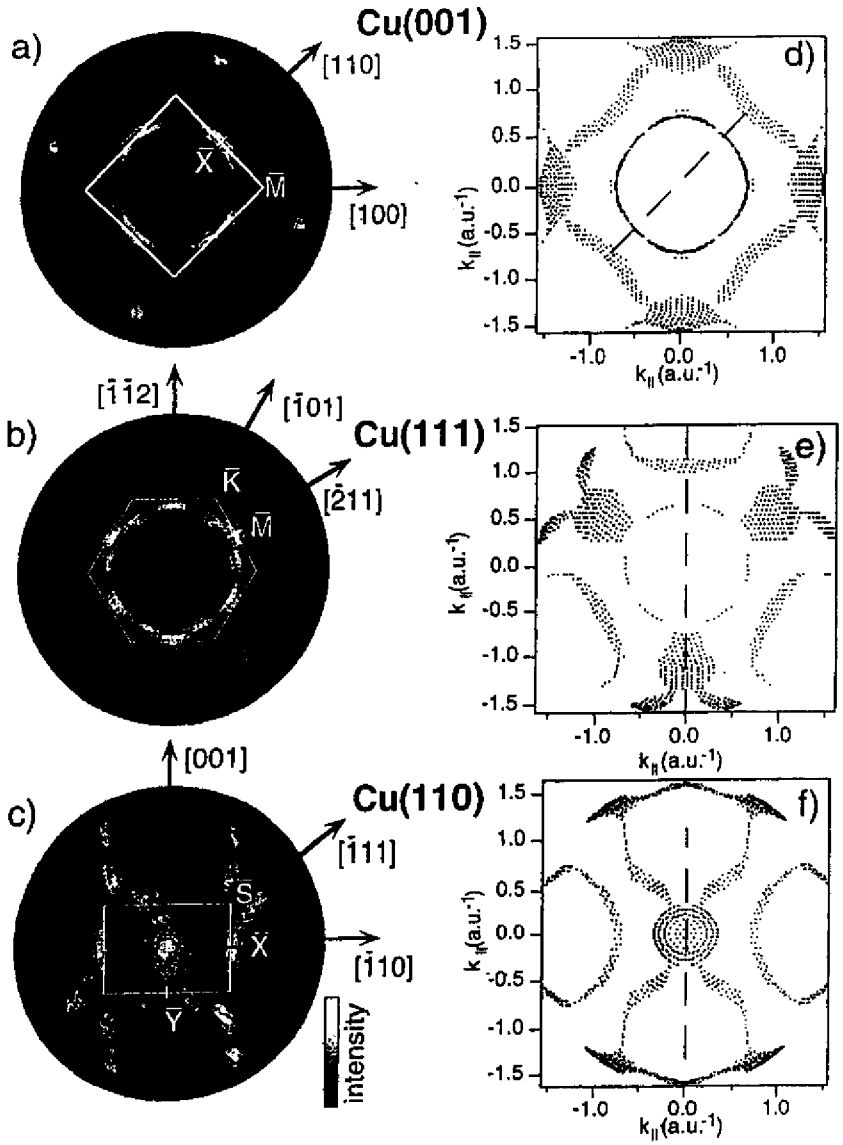

Fig. 10. Same as Fig. 8 but for excitation with He II radiation (40.8 eV).

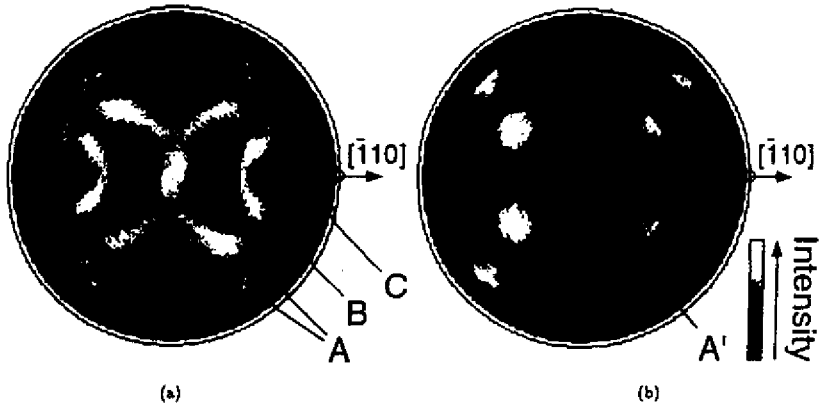

Fig. 11. (a) Room temperature Fermi surface map from Ni(110), excited with He I radiation and using an energy window of 30 meV centered at the Fermi energy. (b) Same as (a), but for a temperature of 700 K, which is above the critical temperature (631 K) of ferromagnetic nickel. Several features are marked by capital letters in order to facilitate their discussion.

This feature can be identified with the well-known Shockley type surface state.[23] It does not appear in the calculation which has been carried out considering bulk Bloch states only. Similar but much weaker surface state features are found near the $\bar{Y}$ point on the Cu(110) surface (see below). Additional structure can be found in the background region between the main contours. Some of this must be due to satellite contributions to the unmonochromatized He I radiation, others due to nondirect transitions. In fact a small step at E_F can be seen for all angles in Fig. 9, also away from the Fermi level crossings of the sp band.

In Figs. 10(a)–10(c) we give a similar presentation of measured FS contours from the same Cu surfaces, measured at a higher photon energy of 40.8 eV (He II). The corresponding final state sphere has been indicated in Fig. 2, and we give in Figs. 10(d)–10(f) again the calculated contours from intersecting it with the Fermi surface. Again, excellent agreement is found. A wider region in k space is accessible at this energy. Quite remarkably, in the Cu(110) measurement the final state sphere touches the Fermi surface in normal emission, producing an extended circular region of higher intensity, modulated by matrix element effects.

4.2. *Nickel, a magnetic case*

While the Fermi surface of Cu has been perfectly accessible with other techniques, Ni presents an interesting case where strong temperature effects are expected on the Fermi surface due to the phase transition from an itinerant ferromagnetic state below a critical temperature of $T_c = 631$ K to a paramagnetic state at higher temperatures. Clearly, dHvA or related experiments cannot be applied in this elevated temperature range as all scattering rates become prohibitively high. In such a situation, photoemission can play an important role in providing unique high resolution Fermi surface information.

A section through the room temperature Fermi surface of Ni, as viewed through the (110) surface analogous to the situation shown in Fig. 2, is given in Fig. 11(a).[24] Various pieces of Fermi surface are contained in this section. We illustrate two different procedures that can be applied to analyze such raw photoemission data when dealing with a less well-known Fermi surface, as is the case here. First we compare the experimental contours, like in the copper case, to calculated Fermi surface contours, now obtained using the spinpolarized LKKR formalism. In this case, Ni is in a ferromagnetic state and we have to consider the two spin systems

separately. The majority spin or spin-up system will have a Fermi surface composed of essentially sp-like states, because the d shell is filled for electrons with their spins aligned parallel to the sample magnetization. This part of the Fermi surface is indicated by blue contours in Fig. 12. The minority spin electrons contribute the red contours. Black regions correspond to k locations where the two Fermi surfaces overlap. Comparing now Figs. 11(a) and 12 we find an excellent agreement as to the positions of Fermi contours, thus providing us with a means for spin assignment of the measured features. Even the fine splitting of minority-and majority-related contours labled $\Sigma_1^{\downarrow}$ and $\Sigma_1^{\uparrow}$ in Fig. 12, which are of sp-like origin as a band structure calculation[25] tells us, can be clearly seen in the experimental data (feature C). This splitting becomes much more apparent in a section through these data along the [$\bar{1}$10] azimuth [Fig. 13(a)]: two intensity maxima are well separated with angular positions of 54.5° and 49.5°. The strong arc-shaped feature B is of minority d-like origin, while for feature A no clear spin assignment can be given from this comparison.

An alternative method for analyzing this sort of data is to compare quantitatively some Fermi surface locations to existing low temperature dHvA measurements.[26] In order to do this, it is useful to project the measured Fermi surface sections, which intersect the final state sphere in the second Brillouin zone (Fig. 2), into the first zone. The procedure is as follows. Using Eqs. (6) and (7) for each intensity measurement $I(\theta_m, \phi_m)$ the corresponding k point inside the solid is calculated. The nearest reciprocal lattice vector G is then determined and subsequently subtracted from this k point, translating it into the first Brillouin zone. Figure 14 shows the image produced that way in the first zone. The measured data set now lies on a series of four spherical sectors, each sphere centered at some reciprocal lattice vector. As before, intensities are given in a linear gray scale, producing bright contours where the measurement surface intersects the Fermi surface. Figure 15 gives a section through this plot, showing one irreducible part of the Brillouin zone in the (001) plane. The measurement surface is indicated by the dashed circular line, and Fermi surface intersections by black ovals. The dHvA data[26] are given by open symbols. We find rather good, though not fully quantitative, agreement between the two techniques. Small deviations may arise due to the use of the free electron final state model, or maybe just because the two measurements were carried out at different temperatures. In any case this indicates the sort of accuracy that can be expected from these experiments given this simple level of interpretation.

Apart from these possible systematic deviations due to this final state approximation, we shall discuss the question of k space resolution. The measured Fermi surface locations are given by black ovals of a size that represents the angular width of the corresponding contour in the measurement. As can be seen from Fig. 13, the two sp band transitions are significantly sharper than the minority d band transition ($\Sigma_2^{\downarrow}$). This difference may be attributed to the more grazing emission angles of the first two transitions. As mentioned earlier, there is some smearing-out associated with $k_\perp$ and essentially none with $k_\parallel$. Consequently, the more weight $k_\parallel$ has at a particular measuring angle, the better that particular k point is defined. This means that different sections of a Fermi surface can be measured with varying precision, depending on the crystal face of the solid one chooses for the photoemission experiment. One should also not forget that the group velocities of the initial state bands will play a role in the measaured contour width. For a flat band like the minority d band a certain energy spread in the detector window will cause a larger k smearing than for the steeper sp band.[19]

We now discuss the changes in the Fermi surface contours as the temperature is raised slightly above the critical point. Without entering much into the ongoing debate about the behavior of the exchange splitting between the two spin subbands, the intensity-versus-angle sections given in Fig. 13 show that the minority and majority contours associated with sp band emission coalesce near the critical temperature but remain otherwise as a well-defined feature in the Fermi contour plot of Fig. 11(b). The minority d band-related features A and B appear to merge, forming a rather extended region of high intensity in between them. There are two physical explanations for the occurrence of such bright regions. A first one we have encountered in the He II excited data from Cu(110) [Figs. 2, 10(c), 10(f)]: when the measuring sphere touches the Fermi surface glancingly, the direct transition condition is fulfilled for many k locations in an extended region. A similar situation can arise in cases where there is a very flat band, and thus a high density of states very near to the Fermi energy. It is not clear which of these two mechanisms is involved in the present case. Closer inspection of this region indicates, however, that some parts of the room temperature Fermi surface remain visible (feature A′), indicating at least partly the coexistence of spin-polarized and paramagnetic

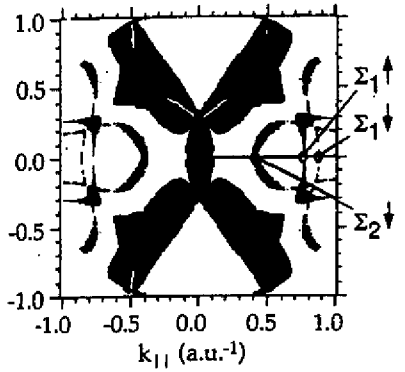

Fig. 12. Calculated section through the bulk Fermi surface of ferromagnetic nickel using the spin-polarized LKKR scheme for the initial state and a free electron final state. Majority spins are given in blue, minority spins in red. Overlapping regions appear in black.

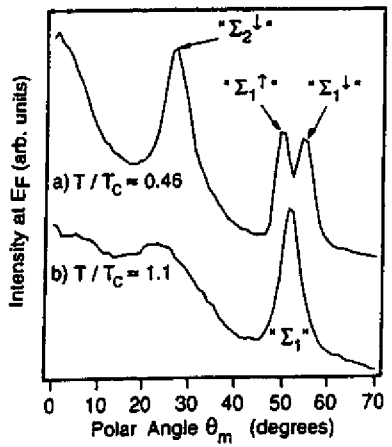

Fig. 13. (a) Polar section through the room temperature Fermi surface map of Fig. 11(a) along the [$\bar{1}$10] azimuth. (b) Same as (a) but for a temperature of 700 K.

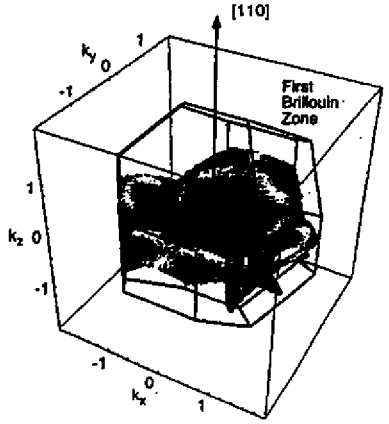

Fig. 14. 3D view of the Fermi surface map of Fig. 11(a) after projection into the first Brillouin zone. Note the reversed order in which the contours appear when moving from the zone center towards the boundaries as compared to Fig. 11(a).

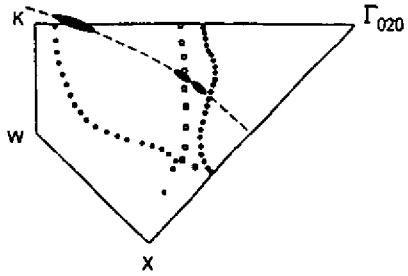

Fig. 15. Fermi surface cross sections of Ni in the (001) plane obtained from de-Haas-van-Alphen experiments (open symbols, from Ref. 26) compared to the data extracted from Fig. 14 (filled ellipses).

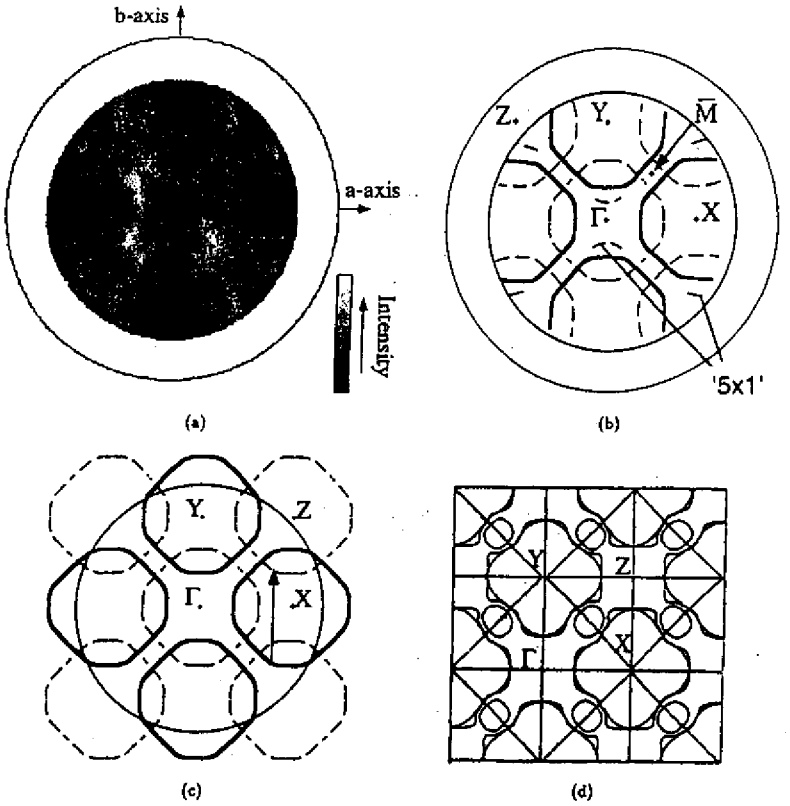

Fig. 16. (a) Fermi surface mapping of $Bi_2Sr_2CaCu_2O_{8+\delta}$(001) using an energy window of 30 meV, centered at E_F. A logarithmic intensity scale is used for gray levels in order to enhance weaker features. (b) Outline of (a), emphasizing the fine lines observed in the measurement and distinguishing between the stronger (thick lines) and weaker (dashed lines) sets of contours. (c) This drawing shows how these lines have the symmetry of a c(2 × 2) superstructure. (d) For comparison, the calculated Fermi surface for this compound from Ref. 29.

bands in these Fermi surface contours above T_c. The significance of the kind of data presented here is that the information is on the Fermi surface directly, which should be closely linked with the driving force for the magnetic phase transition. In conjunction with theoretical models describing the temperature-dependent evolution of the band structure, these data should serve as an important benchmark, in addition to providing some intuitive idea as to the behavior of the various bands over an extended region in k space.

5. Two-Dimensional Systems

5.1. *$Bi_2Sr_2CaCu_2O_{8+\delta}$ high temperature superconductor*

Before addressing truly surface-related Fermi surface contours, we give a brief description of our

experiments on cuprate high temperature superconductors[9,27] which represent quasi-2D systems as far as the relevant electronic bands near the Fermi surface are concerned. $Bi_2Sr_2CaCu_2O_{8+\delta}$ crystals have a layered structure of alternating metal oxide planes.[28] They cleave nicely between two Van-der-Waals-bonded Bi–O planes. The bands forming the Fermi surface are constituted by states that are located on the two Cu–O planes separated by Ca atoms, and they are known to be essentially two-dimensional.[29]

Fermi surface contours have been constructed by Dessau *et al.*[30] by tracing, for various azimuthal directions ϕ_m, $k_\parallel$ locations where a dispersing peak crosses the Fermi level. This procedure relies on a detailed line shape analysis of the spectra near E_F. In these strongly correlated systems where the photoemission signal is composed of a dispersing quasiparticle peak and a large incoherent background, finding the exact crossing point is no simple task. We have therefore conducted Fermi surface mapping experiments on such samples. Complementary to the experiments by Dessau *et al.*,[30] this approach relies on the measurement of the absolute intensities at E_F, a quantity which is not exploited in their approach. Figure 16(a) shows the resulting intensity map. In order to enhance weaker features, intensities are here translated logarithmically into gray levels. Well-defined continuous lines are observed, with some minor but significant deviations from the result of Dessau *et al.* A Fermi surface calculation[29] for this same material [Fig. 16(d)] agrees very well with the most prominent subset of contours seen in the data. Specifically, the general shape of the Fermi surface is well reproduced in the calculation, and the position of the Fermi wave vector along the ΓX direction is quite accurate. On the other hand, the small circular contour halfway between Γ and Z, which the calculation attributes to hole pockets associated with the Bi–O planes, is not seen in the data. Whether it is not present in the bulk electronic structure of $Bi_2Sr_2CaCu_2O_{8+\delta}$, or whether it is solely absent in the surface layer Bi–O plane, cannot be resolved by this experiment. The first bulk like Bi–O plane is buried about 13 Å below the surface and hardly contributes to the measured photoemission intensities. Moreover, in the calculation two Cu–O bands contribute to the Fermi surface, leading to the split contours, especially around the Z point. Experimentally we find that the measured contours have a full width at half maximum in $k_\parallel$ of the order of 0.1 $Å^{-1}$, which is just about the maximum separation of the two bands at the Fermi level and which can thus hardly be resolved. We are here not limited by the angular or energy resolution of the experiment but by the intrinsic width of the features.

In addition to these strong Fermi surface contours, we observed additional features, some of which are due to a c(2 × 2) superstructure on the Fermi surface[9] [dashed lines in Fig. 16(c)] and others due to the quasi-(5 × 1) incommensurate lattice modulation[27] which is a structural peculiarity of these Bi cuprates. The observation of such superstructures may be important in understanding the normal state electronic structure of these materials and will not be discussed at this place. We emphasize, however, that these features had not been seen experimentally before, and that the visualization of photoemission intensities in this 2D fashion greatly enhances the sensitivity to weak extra features.

5.2. *sp surface states on Cu(111) and Cu(110)*

In the discussion of the Cu bulk Fermi surface mapping we have already pointed out that a surface state appears at the center of the surface Brillouin zone on the (111) surface [Fig. 8(b)]. In Fig. 17(a) we give a higher resolution map of this surface state, displaying clearly the free-electron-like circular shape. A polar section through these data shows the high signal-to-background ratio and the width of the surface Fermi surface contour, which is less than 3° full width at half maximum. The existence of this surface state is closely related to the gap in the surface-projected band structure associated with the necks around the L points. Similar gaps in $k_\parallel$ exist on the (110) surface, and a surface state has also been observed here.[31] Figure 17(c) gives a nice view of how this surface state, also rather circular in shape, is situated relative to the bulk Fermi surface contours. If one considers the projected band structure more closely, one finds that this state has already moved out of the projected band gap by the time it reaches the Fermi energy,[31] at least along the $\overline{\Gamma Y}$ direction. Strictly speaking, the circular Fermi contours are thus associated with a surface resonance rather than with a true surface state. Translational symmetry within

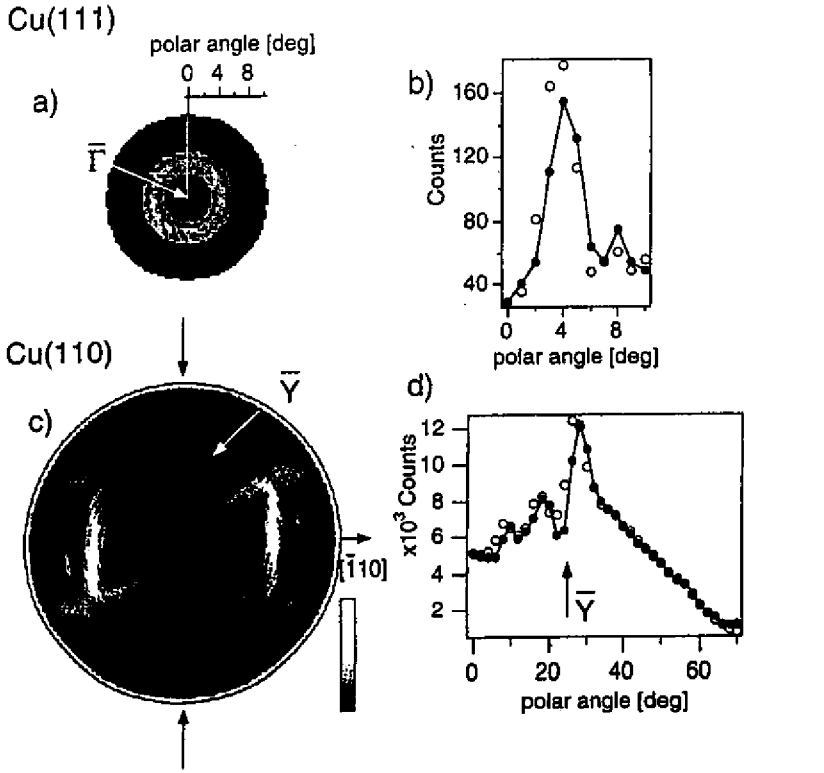

Fig. 17. (a) High resolution map (more than 2000 angular settings) of Fermi level intensities near the center of the surface Brillouin zone of Cu(111), showing the Shockley surface state. (b) Two polar sections through these data (open and closed circles) spaced by 180° in azimuth. (c) Fermi surface map from Cu(110) indicating the surface state centered at the $\overline{Y}$ point. (d) Sections through the data of (c) along the azimuths indicated by black arrows.

the (110) surface demands that this circle be centered precisely on the zone boundary. From this condition we can verify independently the accuracy of our k space mapping procedure. We know the exact location of the $\overline{Y}$ point relative to the $\overline{\Gamma}$ point, the distance being $\overline{\Gamma Y} = \pi/a_0 = 0.87$ Å^{-1} ($a_0 = 3.61$ Å). From Eqs. (3) and (5) we obtain the relation

$$k_\parallel = \frac{1}{\hbar}\sqrt{2m(h\nu - \Phi)}\,\sin\theta_m = \overline{\Gamma Y}\,. \qquad (8)$$

Taking the well-established work function value of 4.48 eV for Cu(110) obtained from photoemission cutoff measurements,[32] we arrive at a polar angle of $\theta_m = 24.5°$ for $\overline{Y}$. Figure 17(d) providing a polar section along the $\overline{\Gamma Y}$ direction, indicates that we ovserve the center of the surface state at a slightly smaller polar angle of 22±1°.

5.3. *sp surface state on Al(001)*

A similar *sp*-derived surface state has been observed on Al(001).[33] In this case the maximum binding energy is 2.75 eV, while it was only 0.4 eV in the case of the Cu sp surface states. Its Fermi surface

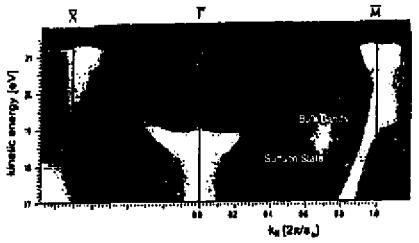

Fig. 18. Series of energy spectra from clean Al(001), representing polar scans along the [100] azimuth ($\overline{\Gamma M}$) and the [110] azimuth ($\overline{\Gamma X}$). The presentation is in a linear gray scale with low intensities in black and high intensities in white. Surface and bulk transitions are indicated.

will therefore cover a much larger area in $k_\parallel$, and it should be interesting to see how it interacts with various bulk bands. Figure 18 shows the highly parabolic dispersion of this state, which can be well fitted with an effective mass of $m^* = 1.18m_e$, in excellent agreement with earlier data.[33,34] This plot represents a series of spectra measured on a dense grid of polar angles along the $\overline{\Gamma X}$ and $\overline{\Gamma M}$ directions which have been mapped onto $k_\parallel$ according to

$$k_\parallel = \frac{1}{\hbar}\sqrt{2m(h\nu - E_B - \Phi)}\,\sin\theta_m\,, \qquad (9)$$

where E_B is the measured binding energy within the spectra. Intensities are given in a linear gray scale much like it is done in the Fermi surface maps, providing a very direct representation of the dispersion.[35] Even though emission from the surface state becomes rather weak away from the $\overline{\Gamma}$ point, this sort of plot permits a clear tracing of the dispersion and of the Fermi level crossing which occurs at 0.60 in units of $2\pi/a_0$.

A Fermi surface map is given in Fig. 19, measured with He I radiation. while the Fermi contours are here much more complex than in Cu, an intuitive understanding of all features is still possible within the simple framework discussed earlier. Figure 20 gives a schematic view of the situation in k space, along the $\overline{\Gamma M}$ direction, i.e. within the (100) plane. A simplified free electron Fermi surface for Al is plotted centered about four reciprocal lattice points which are relevant to this geometry. We neglect here the

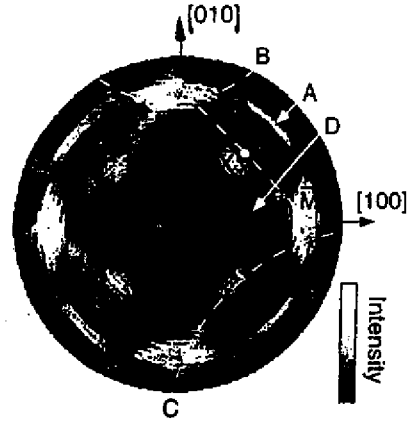

Fig. 19. Fermi surface map from clean Al(001). Several features are emphasized by dashed curves in one of the four symmetry-equivalent places and marked by capital letters. The boundary of the surface Brillouin zone is given at one place by the straight dashed line.

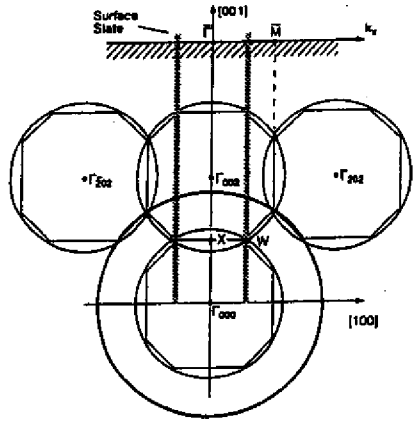

Fig. 20. Section through the reciprocal lattice of Al parallel to the (010) plane, analogous to Fig. 2. The bulk Brillouin zones are given by the polygons, and the idealized free electron Fermi surface of Al is draw around four reciprocal lattice points. The large circle represents the final states for He I excitation. The location of the surface surface state is indicated by the hatched bars.

effects of the lattice potential on the Fermi surface, since we just want to be able to give an assignment to the various measured contours. Like in Fig. 2, a free electron final state for excitation with He I radiation is also given, which here reaches further out due to the smaller Brillouin zone dimensions in Al as compared to Cu. We can now immediately understand the large circular contour A in the data as being due to the intersection with the Γ_{002}-centered Fermi sphere. The Γ_{202} spheres give rise to the arc-shaped contours B, while the Γ_{111} spheres (not shown in Fig. 20) produce the four symmetry-related arcs C. Most of the observed contours are readily accounted for in this simple picture. The surface state appears as a weak circular contour D touching the bulk bands in the $\overline{\Gamma X}$ directions. The corresponding regions of $k_{\parallel}$ are indicated in Fig. 20. This figure suggests that the state might actually be associated with a small gap at the W points and thus be a true surface state even at the Fermi energy. In other directions, especially along $\overline{\Gamma X}$, the $k_{\parallel}$ values would pass near the U points of the bulk Brillouin zone where there is no gap at E_F. This contour D comprises thus both true surface states and surface resonances.

6. Conclusions and Outlook

The examples presented in these notes demonstrate that this new approach to the photoemission experiment provides a very powerful tool for mapping Fermi surfaces directly. It can be applied to any material that can be prepared in single crystalline form of a few mm^2 surface area and thickness down to atomic monolayers. 3D and 2D systems can be measured. Given the wide open parameter space accessible by photoemission experiments (temperature, concentrations, film thickness, dimension (2D $\rightarrow$ 3D), etc.) this technique should be particularly useful for studying phase transitions and their interrelation with the Fermi surface.[36]

While the positions of the Fermi surface contours are well explained within the simple free electron final state model, there is now also a growing understanding of the intensity variations along the contours. A more sophisticated final state wave function is needed here, which takes into account the angular momentum character of the photoelectron wave and the elastic scattering within the surface region.[7,37,38] Finally, the analysis of the widths of such contours might be of considerable interest in studying low energy excitations in correlated systems. The analysis of line widths in energy spectra has attracted a great deal of attention in this context.[19] Very recently we have shown that in momentum space such line widths can be extracted more precisely due to a simpler line shape and a better-defined background.[39,40] It should be mentioned that other constant energy surfaces below the Fermi surface can be measured equally well, such that all the studies discussed here can be extended to higher binding energies.[27,41]

References

1. N. W. Ashcroft and N. D. Mermin, *Solid State Physics* (Holt, Rinehart and Winston, New York, 1976).
2. R. Ribberfors, *Phys. Rev.* **B12**, 3136 (1975).
3. S. Berko, in *Momentum Densities*, eds. R. N. Silver and P. E. Sokol (Plenum, 1989).
4. S. Hüfner, *Photoelectron Spectroscopy* (Springer, Berlin, 1995).
5. R. H. Gaylord, K. Jeong and S. D. Kevan, *Phys. Rev. Lett.* **62**, 203 (1989).
6. A. Santoni, L. J. Terminello, F. J. Himpsel and T. Takahashi, *Appl. Phys.* **A52**, 229 (1991).
7. J. Osterwalder, A. Stuck, T. Greber, P. Aebi, L. Schlapbach and S. Hüfner, in *Proc. 10th Vacuum Ultraviolet Radiation Physics*, eds. F. J. Wuilleumier, Y. Petroff and I. Nenner (World Scientific, Singapore, 1993), p. 475.
8. P. Aebi, J. Osterwalder, R. Fasel, D. Naumovic and L. Schlapbach, *Surf. Sci.* **307–309**, 917 (1994).
9. P. Aebi, J. Osterwalder, P. Schwaller, L. Schlapbach, M. Shimoda, T. Mochiku and K. Kadowaki, *Phys. Rev. Lett.* **72**, 2757 (1994).
10. R. Leckey and J. Riley, *Aust. J. Phys.* **48**, 217 (1995).
11. Zhe Qu, A. Goonewardene, K. Subramanian, J. Karunamuni, N. Mainkar, L. Ye, R. L. Stockbauer and R. L. Kurtz, *Surf. Sci.* **324**, 133 (1995).
12. J. Avila, C. Casado, M. C. Asensio, J. L. Perez, M. C. Munoz and F. Soria, *J. Vac. Sci. Technol.* **A13**, 1501 (1995).
13. S. Doniach, *Phys. Rev.* **B2**, 3898 (1970); N. J. Shevchik, *Phys. Rev.* **B16**, 3428 (1977).
14. D. E. Eastman, J. J. Donelon, C. Hien and F. J. Himpsel, *Nucl. Instrum. Methods* **172**, 327 (1980).
15. J. Osterwalder, T. Greber, A. Stuck and L. Schlapbach, *Phys. Rev.* **B44**, 13764 (1991).
16. R. Fasel and J. Osterwalder, *Surf. Rev. Lett.* **2**, 359 (1995).
17. D. G. Frank, N. Battina, R. Golden, F. Lu and A. T. Hubbard, *Science* **247**, 182 (1990).

18. D. Shoenberg and D. J. Roaf, *Phil. Trans. Roy. Soc.* **225**, 85 (1962).
19. N. V. Smith, P. Thiry and Y. Petroff, *Phys. Rev.* **B47**, 15476 (1993).
20. B. A. McDougall, T. Balasubramaian and E. Jensen, *Phys. Rev.* **B51**, 13891 (1995).
21. J. B. Pendry, *Low Energy Electron Diffraction* (Academic London, 1974), p. 23.
22. T. Greber, J. Osterwalder, S. Hüfner and L. Schlapbach, *Phys. Rev.* **B45**, 4540 (1992).
23. P. O. Gartland and B. J. Slagsvold, *Phys. Rev.* **B12**, 4047 (1975).
24. P. Aebi, T. J. Kreutz, J. Osterwalder, R. Fasel, P. Schwaller and L. Schlapbach, *Phys. Rev. Lett.* **76**, 1150 (1996).
25. H. Eckardt and L. Fritsche, *J. Phys.* **F17**, 925 (1987).
26. Unpublished results of Stark; see C. S. Wang and J. Callaway, *Phys. Rev.* **B9**, 4897 (1974).
27. J. Osterwalder, P. Aebi, P. Schwaller, L. Schlapbach, M. Shimoda, T. Mochiku and K. Kadowaki, *Appl. Phys.* **A60**, 247 (1995).
28. A. Yamamoto, M. Onoda, E. Takayama-Muromachi, F. Izumi, T. Ishigaki and H. Asano, *Phys. Rev.* **B42**, 4228 (1990).
29. S. Massidda, Jaejun Yu and A. J. Freeman, *Physica (Amsterdam)* **C158** 251 (1988).
30. D. S. Dessau, Z.-X. Shen, D. M. King, D. S. Marshall, L. W. Lombardo, P. H. Dickinson, A. G. Loeser, J. DiCarlo, C.-H. Park, A. Kapitulnik and W. E. Spicer, *Phys. Rev. Lett.* **71**, 2781 (1993).
31. P. Heimann, J. Hermanson, H. Miosga and H. Neddermeyer, *Surf. Sci.* **85**, 263 (1979).
32. *CRC Handbook of Chemistry and Physics*, eds. R. C. Weast and M. J. Astle (CRC, Boca Raton, 1980), p. E-82.
33. P. O. Gartland and B. J. Slagsvold, *Solid State Commun.* **25**, 489 (1978); G. V. Hansson and S. A. Flodstrom, *Phys. Rev.* **B18**, 1562 (1978).
34. H. J. Levinson, F. Greuter and E. W. Plummer, *Phys. Rev.* **B27**, 727 (1983).
35. R. Fasel, P. Aebi, R. G. Agostino, J. Osterwalder and L. Schlapbach, *Phys. Rev.* **B54**, 5893 (1996).
36. S. D. Kevan, *Surf. Sci.* **307–309**, 832 (1994).
37. E. L. Shirley, L. J. Terminello, A. Santoni and F. J. Himpsel, *Phys. Rev.* **B51**, 13614 (1995).
38. H. Daimon, S. Imada, H. Nishimoto and S. Suga, *J. Electron Spectrosc. Relat. Phenom.* **76**, 487 (1996).
39. T. J. Kreutz, P. Aebi and J. Osterwalder, *Solid. State Commun.* **96**, 339 (1995).
40. P. Schwaller, P. Aebi, H. Berger, C. Beeli, J. Osterwalder and L. Schlapbach, *J. Electron Spectrosc. Relat. Phenom.* **76**, 127 (1996).
41. T. J. Kreutz, J. Osterwalder and L. Schlapbach, *J. Electron Spectrosc. Relat. Phenom.* **76**, 601 (1996).

INSTITUTE OF PHYSICS PUBLISHING JOURNAL OF PHYSICS: CONDENSED MATTER

J. Phys.: Condens. Matter **13** (2001) 10517–10532 PII: S0953-8984(01)28792-X

Photoelectron and x-ray holography by contrast: enhancing image quality and dimensionality

C S Fadley[1,2], M A Van Hove[1,2,3], A Kaduwela[1,6], S Omori[1,4,5], L Zhao[1,2] and S Marchesini[1]

[1] Materials Sciences Division, Lawrence Berkeley National Laboratory, Berkeley, CA 94720, USA
[2] Department of Physics, University of California, Davis, CA 95616, USA
[3] Advanced Light Source, Lawrence Berkeley National Laboratory, Berkeley, CA 94720, USA
[4] Institute of Industrial Science, University of Tokyo, Tokyo 106-8558, Japan
[5] Sony Corporation Semiconductor Network Company, 4-14-1 Asahi-cho, Atsugi, Kanagawa 243-0014, Japan

Received 13 September 2001
Published 9 November 2001
Online at stacks.iop.org/JPhysCM/13/10517

Abstract

Three forms of electron or x-ray holography 'by contrast' are discussed: they all exploit small changes in diffraction conditions to improve image quality and/or extract additional information. Spin-polarized photoelectron holography subtracts spin-down from spin-up holograms so as to image the relative orientations of atomic magnetic moments around an emitter atom. Differential photoelectron holography subtracts holograms taken at slightly different energies so as to overcome the forward-scattering problem that normally degrades the three-dimensional imaging of atoms, particularly for emitter atoms that are part of a bulk substrate environment. Resonant x-ray fluorescence holography also subtracts holograms at slightly different energies, these being chosen above and below an absorption edge of a constituent atom, thus allowing the selective imaging of that type of atom, or what has been referred to as imaging 'in true colour'.

1. Introduction

The holographic reconstruction of atoms in solids, including surfaces, interfaces and bulk materials, produces real-space images that locate individual atoms in the immediate neighbourhood of selected 'source' atoms [1–14], often to within a fraction of an Ångström. Here we will consider two types of outgoing waves that produce the holograms: photoelectrons and fluorescent x-rays, as produced via core-level excitations. Because such holograms and their associated images are produced by element-specific core processes, a key and well-recognized advantage of such holographies is that they are source-atom specific. That is, the

[6] Present address: California Air Resources Board, Sacramento, CA 95814, USA.

local environment of each type of atom in a complex system can be determined separately. However, such imaging does not readily provide the chemical or magnetic nature of the neighbour atoms. Also, the accuracy of the imaging, particularly with photoelectrons, is limited by effects such as the anisotropy of atomic scattering factors (with forward scattering a major obstacle), multiple scattering and truncation of the experimental data.

By contrasting holographic images measured under slightly different conditions, it is possible to obtain additional information, such as magnetic structure and chemical differentiation, and also to improve the quality of 'normal' holographic images.

This paper describes three methods of such 'holography by contrast'. In spin-polarized photoelectron holography (SPPH) [15] holograms measured with spin-up and spin-down electrons are subtracted from one another to produce a map of the relative orientations of magnetic moments in the neighbourhood of an atom emitting photoelectrons. In differential photoelectron holography (DPH) [16], one exploits the fact that the atomic forward-scattering (FS) peak varies only slowly with energy, such that another difference of holograms, this time at slightly different energies, is found to largely eliminate disruptive FS effects in imaging atoms. In resonant x-ray fluorescence holography (RXFH) [17], one uses the rapid change of the x-ray scattering factors near an absorption edge to selectively image individual chemical neighbours in a compound material.

Before proceeding to specific examples for each case, we note for clarity that a method called 'derivative' PH has been proposed by Chiang and co-workers [18], and this also is based on measurements of photoelectron intensity in slightly different conditions (at two nearby energies). However, the purpose there is to eliminate uncertainties in the experimental intensities I due to the variation of experimental conditions, by first taking logarithmic derivatives $[\partial I/\partial k]/I$ that are then reintegrated into 'self-normalized' intensities; after that step, the holographic reconstruction is 'normal'.

Various reconstruction algorithms [3, 4, 6] and measurement methods [19] have been proposed for photoelectron and x-ray fluorescence holography, many of which are represented by the formula

$$U(\boldsymbol{r}) = \left| \int W\chi(\boldsymbol{k}) \exp[-\mathrm{i}kr + \mathrm{i}\boldsymbol{k}\cdot\boldsymbol{r}]\,\mathrm{d}^3k \right|^2 \tag{1}$$

where U is the image intensity at position $\boldsymbol{r}$, $\chi(\boldsymbol{k}) = (I(\boldsymbol{k}) - I_0)/I_0$ is the normalized hologram based on intensities measured over three-dimensional $\boldsymbol{k}$ space, I_0 is the intensity in the absence of any scattering, and the function or operator W permits describing the difference between algorithms, with $W = 1$ in the original multi-energy formulations [3]. The three methods to be described in the following will start from this basic formula, and deviate from it in different ways.

As a general comment, we note that photoelectron holography involves very strong electron–atom scattering and thus very easily measured modulations in $\chi(\boldsymbol{k})$ that can reach $\pm 30\%$. This strong scattering is nonetheless not ideal for holography, in that it is also very anisotropic and at higher energies above about 300 eV also strongly peaked in the forward direction; it also leads to multiple scattering effects that can distort images or produce artefacts. Multiple-energy images based on equation (1) can improve the image quality and suppress multiple scattering effects, but scattering anisotropy and phase shift effects may remain. X-ray fluorescence holography by contrast involves very weak x-ray-atom scattering and much more difficult to measure modulations in $\chi(k)$ of typically a few tenths of a per cent. However, the weak nature of the scattering leads to holograms that are much more ideal, and to correspondingly more accurate atomic images.

2. Spin-polarized photoelectron holography (SPPH)

There is great interest in studying near-surface magnetism in various types of nanostructures for which magnetic order may be significantly different from that of the corresponding bulk materials. Spin-polarized photoelectron diffraction (SPPD) without direct imaging has already proven capable of detecting changes in short-range magnetic order as a given transition temperature is crossed for both antiferromagnets [20] and a ferromagnet [21], but adding three-dimensional imaging to such measurements would render them much more powerful. It has previously been demonstrated theoretically [15] that it should be possible to image short-range magnetic structure by means of photoelectron holography in which the electron spin is resolved.

The method relies on the difference in the scattering of spin-up versus spin-down electrons by atoms that carry a net spin magnetic moment. The primary interaction involved is thus exchange between the photoelectron and the unpaired valence electrons on the magnetic atom, although spin–orbit effects also may have to be considered for the most accurate description, especially for scattering from heavier atoms. The photoelectron spin can be resolved simply by exploiting the energy separation between multiplet-split core levels in transition metal compounds or ferromagnetic metals. This constitutes an internally referenced source of spin-polarized photoelectrons, giving magnetic moment orientations relative to that of the source atom. Adding an external spin detector and/or exciting spin–orbit split levels with circularly polarized radiation [22] provides the further possibility of making externally referenced measurements, giving absolute magnetic orientations in the laboratory frame.

If we measure separately the two holograms $\chi_\uparrow(\boldsymbol{k})$ and $\chi_\downarrow(\boldsymbol{k})$ for the two different spin orientations, and if $U_\uparrow(\boldsymbol{r})$ and $U_\downarrow(\boldsymbol{r})$ are their respective reconstructed images using 'normal' holographic methods, we can define two separate difference images that focus on just the spin-dependent aspects of the scattering:

$$\Delta(\boldsymbol{r}) = U_\uparrow(\boldsymbol{r}) - U_\downarrow(\boldsymbol{r}) \tag{2}$$

and

$$\Delta'(\boldsymbol{r}) = \left| \int_k \exp(-\mathrm{i}k\boldsymbol{r}) \iint_{\hat{k}} \exp(\mathrm{i}\boldsymbol{k}\cdot\boldsymbol{r}) [\chi_\uparrow(\boldsymbol{k}) - \chi_\downarrow(\boldsymbol{k})] k^2 \, \mathrm{d}k \sin\theta_k \, \mathrm{d}\theta_k \, \mathrm{d}\varphi_k \right|. \tag{3}$$

The latter is the normal three-dimensional holographic transform of equation (1), but now applied to the difference of the spin-up and spin-down holograms.

The expectation is that $\Delta(\boldsymbol{r})$ will show signals of opposite sign at atomic locations with opposite magnetic moment. It should also show no signal at the locations of non-magnetic atoms. Because of the overall absolute value, the second image, $\Delta'(\boldsymbol{r})$, should not show spin-up versus spin-down sensitivity, but should nonetheless show the location of magnetic moments, while again suppressing non-magnetic atoms.

The potential of this method is illustrated in figure 1 for a simulated experiment for a small cluster representing a MnO(001) surface (figure 1(a)) [15, 23]. Atomic magnetic moments are shown in figure 1(a) as cones pointing up or down. Spin-up and spin-down photoelectrons are emitted from the central Mn^{2+} atom, and they can side-scatter from both O and Mn atoms in the same plane so as to yield two different sets of holograms. These holograms have been calculated with full multiple scattering and spin-dependent potentials [24][7]. Spin-up electrons scatter from spin-down Mn^{2+} atoms without the normal exchange potential that is included in the scattering of electrons from same-spin Mn^{2+} atoms, and therefore, two separate sets of phase shifts are needed to calculate the electron scattering. The potential is slightly more attractive

[7] MSCD photoelectron diffraction program package from http://electron.lbl.gov/mscdpack/mscdpack.html.

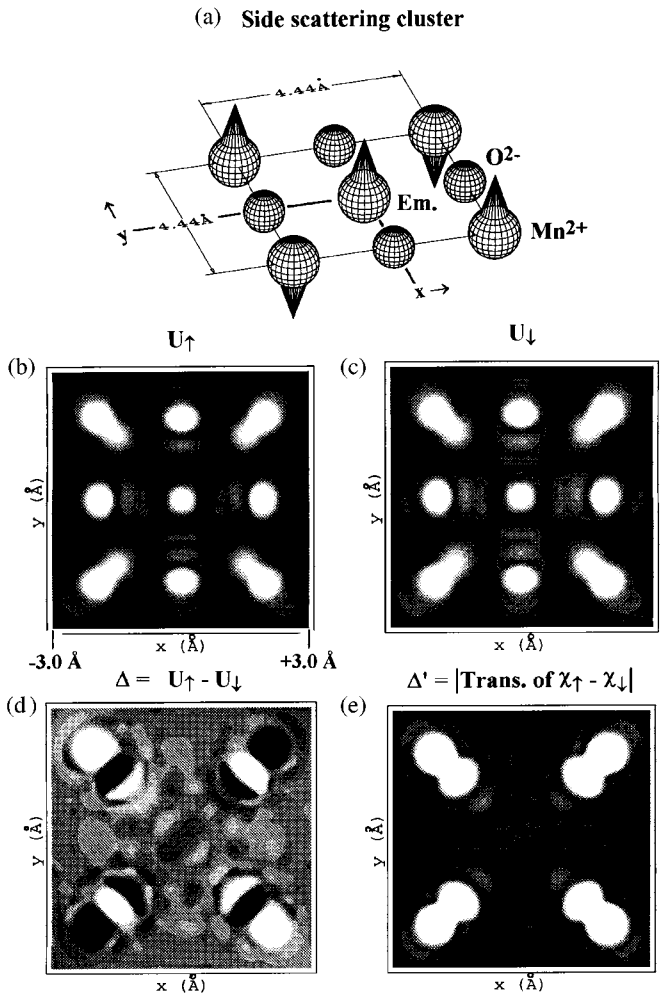

Figure 1. Theoretical simulation of spin-polarized photoelectron holography (SPPH): (a) a nine-atom cluster representing the (001) surface of MnO, with an emitter in its centre and eight side-scattering Mn and O neighbours around it; (b), (c) normal holographic images $U_{\uparrow}(r)$ and $U_{\downarrow}(r)$ generated for the two different photoelectron spins using ten energies between 127 and 278 eV; (d) spin-sensitive holographic image $\Delta(r)$; according to equation (2). (e) Spin-sensitive holographic image $\Delta'(r)$ according to equation (3).

when the spin of the photoelectron and the net spin of the Mn atom are parallel. Holograms were calculated at ten energies between 127 and 278 eV, so as to be able to take advantage of the well known image improvements possible with multi-energy imaging [2, 6, 7]. An important detail in using the spin-dependent image functions in equations (2) and (3) in the most unambiguous way is that the calculations were performed at the same final electron energy for spin-up and spin-down electrons, so that the spatially dependent diffraction conditions remain the same (i.e. same photoelectron wavelength). In practice, this would require an experiment to shift the incoming photon energy by an amount corresponding to the difference in the two spin-resolved photoelectron peaks (e.g., about 6.0 eV for the Mn 3s multiplets in the MnO case considered here) between the spin-up and spin-down measurements, thus again requiring a tunable synchrotron radiation photon source.

Figures 1(b) and (c) show standard multi-energy holographic reconstructions (via equation (1) with $W = 1$) and produced with spin-up and spin-down electrons, respectively. They look much alike, due to the relatively small effect of the exchange potential (5–15% of the total effective scattering potential), and both image the nine atoms of the cluster. Their difference image $\Delta(\boldsymbol{r})$ (equation (2)) is shown in figure 1(d): the Mn^{2+} atoms are imaged with opposite contrast, reflecting their opposite magnetic moments, while the oxygen atoms are effectively suppressed, as expected. Phase variation across the Mn^{2+} images produces oscillations in sign, but it is nonetheless clear that the two pairs of Mn scatterers have opposite orientation. To establish the orientation of the magnetic moments on the scatterers relative to that on the emitter would require further work, e.g. in comparing experimental and theoretical images. The second type of difference image $\Delta'(\boldsymbol{r})$ (equation (3)) shown in figure 1(e) also confirms expectations: it images the magnetic moments without being sensitive to their orientation, and omits the non-magnetic atoms.

Beyond the two simple imaging functions considered here for SPPH, Timmermans *et al* have also discussed from a theoretical point of view more detailed vectorial methods, including spin–orbit contributions to the difference of the spin-up and spin-down photoelectron fluxes [25]. These methods also show promise for even more precise studies of short-range magnetic order in future experimental work.

Thus, spin-polarized photoelectron holography represents an intriguing and challenging experimental possibility for the future, but one well matched to the new synchrotron radiation sources that are now becoming available. Possible applications would be to some of the strongly correlated materials and to complex magnetic alloys, for which the interaction between short-range and long-range magnetic order is thought to play a strong role in producing intriguing properties.

3. Differential photoelectron holography (DPH)

From the first papers on photoelectron holography, it has been clear that the strong electron–atom scattering involved was both a blessing in producing large holographic oscillations and easily measured holograms, and a curse in yielding very anisotropic scattering factors that are strongly peaked in the forward direction at higher energies above a few hundred eV [2, 6, 23]. Since the ideal scattering factor for holography would be weak and isotropic, photoelectron holographic images can often suffer distortions and peak shifts. Some of these aberrations can be corrected by using a sufficiently large multi-energy data set, but it has still proven particularly difficult to image bulk-like atoms that are present in the first few layers below a surface, as recently illustrated for the case of bulk atom emission from W(110) [7].

To overcome the poor imaging quality associated with strong and anisotropic forward scattering (FS) of electrons, a new approach called 'differential holography' has been proposed. This proceeds simply by replacing χ in equation (1) by its derivative with respect to the magnitude of the photoelectron wavevector $\boldsymbol{k}$ (or equivalently by setting $W = \partial/\partial k$) or more conveniently by a numerical difference between two χ at slightly different energies ($\delta\chi = \chi(k+\delta k) - \chi(k)$). FS effects can be greatly suppressed via this method. This method has been applied to both experimental and theoretical multi-energy holograms for Cu 3p emission from Cu(001), and results in images that are improved over prior work in several respects. Applications of this approach in other electron-based holographies also appear possible.

The principle of DPH is as follows: we consider the single-scattering expression of the hologram χ for an emitter–scatterer pair spaced by a vector $\boldsymbol{r}$ [26]:

$$\chi(\boldsymbol{k}) = \frac{I - I_0}{I_0} \approx \frac{2|f(k, \theta_r^k)|}{r} \cos\left[kr(1 - \cos\theta_r^k) + \varphi(k, \theta_r^k)\right] \tag{4}$$

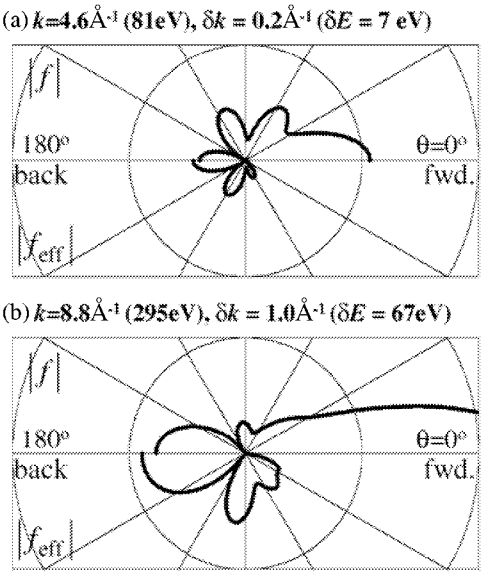

Figure 2. Comparison of the usual scattering amplitude $|f|$ and the effective scattering amplitude of differential holography $|f_{\rm eff}|$, calculated for Cu–Cu nearest neighbours ($r = 2.56$ Å) as a function of scattering angle θ_r^k for two different sets of k and δk in taking the differential of χ: (a) $k = 4.6$ Å^{-1} (81 eV), $\delta k = 0.2$ Å^{-1} (7 eV) and (b) $k = 8.8$ Å^{-1} (295 eV), $\delta k = 1.0$ Å^{-1} (67 eV). The final strong FS data points of $|f|$ at the right of panel (b) are truncated. We have confirmed numerically that equation (3) is a good approximation even in the case of (b), where δk has a larger fractional value.

where I_0 is the intensity that would be observed without atomic scattering and φ is the scattering phase. If δk is sufficiently small so that $\delta|f|/|f| \ll 1$, where $\delta|f|$ is the change in $|f|$, the difference of two holograms at $k_\pm = k \pm \delta k/2$ can be written in a form similar to equation (4):

$$\delta\chi(\boldsymbol{k}) = \chi(k_+\hat{\boldsymbol{k}}) - \chi(k_-\hat{\boldsymbol{k}}) \approx -\frac{2|f_{\rm eff}|}{r}\sin\left[kr\left(1-\cos\theta_r^k\right) + \bar{\varphi}\left(k,\theta_r^k\right)\right] \qquad (5)$$

where the direction $\hat{\boldsymbol{k}}$ is defined by angles θ and ϕ, the 'effective' scattering amplitude is defined as $|f_{\rm eff}| = 2|f|\sin\left[\delta kr\left(1-\cos\theta_r^k\right)/2 + \delta\varphi/2\right]$, and $\bar{\varphi}$ is the average of the φ at $k_\pm$. In the FS region ($\theta_r^k \to 0$), $|f_{\rm eff}|$ is thus very small, approaching zero in the limit of $\delta\varphi \to 0$. If δk is also small, $|f_{\rm eff}|$ is proportional to r; thus, DPH not only suppresses the FS effects, but also enhances the imaging of distant atoms. However, $\bar{\varphi}$ still remains in the sinusoidal holographic oscillation of equation (5), and this could be the origin of small image position shifts.

In figure 2, $|f|$ and $|f_{\rm eff}|$ are plotted as a function of θ_r^k for Cu–Cu nearest neighbours ($r = 2.56$ Å) and two choices of energy and energy difference. For $k = 4.6$ Å^{-1} and $\delta k = 0.2$ Å^{-1}, $|f_{\rm eff}|$ is significant only in the region of $\theta_r^k > \sim 90°$. Therefore, the imaging of side-scattering (SS) and back-scattering (BS) atoms is expected, while it will be difficult for this case to image FS atoms. On the other hand, for $k = 8.8$ Å^{-1} and a larger fractional $\delta k = 1.0$ Å^{-1}, $|f_{\rm eff}|$ is significant not only in the BS region but also in the range of $\theta_r^k \sim$ 30–90°. Since it is well known that near-neighbour FS diffraction fringes extend out beyond 30° [26,27], we might expect the latter choice to also permit imaging FS atoms. In this way, the relative sensitivity of DPH to SS and FS atoms can be 'tuned' by selecting the range and step width of k scans.

To demonstrate DPH experimentally, we have applied the method to measured photoelectron holograms [16]. Photoelectron spectra for Cu 3p emission were measured at 25 energies over $k = 4.5$–9.3 Å^{-1} ($E_k = 77$–330 eV) with a constant step of $\delta k = 0.2$ Å^{-1} (corresponding to $\delta E_k = 7$–14 eV), along 65 different directions over a symmetry-reduced 1/8 of the total solid angle above the specimen, and with a polar angle range from $\theta = 0°$ (surface normal) to 70°. A total of 1625 distinct intensities were thus measured.

The photoelectron intensity $I(\boldsymbol{k} = k, \theta, \phi)$ was fitted by low-order polynomials with three variables to obtain the smooth background intensity I_0 [7,28]. Three kinds of χ were obtained from this fitting: $\chi_{\rm A}$ by fitting a scanned-angle pattern $I_k(\theta, \phi)$ at each fixed k [5], χ_B by

fitting a scanned-energy curve $I_{\hat{k}}(k)$ at each fixed direction $\hat{k}$ [6] and χ_C by fitting to the full data set of $I(k, \theta, \phi)$ at once, with the last being the most accurate from an *a priori* point of view [7]. The k-differences from χ_C were also used for DPH in what we will term method D (i.e. $\chi_D = \delta\chi_C$ as defined in equation (5)). The proper method of I_0 subtraction has been the origin of some controversy concerning the fidelity of reconstructed images, and so warrants a little more discussion here [9]. It has been suggested [9] that method B has an advantage over method A in that low-frequency oscillations due to FS events in $I_{\hat{k}}(k)$ are automatically removed. However, this also means that the I_0 from method B inherently deviates from the true I_0 defined as the intensity without scattering, especially in the FS direction. In addition, since each $I_{\hat{k}}(k)$ is independently normalized without considering the continuity of χ in the whole sampled $\boldsymbol{k}$ space, method B could degrade holographic fringes in $I_k(\theta, \phi)$. Similarly, method A could degrade holographic oscillations in $I_{\hat{k}}(k)$. In contrast, method C takes into account the continuity of χ over the whole data set, but the FS peaks remain in χ_C. Method D (= DPH with χ_C) should suppress these forward scattering effects. Thus, a comparison of methods A–D is of interest in general from the point of view of holographic methodology and it also provides a critical test for the efficacy of DPH in reducing FS effects. The simple original transform was used for all four data sets; but to avoid spurious features due to the abrupt truncation of the integral in equation (1), W was taken to be the product of a Gaussian function of k and a Hanning function $\cos^2\theta$, with an additional multiplication by r to make atoms at larger distances more visible.

Figure 3 shows cross atomic images reconstructed with the four methods in the vertical (100) plane of Cu(001), with methods A–D being applied to experimental data in parts (a)–(d), respectively, and methods C and D being applied to an accurate multiple-scattering simulation of the experimental results in parts (e) and (f), respectively. First considering methods A–C which are different approaches to standard photoelectron holography, we see the qualitatively expected results that method A retains strong FS features, requiring a large enhancement factor of 46× in the bottom part of the image to display BS atoms of types 1 and 3 (figure 3(a)), that method B indeed suppresses these features strongly, with enhancement by 5× now being necessary in the top part of the image to see some SS atoms of type 4 (figure 3(b)); and that method C is intermediate between A and B in requiring somewhat less enhancement (by 29× in experiment and 49× in theory) in the lower part of the image to see some BS and SS atoms (figures 3(c), (e)). Note also that methods A and C also possess strong elongated images of the FS atoms of type 6, as seen in a prior application of method A to Cu(001) [5].

Turning now to DPH in figures 3(d), (f), we find method D to be the most robust for imaging both SS and BS atoms (and to some degree also FS atoms of type 6). All of the BS and SS atoms of types 1, 2, 3 and 4 are seen clearly in these DPH images, with only a small enhancement factor of 5× being required in the top half of the image (as with method B, but with superior image quality to it). Comparing the positions of these images in DPH with the known atomic positions in Cu, there are shifts in position of approximately 0.1 Å for type 1, 0.6 Å for 2, and 0.3 Å for 3. Such peak shifts relative to the true atomic positions, as observed in all methods, can be attributed to the neglect of corrections for both the scattering phase and the inner potential, which have not been included here.

For comparison with experiment, we have also performed multiple-scattering simulations of $I(\boldsymbol{k})$, using a cluster method [24]. The theoretical I_0 was obtained simply as the square of the zeroth-order wave function without scattering. Images reconstructed from the theoretical χ and $\delta\chi$ via methods C and D are shown in figures 3(e) and (f). The main features in figures 3(c) and (d) are well reproduced by our simulations, although the artefacts between the images of atoms 3 are much stronger in experiment for method C, and the relative intensity in the region of FS atom 6 is stronger in experiment for method D.

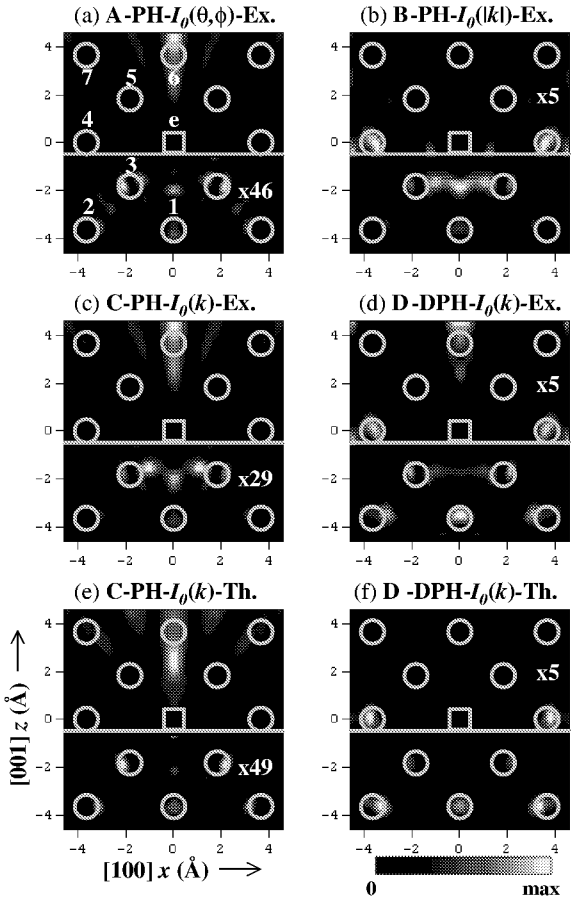

Figure 3. Atomic images in the vertical (100) plane of Cu(001) reconstructed from Cu 3p holograms obtained by normal photoelectron holography (PH, methods A–C) and differential photoelectron holography (DPH, method D), as described in the text. The emitter and scatterer positions are indicated by squares and circles, respectively, and various near-neighbour atoms are numbered. Image intensities above or below $z_c = -0.5$ Å have been rescaled by the factor shown in each panel, with this factor being determined so as to make the maximum intensities above and below z_c equal. *Experimental images*: (a) image obtained by method A: normal holography via equation (1) with I_0 determined by fitting its angular variation at each k value. (b) Image obtained by method B: normal holography with I_0 determined by fitting its k variation along each direction. (c) Image obtained by method C: normal holography with I_0 determined by fitting both its angular and k variations. (d) Image obtained by method D: differential holography with I_0 determined by fitting both its angular and k variations. *Theoretical images*: (e) as (c) but theoretical. (f) As (d) but theoretical.

(This figure is in colour only in the electronic version)

Figures 4 and 5 further show three-dimensional representations of the experimental images in figures 3(a)–(d), with figure 4 first indicating clearly that DPH can effectively image approximately 20 BS and SS atoms around a given emitter e and up to two planes below it. In this image, we find in addition to the atoms of types 1–4 and 6 in figure 3, two other types of near-neighbour BS and SS atoms located in the vertical (110) plane (denoted 2′ and 4′ and situated in the same horizontal layers as 2 and 4, respectively). All of these atoms are

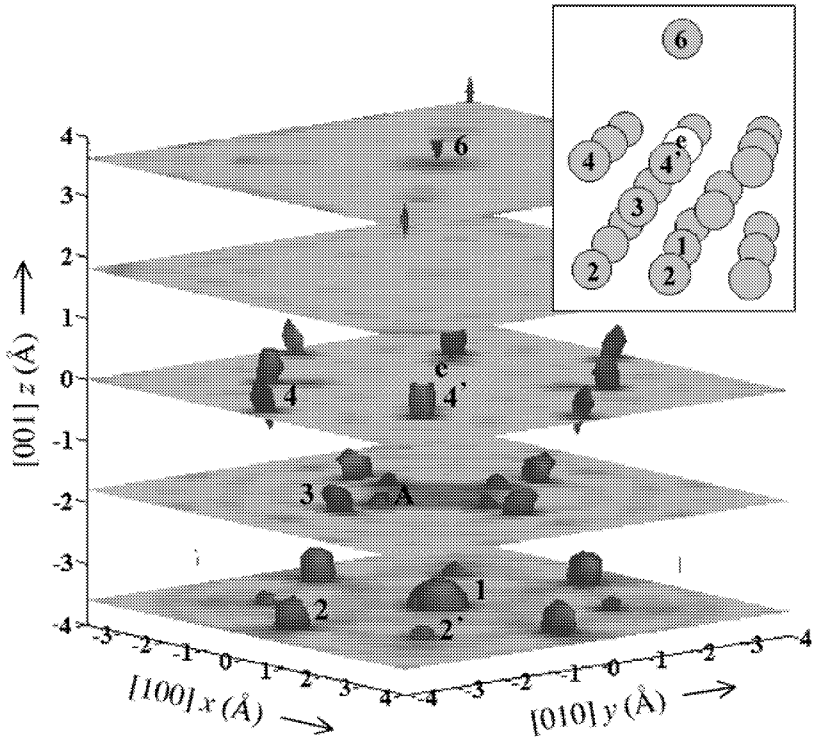

Figure 4. Three-dimensional Cu(001) atomic image reconstructed from the experimental holograms by method D—differential holography with a 3D I_0 function. Image intensities above $z_c = 0.5$ Å have been multiplied by a factor of 4, and isosurfaces at 50% of the maximum intensity are shown together with five slices at $z = 0$ (the emitter plane), ± 1.81 (the first nearest layers) and ± 3.62 Å (the second nearest layers). Reconstructed forward-, side- and back-scattering atoms are numbered, and the corresponding atoms in the crystal model are indicated in the inset. Only the four features labelled A inside the atomic peaks 3 are weak artefacts that cannot be connected with a specific atom.

reasonably well imaged, with only a few, such as 2, being significantly shifted in position, but most within a few tenths of an Å of the correct positions in all directions. Even though four weaker artefacts (labelled A in figure 4) are observed at radii inside of the positions of atoms 3, the three-dimensional image quality is much higher than any of the previous PH images of bulk substrate emission [5, 7].

The experimental images in figure 5 permit a direct comparison of methods A–D in three dimensions, and confirm our earlier comments concerning the relative importance of back, side, and FS atoms, and the superiority of the DPH image.

In conclusion, DPH provides an effective method for reducing FS artefacts in images and significantly improves the imaging of back and SS atoms. With an appropriate choice of the energy difference and $\boldsymbol{k}$-space sampling used, FS atoms should also be imaged more accurately by this method. This method should also be helpful in reducing FS artefacts in other types of electron holography in which energy can be stepped in a controlled way, as e.g. in Kikuchi [9] or LEED [10] holography.

Finally, we for completeness point out briefly a couple of other promising methods that have been suggested by other groups for reducing FS effects and improving images in photoelectron holography.

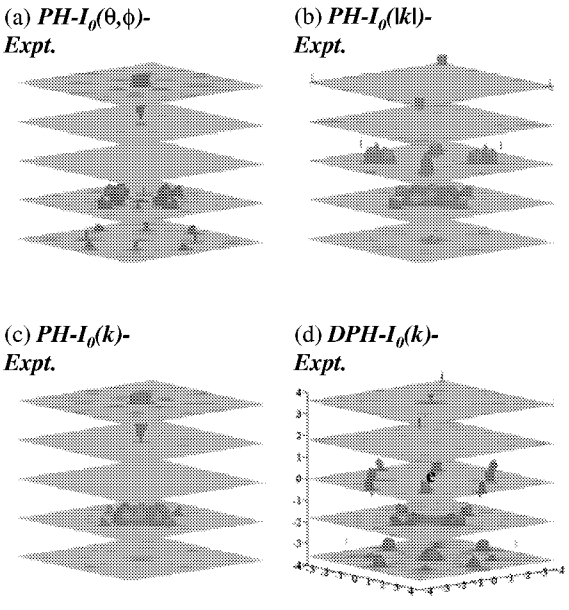

Figure 5. As figure 4, but for all four experimental image cases considered in figures 3(a)–(d).

- *Near-node photoelectron holography.* In this method, as suggested by Greber and Osterwalder [19] and recently demonstrated experimentally by Wider *et al* [29], the experimental geometry is chosen so that the polarization vector is nearly perpendicular to the electron emission direction. Thus, if the photoelectric cross section is roughly p-like (as is rigorously true for dipolar emission from an s-subshell), the strength of the wave emitted in the FS direction is reduced, and significant improvement in imaging BS, SS and FS atoms has been seen in images produced by Al 2s emission from Al(111) [29]. This method requires using a special experimental geometry, and is most effective for s-subshell emission, although many non-s subshells have roughly p-like cross sections at higher photon energies.
- *Circular dichroism in photoelectron holography.* In one method of this type suggested by Daimon *et al* [30], advantage is taken of the fact that photoelectron diffraction features tend to be 'rotated' to the left or right if excited by left or right circularly polarized radiation [31]. The degree of rotation is in first approximation inversely proportional to the distance to the scatterer producing a given peak, and thus a kind of stereoscopic image of the near-neighbour environment can be obtained [30]. In another variant of this, it has been pointed out by Oelsner and Fecher [32] that taking a difference of two holograms obtained with left and right circularly polarized radiation and using this difference in an inversion formula analogous to equation (5) can produce accurate single-energy atomic images, with the theoretical reasons for this being discussed in some detail.

4. Resonant x-ray fluorescence holography (RXFH)

Since Szöke's original suggestion of x-ray fluorescence holography (XFH) as one of the possible inner-source holographies [33], the technique has been pursued first via theoretical feasibility studies [11], and then developed experimentally in both normal [34] and inverse modes [35]. Review articles discussing the first experiments and some likely future directions have also appeared [36, 37]. As examples of the current status of XFH, more recent work

has demonstrated the ability to image up to 100 atoms in a volume of (10 Å)^3 surrounding a given emitter and to see a low-Z atom in the presence of a high-Z atom [38], and to image the local environment in a quasi-crystal lacking long-range periodicity [39]. It has also been shown previously that the local environment of a dopant at the $\sim$0.1% level can be successfully imaged in a semiconductor lattice [40].

Even though XFH in either of the two original modes thus offers a powerful method to probe the local atomic structure around a given atom, it still lacked a key ingredient of the 'ideal' probe: the technique may be element-specific for the central atom in the structure, but there was no simple way to determine the near-neighbour atomic identities. Use can be made of the differences in x-ray scattering strengths between different atoms, but this is only unambiguous when the atomic numbers are very different. It has thus recently been proposed, based on theoretical simulations, to perform resonant x-ray fluorescence holography (RXFH) so as to permit the direct imaging of atoms of a preselected type in solids [17]. This new variant of XFH thus should provide a unique way to determine chemical order and disorder around a given type of atom, through spectroscopic 'true colour' selection. RXFH thus represents an important improvement to XFH in the inverse mode (often termed multi-energy x-ray holography (MEXH) [12]), which should enable the direct discrimination of different atoms in reconstructed images even for the most difficult cases where the atomic numbers of elements involved are very close together.

The principle of RXFH is discussed here with the example of a binary compound with close atomic numbers. As noted above, a considerable amount of experimental work on MEXH has so far demonstrated that atomic images of this kind of crystal can be obtained with reasonable accuracy and resolution without special difficulties by using state-of-the-art facilities based on third-generation synchrotron sources [41]. Thus, it should be technically possible to obtain additional information on the chemical identities of such atomic images that can lead to more complete structural characterization of the crystal.

To illustrate the method, we first label the central atom of the reconstructed images to be of type A: this is the fluorescing atom. The incident photon energy is then tuned across a strong core absorption resonance of some other atom in the lattice that we label B, so that the scattering factor of atom B changes rapidly. The anomalous dispersion for element B which occurs in passing over the absorption resonance is then used to image only atoms of type B. In RXFH, holograms are thus measured at a few energies in the vicinity of the absorption edge of element B, $E^{\mathrm{B}}_{\mathrm{abs}}$.

As an example, we consider the compound $FeNi_3$ with A = Fe and B = Ni. Figure 6 shows the real and imaginary parts of the corresponding scattering factors $f^{\mathrm{A}}(0)$ and $f^{\mathrm{B}}(0)$ in the FS direction, in the vicinity of the K absorption edge of Ni. A choice of three energies for RXFH is also indicated, with these spanning a small energy region ($\Delta E = 197$ eV) around $E^{\mathrm{B}}_{\mathrm{abs}}$ (8333 eV). It is seen that as the energy is swept across $E^{\mathrm{B}}_{\mathrm{abs}}$, the atomic scattering factor $f^{\mathrm{B}}(0)$ of element B changes drastically, while $f^{\mathrm{A}}(0)$ remains nearly constant, because $E^{\mathrm{A}}_{\mathrm{abs}}$ is far outside of this energy range (but still close enough to induce Fe Kα radiation sufficient for realistic experiments).

The portions of an *incident* x-ray wave scattered by atoms constitute the object waves in this inverse form of x-ray fluorescence holography, and they interfere with the unscattered portion of the incident reference-wave to give rise to an interference field at atom A inside the crystal. Since $E > E^{\mathrm{A}}_{\mathrm{abs}}$ (7112 eV), the total strength of the wave field at the atomic positions of element A can be measured by integrating fluorescent x-rays from A over a large solid angle. Thus, an x-ray hologram with the central atom A can be obtained at each energy by recording the intensity $I(k, \theta, \phi)$ of fluorescent x-rays as a function of the x-ray incident direction and then normalizing I by the smooth background intensity I_0, numerically derived

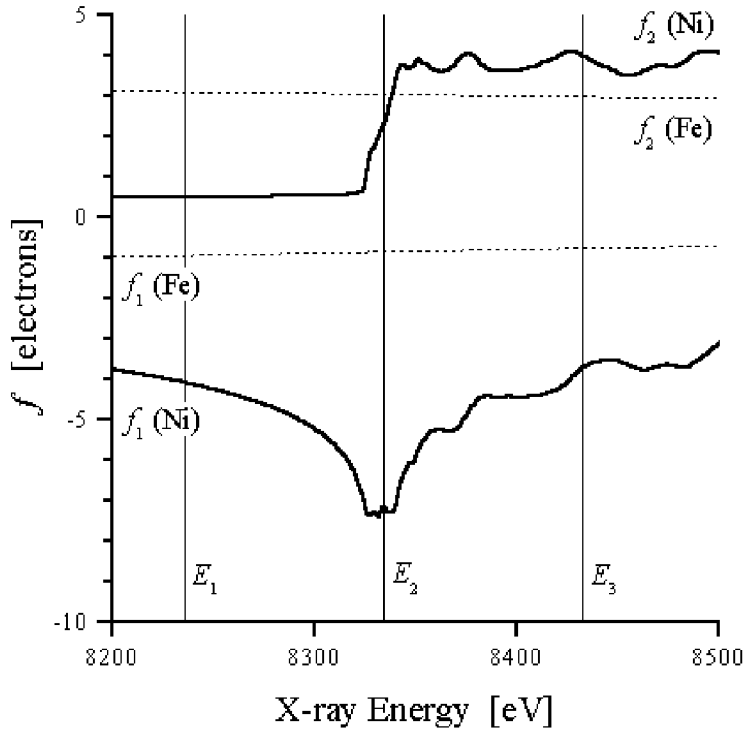

Figure 6. X-ray scattering factors in the forward direction for Fe (dotted lines) and Ni (solid curves) atoms as a function of x-ray energy around the K edge of Ni. The real and imaginary parts are denoted as f_1 and f_2, respectively, and the real parts are shifted down by the atomic numbers. Three energies used for the MEXH and RXFH simulations, E_1, E_2 and E_3, are indicated by vertical solid lines and correspond to 8235 eV ($k = 4.17$ Å^{-1}), 8334 eV ($k = 4.22$ Å^{-1}) and 8433 eV ($k = 4.27$ Å^{-1}), respectively.

from I, as $\chi\,(k, \theta, \phi) = (I - I_0)\,/I_0$. The contribution to the recorded holograms from atoms of type A can be largely cancelled out by taking the difference of two holograms at energies close to $E^{\mathrm{B}}_{\mathrm{abs}}$, while such a differential hologram will receive relatively strong contributions from atoms B resulting from the rapid change in f^{B}.

To more quantitatively develop the holographic transform appropriate for RXFH, the mathematical expression for the differential x-ray hologram in MEXH [17] is discussed next. For simplicity, we consider the normalized hologram χ for a scatterer–absorber pair, which is equivalent to equation (4) but in slightly different form:

$$\chi\,(\boldsymbol{k}) = \frac{f\left(k, \theta^k_R\right)}{R} \exp\left[\mathrm{i}kR - \mathrm{i}\boldsymbol{k}\cdot\boldsymbol{R}\right] + \mathrm{c.c.} \tag{6}$$

where $\boldsymbol{R}$ is the scatterer position, and θ^k_R is the scattering angle between $\boldsymbol{k}$ and $\boldsymbol{R}$. The difference between two holograms at $k_\pm = k \pm \delta k/2$ is given in a form similar to equation (6) but using an effective scattering factor, just as that discussed for DPH above [16, 27]:

$$\delta\chi\,(\boldsymbol{k}) = \frac{f^{\mathrm{eff}}\left(k, \theta^k_R\right)}{R} \exp\left[\mathrm{i}kR - \mathrm{i}\boldsymbol{k}\cdot\boldsymbol{R}\right] + \mathrm{c.c.} \tag{7}$$

and with a more accurate form for the effective scattering factor due to the possibility now of

a non-negligible change in f in crossing a resonance:

$$f^{\text{eff}}\left(k,\theta_{\boldsymbol{R}}^{k}\right)=\delta f\exp\left[\mathrm{i}\frac{\delta k}{2}\left(R-\hat{\boldsymbol{k}}\cdot\boldsymbol{R}\right)\right]+2\mathrm{i}f\left(k_{-},\theta_{\boldsymbol{R}}^{k}\right)\sin\left[\frac{\delta k}{2}\left(R-\hat{\boldsymbol{k}}\cdot\boldsymbol{R}\right)\right]. \tag{8}$$

Equation (8) shows two contributions to $\delta\chi$. The first is due to the change in the scattering factor δf, which can appear even for the smallest δk if there is any abrupt change in f, as at the absorption edge: this term is exploited in RXFH. The second contribution is significant even when δf is nearly zero as long as δk is finite: as discussed earlier, it is used in DPH. In fact, $f^{\text{eff}}=\delta f$ in the limit of $\delta k\to 0$, so that $\delta\chi$ contains structural information about only the resonant species, as measured relative to the central A atom.

In trying to do element-specific imaging via this approach, we first note that the form of the x-ray-atom scattering factor is in general

$$f\left(k,\theta_{\boldsymbol{R}}^{k}\right)=f_{\text{Atom}}\times f_{\text{Thomson}}=\left[f_{0}\left(\theta_{\boldsymbol{R}}^{k}\right)+f_{1}-\mathrm{i}f_{2}\right]\times f_{\text{Thomson}}\left(\theta_{\varepsilon}^{k}\right) \tag{9}$$

where f_{Atom} is the atomic scattering factor, f_{Thomson} is the polarization-dependent Thomson scattering factor, θ_{ε}^{k} is the angle between the scattered x-ray and the light polarization (here assumed linear), f_0 is the tabulated atomic form factor, and f_1 and f_2 are the real (refractive) and imaginary (absorptive) parts of the atomic scattering factor, respectively [42]. The terms f_1 and f_2 are the only quantities which vary strongly with photon energy. One can thus try to exploit the change in f_1, the change in f_2, or both. It is clear from figure 6 that the variations are more gradual in the real part than in the imaginary part, with f_1 showing a broad dip near the resonance that sets in before the K absorption edge for Ni is actually reached, and f_2 showing an abrupt jump right at the edge. To use the variation in the real part, one could use the relatively wide energy spacing shown in figure 6, and contrast holograms taken at one or two off-resonance energies with a hologram taken at the resonance energy. This choice appears to be better than trying to exploit the variation in the imaginary part. In this latter case, two energies should be chosen just below and above $E_{\text{abs}}^{\text{B}}$, so that $\delta f^{\text{A}}\approx 0$ and $\delta f^{\text{B}}\approx -\mathrm{i}\delta f_{2}^{\text{B}}$; while this scheme works in principle, it is found that a very high, but still realistic, signal-to-noise ratio would be required. Thus, although both approaches should probably work in future experiments, we will here focus on using the change in the real part, which appears somewhat easier to achieve in the laboratory.

In the three-energy case shown in figure 6, two differential holograms, $\delta\chi_1=\chi_2-\chi_1$ and $\delta\chi_2=\chi_3-\chi_2$, are obtained from normal holograms at the three energies. The two differential holograms are then summed for extra signal. However, since the change in the real part of the scattering factor f_1^{B} has opposite signs on either side of $E_{\text{abs}}^{\text{B}}$, the differences $\delta\chi_1$ and $\delta\chi_2$ also tend to change signs and would largely cancel out in the sum. Therefore we include a sign $\sigma(k-k_{\text{abs}}^{\text{B}})$ to compensate for this:

$$U\left(\boldsymbol{r}\right)=\int k^{2}\,\mathrm{d}k\,\sigma\left(k-k_{\text{abs}}^{\text{B}}\right)\int\delta\chi\left(\boldsymbol{k}\right)\exp\left[\mathrm{i}\boldsymbol{k}\cdot\boldsymbol{r}\right]\mathrm{d}^{2}\hat{\boldsymbol{k}} \tag{10}$$

where $\sigma\left(k-k_{\text{abs}}^{\text{B}}\right)=+1$ for $k>k_{\text{abs}}^{\text{B}}$ and $\sigma\left(k-k_{\text{abs}}^{\text{B}}\right)=-1$ for $k<k_{\text{abs}}^{\text{B}}$; here the first integral generalizes the summation to more energies, if desired. In this case, the changes δf_2^{B} in the imaginary parts above and below the edge are nearly equal (since E_2 is centred on the edge) so that their contributions nearly cancel out in equation (10). The overall resonant effect is mostly due to the change in the real part δf_1^{B}. Furthermore, that difference is comparable in magnitude to the normal atomic scattering factors of light elements such as C, N and O, with the last having recently been imaged by MEXH [38, 39]. By comparison, the contributions from atoms A are greatly reduced; thus, we have reason to believe that such an element-specific contrasted image should be achievable experimentally. It is also easy to show that if either f or f^{eff} is real, the real part of U has a negative peak at the atomic position [42]. Therefore, we

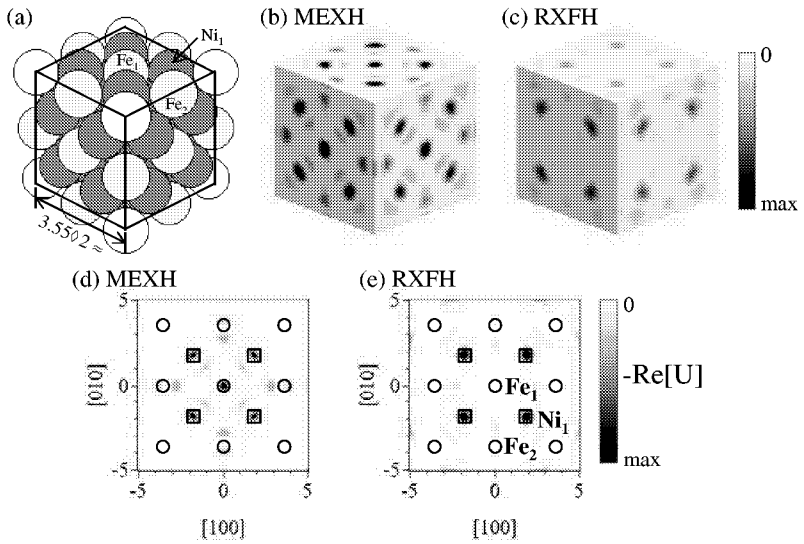

Figure 7. Comparison of multiple-energy x-ray holography (MEXH) and resonant x-ray fluorescence holography (RXFH) based on single-scattering simulations for the $FeNi_3$ crystal. (a) Crystal model of $FeNi_3$ corresponding to the reconstructed images in (b) and (c) and including eight unit cells with the lattice constant of 3.55 Å. The Fe and Ni atoms observed in (b) (marked as Fe_1, Fe_2 and Ni_1) are shown as thin and thick gray circles, respectively, while the Fe atoms not observed in (b) are shown as open circles. (b) Three dimensional reconstructed image from MEXH sliced along six {001} planes. (c) Corresponding image from RXFH. The fluorescing Fe atom is located at the centre of the cubes in (b) and (c). (d) Enlarged reconstructed image from MEXH in the (001) plane. (e) Corresponding enlarged image from RXFH. The true atomic positions of Fe and Ni atoms are shown as circles and squares, respectively, with some key atoms labelled.

have used the negative real part of $U = -\mathrm{Re}\,[U]$ for presenting the reconstructed images in the following, further showing only those parts of this image function that are positive to conform to theoretical expectations: thus, if Re [U] > 0, image $U = 0$, and if Re [U] < 0, U $= -$Re [U].

To quantitatively demonstrate RXFH, x-ray holograms were simulated for the $FeNi_3$ model crystal, which has the fcc structure with Fe atoms at all corners of the cubic unit cell (see figure 7(a)). The simulations use a single-scattering cluster model that is suitable for this application [28]. The spherical cluster has a radius of 30 Å, which includes a fluorescing Fe atom at the centre and approximately 10 000 scatterers. The lattice constant is that for the ordered phase of $FeNi_3$ (3.55 Å). The non-resonant scattering factors $f_0\left(\theta_R^k\right)$ were calculated from the standard tables [43]. The anomalous dispersion corrections for Ni were calculated from the experimental absorption coefficient of Ni [44] by using the computer code developed by Newville and Cross [45], while the slowly varying values for Fe were taken from another database [35]. A hologram at each of the three energies shown in figure 6 was calculated over the full solid angle of 4π steradians with a step width of 3° for both polar and azimuthal scans. Although it is usually impossible to measure a hologram over the full solid angle, in many cases, a measured hologram can be extended over the full solid angle by using the symmetry of the crystal (e.g. inversion symmetry, as is the case for $FeNi_3$), thereby improving the image resolution along the vertical direction. The image resolution and the maximum radius within which the image is reliable for this k-space sampling are expected to be approximately 0.7 and 18 Å, respectively [28].

Three-dimensional atomic images have been reconstructed from the theoretical holograms by both the original MEXH algorithm and the RXFH algorithm based on equation (10), and

are shown in figures 7(b) and (c), respectively. The MEXH image in figure 7(b) yields five Fe peaks and four Ni peaks at the respective sites of these atoms on each crystal plane. The atomic peaks for Fe denoted as Fe_2 in the figure appear to be split into two parts. Such peak splitting is often observed in single-energy holography, and since we have used only three energies here, this could explain this type of image aberration. Nonetheless, all the atomic peaks observed are fairly well resolved, and their positions are close to the true positions, but of course without clear distinction between Fe and Ni. On the other hand, in figure 7(c), using the contrasting mechanism of RXFH, the atomic peaks for Fe are almost completely suppressed, while the peaks for Ni are clearly visible. In figures 7(d) and (e), a more detailed comparison between MEXH and RXFH is presented. This shows that RXFH can very effectively discriminate between two species with close atomic numbers and reveals the chemical order around the fluorescing atom. The maximum image intensity for Ni in RXFH is approximately 18% of that in MEXH. This confirms the previous argument, based on the dispersion curve of f_1, that the experimental challenge associated with RXFH can be comparable to that in MEXH for light elements such as C, N and O, and that RXFH should thus be feasible with current third-generation synchrotron radiation capabilities.

Thus, the RXFH scheme has been demonstrated theoretically and awaits demonstration experimentally. To enhance the resonant effects and suppress the contributions from non-resonant species, the choice of incident x-ray energies is extremely important. From the experimental point of view, the signal-to-noise ratio of the hologram is the most important factor. The accuracy in tuning x-ray energies is also critical. Our simulations show that RXFH should be successful in selectively imaging a single species of atom in a compound. Therefore, not only the atomic arrangement but also the chemical order around each atom can be determined by comparing the reconstructed images via MEXH and RXFH. This technique should be particularly useful for studying such issues as the structural environment of dopant atoms in compound semiconductors and complex oxides, and the order–disorder transition of alloys; and it may ultimately find use in studies of active sites in biological molecules.

Acknowledgments

This work was supported in part by the Director, Office of Science, Office of Basic Energy Sciences, Division of Materials Sciences, of the US Department of Energy under contract no DE-AC03-76SF00098. SO also acknowledges the support of the Japan Society for the Promotion of Science (grant no JSPS-RFTF 98R14101).

References

[1] Szöke A 1986 *Short Wavelength Coherent Radiation: Generation and Applications (AIP Conf. Proc. No. 147)* ed D T Attwood and J Boker (New York: AIP) p 361
[2] Barton J J 1988 *Phys. Rev. Lett.* **61** 1356
[3] Barton J J 1991 *Phys. Rev. Lett.* **67** 3106
Barton J J and Terminello L J 1991 *Structure of Surfaces* vol 3, ed S Y Tong, M A Van Hove, X Xide and K Takayanagi (Berlin: Springer) p 107
Tong S Y, Li H and Huang H 1991 *Phys. Rev. Lett.* **67** 3102
[4] Tonner B P, Han Z L, Harp G R and Saldin D K 1991 *Phys. Rev.* B **43** 14 423
[5] Terminello L J, Barton J J and Lapiano-Smith D A 1993 *Phys. Rev. Lett.* **70** 599
[6] Tong S Y, Li H and Huang H 1995 *Phys. Rev.* B **51** 1850
Wu H and Lapeyre G J 1995 *Phys. Rev.* B **51** 14 549
[7] Len P M, Denlinger J D, Rotenberg E, Kevan S D, Tonner B P, Chen Y, Van Hove M A and Fadley C S 1999 *Phys. Rev.* B **59** 5857
[8] Saldin D K, Harp G R and Chen X 1993 *Phys. Rev.* B **48** 8234

[9] Wei C M, Hong I H and Chou Y C 1994 *Surf. Rev. Lett.* **1** 335
[10] Saldin D K and de Andres P L 1990 *Phys. Rev. Lett.* **64** 1270
Reuter K, Vamvakas J A, Saldin D K, Blum V, Ott M, Wedler H, Döll R and Heinz K 1998 *Phys. Rev.* B **58** 4102
[11] Tegze M and Faigel G 1991 *Europhys. Lett.* **16** 41
Len P M, Thevuthasan S, Fadley C S, Kaduwela A P and Van Hove M A 1994 *Phys. Rev.* B **50** 11 275
[12] Gog T, Len P M, Materlik G, Bahr D, Sanchez-Hanke C and Fadley C S 1996 *Phys. Rev. Lett.* **76** 3132
[13] Korecki P, Korecki J and Ślezak T 1997 *Phys. Rev. Lett.* **79** 3518
[14] Bompadre S G, Petersen T W and Sorensen L B 1999 *Phys. Rev. Lett.* **83** 2741
[15] Kaduwela A P, Wang Z, Thevuthasan S, Van Hove M A and Fadley C S 1994 *Phys. Rev.* B **50** 9656
[16] Omori S, Nihei Y, Rotenberg E, Denlinger J D, Kevan S D, Tonner B P, Van Hove M A and Fadley C S *Phys. Rev. Lett.* at press
[17] Omori S, Zhao L, Marchesini S, Van Hove M A and Fadley C S *Phys. Rev.* B at press
[18] Luh D-A, Miller T and Chiang T-C 1998 *Phys. Rev. Lett.* **81** 4160
[19] Greber T and Osterwalder J 1996 *Chem. Phys. Lett.* **256** 653
[20] Sinkovic B, Hermsmeier B D and Fadley C S 1985 *Phys. Rev. Lett.* **55** 1227
Hermsmeier B D, Osterwalder J, Friedman D J and Fadley C S 1989 *Phys. Rev. Lett.* **62** 478
Hermsmeier B, Osterwalder J, Friedman D J, Sinkovic B, Tran T and Fadley C S 1990 *Phys. Rev.* B **42** 11 895
[21] Tober E D, Palomares F J, Ynzunza R X, Denecke R, Morais J, Wang Z, Biino G, Liesegang J, Hussain Z and Fadley C S 1998 *Phys. Rev. Lett.* **81** 2360
[22] Starke K, Kaduwela A P, Liu Y, Johnson P D, Van Hove M A, Fadley C S, Chakarian V, Chaban E E, Meigs G and Chen C T 1996 *Phys. Rev.* B **53** R10 544
[23] Fadley C S *et al* 1997 *Prog. Surf. Sci.* **54** 341
[24] Chen Y, García de Abajo F J, Chassé A, Ynzunza R X, Kaduwela A P, Van Hove M A and Fadley C S 1998 *Phys. Rev.* B **58** 13 121
[25] Timmermans E M E, Trammell G T and Hannon J P 1994 *Phys. Rev. Lett.* **72** 832
Timmermans E M E, Trammell G T and Hannon J P 1993 *J. Appl. Phys.* **73** 6183
[26] Fadley C S 1993 *Surf. Sci. Rep.* **19** 231
[27] Omori S, Kozakai T and Nihei Y 1999 *Surf. Rev. Lett.* **6** 1085
[28] Len P M 1997 *PhD Thesis* University of California, Davis
[29] Wider J, Baumberger F, Sambi M, Gotter R, Verdini A, Bruno F, Cvetko D, Morgante A, Greber T and Osterwalder J 2001 *Phys. Rev. Lett.* **86** 2337
[30] Daimon H 2001 *Phys. Rev. Lett.* **86** 2034
[31] Daimon H, Nakatani T, Imada S, Suga S, Kagoshima Y and Miyahara T 1993 *Japan. J. Appl. Phys.* **32** 1480
Westphal C, Kaduwela A P, Fadley C S and Van Hove M A 1994 *Phys. Rev.* B **50** 6203
Kaduwela A P, Xiao H, Thevuthasan S, Fadley C S and Van Hove M A 1995 *Phys. Rev.* B **52** 14 297
Ynzunza R X *et al* 2000 *J. Electron Spectrosc.* **106** 7
[32] Oelsner A and Fecher G 1999 *J. Electron Spectrosc. Relat. Phenon.* **101–3** 455
[33] Gabor D 1948 *Nature* **161** 777
[34] Tegze M and Faigel G 1996 *Nature* **380** 49
Kawai J, Hayashi K, Yamamoto T, Hayakawa S and Gohshi Y 1998 *Anal. Sci.* **14** 903
Hiort T, Novikov D V, Kossel E and Materlik G 2000 *Phys. Rev.* B **61** R830
[35] http://www-cxro.lbl.gov/optical_constants/asf.html
[36] Len P M, Fadley C S and Materlik G 1997 *X-ray and Inner-Shell Processes: 17th Int. Conf. (AIP Conf. Proc. No. 389)* ed R L Johnson, H Schmidt-Boeckering and B F Sonntag (New York: AIP) pp 295–319
[37] Faigel G and Tegze M 1999 *Rep. Prog. Phys.* **62** 355–93
[38] Tegze M, Faigel G, Marchesini S, Belakhovsky M and Ulrich O 2000 *Nature* **407** 38
[39] Marchesini S, Schmithüsen F, Tegze M, Faigel G, Calvayrac Y, Belakhovsky M, Chevrier J and Simionovici A S 2000 *Phys. Rev. Lett.* **85** 4723
[40] Hayashi K, Yamamoto T, Kawai J, Suzuki M, Goto S, Hayakawa S, Sakurai K and Gohshi Y 1998 *Anal. Sci.* **14** 987
[41] Marchesini S, Ulrich O, Faigel G, Tegze M, Belakhovsky M and Simionovici A S 2001 *Nucl. Instrum. Methods* A **457** 601
[42] Attwood D T 1999 *Soft X-rays and Extreme Ultraviolet Radiation* (Cambridge: Cambridge University Press) pp 52, 39
[43] C H Macgillavry, G D Rieck and K Lonsdale (ed) 1968 *International Tables for X-ray Crystallography* vol 3 (Birmingham: Kynoch) p 201
[44] http://ixs.csrri.iit.edu/database/
[45] http://cars.uchicago/~newville/dafs/difkk/

INSTITUTE OF PHYSICS PUBLISHING JOURNAL OF PHYSICS: CONDENSED MATTER

J. Phys.: Condens. Matter **14** (2002) L407–L420 PII: S0953-8984(02)36888-7

LETTER TO THE EDITOR

Probing buried interfaces with soft x-ray standing wave spectroscopy: application to the Fe/Cr interface

See-Hun Yang[1], Bongjin S Mun[1,2], Norman Mannella[1,2], Sang-Koog Kim[3], Jeffrey B Kortright[1], James Underwood[1], Farhad Salmassi[1], Elke Arenholz[4], Anthony Young[4], Zahid Hussain[4], Michel A Van Hove[1,2] and Charles S Fadley[1,2,5]

[1] Materials Sciences Division, Lawrence Berkeley Laboratory, Berkeley, CA 94720, USA
[2] Department of Physics, University of California at Davis, Davis, CA 95016, USA
[3] School of Materials Science and Engineering, College of Engineering Seoul National University, Seoul 151-744, Korea
[4] Advanced Light Source, Lawrence Berkeley Laboratory, Berkeley, CA 94720, USA
[5] Department of Physics, University of Hawaii, Honolulu, HI 96822, USA

Received 13 May 2002
Published 30 May 2002
Online at stacks.iop.org/JPhysCM/14/L407

Abstract

The nanometre-scale materials and devices that are under ever more intense study at present often depend for their unique properties on buried interfaces between two phases. Yet the number of experimental techniques that can specifically probe such interfaces, particularly with magnetic sensitivity, is limited. We here report a novel type of non-destructive method for spectroscopically studying buried nanometre-scale interfaces and other nanostructures with soft x-ray standing waves. Strong standing waves with a period of 4.0 nm and approximately 3:1 contrast ratios are created via Bragg reflection from a synthetic multilayer of form $[B_4C/W]_{40}$. By growing a wedge-shaped Fe/Cr bilayer on top of this multilayer, the mechanical translation of the bilayer exposed to a fixed and finely focused synchrotron radiation beam is converted into a translation of the standing wave through the interface. Analysing various core photoelectron intensities as a function of angle and beam position permits derivation of layer thicknesses and interface mixing/roughness scales. Magnetic circular dichroism in photoemission from the 2p and 3p levels of Fe and Cr further permits derivation of the positions and widths of regions with decreased (increased) ferromagnetic alignment for Fe (Cr), showing that normally antiferromagnetic Cr becomes ferromagnetic just below the centre of the interface but with antiparallel alignment with respect to Fe, and that the equal-concentration region in the centre of the interface strongly inhibits magnetic alignment for both species along the direction of net magnetizations that is probed. The magnetically altered regions in both metals are only 1–2 atomic layers in thickness. 3s spectra from Fe and Cr further indicate that the local spin moments on both atoms do not change on crossing the interface. This standing-wave-plus-wedge method should have a range of applications for the characterization of nanostructures and their interfaces.

(Some figures in this article are in colour only in the electronic version)

Many current technological devices consist of layered or sandwich structures, the thickness of whose composite layers is either already in the nanometre (10 Å) range or in the process of shrinking into the nanometre range. These devices include transistors in integrated circuits, solid-state lasers and magnetic elements for storing information and for reading it out. Such interfaces may exhibit intermixing of the components on either side and/or roughness, as well as altered chemical states or states of magnetic order, and their exact nature can affect ultimate properties such as electrical conductivity or magnetic stability in a profound way. As one example of such nanostructures in magnetism, the phenomenon of giant magnetoresistance (GMR) is based on the change in resistance in a sandwich structure consisting of alternating non-magnetic and magnetic layers upon being exposed to an external magnetic field [1, 2]. GMR is today used routinely in the read heads for highest-density information storage, where it is usually combined with another interface-driven effect, exchange biasing [3]. Magnetic tunnel junctions have similar properties and are promising for magnetic random access memory and terabyte-scale hard disk storage device applications [4]. Since interfaces are believed to play a pivotal role in the behaviour of all of these effects, extensive theoretical and experimental work has been carried out in order to unveil the physical and chemical nature of them [1–4]; nonetheless, many fundamental questions remain. Numerous other examples of important interfaces are found, for example in semiconductor science and technology. Beyond this are also various nanometre-scale tubes, wires and clusters which can have buried or hidden interfaces where they make contact with some kind of supporting substrate or with themselves.

It is thus of interest to develop new, non-destructive, element-specific, spectroscopic tools for studying the buried interfaces in such nanostructures. Some of the questions to answer with such a probe are: What are the positions and thicknesses of the compositional intermixing or magnetic transition layers across the interface? What is the roughness of the interface, both chemical and magnetic? What are the chemical and magnetic states of the various atoms involved as a function of position perpendicular to the interface? How does the valence electronic structure and density of electronic states vary across the interface? How does both the short-range and long-range magnetic order depend on position relative to the interface?

Some of these questions can be answered at least partially using currently available methods, and we briefly mention a few of these. One powerful method is scanning transmission electron microscopy (STEM) with electron energy loss spectroscopy (EELS) [5], but this technique requires specialized sample slicing and thinning and thus cannot be considered non-destructive, and in its most sophisticated element-specific form with EELS still cannot provide both element specificity and magnetic sensitivity at the sub-nanometre scale. Hard x-rays in the 5–10 keV range can be reflected from buried interfaces and planar multilayer nanostructures so as to set up standing waves that may permit depth-dependent composition, structure and, via variable light polarization or magnetization direction, also magnetism near buried interfaces to be derived [6,7]. But these hard x-ray measurements are limited as to both energy resolution and spectroscopic characterization, and also may due to their shorter wavelengths ($\sim$1–2 Å) exhibit interference structures from atomic lattice planes that can be much smaller than the nanometre scale it is desired to probe. Another method uses total reflection of soft x-rays in the 0.5–1.5 keV range from a buried interface by tuning the photon energy to a core-level absorption edge [8], and this can determine both chemical and magnetic roughness by working with both right and left circularly polarized radiation (RCP and LCP, respectively) and/or flipping the sample magnetization $\vec{M}$ between two orientations 1 and 2 and measuring a magnetic asymmetry in diffuse reflectivity as $\Delta R_{MCD} \propto R_{RCP} - R_{LCP}$ or $\propto R_{M1} - R_{M2}$. However, this method does not permit detailed spectroscopic studies (e.g. via photoelectron emission) of the buried interface. Finally, soft x-ray spectromicroscopy using secondary electrons as the detecting

medium can achieve some sensitivity to buried interfaces, provided that there are sufficient chemical fingerprints in the x-ray absorption signal to deconvolve the interface contributions to images [9]. However, any method using lower-energy electrons to study buried interfaces is inherently limited by the short inelastic attenuation lengths in the 1–5 nm range, which strongly attenuate the signals.

We here focus on a novel approach making use of photoelectrons (or in future applications also fluorescent soft x-rays) excited by strong *soft x-ray* standing waves that are set up in Bragg reflection from a synthetic multilayer structure of a few nanometres in periodicity. This multilayer is in turn used as the substrate and sample preparation surface in the experiment. Soft x-rays in the 0.5–1.5 keV range have much higher cross sections for exciting outer-shell photoelectrons or fluorescent x-rays than harder x-rays, and these can in turn be analysed with resolutions in the $1{:}10^3$ or $1{:}10^4$ range via suitable spectrometers. By either varying the angle of incidence around the Bragg angle or varying the thickness of the sample on top of the multilayer, the standing wave and the spectroscopy which it excites can effectively be scanned through the interface, thus providing additional depth sensitivity and a method for non-destructively probing chemical composition, chemical state, structure and magnetism through a given interface. Some preliminary aspects of this soft x-ray standing wave approach involving both photoelectron emission [10] and x-ray absorption [11] have been discussed recently. In the present work, we add two key elements: a wedge-shaped (tapered) sample to provide the most unambiguous method of probing the interface, and measurements including magnetic circular dichroism (MCD) and spin-sensitive core-level spectroscopy.

Our basic approach is illustrated in figure 1(a) for the specific example of an Fe/Cr bilayer grown on a B_4C/W multilayer structure consisting of 40 bilayers of period $d = 40.5$ Å. A beam of monochromatized soft x-ray synchrotron radiation at 825.0 eV (wavelength $\lambda_x = 15.0$ Å) emitted from a high-brightness elliptically polarized undulator at the Advanced Light Source in Berkeley is focused down to a spot of about 0.2 mm in diameter, and is incident on the surface of an Fe/Cr bilayer consisting of a wedge-shaped Cr underlayer with thickness varying from 118 Å at one end to 36 Å at the other end and an Fe overlayer with a constant thickness of 16.0 Å. Strong Bragg reflection from the planes in the multilayer will occur when the x-ray incidence angle θ_{hv} satisfies $n\lambda_x \approx 2d \sin\theta_{hv}$, with $n = 1, 2, 3, \ldots$ the order of the reflection. For the strongest reflection at $n = 1$, the resulting standing wave has a period equal to d (in our case thus 40.5 Å = 4 nm) and it will extend many nanometres above the surface of the multilayer.

We have chosen to study the Fe/Cr interface as a first demonstration case because of its importance in GMR, since multilayers of these two materials exhibit one of the highest values for magnetoresistance [1]. It is thus a prototype system for this effect, even though it is not used in actual commercial devices, and its properties have been extensively studied [12–19]. The Fe/Cr interface also is known from prior spectroscopy [12,13], scanning tunnelling microscopy (STM) [14, 15], x-ray diffraction [15] and theoretical modelling [16–18] studies to involve a variable degree of intermixing, depending on exactly how it is grown. It has also been shown from MCD studies in x-ray absorption and photoelectron emission that Cr, which is normally antiferromagnetic, becomes ferromagnetically ordered to some degree near the interface, but anti-parallel to the Fe magnetization, and from this and other work that the Cr magnetic moment may be significantly increased, at least near free surfaces as an overlayer [12, 13, 19]. Also, the degree of ferromagnetic order of Fe, or perhaps its local atomic magnetic moment, is thought to be reduced near the interface [19]. However, much prior work has involved very thin films [12, 13, 17, 19], starting with a single or partial monolayer of Cr and growing upward from there; thus, it is still not clear as to what occurs at a truly buried interface. Our goal here is to directly probe this interface with core-level photoelectron spectroscopy

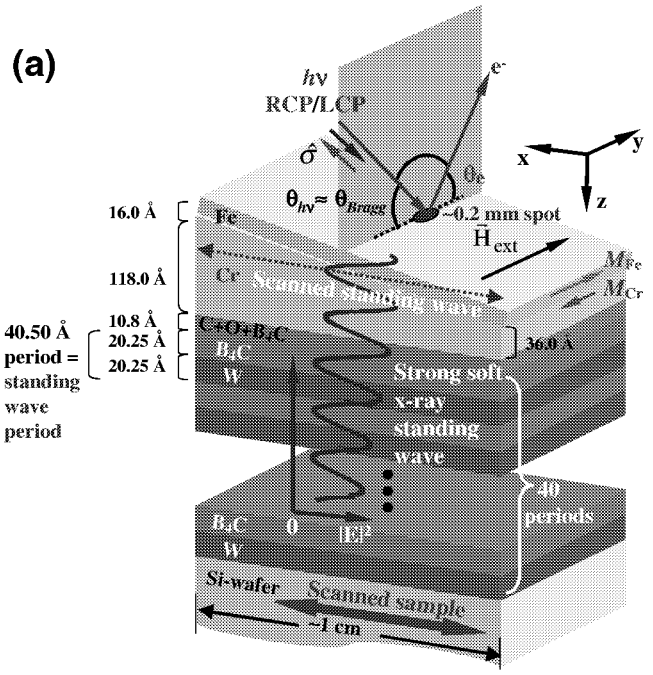

Figure 1. (a) Schematic diagram of our experimental geometry, including a wedge-shaped Fe/Cr bilayer on top of a synthetic multilayer standing wave generator. Note the Cartesian axes, with magnetization along y and the sample scanned along x. (b) Core-level photoemission intensity ratios I(Cr 3p)/I(Fe 3p) as a function of x-ray incidence angle $\theta_{h\nu}$ and Cr wedge thickness d_{Cr} (lines and symbols), together with best-fit calculations (solid curves). (c) The calculated depth-dependent electric field strength $|E|^2$ as a function of d_{Cr}, together with interdiffusion widths at various interfaces (2σ) as derived in this study. The σ for the interface between B_4C and W was determined from hard x-ray reflectometry, while the others were obtained from our analysis of soft x-ray standing-wave photoemission data (see text). Positions B and C are special in that the crest (B) and trough (C) of the standing wave are situated on the Fe–Cr interface, respectively.

as excited by a standing wave, and to make use of both Fe and Cr core spectra, as well as MCD in them, to more quantitatively study the interface compositional mixing/roughness, the individual magnetic moments on both Fe and Cr through the interface and the type and spatial distribution of magnetic order in both constituents through the interface.

Prior to evaporation of Cr and Fe, the structural parameters and reflectivities of the $[B_4C/W]_{40}$ standing-wave generator (SWG) have been measured via standard hard x-ray reflectometry at 8.05 keV, with a theoretical analysis of these data yielding the period d of 40.5 Å and a Gaussian interface interdiffusion length between the two components of $\sigma^{B4C/W} = 4.1$ Å. The top surface of the multilayer (which was air exposed before being inserted into ultrahigh vacuum for Cr and Fe deposition) was also characterized by both STM and atomic force microscopy (AFM), and found to be very smooth, with an average roughness of about 3.0 Å and a root-mean-square (RMS) roughness of about 5 Å.

Cr and Fe layers were then deposited on this top surface from Knudsen-type evaporation cells, at ambient pressures of 1–2 $\times$ 10^{-10} Torr; scanning the sample in the x-direction during growth produced the desired Cr wedge. All bilayer preparation and measurement was done in the advanced photoelectron spectrometer/diffractomer [20] situated on undulator beamline 4.0.2 at the Berkeley Advanced Light Source [21], with the beamline providing

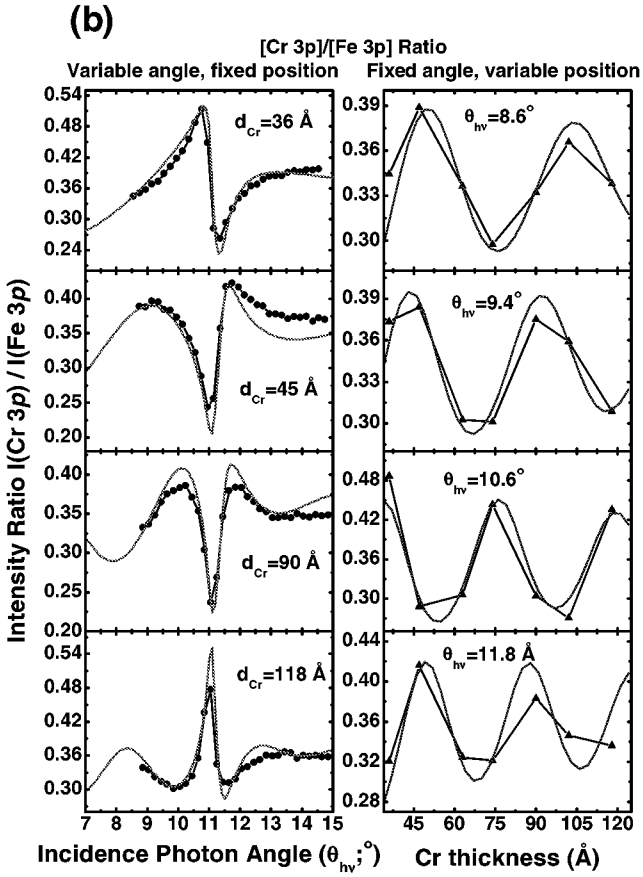

Figure 1. (Continued.)

high-brightness variable-polarization radiation in the soft x-ray range. The Cr/Fe overlayers were polycrystalline or amorphous, as verified by the lack of structure in core photoelectron diffraction patterns. The pressures during subsequent spectroscopic measurements were in the 1×10^{-10} range, with little contamination buildup on the top surface as judged by C 1s and O 1s photoelectron spectra (<2 atomic layers in 24 h). The Fe layer was initially magnetized in plane along the y direction (cf figure 1(a)) by subjecting it to an external field of about 500 Oe. The radiation polarization could be varied from linear polarized (LP) to right circular polarized (RCP) or left circular polarized (LCP) via the undulator involved [21].

As a first measurement procedure, scanning the x-ray incidence angle around the expected first-order Bragg angle for the bare multilayer or multilayer + wedge, thus tracing out its 'rocking curve', and comparing the resulting angular-dependent core-level photoelectron intensities from each constituent (Fe 2p and 3p, Cr 2p and 3p, B 1s, C 1s and W 4f) with theoretical calculations based on classical x-ray optics [10] permits determination of the Bragg angle with high accuracy. For the particular sample studied here, it is $11.05^\circ \pm 0.10^\circ$, in excellent agreement with theoretical calculations, and very close to the 10.70° calculated from the simple formula above. The discrepancy of 0.35° is due to refraction and phase shifts in the waves reflected and refracted at each of the interfaces involved, as a result of the small deviations from unity of the complex optical constants (n_i) in each layer [22]. For the

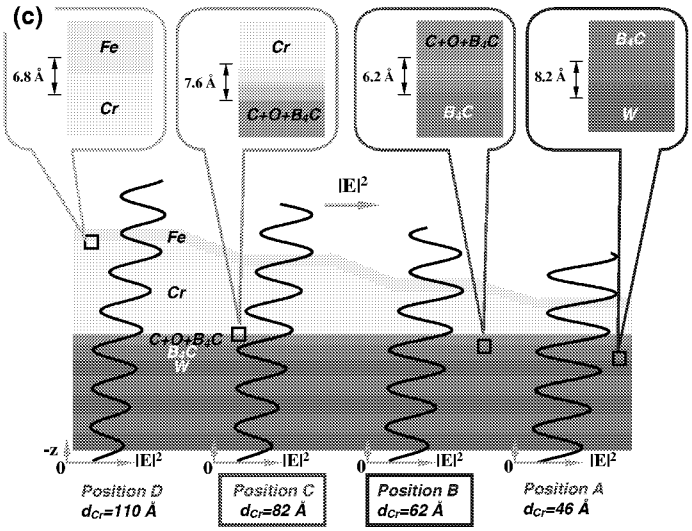

Figure 1. (Continued.)

measurements discussed here, the photon incidence angle and energy were fixed at 11.05° and 825 eV, respectively, with this energy also being far away from any Fe, Cr, B, C, W or O absorption edges.

For these conditions, we have also verified via measurements and theoretical simulations not shown here that the Bragg angle and the phase of the standing wave with respect to the top surface of the multilayer are negligibly altered by the presence of the Fe/Cr bilayer, as judged relative to a native multilayer with no overlayer on top of it [23]. Thus, as our primary measurement procedure, simply moving the sample back and forth along the axis of the slope of the wedge (the x axis in figure 1(a)) will scan the focused x-ray beam along the wedge, but with the net effect also of scanning the fixed-phase standing wave through the buried Fe/Cr interface. In this mode, the number of unknown parameters in the analysis of the data is reduced considerably, as compared, for example, with the significant changes in the standing wave if the rocking curve is instead scanned [11].

As a final characterization step after actual spectroscopic measurements, high-resolution transmission electron microscopy (HRTEM) at a resolution of about 1.6 Å was carried out at the National Center for Electron Microscopy on sections of multilayer with an Fe/Cr bilayer grown on top, with this revealing very smooth interfaces having intermixing and/or roughness over <5–8 Å.

The theoretical calculations used in analysing our photoemission data make use of a specially written computer program [23] which includes single and multiple x-ray reflections at the top surface and all buried interfaces, parametrized compositional intermixing at the interfaces of linear form, several improvements over prior programs for doing such calculations [24] and all information relevant to quantitatively calculating the depth-dependent emission of photoelectrons from the structure (e.g. differential photoelectron cross sections [25] and inelastic electron attenuation lengths [26]) once the depth-dependent exciting electric field strength squared ($\vec{E}(z)^* \cdot \vec{E}(z) = |\vec{E}(z)|^2$) is determined via x-ray optics.

As one example of the results obtained, we have analysed the core-level photoemission intensity ratio I(Cr 3p)/I(Fe 3p) as a function of both x-ray incidence angle θ_{hv} (a rocking curve)

and Cr thickness d_{Cr} so as to derive both the layer thicknesses shown in figure 1(a) and an rms interdiffusion length above the wedge sample of $\sigma^{Fe/Cr} = 3.4$ Å. We have assumed here a linear variation of composition of both species. Measured values for this photoelectron intensity ratio are shown in figure 1(b), and they are in excellent agreement with theory, finally permitting us to determine both the Fe and Cr layer thicknesses (cf figure 1(a)) and the intermixing distances with accuracies of about ±2.0 Å. Further analysing other core intensities yields a $\sigma^{Cr/C+O+B4C}$ of 3.8 Å between Cr and a surface-reacted C + O + B_4C layer of about 10 Å thickness on top of the multilayer, and $\sigma^{C+O+B4C/B4C}$ of 3.1 Å between this reacted layer and the first B_4C layer in the multilayer. The first B_4C layer thus expands by about 50% on air exposure, a result that we have independently confirmed by STEM images (not shown here) [23]. Very accurate layer thickness and interface mixing measurements are thus possible with the standing-wave photoemission technique, and the thicknesses and degrees of interface mixing are shown in figure 1(c). The final calculated standing-wave strengths $|\vec{E}(z)|^2$ in this particular multilayer + bilayer are also shown in figure 1(c), and they exhibit a very strong modulation from the maximum to only about one-third of this value for our experimental incidence angle, with this modulation decreasing somewhat as the Cr layer becomes thicker, but the standing-wave phase remaining constant. This modulation thus permits selective probing of the interface by scanning the x-ray spot over the wedge-shaped bilayer. As noted above, the standing wave is also primarily a property of the multilayer, as verified by both experiment and calculation, and is negligibly influenced by the growth of the bilayer on top of it, as long as the photon energy is chosen well away from any core-level absorption resonances in the bilayer or multilayer constituents. In figure 1(c), we note that the maximum of the electric field intensity lies at the interface between Fe and Cr for beam position B ($d_{Cr} = 62$ Å) while the minimum of the field lies at the interface for position C ($d_{Cr} = 82$ Å). The 20 Å thickness difference between the two positions represents half of the period of the SWG of 40.5 Å.

We now turn to other spectroscopic measurements via the scanning of the standing wave through the interface, and in figure 2(a), we first show MCD data based on spin–orbit-split Fe $2p_{1/2,3/2}$ and Cr $2p_{1/2,3/2}$ photoelectron spectra, with $I_{MCD} = I_{RCP} - I_{LCP}$, and a minimal normalization correction of only a few per cent being needed to bring the left and right background points of I_{RCP} and I_{LCP} to equality. The x positions of the sample were here chosen to have the maximum (position B) and minimum (position C) of the standing wave centred on the interface. Both Fe and Cr show reproducible MCD signals, although that for Fe is much larger, by a factor of about five. The $2p_{1/2}$ and $2p_{3/2}$ MCD signals for both elements are also reversed in sign, being roughly mirror images of one another; this is a well known result for such ferromagnetic metals [27] and confirms the accuracy of our measurements. Note also that the signs of the two signals are reversed, with for example the Fe $2p_{3/2}$MCD going negative, then positive, as binding energy decreases, and the Cr MCD $2p_{3/2}$ MCD going positive, then negative. Because the MCD measurement has an external spin reference, via the polarization in the incoming x-ray beam, which is very close to parallel (anti-parallel) with the Fe layer magnetization direction for RCP(LCP) radiation, we can thus conclude that Cr shows weak ferromagnetism along the y-direction near the interface, but that the orientation of its magnetization is opposite to that of Fe, a result consistent with prior studies [12, 13]. From these measurements alone, we do not derive any information on other components of the magnetization in the two directions x and z perpendicular to the primary Fe magnetization direction, but with modification of the experimental geometry, scanning in both x and y, and the addition of magnetic linear dichroism (MLD) measurements [23, 28], it should be possible in future experiments to determine the x-, and perhaps also the z-magnetization.

Further confirmation of these MCD results is also found in analogous MCD data for Fe 3p and Cr 3p emission (not shown here) [23]. From both the 2p and 3p MCD data, it can also

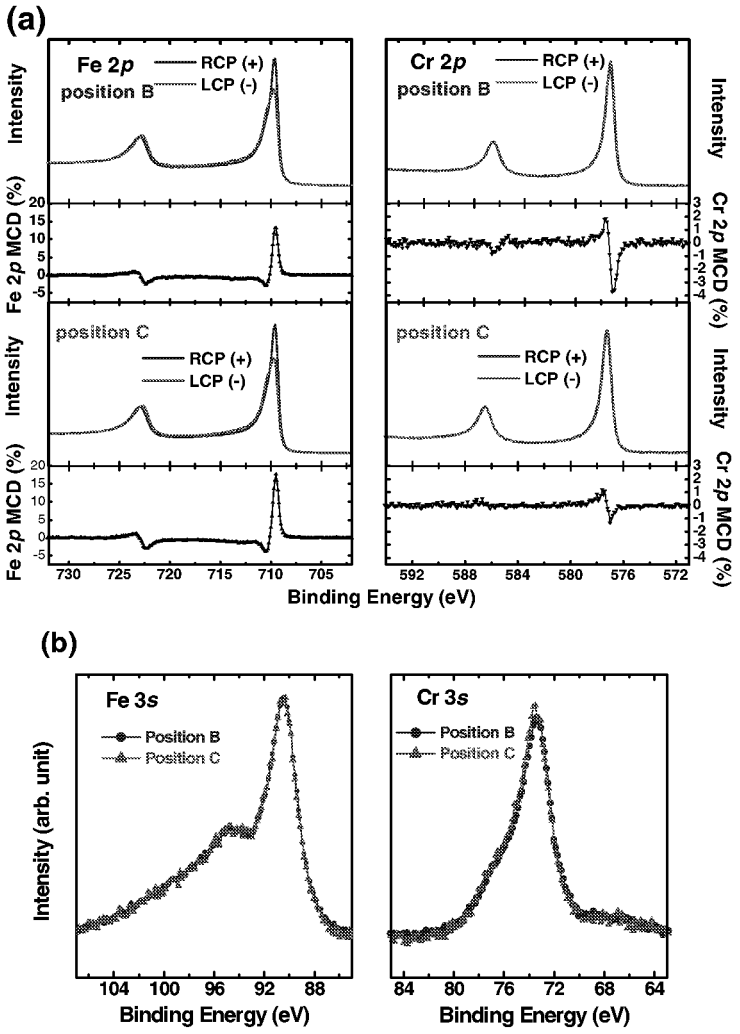

Figure 2. (a) 2p spectra for Fe and Cr for both RCP and LCP excitation, respectively, together with their difference curves (MCD) for the two special x-positions B and C. (b) 3s spectra for Fe and Cr at the same two x-positions. (c) Fe and Cr 2p and 3p MCD results as a function of d_{Cr} (or equivalently of the position of the standing wave with respect to the interface). The experimental data (lines and symbols) are compared with theoretical simulations for the best-fit set of parameters z and σ, as defined in part (d) (solid curves). Vertical black lines represent estimated errors in the MCD measurements. The other curves shown represent some choices at the outside of our estimated error range in determining these parameters. (d) Top panel: model for the variation of composition and y-component of net magnetic moment (magnetization) around the Fe–Cr interface. In the lower panels I and II, the electric field strengths (black solid curve) and distribution of the y-component of ferromagnetic order (blue solid curve: Fe, red solid curve: Cr) are shown as a function of depth from the surface. The single-hatched regions represent Fe (yellow) and Cr (blue) layers while the double-hatched indicate the intermixed region of Fe and Cr. In panels III and IV, the photoelectron intensities from depth z for Fe 2p (blue curves) and Cr 2p (red curves) are shown, and in panels V and VI, the contribution to MCD intensity from depth z due to the ferromagnetic distributions for Fe 2p (blue curves) and Cr 2p (red curves) is plotted. The Cr intensities are amplified for enhanced visibility (compare the left and right ordinates).

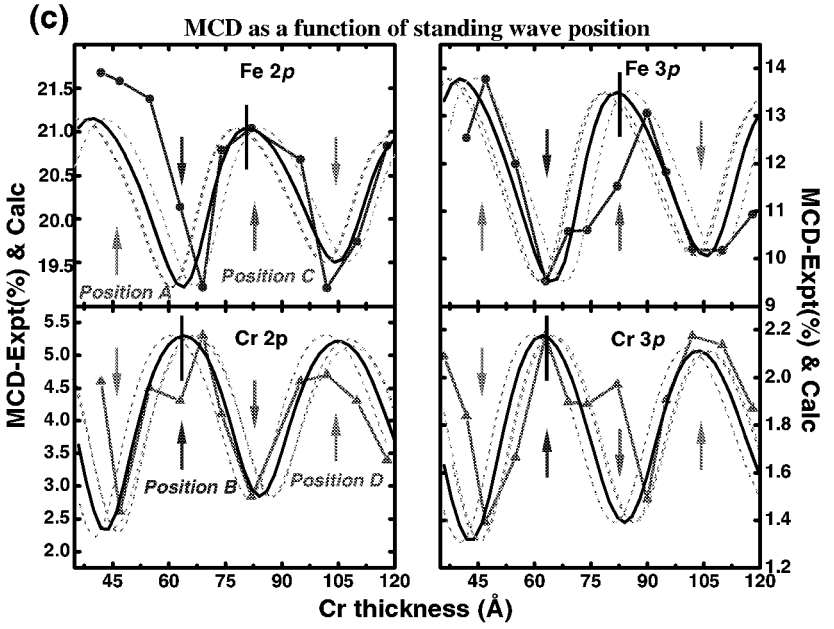

Figure 2. (Continued.)

be clearly seen that the Fe MCD strength in position B is considerably larger than that in position C, while the Cr MCD shows reverse behaviour. This indicates that any long-range (or even short-range) ferromagnetic order shows a strong dependence on depth near the interface, and that the alterations in the y-component magnetizations of Fe and Cr have very different z-dependence.

We now ask via another spectroscopic fingerprint whether these increases (for Cr) or decreases (for Fe) in the MCD signal in crossing from the Fe to the Cr side of the interface can be associated with a reduction in the local atomic spin moment, which is the dominant contributor to the overall magnetic moment on each atom. In figure 2(b), we show a set of Fe 3s and Cr 3s photoelectron spectra obtained with RCP excitation for the key sample x-positions B and C in figure 1(c). Such 3s spectra should not show MCD, as spin–orbit splitting is not present, but are known to provide a qualitative measure of the local atomic spin moment, with the doublet spacing being proportional to this moment and caused by the 3s core–valence exchange interaction [29]. It can be seen that the splitting ($\sim$4.5 eV for Fe and $\sim$3.5 eV for Cr) and overall shape of these two spectra are essentially identical, irrespective of position. Other spectra at much finer steps in position confirm this lack of sensitivity to position [23]. The fact that the curves at different positions do not show any systematic differences from one position to another thus immediately indicates that the local spin moments of both Fe and Cr are essentially unchanged on passing into the interface. In particular, the Fe spin moment does not decrease due to its intermixing with Cr, nor does the Cr moment increase due to its proximity to ferromagnetic Fe, although both of these effects have been suggested previously based on thin-film deposition experiments [12,13,19]. Finally, we note that this kind of core measurement has an implicit internal spin reference [30], and so provides no information on the exact orientation of these moments in the laboratory reference frame, but simply indicates that the *magnitude* of the spin moment does not change through the interface. Adding an *external* spin detector to the measurement in future studies would yield information on the moment orientation.

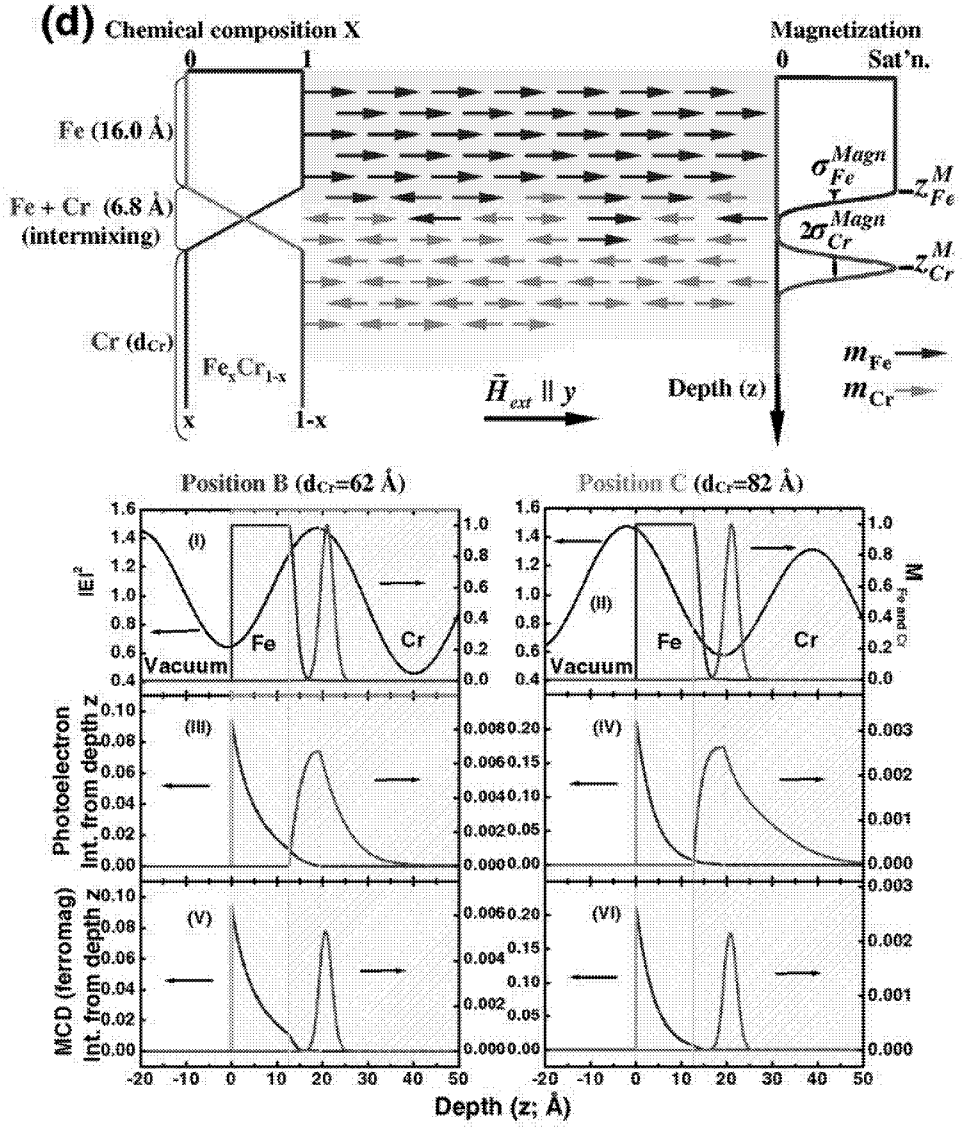

Figure 2. (Continued.)

Turning back to the externally-referenced MCD data, we show in figure 2(c) the experimental variation of the integrated MCD signals for Fe 2p and 3p and Cr 2p and 3p (with a sign change for Cr to permit comparison of relative magnitudes more clearly) as a function of Cr thickness (or equivalently the position of the standing wave relative to the interface). Within estimated experimental errors as shown by the black vertical lines in the figure, there is excellent agreement between the 2p and 3p MCD data for both elements. The positions A, B, C and D of the standing wave (cf figure 1(c)) are also indicated. It is clear from the experimental results that Fe and Cr exhibit very different behaviour across the interface, with Cr showing a maximum in its (negative) dichroism where Fe shows a minimum, and vice versa. Since we know from figure 2(b) that the local atomic spin moments do not change appreciably across

the interface, we can conclude thus far that Cr becomes slightly ferromagnetically ordered on approaching the interface (thus increasing its MCD signal), while the net iron magnetization as seen by MCD is reduced along the reference y direction. This reduction could be due to a random moment alignment, an antiferromagnetic alignment or the existence of a so-called 'spin-flop' transition across the interface in which the Fe moments are aligned along directions to which we are not in this experiment sensitive [31]. Any one of these effects would reduce the present Fe MCD signal.

As a final step in quantifying these results, we now use the measured variation of the Fe and Cr MCD signals with standing-wave position to estimate the positions and thicknesses of the regions over which the Fe shows reduced, and the Cr increased, magnetization. This analysis requires only predicting the *shapes* of the two dichroism curves as a function of depth, rather than their absolute magnitudes. The MCD strengths have been calculated by assuming Gaussian regions of decreased (increased) ferromagnetism for Fe(Cr) near the interface, with the position of the Gaussians (z_{Fe}^{Magn} and z_{Cr}^{Magn}, respectively) and their widths ($\sigma_{\mathrm{Fe}}^{Magn}$ and $\sigma_{\mathrm{Cr}}^{Magn}$, respectively) being adjustable parameters (cf the top panel of figure 2(d)). Thus, the magnetization of Fe is assumed to have some saturated value well away from the interface and to reduce to zero at least by the point at which its concentration goes to zero, and the Cr is assumed to have zero magnetization except for a Gaussian region somewhere near the interface. The previously measured compositional variation (cf discussion of figure 1(b)) at the interface is thus also included in the calculations. The composition of each constituent and the precise form of the standing wave as calculated via x-ray optics are used as combined weighting factors at each depth for calculating the dichroism signal. We have tried to fit our MCD data with a variety of magnetization configurations for both Fe and Cr, especially around the interface at the middle of which the composition of $Fe_{0.50}Cr_{0.50}$ occurs. The quality of these fits has been assessed both visually and by calculating a reliability factor (R-factor) as $R = \sum_j |I_{expt,j}^{MCD} - I_{calc,j}^{MCD}|^2 / \sum_j [I_{expt,j}^{MCD}]^2$. From this analysis, it is found out that our results cannot be reproduced unless the net y magnetization for both Fe and Cr at the 50:50 intermixing region is essentially zero. This is at least consistent with recent results from element-specific MCD in x-ray absorption for a series of Fe–Cr alloys [32], which indicate that neither Fe nor Cr shows any net magnetization in an $Fe_{0.50}Cr_{0.50}$ alloy. The final most self-consistent and reasonable analysis of both the ratio curves for Fe 3p and Cr 3p (cf figure 1(c)) and the MCD data of figure 2(c) leads to the values of $\sigma_{intermix} = 3.4$ Å, $z_{\mathrm{Fe}}^{Magn} = 12.5$ Å, $\sigma_{\mathrm{Fe}}^{Magn} = 2.8$ Å and $z_{\mathrm{Cr}}^{Magn} = 21.1$, $\sigma_{\mathrm{Cr}}^{Magn} = 2.0$ Å and to calculated final forms for the MCD curves as shown by the smooth curves in figure 2(c) (thick black solid curves). There is very good agreement between experiment and theory, if allowance is made for the estimated uncertainty in each MCD value quoted above.

In order to more quantitatively see how sensitive these fits are to these parameters, a few different choices are also illustrated in figure 2(c), in which either the z position or the σ value is changed from the best fit values: $z_{\mathrm{Fe}}^{Magn} = 16.5$ Å, $\sigma_{\mathrm{Fe}}^{Magn} = 2.8$ Å and $z_{\mathrm{Cr}}^{Magn} = 25.1$ Å, $\sigma_{\mathrm{Cr}}^{Magn} = 2.0$ Å (green lines); $z_{\mathrm{Fe}}^{Magn} = 8.5$ Å, $\sigma_{\mathrm{Fe}}^{Magn} = 2.8$ Å and $z_{\mathrm{Cr}}^{Magn} = 17.1$ Å, $\sigma_{\mathrm{Cr}}^{Magn} = 2.0$ Å (pink lines); and $z_{\mathrm{Fe}}^{Magn} = 12.5$ Å, $\sigma_{\mathrm{Fe}}^{Magn} = 7.6$ Å and $z_{\mathrm{Cr}}^{Magn} = 21.1$ Å, $\sigma_{\mathrm{Cr}}^{Magn} = 5.8$ Å (orange lines). These fits show good sensitivity to intermixing width and the forms of the ferromagnetic ordered regions, finally indicating that photoemission spectroscopy via soft x-ray standing-wave excitation can probe buried interfaces with high resolutions in z of the order of ~2–3 Å (about one atomic layer) and in σ of ~4–5 Å (about two atomic layers).

Our final conclusions concerning the variations of both the concentration and magnetization as projected along the x-direction near this Fe–Cr interface are thus as summarized in figure 2(d), where we show not only composition and magnetization, but also

the calculated field strengths and depth-resolved contributions to intensity and MCD for the two key positions B and C. Our results are in agreement with prior work in that MCD effects are reduced in Fe–Cr alloys [32] and that the Cr layers nearest to Fe show some ferromagnetic alignment, but in an antiferromagnetic sense with respect to Fe [12,13]. However, we can also rule out certain other models and conclusions such as a significant change of the local magnetic moments on either Fe or Cr on passing through the interface. Instead spin-flops or frustrated exchange interactions leading to out-of-plane orientations might explain our results because the MCD measurements pick up the majority of magnetic moments aligned with photon helicity orientation only. It is also remarkable from our analysis that the regions over which Fe or Cr show altered magnetic behaviour along the x-direction are only about two atomic layers in thickness. Although the picture of this interface that emerges is simple in some respects and complex in others, we believe that future modelling of it must take account of these effects. The standing-wave-plus-wedge approach has permitted us to delve into its characteristics in a much more quantitative way.

We have thus demonstrated that the use of synthetic multilayers as generators of strong soft x-ray standing waves and as substrates on which various types of nanostructure can be grown represents a promising method for studying buried interfaces. We have used photoelectrons as the emitted particles, with total intensities, MCD and exchange-split core binding energies providing depth-resolved information with a resolution in the few ångstrom range for composition, net magnetization, and local spin moment at the Fe–Cr interface, respectively. In the future, other experimental geometries, linear dichroism and external spin detection should provide additional dimensions of magnetic sensitivity. Future work could also involve chemical shifts in core binding energies (e.g. in tunnel-junctions [4]), valence-band photoemission spectra (thus probing the bonding electrons and densities of states directly), as well as the emission of soft x-ray photons of greater depth penetration and additional symmetry selectivity via dipole selection rules. Due to the greater penetration depths, looking at soft x-ray emission would have the additonal advantage over photoelectron emission of yielding depth-resolved intensity profiles corresponding to those in panels III and IV of figure 2(d) that would much more closely follow the field strengths shown in black in panels I and II, and thus provide even greater buried interface sensitivity. This technique is particularly simple in interpretation when the nanostructure can be grown in (or on top of) a wedge-shaped geometry, thus permitting a fixed standing wave to be scanned through the interface simply by moving a focused x-ray beam along the wedge. Although the multilayer must have a high x-ray optical contrast to set up a strong standing wave (as e.g. the B_4C/W system studied here), various other combinations of materials should be possible[6]. Growing the multilayer *in situ* under better controlled conditions (rather than *ex situ* with subsequent transfer in air as in our experiments) should also permit achievement of better epitaxy and/or structural control in the final structure to be studied. The structure to be studied also does not have to be layered, but might consist of nanoscale 'wires' or 'dots', in which case the top, side and bottom interfaces of these features could be selectively studied. Combining a multilayer + wedge sample geometry with a spectromicroscope [9] should also lead to enhanced depth resolution with this type of experiment. One limitation of the method is that higher-temperature preparation or annealing of the multilayer plus sample will be limited, as going to a sufficiently high temperature will lead to interdiffusion in the multilayer, with resulting loss of reflection efficiency and standing-wave strength. Nonetheless, various possible future applications of this approach to the study of buried interfaces in nanostructures seem possible.

[6] Center for X-Ray Optics, Lawrence Berkeley National Laboratory, summary of multilayer data for various systems at http://www-cxro.lbl.gov/cgi-bin/mldata.pl.

We are indebted to E Gullikson, U Heinzmann and G Rossi for helpful discussions. Also we thank A Rosenhahn for STM measurements and C Y Song, C Kisielowski and U Dahmen for HRTEM experiments at NCEM, LBNL. This work was supported by the US Department of Energy, Office of Science, Office of Basic Energy Sciences, Materials Sciences Division, under contract no DE-AC03-76SF00098. SHY thanks the Korea Science and Engineering Foundation (KOSEF) for additional support.

References

[1] Baibich M N, Broto J M, Fert A, Nguyen van Dau F, Petroff F, Etienne P, Creuzet G, Friederich A and Chazelas J 1988 *Phys. Rev. Lett.* **61** 2472
Binasch G, Grünberg P, Saurenbach F and Zinn W 1989 *Phys. Rev.* B **39** 4828
Barthelemy A, Fert A, Baibich M N, Hadjoudj S, Petroff F, Etienne P, Cabanel R, Lwquien S, Nguyen Van Dau F and Creuzet G 1990 *J. Appl. Phys.* **67** 5908
Dieny B, Speriosu V S, Parkin S S P, Gurney B A, Wilhoit D R and Mauri D 1991 *Phys. Rev.* B **43** 1297
Parkin S S P 1993 *Phys. Rev. Lett.* **71** 1641

[2] See overviews in
Parkin S S P 1995 *Annu. Rev. Mater. Sci.* **25** 357
Vouille C, Barthelemy A, Mpondo F E, Fert A, Schroeder P A, Hsu S Y, Reilly A and Loloee R 1999 *Phys. Rev.* B **60** 6710

[3] See overviews in
Nogués J and Schuller I K 1999 *J. Magn. Magn. Mater.* **192** 203
Berkowitz A E and Takano K 1999 *J. Magn. Magn. Mater.* **200** 552

[4] Moodera J S, Kinder L R, Wong T M and Meservey R 1995 *Phys. Rev. Lett.* **74** 3273 and references therein
Prinz G A 1998 *Science* **27** 1660
Parkin *et al* S S P 1999 *J. Appl. Phys.* **85** 5828

[5] Batson P E 1999 *Ultramicroscopy* **78** 33
Muller D A, Sorsch T, Moccio S, Baumann F H, Evans-Lutterodt K and Timp G 1999 *Nature* **399** 758

[6] Sève L, Jaouen N, Tonnerre J M, Raoux D, Bartolomé F, Arend M, Felsch W, Rogalev A, Goulon J and Gautier C 1999 *Phys. Rev.* B **60** 9662

[7] Schad R, Beliën P, Verbanck G, Potter C D, Fischer H, Lefebvre S, Bessiere M, Moshchalkov V V and Bruynseraede Y 1998 *Phys. Rev.* B **57** 13 692
Schmidt C M, Bürgler D E, Schaller D M, Meisinger F, Güntherodt H-J and Temst K 2001 *J. Appl. Phys.* **89** 181

[8] MacKay J F, Teichert C, Savage D E and Lagally M G 1996 *Phys. Rev. Lett.* **77** 3925
Freeland J W, Chakarian V, Bussmann K, Idzerda Y, Wende H and Kao C C 1998 *J. Appl. Phys.* **83** 6290
Freeland J W, Bussmann K, Idzerda Y U and Kao C-C 1999 *Phys. Rev. Lett.* **60** 9923

[9] Ohldag H, Scholl A, Nolting F, Anders S, Hillebrecht F U and Stöhr J 2001 *Phys. Rev. Lett.* **86** 2878

[10] Yang S-H, Mun B S, Kay A W, Kim S-K, Kortright J B, Underwood J H, Hussain Z and Fadley C S 2000 *Surf. Sci. Lett.* **461** L557

[11] Kim S-K and Kortright J B 2001 *Phys. Rev. Lett.* **86** 1347–50

[12] Xu Zhongde, Liu Y, Johnson P D and Itchkawitz B S 1995 *Phys. Rev.* B **52** 15 393

[13] Panaccione G, Sirotti F, Narducci E and Rossi G 1997 *Phys. Rev.* B **55** 389
Rossi G, Panaccione G, Sirotti F, Lizzit S, Baraldi A and Paolucci G 1997 *Phys. Rev.* B **55** 11 488

[14] Davies A, Stroscio J A, Pierce D T and Celotta R J 1996 *Phys. Rev. Lett.* **76** 4175

[15] Schmid C M, Burgler D E, Schaller D M, Meisinger F, Guntherodt H J and Temst K 2001 *J. Appl. Phys.* **89** 181 and references therein

[16] Vega A, Demangeat C, Dreyssé H and Chouairi A 1995 *Phys. Rev.* B **51** 11 546
Freyss M, Stoeffler D and Dreyssé H 1997 *Phys. Rev.* B **56** 6047

[17] Turtur C and Bayreuther G 1994 *Phys. Rev. Lett.* **72** 1557

[18] Polak M, Fadley C S and Rubinovich L *Phys. Rev.* B at press

[19] Hillebrecht F U, Roth Ch, Jungblut R, Kisker E and Bringer A 1992 *Europhys. Lett.* **19** 711
Idzerda Y U, Tjeng L H, Lin H-J, Gutierrez C J, Meigs G and Chen C T 1993 *Phys. Rev.* B **48** 4144

[20] Fadley C S, Van Hove M A, Hussain Z and Kaduwela A P 1995 *J. Electron Spectrosc. Relat. Phenom.* **75** 273

[21] Young A T, Martynov V and Padmore H A 1999 *J. Electron Spectrosc. Relat. Phenom.* **101–103** 885

[22] Henke B L, Gullikson E M and Davis J C 1993 *At. Data Nucl. Data Tables* **55** 34

[23] Mun B S 2001 *PhD Thesis* University of California, Davis
Yang *et al* unpublished results

[24] Windt D L 1998 *Comput. Phys.* **12** 360
[25] Yeh Y Y and Lindau I 1985 *At. Data Nucl. Data Tables* **32** 1
[26] Powell C J, Jablonski A, Tanuma S and Penn D R 1994 *J. Electron Spectrosc. Relat. Phenom.* **68** 605
[27] Baumgarten L, Schneider C M, Petersen H, Schäfers F and Kirschner K 1990 *Phys. Rev. Lett.* **23** 492
Menchero J G 1997 *Phys. Rev.* B **55** 5505
[28] Menchero J G 1998 *Phys. Rev.* B **57** 993
Rossi G, Sirotti F, Cherepkov N A, Combet Farnoux F and Panaccione G 1994 *Solid State Commun.* **90** 557
[29] Fadley C S and Shirley D A 1970 *Phys. Rev.* A **2** 1109
Bagus P S, Freeman A J and Sasaki F 1973 *Phys. Rev. Lett.* **30** 850
Klebanoff L E and Shirley D A 1986 *Phys. Rev.* B **33** 5301
Johnson P D 1997 *Rep. Prog. Phys.* **60** 1217
[30] Sinkovic B, Friedman D J and Fadley C S 1991 *J. Magn. Magn. Mater.* **92** 301
[31] Koon N C 1997 *Phys. Rev. Lett.* **78** 4865
[32] Kortright J B, Kim Sang-Kook and Ohldag H 2000 *Phys. Rev.* B **61** 64